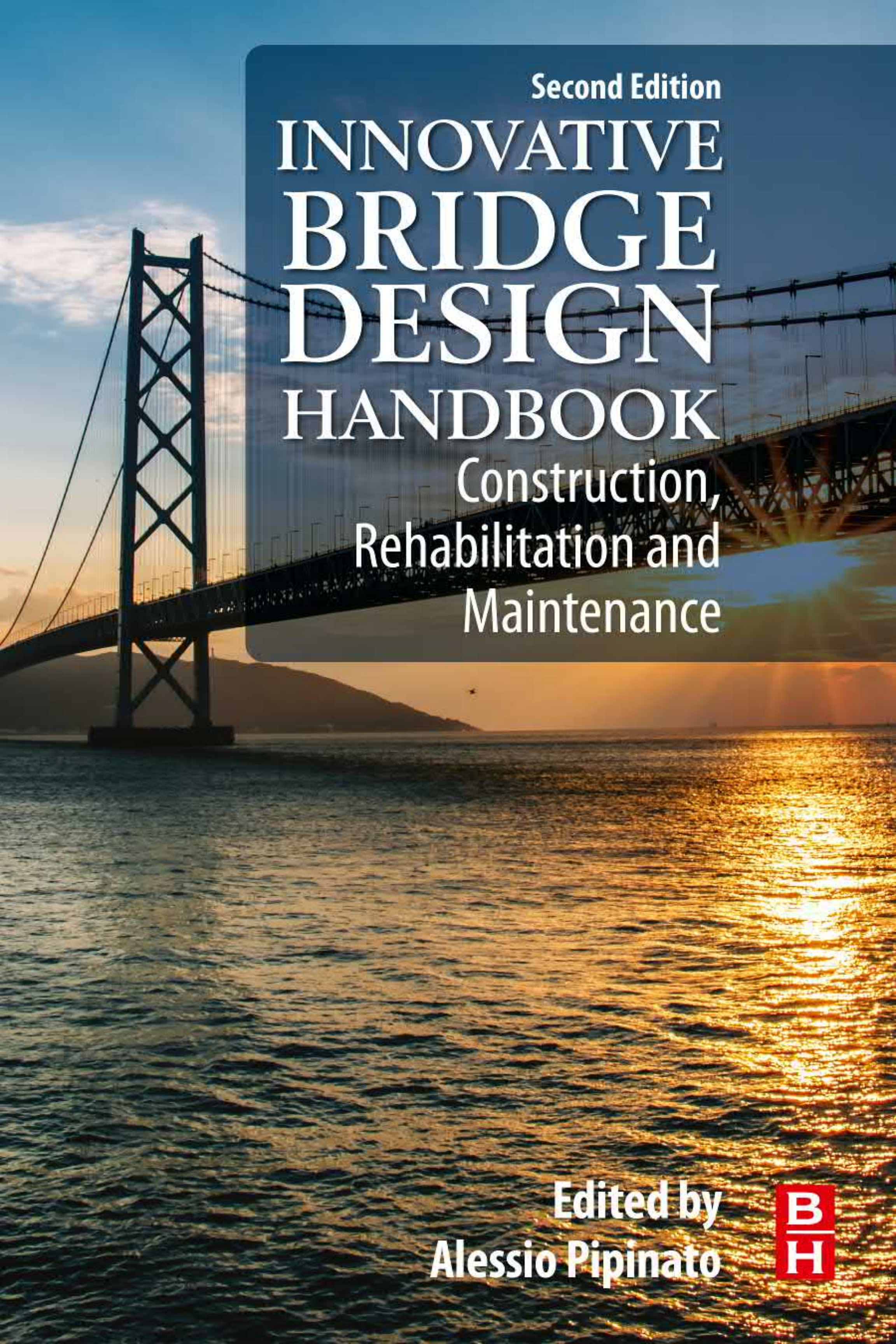

Second Edition

INNOVATIVE BRIDGE DESIGN HANDBOOK

Construction, Rehabilitation and Maintenance

Edited by
Alessio Pipinato

B H

Innovative Bridge Design Handbook

This page intentionally left blank

Innovative Bridge Design Handbook

Construction, Rehabilitation and Maintenance

Second Edition

Edited by

Alessio Pipinato

ELSEVIER

Butterworth-Heinemann
An imprint of Elsevier

Butterworth-Heinemann is an imprint of Elsevier
The Boulevard, Langford Lane, Kidlington, Oxford OX5 1GB, United Kingdom
50 Hampshire Street, 5th Floor, Cambridge, MA 02139, United States

Library of Congress Cataloging-in-Publication Data
A catalog record for this book is available from the Library of Congress

British Library Cataloguing-in-Publication Data
A catalogue record for this book is available from the British Library

ISBN: 978-0-12-823550-8

For information on all Butterworth-Heinemann publications
visit our website at https://www.elsevier.com/books-and-journals

Publisher: Matthew Deans
Acquisitions Editor: Carrie Bolger
Editorial Project Manager: Rachel Pomery
Production Project Manager: Poulouse Joseph
Cover Designer: Victoria Pearson

Typeset by SPi Global, India

Dedication

To Laura, Francesca, Annamaria, and Francesco

This page intentionally left blank

Contents

This page intentionally left blank

Authors' biographies

A. Pipinato
AP&P, Rovigo, Italy
Alessio Pipinato obtained a bachelor's degree in building and structural engineering from the University of Padua and a bachelor's degree in architecture from the University of Venice-IUAV. He earned his PhD in structural design at the University of Trento. He served as an adjunct professor, teaching university courses in bridge engineering and structural design, and has been a research collaborator at the University of Padua in the structural engineering sector (ICAR09-08B3) for more than 10 years. His 18-years engineering career encompasses founding his own engineering consulting firm, AP&P—serving as the CEO, scientific, and technical director—and providing bridge, structural engineering, and research and development (R&D) services, including international research projects in collaboration with numerous universities worldwide and financed by the EU Commission. He is or has been a member of the American Society of Civil Engineers (ASCE), Structural Engineering Institute (SEI), International Association for Bridge and Structural Engineering (IABSE), Collegio Tecnici dell'Acciaio (CTA), International Association for Life Cycle Civil Engineering (IALCCE), International Association for Bridge Maintenance and Safety (IABMAS), Collegio Ingegneri Ferroviari Italiani (CIFI), European Convention for Constructional Steelwork (ECCS), and American Institute of Architects (AIA). He is also the author of more than 260 scientific and technical papers on structures and bridges, the chair of international conference sessions (including IABMAS 2010, Philadelphia, and IABMAS 2012, Milan). In addition, he is peer revisor of many international structural engineering journals, including the *ASCE Journal of Bridge Engineering, Engineering Structures*, *Structure and Infrastructure Engineering*, *International Journal of Fatigue*, and *Journal of Structural Engineering*. He has participated in a number of international research projects. His research interests include the design, analysis, and assessment of bridges; structural analysis and design; fatigue and fracture of steel bridges; reliability analysis; life cycle assessment; design of innovative structure and application of new materials in structures; construction control design; and fast bridge construction. He has won many international and national awards during his professional and academic career, and he served as a volunteer in the evaluation of structures during seismic emergencies for the National Service of the Civil Protection (L'Aquila 2009, Emilia Romagna 2012).

S.E. Abdel Raheem

Faculty of Engineering, Assiut University, Assiut, Egypt

Shehata E. Abdel Raheem was named Professor of Earthquake, Bridge, Structural and Geotechnical Engineering in 2014, Civil Engineering, Assiut University, Egypt. He earned a Dr.-Eng. in 2003. He was named a JSPS fellow in 2006 at Hokkaido University, Japan and an Alexander von Humboldt Fellow in 2005 at Kassel University, Germany. Professor Abdel Raheem has made a significant contribution to nonlinear dynamic analysis of long-span bridges under earthquake excitation, vibration control, seismic performance design, seismic pounding, dynamic of offshore structure, soil structure interaction, damage detection, and structural health monitoring. He was a member of the JSCE, he had worked as professor and an engineering counselor at the general project management and College of Engineering, Taibah University, Madinah, Saudi Arabia. In accordance with his scientific achievements, He has reviewed more than 950 papers and research proposals for more than 100 international journals and funding foundations. He has supervised several PhD and MSc students in the field of earthquake and structural engineering. He has been invited to be an external examiner for several internal and domestic MSc and PhD degrees and participated in several international and national conferences. He has been the recipient of several engineering awards such as the Award of Excellence of First-Class Medal from the Presidency of the Egyptian Republic (2018), Encouragement State Award in Engineering Science (2008 and 2014), Publons Peer Review Awards (2018 and 2019), *ASCE Journal of Bridge Engineering* Outstanding Reviewer Award (2018 and 2019), *Elsevier Engineering Structures* Certificate of Excellence in Reviewing (2013), the Prof. Ahmed Moharram Prize Award in Structural Engineering and Its Practical Applications (2009), and Assiut University Encouragement Prize in Engineering Science (2009). He has coauthored three book and book chapters and has published more than 60 journal papers in the field of earthquake, structural, and geotechnical engineering. Prof. Abdel Raheem is the PI for several international and national research projects. He has been an associate editor of *Innovative Infrastructure Solutions*, the editorial manager of JESAUN, and an editorial board member of a number of international journals.

S. Adriaenssens

Princeton University, Princeton, NJ, United States

Sigrid Adriaenssens is a structural engineer and assistant professor at the Department of Civil and Environmental Engineering at Princeton University in Princeton, New Jersey, where she directs the Form Finding Lab. She has a PhD in lightweight structures from the University of Bath (United Kingdom). She worked as a project engineer for Jane Wernick Associates (London), and Ney+Partners (Brussels), where she was responsible for a series of award-winning bridge projects. Her current research interests include numerical form-finding techniques and lightweight structures. She has coauthored two books, *Shaping Forces: Laurent Ney* (2010) and *Shell Structures for Architecture: Form Finding and Optimization* (2014), and has published over 30 journal papers. She is the recipient of the Alfred Rheinstein '11 Award 2015.

A.K. Agrawal

City College of New York University, New York, NY, United States

Anil Kumar Agrawal is professor of Structural Engineering at the City College University of New York. He is currently involved in structural control systems research, such as passive dampers, tuned mass dampers, active/hybrid and semiactive control systems, have been widely accepted as effective means for protection of civil engineering structures against earthquakes and wind loads. He is also Editor of the *Journal of Bridge Engineering*, the most world-renowned international scientific journal on bridge engineering, edited by ASCE. He is ASCE and IABSE member. He is involved in international technical committee, as ASCE Committee on Engineering Mechanics Member, ASCE Committee on Structural Control Member, ASCE Sub-Committee on Performance of Structures.

M. Amjadian

City College of New York University, New York, NY, United States

Mohsen Amjadian is a research assistant with Department of Civil and Environmental Engineering at the City College of the City University of New York, United States. He received his BSc in Civil Engineering from Razi University in 2006, MSc in Earthquake Engineering from International Institute of Earthquake Engineering and Seismology (IIEES) in 2010, both in Iran. He worked as a professional engineer in construction and consulting companies in Iran from 2010 to 2013. His research interests are Nonlinear Analysis of Structural Systems, Structural Control and Health Monitoring, Structural Risk, Reliability and Safety, Performance-Based Seismic Design, Soil-Structure Interaction, and Seismic Pounding.

H. De Backer

Ghent University, Ghent, Belgium

Hans De Backer, born in 1978, received his civil engineering degree from Ghent University in 2002 and obtained his doctorate in the fatigue behavior of orthotropic steel decks in 2006. He is currently an associate professor in the Department of Civil Engineering of Ghent University and heads the Bridge Research Group. His research focuses on fatigue effects, orthotropic steel decks, tubular structures, and nondestructive in situ testing of bridge construction.

G.L. Balázs

Budapest University of Technology and Economics, Budapest, Hungary

György L. Balázs is a professor at the Budapest University of Technology and Economics in Hungary. His main fields of activity are concrete, reinforced concrete, and prestressed concrete structures; fiber-reinforced concrete (FRC); fiber-reinforced polymers (FRPs) as internally bonded reinforcements; externally bonded reinforcements or near surface mounted reinforcements; durability; service life; fire behavior and design; bond and cracking; high-performance concrete (HPC); and sustainability. He serves as chairman of the Fédération de l'Industrie du Béton (*fib*) Commission on Dissemination of Knowledge, including *fib* courses and *fib* Textbook on Advanced design of concrete structures. He has been a member of the *fib* Presidium since 2002 and was elected president of the organization in 2011 and 2012. He served as the immediate past president of *fib* for 2013 and 2014 and has continued thereafter as honorary president.

R.K. Bharil

Biggs Cardosa Associates, San Jose, CA, United States

Rajneesh (Raj) K. Bharil is a licensed professional civil and structural engineer, certified project management professional (PMP), and an associate with Biggs Cardosa Associates, Orange, California. He obtained his doctorate in structural engineering from the West Virginia University, Morgantown, master's degree in structural engineering from the University of Michigan, Ann Arbor, and bachelor's degree in civil engineering from M. A. National Institute of Technology, India. His 30-year professional engineering career encompasses the cofounding of his bridge specialty consulting firms, serving in key leadership positions with various private consulting firms and public agencies, and performing designs and research in the fields of bridges and structural composites. He is a member of the American Society of Civil Engineers (ASCE), recipient of the AASHTO Value Engineering Award, author of numerous technical papers on bridges and composites, and lead engineer of several major bridge projects in the western United States.

B. Bhattacharya

Indian Institute of Technology Kharagpur, Kharagpur, India

Baidurya Bhattacharya obtained his BTech in civil engineering from the Indian Institute of Technology (IIT) Kharagpur in 1991 and his MS (1994) and PhD (1997) in civil engineering from Johns Hopkins University, Baltimore, Maryland. After continuing as a postdoc at Johns Hopkins, Bhattacharya worked as an R&D engineer at the American Bureau of Shipping in Houston, Texas, for 2 years and as assistant professor at the University of Delaware for 4 years before returning to his alma mater at Kharagpur in 2006. He was promoted to associate professor in 2007, to professor in 2011 and to professor HAG in 2018. Bhattacharya has been a member of the visiting faculty at Stanford (2005) and Johns Hopkins (2012).

Bhattacharya works in probabilistic mechanics and explores how random atomic scale structural defects and fluctuations affect material properties at the microscale and how that randomness, coupled with uncertainties in the environment, affects the performance and safety of structural components and systems. He works on probability-based design and reliability analyses of civil infrastructure systems in structures such as nuclear power plants; ships; and offshore structures, buildings, and bridges. He was an associate editor of the *ASCE Journal of Bridge Engineering* from 2010 to 2018. He has held the position of chairman of civil construction and maintenance and the dean of international relations at IIT Kharagpur. He was elected fellow of the Indian National Academy of Engineering in 2016 and a fellow of the American Society of Civil Engineers in 2018.

A. Boegle

HafenCity Universität Hamburg, Hamburg, Germany

Annette Boegle is full professor for design & analysis of structures at the HafenCity University of Hamburg, Germany. She studied structural and civil engineering at the University of Stuttgart, where she also received her PhD (Dr.-Ing.). She works and teach in the fields of: construction history, conceptual design, design methods in engineering, parametric design, biomimetic structures, analysis of lightweight structures.

Actually she is initiator of an Erasmus+ Strategic Partnership around the Baltic Sea Region on "Intersections in Build Environment." She also has been curator of several exhibitions, e.g., "Leicht Weit–Light Structures" at the DAM Frankfurt, Germany. As a member of several scientific boards she is active participating in the scientific community, e.g., she is member of the scientific board of the "Bautechnik" (*Journal for Civil and Structural Engineering*), Vice Chair of the IABSE working Commission WC5 "Design Methods and Processes," and Vice Chair of the "IngenieurBaukunst e.V." (Association of Structural Art).

E. Brühwiler
EPFL—Swiss Federal Institute of Technology, Lausanne, Switzerland
Eugen Brühwiler has been a professor of structural engineering at EPFL since 1995. His teaching and research activities include modern methods of fatigue and safety assessment of existing bridges using data from monitoring as well as the use of UHPFRC (ultra-high-performance fiber-reinforced cement-based composites) for the rehabilitation and strengthening of bridges. As a consulting engineer, he is involved in numerous UHPFRC projects, mostly related to bridges, including the design and construction of new bridges in UHPFRC, in Switzerland, and abroad. He is also consultant for the Swiss cultural heritage authorities for the restoration, strengthening, and modification of bridges and other highly regarded structures.

Eugen Brühwiler's activities as a professor of structural engineering are motivated by the following principle: Methods for the examination of existing structures ("examineering") must be developed with the ultimate goal to limit construction intervention to a strict minimum. If interventions are necessary, their objective is to improve the structure. In general, ultra-high-performance materials provide smart solutions.

E. Caetano
University of Porto, Porto, Portugal
Elsa Caetano received a civil engineering degree from the Faculty of Engineering of the University of Porto (FEUP) in 1988, a PhD in 2001, and a habilitation in 2011. In 1989, she joined FEUP, where she is presently an associate professor. She was involved in the creation and development of the Laboratory of Vibrations and Monitoring of FEUP. In the context of this laboratory's research and consultancy activities, she has conducted studies of several bridges and special structures. Some relevant projects include the dynamic tests of the Vasco da Gama, Millau (in collaboration with CSTB), and Humber (collaboration with University of Sheffield, United Kingdom) bridges; the dynamic design studies for the new stadium of Braga's cable roof for the Euro 2004 Football Championship; the vibration assessment, design, and instrumentation of TMDs at the new Coimbra footbridge; and the measurement of cable forces at the London 2012 Olympic Stadium roof.

N. Chouw
University of Auckland, Auckland, New Zealand
Dr. Nawawi Chouw is associate professor and director of the University of Auckland Centre for Earthquake Engineering Research. Prior to joining the University of Auckland, he worked at universities in Europe, Japan, and Australia. He earned his diploma

in civil engineering from Ruhr University-Bochum, Germany. After working in a group of consulting engineers in Germany, he returned to the Research Centre for Structural Dynamics at the Ruhr University-Bochum, and in 1993, he was awarded his doctorate. He has been awarded the Gledden Fellowship of the University of Western Australia twice, the Fritz-Peter-Mueller Prize of the Technical University of Karlsruhe, Germany, the Best Research Award of Chugoku Denryoku Research Foundation, Japan, and twice received recognition for excellence in research supervision from the China Scholarship Council. He has been invited to teach at several universities and is an editorial board member of a number of international journals.

M. Dicleli

Middle East Technical University at Ankara, Ankara, Turkey

Murat Dicleli is currently a professor and department head at the Department of Engineering Sciences, Middle East Technical University (METU). Dr. Dicleli received his PhD in structural engineering from the University of Ottawa, Canada, in 1993, and his MSc and BSc degrees from the Civil Engineering Department of METU in 1987 and 1989, respectively. Dr. Dicleli's academic experience include employment both in Illinois, at Bradley University, and in Ankara, Turkey, at METU. His research interests include seismic behavior and retrofitting of buildings and bridges, passive control systems, behavior of integral bridges under thermal and gravity loading, and behavior of steel and reinforced concrete structures under monotonic and cyclic loads. He has considerable industrial experience. He has worked as a structural and head design engineer at MNG Inc. in Ankara, Turkey, as the director of the design and planning division at MITAŞ in Ankara, Turkey, as a structural design consultant at Morrison Hershfield Ltd., in Toronto, Canada, and as senior design engineer and project manager at the Ontario Ministry of Transportation, Toronto-St. Catharines, Canada. He has been involved in the design and rehabilitation of residential and commercial buildings, industrial structures, grain storage silos, power transmission lines, and communication structures, as well as highway and railway bridges. Dr. Dicleli is also the inventor and patent holder of a recently developed torsional hysteretic damper. He serves as an associate editor for the *ASCE Journal of Bridge Engineering* and is an editorial board member of *Earthquake and Structures, American Journal of Civil Engineering, Journal of Civil Engineering and Architecture, ISRN Civil Engineering, International Journal of Engineering and Applied Sciences,* and *The Open Construction & Building Technology Journal.* He is the author of more than 250 technical publications and is also the recipient of the 2006 outstanding paper award from the Earthquake Engineering Research Institute (EERI) and 2012 thesis of the year award from the M. Parlar Foundation of METU.

G. Farkas

Budapest University of Technology and Economics, Budapest, Hungary

G. Farkas graduated in 1971 from the Faculty of Civil Engineering at the Budapest University of Technology and Economics (BME), he earned his Dr. Tech. in 1976, his PhD in 1994, and his Dr. Habil. in 1999 at the BME. Since 1971, he has worked at the Faculty of Civil Engineering of BME. Now a professor emeritus, he also was head of the Department of Structural Engineering from 1995 to 2010, and dean of the

Faculty of Civil Engineering between 1997 and 2005. In addition, he is a member of the Hungarian group of Fédération de l'Industrie du Béton (*fib*) and a member of the Hungarian Academy of Engineers. He is the author of more than 200 publications in the field of reinforced concrete structures.

P.R.A. Fidler
Department of Engineering, University of Cambridge, Cambridge, United Kingdom
Paul Fidler is a computer associate working with the Laing O'Rourke Centre for Construction Engineering & Technology and the Centre for Smart Infrastructure and Construction (CSIC) within the Department of Engineering at the University of Cambridge. He joined the Department of Engineering in 1995. He initially worked with Professor Campbell Middleton on developing software for yield-line analysis of concrete slab bridges. In 2007, he began working with wireless sensor networks, initially on an EPSRC funded project: *Smart Infrastructure—Wireless Sensor Networks for Condition Monitoring and Appraisal*. This project studied potential benefits and challenges of using wireless sensor networks (WSNs) to monitor key aspects of civil infrastructure, including bridges, tunnels, and water pipes. He was part of a team awarded the Telford Gold Medal (2010) from the Institution of Civil Engineers for this work. Later, this research continued with a trial deployment of a WSN on a bridge in Wuxi, China, in 2010 and then with further sensor deployments for the Cambridge Centre for Smart Infrastructure and Construction, an Innovation and Knowledge Centre (IKC) funded by EPSRC and Innovate UK. He is a coauthor of the books *Bridge Monitoring: A Practical Guide* and *Wireless Sensor Networks for Civil Infrastructure Monitoring: A Best Practice Guide*, both published by ICE Publishing. His current research involves the use of fiber-optic sensors and other novel instrumentation as part of a Centre for Digital Built Britain (CDBB) project researching the use of digital twins for the management of railway bridges.

A.J. Gastineau
KPFF Consulting Engineers, Seattle, WA, United States
Andrew J. Gastineau is a licensed professional civil engineer and is currently a project engineer at KPFF Consulting Engineers in Seattle, Washington, where he designs waterfront and bridge structures. He earned his BA in mathematics and physics in 2007 from St. Olaf College in Northfield, Minnesota, and subsequently his MS and PhD in civil engineering from the University of Minnesota in Minneapolis in 2013. He has been published in the *Journal of Bridge Engineering* and the *Journal of Engineering Mechanics* and has written a variety of conference publications and technical reports relating to the response modification and service life extension of existing bridge structures. He also has written about bridge health monitoring.

G. Hegemier
University of California at San Diego, La Jolla, CA, United States
After witnessing the devastation caused by the 1971 San Fernando Valley earthquake and the 1972 Nicaragua earthquake, Gilbert Hegemier, then an aerospace engineer, decided to focus his research on developing systems to retrofit bridges, roadways, and buildings. He helped assemble a team of experts at the University

of California, San Diego (UCSD). He and his colleagues have succeeded in creating and testing full-scale models of bridge column retrofit systems, which have been applied by the California Department of Transportation. These systems stood the ultimate test in the 1994 earthquake that hit Los Angeles, when 114 retrofitted bridges received only minor damage from the quake while several bridges scheduled for retrofit failed. Today, he is working with industry partners to develop and use lightweight fiber-reinforced composites (FRCs) to prevent earthquake damage and restore components of the nation's aging infrastructure. He is also working on blast mitigation techniques using FRCs to protect critical structures such as embassies from terrorist attacks.

K. Humpf
Leonhardt, Andrä, und Partner, Stuttgart, Germany
Karl Humpf graduated as Dipl.-Ing. Structural Engineering from the University of Aachen, Germany, in 1975. He started his career as a project engineer for Ibering S.A. in Spain. In 1976, he went to Leonhardt, Andrä, und Partner, and he was appointed as director of international projects in 1993. He has extensive experience in bridge engineering from numerous bridge projects, including some of the firm's largest cable-stayed, concrete, and composite bridges worldwide, particularly in Spain and Latin America. He is a registered Professional Engineer (PE) in Germany and in the U.S. states of Arizona, Georgia, Kentucky, and Massachusetts; he is also a member of the International Association of Bridge and Structural Engineers (IABSE) and the American Society of Civil Engineers (ASCE). He is the author or coauthor of numerous publications on long-span bridge problems in various German and international technical journals.

F. Huseynov
Laing O'Rourke Centre for Construction Engineering and Technology and the Cambridge Centre for Smart Infrastructure and Construction, University of Cambridge, Cambridge, United Kingdom

Department of Engineering, University of Cambridge, Cambridge, United Kingdom

Farhad Huseynov is a senior research associate in the Department of Engineering at the University of Cambridge. He is a member of the Institution of Engineers Ireland. He holds a PhD from University College Dublin. His PhD research efforts were on structural health monitoring (SHM) of bridges using rotation measurements. Realizing a lack of research in bridge SHM relating to the use of rotations for bridge condition monitoring, he developed a technique using accelerometers that can measure rotations, generated by pendulum behavior caused by gravity, with microradians accuracy. Before joining the university, Farhad had worked as a bridge engineer in several industry-leading consultancy companies for 10 years. He has extensive experience in the design, testing, and assessment of bridges. He has worked on a wide range of projects, including but not limited to medium-and long-span bridge design works and testing some of the iconic bridges in the United Kingdom, such as the Queensferry

Crossing. His research interests lie in the field of bridge performance monitoring using direct measurements, digital twins, bridge weigh-in-motion, and bridge traffic loading. His currently working on a research project, funded by the Centre for Digital Built Britain, looking into developing digital twins of two railway bridges in the United Kingdom.

K.K.G.K.D. Kariyawasam
Department of Civil Engineering, University of Moratuwa, Moratuwa, Sri Lanka
Kasun Kariyawasam is a lecturer at the University of Moratuwa. Kasun worked as a research associate at the Laing O'Rourke Centre for Construction Engineering & Technology after completing his PhD at University of Cambridge as a Gates Cambridge Scholar, working under the supervision of Professor Middleton. As part of his PhD project, Kasun developed a new vibration-based approach for monitoring bridge scour after conducting a series of laboratory centrifuge tests, a field trial, and associated numerical modeling on various types of bridges and forms of scour. This project was nominated for the British Construction Industry Awards and the Engineer Magazine "Collaborate to Innovate" awards. His research interests are in vibration-based condition monitoring, fiber-optic monitoring, bridge scour monitoring, smart infrastructure, and sustainable construction.

K. Kimura
Tokyo University of Science, Shinjuku, Japan
Kichiro Kimura is a professor of structural engineering in the Department of Civil Engineering, Faculty of Science and Technology, Tokyo University of Science, Japan. He earned his PhD at University of Ottawa and his ME in civil engineering at the University of Tokyo in 1987. He was a visiting researcher at the Boundary Layer Wind Tunnel Laboratory, Faculty of Engineering Science, University of Western Ontario, Canada, in 1991–1992. For his work on wind engineering, he has been given awards by the Japan Association for Wind Engineering in the outstanding publication category in 2012, the research paper category in 2008, and the research potential category in 1994. He is a director of the Japan Association for Wind Engineering.

T. Kovács
Budapest University of Technology and Economics, Hungary
Tamás Kovács earned his PhD in 2010 at the Budapest University of Technology and Economics, while being an assistant professor in the Department of Structural Engineering at the same university; in 2013, he became an associate professor. His research interests include dynamic-based damage assessment of concrete structures, life-cycle analysis of structures, reliability of structures, high-performance concrete (HPC) for bridges, modeling of prestressed structures, strengthening of bridges, and concrete pavements. He has been honored to receive the Scholarship of the Scientia et Conscientia Found, 1997; the Tierney Clark Award 2010 for the development of the FI-150 bridge girder family, 2011; and the Innovation Award 2010 of the Hungarian Intellectual Property Office for the development of the FI-150 type bridge girder family, 2011.

K.A. Malo

Norwegian University of Science and Technology, Trondheim, Norway

Kjell A. Malo got his PhD from the Norwegian Institute of Technology in Trondheim. His professional background is in steel-aluminum and timber structures. His current research topics and fields of interest are material models for wood, strength and stiffness of connections for timber structures, vibrations and comfort issues in multistory timber buildings, and design of timber bridges. Since 2002, he has taught university courses on timber engineering and basic mechanics and is supervisor for MSc and PhD students in timber engineering. He is the author of more than 40 professional publications in the field of timber engineering, and he is a national delegate to the European standardization committee on timber structures. In addition, he is the convenor for the committee responsible for the new Eurocode EN 1995-2 Timber Bridges, and he is the coordinator of the European ERA-NET Woodwisdom project DuraTB – Durable Timber Bridges.

B.T. Martin

Modjeski and Masters, Mechanicsburg, PA, United States

Barney T. Martin received his undergraduate degree in civil engineering in 1974 from Louisiana State University, Baton Rouge, Louisiana, and his master's and PhD degrees from Tulane University in New Orleans, Louisiana, in 1981 and 1992, respectively. Dr. Martin is active on the Transportation Research Board, having recently served as chairman of the Concrete Bridge Committee and the Steel Bridge Committee. He has had extensive highway bridge design experience, having been the managing engineer on bridge design projects ranging from simple girder spans to projects involving major suspension bridges. He has significant experience in the evaluation and design of long-span bridges, particularly the inspection and evaluation of parallel wire main cables of suspension bridges. In addition, he has significant experience in the design, structural evaluation, load rating, repair, and construction support of bridges of all types, both fixed and movable. President and CEO of Modjeski and Masters.

C.R. Middleton

Laing O'Rourke Professor of Construction Engineering & Fellow of King's College, University of Cambridge, Cambridge, United Kingdom

Laing O'Rourke Centre for Construction Engineering and Technology, University of Cambridge, Cambridge, United Kingdom

Campbell Middleton is the Laing O'Rourke Professor of Construction Engineering at the University of Cambridge. Prior to Cambridge, he worked for 8 years in professional practice in infrastructure design and construction in Australia and with Arup in London. He is chairman of the UK Bridge Owners Forum, is a member of the Design Panel for HS2, and has acted as an advisor or consultant to a number of organizations including the Department for Transport (UK), Infrastructure UK (now IPA), the Highways Agency (now Highways England), Ministry of Transportation Ontario, and the National Transport Commission in Australia. He has received awards including the IStructE's Henry Adams Award (1999 and 2014), the ICE's Telford Premium Award

(1999) and Telford Gold Medal (2010), and the ASCE's J. James Croes Medal (2019). His research interests focus on a range of topics related to bridge engineering including modern methods of construction, digital engineering applications, satellite and smart sensor applications for structural performance monitoring, risk and asset management, and nondestructive testing. He is a member of the executive team responsible for overseeing the EPSRC/Innovate UK funded Centre for Smart Infrastructure and Construction and coauthor of a recent book titled "Bridge Monitoring: A practical guide."

M. De Miranda
Studio de Miranda Associati, Milan, Italy
Mario de Miranda obtained his civil engineering degree from the Politecnico diMilano, Italy, in 1979. His work, experience, and research are mainly related to the design and construction of cable-stayed and suspension bridges, wind engineering, and the history of construction. He is a partner of Studio de Miranda Associati–Consulting Engineers and has experience in the design and construction of bridges and structures. He has been involved with many major projects, most of these as lead designer, including large cable-stayed bridges in Italy, the Dominican Republic, Brazil, Algeria, and India, as well as with the construction engineering of the Storebaelt suspension bridge in Denmark. He has given lectures on bridge design and construction in many countries and is the author of 60 papers and chapters of books on the same subject. Since 2006, he has been an Invited Professor at the University IUAV of Venice, where he teaches structural design and steel construction.

V. Modeer
Vistra Corporation, Irving, TX, United States
Victor Modeer is the geo-science engineering manager for Vistra Corporation throughout the United States. He has 43 years of geotechnical experience, mainly in the United States but also in Europe and the Middle East. He is a Professional Engineer (PE) and has been awarded certification by the ASCE as a Diplomate in Geotechnical Engineering (DGE). He has a Master of Science with emphasis in geotechnical engineering from Purdue University and a Bachelor of Science in Civil Engineering from Louisiana State University. He is a US Navy Civil Engineer Corps veteran. Victor served as a committee chairman for the Transportation Research Board Committee on Earthworks and served on the Bridge Foundation committee. He served as cochairman of the Illinois Joint Research and Technology Center. He has managed geotechnical foundation investigation, design, and construction projects for cable-stayed, long-span deep-girder and truss bridges. He has also designed cofferdams for bridge foundation construction including evaluation of support for a floating cofferdam system in the Mississippi River. Victor has performed seismic analyses of new and existing bridge foundations on the effects of liquefaction and lateral loads in the New Madrid Fault Region. He has published peer reviewed papers including "Foundation Selection and Construction Performance—Clark Bridge Replacement," that is cable stayed.

A. Nowak

Auburn University, Auburn, AL, United States

Andrzej Nowak is a professor of structural engineering and chair of the Samuel Ginn College of Engineering at Auburnn University, in Auburn, Alabama. In addition, he is vice-chair of the Transportation Research Board-Task Group for LTBP Bridge Traffic and Truck Weight and a member of two American Concrete Institute (ACI) committees: the ACI 343 Committee on Concrete Bridges and ACI 348 Committee on Concrete Bridges. He is the author of more than 100 papers in renowned scientific journals. His research interests include the analysis and design of structures; code calibration procedures for load and resistance factor design (LRFD); the ultimate, serviceability, and fatigue limit states; load models for bridges, including extreme events and their combinations; resistance models for materials and structural components; evaluation of existing structure diagnostics, field testing, and proof loading for bridges; weigh-in-motion procedures for bridges; and mechanical properties and design criteria for lightweight concrete structures.

R. Saul

Leonhardt, Andrä, und Partner, Stuttgart, Germany

Reiner Saul was born at Lünen, Westphalia, Germany, in 1938 and graduated as Dipl.-Ing. in structural engineering from the Technical University of Hannover in 1963. He started his career with steel contractor Hein Lehmann AG Düsseldorf. In 1968, he went to Leonhardt, Andrä, und Partner, where he was appointed managing director in 1992. After his retirement in 2003, he became a consultant. From 1993 to 2006, he was licensed as a Legally Authorized Checking Engineer in Germany. In 1994, he was appointed a lecturer on steel bridges at the University of Stuttgart; in 2003, he received an honorary doctorate in structural engineering from the Technical University Carolo-Wilhelmina Braunschweig. In 2005, he became an honorary member of the Argentine Society for Structural Engineering (AIE). During his professional career, he has been involved in the design, site direction, or checking of about 40 cable-stayed and suspension bridges and numerous other bridges, mainly with steel or steel composite girders. He is the author of numerous papers, mainly on steel, steel composite and cable-stayed bridges and related problems like cables and protection against ship impact.

A.E. Schultz

University of Minnesota, Minneapolis, MN, United States

Arturo Ernest Schultz is a structural engineering researcher and educator. He holds a bachelor's degree in civil engineering from Southern Methodist University in Dallas, Texas, as well as master's and doctoral degrees in civil engineering from the University of Illinois at Urbana-Champaign. He is a fellow of The Masonry Society (TMS) and member of the Precast/Prestressed Concrete Institute (PCI), the American Concrete Institute (ACI), and the American Society of Civil Engineers (ASCE). He is past recipient of the John B. Scalzi Award (TMS), the C.T. Grimm Award (Canada Masonry Design Centre), and the Charles C. Zollman and Martin P. Korn awards (PCI).

S. Stawska
Department of Civil and Environmental Engineering, Auburn University, Auburn, AL, United States
Dr. Sylwia Stawska is a postdoctoral fellow at Auburn University, Alabama. She received her BS and MS degrees in civil engineering from UTP University in Poland, and PhD in civil engineering from Auburn University, Alabama. Dr. Sylwia participated in exchange programs in Sweden, Denmark, Spain, China, and the United States. Her research interests include reliability of structures and bridge engineering including live load models, calibration of design codes, and damage assessment under traffic-induced loads. She worked on research projects sponsored by NCHRP, NSF, state DOTs in California, Alabama, Rhode Island, Montana, and Florida, and other industrial and government sponsors in the United States, European Union, and Canada. She is a member of ASCE, ACI, and PCI. Dr. Sylwia was selected as the most exceptional international student of the Samuel Ginn College of Engineering and received 100+ Woman Strong Leadership award.

L. Stewart
Georgia Institute of Technology, Atlanta, GA, United States
Dr. Lauren K. Stewart, a renowned expert in blast research, came to the School of Civil and Environmental Engineering (CEE), in Atlanta, Georgia, from the University of California, San Diego (UCSD). She earned her bachelor's and doctoral degrees in structural engineering from UCSD, where she was a postdoctoral scholar and lecturer. She is also a National Defense Science and Engineering Graduate Fellow and holds a P.E. license. She has been involved with many blast and earthquake experimental projects, including the blast testing of steel structural columns, steel stud wall systems, and high-performance concrete (HPC) panels using the UCSD blast simulator. She has also conducted advanced finite element analysis for the World Trade Center 7, AFRL Munitions Directorate small munitions program, and programs supported by the Technical Support Working Group. She is considered by many to be among the top blast researchers in the United States, and has served as a senior blast engineering consultant to a number of organizations since 2007.

P.J. Vardanega
Department of Civil Engineering, University of Bristol, Bristol, United Kingdom
Dr. Paul Vardanega is a senior lecturer in civil engineering at the University of Bristol. He holds a PhD in geotechnical engineering from the University of Cambridge. He is a coauthor of the book *Bridge Monitoring: A Practical Guide*, published by ICE Publishing. He has continuing research interests in monitoring of civil infrastructure, geotechnical codes of practice, and development of geodatabases for use in design and modeling studies.

G.T. Webb
WSP, London, United Kingdom
Dr. Graham T. Webb is a chartered civil engineer with 10 years' experience in the infrastructure sector, during which he has worked on a number of high-profile projects

demanding a sound understanding of technical complexities. Prior to joining WSP, Graham completed a PhD on structural health monitoring at the University of Cambridge. His PhD research focused on ways in which data can be interpreted to provide useful information, an area in which surprisingly little work has been published. He has developed an innovative new classification system to aid users of SHM systems to clearly understand how data is used and what information can realistically be obtained. These new findings will help to better target investments in SHM so that results of genuine impact can be delivered. Graham has gained a wide range of experience with remote monitoring of structures, from advising on the interpretation of collected data to the design and specification of monitoring systems targeted to support the assessment of necessary remedial measures for existing structures.

Preface

Integrating new materials, innovative construction practices, and research from a wide variety of other innovative engineering and scientific fields (such as aerospace engineering, materials engineering, and so on), bridge engineering represents the highest intellectual pursuit of the construction and structural engineering fields. Moreover, as the demand for new and retrofitted infrastructure is increasing worldwide, the interest in the bridge engineering field—from both the economic and political points of view—is also increasing to a remarkable extent.

This book is the culmination of 10 years of challenging work, which began when I discovered that a comprehensive work on the state of the art of bridges—including theory, design, construction, research and development (R&D), and innovation—was not present in the existing literature. I hadn't found any existing manuals with useful content on the market, as these usually include a lot of content without precise answers to the most pressing questions relating to the everyday experience in the theory and practice of bridge engineering and design. I realized I wanted to create an innovative reference book that could be updated as innovations were made in the field. This culminated in the first edition of this book.

I initially tried to make a monograph on the matter on my own, spending some years to research books and articles during my doctoral and postdoctoral studies on bridge engineering. I then realized that many of my colleagues, including prominent academicians and engineers from around the world, had the same idea and sought to write an innovative monograph on bridge engineering and design—not a manual, but a reference book in which students, academics, and engineers could find useful information on bridge engineering topics from not merely an academic perspective but also including research and work in the industry. The preparation of this book has been very intensive, with thousands of communications passing between the other authors and myself.

After 5 years, we realized that so much progress in bridge and structural engineering had been made that a second edition was needed.

I hope that this final work has successfully expressed our thoughts and goals. All the chapters in this book have been "built" (this term captures the fatigue and the challenges the contributors overcame while preparing every chapter) and presented by leading experts in the specific area discussed—engineers and academics who have very soundly researched their findings. If you are searching for the best design and research handbook in this area, you can find everything you need to know about bridge design, engineering, construction, and R&D here in this text.

This is not a conventional book because each chapter covers the present body of knowledge, the history, and the most forward-looking, future-oriented information we have on each topic. Most chapters describe research and innovations regarding each topic or where research is going and what the market is dictating. Sometimes these two aspects coincide; other times, not at all. I have personally chosen every contributor, and have included the most prominent authorities in their respective fields and representative authors from around the world in order to prepare a leading book.

I want to acknowledge all the authors and their collaborators, more than 100 academics and professionals from all over the world who have worked to create what is now a real and groundbreaking handbook.

Acknowledgment

I acknowledge all the special men and women I have met during my life. These special people believe in the young and their dreams; they cultivate their good intentions and ambitions, great and small. They are not selfish; they believe in the next generation; they help others and take an interest in them. Special people work in a transparent and fair way, they believe in the possibility of a better future, and they do their best to impact the future for the better during their lives. These individuals truly believe in science, research, and society; they do their work seriously, without the aim of personal gain. Such people want to live life intensely and take the opportunity to spread positivity, courage, respect, selflessness, integrity, and honesty with others. If we all emulate these special people every day, the world will be a better place!

This page intentionally left blank

Note

The views and opinions expressed in the following chapters are those of the authors and not necessarily reflect those of the organizations they belong to or of Elsevier. The reader is cautioned that independent professional judgment must be exercised when information set forth in this handbook is applied. Anyone using this information assumes all liability arising from such actions.

Part I

Fundamentals

This page intentionally left blank

The history, aesthetic, and design of bridges

1

Alessio Pipinato
AP&P, CEO and Technical Director, Rovigo, Italy

1. History of bridge structures

Bridge structures represent a challenge in the built environment: they are the crystallization of forces finalized to keep someone in an unreachable place. Bridges provide the most appropriate connection to what nature has divided by a river or a valley—something that is impossible to be reached. The first bridge was a natural gift to humanity—probably a tree that fell across a small river—and it suggested to the first prehistoric builders that it is possible to overpass obstacles. From this simple structure, a central part of the structural engineering world was inspired and has been perfect over the centuries. In this chapter, a synthesis of the history of bridge construction is presented.

1.1 Pre-Roman era

A simple supported wood beam made the Paleolithic Age was probably the first bridge structure of humankind. In the Mesolithic Period, an increasing amount of bridge structures were built. For example, the Sweet Track, 1800 m long, was recently discovered at Somerset Levels in Great Britain and harked to the early stage of the Neolithic Period (3806 B.C.), according to dendrochronological analysis (Figure 1.1). In Egypt, such small examples as the stone bridge at Gizah (2620 B.C.) have been found (Figure 1.2). Meanwhile, in Greece, the Kasarmi Bridge at Argolide (1400 B.C.) was one of the first type of Miceneus bridges (Figure 1.3). It is a common historical belief that Etruschi taught the Romans how to build arch bridges, even if they left no relevant bridges behind to document this. In fact, the Romans learned about this from defense and hydraulic constructions such as the Volterra arch (fourth century B.C.), which certainly was a masterpiece of the Etruschans that was later altered by the Romans (Figure 1.4). Finally, some wooden structures from the Celtic period have been found; for instance, Figure 1.5 shows the Rodano Bridge in Geneve (58 B.C.). The presence of these bridges was documented in the first century B.C. by Cesare (50 B.C.) in the book *De Bello Gallico*, which lists a large number of wooden bridges in the Gallia territory.

Innovative Bridge Design Handbook. https://doi.org/10.1016/B978-0-12-823550-8.00014-7

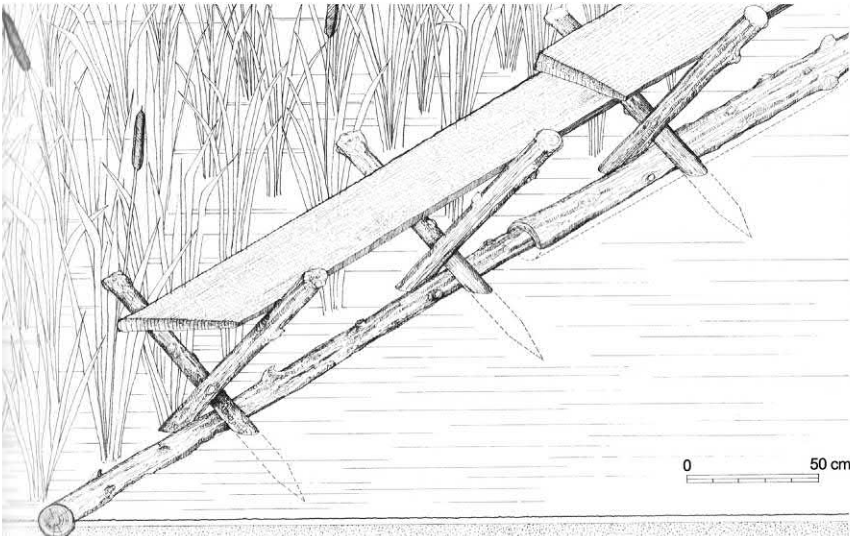

Figure 1.1 Graphic reconstruction of the 1800-m-long Sweet Track (3806 B.C.).

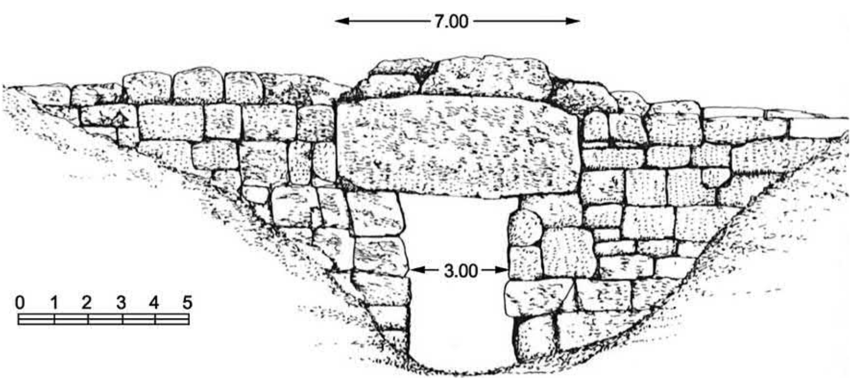

Figure 1.2 Stone bridge, Gizah (2620 B.C.).

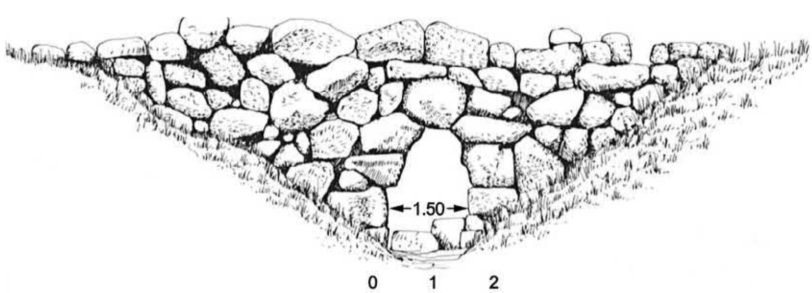

Figure 1.3 Kasarmi Bridge, Argolide (1400 B.C.).

Figure 1.4 Volterra Arch, Volterra (fourth century B.C.).

1.2 Roman era

Although wooden bridges were common at first, stone bridges (especially arch bridges) increasingly dominated until the Middle Ages; as Palladio said: "Stone bridges were built for their longer life, and to glorify their builder" (Palladio, 1570). One of the most incredible periods of bridge construction began during the Roman Empire, when stone arch bridge building techniques were developed. Two fundamental elements form the basis of this development: the first was geopolitical, as the military and political objective to grow faster and faster as an empire required a large amount of infrastructure; the second was technological, as the discovery and growing popularity of the pozzolana strongly impacted bridge construction types. Two notable structures of this period are the Sant'Angelo Bridge (in the year 136) and the Milvio Bridge (100), both in Rome (Figures 1.6 and 1.7). One construction improvement made by the Romans solving the problem of building a foundation in soft soils by the innovative use of cofferdam, in which concrete could be poured. A surviving monument of this period is the Pont du Gard aqueduct near Nîmes in southern France (first century B.C.), which measures 360 m at its longest point; it was built as a three-level aqueduct standing more than 48 m high (Figure 1.8).

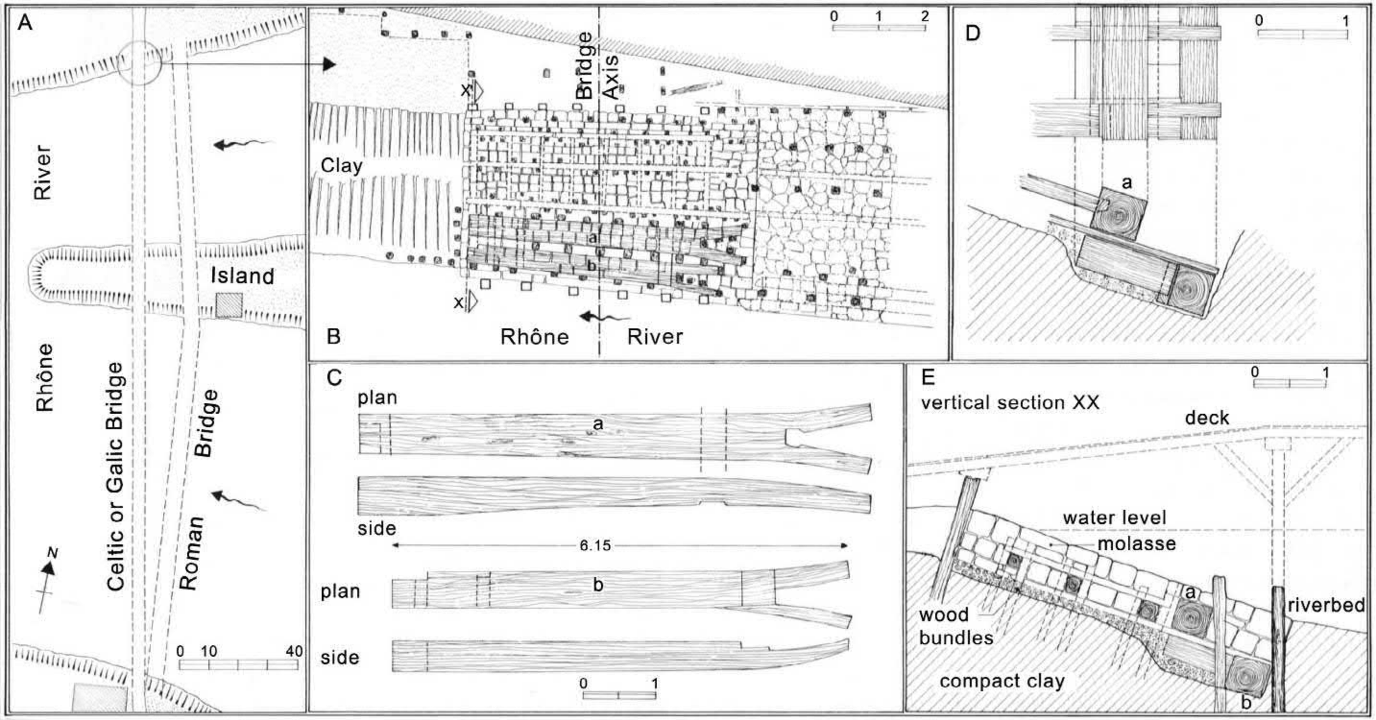

Figure 1.5 Rodano Bridge, Geneve (58 B.C.): (a) plan view, (b) plan of the first pile, (c) wooden platform for the first pile, (d) section of c, (e) built pile section.

Figure 1.6 Sant'Angelo Bridge, Rome (136 B.C.).

Figure 1.7 Milvio Bridge, Rome (first century B.C.).

Figure 1.8 Pont Du Gard aqueduct, Nimes (first century B.C.).

1.3 Middle ages

The fall of the Roman Empire ended the accelerated development of bridge construction for a long time. In the Middle Ages, the inhabited bridge started to be built. One of the most relevant and oldest of these was the Old London Bridge (Figure 1.9), finished in 1209 in the reign of King John and initially built under the direction of a priest and architect named Peter of Colechurch; the bridge was replaced at the end of the 18th century, having stood for 600 years with shops and houses on it. The majority of inhabited bridges still in use are Italian inhabited bridges, such as the Ponte Vecchio in Florence (Figure 1.10a).

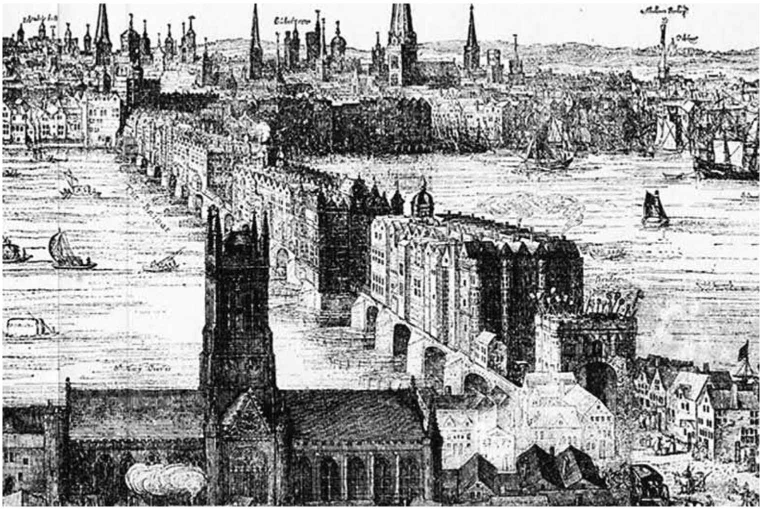

Figure 1.9 Old London Bridge, London (1209).

Figure 1.10 (a) Ponte Vecchio, Florence (1345). (b) Ponte Rialto, Venice (1588).

Figure 1.11 Waterloo Bridge, London (1811).

1.4 The renaissance

A refined use of stone arch bridges came up during the Renaissance. The large variety and quantity of bridges that were built in this period make it impossible to keep a complete list. However, some masterpieces, which represent the innovations of the time, can be cited. The first example is the inhabited Ponte Rialto in Venice (Figure 1.10b), an ornate stone arch made of two segments with a span of 27 m and a rise of 6 m. The present bridge was designed by Antonio da Ponte, the winner of a design competition, who overcame the problem of soft and wet soil by drilling thousands of timber piles straight down under each of the two abutments, upon which the masonry was placed in such a way that the bed joints of the stones were perpendicular to the arch's line of thrust (Rondelet, 1841). Other notable structures of this period include the Pont de la Concorde in Paris, designed by J. R. Perronet at the end of the 18th century; London's Waterloo Bridge (Figure 1.11), designed by J. Rennie beginning in 1811; and, finally, the New London Bridge (designed in 1831).

1.5 The period of modernity: 1900 to present

The 18th-century Industrial Revolution completely changed the use of material not only in traditional buildings, but also in bridges. Wood and masonry were replaced by iron constructions. The famous bridge in Coaldbrookdale, an English mining village along the Severn River, was probably the first to be completely erected with iron (opened in 1779; Figure 1.12): it is a single-span bridge made of cast-iron pieces and a ribbed arch with a nearly semicircular 30 m span. The great reputation of this bridge, due to its shape and robustness (for instance, it was the only bridge that successfully survived a disastrous flood in 1795), spurred the master engineer Thomas Telford to design a great number of arched metal bridges, including the surviving Craigellachie Bridge (1814) over the River Spey in Scotland, a 45 m flat arch made of two curved

Figure 1.12 Coaldbrookdale Bridge, Coaldbrookdale (1779).

Figure 1.13 Craigellachie Bridge, Scotland (1814).

arches connected by X-bracing and featuring two masonry towers at each side (Figure 1.13). Another innovation fostered using iron in construction was the opportunity to build lighter structures and such new structural components as cables. The first structural application in a bridge was probably the Menai Bridge (construction started in 1819, opened in 1826), another of Telford's constructions (Figure 1.14a), spanning 305 m and with a central span of 177 m. This was the world's longest bridge at the time. In 1893, its timber deck was replaced with a steel one, and in 1940, the corroded wrought-iron chains were also replaced with steel. In 1999, the road deck was strengthened, and in 2005, the bridge was fully repainted fully for the first time since 1940. The bridge is still in service today.

Another innovation during the Industrial Revolution was the invention of the Portland cement, patented first by Joseph Aspdin in 1824, which—in conjunction with

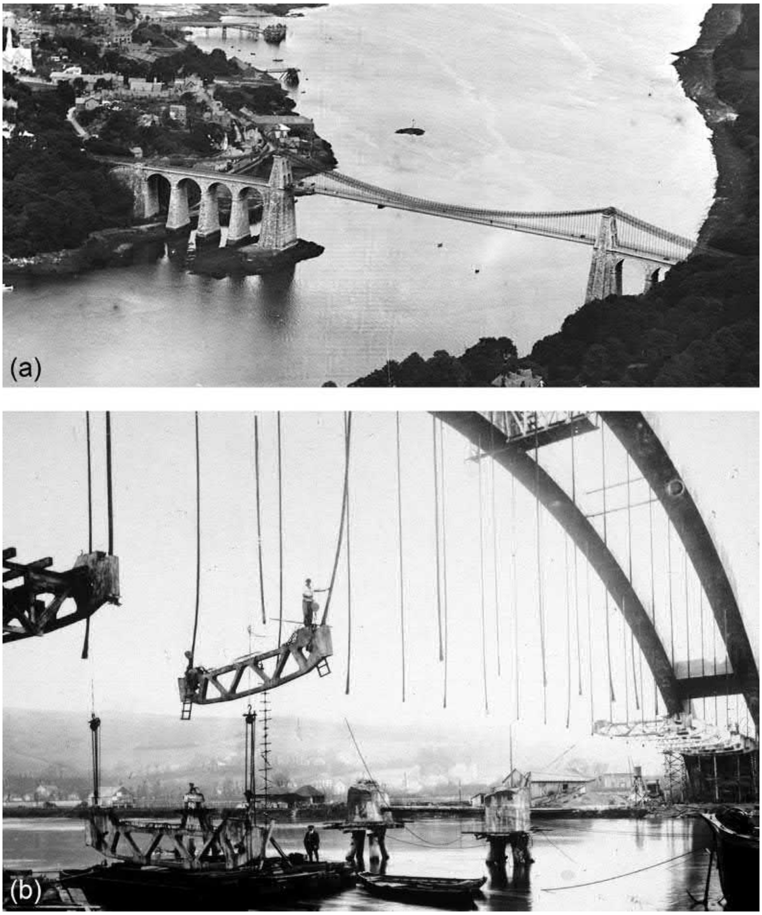

Figure 1.14 (a) Menai Bridge, Wales (1816). (b) Saint-Pierre-du-Vauvray Bridge (1923).

iron industrialization,—boosted the reinforced concrete (RC) era. François Hennebique discovered the reinforced concrete tubs and tanks of Joseph Monier (a French gardener) at the Paris Exposition of 1867 and began experimenting different applications to apply this new material to building construction. Some years later, in 1892, Hennebique patented a complete building system using RC. The first large-scale example of an RC bridge was the Châtellerault Bridge (1899), a three-arched structure with a 48 m central span. Subsequently, Emil Mörsch designed the Isar Bridge at Grünewald, Germany, in 1904 (with a maximum span of 69 m); and Eugène Freyssinet designed the Saint-Pierre-du-Vauvray arched RC bridge over the Seine in northern France (built in 1922, with a maximum span of 131 m; Figure 1.14b); the Plougastel Bridge (Figure 1.15) over the Elorn estuary near Brest, France (built in 1930 with a maximum span of 176 m), and, finally, the Sandö Bridge in northern Sweden (built in 1943 with a maximum span of 260 m). Some of the first problems

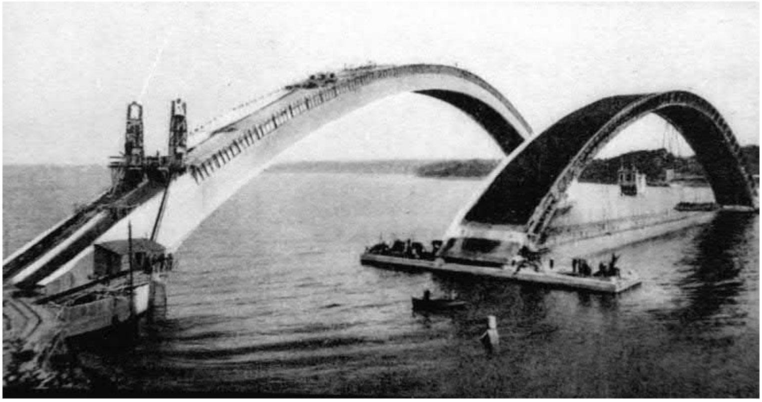

Figure 1.15 Plougastel Bridge, Brest (1930).

that arose with these medium-size structures with vehicle loadings included creep and fatigue. Many innovations were introduced in this period. For instance, in 1901, Robert Maillart, a Swiss engineer, started using concrete for bridges and other structures, and used unconventional shapes. Throughout his life, Maillart built a wide variety of structures still known for their slenderness and aesthetic expression. Some examples include the Tavanasa Bridge over the Vorderrhein at Tavanasa, Switzerland (built in 1905), with a span of 51 m, and the Valtschielbach Bridge (built in 1926), a deck-stiffened arch with a 40 m span. However, undoubtedly the best-known structure is the Salginatobel Bridge, a 90 m three-hinged hollow-box arched span in Graubünden, Switzerland. Maillart probably was the first designer able to merge engineering with the most functional and attractive architectural forms, achieving very high-quality unconventional constructions.

During this period, industries used innovative prestressing methods and RC solutions to build important experimental constructions; this is the case of the railway bridges near Kempten, Germany (1904), the longest span of which was 64.5 m. It was built by DYWIDAG Bau GmbH (at that time Dyckerhoff & Widmann AG). It is also interesting to note that, in 1927, the Alsleben Bridge in Saale was built with prestressed iron ties (designed by Franz Dischinger), a predecessor of today's prestressing technique. And only 1 year later, in 1928, Freyssinet patented the first prestressing technology. Then other bridges were completely realized in prestressed RC—e.g., the Luzancy Bridge (completed in 1946), with a span of 54 m (Figure 1.16). Other notable bridges were the bridge over the Rhine at Koblenz, Germany—completed in 1962, with thin piers and a central span of 202 m, designed by Ulrich Finsterwalder—and, more recently, the Reichenau Bridge over the Rhine (1964)—a deck-stiffened arch with a span of 98 m designed by Christian Menn, a Swiss engineer who made great use of prestressing in bridge construction. More recently, in 1980, Menn built the Ganter Bridge crossing a deep valley in the canton of Valais; this bridge features a cable-stayed structure with a prestressed girder, with its highest column rising 148 m and a central span of 171 m. A wide variety of innovations arising in the late 20th century, together with the use of metal and RC, enabled the achievement of

Figure 1.16 Luzancy Bridge, Luzancy (1946).

Figure 1.17 Brooklyn Bridge, New York (1883).

increased span length. This led to the first suspension bridges; the first such structure was the Brooklyn Bridge (Figure 1.17), which opened in 1883 and was designed by John Roebling and his son, Washington Roebling. This was the first suspension bridge with steel wires, with a total span of 1596 m and a central span of 486 m. Subsequently, in New York, two other bridges were built to accommodate the increasing traffic: the Williamsburg and the Manhattan bridges. The first, spanning 2227 m, was the longest in the world in 1903 after its completion; the second, spanning 1762 m, was completed in 1910. The Manhattan and Williamsburg bridges were the first two such structures in which deflection theory (which took into consideration the stiffening effect of the tension in the main suspension cables) was adopted in order to achieve unprecedented economy in the stiffening trusses. Then, when Ralph Modjeski erected the Philadelphia–Camden Bridge in 1926 (today known as the

Benjamin Franklin Bridge), reaching 2273 m, that became the longest span in the world; this was soon surpassed by the Ambassador Bridge (1929) in Detroit and the George Washington Bridge (1931) in New York. The George Washington Bridge's most astonishing innovations make it a masterpiece of engineering and architecture. Designed by Othmar Ammann, the George Washington Bridge was long enough (1450 m) to shatter the previous record for bridge central span, 1067 m. While the towers and cables were designed to support the future addition of a lower level to expand capacity, the original bridge had single deck and did not include a stiffening truss (unlike other types of suspension bridges built in that era). A stiffening truss was not necessary because the long roadway and cables provided enough dead weight to provide stability for the bridge deck, and the short side spans acted like cable stays, further reducing its flexibility (ASCE, 2020). In addition, the girder depth ratio was innovative for that time at nearly 1:350. Other similar structures followed, such as the Golden Gate Bridge (Figure 1.18), spanning 2737 m (central span 1280 m) and built in 1937, and the Bronx–Whitestone Bridge, spanning 1150 m (central span 701 m) and opened in 1939. The designers of these and other bridges learned a powerful lesson from the collapse of the Tacoma Narrows Bridge, which was destroyed by only a moderate wind in 1940, principally because its deck lacked torsional stiffness. As a result, most of the new bridges were soon after reinforced to prevent similar disaster, adding new bracing systems or inclined suspenders to form a network of cables.

1.6 Recent masterpieces

In contemporary times, a large number of bridges have been built, so it is not easy to decide which recent structures around the world are the most innovative. However, the presence of the following elements helps in the choice: new materials (lighter, more resistant, easier to recycle); new construction methods, finalized to increase productivity; new structural shapes (probably the most fascinating and most difficult task of a

Figure 1.18 Golden Gate Bridge, San Francisco (1937).

Figure 1.19 Grand Harbor Bridge, Ulsan (2015).

Figure 1.20 Providence River Bridge, Providence (2008).

bridge engineer); and finally, elegance, which is a kind of synthesis of the aforementioned characteristics. For each of these categories, a project has been cited as an example:

- Use of new materials: Ulsan Grand Harbor Bridge (Figure 1.19), for its innovative use of materials, such as the super-high-strength steel cables (1960 MPa)
- New construction methods: Providence River Bridge (Figure 1.20), built in a yard and then lifted on-site
- Innovative structural shape: the Sunnibergbrucke (Figure 1.21), combining the cable-stayed scheme with a curved plan, and featuring astonishing bifurcated columns
- Elegance: Erasmus Bridge (Figure 1.22), a masterpiece of construction, its simple shape reflecting the industrial character of Rotterdam

Figure 1.21 Sunnibergbrücke, Klosters (1998).

Figure 1.22 Erasmus Bridge, Rotterdam (2003).

2. Bridge design and aesthetic

2.1 Bridge design

The bridge design phase is probably the most fascinating and most difficult task for an experienced engineer if the design is original design and not industrial/repetitive work. It is unnecessary to provide the definition of the bridge design process, list the various steps required, and detail the bureaucratic procedures involved in this context. Instead, it should be stated that the bridge is a complex structure that introduces into the surrounding landscape relevant variations, dealing with a number of specialist fields: for example, hydraulic, geotechnical, landscaping, structural, architectural, economic, and sociopolitical considerations. For this reason, before starting the design of a bridge, a concept should be developed, with the realization of a scaled model, as a simulation of the three-dimensional (3-D) overview of the construction and of all the considered alternatives. From this initial concept, some parametric considerations need to be performed to estimate the costs. This preliminary analysis is the basis for an open discussion with the client, the managing agencies, and any relevant local government agency on the most suitable solution. Only when costs and the concept are agreed upon can the design stage start: the successive steps of the preliminary, definitive, executive design, finally culminating in a construction project that entails the actual erection of the bridge. For large-scale projects, the preliminary stage includes economic and financial studies as well. It should be known that the majority of the many variables included in the design stage are not fixed, as they depend on the precise place and time of the realization—e.g., there is not the best finite element method (FEM). Rather, the FEM software most suitable for the specific bridge design must be chosen, and the same applies to codes and standards, the amount of human resources, and the hardware instrumentation required. The most successful project is a perfect mix of these various components. Surely, a good project must include an architectural consciousness, the structural engineering knowledge, the professional experience, and a strong informatic infrastructure.

2.2 Bridge aesthetics

There is no one rule to conceive the most perfect or most aesthetically pleasing bridge. However, awful bridges can be found anywhere. A good and well-known definition of the term aesthetic could be "pleasant architecture": consequently, it could be helpful to remember the basic components of architecture. These, according to Vitruvio (27 B.C.), are the following:

- *Firmitas*: This is a key element for infrastructure and is surely the most relevant for bridge structures; it is the ability of a bridge to preserve its physical integrity, surviving as an integral object, at least for its service life.
- *Utilitas*: The practical function of a structure is a common rule; however, it is often not applied; the simple requirement that set the spaces and the components of a bridge structure includes the usefulness for the specific purpose for which the bridge was intended.
- *Venustas*: The sensibilities of those who see or use the bridge structure may arise from one or more factors—including the symbolic meaning; the chosen shape and forms; the materials, textures, and colors; and the elegance to solve practical and programmatic problems. This is obviously a subjective factor that could cause delight in the observers, or not.

3. Research and innovation in bridge design

Research and development (R&D) activities in the particular and fascinating bridge engineering field. Are expected to be carried out by industries, universities, and specialized firms in the coming years. The R&D field in this sector is expected to grow faster and faster, expanding into other fields of construction in the future. The most prominent problems to be faced are the following:

- Sustainable bridges: As generally could be said about the construction sector, a reduction in the use of materials is expected in bridge construction, together with the possibility of conceiving new construction modes and new bridge types that can reduce the need for raw materials and, at the same time, the construction, operation, maintenance, and decommissioning energy and cost consumption. Future bridges hopefully will be able to maintain a skeletal and principle structure over many centuries, updating only superstructures and functional parts during bridges' life.
- Intelligent bridges: Bridges will be more like machines in the future, rather than fixed and completely crystallized constructions. Eventually, intelligent systems able to control the bridge status (such as material decay, unexpected stress/strain levels, and external dangers) in real time will be developed at a reasonable commercial cost, and they will be integrated during the construction process in all new bridges at both large and small scales.
- Intelligent bridge-net: Today, managing authorities are concerned about managing and limiting maintenance costs of old infrastructures of bridges approaching and surpassing 100 years of age. However, apart from highways and railways authorities, where bridges are monitored as a net of constructions and every maintenance cost is planned, not every bridge of municipalities, provinces, and other networks is monitored. Consequently, the application of the aforementioned maintenance procedures should be expanded and applied to all bridges to ensure the maximum safety of users.
- Lifelong solutions: A vast amount of research should be done in the specific sector of materials, as they can easily contribute to build longer-life and more sustainable bridges. Decay characteristics of bridge materials should be investigated and deepened with the goals of discovering and utilizing new materials, beyond the use of common construction materials. In this context, it is useful to observe that many Roman bridges more than 200 years old are still in service, while "modern" bridges are often demolished after 100 years, at best. Are our innovations as effective as we think they are?

References

Palladio, A., 1570. I quattro libri dell'architettura. Translation of the original, 1945, 4 vols. Ulrico Hoepli Editore, Milan, Italy.

Rondelet, A., 1841. Saggio storico sul ponte di Rialto in Venezia. Negretti Edition. Mantova, Italy.

Further reading

Cesare, G., 50 B.C. De Bello Gallico. Original Latin Version. Mursia Editorial Group, Milan, Italy.

Vitruvio, P.M., 1997. 27 B.C. De Architectura. Translation of the original, 2 vols. Einaudi, Milan, Italy.

Part II

Loads on bridges

This page intentionally left blank

Loads on bridges

2

A. Nowak[a], *Alessio Pipinato*[b], *and S. Stawska*[a]
[a]Department of Civil and Environmental Engineering, Auburn University, Auburn, AL, USA, [b]AP&P, CEO and Technical Director, Rovigo, Italy

1. Introduction

In this chapter, information regarding loads is presented: this includes models and load values associated with road traffic, pedestrian activities, rail traffic, dynamic and centrifugal effects, braking, and acceleration actions. Imposed loads defined in codes and standards are intended to be used to design new bridges, including their piers, abutments, upstand walls, wing walls, flank walls, and foundations. Where reduced traffic loads could be used during the structural assessment and imposed in new traffic limitations to avoid bridge retrofitting or reconstruction remains an unanswered question. In fact, in this case, only some nations—for instance, the United States (AASHTO, 2020), the United Kingdom (Highways Agency, 2006; Network Rail, 2006), Denmark (Danish Road Directorate, 1996), Switzerland (Societe‘ Suisse des Ingenieurset des Architects (SIA), 2011), and Canada (Canadian Standards Association, 2006)—provide detailed guidelines or codes for assessing existing bridges, but many countries do not.

2. Permanent loads

2.1 Self-weight of structural elements

Self-weight or dead load consists of the weight of structural components and nonstructural elements permanently attached to the structure, including noise and safety barriers, signals, ducts, cables, and overhead line equipment (except the forces due to the tension of the contact wire, etc.). The self-weight is generally estimated in the first design phase, and then it is updated analytically in the detailed design phase. The actual value can also be estimated using empirical formulae, or it can be assumed based on the designer’s past experience. Special care is required in the analysis of self-weight during the bridge’s construction period, including consideration of the erection equipment (Figure 2.1).

2.2 Self-weight of nonstructural elements

Road and railway equipment, sidewalks, parapets, barriers, channels or pipework, noise wall luminaires, and sign supports are considered as nonstructural elements. The magnitude of load is usually determined using mass/volume unit values specified in design codes and standards.

Innovative Bridge Design Handbook. https://doi.org/10.1016/B978-0-12-823550-8.00008-1

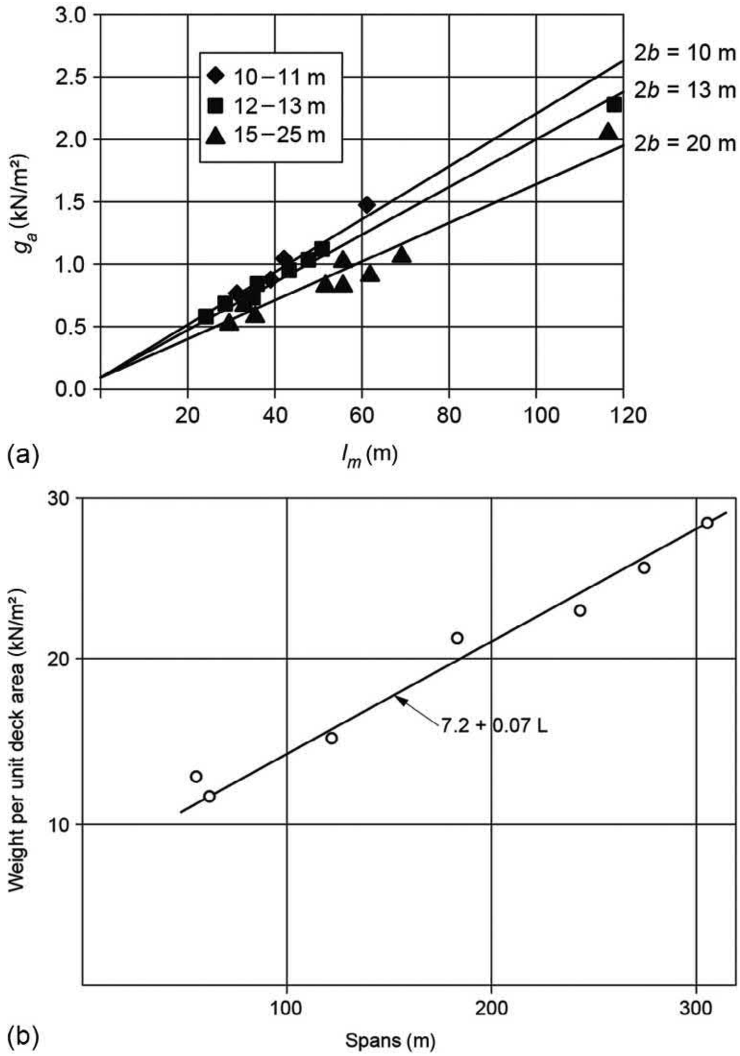

Figure 2.1 (a) Small-span bridges, twin girder composite bridge, self weight of the steelwork (Leben and Hirt, 2012); (b) medium-span bridges—prestressed concrete bridge self weight (O'Connor, 1971).

3. Traffic load provisions

Traffic loads are forces caused by moving vehicles determined by traffic volume—i.e., average daily traffic (ADT) and average daily truck traffic (ADTT), weight of vehicles as gross vehicle weight (GVW), axle weight and spacing—and also vehicle speed, curb distance, and frequent presence of more than one truck in the same lane or in adjacent lanes. Actual traffic load information is available in the form of weigh-in-motion (WIM) measurements. Millions of records have been from collected all over the world. Current traffic is very specific to each bridge site (Babu et al., 2019; Iatsko and Nowak, 2020). The following sections provide information about examples of design live load in various countries.

3.1 Traffic loads: Eurocode

EN 1991-2 (2003) is intended to be used in conjunction with EN 1990 (especially A2). Section 1 of the Eurocode provides general information, definitions, and symbols. Section 2 defines loading principles for road bridges, footbridges (or bicycle-track bridges), and railway bridges. Section 3 covers design situations for critical live load design and provides guidance on combination rules of multiple presence traffic loading. Section 4 defines traffic loads on road bridges, with load combinations including pedestrian and bicycle traffic as well as other actions specific for the design of road bridges. Section 5 describes loads on footways, bicycle tracks, and footbridges, and other actions specific to the design of footbridges. Section 6 defines loading for rail bridges, due to rail traffic and other specific actions for the design of railway bridges and structures adjacent to the railway. Characteristic load values predict road traffic effects associated with the ultimate limit state and with particular serviceability limit states. These values are determined from the analysis of data collected in several countries. The design values were calculated as corresponding to a probability of being exceeded annually and are adjusted using the coefficients αQi and αqi. These coefficients for the traffic load model can be nationally adjusted (in the so-called National Annexes). The code EN 1991-2 (2003) specifies two principal load models for normal highway bridge traffic. For instance, Load Model 1 (LM1) consists of a double-axle system, called tandem (TS), together with a uniformly distributed load, and is intended to cover "most of the effects of the traffic of lorries and cars." It is necessary to first define notional lanes. The normal basic lane width is 3 m, with the exception that roadway widths of 5.4–6 m are assumed to carry two lanes. Generally, a roadway is divided into an integral number of 3 m lanes that may be positioned transversely so as to achieve the worst effect. Of these lanes, the one causing the most unfavorable effect is called Lane 1, the one causing the second most unfavorable effect is Lane 2, and so on. These lanes do not need to correspond to the bridge's marked lanes; indeed, a demountable central safety barrier is ignored in locating the traffic lanes. Space not occupied by the lanes is called a remaining area. The total load models for vertical loads are represented by the following traffic effects:

- Load Model 1 (LM1): Concentrated and uniformly distributed loads that cover most of the effects of the traffic of trucks and cars. This model should be used for general and local verifications (Figure 2.2).
- Load Model 2 (LM2): A single-axle load applied on specific tire contact areas that cover the dynamic effects of the normal traffic on short structural members (Figure 2.3).
- Load Model 3 (LM3): A set of assemblies of axle loads representing special vehicles (e.g., for industrial transport) that can travel on routes permitted for abnormal loads. It is intended for general and local verifications.
- Load Model 4 (LM4): A crowd loading, intended only for general verification.

Location	*Tandem* system *TS*	*UDL* system
	Axle loads Q_{ik} (kN)	q_{ik} (or q_{rk}) (kN/m²)
Lane Number 1	300	9
Lane Number 2	200	2,5
Lane Number 3	100	2,5
Other lanes	0	2,5
Remaining area (q_{rk})	0	2,5

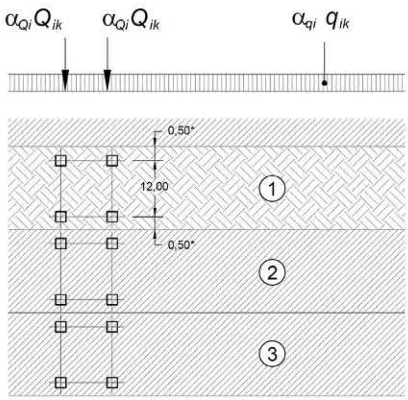

Key
(1) Lane Nr.1: Q_{1k} = 300 kN; q_{1k} = 9 kN/m²
(2) Lane Nr.2: Q_{2k} = 200 kN; q_{2k} = 2,5 kN/m²
(3) Lane Nr.3: Q_{3k} = 100 kN; q_{3k} = 2,5 kN/m²
* For w_l = 3,00 m

Figure 2.2 Load Model 1 (EN 1991-2, 2003).

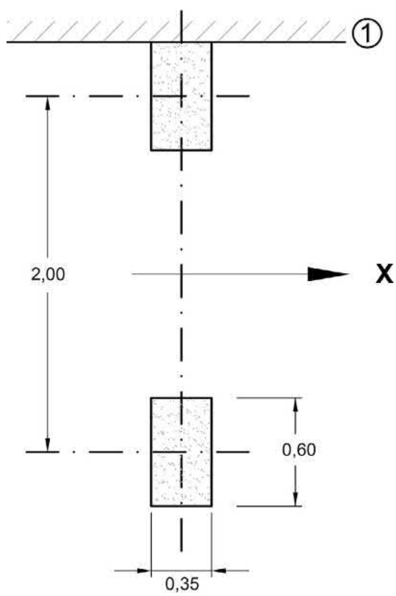

Key
X Bridge longitudinal axis direction
1 Curb

Figure 2.3 Load Model 2 (EN 1991-2, 2003).

3.2 Traffic loads: AASHTO

Highway bridge design loads are established by the American Association of State Highway and Transportation Officials (AASHTO). For many decades, the primary bridge design code in the United States has been the AASHTO "Standard Specifications for Highway Bridges" (Specifications), supplemented by agency criteria as applicable. During the 1990s, AASHTO developed and approved a new bridge design code, entitled "AASHTO LRFD Bridge Design Specifications" (AASHTO, 2020). It is based on the principles of limit states or load and resistance factor design (LRFD). Section 3 deals with loads and load factors and includes information on permanent loads (dead load and earth loads), live loads (vehicular load and pedestrian load), and other loads (wind, temperature, earthquake, ice pressure, and collision forces). The basic vehicular live loading for highway bridges is designated as HL-93, and it consists of a combination of the following:

- Design truck or design tandem
- Design lane load

Each design lane under consideration is occupied by either the design truck or tandem, superimposed with the lane load. The live load is assumed to occupy 10.0 ft. (3.3 m) width within a design lane of 12 ft. (3.6 m). The total live load effect resulting from multilane traffic can be reduced for sites with lower ADTT using the multilane reduction factors. Careful consideration is required in case of site-specific exceptional situations if any of the following conditions apply:

- The legal load of a given jurisdiction is significantly greater than the code-specified load.
- The roadway is expected to carry exceptionally high percentages of truck traffic.
- Traffic flow control devices—such as a stop sign, traffic signal, or tollbooth—cause trucks to congregate on certain areas of a bridge.
- Exceptional industrial loads occur at the considered location of the bridge.

The live load model, consisting of either a truck or tandem coincident with a uniformly distributed load, was developed as a notional representation of a group of vehicles routinely permitted on highways in various states under grandfather exclusions to weight laws. The vehicles considered to be representative of these exclusions were based on a study conducted by the Transportation Research Board (Cohen, 1990). The load model is called "notional" because it is not intended to represent any particular truck. The weights and spacing of axles and wheels for the design truck is as specified in Figure 2.4. A dynamic load allowance is to be considered by increasing the static effects of the design truck or tandem, other than centrifugal and braking forces, by 33% of the truck load effect. That percentage is 75% for deck joints and 15% for fatigue and fracture limit states.

The spacing between two 32.0 kip axles can vary between 4.3 m (14.0 ft) and 9 m (30.0 ft) to produce the extreme force effect. The design tandem consists of a pair of 100 kN (25.0 kip) axles spaced 1.2 m (4.0 ft) apart. The transverse spacing of wheels 1.8 m (6.0 ft). The design lane load consists of a load of 0.64 klf (9.3kN/m) uniformly distributed in the longitudinal direction. Transversely, the design lane load is assumed

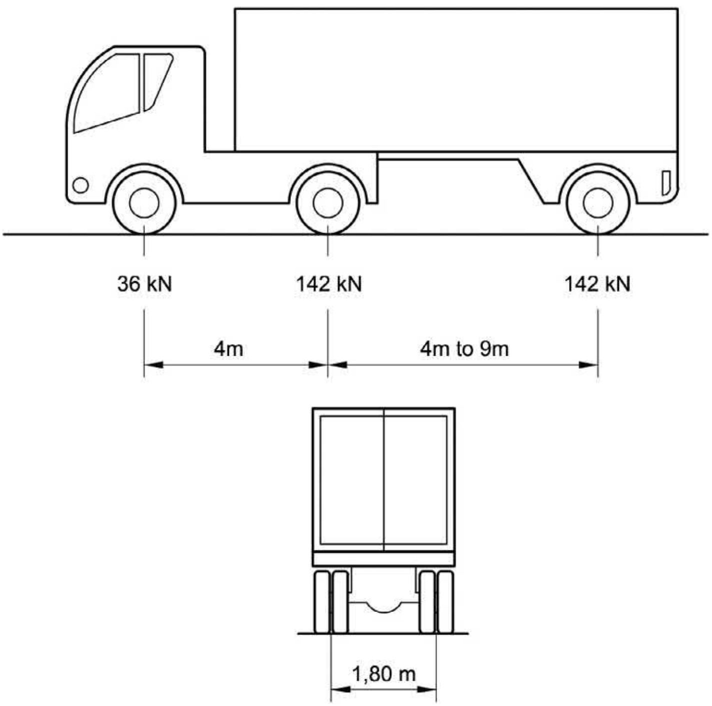

Figure 2.4 Characteristics of the design load (AASHTO, 2014).

to be uniformly distributed over a 3.05 m (10.0 ft) width. The force effects from the design lane load are not subject to a dynamic load allowance.

3.3 Traffic loads: AREMA

The standard loading scheme incorporated by North American Railways and the American Railway Engineering and Maintenance-of-Way Association (AREMA) is the Cooper *E*-Series loading: AREMA (2013) recommends E-80 loadings (two locomotives coupled together in doubleheader fashion, with the maximum axle load of 335 kN) to be used for the design of steel, concrete, and most other structures. The designer must also verify the specific loading to be applied from the railway, as this may require a design loading other than the E-80 Cooper E-Series. More information is given in the specific chapter dedicated to railway bridges (Chapter 20).

3.4 Traffic loads: Australian standard

The Australian Standard (AS) (AS5100, 2017) normal design traffic load includes the following components, each considered separately:

- W80 wheel load comprises an 80 kN load applied over a contact area of 400 mm wide × 250 mm long anywhere on the road surface (Figure 2.5).
- A160 axle load, comprising of two W80 wheels spaced 2 m apart between the center of the wheel contact areas (Figure 2.5).
- M1600 moving load, comprising a combination of axle group and uniformly distributed lane load (UDL), as illustrated in Figure 2.5. The lane width is taken as 3.2 m. The lane UDL is

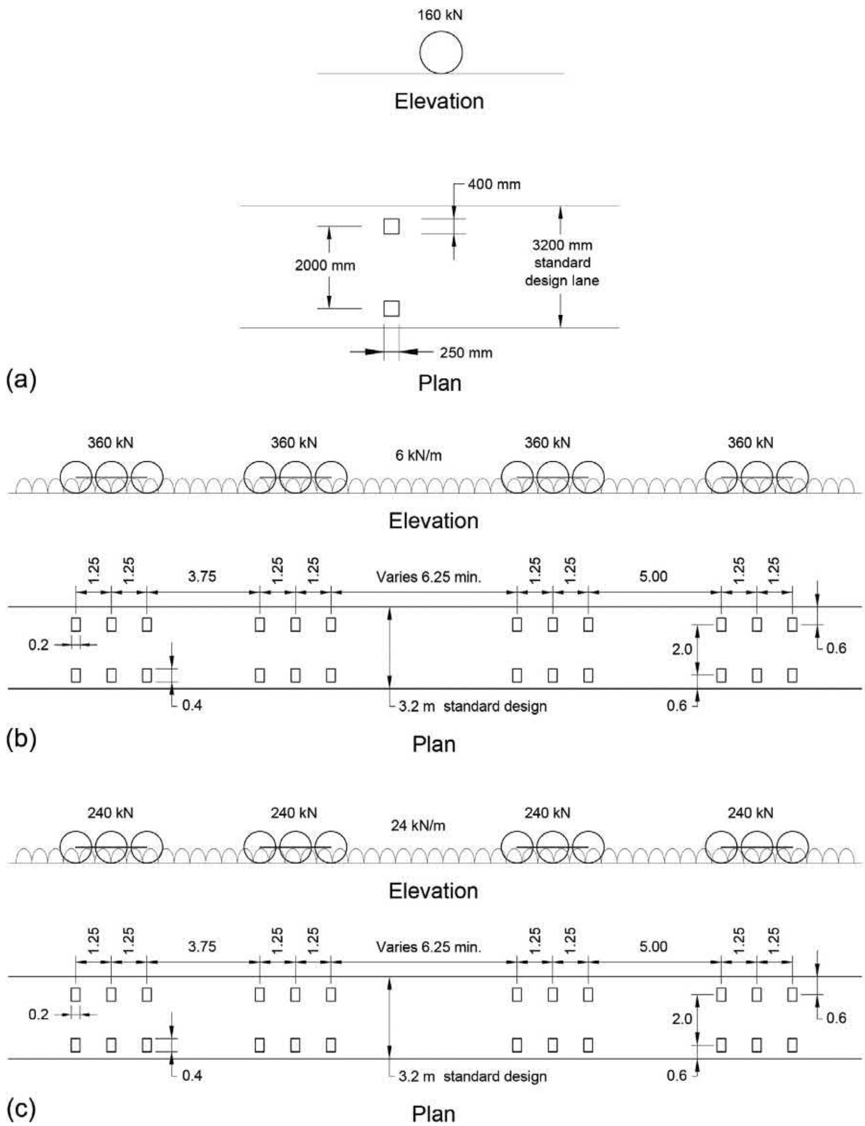

Figure 2.5 AS loading Schemes (AS5100, 2017): (a) AS5100.2 W80 wheel load and A160 axle load configuration; (b) AS5100.2 M1600 moving traffic load configuration; (c) AS5100.2 M1600 stationary traffic load configuration.

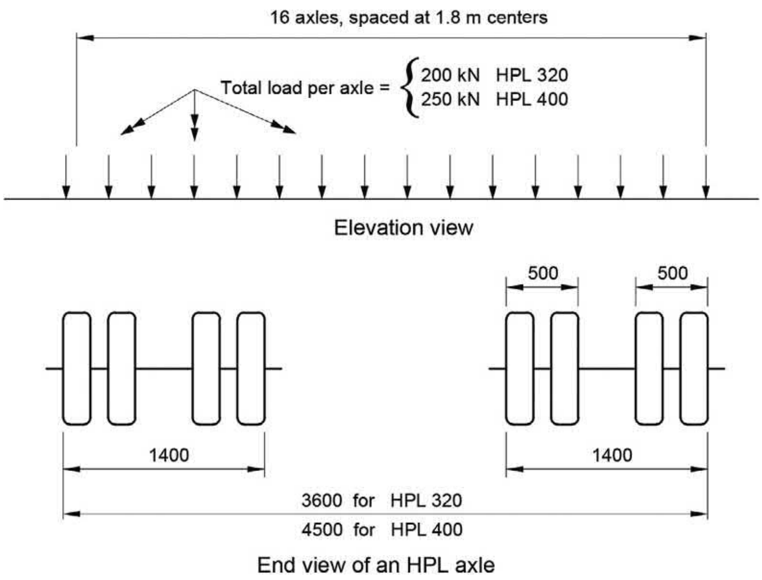

Figure 2.6 AS loading schemes for heavy load platform (AS5100, 2017).

either continuous or discontinuous to produce the most adverse effect. The truck variable length is to be adjusted to produce a most adverse effect.
- S1600 stationary load, comprising the combination of axle group and lane UDL (Figure 2.5), applied in a similar fashion to the M1600 load.

In addition, where required by the authority, bridges are to be designed for heavy load platforms (HLPs). There are two forms of these loads: the HLP 320 load and the HLP 400 load (Figure 2.6). These loads are described as follows:

- 16 rows of axles spaced at 1.8 m center to center
- Total load per axle: 200 kN for the HLP 320 and 250 kN for the HLP 400
- Eight tires per axle row
- Overall width of axles: 3.6 m for the HLP 320 and 4.5 m for the HLP 400
- Tire contact area: 500 mm wide × 200 mm long for each set of dual wheels
- Tire contact areas centered at 250 mm and 1150 mm from each end of each axle
- For continuous bridges, the load is considered as separated into two groups of eight axles, each with a central gap of between 6 m and 15 m, chosen to give the most adverse effect.

AS5100 (2017) defines the standard design lane width as 3.2 m, with the number of design lanes calculated as $n = b/3.2$ (rounded down to the next integer), where n is the number of lanes and b is the width between traffic barriers, in meters. These lanes are to be positioned laterally on the bridge to produce the most adverse effect.

4. Traffic measurement

Traffic measurements are essential for the proper management of highway structures. The roads and bridges are designed to meet transportation demands for a specific number of vehicles and magnitude of load. Therefore, the actual traffic has to be monitored and evaluated. The highway system is a significant part of the national investment, and the condition of roads and bridges is important for an efficient transportation and economic growth. Accurate traffic measurement is required to adequately assess the traffic-induced load effects.

The two major types of vehicle measurement systems are static and in motion. A static system can weigh the truck loads when vehicles are not in motion. In practice, the major limitations of a static system are that it can be applied only to selected vehicles, it takes longer time to measure load, and the driver is fully aware of the measurement. On the other hand, weigh-in-motion (WIM) systems enable the measurement of the truck loads in moving traffic. It is a powerful tool that enables a massive traffic database to be recorded. Static and WIM data collection and analysis are explained in more detail in the next section.

4.1 Static scales

Static scales can measure only nonmoving vehicles or vehicles moving at a very low (crawling) speed. Static scales are considered be to accurate weighing methods and can be used as a reference point while testing and calibrating other weighing systems.

Trucks can be measured statically at truck weigh stations. A station has built-in static scales that can weigh standing or very slow-moving vehicles. Truck weigh stations are located off the road, typically off major highways. All the trucks must exit the road and go through the scales, which are monitored by a police operator.

Another static measurement method uses portable scales, where each wheel has to be measured individually. It requires an operator and a driver, as the truck has to move after each axle is measured. The measured truck has to be parked on a flat surface for about one hour, and it can cause an obstruction to traffic. However, a portable scale can be moved from place to place because it is easy to set up.

4.2 Weigh-in-motion systems

WIM data is an important source of information to evaluate traffic-induced load effects. Today there are many WIM stations in operation all over the world. The traffic is recorded on a continuous basis, which provides a database that can be used in live load model development for bridge design and evaluation. However, the recorded data can contain errors that have to be identified and eliminated. Therefore, the WIM data is checked by specially developed quality-control (QC) procedures to ensure a reliable traffic data analysis. There are numerous studies related to quality checks of the WIM data that are adopted by many US state agencies (Ramesh Babu et al., 2019), (Elkins and Higgins, 2008), (Southgate, 1990), (Ramachandran et al., 2011), (Qu et al., 1997), (Quinley, 2010), (Kulicki et al., 2015). However, there is no universal documented QC procedure. The QC criteria usually include a completeness check to identify any missing data, in case some days and months are not available due to system malfunction. Additionally, the logical tests are used to capture errors, including axle weight tolerances, minimum and maximum weight, axle spacing, etc. QC checks also include the verification of sensor operational problems.

Another method for weighing trucks in motion is a bridge WIM (B-WIM), which collects specific traffic data for the particular bridge. The bridge is treated as a big scale, measuring traffic parameters. The bridge is equipped with the measuring instruments placed under a deck so as not to interfere with the flow of traffic. The weight of a passing vehicle is calculated based on recorded deformations (strain) and adjusted for the thermal material deformations. B-WIM systems allow for the measurement of strain, load distribution factors, and dynamic load factors. They can also be used to supplement bridge inspection and verification of the minimum live load carrying capacity. A B-WIM system has to be calibrated to specific material parameters and bridge-specific sensors.

A portable B-WIM system is an efficient tool for selectively measuring site-specific traffic. A few days' measurements can provide an overview of the traffic-induced load effects acting on the bridge. This overview verifies the vehicle overload—the number of vehicles that can cause excessive overstress and fatigue damage to the bridge.

The WIM system is an excellent source of information that does not require vehicles to stop while they are being weighed. Compared to other systems, it reduces the cost and effort and increases the efficiency and flexibility of traffic measurement. The resulting massive WIM data is needed for the development of the live load model for bridge design and evaluation. However, the collected large WIM data may contain the incorrect records that should be eliminated from the analysis. This is particularly important because the WIM data serves as a basis for the development of design live load used for design and evaluation of existing bridges. The live load should not be underestimated or overestimated. Underestimation can cause premature damage to bridges and roads, and overestimation can result in a significant cost increase.

Recently, a study in Alabama was conducted to check and compare the accuracy of weight measurement systems, including portable scales, truck weigh stations, WIM, and B-WIM (Stawska et al., 2021). Approximately 150 trucks were measured using static and dynamic weighing systems, and the results were compared to assess the accuracy. The conclusion was that all four systems produce the results that are within the required and expected accuracy. Figure 2.8 presents the cumulative distribution functions (CDFs) of the gross vehicle weight (GVW) plotted on the normal probability paper to compare GVW measured by four different techniques. The construction and use of the normal probability paper is presented in textbooks (e.g., Nowak and Collins 2013). The vertical axis is the probability of exceeding the corresponding value of GVW on the horizontal axis. A normal distribution is represented as a straight line on the normal probability paper. The results show that the accuracy of all four systems is comparable and acceptable to use for the live load modeling.

5. Analysis of traffic-induced effects

Bridge load carrying capacity has to exceed the effect of expected loads—i.e., moments and shears. Therefore, the evaluation of bridges requires the knowledge of live load effect. Traffic-induced loads can cause damage to a bridge by overstress and fatigue, which can accelerate corrosion and increase the crack width. To assure bridge safety, the load-carrying capacity has to be systematically inspected and evaluated. The traffic-induced load effects depend on many parameters, including bridge span length, vehicle GVW, axle loads, axle spacings, truck traffic volume (ADTT), number of vehicles on the bridge (multiple presence), etc. The load effects on bridges are considered in terms of bending moment and shear force.

5.1 Truck traffic parameters

The traffic composition is strongly site specific and can vary significantly. Therefore, the development of live load model that accurately represents the traffic is challenging. The WIM database plays a key role in the development of the live load model required for reliability-based calibration—i.e., calculation of load and resistance factors (partial safety factors). The WIM data includes detailed information about vehicle weight and configuration. Data is recorded for every vehicle, including a detailed description of vehicle configuration, vehicle class, measurement date and time, occupied lane, direction, and moving speed, as well as individual axle weights and axle spacings.

The comparative analysis of GVW and first-axle weight was conducted for US and European WIM data. Figure 2.9 shows CDF of GVW for available US databases for Alabama; California, Washington, D.C.; Florida; Montana; Rhode Island; South Dakota; and several European countries, including Slovakia, Poland, Slovenia, Netherlands, and Czech Republic. Figure 2.9 shows the variation of GVW within the United States and selected European countries. The overall weight of the vehicles is higher in Europe than in the United States. Figure 2.10 presents the distribution of the first-axle weight distribution, and the upper tail of the US data shows larger axle weight than for Europe. The collection of truck traffic parameters is essential to assess the load effects necessary for bridge live load development.

5.2 Load effects

Bridge load effects are bending moment and shear force, which can be calculated using influence lines. From the WIM database, which provides detailed information about the axle weight and spacings, the load effects can be assessed for any vehicle. As a truck passes over a bridge, it generates a bending moment at each point along the span, and this moment changes with the moving truck. The influence line analysis allows to determine the critical position of the vehicle that causes the maximum load effects.

Example load effects calculated for the United States and Europe are shown in Figure 2.11. The moment was computed for simply supported bridges with a span length of 27 m (90 ft). Moments calculated for European truck traffic are higher, but this may depend on the vehicle configurations. The moment effect depends on heavy axle groups and GVW, and hence, bending moment is more significant in closely spaced heavy axle groups.

Figure 2.12 presents the CDF plot of shear forces calculated for simply supported bridges with a span length of 27 m (90 ft). The shear forces computed for South Dakota differ significantly from those in other US states. Moreover, the shear effects caused by European WIM trucks are larger than those recorded in the United States. The live load effects can be influenced by heavier single axles or, in longer spans, by axle groups.

5.3 Fatigue

Traffic-induced loads may cause damage to a bridge by fatigue of materials. Every passage of a truck over a bridge creates one or more stress cycles in the structural components, which results in an accumulation of fatigue damage over time. Each passage of a heavy truck consumes a certain amount of the fatigue life of the bridge. Bridges are subjected to variable amplitude stress cycles. A cumulative damage theory defines the effective stress range from variable amplitude stress cycles. The Palmgren–Miner rule (Miner 1945) provides a rational method to account for variable amplitude stress cycles. The Palmgren–Miner rule accounts for the cumulative damage from a spectrum of applied stress ranges of variable amplitude. Using the Palmgren–Miner rule, an equivalent constant amplitude stress range can be calculated.

In the current bridge design code AASHTO LRFD 2020, the stress range is calculated for a code specified AASHTO fatigue design truck to prevent fatigue cracking caused by accumulation of the damage from cyclic truck loading. The AASHTO fatigue design truck is 0.80 of the design truck HL-93 (AASHTO LRFD, 2020), and it is intended to represent truck traffic.

5.4 Overloaded vehicles

Traffic consists of legal and illegal standard vehicles and permit vehicles. Legal limits for regular trucks are imposed to ensure safety of the transportation infrastructure. In the United States, federal law prevents states from setting vehicle weight limits on interstate highways that deviate from established federal weight limits. This means that, for interstate highways, states are subject either to the standard federal weight limits or to state-specific grandfathered limits.

In general, bridge design and assessment codes specify a notional load model for regular traffic, which represents the extremes of standard vehicle loading. Vehicles seeking permits are compared to abnormal vehicles that the bridge has been found to have the capacity to carry.

Permit vehicles are those that require a permit because, according to the regulations on standard vehicles, they are oversized, overweight, or both. Permit vehicles need to follow the limitations specified in their permit, restricting gross vehicle weight, single-axle weight, and group-axle weight. In the United States, states have their own policies on issuing permits but must follow federal rules. Permits allow vehicles of specific configurations and sizes to exceed the standard vehicle size and weight limitations. Permits can be issued for single or multiple trips—usually referred to as special and routine permits, respectively. The permit may have restrictions on designated routes, the number of trips, times of operation, and the necessity (or lack thereof) of escort vehicles. With or without permits, illegal overloaded vehicles belong to an unanalyzed portion of bridge traffic load that is more likely to create an extreme loading case.

Operation of overloaded truck traffic needs to be controlled, since the damage attributed to heavy vehicles is much more extensive and can cause premature bridge consumption. The WIM data can be used to detect overloaded vehicles and assess their effect on infrastructure. Also, the permit vehicles' number and type should be monitored to maintain safety of bridges and roads.

The comparison on the GVW of regular WIM and permit vehicles recorded in Florida is shown in Figure 2.13. The impact of overloaded vehicles can be significant; therefore, monitoring, law enforcement, and bridge inspection are essential.

6. Environmental effects

6.1 Wind

Wind forces must be considered in the design of bridges in two different conditions: during operations (when the bridge is completed) and during construction. Wind loads depend on geometrical form, size, and on constituent material of the structure. Design codes and standards provide numerical values and procedures to determine the wind loads to be applied to structures. The entirety of Chapter 3 of this text is dedicated to wind loads.

6.1.1 Eurocode

EN 1991-1-4 (2005), "Part 1-4: General Actions—Wind actions," provides guidance to determine the characteristic wind actions over the entire structure, some parts of the structure, or a single member of the structure. This code provides a platform to determine the wind action acting on any land-based structures. Eurocode 1 is used as a guide for almost all member countries. Therefore, it is recommended to use the National Annex (NA). The NA provides specific data and methods based on the considered country's geological, topographical, and meteorological characteristics. The current version of the code can only be used for the structures with span lengths of not more than 200 m or heights of 200 m.

6.1.2 AASHTO

According to AASHTO standards, wind loads are assumed to be uniformly distributed over the area exposed to the wind. The exposed area is a sum of the areas of all components—including the floor system, railings, and sound barriers—as seen in elevation taken perpendicular to the assumed wind direction. This direction is selected to determine the extreme force effect in the structure or its components. Areas that do not contribute to the extreme force effect under consideration can be neglected in the analysis. In addition to wind load on the exposed areas of the bridge, the wind pressure is also applied to the vehicles. In AASHTO LRFD (2020), wind load on a vehicle is represented by a concentrated force applied 1.8 m above the wearing surface. Base design wind velocity varies significantly due to local conditions. For small and low structures, the wind usually does not have a significant impact. For large, tall bridges and sound barriers, however, the local conditions should be considered. The pressures on the windward and leeward sides are to be taken simultaneously in the assumed direction of the wind. Typically, a bridge structure should be examined separately under wind pressures from two or more different directions in order to determine if windward, leeward, or side pressure produces the most critical load on the structure.

6.2 Temperature

Two forms of temperature effect can be considered in bridges:

- Overall temperature changes are to be considered in the design of moving bearings and in the selection of their location.
- Differential temperature effects may occur such that at a particular time, the temperature at one point in a structure is not the same as at another, and the temperature difference may cause locked-in stresses and possible failure.

Codes and standards specify temperature changes and variations to be considered during the design stage. If a bridge deck is free to expand, the variation of temperature ΔT implies deformations in the longitudinal direction that have to be accommodated by the expansion joints. Such deformation effects can be calculated using the following equation:

$$\Delta l = \alpha T^* l^* \Delta T$$

where αT is the thermal expansion coefficient, l is the length of the considered element, and ΔT is the uniform temperature variation. Concerning overall temperature changes, in a single-span bridge, it is conventional to permit longitudinal, horizontal movement in the bearings at one end of a span so that the bridge can expand or contract freely under the action of temperature changes or other related effects, such as concrete shrinkage or creep, and elastic strains in the structure under load. They also allow for foundation movement. If a multispan bridge is continuous over its full length or over a number of spans, these longitudinal movements can add up at one location. Alternatively, if the bridge consists of a number of simply supported spans, there can be a moving bearing at one end of each span (O'Connor and Shaw, 2000). Concerning differential temperatures, these can cause damage to bridges (e.g., the major Newmarket Viaduct in Auckland, New Zealand, in the period following its completion in 1966); see Buckle and Lanigan (1971), Leonhardt et al. (1965), Priestley (1972), and White (1979). Temperatures may vary within a cross section: if the variation is linear and the structure is statically determinate, then it can be adopted a deflected shape without the development of stresses due to these temperature differences. If either of these conditions is not satisfied, then stresses can develop due to temperature. These stresses can take the form of longitudinal direct stresses. For example, in a bridge continuous over three spans, it can be expected that the temperatures in the morning in the upper flange are higher than in the lower flange. If the structure were freed from its central piers, these temperatures, when considered alone, would cause the girder to rise. However, it is, in fact, restrained from doing so, and additional downward reaction components are applied to the structure at its intermediate supports. Differential temperatures of this kind can therefore tend to cause restraint tensile stresses in the lower flange. This may not be a problem at the supports themselves, but they will add to other design stresses at midspan. Not only that, but the hold-down reactions developed at the intermediate piers will cause vertical end reactions that add to the end shears in the members. The combination of these effects—the effects of nonlinearity in the temperature distributions and the effects of restraint forces—may cause cracking in a concrete structure and possibly greater distress as well (O'Connor and Shaw, 2000).

6.3 Snow

Design values of the snow load are provided in codes and standards. The designer can consider additional load combinations for greater safety if the region in which the bridge is built is subjected to heavy snowfall.

6.4 Earthquakes

Earthquake events in the vicinity of an existing bridge structure can cause permanent failure. Not all regions are subjected to seismic risk; however, many countries have to face this problem over time. Codes and standards providing procedures for the design and evaluation of bridges with regard to earthquakes are becoming a sort of nightmare for bridge designers due to useless and long procedures to gain results. However, often a simple elastic design procedure can be adopted. The most damaging excitations are horizontal motions in the bridge's longitudinal and transverse direction; these can often lead to a partial collapse (e.g., a single span falling down), bearing damage, abutment and pier damage, or a complete collapse. Seismic devices are used to maintain the superstructure and the structure as a whole in service and during and after a strong earthquake, as discussed in Section VII Bridge Components, chapter 20. In particular, structural details are very important in designing an earthquake-resistant structure.

7. Dynamic amplification

The dynamic load effects of bridge structures include the following main aspects:

- Impact: the maximum vertical loads induced by a moving load will often exceed those produced by an equivalent static load. This is commonly called Impact where I¼(impact factor) defined as the ratio of the additional load (total dynamic minus static) divided by the equivalent static load; experimental studies in the past have revealed the common values of the impact factor (Figure 2.7). In Eurocode, dynamic load is included in static live load, so there is no separate load component to be considered. In AASHTO (2020), dynamic load is specified as 33% of the design truck's live load effect, with dynamic load applied to the uniformly distributed lane load. Extensive field measurements confirm that the dynamic load factor (defined as percentage of static live load) decreases for heavier vehicles, and it is less than 20% for a single vehicle and less than 10% for two trucks side by side (Nassif and Nowak, 1995, 1996; Kim and Nowak, 1997). In the Canadian Highway Bridge Design Code (2014), dynamic load is specified as 25% of static live load.

- Braking/accelerating vehicles: Longitudinal loads can be applied by braking or accelerating vehicles.
- Transverse horizontal centrifugal forces: These forces are expressed by $mV2/R$, where m is the mass of a body moving with tangential velocity V around a circle of radius R. Transverse horizontal centrifugal forces relate to a curved bridge, or when a vehicle changes its direction of movement.
- Earthquake effects.

8. Bridge redundancy

Bridge redundancy can be defined as a bridge structural system's capability to carry loads after one of the structural components (e.g., a girder) reaches capacity or if there is damage to or failure of one or more of its components (AASHTO, 2013). There are three types of redundancy: load path redundancy, structural redundancy, and internal redundancy. A component is considered a load path redundant if an alternative and sufficient load path are determined to exist. The alternative load paths must have sufficient capacity to carry the load redistributed to them from an adjacent failed component. A component is considered structurally redundant if its boundary conditions or supports are such that failure of the component merely changes the boundary or support conditions but does not result in the collapse of the superstructure. Internal redundancy is when a structural component has alternative and sufficient load paths existing within the component itself. For example, a riveted steel component connection is considered internally redundant if it has multiple plies.

9. Conclusions

Consideration of loads is very important during the design stage of a bridge; however, it is mostly considered as a routine step of the project. Apart from a detailed analysis of live loads and other types of loads, it is recommended to evaluate the actual site-specific loads. This is a crucial issue, as magnitude of real traffic loads is often larger than the code-specified traffic loads. Traffic loads should be revisited in design codes, and in particular, this applies to highway loads—and, to a less extent, to railway loads—that are more closely checked by the managing authorities. Although each country has legal restrictions on the vehicle weight and geometries, law enforcement is often not effective (O'Connor and Shaw, 2000). Heywood (1992) reported a study

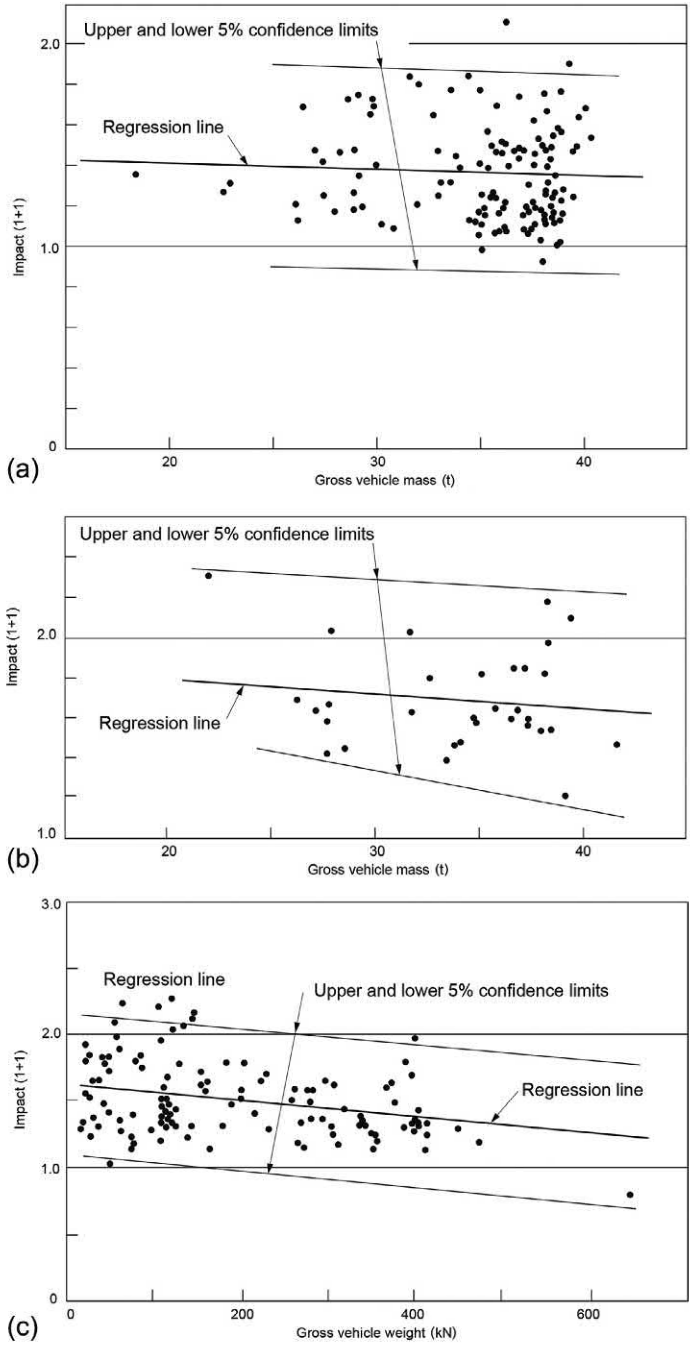

Figure 2.7 Values of impact, I + 1: (a) First impact study of Six Mile Creek Bridge (Pritchard, 1982; O'Connor and Pritchard, 1985); (b) second impact study of Six Mile Creek Bridge (Pritchard, 1982; O'Connor and Pritchard, 1985). (c) Six Mile Creek Bridge (Chan, 1988; Chan and O'Connor (1990).

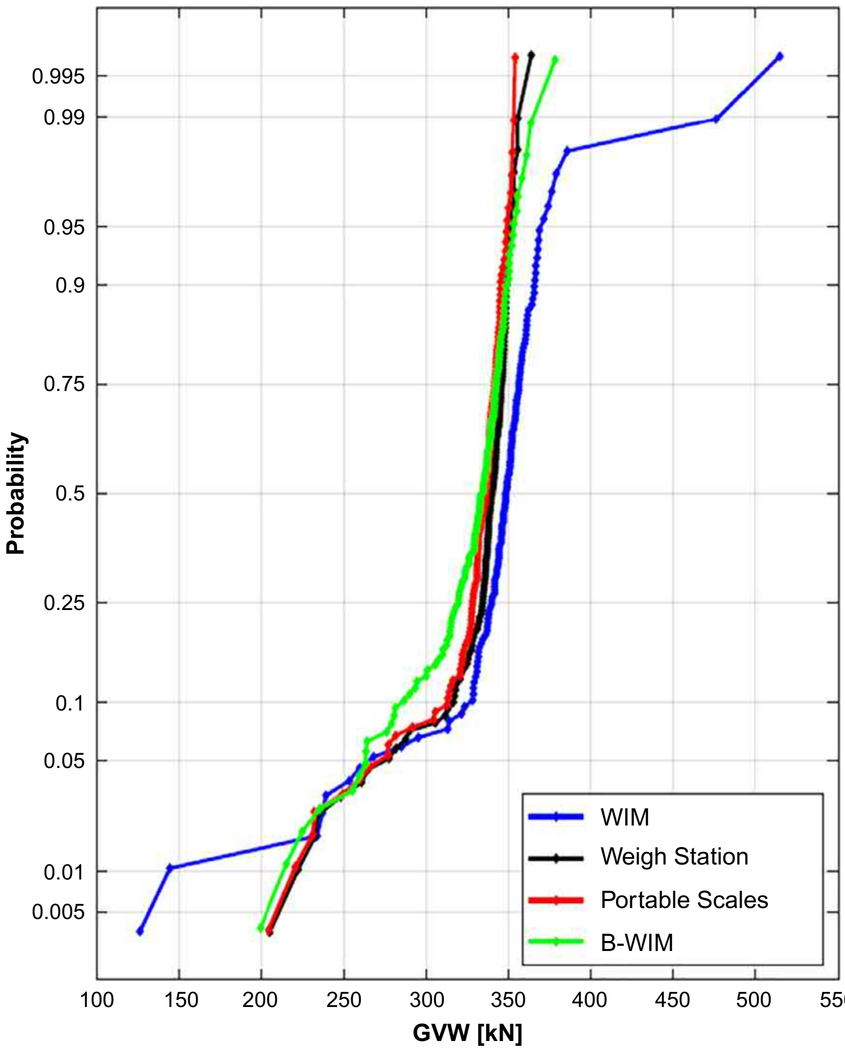

Figure 2.8 CDF of GVW measured by four different measuring systems.

of Australian road traffic loads, with measured values of average extreme daily axle loads for various axle groups, for two classes of sites. The corresponding legal limits for the complete axle groups are (i) single axle–steer 6.0 t (58.8 kN); (ii) tandem–steer 11.0 t (53.9 kN per axle); (iii) tandem–nonsteer 16.5 t (80.9 kN per axle); and (iv) tri-axle group 20.0 t (65.4 kN per axle). The ratios of measured values to legal limits (short, medium, and long spans) were (1.29, 1.14), (1.13, 1.09), (1.26, 1.27), and (1.24, 1.22) for these four-axle configurations. As can be seen, all the categories were exceeded, which agrees with what has been reported by the recent WIM studies (FHWA, 2007). Therefore, for example, bridges are subjected to greater damage than

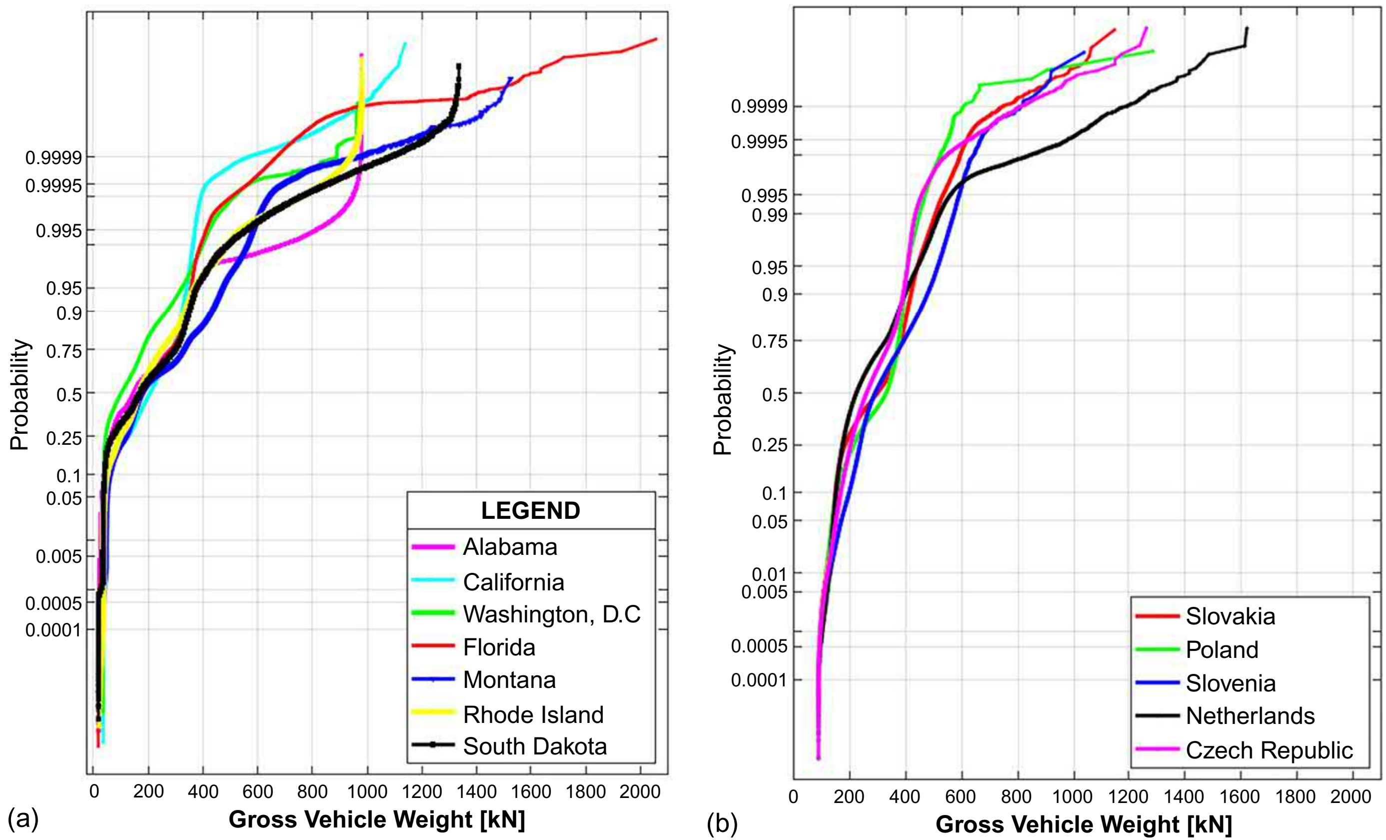

Figure 2.9 CDF of GVW measured in (a) the United States and (b) Europe.

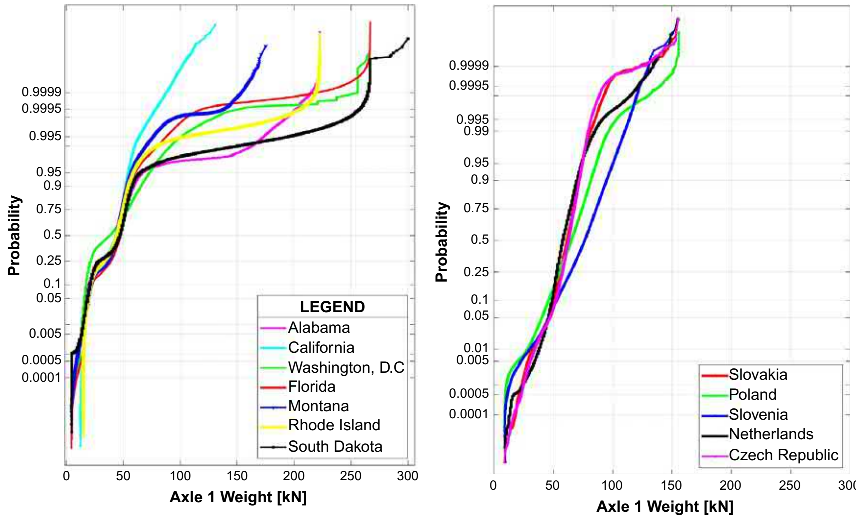

Figure 2.10 CDF of axle load measured in (a) the United States and (b) Europe.

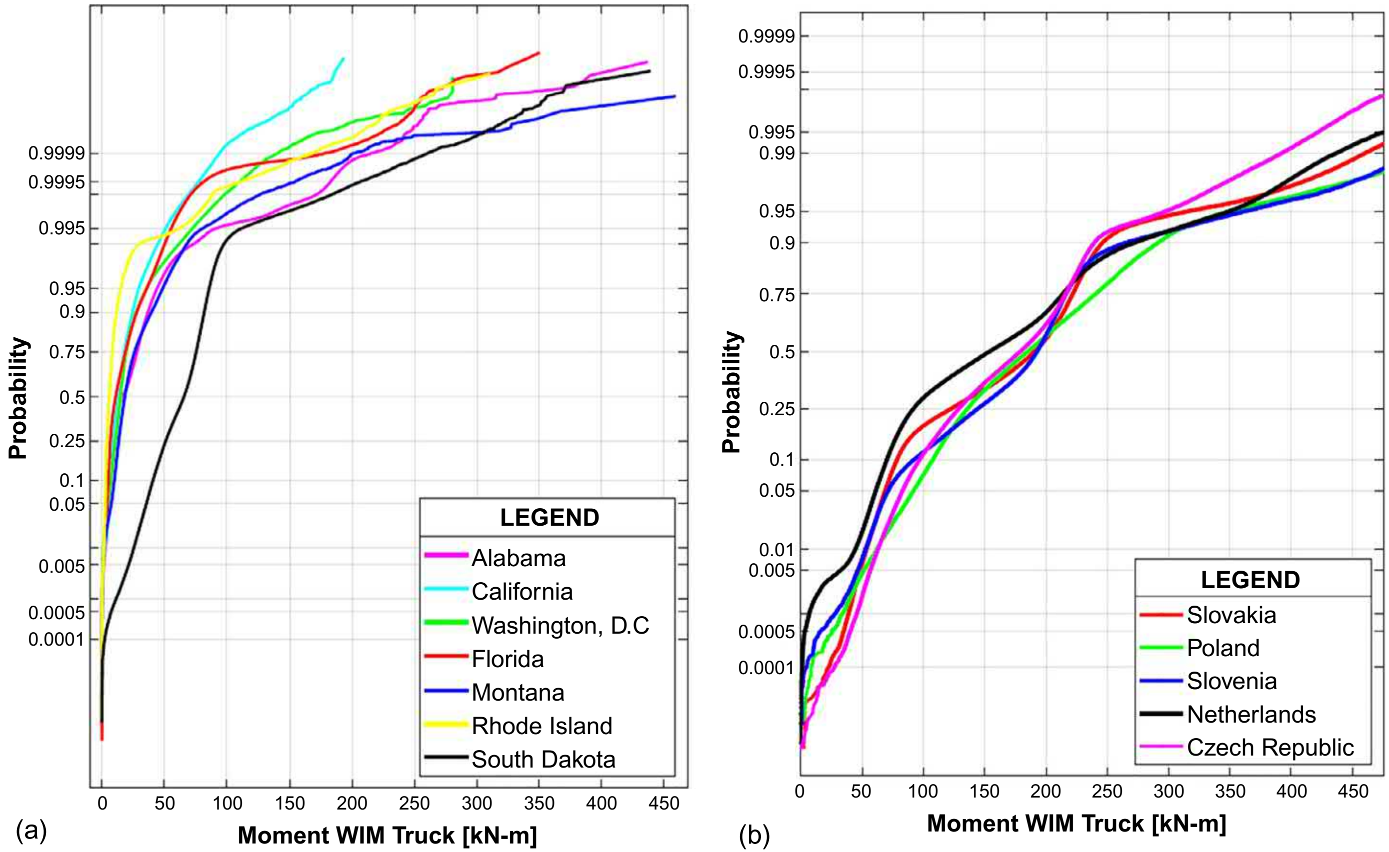

Figure 2.11 CDF of bending moment effect on simply supported bridge with span length 60 ft. in (a) the United States and (b) Europe.

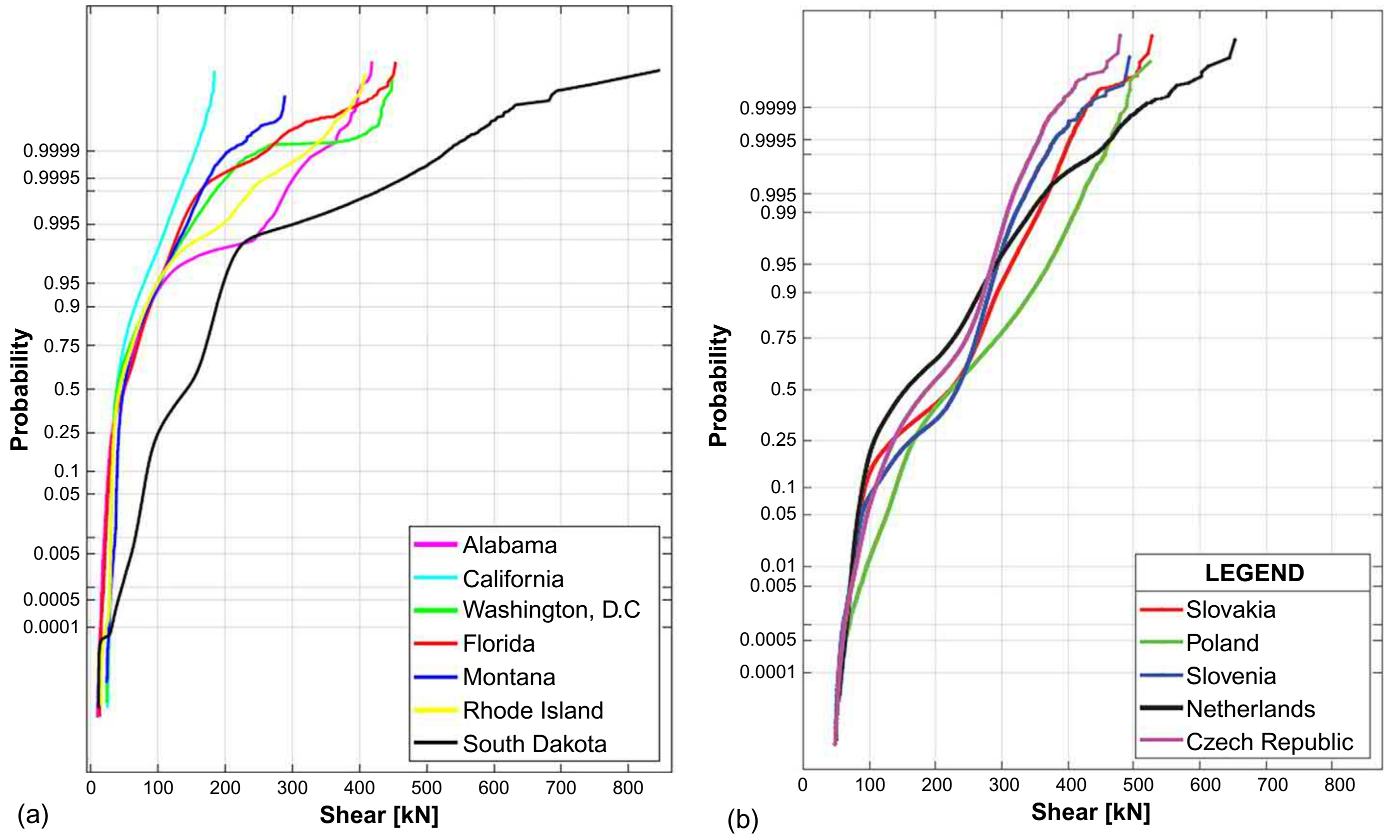

Figure 2.12 CDF of shear effect on simply supported bridge with span length 60 ft. in (a) the United States (b) and Europe.

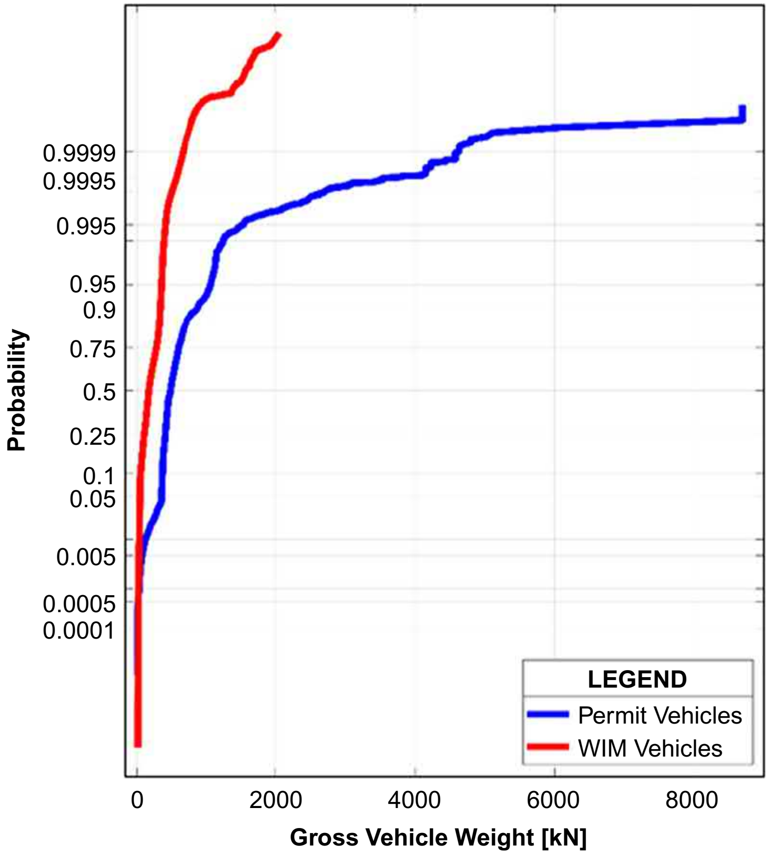

Figure 2.13 CDF of GVW for permit, and WIM traffic.

analytically predicted in the fatigue evaluation performed during the design stage and, of course, to premature deterioration. For this reason, there are significant costs in the use of increased design live loads. However, prior to introduction of more specific changes, it is necessary to perform a cost analysis and then consider three alternatives:

(a) Existing load limits stay as they are, so as to safeguard existing bridges.

(b) Load limits are increased if it is perceived that older design procedures have resulted in bridges with a sufficient reserve of strength.

(c) Economic benefits of the use of heavier vehicles justify the construction of new bridges to a higher standard, accompanied by a program for the strengthening of existing bridges.

References

AASHTO, 2013. Manual for Bridge Evaluation, Second Edition with 2015 Interim Revisions. American Association of State Highway and Transportation Officials, Washington, DC.

AASHTO, 2014. AASHTO LRFD Bridge Design Specifications. American Association of State Highway and Transportation Officials, Washington, DC.

AAHSTO LRFD. (2020). "AASHTO LRFD Bridge Design Specification, 9th Edition." American Association of State Highway and Transportation Officials, Washington D.C.

AREMA, 2013. Practical Guide to Railway Engineering. AREMA–American Railway Engineering and Maintenance-of-Way Association, Lanham, MD.

AS5100, 2017. Australian Standard (AS) 5100, Bridge Design. Department of Main Roads, Road Planning and Design Manual, Sydney, Australia.

Babu, A.R., Iatsko, O., Nowak, A.S., 2019. Comparison of bridge live loads in US and Europe. Struct. Eng. J. 29, 84–93. Taylor and Francis Online.

Buckle, I.G., Lanigan, A.G., 1971. Transient thermal response of box girder bridge decks. In: Third Australasian Conference on the Mechanics of Structures and Materials, Auckland, New Zealand.

CSA S6. (2019), *"Canadian Highway Bridge Design Code, 12th Edition."* Canadian Standard Association.

Canadian Standards Association, 2006. Canadian Highway Bridge Design Code. Mississauga, Ontario, Canada.

Chan, T.H.T., 1988. Highway Bridge Impact. PhD thesis, University of Queensland, Brisbane, Australia.

Chan, T.H.T., O'Connor, C., 1990. Wheel loads from highway bridge strains: field studies. J. Struct. Eng. 116 (7), 1751–1771.

Cohen, H., 1990. Truck Weight Limits: Issues and Options, Special Report 225. Trans. Res. Board, National Research Council, Washington, DC.

Danish Road Directorate, 1996. Calculation of Load-Carrying Capacity for Existing Bridges. Guideline Document, Report 291. Ministry of Transport, Denmark.

Elkins, L., Higgins, C., 2008. Development of Truck Axle Spectra from Oregon Weigh-in-Motion Data for Use in Pavement Design and Analysis.

EN 1991-1-4, 2005. Eurocode 1: Actions on Structures—Part 1–4: General Actions—Wind Actions. European Committee for Standardization (CEN), Brussels, Belgium.

EN 1991-2, 2003. Actions on Structures—Traffic Loads on Bridges. European Committee for Standardization (CEN), Brussels, Belgium.

Federal Highway Administration (FHWA), 2007. Effective Use of Weigh-in-Motion Data: The Netherlands Case Study. U.S. Department of Transportation, Washington, DC.

Heywood, R.J., 1992. Bridge Live Load Models from Weigh-in-Motion Data. PhD thesis, University of Queensland, Brisbane, Australia.

Highways Agency, 2006. Design Manual for Roads and Bridges—Highway Structures Inspection and Maintenance. vol. 3. Sec. 4, London.

Iatsko, O., Nowak, A.S., 2020. Re-visited live load for simple span bridges. ASCE J. Bridge Eng. in print.

Kim, S.-J., Nowak, A.S., 1997. Load distribution and impact factors for I-girder bridges. ASCE J. Bridge Eng. 2 (3), 97–104.

Kulicki, J.M., Wasser, W.G., Mertz, D.R., Nowak, A.S., 2015. Bridges for Service Life Beyond 100 Years: Service Limit State Design. Transportation Research Board, Washington, DC.

Leben, T., Hirt, M., 2012. Steel Bridges: Design and Dimensioning of Steel and Steel-Concrete Composite Bridges. EPFL Press, Lausanne, Switzerland.

Leonhardt, F., Kolbe, G., Peter, J., 1965. Temperature differences endanger prestressed concrete bridges. Beton Stahlbetonbau 60 (7), 231–244.

Nassif, H., Nowak, A.S., 1995. Dynamic load spectra for girder bridges. Transp. Res. Rec. 1476, 69–83.

Nassif, H., Nowak, A.S., 1996. Dynamic load for girder bridges under normal traffic. Arch. Civ. Eng. XLII (4), 381–400.

Network Rail, 2006. Structural Assessment for Underbridges. Guidance Note, London.
Nowak, A. S., and Collins, K. R. (2013). Reliability of Structures, Second Edition. CRC Press, Taylor and Francis Group.
O'Connor, 1971. Design of Bridge Superstructures. Wiley, New York.
O'Connor, C., Pritchard, R.W., 1985. Impact studies on a small composite girder bridge. J. Struct. Div. 111 (3), 641–653.
O'Connor, C., Shaw, P.A., 2000. Bridge Loads. Spon Press, Taylor and Francis Group, New York.
Priestley, M.J.N., 1972. Temperature gradients in bridges: some design considerations. N. Z. Eng. 27 (7), 228–233.
Pritchard, R.W., 1982. Service Traffic Loads on Six Mile Creek Bridge, Queensland. MEngSc thesis, University of Queensland, Brisbane, Australia.
Qu, T., Lee, C.E., Huang, L., 1997. Traffic-load forecasting using weigh-in-motion data. Work 987, 6.
Quinley, R., 2010. WIM Data Analyst's Manual. FHWA Office of Pavement Technology, Washington, DC.
Ramachandran, A.N., Taylor, K.L., Stone, J.R., Sajjadi, S.S., 2011. NCDOT quality control methods for weigh-in-motion data. Public Works Manag. Policy 16 (1), 3–19.
Societe' Suisse des Ingenieurset des Architects (SIA), 2011. SIA 269: Bases pur la Maintenance des Structures Porteuses. Zurich, Switzerland.
Southgate, H.F., 1990. Estimation of Equivalent Axleloads Using Data Collected by Automated Vehicle Classification and Weigh-in-Motion Equipment.
Stawska, S., Chmielewski, J., Bacharz, M., Bacharz, K., Nowak, A., 2021. Comparative accuracy analysis of truck weight measurement techniques. Appl. Sci., Multidiscipl. Digit. Publ. Inst. 11 (2), 745.
White, I.G., 1979. Non-linear Differential Temperature Distributions in Concrete Bridge Structures.

This page intentionally left blank

Wind loads

3

K. Kimura
Department of Civil Engineering, Tokyo University of Science, Noda-shi, Chiba, Japan

1. Introduction

Wind loading is one of primary horizontal loads acting on bridges, and its appropriate consideration is necessary to satisfy the design requirements. The dynamic wind effects are also important particularly for long-span bridges, which may induce significant vibrations not only in along wind direction but also in vertical and torsional directions, and they have to be avoided. In this chapter, wind effects on bridges are overviewed, and a typical procedure for wind resistant design of a long-span bridge is described. Design wind speeds and wind loads in codes, some examples of field measurements of full-scale bridges, and research results on stay cable vibrations are introduced.

2. Overview of wind effects on bridges

Wind effects have to be carefully considered in the design of long-span bridges. The effects are generally dynamic because the fluctuation of wind velocities due to turbulence and the vortices formed around the bridge generate a time-varying wind load. The most dominant component of the wind load is often in the along-wind direction, and its maximum value is mostly taken as the design wind load. For relatively flexible bridges with longer spans and cable-supported bridges, considerations of wind-induced dynamic responses are also important because they can be harmful to the safety and serviceability of the bridge.

The collapse of the old Tacoma Narrows Bridge in Washington in 1940 defined an epoch because it clearly demonstrated the fatal impact of wind-induced vibration as recorded in a film. And since then, bridge engineers have been paying attention to the wind-induced dynamic response, which can be hazardous for long-span bridges. Also, buffeting (a random response caused by turbulence in natural wind) has been considered since the pioneering research by Davenport (1962), who originally presented a buffeting prediction procedure based on random vibration theory. In order to predict and analyze wind-induced responses more accurately, extensive research on bridge aerodynamics has been conducted (e.g., Simiu and Scanlan, 1996; Sockel, 1994; Simiu and Miyata, 2006; Holmes, 2007; Stathopoulos, 2007; Jurado et al., 2011; Fujino et al., 2012; Xu, 2013; Tamura and Kareem, 2013). As another example, there is much construction of long-span bridges in China, and active developments of bridge aerodynamics in these projects were introduced in a summary paper (Ge, 2008).

Innovative Bridge Design Handbook. https://doi.org/10.1016/B978-0-12-823550-8.00031-7

In smooth flow (i.e., wind with very small wind velocity fluctuations), mainly two types of wind-induced vibration of bridges occur: vortex-induced vibration and self-excited vibration. For both of these types of vibrations, the response is affected not only by the aerodynamic forces due to approaching flow, but also by the motion of the bridge itself. This is because the flow around the bridge is influenced by the motion of the bridge, and thus, it significantly changes the aerodynamic forces acting on the bridge. Particularly for self-excited vibrations, the response is also called *aeroelastic* because the elastic motion, or vibration, of the structure plays a significant role in generating these forces. Both vortex-induced vibration and self-excited vibration of bridge decks are mainly caused by fluctuating aerodynamic forces due to vortices around the deck, as shown in Figure 3.1 (Kubo et al., 1992) for a shallow rectangular cylinder model where the flow from the left-hand side was visualized by smoke.

The first type of vibration is caused by vortices formed from separated flows around the bridge, and the wind speed range at which it occurs is limited and usually lower than the onset wind speed of self-excited vibration. The dominant motion of vortex-induced vibration is in the across-wind direction, which is vertical for a bridge deck. However, vortex-induced vibration in torsional motion may also occur. The maximum amplitude of the vibration is sensitive to the structural damping, and the amplitude often becomes much smaller if the damping can be increased. The response amplitude is also sensitive to the turbulence intensity. *Turbulence intensity* is defined as the ratio of standard deviation of fluctuating wind velocity to the mean wind speed, and it represents the intensity of wind velocity fluctuation. In many cases, the maximum amplitude of vortex-induced vibration decreases in a flow with larger turbulence intensity. However, there are exceptions, such as a flat hexagonal cross section where the response amplitude even increases slightly in a more turbulent flow (Fujino et al., 2012).

Self-excited vibration is caused by self-excited aerodynamic forces that are generated due to the vibrating motion of the structure itself. The self-excited vibration is further classified into two types depending on the direction of the vibration. Galloping occurs in an across-wind direction, and for a bridge deck, it is in the vertical direction against the horizontal wind. Flutter occurs mainly in the torsional direction, such as

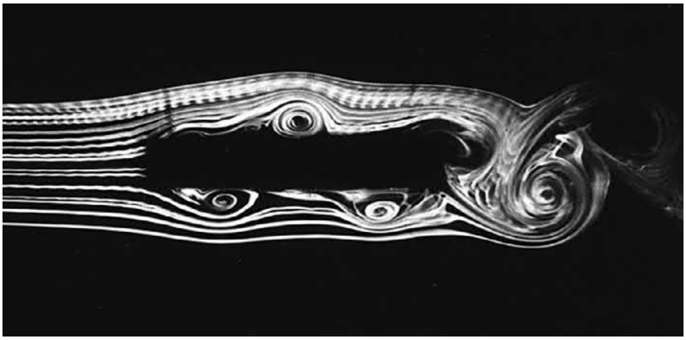

Figure 3.1 Vortices formed around a rectangular cylinder (Kubo et al., 1992).

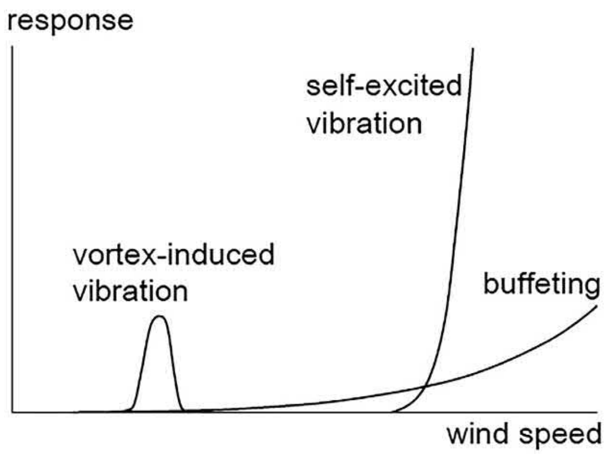

Figure 3.2 Wind-induced vibrations of bridges.

observed in the collapse of the old Tacoma Narrows Bridge. Usually, once the self-excited vibration starts to occur at an onset wind speed, the response amplitude grows more and more if the wind speed is increased. Therefore, it is very important to prevent self-excited vibration for the bridge safety. The allowable design wind speed against the self-excited vibrations is usually set higher than the normal design wind speed by considering the response characteristics that may directly result in the collapse of the bridge. Schematic relationships between the abovementioned responses and wind speed are shown in Figure 3.2.

3. Procedure of wind-resistant design

A typical procedure of the wind-resistant design for a long-span bridge can be briefly summarized as follows. First, the design wind speed and necessary wind characteristics have to be determined. They may be provided in a regional code, but if that is not the case, they should be determined based on meteorological data or simulation of the strong wind speed. Wind speed changes with the bridge's height and profile—that is, a distribution of mean wind speed as a function of height—depend on the surface roughness around the site. Therefore, the height and surrounding roughness of the terrain have to be considered when determining the design wind speed. Then the wind loading due to buffeting is estimated based on buffeting analysis or a simplified formula based on the buffeting analysis. The structure must be confirmed to withstand the maximum response caused by buffeting. Then, when the structure also is considered to be sensitive to dynamic responses other than buffeting, it must be confirmed that the dynamic response occurs neither under the design wind speed nor with an amplitude larger than the allowable one. A simplified judgment as to whether the dynamic response should be considered may be made based on some design rules, such as those found in the United Kingdom (Highways Agency, UK, 2001) or in Japan (Fujino et al., 2012).

4. Design wind speeds provided in design codes

In this section and the next one, descriptions in several codes (EN 1991-1-4:2005, ISO 4354, ASCE Standard ASCE/SEI 7-16, and AASHTO LRFDBDS-9) are briefly introduced. In addition, design rules with respect to the dynamic responses are summarized.

EN 1991-1-4 (European Committee for Standardization, 2010) gives guidance on the determination of natural wind actions for the structural design of civil engineering works. For bridges, it is applicable to those whose spans are not greater than 200 m. Neither bridge deck vibrations from transverse wind turbulence, wind action on cable-supported bridges, nor vibrations in which more than the fundamental mode is important are considered in EN 1991-1-4.

The basic wind speed, v_b, is defined as the 10-min mean wind speed with an annual risk of exceedance of 0.02 (= 2%) at a height of 10 m above flat and open country terrain. The annual risk of exceedance corresponds to a mean return period of 50 years. If necessary, it is modified to account for the directional and seasonal effects. Also, it is modified to account for the effect of terrain roughness and orography. Then, the mean wind speed at a height z above the terrain at the site, $v_m(z)$, which depends on the terrain roughness and orography, is expressed with the basic wind speed as follows:

$$v_m(z) = c_r(z) \times c_o(z) \times v_b, \tag{1}$$

where $c_r(z)$ is the roughness factor and $c_o(z)$ is the orography factor. The roughness factor is given based on a logarithmic profile at a height above the minimum height as follows:

$$c_r(z) = k_r \times ln(z/z_0), \tag{2}$$

where k_r is the terrain factor depending on the roughness length, z_0; z_0 is tabulated with five different terrain categories, from 0 (above a sea or coastal area) to IV (an area in which at least 15% of the surface is covered with buildings with average height exceeding 15 m). In this case, $c_o(z)$ has to be used when the orography (e.g., hills, cliffs, etc.) increases wind speed by more than 5%. Also, the effects of any large and considerably higher neighboring structures must be considered.

The ISO 4354 standard, "Wind Actions on Structures" (ISO, 2009), describes the actions of wind on structures and specifies the methods of calculating wind loads. The peak design wind speed at the site, V_{site}, is given as follows:

$$V_{site} = V_{ref} \times C_{exp}, \tag{3}$$

where the exposure factor, C_{exp}, is determined based on the height above ground level of the structure, the roughness of the terrain, and the topography; and V_{ref} is the maximum wind speed averaged over 3 s referenced to a height of 10 m over flat and open country terrain. V_{ref} for any probability of exceedance in 1 year shall be determined from regionally derived reference wind speeds. The probability of exceedance is determined based on the importance of the structure, and an example of the classification of importance levels is provided. The storm type—such as synoptic storm, tropical cyclone storm, or thunderstorm—has to be appropriately accounted for in a way that is most applicable to both the ultimate limit state and the serviceability design.

In ASCE Standard ASCE/SEI 7-16, "Minimum Design Loads and Associated Criteria for Buildings and Other Structures" (ASCE, 2017), Chapters 26–31 describe wind loads in detail, mainly applicable to buildings. The basic wind speed (which is expressed in terms of 3 s gust speed at 10 m above the ground in open terrain) is provided in maps according to the risk category of the structures, ranging from I (low risk to human life in the event of failure) to IV (in which the failure could pose a substantial hazard to the community). On the maps, special wind regions are shown where unusual wind conditions have to be examined. The same applies for a location in mountainous terrain and gorges. In areas outside hurricane-prone regions, regional climatic data may be used instead of the maps to obtain the basic wind speed if certain conditions are satisfied. In hurricane-prone regions, wind speeds derived from approved simulation techniques may be used instead of the maps, but using regional wind speed data is not permitted. This is because a Monte Carlo simulation model is more appropriate to estimate the hurricane wind speeds of which recurrence rates are much less than non-hurricane wind speeds. Exposure categories shall be determined for the two upwind sectors extending 45° on either side of the selected wind direction. Wind speed-up effects at isolated hills, ridges, and escarpments constituting abrupt changes in the general topography shall be included in the determination of the wind loads when necessary. Finally, velocity pressure is expressed by velocity pressure exposure coefficient, topographic factor, wind directionality factor, ground elevation factor, and the basic wind speed. Tornadoes are not considered in the standard, but considerable information such as on wind speeds, probabilities, and pressures is provided in the commentary.

In AASHTO LRFD Bridge Design Specification (LRFDBDS-9, AASHTO, 2020), the design 3 s gust wind speed is taken from ASCE/SEI 7-10 (ASCE, 2013).

5. Wind loads provided in design codes

In this section, descriptions related to wind loads on bridges from three of the codes described in the previous section are introduced. Also, a few design rules on the dynamic responses of bridges are briefly mentioned.

In EN 1991-1-4 (European Committee for Standardization, 2010), the wind action is represented by a simplified set of pressures or forces whose effects are equivalent to the extreme effects of the turbulent wind. For single-deck bridges with constant depth, guidance of wind actions is provided. When a dynamic response need not be considered, the wind force parallel to the deck width and perpendicular to the span direction (i.e., the x-direction) is expressed as

$$F_{\mathrm{w}} = 0.5 \times \rho \times {v_{\mathrm{b}}}^2 \times C \times A_{\mathrm{ref},x}, \tag{4}$$

where ρ is air density, $A_{\mathrm{ref},x}$ is reference area, and C is the wind load factor and $C = C_{\mathrm{e}} \times C_{\mathrm{f},x}$. Here, C_{e} is the exposure factor that is the ratio of peak pressure at height z and mean pressure caused by v_{b}, and it is expressed as

$$C_e = [1 + 7I_v(z)] \times 0.5 \times \rho \times v_m{}^2(z)/\left(0.5 \times \rho \times v_b{}^2\right), \tag{5}$$

where $I_v(z)$ is the turbulence intensity at height z. A recommended expression of $I_v(z)$ is provided. $C_{f,x}$ represents the force coefficients of bridge decks, and typical values are provided together with the definition of $A_{ref,x}$. Also, recommended values of C are tabulated based on some assumptions for simplicity. Wind forces in the z-direction (i.e., vertical when the deck is horizontal) and y-direction (i.e., along the span) are also described. Wind effects on piers have to be considered as well.

Some information about wind-induced vibration is also provided in EN 1991-1-4. For vortex-induced vibration, empirical formulae of the critical wind speed and largest amplitude are provided, which may be used for bridge members. To determine galloping and flutter, expressions for onset wind speeds are provided, but one should get expert advice when dealing with bridges for which wind-induced dynamic effects are significant. Divergence (i.e., a static torsional instability resulting in huge torsional displacement caused by small torsional rigidity and large aerodynamic moment) is also discussed. For a very-long-span cable-supported bridge or a unique bridge structure with very low torsional rigidity, safety against divergence has to be confirmed. Simple formulae to estimate the dynamic characteristics, such as a fundamental natural frequency, are also provided.

In ISO 4354 (ISO, 2009), equivalent static wind loads that are obtained assuming linear elastic structural behavior are given in two forms:

$$F = q_{\text{site}} \times C_F \times C_{\text{dyn}} \times A_{\text{ref}} \tag{6}$$

$$F = q_{\text{site,m}} \times C_{F_m} \times C_{\text{dyn,m}} \times A_{\text{ref}}. \tag{7}$$

Eqs. (6) and (7) are formulated based on peak and mean wind speed, respectively. In Eq. (6), q_{site} is the site peak dynamic pressure (as discussed next), C_F is a force coefficient, C_{dyn} is a peak dynamic response factor, and A_{ref} is the reference area for force on the overall structure or a part of structure. The site peak dynamic pressure is determined from the regionally derived reference wind speed, V_{site}, as follows:

$$q_{\text{site}} = 0.5 \times \rho \times (V_{\text{site}})^2. \tag{8}$$

In Eq. (7), C_{F_m} is a mean force coefficient, and some examples are provided in the standard. $C_{\text{dyn, m}}$ is expressed as

$$C_{\text{dyn,m}} = C_{\text{dyn}} \times (1 + g_V I_V)^2 \cong C_{\text{dyn}} \times (1 + 2g_V I_V), \tag{9}$$

where g_V is a wind speed peak factor and I_V is turbulence intensity. g_V is defined as

$$V = V_m \times (1 + g_V I_V), \tag{10}$$

where V and V_m are the peak and mean wind speeds, respectively. The approximation on the right side of Eq. (9) is for low turbulence intensity; and $q_{\text{site, m}}$ is the site mean dynamic pressure that is obtained similarly to q_{site} in Eq. (8) based on $V_{site,\,m}$, the mean design wind speed. The dynamic response factors take into account the dynamic action of random wind gusts, fluctuating pressures induced by the wake of the structure, and fluctuating forces induced by the motion of the structure due to wind. Expressions for $C_{dyn,\,m}$ are given based on buffeting analysis, and those for C_{dyn} are derived based on them.

In LRFDBDS-9 (AASHTO, 2020), the wind pressure is given as

$$P_Z = 2.56 \times 10^{-6} V^2 K_Z G C_D, \tag{11}$$

where P_Z is design wind pressure in ksf, V is design 3 s gust wind speed in mph, K_Z is pressure exposure and elevation coefficient, G is gust effect factor, C_D is drag coefficient, and Z is the structure height. The wind pressure is assumed to be uniformly distributed, and the wind load is calculated as the product of the wind pressure and exposed area—that is, the sum of areas of all bridge components as seen in elevation taken perpendicular to the wind direction. For the loads on the substructure from superstructure, skew coefficients may be considered to account for the difference in the load direction. Wind loads on sound barriers and live load, as well as vertical wind load, are specified.

For certain wind-sensitive structures (such as long-span bridges), special supplementary studies are recommended. Wind tunnel tests are often conducted, and standard procedures are briefly given in an annex of ISO 4354 and in ASCE/SEI 7–16. Brief descriptions and design targets are provided in LRFDBDS-9 (AASHTO, 2020).

For the dynamic responses of bridges, more detailed descriptions are given in such documents as in BD 49/01 (Highways Agency, UK, 2001) and a design manual for highway bridges in Japan (Fujino et al., 2012). Simple empirical expressions for the critical wind speeds of flutter, galloping, and vortex-induced response are provided. BD 49/01, "Design Rules for Aerodynamic Effects on Bridges" (Highways Agency, UK, 2001), sets out the design requirements for bridges with respect to aerodynamic effects, including provision for wind tunnel testing. It first provides simple criteria to determine the susceptibility of a bridge to aerodynamic excitation based on the size, mass, natural frequency, and design wind speed. Then the empirical formulae for the critical wind speed and amplitude for vortex-induced vibration, a criterion for buffeting, as well as onset wind speed of galloping and flutter, are given for a number of bridge types. Also, a procedure is specified to estimate the fatigue damage due to vortex-induced vibration. Requirements for wind tunnel tests are given in an annex.

In "Wind-Resistant Design of Bridges in Japan—Developments and Practices," (Fujino et al., 2012), a design manual for highway bridges in Japan is summarized with other bridge related wind codes and their background. The design manual provides empirical formulae for wind-induced responses. To estimate the vortex-induced vibration amplitude, the effects of turbulence intensity of the wind are incorporated.

When the estimated occurrence wind speed of wind-induced vibration is less than the specified design wind speed and the estimated response amplitude is also greater

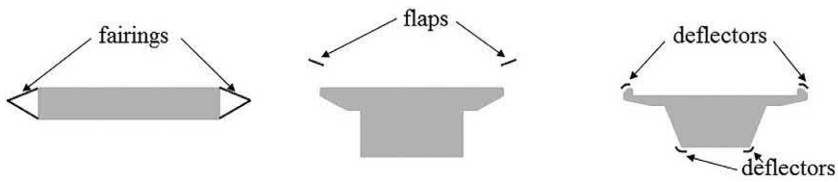

Figure 3.3 Examples of aerodynamic countermeasures.

than the specified allowable amplitude, suppression of the response is necessary. There are two types of countermeasures: one is aerodynamic and the other is mechanical. The aerodynamic countermeasures intend to modify the aerodynamic characteristics by attaching aerodynamic devices such as fairings, flaps, and deflectors (or corner vanes). Schematics of these elements are shown in Figure 3.3. The mechanical countermeasures often increase damping and sometimes increase the stiffness of the structure. Numerous examples of such countermeasures applied for bridges in Japan are listed in Fujino et al. (2012).

6. Wind tunnel test and CFD

Wind tunnel tests have been widely used to predict the wind-induced responses of bridges, as well as to estimate wind loading. Because the bridge model scale is much smaller than the actual bridge, it is difficult to satisfy the Reynolds number similitude, so it is usually disregarded, based on the fact that the flow pattern may not change significantly with the different Reynolds numbers if the bridge and its members consist of sharp edges. But attention has to be paid to a structure with a curved surface or corner cuts because in such cases, the Reynolds number may change the aerodynamic characteristics significantly. Detailed discussions about the similitude and modeling (Tanaka, 1992) and procedures (Fujino et al., 2012) for wind tunnel test of bridges are provided.

It is important to note that just a small difference in the bridge deck cross-sectional shape, such as a modification of the railings, may greatly change the wind-induced response of the bridge. Because it is necessary to have a large-model scale to reproduce the geometric detail and the bridge response to wind is dominantly affected by the response characteristics of the bridge deck, a section model of the bridge deck is often used to check for resistance against dynamic responses. This model is supported with springs so that it represents a dominant response mode of the full bridge. The full bridge model test is also conducted if the three-dimensional effects along the span cannot be disregarded or the wind effects are so significant that a thorough investigation is necessary.

Computational fluid dynamics (CFD) uses computers to determine the flow. Because of the rapid growth of computing capacity and the development of efficient computation schemes, CFD has become popular in many fields of fluid dynamics. However, the separate flows around a structure are complicated, and it generally is difficult to obtain a quantitative prediction of the aerodynamic force and response using CFD. To overcome this problem, extensive studies on utilizing CFD in the field of bridge aerodynamics have been and are currently being performed. For instance, a streamline box girder was analyzed using an elaborate numerical model where even railings were reproduced (Sarwar et al., 2008), and the obtained steady and unsteady aerodynamic coefficients agreed well with experimental results. In another example, a numerically less demanding model was used to obtain the coefficients, which also agreed reasonably well with experimental results (Nieto et al., 2015). Although it may be still difficult to use CFD for the final estimation of the bridge response to wind, the results by CFD are already used at the first stage of wind-resistant design where the general cross-sectional shape of a deck is chosen.

7. Vortex-induced vibration and its countermeasures

Vortex-induced vibration has sometimes been observed in actual bridges. Two such examples are briefly explained next.

The Tokyo Bay Aqua-Line Bridge (Fujino and Yoshida, 2002; Fujino et al., 2012) is a 10-span continuous steel box girder bridge, and its longest span is 180 m. Vortex-induced vibration was observed in a full-bridge-model wind tunnel test, but the decision to install tuned mass dampers (TMDs), which increase damping and decrease or suppress vortex-induced vibration, was made after monitoring the bridge's behavior during construction, because there were still a few years to go before the entire road was to be opened. The observed vortex-induced vibration of the actual bridge had a maximum amplitude of 0.54 m at a wind speed of 16–17 m/s. The observed turbulence intensity was between 4% and 6%, and this small level of turbulence seemed to contribute to the large response amplitude. The TMDs that are designed to suppress the first and second modes were installed inside the box girder, and the response of those modes decreased significantly. Also, small vertical continuous plates attached outside the railings were installed to reduce the third- and fourth-mode response by modifying the aerodynamic characteristics.

The Great Belt East suspension bridge in Denmark (Larsen et al., 2000; Frandsen, 2001) has main span of 1624 m with 535 m side spans. During the final phases of deck erection and surfacing of the roadway, vortex-induced vibration began to be observed. The estimated maximum response amplitude was about 0.35 m at a wind speed of 8 m/s. The vibration was also observed in a wind tunnel test for the final design, and after that, the decision to install a countermeasure was made because there was uncertainty regarding the full-scale structural damping and test results. As the countermeasure, guide vanes with 2 m widths were installed along at the lower side panel joints of the box girder with an opening of 0.6 m. No harmful response was observed after the installation of the guide vanes. Extensive analysis of the full-scale data and comparison with the wind tunnel test results were made.

Towers of cable-supported bridges are also susceptible to vortex-induced vibration and galloping, particularly when they are freestanding at the erection stage. Examples of countermeasures adopted in Japan are given by Fujino et al. (2012).

8. Verification of buffeting analysis based on field measurements

It is always important to compare the estimated responses and full-scale measurements in order to verify the design procedures. There are several examples of such measurements (e.g., Holmes, 1975; Brownjohn et al., 1994; Larose et al., 1998; Miyata et al., 2002; Macdonald, 2003; Xu and Zhu, 2005; Bakht et al., 2013). A few of them are briefly introduced next.

The wind-induced buffeting responses of the Akashi Kaikyō Bridge were measured during two typhoons (Miyata et al., 2002). The mean of the along-wind direction response agreed well with the analysis that was conducted in the design. However, the fluctuating component of the response was generally less than the specified value in the design specification based on buffeting analysis.

Xu and Zhu (2005) made a comparison between the buffeting response of full-scale health monitoring data of the Tsing Ma Bridge in Hong Kong and their elaborate analysis, where the responses under skew wind (i.e., not perpendicular to the bridge axis) were also considered. The agreements were reasonably good.

The results of 10 years of full-scale monitoring data for the Confederation Bridge in Canada are published (Bakht et al., 2013). The Confederation Bridge is a 13 km precast concrete bridge comprised of 43 spans of 250 m. The accuracy of the design wind speed and dynamic characteristics such as natural frequencies were confirmed.

9. Wind-induced vibrations of stay cables

The span length of cable-stayed bridges has become longer over time. Accordingly, their stay cables have also lengthened. Stay cables are very flexible and low-damping, and they are more prone to wind-induced vibration with longer lengths. Extensive studies have been conducted (FHWA, 2007; Caetano, 2007; Fujino et al., 2012). Among the wind-induced vibrations of stay cables, rain- and wind-induced vibration has been clearly noticed by engineers since the mid-1980s, and it is now a common practice to prevent the occurrence of such vibration by installing dampers, modifying the cable surface, or both.

On the other hand, the possibility of wind-induced vibration without rain conditions at relatively high wind speeds has been pointed out, and much research has been conducted on this topic. A possible explanation of the cause is the change of aerodynamic force on cables around the critical Reynolds number range (Jakobsen et al., 2012; Raeesi et al., 2014), and the vibration due to this mechanism is called *dry inclined cable galloping*. Another factor that may be related to this response is the axial flow that forms on the near-leeward side of the cable (Matsumoto et al., 2010). There may be some different causes for the wind-induced vibration of dry stay cables, and experimental (Kimura et al., 2009; Katsuchi and Yamada, 2009; Benidir et al., 2015) and numerical (Yeo and Jones, 2011) studies have been carried out in order to clarify the mechanism.

Related to the wind-induced vibrations of stay cables, attention must be paid to any strong excitation that may occur if the cables are located in parallel. An example of studies was conducted on parallel and unparallel cylinders to clarify their response characteristics (Kim and Kim, 2014).

10. Research and development in wind loads

For longer span bridges, effects of the wind loads become more dominant and further research and development are still required. For example, sometimes it is difficult to design a stiffening girder that does not exhibit vortex-induced vibrations, particularly under large wind inclination angle. In addition, the validation of the wind-resistant design procedure against full-scale bridge behavior is still not enough, and the accumulation of field data and its comparison with prediction made during the design stage are necessary. Aerodynamic countermeasures are often applied to mitigate the wind-induced vibrations, but such countermeasures are often more vulnerable to corrosion than structural members. Countermeasures that are more economical throughout the bridge's long lifetime are hopefully to be developed. Generally, strong winds caused by tropical or extratropical cyclones have been considered for wind loads. On the other hand, research on the effects of non-synoptic wind such as tornadoes and downbursts have begun to be seen (Hao and Wu, 2017; Cao et al., 2019). If the surrounding terrain of the bridge site is complex, its effects on the approaching wind have to be carefully considered, and research is still necessary (Song et al., 2020). Research on the wind effects against vehicles on a bridge is also active due to the high accident rate and the need for regulation that can prevent accidents and minimize bridge closure time.

References

American Association of State Highway and Transportation Officials (AASHTO), 2020. LRFD Bridge Design Specification—9th Edition (LRFDBDS-9). AASHTO, Washington, DC.

American Society of Civil Engineers (ASCE), 2013. ASCE/SEI 7–10—Minimum Design Loads for Buildings and Other Structures. ASCE, Reston, VA.

American Society of Civil Engineers (ASCE), 2017. ASCE/SEI 7–16—Minimum Design Loads and Associated Criteria for Buildings and Other Structures. ASCE, Reston, VA.

Bakht, B., King, J.P.C., Bartlett, F.M., 2013. Wind-induced response and loads for the confederation bridge, part I: on-site monitoring data. Wind Struct. 16 (4), 373–391.

Benidir, A., Flamand, O., Gaillet, L., Dimitriadis, G., 2015. Impact of roughness and circularity-defect on bridge cables stability. J. Wind Eng. Ind. Aerodyn. 137, 1–13.

Brownjohn, J.M.W., Bocciolone, M., Curami, A., Falco, M., Zasso, A., 1994. Humber bridge full-scale measurement campaigns 1990–1991. J. Wind Eng. Ind. Aerodyn. 52, 185–218.

Caetano, E.S., 2007. Cable Vibrations in Cable-Stayed Bridges (Structural Engineering Documents 9). IABSE, Zürich, Switzerland.

Cao, J., Ren, S., Cao, S., Ge, Y., 2019. Physical simulations on wind loading characteristics of streamlined bridge decks under tornado-like vortices. J. Wind Eng. Ind. Aerodyn. 189, 56–70.

Davenport, A.G., 1962. The response of slender, line-like structure to a gusty wind. P. I. Civil Eng. 20, 389–408.

European Committee for Standardization, 2010. EN 1991-1-4:2005+A1, Eurocode 1: Actions on Structures—Part 1–4: General Actions–Wind Actions. CEN, Brussels, Belgium.

Federal Highway Administration (FHWA), 2007. Wind-Induced Vibrations of Stay Cables. US Department of Transportation. Publication No. FHWA-HRT-05-083.

Frandsen, J.B., 2001. Simultaneous pressures and accelerations measured full-scale on the Great Belt east suspension bridge. J. Wind Eng. Ind. Aerodyn. 89, 95–129.

Fujino, Y., Yoshida, Y., 2002. Wind-induced vibration and control of trans-Tokyo Bay crossing bridge. J. Struct. Mech. 128 (8), 1012–1025.

Fujino, Y., Kimura, K., Tanaka, H. (Eds.), 2012. Wind-Resistant Design of Bridges in Japan—Developments and Practices. Springer, Tokyo.

Ge, Y.J., 2008. Recent development of bridge aerodynamics in China. J. Wind Eng. Ind. Aerodyn. 96, 736–768.

Hao, J., Wu, T., 2017. Nonsynoptic wind-induced transient effects on linear bridge aerodynamics. J. Eng. Mech. 143 (9).

Highways Agency, UK, 2001. Design Manual for Roads and Bridges, Vol. 1: Highway Structures, Approval Procedures and General Design, Section 3: General Design, Part 3: BD 49/01, Design Rules for Aerodynamic Effects on Bridges.

Holmes, J.D., 1975. Prediction of the response of a cable stayed bridge to turbulence. In: Eaton, K.J. (Ed.), Proceedings of the Fourth International Conference on Wind Effects on Buildings and Structures, 8–12 September 1975, Heathrow. Cambridge University Press, Cambridge, pp. 187–197.

Holmes, J.D., 2007. Wind Loading of Structures, second ed. Taylor & Francis, Oxon, UK.

International Standard Organization (ISO), 2009. ISO 4354—Wind Actions on Structures, second ed. ISO, Geneva, Switzerland.

Jakobsen, J.B., Andersen, T.L., Macdonald, J.H.G., Nikitas, N., Larose, G.L., Savage, M.G., McAuliffe, B.R., 2012. Wind-induced response and excitation characteristics of an inclined cable model in the critical Reynolds number range. J. Wind Eng. Ind. Aerodyn. 110, 100–112.

Jurado, J.A., Hernández, S., Nieto, F., Mosquera, A., 2011. Bridge Aeroelasticity: Sensitivity Analysis and Optimal Design. WIT Press, Southampton, UK.

Katsuchi, H., Yamada, H., 2009. Wind-tunnel study on dry-galloping of indented-surface stay cable. In: Proceedings of the 11th Americas Conference on Wind Engineering. 11ACWE, June 22–26, 2009, San Juan, Puerto Rico.

Kim, S., Kim, H.K., 2014. Wake galloping phenomena between two parallel/unparallel cylinders. Wind Struct. 18 (5), 511–528.

Kimura, K., Kato, K., Kubo, Y., Oh-hashi, Y., 2009. An aeroelastic wind tunnel test of an inclined circular cylinder. In: Proceedings of the Eighth International Symposium on Cable Dynamics. ISCD 2009, September 20–23, 2009, Paris, pp. 143–150.

Kubo, Y., Hirata, K., Mikawa, K., 1992. Mechanism of aerodynamic vibration of shallow bridge girder sections. J. Wind Eng. Ind. Aerodyn. 41–44, 1297–1308.

Larose, G.L., Johnson, R., Damsgaard, A., 1998. Field measurements of a 1210-m span suspension bridge during erection. In: Proceedings of IABSE Symposium, September 2–4, 1998, Kobe, pp. 217–222. IABSE Rep. No. 79.

Larsen, A., Esdahl, S., Andersen, J.E., Vejrum, T., 2000. Storebaelt suspension bridge: vortex shedding excitation and mitigation by guide vanes. J. Wind Eng. Ind. Aerodyn. 88, 283–296.

Macdonald, J.H.G., 2003. Evaluation of buffeting predictions of a cable-stayed bridge from full-scale measurement. J. Wind Eng. Ind. Aerodyn. 91, 1465–1483.

Matsumoto, M., Yagi, T., Hatsuda, H., Shima, T., Tanaka, M., Naito, H., 2010. Dry galloping characteristics and its mechanism of inclined/yawed cables. J. Wind Eng. Ind. Aerodyn. 98, 317–327.

Miyata, T., Yamada, H., Katsuchi, H., Kitagawa, M., 2002. Full-scale measurement of Akashi–Kaikyo bridge during typhoon. J. Wind Eng. Ind. Aerodyn. 90, 1517–1527.

Nieto, F., Owen, J.S., Hargreaves, D.M., Hernández, S., 2015. Bridge deck flutter derivatives: efficient numerical evaluation exploiting their interdependence. J. Wind Eng. Ind. Aerodyn. 136, 138–150.

Raeesi, A., Cheng, S., Ting, D.S., 2014. A two-degree-of-freedom aeroelastic model for the vibration of dry cylindrical body along unsteady air flow andits application to aerodynamic response of dry inclined cables. J. Wind Eng. Ind. Aerodyn. 130, 108–124.

Sarwar, M.W., Ishihara, T., Shimada Yamasaki, Y., Ikeda, T., 2008. Prediction of aerodynamic characteristics of a box girder bridge section using the LES turbulence model. J. Wind Eng. Ind. Aerodyn. 96, 1895–1911.

Simiu, E., Miyata, T., 2006. Design of Buildings and Bridges for Wind: A Practical Guide for ASCE-7 Standard Users and Designers of Special Structures. John Wiley & Sons, Hoboken, NJ.

Simiu, E., Scanlan, R.H., 1996. Wind Effects on Structures, third ed. John Wiley & Sons, New York.

Sockel, E. (Ed.), 1994. Wind-Excited Vibrations of Structures. Springer-Verlag, Vienna.

Song, J.L., Li, J.W., Flay, R.G.J, 2020. Field measurements and wind tunnel investigation of wind characteristics at a bridge site in a Y-shaped valley. J. Wind Eng. Ind. Aerodyn. 202.

Stathopoulos, T. (Ed.), 2007. Wind Effects on Buildings and Design of Wind-Sensitive Structures. Springer, Wien and New York.

Tamura, Y., Kareem, A. (Eds.), 2013. Advanced Structural Wind Engineering. Springer, Tokyo.

Tanaka, H., 1992. Similitude and modelling in bridge aerodynamics. In: Larsen, A. (Ed.), Aerodynamics of Large Bridges. A.A. Balkema, Rotterdam, pp. 83–94.

Xu, Y.L., 2013. Wind Effects on Cable-Supported Bridges. John Wiley & Sons, Singapore.

Xu, Y.L., Zhu, L.D., 2005. Buffeting response of long-span cable-supported bridges under skew winds, part 2: case study. J. Sound Vib. 281, 675–697.

Yeo, D., Jones, N.P., 2011. Computational study on aerodynamic mitigation of wind- induced, large-amplitude vibrations of stay cables with strakes. J. Wind Eng. Ind. Aerodyn. 99, 389–399.

This page intentionally left blank

Fatigue and fracture

4

Alessio Pipinato[a] *and Eugen Brühwiler*[b]
[a]AP&P, CEO and Technical Director, Rovigo, Italy, [b]E.B.: Professor of Structural Engineering, EPFL - Swiss Federal Institute of Technology, Lausanne, Switzerland

1. Introduction

Fatigue consists of the localized alternating repetitions of concentrated stress cycles in a structure induced by the external application of loads such as vehicles, winds, waves, and temperature. These elements, when impacting the structural capacity of a bridge, could induce fracture and, over a long period, eventually cause total collapse. Bridges are strategic components of a transportation network mostly at the limit of their traffic capacity, due to overloading or simply for a high number of load vehicle repetitions. ASCE Committee on Fatigue and Fracture Reliability (1982a, b, c, d) reported that 80%–90% of failures in steel structures are related to fatigue and fracture; moreover, concrete bridges also could be affected by fatigue failures (Chen et al., 2011). Fatigue damage could lead to very dangerous incidents: for example, Figure 4.1 shows a train derailment on a fracture-critical truss bridge that severed multiple members but did not result in a collapse. These data are also confirmed by Byers et al. (1997). The factors behind these failures have been discussed by a number of researchers, including Brühwiler et al. (1990), Kulak (1992), Åkesson (1994), Pipinato (2008, 2010), and Stephens et al. (2001). The most relevant of these studies deal with geometric imperfections, such as the inclination or deflection of structural elements, and entail the so-called secondary stresses that are difficult to take into account in fatigue safety verifications. However, vibrations, transverse horizontal forces, internal constraints, and localized and diffused defects such as corrosion damage are also causes of fatigue damage (Byers et al., 1997); furthermore, the presence of several joints, detail sizes, and various materials in the same bridge structure lead to different types of fatigue resistance. The most relevant issue of technical and scientific interest concerns how to extend the service duration of existing bridges and how to improve these structures for higher loads, as it is not realistic or economical to consider reconstruction for all service bridges. A relevant question arises in this context: what is old? The notion of a design working life (subsequently called "design service duration") is defined in Eurocode (EN 1990, 2010) as the stipulated period during which a structure or part of it is to be used for its intended purpose with anticipated maintenance but without major repair being necessary. This concept is strictly related to that of maintenance, defined as a set of activities performed during the service duration of the structure in order to enable it to fulfill the requirements for reliability. According to EN 1990 (2010), the intended service duration of the design of a new bridge is generally defined as 100 years, even if, for particular cases, the National Annexes and codes could provide

Innovative Bridge Design Handbook. https://doi.org/10.1016/B978-0-12-823550-8.00033-0

Figure 4.1 A train derailment on a fracture-critical truss bridge that severed several members but did not cause the bridge to collapse.

other values, which would be longer for strategic and monumental structures and shorter for minor structures. In any case, the bridge shall be in service for several generations, and in no way shall the bridge be demolished at the end of its intended service duration but the use of the bridge and its further service duration shall be updated regularly to comply with user demands. The consequent question is how a bridge can be designed to last for more than 100 years of service. Therefore, engineering methods aiming to verify the structural reliability of existing structures (also called assessment procedures) are necessary; however, there are not many existing codes in this field. Only some international guidelines are focused on this point, as explored in the rest of this chapter. The verification of the reliability of an existing structure aims to produce evidence that it will function safely over a specified service duration. In evaluating the reliability of an existing structure, the following points should be considered:

- The application of a risk-based approach while respecting commonly accepted safety levels as defined in codes. Uncertainty is reduced by using nondestructive testing, monitoring, and detailed structural analysis.
- Defining risk acceptance criteria, which requires the consideration of different items—such as redundancy, structural importance in the pertaining network, inspection level, and accessibility for inspection of bridge members.
- Defining adequate safety goals for acceptance criteria, which requires the reliability analysis of the structure, setting up target reliability values, and performing verifications based on calibrated safety factors.

Two main engineering methods are currently applied in the examination of fatigue safety of existing bridges. The first is the traditional *S-N* curve method, in which the relationship between the constant-amplitude stress range, *S*, and the number of cycles to failure, *N*, is determined by appropriate fatigue experiments and described by a curve. The Palmgren-Miner linear damage hypothesis, also called "Miner's rule" (Miner, 1945), extends this approach to variable-amplitude loadings. The second method is the fracture mechanics approach, which is dedicated to describe the crack initiation and growth in consideration of the stress field at the crack tip. In general, the two approaches are applied sequentially, with the *S-N* curve method, used at the bridge design stage or for the evaluation of the fatigue endurance, and the fracture mechanics approach, used for more refined crack-based evaluation of remaining fatigue endurance or effective decision making on inspection and maintenance strategies (Chryssanthopoulos and Righiniotis, 2006; Ye et al., 2014). The most common application of this latter approach is the linear elastic fracture mechanics (LEFM) method (Cheung and Lib, 2003): in this case, Paris' law (Paris et al., 1961), the most common LEFM-based crack growth model, is used. Paris' law is described as

$$\frac{da}{dN} = C \cdot \Delta K^m \tag{1}$$

where a is the crack size, N is the number of stress cycles, C and m are fatigue growth parameters, and ΔK is the stress intensity range. According to LEFM theory (Cheung and Lib, 2003), ΔK can be estimated as

$$\Delta K = F(a, Y) \cdot \Delta\sigma \cdot \sqrt{\pi \cdot a} \tag{2}$$

where $\Delta\sigma$ is the tensile stress range, $F(a,Y)$ is the geometry function taking into account possible stress concentrations, and Y represents a vector of random variables, such as the stress concentration coefficient and the dimensions of the specimen under consideration. In the case of welded details, the geometry function is expressed as the product of four separate factors (Tsiatas and Palmquist, 1999; Cheung and Lib, 2003):

$$F(a, Y) = F_g \cdot F_w \cdot F_s \cdot F_e \tag{3}$$

where F_e, F_s, F_w, and F_g are crack shape, free surface, finite width, and stress gradient correction, respectively (Tsiatas and Palmquist, 1999; Cheung and Lib, 2003):

$$F_e = \frac{1}{\int_0^{\frac{\pi}{2}} \sqrt{1 - \frac{c(a)^2 - a^2}{c(a)^2} \sin^2(\vartheta) d\vartheta}} \tag{4}$$

$$F_s = 1.211 - 0.186\sqrt{\frac{a}{c(a)}} \tag{5}$$

$$F_w = \sqrt{\sec\frac{\pi a}{2t_f}} \tag{6}$$

$$F_g = \frac{-3.539\ \ln\frac{z}{t_f} + 1.981\ \ln\frac{t_{cp}}{t_f} + 5.798}{1 + 6.789\left(\frac{a}{t_f}\right)^{0.4348}} \tag{7}$$

In the preceding expressions, z is the weld leg size, t_f is the flange thickness, t_{cp} is the cover plate thickness, a is the crack depth, b is half the flange width of the girder, c is half the crack length as a function of crack depth, and ϑ is the angle for an elliptical crack. The relation between c and a is given by $c(a) = 3.549\ a^{1.133}$. Hence, the crack propagation law can be written as

$$\frac{da}{dN} = C\left[F(a,Y)\cdot\Delta\sigma\cdot\sqrt{\pi\cdot a}\right]^m \tag{8}$$

According to the LEFM approach, the estimation of the crack growth amplitude vs. the passing time, considering the loading history and the estimated traffic flow, gives an accurate prediction method to analyze the so-called remaining service duration of a structure.

2. Structural redundancy and safety

2.1 Structural redundancy

Redundancy can be defined as an exceedance of what is necessary or normal. The Federal Highway Administration (FHWA, 2012) carefully analyzed three types of structural redundancy in bridges: load-path, structural, and internal redundancy. A member is considered load-path redundant if an alternative and sufficient load path is determined to exist: this is the case for parallel girders, for example, but the existence of a redundant member is not sufficient. The absence of a failed member and the new load path also should be considered to determine if, in this case, the remaining member is able to resist the superimposed loading condition. In the second case, a member is considered structurally redundant if its boundary conditions or supports are such that failure of the member merely changes the boundary or support conditions but does not result in the collapse of the superstructure. In the third case, alternative load paths exist in the same member (for example, multiple plies of a riveted steel member).

2.2 Principles of structural safety

A structure is considered safe if the design has accurately minimized possible economic loss and has ensured the protection of people during its whole service duration. The first systematic study of the matter was made by Freudenthal (1945), publishing the first paper on the safety of structures. Safety is strictly related to the concept of reliability, referring to the probability that failure will not occur or that a specified criterion will not be exceeded. As an example, to design a structural system, the value of the maximal load parameter or the carrying capacity of the structure as expressed by the load parameter value in the limit situation (the ultimate resistance) raises the following safety question: how much higher than the maximal load parameter (the action effect) calculated with a deterministic procedure should the ultimate load value be in the carrying capacity model for the engineer to guarantee that there is either no risk or an extremely small and acceptable risk that a failure will occur? The difference between the two values is called the safety margin (Ditlevsen and Madsen, 2005). The safety documentation for a structure has in the past often been based on the ratio between a calculated carrying capacity R (resistance) and a corresponding loading action effect S (stress). This ratio $N = R/S$ is the safety factor. Since $N > 1$ if and only if $R > S$, the statement $N > 1$ proves that the structure corresponds to a point in the safe set, while $N \leq 1$ says that the structure corresponds to a point in the failure set. In a probabilistic formulation, the safety factor is a random variable ($N = R/S$), where R and S are random variables corresponding to the chosen resistance definition. The probability that the structure is not failing is, then,

$$P(N > 1) = P(R > S) \tag{9}$$

Unlike the safety factor, this probability does not vary with respect to the definition of R. Of course, it is required that all considered resistance definitions with respect to a given limit state and corresponding action effects are defined in the same probability space. Let us assume that R and S are mutually independent and distributed according to the normal distribution with parameters (μ_R, σ_R) and (μ_S, σ_S), respectively (with μ mean value, σ^2 variance). Then,

$$P(N > 1) = P(S - R < 0) = \Phi\left(\frac{\mu_R - \mu_S}{\sqrt{\sigma_R^2 + \sigma_S^2}}\right) \tag{10}$$

where ϕ is the distribution function of the standardized normal distribution (Ditlevsen and Madsen, 2005).

2.3 Inspection and monitoring

2.3.1 Inspection

Field inspections are necessary for fatigue damage detection, given the implicit uncertainties of key elements related to fatigue like loading history analysis and future traffic estimation. Concurring causes of the constituent material deterioration like corrosion, cracking, and other kinds of damage can affect the structural safety of a bridge. Therefore, all of the elements that directly affect the performance of the bridge—including the footing, substructure, deck, and superstructure—must be periodically inspected or monitored. Inspection is the primary nondestructive evaluation method used to evaluate the condition of bridges. Periodic inspections are conducted at defined intervals to survey the actual condition of bridges: the periodicity and inspection methods are commonly regulated by the bridge owners or by code rules. One of the most advanced processes is included in the National Bridge Inspection Standards (NBIS, 2004), developed by FHWA: this encompasses a manual guide, and all data from the inspections are then migrated into a bridge inventory, a national database in which all bridges are catalogued and in which inspection data are reported. Outside the United States, every managing agency—including those in the same nation—has developed a different standard, which is not a very useful engineering method. Other methods adopted for the fatigue examination of existing bridges include dynamic testing, radiographic inspection, electric inspection, sonic and ultrasonic methods, acoustic emission methods, and dye penetration to detect fatigue cracks. Regular field inspection combined with an accurate testing program could also provide managing authorities with accurate monitoring of cracks and a more precise prediction of the remaining service duration.

2.3.2 Monitoring

Today, simple monitoring has been replaced with structural health monitoring (SHM), which is a long-term process that includes an integration of structural analytical skills, a bridge design process, construction issues, management, and inspection procedures. These procedures provide accurate information with the support of online SHM systems, which are directly controlled by infrastructural agencies. SHM systems incorporate the use of advanced technologies in sensing, data acquisition, computing, communication, and information and communication technologies (ICT).

3. Codes and standards

3.1 Eurocode

Eurocode Part 3, Section 1-9 (EN 1993-1-9), is the European standard that gives methods for the structural fatigue design of members, connections, and joints of steel structures subjected to variable loadings. The fatigue design and verification provided in this code is derived from fatigue tests of common structural details, including the effects of geometrical and manufacturing imperfections, material production, and execution (for example, the effects of tolerances and residual stresses from welding). Materials should conform to the toughness requirements of EN 1993-1-10 (2009). The fatigue strengths provided in this code apply to structures operating under normal atmospheric conditions and with sufficient corrosion protection and regular maintenance, but do not provide any information on different environmental conditions; for example, the effect of seawater corrosion and microstructural damage from high temperatures (>150°C) is not covered. Two methods are provided for fatigue safety verification: the damage-tolerant method and the safe-life method. The first should provide an acceptable reliability that a structure will perform satisfactorily over its service duration, provided that a prescribed inspection and maintenance regime for detecting and correcting fatigue damage is implemented throughout the design life of the structure. The second method should provide an acceptable level of reliability that a structure will perform satisfactorily for its intended service duration without the need for regular in-service inspection for fatigue damage. The methods presented in EN 1993-1-9 describe fatigue resistance in terms of fatigue strength curves for standard details applicable to nominal stresses and discuss weld configurations applicable to geometric stresses. The National Annex may give the choice of the verification method, definitions of classes of consequences, and numerical values for γ_{Mf}. Recommended values for γ_{Mf} are given in Table 4.1. Concerning stresses from fatigue actions, modeling for nominal stresses should consider all action effects, including distortions, and should be based on linear elastic analysis of members and connections. Provided that the stresses due to external loading applied to members between joints are taken into account, the effects from secondary moments due to the stiffness of the connection are considered by adopting a $k1$-factor (as given in the code tables, for circular hollow sections under in-plane loading and for rectangular hollow sections under in-plane loading). The relevant stresses are nominal direct stresses σ and nominal shear stresses τ, while the relevant stresses in welds (Figure 4.2) are normal stresses σ_{wf} transverse to the axis of the weld and shear stresses τ_{wf} longitudinal to the axis of the weld, for which two separate checks should be performed. Stresses should be calculated at the serviceability limit state and the site of potential fatigue

Table 4.1 Recommended Values for Partial Factors γ_{Mf} for Fatigue Strength (Table 3.1, EN 1993-1-9)

Assessment Method	Consequence of Failure	
	Low Consequence	**High Consequence**
Damage tolerant	1.00	1.15
Safe life	1.15	1.35

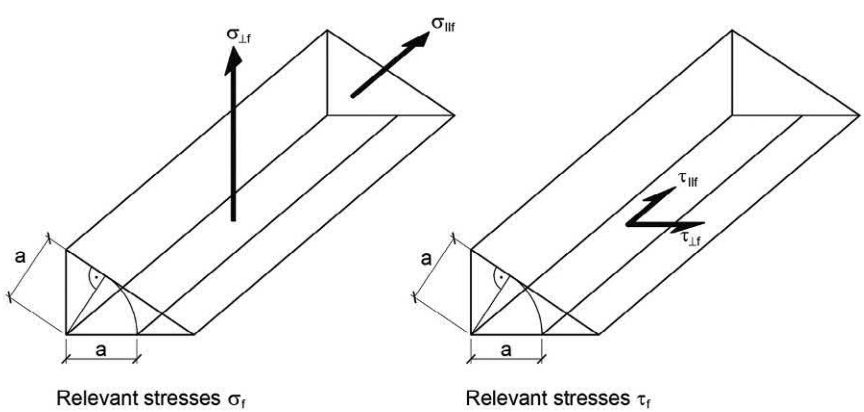

Figure 4.2 Relevant stresses in the fillet welds.

initiation. Effects producing stress concentrations at the investigated structural detail should be generally accounted for by using a stress concentration factor (SCF): these values are provided in the code for every detail category. When using geometric (hot spot) stress methods for specific details included in the code, the stresses should be calculated as reported in the code. The fatigue design should be carried out using nominal stress ranges for such details as plain members and mechanically fastened joints, welded built-up sections, transverse butt welds, weld attachments and stiffeners, load-carrying welded joints, hollow sections, lattice girder node joints, orthotropic decks (open and closed stringers), top-flange-to-web junctions of runway beams, and modified nominal stress ranges, in which consistent changes of section occur close to the initiation site that are not included in the code; and geometric stress ranges, where high stress gradients occur close to a weld toe. The design value of the stress range to be used for the fatigue design should be the stress ranges $\gamma_{Ff}\,\Delta\sigma_{E,2}$ corresponding to $N_C = 2 \times 10^6$ cycles. The design value of nominal stress ranges $\gamma_{Ff}\,\Delta\sigma_{E,2}$ and $\gamma_{Ff}\,\Delta\tau_{E,2}$ should be determined as follows:

$$\gamma_{Ff}\,\Delta\sigma_{E,2} = \lambda_1 \times \lambda_2 \times \lambda_i \times \cdots \times \lambda_n \times \Delta\sigma\left(\gamma_{Ff}\,Q_k\right) \tag{11}$$

$$\gamma_{Ff}\,\Delta\tau_{E,2} = \lambda_1 \times \lambda_2 \times \lambda_i \times \cdots \times \lambda_n \times \Delta\tau\left(\gamma_{Ff}\,Q_k\right) \tag{12}$$

where $\Delta\sigma$ ($\gamma_{Ff}\,Q_k$), $\Delta\tau$ ($\gamma_{Ff}\,Q_k$) is the stress range caused by the fatigue loading specified in EN 1991-2 (2010), and λ_i are damage-equivalent factors depending on the spectra, as specified in EN1993. The other cases are reported and specified in the code. The fatigue strength for nominal stress ranges is represented by a series of (log $\Delta\sigma_R$) − (log N) curves and (log $\Delta\tau_R$) − (log N) curves (S-N curves), which correspond to typical detail categories. Each detail category is designated by a number that represents, in N/mm^2, the reference value $\Delta\sigma_C$ and $\Delta\tau_C$ for the fatigue strength at 2 million cycles. For constant amplitude nominal stresses, fatigue strengths can be obtained by the following:

$$\Delta\sigma_R{}^{\mathrm{m}}\,N_R = \Delta\sigma_C{}^m\,2 \times 10^6 \tag{13}$$

with $m = 3$ for $N \leq 5 \times 10^6$, and

$$\Delta\tau_R{}^m\,N_R = \Delta\tau_C{}^m\,2 \times 10^6 \tag{14}$$

with $m = 5$ for $N \leq 10^8$

while

$$\Delta\sigma_D = (2/5)^{1/3} \times \Delta\sigma_C = 0.737\,\Delta\sigma_C \tag{15}$$

is the constant amplitude fatigue limit, and

$$\Delta\tau_L = (2/100)^{1/5} \times \Delta\tau_C = 0.457\,\Delta\tau_C \tag{16}$$

is the cutoff.

Finally, for nominal stress spectra with stress ranges above and below the constant amplitude fatigue limit $\Delta\sigma_D$, the fatigue strength should be based on the extended fatigue strength curves as follows:

$$\Delta\sigma_R{}^m N_R = \Delta\sigma_C{}^m 2 \times 10^6 \tag{17}$$

with $m = 3$ for $N \le 5 \times 10^6$, and

$$\Delta\sigma_R{}^m N_R = \Delta\sigma_C{}^m 5 \times 10^6 \tag{18}$$

with $m = 5$ for $5 \times 10^6 \le N \le 10^8$
while

$$\Delta\sigma_L = (5/100)^{1/5} \times \Delta\sigma_D = 0.549\,\Delta\sigma_D \tag{19}$$

is the cutoff. The *S-N* curves have a slope of 3 for up to 5 million cycles where the corresponding stress range is the constant amplitude fatigue limit (CAFL) for that curve. From 5 million cycles to 100 million cycles, a slope of 5 is used. Fatigue strength curves for direct and shear stress ranges are shown in Figures 4.3 and 4.4, respectively: test data used to determine the appropriate detail category for a particular constructional detail refer to the value of the stress range $\Delta\sigma_C$ corresponding to a value of $N_C = 2$ million cycles calculated for a 75% confidence level of 95% probability of

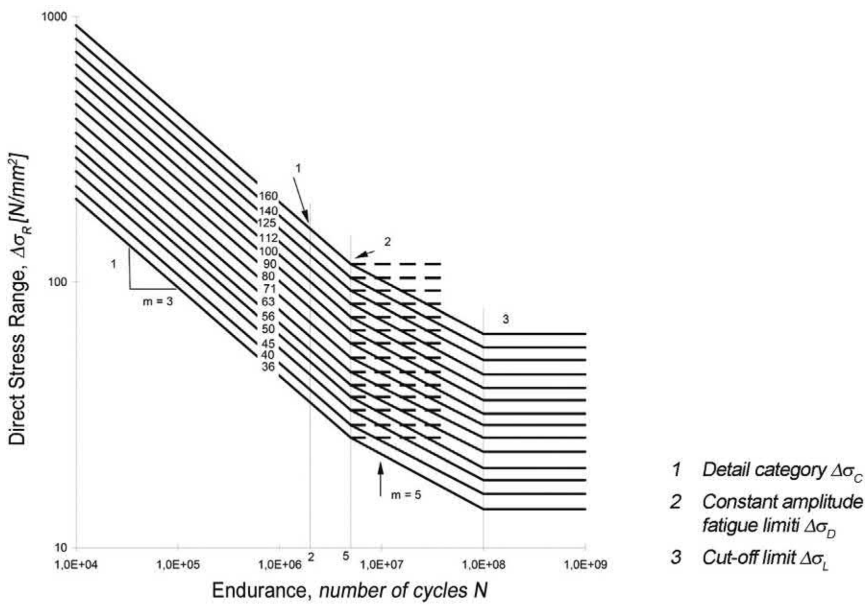

Figure 4.3 Fatigue strength curves for direct stress ranges (EN 1993-1-9).

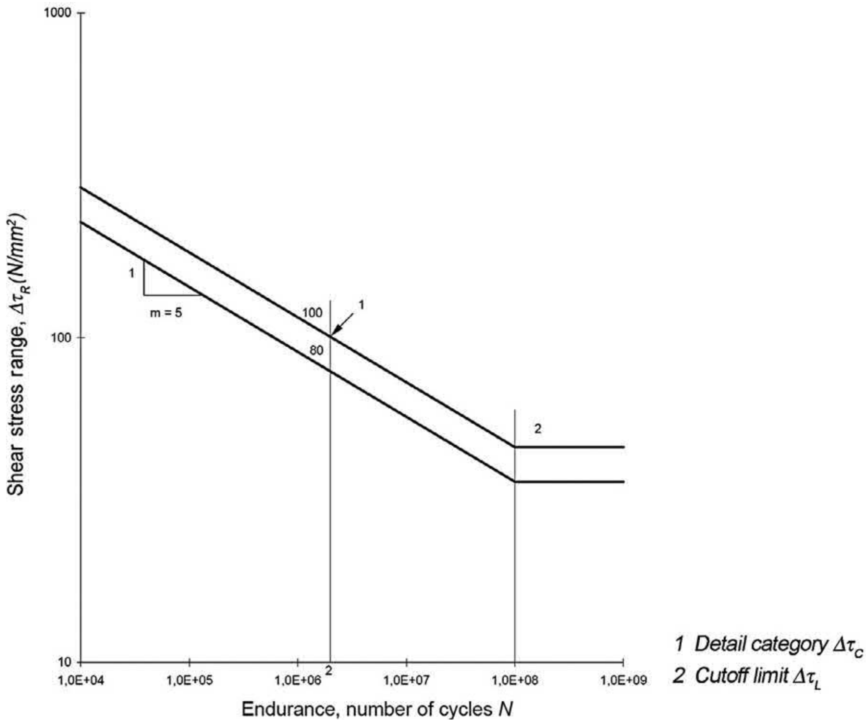

Figure 4.4 Fatigue strength curves for shear stress ranges (EN 1993-1-9).

survival for log N, taking into account the standard deviation, the sample size, and residual stress effects. The number of data points (not lower than 10) was considered in the statistical analysis, as reported in Annex D of EN 1990 (2010). Moreover, the National Annex of European countries may permit the verification of a fatigue strength category for a particular application, in accordance with the aforementioned procedure. Concerning fatigue verification, nominal, modified nominal, and geometric stress ranges due to frequent loads $\psi_1 Q_k$ (see EN 1990, 2010), it should be verified that under fatigue loading:

$$\gamma_{Ff}\,\Delta\sigma_{E,2}/\left(\Delta\sigma_C/\gamma_{Mf}\right) \leq 1 \tag{20}$$

$$\gamma_{Ff}\,\Delta\tau_{E,2}/\left(\Delta\tau_C/\gamma_{Mf}\right) \leq 1 \tag{21}$$

Unless otherwise stated in the fatigue strength categories, for combined stress ranges, it should be verified that

$$\left(\frac{\gamma_{Ff}\Delta\sigma_{E,2}}{\Delta\sigma_C/\gamma_{Mf}}\right)^3 + \left(\frac{\gamma_{Ff}\Delta\tau_{E,2}}{\Delta\tau_C/\gamma_{Mf}}\right)^5 \leq 1{,}0 \tag{22}$$

3.2 North American practice

The North American standards include American Association of State Highway and Transportation Officials (AASHTO, 2013), American Institute of Steel Construction (AISC, 2011), American Welding Society (AWS, 2010), and American Railway Engineers Association (AREA) documents. Welded and bolted details for bridges and buildings are designed with reference to the nominal stress range rather than the local "concentrated" stress at the weld detail. Fatigue design is carried out adopting service loads. Usually, nominal stress in the members can be easily calculated without great error. It is a standard practice in fatigue design to separate the details into categories with similar fatigue resistance in terms of nominal stress. Each category detail has an associated *S-N* curve. The *S-N* curves for steel details in the AASHTO (2013), AISC (2011), AWS (2010), and AREA provisions are presented for various detail categories in order of decreasing fatigue strength. These *S-N* curves are based on a lower bound of a large number of full-scale fatigue test data with a 97.5% survival limit. Generally, the slope of the regression line fitting to the test data is typically in the range 2.9–3.1 (Dexter and Fisher, 1996, 2000). Therefore, in the AISC and AASHTO codes as well as in Eurocode, the slopes have been standardized at 3.0. The fatigue threshold and CAFLs for each category are marked as horizontal dashed lines. When constant-amplitude tests are performed at stress ranges below the CAFLs, noticeable cracking should not occur. The number of cycles associated with the CAFLs is whatever number of cycles corresponds to that stress range on the *S-N* curve for that category or class of detail. The CAFL occurs at an increasing number of cycles for lower fatigue categories or classes. Different details, which share a common *S-N* curve (or category) in the finite-life regime, have different CAFLs (Dexter and Fisher, 2000). The AASHTO Load and Resistance Factor Design (LRFD) Specifications define eight detail categories for fatigue: A, B, B′, C, C′, D, E, and E′. Figure 4.5 shows the fatigue-resistance

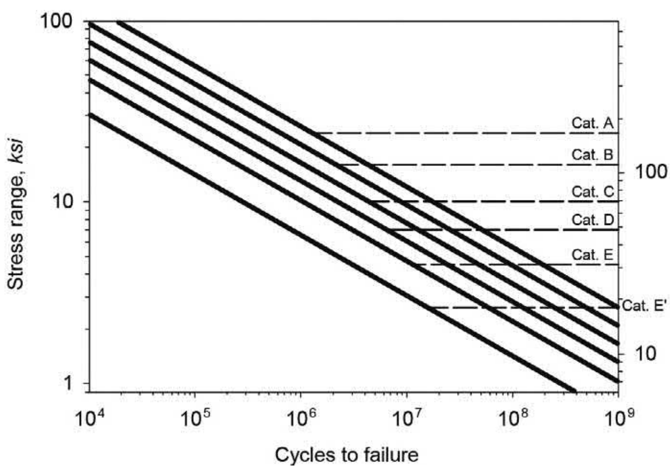

Figure 4.5 Nominal stress S-N curves used in AASHTO, AISC, AWS, and AREMA specifications.

curves given in the LRFD Specifications. The plot shows stress ranges on the vertical axis and number of cycles on the horizontal axis for the various categories. Both axes are logarithmic representations. Over some portion of the range, each detail category is a straight line with a constant slope equal to 3. Beyond a certain point, which varies depending on the detail category, the fatigue-resistance line is horizontal.

3.3 S-N *curve comparison*

To compare EN 1993-1-9 (2005) with North American codes, test results of correspondent categories are needed. A first comparison includes riveted details of different experimental investigations and structural types (Adamson and Kulak, 1995; Baker and Kulak, 1982; Mang and Bucak, 1993; Åkesson, 1994; Fisher et al., 1987; Forsberg, 1993; Abe, 1989; Al-Emrani, 2000; Rabemanantso and Hirt, 1984; Brühwiler et al., 1990; Out et al., 1984; Reemsnyder, 1975; Helmerich et al., 1997; Di Battista and Kulak, 1995; Xiulin et al., 1996; ATLSS, 1993): these have been analyzed and compared with Eurocode Category C = 63, AASHTO, and AREA (Figure 4.6). The second comparison deals with the specific category of riveted shear

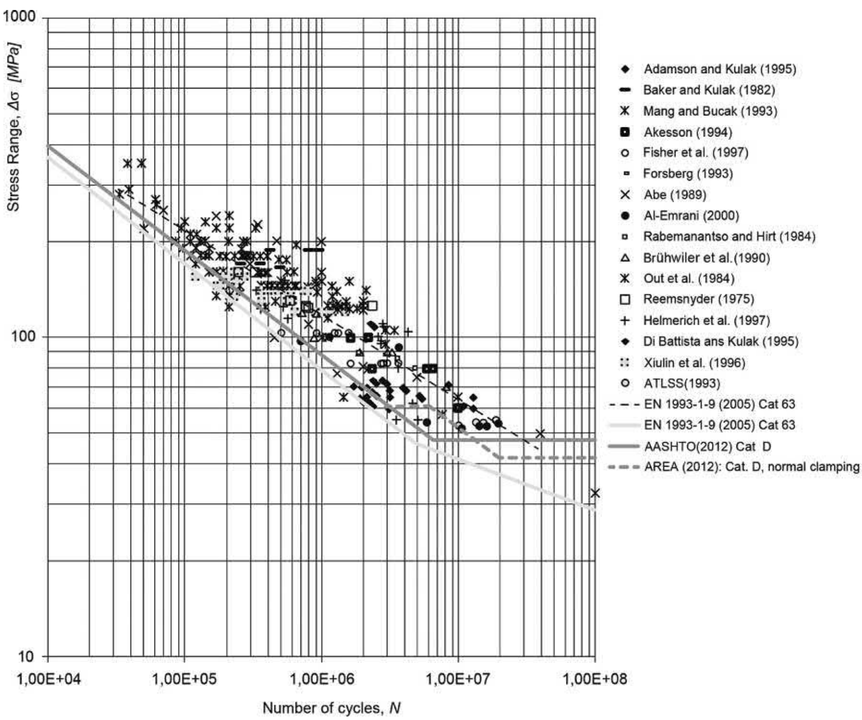

Figure 4.6 Comparison between riveted connection test results and Eurocode versus AASHTO and AREA provisions.

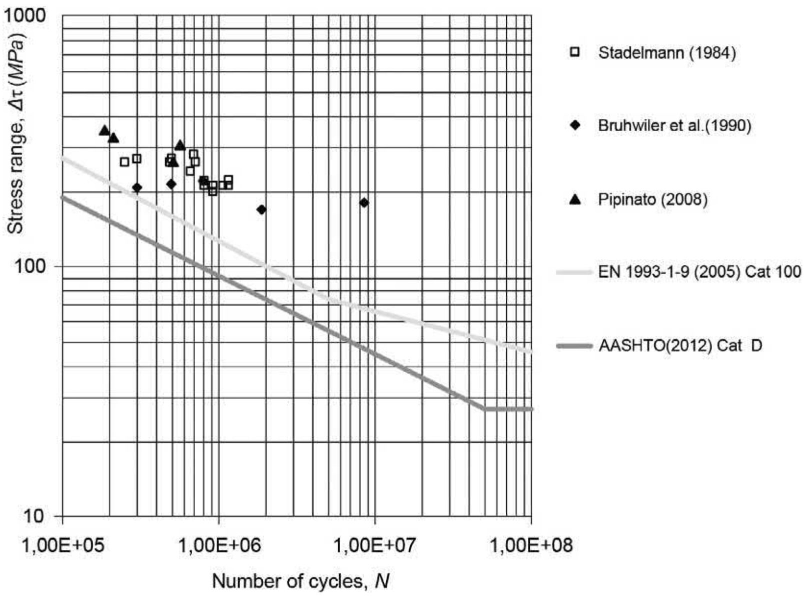

Figure 4.7 Comparison between shear-riveted connection test experimental results and Eurocode versus AASHTO and AREA provisions.

details tests data (Stadelmann, 1984; Brühwiler et al., 1990; Pipinato, 2008) compared to Eurocode Category C = 100 and the AASHTO standards (Figure 4.7); finally, the specific category in transverse connection plates due to distortion-induced fatigue strength (Fisher et al., 1990) has been analyzed and compared with Eurocode Category C = 80 and with the AASHTO standards (Figure 4.8). Considering the first and second comparisons, failures often occur over the design curves: this knowledge could help with understanding that more accurate subdivision of precise details in their specific category works better than grouping details into common categories. This problem relates to the design stage, where deep analysis of the structural details is needed to divide each substructure into its specific category, in order to avoid excessive material and to build lightweight structures. Moreover, this also implies a more efficient detailed study of the examination of existing bridges, as a precise choice of category detail implies a more accurate estimation of the remaining service duration of the considered structure. Concerning AASHTO Category C, the *S-N* curve could be a reasonable way to show the distortion-induced fatigue cracking at the ends of transverse connection plates. Both the AASHTO and Eurocode *S-N* curves seem to equally fit the test data, even though some failures appear at the limit in the high-cycle region. For all the tests and comparisons considered, a change of the nature of the current AASHTO fatigue curves from a linear to a bilinear slope would increase the effort required to calculate the fatigue endurance period.

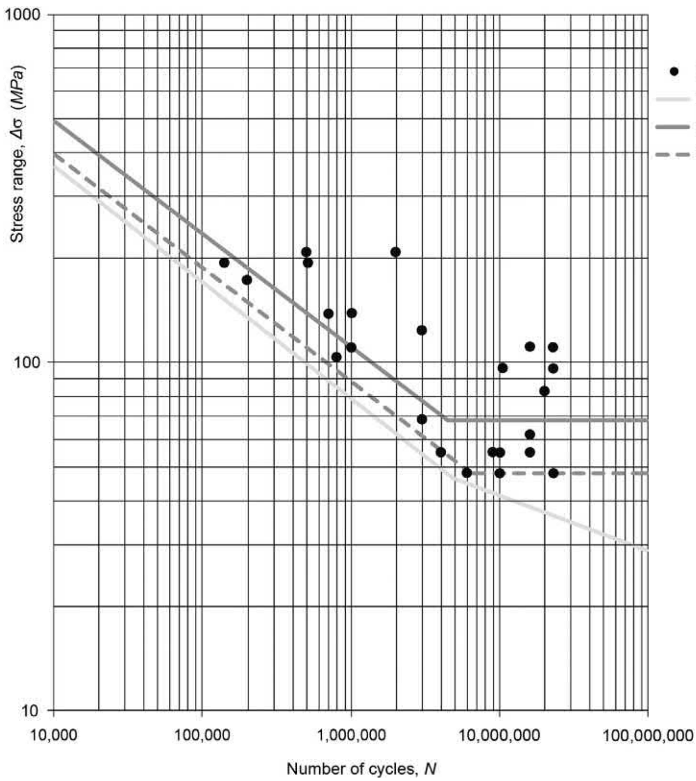

Figure 4.8 Comparison between transverse connection plate test experimental results and Eurocode versus AASHTO provisions.

3.4 Recent code background and pre-standard studies

In the examination of existing structures, as code provisions for new structures do not cover this issue, bridge engineers should cover this gap using guidelines or specific procedures provided by the managing agencies. The most comprehensive recent document on the matter in the United States is "Fatigue Evaluation of Steel Bridges," prepared by the National Cooperative Highway Research Program (NCHRP, 2012); this report summarizes the results of the research effort undertaken as part of NCHRP Project 12-81. This project has a focus on Section 7, dealing with "Fatigue Evaluation of Steel Bridges." Items identified as in need of improvement include utilizing a reliability-based approach to investigating fatigue behavior and aid bridge owners in making appropriate operational decisions; guidance on the evaluation of retrofit and repair details used to stop fatigue cracking; and guidance for the evaluation of distortion-induced fatigue cracks (NCHRP, 2012). To address these needs, several analytical and experimental studies were performed; the analytical studies were used to examine various aspects that influence the fatigue behavior. These topics ranged from truck-loading effects on bridge structures to fatigue resistance-related factors that affect the predicted fatigue duration. Both analytical and experimental methods were used to further develop an understanding of distortion-induced deformations and the structural behavior of various retrofit details used to improve a bridge suffering from distortion-induced fatigue cracking. Moreover, early in the study, it was decided that it would be beneficial to perform a series of experimental tests to study the influence of tack welds on riveted joints (NCHRP, 2012). The European document that it could be compared to is "Assessment of Existing Steel Structures: Recommendations for Estimation of Remaining Fatigue Life" (Kuhn et al., 2008): the document provides background and support for the implementation, harmonization, and further development of the Eurocodes. It has been prepared to provide technical insight on the existing steel structures, how they could be analyzed, and how the remaining fatigue endurance period could be estimated. It may be used as a main source of support to further harmonize design rules across different materials and develop the Eurocodes. The European Convention for Constructional Steelwork (ECCS) has initiated the development of this report in the frame of the cooperation between the European Commission (Joint Research Centre) and the ECCS on the further evolution of the Eurocodes. It is, therefore, published as a joint JRC-ECCS report. The aims of these recommendations are the following: (i) to present a stepwise procedure, which can be generally used for the examination of existing structures and steel bridges; (ii) to illustrate all factors to be considered about resistance and to describe ways to get more detailed information on these factors; (iii) to illustrate the remedial measures that can be chosen after fatigue verification showing insufficient fatigue safety and fatigue endurance period; and (iv) to present examples explaining the use of the proposed assessment procedure. The procedure incorporates four phases, differentiating the first phase of investigation from the deeper analysis in which experts are involved (see Figure 4.9). In 2011, the Swiss Society of Engineers and Architects (SIA) published a series of standards for existing structures. The standard entitled "Existing Structures—Bases for Examination and Interventions" (Brühwiler et al., 2012) specifies the principles, terminology, and appropriate methodology for dealing with existing structures. This standard is complemented by a series of standards that treat specific items regarding "actions on existing structures," "existing concrete, steel, composite, timber, and masonry structures," and "geotechnical and seismic aspects of existing structures." These standards provide effective ways to address issues such as higher live loads, accidental actions, and the restoration and improvement of the durability of existing structures. In particular, the following typical challenges concerning fatigue are addressed: if the structural safety for higher live loads can be verified, fatigue safety, the remaining fatigue endurance period (of fatigue-vulnerable structures such as bridges), and serviceability become predominant issues requiring advanced analysis methods; SIA standard 269/1, "Actions on Existing Structures," states that for fatigue safety verification, one must consider correction factors such as past and planned future road or rail traffic and favorable load-carrying effects due to curbs, parapets, road pavement, and railway track (for example, continuous rails on short-span bridges) to determine fatigue action effects. SIA standard 269/2,

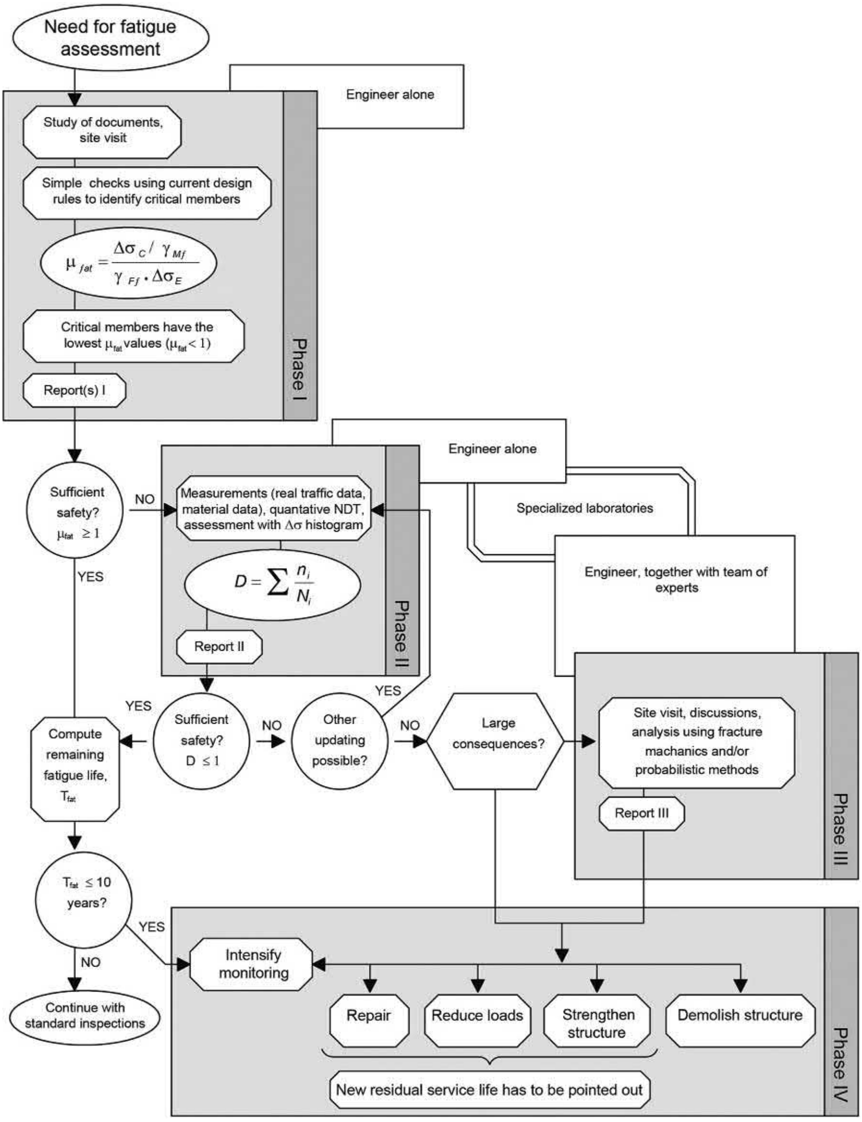

Figure 4.9 Assessment procedure for existing steel structures and recommendations for the estimation of remaining fatigue life (Kuhn et al., 2008).

"Existing Concrete Structures," covers the fatigue resistance of steel reinforcement, and SIA standard 269/3, "Existing Steel Structures," gives provisions regarding the ultimate resistance (including stability) and fatigue resistance (*S-N* curves) for riveted connections and structural elements.

4. Fatigue and fracture resistance of steel and concrete bridges

4.1 Fatigue

Fatigue is the most common cause of reported damage to steel bridges (ASCE Committee on Fatigue and Fracture Reliability, 1982a), and it is also an issue with concrete bridges (Chen et al., 2011). However, while the fatigue design of steel bridges is clearly discussed in codes and standards, the same does not hold for the examination of existing bridges. Moreover, while steel bridges built in the last two decades have had no significant problems with fatigue and fracture (and should not in the future), bridges designed before the introduction of modern specifications will continue to be susceptible to the development of fatigue cracks and to fracture. In order to avoid stress concentrations and induced deformations in specific key points of bridge structures and to control fatigue and avoid fracture, detailed rules have been found to be the most important part of fatigue and fracture design and examination procedures. While for steel bridges, a wide amount of information has been given, the following discussion will deal with concrete bridges, which are typically less prone to fatigue than welded steel and aluminum structures. Plain concrete under high force-controlled compression or tension fatigue loading exhibits strongly increasing strains within a first brief period of fatigue endurance (Dyduch et al., 1994; Cornelissen and Reinhardt, 1984; Schlafli and Brühwiler, 1998), followed by a phase of steady but only slightly increasing strains. During the last phase, strains again increase significantly before the specimen fractures (Figure 4.10). The apparent modulus of elasticity of concrete decreases significantly during the test, mainly due to crack formation on a microscopic level. Under uniaxial compression, the concrete matrix shows extensive microcracking during this last period of time. An increasing number of cracks appear parallel to the loading direction on the outer surface of the specimen with subsequent failure. Concrete behavior under tension fatigue loading is also dominated by crack propagation; early age microcracks in the cement matrix and at the interface between aggregates and the cement matrix propagate steadily and perpendicular to the loading direction until the specimen shows one discrete crack. Concrete subjected to tension-compression stress reversals deteriorates more rapidly,

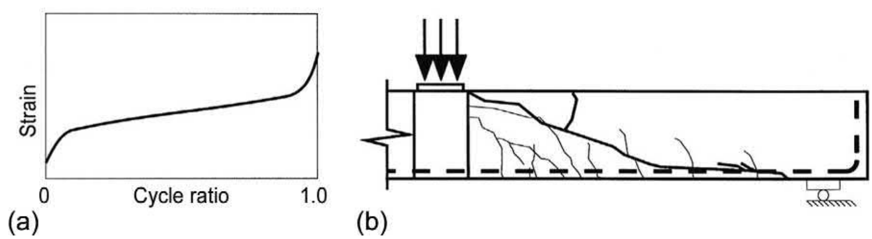

Figure 4.10 (a) Diagram of idealized strain versus cycle ratio for compression fatigue of plain concrete; (b) shear crack pattern due to fatigue loading of a beam without shear reinforcement (Frey and Thurlimann, 1983).

which is explained by the interaction of differently oriented microcracks due to compression and tension loading (Weigler and Rings, 1987; Cornelissen and Reinhardt, 1982). Fatigue behavior of steel reinforcement bars can be divided into a crack initiation phase, a steady crack propagation phase, and final fracture with little deformation of the remaining rebar section. Crack initiation on a ribbed, high-yield steel bar usually starts at the root of a rib, which typically is the location of stress concentration. Welds, the curvature of bent bars, and corrosion favor crack initiation and lead to low fatigue strength. The fatigue behavior of reinforced concrete elements is also characterized by progressive deterioration of the bond between reinforcement and concrete. Larger cracks and a smaller contribution of concrete in tension between the cracks result in larger deflection. Failure normally occurs due to fatigue fracture of steel rebars; another failure mechanism may be spalling of concrete in the compression zone, but then it is possible that the basic ductility criterion for the reinforced concrete section is not fulfilled or the concrete strength is too low (and thus not respecting type 2 verification of structural safety at ultimate static resistance). In fact, fatigue tests show that even overreinforced beams (i.e., concrete compression failure under static loading) fail due to reinforcement fatigue fracture when subjected to fatigue loading. Beams (without transverse reinforcement, hence not respecting basic rules of good detailing in structural concrete) subjected to predominant shear develop a shear crack pattern after the first few cycles when deformation increases only slightly (Figure 4.10). Subsequently, a critical shear crack that crosses the bending cracks appears. The rather large width of this crack does not allow any stress transfer; as a result, the beam fails due to fatigue of the compression strut (upper flange; Frey and Thurlimann, 1983). Beams with shear reinforcement show fatigue failure of stirrups, accompanied by spalling of surrounding concrete; failure is ductile. Fatigue tests of scaled deck slabs have shown a punching shear failure mode, and moving wheel loads leading to stress reversals are more detrimental to fatigue strength than stationary pulsating loads (Sonoda and Horikawa, 1982; Perdikaris and Beim, 1988).

4.2 Fracture

Fracture may be defined as rupture in tension or rapid propagation of a crack, leading to large deformation, loss of function or serviceability of the structural element, or complete separation of the component (Anderson, 1995). Even if prevention should be focused on fatigue, however, for structural components that are not subjected to significant cyclic loading, fracture could still possibly occur without prior fatigue crack growth. In general, fracture toughness (K_{IC}) has been found to decrease with increasing yield strength of a material, suggesting an inverse relationship between the two properties (Dexter and Fisher, 2000; Crooker and Lange, 1970); moreover, K_{IC} values are largely accepted for steel, while $K_{IC,c}$ for concrete has little meaning. However, fracture toughness is more complex than this simple relationship since steels with similar strength levels can have widely varying levels of fracture toughness (Dexter and Fisher, 2000). Steel exhibits a transition from brittle to ductile fracture behavior as the temperature increases. For example, Figure 4.11 shows a plot of the energy required to fracture CharpyV-notch impact test specimens of A588

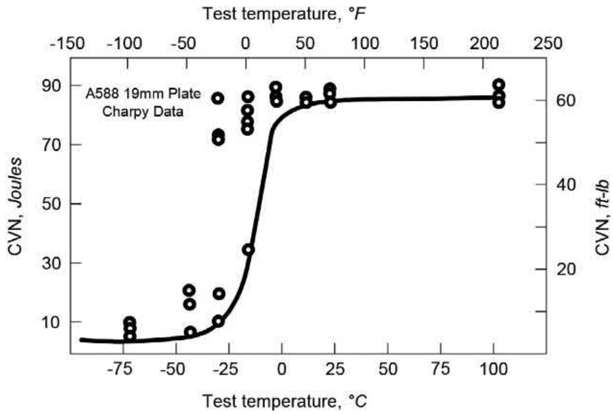

Figure 4.11 Charpy energy transition curve for A588 Grade 50 (350 MPa yield strength) structural steel.

structural steel at various temperatures. These results are typical for ordinary hot-rolled structural steel. The transition phenomenon shown in Figure 4.11 is a result of changes in the underlying microstructural fracture mode (Dexter and Fisher, 2000). Codes and standards do not provide any specific verification procedures in order to check for fracture in constituent materials. For example, according to Eurocode (EN 1993-1-10, 2009), the material should have the required toughness to prevent brittle fracture within the intended design service duration of the structure, and no further checks against brittle fracture need to be made if the conditions given in EN 1993-1-10 (2009) are met for the lowest service temperature. The National Annex may specify additional requirements depending on the plate thickness. Three main types of fracture with different behavior can be addressed. The first is brittle fracture, which is associated with cleavage of individual grains on selected crystallographic planes. This type of fracture occurs at the lower end of the temperature range, although the brittle behavior can persist up to the boiling point of water in some materials with low toughness. This part of the temperature range is called the lower shelf because the minimum toughness is fairly constant up to the transition temperature. Brittle fracture may be analyzed with LEFM because the extent of plastic deformation at the crack tip is generally negligible. The second type, ductile fracture, is associated with a process of void initiation, growth, and coalescence on a microstructural scale, a process requiring considerable energy. This higher end of the temperature range is referred to as the upper shelf because the toughness levels off and is essentially constant for higher temperatures. Ductile fracture is also called fibrous fracture, due to the fibrous appearance of the fracture surface, or shear fracture, due to the usually large, slanted shear lips on the fracture surface (Dexter and Fisher, 2000). The third type is transition-range fracture, which occurs at temperatures between the lower shelf and the upper shelf and is associated with a mixture of cleavage and fibrous fracture on a microstructural scale. Because of the mixture of micro mechanisms, transition-range fracture is characterized by extremely large variability.

5. Traffic loading and action effects on bridge elements

Traffic running on bridges produces a stress spectrum that may cause fatigue damage. This stress spectrum depends on the geometry of the vehicles, the axle loads, the vehicle spacing, the composition of the traffic, and its dynamic effects. For simplicity, only fatigue loading mentioned in the Eurocodes is reported here: five fatigue load models of vertical forces are defined and given in EN 1991-2 (2010) for road traffic. The use of the various fatigue load models is defined in EN 1992 to EN 1999, and further information is given next. Fatigue load models 1, 2, and 3 are intended to be used to determine the maximum and minimum stresses resulting from the possible load arrangements on the bridge of any of these models; in many cases, only the algebraic difference between these stresses is used in EN 1992 to EN 1999. Fatigue load models 4 and 5 are intended to be used to determine stress range spectra resulting from the passage of trucks on the bridge. Fatigue load models 1 and 2 are intended to be used to check whether the fatigue endurance period may be considered unlimited when a constant stress amplitude fatigue limit is given. Therefore, they are appropriate for steel constructions but may be inappropriate for other materials. Fatigue load model 1 is generally conservative and covers multilane effects automatically. Fatigue load model 2 is more accurate than fatigue load model 1 when the simultaneous presence of several trucks on the bridge can be disregarded for fatigue verification. If that is not the case, it should be used only if it is supplemented by additional data. The National Annex may give the conditions of use of fatigue load models 1 and 2. Fatigue load models 3, 4, and 5 are intended to be used for the estimation of fatigue endurance period by referring to fatigue strength curves defined in EN 1992 to EN 1999. They should not be used to check whether fatigue endurance can be considered unlimited. For this reason, they are not numerically comparable to fatigue load models 1 and 2. Fatigue load model 3 may also be used for the direct verification of designs by simplified methods in which the influence of the annual traffic volume and of some bridge dimensions is taken into account by a material-dependent adjustment factor λ_e. Fatigue load model 4 is more accurate than fatigue load model 3 for a variety of bridges and for the traffic when the simultaneous presence of several trucks on the bridge can be disregarded. If that is not the case, it should be used only if it is supplemented by additional data, as specified or defined in the National Annex. Fatigue load model 5 is the most general model, using actual traffic data. A list of road load fatigue models is depicted in Figure 4.12. A traffic category on a bridge should be defined, for fatigue verification at least, in terms of the following:

- The number of slow lanes
- The number N_{obs} of heavy vehicles (maximum gross vehicle weight of more than 100 kN), observed or estimated, per year and for a slow lane (i.e., a traffic lane used predominantly by trucks)

Indicative values for N_{obs} are given in EN 1991-2 (2010) for a slow lane when using fatigue load models 3 and 4: for example, roads and motorways with two or more lanes per direction with high flow rates of trucks imply $N_{obs} = 2 \times 10^6$ per year for a slow lane, whereas on each fast lane (i.e., a traffic lane used predominantly by cars), 10% of

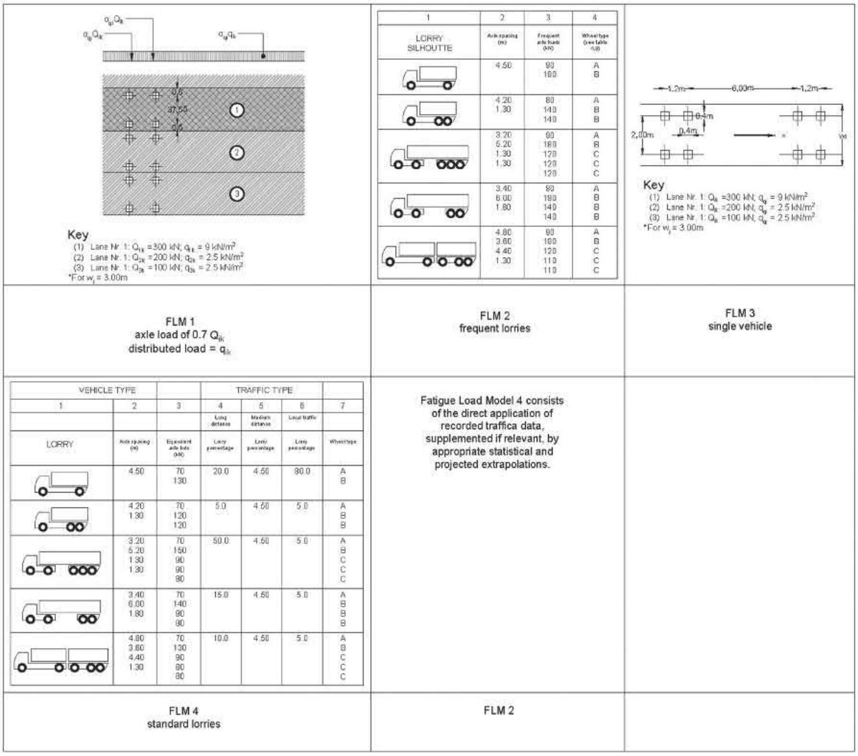

Figure 4.12 Road fatigue load model.

N_{obs} also may be considered. It should be noticed that these tables are not sufficient to characterize the traffic for fatigue verifications. Other parameters may have to be considered, such as percentages of vehicle types, which depend on the traffic type (i.e., parameters defining the distribution of the weight of vehicles or axles of each type). Other specifications, such as the statistical distribution of the transverse location of loads, should be taken into account according to the code notations. Finally, note that dynamic amplification factors are implicitly accounted in the code (for FLM 1–4); however, an additional factor should be added in expansion joints and applied to all loads (see EN 1991-2, 2010). In the specific case of railway bridges, other loading schemes are given. A fatigue damage assessment shall be carried out for all structural elements, which are subjected to alternating stresses. For normal traffic based on characteristic values of Load Model 71 (Figure 4.13), including the dynamic factor Φ, the fatigue safety verification should be carried out on the basis of one of the traffic mixes—“standard traffic,” “traffic with 250 kN-axles,” or “light traffic mix”—depending on whether the structure carries mixed traffic, predominantly heavy freight traffic, or lightweight passenger traffic in accordance with the requirements specified. Details of the service trains and traffic mixes considered and the dynamic amplification to be applied are given in Annex D of EN 1991-2 (2010). Where the traffic mix

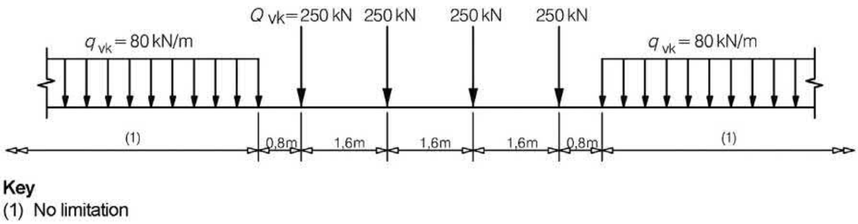

Figure 4.13 Railway fatigue load model LM71.

does not represent the real traffic (for example, in special situations where a limited number of vehicle types dominate the fatigue loading), an alternative traffic mix should be specified. It should be noted that the dynamic factor Φ is significantly higher than the results from measurements of the dynamic response in bridge elements, as shown by many studies, particularly in the case of ballasted tracks on bridges; hence, the dynamic factor Φ is like an additional partial safety factor—which, however, should be considered carefully in the examination of existing bridges (Herwig, 2008; Herwig and Brühwiler, 2011).

6. Common failures

Concerning steel and composite bridges, most failures relate to fatigue cracking from weld defects (Wichtowski, 2013), details with change in section (IIW, 1996; Miki et al., 2003), vibration-induced fatigue cracking in bridge hangers (for example, in the Skellefte River in Sweden as reported by Åkesson, 1991), bridge girders and stringers at timber tie connections (Soudki et al., 1999), diaphragms and cross-bracing connections (Pipinato et al., 2012a), stringer-to-floor-beam connections (Chotickai and Kanchanalai, 2010), elements with coped cut-short flanges (Fisher, 1984), connections between girder splices or welded cover plates (Kuhn et al., 2008), short diaphragm connections (Pipinato et al., 2009), and riveted connections (Brühwiler et al., 1990). Concerning reinforced concrete (RC)-steel composite bridges, a broad assessment of various details is given by Leitão et al. (2011), and for shear studs in particular, some tips can be found in Lee et al. (2005). For concrete bridges, a general study could be found in CEB (1988). Fatigue damage of reinforced concrete deck slab of road bridges has been identified in Japan in the 1980s after 20 years of service; this damage was due to low concrete strength, inadequate detailing of rebars, and overloaded trucks. Other countries also reported some fatigue damage. Recurrent fatigue-induced problems in RC decks have been found in literature (Rodrigues et al., 2013) from the inspection data collected in 40 bridges, in which systematic damages and defects were associated with a particular structural arrangement usually found in two-girder-slab RC bridges, with cantilever girders at the extremities. For economic reasons and due to the relative simplicity of construction, a great number of these structures can be found along the main roadways analyzed in Rodrigues et al. (2013). The superstructure is composed of a cast-in-situ concrete deck upon

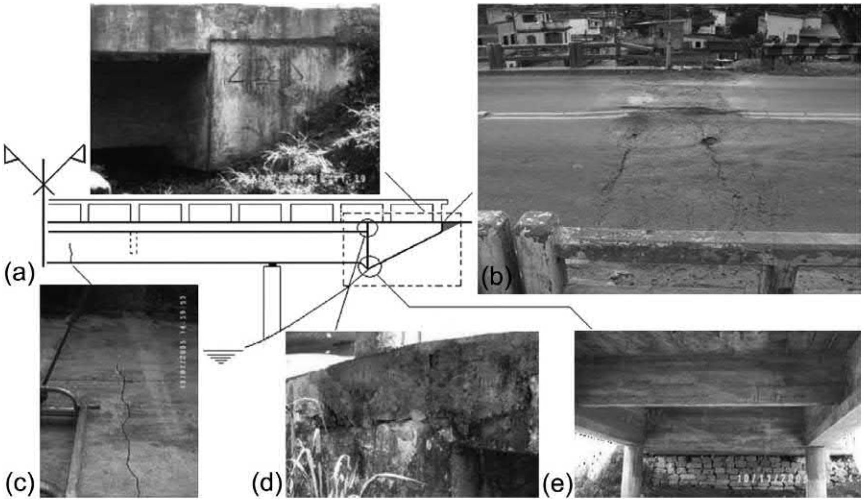

Figure 4.14 (a) Detail of cantilevered deck extremities and inclined embankments; (b) roughness of the access to bridges; (c) cracking at a midspan girder of one of the investigated bridges; (d) damage observed next to the extremities of a cantilevered deck bridge; (e) a rock barrier to restrain embankment slide under deck extremities (Rodrigues et al., 2013).

two concrete girders. In some of the investigated bridges, cracks at the midspan were also observed clearly, and in others, evidence of crack repairs in the same region was observed (Figure 4.14).

7. Crack detection, intervention methods and techniques

7.1 Crack detection

Visual inspection is the most common and useful way to discover fatigue cracks and failures. To further aid observation, two common nondestructive techniques used to expose cracks are dye penetrant and magnetic particle inspection. For the former, a cleaning procedure is first undergone to remove contaminants, then a red dye is sprayed on the surface, and finally, the excess is wiped out and a developer is sprayed on so that the volatile solvent will couple the flaw-entrapped dye penetrant to the powder and speed the penetrant's return to the surface for viewing. With this technique, cracks are shown precisely. Magnetic inspection is used with an electromagnetic yoke, inducing a magnetic field that is eventually disrupted by the crack presence, and then a fine iron filler is sprinkled on the area and is attracted by the magnetic concentration. In this latter case, rust or paint should be completely removed. Eddy current, ultrasonic testing (either manual or automatic), and time-to-flight-diffraction are other techniques employed for the same purpose.

7.2 Local intervention methods

Local intervention is needed when cracks or defects are evidenced only in a small part of the entire structure and when these are not loading- or distortion-induced fatigue problems. But these flaws should arise from local damage or flaws.

7.2.1 Surface treatment for welded structures

For the case of surface treatment for welded structures, the following solutions can be adopted:

- Grinding: The aim is to remove or reduce the size of the weld toe flaws from which fatigue cracks propagate. At the same time, the aim of grinding is to reduce the local stress concentration effect of the weld profile by smoothly blending the transition between the plate and the weld face (Figure 4.15; Haagensen and Maddox, 2001).
- TIG dressing: The aim of tungsten inert gas (TIG) dressing is to remove weld toe flaws by remelting the material at the weld toe, reducing the local stress concentration effect of the local weld toe profile by providing a smooth transition between the plate and the weld face (Figure 4.16; Haagensen and Maddox, 2001).
- Hammer and needle peening: Compressive residual stresses are induced by repeatedly hammering the weld toe region with a blunt-nosed chisel. It is not applicable to connections with main plate thicknesses of less than 4 mm for steel; for larger areas, needle peening is preferred (Figure 4.17; Haagensen and Maddox, 2001).
- Shot peening: Compressive residual stresses are induced by small spherical media shot bombarding the welding surface (Bandini, 2004).

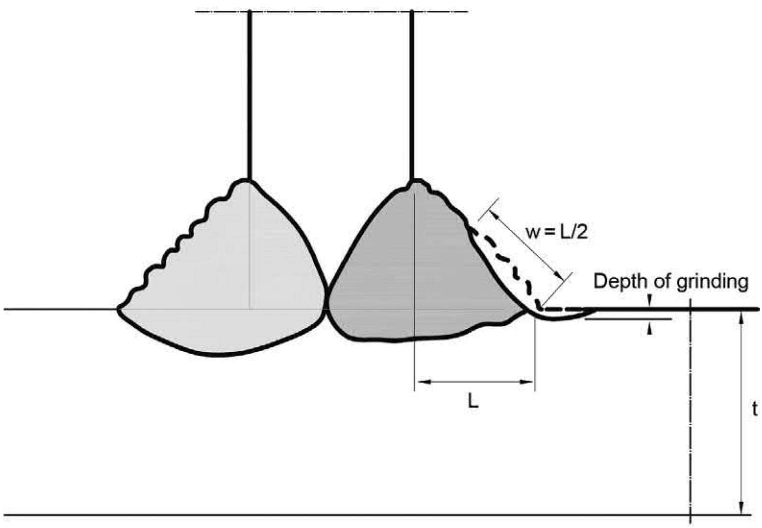

Figure 4.15 The burr grinding technique: the depth of grinding should be 0.5 mm below the bottom of any visible undercut, with a maximum of 2 mm, or 7% of plate thickness. Adapted from Haagensen and Maddox (2001).

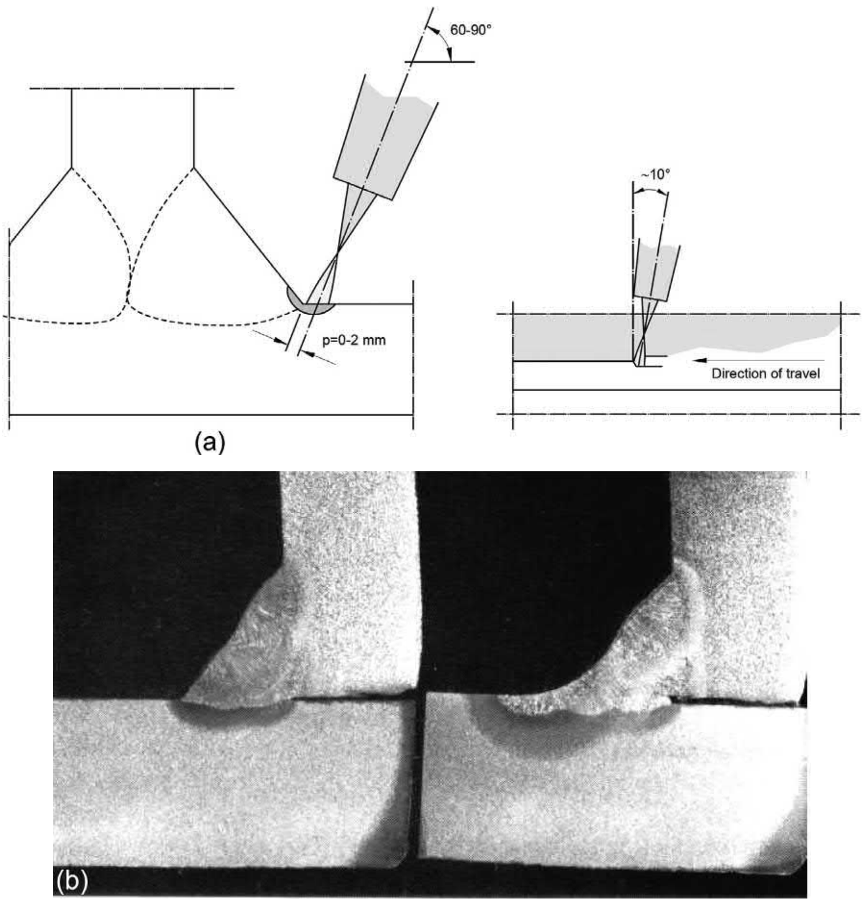

Figure 4.16 A weld toe threated with tungsten inert gas (TIG) dressing: (a) front (on left) and lateral view (on right) of the application; (b) before (on left) and after (on right) the application. Adapted from Haagensen and Maddox (2001).

- Ultrasonic impact treatment: This technique involves deformation treatment of the weld toe by a mechanical hammering at a frequency of around 200 Hz superposed by ultrasonic treatment at a frequency of 27 kHz. The objective of this treatment is to introduce beneficial compressive residual stresses at the weld toe by plastic deformation of the surface and to reduce the stress concentration by smoothing the weld toe profile (Gunther et al., 2005; Kudryavtsev et al., 2007).

7.2.2 Arresting cracks

Classical solutions for stopping cracks include the following:

- Stop holes: The execution of a stop hole is the method most widely used to repair fatigue cracks or to correct details prone to fatigue. It is often used as a temporary measure to stop the propagation of cracks, which might be followed by more extensive repairs. It is rare to

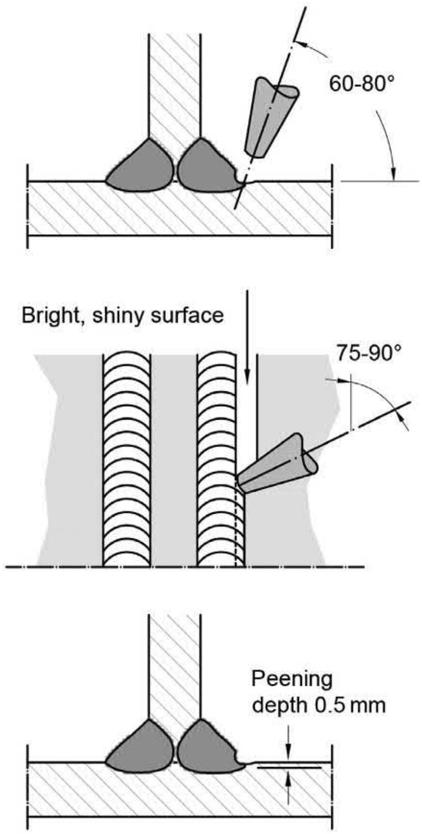

Figure 4.17 Hammer peening.

implement a remedial action that does not include the drilling of a hole at the top of the crack. In the case of critical details, the hole is often drilled to isolate the detail or to intercept a potential crack before it can propagate far into the root (Connor et al., 2005); the hole dimension could be dimensioned according to Fisher et al. (1990).

- Cover plating: Reinforcement plates introduce additional material to the cross section to increase the resisting area. Typically, cracks are repaired with protection plates with this method. The plates can be bolted or welded to the repaired part. However, from the point of view of the fatigue resistance, the bolted connection is the best option because connections with high-strength bolts may be considered as details of Category B (i.e., Category 125 of EC3), while the welded details may be considered details of Category E (i.e., Category 56 of EC3) or lower. It follows that for permanent repairs, the use of bolted plates is recommended (Connor et al., 2005).
- Welding: Welding can be used to repair cracks to restore the continuity of the element; at times, this appears to be the only solution, as the structure to be repaired cannot withstand the reduction of a section required by an intervention that uses bolts. However, welding should be done with caution, as it can introduce unfavorable conditions regarding fatigue strength, as discontinuity and residual stresses are inherent in the process (Dexter, 2004).

- Local heating: This approach consists of artificially introducing compressive residual stresses to an existing through-thickness crack by local heating near the crack tip. In spot heating, the structure is heated locally, usually with a gas torch, to produce local yielding resulting in compressive thermal stresses. As the locally heated metal cools, it shrinks, causing residual stresses (Jang et al., 2002).

An economic consideration needs to be made here, as the global economy of a new bridge should include maintenance costs, not just construction costs. Considering that repair and any further interventions imply significant costs, an important choice must be made at the design stage. From this perspective, bolted structures offer more advantages in the maintenance stage than welded structures because while a riveted/bolted member will not fail until additional cracks form in one or more additional elements, as they are inherently redundant, in a welded structure, one crack could propagate along the whole structural element and can easily cause global failure. For this reason, bolted structures, especially if subjected to cyclic live traffic loadings, are better than welded structures; however, they do require a particular kind of experience in both the design and the construction stages.

7.3 Global interventions

Large interventions are needed when cracks or defects are widely diffused throughout the whole structure, and local retrofits do not produce improvement in the structural behavior. Here are some examples:

- Load reduction: An increase in bearing capacity of the structure is obtained through the reduction of permanent loads via the construction of a lighter bridge deck slab. The replacement of the existing slab can appear to be an attractive solution if the high weight of the concrete constituent can be replaced with a system of lower weight. The literature recognizes these main types of system: in situ and precast concrete deck slabs of reduced dimensions using higher-strength concrete, metal gratings with and without fillings, orthotropic steel or aluminum deck slabs, composite fiber-reinforced polymer (FRP) deck slabs, and wooden slabs (Wipf et al., 1993). Deck slabs made of ultra-high-performance fiber-reinforced cement (UHPFRC)-based composites (strengthened with steel rebars) represent a further improvement because of their reduced weight and significantly improved fatigue and ultimate strength (Makita and Brühwiler, 2014a, b), together with FRP or a sandwich plate system (SPS), which may also represent suitable solutions, particularly where accelerated reconstruction is required.
- Composite action: In the case of simply supported deck systems, composite action could be introduced as a strengthening method to upgrade the loading capacity of the structural system and to reduce hot spot stresses; the structural design is similar to that of new structures; post-installed connectors should be used (Kwon et al., 2007).
- Cover plating: The same use of local retrofits could be realized in the whole structure; however, specific interventions could be adopted to gain a larger cross-resistant area, as new angles or members (Figure 4.18).
- Post-tensioning: Prestressing can be used as a means to introduce redundancy in critical elements to fracture. It can also be used to repair damaged zones where there are cracks. In this case, the method can provide the control of the propagation of the crack caused by traffic loads. For example, the total prestressing element of a tensile chord or tensile diagonal,

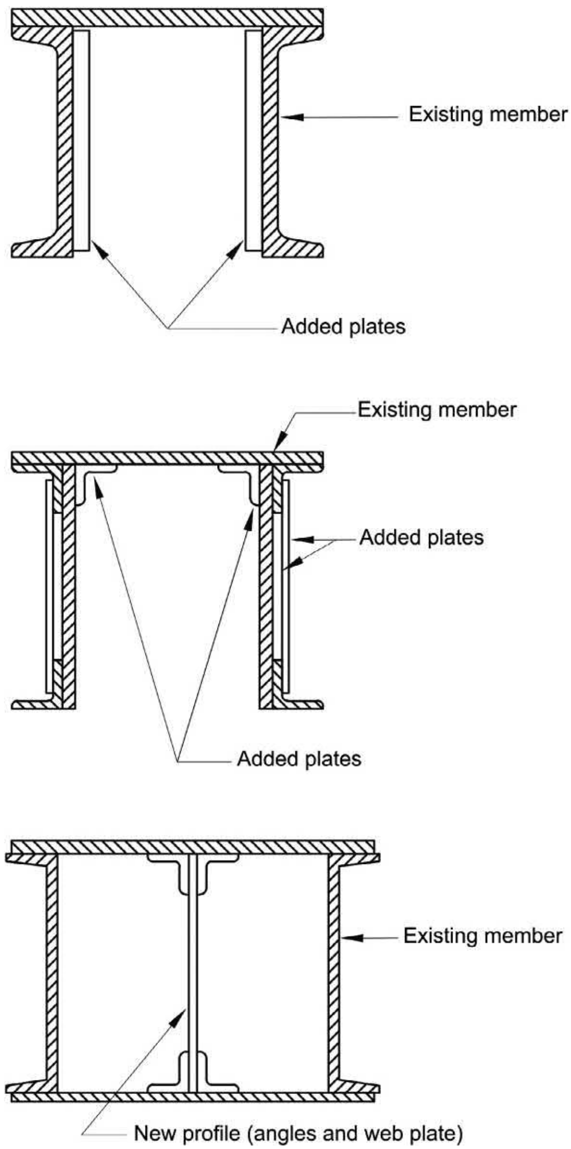

Figure 4.18 Cover plating options.

belonging to a lattice, can ensure permanent compression, preventing the crack to propagate and reach the critical size. If this option is not feasible due to the high levels of stress in other parts of the structure, one can choose a partial prestressing; external prestressing by means of high-strength bars or cables attached to the steel beams has been used as an effective technique for upgrading the load-carrying capacity of composite steel-concrete girders (Albrecht and Lenwari, 2008; Figure 4.19).

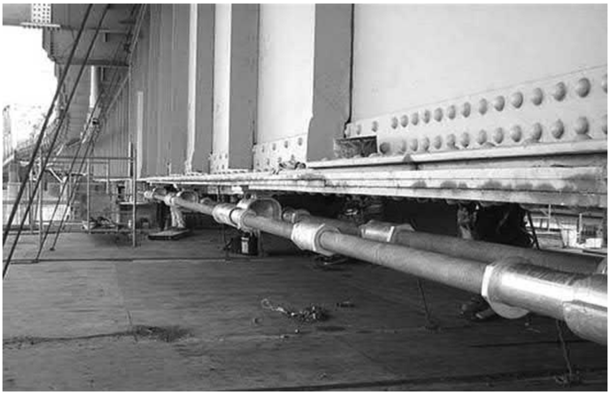

Figure 4.19 Post-tensioning steel bar application on an existing girder.

- High-strength pretensioned steel plates: This technique is applicable to beam elements, such as flooring system-bearers of girders and lattice girder bridges. Pretensioned plates are applied to the tension zone.
- TPSM: The thermal prestressing method (TPSM) has been proposed for innovative construction of continuous composite girder bridges as an effective prestressing method to prevent the occurrence of tensile transverse cracks in the concrete deck at the negative bending moment regions (Kim et al., 2010).
- FRP: An alternative technique for strengthening steel structures consists of the application of externally bonded FRP sheets, to increase mainly the tensile and flexural capacity of the structural elements. FRP materials have a high strength-to-weight ratio, do not give rise to problems due to corrosion, and are manageable. However, this technique is not flame resistant and should be shielded from fire.
- Modification of the static system: Although not applicable in all cases, modification of static conditions could be applied to improve fatigue resistance, avoiding stress concentrations and reducing stress amplitudes, for example, by introducing intermediate supports or transforming isostatic spans into hyperstatic systems.

A deeper focus is needed for the strengthening of RC bridge deck slabs and bridge girders using UHPFRC (ultra-high-performance fiber-reinforced cementitious composite): UHPFRC has properties such as high compressive strength (>150–200 MPa) and tensile strength (>10–14 MPa), tensile strain-hardening deformation of 0.2%–0.5%, and very low permeability because of an optimized dense cement-based matrix, making the material virtually waterproof (Brühwiler and Denarié, 2013). These properties make UHPFRC suitable for strengthening those parts of structural members that are subjected to mechanically and environmentally severe actions. The tensile behavior of UHPFRC may be effectively improved by arranging steel rebars to create reinforced UHPFRC (R-UHPFRC). In recent years, the necessity to improve the durability, load-bearing capacity, and fatigue resistance of bridge elements (primarily deck slabs) is growing due to the increase of traffic loads and volume. The strengthening of concrete bridge deck slabs is efficiently achieved by adding a 30–60 mm thick layer of UHPFRC (combined with steel rebars) on top of the existing RC deck slab without an increase or with only a minor increase in self-weight (thereby avoiding the need to strengthen other structural members like main beams or boxes). The UHPFRC layer increases the fatigue strength and ultimate resistance (in bending and shear) of the deck slab and improves durability due to its waterproofing properties protecting the reinforced concrete, making the UHPFRC strengthening technology efficient and economical. The technology has been applied since 2004, mostly in Switzerland, in more than 200 applications up to the year 2020. A recent large-scale application is the strengthening of the 2.1 km long Chillon Highway Viaduct in Switzerland, implying an increase in ultimate bending and shear resistance as well as fatigue strength of the deck slab, an increase of the hogging moment resistance of the main bridge girder, and waterproofing protection of the post-tensioned concrete structure for low intervention cost (Figure 4.20).

8. Research on fatigue and fracture

In view of a modern structural engineering approach, some changes are required in the common construction of steel and RC structures to avoid well-known concerns due to material deterioration. For this reason, bolting should be preferred over welding to take advantage of this connection type, which features relatively high fatigue strength and rapid construction is also easy to inspect, change, or improve. Moreover, high-strength materials should be used for both steel and RC structures, as they are able to sustain higher stresses in hot spots, prolonging their fatigue endurance. New materials are necessary, not only for retrofit interventions on existing structures, but also for new constructions, to gain new levels of sustainability, and to reduce economic costs. The most promising areas of research specific to the aforementioned goals are as follows:

- Testing: Testing techniques could be adopted for existing or new structures, at the scale of a single member/component up to an entire structure. This procedure helps in finding the most accurate solution for structural retrofit in existing bridges; in new bridges, it is able to anticipate the structural performance of components or entire structures (at the scaled or real size), obtaining more sustainable and more efficient design solutions. This method has been well established in the area of fatigue since the second half of the 18th century, either on a small scale or on a realistic scale. Small-scale specimen tests give longer apparent fatigue lives, either if testing is related to new structures or to FRP-strengthened specimens (Dexter and Fisher, 2000; Pipinato et al., 2012b); therefore, the *S-N* curve must be based on full-size testing of structural components such as girders, cross bracings, and stringer-to-floor connections. Moreover, testing on full-scale welded members has indicated that the primary effect of constant-amplitude fatigue loading can be accounted for in the live-load stress range. Relevant experiences with steel bridge testing are shown in Table 4.2 (for small- and full-scale tests of unreinforced steel structures) and Table 4.3 (for small- and full-scale tests of reinforced steel structures).
- Innovative materials (FRP): Some examples of guidelines for the design and construction of externally bonded FRP systems for strengthening of existing metallic structures include the ICE (Institution of Civil Engineers) "FRP Composites: Life Extension and Strengthening of Metallic Structures" (ICE, 2001), the Construction Industry Research and Information Association (CIRIA) Design Guide (Cadei et al., 2004), and the CNR-DT 202/2005 (Italian

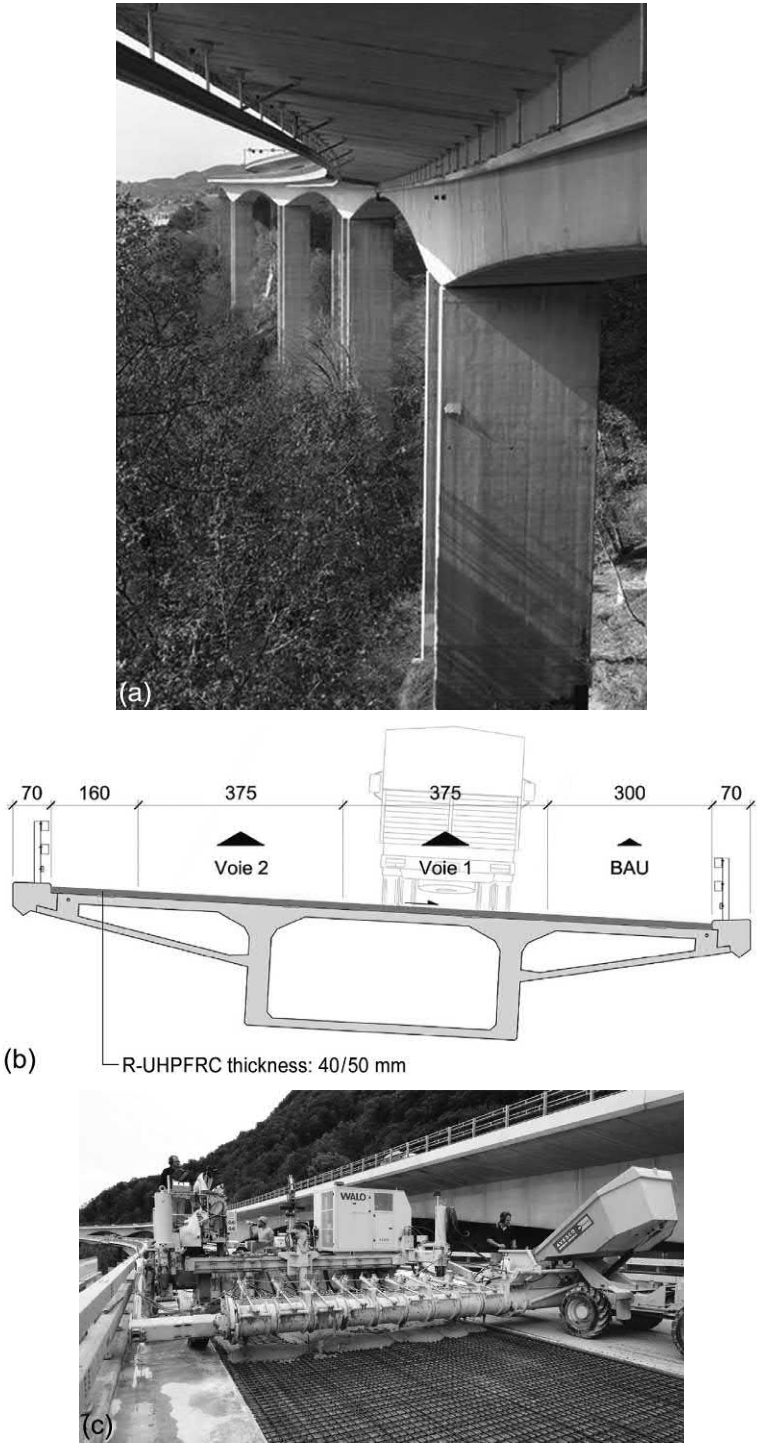

Figure 4.20 Strengthening of the deck slab of the 2.1 km long Chillon Highway Viaduct in Switzerland using R-UHPFRC: (a) a view of the viaduct; (b) a typical section; and (c) R-UHPFRC deck realization.

Table 4.2 Full- and Small-Scale Test of Non-Reinforced Structures

Author	**Year**	**Experimental Data**	
Reemsnyder	**1975**	**Type of test**	**Axial loading constant amplitude test**
		Specimens	Riveted gusset plate connections
		Structure	Ore unloading bridge
		Hot spot detail	Tension chord at its connection to a gusset plate
		Note	Five test results have been obtained by newly fabricated specimens
Baker and Kulak	1982	Type of test	Bending and shear test
		Specimens	Built-up hanger members
		Structure	Highway bridge
		Hot spot detail	Built-up hanger members
Out et al.	1984	Type of test	Bending test
		Specimens	Stringers
		Structure	Railway stringers
		Hot spot detail	Continuous riveted connection between the web and the flange angles
		Note	Not shown results from corroded specimens
Fisher et al.	1987	Type of test	Bending test
		Specimens	Built-up hanger members
		Structure	Railway stringers
		Hot spot detail	Web-to-flange connection
Brühwiler et al.	1990	Type of test	Bending test
		Specimens	Built-up plate girders and lattice girders, wrought iron and rolled mild steel
ATLSS	1993	Type of test	Bending test
		Specimens	Flanged angle to web
		Structure	Railway stringers
		Hot spot detail	Web-to-flange connection

Adamson and Kulak	1995	Type of test	Bending test
		Specimens	Stringers
		Structure	Built-up railway stringers
		Hot spot detail	Horizontal bracing attachment riveted to the tension flange
Di Battista and Kulak	1995	Type of test	Axial tension
		Specimens	Diagonals
		Structure	Railway truss bridge
		Hot spot detail	Riveted connection of the outstanding legs of these angles to gusset plates
Åkesson and Edlund	1996	Type of test	Bending test
		Specimens	Flange angles riveted to web plate
		Structure	Built-up railway stringers
		Hot spot detail	Angle to web connection
Helmerich et al.	1997	Type of test	Bending and axial test
		Specimens	Truss members
		Structure	—
		Hot spot detail	Built-up plate girders
Matar and Greiner	2006	Type of test	Bending test
		Specimens	Secondary members
		Structure	Railway bridge
		Hot spot detail	Flange-to-web connection
		Note	Only not corroded specimens were tested
Pipinato	2008	Type of test	Bending test
		Specimens	Full-scale girders
		Structure	Railway bridge
		Note	Only not corroded specimens were tested
Pipinato	2008	Type of test	Shear test
		Specimens	Short diaphragm connection
		Structure	Railway bridge
		Hot spot detail	Short diaphragm connection
		Note	Only not corroded specimens were tested

Table 4.3 Full- and Small-Scale Tests of Reinforced Structures

Reference	Details	Test Type
Bocciarelli, 2009	S275 specimens reinforced on each side with Sika Carbo Dur M614	Normal tension
Iwashita, 2007	Single-lap shear steel specimens	Normal tension
Jones, 2003	5 steel specimens not reinforced and 24 each side reinforced specimens	Normal tension
Monfared, 2008	15 plates of steel reinforcing or not the specimens with FRP, treating the surface with blasting or less, and applying the reinforcements on one or both sides	Normal tension
Zheng, 2006	6 steel specimens with a hollow center and provided with 2 cracks reinforced with CFRP on one or both side	Normal tension
Colombi, 2003	Perforated steel specimens with 2 crack, reinforced with 2 CFRP straps on each side	Normal tension
Taljsten, 2009	5 historical steel specimens perforated, with 2 cracks	Normal tension
Liu, 2005	12 steel joints composed by 2 steel plates CFRP reinforced, with normal or HM on each side	Normal tension
Tavakkolizadeh, 2003	5 steel beams hollowed in the flanges and CFRP reinforced on the lower and midspan flange	Bending
Deng, 2007	Steel beams CFRP reinforced on the lower and midspan flange	Bending
Bassetti, 1999	Truss-riveted beams with I-section, traditionally reinforced	Bending
Bassetti, 2001	Truss-riveted beams traditionally reinforced	Bending
	Truss-riveted beams reinforced with 2 CFRP laminates and 3 CFRP post-tensioned laminates on the lower flange	Bending

Research Council, 2005). The benefits of composite strengthening have been applied, for example, in a steel bridge on the London Underground (Moy and Bloodworth, 2007). The benefits of strengthening large cast-iron struts with carbon FRP (CFRP) composites in the London Underground are illustrated in Moy and Lillistone (2006). A state-of-the-art review of FRP-strengthened steel structures has been provided by Zhao and Zheng (2007). Among these materials, apart from the well-known e-glass, high-strength (HS) CFRP, and aramid, high-modulus CFRP (HM CFRP) materials are being widely used and have been developed with a tensile modulus that is approximately twice that of steel. We are still far from real improvements in industrial and general use of new materials, but composite material industries have the right bases to go toward real innovations.

- Innovative materials like UHPFRC (ultra-high-performance fiber-reinforced cementitious composite): The static behavior of UHPFRC and R-UHPFRC has been investigated by many researchers; however, few findings have been reported so far in the literature. The fatigue behavior of tensile-strain-hardening UHPFRC and R-UHPFRC has been investigated by

Makita and Brühwiler (2014a, b) with the purpose of using this material for the fatigue strengthening of RC bridge deck slabs. Other concurring recent research on this issue includes the local bending tests and punching failure of a ribbed UHPFRC bridge deck (Toutlemonde et al., 2007) and the study of UHPFRC overlays to reduce stresses in orthotropic steel decks (Lamine et al., 2013). The biaxial flexural fatigue behavior of thin slab elements made of strain-hardening UHPFRC was investigated experimentally by Shen and Brühwiler (2020). Test results presented in the *S-N* diagram reveal a fatigue endurance limit under biaxial flexural fatigue at $S = 0.54$. Fatigue strength was similar to the one obtained from direct tensile fatigue tests.

References

Abe, H., 1989. Fatigue strength of corroded steel plates from old railway bridges. In: IABSE Symposium, Lisbon, pp. 205–210.

Adamson, D.E., Kulak, G.L., 1995. Fatigue Test of Riveted Bridge Girders. Structural Engineering Report No. 210, Department of Civil Engineering, University of Alberta.

AISC (Ed.), 2011. Steel Construction Manual, fourteenth ed. AISC-American Institute for Steel Construction, Chicago.

Åkesson, B., 1991. Older Railway Bridge-Load-Carrying Capacity, Condition and Service Life. Department of Structural Engineering, Chalmers University of Technology, Gothenburg, Sweden.

Åkesson, B., 1994. Fatigue Life of Riveted Railway Bridges. Thesis (PhD), Division of Steel and Timber Structures, Chalmers University of Technology, Publ. S94, Goteborg, Sweden, p. 6.

Albrecht, P., Lenwari, A., 2008. Fatigue strength of repaired prestresses composite beams. J. Bridge Eng. 13 (4), 409–417.

Al-Emrani, M., 2000. Two Fatigue-Related Problems in Riveted Railway Bridges. Thesis (Licentiate), Department of Structural Engineering, Chalmers University of Technology, Goteborg, Sweden.

American Association of State Highway and Transportation Officials (AASHTO), 2013. LRFD Bridge Design Specifications, sixth ed. with 2013 Interim Revisions. Washington, DC.

Anderson, T.L., 1995. Fracture Mechanics—Fundamentals and Applications, second ed. CRC Press, Boca Raton, FL.

ASCE Committee on Fatigue and Fracture Reliability, 1982a. Fatigue reliability: introduction. J. Struct. Div. 108 (1), 3–23.

ASCE Committee on Fatigue and Fracture Reliability, 1982b. Fatigue reliability: quality assurance and maintainability. J. Struct. Div. 108 (1), 25–46.

ASCE Committee on Fatigue and Fracture Reliability, 1982c. Fatigue reliability: variable amplitude loading. J. Struct. Div. 108 (1), 47–69.

ASCE Committee on Fatigue and Fracture Reliability, 1982d. Fatigue reliability: development of criteria for design. J. Struct. Div. 108 (1), 71–88.

ATLSS (Center for Advanced Technology for Large Structural Systems), 1993. Assessment of Remaining Capacity and Life of Riveted Bridge Members. Draft Project Report to Canadian National Railways, 1993, ATLSS, Lehigh University, Bethlehem, Pennsylvania.

AWS, 2010. D1.5M/D1.5:2010 Bridge Welding Code. American Welding Society, a Joint Publication of American Association of State Highway and Transportation Officials. Miami.

Baker, K.A., Kulak, G.L., 1982. Fatigue Strength of Two Steel Details. Structural Engineering Report No. 105, Department of Civil Engineering, University of Alberta.

Bandini, M., 2004. La pallinatura controllata e le sue applicazioni. In: International Conference on Innovative Solutions, Components and Materials for Transport Industries, Proceedings of the Conference, Verona, Italia, pp. 122–138.

Brühwiler, E., Denarié, E., 2013. Rehabilitation and strengthening of concrete structures using ultra-high-performance fibre-reinforced concrete. SEI 23 (4), 450–457.

Brühwiler, E., Smith, I.F.C., Hirt, M.A., 1990. Fatigue and fracture of riveted bridge members. J. Struct. Eng. 116 (1), 198–214.

Brühwiler, E., Vogel, T., Lang, T., Lüch, P., 2012. Swiss standards for existing structures. SEI 22 (2), 275–280.

Byers, W.G., Marley, M.J., Mohammadi, J., Nielsen, R.J., Sarkani, S., 1997. Fatigue reliability reassessment applications: state of the-art paper. J. Struct. Eng. 123 (3), 277–285.

Cadei, J.M.C., Stratford, T.J., Hollaway, L.C., Duckett, W.G., 2004. Strengthening Metallic Structures Using Externally Bonded Fibre-Reinforced Polymers (C595). CIRIA Design Guide, CIRIA, London.

Chen, Y., Ni, J., Zheng, P., Azzam, R., Zhou, Y., Shao, W., 2011. Experimental research on the behavior of high frequency fatigue in concrete. Eng. Fail. Anal. 18, 1848–1857.

Cheung, M.S., Lib, W.C., 2003. Probabilistic fatigue and fracture analyses of steel bridges. Struct. Saf. 23, 245–262.

Chotickai, P., Kanchanalai, T., 2010. Field testing and performance evaluation of a through plate girder railway bridge. Transport. Res. Rec. 2172, 132–141.

Chryssanthopoulos, M.K., Righiniotis, T.D., 2006. Fatigue reliability of welded steel structures. J. Const. Steel Res. 62 (11), 1199–1209.

Confederation Europeene de Billiard (CEB), 1988. Fatigue of Concrete Structures, Bulletin 188. State-of-the-Art Report, Lausanne.

Connor, R.J., Dexter, R., Mahmoud, H., 2005. Inspection and Management of Bridges with Fracture-Critical Details. NCHRP Synthesis 354, Transportation Research Board, Washington, DC.

Cornelissen, H.A.W., Reinhardt, H.W., 1982. Fatigue of plain concrete in uniaxial tension and in alternating tension-compression loading. IABSE Rep. 37, 273–282.

Cornelissen, H.A.W., Reinhardt, H.W., 1984. Uniaxial tensile fatigue failure of concrete under constant-amplitude and programme loading. Mag. Concr. Res. 36 (129), 216–226.

Crooker, T.W., Lange, E.A., 1970. How yield strength and fracture toughness considerations can influence fatigue design procedures for structural steels. Weld. Res. Suppl. 489-s.

Dexter, R.J., 2004. Sign, signal, and light support structures and manual for repair fatigue cracks. In: Third Annual Bridge Workshop: Fatigue and Fracture.

Dexter, R.J., Fisher, J.W., 1996. The effect of unanticipated structural behavior on the fatigue reliability of existing bridge structures, structural reliability in bridge engineering. In: Frangopol, D.M., Hearn, G. (Eds.), Proceedings of a Workshop at the University of Colorado at Boulder. McGraw Hill, New York, pp. 90–100.

Dexter, R.J., Fisher, W.F., 2000. Fatigue and fracture. In: Chen, W.-F., Duan, L. (Eds.), Bridge Engineering Handbook. CRC Press, Boca Raton.

Di Battista, J.D., Kulak, G.L., 1995. Fatigue of Riveted Tension Members. Structural Engineering Report No. 211, Department of Civil Engineering, University of Alberta.

Ditlevsen, O., Madsen, H.O., 2005. Structural Reliability Methods. John Wiley & Sons, Chichester.

Dyduch, K., Szerszen, M., Desterbecq, J.-F., 1994. Experimental investigation of the fatigue of plain concrete under high compressive loading. Mater. Struct. 27, 505–509.

EN 1990, 2010. Eurocode—Basis of Structural Design. CEN, Brussels.

EN 1991-2, 2010. Actions on Structures—Traffic Loads on Bridges. CEN, Brussels.

EN 1993-1-10, 2009. Eurocode 3: Design of Steel Structures—Parts 1–10: Material Toughness and Through-Thickness Properties. CEN, Brussels.

EN 1993-1-9, 2005. Eurocode 3: Design of Steel Structures—Parts 1–9: Fatigue. CEN, Brussels.

Federal Highway Administration (FHWA), 2012. Steel Bridge Design Handbook: Redundancy. Publication No. FHWA-IF 12-052—Vol. 9.

Fisher, J.W., 1984. Fatigue and Fracture in Steel Bridges. Wiley-Interscience, Hoboken, NJ.

Fisher, J.W., Yen, B.T., Wang, D., 1987. Fatigue and Fracture Evaluation for Rating Riveted Bridges. Transportation Research Record 302, Transportation Research Board, Washington, DC, pp. 25–35.

Fisher, J.W., Yen, B.T., Wang, D., 1990. Fatigue strength of riveted bridge members. J. Struct. Eng. 116 (11), 2968–2981.

Forsberg, B., 1993. Utmattningsha llfasthet hos äldre konstruktionssta l med korrosionsskador. Master Thesis, Division of Steel Structures Lulea University of Technology. ISSN 0349-6023.

Freudenthal, A.M., 1945. Safety of structures. Trans. ASCE 112 (1947), 125–180.

Frey, R., Thurlimann, B., 1983. Ermüdungsversuche an Stahlbetonbalken mit und ohne Schubbewehrung. Institute für Baustatik und Konstruktion Bericht Nr 7801-1, ETH Zurich.

Gunther, H.P., Kuhlmann, U., Dürr, A., 2005. Rehabilitation of welded joints by ultrasonic impact treatment (Uit). In: IABSE Symposium, Lisbon.

Haagensen, P.J., Maddox, S.J., 2001. IIW recommendations on post-weld improvement of steel and aluminum structures. In: IIW Commission XIII Working Group 2—Improvement Techniques, Paris.

Helmerich, R., Brandes, K., Herter, J., 1997. Full scale laboratory fatigue tests on riveted railway bridges, evaluation of existing steel and composite bridges. In: IABSE Workshop, Lausanne, pp. 191–200.

Herwig, A., 2008. Reinforced Concrete Bridges Under Increased Railway Traffic Loads—Fatigue Behaviour and Safety Measures. Doctoral Thesis EPFL No. 4010, EPFL Press, Lausanne.

Herwig, A., Brühwiler, E., 2011. In situ dynamic behavior of a railway bridge girder under fatigue causing traffic loading. In: Proc. ICASP 11—11th Intl. Conf. Appl. Stat. Prob. Civil Eng., Zurich, August 1–4.

ICE-Institution of Civil Engineers, 2001. FRP composites: life extension and strengthening of metallic structures. In: ICE Design and Practice Guide. Thomas Telford, London, ISBN: 978-0-7277-3009-1.

International Institute of Welding (IIW), 1996. Fatigue of Welded Components and Structures. International Institute of Welding—Working Group 5 (WG5): Repair of Fatigue-Loaded Welded Structures. IIW, Villepinte.

Italian Research Council, 2005. Guidelines for the Design and Construction of Externally Bonded FRP Systems for Strengthening Existing Structures. Preliminary Study. Metallic Structures (CNR-DT 202/2005). Italian Research Council, Rome.

Jang, C.D., Song, H.C., Lee, C.H., 2002. Fatigue life extension of a through-thickness crack using local heating. In: International Offshore and Polar Engineering Conf, May. ISOPE edition, Kitakyushu, Japan.

Kim, S.H., Kim, J.H., Ahn, J.A., 2010. Life-cycle cost analysis of a TPSM applied continuous composite girder bridge. Int. J. Steel Struct. 10 (2), 115–129.

Kudryavtsev, Y., Kleiman, J., Lugovskoy, A., Lobanov, L., Knysh, V., Voitenko, O., Prokopenko, G., 2007. Rehabilitation and Repair of Welded Elements and Structures by Ultrasonic Peening. IIW Document XIII-2076-05, International Institute of Welding, Paris.

Kuhn, B., Lukić, M., Nussbaumer, A., Gunther, H.-P., Helmerich, R., Herion, S., Kolstein, M. H., Walbridge, S., Androic, B., Dijkstra, O., Bucak, O., 2008. Assessment of Existing Steel Structures: Recommendations for Estimation of Remaining Fatigue Life. Joint report prepared under the JRC-ECCS cooperation agreement for the evolution of Eurocode 3 (program of CEN/TC 250).

Kulak, G., 1992. Discussion of "Fatigue Strength of Riveted Bridge Members" by John W. Fisher, Ben T. Yen, and Dayi Wang (November 1990, Vol. 116, No. 11). J. Struct. Eng. 118 (8), 2280–2281.

Kwon, G., Hungerford, B., Kayir, H., Schaap, B., Kyu Ju, Y., Klingner, R., Engelhardt, M., 2007. Strengthening Existing Non-Composite Steel Bridge Girders Using Post-Installed Shear Connectors. Report FHWA/TX-07/0-4124-1, Texas Department of Transportation.

Lamine, D., Marchand, P., Gomes, F., Tessier, C., Toutlemonde, F., 2013. Use of UHPFRC overlay to reduce stresses in orthotropic steel decks. J. Construct. Steel Res. 89, 30–41.

Lee, P.G., Shim, C.S., Chang, S.P., 2005. Static and fatigue behavior of large stud shear connectors for steel-concrete composite bridges. J. Construct. Steel Res. 61 (9), 1270–1285.

Leitão, F.N., da Silva, J.G.S., de Andrade, S.A.L., da Vellasco, P.C.G.S., de Lima, L.R.O., 2011. Fatigue analysis of composite (steel-concrete) highway bridges subjected to dynamic actions of vehicles. In: CC 2011—The Thirteenth International Conference on Civil, Structural and Environmental Engineering Computing. vol. 1. Civil-Comp Press, Chania, Crete, Greece, pp. 1–17.

Makita, T., Brühwiler, E., 2014a. Tensile fatigue behaviour of ultra-high performance fibre reinforced concrete combined with steel rebars (R-UHPFRC). Int. J. Fatigue 59, 145–152.

Makita, T., Brühwiler, E., 2014b. Tensile fatigue behaviour of ultra-high performance fibre reinforced concrete. Mat. Struct. 47, 475–491.

Mang, F., Bucak, Ö., 1993. Application of the S-N line concept for the assessment of the remaining fatigue life of old bridge structures. In: Bridge Management 2. Inspection, Maintenance Assessment and Repair. ISBN: 0 7277 1926 2.

Miki, C., Ito, Y., Sasaki, E., 2003. Fatigue and Repair Cases in Steel Bridges. Tokyo Institute of Technology, Department of Civil Engineering, Miki Laboratory, Tokyo.

Miner, M.A., 1945. Cumulative damage in fatigue. J. Appl. Mech. 12 (3), 159–164.

Moy, S.S.J., Bloodworth, A.G., 2007. Strengthening a steel bridge with CFRP composites. Proc. ICE. Struct. Build. 160, 81–93.

Moy, S.S.J., Lillistone, D., 2006. Strengthening cast iron using FRP composites. Proc. ICE. Struct. Build. 159 (6), 309–318.

National Bridge Inspection Standards (NBIS), 2004. U.S. Department of Transportation, Federal Highway Administration (FHWA), Washington, DC.

National Cooperative Highway Research Program (NCHRP), 2012. Fatigue Evaluation of Steel Bridges. National Cooperative Highway Research Program. Report 721/2012, Transportation Research Board, Washington, DC.

Out, J.M.M., Fisher, J.W., Yen, B.T., 1984. Fatigue strength of weathered and deteriorated riveted members. Transport. Res. Rec. 950 2, 10–20.

Paris, P.C., Gomez, M.P., Anderson, W.E., 1961. A rational analytic theory of fatigue. Trend Eng. 13, 9–14.

Perdikaris, C., Beim, S., 1988. RC bridge decks under pulsating and moving load. J. Struct. Eng. 114 (3), 591–607.

Pipinato, A., 2008. High-Cycle Fatigue Behaviour of Historical Metal Riveted Railway Bridges. PhD Thesis, University of Trento, Trento, Italy.

Pipinato, A., 2010. Step-level procedure for remaining fatigue life evaluation of one railway bridge. Baltic J. Road Bridge Eng. 5 (1), 28–37. https://doi.org/10.3846/bjrbe.2010.04.

Pipinato, A., Pellegrino, C., Bursi, O.S., Modena, C., 2009. High-cycle fatigue behavior of riveted connections for railway metal bridges. J. Construct. Steel Res. 65 (12), 2167–2175.

Pipinato, A., Pellegrino, C., Modena, C., 2012a. Assessment procedure and rehabilitation criteria for the riveted railway Adige Bridge. Struct. Infrastruct. Eng.: Main Manage Life-Cycle Des. Perform. 8 (8), 747–764. https://doi.org/10.1080/15732479.2010.481674.

Pipinato, A., Pellegrino, C., Modena, C., 2012b. Fatigue behavior of steel bridge joints strengthened with FRP laminates. Mod. Appl. Sci. 6 (9), 1–15.

Rabemanantso, H., Hirt, M.A., 1984. Comportement a la Fatigue de Profiles Lamines avec Semelles de Renfort Revetees, ICOM Report 133. Swiss Federal Institute of Technology, Lausanne, Switzerland.

Reemsnyder, H.S., 1975. Fatigue life extension of riveted connections. J. Struct. Div. Proc. Am. Soc. Civ. Eng. 101 (ST12), 2591–2608.

Rodrigues, J.F.S., Casas, J.R., Almeida, P.A.O., 2013. Fatigue-safety assessment of reinforced concrete (RC) bridges: application to the Brazilian highway network. Struct. Infrastruct. Eng.: Main. Manage Life-Cycle Des. Perform. 9 (6), 601–616.

Schlafli, M., Brühwiler, E., 1998. Fatigue of existing reinforced concrete bridge deck slabs. Eng. Struct. 20 (11), 991–998.

Shen, X., Brühwiler, E., 2020. Biaxial flexural fatigue behavior of strain-hardening UHPFRC thin slab elements. Int. J. Fatigue 138.

Sonoda, K., Horikawa, T., 1982. Fatigue strength of reinforced concrete slabs under moving loads. IABSE Rep. 37, 455–462.

Soudki, K., Rizkalla, S., Uppal, A., 1999. Performance of bridge timber ties under static and fatigue loading. J. Bridge Eng. 4 (4), 263–268.

Stadelmann, W., 1984. Compiling of material tests on wrought iron rivets at EMPA, St. Gallen. Private communication [in German], cited in Brühwiler, E., Smith, I.F.C., and Hirt, M. 1990. Fatigue and fracture of riveted bridge members. J. Struct. Eng. 116 (1), 198–213.

Stephens, R.I., Fatemi, A., Stephens, R.R., Fuchs, H.O., 2001. Metal Fatigue in Engineering. John Wiley & Sons, New York.

Toutlemonde, F., Renaud, J.-C., Lauvin, L., Brisard, S., Resplendino, J., 2007. Local bending tests and punching failure of a ribbed UHPFRC bridge deck. In: Proc. 6th Intl. Conf. Fracture Mech. Concrete and Concrete Struct., vol. 3, pp. 1481–1489, 2007.

Tsiatas, G., Palmquist, S.M., 1999. Fatigue evaluation of highway bridges. Prob. Eng. Mech. 14, 189–194.

Weigler, H., Rings, K., 1987. Unbewehrter und bewehrter Beton unter Wechselspannungen. Deutscher Ausschuss für Stahlbeton 383, 52.

Wichtowski, B., 2013. Assessment of fatigue and selection of steel on constructions of steel bridges welded according to Eurocode 3. Weld. Intl. 27 (5), 345–352.

Wipf, T.J., Klaiber, F.W., Besser, D.M., Laviolette, M.D., 1993. Manual for Evaluation, Rehabilitation and Strengthening of Low Volume Bridges. Iowa Department of Transportation, Ames.

Xiulin, Z., Zhen, L., Yongi, S., Yanman, Y., Zhijiang, S., 1996. Fatigue performance of old bridge steel and the procedures for life prediction with given survivability. Eng. Fract. Mach. 53 (2), 251–262.

Ye, X.W., Su, Y.H., Han, J.P., 2014. A state-of-the-art review on fatigue life assessment of steel bridges. Math. Prob. Eng. 2014, 1–13. Article ID 956473.

Zhao, X.L., Zheng, L., 2007. State-of-the-art review on FRP strengthened steel structures. Eng. Struct. 29, 1808–1923.

Further reading

Åkesson, B., Edlund, B., 1996. Remaining fatigue life of riveted railway bridges. Der Stahlbau 65 (11), 429–436.

Fisher, J.W., Mertz, D.R., Zhong, A., 1983. Steel Bridge Members Under Variable Amplitude Long Life Fatigue Loading. Transportation Research Record 267, National Research Council, Washington, DC.

Pipinato, A., Molinari, M., Pellegrino, C., Bursi, O.R., Modena, C., 2011. Fatigue tests on riveted steel elements taken from a railway bridge. Struct. Infrastruct. Eng. 7 (12), 907–920. https://doi.org/10.1080/15732470903099776.

Part III

Structural analysis

This page intentionally left blank

Bridge structural theory and modeling

5

Alessio Pipinato
AP&P, CEO and Technical Director, Rovigo, Italy

1. Introduction

The bridge engineering and design process involves a number of disciplines, at the basis of which undoubtedly lies the structural analysis theory. This chapter deals with the most interesting aspects of the structural analysis of bridges. Later, the text focuses on finite element method (FEM) theory and its applications to bridges, to emphasize the importance of this design instrument, commonly used by bridge engineers in their everyday applications.

2. Structural theory

Stresses inside a body generated by external excitations (volume and surface forces) can be obtained using equilibrium equations. Three equilibrium equations relate to the six components of the σ_{ij} stress tensor for an infinitesimal element in a static state; in the dynamic case, equations of motion are needed, including second-order derivatives of displacement (with respect to time). Considering the geometrical conditions, strains and displacement could be linked by using strain–displacement equations of kinematics expressing the components of strain ε_{ij} by the displacement components (u_i). The constitutive laws exert a material influence on these mathematical relations. The 15 variables are described and can be connected by 15 equations (three equilibrium equations, six kinematics equations, and six constitutive equations). To solve the general problem of solid mechanics, two basic methods are available: the displacement method and the stress method. A combination of these two methods can also be used. In fact, while these methods could be directly applied for simple elastic problems, the discretization procedure is applied today for complex and irregular structural forms and components, as in bridge engineering. This implies a preference for the use of the so-called FEM model, which can subdivide every complex body into finite small elements, solving every variable in the investigated discretized body with direct or iterative procedures. It is the method most widely adopted by automated software for the solution of real-life structural analysis problems. The systematic method adopted in computational analysis is matrix analysis, a computer code procedure implementing the classical methods used for handmade structural calculations

Innovative Bridge Design Handbook. https://doi.org/10.1016/B978-0-12-823550-8.00017-2

(i.e., the principle of virtual displacement, the minimization of the total potential energy, and the minimization of the total complementary energy). When using matrix analysis to solve issues, two methods are available: the force method (with unknown internal forces) and the displacement method (with unknown displacement). In every case, the solving equations are based on a joint equilibrium and compatibility, giving as a result the stresses, strains, and displacements of every element of the investigated structure. Whenever FEM results are available, human judgment is needed: FEM solutions cannot be used without an expert overview of the reliability of the given output.

2.1 Equilibrium

Newton's first law of motion states that an object will remain at rest or in uniform motion in a straight line unless acted upon by an external force. It may be seen as a statement about inertia, that objects will remain in their state of motion unless a force acts to change the motion. This is what we call "equilibrium" state, in which—if the resultant force acting on a body is zero—the particle will remain at rest or will move at a constant velocity. Static is essentially concerned with the case where the particle or body remains at rest. A complete free-body diagram is essential for the solution of problems concerning the equilibrium. In a three-dimensional (3-D) case, the conditions of equilibrium require the satisfaction of the following equations of static:

$$\begin{gathered}\sum F_x=0 \ \sum F_y=0 \ \sum F_z=0 \\ \sum M_x=0 \ \sum M_y=0 \ \sum M_z=0\end{gathered} \tag{1}$$

The previous equations state that the sum of all forces acting on a body in any direction must be zero, and the sum of all moments about any axis must be zero. A structure is *statically determinate* when all forces on its members are found by using only equilibrium conditions. If there are more unknowns than available equations of statics, the problem is called *statically indeterminate*. The degree of static indeterminacy is equal to the difference between the number of unknown forces and the number of relevant equilibrium conditions. Any reaction that is in excess of those that can be obtained by statics alone is termed a *redundant*. The number of redundants is, therefore, the same as the degree of indeterminacy. The generalization of the foregoing is analyzed in a free body of volume V (Ansel and Saul, 2011).

The body with all the appropriate forces, both known and unknown, acting on it is represented in Figure 5.1. An element of area ΔA, located at the internal point Q on the cut surface, is acted on by force ΔF. Put the origin of coordinates at point Q, with x normal and y and z tangent to ΔA, and assume that ΔF is not lying along x, y, or z. Decomposing ΔF into components parallel to x, y, and z (Figure 5.1c), we can define the normal (perpendicular) stress σ_x and the shearing (tangent) stresses τ_{xy} and τ_{xz} as follows:

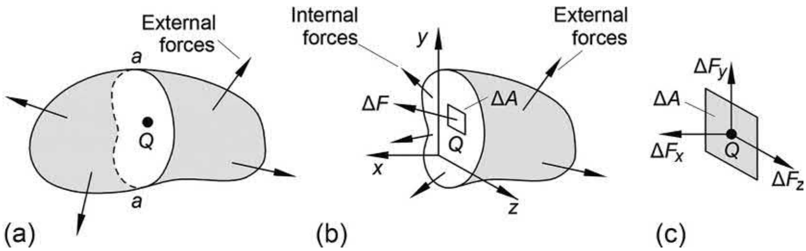

Figure 5.1 Derivation of equations of equilibrium: (a) a loaded body; (b) body with external and internal forces; (c) enlarged area ΔA with force components.

$$
\begin{aligned}
\sigma_x &= \lim_{\Delta A \to 0} \frac{\Delta F_x}{\Delta A} = \frac{dF_x}{dA} \\
\tau_{xy} &= \lim_{\Delta A \to 0} \frac{\Delta F_y}{\Delta A} = \frac{dF_y}{dA} \\
\tau_{xz} &= \lim_{\Delta A \to 0} \frac{\Delta F_z}{\Delta A} = \frac{dF_z}{dA}.
\end{aligned}
\tag{2}
$$

In the generalized 3-D case, distributed forces within a load-carrying member can be represented by a statically equivalent system consisting of a force and a moment vector acting at any arbitrary point (usually the centroid) of a section. These internal force resultants (also called *stress resultants*), exposed by an imaginary cutting plane containing the point through the member, are usually resolved into components that are normal and tangent to the cut section (Figure 5.2). The sense of moments follows the right-hand-screw rule, often represented by double-headed vectors, as shown in the figure. Each component can be associated with one of four modes of force transmission: (i) The axial force P or N tends to lengthen or shorten the member; (ii) the shear forces Vy and Vz tend to shear one part of the member relative to the adjacent part; (iii) the torque or twisting moment T is responsible for twisting the member; (iv) the bending moments My and Mz cause the member to bend.

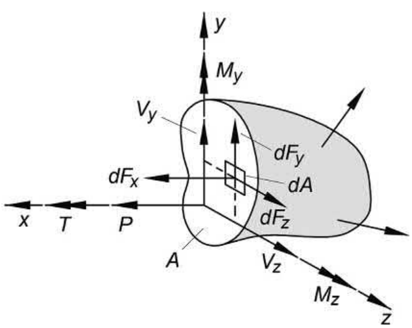

Figure 5.2 Forces and moments on a section of a 3-D body.

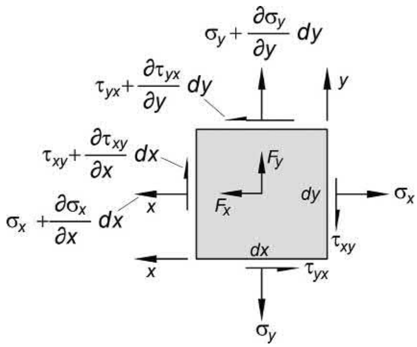

Figure 5.3 3-D infinitesimal element with body forces and stresses.

According to the general case, components of stresses vary from point to point in a stressed body, where stress variations are governed by the conditions of equilibrium and mathematically from the differential equations of equilibrium.

Considering a planar infinitesimal element of sides *dx* and *dy* (Figure 5.3), being σ_x, σ_y, σ_{xy}, τ_{yx} functions of *x* and *y,* but independent from *z* (not varying in thickness), and all the other components being zero, this is a typical plane stress situation. In this scenario, the variation of stresses (e.g., along the *x*-axis could be denoted by a truncated Taylor's series with partial derivatives, with σ_x a function of *x* and *y*) is

$$\left(\partial\sigma_x + \frac{\partial\sigma_x}{\partial x}dx\right). \tag{3}$$

All the other variations are similarly obtained. By the use of Eq. (1), the equilibrium of *x* forces, $\Sigma F_x = 0$, considering the equilibrium of an element of unit thickness, taking moments of force about the lower-left corner ($\Sigma M_z = 0$), neglecting the triple products involving *dx* and *dy*, this reduces to $\tau_{xy} = \tau_{yx}$. In a like manner, it may be shown that $\tau_{yz} = \tau_{zy}$ and $\tau_{xz} = \tau_{zx}$. Consequently:

$$\left(\sigma_x + \frac{\partial\sigma_x}{\partial x}dx\right)dy - \sigma_x dy + \left(\tau_{xy} + \frac{\partial\tau_{xy}}{\partial y}dy\right)dx - \tau_{xy}dx + F_x dxdy = 0 \tag{4}$$

$$\left(\frac{\partial\sigma_x}{\partial x} + \frac{\partial\tau_{xy}}{\partial y} + F_x\right)dxdy = 0 \tag{5}$$

$$\begin{aligned}\frac{\partial\sigma_x}{\partial x} + \frac{\partial\tau_{xy}}{\partial y} + F_x = 0\\ \frac{\partial\sigma_y}{\partial y} + \frac{\partial\tau_{xy}}{\partial x} + F_y = 0\end{aligned} \tag{6}$$

The 3-D case could be similarly obtained giving the following result:

$$\begin{aligned}
&\frac{\partial \sigma_x}{\partial x}+\frac{\partial \tau_{xy}}{\partial y}+\frac{\partial \tau_{xz}}{\partial z}+F_x=0\\
&\frac{\partial \sigma_y}{\partial y}+\frac{\partial \tau_{xy}}{\partial x}+\frac{\partial \tau_{yz}}{\partial z}+F_y=0\\
&\frac{\partial \sigma_z}{\partial z}+\frac{\partial \tau_{xz}}{\partial x}+\frac{\partial \tau_{yz}}{\partial y}+F_z=0
\end{aligned}\tag{7}$$

Or, more synthetically:

$$\frac{\partial \tau_{ij}}{\partial x_j}+F_i=0, \quad i,j=x,y,z \tag{8}$$

which is denoted also as

$$\tau_{ij,j}+F_i=0 \tag{9}$$

When all forces are balanced, the problem to find the configuration of the system, subjected to whatever constraints there may be, is solved by the principle of virtual work. Only if the virtual work equality for all arbitrary variations of displacement is ensured would the equilibrium be complete (Zienkiewicz and Taylor, 2000).

2.1.1 Numerical method in structural analysis

The minimization of the total potential energy (TPE) is the basic principle of FEM: according to this, the sum of the internal strain energy and external works must be stationary when equilibrium is reached; for elastic problems, the TPE is stationary and minimal. This concept is mathematically expressed as (Zienkiewicz and Taylor, 2000) the following:

$$\frac{\partial \Pi}{\partial \boldsymbol{a}}=\left\{\begin{array}{c}\dfrac{\partial \Pi}{\partial \boldsymbol{a}_1}\\ \dfrac{\partial \Pi}{\partial \boldsymbol{a}_2}\\ \vdots\end{array}\right\}=\mathbf{0}, \tag{10}$$

where a_i represents displacements and Π is the total potential energy (Π = U + W, and U and W are the total strain energy and the total potential energy, respectively). It is of interest to note that if true equilibrium requires an absolute minimum of total potential energy (Π), a finite element solution by the displacement approach will always provide an approximate (Π) greater than the correct one. Thus, a bound on the value of the total potential energy is always achieved. If the functional Π could be specified a priori, then the finite element equations could be derived directly by Eq. (10). The Ritz (1909) process of approximation frequently used in elastic analysis uses precisely this approach. The total potential energy expression is formulated, and the displacement pattern is assumed to vary with a finite set of undetermined parameters (Zienkiewicz and Taylor, 2000). According to this interpretation, the static relation between unknown nodal displacements and known external loads is

$$[\mathbf{F}] = \{\mathbf{k}\}[\boldsymbol{\delta}] \tag{11}$$

$[\mathbf{F}]$ is the external loads vector, $\{\mathbf{k}\}$ is the stiffness matrix, and $[\boldsymbol{\delta}]$ is the nodal displacement vector. In the force method, $\{\mathbf{k}\}$ is substituted by the force transformation matrix, and $[\boldsymbol{\delta}]$ by the internal force vector. To exemplify, for a plane truss, member (11) becomes

$$[\mathbf{F}] = \begin{bmatrix} \bar{f}_{xi} \\ \bar{f}_{yi} \\ \bar{f}_{xj} \\ \bar{f}_{yj} \end{bmatrix} = \frac{EA}{L} \begin{bmatrix} 1 & 0 & -1 & 0 \\ 0 & 0 & 0 & 0 \\ -1 & 0 & 1 & 0 \\ 0 & 0 & 0 & 0 \end{bmatrix} \begin{bmatrix} \bar{u}_{xi} \\ \bar{u}_{yi} \\ \bar{u}_{xj} \\ \bar{u}_{yj} \end{bmatrix} = \{\mathbf{k}\}[\boldsymbol{\delta}], \tag{12}$$

where EA/l is the axial stiffness of the truss member.

2.1.2 Influence lines and surfaces

The maximization of stress and strains in an intricate section of a structural member is relevant to bridge structure, and it is affected by moving loads during the whole life of the bridge. For this reason, influence lines (ILs) are used. To define an IL, suppose there is a generic structure with its boundary condition and an applied load F at the x_1 position in the x-axis (Figure 5.4). Considering the investigated quantity Q (normal tension, shear, bending moment, rotation, displacement, etc.) in the generic section S at the x_s position, this could be defined by

$$Q = Q(x_1, x_s, \mathrm{F}) \tag{13}$$

The following situations apply: (i) if x_s is variable, solicitation diagrams are represented, describing the precise position of F solicitations and deformations; (ii) if x_1 is variable, solicitation diagrams are represented, describing the various position of F solicitations and deformations at point S. Dimensions of ILs include force $\times$ length/force for moments, the pure number for normal forces and shear, and length/forces for displacements. According to this definition, ILs could be defined as

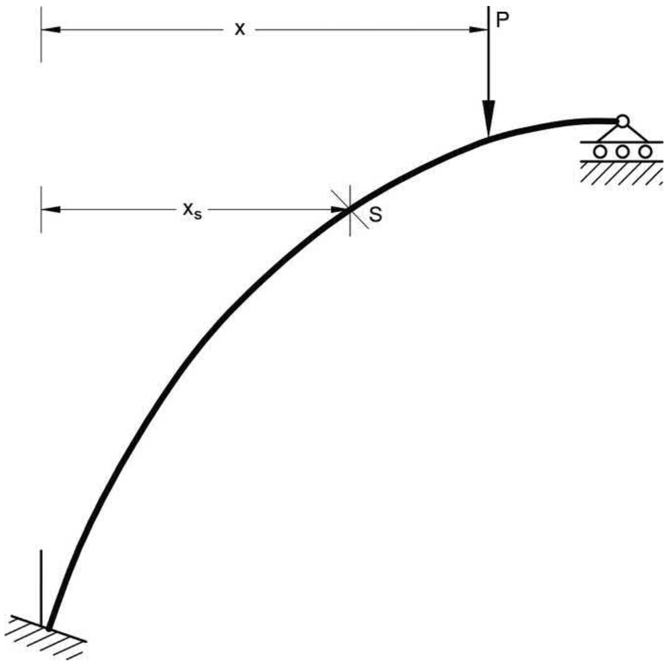

Figure 5.4 IL trivial representation.

$$
\begin{aligned}
vs &= \int_0^l v_S^F(x_{S'}x)p(x)dx \\
ws &= \int_0^l w_S^F(x_{S'}x)p(x)dx \\
Ms &= \int_0^l M_S^F(x_{S'}x)p(x)dx \\
Ns &= \int_0^l N_S^F(x_{S'}x)p(x)dx \\
Ts &= \int_0^l T_S^F(x_{S'}x)p(x)dx,
\end{aligned}
\tag{14}
$$

where the ILs of *v, w, M, N,* and *T,* respectively, are described in the investigated section S along the *x*-axis under the moving load. By different notation, for a generic variable distributed load *q(x),* the investigated generic quantity *Q* is

$$
Q = \int_{x_1}^{x_2} q(x)\eta dx. \tag{15}
$$

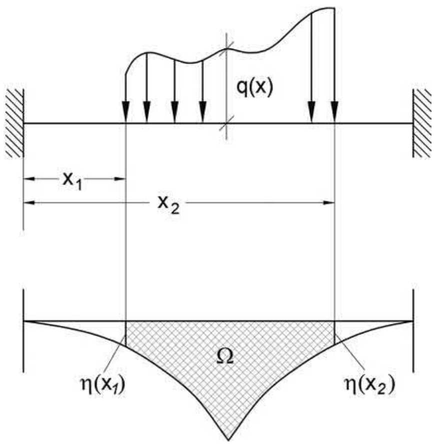

Figure 5.5 IL of a distributed load.

For an uniform load, $q = \text{cost}$, Eq. (14) becomes

$$Q = \mathrm{q} \cdot \Omega, \tag{16}$$

where Ω is the surface area under the IL. In this specific case of a uniform distributed load, the position of the maximum of Q can be found easily as follows (Figure 5.5):

$$\mathrm{d}\,\Omega = \eta_{x1} \cdot \mathrm{dx} - \eta_{x2} \cdot \mathrm{dx} \tag{17}$$

$$\frac{d\Omega}{dx} = 0 \tag{18}$$

$$\text{and } \eta_{x1} = \eta_{x2}. \tag{19}$$

The typical solution of the shear and moment maximization on a continuous bridge is displayed in Figure 5.6.

2.2 Compatibility

The deformation of a continuum is described in strain analysis without any reference to the material property: both the Lagrangian and Eulerian strain tensor are used to describe the deformation; however, in the first, the position and physical properties of the particles are described in terms of the material or referential coordinates and time, and in the second, they are described in terms of the spatial coordinates. In the latter case, this is called the *spatial description* or *Eulerian description;* i.e., the current configuration is taken as the reference configuration. However, strain equations of compatibility for infinitesimal strains could be also written in a different

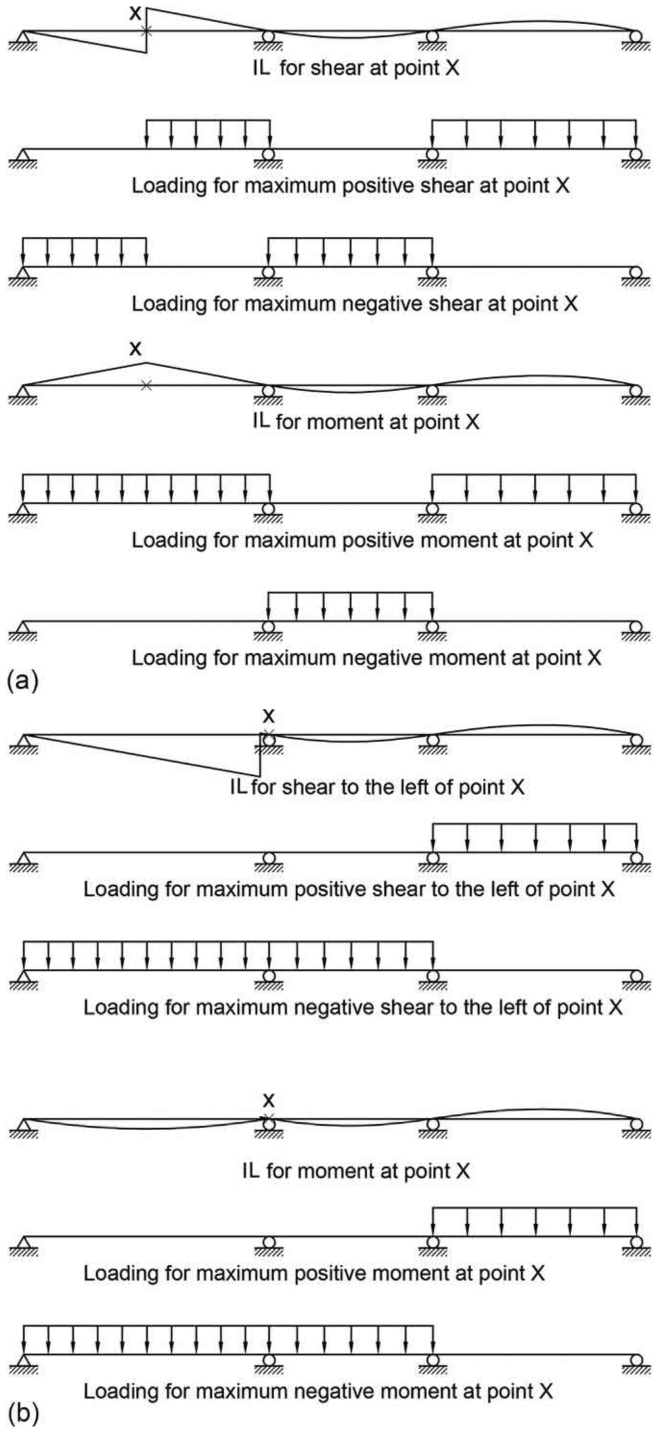

Figure 5.6 ILs of a continuous bridge: (a) shear and moment maximization at point X and the associated critical load diagrams; (b) shear and moment maximization at point X and the associated critical load diagrams.

way: given the strain field, it is possible to compute the displacements in the case of *infinitesimal deformations*. For infinitesimal motions, the relation between strain and displacement is

$$\varepsilon_{ij}=\frac{1}{2}\left(\frac{\partial u_i}{\partial x_j}+\frac{\partial u_j}{\partial x_i}\right) \tag{20}$$

Given that there are six strain components (since $\varepsilon_{ij}=\varepsilon_{ji}$), we can determine the three displacement components u_i. First, it should be noted that the displacement field that gives rise to a particular strain field cannot be completely recovered, so the displacements can be determined only if there is some additional information about how much the solid has rotated and translated. Second, the strain–displacement relations can be integrated (a strain field is a symmetric second-order tensor field, but a symmetric second-order tensor field is not always a strain field). The strain–displacement relations amount to a system of six scalar differential equations for the three displacement components u_i. To be integrable, the strains must satisfy the compatibility conditions, which may be expressed as

$$\frac{\partial^2\varepsilon_{ij}}{\partial x_k\partial x_l}+\frac{\partial^2\varepsilon_{ld}}{\partial x_i\partial x_j}-\frac{\partial^2\varepsilon_{il}}{\partial x_j\partial x_k}-\frac{\partial^2\varepsilon_{ik}}{\partial x_i\partial x_l}=0. \tag{21}$$

Alternatively, expanding this expression in the (1,2,3) principal axis notation:

$$\begin{gathered}
\frac{\partial^2\varepsilon_{11}}{\partial x_2^2}+\frac{\partial^2\varepsilon_{22}}{\partial x_1^2}-2\,\frac{\partial^2\varepsilon_{12}}{\partial x_1\partial x_2}=0\\
\frac{\partial^2\varepsilon_{11}}{\partial x_3^2}+\frac{\partial^2\varepsilon_{33}}{\partial x_1^2}-2\,\frac{\partial^2\varepsilon_{13}}{\partial x_1\partial x_3}=0\\
\frac{\partial^2\varepsilon_{22}}{\partial x_3^2}+\frac{\partial^2\varepsilon_{33}}{\partial x_2^2}-2\,\frac{\partial^2\varepsilon_{23}}{\partial x_2\partial x_3}=0\\
\frac{\partial^2\varepsilon_{11}}{\partial x_2\partial x_3}-\frac{\partial}{\partial x_1}\left(-\frac{\partial\varepsilon_{23}}{\partial x_1}+\frac{\partial\varepsilon_{31}}{\partial x_2}+\frac{\partial\varepsilon_{12}}{\partial x_3}\right)=0\\
\frac{\partial^2\varepsilon_{22}}{\partial x_3\partial x_1}-\frac{\partial}{\partial x_2}\left(-\frac{\partial\varepsilon_{31}}{\partial x_2}+\frac{\partial\varepsilon_{12}}{\partial x_3}+\frac{\partial\varepsilon_{23}}{\partial x_1}\right)=0\\
\frac{\partial^2\varepsilon_{33}}{\partial x_1\partial x_2}-\frac{\partial}{\partial x_3}\left(-\frac{\partial\varepsilon_{12}}{\partial x_3}+\frac{\partial\varepsilon_{23}}{\partial x_1}+\frac{\partial\varepsilon_{31}}{\partial x_2}\right)=0.
\end{gathered} \tag{22}$$

All strain fields must satisfy these conditions.

2.3 Constitutive laws

The concepts introduced in this chapter so far, in the framework of nonrelativistic mechanics, are essential to characterize stresses, kinematics, and balance principles. However, they cannot be used alone to distinguish one material from another. As the response (displacement of the body due to an applied force) of a deformable body cannot be determined using balance laws alone, they must be combined with the use of additional equations, the constitutive laws, which depend on the material that the body is made of. A constitutive law describes the physical behavior of a specific material under defined conditions of interest.

2.4 Elastic and plastic behavior

The deformations of a body subjected to external actions are principally described by two main behaviors: elastic and plastic behaviors (Figure 5.7). Elastic materials, if subjected to an external force, return to their initial configurations at release; this behavior could be linear or nonlinear, representing the so-called linear elastic and nonlinear elastic laws. Plastic materials, on the other hand, have a final configuration that is different from the initial one at the release of the applied force.

Elastic behavior can be defined in three different ways: (i) the processes in which the original size and shape can be recovered, called *elasticity;* (ii) the processes in which the value of state variables in a given configuration are independent of how the configuration was reached, called elastic; or (iii) a nondissipative process called an *elastic process*. It can be shown that the Cauchy stress, σ, in an elastic process would depend on the deformation gradient, F; three material unit vectors, D_i; and the state of Cauchy stress in the reference configuration, with σ_R being

$$g\left(\sigma, F, \sigma_R, D_1, D_2, D_3\right) = 0. \tag{23}$$

This is an assumption about how the state variable varies with the motion of the body. Considering definition (ii), it is certain that there is an implicit function that relates to the Cauchy stress and the deformation gradient. Assuming that $\sigma_R = 0$ (the reference configuration is stress free) and that the Cauchy stress is related explicitly to the deformation gradient, g() could be simplified as follows:

$$\sigma = h\left(F, D_1, D_2, D_3\right). \tag{24}$$

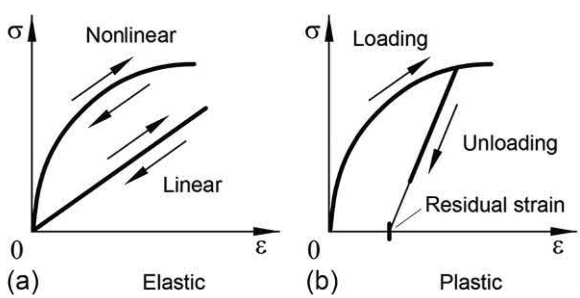

Figure 5.7 Constitutive laws: (a) linear and nonlinear elastic laws; (b) plastic law (stress versus strain plot).

Moreover, assuming an isotropic material, the Cauchy stress is

$$\sigma = f\,(F). \tag{25}$$

The general relation between the components of the Cauchy stress (σ_{ij}) and deformation gradient (F_{kl}) is linear and takes the following form:

$$\sigma_{ij} = B_{ijkl}\,(F_{kl} - \delta_{kl}) = B_{ijkl}F_{kl} - B_{ijkl}\,\delta_{kl}, \tag{26}$$

where B_{ijkl} is the components of a constant fourth-order tensor and δ_{kl} is the Kronecker delta. If Eq. (25) assumes the form

$$\sigma_{ij} = B_{ijkl}\,F_{kl}, \tag{27}$$

The generalization of the Hook principle is described. Whenever the elastic response is not linear, the elastic behavior of the material is not constant; however, deformations remain reversible.

2.4.1 Nonlinear effects

Four sources of nonlinearity could affect the structures: they are the geometric nonlinearity, material linearity, force boundary conditions, and displacement boundary conditions. The most relevant for bridge engineers are discussed in the following sections.

Geometric nonlinearity

If nonlinear terms cannot be neglected, or if displacements are so large that evident (not infinitesimal) changes in the structure are effected, geometric nonlinearity arises. One of the analytical consequences is the introduction of the geometric stiffness matrix, which takes this effect into consideration. A mathematical explanation could be found in Chen and Lui (1987). However, the most relevant consequences are the following:

- Equilibrium is formulated with respect to the deformed geometry of the structure, and a second-order analysis taking into account second-order effects must be performed: second-order analysis considering the $P-\Delta$ effect (the influence of axial forces acting through displacement associated with member chord rotation) and the $P-\delta$ effect (the influence of axial forces acting through displacement associated with the member's flexural curvature).
- In the hypothesis of large displacement, the analysis is based on small-strain and small-member deformation, but moderate rotations and large displacement theory (Akkari and Duan, 2000).

An example of geometric nonlinearity behavior of a structure is reported in Figure 5.8.

Figure 5.8 The Olive View Hospital, after the San Fernando, California, earthquake (magnitude 6.7) in 1971.

Material nonlinearity

Steel Figure 5.9, depicting four phases (elastic, plastic, strain hardening, and softening), represents the stress–strain behavior of structural steel. This is generally described by the following relations:

$$f_s = \begin{cases} E_s\varepsilon_s 0 \le \varepsilon_s \le \varepsilon_y & \\ f_y\varepsilon_{sy} & \text{lt;}\ \ \varepsilon_s \le \varepsilon_{sh} \\ f_y + \dfrac{\varepsilon_s - \varepsilon_{sh}}{\varepsilon_{su} - \varepsilon_{sh}}\left(f_{su} - f_y\right)\varepsilon_{sh} & \text{lt;}\ \ \varepsilon_s \le \varepsilon_{su} \\ f_u\left[1 - \dfrac{\varepsilon_s - \varepsilon_{su}}{\varepsilon_{sb} - \varepsilon_{su}}\right.(f_{su} - f_{sb})\varepsilon_{cu} & \text{lt;}\ \ \varepsilon_s \le \varepsilon_{sb} \end{cases}, \tag{28}$$

where f_s and ε_s is the stress of strain in steel; E_s is the modulus of elasticity of steel; f_y and ε_y are yield stress and strain; ε_{sh} is hardening strain; f_{su} and ε_{su} are maximum

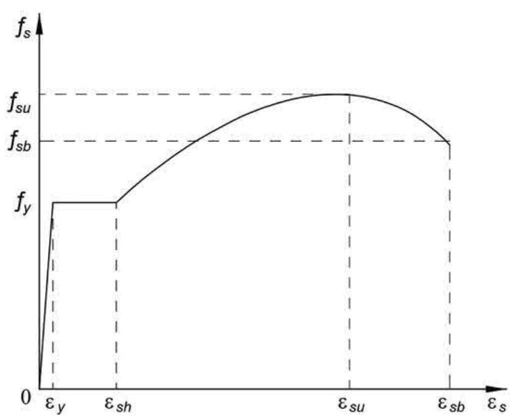

Figure 5.9 Stress-strain graph theoretical curve.

stress and the corresponding strain; f_{sb} and ε_{sb} are rupture stress and corresponding strain.

Phenomenological models including nonlinear equations are calibrated on the basis of experimental data. The first model of this type was proposed by Ramberg and Osgood (1943); another noteworthy model came from Menegotto and Pinto (1973). In addition, many other models have been studied in the literature. The Menegotto and Pinto (1973) model is an evolution of the model proposed by Giuffrè and Pinto (1970) and is laid out as follows: for $\varepsilon_s \to 0$, $\sigma_S = E_{S0}\varepsilon_s$; and for $\varepsilon_s \to \infty$, $\sigma_S = E_\infty \varepsilon_s + (E_{S0} - E_\infty)$:

$$\sigma_s = E_\infty \varepsilon_s + \frac{(E_{s0} - E_\infty)\varepsilon_s}{\left[1 + (\varepsilon_s/\varepsilon_0)^R\right]^{1/R}}, \tag{29}$$

where E_{s0} is the initial tangent modulus of the stress–strain curve, E_∞ is the secondary tangent modulus (for large strain), R is the independent parameter that defines the curvature; and $\varepsilon_0 = \sigma_0/E_{s0}$ is the strain at the intersection point between the tangent at the origin and the asymptote. This model has some advantages with respect to the implicit Ramberg–Osgood law. One relevant advantage is that each parameter (E_0, E_∞, σ_0, ε_0, R) in Eq. (28) defines a separate aspect of the curve's geometry, so these can be modified independently (Figure 5.10).

Concrete Figure 5.10, which depicts confined and unconfined concrete situations, represents the stress–strain behavior of structural concrete. Analytical models describing the stress–strain model proposed for monotonic loading of confined and unconfined concrete are influenced by the shape of the reinforced concrete (RC) section and the transverse reinforcement type and disposition. Phenomenological models including nonlinear equations are calibrated on the basis of experimental data. The more diffused model of this type is that proposed by Mander et al. (1988), based on the assumptions of other studies (mainly Willam and Warnke, 1975; Schickert and Winkler, 1977; Elwi and Murray, 1979). To determine the confined concrete compressive strength f'_{cc}, a constitutive model involving a specified ultimate strength

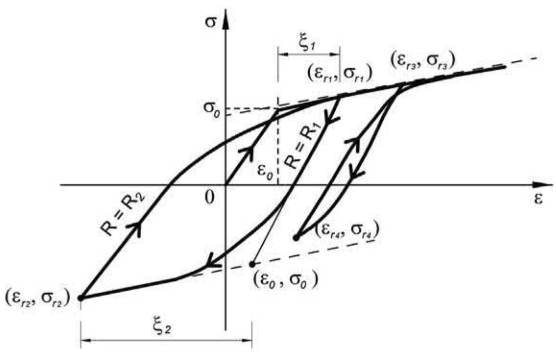

Figure 5.10 The Menegotto and Pinto (1973) model.

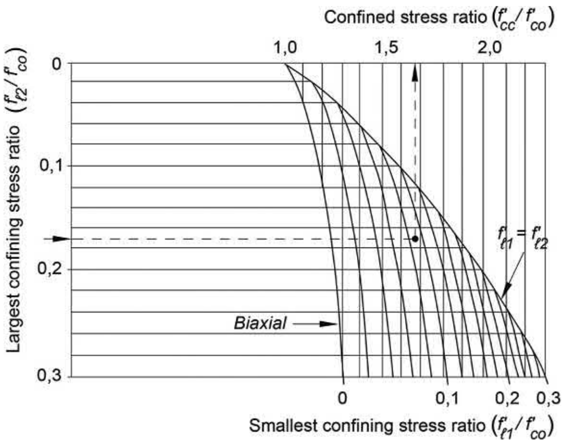

Figure 5.11 Confined strength determination from lateral confining stresses for rectangular sections (Mander et al., 1988).

surface for multiaxial compressive stresses is used. The general solution of Mander et al. (1988) is depicted in Figure 5.11, the model is shown in Figure 5.12, and the effectively confined core for circular and rectangular hoop reinforcement is illustrated in Figure 5.13. According to this model, when the confined core is placed in triaxial compression with equal effective lateral confining stresses f'_l from spirals or circular hoops, the confined compressive strength is

$$f'_{cc} = f'_{c0}\left(-1.254 + 2.254\sqrt{1+\frac{7.94f'_l}{f'_{c0}}} - 2\frac{f'_l}{f'_{c0}}\right), \tag{30}$$

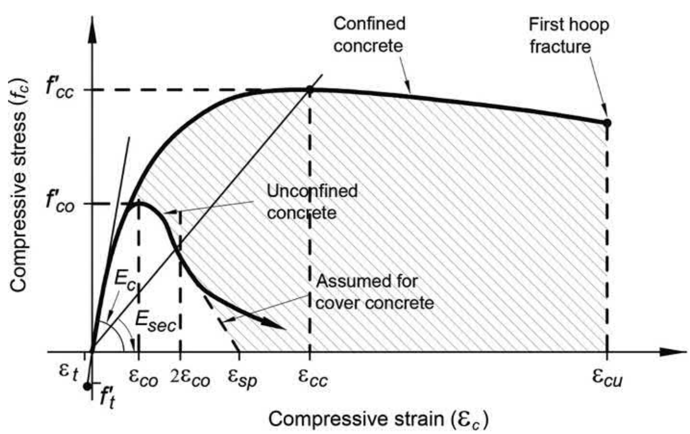

Figure 5.12 Stress–strain model proposed for monotonic loading of confined and unconfined concrete (Mander et al., 1988).

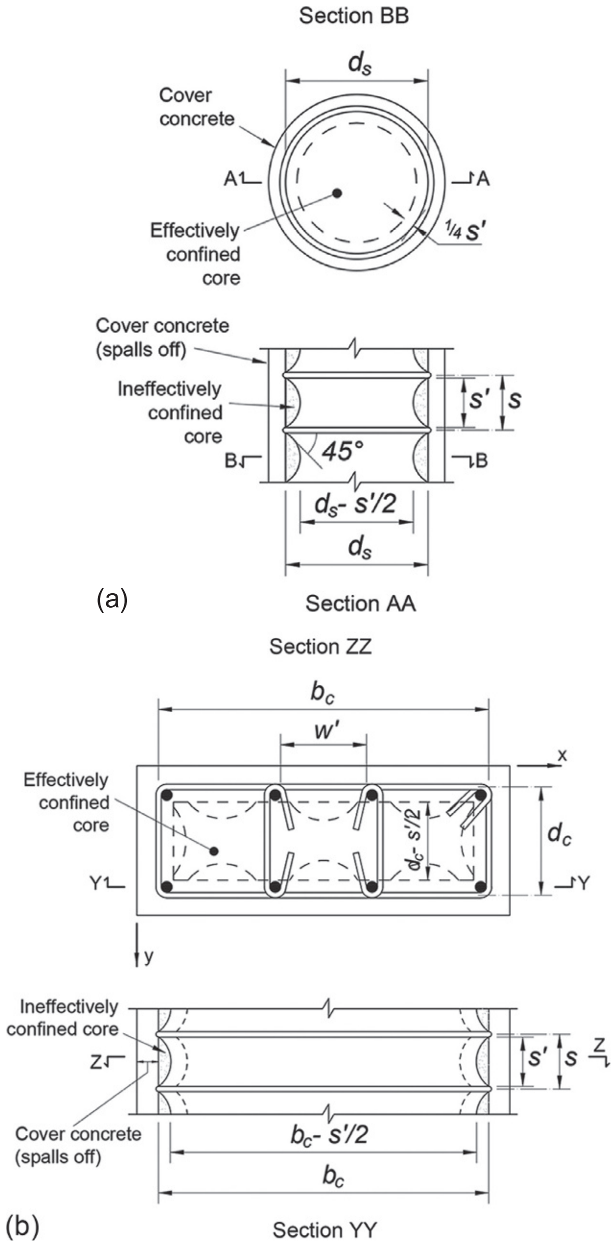

Figure 5.13 Effectively confined core for (a) circular (b) and rectangular hoop reinforcement (Mander et al., 1988).

where f'_{cO} is the unconfined concrete compressive strength; and the effective lateral confining stress on the concrete f'_1 is

$$f_l' = 0.5 k_e \rho_s f_{yh}. \tag{31}$$

Rectangular concrete sections: The rectangular hoops produce two unequal, effective, confining pressures; in the principal x- and y-direction, they are defined as

$$f_{lx}' = k_e \rho_x f_{yh} \tag{32}$$

$$f_{ly}' = k_e \rho_y f_{yh}, \tag{33}$$

where

$$K_e = \frac{\left[1 - \sum_{i=1}^{n} \frac{\left(w_i'\right)^2}{6 b_c d_c}\right]\left(1 - \frac{s'}{2b_c}\right)\left(1 - \frac{s'}{2d_c}\right)}{(1 - \rho_{cc})} \tag{34}$$

and

$$\rho_x = \frac{A_{sx}}{s d_c}, \quad \rho_y = \frac{A_{sy}}{s b_c}, \tag{35}$$

and, for concrete circular section by circular hoops or spirals,

$$f_l' = 0.5\, k_e \rho_s f_{yh} \tag{36}$$

$$K_e = \begin{cases} \left(1 - \frac{s'}{2d_s}\right)^2 / (1 - \rho_{cc}) & \textit{for circular hoops} \\ \left(1 - \frac{s'}{2d_s}\right) / (1 - \rho_{cc}) & \textit{for circular spirals} \end{cases} \tag{37}$$

$$\rho_s = \frac{4A_{sp}}{s d_s}, \tag{38}$$

where K_e is the confinement effectiveness coefficient; f_{yh} is the yield stress of the transverse reinforcement; s' is the clear vertical spacing between transverse reinforcement; s is the center-to-center spacing of the transverse reinforcement; *ds* is the centerline diameter of the transverse reinforcement; ρ_{cc} is the ratio of the longitudinal reinforcement area to section core area; ρ_s is the ratio of the transverse confining steel volume to the confined concrete core volume; A_{sp} is the bar area of transverse reinforcement; w'_i is the ith clear distance between adjacent longitudinal bars; b_c and d_c are core dimensions to the center lines of the hoop in the x- and y-directions (where $b \geq d$), respectively; A_{sx} and A_{sy} are the total area of transverse bars in the x- and

Figure 5.14 The Hanshin Expressway after a magnitude-6.9 earthquake hit Kobe, Japan, in 1995.

y-directions, respectively. A trivial example of the application of this method is given here: Consider a column with an unconfined strength of $f'_{cO} = 30$ MPa and with confining stresses (Eqs. 30 and 31) of $f'_{lx} = 5{,}1$ MPa, and $f'_{ly} = 2.7$ MPa. The compressive strength of the confined concrete could be inferred from looking at Figure 5.11, finding that $f'_{cc} = 1.65 * 30 = 49.5$ MPa (dotted line in the figure).

An example of the geometric nonlinearity behavior of a structure is reported in Figure 5.14.

3. Structural modeling

3.1 Introduction

Although structural modeling using numerical methods has been applied in FEM solutions for many years, we cannot forget the sense and the procedures involved when an FEM procedure is ongoing. The common FEM procedure is well explained by Bathe (2014): A mathematical model—including differential equations describing the geometry, kinematics, material law, loading and boundary conditions, and other elements—describes the investigated physical problem. The FEM solution passes through the identification of finite element types, the mesh density, and the solution parameters. An assessment of the accuracy of the FEM solution is investigated. Eventually, the mesh is refined, and some changes are made to the model.

In the final phase, the results are interpreted, and the analysis may be done again to account for the improvements to the structure (Figure 5.15). One of the implicit limits of the FEM procedure is that it represents only a simplified description of a physical model, as the most refined mathematical model is not able to reproduce all the information that is present in nature. A further consideration concerns the implicit FEM representation: FEM models are mathematical models and are able to represent physical problems only if they are accurately described. For this reason, a FEM model

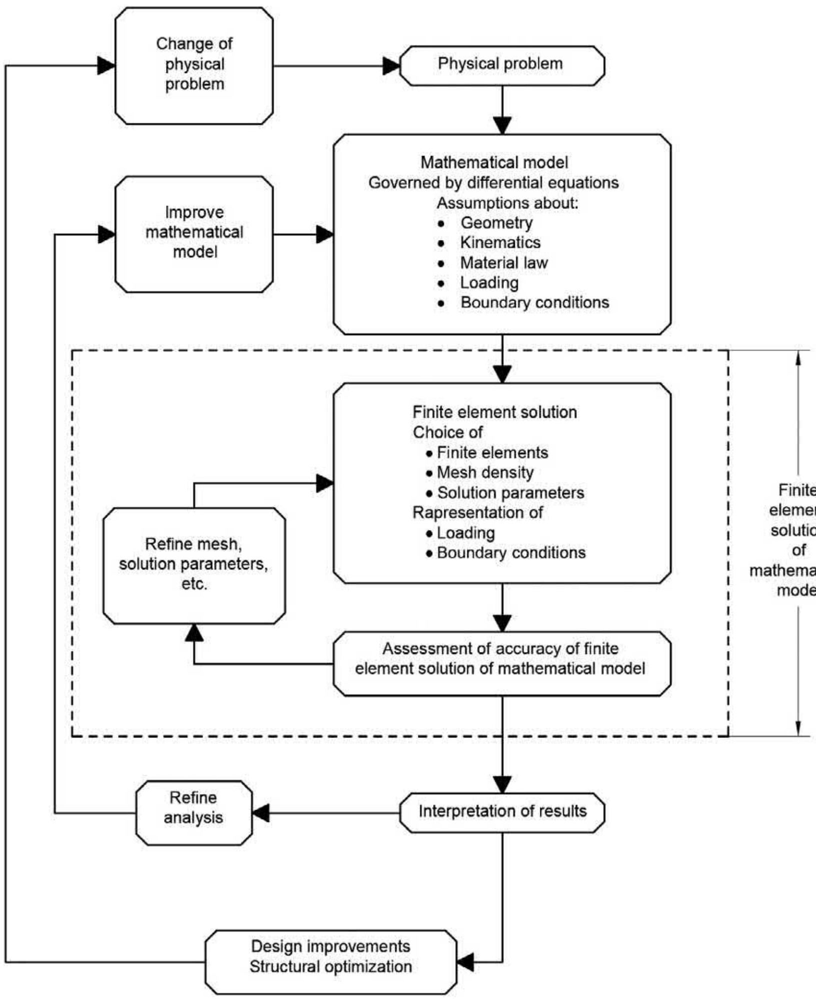

Figure 5.15 The FEM-finite element method process (adapted from Bathe, 2014).

must be checked for its reliability with an accurate final assessment. One suggested step-by-step solution, which may be able to simplify engineering complexities during the design process, is the hierarchy of models, in which a sequence of increasingly complex mathematical models and effects is investigated. For example, a beam structure may be analyzed first with the Bernoulli beam theory, next with the Timoshenko beam theory, then with 2-D plane stress theory, and finally with a fully 3-D continuum model, including in each case the nonlinear effects (Bathe et al., 1990). The hierarchy of models should take into consideration the time-consuming nature of the procedures, which may be adopted for unknown or rather complicated structural solutions, or whenever doubts about the interpretation of a complex FEM model are found. Some preliminary conclusions could be drafted as follows:

- The response to be predicted by an FEM analysis is correlated with the mathematical solution adopted.
- The most effective FEM requires a minimal amount of effort while providing, with an acceptable margin of error, the most effective answer to the design question.
- Every specific mathematical model is able to illustrate only the effects that it can describe and nothing more (e.g., a beam analysis is not able to predict any further information than that provided by the beam theory).
- Unreliable peak stresses could be found in an FEM model, and it is important to be able to show that these are solely due to the simplifications introduced in the model.

3.2 Modeling elements

In order to model a bridge structure, different elements provided in the common FEM software solution are available, including those described in the following sections (HSH, 2007).

3.2.1 1-D elements

- *Truss*: A linear member with a constant section along the axis, subject to compression/tension forces. The degree of freedom (DOF) of a truss is the only axial displacement at the nodes.
- *Beam*: Six DOFs at each node (three translations and three rotations) describe the beam element type, which could be subjected to axial and lateral loads and moments. Standard beams include axial, bending, and torsional stiffness.
- *Spring/damper*: A longitudinal spring-damper option is a uniaxial tension–compression element with up to three DOFs at each node. Translations in the nodal *x-, y-,* and *z*-directions. No bending or torsion is considered. The torsional spring-damper option is a purely rotational element with three degrees of freedom at each node: rotations about the nodal *x-, y-,* and *z*-axes. No bending or axial loads are considered; the spring-damper element has no mass, although masses can be added by using the appropriate mass element.
- *Cable*: The cable element is based on the catenary formulation, and it may have a free length that is different from the distance between the end nodes.

3.2.2 2-D elements

- *Plane strain:* For modeling very thick structures such as stress analysis through the section of a dam.
- *Plane stress:* For modeling thin 2-D sheets subject to in-plane loads.
- *Plate/shell:* For modeling general 3-D structures made of relatively thin material. Plate elements in some software may be either thin or thick. Thick plates consider the effects of shear deformation.
- *3-D membrane:* For modeling very flexible structures such as draped membranes.
- *Shear panel:* For modeling flat sheets that carry only in-plane shear loads.

3.2.3 3-D elements

Tetrahedral: Featuring either 4 or 10 node elements.
Wedge: Featuring either 6 or 15 node elements.
Pyramid: Featuring either 5 or 13 node elements.
Hexahedral: Featuring 8, 16, or 20 node elements.

3.2.4 Constraints

- *Rigid link*: Used to rigidly connect nodes. Both translations and rotations may be coupled selectively. For modeling rigid diaphragms on specific planes (e.g., the floor of a building), automatic tools are available to assign the rigid links, create the master node, and set the required DOFs.
- *Pinned link*: Displays similar behavior as rigid links, except that pinned links only the translational DOFs.
- *Master/slave link*: Used to force nodes to share DOFs. For example, the X displacement of one node can be forced to be the same as the X displacement of another node. Master/slave links may be applied in the global Cartesian system or in any user-defined coordinate system (UCS).

A similar identification of finite elements, including their applications, is reported in Table 5.1.

3.3 Modeling methods

Depending on the level of refinement expected, 2-D or 3-D models are commonly used in FEM models. At first glance, beam models are used, as they provide very useful and fast results, in terms of force and moments (Figure 5.16).

The FEM should be built with the aim to anticipate key locations in which principal (axial, shear, torsion, and bending) actions are desired. Excessively refined meshing could negatively influence the modeling procedure, as it wastes time; a combination of proper mesh refining and component size is the basis of reliable results. The technical judgment at this design stage is a balanced choice involving time, costs, and accurate results, depending on the expected solution. For instance, whereas in a static analysis of precast reinforced concrete (PRC) beams, an accurate model of reinforcement is needed, this is not useful in a dynamic analysis, for which lumped parameter models are enough. With increasing geometric and structural complications, which necessitate detailed FEMs (e.g., composite beam, skewed, and curved bridges) and the local evaluation of stress–strain components, the complexity of the model increases (Figure 5.17).

3.4 Materials and cross sections

The material properties are described in the FEM model in order to simulate the aforementioned constitutive laws during the procedure. While most of the structural theories concern homogenous and isotropic materials, and such materials as steel are well described by FEM models using the actual section, other materials such as concrete, characterized by a composite nonlinear performance, should be modeled accordingly, particularly when the ultimate behavior is investigated (as this implies the section partialization). Software libraries are commonly used for linear constitutive laws, and constitutive laws also could be inferred from structural sampling and testing of specimens for nonlinear models. Finally, given the material grade, theoretical laws could be employed also (see Section 2.4.1, earlier in this chapter).

Table 5.1 Identification of FEM Elements (Young and Budynas, 2002)

Element Type	Name	Shape	Number of Nodes	Applications
Line	Truss		2	Pin-ended bar in tension or compression
	Beam	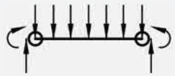	2	Bending
	Frame	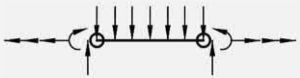	2	Axial, torsional, and bending; with or without load stiffening
Surface	Four-node quadrilateral	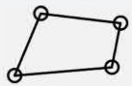	4	Plane stress or strain, axisymmetry, shear panel, thin flat plate in bending
	Eight-node quadrilateral	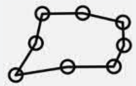	8	Plane stress or strain, thin plate or shell in bending
	Three-node triangular	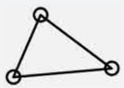	3	Plane stress or strain, axisymmetry, shear panel, thin flat plate in bending; prefer quad where possible; used for transitions of quads
	Six-node triangular	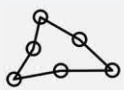	6	Plane stress or strain, axisymetry, thin plate or shell in bending; prefer quad where possible; used for transitions of quads
Surface	Eight-node hexagonal (brick)	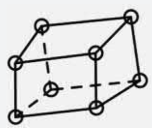	8	Solid, thick plate (using midside nodes)

	Six-node pentagonal (wedge)	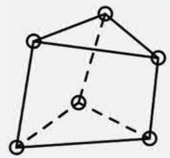	6	Solid, thick plate (using midside nodes); used for transition
	Four-node tetrahedron (tet)	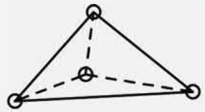	4	Solid, thick plate (using midside nodes); used for transition
Special purpose	Gap	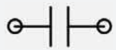	2	Free displacement for prescribed compressive gap
	Hook		2	Free displacement for prescribed compressive gap
	Rigid	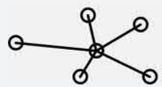	Variable	Rigid constraints between nodes

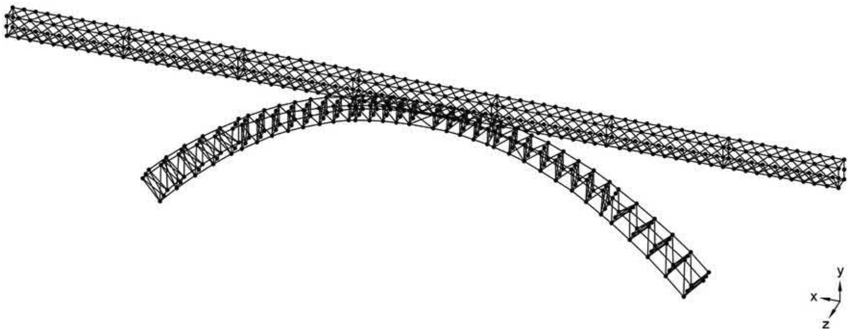

Figure 5.16 Beam model of the Paderno arched railway and road structure (Pipinato, 2010).

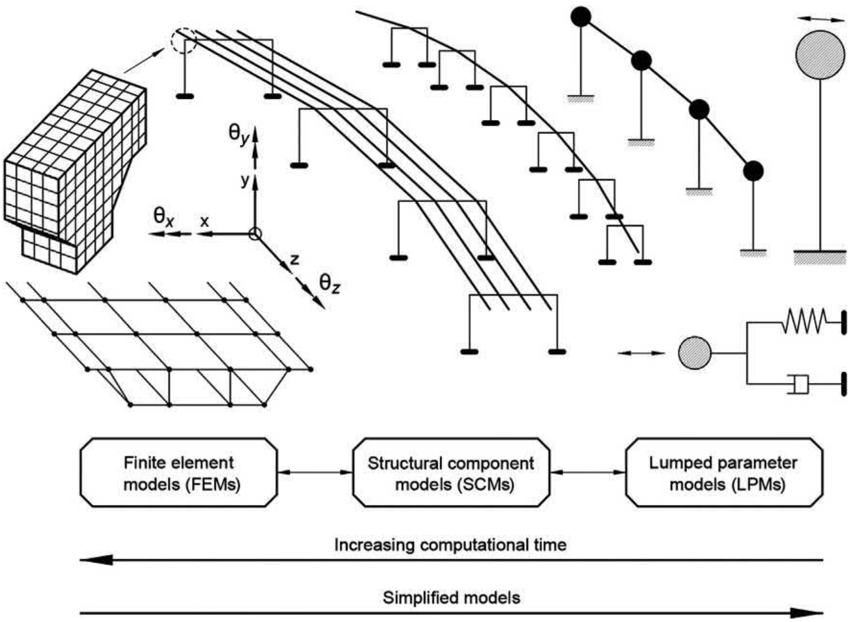

Figure 5.17 FEM modeling methods.

3.5 Boundaries

The real situation of the boundary condition is expected to be introduced into the model. An error of the imposed boundary conditions could lead the designer to unexpected solutions. To avoid this situation, such boundaries as support conditions, bearings, and expansion joints must be carefully analyzed and designed. Moreover, for simple linear static analysis, boundaries are commonly represented only by fixed/pinned/roller possibilities, avoiding structure/soil interaction, whereas for dynamic analysis, the structure/soil interaction should be carefully analyzed.

3.6 Modeling strategies

Different strategies are used in order to investigate specific problems of the structure throughout its service life, including the following:

- *Global models:* These are used for the global static analysis of the structure and for the seismic design.
- *Local models:* Submodels are able to amplify the structural behavior at a higher scale, highlighting specific parameters to be deepened by the use of FEM refinement and FEM hierarchy applications (a sequence of mathematical models that includes increasingly more complex effects).
- *Tension and compression models:* To avoid hammering, the tension and compression models are used to capture nonlinear responses for bridges with expansion joints in order to model the nonlinearity of the hinges with cable restrainers. Maximum response quantities from the two models are used for seismic design (Caltrans, 2007). Tension and compression models are able to capture the out-of-phase and in-phase frame movement, respectively.
- *Frame models:* Isolating the structural portion extending from one expansion joint to another, the bridge always becomes simpler and has upper-bound dynamic behavior; in this situation, seismic characteristics of individual frame responses are controlled by the mass of the superstructure and the stiffness of individual frames. Transverse stand-alone frame models shall assume lumped masses at the columns. Hinge spans shall be modeled as rigid elements with half of their mass lumped at the adjacent column. Effects from the adjacent frames can be obtained by including boundary frames in the model (Caltrans, 2010).
- *Bent models:* A simplified model, including only transverse bent caps together with their columns, is used to obtain the maximum solicitation values; in this model, accurate design includes foundation flexibility and a parametrical analysis of different ground motion inputs versus response.

3.7 Modeling approach

3.7.1 Superstructure

Spine models

In this section, a 3-D space frame is modeled in which the superstructure is made of a series of straight-beam elements located along the center line of the superstructure at its center of gravity in the vertical direction. Substructure elements are modeled as beams that are oriented so that their member properties coincide with the 3-D orientation of the piers or columns (Figure 5.18).

Grillage models

A 3-D space grid of beam elements in which the superstructure is comprised of both longitudinal and transverse beams located at the vertical center of gravity of the superstructure is modeled. Longitudinal members are located at the center of gravity of each girder line (web and slabs). Transverse beams are intended to model the bridge deck and transverse diaphragms. Substructure elements are also modeled as beams that are oriented so that their member properties coincide with the 3-D orientation of the piers or columns (Figure 5.18).

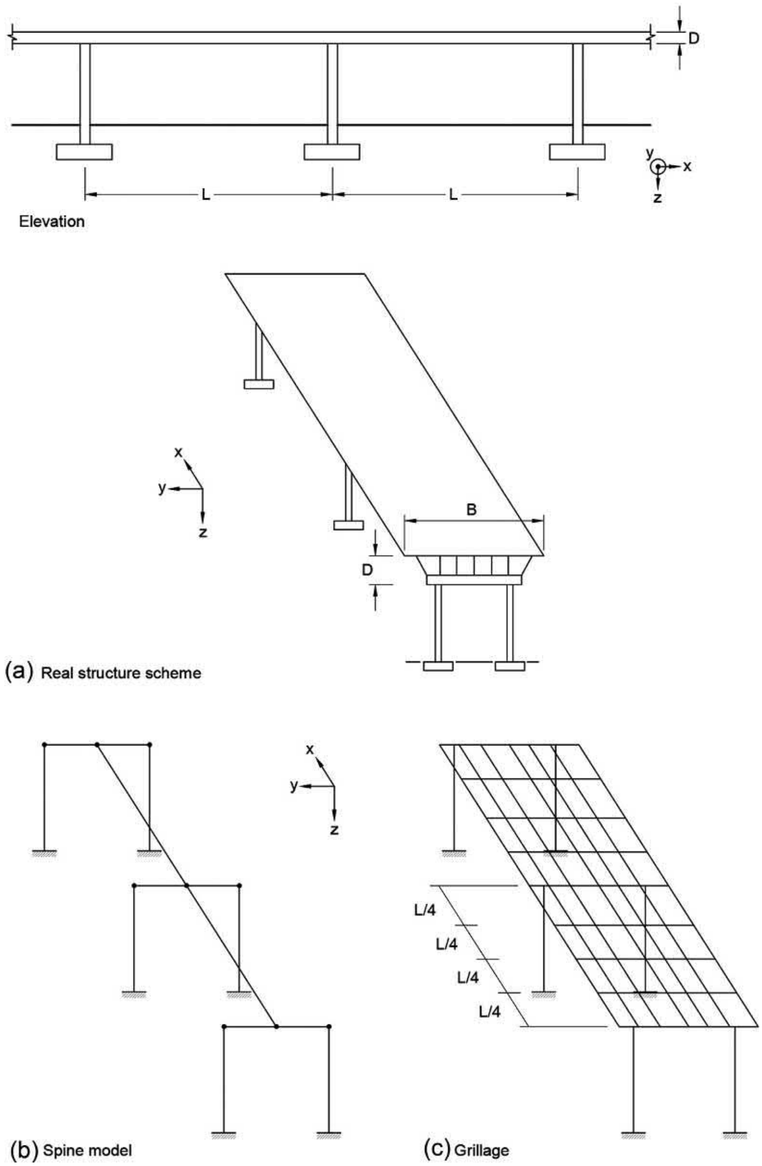

Figure 5.18 Superstructure model: (a) Real structure scheme, (b) spine model, (c) grillage model.

Isotropic and orthotropic plates

Isotropic or orthotropic superstructure differences are defined in Figure 5.19. In this subset, special attention should be given to the orthotropic deck, which can be solved with the following nonhomogeneous differential equation (Huber, 1923):

$$D_x \frac{\partial^4 w}{\partial x^4} + 2\mathrm{H} \frac{\partial^4 w}{\partial x^2 \partial y^2} + D_y \frac{\partial^4 w}{\partial y^4} = p\,(x, y), \tag{39}$$

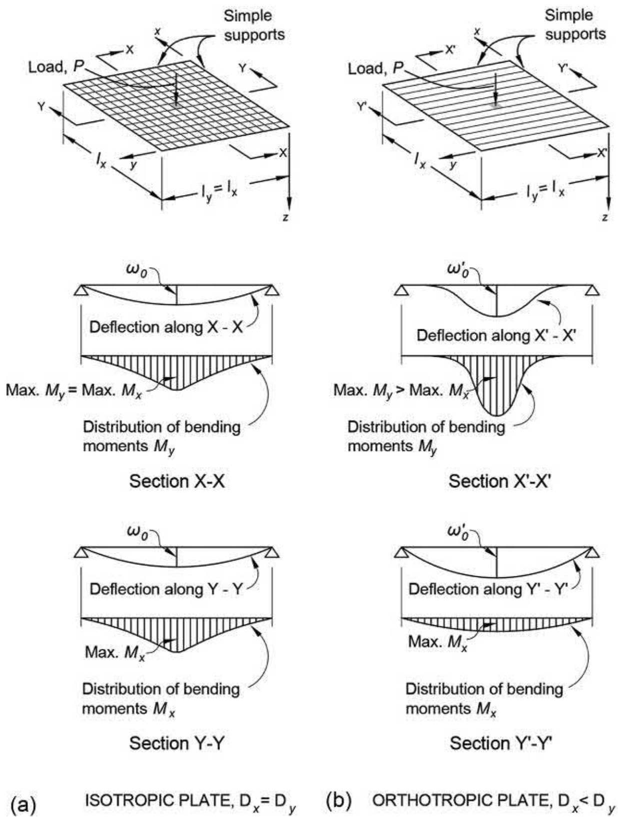

Figure 5.19 Comparison of deflections and bending moment in a square isotropic and a square orthotropic plate.

where w is the deflection of the middle surface of the plate at any point (x, y) (Figure 5.20); D_x, D_y, and H are the rigidity coefficients defined by

$$
\begin{aligned}
D_x &= \frac{E_x t^3}{12\left(1 - v_x v_y\right)} \\
D_y &= \frac{E_y t^3}{12\left(1 - v_x v_y\right)}
\end{aligned} \tag{40}
$$

$$2H = 4C + v_y D_x + v_x D_y, \tag{41}$$

and p (x,y) is the loading intensity at any point as a function of the coordinates x and y. Consequently, the solutions to the equations have been inferred (Girkman, 1959). When modeling an orthotropic deck, a rough model could be built up with a plate element, considering different bending stiffnesses in the two principal directions. An advanced model—such as a model considering local effects, the choice of the specific type of rib, a refined analysis of transverse-to-rib connection, and so on—should be made of plate elements representing the local portion of the substructure.

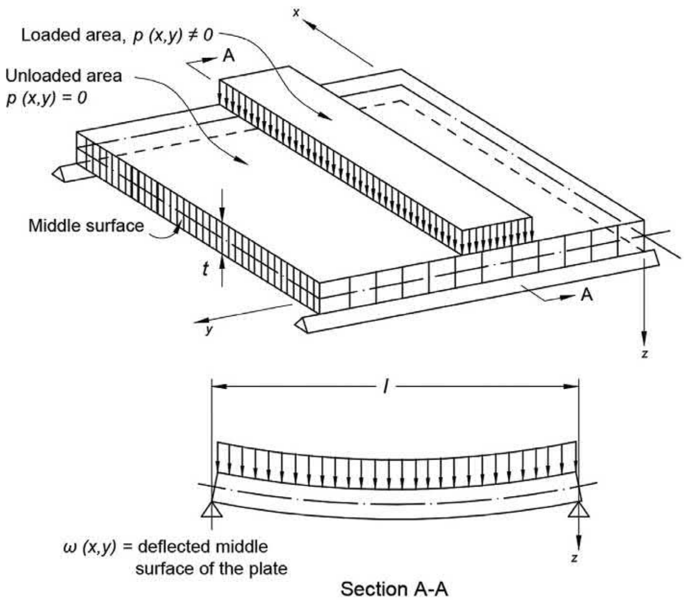

Figure 5.20 Basic designations of an orthotropic superstructure.

Bent model

In the hypothesis in which the bridge superstructure could be considered a rigid body under seismic loads, the bent models could be used. Discretizations are reported in Figure 5.21.

Thermal expansion joints

Thermal expansion joints allow movements in long superstructures; these should be modeled as hinges—6 DOF, free to rotate in the longitudinal direction and pin in the transverse direction to represent shear.

3.7.2 Substructure modeling

Substructure modeling should adhere to the following guidelines (Figure 5.22A–C):

- *Spring modeling of the foundation node:* The fixed-base connection is generally used in the single-column scheme, whereas a pin-base scheme is adopted in the multicolumn bents,.
- *Column-bent cap model:* A simplified model including only transverse bent caps together with their columns is used to obtain the maximum level of moment and shear; the design should adhere to the aforementioned rules.

An equivalent fixity model (Figure 5.22D) is used for the pile shaft (Figure 5.22E) for nonseismic loading. For seismic loading, a soil-spring model (Figure 5.22F) should be considered to capture the soil–structure interaction.

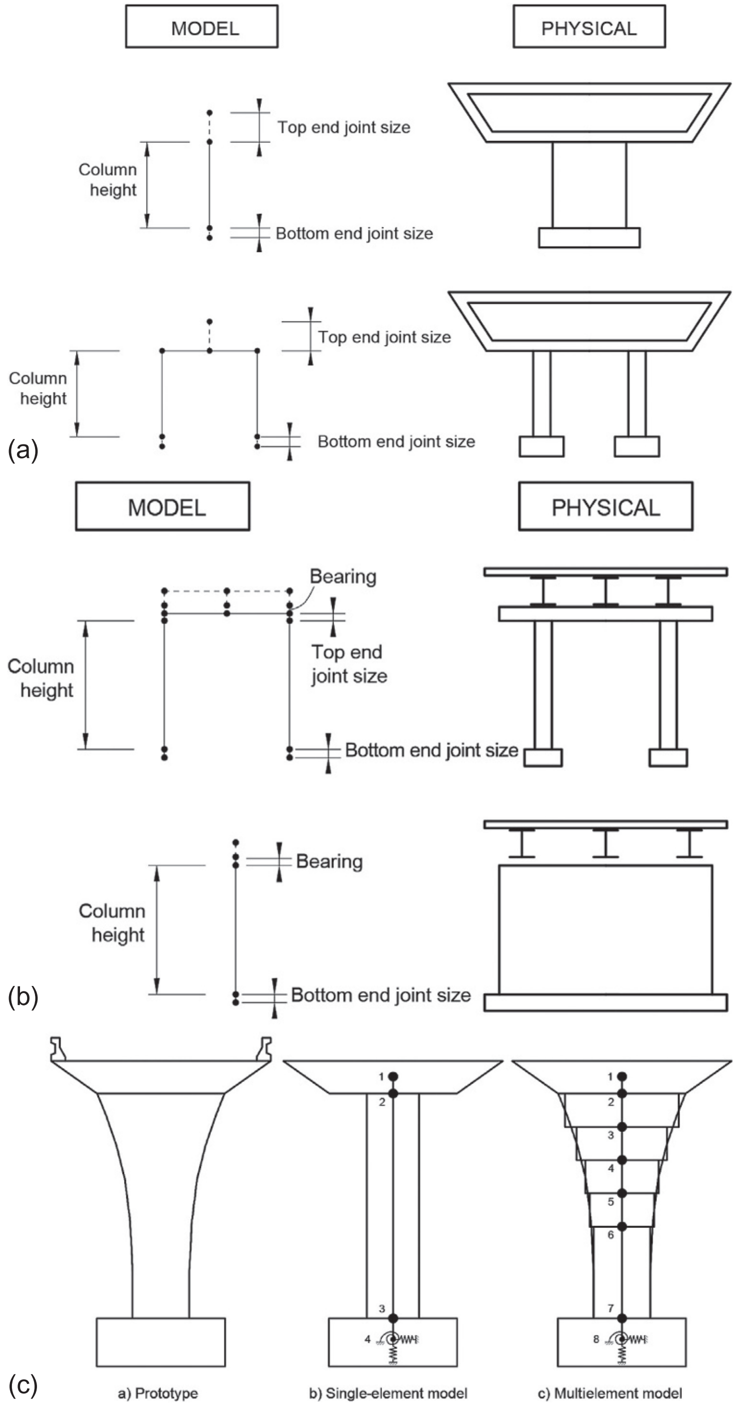

Figure 5.21 Bent models: (a) model discretization for monolithic connection; (b) bearing supported connections for precast concrete girders or steel superstructures on drop cap; (c) single-column bent model.

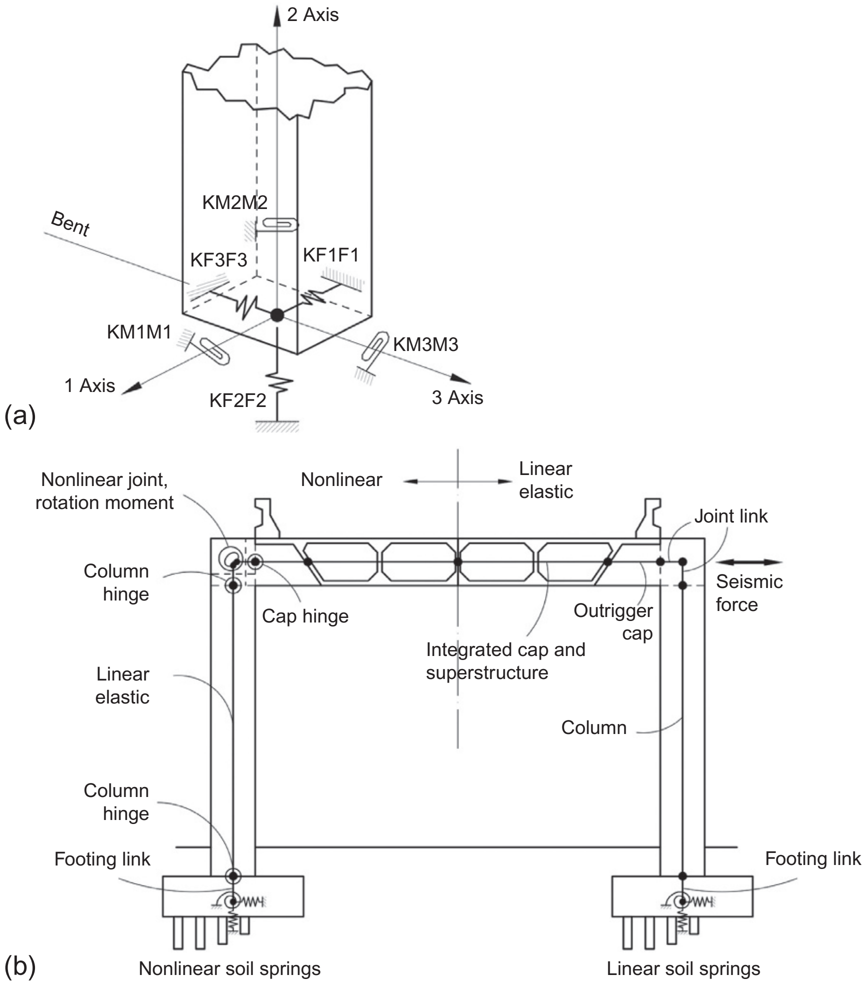

Figure 5.22 Substructure FEM modeling: (a) spring modeling of the foundation node; (b) column-bent cap model;

(Continued)

3.8 Modeling by bridge type

3.8.1 RC bridges

Slab bridges represent the simplest solution. In this case, an equivalent beam or a grid of equivalent beams model is suggested by the use of equivalent stiffness; otherwise, an adequate number of quadrilateral isotropic plate elements should be modeled, representing the continuous bridge slab, all lying in a plane and connected at a finite number of nodes. In this case, in-plane distortions are not considered, and an accurate analysis should be undergone if the particular details of the bridge require in-plane distortions. Some basic recommendations for slab bridges are as follows:

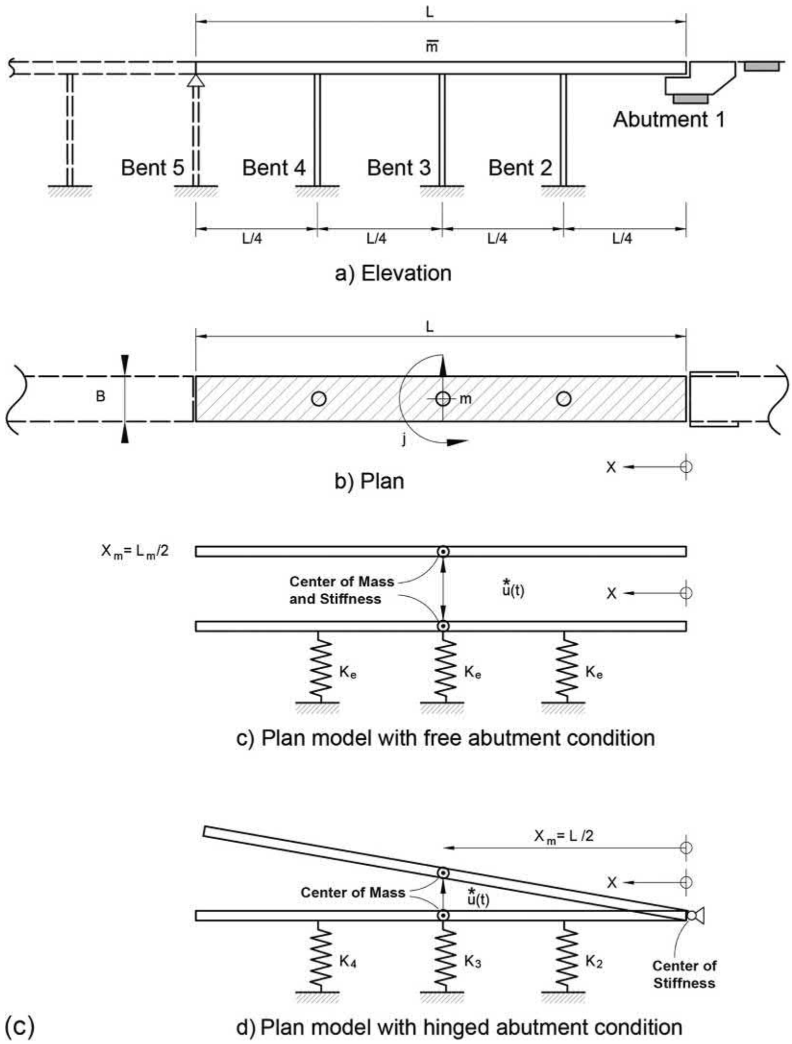

Figure 5.22, cont'd (c) multiframe model;

(Continued)

(i) Regular-shaped plates should be designed with quadrilateral elements, not exceeding 2:1 proportion. If triangular elements are adopted, regular equilateral triangles are preferred. (ii) Avoid discontinuities and the irregular subdivision of elements. (iii) Bearing locations and pier locations are identified with specific nodes.

In a retrofitting analysis, the fiber-reinforced polymer (FRP) retrofit of RC beams or slabs could be modeled with solid elements, with eight nodes and three DOFs at

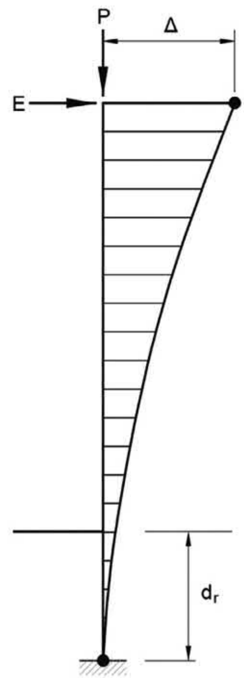

Figure 5.22, cont'd (d) equivalent fixity model;

(Continued)

each node, including information on creep, plastic deformation, crushing, and cracking. The special case of curved concrete bridges has three modeling solutions: the spine model, the grillage model, and the 3-D FEM model. Depending on the complexity of the structure, it is recommended to adopt the most time-consuming modeling approach at the final design stage only.

3.8.2 Prestressed/post-tensioned concrete bridges

Basic FEM solutions (not including prestressing or post-tensioned elements) could be used by introducing applied loading instead of dedicated resisting elements. When prestressing or post-tensioned elements are included in the FEM package, the elements should account for tendon type, immediate loss, elastic shortening, long-term losses, and changes in stress for bending. Different analyses are available for the particular FEM solution adopted, such as beam type, tendon type, plane stress, and solid type. The beam analysis is the most diffused; it considers the current beam section and truss elements representing the tendons, including pretensioning forces.

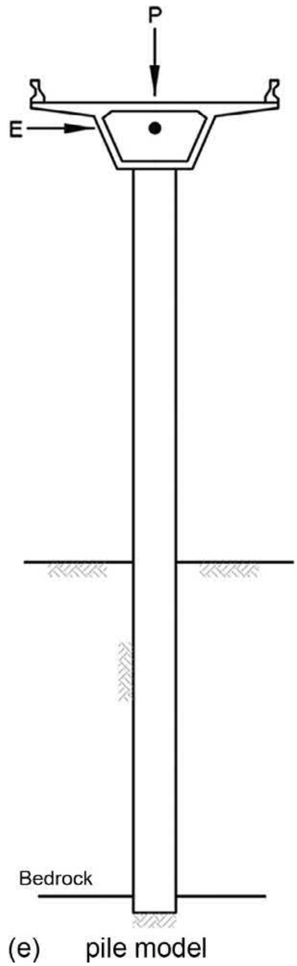

Figure 5.22, cont'd (e) pile model;

(Continued)

3.8.3 Steel girder bridges

Beam models are sufficient to satisfy the steel girder bridge design at the approximate analysis stage, or to provide a local approximate analysis of the results of complex models where the vast amount of elements and the information modeled could give the wrong results. Another way to provide an approximate analysis is with line-girder analysis: in this case, load distribution factors are used to isolate a single girder from the rest of the superstructure system, evaluating that girder individually. The load distribution factors are determined by approximate formulae for both straight bridges and

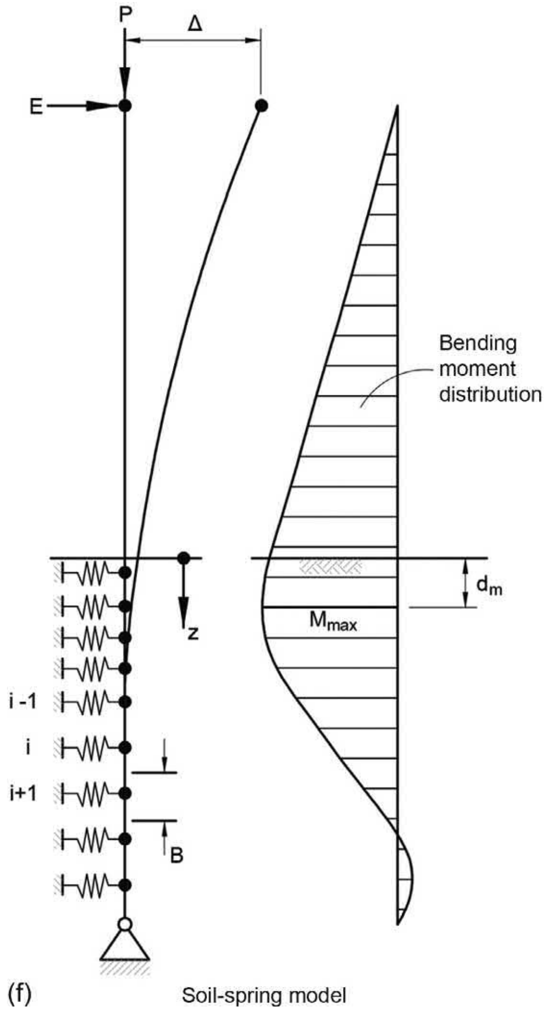

Figure 5.22, cont'd (f) soil-spring model.

curved bridges—as reported, for example, by AASHTO (2015), Kim et al. (2007), and Zhang et al. (2005). FEM solutions include the following:

- *2-D grid analysis method*: In this method, the structure is divided into plane grid elements with three DOFs at each node (vertical displacement, rotation angles about the longitudinal and transverse axes, or the first derivative of the rotational angle about the longitudinal axis, or both). The element choice, node spacing, and other modeling parameters are often set following simplified guidelines (e.g., AASHTO, 2015).
- *Plate and eccentric beam analysis methods*: The deck is modeled using plate or shell elements, while the girders and cross frames are modeled using beam elements offset from the plate elements to represent the offset of the neutral axis of the girder or cross frame from

the neutral axis of the deck. This approach is covered by AASHTO (2015). The offset length is typically equal to the distance between the centroids of the girder and deck sections. This method is somewhat more refined than the traditional 2-D grid method. For this modeling approach, beam element internal forces obtained from this method need to be eccentrically transformed to obtain the composite girder internal forces (bending moment and shear) used in the bridge design.

- *Grid analysis method*: This method offers an enhancement of the aforementioned solution—including modeling of cross frames or diaphragms with consideration of shear deformation in addition to flexural deformation, modeling of the warping stiffness of open cross-section shapes (such as I-shaped girders), modeling of girder supports, lateral bracing, cross frames, or diaphragms at their physical elevation within the structure.
- *3-D FEM analysis methods*: This method includes a computerized structural analysis model where the superstructure is modeled in three dimensions—including girder flanges using line/beam elements or plate/shell/solid type elements; modeling of girder webs using plate/shell/solid type elements; modeling of cross frames or diaphragms using line/beam, truss, or plate/shell/solid type elements (as appropriate); and modeling of the deck using plate/shell/solid elements. This method is dedicated to three main categories of design issues: complicated situations such as severe curvature, skew, or both; unusual framing plans, unusual support/substructure conditions, or other complicating features (AASHTO, NSBA, 2011); and refined analysis of structure submodels. However, a further complication arises with this solution type, as solicitation parameters are not directly calculated. Instead, the model reports stresses in flanges, webs, and deck elements. If the designer wishes to consider girder solicitations, some type of conversion/integration of the stresses over the depth of the girder cross section is required. The procedure is long and time consuming, and using it increases the potential for error.

3.8.4 Truss bridges

For truss bridges, an initial 2-D model should be sufficient, incorporating the 2-D information of the planar truss. In this case, only one side truss is modeled, and the vertical loads are applied directly to that. In the final design stage, a 3-D model including the two trusses, the deck, and all the structural components is required. In this last case, an assemblage of beams, carefully considering the mutual connections, represents the deck: the designer should avoid stress concentrations in connection points, as well-known fatigue-prone details are present in truss–deck connections (Pipinato, 2012).

3.8.5 Arch bridges

In the case of arch bridges, dedicated FEM solutions, including multiphase construction and hanger/cable analysis, are available on the market. The analysis of steel or steel/concrete arch bridges includes the following elements:

- *Arch structure*: For the arch structure, 3-D models that introduce a correct amount of straight-beam elements to reproduce the cross-frame arched geometry are necessary. The global stability analysis in the two principal planes (arch plane and horizontal plane) is required for the common high compression value in the arch itself. The influence of initial stress in arches should be carefully considered (e.g., an initial tension level in hangers helps to maintain arches in position in deck-through arches). Fatigue analysis of cables and

hangers is required. A parametric analysis of cable spacing and geometry, including different arch geometry solutions, could help to reduce the weight and optimize the shape of the structure.
- *Deck structure*: Stringers and floor beams, together with the deck permanent loads (e.g., special equipment), should be modeled in a 3-D FEM solution to account for the correct stiffness of each component.
- *Hangers*: Hangers can be initially modeled as truss elements, even though special elements are introduced in dedicated FEM solutions.

General FEM software is used to perform the very simple modeling required for masonry arches.

3.8.6 Cable-stayed bridges

For cable-stayed bridges, 3-D modeling is recommended. This includes the following elements:

- *Main girder*: Steel or concrete boxes or composite I-girders are basic solutions. In the first case, the girder can be modeled as a beam at the centroid of its cross section with a longitudinal development, linking the beam to a cable's anchor point by a rigid link. If transverse-stiffened beams are used instead of rigid links, bending and shear stiffness along the length of the bridge should be carefully calculated. If composite I-girders are used, the girder can be modeled as a grid of beams.
- *Pylons*: 3-D beam elements are usually used to model pylons, changing the cross-section shape/geometry/direction according to the vertical development.
- *Cables*: Truss elements are commonly used, except in those cases where sag effect should be accounted for. In this case, appropriate elements should be introduced in the model (namely cable element), considering the equivalent Young's modulus.
- *Pylon/girder connection*: According to the specific connection (full separation, rigid connection, vertical support, etc.) the connection is introduced into the 3-D model. If a damping system is adopted in the bridge, accurate calibration of this element, checking for the allowable displacement versus movement, should be provided.

3.8.7 Suspension bridges

Three-dimensional modeling is also recommended for suspension bridges. This includes the following items:

- *Main cables and saddles*: If truss elements are used, cables are meshed at the hanger locations. Otherwise, specific catenary cable elements are included in particular FEM solutions. The modeling and analysis should account for saddles' role in the various erection and exercise phases (moveable/fixed, according to the type of bridge). Considering saddles' relevant role in the whole bridge structure, a 3-D submodel should be considered.
- *Hangers*: Truss elements can be used except for the principal rigid connection between the girder and the main cables (at midspan), where beam elements are preferred, together with a specific submodel of the structure, including solid elements, to account for hot spot stress checks.
- *Pylons and Girders*: The same procedure described for cable-stayed bridges should be adopted.

4. Research and development

Looking ahead to the future development of these relevant structural engineering instruments as FEM software, some improvements are required, as suggested in the following items:

- *Full integration of the modeling procedures:* The output of the analysis should be usable/readable for an extended number of engineers involved in the bridge design and production and should facilitate understanding of the model. The close native format of every different software is a commercial, understandable choice; however, this is a clear limit to the public, who cannot easily manage and handle the structural design. One possibility of solving this issue is the introduction of a dedicated free software interface, in order to enable everyone to read the output of the FEM.
- *Full integration of FEM and BIM:* Today, construction solutions integrate a wide variety of information about element types, materials, geometries, and construction issues. All this information is included in bridge design output that is generated separately from the FEM modeling and also apart from building information modeling (BIM) models. Some software solutions are now trying to close the gap among these three phases. However, a great amount of work must done in this specific field in order to give bridge engineers a unique software solution that integrates all steps of design production.
- *Coded output:* Not all codes and standards are clearly related to the postprocessed FEM structural output content that should be produced for the authority, the official deposit. However, it seems that software companies do not understand that it is not acceptable to produce code tabulations that are almost impossible understand. A coded tabulation must be produced in a clear format, allowing the designer make further specific calculation output (or not), and should include a clear description of the adopted code and standard procedure. This would also be very useful to ensure the repeatability of the structural assumptions and calculations.

References

Akkari, M., Duan, L., 2000. Nonlinear analysis of bridge structures. In: Chen, W.-F., Duan, L. (Eds.), Bridge Engineering Handbook. Boca Raton Press, Boca Raton, FL.

American Association of State Highway and Transportation Officials (AASHTO), 2015. AASHTO LRFD Bridge Design Specifications, seventh ed. American Association of State Highway and Transportation Officials, Washington, DC. with 2015 interim revisions.

American Association of State Highway and Transportation Officials–National Steel Bridge Alliance (AASHTO, NSBA), 2011. Guidelines for Steel Girder Bridge Analysis. AASHTO/NSBA Steel Bridge Collaboration Task Group—Analysis of Steel Girder Bridges. American Association of State Highway and Transportation Officials–National Steel Bridge Alliance, Washington, DC.

Ansel, C., Saul, F.K., 2011. Advanced Mechanics of Materials and Applied Elasticity: Analysis of Stress. Prentice Hall, Pearson PLC, London.

Bathe, K.J., 2014. Finite Element Procedures. Monograph. Prentice Hall, Upper Saddle River, NJ.

Bathe, K.J., Lee, N.S., Bucalem, M.L., 1990. On the use of hierarchical models in engineering analysis. Comput. Methods Appl. Mech. Eng. 82, 5–36.

Caltrans, 2007. Memo to Designers 20–4—Earthquake Retrofit for Bridges. California Dept. of Transportation, Sacramento, CA.

Caltrans, 2010. Seismic Design Criteria, Version 1.6. California Dept. of Transportation, Sacramento, CA.

Chen, W.F., Lui, E.M., 1987. Structural Stability: Theory and Implementation. Elsevier, New York.

Elwi, A.A., Murray, D.W., 1979. A 3-D hypoelastic concrete constitutive relationship. J. Eng. Mech. Div. ASCE 105 (4), 623–641.

Girkman, K., 1959. Flachentragwerke, fifth ed. Springer Verlak, Vienna.

Giuffrè, A., Pinto, P.E., 1970. Il comportamento del cemento armato per sollecitazioni cicliche di forte intensità. Giornale del Genio Civile 5, 391–408. Maggio.

HSH, 2007. Strand 7 User Manual. Strand7 Pty Ltd.

Huber, M.T., 1923. Die Theorie der kreuzweise bewehrten Eisenbetonplatten. Der Bauingenieur 4, 354–392.

Kim, W.S., Laman, J.A., Linzell, D.G., 2007. Live load radial moment distribution for horizontally curved bridges. ASCE J. Bridge Eng. 12 (6), 727–736.

Mander, J.B., Priestley, M.J.N., Park, R., 1988. Theoretical stress-strain model for confined concrete. J. Struct. Eng. 114 (8), 1804.

Menegotto, M., Pinto, P.E., 1973. Method of analysis for cyclically loaded reinforced concrete plane frames including changes in geometry and non-elastic behavior of elements under combined normal force and bending. In: Proc., IABSE Symp. Resistance and Ultimate Deformability of Structures Acted on by Well-Defined Repeated Loads, Intl. Assoc, Bridge Struct. Eng., Libson, Portugal. 13, pp. 15–22.

Pipinato, A., 2010. Structural analysis and fatigue reliability assessment of the Paderno bridge. Practice period. Struct. Des. Construct. 15 (2), 109–124. https://doi.org/10.1061/(ASCE)SC.1943-5576.0000037.

Pipinato, A., 2012. Assessment procedure and rehabilitation criteria for the riveted railway Adige bridge. Struct. Infrastruct. Eng. 8 (8), 747–764. https://doi.org/10.1080/15732479.2010.481674.

Ramberg, W., Osgood, W.R., 1943. Description of Stress-Strain Curves by Three Parameters. Technical Note No. 902. National Advisory Committee for Aeronautics, Washington, DC.

Ritz, W., 1909. Uber eine neue Methode zur Losung gewissen Variations Probleme der mathematischen. Physik. J. Reine Angew. Math. 135, 1–61.

Schickert, G., Winkler, H., 1977. Results of Test Concerning Strength and Strain of Concrete Subjected to Multiaxial Compressive Stress. Deutcher Ausschuss fur Stahlbeton, Heft 277, Berlin.

Willam, K.J., Warnke, E.P., 1975. Constitutive models for the triaxial behavior of concrete. Proc. Int. Assoc. Bridge Struct. Eng. 19, 1–30.

Young, W.C., Budynas, R.G., 2002. Roark's Formulas for Stress and Strain, seventh ed. McGraw-Hill, New York.

Zhang, H.L., Huang, D.H., Wang, T.L., 2005. Lateral load distribution in curved steel I- girder bridges. J. Bridg. Eng. 10 (3), 281–290.

Zienkiewicz, O.C., Taylor, R.I., 2000. The Finite Element Method, fifth ed. Butterworth Heynemann, New York.

Dynamics of bridge structures

6

N. Chouw
Department of Civil and Environmental Engineering, The University of Auckland, Auckland, New Zealand

1. Linear idealization of bridge structures

Bridge structures can be idealized as either a single degree-of-freedom (SDOF) system, a multi-DOF system, or an infinite-DOF system. The equation of motion of each of these models describes the relationship between the loading and the response of the system. As anticipated, the more information that must be obtained, the greater the number of DOFs needed. For an initial and approximate estimate of bridge response, an SDOF system is sufficient.

1.1 SDOF system

Figure 6.1 shows a bridge with two segments under a dynamic loading P(t). As an example, the response of the left segment is considered. For simplicity, it is assumed that the bridge girder is much stiffer than the pier bending stiffness. Hence, a rigid girder is assumed, and the response of the bridge structure to a horizontal dynamic loading P(t) can be described by considering only one DOF, i.e., the horizontal girder response u(t).

The stiffness of the structure of the DOF considered is the force required to cause a unit displacement in the DOF. The rigid girder can be represented by a fixed-base boundary condition (see Figure 6.1, on the right, showing a top boundary condition). The force required to produce unit displacement at the top of one pier is equal to the pier stiffness $k_p = 12EI/h^3$, where EI and h are the bending stiffness and the height of the pier, respectively. The mass m of the SDOF system can be assumed to be the total girder mass and the mass of the top half of the piers. When the bridge girder vibrates to the left, the inertia force $F_I = m\,\ddot{u}(t)$ is initiated and acts in the opposite direction, and each bridge pier will resist the deformation. The resisting force is $F_S = k\,u(t)$. The energy loss during the vibrations (e.g., due to friction at the pier-girder connections) can be described in terms of viscous damping; i.e., the velocity-dependent damping force $F_D = c\,\dot{u}(t)$, where c is the damping coefficient.

The equation that governs the response of the bridge structure to the load P(t) can be derived from the equilibrium of all forces:

$$m\,\ddot{u}(t) + c\,\dot{u}(t) + k\,u(t) = P(t). \tag{1}$$

Innovative Bridge Design Handbook. https://doi.org/10.1016/B978-0-12-823550-8.00004-4

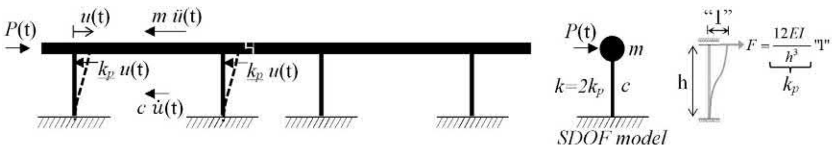

Figure 6.1 A two-segment bridge structure with an assumed fixed base.

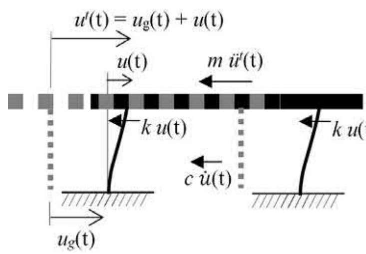

Figure 6.2 SDOF bridge system under an earthquake loading.

In the case of a ground excitation $\ddot{u}_g$(t), the inertia force F_I is determined by the absolute acceleration $\ddot{u}^t$(t) (Figure 6.2), while the pier restoring force F_S(t) and the damping force F_D(t) depend on the relative response.

Thus, the governing equation is

$$m\,\ddot{u}^t(t) + c\,\dot{u}(t) + k\,u(t) = 0 \text{ or } m\,\ddot{u}(t) + c\,\dot{u}(t) + k\,u(t) = -m\,\ddot{u}_g(t) \tag{2}$$

1.2 MDOF system

In the previous section, the girder is assumed to be rigid. Consequently, the system can be described by the SDOF u_1(t). Should the girder flexibility be considered, however, depending on the bending stiffness ratio of girder to pier, the rotational DOF u_2(t) and u_3(t) at the pier-girder connections can be influential. The bridge segment is then described by three DOFs (Figure 6.3).

The stiffness coefficient of each bridge member (i.e., the nodal forces due to unit nodal displacement or rotation) can be determined by a number of approaches. One of

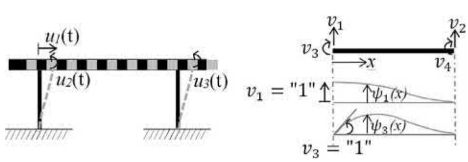

Figure 6.3 MDOF bridge model and member deflection due to unit left nodal deformation.

these is the principle of virtual deformation, where the following shape functions are considered:

$$\begin{aligned}
\psi_1(x) &= 1 - 3\left(\frac{x}{L}\right)^2 + 2\left(\frac{x}{L}\right)^3, \\
\psi_2(x) &= 3\left(\frac{x}{L}\right)^2 - 2\left(\frac{x}{L}\right)^3, \\
\psi_3(x) &= x\left(1 - \frac{x}{L}\right)^2 \text{and} \\
\psi_4(x) &= \frac{x^2}{L}\left(\frac{x}{L} - 1\right)
\end{aligned} \tag{3}$$

The deflected shape $v(x) = \psi_1(x)v_1 + \psi_2(x)v_2 + \psi_3(x)v_3 + \psi_4(x)v_4$ of the structural member can now be expressed in terms of its nodal displacements v_1 and v_2 and the nodal rotations v_3 and v_4.

With the stiffness coefficient $k_{ij} = \int_0^L EI(x)\psi_i''(x)\psi_j''(x)dx$ (i.e. the force developed at the i^{th} DOF due to a unit deformation at the j^{th} DOF), the stiffness $\boldsymbol{k}_e$ of the structural member of length L with a bending stiffness EI relates the deformation $\boldsymbol{v}$ of each member DOF to the corresponding elastic nodal force $\boldsymbol{f}_s$:

$$\underbrace{\frac{2EI}{L^3}\begin{bmatrix} 6 & -6 & 3L & 3L \\ -6 & 6 & -3L & -3L \\ 3L & -3L & 2L^2 & L^2 \\ 3L & -3L & L^2 & 2L^2 \end{bmatrix}}_{\boldsymbol{k}_e} \begin{bmatrix} v_1 \\ v_2 \\ v_3 \\ v_4 \end{bmatrix} = \begin{bmatrix} f_{s1} \\ f_{s2} \\ f_{s3} \\ f_{s4} \end{bmatrix}. \tag{4}$$

By transforming the local member coordinate to the global DOF, the system stiffness $\boldsymbol{K}$ of the whole system can be obtained using the direct stiffness approach (see e.g. Martin, 1966).

$$\boldsymbol{K} = \sum_{e=1}^{n} \boldsymbol{k}_e, \tag{5}$$

where n is the number of structural members.

With regard to the mass matrix of the bridge segment, a lumped-mass model can be assumed; i.e., each structural member will be divided into two segments of $L/2$, with masses concentrated at the segment ends. The mass matrix of the system is, then, a diagonal matrix.

A more realistic model of the inertia forces can be achieved by assuming that the inertia forces initiated along the structural members by unit nodal lateral or angular accelerations are proportional to the corresponding shape function ψ_i. The mass coefficient of the so-called consistent mass model is $m_{ij} = \int_0^L m(x)\psi_i(x)\psi_j(x)dx$; i.e., the force developed at the ith DOF due to a unit acceleration at the j^{th} DOF. Hence, the mass matrix $\boldsymbol{M}_e$ of the structural member of the length of L with mass per unit length $\overline{m}$ relates the acceleration at each DOF to the corresponding inertial force f_I:

$$\underbrace{\frac{\overline{m}L}{420}\begin{bmatrix} 156 & 54 & 22L & -13L \\ 54 & 156 & 13L & -22L \\ 22L & 13L & 4L^2 & -3L^2 \\ -13L & -22L & -3L^2 & 4L^2 \end{bmatrix}}_{\boldsymbol{M}_e}\begin{bmatrix} \ddot{v}_1 \\ \ddot{v}_2 \\ \ddot{v}_3 \\ \ddot{v}_4 \end{bmatrix} = \begin{bmatrix} f_{I1} \\ f_{I2} \\ f_{I3} \\ f_{I4} \end{bmatrix}, \tag{6}$$

and the system mass matrix $\boldsymbol{M}$ can be obtained using the direct stiffness approach (see e.g. Martin, 1966).

$$\boldsymbol{M} = \sum_{e=1}^{n} \boldsymbol{M}_e \tag{7}$$

where n is the number of structural members.

In order to have the same matrix properties, the Rayleigh damping $\boldsymbol{C} = \lambda\,\boldsymbol{M} + \mu\,\boldsymbol{K}$ is often used; i.e., the damping matrix is stiffness and mass matrices proportional (Clough and Penzien, 1993). By introducing the orthogonality property of the natural modes $\boldsymbol{\phi}_r$ with the corresponding frequency ω_r(i.e., $\boldsymbol{\phi}_j^T M \boldsymbol{\phi}_i = \boldsymbol{\phi}_j^T \boldsymbol{K} \boldsymbol{\phi}_i = \boldsymbol{\phi}_j^T \boldsymbol{C} \boldsymbol{\phi}_i = 0$), λ and μ can be calculated from two selected damping ratios $\xi_r = \frac{1}{2}\left(\frac{\lambda}{\omega_r} + \mu\,\omega_r\right)$.

Thus, the governing equation is

$$\boldsymbol{M}\,\ddot{\boldsymbol{u}}(t) + \boldsymbol{C}\,\dot{\boldsymbol{u}}(t) + \boldsymbol{K}\,\boldsymbol{u}(t) = \boldsymbol{P}(t), \tag{8}$$

where bold uppercase letters $\boldsymbol{M}$, $\boldsymbol{C}$ and $\boldsymbol{K}$ denote respectively the mass, damping and stiffness matrices of the bridge structure, and bold lower and uppercase letters $\boldsymbol{u}$, $\dot{\boldsymbol{u}}$, $\ddot{\boldsymbol{u}}$ and $\boldsymbol{P}$ denote the displacement, velocity, acceleration response and load vectors, respectively.

1.3 IDOF system

Unit deformations described by the shape functions of Eq. (3) fulfill the differential equation of a flexural beam exactly. For calculating the structural response to a static loading, the stiffness matrix [Eq. (4)] is exact. For analyzing the structural response to dynamic loading, the stiffness and mass matrices of Eq. (5) and Eq. (7), resulting from the member stiffness and mass matrices (Eqs. 4 and 6), can only describe the dynamic properties of the structure approximately.

The vibration of a structural member with uniformly distributed mass $\overline{m}$, bending stiffness EI, and viscous damping c_t is governed by a partial differential equation (see also Figure 6.4 and Chouw, 1994).

$$\overline{m}\,\ddot{v} = -EI\,v_{,xxxx} - c_t\dot{v} \tag{9}$$

where $(\dot{\ }) = \frac{d}{dt}()$ and $()_{,x} = \frac{d}{dx}()$. Eq. (9) can be transformed into the Fourier or Laplace domain and an analytically solvable normal differential equation can be obtained. The solution of this equation can be expressed in terms of nodal displacement and rotation

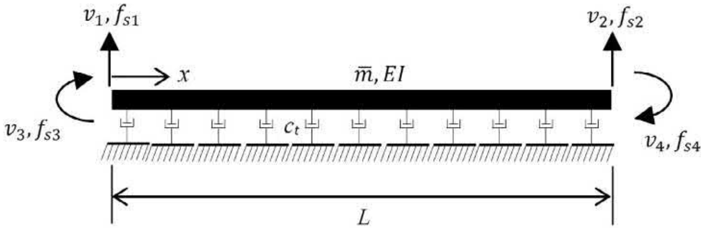

Figure 6.4 Structural member with continuously distributed mass $\overline{m}$, stiffness EI, and damping c_t.

$\widetilde{v}$, and corresponding force and moment $\widetilde{f}_s$. In the following the tilde indicates the variable in the Laplace domain.

The Laplace transformation of Eq. (9) leads to

$$4f^4\ \widetilde{v} = -\widetilde{v}_{,xxxx} \tag{10}$$

where $f^4 = \frac{ms^2 + c_t s}{4EI}$, and the Laplace parameter s is $\delta + i\,\omega$ and $i = \sqrt{-1}$;$\delta = \frac{8}{T}$; T is the time window considered.

The solution in the Laplace domain is $v = (A\cos f\ x + B\sin f\ x\ )e^{fx} + (C\cos f\ x + D\sin f\ x\ )e^{-fx}$, with the four constant values A, B, C and D being obtained from four boundary conditions involving both ends of the structural member. By relating the nodal deformation to the nodal forces $\widetilde{f}_{s1} = -EI\widetilde{v}_{,xxx}(x=0,s)$ and $\widetilde{f}_{s2} = EI\widetilde{v}_{,xxx}(x=L,s)$ and moments $\widetilde{f}_{s3} = -EI\widetilde{v}_{,xx}(x=0,s)$ and $\widetilde{f}_{s4} = EI\widetilde{v}_{,xx}(x=L,s)$ the exact member stiffness $\widetilde{k}_e$ can be obtained. It is worth mentioning that in the stiffness coefficient the mass and stiffness component can no longer be separated. Hence, the stiffness $\widetilde{k}_e$ is called the *dynamic stiffness* of the structural member:

$$\underbrace{\begin{bmatrix} \widetilde{k}_{11} & \widetilde{k}_{12} & \widetilde{k}_{13} & \widetilde{k}_{14} \\ \widetilde{k}_{21} & \widetilde{k}_{22} & \widetilde{k}_{23} & \widetilde{k}_{24} \\ \widetilde{k}_{31} & \widetilde{k}_{32} & \widetilde{k}_{33} & \widetilde{k}_{34} \\ \widetilde{k}_{41} & \widetilde{k}_{42} & \widetilde{k}_{43} & \widetilde{k}_{44} \end{bmatrix}}_{\widetilde{k}_e} \begin{bmatrix} \widetilde{v}_1 \\ \widetilde{v}_2 \\ \widetilde{v}_3 \\ \widetilde{v}_4 \end{bmatrix} = \begin{bmatrix} \widetilde{f}_{s1} \\ \widetilde{f}_{s2} \\ \widetilde{f}_{s3} \\ \widetilde{f}_{s4} \end{bmatrix}, \tag{11}$$

where

$$\widetilde{k}_{11} = \widetilde{k}_{33} = 2\gamma f^2(e^{4\alpha} + 2e^{2\alpha}\sin 2\alpha - 1);$$
$$\widetilde{k}_{12} = \widetilde{k}_{21} = -\widetilde{k}_{34} = -\widetilde{k}_{43} = \gamma f(-e^{4\alpha} + 2e^{2\alpha}\cos 2\alpha - 1);$$
$$\widetilde{k}_{13} = \widetilde{k}_{31} = 4\gamma f^2\{-e^{3\alpha}(\sin\alpha + \cos\alpha) + e^{\alpha}(-\sin\alpha + \cos\alpha)\};$$
$$\widetilde{k}_{14} = \widetilde{k}_{41} = -\widetilde{k}_{23} = -\widetilde{k}_{32} = 4\gamma f\ (\sin\alpha(e^{\alpha} - e^{3\alpha});$$
$$\widetilde{k}_{22} = \widetilde{k}_{44} = \gamma\ (e^{4\alpha} - 2e^{2\alpha}\sin 2\alpha - 1);$$

$$\tilde{k}_{24} = \tilde{k}_{42} = 2\gamma\left\{e^{3\alpha}(\sin\alpha - \cos\alpha) + e^{\alpha}(\sin\alpha + \cos\alpha)\right\};$$

$$\alpha = \sqrt{\frac{(ms + c_t)sL^4}{4EI}};\ \gamma = \frac{2EIf_t}{e^{4\alpha} - 2e^{\alpha}(1 + 2\sin^2\alpha) + 1}$$

The dynamic stiffness $\tilde{\boldsymbol{K}}$ of the bridge structure can be obtained using the same direct stiffness approach [Eq. (5)] in the Laplace domain. The equation of motion of the bridge structure with infinite DOF in the Laplace domain is an algebraic equation:

$$\tilde{\boldsymbol{K}}\ \tilde{\boldsymbol{u}} = \tilde{\boldsymbol{P}}\,. \tag{12}$$

2. Bridge response to dynamic loading

The equation of motion relates loading to structural response. For a given loading, the responses u(t), $\dot{u}$(t) and $\ddot{u}$(t) can obtained from the equation of motion. Depending on loading types and the number of DOFs, the equation can be solved analytically or numerically.

2.1 SDOF system

2.1.1 Harmonic loading

In the case of a harmonic loading [e.g. $P(t) = P_e \sin(\omega_e t)$], the excitation is characterized only by its amplitude $P_e = kA_e$ and frequency $f_e = \omega_e/2\pi$. Because of structural damping c, the free vibration determined solely by the dynamic properties of the structure, will die away with the time. The remaining steady-state response is determined by the magnitude and frequency of the load (i.e. A_e, f_e), and the natural frequency and damping ratio of the structure (i.e. f_s and ξ). The damping ratio ξ is c/c_{crit}, where c and $c_{crit} = 2\sqrt{mk}$ are the actual structural damping and the critical damping that results in monotonic decay of vibration with time, respectively.

The particular solution for Eq. (1) can be assumed as $u(t) = C\sin\omega_e t + D\cos\omega_e t$ and by substituting this solution and its first and second time derivatives into Eq. (1), while equating the sine and cosine terms of both sides of the equation, the coefficients C and D can be obtained. The steady-state response is then

$$u(t) = \sqrt{C^2 + D^2}\sin(\omega_e t - \varphi) \tag{13}$$

where $\varphi = \tan^{-1}\left(\frac{-D}{C}\right) = \tan^{-1}\left(\frac{2\xi\beta}{1-\beta^2}\right)$, $C = A_{st}\frac{1-\beta^2}{\left(1-\beta^2\right)^2 + (2\xi\beta)^2}$, $D = A_{st}\frac{-2\xi\beta}{\left(1-\beta^2\right)^2 + (2\xi\beta)^2}$, $A_{st} = \frac{P_e}{k}$ and $\beta = \frac{f_e}{f_s}$.

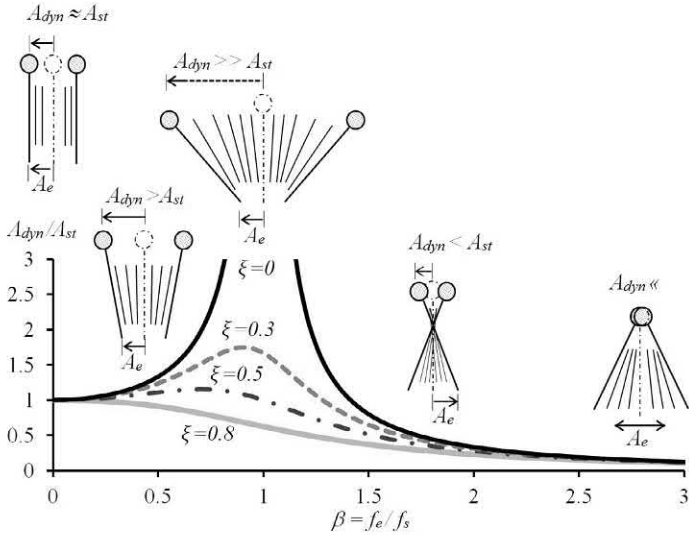

Figure 6.5 Consequence of excitation-to-structural frequency ratio β and damping ratio ξ for the structural response ratio A_{dyn}/A_{st} (A_e = excitation amplitude; A_{dyn} and Ast¼ dynamic and static response of the structure; f_e and f_s = the frequency of the harmonic excitation and the structure, respectively).

The amplitude A_{dyn} of the dynamic response is $\sqrt{C^2 + D^2}$. The maximum response ratio A_{dyn}/A_{st} shows an amplification or a reduction of the dynamic response relative to the maximum static response A_{st}. In Figure 6.5, the dynamic response amplitude A_{dyn} of a number of SDOF structures due to the same harmonic excitation is displayed relative to the constant static response amplitude A_{st}, as a function of frequency ratio β and damping ratio ξ. A plot of the maximum dynamic response of the SDOF structures to the same dynamic loading is called the response spectrum of the harmonic loading (even though it is not a real spectrum), because the maximum response of one structure is independent of the response of another structure, while the spectrum values of a real spectrum (e.g. the Fourier spectrum), are linked to each other. The display of the response is only spectrum-like because the amplitude is shown as a function of the natural undamped frequency f_s of the structures. The spectrumlike display is still useful, since it reveals the consequence of the structural frequency f_s relative to the excitation frequency f_e, and the actual damping c relative to the critical damping c_{crit}.

If β is very small, $A_{dyn} \approx A_{st}$; i.e., the structure responds to the dynamic loading like responding to a static load. This is the case when the structure is very stiff; i.e., f_s is very high relative to the excitation frequency f_e. The excitation is so slow relative to the speed of the natural vibration of the structure, that the structure responds to the excitation as a static-like loading.

In the case of harmonic ground excitation, the structure moves with the ground with the same amplitude (see top left sketch of the response in Figure 6.5). Since the structure moves like a rigid body, there is no relative deformation along the structure.

Consequently, the damping has no effect and no force will be generated in the structure. Because of this damage to structures resulting from deformation-related forces can be avoided. Since rigid body like movement occurs, the whole structure will experience the ground acceleration. This induced acceleration might cause excessive loading for secondary structures attached to the main structure (Lim and Chouw, 2015).

With increasing excitation frequency or with a more flexible structure, the steady-state response becomes larger than the static response. For common civil infrastructure with a damping ratio less than 20%, the influence of damping is not so significant. When the excitation frequency coincides with the natural frequency of the structure ($\beta = 1$) the structure is in resonance with the excitation. Without damping, it is only a question of time before the structure will collapse due to the accumulation of induced energy. The response of the strongly excited structure is controlled solely by the damping. Following this observation, structures in earthquake-prone regions should be built with a fundamental frequency as far as possible from dominant frequencies of ground motions predicted for those regions.

With either or both further increases of the excitation frequency or flexibility of the structure, the amplitude of the dynamic response becomes smaller than the static response. The structure responds in the opposite direction to that of the loading (see the sketch on the right side, $\beta > 1$, $A_{dyn} < A_{st}$ in Figure 6.5). The damping plays a less important role than the ratio of the excitation frequency to the structural frequency.

In the case of a very flexible structure, or a very fast-moving excitation, the structure hardly responds to the excitation; i.e., A_{dyn} is very small relative to the excitation amplitude A_e. Before the slow-moving structure can react, the load already moves to the other direction. The load is too fast for the structure to have the opportunity to respond (see the right sketch in Figure 6.5). In the case of a ground excitation the structure hardly experiences induced acceleration (A_{dyn} «). Consequently, secondary structures (e.g. non-structural components such as ceilings, cladding piping system) will likely survive the ground motion without difficulty. However, the structure will likely suffer damage due to large relative deformation along the height of the structure.

The advantage of a structure with both a very small β (rigid structure) and a very large β (flexible structure) at the same time can be created by installing a base isolator at the interface between the footing and the supporting ground. The flexibility of the isolator in the lateral direction simulates a flexible system. The system itself is the rigid structure. Hence, when the ground moves the isolator will be displaced laterally, while the structure performs only rigid body movement (i.e. no deformation in the structure and thus no forces will be generated in the structure). In the worst case the strongly dislocated isolator will be damaged and needs to be replaced prior to seismic motion (e.g. aftershock shaking). The structure itself can survive the earthquake without significant damage.

Although a steady-state response is unlikely in the case of earthquakes, a long duration and harmoniclike ground motion is possible; e.g., when a site with soft sediment is excited by the incoming seismic waves, resulting in harmoniclike ground excitation of the ground surface and the structure. The ground motions have the dominant frequency of the sediment, such as that observed in the 1985 Mexico City earthquake.

At the Secretaria de Comunicaciones (SCT) station, the harmoniclike earthquake motion lasted more than 2 min. (Chouw, 1994).

2.1.2 Pulse excitation

Should the excitation have a pulselike nature that does not last long, the load can be broken into a sequence of very short impulses. The load duration td is short, relative to the fundamental period of the structure, of the order of a few multiples of the fundamental period of the structure. Once the response of the structure to each of these very short impulses has been determined, the response to the total pulselike excitation can be obtained by superimposing the effect of these very short impulses. This consideration of the influence of each impulse on the structure and the superposition of each influence as the total effect of the loading is also called the *Duhamel integral approach* (Figure 6.6).

It is known that an impulse I reflects the change in momentum $\Delta(m\dot{u})$. Consequently, for a structure with a constant mass throughout the time window considered, the impulse causes a sudden change in velocity $\Delta\dot{u} = I/m$. The effect of this sudden velocity change on an SDOF system, initially at rest with $u(0)=0$, can be considered as initial velocity $\dot{u}(0) = \frac{I}{m}$ at the time τ of occurrence of the impulse. For an assumed free vibration $u(t) = G\sin(\omega_d t - \alpha)$ the constants G and α can be obtained from introducing the initial conditions $u(0)$ and $\dot{u}(0)$ into the free vibration equation.

With $G = \frac{I}{m\,\omega_d}, \alpha = \frac{\pi}{2}$ the response to the very short impulse is

$$u(t) = \frac{I(\tau)}{m\,\omega_d} e^{-\xi\omega(t-\tau)} \sin\omega_d(t-\tau),\ at\ t=\tau, I(\tau) = P(\tau)\,d\tau, t > \tau \tag{14}$$

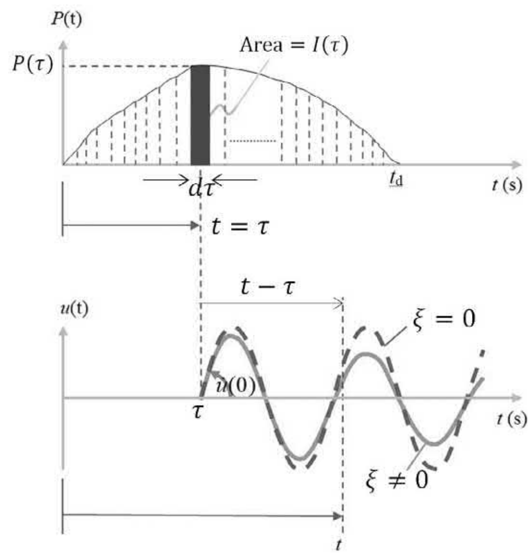

Figure 6.6 Duhamel integral approach.

The total response to the pulse excitation can be obtained by superposition of each impulse response:

$$u(t) = \int_{\tau=0}^{\tau=t} \frac{P(\tau)}{m\,\omega_d} e^{-\xi\omega(t-\tau)} \sin\omega_d(t-\tau)d\tau \tag{15}$$

Since superposition is applied, only a linear system can be considered; i.e., damage to the structure during the loading cannot be incorporated into the analysis. However, for estimating the impact of the pulse loading on the nonlinear behavior of the structure, an analysis of the linear structure is always useful. It serves as a reference case to reveal the consequence of nonlinear material behavior due to structural damage (i.e., reduction of the structural stiffness resulting from damage).

In near-source earthquake regions, the hypocentral distance of the structure to the source of the earthquake is short (typically within 20 km). The ground motion can have a vertical component that is much stronger than the horizontal ones (Chen et al., 2016) and it may also have strong pulses due to directivity effects of seismic wave propagation. For simplicity the ground motion can be described by the strong pulse; i.e., $P(\tau) = -m\,\ddot{u}_g(\tau)$. Pulse-like loadings can also be triggered by underground explosions, such as those due to mining activities. To incorporate possible damage during a strong earthquake, the step-by-step approach described in the next section can be used.

As an example, the response $u(t)$ of the structure to a ground acceleration pulse induced by an underground explosion can be calculated using Eq. (15). It is assumed that the load $P(\tau) = -m\,\ddot{u}_g(\tau)$ can be described by a half sine $\ddot{u}_g(t) = \ddot{u}_{go}\sin\pi t$ with a duration t_d of 1 s. For simplicity, the damping effect of this short duration pulse loading can be ignored:

$$u(t) = \int_{\tau=0}^{\tau=t} \frac{\ddot{u}_{go}\sin\pi\tau}{m\,\omega} \sin\omega(t-\tau)d\tau = \frac{\ddot{u}_{go}}{\omega} \frac{\pi\sin\omega t - \omega\sin\pi t}{\pi^2 - \omega^2},\ t \le 1s \tag{16}$$

2.1.3 Earthquake loading

Ground motion due to an earthquake has a seemingly random development over time. A closed-form solution as derived in Section 2.1.1 for harmonic loading, and utilization of a short pulse excitation using the Duhamel integral approach, as described in Section 2.1.2, are not usually an option. The so-called step-by-step approach is commonly used. Since no superposition is performed, nonlinear geometry and material behavior can be incorporated into the analysis. The approach is based on an assumption of the acceleration development within one time step; i.e., it is assumed that the response acceleration one step later relative to the current acceleration is known. Based on this assumption, a number of step-by-step numerical approaches have been developed (see e.g., Figure 6.7).

In the following, the step-by-step approach based on an assumption of constant acceleration development within one time step $\ddot{u}(\tau) = \frac{1}{2}(\ddot{u}_i + \ddot{u}_{i+1})$ is described.

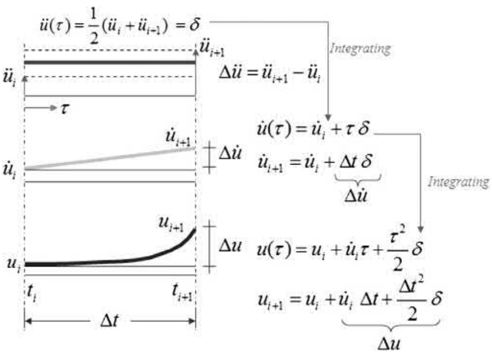

Figure 6.7 Constant acceleration assumption $\ddot{u}(\tau)$ within one time step yielding the velocity $\dot{u}_{i+1}$ and displacement u_{i+1}.

With $\frac{c}{m} = 2\xi\omega$ and $\frac{k}{m} = \omega^2$ the equation of motion for a load increment is $m\,\Delta\ddot{u} + c\,\Delta\dot{u} + k\,\Delta u = \Delta P$, which can be rearranged as follows:

$$\Delta\ddot{u} + 2\xi\omega\,\Delta\dot{u} + \omega^2\,\Delta u = \frac{\Delta P}{m} \tag{17}$$

With δ, $\Delta\ddot{u}$ and Δu:

$$\Delta u = \frac{(2\ddot{u}_i + \Delta\ddot{u})\Delta t^2}{4} + \dot{u}_i\,\Delta t$$

and a rearrangement leads to

$$\Delta\ddot{u} = \frac{4(\Delta u - \dot{u}_i\Delta t)}{\Delta t^2} - 2\,\ddot{u}_i \tag{18}$$

With $\Delta\dot{u}$ and Δu:

$$\Delta\dot{u} = \frac{2\Delta u}{\Delta t} - 2\dot{u}_i \tag{19}$$

By substituting Eqs. (18) and (19) into Eq. (17), the response increment within one time step can be defined:

$$\Delta u = \frac{\frac{4\dot{u}_i}{\Delta t} + 2\ddot{u}_i + 4\xi\omega\dot{u}_i + \frac{\Delta P}{m}}{\frac{4}{\Delta t^2} + \frac{4\xi\omega}{\Delta t} + \omega^2} \tag{20}$$

With the response increment the response one time step later at $t+\ \Delta t$, i.e. Δu, $u_{i+1}, \dot{u}_{i+1}$, and $\ddot{u}_{i+1}$, can then be calculated.

Since the development of responses in the future cannot be predicted, the assumption of the development is only an estimate. Hence, the time step is relevant, leading to

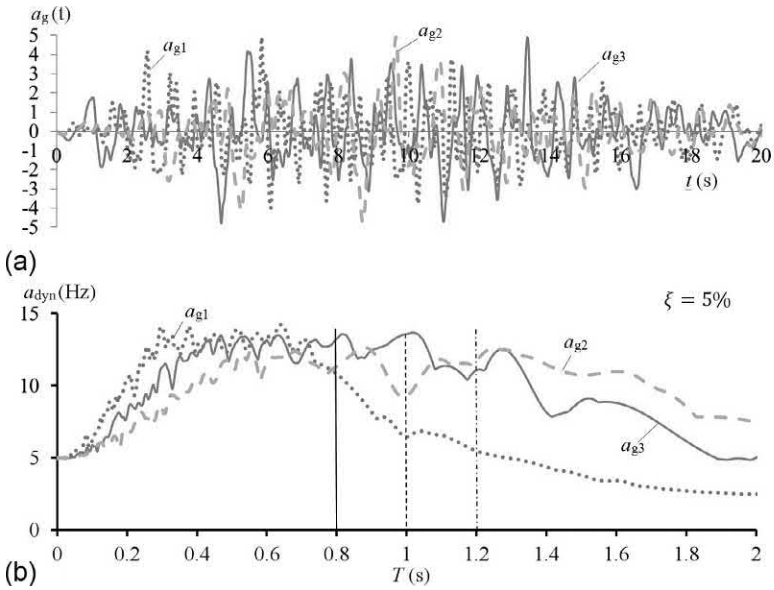

Figure 6.8 Influence of *PGA* and frequency content on the structural response: (a) Time history of ground motions; (b) response spectra of the ground motions.

what is referred to as a *conditionally stable computation scheme* (see, e.g., Clough and Penzien, 1993). A large time step, relative to the natural period T of the structure, will lead to an inaccurate result. Time steps that are too small will also lead to inaccuracies. A time step $\Delta t \leq 0.1\,T$ is recommended; i.e., if the structure vibrates in its natural mode, 10 discrete values will be available to describe one natural vibration of the structure appropriately.

Figure 6.8a and b show the simulated ground accelerations based on JSCE (2000) and their corresponding response spectra, respectively. The maximum response of the structure to each ground motion can be obtained using Eq. (20), and a_{g1}(t), a_{g2}(t) and a_{g3}(t) are ground motions for hard, soft, and medium soil conditions, respectively. In order to reveal the role of the peak ground acceleration (*PGA*), the ground motions considered have the same *PGA* ($5\,\text{m/s}^2$).

This same *PGA* is evident for all response spectrum values at the zero period in Figure 6.8b. As is demonstrated in Figure 6.5, a totally rigid structure (i.e., with the natural period $T = 0\,\text{s}$) will move identically with the ground (see top left sketch in Figure 6.5). Hence, it will experience exactly the same acceleration as the ground. Consequently, the maximum response of the structure to the ground motion is the *PGA* of the ground excitation; i.e., the *PGA* is the total acceleration.

Based on a quasi-static approach (i.e., the maximum inertia force FI is *PGA* times the mass of the structure), a structure under this loading could be anticipated to have the same maximum force. However, Figure 6.8b clearly shows that this is not the case. The reason for this is that the assumption of the quasi-static approach is based solely on one quantity of the loading (i.e., *PGA*), while both the other significant property of the loading (i.e., its frequency content) and the dynamic property of the structure (i.e., its natural period) are ignored. Even though all ground motions have the same *PGA*, depending on the period of the structure relative to the dominant frequencies of the loading, the structure will respond differently. Consequently, the maximum response acceleration is not the same for structures with different natural periods. The vertical solid, dashed, and dashed-dotted lines in Figure 6.8b indicates the response of a structure with the natural period of 0.8 s, 1 s, and 1.2 s, respectively. While for a structure with the natural period of 0.8 s, the maximum responses due to ground motions of hard-and soft-soil conditions are similar, the excitation of medium-soil condition results in the largest response. In contrast, for a structure with the natural period of 1.2 s, similar maximum responses occur due to excitations of soft-and medium-soil conditions. For a structure with a natural period of 1 s, the excitation of each soil condition evokes very different responses. The largest response occurs when the excitation of medium-soil condition is considered.

These results clearly show that the commonly used approach, which is solely based on *PGA*, is unreliable. It is advised that the combined effect of the whole dynamic properties of loading and structure should be considered in the analysis of structural responses.

2.2 MDOF system

In contrast to an SDOF system, the equation of motion cannot be solved directly for each DOF. Even if a lumped-mass model is assumed, the damping and stiffness matrices have coupled terms. Hence, the equation of motion [Eq. (8)] needs to be solved simultaneously for all DOFs. For a system with more than two DOFs, a hand calculation will be time consuming. However, this difficulty can be overcome by expressing the total response using the modal response $\boldsymbol{Y}$(t):

$$\boldsymbol{u}(\boldsymbol{t}) = \sum_{r=1}^{n} \boldsymbol{\Phi}_r \boldsymbol{Y}_r(t) = \boldsymbol{\Phi}\boldsymbol{Y}(t)\,, \tag{21}$$

where $\boldsymbol{\Phi}_r$ is the r^{th} mode shape which does not vary with time.

By substituting Eq. (21) and its time derivatives $\dot{\boldsymbol{u}}(t) = \boldsymbol{\Phi}\dot{\boldsymbol{Y}}(t)$ and $\ddot{\boldsymbol{u}}(t) = \boldsymbol{\Phi}\ddot{\boldsymbol{Y}}(t)$ the equation of motion (Eq. (8)) becomes

$$\boldsymbol{M}\boldsymbol{\Phi}\ddot{\boldsymbol{Y}} + \boldsymbol{C}\boldsymbol{\Phi}\dot{\boldsymbol{Y}} + \boldsymbol{K}\boldsymbol{\Phi}\boldsymbol{Y} = \boldsymbol{P} \tag{22}$$

The natural frequency of the system can be obtained from its undamped free vibrations, i.e. $\boldsymbol{C}$ and $\boldsymbol{P}$ are not considered. By substituting the assumed solution to be $Y(t) = A\cos\omega t + B\ \ sin\omega t$ and its second time derivative, Eq. (22) becomes $(\boldsymbol{K} - \omega^2\boldsymbol{M})\boldsymbol{\Phi}\boldsymbol{Y} = \boldsymbol{0}$. Since $\boldsymbol{Y} \neq \boldsymbol{0}$, the frequency equation $(\boldsymbol{K} - \omega^2\boldsymbol{M})\boldsymbol{\Phi} = \boldsymbol{0}$ can be obtained. For non-trivial solutions, i.e. $\boldsymbol{\Phi} \neq \boldsymbol{0}$, det $|\boldsymbol{K} - \omega^2\boldsymbol{M}| = 0$ and provides the eigenvalues of the system, i.e. the natural circular frequencies ω_r, $r = 1, n$ of the structure. By substituting the natural frequency ω_r into the frequency equation, the corresponding natural mode shape $\boldsymbol{\Phi}_r$ can be determined.

Multiply Eq. (22) by any mode $\boldsymbol{\Phi}_i^T$ to obtain:

$$\boldsymbol{\Phi}_i^T \boldsymbol{M} \boldsymbol{\Phi} \ddot{\boldsymbol{Y}} + \boldsymbol{\Phi}_i^T \boldsymbol{C} \boldsymbol{\Phi} \dot{\boldsymbol{Y}} + \boldsymbol{\Phi}_i^T \boldsymbol{K} \boldsymbol{\Phi} \boldsymbol{Y} = \boldsymbol{\Phi}_i^T \boldsymbol{P} \tag{23}$$

and by decoupling the system matrices using the orthogonality properties of the natural modes of the system $\boldsymbol{\Phi}_j^T \boldsymbol{M} \boldsymbol{\Phi}_i = \boldsymbol{\Phi}_j^T \boldsymbol{C} \boldsymbol{\Phi}_i = \boldsymbol{\Phi}_j^T \boldsymbol{K} \boldsymbol{\Phi}_i = 0$.

$$\boldsymbol{\Phi}_i^T \boldsymbol{M} \boldsymbol{\Phi}_i \ddot{Y}_i + \boldsymbol{\Phi}_i^T \boldsymbol{C} \boldsymbol{\Phi}_i \dot{Y}_i + \boldsymbol{\Phi}_i^T \boldsymbol{K} \boldsymbol{\Phi}_i Y_i = \boldsymbol{\Phi}_i^T \boldsymbol{P} \tag{24}$$

Since all system matrices are diagonal matrices, $\boldsymbol{\Phi}_i^T \boldsymbol{M} \ \boldsymbol{\Phi}_i = M_i$, $\boldsymbol{\Phi}_i^T \boldsymbol{C} \ \boldsymbol{\Phi}_i = C_i$, $\boldsymbol{\Phi}_i^T \boldsymbol{K} \ \boldsymbol{\Phi}_i = K_i$ and $\boldsymbol{\Phi}_i^T \boldsymbol{P} = P_i$ are scalar. The coupled equations of motion [Eq. (22)] for n-DOF are now de-coupled into n number of independent equations of motion, and instead can be solved separately in the manner of SDOF equations. n is the total number of DOFs considered.

$$M_i \ddot{Y}_i(t) + C_i \dot{Y}_i(t) + K_i Y_i(t) = P_i(t), i = 1, n \tag{25}$$

Once all modal responses $Y_i(t)$ due to $P_i(t)$ are calculated, the total response of the structure can be obtained. To solve Eq. (25) all previously discussed approaches for SDOF systems can be applied (Chouw, 2020).

2.3 IDOF system

The algebraic equation of motion, Eq. (12) can be solved easily, once the load is transformed into the Laplace domain. Thus

$$\tilde{\boldsymbol{P}} \, (\delta + i \, r \, \Delta\omega) = \sum_{r=0}^{N-1} \boldsymbol{P}(n \, \Delta t) \, e^{-\delta \, (n \, \Delta t)} \, e^{-i \, (r \, \Delta\omega)(\mathrm{n} \, \Delta t)} \, \Delta t, \tag{26}$$

the response $\tilde{\boldsymbol{u}} = \frac{\tilde{\boldsymbol{P}}}{\tilde{\boldsymbol{K}}}$ can be calculated. A back transformation of the response $\tilde{\boldsymbol{u}}$ into the time domain gives

$$\boldsymbol{u}(n \, \Delta t) = \frac{e^{\delta (n \, \Delta t)}}{2 \, \pi} \sum_{r=0}^{N-1} \tilde{\boldsymbol{u}} \, (\delta + i \, r \, \Delta\omega) \, e^{i \, (r \, \Delta\omega)(\mathrm{n} \, \Delta t)} \, \Delta\omega, \tag{27}$$

where $r = n = 0, \ldots, N\text{-}1$; $i = \sqrt{-1}$; $\delta = \frac{8}{T}$; $\Delta t = \frac{T}{N}$; $\Delta\omega = \frac{2\pi}{T}$. The largest circular frequency considered is $\omega_{max} = \frac{N}{2} \Delta\omega$, and N is the number of time steps considered.

For structures with material or geometrical nonlinearities, the nonlinear behavior can be approximated by a sequence of linear behavior; i.e., within each sequence, the structure behaves in a linear manner. The calculation is performed in the Laplace domain while the correction of the result is performed in the time domain (i.e., determination of the unbalanced forces as loading for the subsequent analysis). Details of this Laplace and time domain analysis are given in Chouw (1994, 2002).

3. Influence of supporting soil

In current bridge design, a fixed-base structure is often assumed due to the intrinsic difficulties in modeling coupled soil-foundation-bridge structure response. This design practice of neglecting soil effects is used, although the bridge is always supported by soil, and the significant impact of local soil has been observed in most major earthquakes (Chouw, 1995; Chouw and Hao, 2012).

3.1 Dynamic properties of the soil-structure system

For simplicity, a bridge segment is modeled as an SDOF system. The natural period or frequency of the system can be obtained by observing the free vibration (i.e., vibration behavior after the load that causes the free vibrations is outside the time window under consideration).

Figure 6.9a shows a simplified model of a bridge segment (shown in Figure 6.9b) with an assumed fixed base; i.e., the influence of the supporting subsoil is ignored as commonly performed in the current design. From the equation of motion for undamped free vibrations [i.e., Eq. (1), with no damping and loading], $m\ddot{u}(t) + k\,u(t) = 0$, the natural circular frequency ($\omega = \sqrt{\frac{k}{m}}$), and the natural period ($T = \frac{2\pi}{\omega} = 2\pi\sqrt{\frac{m}{k}}$) of the structure can be determined by substituting the mass $m = \frac{u_{st}}{k\,a}$, where u_{st} is the static displacement due to a load that causes an acceleration a of the mass:

$$T = \frac{2\pi}{\sqrt{a}}\sqrt{u_{st}} \tag{28}$$

Figure 6.9c shows the simplified SDOF model of the bridge segment with the subsoil. For simplicity the mass of the footing is not considered. The influence of the flexibility of the supporting soil is given by the horizontal and rotational springs with stiffness k_x and k_θ, respectively. u, u_x and u_θ are the static displacement due to a load W induced deformation of the structure, elongation of the horizontal spring, and the rotation of the rotational spring, respectively. The relationship between the load and induced

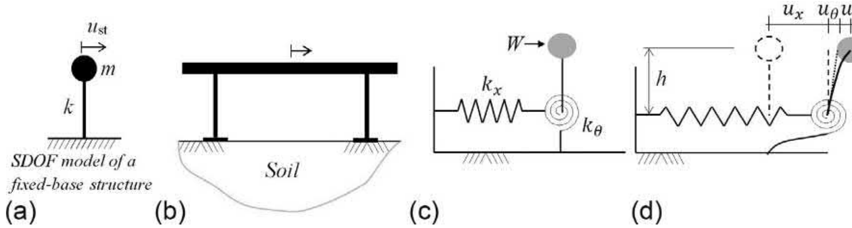

Figure 6.9 Influence of subsoil on the fundamental period of the system. (a) Fixed based and (b) soil supported structure, (c) simplified SDOF soil-structure system and (d) its static deformation.

rotation, $k_\theta \frac{u_\theta}{h} = W\,h$, can be obtained from the base moment. The total static displacement is

$$\overline{u}_{st} = \frac{W}{k} + \frac{W}{k_x} + \frac{Wh^2}{k_\theta} \tag{29}$$

From Eq. (28), the natural period $\overline{T}$ of the soil-structure system is

$$\overline{T} = \frac{2\pi}{\sqrt{a}}\sqrt{\overline{u}_{st}} = T\sqrt{1 + \frac{k}{k_x}\left(1 + \frac{k_x\,h^2}{k_\theta}\right)}. \tag{30}$$

When the structure vibrates the interaction between the vibrating footing and the supporting soil causes waves in the ground. These waves propagate from the footing-soil interface and transfer part of the vibration energy away. The vibrating footing therefore experiences energy loss. This process is termed radiation damping, i.e. due to radiation of waves in the soil. This damping and the soil resistance, i.e. soil stiffness, depends on the frequency of the vibrating footing, the direction of footing vibration and the dynamic soil properties, e.g. velocities of waves propagating in the soil. The frequency-dependent soil stiffness can be calculated e.g. using boundary element method (Chouw, 1994) or obtained from the handbook of impedance functions (Sieffert and Cevaer, 1992).

For simplicity the following static soil stiffness and frequency-independent damping can be used in Eqs. (29) and (30).

For the half-space case shown in Figure 6.10,

$$k_x = \frac{8GR}{2-\upsilon} \text{ and } k_\theta = \frac{8GR^3}{3(3-\upsilon)} \tag{31}$$

where R and υ are the equivalent radius of the assumed circular footing and Poisson's ratio, respectively.

For a soil layer of thickness H over bedrock with a footing embedment D shown in Figure 6.11,

$$k_x = \frac{8GR}{2-\upsilon}\left(1 + \frac{R}{2H}\right)\left(1 + \frac{2D}{3R}\right)\left(1 + \frac{5D}{4H}\right)$$

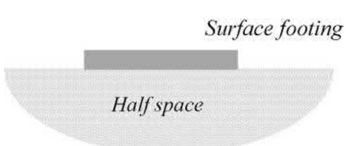

Figure 6.10 Surface footing on subsoil.

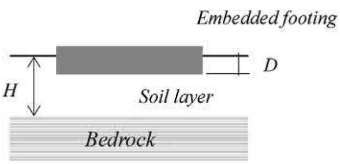

Figure 6.11 Footing with embedment D on soil layer over bedrock.

and

$$k_\theta = \frac{8GR^3}{3(3-\upsilon)}\left(1+\frac{R}{6H}\right)\left(1+2\frac{D}{R}\right)\left(1+0.7\frac{D}{H}\right) \tag{32}$$

where G is the shear modulus of the soil.

$$\overline{\xi} = \xi_s + \frac{\xi}{\left(\frac{\overline{T}}{T}\right)^3} \tag{33}$$

where $\xi = \frac{c}{c_{crit}}$, $c_{crit} = 2\ m\ \omega$, ξ_s is material and radiation damping of the soil, $\overline{T}$ the natural period of the soil-structure system, and T is the natural period of the assumed fixed-base structure.

Eq. (33) shows that the larger the period ratio $\frac{\overline{T}}{T}$ the less the structural damping will contribute to the system damping. In other word, the more flexible the system is, e.g. due to soft soil, the smaller the effects of structural damping. Details regarding soil-foundation-structure system are given by Chouw (2013).

3.2 Effect of spatially varying ground motion

In the case of a long, extended structure (e.g. pipe lines or long bridges), the excitation of adjacent bridge supports is normally not the same, since seismic waves need time to travel from one bridge support to the other. Even if the adjacent bridge structures have the same fundamental frequency, relative response will nevertheless still occur, because spatially non-uniform ground excitation is to be expected, due to the effect of wave passage, site response and coherency loss.

Despite this knowledge most design specifications still consider spatially uniform ground motions as the design seismic loading. The consequence of this assumption of uniform loading can be seen in severe damage to bridges in almost all major earthquakes in the past (see Figure 6.12).

With an assumption of uniform ground excitation Eq. (2.2) can be rewritten with the stiffness $k = k_1 + k_2$, $\xi = \frac{c}{2m\,\omega}$ and $\omega = \sqrt{\frac{k_1+k_2}{m}}$

$$\ddot{u}(t) + 2\xi\omega\,\dot{u}(t) + \omega^2\,u(t) = -\,\ddot{u}_g(t) \tag{34}$$

Figure 6.12 Unseating damage to Llacolen Bridge due to the 2010 Chile earthquake induced relative movements of adjacent segments.

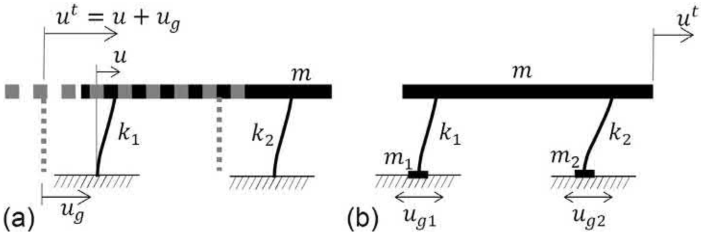

Figure 6.13 Bridge segment under (a) uniform and (b) spatially nonuniform ground motions.

Figure 6.13a shows the bridge structure under uniform ground excitation. When spatially varying ground motions are considered, it is useful to incorporate the effect of footings. Figure 6.13b shows that the left and right footing is of mass m1 and m2, respectively. With an assumption of the lumped-mass model, the equation of motion for the three-DOF system is

$$\begin{bmatrix} m & 0 & 0 \\ 0 & m_1 & 0 \\ 0 & 0 & m_2 \end{bmatrix} \begin{bmatrix} \ddot{u}^t \\ \ddot{u}_{g1} \\ \ddot{u}_{g2} \end{bmatrix} + \begin{bmatrix} c & 0 & 0 \\ 0 & 0 & 0 \\ 0 & 0 & 0 \end{bmatrix} \begin{bmatrix} \dot{u}^t \\ \dot{u}_{g1} \\ \dot{u}_{g2} \end{bmatrix} + \begin{bmatrix} k_1+k_2 & -k_1 & -k_2 \\ -k_1 & k_1 & 0 \\ -k_2 & 0 & k_2 \end{bmatrix} \begin{bmatrix} u^t \\ u_{g1} \\ u_{g2} \end{bmatrix} = \begin{bmatrix} 0 \\ 0 \\ 0 \end{bmatrix}. \tag{35}$$

While the quasi-static response of the uniformly excited bridge segment does not occur because of the rigid-body movement of the whole structure, the spatially varying ground motions does cause a quasi-static response since both bridge piers will move differently. By substituting the relationship between dynamic response u and quasi-static response u^{qs},

$$\begin{bmatrix} u^t \\ u_{g1} \\ u_{g2} \end{bmatrix} = \begin{bmatrix} u \\ 0 \\ 0 \end{bmatrix} + \begin{bmatrix} u^{qs} \\ u_{g1} \\ u_{g2} \end{bmatrix} \tag{36}$$

into Eq. (35), and by ignoring all dynamic components the quasi-static response can be determined

$$(k_1 + k_2)u^t - k_1 u_{g1} - k_2 u_{g2} = 0 \text{ and with } u = 0, u^{qs} = \frac{k_1 u_{g1} + k_2 u_{g2}}{k_1 + k_2} \tag{37}$$

For equal pier bending stiffness $k_1 = k_2 = \frac{k}{2}$: $u^{qs} = \frac{u_{g1} + u_{g2}}{2}$ which indicates an average of ground motions.

From Eq. (35), by ignoring the quasi-static response the equation of motion for spatially varying ground excitation can be defined:

$$m\,\ddot{u} + c\,\dot{u} + (k_1 + k_2)\,u(t) = k_1 u_{g1} + k_2 u_{g2},$$

or for equal pier bending stiffness case $k_1 = k_2 = \frac{k}{2}$, and

$$\ddot{u} + 2\xi\omega\,\dot{u} + \omega^2\,u = \frac{k}{2\,m}\left(u_{g1} + u_{g2}\right) = \frac{\omega^2}{2}\left(u_{g1} + u_{g2}\right) \tag{38}$$

For a MDOF system the equation for dynamic and quasi-static response can be derived in the same manner.

Eq. (35) becomes

$$\begin{bmatrix} \boldsymbol{M}_{bb} & \boldsymbol{M}_{bs} \\ \boldsymbol{M}_{sb} & \boldsymbol{M}_{ss} \end{bmatrix} \begin{bmatrix} \ddot{\boldsymbol{u}}^t \\ \ddot{\boldsymbol{u}}_g \end{bmatrix} + \begin{bmatrix} \boldsymbol{C}_{bb} & \boldsymbol{C}_{bs} \\ \boldsymbol{C}_{sb} & \boldsymbol{C}_{ss} \end{bmatrix} \begin{bmatrix} \dot{\boldsymbol{u}}^t \\ \dot{\boldsymbol{u}}_g \end{bmatrix} + \begin{bmatrix} \boldsymbol{K}_{bb} & \boldsymbol{K}_{bs} \\ \boldsymbol{K}_{sb} & \boldsymbol{K}_{ss} \end{bmatrix} \begin{bmatrix} \boldsymbol{u}^t \\ \boldsymbol{u}_g \end{bmatrix} = \begin{bmatrix} \boldsymbol{0} \\ \boldsymbol{0} \end{bmatrix} \tag{39}$$

Here, the subscripts b and s stand for bridge and soil, respectively.

By ignoring the dynamic response, Eq. (39) gives the quasi-static response

$$\boldsymbol{u}^{qs} = -\boldsymbol{K}_{bb}^{-1}\,\boldsymbol{K}_{bs}\,\boldsymbol{u}_g, \tag{40}$$

and the dynamic response can be obtained from the equation of motion

$$\boldsymbol{M}_{bb}\,\ddot{\boldsymbol{u}} + \boldsymbol{C}_{bb}\,\dot{\boldsymbol{u}} + \boldsymbol{K}_{bb}\,\boldsymbol{u} = \boldsymbol{P}_{eff}, \tag{41}$$

where $\boldsymbol{P}_{eff} = -\left(\boldsymbol{M}_{bb}\boldsymbol{K}_{bb}^{-1}\boldsymbol{K}_{bs} + \boldsymbol{M}_{bs}\right)\ddot{\boldsymbol{u}}_g - \left(\boldsymbol{C}_{bb}\boldsymbol{K}_{bb}^{-1}\boldsymbol{K}_{bs} + \boldsymbol{C}_{bs}\right)\dot{\boldsymbol{u}}_g$.

The total response can be obtained.

$$\begin{bmatrix} \boldsymbol{u}^t \\ \boldsymbol{u}_g \end{bmatrix} = \begin{bmatrix} \boldsymbol{u} \\ \boldsymbol{0} \end{bmatrix} + \begin{bmatrix} \boldsymbol{u}^{qs} \\ \boldsymbol{u}_g \end{bmatrix} \tag{42}$$

4. Bridge integrity: Consequences of relative response of adjacent bridge structures

Despite the most advanced bridge design specifications, almost all major earthquakes have shown that large relative movements between bridge girders and between bridge girders and between bridge decks and abutments can have severe consequences for the structural integrity of a bridge. Normally, the available gap is designed to cope with a relative closing movement due to a large change in temperature. In strong earthquakes large relative opening and closing displacements may occur. If the relative closing displacement is larger than the available gap, then pounding will take place. To estimate pounding-induced damage the pounding force needs to be determined (see e.g., Khatiwada et al., 2014). Pounding can be affected by several influence factors, e.g. aftershock (Qin and Chouw, 2017), multi-axial ground excitation (Lim et al., 2017; Lim and Chouw, 2018), skew angle of the bridge girders (Kun et al., 2017, 2018a, b; Kun and Chouw, 2019a,b), supporting soil (Barrios et al., 2020) and activated rigid-like body movement in the low-damage seismic design (Chouw, 2017). Should the relative opening response exceed the seat length then the bridge deck will lose its support and collapse (see Figure 6.12, Chouw, 1995; Chouw and Hao, 2012).

The main causes of relative response are

- Different dynamic properties of adjacent bridge structures
- Non-coherent ground motions at adjacent bridge supports
- Non-uniform soil-structure interaction
- Combined effect of the three above mentioned factors

To avoid or minimize relative responses, current design specifications (e.g., CALTRANS, 2010), suggest identical or similar fundamental frequencies of adjacent bridge structures. The fundamental period of the less flexible bridge structure should be at least equal to or larger than 70% of the fundamental period of the more flexible adjacent structure. With equal or similar frequencies, the adjacent structures will then respond approximately in phase. Consequently, the relative response is negligible and pounding and unseating can be avoided. However, this recommendation of similar frequencies is based on uniform excitation, i.e., all bridge structures will experience the same ground motions at the same time. However, in actuality, this rarely is the case, and so instead of reducing relative response, constructing adjacent structures at the same or similar frequencies becomes one of the significant causes of relative response. Thus the good intentions of most current design specifications could in many cases worsen, and not improve, bridge performance. This is because adjacent structures of the same or similar structural frequencies will cause relative response, if spatially non-uniform ground motions occur (Chouw and Hao, 2005; Bi et al., 2010; Li et al., 2013).

Spatially varying ground motions occur mainly due to the effect of

- Wave passage due to finite speed of the propagating seismic waves
- Site response due to spatially non-uniform soil profiles
- Coherency loss due to refraction and reflection of waves in the wave path

Since the soil along the bridge is never uniform, spatial variation of ground excitations is unavoidable.

Most current design specifications are based on uniform ground excitation. For example the *New Zealand Transport Agency* (NZTA, 2004) Bridge Manual defines the requirement for the minimum seat length to prevent unseating as

$$SL = 2E + 0.1 \geq 0.4\,m \tag{43}$$

where E is the relative movement between span and support.

According to the AASHTO LRFD bridge design specification (AASHTO, 2010) for straight bridges the length of seating required (in metres) is

$$SL = 0.203 + 0.00167\,l + 0.00666H \tag{44}$$

where l and H are the effective length of the bridge deck to the adjacent expansion joint or to the end of the bridge deck and the average height of columns supporting the bridge deck from the abutment to the next expansion joint or pier height, respectively.

In contrast to AASHTO and NZTA specifications, the seat length according to the Japan Road Association (JRA, 2004) is

$$SL = u_{rel} + u_G \geq SL_m \tag{45}$$

where u_{rel} is the relative displacement of the adjacent structures and u_G describes the relative ground displacement which depends on the soil strain $u_G = \varepsilon_G L$ and the distance L between the substructures in metres. For hard, medium and soft soil conditions the soil strain ε_G has the value of 0.0025, 0.00375 and 0.005, respectively. The minimum value of $SL_m = 0.7 + 0.005\,l$.

To reveal the consequence of the spatial variation of ground motions for the relative opening and closing displacements at an expansion joint, two bridge segments with the same damping ratio of 5% on an assumed half-space with a shear wave velocity of 100 m/s, soil density of 2000 kg/m^3, and Poisson's ratio of 0.33 are considered (Figure 6.14a). The ground motions are stochastically simulated based on the Japanese design spectrum (JDS) for soft-soil conditions [Figure 6.14b]. For simplicity, each bridge segment is modeled by an SDOF system. It is assumed that the surface footings have the dimensions of 9 m × 9 m. The bridge structures and subsoil are modeled by finite and boundary elements. While the calculation of the response is performed in the Laplace domain, the unbalanced forces for correcting the response due to pounding and girder separation are determined in the time domain. Details can be found in Chouw (1994, 2002), Chouw and Hao (2006), and Chouw (2008).

To limit the number of influence factors, it is assumed that both bridge structures have the same fixed-base fundamental frequency of 1 Hz, and the effect of spatial variation of the ground excitation is not considered for the moment. The height of the left structure ($h_2 = 9$ m) is kept constant. Since both structures have the same fixed-base fundamental frequency, they experience the same soil-structure interaction (SSI) and

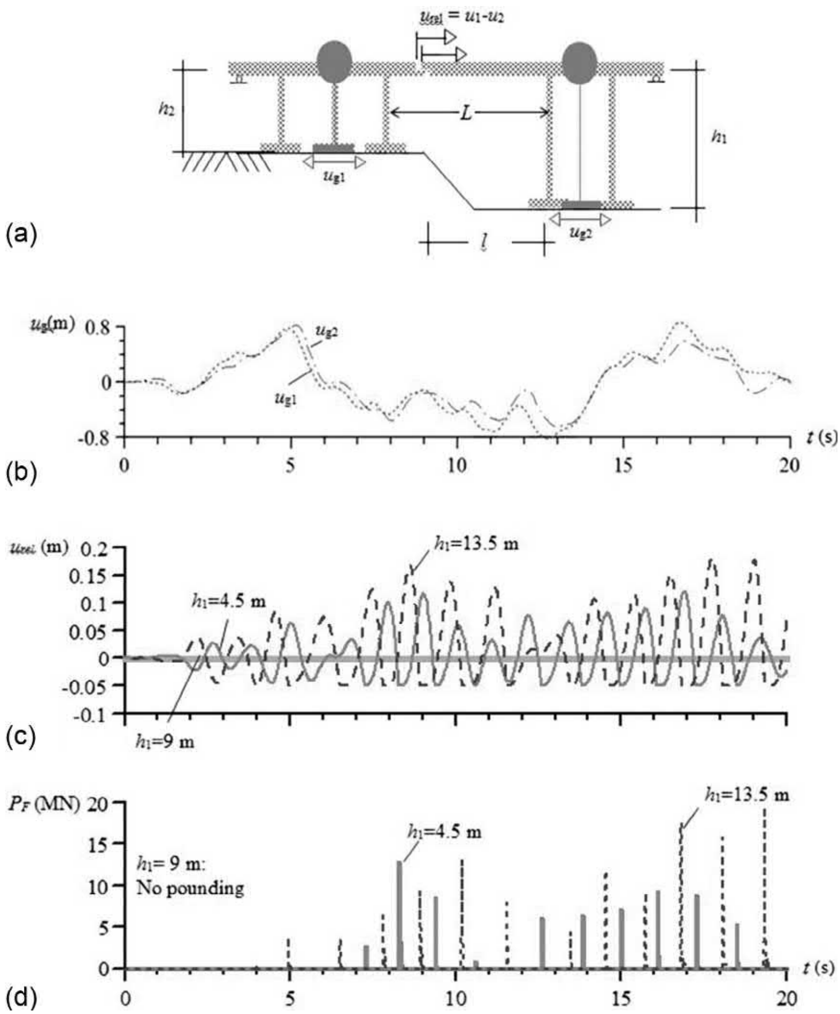

Figure 6.14 Two bridge structures with $h_2 = 9$ m. (a) Simplified double SDOF model, (b) spatially varying ground motion, (c) relative displacement u_{rel} at the joint, and (d) pounding force PF.

uniform ground excitation; i.e., there is no relative displacement between the girders [shown by the bold line in Figure 6.14c for $h_1 = h_2 = 9$ m]. Should the bridge piers have different heights, different SSIs will result in relative responses between the girders. While structures with tall piers are mainly controlled by the rotational stiffness of the soil, the response of structures with short piers will likely be determined by the horizontal soil stiffness (see Figure 6.9). Consequently, bridge segments with different slenderness ratios will not respond in phase, even though both structures may have the same fixed-base fundamental frequency. In this example, a height ratio (h_1/h_2) of 0.5 produces a seat length of 12 cm (see Figure 6.14c, the thin-solid line

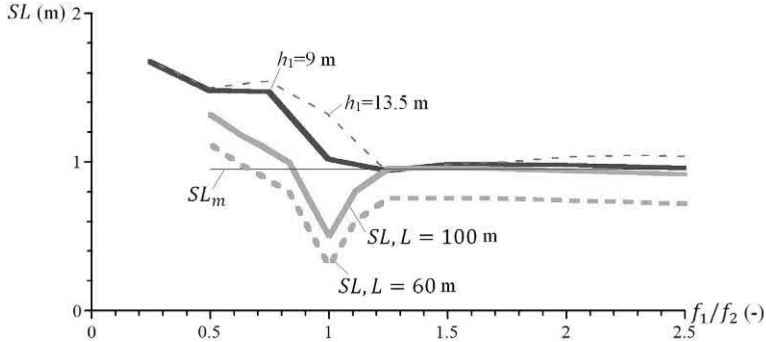

Figure 6.15 Influence of soft-soil JDS spatially nonuniform ground motions on the minimum seat length *SL* required to prevent unseating, according to JRA.

at 16.96 s). In contrast, a height ratio of 1.5 produces a seat length of 17.9 cm (see Figure 6.14c, the dashed line at 17.8 s).

The results clearly show the significance of considering SSI. While using the common assumption of a fixed-base structure, unseating will not take place, but including SSI will result in seat length requirements that cannot be revealed by following a conventional analysis of a fixed-base structure, even if uniform ground excitation can be justified. An assumption of a fixed-base structure clearly may underestimate the damage potential due to unseating and pounding between bridge girders.

When SSI is ignored in the analysis, the influence of the height ratio h_1/h_2 also cannot be revealed. Figure 6.15 shows the consequence of the height ratio h_1/h_2 and SSI for the seat length SL required to prevent unseating, where *SL* is shown as a function of the frequency ratio f_1/f_2 and the effect of pounding is not considered. The results show that the slender structure with $h_1 = 13.5$ m has the largest required seat length (thin dashed line). In addition, $h_1 = 9$ m results in a large seat length (see bold, solid black line in Figure 6.15). In the frequency ratio range between 0.5 and 1.2, and above 1.8, bridge structures with $h_1 = 13.5$ m need the longest seat length.

The horizontal solid thin line in the figure shows the minimum seat length values SLm according to the Japanese design specifications. Assuming a distance between bridge piers to be $L = 60$ m, the seat length [according to Eq. (45)] is the shortest (as indicated by the bold, dashed line). The consequence of the spatially varying ground movement for the seat length required can be clearly seen to have a nonzero value at the frequency ratio f_1/f_2 of 1. In contrast to reality, an assumption of constant soil strain for all cases causes a constant quasi-static contribution of 0.3 m. Even though the assumption does not reflect the reality, it is still the most advanced knowledge considered in the current Japanese design specifications. To this author's knowledge, this soil strain factor has not been considered in other specifications. The results show that even if a larger distance ($L = 100$ m) between the substructures is chosen, *SL* is still smaller than the values calculated using a more realistic numerical soil-structure model (see the bold, solid, black line).

A large number of physical experiments on the effects of spatial variation of ground motions using multiple shake tables had been performed at the University of

Auckland's Centre for Earthquake Engineering Research (UACEER). The ground motions were stochastically simulated based on the New Zealand loadings code (NZS1170.5, 2004) for soft-, medium-, and hard-soil conditions. Field tests on sand (Li, 2013), and fixed-base tests in the laboratory were considered, and these revealed the influence of soil-foundation-bridge structure interaction under spatially varying ground excitations.

Based on the experimental results, the following empirical equation for seat length, SLg of girders is proposed:

$$SL_g = (5.6f_r - 3.3)d_{ave} + d_{uni} \tag{46}$$

where d_{ave} and d_{uni} are the maximum relative displacements of fixed-base structures due to uniform ground motion, and the mean of the maximum girder displacements of two adjacent bridge segments with an assumed fixed base, respectively.

At least three ground motions should be considered. The maximum relative displacement between girders under uniform ground motions should consider excitation along two mutually perpendicular directions. Once the average maximum displacement of the bridge structures under the selected ground motions is determined, the seat length can be obtained from Eq. (46). These steps should be repeated for the other ground excitations. The largest seat length possible should be determined to be the seat length required to prevent unseating.

An empirical equation is proposed for the seat length S_{La} at the abutments:

$$S_{\mathrm{La}} = 1.4\,d_{uni}. \tag{47}$$

The background of the development of these empirical equations is given by Li et al. (2013).

To mitigate possible damage to bridge structures due to their relative responses, a number of measures have been developed and applied (e.g., hinge restrainers to prevent excessive relative opening displacements at a joint) so that seat extenders to ensure unseating does not occur through inadequate seat width. Recently, the author has proposed the use of modular expansion joints (MEJs) to cope with relative opening and closing displacements. These would help prevent the unseating and pounding of a bridge girder with adjacent girders or abutments. Details of a MEJ application are given in Chouw and Hao (2008).

Figure 6.16a shows a sketch of a modular expansion joint. It consists of a number of intermediate gaps so that in total, the joint can have a gap that is wide enough to cope with the largest relative movements expected at the joint. To determine the largest expected relative movements, fixed-base and field tests have been performed. From the newly developed relative displacement response spectrum at UACEER, the total gap that the joint has to cope with can be determined. Figure 6.16b shows the relative displacement response spectrum developed for ground motions according to the Japanese design spectrum (JSCE, 2000).

From Figure 6.16b, suppose that the left and right bridge structures have the fundamental periods T1of1 sand T2 of 2.5 s, respectively. Referring to the spectrum, the total gap required of the modular expansion joint can be calculated; in this case, it is 1.4 m.

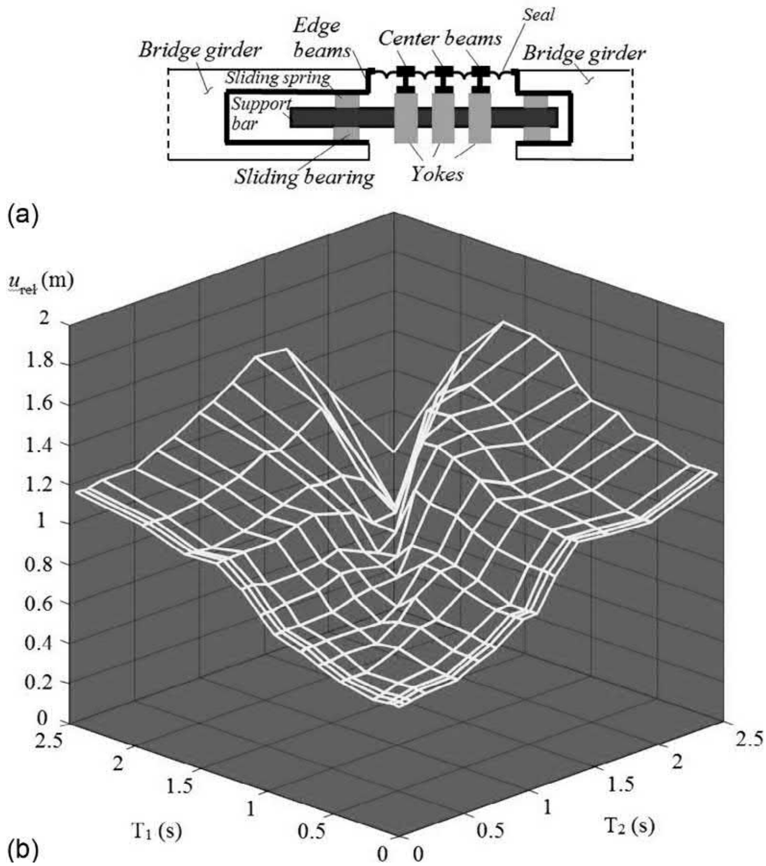

Figure 6.16 Mitigation measure: (a) Modular expansion joint; (b) relative displacement spectrum.

In the case of a strong earthquake and poor soil, nonlinear soil behavior can be observed (e.g., due to liquefaction, as observed in Kobe and Christchurch earthquakes; see Chouw, 1995; Chouw and Hao, 2012). The nonlinear soil behavior can be described using macro elements with a predefined yield surface (e.g., Chouw and Rincon, 2011). The nonlinear soil-foundation-bridge structure interaction can significantly influence the structural response.

5. Conclusions

Idealization of bridge structures can provide a quick insight into the dynamic behavior of the structure under loading, but with the drawback of limiting the information that otherwise could be obtained by more realistic analyses. Similarly, the idealization of dynamic loadings can be limiting when attempting to estimate the response of the structure, since the result will only be as good as the original correct assumptions of the loading. This chapter has suggested possibilities that may allow for going beyond the conventional analysis of bridge structural response under dynamic loadings.

Possible SDOF modeling, multi-DOF, and infinite DOF descriptions of the bridge structure were introduced. Approaches to solve the governing equations were provided, together with insights into the relationship between loading and structural response characteristics. In particular, the role of peak ground acceleration and the frequency content of the loading in the response of a structure were explored.

In contrast to the conventional consideration of fixed-base structures, the consequences of supporting soil for the dynamic properties of the soil-structure system and for the spatial variation of ground motions were considered and described. The structural response of the soil-structure system, which otherwise cannot be revealed from the assumption of fixed-base structures, was introduced. The relative response resulting from spatially varying ground excitation and spatially nonuniform soil-structure interaction was considered, especially with the aim to estimate its damage potential. Recent developments in mitigating damage development due to the relative response between bridge structures were also described.

Acknowledgments

The author would like to thank the Ministry of Business, Innovation, and Employment through the Natural Hazards Research Platform for the support of the research on “Seismic response of New Zealand bridges” under the Award UoA 3701868.

References

American Association of State Highway and Transportation Officials (AASHTO), 2010. Load and Resistance Factor Design (LRDF) Specification for Highway Bridges. AASHTO, Washington, DC.

Barrios, G., Larkin, T., Chouw, N., 2020. Influence of shallow footings on the dynamic response of saturated sand with low confining pressure. Soil Dyn. Earthq. Eng. 128, 105872.

Bi, K., Hao, H., Chouw, N., 2010. Required separation distance between decks and at abutments of a bridge crossing a canyon site to avoid seismic pounding. Earthq. Eng. Struct. Dyn. 39 (3), 303–323.

CALTRANS, 2010. Seismic Design Criteria, Version 1.6. November.

Chen, Y., Kun, C., Larkin, T., Chouw, N., 2016. Impact of vertical ground excitation on a bridge with footing uplift. J. Earthq. Eng. 20, 1035–1053.

Chouw, N., 1994. Analysis of Structural Vibration Considering the Dynamic Transmitting Behaviour of Soil. Technical Report. Ruhr University, Bochum, Germany.

Chouw, N., 1995. Effect of the earthquake on 17th of January 1995 on Kobe. In: Proc. DACH Meeting of the German, Austrian, and Swiss Society for Earthquake Engineering and Structural Dynamics, pp. 135–169.

Chouw, N., 2002. Influence of soil-structure interaction on pounding response of adjacent buildings due to near-source earthquakes. JSCE J. Appl. Mech. 5, 545–553.

Chouw, N., 2008. Unequal soil-structure interaction effect on seismic response of structures. In: Proc. 18th New Zealand Geotechnical Society, Geotechnical Symp. Soil-Structure

Interaction—From Rules of Thumb to Reality, September 4–5. University of Auckland, New Zealand, pp. 214–219.

Chouw, N., 2013. Advanced Structural Dynamics, Civil710 Course Note. University of Auckland, New Zealand.

Chouw, N., 2017. Low-damage design philosophy for future earthquake-resistant structures. In: Proceedings of the 2017 PVP Conference, July 16–20, Waikoloa, Hawaii, USA.

Chouw, N., 2020. Structural Dynamics, Civil314 Course Note. University of Auckland, New Zealand.

Chouw, N., Hao, H., 2005. Study of SSI and non-uniform ground motion effect on pounding between bridge girders. Soil Dyn. Earthq. Eng. 25 (7), 717–728.

Chouw, N., Hao, H., 2006. Comments on bridge girder seating length under current design regulations. JSCE J. Appl. Mech. 9, 691–699.

Chouw, N., Hao, H., 2008. Significance of SSI and non-uniform near-fault ground motions in bridge response. II: Effect on response with modular expansion joint. Eng. Struct. 30, 154–162.

Chouw, N., Hao, H., 2012. Pounding damage to buildings and bridges in the 22 February 2011 Christchurch earthquake. Intl. J. Protect. Struct. 3 (2), 123–139.

Chouw, N., Rincon, E.W., 2011. Numerical simulation of adjacent bridge structures with nonlinear SSI. In: 3rd Intl. Conf. Computational Methods in Structural Dynamics and Earthquake Engineering, Corfu, May 26–28, Greece.

Clough, R.W., Penzien, J., 1993. Dynamics of Structures. McGraw-Hill, Singapore.

Japan Road Association (JRA), 2004. Specification for highway bridges -Part V: Seismic design, fifth ed. Tokyo (in Japanese).

Japan Society of Civil Engineers (JSCE), 2000. Earthquake Resistant Design Codes in Japan. JSCE, Maruzen, Tokyo.

Khatiwada, S., Chouw, N., Butterworth, J.W., 2014. A generic structural pounding model using numerically exact displacement proportional damping. Eng. Struct. 62, 33–41.

Kun, C., Chouw, N., 2019a. Influence of ground motion characteristics on seismic response of skewed bridges. Struct. Infrastruct. Eng. 15 (6), 798–811.

Kun, C., Chouw, N., 2019b. Estimation of response of skewed bridges considering pounding and supporting soil. Eng. Struct. 184, 469–479.

Kun, C., Jiang, L., Chouw, N., 2017. Influence of pounding and skew angle on seismic response of bridges. Eng. Struct. 148, 890–906.

Kun, C., Yang, Z., Chouw, N., 2018a. Seismic response of skewed bridges including pounding effects. Earthq. Struct. 14 (5), 467–476.

Kun, C., Yang, Z., Chouw, N., 2018b. Seismic performance of skewed bridges with simultaneous effects of pounding and supporting soil. Eng. Struct. 174 (15), 26–38.

Li, B., 2013. Effects of Spatially Varying Ground Motions on Bridge Response. Ph.D. thesis, University of Auckland, Auckland, New Zealand.

Li, B., Bi, K., Chouw, N., Butterworth, J.W., Hao, H., 2013. Effect of abutment excitation on bridge pounding. Eng. Struct. 54, 57–68.

Lim, E., Chouw, N., 2015. Review of approaches for analysing secondary structures in earthquakes and evaluation of floor response spectrum approach. Intl. J. Protect. Struct. 6 (2), 237–261.

Lim, E., Chouw, N., 2018. Influence of simultaneous multi-axial ground motions and a compliant base on the response of a non-structural component with multiple supports. Eng. Struct. 174, 618–628.

Lim, E., Jiang, L., Chouw, N., 2017. Dynamic response of a non-structural component with three supports in multi-directional earthquakes. Eng. Struct. 150, 143–152.

Martin, H., 1966. Introduction to Matrix Methods of Structural Analysis. McGraw-Hill, New York.

New Zealand Standards, 2004. NZS1170.5 Structural Design Actions, Part 5: Earthquake Actions. Wellington, ISBN 1-86975-018-7.

New Zealand Transport Agency (NZTA), 2004. Bridge Manual, Section 5: Earthquake-Resistant Design. September.

Qin, X., Chouw, N., 2017. Shake table study on the effect of mainshock-aftershock sequences on structures with SFSI. Shock. Vib., 9850915.

Sieffert, J.G., Cevaer, F., 1992. Handbook of Impedance Functions. Quest Editions Presses Academiques, Nantes.

Risk and reliability in bridges

7

Baidurya Bhattacharya
Indian Institute of Technology Kharagpur, Kharagpur, India

1. Overview

In probability-based design, we explicitly account for uncertainties and variabilities in (i) the inputs (loads, etc.), (ii) the properties (including strength), and (iii) the model of the system. We then design and assess the system so that it satisfies its safety and performance objectives with acceptable probabilities for its intended function, under expected service conditions and throughout the projected service life. When a design code is used instead of an explicit probability-based approach, such uncertainties are often accounted for indirectly in the form of partial safety factors, load combination schemes, and other codal provisions.

Consider the entire life of a bridge from its conception, which begins at the determination of functional requirements. Suppose the bridge is part of the national highway network at some location, over a major river, and must be able to carry four lanes of unrestricted traffic, in addition to a shoulder on each side. The waterway below is used for cargo and passenger transport. Thus, some clear span and height must be provided. The design life of the bridge has to be specified.

After functional requirements are determined, a concept design follows. Economic considerations impact this stage; at some point in the design cycle, the owner has to justify if the bridge will be worth the expense. For the given geometry, location, design life, and expected loading, the most economical form (box girder, truss, cable-stayed, etc.) and material (steel, prestressed, or reinforced concrete) are selected. For signature bridges, aesthetics are considered in the selection of form and materials.

Next, material properties are determined. A finite element model of the structure is developed, and loads have to be obtained. Is the bridge going to be in earthquake-prone area? Will there be tidal waves, scouring, or barge impact? What kind of wind forces are typical of the location? What are the uncertainties in the loads, and what load magnitudes shall be designed for? How do are loads to be combined? Is data collected, and, if so, how large should the data set be?

The cycle of design and analysis continues until a final solution is obtained. Costs must be contained, functional requirements must be met, and safety must be ensured. How are failure criteria to be defined—both for collapse and functionality—and how safe is safe enough? Is an explicit dynamic analysis of the bridge structure necessary? Is the finite element model of the structure accurate enough? Does it account for nonlinearities near failure, and does it represent realistic boundary conditions? What are the uncertainties in the model?

Innovative Bridge Design Handbook. https://doi.org/10.1016/B978-0-12-823550-8.00010-X

Construction begins, and quality must be maintained. Once construction is complete, the bridge is put into service. Periodic inspection and maintenance must be performed to determine if the bridge is deteriorating and if traffic is becoming heavier. It must be determined how often the bridge should be inspected and how extensively it should be repaired. During repairs, can the bridge be kept closed to traffic—for a month, for a day, for 6 h? Should the bridge be made stronger or more durable at the construction stage so that maintenance actions can be minimized?

Finally, the bridge may become unfunctional, too costly to maintain, and/or too risky to operate. It is then demolished, and a new bridge takes its place. The cycle begins again.

In this chapter, we isolate the key concepts from the preceding discussion and treat them systematically.

2. Uncertainty in bridge modeling and assessment

2.1 Probabilistic modeling of uncertain phenomena

In the context of probability theory, the "sample space" is the universal set of all possible events. Probabilities are assigned to an appropriately defined collection of subsets or "events" (called sigma-algebras) of the sample space. A (random) experiment implies the occurrence of an event. When the outcome of an experiment can be given in numerical terms, then we have an RV in hand. Any possible outcome of an RV is called a "realization." An RV can be either discrete or continuous. If a quantity varies randomly with time, we model it as a stochastic process. A stochastic process can be viewed as a family of RVs indexed by time. If a quantity varies randomly in space, we model it as a random field, which is the generalization of a stochastic process in two or more dimensions. It is assumed that the reader is familiar with the basic concepts of probability theory and RVs and processes, and may refer to standard texts (Ang and Tang, 1975; Papoulis and Pillai, 2002; Hines et al., 2003) for a refresher.

2.1.1 Common random variables encountered in structural reliability

An RV is governed by its probability laws. The probability law of an RV can be described by any of the following equivalent ways: a cumulative distribution function (CDF), a probability density function (PDF) for continuous RVs, a probability mass function (PMF) for discrete RVs, a characteristic function (CF), a moment generating function (MGF), etc.

Although any non-decreasing function bounded by 0 and 1 can be a candidate cumulative distribution function for a random variable X, only a few models (e.g., normal, Poisson, geometric, Weibull, etc.) are commonly used by the scientific and engineering communities in their work. This is because the underlying process appears repeatedly in a wide class of problems. Deriving models solely from data, without basing it on the underlying physics, may be very expensive and often inconclusive.

The uniform distribution arises naturally when there is no reason to favor one outcome over another from the sample space, making all sample points equally likely. This distribution also corresponds to the state of maximum Shannon entropy.

The Bernoulli trial refers to a binary outcome $X = 0$ (often called failure), which occurs with probability q, and $X = 1$ (often called success), which occurs with probability p so that $p + q = 1$. A sequence of independent and identical Bernoulli trials can help model large classes of phenomena of engineering interest. The number of trials to the first success gives rise to the geometric distribution. Generalizing the number of trials to the rth success gives rise to the Pascal (or negative binomial) distribution. The number of successes in a fixed number of Bernoulli trials, on the other hand, follows the binomial distribution.

The concept of mean (or average) return period (also called mean recurrence interval) arises from a sequence of independent and identically distributed (IID) Bernoulli trials. Let success in the Bernoulli trial refer to the occurrence of an event A (so that failure means nonoccurrence of A)—typically a relatively rare phenomenon, like annual rainfall exceeding 50 in., annual maximum wave height exceeding 20 m, annual maximum wind speed exceeding 150 km/h, earthquake magnitude exceeding 7 on the Richter scale, etc. The time (or, more literally, the number of trials), T, between successive occurrences of the event A in a sequence of Bernoulli trials is a random variable. T follows the geometric distribution due to the IID nature of the trials; hence, the mean of T is $1/p_A$ time units where p_A is the probability of occurrence of A in each trial (or time unit). This mean of T is the so-called mean recurrence interval of the event A. In the continuous time scenario, the time between occurrences is exponentially distributed, and the mean occurrence time is the reciprocal of the occurrence rate of the underlying Poisson process. For example, a "10% in 50 year" magnitude of earthquake corresponds to a return period of about 475 years and not 500 years (this is left as an exercise here).

The Gaussian (or normal) distribution appears as the limiting form for the sum of a number of random variables, subject to certain conditions, (Resnick, 1999) and is the most widely used model for continuous random variables. In structural engineering, dead loads are almost exclusively modeled as Gaussian. In fact, in the absence of evidence to the contrary, the Gaussian distribution is the default choice. The exponentiated Gaussian gives the lognormal random variable and is popular in the literature of structural reliability, especially for nonnegative quantities. Extreme value theory has given rise to three limiting forms (Galambos, 1987)—Gumbel, Frechet, and Weibull—and is often adopted for the distribution of the maximum (like wind, wave, traffic, etc.) or the minimum (like strength) of a sequence.

The typical loads considered in bridge analysis and design are dead loads, live loads (mostly traffic loads (Wen, 1990; Bhattacharya, 2008; Guzda et al., 2007; Nowak, 1993; Enright et al., 2013; Anitori et al., 2017)), wind loads, and earthquake loads. Dead loads represent the gravity loads (i.e., self-weight) of various components of the bridge, from prefabricated elements and cast-in-situ members to wearing surfaces and fixtures. Depending on the location of the bridge, snow load, wave load, impact load, etc., may also be considered. NBS 577 (Ellingwood et al., 1980) lists the mean bias and coefficient of variation and distribution for common material resistance and load random variables, and these are widely adopted in the structural reliability literature.

Uncertainties in material properties—and, to a lesser extent, those in geometries—lead to uncertainties in strength. Uncertainties in boundary condition—e.g., the extent of joint fixity—are typically listed under modeling uncertainties.

2.1.2 Common stochastic processes encountered in structural reliability

Various types of stochastic processes appear in the analysis of structural reliability. They mostly represent load processes. In some cases, however, strength degradation also need to be modeled as stochastic processes (e.g., fatigue crack growth). Broadly, load processes are either sustained or intermittent. Sustained load processes can be further subdivided into (approximately) time-invariant loads, such as dead loads, and fluctuating loads, such as occupant live loads. Sustained loads can be modeled as random variables. Intermittent loads, such as seismic loads, are present during a very short duration compared to the life of the structure. In the limit, intermittent loads can be modeled as pulses with random magnitudes occurring at random instants of time. Wind loads and traffic loads can have both fluctuating components (which are low-level continuous) and intermittent pulses (such as storms and heavy trucks). In many cases, it is only the lifetime maximum of the fluctuating or intermittent load processes rather than detailed temporal characteristics that are of importance in structural reliability analysis. In such cases, the said maximum is modeled as a random variable. The corresponding design quantity is a characteristic value of the distribution of the random variable, which may be defined as n-year return period value or some other quantile.

Pulse processes, occurring randomly in time with random pulse magnitudes, are particularly suited for modeling the occurrence of heavy trucks, high winds, high waves, and earthquakes on bridges—as long as the within-event variations are not important. If the within-event variations need to be considered—e.g., to determine the response history (of the order of a minute) of a bridge due to a strong motion earthquake—then the occurrence can still be modeled as a pulse, but the frequency content, envelope function, etc., of the load time history will also be needed. The Poisson process is the most common model of pulse processes.

The stationary Gaussian process is the most common model for continuous stochastic processes. It can be fully defined in terms of the mean and the covariance functions. Non-stationary and/or non-Gaussian processes may be created through various transformations and filtering of the stationary Gaussian process. (Shinozuka and Sato, 1967; Ghanem and Spanos, 2012; Vanmarcke, 1983)

2.2 Types of uncertainty

Uncertainties in engineering problems occur as a result of natural variability, incomplete information, or imperfect knowledge. Uncertainties are typically classified as either type I or type II uncertainties. Type I uncertainties (also known as natural, inherent, or aleatory uncertainties) cannot be reduced, as they are intrinsically associated with the quantity. Type II uncertainties (also known as modeling or epistemic uncertainties), on the other hand, can be reduced with increased information or sophistication. As early as 1947, Freudenthal (Freudenthal, 1947) was able to state the essential difference between type II and type I uncertainties: "With increasing perfection of design methods the element of 'ignorance' can be largely eliminated, but the element of 'uncertainty' is caused by circumstances that can be changed, to a certain extent, but never be removed." A more modern classification of uncertainty is statistical vs. parameter vs. modeling; this classification is preferred because it gives a greater resolution to the analyst.

Regardless of classification, the mathematical representation of uncertainty must follow the laws of probability and is generally described by random variables. Apart from the type of distribution, two dimensionless constants are popularly used to describe a random variable: the mean bias, B, which is the ratio of the mean to the nominal (or predicted or handbook) value,

$$B = \frac{\mu}{X_n}, \tag{1}$$

(the *median bias* can also be defined similarly) and the coefficient of variation (COV), which is the normalized standard deviation,

$$V = \frac{\sigma}{\mu}. \tag{2}$$

2.2.1 Statistical uncertainty

Suppose the mathematical model of a phenomenon requires the use of a random variable X with the distribution function F_X. Rather than probing further where the uncertainty in X is coming from; X will be treated as random, and $F_X$will be treated as a black box. Either an empirical form can be used for F_X, or a parametric form (e.g., normal, Weibull, etc.) can be used, and its parameters can be obtained from data. Most random variables used in structural reliability problems represent this kind of uncertainty.

2.2.2 Parameter uncertainty

Suppose it is known from analytical, subjective, or experimental considerations that a random variable X follows the distribution g that is governed by a set of parameters θ. However, there may be uncertainties about the exact value of θ . In that case, for any fixed value of θ, g is the *conditional* distribution of X. If the parameters are now expressed as a random variable, Θ, then

$$\begin{gathered} P[X \le x | \underline{\Theta} = \underline{\theta}] = g(x; \underline{\theta}) \\ F_X(x) = P[X \le x] = \int_{\text{all } \underline{\theta}} g(x; \underline{\theta}) f_{\underline{\Theta}}(\underline{\theta}) d\underline{\theta} \end{gathered} \tag{3}$$

to obtain the unconditional distribution of X.

According to Zio and Apostolakis, (Zio and Apostolakis, 1996) some model uncertainties can, in fact, be used as parameter uncertainties—e.g., when using a Monte Carlo simulation, a flag can be used to switch some models on or off, or a "switch case" parameter that will select one model at a time in repeated simulations can be used. It also may not always be possible to separate model uncertainties for parameter uncertainties—for example, in cases where there are parameters whose values need to be estimated from the available data, but how the estimates themselves are computed may depend on the model chosen in the first place.

Regardless of the classification, probability theory allows one to treat all uncertainties as random variables. For some, though, conditional distributions may be necessary.

2.2.3 Modeling uncertainty

Analysis tools for predicting global response, stress analysis, etc., are commonly deterministic in nature. The model predictions deviate from the actual events due to three broad classes of reasons: mathematical idealizations, numerical errors, and ignorance. Mathematical idealization includes simplifications such as neglect of nonlinearities. Ignorance effectively leads one to neglect a group of variables. The difference between idealization and ignorance is that in the former, one knows what is being left out, whereas in the latter, one does not. Gallegos and Bonano (Gallegos and Bonano, 1993) named these uncertainties (i) mathematical model uncertainty, (ii) conceptual uncertainty, and (iii) computer code uncertainty.

All three uncertainties introduce new random variables into the reliability problem and, hence, into the limit state. Ditlevsen (Ditlevsen, 1982) incorporated modeling uncertainty in the limit state equation by transforming the vector of basic variables into another random vector of the same dimension, i.e., by substituting the basic variables $\underline{X}$ with $\underline{V}(\underline{X})$.

In the aggregate sense, the model uncertainty, M, in predicting some property or response may be expressed as

$$M = \frac{\text{actual}}{\text{predicted}\,(\text{or} \quad \text{nominal})} \quad (\text{predicted} \neq 0). \tag{4}$$

M is a random variable because the exact deviation is unknown. Of course, in many situations, actual results—e.g., failure pressure of an actual nuclear power plant containment under pressurization due to an actual core meltdown—may just not be available. For such phenomena, we can have only competing models and, in some cases, scaled model test results under idealized conditions.

Some modeling uncertainty distributions cannot be estimated from data. They can only be estimated from *subjective* probabilities given by a group of experts. (Lind and Nowak, 1988; Cooke and Goossens, 2008; Keeney and Dv, 1991)

Examples of treatment of modeling uncertainty

(i) In one of the earliest examples of modeling uncertainty in structural reliability analysis, (Ellingwood et al., 1980) the random yield strength, Y, of a steel member, was considered to be the product of three random variables representing intrinsic and extrinsic uncertainties and the nominal value, Y_n:

$$Y = B_P B_M B_F Y_n, \tag{5}$$

where B_P accounts for professional or modeling error, B_M is the material variability, and B_F is the fabrication error. If these three factors are considered to be mutually statistically independent and lognormally distributed, then the yield strength Y also is lognormal.

(ii) Nikolaidis and Kaplan (Nikolaidis and Kaplan, 1991) performed a survey of uncertainties in FEA in marine and other industries (automobile, aerospace, etc). Their conclusions and findings were as follows: Depending on the loading case, the mean bias in FEA of containership ranged from 0.9 to 1.4, and the COV ranged from 0.1 to 0.4. For aerospace structures, the stress modeling uncertainty is uniformly distributed with mean 1.0 and COV 0.12. In the automobile industry, FEA underestimates flexibility of a car body. The error in predicting deflection due to bending or torsion ranges between 10% and 20%. For offshore structures, the uncertainty in modeling members forces has a mean bias between 0.8 and 1.1 with COV between 0.2 and 0.4.

(iii) In fatigue strength computation, (Fricke and Muller-Schmerl, 1998) the permissible stress range, $\Delta\sigma_P$, in a component may be determined by the use of several adjustment factors on the S-N curve-based reference stress range, $\Delta\sigma_R$, which corresponds to $N = 2 \times 10^6$

$$\Delta\sigma_{\max} \leq \Delta\sigma_P = \Delta\sigma_R f_n f_m f_R f_t f_s f_w f_c \tag{6}$$

where f_n takes into account the effect of the stress spectrum (compared to the constant amplitude assumption of the S-N curve); f_m accounts for material type; f_R accounts for the mean-stress effect; f_t accounts for the plate thickness effect; f_s accounts for imperfections; f_w accounts for weld shape improvements; and f_c accounts for corrosive environments. Of these, the factors f_n, f_R, and f_t may be considered as representing modeling uncertainty.

(iv) Similar approaches have been taken to derive strain-based limit states for nuclear power plant containments. Cherry and Smith (Cherry and Smith, 2001) adopted the Hancock model in their fragility analysis of steel containments. They defined the equivalent plastic strain at failure, $\varepsilon_{fail,}$ in terms of the uniaxial fracture ductility, $\varepsilon_{f,uni}$, and four correction factors (f_1, …, f_4) as follows:

$$\varepsilon_{fail} = \varepsilon_{f,uni} \times f_1 \times f_2 \times f_3 \times f_4, \tag{7}$$

where $f_1 = 1.6 \exp.(-3\sigma_m/2\sigma_{\text{von}})$ accounts for multiaxial stress state, f_2 accounts for model sophistication (i.e., modeling error), f_3 accounts for material variability, and f_4 accounts for variability in corrosion degradation (reduction of ductility). This failure criteria can be applied locally in conjunction with a finite element analysis.

(v) In seismic design, the target displacement, δ_t, of the control node on the rooftop of a building may be calculated as (Whittaker et al., 1998)

$$\delta_t = C_0 C_1 C_2 C_3 S_a \frac{T_e^2}{4\pi^2}. \tag{8}$$

C_0 is the modification factor to relate spectral displacement and expected maximum inelastic displacement at the roof; C_1 is the modification factor to relate expected maximum inelastic displacements to displacements calculated for linear elastic response; C_2 is the modification factor to represent the effects of stiffness degradation, strength deterioration, and pinching on the maximum displacement response; C_3 is the modification factor to represent increased displacements due to dynamic second order effects; S_a is the response spectrum acceleration at the effective fundamental period and damping ratio of the building; T_e is the effective fundamental period of the building in the direction under consideration calculated using the secant stiffness at a base shear force equal to 60% of the yield force. The factors $C_{1,}$ C_2, and C_3 serve to modify the relation between mean elastic and mean inelastic displacements where the inelastic displacements correspond to those of a bilinear elastic plastic system. The factors C_0 through C_3 represent modeling error.

(iv) The environmental load effect due to sea load, wind, ice, and earthquakes is (Moan, 1997)

$$S = K C_1 C_2 \ldots E^{\alpha}, \tag{9}$$

where K is a constant, C_1 represents the transfer from environmental condition to load, C_2 represents the transfer from load to load effect, E is a characteristic environmental parameter, and α is a constant. E usually follows an extreme value distribution—e.g., Gumbel. K, C_1,C_2, … are generally random and may be assumed to be lognormal. Each of the preceding transfer functions may be decomposed into a nominal value and a modeling error variable.

(vi) In seismic code development, Cornell et al. (Cornell et al., 2002) separated uncertainty into four parts—β_{DU} (*uncertainty in estimating* the median demand), β_{DR} (the *record to record* variability in demand),β_{CU} (the *uncertainty in estimating* the capacity), andβ_{CR} (the *randomness* in capacity—so that the total uncertainty (in the lognormal standard deviation sense) in demand and capacity are, respectively,

$$\begin{aligned} \beta_D^2 &= \beta_{DU}^2 + \beta_{DR}^2 \\ \beta_C^2 &= \beta_{CU}^2 + \beta_{CR}^2. \end{aligned} \tag{10}$$

β_{DU} andβ_{CU} correspond to modeling uncertainty type, whereas β_{DR} and β_{CR} correspond to the statistical uncertainty type. In a related work, Yun et al. (Yun et al., 2002) took into account β_{NTH}, the uncertainty in nonlinear time history analysis, and assumed it to be 0.15, 0.20, and 0.25 for three-, nine-, and 20-story buildings, respectively.

(vi) Stewart et al. (Stewart et al., 2019) performed a series of 60 air blasts using plastic explosives. They found the model error describing peak incident pressure had a COV of 15% while that for impulse duration was 21%. The mean for both was close to unity, and the lognormal distribution was the best fit for either variable. The model in this case was the polynomial fit developed by the US Army (Kingery and Bulmash, 1984).

3. Reliability of bridges

For a structure with several critical locations subject to time-dependent loads and possessing time- and space-dependent material properties, the reliability function estimates the probability that the capacity, C, exceeds the demand, Q, at all locations at all times that the structure is in service:

$$\mathrm{Rel}(t) = 1 - P_f(t) = P\left[C^j(\underline{x}, \tau) \geq Q^j(\underline{x}, \tau), \forall \tau \in (0, t), \forall \underline{x} \in \Omega, j \in J\right], \tag{11}$$

where Ω is the set of critical locations of the structure and t is the total time horizon. Both capacity and demand of the structure are generally functions of space and time and constitute a multidimensional stochastic process. Capacity can change randomly due to aging or other time-dependent effects, and it can recover due to maintenance operations. Capacity can also be a time-invariant constant, such as a deflection limit for decks. Further, there may be several modes of failure j (e.g., shear, flexural, deflection, lateral torsional buckling, etc.), as indicated by the superscript to C and Q, associated with any given location/member. The demand represents the effect of all loads acting simultaneously on the structure (e.g., dead, live, wind, etc.) and may be expressed either in load space or in load effect space:

$$Q^j(\underline{x}, \tau) = DL^j(\underline{x}, \tau) + LL^j(\underline{x}, \tau) + WL^j(\underline{x}, \tau) + \ldots \tag{12}$$

The + sign indicates combination, not necessarily superposition, and thus may involve nonlinear effects.

The structural reliability problem in its most general formulation is thus infinite dimensional both in time and space—which, of course, makes it computationally intractable; hence, engineering judgment and various simplifications and restrictions are adopted. Several levels of simplification can be implemented, as will be described in Section 5.1. In general terms, Eq. (11) can be made tractable by identifying the key sets of (i) failure modes, (ii) load combinations, (iii) critical locations, and (iv) temporal statistics of the relevant stochastic processes, so that reliability computations may be undertaken efficiently and checked against acceptance criteria.

Figure 7.1 shows the important steps involved in structural reliability analysis. The concept of limit states, various solution techniques for the reliability problem, and the introduction of explicit time-dependence into the reliability problem are discussed next.

3.1 Limit states

One of the first steps in a structural reliability analysis is to identify the failure modes (or, more generally, nonperformance modes) of the structure. A limit state is the boundary between the *safe* (or acceptable) and *failed* (or unacceptable) domains of

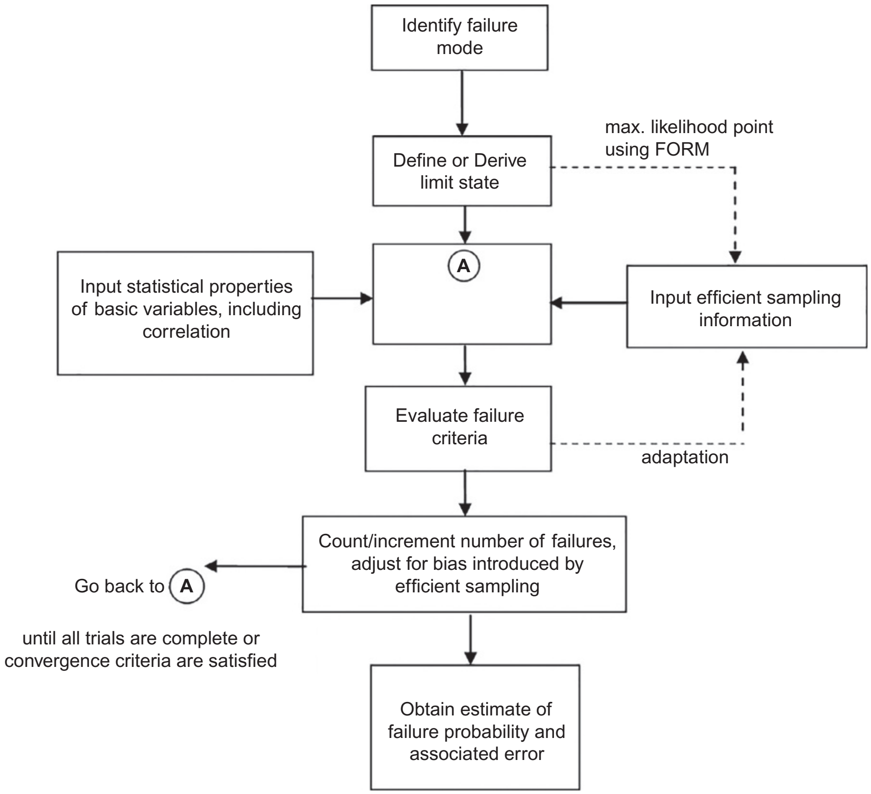

Figure 7.1 General scheme for reliability analysis.

structural performance in the failure mode under consideration. It is represented with the help of the limit state function (also called the performance function), $g(\underline{X})$, in the following manner:

$$\begin{aligned} &g(\underline{X}) < 0, \text{unacceptable or failed domain} \\ &g(\underline{X}) \geq 0, \text{acceptable or safe domain} \\ &\text{so that}, g(\underline{X}) = 0 \text{ is the limit state equation} \end{aligned} \tag{13}$$

The boundary between the two regions, $g(\underline{X}) = 0$, is called the limit state equation. $\underline{X}$ is the set of basic variables, which consists of the complete set of quantities used to describe structural performance in the failure mode under consideration. They may include material properties, loads or load effects, environmental parameters, geometric quantities, modeling uncertainties, etc. Basic variables in a limit state are usually modeled as random variables; however, those with negligible uncertainties may be treated as deterministic.

Limit states may be defined for elements as well as the system (Figure 7.2). The difference between "element" and "system" in reliability analysis has less to do with

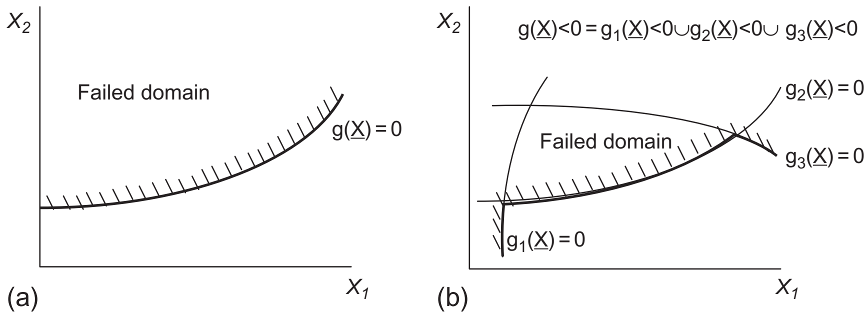

Figure 7.2 Limit state functions (a) for an element and (b) for a series system. The failure domain is indicated by the hashing.

the scale and complexity of the participating component/assembly/substructure and more to do with the form of the limit state function and whether one needs to undertake Boolean combinations, which are discussed next.

3.1.1 Structural limit states and load combinations used in bridges

There are, broadly, two kinds of failure for a structure: *irreversible* and *reversible*. Irreversible failure can be divided into two types:

(i) Overload—e.g., ultimate failure that happens under a single high-loading event. Design codes refer to these as strength/extreme/accidental limit states. This type of failure is irreversible in nature. The structure needs to be replaced/repaired after such failure. Consequences of such failure is serious—even catastrophic.

(ii) Cumulative damage—e.g., fatigue cracking. It, too, is irreversible in nature, and the structure needs to be replaced/repaired after such failure. The consequence of such failure can be serious. However, this damage proceeds gradually and can be detected through inspection before failure occurs.

Reversible structural damage is temporary in nature and typically has to do with functional requirements of the bridge (e.g., deflection, vibration, etc.). There is no lasting damage, but the structure is not available for the duration of this kind of failure. The consequence of such failure is usually minor. Most serviceability limit states listed in design codes fall under this category.

Strength and serviceability limit states can be formulated both as element- and system-level limit states depending on the objective and available information. For each of these limit states, several load combinations need to be evaluated (Eq. 12). For example, the AASHTO bridge LRFD code (AASHTO, 2012) specifies five *strength*-type load combinations (involving dead loads and various live loads, with or without wind loads), two extreme event load combinations (involving dead loads and reduced live loads with earthquake or ice/collision/flood, etc., loads), four service load combinations (involving dead loads, various live loads, wind loads, etc.), and two fatigue load combinations (involving only live loads).

Eq. (11) therefore simplifies to checking the following groups of limit states one at a time:

$$\begin{aligned}&\text{overload}: \quad C^j(\underline{x}_i) \geq Q^j(\underline{x}_i; \mathrm{LC}_k(t))\\&\vdots\\&\text{cumulative}: \ C^{j'}(\underline{x}_{i'}) \geq Q^{j'}(\underline{x}_{i'}, \mathrm{LC}_{k'}(t))\,.\\&\vdots\\&\text{reversible}: \ C^{j''}(\underline{x}_{i''}) \geq Q^{j''}(\underline{x}_{i''}; \mathrm{LC}_{k''})\end{aligned} \tag{14}$$

3.1.2 Element-level limit states

If it is possible to define a single differentiable performance function $g(\underline{X})$ of the basic variables for a given failure mode, then we have what is known as an element reliability problem at hand. An element reliability problem is most naturally realized in the case of a *single* critical cross section of one structural component in a *single* failure mode (such as flexural failure); in such cases, the function g is commonly derived from analytical/mechanistic modeling. It can be the same function used in a corresponding deterministic analysis, with some or all of the variables now treated as random variables. However, it is entirely possible that the performance function corresponding to the roof displacement of a tall building under wind loading can be derived in the form of a *single* response surface given in terms of a relevant set of basic variables (obtained from a set of finite element analyses of the structure); in this case, the reliability problem of excessive roof displacement for the building will also qualify as an element reliability problem.

An element-level limit state naturally arises from Eq. (11) if it is restricted to only one critical location with only one failure mode, and demand and capacity variables that are time invariant:

$$\mathrm{Rel} = P[C_0 - Q_0 > 0]. \tag{15}$$

This is a two-variable linear element-level reliability problem. The basic variables are $\underline{X} = [C_0, Q_0]^T$, and the limit state equation is

$$g(\underline{X}) = C_0 - Q_0. \tag{16}$$

Eq. (15) can easily be computed with the help of the joint PDF of C_0 and Q_0:

$$\begin{aligned}\mathrm{Rel} &= \int_{-\infty}^{\infty}\int_{c=q}^{\infty} f_{C_0,Q_0}(c,q)\,dc\,dq\\ &\left.\begin{aligned}&= \int_{-\infty}^{\infty} [1 - F_{C_0}(q)] f_{Q_0}(q)\,dq\\ &= \int_{-\infty}^{\infty} F_{Q_0}(c) f_{C_0}(c)\,dc\end{aligned}\right\}\text{if } \mathrm{C}_0 \text{ is indepdent of } Q_0\end{aligned}\,. \tag{17}$$

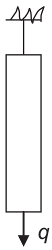

Figure 7.3 A cable in tension.

Typical modes of failures in bridge structures that give rise to element reliability problem include yielding, crushing, buckling, fatigue failure, etc. Element reliability problems are easy are to formulate but inexpensive to compute.

Example 7.1. A small structural design problem.

Consider a cable (with an 8-in. diameter) in a suspension bridge made of A36 steel with random yield strength Y (time invariant) (Figure 7.3). Let Y be Weibull distributed with COV 15%. It is a one RV problem. No modeling uncertainty is considered. The axial load $q = 1600$ kip and the cross-sectional area $a = 50.3$ in^2 are deterministic. Let cable failure be defined as yield of the cross section. Find the failure probability of the cable. The target failure probability is 0.001. Redesign if necessary.

The given Y is Weibull distributed with COV 15%. The mean yield strength of A36 steel is 38 ksi. The shape and location parameters of Y are, therefore,$V_Y = 15\,\% \Rightarrow k = 8$ and $u = \frac{\mu}{\Gamma(1+1/8)} = \frac{38}{.94} = 40.4\,\text{ksi}$. The failure event is

$$\{\text{Failure}\} = \left\{\frac{q}{a} > Y\right\}. \tag{18}$$

The probability of failure is derived by evaluating the Weibull CDF:

$$\begin{aligned} P_f &= P[\text{failure}] = P\left[Y < \frac{1600\,\text{kip}}{50.3\,\text{in}^2}\right] \\ &= P[Y < 31.8] = 1 - e^{-\left(\frac{31.8}{40.4}\right)^8} = 0.14 \end{aligned}. \tag{19}$$

Since it is required that $P[\text{failure}] < .001$, the cable is inadequate. Reliability can be increased in four ways for this problem: increasing the area, reducing the load, increasing the mean strength, and decreasing the variability of strength. Of these, the second is not possible without restricting traffic, and the third and fourth would require a different material and possibly be very expensive. Thus, we decide to first try to increase the cross-sectional area.

The revised cross-sectional area can be found by finding the inverse of the CDF at the target P_f:

$$\therefore P\left[Y < \frac{q}{a_{new}}\right] = .001 \Rightarrow 1 - e^{-\left(\frac{q}{a_{new}40.4}\right)^8} = .001. \tag{20}$$

which yields

$$a_{new} = \frac{1600}{40.4 \times .4217} = 93.9\,\text{in}^2. \tag{21}$$

Suppose the resultant diameter, about 11 in., proves to be impractical from the point of view of anchoring requirements. The next option is to try a different grade of steel without changing the diameter. Assume the distribution of Y_{new} remains Weibull and its COV remains 15%. The approach now is to select a new mean. The target probability of failure remains 0.001:

$$P\left[Y_{new} < \frac{q}{a}\right] = .001, \tag{22}$$

which yields

$$\begin{aligned} &\exp\left[-\left(\frac{31.8}{u_{new}}\right)^8\right] = .999 \\ &\Rightarrow u_{new} = 75.4 \\ &\Rightarrow \mu_{new} = 75.4\Gamma(1+1/8) = 70.9\,\text{ksi} \end{aligned} . \tag{23}$$

The new mean strength is acceptable, provided this new grade of steel has sufficient ductility, corrosion resistance, and other desirable properties. Otherwise, a totally new design may need to be adopted.

3.1.3 System-level limit states

As should be clear by now, the difference between an *element* and a *system* in a reliability analysis context is somewhat arbitrary and largely dependent on the available information and scale of interest. Indeed, a problem of tensile failure of a prismatic rod made of a brittle material that can be treated as a simple element reliability problem from a continuum viewpoint may amount to an intractable system reliability problem from microstructural considerations. For practical purposes, it is mostly the availability of a single, differentiable, and closed-form performance function that separates an element reliability problem from a system reliability problem.

It would be highly desirable, then, to somehow cast the performance of a structural *system* in terms on a single-limit state (perhaps using approximate numerical techniques such as a response function fit) and thereby take advantage of the speed, elegance, and accuracy of element reliability solution techniques; such a formulation unfortunately remains elusive more often than not. It is needless to add that structural system failure events are thankfully so rare (and, in any case, structural systems can hardly be deemed to constitute a nominally identical sample) that the other alternative—a frequentist interpretation of structural system reliability—is not feasible. The usual systems reliability formulation therefore is presented in terms of Boolean combinations of element limit states depending on the logical construct of the system in terms of its components and the definition of *failure* at the systems level (Bhattacharya et al., 2009).

If the system failure event can be cast as an intersection of m element failure events (i.e., a classical parallel system), then the system failure probability is

$$\text{Parellel system}: \; P_{f,sys} = P\left[\bigcap_{i=1}^{m} g_i \leq 0\right], \tag{24}$$

where g_i is the element limit state surface in the basic variable space ($\underline{X}$). For a series system–type configuration, the system failure probability is

$$\text{Series system}: \; P_{f,sys} = P\left[\bigcup_{i=1}^{m} g_i \leq 0\right]. \tag{25}$$

For systems more general than the simple series and parallel organizations, the greatest challenge is to identify the minimal cut sets (at least the dominant ones), particularly in light of the circumstances peculiar to the previously mentioned structural systems. A set of elements of a system is a *cut set* if the failure of all members of the cut set causes system failure. (Birolini, 1999) A *minimal cut set* is one in which if any element is removed from it, the subset no longer remains a cut set.

If the cut sets C_i, $i = 1, \ldots, n_c$ can be identified for the system, the system failure probability becomes

$$\text{Series} - \text{parallel system}: \quad P_{f,sys} = P\left[\bigcup_{i=1}^{n_c} C_i\right] = P\left[\bigcup_{i=1}^{n_c}\left\{\bigcap_{j=1}^{n_i} g_{ij} \leq 0\right\}\right], \tag{26}$$

where $g_{ij}$is the jth limit state in cut set I, and there are n_i elements in the ith cut set. The exact solution of Eq. (26) may be impossible to obtain; thus, bounds on system reliability, based on marginal events (Cornell, 1967), pairs of joint events (Ditlevsen, 1979), or triplets of joint events (Hohenbichler and Rackwitz, 1983) are available.

The n_i elements in the i^{t}h minimal cut set can be ordered in $n_i!$ ways. All of these orderings are unique failure sequences, and they are mutually exclusive. If all sequence probabilities can be determined for all the n_c minimal cut sets, the system failure probability is given by the summation:

$$\text{All sequences in minimal cut sets}: \quad P_{f,sys} = \sum_{i=1}^{n_c}\left\{\sum_{k=1}^{n_i!} P\left(\bigcap_{j=1}^{n_i} g_{ij}^{(k)} \leq 0\right)\right\}, \tag{27}$$

where $g_{ij}^{(k)} \leq 0$ indicates the jth element of the ith minimal cut set being part of the kth failure sequence. For elastic perfectly plastic structures, it is not necessary to consider sequences in any minimal cut set.

Though the binary nature of elements (being either in failed or safe states) is not a necessity, it facilitates the use of standard methods such as fault or event trees (or a combination of the two), including their variants to suit the peculiarities of structural systems, to describe system failure in terms of component failure events and, hence, to identify minimal cut and/or minimal path sets of the system. System reliability computation for structures is not straightforward since the component failures are not mutually independent events on account of (i) active redundancy in the structure leading to load sharing, (ii) load path dependence in case of successively applied multiple yet sustained loads, (iii) load redistribution after initial member failures for redundant structures, (iv) nonlinear behavior and non-brittle failure of the components, (v) failure sequences of different probabilities for the same cut set in a progressive collapse or incremental loading situation, and (vi) possible statistical dependence among the basic variables.

3.2 Computation of reliability

The failure probability corresponding to Eq. (13) is given by the multidimensional integral in the basic variable space:

$$P_f = P(g(\underline{X}) < 0) = \int\limits_{g(\underline{x})<0} f_{\underline{X}}(\underline{x}) d\underline{x}, \tag{28}$$

where $f_{\underline{X}}(\underline{x})$ is the joint probability density function for $\underline{X}$. The reliability of the structure would then be defined as $\text{Rel} = 1 - P_f$.

Closed-form solutions to Eq. (28) are generally unavailable. Two different approaches are in wide use: (i) analytic methods based on constrained optimization and normal probability approximations and (ii) simulation-based algorithms with or without variation reduction techniques. Both can provide accurate and efficient solutions to the structural reliability problem. The first approach, grouped under first-order reliability methods (or FORMs), holds a distinct advantage over the simulation-based methods in that the design point(s) and the sensitivity of each basic variable can be explicitly determined.

3.2.1 First-order reliability method

FORM calculates the reliability of a system by mapping the failure surface onto the standard normal space and then approximating it with a tangent hyperplane at the design point (defined as the point on the limit state surface in the standard normal space that is closest to the origin). (Shinozuka, 1983) Provided the limit state surface is well behaved, the solutions obtained by FORM are reasonably close to that obtained by the relatively expensive simulation-based solutions.

The two important steps of FORM are described in detail as follows.

1. Map the basic variables $\underline{X}$ on to the independent standard normal space $\underline{Y}$ and hence $g(\underline{X})$ to $g_I(\underline{Y})$. Several mappings are possible, such as (i) Hasofer–Lind (Hasofer and Lind, 1974) or

second moment transformation, which uses information only on the first two moments of each X; (ii) Nataf transformation, (Melchers, 1987) which uses marginal distribution of each X and the correlation matrix of the $\underline{X}$ vector, (iii) Rosenblatt transformation (Melchers, 1987), which uses nth-order joint distribution information, a special case of which is the so-called full distribution transformation, valid when the $\underline{X}$ are mutually independent; (iv) the Rackwitz–Fiessler (Rackwitz and Fiessler, 1978) transformation, which converts each X point by point into an equivalent normal U through a marginal distribution and density equivalence, and then the vector $\underline{U}$ into the independent standard normal vector $\underline{Y}$ through a Nataf-type transformation.

2. Locate on g_1 the point $\underline{y}^*$ closest to the origin,

$$\begin{aligned} &\min F = \underline{y}^T \underline{y} \\ &\text{subject to}\, G = g_1\left(\underline{y}\right) = 0 \end{aligned} \quad . \tag{29}$$

Let the solution to this optimization problem be $\underline{y}^*$,and let β be the distance of this optimal point from the origin. This minimum norm point, $\underline{y}^*$, is known as the checking or the design point. The limit state surface, g_1, can be approximated by a tangent hyperplane at y*, yielding the approximate probability of failure as

$$P_f = \Phi\left(-\beta\, \mathrm{sgn}\left[g_1\left(\underline{0}\right)\right]\right). \tag{30}$$

The signum function determines whether or not the origin is in the safe domain. The drawback of FORM is that it provides the exact solution only if the original limit state is linear and the basic variables are normally distributed. Otherwise, the extent of error depends on the curvature of the limit state and the method of mapping of $\underline{X}$ onto $\underline{Y}$.

After performing a FORM analysis, the design point $\underline{y}^*$ can be transformed back into the basic variable space, yielding the checking point, $\underline{x}^*$, which cannot be obtained from simulation-based solutions. It is implied that if the structural element in question is designed using this combination, $\underline{x}^*$, the reliability of the component would be β (within the approximations of FORM). This, in fact, is the basis of load and resistance factor design, discussed subsequently.

The gradient projection method, originally developed by Rosen, (Rosen, 1961) is well suited to tackle the constrained nonlinear optimization problem in Eq. (29).

3.2.2 Monte Carlo simulations

Except in very special situations, a closed-form solution to the structural reliability problem (Eq. 28) does not exist, and numerical approximations are needed. The true probability of failure, P_f,

$$P_f = \int_{\text{all } \underline{x}} \mathbb{I}[\{\text{Failure}\}] f_{\underline{X}}(\underline{x}) d\underline{x} = \int_{\text{all } \underline{u}} \mathbb{I}[\{\text{Failure}\}] f_{\underline{U}}(\underline{u}) d\underline{u}, \tag{31}$$

can be estimated using basic (also known as brute-force or crude) Monte Carlo simulations (MCS) in practice as

$$\hat{P}_f = \frac{1}{N}\sum_{i=1}^{N}\mathbb{I}[g(T(\underline{U}_i)) < 0]\,, \tag{32}$$

where a zero-mean normal vector $\underline{U}$ with the same correlation matrix $\boldsymbol{\rho}$ as the basic variables is generated first and then transformed element by element according to the full distribution transformation:

$$T(\underline{u}) = \underline{x} \;\Rightarrow F_{X_i}(x_i) = \Phi(u_i). \tag{33}$$

The use of the same $\boldsymbol{\rho}$ for $\underline{U}$ as for $\underline{X}$ results in error, but the error is generally small. (der Kiureghian and Liu, 1986) N is the total number of times the random vector $\underline{U}$ is generated, and $\underline{U}_i$ is the ith realization of the vector. It is well known that the basic Monte Carlo simulation–based estimate of P_f has a relatively slow and inefficient rate of convergence. The coefficient of variation (COV) of the estimate is

$$\hat{V}\left(\hat{P}_f\right) = \sqrt{\left(1 - P_f\right)/\left(NP_f\right)} \approx \sqrt{1/\left(NP_f\right)}, \tag{34}$$

which is proportional to $1/\sqrt{N}$and points to an inefficient relation between sample size and accuracy (and stability) of the estimate. Such limitations of the basic Monte Carlo simulation technique have led to several variance-reducing refinements. Notable among them are Latin hypercube sampling, (Ayyub and McCuen, 1995) importance sampling and its variants, (Melchers, 1990; Bjerager, 1988) and subset simulations (Au and Beck, 2001)—which, if performed carefully, can significantly reduce the required sampling size. Nevertheless, importance sampling and other variance-reducing techniques should be performed with care, as their results may be quite sensitive to the type and the point of maximum likelihood of the sampling distribution, and an improper choice can produce erroneous results. (Sen and Bhattacharya, 2015)

3.2.3 System reliability computation

An ordered sequence of failure events from a cut set is known by several different terms in structural systems reliability analyses, sometimes with subtle differences among the terms, such as *failure sequence* or *failure path*. To be specific, a *failure sequence* under incremental loading accounts for load redistribution after each component failure whereas a *failure path* does not; a failure path leads to different events whenever load redistribution occurs after each successive component failure (Bjerager et al., 1987). The terms *failure mode* and *collapse mode* unfortunately have been used in the literature to denote a cut set both with and without regard to the order of failure events, and this has led to confusion in some cases. The authors prefer *collapse mode*, to imply a cut set without reference to failure order, and *failure sequence*, to imply an ordered sequence from a cut set. A path set is sometimes referred to as a *stable configuration (*Bennet and Ang*, 1986)* although this term is rarely used in structural problems.

Depending on the structural complexity and desired accuracy of the solution, the dominant failure sequences (or collapse modes) can be found in a variety of ways. Some methods involve only a deterministic analysis of the structural system, some employ a fully probabilistic analysis, and still others use some limited probabilistic information. The assumption of rigid perfectly plastic material behavior is fairly popular in structural system reliability analysis as it eliminates load history dependence. It is well known that deterministic plastic mechanism analysis can lead to collapse mode identification in the case of rigid plastic–framed structures, but the number of modes generated quickly becomes excessively large (Watwood, 1979; Gorman, 1981). Such deterministic rules have been variously adapted to search for probabilistically dominant collapse modes—for example, by (i) creating linear combinations of those basic mechanisms that have the lowest reliability indices (the beta-unzipping method (Thoft-Christensen and Murotsu, 1986)), (ii) using linear programming (Corotis and Nafday, 1989), (iii) using stochastic programming, (Zimmerman et al., 1993) (iv) and employing genetic algorithms. (Shao and Murotsu, 1999) The probabilistically dominant failure *sequences* can be searched for by using truncated enumeration schemes that include the branch and bound method (Thoft-Christensen and Murotsu, 1986) and, importantly, the incremental loading method (Karamchandani, 1987; Moses, 1997). The incremental loading method is particularly useful (and often the only solution) when component failure is multistate instead of the usual binary; (Karamchandani and Cornell, 1992a) when material behavior is brittle, semi-brittle, or nonlinear instead of ideal plastic; (Karamchandani and Cornell, 1992b) and when system failure occurs not due to formation of a mechanism but due to excessive deformation or a specified drop in structural stiffness with regard to specified degrees of freedom. Nevertheless, one potential drawback of the incremental analysis method is its quasi-static assumption of structural behavior: the load duration needs to be sufficiently long to allow potential redistribution of load effects throughout the system.

Example 7.2. A portal frame system.

A portal frame consists of two columns and one beam (Figure 7.4). It has four nodes and 12 DOFs in all, of which six are constrained DOFs (at nodes 1 and 4). The three members are of equal length ($a = b = 20$ ft). A horizontal load, H, acts on the left beam column junction (node 2, DOF 4). A, E, I, and Y for each member are random. The statistics and dependence structure are given in Table 7.1. Three failure modes are to be considered: sway of node 3, flexural failure of member 1 at base, and flexural failure of member 2 at base. System failure is defined as frame failure if sway exceeds deltamax or failure of both legs in flexure. In this case, the system reliability of the frame needs to be found, and an elastic analysis is to be performed. A yield of extreme fiber in flexure constitutes failure, and the limiting sway is $b/80$.

$$\begin{array}{l}\text{Frame fails if }\{\text{sway exceeds deltamax}\}\text{ OR }\{\text{both legs fail in flexure}\}\\ F_{sys} = \{g_1 \leq 0\} \cup [\{g_2 \leq 0\} \cap \{g_3 \leq 0\}]\end{array} \quad . \tag{35}$$

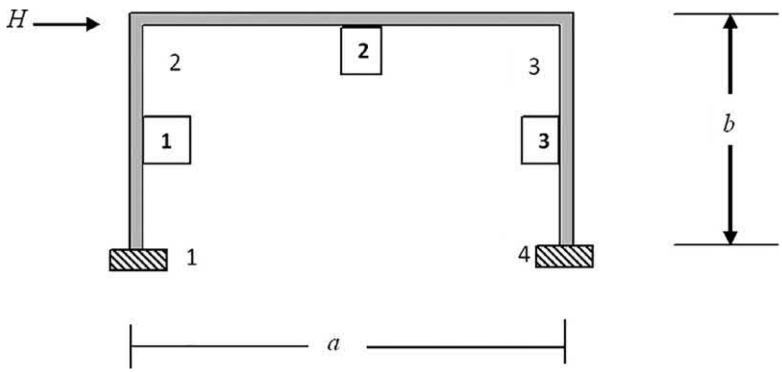

Figure 7.4 A portal frame. Nodes 1–4 (without borders) and members 1–3 (within boxes) are indicated.

Table 7.1 Random Variables in the Portal Frame Example

Random Variable	Distribution	Dependence Structure
Cross-sectional area, A_i, $i=1, 2, 3$	Normal with mean 12 in^2 and COV 10%	$\rho(A_i,A_j)=0.5,\ i\neq j$ Each A_i is independent of each E_j, each I_k and each Y_m. $I=1, 2, 3$; $j=1, 2, 3$; $k=1, 2, 3$; $m=1, 2, 3$
Stiffness, E_i $i=1, 2, 3$	Lognormal with mean 29,000 ksi and COV 5%	$\rho(E_i,E_j)=0.5,\ i\neq j$ Each E_i is independent of each A_j, each I_k and each Y_m. $I=1, 2, 3$; $j=1, 2, 3$; $k=1, 2, 3$; $m=1, 2, 3$
Moment of inertia, I_i $i=1, 2, 3$	Weibull with mean 600 in^4 and COV 25%	$\rho(I_i,I_j)=0.5,\ i\neq j$ Each I_i is independent of each A_j, each E_k and each Y_m. $I=1, 2, 3$; $j=1, 2, 3$; $k=1, 2, 3$; $m=1, 2, 3$
Yield strength, Y_i $i=1, 2, 3$	Lognormal with mean 36 ksi and COV 10%	$\rho(Y_i,Y_j)=0.5,\ i\neq j$ Each Y_i is independent of each A_j, each E_k and each I_m. $I=1, 2, 3$; $j=1, 2, 3$; $k=1, 2, 3$; $m=1, 2, 3$
Horizontal load H	Gumbel with mean 50 kip and COV 20%	H is independent of all member properties

The three limit state functions are

$$\begin{array}{l} \text{Limit state 1}: \ g_1 = \text{deltamax} - \text{sway} \\ \text{Limit state 2}: g_2 = Y_2 I_2/(c/2) - Mapp_2 \\ \text{Limit state 3}: g_3 = Y_3 I_3/(c/2) - Mapp_3 \\ \text{where deltamax} = L/80, c = L/30 = 8\,\text{inch} \end{array} . \tag{36}$$

Discussion of Solution.

The failure probabilities corresponding to the three individual limit states are found through FORM analyses:

$$\begin{aligned} P_{f_1} &= P[g_1 \le 0] = 0.18 \\ P_{f_2} &= P[g_2 \le 0] = 0.076\,. \\ P_{f_3} &= P[g_3 \le 0] = 0.074 \end{aligned} \tag{37}$$

The problem is solved using Monte Carlo simulations. Note that the failure probabilities in limit states 2 and 3 should be identical due to the symmetry of the problem.

The system failure probability, as found by Calrel through Monte Carlo simulations, is

$$P_{f_{sys}} = P[g_1 \le 0 \cup (g_2 \le 0 \cap g_3 \le 0)] = 0.21, \tag{38}$$

which is larger than any individual element failure probability.

Example 7.3. A system reliability problem where sequence effects matter. Consider the square truss with two diagonals (Figure 7.5). Each element has the same axial stiffness, EA. Material behavior is linear elastic up to failure; failure is brittle. Each element can fail either in compression or in tension. It is assumed that the element strength magnitude is the same in tension and compression. The six strength magnitudes, $C_1, \ldots, C_6$ are normally distributed with means (200200250250250200) kN and a common COV of 20%. The three elements that connect to the point of application of load (elements 3, 4, and 5) are stronger and have a 25% higher mean strength. The external force, H, is random: $H \sim$ N (100 kN, 30%). The seven random variables are mutually independent. Each normal variable is left truncated at 0.

The truss has 15 cut sets, $\{1,2\}$, $\{1,3\}$, …, $\{5,6\}$, which are neither disjoint nor independent. The system failure event is

$$F_{sys} = \{F_1F_2\} \cup \{F_1F_3\} \cup \ldots \cup \{F_5F_6\}, \tag{39}$$

where F_i is failure of the ith element. Accounting for failure sequences in each cut set, we express the system failure event in terms of mutually exclusive events as follows:

$$\begin{aligned} \{F_iF_j\} = &\left\{F^0_{i(1)j(2)} \cup F^0_{j(1)i(2)} \cup F^0_{i\&j \text{ fail together}}\right\} \\ &\cap \{\text{other elements}\,(\text{not}\, i, j)\, \text{survive}\}, \end{aligned} \tag{40}$$

where the superscript 0 indicates the current system state as intact, $i\,(1)$ means element i fails first, and $j\,(2)$ means element j fails second. Although not usually considered and not always significant, the simultaneous failure of two elements has been considered here for the sake of completeness. The probability of system failure is then

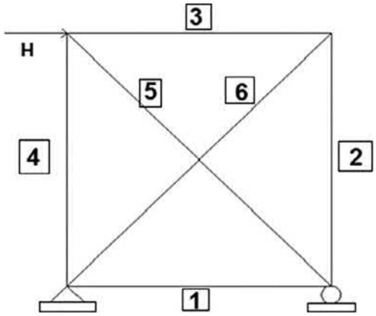

Figure 7.5 A square truss made up of six brittle elements. The failure of any two elements leads to system instability.

$$P\left[F_{sys}\right] = \sum_{\substack{\text{all } i,j \\ i \neq j}} \left\{ \begin{array}{l} P\left[F^0_{i(1)j(2)} \cap \{\text{other elements (not } i,j) \text{ survive}\}\right] + \\ P\left[F^0_{i\&j \text{ fail together}} \cap \{\text{other elements (not } i,j) \text{ survive}\}\right] \end{array} \right\}. \tag{41}$$

In order to compute their probabilities, the events $F^0_{i(1)j(2)}$ and$F^0_{i\&j\text{fail together}}$intersecting with the event "other elements survive" need to be expressed in terms of element capacities and demands:

$$\begin{aligned} F^0_{i(1)j(2)} \cap \{\text{other elements survive}\} = C_1 \leq D^0_1, C_2 > D^0_2, \ldots, C_6 > D^0_6, \\ C_2 \leq D^1_2, C_3 > D^1_3, \ldots, C_6 > D^1_6 \end{aligned} \tag{42}$$

$$\begin{aligned} F^0_{i\&j\text{fail together}} \cap \{\text{other elements survive}\} = C_1 \leq D^0_1, C_2 \leq D^0_2, C_3 > D^0_3 \ldots, \\ C_6 > D^0_6 \end{aligned} \tag{43}$$

Table 7.2 shows the element loads in intact and damaged conditions for the truss in Figure 7.5. The reliability of the intact system is $R_{sys} = 0.999072$. Sequence failure events, as opposed to "fail together" events, contribute almost entirely to the system failure probability: only 1.5% of PF_{sys} arise from the "fail together" events. The three most dominant sequences are: (6–5), (6, 113) and (6–1) accounting for 75% of PF_{sys}; 12 sequences have zero probability of occurrence.

3.3 Specifying target reliabilities for design and assessment

It has become increasingly common to express safety requirements, as well as some functionality requirements, in reliability-based formats. A reliability-based approach to design, by accounting for randomness in the different design variables and uncertainties in the mathematical models, provides tools for ensuring that the performance requirements are violated as rarely as considered acceptable. Such an approach comes

Table 7.2 Element Loads in Intact and Damaged Conditions

Element ID, k	Member Forces						
	D_k^0	D_k^1	D_k^2	D_k^3	D_k^4	D_k^5	D_k^6
1	H/2	NA	H	H	0	0	H
2	H/2	H	NA	0	H	H	0
3	H/2	H	0	NA	H	H	0
4	H/2	0	H	H	NA	0	H
5	$H/\sqrt{2}$	0	$\sqrt{2}H$	$\sqrt{2}H$	0	NA	$\sqrt{2}H$
6	$H/\sqrt{2}$	$\sqrt{2}H$	0	0	$\sqrt{2}H$	$\sqrt{2}H$	NA

D_k^0 = demand in element k when structure is intact.
D_k^i = demand in element k when element i has failed.
NA = not applicable.

under the broad classification of performance-based design (PBD). In structural engineering, the seismic engineering community has most enthusiastically espoused PBD, as evident in SEAOC, (SEAOC, 1995) ATC-40 (ATC, 1996), FEMA 273 (FEMA, 1997), and FEMA 350. (FEMA, 2000)

Mathematically, we go back to Eq. (14) and set a lower limit to the reliability—or, equivalently, an upper limit to the failure probability for each limit state:

$$1 - \mathrm{Rel}(t) = P_f(t) \le P_f^* = \Phi^{-1}(-\beta_T), \tag{44}$$

where P_f^* is the maximum permissible failure probability and β_T is the equivalent target reliability index. The cause, reference period, and consequences of violation of different limit states may vary, and the target reliability for each limit state must take such difference into account. (ISO, 2015; JCSS, 2015; Bhattacharya et al., 2001; Wen, 2001; Eurocodes, 2002) For example, if the structure gives appropriate warning before collapse, the failure consequences reduce, and that, in turn, reduces the target reliability for that mode. (JCSS, 2015; DNV, 1992) Eurocodes (Eurocodes, 2002) classifies buildings into three consequence classes: CC1 (agricultural buildings and greenhouses), CC2 (residences and offices), and CC3 (grandstands and public buildings). ASCE (ASCE, 2016) classifies structures into four risk categories based on the number of persons at risk and specifies target reliabilities for each category, corresponding to three types of failure (including specifying whether the failure is sudden and/or it leads to widespread damage).

Functionality target reliabilities may be developed exclusively from economic considerations. The safety target reliability levels required of a structure (i.e., in strength or ultimate type limit states), on the other hand, cannot be left solely to the discretion of the owner or derived solely from a minimum total expected cost consideration, since structural collapse causing a large loss of human life and/or property, even if an “optimal” solution in some sense, may not be acceptable to either the society or the regulators. Design codes, therefore, often place a lower limit on the reliability of safety-related limit states (Bhattacharya et al., 2001; Galambos, 1992).

3.3.1 Code-specified target reliabilities

Conventional structures that have a history of successful service—such as concrete buildings, highway bridges, and steel vessels—can be deemed sufficiently safe, and their calculated reliability levels may be used as the targets for new structures of the same kind. This, in principle, is done when a new reliability-based code is developed for a given class of structures having a successful history of use and a wide knowledge base about their performance. (Ellingwood and Galambos, 1982) The objective is to produce more uniform levels of safety and more optimal structures. ISO 2394 (ISO, 2015) and, later, JCSS (JCSS, 2015) proposed three levels of requirements with appropriate degrees of reliability: (i) serviceability (adequate performance under all expected actions), (ii) ultimate (ability to withstand extreme and/or frequently repeated actions during construction and anticipated use), and (iii) structural integrity (i.e., progressive collapse in ISO 2394 and robustness in JCSS). Target reliability values were suggested based on the consequences of failure (C) and relative cost of safety measure (S). (JCSS, 2015) In ultimate limit state, these ranged from 10^{-3}/year for minor C and large S to 10^{-5}/year for moderate C and normal S, down to 10^{-6}/year for large C and small S. In serviceability limit state, the maximum annual failure probability ranged from 0.1 (high S) to 0.01 (low S). For existing structures, ISO 13822 (ISO, 2012) recommends a fatigue reliability index of 2.3 for inspectable structures and 3.1 for non-inspectable structures, which is valid for the remainder of their working lives.

The Canadian Standards Association (CSA, 1992) defines two safety classes and one serviceability class (and corresponding annual target reliabilities) for the verification of the safety of offshore structures: (i) Safety Class 1, where there is great risk to life or high potential for environmental pollution or damage; (ii) Safety Class 2, where there is low risk to life or low potential for environmental pollution or damage; and (iii) Serviceability Impaired, where neither function nor the two safety classes are violated. Det Norske Veritas (DNV, 1992) specifies three types of structural failures for offshore structures and target reliabilities for each, corresponding to the seriousness of the consequences of failure. The American Bureau of Shipping (ABS, 1999) identified four levels of failure consequences for various combinations of limit states and component classes for the mobile offshore base concept and assigned target reliabilities for each.

3.3.2 Bridge structures

Ghosn and Moses (Ghosn and Moses, 1998) suggest three levels of performance to ensure adequate redundancy of bridge structures corresponding to functionality, ultimate, and damaged condition limit states, whereas Nowak et al. (Nowak et al., 1997) recommend two different reliability levels for bridge structures corresponding to ultimate and serviceability limit states.

Nowak et al. (Nowak et al., 1997) recommend a (lifetime) target component reliability index of 3.5 and a target system reliability index of 5.5 in the ultimate limit states for bridge structures. For serviceability limit states, they recommend a target component (i.e., girder) reliability index of 1.0 in tension and 3.0 in compression. They also compute component reliabilities of different kinds of bridges (reinforced concrete, prestressed concrete, and steel built to AASHTO 1992 and BS 5400 specifications) in bending, shear, and serviceability limit states.

Ghosn and Moses (Ghosn and Moses, 1998) suggest the following reliability requirements to ensure adequate redundancy of a highway bridge structure:

$$\beta_u - \beta_1 \geq 0.85,\ \beta_f - \beta_1 \geq 0.25,\ \beta_d - \beta_1 \geq -2.7. \tag{45}$$

The subscripts $1, f, u$, and d refer to first member failure, functionality limit state, ultimate state, and damaged condition limit state, respectively.

The design of the Confederation Bridge (Northumberland, Canada) required that load and resistance factors be calibrated to "a β of 4.0 for ultimate limit states, for a 100 year life" (MacGregor et al., 1997). Sarveswaran and Roberts (1999) chose an acceptable annual failure probability of bridge collapse in UK equal to 2×10^{-5}, which corresponded to an FAR of 2 (FAR is discussed in Section 3.3.4).

3.3.3 Loss-based approaches

The risk of an undesirable event is commonly defined as the product of p, the probability of occurrence of the event, and C, the consequence of the event (lives lost, lost revenue, monetary compensation, lost utility, etc.). Rather than having only one level of undesirable consequence, a more general expression for risk would be

$$\text{Risk} = \sum p_i \times C_i. \tag{46}$$

The term *risk* is also used in the sense of an individual's probability of death in the public health and actuarial literature. Definition of risk and what constitutes consequences of failure depend on whose risk is it—the public's, a corporation's, or an individual's. Once the tolerable risk, R^*, is known and C can be quantified, the maximum permissible failure probability can be set:

$$P_f^* = \frac{R^*}{C}. \tag{47}$$

The actual risk from an activity may be markedly different from the risk perceived by the public. Society's general reaction to hazards of different levels can range from indifference to rational to dread. If exposure to an activity is voluntary, the acceptable level of risk is generally higher. Involuntary activities, on the other hand, have a much lower acceptable risk to an individual. In the absence of proper information about a perceived hazardous activity, the public may have a dread risk. Appreciating this, in the Netherlands, the maximum tolerable risk suggested for existing situations is

10^{-5}/person/year, and for new situations, it is 10^{-6}/person/year (Bottelberghs, 1995). However, it needs to be underlined that a society's sense of tolerable risk for a given activity may change with time.

3.3.4 Fatality-based approaches

When the loss from failure is measured in terms of human lives lost, there are several fatality-based approaches to setting target reliabilities. It is controversial to put a monetary value on human life.

Various agencies and researchers have investigated levels of probability that are acceptable to society for events causing fatalities, as described in the following. The acceptable probabilities depend on the nature of the hazard, advanced warning, etc., and decrease with an increasing number of fatalities, n. The general form is as follows:

$$P_f \leq C n^{-\alpha}/yr, \tag{48}$$

where C accounts for the nature of hazard, warning, etc., and α signifies the impact of the number of lives lost in a single event. As reported in MSC 72/16, (IMO, 2000) UK's HSE suggests 10^{-4}/person/year as the limit of fatality risk to members of the general public. In a CIRIA (CIRIA, 1977) report, Flint developed an empirical formula with $\alpha = 1$. On the other hand, Allen (Allen, 1981) proposed an annual target failure probability with $\alpha = 0.5$ and $C = 10^{-5}(A/W)$, where A = activity factor and W = warning factor. The factor 10^{-5} was ascertained from data on building collapse in Canada. For normal activities, A ranges from 1 (in buildings) to 10 (in high-exposure structures like offshore structures) and equals 3.0 for bridges. W ranges from 0.01 (fail-safe condition) to 1.0 (for failure without warning). Note that $\alpha = 0.5$ implies that the rate of growth in risk aversion decreases with the number of fatalities. Later, ISO (ISO, 2015) specified $\alpha = 2$ and tied the acceptable failure probability to the square of the number of lives involved, perhaps signifying a decrease in the public's sense of tolerable risk in large engineered systems. Steenbergen et al. (Steenbergen et al., 2015) took $C = 0.01$ and $\alpha = 2$ and assumed that n is related to the span of the bridge (S). Table 7.3 shows the one-year annual target β values Steenbergen et al. found.

A somewhat different measure of hazardous activities that accounts for exposure time is the fatal accident rate (FAR). The FAR for an activity is the number of fatalities

Table 7.3 Annual Target Reliability Index as a Function of Bridge Span

Span Length S (m)	Annual Target β
$S < 20$	2.7
$20 < S < 50$	3.3
$50 < S < 100$	3.7
$S > 100$	4.4

per 100 million hours of exposure to that activity (i.e., 1000 people working 2500 h a year and having careers of 40 years each):

$$\mathrm{FAR} = 10^8 P[F]/T_h, \tag{49}$$

where $P(F)$ is probability of fatality, and T_h is the exposure time in person-hours. Typical values of FAR in the UK (Mander and Elms, 1993) range from 5 (in the chemical processing industry) to 67 (in the construction industry). FARs for various activities in Japan (Suzuki, 1999) range from 0.2 for fires and 4.3 for railway travel to 46.3 for civil aviation.

4. Reliability-based design codes of bridges

4.1 Partial safety factors

Reliability-based partial safety factor (PSF) design is intended to ensure a nearly uniform level of reliability across a given category of structural components for a given class of limit state under a particular load combination (Ellingwood, 2000). We approach the topic of optimizing PSFs by noting that any arbitrary point, $\underline{x}^a$, on the limit state surface, by definition, satisfies

$$g(\underline{x}^a) = 0. \tag{50}$$

For example, each member of $\underline{x}^a$ can be chosen to correspond to a particular quantile of the respective element of the random vector $\underline{X}$, such that Eq. (50) defines a functional relation among these quantiles. By choosing different values for $\underline{x}^a$, the joint density function of $\underline{X}$ can effectively be moved with respect to the limit state surface. Clearly, this relative movement in the basic variable space affects the limit state probability. In other words, by specifying a functional relation among quantiles (or some other statistics) of the basic variables $\underline{X}$, one can affect the reliability of the structure.

Extending this idea, a design point $\underline{x}^d$ on the limit state surface can be carefully chosen so that it locates the limit state in the space of basic variables such that a desired target reliability is ensured for the design. The ensuing design equation,

$$g\left(\underline{x}^d\right) = 0, \tag{51}$$

is essentially a relationship among the parameters of the basic variables and gives a minimum requirement type of tool in the hand of the design engineer to ensure target reliability for the design in an indirect manner. Since nominal or characteristic values of basic variables are typically used in design, Eq. (51) may be rewritten as

$$g\left(\frac{x_1^n}{\gamma_1}, \ldots, \frac{x_k^n}{\gamma_k}, \gamma_{k+1}x_{k+1}^n, \ldots, \gamma_m x_m^n\right) \geq 0, \tag{52}$$

where the superscript n indicates the nominal value of the variable. The vector of basic variables has been partitioned into k resistance–type and $m-k$ action–type quantities. The partial safety factors, γ_i, are typically greater than 1: for resistance-type variables, the nominal values are divided, whereas for action-type variables, the nominal values are multiplied to obtain the design point:

$$\begin{aligned} &\text{resistance PSFs}: \gamma_i = \frac{x_i^n}{x_i^d}, \quad i = 1, \ldots, k \\ &\text{action PSFs}: \gamma_i = \frac{x_i^d}{x_i^n}, \quad i = k+1, \ldots, m \end{aligned} \tag{53}$$

If the design equation (52) can be separated into a strength term and a combination of load effect terms, the following safety checking scheme may be adopted for design:

$$R_n\left(\frac{S_i^n}{\gamma_i^s}, i = 1, \ldots, k\right) \geq l\left(\sum_{i=1}^{m-k} \gamma_i^q Q_i^n\right), \tag{54}$$

where R_n = the nominal resistance and a function of factored strength parameters, l = load effect function, S_i^n = nominal value of ith strength/material parameter, γ_i^s = ith strength/material factor, Q_i^n = the nominal value of the ith load, and γ_i^q = ith load factor. Note that there is no separate resistance factor multiplying the nominal resistance (as in LRFD) since material partial safety factors have already been incorporated in computing the strength.

The nominal values generally are fixed by professional practice and thus are inflexible. Some of the m partial safety factors (often those associated with material properties) can also be fixed in advance. The remaining PSFs can be chosen by the code developer so as to locate the design point, locate the limit state as alluded to before, and, hence, achieve a desired reliability for the structure.

4.2 Calibration of partial safety factors

By normalizing the limit state with the design equation in a two-variable problem, the reliability problem can be written as

$$\begin{aligned} &\text{Find } \gamma_1^s, \ldots, \gamma_k^s, \gamma_1^q, \ldots, \gamma_{m-k}^q \text{ such that} \\ &P\left[\frac{C}{C^n\left(\gamma_1^s, \ldots, \gamma_k^s\right)} - \frac{Q}{Q^n\left(\gamma_1^q, \ldots, \gamma_{m-k}^q\right)} \leq 0\right] = \Phi(-\beta_T) \end{aligned} \tag{55}$$

where β_T is the target reliability index, C is the random capacity and C^n is its nominal value. Of course, this is an under-defined problem, and even though some of the PSFs may be fixed in advance, as stated before, it has an infinite number of solutions. Additional considerations are needed to improve the problem definition. Such considerations naturally arise when PSFs need to be optimized for a class of structures, as discussed next.

It is common to expect that the design equation be valid for r representative structural components (or groups). Let w_i be the weight (i.e., relative importance or relative frequency) assigned to the ith such component (or group). These r representative components may differ from each other in location, geometric dimension, nominal load, material grades, etc. For a given set of PSFs, let the reliability of the ith group be β_i. Choosing a new set of PSFs gives us a new design, a new design point, and, consequently, a different reliability index. If there has to be one design equation—i.e., one set of PSFs—for all the r representative components, the deviations of all β_i from $\beta_T$must be minimized in some sense. When using the optimal PSFs obtained this way, design equation (52) can ensure a nearly uniform reliability for the range of components. Several constraints may be introduced to the optimization problem to satisfy engineering and policy considerations (as summarized in Agrawal and Bhattacharya (Agrawal and Bhattacharya, 2010)). Moreover, some partial safety factors, such as those on material strengths, may be fixed in advance, as stated before. The PSF optimization exercise has the following form:

$$\begin{aligned}
&\min\left[\sum_{i=1}^{r} w_i\left(\beta_i\left(\gamma_1^q,\ldots,\gamma_{m-k}^q\right)-\beta_T\right)^2\right] \text{ where } \sum_{i=1}^{r} w_i = 1\\
&\text{subject to}: \min\left(\beta_i\right) > \beta_T - \Delta\beta,\quad i=1,\ldots,r \\
&\gamma_i^{\min} \le \gamma_i^q \le \gamma_i^{\max},\ i=1,\ldots,m-k\\
&\gamma_i^s = m_i, i=1,\ldots,k
\end{aligned} \tag{56}$$

The weighted squared error from the target reliability index over all groups is minimized while ensuring that the lowest reliability among all the groups does not drop by more than $\Delta\beta$ below the target. The material PSFs are fixed while the load PSFs have upper and lower limits.

5. Bridge life cycle cost and optimization

In life cycle cost analysis of bridges, costs to owners (also refer to as agencies) as well as the public (also known as users) need to be taken into account (NCHRP, 2003). Agency costs include design, construction, maintenance, repair, and replacement (less salvage value). If failure occurs, then costs may include compensation, cleanup, etc. For users, costs arise from accidents, delays, and detours. Since some costs are fixed (i.e., deterministic) and some are outcome dependent (i.e., random), the total cost (i.e., life cycle cost),

$$C_T = C_I + \sum_{n_i} C_M(t_i) + \sum_{n_j} C_U(t_j) + C_F, \tag{57}$$

is probabilistic in nature. C_F is either the replacement cost (C_{rep}) at the end of life or the failure cost (C_f), which occurs at some random instant T_f. The maintenance and user costs, C_M and C_U, are also uncertain, as they depend on future loading and aging effects and whether the bridge fails prematurely or not. Hence, the total expected cost can be written as

$$E[C_T] = C_I + \sum_{n_i} E[C_M(t_i)I(t_i)] + \sum_{n_j} E\left[C_U\left(t_j\right)I\left(t_j\right)\right] + \left(1-P_f\right)C_{rep} + P_f C_f. \tag{58}$$

The indicator function I verifies whether or not the bridge has survived up to the indicated time. Discounting of future costs can also be included (Lind, 1993). Examples of various costs in for a system of highway bridges can be found in Almeida et al. (Almeida et al., 2015) In a decision context, the total expected cost is minimized, and subjected to constraints like available budget, target reliability, etc.; see, for example, Frangopol et al. (Frangopol et al., 2017)

Decisions regarding new design as well as maintenance therefore require explicit determination of the bridge's time-dependent reliability function, which is discussed next.

5.1 Time-dependent structural reliability

5.1.1 Descriptors of the time to failure

Let T denote the random time to failure (or TTF, also known as failure-free operating time or lifetime) of an item. The reliability function Rel(t) evaluated at time t is the probability that the item survives beyond t (cf. Eq. (11)):

$$\mathrm{Rel}(t) = P[T > t] = \int_t^{\infty} f_T(\tau)d\tau, \tag{59}$$

where f_T is the probability density function of T. The hazard function, $h(t)$, which is the conditional density of the TTF, presents the same information differently and can be very useful in revealing unsafe conditions:

$$h(t) = \frac{f_T(t)}{\mathrm{Rel}(t)} \text{ so that } \mathrm{Rel}(t) = \exp\left[-\int_0^t h(\tau)d\tau\right]. \tag{60}$$

Statistics of T are routinely obtained for electronic/electrical components through (accelerated) testing programs. This is possible because (i) an abundant number of nominally identical specimens can be obtained, (ii) a large number of test data can be generated in a relatively short time, (iii) tests can be performed in near actual conditions, (iv) tests are not hazardous, and (v) tests are relatively inexpensive.

For civil engineering structures, very seldom are all five points satisfied. Actual failure data are also, thankfully, rare. In the parlance of system reliability, structures constitute active redundant systems with load sharing and dependence—the most difficult type of system to model for reliability analysis.

Nevertheless, time-dependent reliability functions are useful for civil engineering systems not only at the new design stage but also for scheduling future maintenance, posting load restrictions, and managing life cycle costs, as explained previously. The reliability function is obtained from the mechanics of the problem where time-varying behavior of some of the basic variables is now brought into the picture explicitly.

5.1.2 Capacity and demand both vary nonrandomly in time

Without loss of generality, we look at only one critical location and one failure mode of the structure in Eq. (11). For multiple critical locations and failure modes, the limit state that follows can be augmented by unions of individual failure events.

At a given location and for a given failure mode, let the capacity and demand vary deterministically in time:

$$\begin{aligned} C(\tau) &= C_0\, d(\tau) \\ Q(\tau) &= Q_0\, h(\tau) \end{aligned}. \tag{61}$$

C_0 and D_0 are random variables, and d and h are nonrandom functions of time, $d > 0$, $h > 0$. That is, if the process $C(\tau)$ is known at any instant t_1, its value can be known precisely at all other instants of time, and likewise for $Q(\tau)$. Due to the nonrandom nature of d and h, the reliability function,

$$\mathrm{Rel}(t) = P[C_0\, d(\tau) - Q_0\, h(\tau) > 0, \text{for all } \tau \in (0, t]] \tag{62}$$

can be written as

$$\mathrm{Rel}(t) = P\left[C_0 - Q_0 \max_{0<\tau\le t} \frac{h(\tau)}{d(\tau)} > 0\right]; \tag{63}$$

d is commonly the aging function. Its form can be derived from the mechanics of damage growth (e.g., corrosion loss, (Bhattacharya et al., 2008a) fatigue crack growth (Kwon and Frangopol, n.d.), etc.) and the loading history. $d = 1$ implies the capacity does not degrade with time, and $h = 1$ implies the load is sustained in time. The preceding approach will be still valid for several simultaneously occurring loads (cf. Eq. (12)) if

$$Q_0\, h(\tau) = Q_0^{(1)} \cdot h_1(\tau) + Q_0^{(2)} \cdot h_2(\tau) + Q_0^{(3)} \cdot h_3(\tau) + \ldots \tag{64}$$

in which all h are nonrandom functions of time and the initial load magnitudes $Q_0^{(i)}$ are random variables.

Example 7.4. We define a time-dependent problem based on Example 7.1. The cable is subject to uniform corrosion causing its radius, whose initial value $r_0 = 4$ in, to deteriorate as $\Delta r(t) = b_1 t^{b_2}$, where $b_1 = 0.1$ in/yr^{b_2}, $b_2 = 0.9$ are the corrosion law constants. The cross-sectional area thus deteriorates according to $a(t) = \pi(r_0 - \Delta r)^2$. The cable is made of A36 steel, whose yield strength Y is now assumed to be normally distributed with mean $\mu_Y = 38$ ksi and COV $V_Y = 15\%$. The load, Q_0, is invariant and sustained in time, and is now considered a normal random variable. Its mean is $\mu_Q = 1000$ kip, and the COV is $V_Q = 20\%$. In the context of Example 7.1, the mean bias of the load is then $1000/1600 = 0.625$. The load and capacity are independent. The reliability function (Eq. 63) for this problem can be simplified as follows:

$$\begin{aligned} \mathrm{Rel}(t) &= P\left[Y - Q_0 \max_{0<\tau\le t} \frac{1}{\pi\left(r_0 - b_1 \tau^{b_2}\right)^2} > 0\right] \\ &= P\left[Y - Q_0 \frac{1}{\pi\left(r_0 - b_1 t^{b_2}\right)^2} > 0\right] \\ &= P\left[\pi\left(r_0 - b_1 t^{b_2}\right)^2 Y - Q_0 > 0\right] \\ &= P[M(t) > 0] \end{aligned}. \tag{65}$$

Note that, due to the monotonically decreasing nature of $d(\tau)$, the limit state is evaluated *only at the right end point* of the interval $(0,t)$. In any other situation, this simplification would be wrong and would lead to dangerous overprediction of reliability.

The margin process M is normally distributed being a linear combination of normals. Its mean and variance at time t are

$$\begin{aligned} \mu_M(t) &= a(t)\mu_Y - \mu_Q \\ \sigma_M^2(t) &= a^2(t)\sigma_Y^2 + \sigma_Q^2 \end{aligned}. \tag{66}$$

The reliability function therefore can be expressed as the normal CDF:

$$\mathrm{Rel}(t) = \Phi\left(\frac{\mu_M(t)}{\sigma_M(t)}\right). \tag{67}$$

Differentiating the reliability function leads to the hazard function:

$$h(t) = -\frac{\phi\left(\frac{\mu_M(t)}{\sigma_M(t)}\right)}{\Phi\left(\frac{\mu_M(t)}{\sigma_M(t)}\right)} \frac{\dot{\mu}_M(t)\sigma_M(t) - \mu_M(t)\dot{\sigma}_M(t)}{\sigma_M^2(t)}. \tag{68}$$

These two functions are plotted in Figure 7.6. The choice of normal distribution for both random variables in the problem leads to the closed-form expressions for the preceding reliability and hazard functions. For other distributions, FORM or Monte Carlo simulations may be adopted.

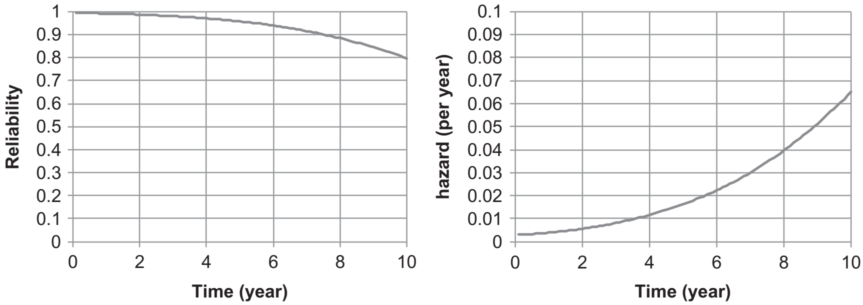

Figure 7.6 Reliability and hazard functions of corroding cable.

5.1.3 Load occurs as a pulsed sequence with random magnitudes

Known number of load pulses and no aging

We first consider the case when C is time invariant (i.e., $d \equiv 1$ in Eq. 61) and the load occurs as pulses of random magnitude Q_1, Q_2, …, $Q_{n(t)}$ where the number of load pulses n in time t are known. We assume that the loads are IID—that is, all Q_i are mutually independent and each Q_i has the same distribution, F_Q. Further, the loads are independent of the capacity. The reliability function,

$$\mathrm{Rel}(t) = P\left[Q_1 < C_0, Q_2 < C_0, Q_3 < C_0, \ldots, Q_{n(t)} < C_0\right], \tag{69}$$

can be simplified by first conditioning it on an arbitrary value of C_0 and then using the IID property of the Q_i:

$$\mathrm{Rel}(t|\, C_0 = c) = \left[F_Q(c)\right]^{n(t)}. \tag{70}$$

The total probability theorem is then applied to yield:

$$\mathrm{Rel}(t) = \int_0^\infty \left[F_Q(c)\right]^{n(t)} f_{C_0}(c)\, dc. \tag{71}$$

Q is a Poisson pulse process and no aging

A *point process* $N(t)$ on the line $\mathbb{R}^+ = [0, \infty)$ is a set of randomly occurring points such that (i) any finite interval contains a finite number of points with probability 1, and (ii) the number of points in disjoint intervals is the sum of the individual counts (Kovalenko et al., 1996). The points are commonly designated as arrival times: T_1, T_2, …, $T_i \geq 0$. The interarrival times are $\tau_1 = T_1$, $\tau_2 = T_2 - T_1$, . …, so that $T_n = \tau_1 + \tau_2 + \cdots + \tau_n$. The point process can be described by the joint distribution of

(i) the arrival times, (ii) the interarrival times, or (iii) the increments in disjoint intervals. $N(t)$ is a renewal process if the interarrival times are mutually independent and identically distributed. A renewal process is Poisson if the interarrival times are exponentially distributed or, equivalently, if the increments in disjoint intervals are independent.

A Poisson process $N(t)$ is completely defined by its rate of occurrence, λ. The Poisson random variable, N_t, with its mean being equal to λt, represents the number of arrivals in the Poisson process $N(t)$ in the interval $(0,t)$. The joint distribution of the interarrival times T_1, T_2, $\ldots T_n$ given $N(t) = n$ is (Kingman, 2002)

$$f_{T_1,T_2,\ldots,T_n|N(t)=n}(t_1, t_2 \cdots t_n) = \begin{cases} \dfrac{n!}{t^n} & 0 < t_1 < \ldots < t_n < t \\ 0, & \text{otherwise} \end{cases}. \tag{72}$$

We generalize the preceding situation and consider the loads to occur according to a Poisson pulse process (with rate λ). As before, the magnitude of the pulses are IID and independent of capacity. No aging is considered. Since the number of pulses in time interval (0,t) is random, the reliability function is expressed as

$$\begin{aligned} \mathrm{Rel}(t) &= \sum_{n=0}^{\infty} P\left[\bigcap_{i=1}^{n} Q_i < C_0 | N(t) = n\right] P[N(t) = n] \\ &= \int_{c=0}^{\infty} \sum_{n=0}^{\infty} P\left[\bigcap_{i=1}^{n} Q_i < c | N(t) = n, C_0 = c\right] P[N(t) = n] \, f_{C_0}(c) dc \end{aligned}. \tag{73}$$

By using the form of the Poisson PMF, the reliability function simplifies to

$$\mathrm{Rel}(t) = \int_0^{\infty} e^{-\lambda t\left(1 - F_Q(c)\right)} f_{C_0}(c) \, dc. \tag{74}$$

Q is a Poisson pulse process, and structure ages deterministically

We now introduce aging, as in Eq. (61). Figure 7.7 shows a schematic of this situation. Since the loads occur as a Poisson pulse, the occurrence times, T_i, are random in nature, and the individual limit states are evaluated at these random instants of time:

$$\mathrm{Rel}(t) = \sum_{n=0}^{\infty} P\left[\bigcap_{i=1}^{n} Q_i < C_0 d(T_i) | N(t) = n\right] P[N(t) = n]. \tag{75}$$

Since these random occurrence times are ordered, $T_1 < T_2 < \ldots < T_i < T_{i+1} < \ldots$, their conditional joint PDF given that n pulses occurred in (0,t) is $1/t^n$ (cf. Eq. 72). The reliability function, conditioned on a fixed value of C_0, then can be written as

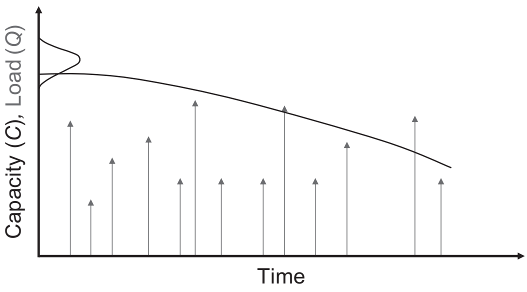

Figure 7.7 Deteriorating capacity and Poisson pulse loads with random magnitudes.

$$\begin{aligned}\mathrm{Rel}\,(t|\,C_0=c) &= \sum_{n=0}^{\infty}\iiint\limits_{\mathrm{all}\,\tau_i} P\left[\bigcap_{i=1}^{n} Q_i < c\,d(\tau_i)|N(t)=n, T_i=\tau_i, T_i<T_j, 1\le i<j\le n\right]\times \\ &\quad f_{\underline{T}}(\underline{\tau})d\underline{\tau}P[N(t)=n] \\ &= \sum_{n=0}^{\infty}\left[\frac{1}{t}\int_{\tau=0}^{t} F_Q[c\,d(\tau)]d\tau\right]^n P[N(t)=n]\end{aligned} \tag{76}$$

By using the form of the Poisson PMF and removing the conditioning on C_0, the reliability function simplifies to

$$\mathrm{Rel}(t) = \int_0^{\infty} e^{-\lambda t\left(1-\frac{1}{t}\int_{\tau=0}^{t} F_Q[c\,d(\tau)]d\tau\right)} f_{C_0}(c)\,dc \quad . \tag{77}$$

Note that Eq. (77) reduces to Eq. (74) when d is identically equal to 1.

5.1.4 Load and capacity both vary randomly in time

This is the most general case and constitutes a first passage problem. (Ditlevsen and Bjerager, 1986; Lin, 1976) The rate at which the margin process $M(\tau)=C(\tau)-Q(\tau)$ crosses the zero barrier (i.e., enters or leaves the "safe" domain) at an arbitrary time t is given by the joint PDF of the process and its derivative, $\dot{M}$,at that instant:

$$\overline{\nu}_0(t) = \int_{-\infty}^{\infty} |\dot{m}(t)|\, f_{M(t)\dot{M}(t)}(0,\dot{m})d\dot{m}. \tag{78}$$

If the margin process is statistically stationary, the passages into the unsafe domain become asymptotically Poisson, so that the reliability function represents the probability of the first passage into the unsafe domain beyond time t:

$$\mathrm{R}(t) = (1 - F_T(0))e^{-\nu_0^- t}, \tag{79}$$

where $F_T(0)$ is the probability that the margin is negative at $t = 0$. In this stationary case, the constant rate of downcrossing (into the unsafe domain) is

$$\nu_0^- = \int_0^\infty \dot{m} f_{M\dot{M}}(0, \dot{m}) d\dot{m}. \tag{80}$$

Further, if the margin is stationary Gaussian, it is independent of its derivative at the same instant, and the downcrossing rate becomes

$$\nu_0^- = \frac{\sigma_{\dot{M}}}{\sqrt{2\pi}} \frac{1}{\sigma_M} \phi\left(\frac{\mu_M}{\sigma_M}\right) \text{ if } M \text{ is stationary Gaussian.} \tag{81}$$

5.2 Reliability-based maintenance of bridges

Reliability-based maintenance of irreparable systems is preventive in nature, as opposed to corrective maintenance performed to maintain availability of repairable systems. Consider the reliability function shown in Figure 7.6. If the target reliability is 0.9 and the remaining life is 10 years, then this item becomes unacceptable in around $t_u = 8$ years. Four options are available:

(1) Replace item by new item at t_u.
(2) Repair item before t_u(preventive maintenance).
(3) Make a stronger item so that no repair becomes necessary.
(4) Restrict loads.

This section is about the second option. It can be placed in the context of minimizing the total expected cost (Eq. 58) subject to constraints like budget and reliability. Repair can be either perfect (in which the item is made as new) or partial (only a fraction of original strength is restored). The question is, how is the reliability function altered due to periodic maintenance? In other words, how can the conditional reliability $\mathrm{Rel}(t|M_{0:t})$, given the maintenance plan, M, up to time t, be described? Please note that one is still looking into the future when trying to predict $\mathrm{Rel}(t|M_{0:t})$—i.e., the analyst's position on the time axis is $t = 0$. Thus, the conditional reliability function would still have the essential properties of the unconditional reliability—namely, it is a non-increasing function that drops from 1 to 0 with time.

Although not recommended, but as some authors do, one could also add the survival history up to time t and repeat the question. The difference is subtle but important. This would happen if the analyst were placed at some point in time in the future—

say, at t_0—and asked how the reliability function would behave henceforth. That is, one would estimate the conditional reliability $\mathrm{Rel}(t|M_{0:t}, S_{0:t})$ where S gives the survival information up to time t. The plot of $\mathrm{Rel}(t|M_{0:t}, S_{0:t})$ would no longer behave monotonically but would jump to 1 at each discontinuous point t_0 where the structure is known to have survived. It is easy to show that this jump would happen even in the absence of any maintenance operation, just due to the fact that the structure survived up to t_0. $\mathrm{Rel}(t|M_{0:t}, S_{0:t})$ is not a reliability function in the strict sense; rather, it is a piecewise juxtaposition of several reliability functions and must be interpreted cautiously.

5.2.1 Perfect vs. imperfect repair

To illustrate, assume that only one maintenance operation is performed on the structure, which occurs at time t_R. It is convenient to start with the hazard function. It is altered due to the maintenance operation:

$$h(t) = \begin{cases} h_0(t), t < t_R \\ h_1(t), t \geq t_R \end{cases}. \tag{82}$$

The reliability function (Eq. 60) then becomes

$$\mathrm{Rel}(t) = \begin{cases} \mathrm{Rel}(t), & t < t_R \\ \mathrm{Rel}(t_R)\exp\left[-\int_{t_R}^{t} h_1(\tau)d\tau\right], & t \geq t_R \end{cases}. \tag{83}$$

If perfect repair is undertaken at t_R, then the hazard function undergoes a time shift:

$$\text{Perfect repair at } t_R : h_1(t) = h_0(t - t_R),\ \ t \geq t_R, \tag{84}$$

and the reliability function is repeated as a scaled version of itself:

$$\text{Perfect repair at } t_R : \mathrm{Rel}\left(t|\, M_{t_R}^{100\%}\right) = \begin{cases} \mathrm{Rel}(t), & t < t_R \\ \mathrm{Rel}(t_R)\cdot \mathrm{Rel}(t - t_R), & t \geq t_R \end{cases}. \tag{85}$$

The event ${M_{t_R}}^{100\%}$ signifies 100% repair at time t_R.

Generalizing, if the repair is imperfect, one starts with the second factor in Eq. (83) for$t \geq t_R$ and rewrites it as

$$\begin{aligned} \exp\left[-\int_{t_R}^{t} h_1(\tau)d\tau\right] &= \exp\left[-\int_{0}^{t-t_R} h_1(\tau + t_R)d\tau\right] \\ &= \exp\left[-\int_{0}^{t-t_R} h_1^{'}(\tau)d\tau\right] \\ &= \mathrm{Rel}^{'}(t - t_R) \end{aligned}, \tag{86}$$

where $h_1^{'}$ is a legitimate hazard function (generally different from h_0, due to the imperfect nature of the repair), and Rel'(t) is the corresponding reliability function, which is generally different from (and less benign than) Rel(t). The reliability function due to imperfect repair can then be written as

$$\text{Imperfect repair at } t_R : \mathrm{Rel}\left(t \middle| M_{t_R}^{\alpha\%}\right) = \begin{cases} \mathrm{Rel}(t), & t < t_R \\ \mathrm{Rel}(t_R) \cdot \mathrm{Rel}^{'}(t - t_R), & t \geq t_R \end{cases}. \tag{87}$$

${M_{t_R}}^{\alpha\%}$ represents imperfect repair at time t_R in which the strength is restored to $\alpha\%$ of the initial value.

If, in addition, the condition is imposed that the structure is found to survive at t_R, then the conditional reliability starts from 1 at t_R, as stated before, and all past information is erased:

$$\begin{aligned} \mathrm{Rel}\left(t \middle| T > t_R, M_{t_R}^{\alpha\%}\right) &= \frac{P\left[T > t \middle| M_{t_R}^{\alpha\%}\right]}{P\left[T > t_R \middle| M_{t_R}^{\alpha\%}\right]}, \quad t \geq t_R \\ &= \frac{\mathrm{Rel}\left(t \middle| M_{t_R}^{\alpha\%}\right)}{\mathrm{Rel}(t_R)}, \quad t \geq t_R \\ &= \mathrm{Rel}^{'}(t - t_R), \quad t \geq t_R \end{aligned}. \tag{88}$$

Example 7.5. We repeat Example 7.4 with (i) perfect repair (i.e., $\alpha = 100\%$) and (ii) imperfect repair ($\alpha = 90\%$) of the cable performed at 5 years. The red lines in Figure 7.8 depicts the effect of perfect repair. It is clear that, due to the repair, the reliability function stays above 0.9 at the end of the 10-year life, as required. However, note that the reliability function never increases with time: at t_R, its slope changes to a more benign value due to repair. The green lines in Figure 7.8 correspond to $\alpha = 90\%$. The effect is not as good as perfect repair, as can be expected.

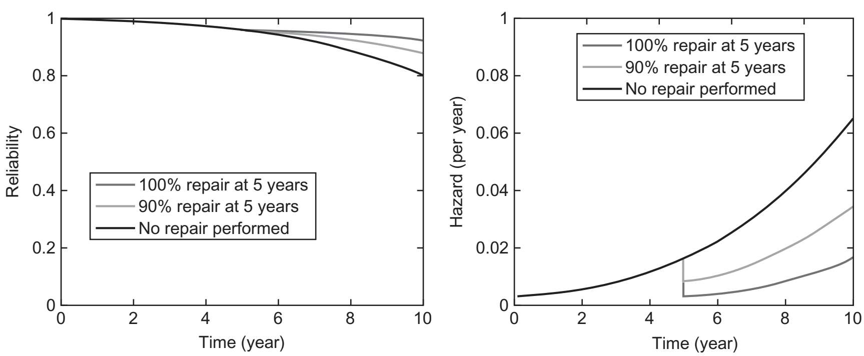

Figure 7.8 Effect of perfect and partial repair on reliability and hazard functions.

Table 7.4 Benefit–Cost Analysis for Cable Repair Options

Option	C_R	$h(t)\Delta(t)$	Risk of Failure	Risk Reduction	BCR
100% repair	\$100,000	0.004	\$40,000	\$160,000	1.6
90% repair	\$50,000	0.01	\$100,000	\$100,000	2.0
No repair	0	0.02	\$200,000	0	1

5.2.2 Benefit–cost ratio of repair strategies

A benefit–cost ratio is a useful metric in decision making. In the context of repair strategies, the cost of repair, C_R, is deterministic; however, if the purpose of repair is prevention of failure, then the benefit is uncertain. An appropriate measure of benefit in this case is risk reduction, and the benefit–cost ratio becomes

$$\mathrm{BCR} = \frac{\Delta(\mathrm{Risk})}{C_R} = \frac{\Sigma PC - \Sigma P'C'}{C_R}, \tag{89}$$

where the primes indicate the values after repair. This ratio can be further improved by bringing in consideration of probability weighting and subjective value of cost (Cha and Ellingwood, 2013).

Example 7.6. Consider the repair strategies for the cable in Example 7.5. The cost of failure of the cable is \$10,000,000. The 100% repair costs \$100,000, whereas the 90% repair costs \$50,000. Which option is better from a BCR point of view?

We consider annual risk reduction for the year immediately after the repair. The probability of failure is approximately $h(t)\Delta(t)$, where h is the hazard function, and here $\Delta(t)$ is 1 year. Table 7.4 shows the expected benefit for the three options. For this example, partial repair turns out to be the best option.

6. Load and resistance factor design and rating methodologies

The Ontario Highway Bridge Design Code (OHBDC) released in 1978 was the first-ever reliability-based standard for bridges (Csagoly and Dorton, 1978); it was subsequently replaced by the national standard CSA S6-00 in 2000. In 1988, the Transportation Research Board in Washington, D.C., commissioned NCHRP Project 12–33 in order to assess the feasibility of revising the existing working stress design methodology for highway bridges on a probabilistic basis. The result was the publication of the first edition of AASHTO LRFD Highway Bridge Design Specifications in 1994 (it is currently in its ninth edition (AASHTO, 2020)); the load and resistance factors (LRFs) were calibrated on the basis of a global population of bridges (Nowak, 1995; NCHRP, 2001).

As part of periodic inspection, a bridge may need to be rated for load carrying capacity. Load-rating a bridge gains urgency in face of changed traffic pattern or due to any change in health of the bridge. When load-rating a bridge, the best model is the bridge itself. By monitoring the bridge, one can gather in-service traffic and performance data and conduct in-service evaluations.

NCHRP Project 12–46 (NCHRP, 2001) led to the development of a reliability-based bridge rating manual (AASHTO, 2003) that was consistent with AASHTO's reliability-based LRFD approach for design of new bridges. The method was termed *load and resistance factor rating* (LRFR), and like LRFD, LRFR specifications were still based on design parameters and non-site-specific data. Nevertheless, they did open the door for using site-specific information to load-rate bridges—e.g., by using weigh-in-motion data and obtaining site-specific live load factors. The recent AASHTO Manual for Bridge Evaluation (AASHTO, 2015) includes the older deterministic allowable stress and load factor rating methodologies in addition to the modern LRFR approach for condition evaluation of bridges.

The load-rating equation for existing bridges is of the general form (Wang et al., 2011a)

$$RF = \frac{\phi C_n - \gamma_D D_n}{\gamma_L (L_n + I_n)}, \tag{90}$$

where I is the nominal capacity, D_n is the nominal dead load, L_n is the nominal live load, and I_n is the nominal impact. ϕ, γ_D, γ_L are, respectively, the capacity, dead load and live load factors. The rating may be performed at various live load levels—inventory, operating,etc. The factors may be derived from probabilistic considerations.

It may be relatively time consuming and expensive to inspect and instrument every bridge in a jurisdiction's inventory. (Bhattacharya et al., 2005) If in-service response from a limited number of sites can be deemed representative of a larger suite of bridges, the rating factors can be optimized for the entire suite of bridges (similar to the principle applied in LRFD and LRFR), and bridge owners may determine the safety of bridges in their inventory using such optimized rating equations. The factors can be adjusted to take care of aging (Bhattacharya et al., 2008b) and system (Wang et al., 2011b) effects.

7. Summary

Various sources of uncertainty affect a bridge structure during its life: first at the design stage, then during construction, and then throughout its useful life after it has been put into service. These uncertainties are modeled as random variables, random processes, or random fields, as appropriate. Performance requirements of a bridge are described in terms of limit state functions. The exceedance probabilities of these limit states—i.e., the probabilities of nonperformance—need to be kept within acceptable limits. Reliability-based design and maintenance, whether through first principles or by using codes of practice, can ensure compliance. There are various methods of deciding acceptable failure probabilities (or, equivalently, target reliabilities). Once the bridge is put into service, its load characteristics may change, and the structure may be subjected to various forms of (generally random) deterioration. Time-dependent reliability analyses of an aging bridge, coupled with preventive maintenance, can ensure that reliability does not fall below acceptable limits. A suite of bridges can be rated in service by optimized site-specific partial safety factors.

As bridge inventories around the world grow in size and diversity, the owners and managers are faced with an increasing population of aging bridges under their care. Not only do they need to build new bridges to satisfy the growing needs of travel and commerce; they also need to allocate enough resources to maintain the existing ones safely and economically. As a consequence, the need to address robustness in design (Bhattacharya, 2021) and resilience of an infrastructure system (Koliou et al., 2018) has gained urgency.

References

AASHTO, 2003. Guide Manual for Condition Evaluation and Load and Resistance Factor Rating (Lrfr) of Highway Bridges. American Assoc. of State Highway and Transportation Officials, Washington, DC.

AASHTO, 2012. Lrfd Highway Bridge Design Specifications, sixth ed. Washington, DC, American Assoc. of State Highway and Transportation Officials.

AASHTO, 2015. Manual for Bridge Evaluation. American Assoc. of State Highway and Transportation Officials, Washington, DC.

AASHTO, 2020. Lrfd Highway Bridge Design Specifications, ninth ed. American Assoc. of State Highway and Transportation Officials, Washington, DC.

ABS, 1999. Draft mobile offshore base classification guide.

Agrawal, G., Bhattacharya, B., 2010. Optimized partial safety factors for the reliability based design of rectangular prestressed concrete beams. J. Struct. Eng. 37, 263–273. SERC Madras.

Allen, D.E., 1981. Criteria for design safety factors and quality assurance expenditure. In: Third International Conference on Structural Safety and Reliability, pp. 667–678.

Almeida, J.O., Teixeira, P.F., Delgado, R.M., 2015. Life cycle cost optimisation in highway concrete bridges management. Struct. Infrastruct. Eng. 11, 1263–1276.

Ang, A.H.S., Tang, W.H., 1975. Probability Concepts in Engineering Planning and Design. Wiley, New York.

Anitori, G., Casas, J.R., Ghosh, M., 2017. Wim-based live-load model for advanced analysis of simply supported short- and medium-span highway bridges. J. Bridge Eng., ASCE 22, 04017062.

ASCE, 2016. Asce 7–16: Minimum Design Loads and Associated Criteria for Buildings and Other Structures. Reston, USA, American Society of Civil Engineers.

ATC, 1996. Atc-40 siesmic evaluation and retrofit of existing concrete buildings.

Au, S., Beck, J., 2001. Estimation of small failure probabilities in high dimensions by subset simulation. Probabil. Eng. Mech. 16, 263–277.

Ayyub, B.M., McCuen, R.H., 1995. Simulation-based reliability methods. In: Sundararajan, C. (Ed.), Probabilistic Structural Mechanics Handbook : Theory and Industrial Applications. Chapman Hall, New York.

Bennet, R.M., Ang, A.H.-S., 1986. Formulation of structural system reliability. J. Eng. Mech., ASCE 112, 1135–1151.

Bhattacharya, B., 2008. The extremal index and the maximum of a dependent stationary pulse load process observed above a high threshold. Struct. Saf. 30, 34–48.

Bhattacharya, B., 2021. A reliability based measure of structural robustness for coherent systems. Struct. Saf. 89. Elsevier.

Bhattacharya, B., Basu, R., Ma, K.-T., 2001. Developing target reliability for novel structures: the case of the mobile offshore base. Mar. Struct. 14, 37–58.

Bhattacharya, B., Li, D., Chajes, M.J., Hastings, J., 2005. Reliability-based load and resistance factor rating using in-service data. J. Bridge Eng., ASCE 10, 530–543.

Bhattacharya, B., Li, D., Chajes, M.J., 2008a. Bridge rating using in-service data in the presence of strength deterioration and correlation in load process. Struct. Infrastruct. Eng. 4, 237–249. Taylor and Francis.

Bhattacharya, B., Li, D., Chajes, M.J., 2008b. Bridge rating in the presence of strength deterioration and correlation in load process. Struct. Infrastruct. Eng. 4, 237–249.

Bhattacharya, B., Lu, Q., Zhong, J., 2009. Reliability of redundant ductile structures with uncertain system failure criteria: a study on a highway steel girder bridge. Sadhana 34, 903–921. Indian Academy of Sciences.

Birolini, A., 1999. Reliability Engineering Theory and Practice. Springer-Verlag New York, Inc.

Bjerager, P., 1988. Probability integration by directional simulation. J. Eng. Mech., ASCE 114, 1285.

Bjerager, P., Karamchandani, A., Cornell, C.A., 1987. Failure tree analysis in strucutral system reliability. In: ICASP 5.

Bottelberghs, P.H., 1995. Qra in the Netherlands. Conference on Safety Cases. IBC/DNV.

Cha, E.J., Ellingwood, B.R., 2013. The role of risk aversion in nuclear plant safety decisions. Struct. Saf. 44, 28–36. Elsevier.

Cherry, J.L., Smith, J.A., 2001. Capacity of Steel and Concrete Containment Vessels with Corrosion Damage, Nureg/Cr-6706.

CIRIA, 1977. Construction industry research and information association. Rationalization of safety and serviceability factors in structural codes, CIRIA, report no. 63.

Cooke, R.M., Goossens, L.L.H.J., 2008. Tu delft expert judgment data base. Reliab. Eng. Syst. Saf. 93, 657–674.

Cornell, C.A., 1967. Bounds on the reliability of structural systems. J. Struct. Div. ASCE ST1, 171–200.

Cornell, C., Jalayer, F., Hamburger, R., Foutch, D., 2002. Probabilistic basis for 2000 sac federal emergency management agency steel moment frem guidelines. J. Struct. Eng. ASCE 128, 526–533.

Corotis, R.B., Nafday, A.M., 1989. Structural system reliability using linear programming and simulation. J. Struct. Eng. ASCE 115, 2435–2447.

CSA, 1992. General requirements, design criteria, the environment, and loads. A national standard of Canada.

Csagoly, P., Dorton, R.A., 1978. The development of the ontario highway bridge design code. Transportation Research Record No. 665, Bridge Engineering, Volume 2.

der Kiureghian, A., Liu, P.-L., 1986. Structural reliability under incomplete probability information. J. Eng. Mech., ASCE 112, 85–104.

Ditlevsen, O., 1979. Narrow reliability bounds for structural systems. J. Struct. Mech. 7, 453–472.

Ditlevsen, O., 1982. Model uncertainty in structural reliability. Struct. Saf. 1, 73–86.

Ditlevsen, O., Bjerager, P., 1986. Methods of structural systems reliability. Struct. Saf. 3, 195–229.

DNV, 1992. Structural reliability analysis of marine structures, classification notes no. 30.6.
Ellingwood, B.R., 2000. Lrfd: implementing structural reliability in professional practice. Eng. Struct. 22, 106–115.
Ellingwood, B.R., Galambos, T.V., 1982. Probability-based criteria for structural design. Struct. Saf. 1, 15–26.
Ellingwood, B.R., Galambos, T.V., MacGregor, J.G., Cornell, C.A., 1980. Development of a Probability Based Load Criterion for American National Standard a58. nbs Special Publication 577.
Enright, B., Carey, C., Caprani, C.C., 2013. Microsimulation evaluation of Eurocode load model for American long-span bridges. J. Bridge Eng., ASCE 18, 1252–1260.
Eurocodes, 2002. En 1990, eurocode–basis of structural design. European Committee for standardization, Brussels, Belgium.
FEMA, 1997. Fema-273 nehrp guidelines for the siesmic rehabilitation of buildings.
FEMA, 2000. Fema-350 recommended seismic design criteria for new steel moment-frame buildings.
Frangopol, D.M., Dong, Y., Sabatino, S., 2017. Bridge life-cycle performance and cost: analysis, prediction, optimisation and decision-making. Struct. Infrastruct. Eng. 13, 1239–1257.
Freudenthal, A.M., 1947. The safety of structures. Trans. Am. Soc. Civ. Eng. 112.
Fricke, W., Muller-Schmerl, A., 1998. Uncertainty modeling for fatigue strength assessment of welded structures. J. Offshore Mech. Arctic Eng. 120, 97–102.
Galambos, J., 1987. The Asymptotic Theory of Extreme Order Statistics. Krieger, Malabar, FL.
Galambos, T.V., 1992. Design codes. In: Blockley, D. (Ed.), Engineering Safety. McGraw Hill, pp. 47–69.
Gallegos, D.P., Bonano, E.J., 1993. Consideration of uncertainty in the performance assessment of radioactive waste disposal from an international regulatory perspective. Reliab. Eng. Syst. Saf. 42, 111–123.
Ghanem, R.G., Spanos, P.D., 2012. Stochastic Finite Elements: A Spectral Approach. Dover.
Ghosn, M., Moses, F., 1998. Redundancy in Highway Bridge Superstructures, Report 406.
Gorman, M.R., 1981. Automatic generation of collapse mode equations. J. Struct. Div.ASCE 107, 1350–1354.
Guzda, M., Bhattacharya, B., Mertz, D., 2007. Live load distribution on highway bridges using in-service bridge monitoring system. J. Bridg. Eng. 12, 130–134.
Hasofer, A.M., Lind, N.C., 1974. Exact and invariant second-moment code format. J. Eng. Mech., ASCE 100, 111–121.
Hines, W.W., Montgomery, D.C., Goldsman, D.M., Borror, C.M., 2003. Probability and Statistics in Engineering. Wiley, Hoboken, NJ.
Hohenbichler, M., Rackwitz, R., 1983. First-order concepts in system reliability. Struct. Saf. 1, 177–188.
IMO, 2000. Formal safety assessment.
ISO, 2012. Iso 13822:2010 bases for design of structures - assessment of existing structures.
ISO, 2015. General principles on reliability for structures iso 2394. International Organization for Standardization, Geneva.
JCSS, 2015. Probabilistic model code, 12th draft. 2001.
Karamchandani, A., 1987. Structural system reliability analysis methods. In: Reliability of Marine Structures Program.
Karamchandani, A., Cornell, C.A., 1992a. Reliability analysis of truss structures with multistate elements ii. J. Struct. Eng. ASCE 118, 910–925.
Karamchandani, A., Cornell, C.A., 1992b. An event-to-event strategy for nonlinear analysis of truss structures i. J. Struct. Eng. ASCE 118, 895–909.

Keeney, R.L., Dv, W., 1991. Eliciting probabilities from experts in complex technical problems. IEEE Trans. Eng. Manag. 38, 191–201.
Kingery, C., Bulmash, G., 1984. Airblast Parameters from tnt Spherical Air Burst and Hemispherical Surface Burst. U.S. Army Armament Research and Development Centre, Aberdeen Proving Ground, MD, USA.
Kingman, J.F.C., 2002. Poisson Processes. Oxford,.
Koliou, M., Lindt, J., McAllister, T., Ellingwood, B., Dillard, M., Cutler, H., 2018. State of the research in community resilience: Progress and challenges. Sustain. Resil. Infrastruct. 5, 131–151. Taylor and Francis.
Kovalenko, I.N., Kuznetsov, N.Y., Shurenkov, V.M., 1996. Models of Random Processes: A Handbook for Mathematicians and Engineers. CRC Press, Inc, Boca Raton.
Kwon K, Frangopol DM. Bridge fatigue assessment and management using reliability-based crack growth and probability of detection models. Probabil. Eng. Mech..26:471–480.
Lin, Y.K., 1976. Probabilistic Theory of Structural Dynamics. Krieger, Huntington, NY.
Lind, N.C., 1993. Target reliability levels from social indicators. In: 6th International Conference on Structural Safety and Reliability.
Lind, N.C., Nowak, A.S., 1988. Pooling expert opinions on probability distributions. J. Eng. Mech. 114, 328–341.
MacGregor, J.G., Laurie Kennedy, D.J., et al., 1997. Design criteria and load and resistance factors for the confederation bridge. Can. J. Civ. Eng. 24, 882–897.
Mander, J., Elms, D., 1993. Quantitative risk assessment of large structural systems. In: Sixth International Conference on Structural Safety and Reliability, pp. 1905–1912.
Melchers, R.E., 1987. Structural Reliability Analysis and Prediction. Ellis Horwood, Chricester, UK.
Melchers, R.E., 1990. Radial importance sampling for structural reliability. J. Eng. Mech., ASCE 116, 189–203.
Moan, T., 1997. Current trends in the safety of offshore structures. In: 7th ISOPE Conference.
Moses, F., 1997. Problems and prospects of reliability-based optimization. Eng. Struct. 19, 293–301.
NCHRP, 2001. Calibration of load factors for lrfr bridge evaluation, report 454.
NCHRP, 2003. Bridge life-cycle cost analysis, report 483.
Nikolaidis, E., Kaplan, P., 1991. Uncertainties in Stress Analyses on Marine Structures.
Nowak, A.S., 1993. Live load model for highway bridges. Struct. Saf. 13, 53–66.
Nowak, A.S., 1995. Calibration of lrfd bridge code. J. Struct. Eng. ASCE 121, 1245–1251.
Nowak, A.S., Szerszen, M.M., Park, C.H., 1997. Target safety levels for bridges. In: 7th International Conference on Structural Safety and Reliability.
Papoulis, A., Pillai, S.U., 2002. Probability, Random Variables, and Stochastic Processes. McGraw-Hill, New York.
Rackwitz, R., Fiessler, B., 1978. Structural reliability under combined random load sequences. Comput. Struct. 9, 489–494.
Resnick, S., 1999. A Probability Path. Birkhauser, Boston.
Rosen, J.B., 1961. The gradient projection method for nonlilnear programming. Part ii. Nonlinear constraints. J. Soc. Ind. Appl. Math. 9, 514–532.
Sarveswaran, V., Roberts, M., 1999. Reliability analysis of deteriorating structures - the experience and needs of practising engineers. Struct. Saf. 21.
SEAOC, 1995. Vision 2000, performance based seismic engineering of buildings. I and II:Conceptual framework.
Sen, D., Bhattacharya, B., 2015. On the pareto optimality of variance reduction simulation techniques in structural reliability. Struct. Saf. 53, 57–74. Elsevier.

Shao, S., Murotsu, Y., 1999. Approach to failure mode analysis of large structures. Probabil. Eng. Mech. 14, 169–177.

Shinozuka, M., 1983. Basic analysis of structural safety. J. Struct. Eng. ASCE 109, 721–740.

Shinozuka, M., Sato, Y., 1967. Simulation of nonstationary random processes. J. Eng. Mech. Div., ASCE 93, 11–40.

Steenbergen, R.D.J.M., Sykora, M., Diamantidis, D., Holicky, M., Vrouwenvelder, T., 2015. Economic and human safety reliability levels for existing structures. Struct. Concr.

Stewart, M.G., Netherton, M.D., Baldacchino, H., 2019. Observed airblast variability and model error from repeatable explosive field trials. Int. J. Protect. Struct. 11, 235–257. Sage.

Suzuki, H., 1999. Safety target of very large floating structure used as a floating airport. In: Third International Workshop on Very Large Floating Structures, pp. 607–612.

Thoft-Christensen, P., Murotsu, Y., 1986. Application of Structural Systems Reliability Theory. Springer-Verlag, Berlin.

Vanmarcke, E., 1983. Random Fields: Analysis and Synthesis. MIT Press, Cambridge, MA.

Wang, N., O'Malley, C., Ellingwood, B.R., Zureick, A.-H., 2011a. Bridge rating using system reliability assessment. I: assessment and verification by load testing. J. Bridge Eng., ASCE 16, 854–862.

Wang, N., O'Malley, C., Ellingwood, B.R., Zureick, A.-H., 2011b. Bridge rating using system reliability assessment. Ii: improvements to bridge rating practices. J. Bridge Eng., ASCE 16, 863–871.

Watwood, V.B., 1979. Mechanism generation for limit analysis of frames. J. Struct. Div. ASCE 109, 1–15.

Wen, Y.-K., 1990. Structural Load Modeling and Combination for Performance and Safety Evaluation. Elsevier, Amsterdam.

Wen, Y.-K., 2001. Minimum lifecycle cost design under multiple hazards. Reliab. Eng. Syst. Saf. 73, 223–231.

Whittaker, A., Constantinou, M., Tsopelas, P., 1998. Displacement estimates for performance-based seismic design. J. Struct. Eng. 124, 905–912.

Yun, S., Hamburger, R.O., Cornell, C.A., Foutch, D.A., 2002. Seismic performance evaluation of steel moment frames. J. Struct. Eng. 128, 534–545.

Zimmerman, J.J., Ellis, J.H., Corotis, R.B., 1993. Stochastic optimization models for structural reliability analysis. J. Struct. Eng. ASCE 119, 223–239.

Zio, E., Apostolakis, G.E., 1996. Two methods for the structures assessment of model uncertainty by experts in performance assessments of radioactive waste repositories. Reliab. Eng. Syst. Saf. 54, 225–241.

This page intentionally left blank

Innovative structural typologies

8

Sigrid Adriaenssens[a] *and Annette Boegle*[b]
[a]Princeton University, NJ, USA, [b]HafenCity Universität, Hamburg, Germany

1. Introduction: Aim and context

The objective of this chapter is to demonstrate how advances in computational form-finding, optimization, and digital fabrication techniques have brought about a new realm of bridge typologies. The engineering design of bridges requires the solution of a complex brief that stipulates economic cost, technical quality, ease of maintenance, durability, site suitability, and esthetic appeal. Solutions that satisfy these criteria are not unique. In the past, engineers identified feasible instances using trial and error, accumulated knowledge, and deductive reasoning. Today, computational tools are available to the bridge designer to aid decision making and steer the design process to novel typology solutions. These tools in the engineer's toolbox are most useful in the preliminary design stage, where they can achieve the most gain in terms of economic and environmental cost (Mueller, 2014).

There are at least five distinct reasons that these new techniques have not been widely embraced. First, form-finding and optimization techniques are perceived as implying a large computational cost, which is undesirable in a preliminary design context. Second, the design solutions generated by these techniques are wrongly thought to entail fragility and lack robustness or redundancy. Third, in contrast with products from the automotive and aerospace industries, the uniqueness of each bridge project excludes the repetition of gains. Fourth, the limitations of overconstrained bridge design codes might not allow unconventional typologies generated by these computational techniques. Finally, with the exception of a few instances, these computational methods are not taught in a traditional undergraduate or graduate civil engineering curriculum and, hence, require expert knowhow, which is unlikely to be available in standard structural design offices.

2. Literature review

This section provides a succinct literature review of numerical form finding, optimization, and computer numerically controlled (CNC) machine techniques that have been integrated into the preliminary design of bridges.

Structural form finding can be defined as a forward process in which parameters are directly controlled to find an "optimal" geometry of a structural system, which is in static equilibrium with one design loading (Adriaenssens et al., 2014). This process is particularly suited for "form-active" and certain "form-passive" bridge typologies that resist external loads, predominantly through axially loaded members or membrane

Innovative Bridge Design Handbook. https://doi.org/10.1016/B978-0-12-823550-8.00035-4

action. The axially loaded members could include the main and the hanger cables of a suspension bridge, the hangers in a bowstring arch bridge, the elements forming an arch, and the struts connecting the bridge deck to a below-deck arch. Membrane stresses, on the other hand, could be taken within the thickness of a structural surface, as in the case of thin shell systems supporting a bridge deck. Initially, the geometry of a structural system is unknown. However, the process may require some arbitrary starting geometry. To steer the form-finding process, the structural designer can manipulate certain parameters, such as (i) the boundary conditions and external loads, (ii) the topology of the model, and (iii) the internal forces and their relationship to the geometry. Once the final shape is found, the numerical model is updated by assigning real physical material and member properties. The rapid feedback of the form-finding program and the interactive designer experience are key to making informed decisions in the preliminary design process. After the form-finding procedure, the designer needs to carry out a rigorous static and dynamic analysis according to relevant bridge design codes.

Several form-finding methods have been used. The force density method (Scheck, 1974) for instance solves the problem of static equilibrium without requiring material properties. Descamps et al. (2011), for example, used this method for generation of the geometry of three-dimensional (3D) systems of suspension bridges and arches. To balance stress levels in the hanger attached to a rigid bowstring, Caron et al. (2009) used the same force density technique. An extended form of this technique was developed by Quagliaroli and Malerba (2013) for flexible bridge decks suspended by cable nets. An alternative computational form-finding approach, the dynamic relaxation method (Day, 1965), incorporates fictitious material stiffness and element properties to solve for equilibrium. Methodologies have been presented based on dynamic relaxation to find the shape of a shallow arch (Halpern and Adriaenssens, 2014), suspension (Segal et al., 2015) and tensegrity (Rhode-Barbarigos et al., 2010) bridges.

Most academic work related to bridge optimization can be found in the domain of economic cost and maintenance optimization (Ayd and Ayvaz, 2013; Hassan et al., 2013); however, this chapter focuses on optimization approaches that affect the bridge topology, not their shape or the size of their elements. In this context, structural optimization is an inverse process in which parameters are indirectly optimized to find the optimal structural layout of a bridge system such that an objective function or fitness criterion is minimized. Fauche et al. (2010) demonstrated the use of topology optimization as a design tool for a thin-shelled bridge structure. Their optimization routine, which was coupled to a finite element analysis, aimed at maximizing compliance and finds its solution using the fixed point iteration method. Briseghella et al. (2013) also proposed a slightly different topology optimization approach for shell bridge design by minimizing compliance using a solid isotropic material with penalization algorithm. Nagase and Skelton (2014) presented a design methodology for tensegrity bridges, which is based on parametric design concepts, fractal geometry, and mass minimization through an iterative linear programming approach. To minimize operational energy, Thrall et al. (2012) employed simulated annealing to optimize the topology of deployable linkage bridges. Rahmatalla and Swan (2003) developed a methodology that optimizes the topology of truss bridges to maximize buckling stability. Using the homogenization method with the objective of maximizing stiffness, Lochner-Aldinger (2011) demonstrated how two-dimensional (2D) bridge topologies could be generated to inform footbridge design using the homogenization method. Islam et al. (2014) used a global optimization algorithm, evolutionary operation (EVOP), to minimize the cost of a network arch bridge by varying geometric shape, rise-to-span ratio, cross-section of arch and hangers, and topology of the hangers.

In traditional bridge construction, techniques to manufacture members rely on material subtraction, deformation (such as bending), and casting methods. Many of these methods predate the arrival of the computer and have recently been adjusted to suit a numerical control process (Schodek et al., 2005). As a result, a person no longer directly operates the machine; computer algorithms do. Other more recent manufacturing processes (such as lasers) completely depend upon computer technologies for both their operation and control. Based on a computer-aided design (CAD) manufacturing layout file, the machine itself prepares a set of commands, reads them, and instructs tools to execute coded movements. There are two benefits of CNC tools for the design and construction of bridges. First, these tools can be more accurate, faster, and more economical than conventional machines for the manufacture of bridge components. Second, they can facilitate the construction of novel components needed for nontraditional bridge typologies (Adriaenssens et al., 2009).

3. 3D bridges force-modeled for one loading condition

Throughout history, engineers have been shaping bridge systems (or, more specifically, their structural elements) to follow the flow of forces. Their objective was to obtain a dominant load-bearing behavior with tension or compression, minimizing any shear and avoiding bending. In particular, since the 17th century, when the first interactions between science and building practice became visible, various form-finding methods were developed. Long before the development of numerical methods, these form-finding techniques were based on physical experiments. It was, for example, British architect-philosopher Robert Hooke (1635–1703) who formulated the ideal shape of an arch through a hanging model and its inversion. Experimental form finding was (and still is) considered to be good practice, but a strong restriction remains—namely, that it can be applied for only one load condition.

Thus, the geometry of early force-modeled bridges is carefully formed, but it only works because of a larger self-weight and a comparatively lower life load. One of the pioneers of using physical hanging models for form finding was Spanish architect Antoni Gaudi (1852–1926), known for his virtuously shaped arches and vaults. For example, the crypt in his Güell Chapel and the arches in his Casa Mila are all perfectly shaped for a high self-weight, which is true of the stone material they are constructed from. Connected to his garden designs, he developed a number of bridge designs. Some were realized as viaducts, like the Park Güell (shown in Figure 8.1), while others were unrealized, like the bridge over the Torrent de Pomeret between Sarrià and Sant Gervasi, on the outskirts of Barcelona, Spain.

Figure 8.1 Gaudí's design and construction of a force-modeled viaduct in the Park Güell (https://creativecommons.org/licenses/by-sa/2.0/legalcode; Valerie Hinojosa).

Physical form finding methods were essential for the visionary structures of Italian architect Sergio Musmeci (1926–1981). At a time where numerical methods were not available, he designed prestressed spatial membrane structures based on the idea of minimal surfaces and inverted them into shell structures under compression. Thereby, the Basento Viaduct in Potenza, built in 1969, is said to be his masterpiece (Figure 8.2). A slender continuous shell structure serves as the load-bearing system and experiences uniform but not isotropic compression stresses. The form-finding process started with soap models, but the most promising results were achieved with the second generation of experiments. With this viaduct, Musmeci used a neoprene material; the model was not only more stable than the soap models, but also able to model the nonisotropic behavior typical of a concrete membrane. Last, but not least, a large-scale model (two segments, scale 1:10) made of microconcrete was created in Bergamo's laboratory. This model was essential to optimize the form, to obtain

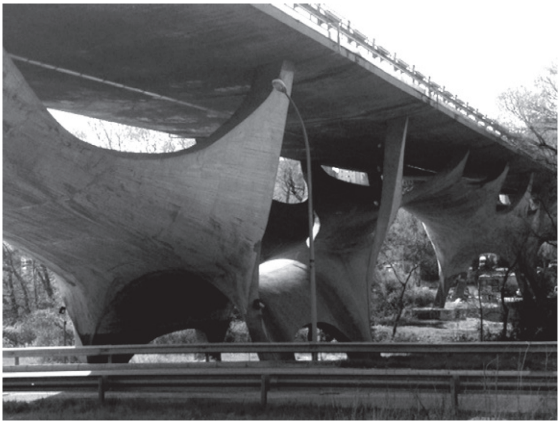

Figure 8.2 The form finding process of the Basento Bridge employed several physical techniques, including the pre-stressing of membranes.

information about the strains and stresses, and to discuss details and questions concerning the construction process. The resulting bridge is a magnificent, spatial, concrete structure that gets its aesthetics directly from its efficiency.

Another typology, where spatial equilibrium is achieved through geometry, is the circular ring girder bridge, a pioneering work in efficient 3D load-bearing behavior. These bridges have a distinctive, nonlinear layout of their deck trajectory. Traditionally, the plan layout of a bridge is straight or only slightly curved, which has no major effect on the load-bearing behavior. In contrast, the principle of the circular ring girder allows much more design freedom for footbridges.

The general structural principle behind the circular ring girder, shown in Figure 8.3, is that it needs only a single hinged support either on the inner or outer edge, without flipping downward or being stressed with torsion. Similarly, a straight slab strip needs either a support on both sides or, if only supported on one side, a fixed support. Instead, the circular girder transfers the overturning moment—resulting from dead load or any uniform distributed load—along the supported edge into a bending moment along the horizontal axis. This overturning moment can be replaced by a pair of radial distributed forces along the length of the ring girder, one facing the center of

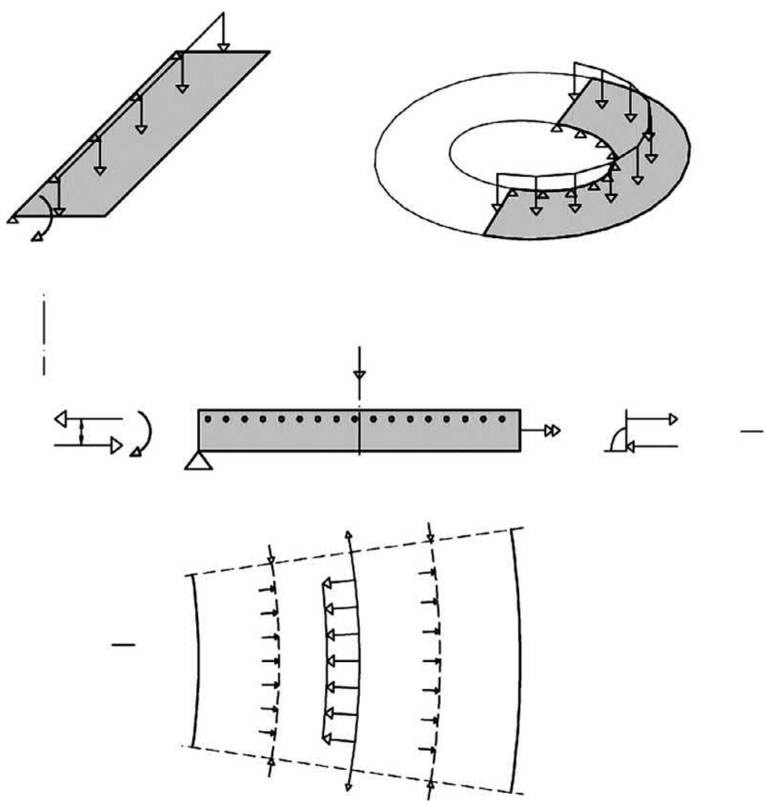

Figure 8.3 Principles behind the structural behavior of the ring girder (Bögle et al., 2003).

the circle, the other pointing in the opposite direction. As in a thin-walled pressure vessel, any radial distributed force along a circular line causes a normal force in the longitudinal direction. Thus, if the circular ring girder rests on the inner edge, a line load causes ring tension on the upper side and ring compression on the lower side of the slab, or vice versa for a line support on the outer edge. Any load with geometric affinity may be supported in this manner, but any loads without geometric affinity, such as point loads or unbalanced live loads, cause moments in the girder that require an appropriate stiffness in the horizontal axis.

Circular ring girders are mostly supported by a suspension cable and inclined hangers. The inclination of the hangers introduces other horizontal forces into the bridge deck, creating other compression ring forces in the deck when supported at the inner edge, and other tension ring forces when supported at the outer edge. The spatial load-bearing behavior of the ring girder, under geometric affined loads, is quite descriptive and does not truly require numerical form-finding techniques. However, the spatial geometry of the suspension cable, the exact inclination of the hangers, and their analysis necessitate numerical form-finding techniques. With the aid of numerical methods, this idea can be developed further (Bögle et al., 2003).

The earliest suspension bridge built on this principle is the footbridge over the Rhine-Main-Danube Canal in Kehlheim, Germany (built in 1987 by the architectural firm schlaich bergermann and partner), which features a compact, prestressed concrete cross section that is supported on the inner edge by inclined hangers. These are attached to a suspension cable, and eventually to a mast and foundations. The compact cross section is structurally inefficient, as only the top layer is structurally fully used. Thus, in later designs, the cross section has been transformed into a network of cables and struts subjected to tension or compression, respectively. The Westpark Bridge in Bochum, Germany (built in 2003 by schlaich bergermann and partner; see Figure 8.4) elegantly illustrates this circular girder typology with network. In this case, the S-shaped walkway (66 m long, each half with a radius of 46 m) is supported on the inner perimeter. The flow of forces is expressed in a lightweight deck, to handle the tensile ring forces, and a circular compact steel strut, to take the compression ring forces beneath the deck. This bridge shows an additional novelty: two inclined masts, each inside one of the semicircles, are stabilized only by the main suspension cable cables (see Figure 8.5). The mast tip, the geometry of the main suspension cable, and the hangars are in spatial balance for one load case. This structural arrangement is sufficient for different load cases even without stay cables because the foundations of the masts are placed lower than the anchorages of the cables. Then, each individual load case leads to a new equilibrium geometry, and here, stability is coupled to deformation.

Further optimization will be reached if any overturning moment due to self-weight or any uniformly distributed load is completely avoided. This equilibrium can be achieved if the resulting force of the hangers passes through the gravity center of the deck. In the practical sense, this requires a deck with cantilevers of different heights to connect to the hangers as in the "balcony to the sea" bridge in Saßnitz, Germany (built in 2007 by schlaich bergermann and partner). This 120-m span suspension bridge only acts as a circular ring girder when a lateral pedestrian load is applied, with both a compression ring below and a tension ring on the deck level.

Figure 8.4 The spatial geometry of the circular ring girder, suspension cables, and inclined mast of the West Park Bridge, Bochum, Germany © Nicolas Janberg (www.structurae.de).

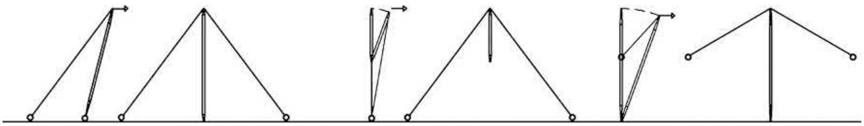

Figure 8.5 The geometry of the inclined masts in spatial equilibrium.

Other realized projects have added to the potential of the principle of circular ring girders. For example, the Footbridge Harbor Grimberg in Gelsenkirchen, Germany (built in 2009 by schlaich bergermann and partner) is supported on the outside perimeter of the curve. Its main cables are not anchored on the abutments, but instead are 24 m in front of them (see Figure 8.6). In this case, the bridge has to be designed for torsion and bending as well. The challenge of the form-finding process was to find a stable equilibrium between the anchorage of the main suspension cables, the position and inclination of the mast and hangars, the slenderness of the deck, and the stiffness of the abutment.

According to the principle of inversion, which dates back as far as the 17th century, the inversion of a cable-suspended bridge leads to an arch bridge, including all the structural challenges arising from a thin arch under compression. There are various examples existing, a few of them already exploring spatial values concerning aesthetics and structural behavior. Further, by inverting the spatial main cable of a cable-suspended ring girder, an impressive spatial curve arises. This lightweight solution provides a structural answer to the challenge of bringing an arch in longitudinal view together with a curve in the plan layout. Initial approaches have been made by

Figure 8.6 Spatial static equilibrium between the different elements of the Footbridge Harbor Grimberg, Gelsenkirchen, Germany (© schlaich bergermann and partner, Michael Zimmermann).

schlaich bergermann and partner (e.g., the footbridge over the Rhine-Herne-Canal, Germany, and footbridges in Esslingen, Germany, and Belfast, Ireland). One of the most recent examples is the design of FEHCOR for the Salford Meadows Bridge Competition in Salford, UK, shown in Figure 8.7 (2014). A 130-m-long curved pathway, supported on only one side, will be carried by one spatial arch. The form of the spatial arch follows the efficient flow if forces of a circular curved girder are supported on only one side. This extraordinary form is not the result of pure architectural expression, but instead, the result of structural optimization with an arch only under compression for evenly distributed loads. The proposal goes even further when it entirely exploits the possibilities of contemporary structural steel manufacturing, with its capacity to construct spatial and complex shapes without a significant cost increase.

Figure 8.7 The spatial form of the arch follows the flow of forces of the circular deck girder only supported on one side; competition entry, Salford Meadow Bridge (© FEHCOR).

4. 3D bridges, optimized for one or more criteria and composed of surface elements

The advances of CAD manufacturing technologies have introduced a new bridge design vocabulary that is starting to result in new bridge typologies. It is no longer difficult to fabricate designs that involve highly complex, geometrical 3D forms that cannot be described by straight lines and circular arcs. Likewise, the form-finding methods have developed. Originally, numerical form-finding methods could focus on only one parameter and search for the one equilibrium of forces using mainly linear elements. Now, the new numerical methods allow multiobjective optimization. Therefore, the structural focus shifts toward surface elements.

The development of the so-called steel sails is the enhancement of a continuous trough bridge with the webs shaped according to the bending moments. Just like the main cables and hangers in a suspension bridge, these webs experience mainly tensile stress, suggesting that they should be made out of steel. The deck, in compression, is ideally realized in concrete. Dissolving the steel webs more and more leads to elegantly curved sail-like steel plates, suspended from short, reinforced concrete (r.c.) masts. Structurally, this assembly is related to "extradosed bridges," a Japanese variation of multispan cable-stayed bridges with small deflections under heavy loads. Thus, these structures are often used for railway bridges. The load-bearing behavior becomes immediately obvious when flipping its orientation upside down into an inverted strutted frame, as seen in the Felsegg Bridge (designed in 1932 by Robert Maillart), shown in Figure 8.8, or the Ganter Bridge (designed in 1980 by Christian Menn), both in Switzerland. An example of such a bridge with steel sails is the Neckar Rail Bridge (schlaich bergermann and partner), a train bridge in Germany with two main spans of 72 and 78 m and two small side spans (see Figure 8.9).

The idea of using structural steel surface elements aligns with the potential offered by new CNC manufacturing methods (particularly steel-laser-cutting techniques);

Figure 8.8 The shape of the Felsegg Bridge (1932) reflects the inverted form of the Rail Bridge Bad Cannstatt (photo taken by authors).

Figure 8.9 A continuous trough bridge with sidewise webs shaped according to the bending moments, giving the appearance of sails; Rail bridge, Bad Cannstatt, Stuttgart, Germany (competition 1998, completion 2021).

existing typologies can be reinterpreted and constructed more economically and efficiently while new typologies can be envisaged.

The process of fabrication of the Abetxuko Bridge, located in Vitoria, Spain (Pedelta, 2006) across the Zadorra River, illustrates the enormous possibilities available through CAD/CNC techniques (see Figure 8.10). The structural system is a

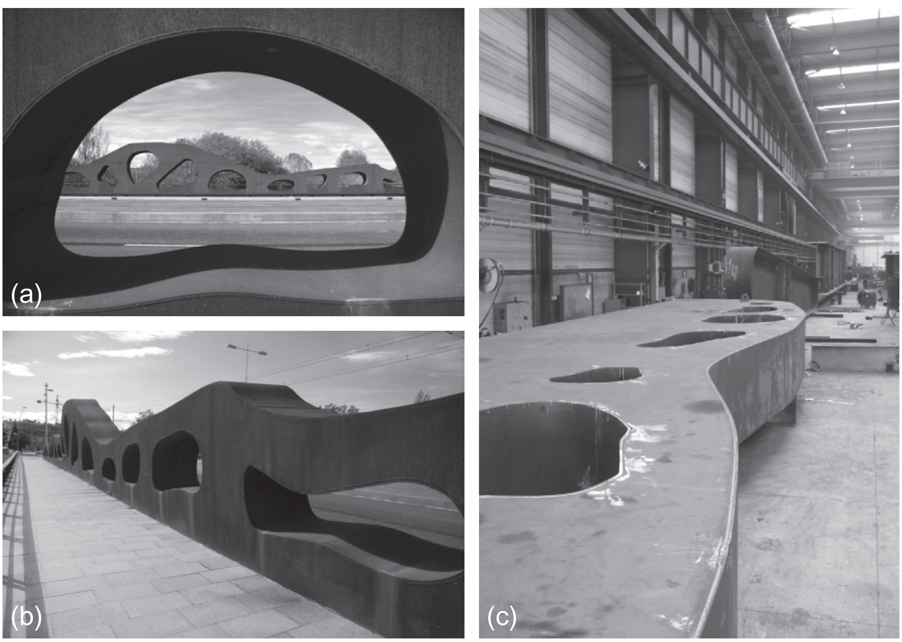

Figure 8.10 The design of the Abetxuko Bridge across the Zadorra River exploited the new formal possibilities of CNC technologies (Pedelta). (Copyright Ricardo Ferraz, TU Berlin, Fachgebiet Entwurf und Konstruktion – Massivbau).

continuous beam is quite simple, with spans of 26 m on its sides and 40 m in the center, but the two trusses make it a true landmark. The organic curved trusses are above the deck and separate the road traffic from the pedestrian walkway on both sides. With its irregular and curved forms, this bridge mirrors a different engineering attitude than the classical one of purity and flow of forces. Still, the dimensions are adjusted according to the structural analysis. The expressive forms were cut, bent, and welded at a local steelyard. Segments were transported to the building site to be finally assembled. Thus, these fabrication techniques allow for divergence from standard geometry.

The last design case study presented here draws on the concepts of the plate-stayed bridge but uses form finding and topology optimization to generate a new bridge typology: the hanging shell bridge, entirely constructed out of surface elements. The Knokke-Heist footbridge in Belgium (designed in 2008 by Ney and Partners), shown in Figure 8.11, was designed unlike traditional structures, where the loads in the longitudinal and transverse directions are decoupled (Adriaenssens et al., 2010). From a topological point of view, the bridge is based on a cutout, curved shape that efficiently carries external loads through membrane action and satisfies the site requirements. The shape of the steel bridge was numerically form-found, like a network of connected springs supported at the abutments and the mast heads. The grid is allowed to relax or "fall" under gravity loads applied at the spring connections. The idea behind the curved structural form is to carry all loads within the steel surface shell without needing additional structural elements (see Figure 8.12).

Once the overall shape has been found, the geometry is further refined to comply with the CNC manufacturing constraint of single-curvature steel sheet bending, and then it is numerically optimized to maximize the overall stiffness of the bridge. The latter task presents a typical topology optimization problem that consists of distributing a given amount of material in a design domain subject to load and support conditions, such that the stiffness of the structure is maximized. Figure 8.13a shows the optimal thickness distribution in the shell for different values and the mean thickness ρ_{mean}, which is a measure of the total material volume constraint. Figure 8.13b

Figure 8.11 Side view of the Knokke-Heist footbridge in Knokke, Belgium (Ney and Partners); photo credit Jean-Luc Deru.

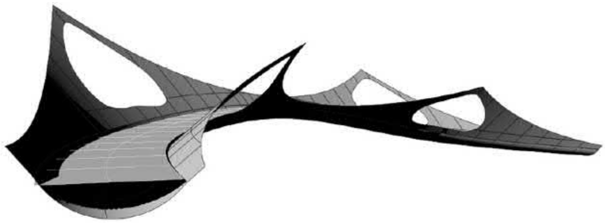

Figure 8.12 The force-modeled bridge shape; photo credit Ney and Partners.

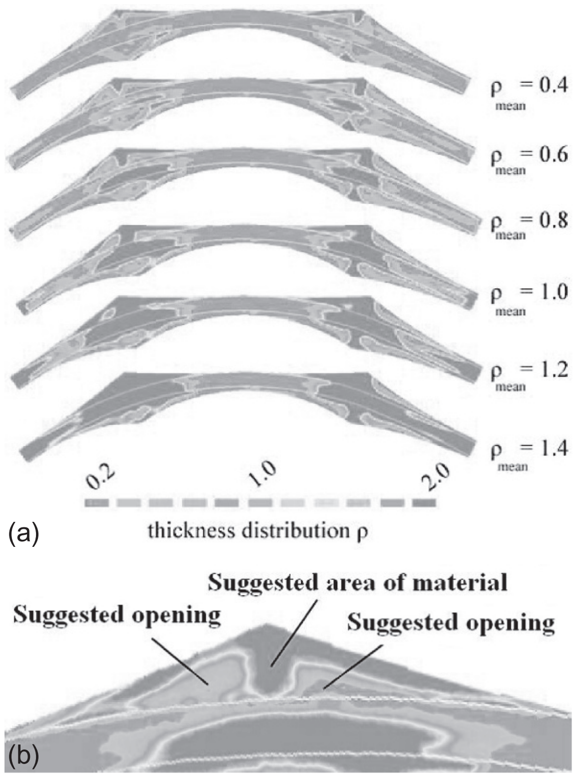

Figure 8.13 (a) Optimal shell thickness distribution; (b) suggestion of location of openings (images from authors).

shows a close-up of the results of the topology optimization for the area around the intermediate supports, and also suggests the optimal location for openings and shows where the steel plate thickness must be increased. Topology optimization provided a powerful tool for the preliminary design of this thin-shelled bridge. By combining topology optimization with form finding and CNC manufacturing constraints, a 3D typology that might not have been conceivable in a purely analytical or intuitive fashion was generated.

5. Future prospects and conclusions: Role of the designer and the toolbox

Most of this chapter focused on constructed bridges made of steel components. However, many historic bridges that articulate their force flow, such as the Felsegg Bridge and the Basento Viaduct, were made of r.c. and were constructed at a time and place where manual labor was cheap. Over recent years, a gap has developed between the formal opportunities offered by digital additive fabrication techniques and available construction methods for r.c. systems. Current additive methods focus on nonstructural materials, produce small components, and rely on an additive layering approach. Therefore, these approaches not suitable for r.c. bridge systems. To overcome these challenges, recent research progress has developed techniques such as smart dynamic casting, which combines digital fabrication with slipforming (Lloret et al., 2015) and robotic swarm printing (Oxman et al., 2014). However, it is yet to be seen how these techniques will influence the discovery of new r.c. bridge typologies and drive their construction.

It is said that "an engineer is a (wo)man who can do for a dime what any fool can do for a dollar." While it is customary for an engineer to be responsible for achieving a specific technological need for the lowest economic cost, this saying is crippling to both the engineer's creativity and the design's potential. With the available new tools, the role of the bridge designer needs to be emphasized. Traditionally, designers use tools such as back-of-the-envelope hand calculations, physical experiments and tests, design charts, and 2D sketches to develop and advance the preliminary design process. The computational techniques presented in this chapter are new tools in this existing toolbox; they allow for the rapid generation of a large set of design alternatives that fulfill specific requirements. These alternatives might be unusual and surprising to the traditional bridge designer, who is grounded in intuition and accumulated knowledge; yet they present unexplored feasible domains in the design space. These instances can inform the bridge designer of new typologies beyond the existing archives of acceptable systems, developed from 19th- and 20th-century analytical and construction techniques. Prior studies of existing successful designs are important, but the use of previous typologies might exclude the creation of more efficient ones. Instead, this chapter argues that by drawing on a broad body of existing knowledge and utilizing 21st-century computational tools, the designer might uncover a range of novel bridge typologies, waiting to be discovered.

References

Adriaenssens, S., Ney, L., Bodarwe, E., Dister, V., 2009. Centner footbridge bridges the gap between structural design and digital fabrication. Steel Construct. 2 (1), 33–35.

Adriaenssens, S., Devoldere, S., Ney, L., Strauven, I., 2010. Shaping Forces: Laurent Ney. Bozar Books - A+ Editions, Brussels.

Adriaenssens, S., Block, P., Veenendaal, D., Williams, C., 2014. Shell Structures for Architecture: Form Finding and Optimization. Routledge, Abingdon, UK.

Ayd, Z., Ayvaz, Y., 2013. Overall cost optimization of a prestressed concrete bridge using genetic algorithm. J. Civ. Eng. 17 (4), 769–776.
Bögle, A., Schmal, P., Flagge, I., 2003. Leicht Weit—Light Structures, Jorg Schlaich, Rudolf Bergermann. Prestel, Munich.
Briseghella, B., Fenu, L., Feng, Y., Mazzarolo, E., 2013. Topology optimization of bridges supported by a concrete shell. Struct. Eng. Int. 3, 285–294.
Caron, J., Julich, S., Baverel, 2009. Self-stressed bowstring footbridge in FRP. Compos. Struct. 89 (3), 489–496.
Day, A., 1965. The Engineer 29, 218–221.
Descamps, B., Coelho, R.F., Ney, L., Bouillard, P., 2011. Multicriteria optimization of lightweight bridge structures with a constrained force density method. Compos. Struct. 89, 277–284.
Fauche, E., Adriaenssens, S., Prevost, J., 2010. Topology optimization of a thin shell structure. J. Intl. Assoc. Shell Spatial Struct. 51 (2), 153–160.
Halpern, A., Adriaenssens, S., 2014. In-plane optimization of truss arch footbridges using stability and serviceability objective functions. Struct. Multidiscip. Optim. 51 (4), 971–985.
Hassan, M., Nassef, A., El Damatty, A., 2013. Optimal design of semi-fan cable-stayed bridges. Can. J. Civ. Eng. 40, 285–297.
Islam, N., Rana, S., Ahsan, R., Ghana, S., 2014. An optimized design of network arch bridge using global optimization algorithm. Adv. Struct. Eng. 17 (2), 197–210.
Lloret, E., et al., 2015. Complex concrete structures: merging existing casting techniques with digitak fabrication. Comput. Aided Des. 60, 40–49.
Lochner-Aldinger, I., 2011. Formfindung und Optimierung im Brückenbau. Altair University, Bonn.
Mueller, C., 2014. Ph.D. thesis: Computational Exploration of the Structural Design Space. Massachusetts Institute of Technology (MIT), Cambridge, MA.
Nagase, K., Skelton, R.E., 2014. Minimal mass design of tensegrity structures. In: SPIE Smart Structures and Materials + Nondestructive Evaluation and Health Monitoring. International Society for Optics and Photonics, p. 90610W.
Oxman, N., et al., 2014. Towards robotic swarm printing. Arch. Des., 108–115. May–June.
Quagliaroli, M., Malerba, P., 2013. Flexible bridge decks suspended by cable nets: a constrained form finding approach. Int. J. Solids Struct. 50 (14–15), 2340–2352.
Rahmatalla, S., Swan, C., 2003. Form finding of sparse structures with continuum topology optimization. J. Struct. Eng. 129 (12), 1707–1716.
Rhode-Barbarigos, K., Bel Hadj, N., Motro, R., Ifc, S., 2010. Designing tensegrity modules for pedestrain bridges. Eng. Struct. 32 (4), 1158–1167.
Scheck, H., 1974. The force density method for the form-finding and computation of general networks. Comput. Methods Appl. Mech. Eng. 3, 115–134.
Schodek, D., Bechthold, M., Griggs, K., Kao, K.M., Steinberg, M., 2005. Digital Design and Manufacturing: Cad/CAM Applications in Architecture and Design. John Wiley & Sons, Hoboken, NJ.
Segal, E., Rhode-Barbarigos, L., Adriaenssens, S., Filomeno Coelho, R., 2015. Multi-objective optimization of polyester-rope and steel-rope suspended footbridges. Eng. Struct. 99, 559–567.
Thrall, A., et al., 2012. Structural optimization of deploying steel pantographs. ASCE J. Comput. Civ. Eng. https://doi.org/10.1061/(ASCE)CP.1943-5487.0000272.

Soil–structure interaction for seismic analysis and design of bridges

9

Shehata Eldabie Abdel Raheem
Professor of Earthquake, Bridge, Structural and Geotechnical Engineering, Civil Engineering Department, Faculty of Engineering, Assiut University, Egypt

1. Introduction

The observed damage and postprocessing of strong ground motion recordings obtained from soft soil sediments during the 1985 Mexico City earthquake and the 1989 Loma Prieta earthquake revealed the great importance of the seismic site response and soil–structure interaction (SSI) to the response of the affected bridge structures (Seed et al., 1992, Torabi and Rayhani, 2014). The collapse of the Hanshin Expressway during the 1995 Kobe earthquake due to significant detrimental SSI impacts (up to a 100% increase) is a prominent example of the important interaction of the soil, bridge, and earthquake characteristics (Mylonakis et al., 2006a, 2006b). Other studies (Sextos et al., 2003a, 2003b) have also highlighted the importance of local soil and site conditions when considering soil and bridge interaction issues. The impact of SSI impacts on displacement response requirements for seismic bridges can be underestimated by a maximum factor of 1.5–2.5 (Sextos, 2013). Most studies on the seismic performance of heavy structures have assumed that the foundation system of the structure is rigid, and thus, the interaction between soil and structure is rarely considered. But it should be noted that the prevailing soil conditions only play an important role in the event that any structure is damaged by an earthquake. This fact becomes even more evident when structures are built on soft soil and are subject to earthquakes. Hence, to minimize the damage caused by this seismic excitation, the SSI phenomenon should be considered. SSI plays a prominent role in important structures such as bridges, and bridges play an important part of the transportation network and form an important link within the lifelines of a nation. Most bridges have their fundamental natural period in the range of 0.2–1.2 s. Structural responses will be high during this range because it is close to the predominant periods of earthquake-induced ground movements of 0.2 to 0.6 s (Neethu and Das, 2019).

Both past and recent earthquakes show that the overall structure response suffers from the foundation and its response from the soil. SSI becomes a big reason that massive structures to collapse when exposed to earthquakes. Engineers who are not aware of this phenomenon usually ignore its implications for seismic analyses, which are not always conservative. Information from instrumented sites can be used to verify analytical methods developed for SSI impact prediction, and to calibrate numerical

Innovative Bridge Design Handbook. https://doi.org/10.1016/B978-0-12-823550-8.00024-X

methods and soil constitutive models as well. The main objective of this chapter is to provide a solid understanding of SSI and its application to different types of bridge structures and foundations. Realistic modeling of a bridge foundation system can greatly influence the prediction of structural response. For relatively strong ground motion, the nonlinear analysis can be more realistic; when the structural response is nonlinear, the frequency domain analysis cannot be valid, and the response must be calculated in the time domain. It seems difficult to determine whether SSI will increase or decrease the bridge response requirements (Anand and Kumar, 2018). The observed phenomena and the discussed interaction between the different natural periods of the bridge system and the predominant periods of ground excitation often assist in qualitatively predicting the response in other situations or in interpreting the results of numerical studies. The effects of soil–structure interaction should be considered for light and heavy infrastructures, regardless of the stiffness of the foundation and underneath soil. For soft soil conditions, the effects of soil–structure interaction must be considered regardless of the type of bridge (Dicleli et al., 2004).

2. Soil–structure interaction (SSI)

SSI can be defined as a process in which the response of soil affects the motion of structure and the motion of the structure influences the response of the soil. When external forces, such as earthquakes, act on bridge systems, neither structural displacements nor ground displacements are independent of each other. Each structure has a load transfer system to the ground. The amount of load transferred through each foundation depends on the location of the foundation, the foundation flexibility, and the soil behavior on which the foundation is supported. The bridge pier's reaction to the loads depend on the soil and foundation type. The same pier can behave differently in different soil conditions. Most designers do not consider the effect of SSI; they consider the foundation as glued to the structure since neglecting SSI tremendously reduces the complication of the analysis of the structure. As a result, such analysis does not lead to a more realistic modeling of the structure and, thus, either leads to an overestimation or underestimation of structural response demands. In SSI problems, the ability to predict the coupled behavior of the soil and the structure is essential and requires combined soil and structure models. The response of soil and movement of the structure influence each other through mutual effects that the vibrating structure, the foundation, and the ground have on one other, causing alterations in the vibrational characteristics of each. Basically, two mechanisms dominate SSI: **kinematic and Inertial interaction**, as shown in Figure 9.1.

Earthquake ground motion causes soil displacement in what is known as free-field motion. The kinematic interaction effect results from the inability of a stiff foundation in or on the soil to move in the same way as the free-field motion of the sediment. The main factors contributing to the kinematic interaction include the foundation embedment, the motion-producing wave inclination, and incoherency. The kinematic interaction effect is usually quantified by a frequency-dependent transfer function. This is defined as the ratio of the foundation motion to the free-field ground motion assuming a massless foundation and structure (Veletsos et al., 1997). Inertial interactions also

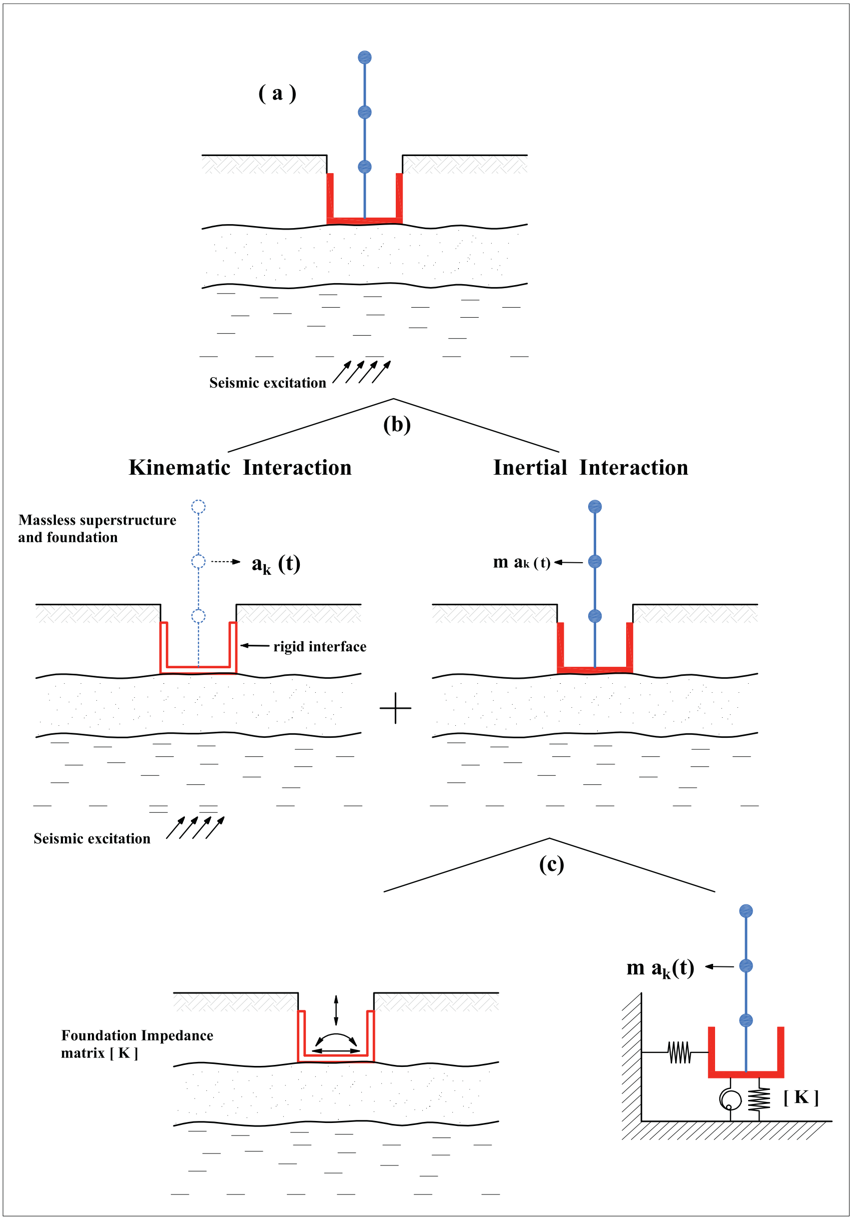

Figure 9.1 (a) The geometry of SSI problem; (b) kinematic and inertial response; (c) two-step analysis of inertial interaction (Kausel et al., 1976; Mylonakis et al., 2006a, 2006b).

affect the vibrational characteristics of structures. The inertial force of the vibrating structure produces base shear and moment effects at the foundation level, resulting in relative displacement between the foundation and the soil. More importantly, inertial interactions result in changes in the modal characteristics of the structure, including variations in modal frequencies and damping factors. In Part 2 of FEMA P-750, NEHRP Recommended Seismic Provisions for New Buildings and Other Structures (FEMA, 2009), SSI effects are categorized as inertial interaction effects, kinematic interaction effects, and soil–foundation flexibility effects. When the ground shaking is of low level, the kinematic effect of SSI is more prominent. This results in period lengthening and an increase in radiation damping. When stronger shaking commences, the radiation damping is limited by the soil modulus degradation in the near field and the soil pile gaping. In this situation, the inertial damping is more prominent. This will therefore cause excessive displacements near the ground surface, which damages foundations.

2.1 Kinematic interaction

When an embedded rigid shallow foundation is subjected to a strong ground motion, kinematic interaction causes the foundation motion to deviate from that in the free field. Accordingly, a reduction in the amplitude of the foundation's transitional motion occurs, while a rocking motion is introduced in the foundation as a result. **Kinematic interaction** effects exist due to the change in wave propagation media because of the change in density and elasticity of the media. It changes the wave propagation velocity and leads to reflection and refraction of incoming seismic waves. Kinematic effects of SSI represent the change in response of the structure when the response is obtained using free-field motions and when the presence of the structure is considered. It does not depend on the mass of the structure; but it is affected by the geometry and configuration of structure, the foundation embedment, the composition of incident free-field waves, and the angle of incidence of these waves. Kinematic interaction can be neglected for structures with no embedment excited by vertically propagating shear waves. Foundation input motions and free-field motions can differ because of *kinematic interaction*, in which stiff foundation elements placed at or below the ground surface cause foundation motions to deviate from free-field motions due to base slab averaging, wave scattering, and embedment effects in the absence of structure and foundation inertia, as well as relative displacements and rotations between the foundation and the free-field associated with structure and foundation inertia.

2.2 Inertial interaction

Inertial effects result from the combined dynamic behavior of the structure, foundation, and supporting soil media. Soil media, owing to its elastic and inertial properties, increases the degrees of freedom of the structure and makes it possible to dissipate the energy of the incoming seismic waves by radiation of the waves away from the structure and hysteretic deformation of the supporting soil media. The inertial effect depends on the relative flexibility of the supporting soil media to the structure, which implies that the effect is not significant for regular structures in stiff soils or rock but could be significant for stiff and massive structures. The inertial force of the vibrating structure produces base shear and moment effects at the foundation level, resulting in relative displacement between the foundation and the soil. More importantly, inertial interactions also result in changes in the modal characteristics of the structure, including variations in modal frequencies and damping factors. The analysis for SSI simulates the flexible-base model analysis that refers to a building founded on a soil deposit that enables the foundation of the building to vibrate when subjected to dynamic loadings. These conditions alter the vibrational characteristics of a fixed-base foundation compared to buildings founded on a rigid base.

Inertia developed in a vibrating structure gives rise to base shear, moment, and torsion. These forces generate displacements and rotations at the soil–foundation interface. These displacements and rotations are only possible because of the flexibility in the soil–foundation system, which significantly contributes to overall structural stability. Moreover, these displacements give rise to energy dissipation via radiation damping and hysteretic soil damping, which can significantly affect overall system damping.

Ground motions at the foundation level of structures differ from those in the free field because of inertial and kinematic interaction effects. Inertial interaction effects tend to produce narrow-banded ground motion modification near the fundamental period of the soil–structure system, whereas kinematic effects are relatively broad-banded but most significant at high frequencies. Kinematic interaction effects can be predicted using relatively costly finite element analyses with incoherent input or simplified models. Foundation damping incorporates the combined effects of energy loss due to waves propagating away from the vibrating foundation in translational and rotational modes (radiation damping), as well as hysteretic action in the soil (material damping). The kinematic interaction effects are far more difficult to evaluate rigorously than inertial interaction effects are.

2.3 Soil nonlinearity

As the earthquake intensity increases, the behavior of the supporting soil deposits quickly becomes nonlinear, thus introducing additional flexibility and damping at the soil–foundation interface. Many sophisticated constitutive laws for soil materials have been developed and incorporated into modern FE codes. Nevertheless, the numerical simulation of concurrent inelastic mechanisms developing at the soil, foundation, and structure simultaneously is still computationally demanding and a major challenge due to material and epistemic uncertainties. The effect of soil nonlinearity, foundation rigidity and embedment, as well as the friction coefficient between soil–foundation interfaces during seismic excitation are investigated. The soil beneath the foundation is assumed to be a nonlinear hysteretic continuum with unit weight $g = 18$kN/m3 and Poisson's ratio $n = 0.35$. The low-strain shear modulus of the soil varies based on the square root of the depth, with values of zero at the surface and 213 MPa 10 m deep. The variations of shear moduli and damping ratios with shear strain are those recommended by Seed and Idriss (1970) for sand. The surface soil layer overlies a hard stratum at 10 m. For the PILE-3D (Wu and Finn, 1997; Finn et al., 2019) finite element mesh, the soil deposit was divided into 10 sublayers of varying thicknesses. Sublayer thicknesses decrease toward the surface where soil–pile interaction effects are stronger. For seismic design in accordance with site conditions in most design guides, the site effects are quantified according to the mean shear wave velocity V_s to a depth of 30 m ($V_{s;30}$) and the corresponding site classes. Accordingly, in the usual seismic codes, the site characterization for a site class is based only on the top 30 m of the ground. The site class is determined unambiguously by this single parameter $V_{s;30}$. For a profile consisting of n soil and/or rock layers, $V_{s;30}$ (in units of m/s) can be given by

$$V_{s,30} = \sum_i^n h_i / \sum_i^n \frac{h_i}{V_{si}}, \tag{1}$$

where h_i is the thickness of the ith layer between 0 and 30 m and V_{si} is the shear wave velocity in the ith layer. Another property that characterizes each soil category is the characteristic period of soil Tc, defined as the transition period between constant acceleration and constant velocity segment of the elastic spectrum. The random and nonlinear behavior of soil may lead to insufficient reliability levels. For this reason, it is necessary to consider the variability of soil properties that can significantly affect the bridge behavior regarding ultimate and serviceability limit states.

2.4 Foundation deformations

Flexural, axial, and shear deformations of structural foundation elements occur because of forces and displacements applied by the superstructure and the soil medium. These represent the seismic demands for which foundation components should be designed, and they could be significant, especially for flexible foundations such as rafts and piles.

3. SSI potential effects

SSI can be both beneficial and detrimental for a particular structure–foundation–soil system, depending on the characteristics of the seismic motions exciting the system. Based on conventional theories, it has been said that the soil–structure interaction has effects that are beneficial for the structural response. Most design codes for structures recommends neglecting the effect of SSI in the seismic analysis of the structure because of the myth that the SSI enables favorable response of the structure and hence can increase the safety margins. More flexible structural designs can be obtained if we consider the effects of soil–structure interaction. This helps to increase the natural period and the damping ratio of the structure, which provides an improved structure when compared to a corresponding rigid structure. This means that the myth that the SSI effects are good for structures is not true. In fact, SSI can bring detrimental effects to structures. Neglecting the SSI effect can bring unsafe design of the superstructure and the substructure.

In the seismic analysis of a structure founded on ground, the ground motion passes to the base of structure and then loads on structure. The response of the foundation system affects the response of the structure and vice versa, which is called dynamical soil–structure interaction (SSI). Theoretical results (Wolf, 1985; Mylonakis and

Gazetas, 2000) indicate that SSI is sometimes beneficial and sometimes detrimental to structural performance. Therefore, the effect of soil cannot be neglected because SSI phenomenon is closely related to its dynamic characteristics (Lou et al., 2001), especially the damping of the whole system (Zhang et al., 2010). To explore the effect of SSI on the seismic performance of engineering structures, the finite element methods and theoretical analysis are often used. However, the uncertainties and boundary conditions existing in SSI system have not been simulated properly by these methods (Gilles et al., 2011; Mirzaie et al., 2017). Current design practice for structures subject to earthquake loading regards dynamic soil–foundation–structure interaction to be mainly beneficial to the behavior of structures; for example, the flexibility of the foundation reduces the overall stiffness of a system and therefore reduces peak loads caused by a given ground motion. Even if this is true in most cases, there is the possibility of resonance occurring because of a shift of the natural frequencies of the soil–foundation–structure system. This can lead to large inertial forces acting on a structure. As a result of these large inertial forces caused by the structure oscillating in its natural frequency, the structure as well as the soil surrounding the foundation can undergo plastic deformations. This in turn further modifies the overall stiffness of the soil–foundation–structure system and makes any prediction of its behavior very difficult. A good numerical model of a soil–foundation-structure system can therefore not only prevent the collapse or damage of a structure but also help to save money by optimizing the design to withstand an earthquake with a certain return period.

3.1 Beneficial effects of SSI

The demands imposed by the earthquake are more significant in the short period range; hence, the fixed-base model experiences higher demands than the model with soil springs. SSI has been traditionally considered to be beneficial for seismic response. Neglecting SSI effects is currently being suggested in many seismic codes (ATC, 1978; NEHRP, 1997) as a conservative simplification that would supposedly lead to improved safety margins. Through a comparison of conventional code design spectra to actual response spectra, it was shown that an increase in fundamental natural period of a structure due to SSI does not necessarily lead to lower seismic response, and, therefore, the prevailing view in structural engineering that SSI is always beneficial is an oversimplification that may lead to unsafe design (Mylonakis and Gazetas, 2000).

3.2 Detrimental effects of SSI

The spectral demands are initially higher in the short period range for this record; however, it is likely that the fixed-base model moves into a region of slightly lower demands (just beyond 0.5 s) since the degree of inelasticity is not severe. The shift in the period from 1.24 s of the soil-spring based model takes it into a region of increased demand, thus causing higher drifts. The dynamic response is extremely sensitive to shifts in the fundamental period as the structure moves from the elastic state to the inelastic state. Such sensitivity makes it difficult to develop simplified guidelines for designing structures incorporating SSI. The effects of SSI are more focused on its detrimental effects. As mentioned, even if studies have shown that the design based on soil–structure interaction increases the time, the increase in period is not always a beneficial factor. The elongation of seismic waves when it is on a site of soft soil sediments results in the increase of the natural period, hence leading to resonance. This happens with a long period vibration. If the natural period increases, the demand for ductility also increases. This may result in permanent deformation and soil failure that will further worsen the structural seismic response.

4. SSI analysis approaches

The various ways of accounting for SSI in design and analysis in practice range from a complete analysis of the total combined system of foundation, soil, and structure to approximate models of the system. Methods used to evaluate the SSI effects can be categorized as direct and substructure approaches. In a *direct analysis*, the soil and structure are included within the same model and analyzed as a complete system. In a *substructure approach*, the SSI problem is partitioned into distinct parts that are combined to formulate the complete solution.

4.1 Direct analysis method

The direct approach is one in which the soil and structure are modeled together in a single step, accounting for both inertial and kinematic interaction. Inertial interaction develops in the structure due to its own vibrations giving rise to base shear and base moment, which in turn causes displacements of the foundation relative to the free field, whereas kinematic interaction develops due to the presence of stiff foundation elements on or in the soil, causing foundation motion to deviate from free-field motions. The soil–structure system is modeled and analyzed in one step and, hence, responds to the two simultaneous numerical methods, FEM and FDM. In this type of analysis, the soil and the structure are used in the same model for analysis and are analyzed as a complete system. As illustrated in Figure 9.2, the soil system is represented as a continuum. For example, finite elements are represented along with foundation and structural elements, transmitting boundaries at the limits of the soil mesh, and interface elements at the edges of the foundation. The foundation, structural elements, load-transmitting boundaries, and elements at the interface located on the edges of foundation are also included. Evaluation of site response using wave propagation analysis through the soil is important to this approach. Such analyses are most often performed using an equivalent linear representation of soil properties in finite element, finite difference, or boundary element numerical formulations (Wolf, 1985; Lysmer et al., 1999). Direct analyses can address all the previously described SSI effects, but incorporating kinematic interaction is challenging because it requires the specification of spatially variable input motions in three dimensions. Because the direct solution of the SSI problem is difficult from a computational standpoint, especially when the system is geometrically complex or contains significant nonlinearities in the soil or structural materials, the model may be too complex to analyze. It may include parameters that are difficult for structural engineers to understand, involve a great amount of computation, so it is

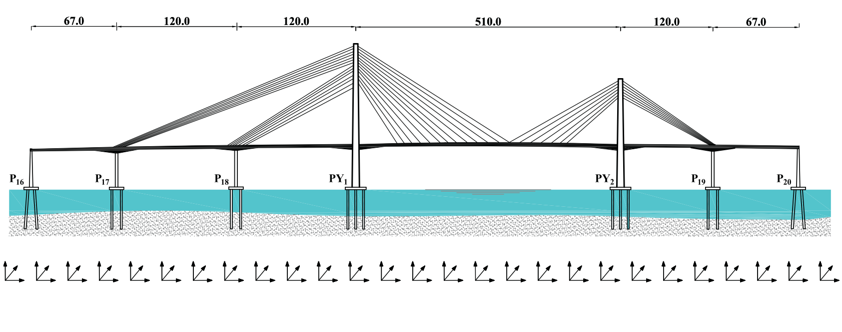

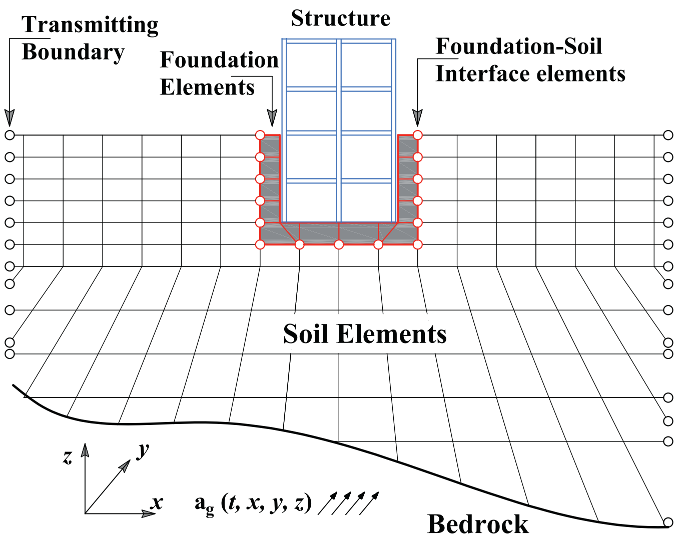

Figure 9.2 Schematic illustration of direct approach to analysis of the SSI problem using continuum modeling and finite elements (NIST, 2012).

rarely used in practice. The direct approach of modeling the entire SSI system in one step can be computationally costly.

4.2 Substructure method

In the substructure method, the analysis is broken down into several steps. The principle of superposition is used to isolate the two primary causes of SSI's inability to make the foundation to match the free-field deformation and the effect of the dynamic response of the structure foundation system on the movement of the supporting soil. In the analysis and design of engineered structures in the past, it was assumed that the foundation of structure was fixed to a rigid underlying medium. In the last few decades, however, it has been recognized that SSI has altered the response characteristics of a structural system because of the massive and stiff nature of structure and often the softness of the soil. The literature contains various studies on the effect of SSI on the dynamic response of structures such as nuclear power plants, high-rise

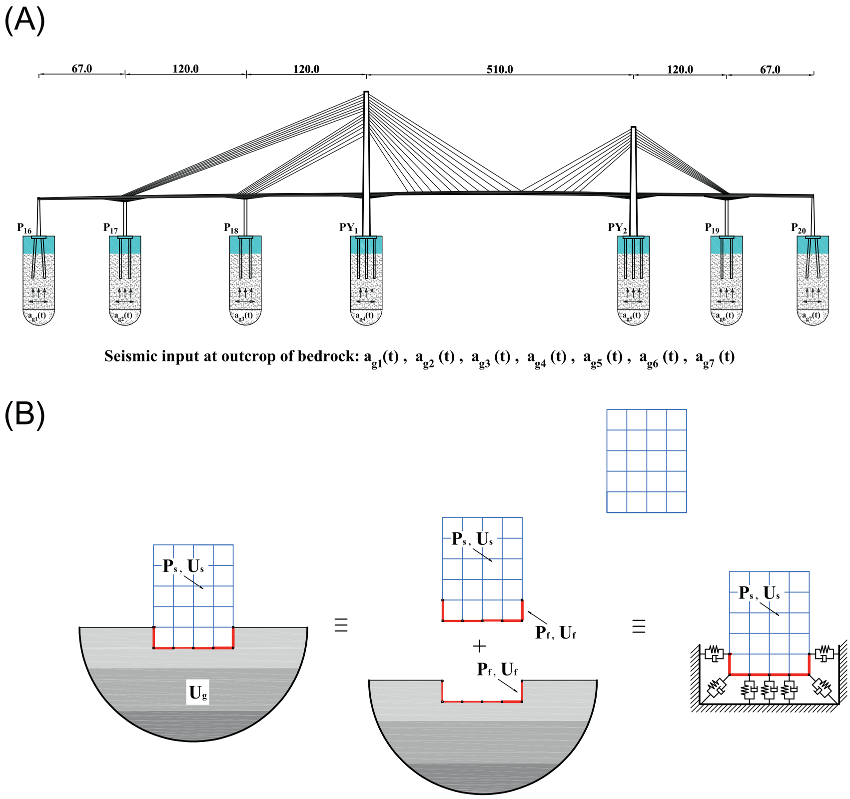

Figure 9.3 Schematic illustration of the substructure approach in the soil–structure analysis (Kamali, 2018).

structures, and elevated highways. In the substructure method, each problem is evaluated separately, and the combination of the results will give the final solution, as illustrated in Figures 9.3 and 9.4.

In substructure approach, a model is generated with certain requirements:

- **(i)** Complete System: The complete soil–foundation-structure system is excited by an incident wave field represented by a free-field ground motion.
- **(ii)** Kinematic Interaction: A non-embedded rigid foundation excited by vertically propagating seismic incident waves would theoretically experience the motion.
- **(iii)** Foundation–Soil Flexibility and Damping: The seismic loading at the foundation level introduces an inertial response into the building. This process is known as inertial interaction and is captured in the substructure approach by using frequency-dependent soil springs and dashpots. These springs and dashpots can be applied in a simple manner for a rigid foundation or dispersed in a series of springs and dashpots for flexible foundations.
- **(iv)** Excitation with foundation input motion of structure with foundation flexibility/damping: The substructure approach does not account for soil nonlinearities introduced by the inertial response, which may affect the incoherent demand distribution and impedance. Nonlinearity can be incorporated in an approximate way through the site response (Jeremić et al., 2004; Chaudhary, 2016).

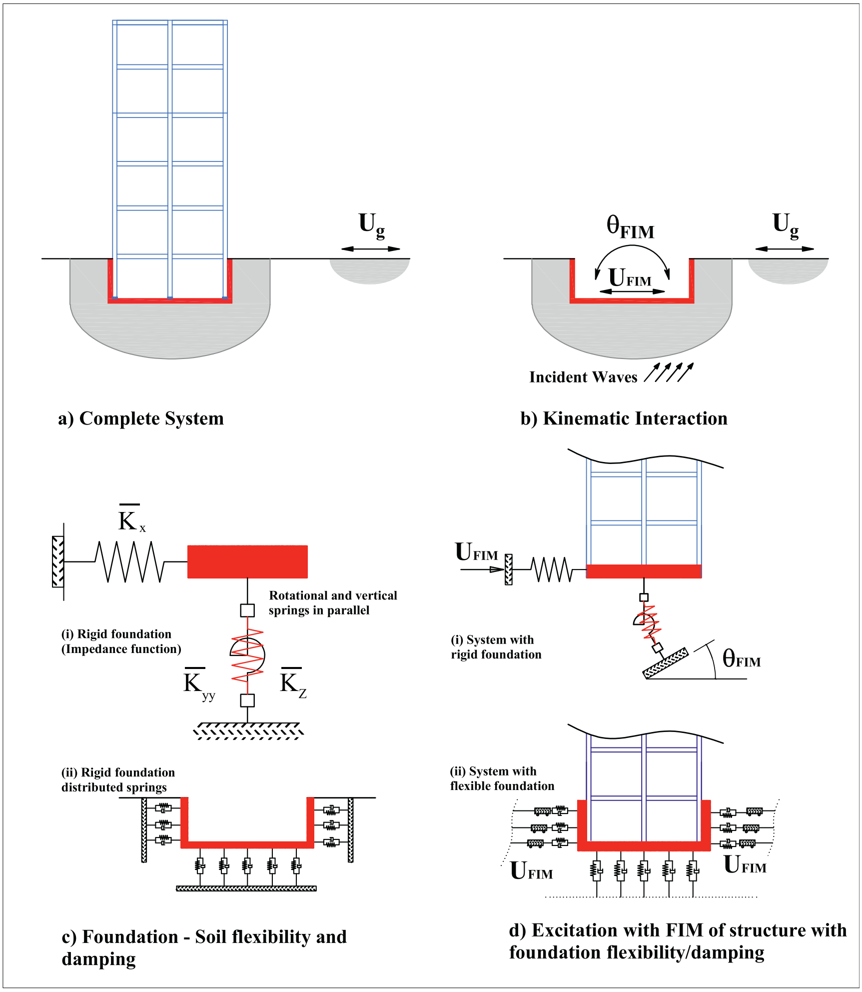

Figure 9.4 Schematic illustration of a substructure approach to analysis of SSI (NIST, 2012) using either (i) rigid foundation or (ii) flexible foundation assumptions.

4.3 Free-field site response

The evidence of severe damage and the recorded strong ground motions in soft soil deposits during the 1989 Loma Prieta and 1985 Mexico City earthquakes demonstrated the capability of this type of soil to amplify the bedrock motion (Seed et al., 1988). Subsequent investigation into this phenomenon led to the development of site categories, which were implemented in building design code provisions (NEHRP, 1997, NRCC, 2010). According to this classification, which is based on average shear wave velocity in the top 30 m ($v_{s,30}$), soft soil deposits with $v_{s,30}$ less than 180 m/s are classified as group E. In this study, site-specific analysis was conducted on a 30 m soil deposit with a shear wave velocity of 78 m/s (site class E). The site response spectra and site amplification factor, which is the ratio of the response spectra of the free field and base motion in the frequency domain, show that three local peaks in the amplification function mark the fundamental modes of soil deposit vibrations.

The potential resonance between components involved in SSI phenomenon must be considered in any seismic analysis. This hazardous event is of great significance in thick deposit of soils with low shear wave velocities, in which modal fundamental periods of the site are likely to coincide the natural periods of structure. It was concluded that resonance can occur between the structure, input excitation, and soil deposit. A detailed characterization of soil–structure interaction is crucial for this type of site-structure setting in order to avoid hazardous events like resonance, foundation rocking, and excessive base shear demand (Eduardo, 2010). The influence of local site conditions can be demonstrated using a simple site response analysis; the softer site amplifies bedrock motion at a low-frequency range while the stiffer site amplifies high-frequency rock motion. Since earthquakes produce bedrock motion over a range of frequencies, some components of the bedrock motion will be amplified more than others.

4.4 Current design practices

Current design practice does not account for the nonlinear behavior of soil–foundation interface, primarily due to the absence of reliable nonlinear SSI modeling techniques that can predict the permanent and cyclic deformations of the soil as well as the effect of nonlinear soil–foundation interaction on the response of structural members. Safe and economic seismic designs of bridge structures directly depend on the level of understanding of the seismic excitation and the influence of supporting soil on the structural dynamic response. Long-span bridges are more susceptible to relatively severe SSI effect during earthquakes when compared to buildings, due to their spatial extent, varying soil conditions at different supports, and possible incoherence in the seismic input. The necessity of incorporating soil–structure interaction in the design of a wide class of bridge structures has been pointed out by several post-earthquake investigations, experiments, and analytical studies (Committee of Earthquake Engineering, 1996; Vlassis and Spyrakos, 2001; Trifunac and Todorovska, 1996; Megawati et al., 2001). Recently, several cable-stayed bridges have been constructed on relatively soft ground, which creates a great need to evaluate the effect of soil–structure interaction on the seismic behavior of bridges and properly reflect it in seismic design to accurately capture the response, enhance the safety level, and reduce design and construction costs.

Due to material and geometrical nonlinearities, the dynamic characteristics of soil–structure system change during a severe earthquake. These nonlinearities are sometimes treated using an equivalent linear model (Abdel Raheem et al., 2003, Chaojin and Spyrakos, 1996, Spyrakos, 1997). However, the dynamic characteristics of soil–structure system are dependent on the soil stress level during a severe earthquake (Ahn and Gould, 1992; Gazetas and Dobry, 1984; Kobayashi et al., 2002). Foundation rocking and uplifting are important for short-period structures on a relatively soft-soil site (Yim and Chopra, 1984; Harden et al., 2006). For nonlinear structures, effects of soil–structure interaction due to rocking can result in significantly larger ductility demands under certain conditions (Tang and Zhang, 2011; Zhang and Tang, 2009). These findings necessitate the evaluation of structural responses that consider SSI using foundation models that can realistically capture the nonlinear force, displacement behaviors, and energy dissipation mechanisms. Nonlinear foundation movements and associated energy dissipation may be utilized to reduce the force and ductility demands of a structure, particularly in high-intensity earthquake events (Raychowdhury, 2011).

The finite element method has proven to be a very useful method for studying the soil–structure interaction effect with rigor. In fact, the technique is useful in incorporating the effect of material nonlinearity, inhomogeneity, and interface modeling of soil and foundation. To perform nonlinear soil–structure interaction analysis, an incremental iterative technique is found to be the most suitable and general one. For practical purposes, the Winkler hypothesis should at least be employed instead of carrying out an analysis with a fixed-base idealization of structures. The preferred method of capturing the effect of superstructure interaction is to consider the bridge structure and the foundation as a fully coupled system in the finite element analysis. However, a fully coupled analysis would not be feasible in practice because it would require enormous amounts of computational storage and time, using the more sophisticated computer codes.

5. Modeling of soil–structure interaction

A crucial goal of current seismic foundation design particularly as entrenched in the respective codes (European Committee for Standardization, 1998; CEN, 2004), is to avoid the full mobilization of the foundation's strength by guiding failure to the aboveground structure. The designer must ensure that the (difficult-to-inspect) belowground support system will not even reach thresholds that would statically imply failure: the mobilization of the soil bearing capacity, significant foundation uplifting, sliding, and any combination of these actions are prohibited or severely limited. To this end, the norms of capacity design, overstrength factors, and safety factors (explicit or implicit) are followed against those failure modes. A series of time-domain-inelastic finite-element simulations of seismic behavior of a bridge bent and subjected to various earthquake events is carried out using two separate models of the system (Jeremić et al., 2004).

Structures are generally assumed to be fixed at their bases in the process of analysis and design under dynamic loading. But the consideration of actual support flexibility reduces the overall stiffness of the structure and increases the period of the system. Considerable change in spectral acceleration with the natural period is observed from the response spectrum curve. Thus, the change in natural period may alter the seismic response of any structure considerably. In addition to this, soil medium imparts damping due to its inherent characteristics. The issues of increasing the natural period and involving high damping in soil due to soil–structure interaction in building structures are also discussed in some of the studies. Moreover, the relationship between the periods of structural vibration and the supporting soil is profoundly important as regards the seismic response of the structure. The destruction of a part of a factory as a result of the 1970 earthquake at Gediz, Turkey, and the destruction of buildings during the 1967 Caracas earthquake raised the importance of this issue.

The effects of soil–structure interaction on the seismic response and dynamic performance of the cable-stayed bridge towers with spread foundation are assessed. The seismic responses of two different modeling approaches, the nonlinear Winkler soil model and the linear lumped-parameter soil model for the soil foundation interaction, are investigated and compared. In the lumped-parameter soil model, the soil–structure interaction is simulated with their translational, rotational, and coupling linear springs acting at the centroid of the spread foundation at footing base level. While in the nonlinear Winkler soil model, the soil–structure interaction is simulated with a continuous spring (Winkler) system along the embedded depth of tower pier and underneath the spread foundation. Soil strain-dependent material nonlinearity is considered through a hysteretic element, whereas geometrical nonlinearity by base mat uplift is considered through a gap element. The massive pier of the tower model activates the rocking response of the spread foundation under strong earthquake ground motion and, hence, results in the foundation uplift and yield of the underlying soil (Kawashima and Hosoiri, 2002; Gelagoti et al., 2012). The results of the nonlinear Winkler soil model approach are compared with those from the linear lumped soil model approach.

5.1 Fixed-base model

The fixed-base model assumes the bridge columns to be rigidly connected to the foundation without SFS interaction. A structure, when analyzed by considering its foundation to be rigid, is said to have no soil–structure interaction effects. This case is considered even if the interaction force impacts the foundation. The base mat acceleration and the inertia of the structure can be used to estimate the value of interaction forces. The heavier the structure, the more the soil–structure interaction effects are for a particular soil site and for a given free-field seismic excitation. Most of the civil structure, whether lying on hard or medium soil, does not show any sign of SSI effects. Fixed-base capacity models are commonly adopted in seismic assessment of bridge structures. However, structural response can be strongly influenced by dynamic interaction with underlying soil (Mylonakis and Gazetas, 2000; Kausel, 2010). Soil–structure interaction (SSI) can produce a reduction in the fundamental frequency of the soil–foundation–structure system as well as additional energy dissipation by means of wave radiation and hysteresis of soil (Mylonakis et al., 2006a, 2006b; Givens et al., 2016). These SSI effects can be associated with the soil's compliance to the structural motion, which is usually referred to as inertial interaction. This type of interaction produces the modification of the period and damping of the whole system, affecting the structural response in terms of displacements and/or accelerations. As the foundation embedment increases, another SSI effect due to the relative soil–foundation stiffness is observed and is referred to as kinematic interaction (Kim and Stewart, 2003). This consists of a modification of seismic motion transmitted from the soil to the structure with respect to free-field conditions.

5.2 Simplified soil–structure interaction model

The simplified SSI model incorporates structure–foundation–soil interaction using equivalent springs, as illustrated in Figure 9.5. The spring properties are derived from three-dimensional finite element analysis of the pile foundation in a layered soil system. The analysis is based on nonlinear inelastic characteristics of the concrete substructure and linear elastic behavior of the soil–foundation system. Results of the analysis indicate that structure–foundation–soil interaction can have both beneficial and detrimental effects on structural behavior and is dependent on the characteristics of the earthquake motion. The Applied Technology Council's development of seismic regulations (ATC, 1978; NEHRP, 1997) proposes simple formulae for computing the fundamental period and the effective dumping ratio of structures founded on mat foundations on a homogeneous half-space. All codes today use idealized envelope response spectra that attain constant acceleration values up to a certain period (of order of 0.4–1.0 s at most) and then decrease monotonically with the period. Therefore, SSI leads to smaller accelerations and stresses in the structure and thereby smaller forces on the foundation.

Another condition relevant to SSI effects is the soil flexibility. The softer the soil, the greater the chance that SSI effects occur. This is for a given structure and a site that have a free-field seismic excitation. The main characteristic of soil stiffness can be the shear wave velocity Vs less than 300 m/s for soft soil, greater than 800 m/s for hard soil, and greater than 1100 m/s for rigid soil. The SSI effects are essential for the analysis of heavy structures such as hydraulic structures and nuclear structures; for those structures where the P-delta effects are prominent, the analysis based on soil–structure interaction is helpful. Moreover, the SSI has a significant role in deep-seated foundations, structures supported over soft soil, and tall or slender structures that have an average shear velocity of 100 m/s.

Preliminary analytical studies comparing the response of fixed-base models with simplified soil–foundation models provide important information on the need for considering SSI effects in the design process (Jeremić et al., 2004). A simulation model of the highway structure is being developed systematically to increase the level of detail and complexity: a three-dimensional finite-element model utilizing a linear elastic single degree of freedom (SDOF) structure and a nonlinear elasto-plastic constitutive model for soil behavior to capture the nonlinear foundation–soil coupled response under seismic loadings (Torabi and Rayhani, 2014). The results of parametric study demonstrate that rigid, slender, tall structures are highly susceptible to the SSI effects—including the alteration of natural frequency, foundation rocking, and excessive base shear demand. Structure–foundation stiffness and aspect ratios were found to be crucial parameters in controlling coupled foundation–structure performance in flexible-base structures. Furthermore, frequency content of input motion, site response, and structure must be considered to avoid a resonance problem.

To account for inertial interaction effects in seismic performance assessment, more or less refined models of soil and structure have been proposed. The use of finite-element models is generally adopted for critical cases because of their huge computational demand. The simplest model of SSI system using a single-degree-of-freedom

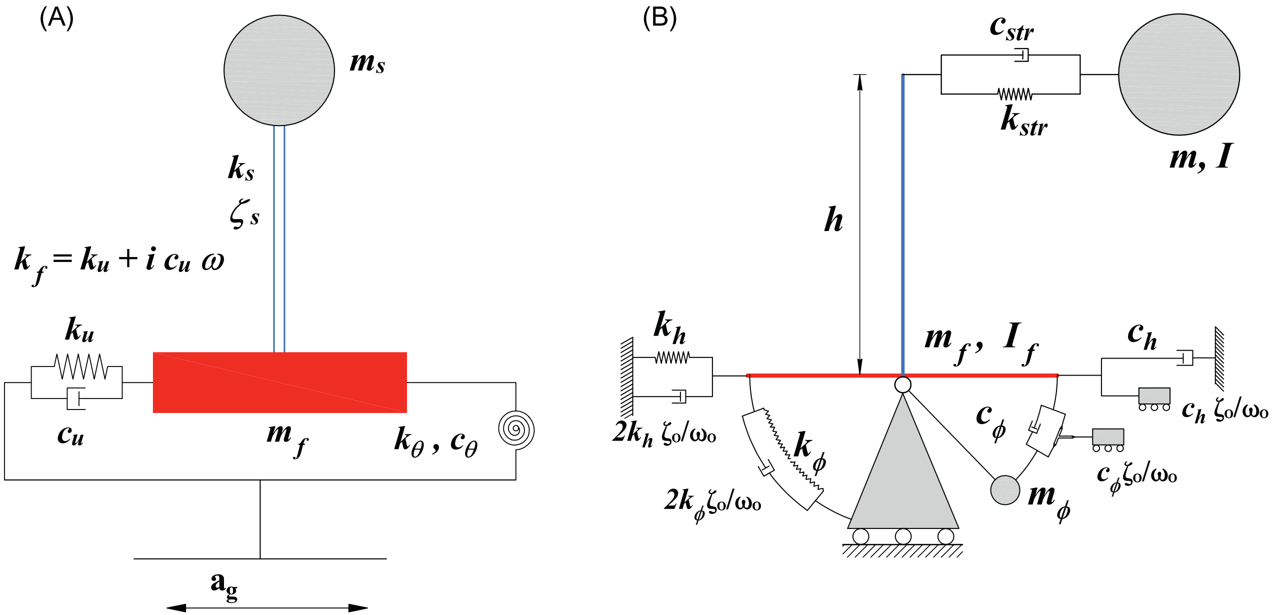

Figure 9.5 Simplified SSI models. (a) Soil equivalent springs (Torabi and Rayhani, 2014). (b) Soil–structure SDOF system (Cone model) (Hassani et al., 2018).

(SDOF) system is frequently adopted. This model is equipped at the base with a combination of linear springs, which are associated with translational and rotational motion, plus as many viscous dashpots simulating the impedance of a homogeneous, linear elastic half-space underlying a circular rigid foundation at the ground surface. A system commonly employed for simplified analysis of inertial interaction consists of an SDOF structure on a flexible foundation medium represented by the frequency-dependent and complex-valued translational and rotational springs. The effective properties of profiles that have a gradual increase in stiffness with depth can often be approximately modeled by an equivalent half-space. The soil properties are used to define the half-space, where the shear wave velocity and hysteretic damping ratio are representative of the site stratigraphy and the level of ground shaking (Piro et al., 2020). Depending on the level of the strain, the dynamic behavior of the soil–structure system can be considered linear or nonlinear, and different simulation techniques exist for each case. For the linear case, the most commonly used model to capture the nonlinear behavior of the soil–structure system is a discretized numerical model using the finite-element method (FEM). Nonlinear analyses are usually carried out in the time domain (TD) using time-integration techniques. Nonetheless, applying the FEM for the soil system cannot capture the real endless dimension and requires significant number of degrees of freedom (DOFs). Therefore, the FEM requires a special extension to account for the frequency-dependent properties of the soil. Different direct and substructuring methods could be used for nonlinear SSI. These range from simple 1-D spectral methods to 3-D transient approaches. A simplified model has generally been used to investigate the inertial interaction phenomenon in theoretical and analytical studies (Veletsos and Meek, 1974; Bielak, 1975; Mita and Luco, 1989; Gazetas, 1991). This SDOF system consists of frequency-dependent translational and rotational springs, which represent dynamic stiffness and damping of a flexible foundation–soil system.

5.3 Linear lumped-parameter soil model

The soil–structure interaction is modeled using the sway rock model available in the literature (Mikami and Sawada, 2004), as illustrated in Figure 9.6. For the modeling of SSI employed in this study, the effect of kinematic interaction and the off-diagonal components of the stiffness and damping matrices are ignored considering the foundation geometry's depth is small enough compared to its width. It is to be noted that the same bridge model has been used in previous studies (Tongaonkar and Jangid, 2003; Ucak and Tsopelas, 2008) in which the SSI for the soil supporting the pier foundation has been modeled as a spring and damper acting in the horizontal and rotational directions. The foundation was represented for all motions using a spring–dashpot–mass model with frequency-independent coefficients. A lumped-parameter model is a block of springs, dashpots, and masses that is able to reproduce the dynamic behavior of a soil–foundation system. Its real frequency-independent coefficients are found by approximating the dynamic impedance or compliance functions by a ratio of two polynomials. Extended LPM is developed for horizontally layered soil and different forms of the foundation. In the linear lumped-parameter soil model, the

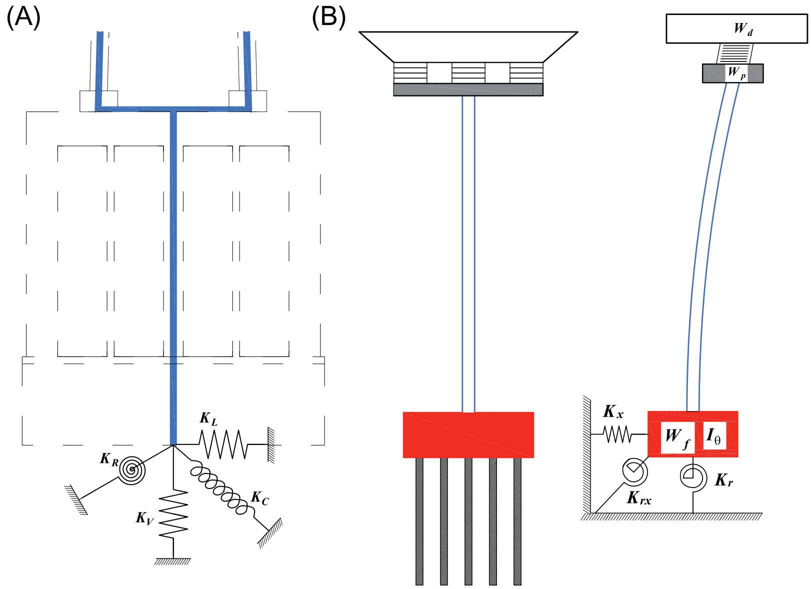

Figure 9.6 Linear lumped-parameter SSI model (Abdel Raheem and Hayashikawa, 2013; Ucak and Tsopelas, 2008).

interaction between the soil and the structure is simulated with translational, rotational, and coupled spring systems. The spring stiffness values in both the bridge axis and right-angle directions are determined. The stiffness is calculated based on foundation geometry and soil profile underneath and along the embedded depth of the foundation, as specified in the Japanese Highway Specification (Japan Road Association, 1996a, 1996b).

5.4 Winkler model for shallow foundation soil–structure interaction

Like for the linear case, the most commonly used model to capture the nonlinear behavior of the soil–structure system is a discretized numerical model using FEM. Nonlinear analyses are usually carried out in the time domain (TD), using time-integration techniques. Nonetheless, applying the FEM for the soil system cannot capture the real endless dimension and requires significant number of DOFs. Therefore, the FEM requires a special extension to account for the frequency-dependent properties of the soil. Different direct and substructuring methods for nonlinear SSI range from simple 1-D spectral methods to 3-D transient approaches. Beam-on nonlinear Winkler foundation (BNWF) models have been used for many years for analyzing the response of foundations, most notably piles, for static loads (Matlock, 1970; Cox et al., 1974) and dynamic loads (Nogami et al., 1992; Boulanger et al., 1999). Key advantages of these models over continuum formulations are their ability to describe soil–structure interaction phenomena by one-dimensional nonlinear springs distributed along the soil–foundation interface. It is well known that the modulus of the springs (also known as modulus of subgrade reaction) is not uniquely a soil property, but also depends on foundation stiffness, geometry, frequency, response mode, and level of strain. A limitation of the approach relates to its one-dimensional nature. A spring responds only to loads acting parallel to its axis, so loads acting in a perpendicular direction have no effect on the response of the spring. Accordingly, the concept of plastic potential and flow rule cannot be explicitly incorporated. Nevertheless, the BNWF approach is popular because of its simplicity and predictive abilities on a variety of problems.

The soil–structure interaction is simulated with nonlinear spring-dashpot system along the pier embedded depth. Strain-dependent material nonlinearity is implemented using the nonlinear Hardin–Drnevich soil model (Hardin and Drnevich, 1972a, 1972b). Geometrical nonlinearity by base mat uplift is considered through nonlinear soil element connected in series with gap element spring system, as shown in Figure 9.7. The spring constants in both bridge axis directions are calculated based on foundation geometry and soil profile underneath and along the embedded depth of foundation, as specified in the Japanese Highway Specification (Japan Road Association, 1996a, 1996b). Soil properties from the SPT data and logs of boreholes at the tower site are used to determine the coefficients of vertical and horizontal subgrade reactions. The subgrade reaction coefficients are obtained from the ground stiffness, corresponding to the deformation caused in the ground during an earthquake.

5.5 Soil nonlinearity idealization

One of the most important factors in the analysis of soil–foundation interactive behavior is the nonlinear constitutive laws of the soil (material nonlinearity). In this study, the Hardin–Drnevich model is proposed to represent the soil material nonlinearity.

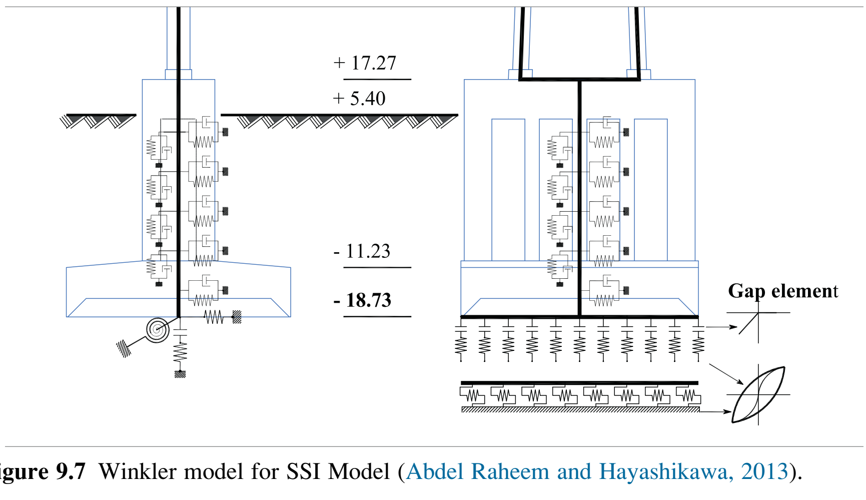

Figure 9.7 Winkler model for SSI Model (Abdel Raheem and Hayashikawa, 2013).

The model is often used for its capacity to trace the degradation of stiffness. The parameters used to define the skeleton curve and family of hysteresis stress–strain curves are indicated in Figure 9.8. The skeleton curve is expressed as follows:

$$\tau = G_0\gamma/(1+|\gamma/\gamma_r|), \gamma_r = \tau_{max}/G_0, \tag{2}$$

where G_0 is the initial shear modulus, τ is the generalized soil shear stress, τ_{max} is the shear stress at failure, γ_r is the reference strain, and γ is the generalized strain. The hysteretic curve can be constructed using the Masing rule (Masing, 1926) and is given as follows:

$$\tau \pm \tau_m = G_0(\gamma \pm \gamma_m)/\{1+|(\gamma \pm \gamma_m)/2\gamma_r|\}, \tag{3}$$

where τ_m and γ_m indicate the coordinates of the origin of the curve—that is, the point of the most recent load reversal. The hysteresis curve is the same in shape as the skeleton curve but is twice as large. The nonlinear dynamic soil parameters in this study, including the dynamic shear moduli and the damping ratios for the employed soil models, are modulated based on the shear strain–dependent relationships for gravel, sand, and clay shown in Figure 9.8. The soil exhibits nonlinear nature even at small strains. The shear modulus (G) can be described as follows:

$$G/G_0 = 1/(1+\gamma_m/\gamma_r). \tag{4}$$

The decay of normalized shear modulus, G/G_0, and the variation of the damping ratio, D, with the shear strain, were defined by resonant column tests. The soil element stiffness is idealized by the Winkler model. For practical use, frequency-independent spring coefficients are computed based on the Japanese Specification for Highway Bridges (Japan Road Association, 1996a, 1996b). Each spring consists of a gap element and a soil element. The gap element transmits no tensile stress, which can express the geometrical nonlinearity of base mat uplift.

5.6 Soil-damping idealization

The hysteretic damping characteristic of the soil, which resulted from the deformations produced by the interaction with the pier, is represented by nonlinear viscous dashpots. The damping ratio of the soil dashpot strain-dependent material nonlinearity is described by a simple relationship between the shear modulus and damping, as shown in Figure 9.9:

$$h = (\Delta w/w)/2\pi = (2/\pi)\left[\left(\frac{2G_0}{G}\right)\left\{\left(\frac{\gamma_r}{\gamma_m}\right) - \left(\frac{\gamma_r}{\gamma_m}\right)^2 \log\left(1+\frac{g_r}{g_m}\right)\right\} - 1\right]. \tag{5}$$

The material-damping ratio h is defined as follows:

$$h = C_m/C_r,\ C_r = 2(k/m)^{0.5}. \tag{6}$$

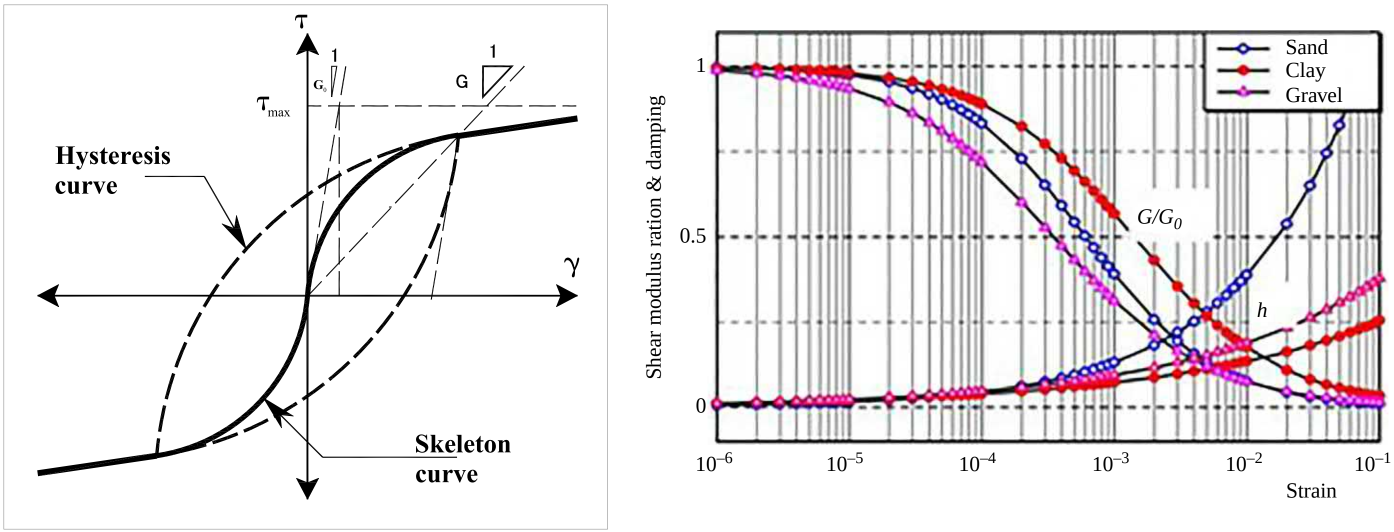

Figure 9.8 Strain-dependent soil material nonlinearity. (a) Hardin–Drnevich model and Masing rule hysteresis loop. (b) Shear modulus and damping ratio versus shear–strain relationship.

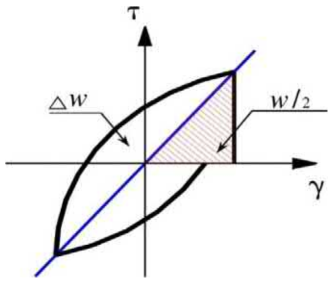

Figure 9.9 Soil hysteretic damping.

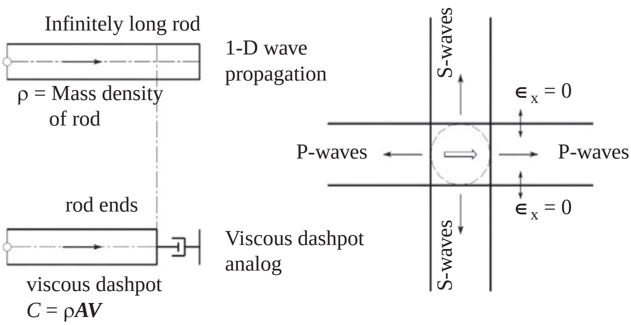

Figure 9.10 One-dimensional radiation-damping model.

in which C_m is the coefficient of material damping, C_r is the coefficient of material critical damping, and k and m are the soil spring stiffness and pier mass per unit length, respectively. The coefficient of material damping of the soil C_{soil} is obtained as follows:

$$C_{soil} = 2h_{max}\left(1 - \frac{k}{k_0}\right)\left(\frac{k}{m}\right)^{0.5}. \tag{7}$$

The radiation-damping characteristic of soil is represented through an approximation of a para-axial boundary, where viscous dampers can be used to represent a suitable transmitting boundary for many applications involving both dilatational waves and shear waves. A one-dimensional viscous boundary model is selected for this study. It is assumed that a horizontally moving pier cross section would solely generate one-dimensional P waves traveling in the direction of shaking and one-dimensional S waves in the direction perpendicular to shaking, as shown in Figure 9.10. Based on the previous assumption, the coefficient of viscous dashpot that will absorb the energy of the waves originating at soil–pier interface is evaluated.

5.7 Winkler model for pile–structure–soil interaction model

As opposed to spread footings, for which a single method of analysis to determine the forces transmitted by the foundation emerges in practice (based on a substructuring approach and the definition of the foundation stiffness matrix and damping), several modeling techniques are used to model piled foundations for seismic response studies; the most common methods are the simplified beam on Winkler foundation (BNWF) model and the substructuring coupled foundation stiffness matrix (Lam and Law, 2000; Pecker, 2015), as illustrated in Figures 9.11 and 9.12. The BNWF is considered to be a simplified approach capable of modeling nonlinear soil–pile–structure interaction. Soil nonlinearity is modeled through a series of *p*-*y* curves where *p* is soil resistance per unit length of pile and *y* is pile lateral displacement (Liyanapathirana and Poulos, 2005). The approach has been adopted by many researchers (El-Naggar and Bentley, 2000; Brandenberg et al., 2001; Allotey and El-Naggar, 2008; Castelli and Maugeri, 2009; Armstrong et al., 2014). Kimiaei et al. (2004) introduced a practical BNWF model for estimating the lateral response of flexible piles embedded in layered soil deposits subjected to seismic loading. Their approach is applied to offshore piles, and it was reasonably able to model recorded centrifuge responses specifically for moderate rates of peak base accelerations. Zhong and Huang (2013) developed a simplified Winkler model for the lateral vibration of the composite caisson-pile foundations. The reliability of that model is demonstrated by conducting comparisons against results of the finite element simulations.

The pile–soil interaction is of great concern in structural behavior. For piled foundations, the nonlinear behavior of the axial and lateral pile–soil support is explicitly modeled to ensure load-deflection compatibility between the structure and pile–soil system. For a pile analysis, the effects of geometrical and material nonlinearities are considered within the structure–pile–soil system. The soil parameters based on geotechnical investigations and bore hole data at the platform site are determined in terms of submerged unit weight (γ'), undrained shear strength (Su), soil–pile friction angle (δ), and over-consolidation ratio (OCR) for piled foundation analysis. These values were used to generate the pile axial adhesion, skin friction, and bearing capacity based on API-RP2A recommendations (Det Norske Veritas (DNV), 1977, API, 2014). Soil basic properties at the site were also used to generate the pile lateral soil properties in the form of load-deflection curves. The modeling of foundation piles and conductor piles is constructed based on the pile and conductor size and penetration as defined in the design drawings. The foundation is simulated in the structural model by considering the pile stiffness; the lateral behavior of the soil and the nonlinear soil–pile–jacket interaction based on the API guidelines

$$p_u = \min\begin{pmatrix} (C_1 \times h + C_2 \times D) \times \gamma' \times h \\ C_2 \times D \times \gamma' \times h \end{pmatrix}. \tag{8}$$

p_u is the ultimate resistance, (kN/m); γ' is the effective soil unit weight, (kN/m^3); h is the depth, (m); and D is average pile diameter from surface to depth h, (m). C_1, C_2, C_3 are coefficients determined from the API guidelines. The lateral soil resistance–deflection (*p*–*y*) relationships for sand are nonlinear and may be approximated by the following expression:

$$P_s = A \times p_u \times \tanh\left(\frac{\kappa \times h}{A \times p_u} y\right), \tag{9}$$

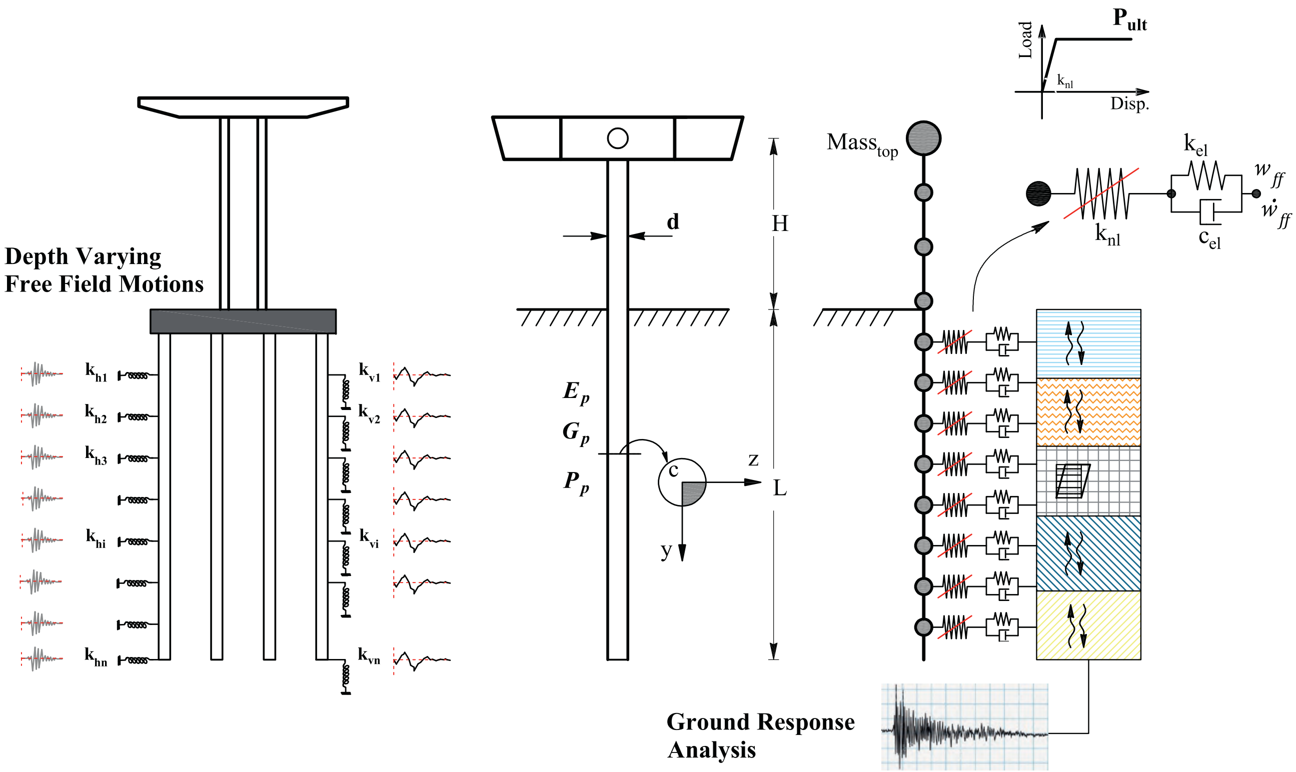

Figure 9.11 Winkler soil–pile–structure interaction model (Lam et al., 2007; Kampitsis et al., 2013; Pecker, 2015).

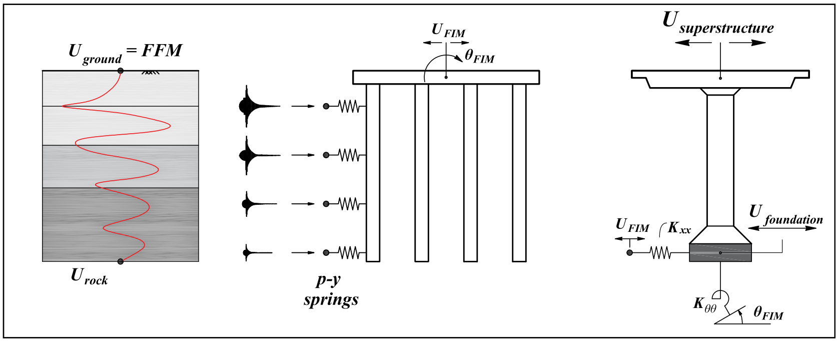

Figure 9.12 Substructure method of analysis for bridge bent supported on a pile group (Turner et al., 2017). (a) Ground response analysis, (b) BDNWF pile–soil interaction, (c) Superstructure analysis.

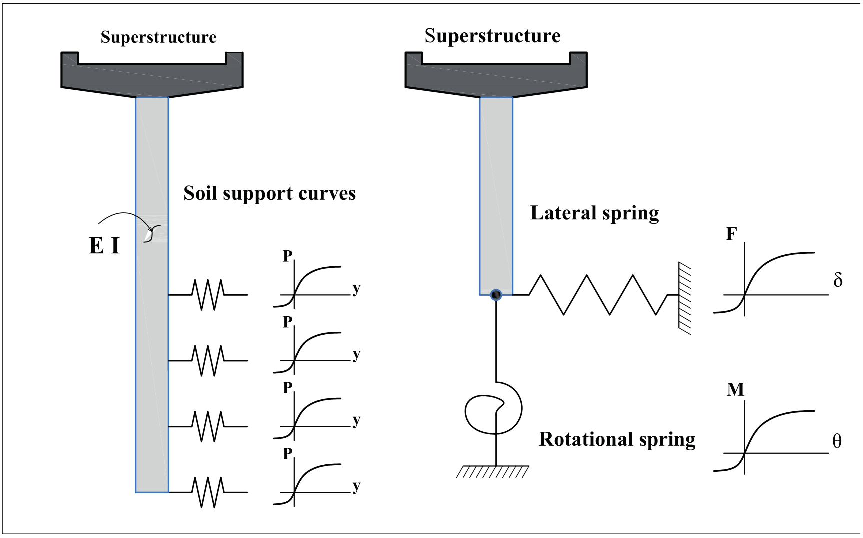

Figure 9.13 Nonlinear Winkler soil–pile–structure interaction model (Lam and Law, 2000).

where A is the factor to account for cyclic or static loading ($A = 0.9$ for cyclic, $A = (3.0–0.8*(h/D)) \geq 0.9$ for static), p_u is the ultimate resistance at depth h, and κ is the initial modulus of the subgrade reaction determined from the API specifications. The vertical soil resistance along the pile shaft and at the pile toe is a function of the level and rate of loading. The soil resistance to the vertical movement of the pile is modeled using axial shear transfer functions that depend on local pile deflection ($t–z$ curves). The soil resistance at the pile toe is modeled using $q–z$ curves. The soil conditions are modeled as a set of nonlinear springs, as shown in Figure 9.13. Geotechnical data in the form of soil lateral capacities ($p–y$), axial values ($t–z$), and end bearing values ($q–z$) curves are obtained from the soil and foundation report (Abdel Raheem and Hayashikawa, 2013; Abdel Raheem et al., 2020).

5.8 3-D continuum model

Three-dimensional (3-D) dynamic FE simulation is developed to capture seismic site response and coupled soil–foundation–structure interaction by considering the progressive softening (inelasticity) of soft saturated clay. This was accomplished by implementing an elasto-plastic constitutive model of soil to capture the elasto-plastic foundation–soil coupled response under irregular seismic loadings. It was shown that the variation in the underlying soil profiles leads to a different dynamic response of the system. This effect depends on the ratio between the flexural stiffness of the bridge and the dynamic stiffness of the foundation–soil system but also on the ratio between the resonant frequency of the soil layer and the fundamental frequency of the bridge, as shown in Figures 9.14 and 9.15.

The results of parametric study demonstrate that rigid, slender (tall) structures are highly susceptible to the SSI effects including the alteration of natural frequency, foundation rocking, and excessive base shear demand. Structure–foundation stiffness and aspect ratios were found to be crucial parameters controlling coupled foundation–structure performance in flexible-base structures. Furthermore, the frequency content of input motion, site response, and structure must be considered to avoid the occurrence of resonance problems (Torabi and Rayhani, 2014).

5.9 Soil–structure interaction of integrated abutment

Although the concept of IAB provides many advantages and avoids many complications in construction, the most important concern in analyzing and designing an IAB is the possible reaction of soil to the rear of abutment walls and nearby piles. When a bridge is thermally expanded, there are substantial degrees of force exerted by the soil, and this can significantly impact the whole bridge structure. Such inherently nonlinear activity of soil is dependent on the amount and form of displacement of the wall,

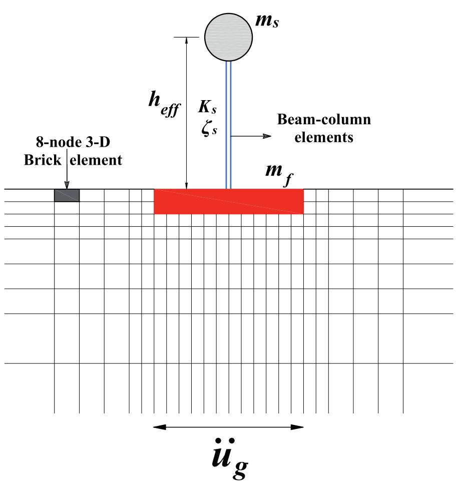

Figure 9.14 Finite element method (Torabi and Rayhani, 2014).

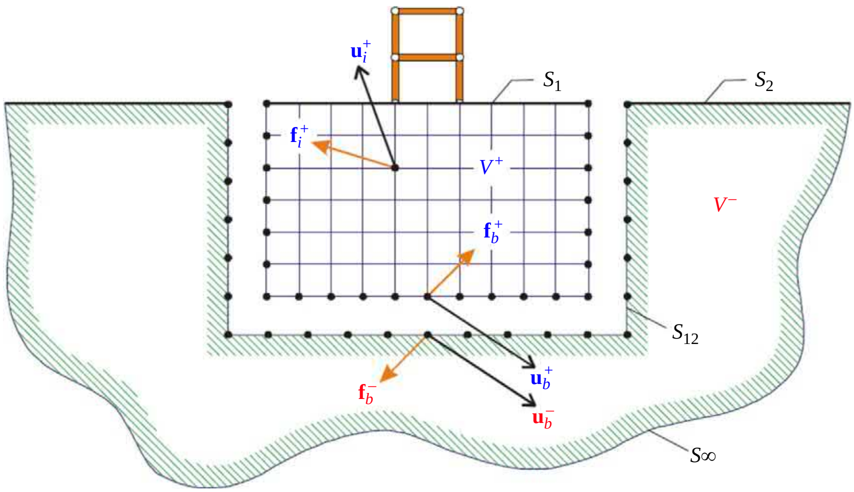

Figure 9.15 Finite domain interacting with an infinite surrounding medium (Andersen, 2004).

which brings about translation and rotation. The problem affects to the soil–structure and is stated as a drag of SSI, whereby there is independence in the amount and form of soil and deformations in structure and stresses (Jeremić et al., 2004; Fennema et al., 2005). However, soil conditions can vary from loose to dense states, the soil pressure that builds up behind the abutment increases more than 400%, axial forces in the bridge deck increase by about 50%, and bending moments in the composite deck increase by about 40% (Clayton et al., 2006; Shamsabadi et al., 2007; Mahjoubi and Maleki, 2018). Generally, the integral bridge concept has been proven to be less expensive to construct for wide-ranging span lengths; it has also been shown to be successful from the technical point of view as it eliminates problems of joint and bearings expansion. However, it may be troubled by geotechnical issues, which are potentially the result of reaction of the complicated structure of the soil to relative movement of the bridge abutment and surrounding retained soil. Primarily, as this movement is due to both natural and seasonal variations in weather and other longitudinal movements such as seismic loads, it is a potential problem for all integral bridges (Huffman et al., 2015; Gorini and Callisto, 2019; Najia et al., 2020). The seismic response should be evaluated by using a comprehensive methodology that takes into consideration the local response of deposits, the different response of each foundation, and the real structural configuration to capture the effects of deck deformability and of the substructures (Carbonari et al., 2011).

5.10 Spatial variation of earthquake ground motion

The observed amplitude and phase differences of seismic ground motions recorded at different locations over extended areas or within the dimensions of an engineered structure are termed as spatial variability of earthquake ground motions (SVGMs). The main causes of SVGMs have been identified as the wave passage effect, the loss of coherence, the extended source affect, the scattering effect, and the attenuation effect (Abrahamson, 1993, Shinozuka et al., 2000, Sextos et al., 2003a and b). The wave passage effect corresponds to the difference in arrival times of seismic waves at different locations. The loss of coherence of seismic waves is due to multiple reflections and refraction as they propagate through the highly inhomogeneous soil medium. Differences in the way that multiple waves are combined when arriving from an extended source cause differences in the phase and amplitude content of the ground motions of two distant points. The attenuation effect of the waves as they travel away from the source to the site contributes to the variations of seismic ground motion; moreover, the change in the amplitude and frequency content of seismic ground motion is due to different local soil conditions. Different supports of long structures or continuous parts of the foundations of a large structure may undergo different motions during an earthquake.

Past research studies have demonstrated that seismic ground motion can vary significantly over distances comparable to the length of the majority of highway bridges on multiple supports. As a result, such bridges are subjected to ground motions at their supports that can differ considerably in amplitude, phase, and frequency content, referred to as asynchronous support ground motions. In some cases, these differential motions can induce additional internal forces in the structures when compared to the case of identical support ground motion. This, in turn, might have a potentially detrimental effect on the safety of a bridge during a severe earthquake event. It is therefore of paramount importance to be able to account for the effect of spatial variability of earthquake ground motion on the response of the highway bridges. The spatial variability of input ground motion at supporting foundations plays a key role in the structural response of cable-stayed bridges (CSBs); therefore, spatial variation effects should be included in the analysis and design of effective vibration control systems. For long-span bridge structures, when the fundamental frequency may be close to the frequency of large-amplitude surface waves, long-period differential support motions may significantly influence the dynamic response of the bridge. Since strong motion accelerograms are the basic source of data for earthquake engineering research, it is important that highway bridges in seismic regions continue to be instrumented, especially to include a sufficient deployment of instruments on long-span bridges so that both spatial and temporal variations in support motions can be evaluated (Wilson and Jennings, 1985; Abdel Raheem et al., 2011).

6. Conclusions

The present chapter is an attempt to critically review the currently available structural analysis capabilities for the assessment of SSI and spatial variability effects in the framework of seismic design and assessment of bridges. Having discussed the most widely applied approaches and highlighted a set of reasonable approximations together with their limitations, this chapter was intended to fill the gap between state-of-the-art research and state of practice.

Soil conditions have a great deal to do with damage to structures during earthquakes. Hence, the investigation on the energy transfer mechanism from soils to structures during earthquakes is critical for the seismic design of bridge structures (Abdel Raheem et al., 2015). Preliminary analytical studies comparing the response of fixed-base models with simplified soil–foundation models are expected to provide important information about the need for considering SSI effects in the design process. It is important that highway bridges in seismic regions continue to be instrumented, especially to include a sufficient deployment of instruments on long-span bridges so that both spatial and temporal variations in support motions can be evaluated. It appears difficult to determine a priori whether SSI will increase or decrease the response of a bridge (Anand and Kumar, 2018). The observed phenomena and the discussed interplay between various natural periods of the system and dominant periods of the ground excitation can be helpful in predicting qualitatively the response in other cases or in interpreting the results of numerical studies.

- The system damping: If the fundamental period of the flexibly supported bridge is significantly smaller than the cutoff frequency of the soil (e.g., a rigid pier on a deep and soft deposit), radiation damping will be significant, and the response of the system will decrease. In particular, if the cutoff period of the soil is very large (e.g., a thick deposit), radiation damping may be substantial regardless of the natural period of the system. This implies that modeling the soil as a half-space, as done in existing seismic regulations (ATC-3, NEHRP-2003), may lead to unconservative estimates of the response.
- Resonance between structure and soil: If the increase in the fundamental natural period due to SSI brings the period of the bridge close to an "effective" natural period (especially the first or second) of the soil, resonance will develop, which will tend to increase the response. However, if the frequency content of the excitation is not rich in that period, the increase may be insignificant.
- Double resonance: If the fundamental natural period of the system coincides with both the natural period of the soil and the predominant period of the earthquake motion (at rock level), double resonance will develop (i.e., between structure, soil, and excitation). In this case, the response may increase dramatically. Whether or not this will result in damage is related to several additional parameters that are not discussed in this study.
- Nonlinear effects: The development of plastic deformations in the structure and soil, including development of pore water pressure and uplift, may increase the effective natural period of the structure and the soil. This shift in period may lead to either de-resonance or resonance (e.g., bringing the structure closer to the predominant period of the excitation)—which, in turn, may lead to "progressive collapse." To date, such strong nonlinearities are beyond the state-of-the-art seismic SSI.
- In conclusion, in complex structures such as bridges, it is not possible to state that the effects of SSI are beneficial or detrimental with respect to the structure as a whole, but only with respect to each structural element (deck, piers, abutments, and foundations).

References

Abdel Raheem, S.E., Hayashikawa, T., 2013. Soil–structure interaction modeling effects on seismic response of cable-stayed bridge tower. Int. J. Adv. Struct. Eng. 5 (8), 1–17.

Abdel Raheem, S.E., Hayashikawa, T., Hashimoto, I., 2003. Effects of soil–foundation superstructure interaction on seismic response of cable-stayed bridges tower with spread footing foundation. J. Struct. Eng. 49A, 475–486.

Abdel Raheem, S.E., Hayashikawa, T., Dorka, U., 2011. Ground motion spatial variability effects on seismic response control of cable-stayed bridges. Earthq. Eng. Eng. Vib. 10 (1), 37–49. https://doi.org/10.1007/s11803-011-0045-5.

Abdel Raheem, S.E., Ahmed, M.M., Alazrak, T.M.A., 2015. Evaluation of soil–foundation–structure interaction effects on seismic response demands of multi-story MRF buildings on raft foundations. Int. J. Adv. Struct. Eng. 7, 11–30. https://doi.org/10.1007/s40091-014-0078-x.

Abdel Raheem, S.E., Abdel, A.E., Abdel Shafy, A.G., Fahmy, M.F.M., Mansour, M.H., 2020. Pile-soil–structure interaction effect on structural response of piled jacket-supported offshore platform through in-place analysis. Earthq. Struct. 18 (4), 407–421.

Abrahamson, N.A., 1993. Spatial variation of multiple support inputs. In: Proceedings of the 1st US Seminar on Seismic Evaluation and Retrofit of Steel Bridges. A Caltrans and University of California at Berkeley Seminar, San Francisco, CA.

Ahn, K., Gould, P.L., 1992. Interactive base-isolation foundation system: I. Finite element formulation. J. Eng. Mech., ASCE 118 (10), 2048–2058.

Allotey, N., El-Naggar, M.H., 2008. Generalized dynamic Winkler model for nonlinear soil–structure interaction analysis. Can. Geotech. J. 45 (4), 560–573.

Anand, V., Kumar, S.R.S., 2018. Seismic soil–structure interaction: a state-of-the-art review. Structures 16, 317–326. https://doi.org/10.1016/j.istruc.2018.10.009.

Andersen, L., 2004. Elastodynamics and Finite Element Analysis in Wave Propagation Problems. Course Notes. Department of Civil Engineering, Aalborg University, Denmark.

API (American Petroleum Institute), 2014. Recommended Practice for Planning, Designing and Constructing Fixed Offshore Platforms-Working Stress Design, API RP-2A - WSD, twenty-second ed. Washington.

Armstrong, R.J., Boulanger, R.W., Beaty, M.H., 2014. Equivalent static analysis of piled bridge abutments affected by earthquake induced liquefaction. ASCE J. Geotechn. Geoenviron. Eng. 140 (8), 1–10.

ATC, 1978. Tentative provisions for the development of seismic regulations for buildings. In: ATC 3–06, Applied Technology Council, Redwood City, CA.

Bielak, J., 1975. Dynamic behavior of structures with embedded foundations. Earthq. Eng. Struct. Dyn. 3 (3), 259–274.

Boulanger, R.W., Curras, C.J., Kutter, B.L., Wilson, D.W., Abghari, A., 1999. Seismic soil-pile-structure interaction experiments and analyses. J. Geotech. Geoenviron. 125 (9), 750–759. https://doi.org/10.1061/(ASCE)1090-0241(1999)125:9(750).

Brandenberg, S.J., Singh, P., Boulanger, R.W., Kutter, B.L., 2001. Behavior of piles in laterally spreading ground during earthquakes. In: Proceedings of the 6th Caltrans Seismic Research Workshop, CA, 2001, pp. 2–106.

Carbonari, S., Dezi, F., Leoni, G., 2011. Seismic soil–structure interaction in multi-span bridges: application to a railway bridge. Earthq. Eng. Struct. Dyn. 40 (11), 1219–1239. https://doi.org/10.1002/eqe.1085.

Castelli, F., Maugeri, M., 2009. Simplified approach for the seismic response of pile foundation. Am. Soc. Civil Eng., ASCE J. Geotechn. Geoenviron. Eng. 135 (10), 1440–1451.

CEN, 2004. EN 1998–1 Eurocode 8: Design of Structures for Earthquake Resistance, Part 1: General Rules, Seismic Actions, and Rules for Buildings. European Committee for Standardization.

Chaojin, X., Spyrakos, C.C., 1996. Seismic analysis of towers including foundation uplift. Eng. Struct. 18 (4), 271–278.

Chaudhary, M.T.A., 2016. Effect of soil–foundation structure interaction and pier column nonlinearity on seismic response of bridges supported on shallow foundations. Aust. J. Struct. Eng. 17 (1), 67–86. https://doi.org/10.1080/13287982.2015.1116178.

Clayton, C.R.I., Xu, M., Bloodworth, A., 2006. A laboratory study of the development of earth pressure behind integral bridge abutments. Géotechnique 56 (8), 561–571.

Committee of Earthquake Engineering, 1996. The 1995 Hyogoken-Nanbu Earthquake, Investigation into Damage to Civil Engineering Structures. Japan Society of Civil Engineers, Tokyo.

Cox, W.R., Reese, L.C., Grubbs, B.R., 1974. Field testing of laterally loaded piles in sand. In: Proc. 6th Offshore Technol. Conf., Houston, TX. 2, pp. 459–472.

Det Norske Veritas (DNV), 1977. Result for the Design, Construction and Inspection of Offshore Structures. Oslo (Reprint with correction 1981) http://www.dnv.com.

Dicleli, M., Lee, J.-Y., Mansour, M., 2004. Importance of soil-bridge interaction modeling in seismic analysis of seismic-isolated bridges. In: 13th World Conference on Earthquake Engineering, Vancouver, BC, Canada, August 1–6, 2004. Paper No. 3147.

Eduardo, K., 2010. Early history of soil–structure interaction. Soil Dyn. Earthq. Eng. 30, 822–832.

El-Naggar, M.H., Bentley, K.J., 2000. Dynamic analysis for laterally loaded piles and dynamic p-y curves. Can. Geotech. J. 37, 1166–1183.

European Committee for Standardization, 1998. EC8: Design Provisions for Earthquake Resistance of Structures, Part 5: Foundations, Retaining Structures and Geotechnical Aspects. European Committee for Standardization, Brussels.

FEMA, 2009. NEHRP Recommended Seismic Provisions for New Buildings and Other Structures, FEMA P-750/2009 Edition, Prepared by the Building Seismic Safety Council of the National Institute of Building Sciences for the Federal Emergency Management Agency. Washington, DC.

Fennema, J.L., Laman, J.A., Linzell, D.G., 2005. Predicted and measured response of an integral abutment bridge. J. Bridg. Eng. 10 (6), 666–677.

Finn, W.D.L., Pandey, B.H., Ventura, C.E., 2019. Modeling soil–foundation–structure interaction. Struct. Des. Tall Spec. Build. 20, S47–S62. https://doi.org/10.1002/tal.735.

Gazetas, G., 1991. Formulas and charts for impedances of surface and embedded foundations. J. Geotechn. Eng. (ASCE) 117 (9), 1363–1381.

Gazetas, G., Dobry, R., 1984. Horizontal response of piles in layered soils. J. Geotechn. Eng. Div. - ASCE 110 (1), 20–40.

Gelagoti, F., Kourkoulis, R., Anastasopoulos, I., Gazetas, G., 2012. Rocking isolation of low-rise frame structures founded on isolated footings. Earthq. Eng. Struct. Dyn. 41, 1177–1197.

Gilles, D., McClure, G., Chouinard, L.E., 2011. Uncertainty in fundamental period estimates leads to inaccurate design seismic loads. Can. J. Civ. Eng. 38 (8), 870–880.

Givens, M.J., Mylonakis, G., Stewart, J.P., 2016. Modular analytical solutions for foundation damping in soil structure interaction applications. Earthquake Spectra 32 (3), 1749–1768.

Gorini, D.N., Callisto, L., 2019. A coupled study of soil-abutment-superstructure interaction. In: National Conference of the Researchers of Geotechnical Engineering. Springer, Cham, pp. 565–574.

Harden, C., Hutchinson, T., Moore, M., 2006. Investigation into the effects of foundation uplift on simplified seismic design procedures. Earthquake Spectra 22 (3), 663–692.

Hardin, B.O., Drnevich, V.P., 1972a. Shear modulus and damping in soil: measurement and parameter effects. J. Soil Mech. Found. Eng. Div. ASCE 98 (6), 603–624.

Hardin, B.O., Drnevich, V.P., 1972b. Shear modulus and damping in soils: design equations and curves. J. Soil Mech. Found. Div. ASCE 98 (7), 667–692.

Hassani, N., Bararnia, M., Amiri, G.G., 2018. Effect of soil–structure interaction on inelastic displacement ratios of degrading structures. Soil Dyn. Earthq. Eng. 104, 75–87.

Huffman, J.T., Xiao, F., Chen, G., Hulsey, J.L., 2015. Detection of soil-abutment interaction by monitoring bridge response using vehicle excitation. J. Civ. Struct. Heal. Monit. 5 (4), 389–395.

Japan Road Association, 1996a. Specification for Highway Bridges - Part V Seismic Design. Japan Road Association, Tokyo.

Japan Road Association, 1996b. Reference for Highway Bridge Design, Specification for Highway Bridges - Part IV Substructures. Japan Road Association, Tokyo.

Jeremić, B., Kunnath, S., Xiong, S., 2004. Influence of soil–foundation-structure interaction on seismic response of the I-880 viaduct. Int. J. Eng. Struct. 26 (3), 391–402.

Kamali, A.Z., 2018. Dynamic Soil Structure Interaction Analysis of Railway Bridges Numerical and Experimental Results. Licentiate Thesis, KTH Royal Institute of Technology School of Architecture and the Built Environment, Department of Civil and Architectural Engineering Division of Structural Engineering and Bridges SE-100 44, Stockholm, Sweden.

Kampitsis, A.E., Sapountzakis, E.J., Giannakos, S.K., Gerolymos, N.A., 2013. Seismic soil–pile–structure kinematic and inertial interaction-a new beam approach. Soil Dyn. Earthq. Eng. 55, 211–224.

Kausel, E., 2010. Early history of soil–structure interaction. Soil Dyn. Earthq. Eng. 30, 822–832.

Kausel, E., Roesset, J.M., Christian, J.T., 1976. Nonlinear behavior in soil–structure interaction. J. Geotech. Eng. Div. ASCE 102 (GT12), 1159–1178.

Kawashima, K., Hosoiri, K., 2002. Effect of nonlinear rocking response of direct foundations on the hysteretic behavior of bridges. J. Struct. Mech. Earthq. Eng.-JSCE 703 (I-59), 97–111.

Kim, S., Stewart, J.P., 2003. Kinematic soil–structure interaction from strong motion recordings. J. Geotech. Geoenviron. Eng. 129, 323–335.

Kimiaei, M., Shayanfar, M.A., El Naggar, M.H., Aghakouchak, A.A., 2004. Nonlinear response analysis of offshore piles under seismic loads. In: Proceedings of 13th World Conference on Earthquake Engineering, Vancouver, BC, Canada, August 1–16, 2004. Paper No. 3056.

Kobayashi, T., Yoshikawa, K., Takaoka, E., Nakazawa, M., Shikama, Y., 2002. Time history nonlinear earthquake response analysis considering materials and geometrical nonlinearity. Nucl. Eng. Des. 212 (1–3), 145–154.

Lam, I.P., Law, H., 2000. Soil Structure Interaction of Bridges for Seismic Analysis. MCEER-00-0008. Multidisciplinary Center for Earthquake Engineering Research.

Lam, P.I., Law, H., Martin, G.R., 2007. Bridge Foundations: Modeling Large Pile Groups and Caissons for Seismic Design. MCEER-07-018. Multidisciplinary Center for Earthquake Engineering Research.

Liyanapathirana, D.S., Poulos, H.G., 2005. Seismic lateral response of piles in liquefying soil. Am. Soc. Civil Eng. ASCE J. Geotechn. Eng. 131 (12), 1466–1479.

Lou, M.-L., Wang, W.-J., Ma, H.-C., Zhu, T., 2001. Study on soil pile-structure interaction system by shaking table model test. J. Tongji Univ. 29 (7), 763–768.

Lysmer, J., Ostadan, F., Chen, C., 1999. Computer Program SASSI2000, Geotechnical Division. University of California, Berkeley, California.

Mahjoubi, S., Maleki, S., 2018. Finite element modelling and seismic behaviour of integral abutment bridges considering soil–structure interaction. Eur. J. Environ. Civ. Eng., 1–20.

Masing, G., 1926. Eigenspannungeu und verfertigung beim Messing. In: Proceedings of the 2nd International Congress on Applied Mechanics, Zurich.

Matlock, H., 1970. Correlations for design of laterally loaded piles in soft clay. In: Proc. 2nd Offshore Technol. Conf., Houston, TX. 1, pp. 577–594.

Megawati, K., Higashihara, H., Koketsu, K., 2001. Derivation of near-source ground motions of the 1995 Kobe (Hyogo-ken Nanbu) earthquake from vibration records of the Akashi Kaikyo bridge and its implications. Eng. Struct. 23 (10), 1256–1268.

Mikami, A., Sawada, T., 2004. Time-domain identification system of dynamic soil–structure interaction. In: Proceedings of the 13th World Conference on Earthquake Engineering, Vancouver.

Mirzaie, F., Mahsuli, M., Ghannad, M.A., 2017. Probabilistic analysis of soil–structure interaction effects on the seismic performance of structures. Earthq. Eng. Struct. Dyn. 46 (4), 641–660.

Mita, A., Luco, J.E., 1989. Dynamic response of square foundation embedded in an elastic half-space. Soil Dyn. Earthq. Eng. 8 (2), 54–67.

Mylonakis, G., Gazetas, G., 2000. Seismic soil-structure interaction: beneficial or detrimental. J. Earthq. Eng. 4 (3), 277–301. https://doi.org/10.1080/13632460009350372.

Mylonakis, G., Syngros, C., Gazetas, G., Tazoh, T., 2006a. The role of soil in the collapse of 18 piers of hanshin expressway in the Kobe earthquake. Earthq. Eng. Struct. Dyn. 35 (5), 547–575.

Mylonakis, G., Nikolaou, S., Gazetas, G., 2006b. Footings under seismic loading: analysis and design issues with emphasis on bridge foundations. Soil Dyn. Earthq. Eng. 26, 824–853.

Najia, M., Akbar, F.A., Asghar, F.A., 2020. Review: study of integral abutment bridge with consideration of soil–structure interaction. Latin Am. J. Solids Struct. 17 (2), e252. 25/27.

National Institute of Standards and Technology (NIST), 2012. Soil-Structure Interaction for Building Structures, Report NIST/GCR 12-917-21, Presented by NEHRP Consultants Joint Venture, J.P. Stewart (Project Director), September. NIST, U.S. Department of Commerce.

Neethu, B., Das, D., 2019. Effect of dynamic soil–structure interaction on the seismic response of bridges with elastomeric bearings. Asian J. Civil Eng. 20, 197–207. https://doi.org/10.1007/s42107-018-0098-0.

NEHRP, 1997. Recommended Provisions for Seismic Regulations for New Buildings and Other Structures. National Earthquake Hazard Reduction Program. Building Seismic Safety Council, Washington, DC.

Nogami, T., Otani, J., Konagai, K., Chen, H.-L., 1992. Nonlinear soil-pile interaction model for dynamic lateral motion. J. Geotech. Eng. 118 (1), 89–106.

NRCC, 2010. National Building Code of Canada, Associate Committee on the National Building Code. National Research Council of Canada, Ottawa, ON.

Pecker, A., 2015. Seismic analyses and design of foundation soil structure interaction. In: Ansal, A. (Ed.), Perspectives on European Earthquake Engineering and Seismology. Geotechnical, Geological and Earthquake Engineering. vol. 39. Springer, Cham, https://doi.org/10.1007/978-3-319-16964-4_6.

Piro, A., Silva, F., Parisi, F., Santolo, A., Silvestri, F., 2020. Effects of soil-foundation-structure interaction on fundamental frequency and radiation damping ratio of historical masonry building sub-structures. Bull. Earthq. Eng. 18, 1187–1212. https://doi.org/10.1007/s10518-019-00748-4.

Raychowdhury, P., 2011. Seismic response of low-rise steel moment-resisting frame (SMRF) buildings incorporating nonlinear soil–structure interaction (SSI). Eng. Struct. 33, 958–967.

Seed, H.B., Idriss, I.M., 1970. Soil Moduli and Damping Factors for Dynamic Response Analysis. Report No. EERC70-10. Earthquake Engineering Research Center, University of California, Berkeley, CA.

Seed, H.B., Romo, M.P., Sun, J.I., Lysmer, J., 1988. The Mexico earthquake of September 19, 1985-relationships between soil conditions and earthquake ground motions. Earthq. Spectr. (EERI) 4 (4), 687–729.

Seed, R.B., Dickenson, S.E., Mok, C.M., 1992. Recent lessons regarding seismic response analyses of soft and deep clay sites. In: Proceedings of Seminar on Seismic Design and Retrofit of Bridges. Earthquake Engineering Research Center, Univ. of California at Berkeley, California, Dept. of Transportation, Sacramento, CA, pp. 18–39.

Sextos, A., 2013. Effect of soil–structure interaction and spatial variability of ground motion on seismic risk assessment of bridges (Chapter 22). In: Tesfamariam, S., Goda, K. (Eds.), Handbook of Seismic Risk Analysis and Management of Civil Infrastructure Systems, first ed. Woodhead Publishing, https://doi.org/10.1533/9780857098986.4.597.

Sextos, A.G., Pitilakis, K.D., Kappos, A.J., 2003a. Inelastic dynamic analysis of RC bridges accounting for spatial variability of ground motion, site effects and soil–structure interaction phenomena. Part 1: methodology and analytical tools. Earthq. Eng. Struct. Dyn. 32 (4), 607–627. Available at: http://doi.wiley.com/10.1002/eqe.241.

Sextos, A.G., Kappos, A.J., Pitilakis, K.D., 2003b. Inelastic dynamic analysis of RC bridges accounting for spatial variability of ground motion, site effects and soil–structure interaction phenomena. Part 2: parametric study. Earthq. Eng. Struct. Dyn. 32 (4), 629–652. Available at: http://doi.wiley.com/10.1002/eqe.242.

Shamsabadi, A., Rollins, K.M., Kapuskar, M., 2007. Nonlinear soil–abutment–bridge structure interaction for seismic performance-based design. J. Geotech. Geoenviron. 133 (6), 707–720.

Shinozuka, M., Saxena, V., Deodatis, G., 2000. Effect of Spatial Variation of Ground Motion on Highway Structures. MCEER-00-0013.

Spyrakos, C.C., 1997. Soil–structure-water interaction of intake-outlet towers allowed to uplift. Soil Dyn. Earthq. Eng. 16 (2), 151–159.

Tang, Y., Zhang, J., 2011. Probabilistic seismic demand analysis of a slender RC shear wall considering soil–structure interaction effects. Eng. Struct. 33, 218–229.

Tongaonkar, N.P., Jangid, R.S., 2003. Seismic response of isolated bridges with soil–structure interaction. Soil Dyn. Earthq. Eng. 23, 287–302. https://doi.org/10.1016/S0267-7261(03)00020-4.

Torabi, H., Rayhani, M.T., 2014. Three-dimensional finite element modeling of seismic soil–structure interaction in soft soil. Comput. Geotech. 60, 9–19. https://doi.org/10.1016/j.compgeo.2014.03.014.

Trifunac, M.D., Todorovska, M.I., 1996. Nonlinear soil response - 1994 Northridge, California, earthquake. J. Geotech. Eng. 122 (9), 725–735.

Turner, B.J., Brandenberg, S.J., Stewart, J.P., 2017. Influence of Kinematic SSI on Foundation Input Motions for Bridges on Deep Foundations. PEER Report No. 2017/08. Pacific Earthquake Engineering Research Center PEER, Department of Civil and Environmental Engineering, University of California, Los Angeles.

Ucak, A., Tsopelas, P., 2008. Effect of soil–structure interaction on seismic isolated bridges. J. Struct. Eng. 134 (7), 1154–1164. https://doi.org/10.1061/(asce)0733-9445(2008)134:7(1154).

Veletsos, A.S., Meek, J.W., 1974. Dynamic behavior of building-foundation systems. Earthq. Eng. Struct. Dyn. 3 (2), 121–138.

Veletsos, A.S., Prasad, A.M., Wu, W.H., 1997. Transfer functions for rigid rectangular foundations. Earthq. Eng. Struct. Dyn. 26 (1), 5–17.

Vlassis, A.G., Spyrakos, C.C., 2001. Seismically isolated bridge piers on shallow soil stratum with soil structure interaction. Comput. Struct. 79 (32), 2847–2861.

Wilson, J.C., Jennings, P.C., 1985. Spatial variation of ground motion determined from Accelerograms recorded on a highway bridge. Bull. Seismol. Soc. Am. 75 (6), 1515–1533.

Wolf, J.P., 1985. Dynamic Soil–Structure Interaction. Prentice-Hall, Englewood Cliffs, NJ.

Wu, G., Finn, W.D.L., 1997. Dynamic nonlinear analysis of pile foundations using the finite element method in the time domain. Can. Geotech. J. 34, 144–152.

Yim, S.C.S., Chopra, A.K., 1984. Dynamics of structures on 2-spring foundation allowed to uplift. J. Eng. Mech. 110 (7), 1124–1146.

Zhang, J., Tang, Y., 2009. Dimensional analysis of structures with translating and rocking foundations. Soil Dyn. Earthq. Eng. 29 (10), 330–346.

Zhang, Z., Cho, C., Lu, X., Lou, M., 2010. Shaking table tests of the damping behavior of SSI systems. China Civ. Eng. J. 43 (2), 100–104.

Zhong, R., Huang, M., 2013. Winkler model for dynamic response of composite caisson-piles foundations: lateral response. Soil Dyn. Earthq. Eng. 55 (4), 182–194.

This page intentionally left blank

Part IV

Bridge design based on construction material type

This page intentionally left blank

Reinforced and prestressed concrete bridges

10

G.L. Balázs, G. Farkas, and T. Kovács
Budapest University of Technology and Economics, Budapest, Hungary

1. Types of reinforced concrete bridges

The type of a reinforced or prestressed concrete bridge deck built depends mainly on the functional requirements, the structural form, and the main span length of the construction. Precast or cast-in-situ reinforced concrete bridge decks can be practically applied for all structural types, like arch, cable-stayed, extradosed, suspension bridges, and the majority of girder bridges. In this chapter, we mainly discuss simply supported and continuous girder bridges, which differ from each other mainly by their cross section. The structural depths of reinforced concrete girders largely depend on the selected cross section.

Solid slabs with rectangular cross sections are suitable for spans up to 15 m. If self-weight is reduced by using side cantilevers, the spans from 18 to 20 m are particularly economical (Figure 10.1). The main benefits of this type of cross section are the relatively high torsional rigidity, the smaller structural depth than beams, and easily fixable reinforcement. These types of bridge decks requiring prestressed solid slabs can be economically used due to the these benefits for spans of 15 to 23 m owing to less formwork than for beams and fewer earthworks in the approach embankments. The disadvantages of this construction are the greater quantities of reinforcement and concrete beams required and, consequently, the increased self-weight of the deck.

Voided slabs with rectangular cross sections or side cantilevers are used for spans longer than about 20 m in order to reduce the self-weight (Figure 10.2). This type of cross section can be economical up to 25 m with a constant depth or up to 35 m with variable depth. Voids are produced by excluding the concrete by appropriate materials—for example, cardboard, expanded polystyrene, etc.—and are located near the mid-depth, causing a minimal reduction in inertia. Preventing the lifting of void formers due to the upward pressure of fresh concrete requires particular attention during casting.

Ribbed slabs can be used for spans between 20 and 40 m (Figure 10.3). The reduction in self-weight of this type of bridge decks is significant compared to solid slabs. For simply supported spans with constant depth, the typical span/depth ratio is between 22 and 25. This value may be about 30–35 for continuous prestressed concrete structures. For continuous reinforced concrete bridge decks with variable depth, the span/depth ratio can be 40 in the middle of the span and 25 over intermediate supports. The disadvantage of this type of cross section is the deep section at ribs.

Innovative Bridge Design Handbook. https://doi.org/10.1016/B978-0-12-823550-8.00009-3

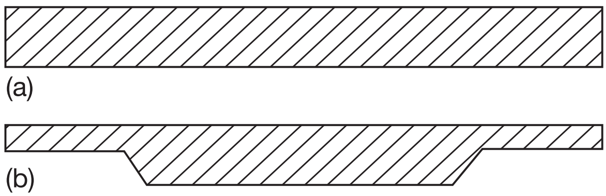

Figure 10.1 Solid slabs.

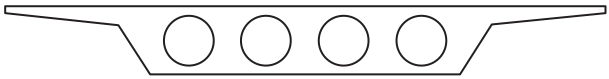

Figure 10.2 Voided slab.

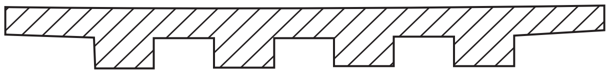

Figure 10.3 Ribbed slab.

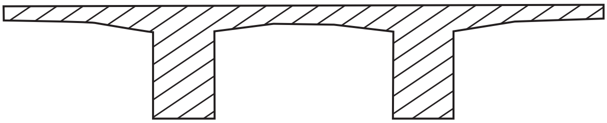

Figure 10.4 Beam and slab system.

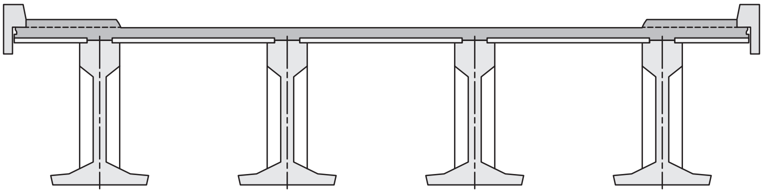

Figure 10.5 Beam and slab system with precast elements.

The construction requires relatively complicated formwork and special construction techniques.

Cast-in-situ beam and slab systems are developments of the ribbed slab, which is used for longer spans (Figure 10.4). For simply supported spans with post-tensioned beams, the range of use is 30–50 m.

Beam and slab systems with precast elements are most often used for simply supported spans (Figure 10.5). The continuity of the deck can be achieved by additional ordinary reinforcement over the piers or by post-tensioning. It provides an economic solution with pre-tensioned beams for span up to 30 m and to 50 m in case of post-tensioning. Many different cross sections can be used for precast beams. The most usual is an I shape section, placed at 0.6 m to about 4.0 m apart with cast

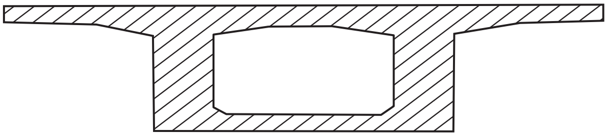

Figure 10.6 Box-girder cross section.

in situ concrete slab. The formwork of the slab is often created by a series of thin precast concrete slab elements. The span/depth ratio of 18 is usual for decks with beams 2–3 m apart. A span/depth ratio of 25 is possible for continuous bridge decks.

Box-girder bridge decks with single or multiple cells are necessary for spans longer than 80 m (Figure 10.6). The longest span constructed with box-girder cross section is about 300 m. The main benefit of these structures is their significant torsional rigidity. For reinforced concrete decks of constant depth, the span/depth ratio is normally within the range of 14–30. The optimum span/depth ratio for constant depths is between 18 and 22. For spans that exceed 60 m, it is structurally and economically favorable to apply longitudinally varying depth. For spans in excess of 150 m, variable depth is essential. The span/depth ratio at the piers in this case can be between 15 and 22, the span/depth ratio at midspan will be in the range of 35–22 for decks simply supported on the piers, and the ratio will be between 40 and 45 for decks embedded in the head of piers.

2. Prestressing in bridges

The cross section of a bridge deck subjected to bending moments will carry the load by the development of internal compressive and tensile stresses. In reinforced concrete elements, cracks will be formed in zones where high tensile stresses develop. An efficient possibility to reduce, or even avoid, the tensile stresses is the use of prestressing. The prestressing technology is widely applied in bridges, especially when using modern construction methods—e.g., bridge decks built using large precast elements, incremental launching, or other cantilever constructions.

2.1 Principle of prestressing

Prestressing artificially creating a stress distribution in the structure before loading, which will contribute balancing the external loads. One way to produce the suitable stress distribution is to apply a compressive force to the structural element. This can be achieved by use of high-strength steel tendons, which are stressed before the loading of the structure (Figure 10.7). The anchorage forces at the ends of the tendons provide compression in the concrete, straight tendons with eccentricity give additional bending effect, and the use of curved tendons can reduce axial bending as well as shear effects due to external loads.

Prestressing reduced the external forces in case of curved tendons, increases the rigidity by delaying the cracking of the reinforced concrete elements, and reduces deflections under service conditions.

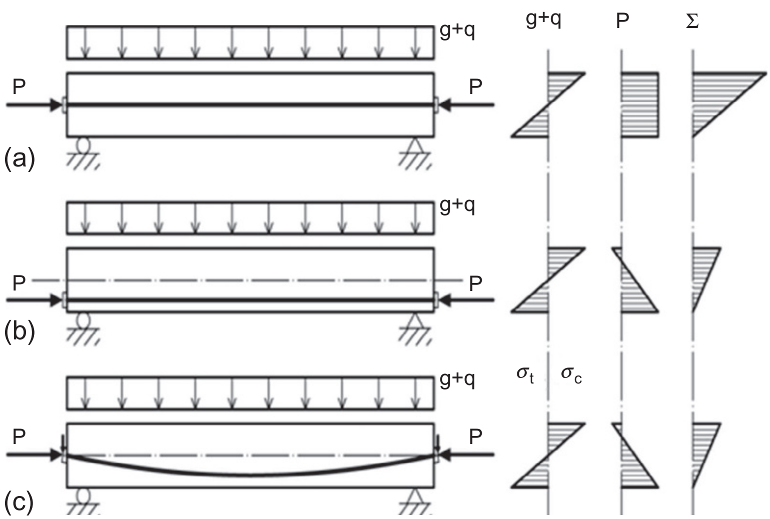

Figure 10.7 Stresses in the midspan cross section due to external loads and prestressing forces.

2.2 Prestressing systems

The main systems of prestressing are the *pretensioning* and the *post-tensioning*.

In the case of *pretensioning,* the prestressing tendons are tensioned before the casting of concrete. The prestress will be released from the temporary anchorages and transferred to the element after the hardening of the concrete. The transmission of the prestressing force to the structural element is generally ensured by bond over the interface of prestressing tendon and concrete. The common types of prestressing steels are eccentrically placed straight strands with a nominal diameter of 13 or 15 mm. This technology is mainly used to produce precast bridge girder beam elements in precast plants.

Post-tensioning is the commonly used technology in long-span cast in-situ reinforced concrete bridge constructions. In this case, the prestressing tendons are tensioned after the hardening of the concrete. Special end anchorages are fixed to the concrete; they transfer the prestressing forces into the structural element. Prestressing can be provided by prestressing wires, strands, cables or bars. Cables usually consist of 3–55 strands as a function of the prestressing force. The layout of tendons for post-tensioning can be selected to have optimal effect of prestressing.

The tendon must be freely movable in the element to be tensioned after hardening the concrete. To achieve this, the tendons are enclosed in metal or plastic ducts. The ducts are generally filled by cement grout to improve corrosion protection and provide a bond between tendons and surrounding concrete (Figure 10.8).

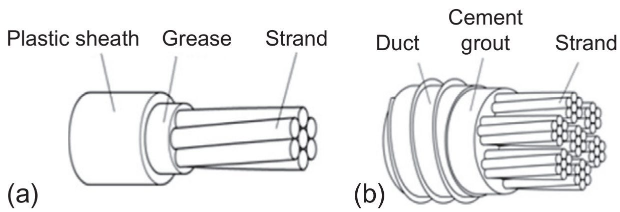

Figure 10.8 A seven-wire strand protected by plastic sheath and a cable formed by strands grouted in a duct.

In the case of conventional (internal) prestress, the cables are embedded in the concrete part of the cross section. For construction of post-tensioned bridge decks, the use of external prestressing is more and more frequent as part of current construction technologies. In the case of external prestressing, the tendons are outside of the concrete cross section. A polygonal layout of tendons is favorable in order to follow the internal forces due to the external loads (Figure 10.9).

Post-tensioning of bridge girders can be provided by bonded or unbonded tendons. Bonded tendons are considered if ducts are cement grouted and the tendons are in direct contact with the cement grout. In the case of bonded tendons, the strain variations due to live load are equal both in the tendon as well as in the surrounding concrete at the same level of the cross section. Cracks are well distributed along the length of the structural element.

External prestressing, or tendons in plastic sheaths, represent unbonded behavior. In principle, there is no friction between the tendon and concrete—therefore, no local increase of strain in prestressing steel—and, consequently, cracks will be concentrated and have wide openings without the ordinary reinforcement (Figure 10.10).

Figure 10.9 An example of external prestressing applied both in longitudinal and transverse directions with unbonded tendons.

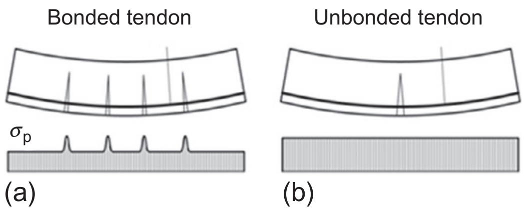

Figure 10.10 Stresses and cracks with (a) bonded and (b) unbonded tendons.

2.3 Detailing rules

In post-tensioning systems, special anchorage devices are used to transfer the prestressing forces to the concrete (Figure 10.11). The so-called *active anchorage* enables the tensioning of the tendon; the *passive anchorage* fixes the end of the tendon without tensioning. The so-called *coupling device* connects the end of one of the tensioned tendons to another tendon, which will be tensioned in a second phase. *Ducts* for post-tensioning systems connected to the anchorages form a channel inside the concrete element for the installation of tendons and provide an interface suitable for the transfer of bond stresses in the case of bonded tendons (using cement grout) for internal prestressing. For external prestressing, the duct can be placed inside or outside the concrete element, including single or multiple strands that are covered by grease, allowing longitudinal movement of strands without developing bond stresses (unbonded prestressing). Post-tensioning systems are developed and produced by qualified specialist companies that can be used for bridges.

For external prestressing, deviating devices must be placed between the tendon and the structural element to ensure the required layout of the cable (see Figure 10.9). These devices are designed to transfer the cable deviation forces to the structure. The minimum radii of curvature for tendons must meet the requirement so that the maximum tensile stress in the curvature complies with the tensile strength requirement. This minimum curvature must be declared by the tendon supplier in the prestressing system documentation.

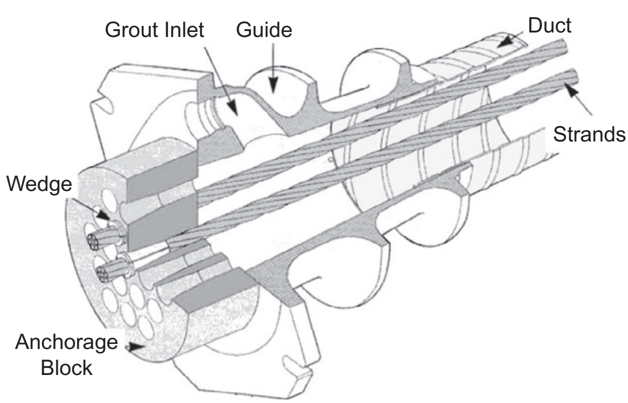

Figure 10.11 System of active Freyssinet anchorage for post-tensioning.

2.4 Losses and time-dependent effects on prestressing forces

The prestressing force applied to the structure decreases along the tendon length and also with time.

Immediate losses of prestress occurring during stressing are the following.

- *Losses due to elastic shortening of concrete* develop when tendons cannot be tensioned at the same time. The loss in tendon stress corresponds to the elastic deformation of concrete during prestressing. The range of the average loss for bridge decks is about 25 MPa, which is not very much compared to the level of prestressing.
- *Losses due to friction between the prestressing steel and the duct* in the case of post-tensioning at a distance x from the stressing anchorage depend on the stress of the tendon at the anchorage, σ_{po}; the coefficient of friction between the prestressing steel and the duct, μ; the sum of the angular deviation in radian from a distance x to the anchorage, α; and the unintentional angular deviation per unit length of the tendon, k. The stress in the tendon at a distance x from the anchorage is given by the following formula:

$$\sigma_{px} = \sigma_{po} e^{-\mu(\alpha + kx)} \approx \sigma_{po} \mu(\alpha + kx).$$

- Values of μ and k are obtained by experiments and are given in the system documentations. The coefficient of friction for bare strands or wires over the steel duct is between 0.25 and 0.30; for seven-wire strands over plastic ducts, it is in the range of 0.15–0.20; and for individually greased strands in plastic sheaths, it is 0.05–0.07.
- *Losses due to draw-in of prestressing anchoring wedges* occur before the wedges fully grip onto the surface of prestressing tendon at the anchorage during prestressing. This displacement causes a reduction of the prestress of the tendons in the anchorage zone. The loss of prestress can be calculated as a function of the draw-in value divided by the overall length of the tendon. Therefore, this type of loss is considerable for short tendons and almost negligible for long tendons.

Time-dependent losses of prestress due to shrinkage and creep of concrete and the relaxation of prestressing tendons may occur during the whole lifetime of the structure. The national and international codes give different expressions for the time-dependent losses, but the fundamental expression is

$$\Delta\sigma_p = E_p\, \varepsilon_{cs} + E_p\, \varphi\, \sigma_{cp}/E_c + \varkappa \sigma_p,$$

where E_p is the modulus of elasticity of prestressing steel;
E_c is the modulus of elasticity of concrete;
ε_{cs} is the shrinkage of concrete;
φ is the creep coefficient of concrete;
σ_{cp} is the compressive stress of the concrete for quasi-permanent load at level of tendons;
$\varkappa$ is the relative relaxation loss of the prestressing steel;
σ_p is the stress in the tendon.

The value of the time-dependent losses for bridge constructions is between 10% and 15% of the initial prestress.

2.5 Effective values of prestressing force

The effective value of the prestressing force, $P(t)$, at time t is

$$\mathrm{P(t) = A_p\,\sigma_p(t)},$$

where A_p is the cross section of the prestressing reinforcement, and $\sigma_p(t)$ at the time t is the initial prestress reduced by the losses of prestress:

$$\sigma_p(t) = \sigma_{po} - \Delta\sigma_p(t).$$

The maximum value of the initial prestress cannot exceed the minimum of $k_1 \cdot f_{pk}$ or $k_2 \cdot f_{p0,1k}$, where f_{pk} and $f_{p0,1k}$ are the characteristic tensile strength and the characteristic 0.1% proof-stress of the prestressing steel, respectively. The values of k_1 and k_2 may be given in national and international codes; the recommended values are 0.8 and 0.9, respectively.

2.6 Effects of prestressing

Two basic methods can be used in order to take into account the effects of prestressing in the structure.

Effects of prestressing can be considered as *internal forces* by introducing a normal force, $N_p = P\cos\alpha$; a shear force, $V_p = P\sin\alpha$; and a bending moment, $M_p = eP\cos\alpha$, in each concrete cross section, where P is the prestressing force, e is its eccentricity, and α is the angle between the prestressing reinforcement and the neutral axis of the structural element in the considered cross section. These isostatic forces can also produce additional hyperstatic effects in the case of hyperstatic structures.

Prestressing effects can be considered as *external loads* by introducing forces created by the prestressing onto the concrete element. These forces represent the anchorage forces, the distributed normal forces due to the tendon curvature perpendicular to the tendon $P(x)/R(x)$, and the distributed friction force parallel to the tendon $dP(x)/dx$. If the tendon layout has a quadratic parabolic shape, or for tendon shape with constant curvature, the effect of prestressing as external forces is shown in Figure 10.12.

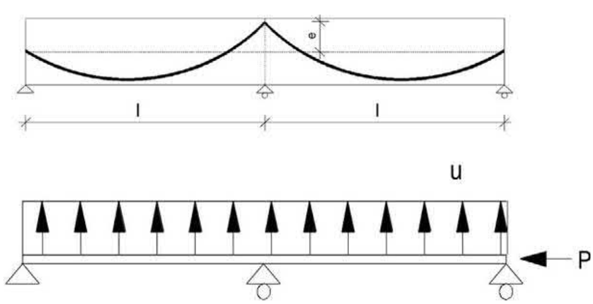

Figure 10.12 Effects of prestressing as an external force in the case of a quadratic parabolic tendon layout.

The intensity of the uniformly distributed equivalent external load perpendicular to the neutral axis of the element is given in this case by

$$u = 8Pf/l^2.$$

This formula enables one to determine the necessary value of the prestressing force, which can be directly balanced as part of a uniformly distributed external force q in an uncracked elastic state:

$$P_{nec} = ql^2/8f.$$

3. Design of reinforced and prestressed concrete bridge decks

3.1 Conceptual design

The main objective of the conceptual design is to find the optimal structural form of the bridge to satisfy the needs of the client as well as satisfy aesthetic, economical, and social aspects by the different possible alternatives. The design procedure at this stage is based on a relatively simple analysis to determine the main dimensions of the primary members of the structure to compare different possible solutions, which can differ in the following aspects:

- The structural system, including the longitudinal configuration, and the corresponding distribution of spans.
- The construction materials, such as the use of reinforced or prestressed concrete; and normal, high-performance, or lightweight concrete.
- The type and the dimensions of the cross section, slab, beam, box girder, etc.
- The erection technique, precast system, or cast-in-situ concrete including the definition of the main steps of the construction sequences.

All these elements are correlated; that is why a good conceptual design must be based on the intuition, the knowledge, and the experience of the engineer responsible for the project.

3.2 Structural modeling and analysis

Structural analysis consists of the evaluation of the response of the bridge to external effects. For structural analysis, the structure has to be idealized by suitable models. A reinforced concrete structure consists of a combination of structural elements, like beams, columns, slabs, shells, etc. The response of the global structure—for example, the distribution of the internal forces due to external loads—is determined using analytical or numerical methods. However, the idealizations of the behavior used for the analysis of the structural elements are the following.

In the current design codes for structural analysis of reinforced or prestressed concrete structures, four methods are proposed.

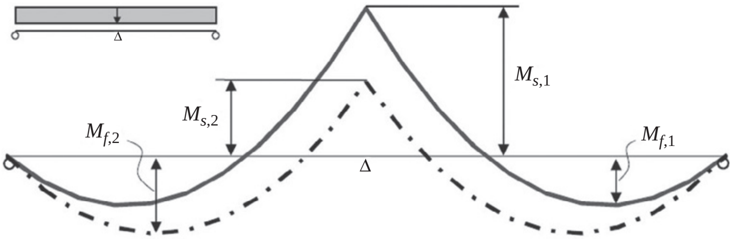

Figure 10.13 Example of redistribution of bending moments for a continuous bridge deck.

Linear elastic analysis may be used for the determination of action effects for both the serviceability and the ultimate limit states assuming linear stress-strain relationships for concrete and steel with uncracked cross sections. The results are realistic with the assumption that actions are low.

Linear elastic analysis with limited redistribution for analysis of structural members in ULS can be used for continuous beam or slab decks predominantly subjected to bending when the ratio of the length of adjacent spans is between 0.5 and 2 (Figure 10.13). The redistribution of bending moments can be applied only if sufficient rotation capacity of the considered sections of the structural member is provided. National and international codes require the rotation capacity to be checked. The reinforcements of the cross sections are determined according to the redistributed bending moments.

Theory of plasticity should be only used to check at ultimate limit state conditions of reinforced concrete bridges. In this case, the sufficient deformation capacity of the critical regions of the structure corresponding to the envisaged plastic mechanisms must be ensured. According to European Standard EN 1992-2 the required rotation capacity in the region of plastic hinges for beams, slabs, or frames generally may be considered to be ensured if the area of reinforcement of a cross section fulfills the following:

$$x_u/d \leq 0.30 \text{ for concrete strength classes} \leq \text{C50/60 and}$$

$$x_u/d \leq 0.23 \text{ for concrete strength classes} \geq \text{C55/67,}$$

where x_u is the neutral axis depth in ULS, and d is the effective depth of the cross section.

Nonlinear modeling for dimensioning of reinforced concrete bridges may be used under the conditions that equilibrium and compatibility of the structure are satisfied and, for materials, the condition that accurate nonlinear behavior is applied. The model must properly cover all failure modes, like due to axial forces, bending, shear, etc. The resistance should be evaluated in incremental steps. The process should be continued until the structure reaches its ultimate capacity.

4. Methods of construction

Construction of bridge decks with **precast prestressed concrete beams** connected by in situ concrete deck slabs is economical for spans up to 50 m, mainly for structures such as long viaducts, where a large number of beams is required.

In the case of in situ concrete construction, the use of **classical scaffolding** to support the formwork is suitable, particularly for bridges built over land if the ground can provide a suitable foundation and the structure is neither too high nor too long (Figure 10.14).

The use of **launching girders** is a particular application to support the formwork of an incrementally concreted bridge deck, which requires the use of a special movable girder supported from the previously completed part of the structure.

Prestressed concrete bridge decks built by the **balanced cantilever construction method** can be used for spans from about 50 m to even up to 300 m. This method involves assembling the elements of the deck by building outwards from either side of the piers symmetrically. Each segment of the construction is prestressed to the previously completed part of the structure (Figure 10.15).

In the case of **in situ construction**, each segment is cast in situ using a formwork usually suspended from a steel frame supported by the previously cast segment. In order to limit its weight and avoid the problems with deformations during construction, the length of each segment is limited to between 3 and 5 m. The length of the segment at the piers is approximately twice the length of a subsequent segment. The typical length of the segments in the case of the **use of precast elements** is between 2 and 4 m, depending upon their depth and width, and is considered in order to limit the bending moment and avoid a large amount of prestress at one location. The treatment of the joints between segments is an important factor of precast

Figure 10.14 Scaffolding of the middle part of the railway bridge at Zalalövő, Hungary.

Figure 10.15 Construction of the highway viaduct at Köröshegy, Hungary.

construction. The main types of joints are the coupled joint, the mortared joint, and the in situ concreted joint—the most common type being coupled joints, where joints are filled usually by epoxy resin.

The principle of construction by **the incremental launching method** is to concrete the deck on the ground in successive segments, located at one or two ends of the bridge. When a segment is completed, it is prestressed to the previously completed part of the structure. Then the whole assembled structure is advanced forward to its final position to clear the casting area for the construction of the next segment. This method is suitable to building long bridge decks with various spans. The range of spans varies between 15 and 20 m for slab decks, and from 40 to 70 m for box girders. The length of each segment can be between 12 m and the full length of the span. During construction, each section of the structure will be subjected to considerable bending moments, which vary in function of the current position of the section. For this reason, it is beneficial to provide a uniform prestress to the intermediate sections of the bridge while launching. Although in the first span, where mainly the hogging moments are high, eccentric prestress is favorable. The most common way to reduce the high hogging moment in the first span is to use a launching nose (Figure 10.16).

The launching noses are usually light and rigid steel constructions with lengths equal to 60% or 80% of the span. The easiest solution to reduce the excessive hogging moments during construction is to use temporary intermediate supports placed

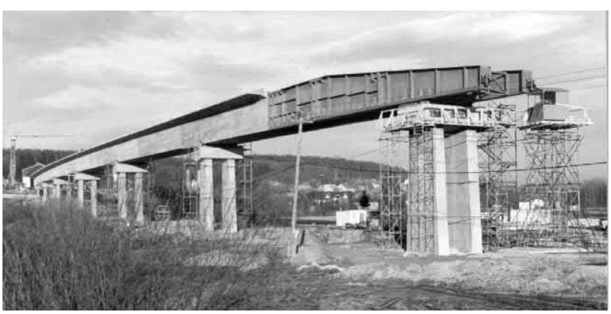

Figure 10.16 Construction of the main part of the 1670 m length railway viaduct at Zalalövő.

midway between piers. Another way to reduce hogging moments is to apply a mast located approximately a span length behind the end of the deck to support cable stays when launching. For the longest spans, cable stays with a launching nose.

5. Design example 1

The following simplified structural analysis of the main longitudinal girder for static loads, according to Eurocode practice (see details in Section 5.1.2), is presented for a cast-in-situ beam and slab-type superstructure.

5.1 Basic design data

5.1.1 Geometry

The longitudinal axis of the deck is assumed to be straight in plane and perpendicular to the planes of supports (Figures 10.17 and 10.18).

- Main sizes:

Span: $L = 19.00$ m
Total height of main girder: $h = 1.4$ m (at girder axis)
Carriageway width: $w = 8.0$ m
Thickness of deck slab: $v = 220$ mm (at the symmetry axis).
Pavement structure:

4 cm wearing layer
6 cm binding layer
4 cm protective layer
1 cm waterproofing
20–25 cm reinforced concrete deck slab.

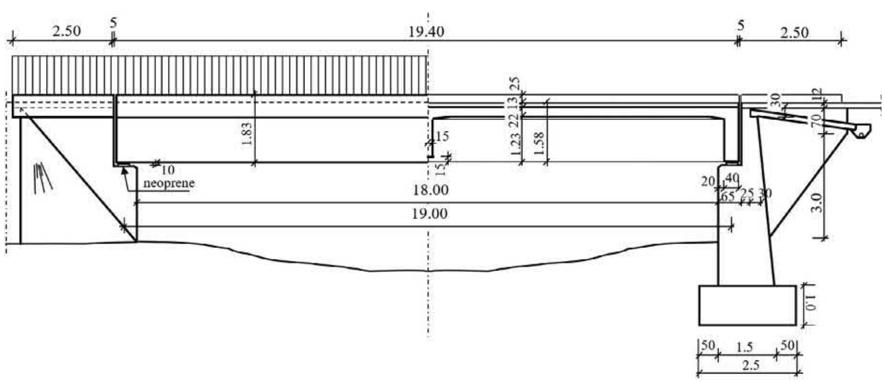

Figure 10.17 Longitudinal section and side view.

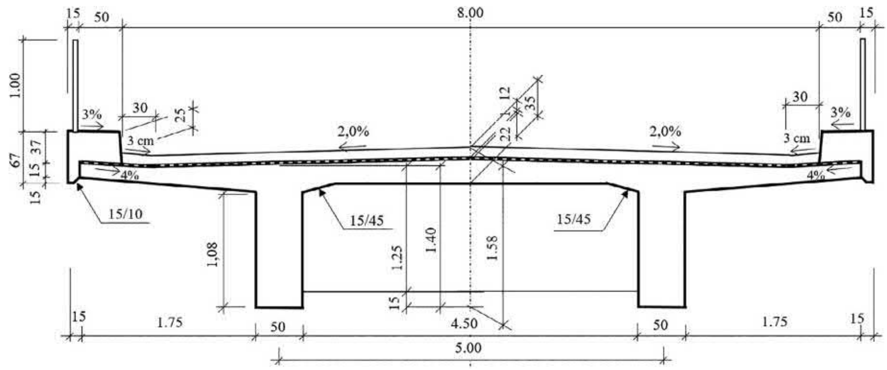

Figure 10.18 Cross section at midspan.

5.1.2 Design codes

EN 1990: Eurocode—Basis of structural design
EN 1991-2: Eurocode 1—Actions on structures. Traffic loads on bridges
EN 1992-1-1: Eurocode—Design of concrete structures. General rules and rules for buildings
EN 1992-2: Eurocode 2—Design of concrete structures. Concrete bridges

5.1.3 Material properties

Concrete	**C35/45**
Characteristic value of compressive strength, f_{ck} [N/mm^2]	35
Mean value of tensile strength, f_{ctm} [N/mm^2]	3.2
Mean value of the modulus of elasticity, E_{cm} [N/mm^2]	34,000
Long-term modulus of elasticity, $E_{c.eff} = E_{cm}/(1 + \phi)$ (ϕ: final creep coefficient)	
Ultimate strain, ε_{cu} [‰]	3.5

Strength reduction factor for bridges: $\alpha = 0.85$.
Partial factor for concrete: $\gamma_c = 1.5$.

Reinforcing Steel	**B500B**
Characteristic value of yield strength, f_{yk} [N/mm^2]	500
Characteristic value of the elongation at maximum load, ε_{uk} [‰]	No limit
Modulus of elasticity, E_s [N/mm^2]	200,000

Partial factor for steel: $\gamma_s = 1.15$.

5.1.4 Actions

Permanent actions

For simplification, only self-weight of the superstructure is considered as permanent action.

Self-weight

Specific weights: concrete: 25.0 kN/m^3

Asphalt: 24.0 kN/m^3

Waterproofing: 0.25 kN/m^2

Safety barrier: 0.50 kN/m.

The self-weight of the superstructure is calculated for the half of the cross section (for one longitudinal girder) as follows:

- Self-weight of structural parts (load bearing structure): $g_1 = 40.28$ kN/m
- Self-weight of nonstructural parts (curb, pavement, barrier, equipment): $g_2 = 19.22$ kN/m
- Total self-weight: $g = g_1 + g_2 = 40.28 + 19.22 =$ **59.50** kN/m.

Variable actions

Wind and temperature action will be introduced as typical variable actions on bridge decks, vertical, and horizontal traffic loads. However, for simplification, only vertical traffic loads (LM1) will be considered in further calculation.

Traffic loads

Number of notional lanes (6 m $\leq w = 8.0$ m): 2.

Width of

Traffic lanes: $w_l = 3.0$ m;

Remaining area $w_r = 2.0$ m.

➢*Vertical traffic loads*

For simplification, only Load Model 1 (LM1) is considered. Characteristic values of LM1 ($\alpha_{Qi}Q_{ik}$, $\alpha_{qi}q_{ik}$, and $\alpha_{qr}q_{rk}$) are shown in Table 10.1 and Figure 10.19.

For simplification:

- The tandem system on each lane is replaced by a one-axle load of equal weight ($L > 10$ m).
- The values of adjustment factors are set as $\alpha_{Qi} = \alpha_{qi} = \alpha_{qr} = 1.0$.

Table 10.1 Characteristic Values of LM1

Lane	Tandem System (TS) Axle weight, Q_{ik} (kN)	UDL q_{ik} (or q_{rk}) (kN/m^2)
Lane 1	300	9.0
Lane 2	200	2.5
Remaining area (q_{rk})	0	2.5

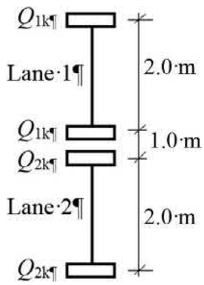

Figure 10.19 Axle positions.

Traffic loads on footways and cycle tracks: $q_{fk} = 0.0$ kN/m^2 (no footway and cycle track in this case).

➢ *Horizontal forces*

Centrifugal force is disregarded due to the straight longitudinal axis of the deck.

- Braking and acceleration force ($Q_{\ell k}$)

The $Q_{\ell k}$ force acts at the top level of the pavement in the longitudinal axis of the carriageway.

$$Q_{\ell k} = 0.6\alpha_{Q1}\,(2Q_{1k}) + 0.10\alpha_{q1}\,q_{1k}\,wL = 497\,\text{kN}\,\left(\text{but } 180\alpha_{Q1} = 180\,\text{kN} \le Q_{\ell k} \le 900\,\text{kN}\right).$$

Wind action (F_{wk})

For simplification, the vertical and longitudinal (horizontal) components of wind are disregarded.

The height of the reference area, d_{tot}, as a function of parapet type as well as calculation of the reference area, $A_{ref,x}$, and the associated force coefficient, $c_{f,x}$, are seen in Figure 10.20.

The horizontal component (horizontal wind force) uniformly distributed along the superstructure length acts perpendicularly to the longitudinal axis of the superstructure:

$$F_{wk,x} = ½\rho v^2{}_b C_x A_{ref,x} = 0.5 \times 1.25\,\left[\text{kg/m}^3\right] \times (20\,[\text{m/s}])^2 \times 2.34 \times 44.65$$
$$= 26.1\,\text{kN},$$

where the wind load factor, C_x, is calculated assuming the usual suburban terrain (terrain category II) and a distance $z = 5$ m of the superstructure from the ground level, which result in a terrain roughness factor, $\underline{c}_e(z) = 1.8$, as follows: $C_x = c_{f,x}\,c_e(z) = 1.3 \times 1.8 = 2.34$. The basic wind velocity, v_b, is a nationally determined parameter (NDP); here $v_b = 20$ m/s is taken.

Temperature action (T_k)

Determination of bridge temperatures as function of air temperatures (NDP):

- Minimum bridge temperature (for –15°C minimum air temperature): $T_{e,min}$ = –7°C
- Maximum bridge temperature (for +35°C max. air temperature): $T_{e,max}$ = +37°C

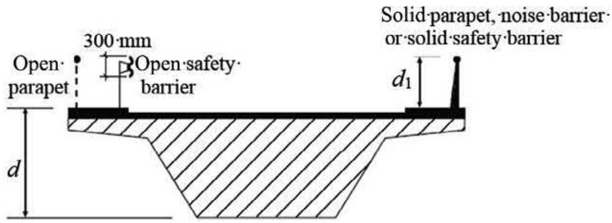

Type of parapet	On one side	On both sides
Open parapet or open safety barrier	d + 0,3 m	**d + 0,6 m**
Solid parapet or solid safety barrier	d + d_1	d + 2d_1
Open parapet and open safety barrier	d + 0,6 m	d + 1,2 m

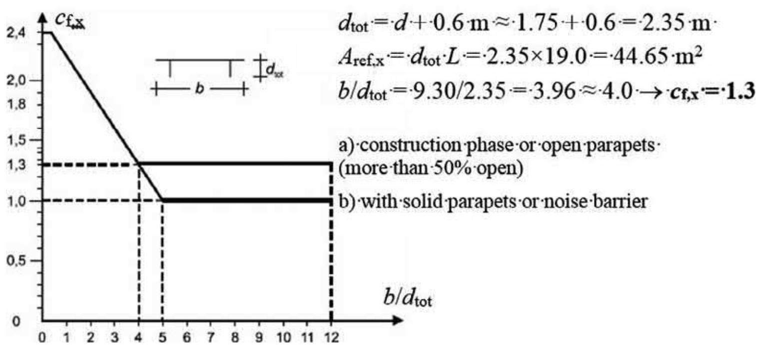

Figure 10.20 Definition of reference area, $A_{ref,x}$, for horizontal wind component.

Assumed initial temperature: $T_0 = +10°C$.

- *Uniform temperature component*
  - Maximum contraction: $\Delta T_{N,con} = T_0 - T_{e,min} = 10 - (-7) = 17°C$
  - Maximum expansion: $\Delta T_{N,exp} = T_{e,max} - T_0 = 37 - 10 = 27°C$
- *Uneven (linear) temperature component (in vertical plane)*

Temperature differences between the bottom and top fibers of the main girder (for 150 mm thick pavement):

- Top face warmer: $\Delta T_{M,heat} = 15°C \times 0.5 = 7.5°C$
- Bottom face warmer: $\Delta T_{M,cool} = 8°C \times 1.0 = 8°C$

Simultaneity of temperature components

The simultaneity of the uniform and linear temperature components is assumed to be as follows:

$$T_k = \max \begin{cases} \Delta T_{N,con} \left(\text{or}\, \Delta T_{N,\exp} \right) + 0.75 \Delta T_{M,cool} (\text{or } \Delta T_{M,heat}) \\ 0.35\, \Delta T_{N,con} \left(\text{or}\, \Delta T_{N,\exp} \right) + \Delta T_{M,cool} (\text{or } \Delta T_{M,heat}) \end{cases}$$

5.1.5 Combination of actions

For simplification, only self-weight and LM1 vertical traffic load are considered in further calculations.

Partial and combination factors

Partial factors for permanent actions (NDP):

- $\gamma_{G,inf} = 1.00$ if favorable
- $\gamma_{G,sup} = 1.35$ if unfavorable
- $\xi = 0.85$ reduction factor for unfavorable permanent actions

Partial factor for variable actions (NDP):

- Traffic load: $\gamma_Q = 1.35$
- Other variable actions: $\gamma_Q = 1.5$

ψ factors (NDP) for traffic loads:

- UDL: $\psi_{0,q} = \psi_{0,r} = 0.4$; $\psi_{1,q} = \psi_{1,r} = 0.3$; $\psi_{2,q} = \psi_{2r} = 0.0$
- TS: $\psi_{0,Q} = 0.75$; $\psi_{1,Q} = 0.6$; $\psi_{2,Q} = 0.0$

Combination of traffic loads with other actions

For simplification, only group gr1a of traffic loads (including LM1 + loads on footways and cycle tracks) is considered.

For ultimate limit state (ULS) verifications, actions will be combined according to the alternative combinations, as follows:

$$E_{Ed} = \max \begin{cases} \gamma_{G,\,\mathrm{sup}} E_G + \gamma_Q \left(\psi_{0,q} E_q + \psi_{0,Q} E_Q\right) \\ \xi \gamma_{G,\,\mathrm{sup}} E_G + \gamma_Q \left(E_q + E_Q\right) \end{cases}.$$

Combinations of actions for serviceability verifications (SLS):

- Characteristic combination: $E_{car} = E_G + (E_q + E_Q)$
- Frequent combination: $E_{fr} = E_G + (\psi_{1,q} E_q + \psi_{1,Q} E_Q)$
- Quasi-permanent combination: $E_{qp} = E_G + (\psi_{2,q} E_q + \psi_{2,Q} E_Q)$

5.2 Calculation of internal forces

5.2.1 Influence line in transverse direction

For simplification, a linear influence line is assumed (Figure 10.21). Traffic loads are reduced, due to LM1 to one longitudinal girder using the one-axle model for the concentrated vehicle load:

Reduction of UDL to one girder (influence area below the ith notional lane: $A_\eta^1 = 3.0$ m; $A_\eta^2 = 1.2$ m; $A_\eta^r = 0.025$ m; $A_\eta^{fw} = 0.89$ m):

$$q_{red} = \alpha_{q1}\, q_{1k}\, A_\eta^1 + \alpha_{q2}\, q_{2\mathrm{k}}\, A_\eta^2 + \alpha_{qr}\, q_{rk}\, A_\eta^r + q_{fk}\, A_\eta^{fw}$$
$$= 1.0 \times 9.0 \times 3.0 + 1.0 \times 2.5 \times 1.2 + 1.0 \times 2.5 \times 0.025 + 0.0 \times 0.89 = 30.06\,\mathrm{kN/m}.$$

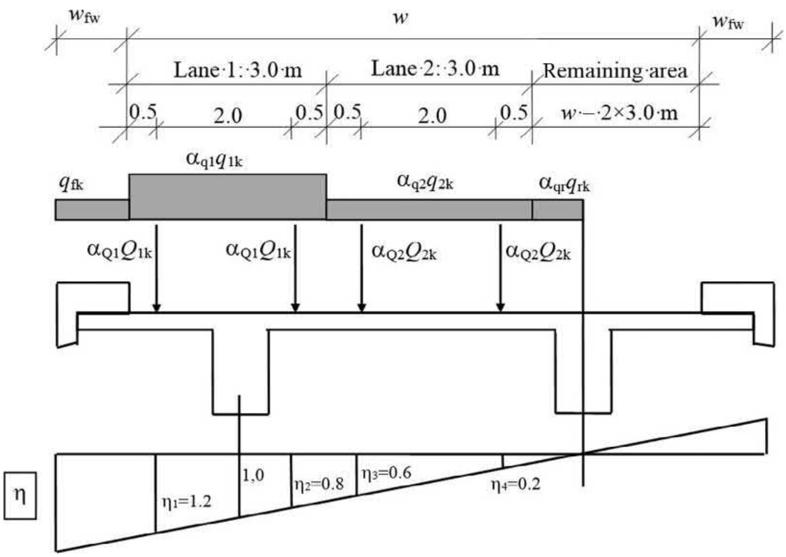

Figure 10.21 Reduction of traffic loads to one longitudinal girder.

Reduction of TS (one-axle concentrated vehicle load) to one girder:

$$Q_{red} = \alpha_{Q1}Q_{1k}\,(\eta_1 + \eta_2) + \alpha_{Q2}Q_{2k}\,(\eta_3 + \eta_4)$$

$$= 1.0 \times 300 \times (1.2 + 0.8) + 1.0 \times 200 \times (0.6 + 0.2) = 760 \text{ kN}.$$

5.2.2 Bending moments

For design purposes, bending moments are calculated only at cross section *K*. Load arrangement (of self-weight and reduced traffic loads) is shown in Figure 10.22.

Design bending moment:

$$M_{Ed}^{K} = \max\begin{cases}\gamma_{G,\sup}M_G^K + \gamma_Q\left(\psi_{0,q}M_q^K + \psi_{0,Q}M_Q^K\right)\\[2ex] \xi\gamma_{G,\sup}M_G^K + \gamma_Q\left(M_q^K + M_Q^K\right)\end{cases}$$

$$= \max\begin{cases}1.35 \times 2685 + 1.35(0.4 \times 1357 + 0.75 \times 3610)\\[2ex] 0.85 \times 1.35 \times 2685 + 1.35(1357 + 3610)\end{cases} = 9786\,\text{kNm}$$

Frequent value of bending moment:

$$M_{fr}{}^{K} = M_G{}^{K} + \left(\psi_{1,q}M_q{}^{K} + \psi_{1,Q}\,M_Q{}^{K}\right) = 2685 + (0.3 \times 1357 + 0.6 \times 3610)$$
$$= 5258\,\text{kNm}.$$

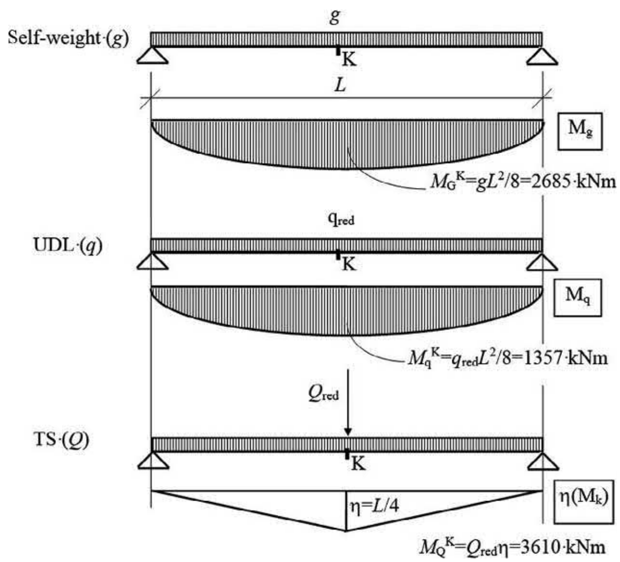

Figure 10.22 Load arrangement resulting in maximum bending moment in the longitudinal girder.

Quasi-permanent value of bending moment:

$$M_{qp}{}^K = M_G{}^K + \left(\psi_{2,q} M_q{}^K + \psi_{2,Q} M_Q{}^K\right) = 2685 + (0.0 \times 1357 + 0.0 \times 3610)$$
$$= 2685\,\text{kNm}.$$

5.2.3 Shear forces

For design purposes, design shear force is calculated at cross sections A and A'. Load arrangement (of self-weight and reduced traffic loads) is shown in Figure 10.23.

Design shear forces:

$$V_{Ed}^{A} = \max \begin{cases} \gamma_{G,\sup} V_G^A + \gamma_Q \left(\psi_{0,q} V_q^A + \psi_{0,Q} V_Q^A\right) \\ \xi \gamma_{G,\sup} V_G^A + \gamma_Q \left(V_q^A + V_Q^A\right) \end{cases}$$

$$= \begin{cases} 1.35 \times 565 + 1.35(0.4 \times 286 + 0.75 \times 760) \\ 0.85 \times 1.35 \times 565 + 1.35(286 + 760) \end{cases} = 2175\text{kN},$$

$$V_{Ed}^{A'} = \max \begin{cases} \gamma_{G,\sup} V_G^{A'} + \gamma_Q \left(\psi_{0,q} V_q^{A'} + \psi_{0,Q} V_Q^{A'}\right) \\ \xi \gamma_{G,\sup} V_G^{A'} + \gamma_Q \left(V_q^{A'} + V_Q^{A'}\right) \end{cases}$$

$$= \begin{cases} 1.35 \times 490 + 1.35(0.4 \times 249 + 0.75 \times 710) \\ 0.85 \times 1.35 \times 490 + 1.35(249 + 710) \end{cases} = 1956\text{kN}.$$

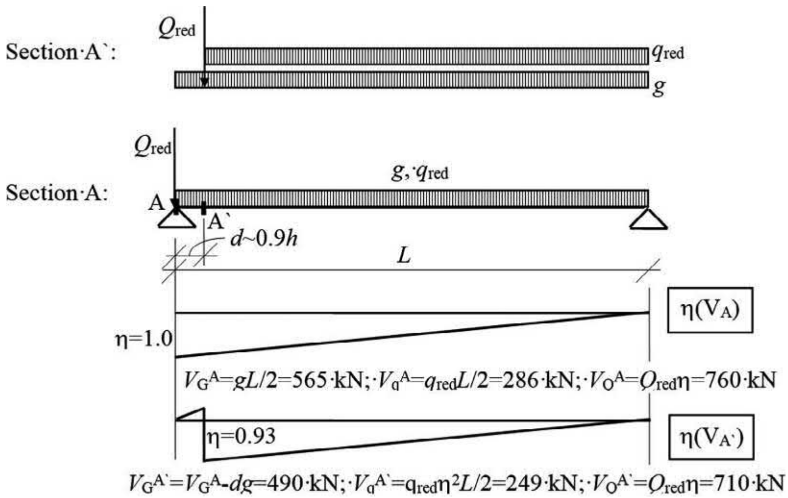

Figure 10.23 Load arrangement resulting in maximum shear force in the longitudinal girder.

5.3 Ultimate limit states

5.3.1 Effective width of flange

Effective width of flange (Figure 10.24)

- On the outer side of the beam (cantilever side):

$$\begin{aligned} b_{eff,o} &= \min(0.2l_c + 0.1l_0;\, l_c;\, 0.2l_0) \\ &= \min(0.2 \times 1.75 + 0.1 \times 19.0,\, 1.75;\, 0.2 \times 19.0) = 1.75\,\text{m} \end{aligned}$$

- On the inner side of the beam (toward the symmetry axis):

$$\begin{aligned} b_{eff,I} &= \min(0.2l_r/2 + 0.1l_0;\, l_r/2;\, 0.2l_0) \\ &= \min(0.2 \times 2.25 + 0.1 \times 19.0,\, 2.25;\, 0.2 \times 19.0) = 2.25\,\text{m}, \end{aligned}$$

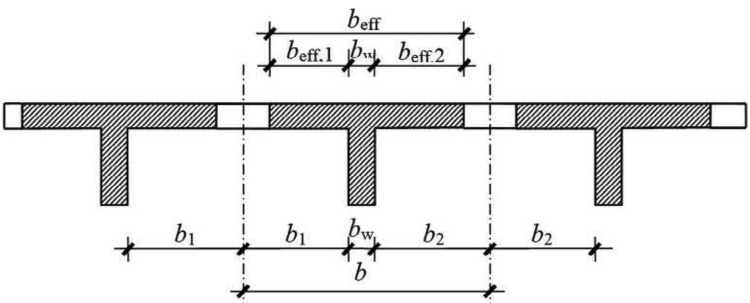

Figure 10.24 Effective width of flange.

where $l_0 = 19$ m is the distance along the beam between sections with zero bending moment (here equal to the span); $l_c = 1.75$ m is the length of the cantilevered deck slab; and $l_r = 4.5$ m is the clear distance between the longitudinal beams.

Total effective width of flange:

$$b_{eff} = b_w + b_{eff.o} + b_{eff,i} = 0.5 + 1.75 + 2.25 = 4.5\,\text{m}.$$

5.3.2 Design for flexure

For simplification, only cross section K is sized.

Applied σ-ε diagrams (Figure 10.25): for concrete and reinforcing steel

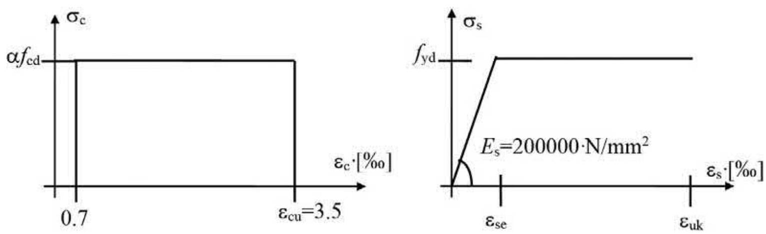

Figure 10.25 Stress-strain diagrams for materials.

Estimation of the effective depth (d), assuming the following:

- Concrete cover: $c = 40$ mm (corresponding to exposure class XD3)
- Design increase of cover: $\Delta c_{dev} = 10$ mm
- Diameter of longitude. bars: $\phi = 36$ mm (arranged in three rows)
- Diameter of stirrups: $\phi_k = 16$ mm

$$d \approx h - (c + \phi_k + 2.5\phi + \Delta c_{dev}) = 1400 - (4.0 + 1.6 + 2.5 \times 3.6 + 1.0)$$
$$= 1244\,\text{mm}.$$

Calculation of the depth of compression zone (x_c):

$$M_{Ed}{}^{K} = x_c\, b_{eff}\, \alpha f_{cd}\, (d - x_c/2) \Rightarrow 9786\,\text{kNm}$$
$$= x_c \times 4500 \times 0.85 \times (35/1.5) \times (1244 - x_c/2) \Rightarrow x_c$$
$$= 92\,\text{mm (remains in flange)}.$$

Strain at the level of longitudinal bars:

$$\varepsilon_s = \varepsilon_{cu}(d - 1.25x_c)/(1.25x_c) = 0.035(1244 - 1.25 \times 92)/(1.25 \times 92)$$
$$= 0.0346 > \varepsilon_{se} = f_{yd}/E_s = 0.0022\ \text{(yields)}.$$

Required amount of longitudinal tension reinforcement:

$$A_s = x_c\, b_{eff}\, \alpha f_{cd}/f_{yd} = 92 \times 4500 \times 0.85 \times (35/1.5)/(500/1.15)$$
$$= 18{,}784\,\text{mm}^2\ (19\,\phi 36 \rightarrow 3 \times 6 + 1\ \text{pieces of bars}).$$

Minimum amount of tension reinforcement:

$$A_{s,\min} = \max \begin{cases} 0.26\dfrac{f_{ctm}}{f_{yk}} b_w d \\ 0.0013 b_w d \end{cases} = \max \begin{cases} 0.26\dfrac{3.2}{500} 500 \times 1244 \\ 0.0013 \times 500 \times 1244 \end{cases}$$

$$= 1035\,\text{mm}^2 \ll A_s (OK).$$

Bars shall be spaced according to the relevant detailing rules, and then recalculation of the bending resistance of the section on the basis of the provided amount and position of reinforcement is necessary!

5.3.3 Design for shear

For simplification, the resistance of compression struts is verified at cross section A and the shear reinforcement is sized only at cross section A'.

As shear reinforcement, only vertical stirrups are applied ($\alpha = 90°$).

Design for shear is carried out based on the variable strut inclination method, as follows (Figure 10.26):

Data necessary to calculate shear resistance:

Strength reduction factor:

$$\nu = 0.6(1 - f_{ck}/250) = 0.52$$

Size effect factor:

$$k = \min\left(1 + \sqrt{\frac{200}{d[mm]}}; 2.0\right) = \min\left(1 + \sqrt{\frac{200}{1244}}; 2.0\right) = 1.40.$$

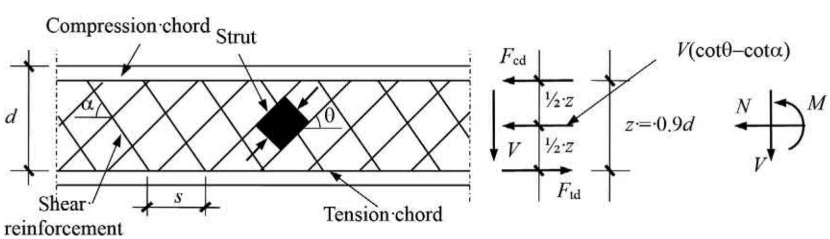

Figure 10.26 Calculation model for shear.

Longitudinal steel ratio (assuming 50% of A_{sl} required at midspan (cross section K) is fully anchored behind the supports):

$$\rho_l = \min(A_{sl}/(b_w d); 0.02) = \min(0.5 \times 18,784/(500 \times 1244); 0.02) = 0.015.$$

Assumption of the compression strut inclination (angle between compression strut and longitudinal axis of the beam):

cot $\theta = 1.3$ corresponding to $\theta = 37.5°$ ($1.0 \leq \cot\theta \leq 2.5$ condition is fulfilled).

Verification of compression struts (maximum shear force at cross section A):

$V_{Rd,\max} = 1{,}0\ \nu f_{cd}\, b_w\, 0.9\ d\, \frac{\cot\theta}{1+\cot^2\theta}$

$= 1.0 \times 0.52 \times (35/1.5) \times 500 \times 0.9 \times 1244 \times \frac{1.3}{1+1.3^2}$

$= 3257\ \text{kN} \geq V_{Ed}^{A} = 2175\ \text{kN}$ (OK)

Check whether design shear reinforcement is necessary:

$V_{Rd,c} = [0.18/\gamma_c\ k\ (100\ \rho_l f_{ck}\ [\text{N/mm}^2])^{1/3}]\ b_w\ d$

$= [0.18/1.5 \times 1.4(100 \times 0.015 \times 35)^{1/3}]500 \times 1244$

$= 392\ \text{kN} < V_{Ed}^{A'} = 1956\ \text{kN}.$

(shear reinforcement is required)

Required amount of shear reinforcement (from condition $V_{\text{Rd,s}} = V_{Ed}^{A'}$)

$A_{sw}/s = \frac{V_{Ed}^{A'}}{0.9df_{yd}\cot\theta} = \frac{1956}{0.9\times1244\times500\times1.3}$

$= 3091\ \text{mm}^2/\text{m}$ (ϕ 16/125 vertical stirrups, $(A_{sw}/s)_{prov} = 3217\ \text{mm}^2/\text{m}$).

Minimum amount of shear reinforcement:

$\rho_{w,\min} = 0.08\,\frac{\sqrt{f_{ck}}}{f_{yk}} = 0.08\,\frac{\sqrt{35}}{500} = 0.00095 \ll \rho_{w,\text{prov}} = (A_{sw}/s)_{\text{prov}}/b_w = \frac{3217}{500}$

$= 0.0064$ (OK).

Stirrups shall be spaced according to the relevant detailing rules, and then recalculation of the shear resistance of the section on the basis of the provided shear reinforcement is necessary!

5.4 Serviceability limit states

5.4.1 Crack control

Crack control is carried out by calculating crack width on the frequent level of actions (NDP). For simplification, only cross section K is analyzed.

Applied crack width limit: $w_{\text{lim}} = 0.3$ mm (for exposure class XD3).

Cross-sectional data necessary for crack-width calculation (omitting calculation details):

Final value of creep coefficient: $\phi_c = 1.65$ (RH = 80%, 28 days of concrete age at initial loading).

Effective modulus of elasticity:

$$E_{c,\mathrm{eff}} = E_{cm}/(1+\phi_c) = 34{,}000/(1+1.65) = 12{,}853\,\mathrm{N/mm^2}.$$

Depths of the neutral axis and moments of inertia assuming uncracked (I) stage:
for short-term loading: $y_{\mathrm{I},0}$ = 422 mm, $I_{\mathrm{I},0}$ = 0.33 m^4
for long-term loading: $y_{\mathrm{I},t}$ = 510 mm, $I_{\mathrm{I},t}$ = 0.45 m^4
cracked (II) stage:
for short-term loading: $y_{\mathrm{II},0}$ = 237 mm, $I_{\mathrm{II},0}$ = 0.15 m^4
for long-term loading: $y_{\mathrm{II},t}$ = 386 mm, $I_{\mathrm{II},t}$ = 0.33 m^4.
Effective depth of the outer row of longitudinal bars: d_{so} = 1326 mm.
Division of the frequent value of bending moment into short-term and long-term parts:
long-term part: $M_{fr,t} = M_G^K$ = 2685 kNm,
short-term part: $M_{fr,0} = M_{fr}^K - M_{fr,t}$ = 5258 − 2685 = 2573 kNm.
Cracking moment:

$$M_{cr} = f_{ctm}\frac{I_{\mathrm{I},0}}{h - y_{\mathrm{I},0}} = 3.2\frac{0.33\times 10^{12}}{1400-422} = 1078\,\mathrm{kNm}.$$

Calculation of steel stresses:
from the cracking moment at the outer bar ($\alpha_0 = E_s/E_{cm}$ = 200,000/34,000 = 5.9):

$$\sigma_{sr} = \alpha_0\frac{M_{cr}}{I_{\mathrm{II},0}}(d_{so} - y_{\mathrm{II},0}) = 5.9\frac{1078\times 10^6}{0.15\times 10^{12}}(1326-237) = 47\,\mathrm{N/mm^2}.$$

from the quasi-permanent value of moment at the outer bar

($\alpha_t = E_s/E_{c,eff}$ = 200000/12853 = 15.6):

$$\sigma_{s,qp} = \alpha_t\frac{M_{qp}}{I_{\mathrm{II},t}}(d_{so} - y_{\mathrm{II},t}) = 15.6\frac{2685\times 10^6}{0.33\times 10^{12}}(1326-386) = 121\,\mathrm{N/mm^2}.$$

from the frequent value of moment at the outer bar:

$$\sigma_s = \alpha_t\frac{M_{fr,t}}{I_{\mathrm{II},t}}(d_{so} - y_{\mathrm{II},t}) + \alpha_0\frac{M_{fr,0}}{I_{\mathrm{II},0}}(d_{so} - y_{\mathrm{II},0})$$
$$= 15.6\frac{2685\times 10^6}{0.33\times 10^{12}}(1326-386) + 5.9\frac{2573\times 10^6}{0.15\times 10^{12}}(1326-237) = 232\,\mathrm{N/mm^2}.$$

Effective tension area and corresponding steel ratio (Figure 10.27):
effective tension area:
$h_{c,eff}$ = min[2.5(h-d-Δc_{dev}); (h-$y_{\mathrm{II},t}$)/3, h/2] = 365 mm,

Figure 10.27 Effective tension area.

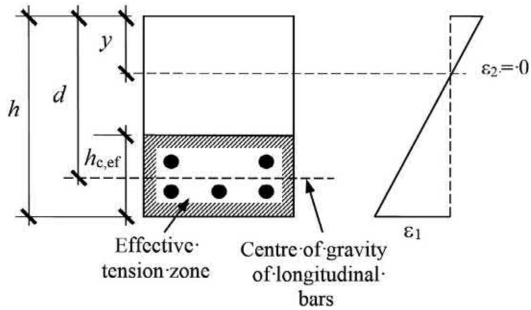

$A_{c,eff} = b_w\ h_{c,eff} = 500 \times 365 = 182{,}500\ \text{mm}^2$,
effective steel ratio:
$\rho_{s,eff} = A_s/A_{c,eff} = 18{,}784/182{,}500 = 0.103$.

Calculating the difference of average strain in steel (ε_{sm}) and average strain in concrete (ε_{cm}) (for simultaneous long-term and short-term loading: $k_t = 0.5$):

$$\varepsilon_{sm} - \varepsilon_{cm} = \max\left[\frac{\sigma_s - k_t \dfrac{f_{ctm}}{\rho_{s,eff}}\left(1 + \alpha_0 \rho_{s,eff}\right)}{E_s}, 0.6\frac{\sigma_s}{E_s}\right]$$

$$= \max\left[\frac{232 - 0.5\dfrac{3.2}{0.103}(1 + 5.9 \times 0.103)}{200{,}000}, \frac{0.6 \times 232}{200{,}000}\right] = 0.00104.$$

Calculation of maximum crack spacing (for ribbed bars: $k_1 = 0.8$; for bending: $k_2 = 0.5$):

$$\begin{aligned} s_{r,\max} &= 3.4c + 0.425 \cdot k_1 \cdot k_2 \cdot \phi/\rho_{s,eff} \\ &= 3.4 \times 40 + 0.425 \times 0.8 \times 0.5 \times 36/0.103 = 171\,\text{mm}. \end{aligned}$$

Calculation of crack width:

$$w_k = s_{r,\max} \cdot (\varepsilon_{sm} - \varepsilon_{cm}) = 171 \times 0.00104 = 0.18\,\text{mm} < w_{\lim} = 0.3\,\text{mm (OK)}.$$

5.4.2 Deflection control

With regard to appearance and drainage, the longitudinal beams are generally designed with a camber equal to the deflection due to self-weight. For simplification, the effect of cracking on deflections is assessed by the use of distribution coefficient ζ, which allows for tension stiffening and enables an interpolation between the uncracked and the cracked state of the structure, as follows.

Distribution coefficient allowing for tension stiffening (for sustained and repeated loading: $\beta = 0.5$; for σ_{sr} and $\sigma_{s,}$ see Section 10.5.4.1):

$$\text{for quasi} - \text{permanent level of actions}: \zeta_{qp} = 1 - \beta\left(\frac{\sigma_{sr}}{\sigma_{s,qp}}\right)^2 = 1 - 0.5\left(\frac{47}{121}\right)^2 = 0.92,$$

$$\text{for frequent level of actions}: \zeta_{fr} = 1 - \beta\left(\frac{\sigma_{sr}}{\sigma_{s,fr}}\right)^2 = 1 - 0.5\left(\frac{47}{232}\right)^2 = 0.98.$$

Deflection control at midspan (cross section K) to avoid unacceptable appearance of the structure (quasi-permanent level of actions):

$$e_{qp}{}^{K} = \frac{5}{48}\frac{M_{qp}L^2}{E_{c,eff}}\left(\frac{1-\zeta_{qp}}{I_{\mathrm{I},t}} + \frac{\zeta_{qp}}{I_{\mathrm{II},t}}\right)$$

$$= \frac{5}{48}\frac{2685 \times 10^6 \times \left(19.0 \times 10^3\right)^2}{12853}\left(\frac{1-0.92}{0.45 \times 10^{12}} + \frac{0.92}{0.33 \times 10^{12}}\right) = 23.6\,\text{mm}.$$

verification condition: $e_{qp}^{K} = 23.6$ mm $\leq \frac{L}{500} = 38$ mm (OK).

Deflection control at midspan (cross section K) to avoid user discomfort (assuming a camber at midspan, $e_0^K = -\mathrm{e}_{\mathrm{qp}}^{\mathrm{K}}$):

deflection from UDL (q):

$$e_q{}^{K} = \frac{5}{48}\frac{M_q^K L^2}{E_{cm}}\left(\frac{1-\zeta_{fr}}{I_{\mathrm{I},0}} + \frac{\zeta_{fr}}{I_{\mathrm{II},0}}\right)$$

$$= \frac{5}{48}\frac{1357 \times 10^6\left(19 \times 10^3\right)^2}{34{,}000}\left(\frac{1-0.98}{0.33 \times 10^{12}} + \frac{0.98}{0.15 \times 10^{12}}\right) = 10.1\,\text{mm},$$

deflection from TS (Q)

$$e_Q{}^{K} = \frac{1}{12}\frac{M_Q^K L^2}{E_{cm}}\left(\frac{1-\zeta_{fr}}{I_{\mathrm{I},0}} + \frac{\zeta_{fr}}{I_{\mathrm{II},0}}\right)$$

$$= \frac{1}{12}\frac{3610 \times 10^6\left(19 \times 10^3\right)^2}{34000}\left(\frac{1-0.98}{0.33 \times 10^{12}} + \frac{0.98}{0.15 \times 10^{12}}\right) = 21.4\,\text{mm},$$

deflection from frequent value of traffic load:

$e_{q+Q,fr,}{}^{K} = \psi_{1,q}\, e_q{}^{K} + \psi_{1,Q}\, e_Q{}^{K} = 0.3 \times 10.1 + 0.6 \times 21.4 = 15.9$ mm,

verification condition:

$e_{fr}{}^{K} = e_0{}^{K} + e_{qp}{}^{K} + e_{q+Q,fr}{}^{K} = -23.6 + 23.6 + 15.9 = 15.9$ mm $\leq \frac{L}{400} = 47.5$ mm (OK).

6. Design example 2

Herein a simplified structural analysis for static loads according to the Eurocode practice (see details in Section 6.1.2) is presented for a cast-in-situ, one-cell, post-tensioned, box-girder-type superstructure. The post-tensioning system consists of polygonal external (unbonded) cables running inside the box (no internal tendons). The superstructure is supported by two bearings on each abutment.

6.1 Basic data

6.1.1 Geometry

The longitudinal axis of the deck is straight and perpendicular to planes of supports (Figures 10.28 and 10.29).

Main sizes:	
Span:	$L = 40.0$ m
Total box height:	$h = 2.0$ m (at axis of symmetry)
Box width:	$b_{box} = 6.0$ m
Web thickness:	$b_w = 0.5$ m
Thickness of deck slab:	$v = 250$ mm (at axis of symmetry)
Carriage width:	$w = 9.5$ m
Pavement structure:	4 cm wearing layer
	4 cm binding layer
	4 cm protective layer
	1 cm waterproofing

6.1.2 Design codes

EN 1990	Eurocode—Basis of Structural Design
EN 1991-2	Eurocode 1—Actions on Structures: Traffic Loads on Bridges
EN 1992-1-1	Eurocode 2—Design of Concrete Structures: General Rules and Rules for Buildings
EN 1992-2	Eurocode 2—Design of Concrete Structures: Concrete Bridges

6.1.3 Material properties

➢**Concrete**		**C40/50**
Characteristic compressive strength, f_{ck} [N/mm^2]		40
Mean tensile strength, f_{ctm} [N/mm^2]		3.5
Modulus of elasticity, E_{cm} [N/mm^2]		35,000
Ultimate strain, ε_{cu} [‰]		3.5
Strength reduction factor for bridges:	$\alpha = 0.85$	
Partial factor for concrete:	$\gamma_c = 1.5$	

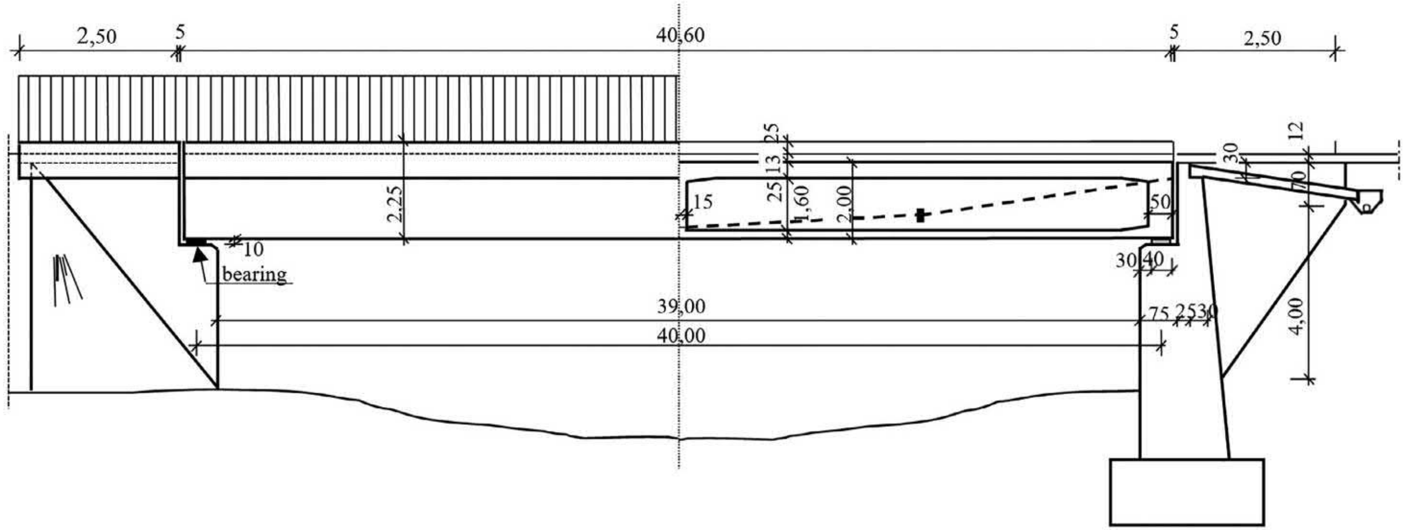

Figure 10.28 Longitudinal section and side view.

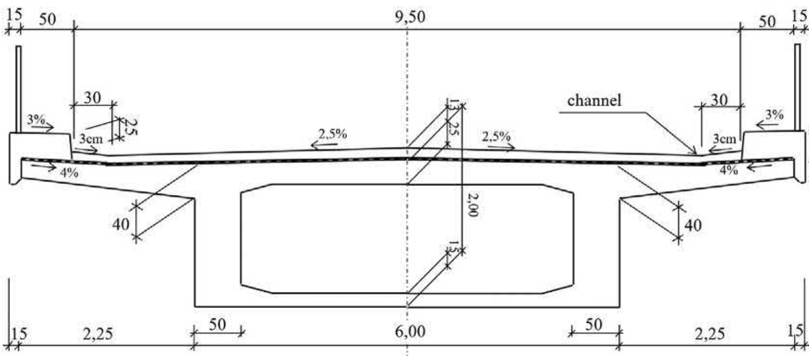

Figure 10.29 Cross section of the deck at midspan.

➢Reinforcing Steel		**B500B**
Characteristic yield strength, f_{yk} [N/mm^2]		500
Characteristic elongation at maximum load, ε_{uk} [‰]		no limit
Modulus of elasticity, E_s [N/mm^2]		200000
Partial factor for reinforcing steel:	$\gamma_s = 1.15$	

➢Prestressing Steel		**Y1860**
Characteristic tensile strength, f_{pk} [N/mm^2]		1860
Characteristic 0.1% proof-stress, $f_{p0,1k}$ [N/mm^2]		1580
Characteristic elongation at maximum load, ε_{uk} [‰]		35
Modulus of elasticity, E_s [N/mm^2]		195,000
Partial factor for prestressing steel:	$\gamma_s = 1.15$	

6.1.4 Actions

This example does not cover design for accidental actions and seismic forces.

Permanent actions

For simplifications, only the self-weight of the deck is considered as permanent action.

Self-weight

Specific weights for the calculation of self-weight of

• pavement layers:	
asphalt:	24 kN/m^3
waterproofing:	10 kN/m^3
handrail:	0.35 kN/m
• load-carrying structure (reinforced concrete):	25 kN/m^3

The self-weight of the superstructure is calculated for the half of the cross section (including one web), as follows:

- structural parts (load-carrying structure): $g_1 = 64.25$ kN/m
- nonstructural parts (curb, pavement, barrier, equipment): $g_2 = 21.42$ kN/m
- total self-weight: $g = g_1 + g_2 = 64.25 + 21.42 =$ **85.67** kN/m

Variable actions

Normally, as variable actions, vertical and horizontal traffic loads, wind, and temperature actions should be considered in bridge superstructures. However, for simplification, only vertical traffic loads (LM1) will be considered in the following. An example for the introduction and the application of the remaining variable actions on bridge decks can be found in Section 5.1.4.

Traffic loads

Number of notional lanes (9 m $\leq w = 9.5$ m $\leq$ 12 m): 3.

Width of

traffic lanes: $w_\ell = 3.0$ m;

remaining area $w_r = 0.5$ m

➢*Vertical traffic loads*

For simplification, only Load Model 1 (LM1) is considered. Characteristic values of LM1 ($\alpha_{Qi}Q_{ik}$, $\alpha_{qi}q_{ik}$, and $\alpha_{qr}q_{rk}$) are shown in Table 10.2 and Figure 10.30.

For simplification:

- The tandem system in each lane is replaced by a one-axle load of equal weight ($L > 10$ m).
- The values of adjustment factors are set as $\alpha_{Qi} = \alpha_{qi} = \alpha_{qr} = 1.0$.

Traffic loads on footways and cycle tracks: $q_{fk} = 0.0$ kN/m^2 (no footway and cycle track in this case).

Partial factors and ψ factors

Partial factors for permanent actions (NDP):

- $\gamma_{G,inf} = 1.00$ if favorable
- $\gamma_{G,sup} = 1.35$ if unfavorable
- $\xi = 0.85$ reduction factor for unfavorable permanent actions
- $\gamma_P = \gamma_{P,inf} = \gamma_{P,sup} = 1.0$ for prestressing in global analysis

Table 10.2 Characteristic Values of LM1

	Tandem System (TS)	**UDL**
Lane	**Axle Weight, Q_{ik} (kN)**	**q_{ik} (or q_{rk}) (kN/m^2)**
Lane 1	300	9.0
Lane 2	200	2.5
Lane 3	100	2.5
Remaining area (q_{rk})	0	2.5

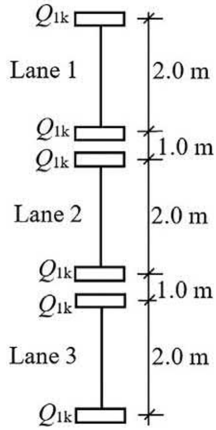

Figure 10.30 Axle positions.

Partial factor for variable actions (NDP):

- traffic load: $\gamma_Q = 1.35$
- other variable actions: $\gamma_Q = 1.5$

ψ factors for traffic loads (NDP):

- UDL: $\psi_{0,q} = 0.4$; $\psi_{1,q} = 0.3$; $\psi_{2,q} = 0.0$
- TS: $\psi_{0,Q} = 0.75$; $\psi_{1,Q} = 0.6$; $\psi_{2,Q} = 0.0$

Combination of traffic loads with other actions

For simplification, only group *gr1a* of traffic loads (including LM1 + combined value of loads on footways and cycle tracks) is considered.

For ultimate limit state (ULS) verifications, actions are combined according to

- either the basic combination (preliminary analysis; see Section 6.2):

$$E_{Ed} = \gamma_{G,\,\sup} E_G + \gamma_Q \left(E_q + E_Q \right)$$

- or the alternative combinations (detailed analysis; see Section 6.3):

$$E_{Ed} = \max \begin{cases} \gamma_{G,\,\sup} E_G + \gamma_Q \left(\psi_{0,q} E_q + \psi_{0,Q} E_Q \right) \\ \xi \gamma_{G,\,\sup} E_G + \gamma_Q \left(E_q + E_Q \right) \end{cases}$$

Combinations of actions for serviceability verifications (SLS):

- Characteristic combination: $E_{car} = E_G + (E_q + E_Q)$
- Frequent combination: $E_{fr} = E_G + (\psi_{1,q} E_q + \psi_{1,Q} E_Q)$
- Quasi-permanent combination: $E_{qp} = E_G + (\psi_{2,q} E_q + \psi_{2,Q} E_Q)$.

6.2 Preliminary design

The necessary amount of prestress in calculated based on the following governing principles:

- Total construction cost is expected as minimum for partial post-tensioning with ~70% prestress rate. That means that ~70% of the required total longitudinal tension force in ULS is carried by post-tensioning, and the remaining ~30% is resisted by reinforcing steel (ULS verification; see Section 6.2.2).
- It is assumed that the superstructure operates under environmental conditions corresponding to either of the exposure classes, XD1 or XD3 (chloride attack), which requires decompression under the frequent combination of actions. Thus, the necessary amount of prestress is also controlled by this requirement (SLS verification; see Section 6.2.3).

6.2.1 Calculation of bending moments at midspan

For simplification, a linear influence line and the critical transverse position of LM1 using the one-axle model for TSs are assumed (Figure 10.31) to calculate bending moments at midspan (here $q_{fk}^* = 0$) for one-half of the box (Figure 10.32).

Bending moments at midspan (section K)

- due to self-weight:

$$M_g^K = \frac{gL^2}{8} = \frac{85.67 \times 40^2}{8} = 17134 \text{ kNm}$$

- due to UDL part of LM1 (assuming that 2/3 of UDL on the carriageway subjects one-half of the box):

$$M_q^K = q_{red}\frac{L^2}{8} \approx \frac{2}{3}\left[\sum_{i=1}^{3}(\alpha_{qi}q_{ik})w_\ell + \alpha_{qr}q_{rk}w_r\right]\frac{L^2}{8}$$

$$= \frac{2}{3}[(1.0 \times 9.0 + 2 \times 1.0 \times 2.5) \times 3.0 + 1.0 \times 2.5 \times 0.5]\frac{40^2}{8} = 5767 \text{ kNm}$$

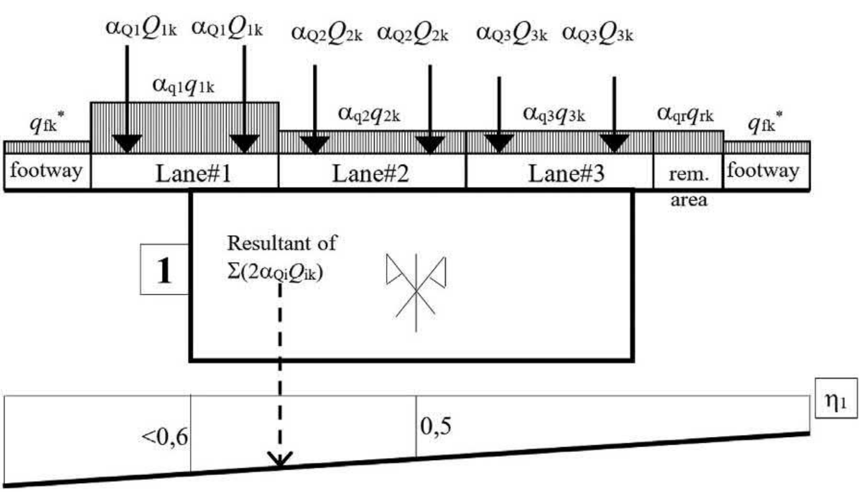

Figure 10.31 Transverse position of traffic loads critical to one one-half (1) of the box.

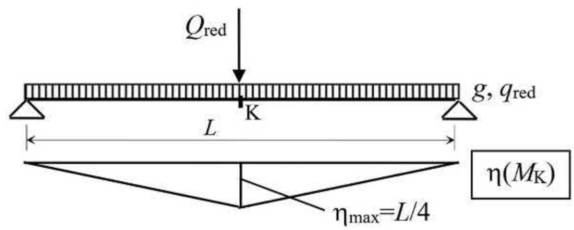

Figure 10.32 Longitudinal positions of loads critical to bending moment at midspan.

- due to TS part of LM1 (assuming that 60% of the sum of TSs subjects one-half of the box):

$$M_Q^K = Q_{red}\frac{L}{4} = \left[0.6\sum_{i=1}^{3}\alpha_{Qi}(2Q_{ik})\right]\frac{L}{4}$$

$$= [0.6\times 2\times(1.0\times 300 + 1.0\times 200 + 1.0\times 100)]\frac{40}{4} = 7200 \text{ kNm}$$

Combination of bending moments at midspan:

- design bending moment (based on the basic combination of actions):

$$M_{Ed}{}^K = \gamma_{G,\sup}M_g{}^K + \gamma_Q\left(M_q{}^K + M_Q{}^K\right) = 1.35\times 17{,}134 + 1.35\times(5767+7200)$$
$$= 40{,}636 \,\text{kNm}$$

- frequent moment (based on the frequent combination of actions):

$$M_{fr}{}^K = M_g{}^K + \left(\psi_{1,q}M_q{}^K + \psi_{1,q}M_Q{}^K\right) = 17{,}134 + (0.3\times 5767 + 0.6\times 7200)$$
$$= 23{,}184\,\text{kNm}.$$

6.2.2 Design for ULS (bending) at midspan

Approximation of internal lever arm:

$z = 0.8h - 0.5v = 0.8\times 2.0 - 0.5\times 0.25 = 1.48$ m

Total longitudinal force to resist:

$$H_{tot} = \frac{M_{Ed}^K}{z} = \frac{40{,}636}{1.48} = 27{,}550 \text{ kN}$$

Effective prestress:

- applied strand type in cables: Y1860-S7 (cross-sectional area: $A_{p0} = 150$ mm^2)
- effective (unbonded) strand force (assuming an initial prestress of $\sigma_{p0} = 0.7f_{pk}$ and 30% total loss of prestress):

$$P_{eff}^t = 0.7\times 0.7f_{pk}A_{p0} = 0.7\times 0.7\times 1860\times 150 = 137 \text{ kN}$$

Necessary number of strands (post-tensioning resists 70% of H_{tot}) in half of the box:

$$n_{s,\text{ULS}} = \frac{0.7H_{tot}}{\gamma_{P,\inf}P_{eff}^t} = \frac{0.7\times 27{,}550}{1.0\times 137} = 141.1$$

6.2.3 Design for SLS (decompression) at midspan

The cross-sectional data for the half of the midspan section are calculated on the basis of the gross concrete section and obtain as follows:

- cross-sectional area: $A_c = 2.67\ \text{m}^2$
- section modulus to the bottom extreme fiber: $W_c = 1.09\ \text{m}^3$

The eccentricity of the resulting tendon force at midspan is estimated by considering that the cable groups should run at the possible lowest position inside the box. Thus, it results in $e_P = 889$ mm measured from the center of gravity of the gross concrete section.

Condition equation of decompression:

$$-\frac{n_{s,\text{SLS}} P^t_{eff}}{A_c} - \frac{n_{s,\text{SLS}} P^t_{eff} e_P}{W_c} + \frac{M^K_{fr}}{W_c} = -\frac{n_{s,\text{SLS}} 137}{2.57} - \frac{n_{s,\text{SLS}} 137 \times 0.889}{1.09} + \frac{23,184}{1.09} = 0,$$

from which the necessary number of (unbonded) strands in half of the box obtains as

$$n_{s,\text{SLS}} = 130.8.$$

6.2.4 Applied reinforcement and cable layout

Assuming 37 strand cables ($n_0 = 37$), the applied number of cables, n_c, and the total amount of prestressing steel, A_p, in half of the box obtains as follows:

$$n_c = \frac{\max(n_{s,\text{ULS}}; n_{s,\text{SLS}})}{n_0} = \frac{141.1}{37} = 3.53 \rightarrow 4 \rightarrow A_p = n_c n_0 A_{p0} = 4 \times 37 \times 150$$
$$= 22,200\,\text{mm}^2.$$

Necessary amount of reinforcing steel in half of the box (equal to the part of H_{tot} that is not resisted by post-tensioning according to Section 6.2.2):

$$A_{s,req} = \frac{H_{tot} - n_c n_0 \gamma_{P,\inf} P^t_{p,eff}}{f_{yk}/\gamma_s} = \frac{27550 - 4 \times 37 \times 1.0 \times 137}{500/1.15} = 16,828\ \text{mm}^2$$
$$\rightarrow \text{provided} : 35\phi 25$$

$$\rightarrow A_s = 17,181\,\text{mm}^2\ (\text{effective depth} : d_s = 1700\,\text{mm}).$$

Minimum amount of reinforcing steel (assuming the effective depth as $d = 0.85h$):

$$A_{s,\min} = \max\left(0.26\frac{f_{ctm}}{f_{yk}}; 0.0015\right) b_w d$$
$$= \max\left(0.26\frac{3.5}{500}; 0.0015\right) \times 500 \times 0.85 \times 2000 = 1547\ \text{mm}^2.$$

Bars of the provided reinforcing steel, $A_{s,}$ shall be uniformly distributed along the perimeter of the effective tension zone, which includes the bottom slab and the bottom $2.5(h\text{-}d_s)$ high part of the webs.

6.2.5 Cable layout

The individual external tendons run along polygons that are defined by the locations of deviation points (here, two anchorages and three deviators are assumed along the full span, as shown in Figure 10.33). To fit the equivalent tendon polygon (the dashed line in Figure 10.33) to a parabola, the vertical locations of deviation points are assumed as $a_K = 23$ cm (as function of cable size), a_B ($\sim 0.3h_{box}$) = 52.5 cm and a_A ($\sim 0.85h_{box}$) = 135 cm (Figure 10.34).

For technological reasons, the anchorages are assumed to be located at ~10 cm behind the end section. Thus, the horizontal projection of cables is equal to $L_c = L_{tot} - 2 \times 0.1\,\text{m} = 40.4$ m, and the associated inclinations of the equivalent tendon obtain as $\alpha_2 = 0.082$ rad and $\alpha_1 = 0.029$ rad.

6.3 Detailed design

In the presented detailed design, the following assumptions are used:

- The hunches between webs and (top and bottom) slabs are neglected, and, thus, the gross concrete section of the superstructure is prismatic along the full length.
- The longitudinal reinforcing steel provided at midspan is constant along the full length and fully anchored behind the supports.

6.3.1 Cross-sectional data

Based on the provided amount and arrangement of mild reinforcement according to Section 6.2.4, the ideal cross-sectional data (including reinforcing steel and excluding prestressing steel, subscript "i") for the uncracked stage were calculated for half of the box to both short-term (excluding creep of concrete, subscript "0", $\alpha_0 = E_s/E_{cm} = 5.71$) and long-term loading (including creep of concrete, subscript "t", $\alpha_t = E_s/E_{c,eff} = 14.97$). The results are as follows:

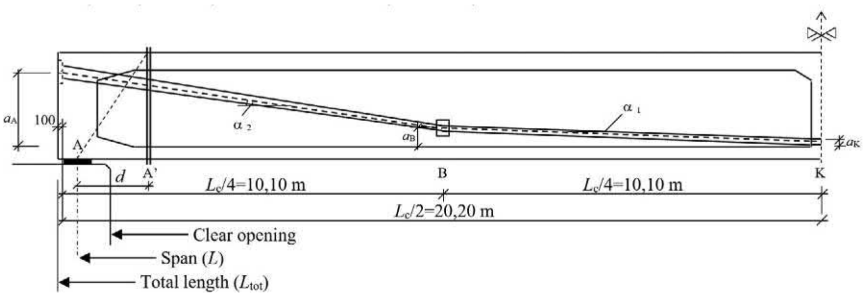

Figure 10.33 Vertical tendon layout.

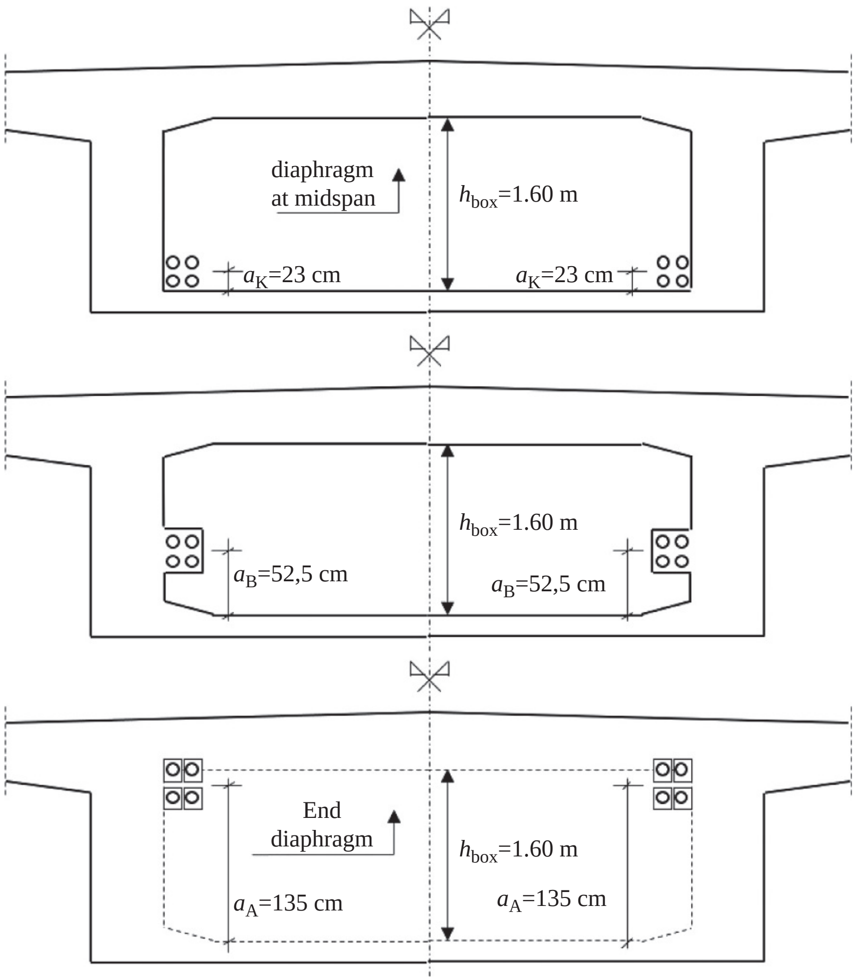

Figure 10.34 Cable arrangements at anchorages and deviators.

- cross-sectional area: $A_{i0} = 2.65\ \text{m}^2$; $A_{it} = 2.81\ \text{m}^2$;
- center of gravity measured from the top: $y_{i0} = 806$ mm; $y_{it} = 856$ mm;
- moment of inertia: $I_{i0} = 1.37\ \text{m}^4$; $I_{it} = 1.49\ \text{m}^4$

The eccentricity of the equivalent tendon at anchorages and deviators:

- at section A: $e_{Pi0,A} = -313$ mm $e_{Pit,A} = -376$ mm;
- at section B: $e_{Pi0,B} = 519$ mm $e_{Pit,B} = 469$ mm;
- at section K: $e_{Pi0,K} = 814$ mm $e_{Pit,K} = 764$ mm

6.3.2 Losses of prestress, effective prestress

The maximum stress in tendons occur during the stressing procedure. Thus, using the initial prestress according to Section 6.2.2:

$$\begin{aligned}\sigma_{\max} &= \sigma_{p0} = 0.7f_{pk} = 0.7\times 1860\\ &= 1302\,\mathrm{N/mm^2}\left(< \min\left(0.8f_{pk}, 0.9f_{p0.1k}\right) = 1422\,\mathrm{N/mm^2}\right).\end{aligned}$$

The strands in a cable are assumed to be stressed individually in one step from alternate ends. The stressing operation remains always symmetric. Therefore, simultaneous stressing of two strands being symmetric locations in the cross section is assumed. Thus, altogether, $n_c \times n_0 = 4 \times 37 = 148$ stressing operations take place.

Losses of prestress

Assuming a friction coefficient of $\mu_\alpha = 0.12$ 1/rad and an unintentional deviation as $k = 0.007$ 1/m for the applied unbonded tendons, the loss of friction at midspan (section K) obtains as

$$\Delta\sigma_\mu^K = \sigma_{p0}\left[1 - e^{-\mu_\alpha(\alpha_2 + k0.5L_c)}\right] = 1302\left[1 - e^{-0.12(0.082 + 0.007\times 0.5\times 40.4)}\right] = 34\ \mathrm{MPa}.$$

A technology-related $g = 6$ mm wedge slip is assumed for the applied unbonded tendons. Based on the preceding μ_α and k values and assuming a linear $\Delta\sigma_\mu(x)$ function, the slip length is calculated as $l_{sl} = 25.71$ m, which results in loss due to slip at the anchorage as

$$\Delta\sigma_{sl}^A = 2\sigma_{p0}l_{sl}\left[\frac{\alpha_2}{0.5L_c} + k\right] = 2\times 1302\times 25.71\left[\frac{0.082}{0.5\times 40.4} + 0.007\right] = 89\ \mathrm{MPa}$$

and at midspan as

$$\Delta\sigma_{sl}^K = \Delta\sigma_{sl}^A\frac{l_{sl} - 0.5L_c}{l_{sl}} = 89\frac{25.71 - 0.5\times 40.4}{25.71} = 19\ \mathrm{MPa}.$$

The concrete stresses due to one stressing operation are calculated along the line between the anchorages at sections A ($\Delta\sigma_c^A = -3.00/n_0$ MPa) and K ($\Delta\sigma_c^K = -1.35/n_0$ MPa) by considering the preceding losses due to friction and wedge slip and then averaged as

$$\Delta\sigma_c^{ave} = \left(\Delta\sigma_c{}^A + \Delta\sigma_c{}^K\right)/(2n_0) = -(3.00 + 1.35)/(2\times 37) = -0.059\,\mathrm{MPa}.$$

The loss of prestress due to elastic deformation of concrete is calculated as

$$\Delta\sigma_c = \frac{n_c n_0 - 1}{2}\alpha_0\Delta\sigma_c^{ave} = \frac{4\times 37 - 1}{2}5.71\times|0.059| = 25\ \mathrm{MPa}.$$

The stress in tendons immediately after all stressing operations results in $\sigma_{pm0}^A = 1189$ MPa at anchorages (section A) and $\sigma_{pm0}^K = 1224$ MPa at midspan (section K); thus,

$$\max\left(\sigma_{pm0}{}^A; \sigma_{pm0}{}^K\right) = 1224\,\mathrm{MPa} < \min\left(0.75f_{pk}, 0.85f_{p0.1k}\right) = 1343\,\mathrm{MPa}.$$

The calculation of long-term losses is based on the final value of concrete shrinkage of $\varepsilon_{cs} = -0.31‰$, the final creep coefficient of $\varphi(t,t_0) = 1.62$, and the total relaxation loss in strands of $\Delta\sigma_{pr} = 44$ MPa. The average concrete compression stress along line between the anchorages obtained as $\sigma_{cg}{}^{ave} = -1.92$ MPa due to self-weight and $\sigma_{cp0}{}^{ave} = -8.53$ MPa due to post-tensioning. Thus, using the cross-sectional data given in Section 6.3.1, the total long-term loss arises as

$$\Delta\sigma_{csr} = \frac{\varepsilon_{cs}E_p + 0.8\Delta\sigma_{pr} + \alpha_0\varphi(t,t_0)\left|\sigma_{cg}^{ave} + \sigma_{cp0}^{ave}\right|}{1 + \alpha_0\dfrac{A_p}{A_{i0,A}}\left[1 + \dfrac{A_{i0}}{I_{i0}}e_{Pi0,A}{}^2\right][1 + 0.8\varphi(t,t_0)]}.$$

$$= \frac{0.00031 \times 195{,}000 + 0.8 \times 44 + 5.71 \times 1.62 \times |1.92 + 8.53|}{1 + 5.71\dfrac{22{,}200}{2.65 \times 10^6}\left[1 + \dfrac{2.65 \times 10^6}{1.37 \times 10^{12}}313^2\right][1 + 0.8 \times 1.62]} = 176 \text{ MPa}$$

Effective prestress

Using the preceding losses, the effective prestress is calculated by the following formula:

$$\sigma_{p.eff} = \sigma_{p0} - \Delta\sigma_\mu - \Delta\sigma_{sl} - \Delta\sigma_c - \Delta\sigma_{csr}.$$

It obtains at sections A and A' (see Figure 10.33) as $\sigma_{p,\ eff}^{A} = 1012$ MPa and $\sigma_{p,\ eff}^{A'} = 1043$ MPa as well as at midspan as $\sigma_{p,\ eff}^{K} = 1048$ MPa. The latter results in the $\sigma_{p,\ eff}^{K}/\sigma_{p0} = 1048/1302 = 0.80$ ratio of the initial stress. The corresponding effective post-tensioning forces on half of the box are as follows: $P_{eff}^{A} = 22,\ 474$ kN, $P_{eff}^{A'} = 23,\ 144$ kN and $P_{eff}^{K} = 23,\ 257$ kN.

6.3.3 Analysis (calculation of internal forces)

This section aims to introduce the procedure of internal forces necessary to complete the most important ULS and SLS verifications in Sections 6.3.4 and 6.3.5 without providing the details of the relevant calculation formulae.

Thus, only internal forces that are necessary for bending-governed ULS and SLS verifications at the midspan section (section K) as well as shear-governed ULS verifications close to supports (section A', see Figure 10.33) are addressed in the following.

Design internal forces at midspan (section K)

The maximum loading on one-half of the box is calculated on the basis of the influence lines at section K according to the Cornelius model (η_K is intended to determine maximum load on one half of the box and η_t is used the calculate maximum torsion on the whole box).

The rotation of the middle section of the box due to unit torsional moment acting at the same section characterizes the

- Torsional behavior of the box if a rigid crossbeam effect is assumed and is calculated as follows (using the torsional moment of inertia of the box equal to $I_t = 5.95$ m^4):

$$\alpha_G = \frac{(1\text{ kNm})L}{4GI_t} = \frac{40}{4 \times 0.417 \times 35{,}000 \times 5.95} = 1.15 \times 10^{-7} \text{ rad}$$

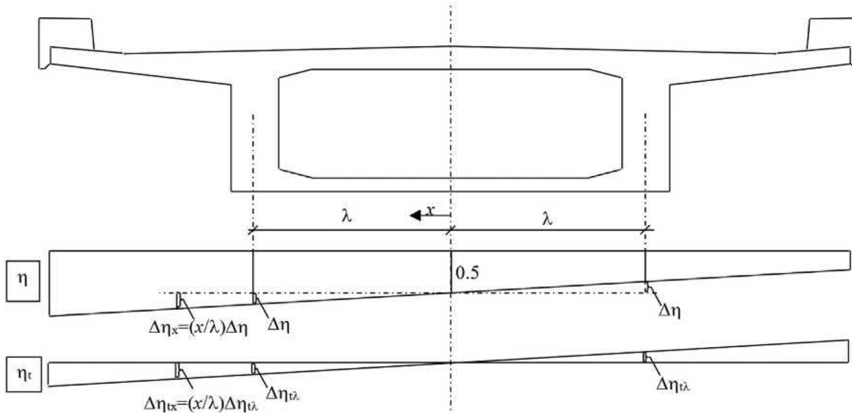

Figure 10.35 Influence lines according to the Cornelius model.

- Flexural behavior of the box if a simply supported crossbeam effect is assumed and is calculated as follows:

$$\varphi_M = \frac{\dfrac{1\ \text{kNm}}{2\lambda}L^3}{48E_{cm}I_{i0}\lambda} = \frac{\dfrac{40^3}{2\times 2.75}}{48\times 35{,}000\times 1.37\times 2.75} = 1.84\times 10^{-6}\ \text{rad}$$

Based on these midspan rotations, the basic parameters of the influence lines in Figure 10.35 are calculated as follows:

$$\Delta\eta = \frac{\alpha_G}{\alpha_G + \varphi_M} = \frac{1.15}{1.15 + 1.84} = 0.059$$

and

$$\Delta\eta_{t\lambda} = \lambda\,(1 - 2\Delta\eta) = 2.75\,(1 - 2\times 0.059) = 2.43\,\text{m}.$$

Transverse positions of traffic loads critical to maximum bending moment at midspan and the associated lane numbering are shown in Figure 10.36 (similar to Figure 10.31; here $q_{fk*} = 0$).

The resulting traffic forces obtained as follows:

• UDL on half of the box:	$q_{red} = 22.98$ kN/m
• UDL-induced torsion moment on the whole box:	$t_{red} = 55.92$ kNm/m
• TS load on half of the box:	$Q_{red} = 632$ kN
• TS-induced torsion moment on the whole box:	$T_{red} = 1324$ kNm

These loads (also including self-weight) are positioned longitudinally, as shown in Figure 10.37.

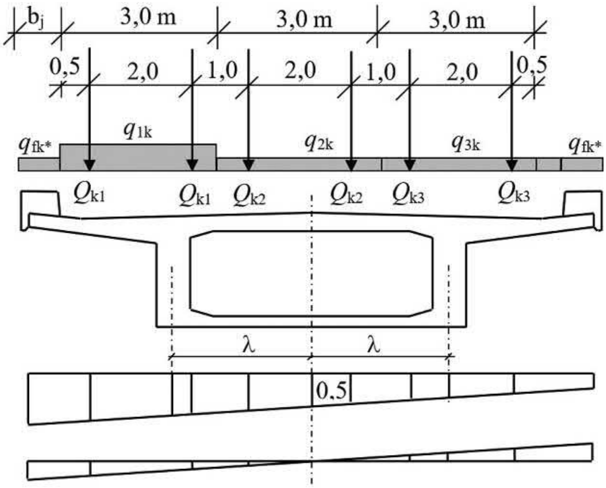

Figure 10.36 Transverse position of traffic loads.

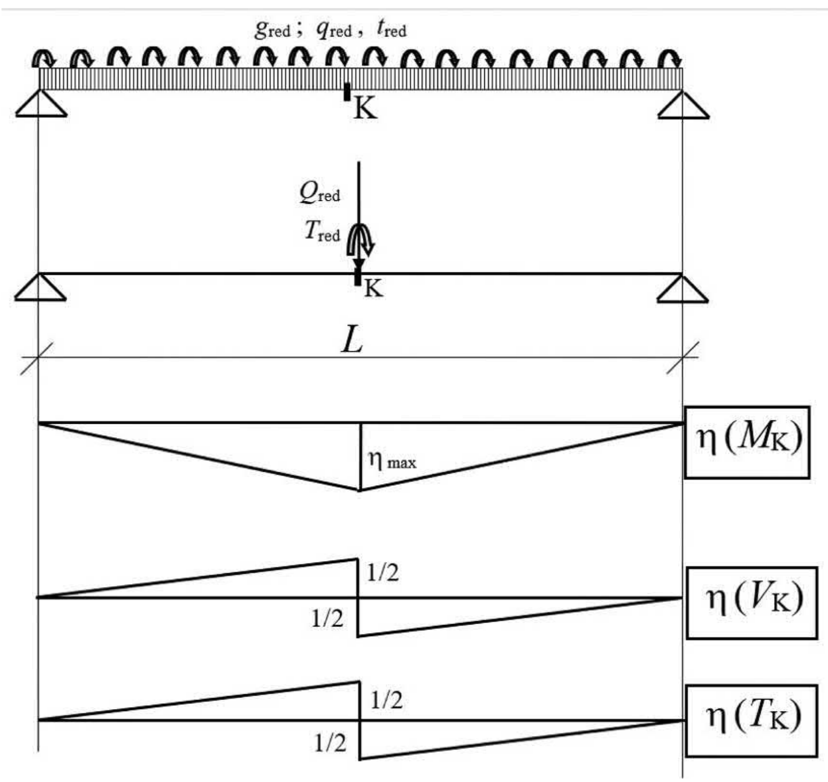

Figure 10.37 Longitudinal position of traffic loads.

By the use of the relevant influence lines, the associated internal forces arise as follows (comparable to the corresponding one in Section 6.2.1):

- Bending moment on half of the box due to UDL: $M_{q,K} = 4596$ kNm
- Bending moment on half of the box due to TS: $M_{Q,K} = 6321$ kNm
- Borsion moments on the whole box: $T_q = T_Q = 0$

Using the alternative combinations of actions given in Section 6.1.4 ($M_g^K = 17{,}134$ kNm; see Section 6.2.1), the design and representative values of bending moment in section K result as follows:

- Design bending moment: $M_{Ed,K} = 34{,}398$ kNm
- Frequent value of bending moment: $M_{fr,K} = 22305$ kNm
- Quasi-permanent value of bending moment: $M_{\mathrm{qp,K}} = 17134$ kNm.

Design internal forces close to support (sections A and A′)

Because direct supports limit the difference in deflection between the webs (longitudinal girders) in their close vicinity, a much less effective transverse distribution of eccentric (traffic) loads between the halves of the box develop in this region compared to that at midspan. Here the deck slab behaves like a "transition beam," distributing the traffic loads between webs, similar to a simply supported beam. As a consequence, $\Delta\eta$ becomes equal to 0.5, and $\Delta\eta_{t\lambda}$ results in zero (no torsion occurs).

Accordingly, when calculating $V_{Q,A}$ and $V_{Q,A'}$ (Q_{red} is located in sections A and A') from the TS load, the transverse distribution of traffic loads is considered according to the safe-side "transition beam" analogy following the procedure used for the midspan section.

For the q_{red} load (UDL), the transverse distribution assumed at midspan may be taken as applicable because the majority of the loaded length by q is far from supports, and only short parts of the loaded length locate close to them. However, for simplification (and safe-side approximation), here $V_{q,A}$ and $V_{q,A'}$ will also be calculated by the use of the "transition beam" analogy.

Accordingly, the "transition beam"-like influence line as well as the transverse position of TSs are shown in Figure 10.38.

The resulting traffic forces obtain as follows:

- UDL on half of the box: $q_{\mathrm{red},A} = 34.06$ kN/m
- TS load on half of the box: $Q_{\mathrm{red},A} = 873$ kN.

The longitudinal positions of these loads (also including self-weight are shown in Figure 10.39 for section A and Figure 10.40 for section A'.

By the use of the relevant influence lines, the associated internal shear forces arise as follows:

- At section A:
  - shear force on half of the box due to self-weight: $V_{g,A} = 1713$ kN
  - shear force on half of the box due to UDL: $V_{q,A} = 681$ kN
  - shear force on half of the box due to TS: $V_{Q,A} = 873$ kN

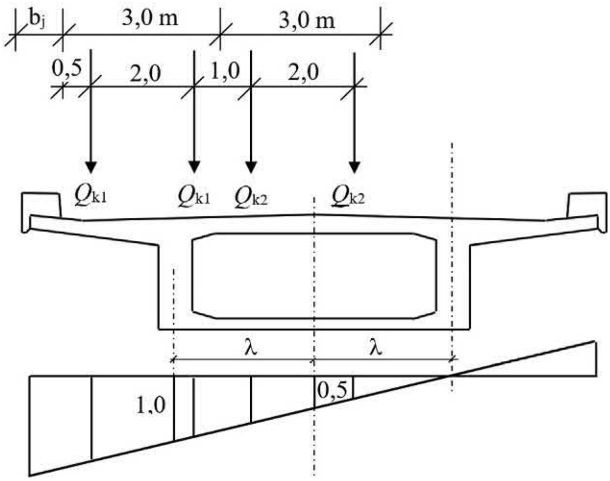

Figure 10.38 Transverse position of TS when calculating shear forces in the close vicinity of supports.

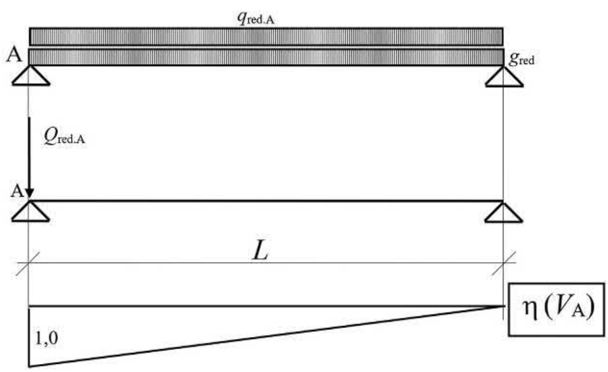

Figure 10.39 Longitudinal position of traffic loads to calculate shear forces at section A.

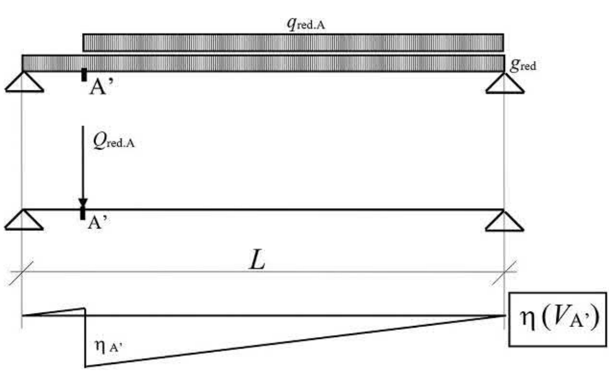

Figure 10.40 Longitudinal position of traffic loads to calculate shear forces at section A'.

- At section A':
  - shear force on half of the box due to self-weight: $V_{g,A'} = 1548$ kN
  - shear force on half of the box due to UDL: $V_{q,A'} = 617$ kN
  - shear force on half of the box due to TS: $V_{Q,A'} = 830$ kN.

Using the alternative combinations of actions given in Section 6.1.4, the design shear forces at sections A and A' are calcuated as follows:

- Design shear force at section A: $V_{Ed,A} = 4064$ kN;
- Design shear force at section A': $V_{Ed,A'} = 3730$ kN.

6.3.4 ULS verifications

For simplification, only bending resistance at midspan (section K) and shear resistance in the close vicinity of support (sections A and A') will be verified.

Owing to either the critical traffic load position (section K) or the applied analysis model (sections A and A') no simultaneous torsion effect needs to be considered at these sections; however, the effect of torsion at other sections and at the traffic load locations cannot be neglected for this superstructure.

Bending Verification at Midspan (section K)

In accordance with the associated design internal forces (see Section 6.3.3), the verification is also directed to half of the box.

For simplification (see Figure 10.41),

- The full width of both the top (deck) and the bottom slab is considered as effective; thus, $b_{eff} = 5.25$ m.
- The height of the section, h', is considered as constant along the full width, b_{eff}, and taken equal to the height of the actual section at the axis of the web as $h' = 1.931$ m.
- An equivalent thickness, t_{eff}, for the deck slab is defined on the basis of the equality of areas of the actual (Figure 10.29) and the simplified (Figure 10.41) gross concrete sections as follows:

$$h'b_w + \left(b_{eff} - b_w\right)t_{eff} + \left(\frac{b_{box}}{2} - b_w\right)t_b = A_c \rightarrow t_{eff} = 259 \text{ mm}.$$

Figure 10.41 Simplified cross section with effective sizes.

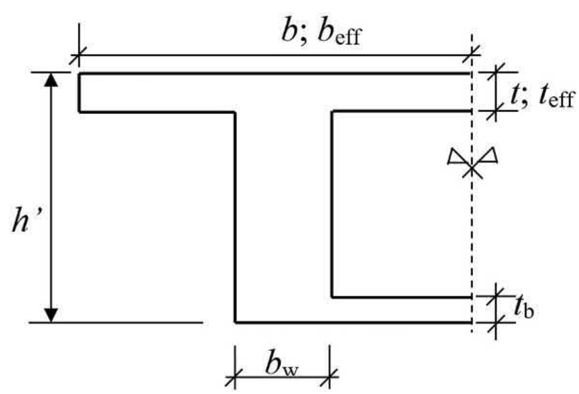

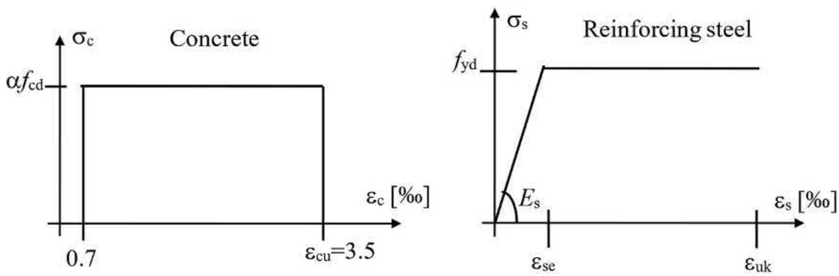

Figure 10.42 Stress-strain diagrams for materials.

The stress-strain (σ-ε) diagram of the applied materials is shown in (Figure 10.42). Prestressing is fully unbonded.

The provided amount, A_s, of reinforcing steel is given in Section 6.2.4, and its effective depth, d_s^K, is recalculated accordingly (also allowing for the unintentional deviation in position as $\delta = 10$ mm):

- At the center of reinforcement:
$$d_s^K = d_s - (h - h') - \delta = 1700 - (2000 - 1931) - 10 = 1621 \text{ mm}$$
- At the outer row of reinforcing steel bars (assuming $c = 40$ mm cover as well as bar diameters as $\phi = 25$ mm for main longitudinal reinforcement and $\phi_t = 12$ mm for transverse reinforcement):
$$d_{s1}^K = h' - c - \phi_t - 0.5\phi - \delta = 1931 - 40 - 12 - 0.5 \times 25 - 10 = 1857 \text{ mm}$$

Owing the static determinacy of the superstructure, the effect of post-tensioning on the section is calculated from its exact geometric position relative to the section (instead of considering it as a compression force at the center of the section and calculating the associated bending moment at section K from the global bending effect of post-tensioning on the superstructure). To consider tendon inclination, the intensity of the compression force due to post-tensioning is calculated immediately before the considered section (see Figure 10.33) as

$$N_{Pd}^K = \gamma_{P,\,\inf} P_{eff}^K \cos(\alpha_1) = 1.0 \times 23257 \times 0.9996 = 23247 \; kN,$$

and the effective depth obtains accordingly as

$$d_P^K = h' - t_b - a_K - \delta = 1931 - 150 - 230 - 10 = 1541 \text{ mm}.$$

Calculation of the depth of compression zone (assuming that reinforcement yields):

$$x_c = \frac{A_s f_{yd} + N_{Pd}^K}{b_{eff}\alpha f_{cd}} = \frac{17{,}181 \times 435 + 23{,}247 \times 10^3}{5250 \times 0.85 \times 26.7} = 258 \text{ mm} < t_{eff}$$
$$= 259 \text{mm} \,(\text{remains in flange})$$

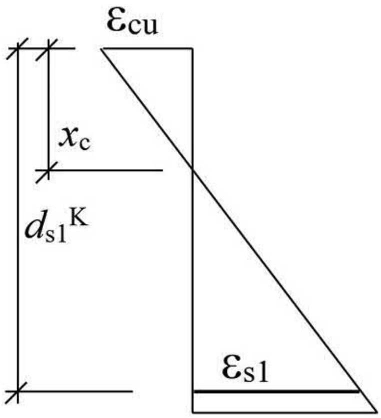

Figure 10.43 Strain distribution over the section in ULS.

Strain at the outer row of longitudinal bars (see Figure 10.43):

$$\varepsilon_{s1} = \frac{\varepsilon_{cu}}{1.25x_c}\left(d_{s1}^K - 1.25x_c\right) = \frac{0.35}{1.25\times 258}(1857 - 1.25\times 258) = 1.66\% < \varepsilon_{uk} = 3.5\%$$

$> \varepsilon_{se} = f_{yd}/E_s = 0.22\%$ (yields).

Bending capacity of the section:

$$M_{Rd}^K = A_s f_{yd}\left(d_s^K - \frac{x_c}{2}\right) + N_{Pd}^K\left(d_P^K - \frac{x_c}{2}\right) =$$
$$= 17181\times 435\left(1621 - \frac{258}{2}\right) + 23247\times 10^3\left(1541 - \frac{258}{2}\right) = 43976\ kNm$$
$$> M_{Ed,K} = 34398\ kNm$$

Shear verification close to support (section A and A′)

In accordance with the associated design internal forces (see Section 6.3.3), the introduced shear verification is directed to the half of the box and based on the following assumptions:

- Only vertical stirrups are used as shear reinforcement ($\alpha = 90°$).
- The total longitudinal reinforcement at midspan, A_s, is fully anchored behind supports.
- The effective depth of the longitudinal reinforcement is equal to that belonging to the outer row of bars ($d_s^A = d_s^{A'} = d_{s1}^K$).

The normal (compressive) and shear (upward) components of post-tensioning at sections A and A’ are calculated on the basis of effective stresses given in Section 6.3.2 as

$$N_{Pd}^A = \gamma_{P,\inf} P_{eff}^A \cos(\alpha_2) = 1.0\times 22{,}474\times 0.997 = 22399\ \text{kN}$$
$$N_{Pd}^{A'} = \gamma_{P,\inf} P_{eff}^{A'} \cos(\alpha_2) = 1.0\times 23{,}144\times 0.997 = 23068\ \text{kN}$$
$$V_{Pd}^{A'} = \gamma_{P,\inf} P_{eff}^{A'} \sin(\alpha_2) = 1.0\times 23{,}144\times 0.081 = 1884\ \text{kN}$$

and the resulting average compressive stresses as

$$\sigma_{cp}^{A} = \frac{N_{Pd}^{A}}{A_c} = \frac{22,399 \times 10^3}{2.57 \times 10^6} = 8.72 \text{ MPa} > 0.25 f_{cd} = 0.25 \times 26.7 = 6.67 \text{ MPa}$$

$$\sigma_{cp}^{A'} = \frac{N_{Pd}^{A'}}{A_c} = \frac{23,068 \times 10^3}{2.57 \times 10^6} = 8.98 \text{ MPa}$$

The compression strut inclination (the angle between compression strut and the longitudinal axis of the superstructure) is assumed as $\cot(\theta) = 1.638$, which corresponds to $\theta = 31.4°$ and fulfills the relevant $1.0 \leq \cot\theta \leq 2.5$ condition.

The resistance of compression chords is verified by applying the strength reduction factor, ν, as

$$\nu = 0.6\left(1 - \frac{f_{ck}[\text{MPa}]}{250}\right) = 0.6\left(1 - \frac{40}{250}\right) = 0.50,$$

the stress state coefficient, $\alpha_{cw} = 1.25$ (if $0.25 f_{cd} < \sigma_{cp}^{A} \leq 0.5 f_{cd}$) and assuming the internal lever arm as $z = 0.9\ d_s^A$ as follows:

$$\begin{aligned} V_{Rd,}\text{max} &= \frac{\alpha_{cw} b_w 0.9 d_s^A \nu_1 f_{cd}}{\cot(\theta) + \tan(\theta)} \\ &= \frac{1.25 \times 500 \times 0.9 \times 1857 \times 0.50 \times 26.7}{1.638 + 1/1.638} = 6243\ kN \end{aligned} > V_{Ed,A} = 4064 \text{kN}.$$

Check whether design shear reinforcement at section A', as necessary, requires the size effect factor, k, as

$$k = \min\left(1 + \sqrt{\frac{200}{d_s^{A'}[\text{mm}]}}; 2.0\right) = \min\left(1 + \sqrt{\frac{200}{1857}};\ 2.0\right) = 1.33,$$

the longitudinal steel ratio, ρ_l (assuming that the total longitudinal reinforcement at midspan, A_s is fully anchored behind supports), as

$$\rho_l = \min\left(\frac{A_s}{b_w d_s^{A'}}; 0.02\right) = \min\left(\frac{17181}{500 \times 1857};\ 0.02\right) = 0.019,$$

and the minimum shear strength as

$$v_{\min} = 0.035 k^{1.5} (f_{ck}[\text{MPa}])^{0.5} \text{MPa} = 0.035 \times 1.33^{1.5} 40^{0.5} = 0.34 \text{ MPa},$$

based on which the shear resistance of section A' without design shear reinforcement is calculated as follows:

$$V_{Rd,c}^{A'} = \max\left(\frac{0.18}{\gamma_c}k(100\rho_l f_{ck}[\text{MPa}])^{0.33}\text{MPa} + 0.15\sigma_{cp}^{A'};\ v_{\min} + 0.15\sigma_{cp}^{A'}\right)b_w d_s^{A'}$$

$$= \max\left(\frac{0.18}{1.5}1.33(100\times 0.019\times 40)^{0.33}\text{MPa} + 0.15\times 8.98;\ 0.34 + 0.15\times 8.98\right)500\times 1857$$

$$= 1862\ \text{kN} \quad > \quad V_{Ed,A'} - V_{Pd}^{A'} = 3730 - 1884 = 1845\ \text{kN}.$$

Formally, it seems that no design shear reinforcement is necessary. However, if applying a relatively low amount of shear reinforcement comprising of (two legs) stirrups as ϕ12/125 B500B (a_{sw} = 226/125 mm) in each web of the box that corresponds to a specific amount of

$$\rho_w = \frac{a_{sw}}{b_w} = \frac{226/125}{500} = 0.0036 > \rho_{w,\min} = 0.08\frac{\sqrt{f_{ck}[\text{MPa}]}}{f_{ywk}} = 0.08\frac{\sqrt{40}}{500} = 0.0010,$$

then the shear capacity of section A' arises as follows:

$$V_{Rd,s}^{A'} = a_{sw}0.9d_s^{A'}f_{ywd}\cot(\theta) = \frac{226}{125}0.9\times 1857\times 435\times 1.638$$

$$= 2154\ \text{kN} > \quad V_{Ed,A'} - V_{Pd}^{A'} = 3730 - 1884 = 1845\ \text{kN}$$

6.3.5 SLS verifications

For simplification, SLS verifications addresses only

- Normal stress limitation in concrete and steels under the characteristic combination of actions
- Decompression under the frequent combination of actions
- Deflection control under the quasi-permanent and the frequent combinations of actions.

In all serviceability limit states, the structure is assumed to remain elastic. For stress calculations, the effects of long-term and short-terms loads are distinguished.

For serviceability verifications, the effects of possible variations in prestress on the characteristic value of (unbonded) post-tensioning force are considered by the use of $r_{k,inf} = 0.95$ and $r_{k,sup} = 1.05$ factors associated with the characteristic value of post-tensioning force as follows (for section K):

$P_{k,inf} = r_{k,inf}\, P_{eff}^{K} = 0.95 \times 23257 = 22{,}094$ kN and

$P_{k,sup} = r_{k,sup}\, P_{eff}^{K} = 1.05 \times 23257 = 24420$ kN.

For simplification and safe-side approximation, any stress increase in tendons due to deformation of the whole superstructure in serviceability limit states are neglected ($\Delta\sigma_p = 0$).

Normal stress limitation (under characteristic combination of actions)

Maximum normal stresses in both concrete and steels occur at midspan; therefore, all verifications focus on section K.

Tension stress in concrete at the bottom extreme fiber of section K:

$$\sigma^K_{ct,car} = -\frac{P_{k,\inf}\cos(\alpha_1)}{A_{it}} - \frac{P_{k,\inf}\cos(\alpha_1)e_{Pit,K}}{I_{it}}(h-y_{it}) + \frac{M^K_g}{I_{it}}(h-y_{it}) + \frac{M^K_q + M^K_Q}{I_{i0}}(h-y_{i0})$$

$$= -\frac{22{,}094\times 10^3\times 0.9996}{2.81\times 10^6} - \frac{22{,}094\times 10^3\times 0.9996\times 764}{1.49\times 10^{12}}(2000-856)$$

$$+\frac{17134\times 10^6}{1.49\times 10^{12}}(2000-856) + \frac{(4596+6321)\times 10^6}{1.37\times 10^{12}}(2000-806)$$

$$= 3.68\text{ MPa} \approx f_{ctm} = 3.50\text{ MPa}.$$

Formally, it seems that the section just cracks, but, for simplification, the uncracked stage is considered in the following.

Axial (compression) stress in concrete at the top extreme fiber of section K (the use of $r_{k,inf}$ less unfavorable than that of $r_{k,sup}$):

$$\sigma^K_{cc,car} = -\frac{P_{k,\inf}\cos(\alpha_1)}{A_{it}} + \frac{P_{k,\inf}\cos(\alpha_1)e_{Pit,K}}{I_{it}}y_{it} - \frac{M^K_g}{I_{it}}y_{it} + \frac{M^K_q + M^K_Q}{I_{i0}}y_{i0}$$

$$= -\frac{22{,}094\times 10^3\times 0.9996}{2.81\times 10^6} + \frac{22{,}094\times 10^3\times 0.9996\times 764}{1.49\times 10^{12}}856$$

$$+\frac{17{,}134\times 10^6}{1.49\times 10^{12}}856 + \frac{(4596+6321)\times 10^6}{1.37\times 10^{12}}806$$

$$= -16.6\text{ MPa} \;<\; 0.6f_{ck} = 0.6\times 40 = 24.0\text{ MPa}.$$

In terms of reinforcing steel, stress limitation is not required because concrete stress at the level of reinforcing steel at section K remains necessarily less than $\sigma^K_{ct,\,car}$. If steel stress, $\sigma^K_{s,\,car}$, is safe-side approximated accordingly, then

$\sigma^K_{s,\,car} = \alpha_t\,\sigma^K_{ct,\,car} = 14.97\times 3.68 = 55\text{ MPa} \ll 0.8f_{yk} = 0.8\times 500 = 400\text{ MPa}.$

Because of unbonded post-tensioning, the maximum stress is prestressing steel is given in Section 6.3.2 as

$\sigma^K_{p,\,car} = \sigma^K_{p,\,eff} = 1048\text{ MPa} \ll 0.75f_{pk} = 0.75\times 1860 = 1395\text{ MPa}.$

Verification of decompression (under frequent combination of actions)

Maximum axial tension stress in concrete occurs at midspan; therefore, this verification focuses on section K.

Tension stress in concrete at the bottom extreme fiber of section K:

$$\sigma^K_{ct,fr} = -\frac{P_{k,\inf}\cos(\alpha_1)}{A_{it}} - \frac{P_{k,\inf}\cos(\alpha_1)e_{Pit,K}}{I_{it}}(h-y_{it}) + \frac{M^K_g}{I_{it}}(h-y_{it})$$

$$+\frac{\psi_{1,q}M^K_q + \psi_{1,Q}M^K_Q}{I_{i0}}(h-y_{i0})$$

$$= -\frac{22{,}094\times 10^3\times 0.9996}{2.81\times 10^6} - \frac{22{,}094\times 10^3\times 0.9996\times 764}{1.49\times 10^{12}}(2000-856)$$

$$+\frac{17{,}134\times 10^6}{1.49\times 10^{12}}(2000-856) + \frac{(0.3\times 4596+0.6\times 6321)\times 10^6}{1.37\times 10^{12}}(2000-806)$$

$$= -2.37\text{ MPa} < 0.$$

Consequently, possible cracks close under the frequent load level.

Deflection control

Deflection control under the quasi-permanent combination of actions (here only self-weight) is reasoned by the acceptable appearance of the superstructure. Based on the results of the stress limitations, the superstructure remains uncracked under the quasi-permanent load.

Deflections due to long-term loads are calculated by the use of the effective modulus of elasticity, which is based on the final creep coefficient, $\varphi(t,t_0) = 1.62$, as follows:

$$E_{c,eff} = \frac{E_{cm}}{1+\varphi(t,t_0)} = \frac{35{,}000}{1+1.62} = 13361 \text{ MPa}.$$

➢*Deflection control at midspan (section K) to avoid unacceptable appearance of the superstructure*

Deflection at midspan due to self-weight:

$$a_g^K = \frac{5}{48}\frac{M_g^K L^2}{I_{it}E_{c,eff}} = \frac{5}{48}\frac{17{,}134\times10^6\times\left(40\times10^3\right)^2}{1.49\times10^{12}\times13361} = 144 \text{ mm}.$$

The bending moment distribution due to post-tensioning is shown in Figure 10.44 from which the deformation of the uncracked superstructure can be simply calculated. The procedure ends with a midspan upward deflection as

$$a_P^K = -116\text{mm}.$$

The sum of the two deflections results in the midspan deflection of the superstructure due to the quasi-permanent load as follows:

$$\mathrm{a}_{qp}^K = \mathrm{a}_g^K + \mathrm{a}_P^K = 144 - 116 = 27.6 \text{ mm},$$

which is far less than the relevant deflection limit of $L/500 = 40{,}000/500 = 80$ mm.

➢*Deflection control at midspan (section K) to avoid user discomfort*

For simplification, a camber at midspan, $a_0^K = -a_{qp}^K$, is assumed. Deflections from traffic loads are calculated assuming uncracked superstructure.

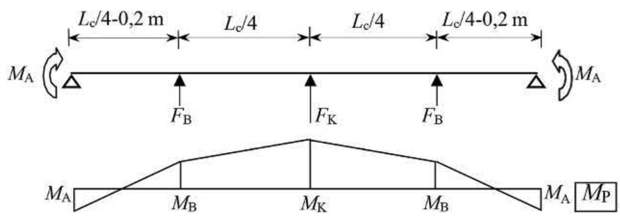

Figure 10.44 Equivalent prestress and its bending effect.

Deflection due to UDL is given as

$$a_q^K = \frac{5}{48}\frac{M_q^K L^2}{I_{i0}E_{cm}} = \frac{5}{48}\frac{4596\times10^6\times\left(40\times10^3\right)^2}{1.37\times10^{12}\times34000} = 16.0\ mm.$$

Deflection due to TS load is given as

$$a_Q^K = \frac{1}{12}\frac{M_Q^K L^2}{I_{i0}E_{cm}} = \frac{1}{12}\frac{6321\times10^6\times\left(40\times10^3\right)^2}{1.37\times10^{12}\times34{,}000} = 17.6\ \text{mm}.$$

Deflection at midspan due to the frequent value of traffic load is combined as

$$a_{q+Q,fr}^K = \psi_{1,q}a_q^K + \psi_{1,Q}a_Q^K = 0.3\times16.0 + 0.6\times17.6 = 15.4\ \text{mm}.$$

Deflection at midspan due to the frequent combination of actions (verification):

$$\begin{aligned} a_{fr}^K &= a_0^K + a_{qp}^K + a_{q+Q,fr}^K = -27.6 + 27.6 + 15.4 = 15.4\ \text{mm} \ll L/400 \\ &= 40{,}000/400 = 100\text{mm}. \end{aligned}$$

7. Research and development

7.1 Shell pedestrian bridge in Madrid

Two pedestrian bridges (Matadero and Invenadero Bridges) with the cover of a concrete shell have been constructed in Madrid on the banks of Manzanares River (Corres et al., 2012; Figure 10.45). These pedestrian bridges are excellent examples of creativity, the optimal use of material, and intentional, extraordinary appearance. The purpose of these special bridges was to establish communication between downtown Madrid and its surroundings. The structural solution consists of a reinforced concrete arch-vault with suspended composite deck spanning 43.5 and 7.7 m rise. The deck is suspended by means of two series of 8.1 mm diameter ties every 0.6 m at both sides.

7.2 Large-span arch bridge, Colorado, USA

With a main span of 323 m, the Hoover Dam Bypass Bridge (also known as the Mike O'Callaghan-Pat Tillman Memorial Bridge) is the fourth-longest single-span concrete arch bridge in the world (Figure 10.46). Each half-arch rib is made up of 26 cast-in-place sections, with construction starting from the canyon walls and a closure pour that locks the two halves together. Approximately 6880 m^3 of concrete of 69 MPa strength of concrete is cast in the arches. The outer dimensions of each hollow arch rib are 6 m wide by 4.26 m long. Structural steel struts connect the arches at each column and are covered with precast concrete panels. The largest struts weigh nearly 40 tons. The 440 concrete segments, each 3 m tall, were precast off-site and erected to form the pier columns. The precast columns are 90 m tall. The structural steel tub girders were

Figure 10.45 Shell pedestrian bridge in Madrid, Spain.
Courtesy of Hugo Corres, Fhecor, Madrid, Spain.

Figure 10.46 Hoover Dam Bridge, photo is taken from the Hoover Dam.
Photo by Balázs.

fabricated off-site and placed with cableway cranes. The temporary cable-stay tower and support system for the erection of the arch incorporated more than 600,000 m of cable-stayed strand. The bridge design satisfies the objectives for both architecture and performance.

7.3 Lightweight concrete for bridges, Stolma Bridge, Norway

The Stolma Bridge in Norway had the longest span of lightweight aggregate concrete bridges in 2000 (Figure 10.47), with the main span measuring 301 m (total length 467 m). The concrete grade was LC 60 with a density of 1930 kg/m^3.

Figure 10.47 Lightweight aggregate concrete bridge under construction in Norway (**fib** bulletin 7).

Figure 10.48 View of Passarelle de Sherbrooke, Canada.
Photo by Balázs.

7.4 UHPC bridge, Sherbrooke

The first large-span (60 m) RPC (reactive powder concrete) or UHPC (ultra high-performance concrete) pedestrian bridge has been erected in Sherbrooke, Canada, in 1997 (Figure 10.48). It is called Passerelle de Sherbrooke. It consists of six pieces of 10 m long match-cast elements with two post-tensioned bottom arches and post-tensioned inclined diagonals. The structure has been completed by external post-tensioning (Figure 10.48; Aitcin, 2014). The selection of materials was done by the University of Sherbrooke under the supervision of Prof. Pierre-Claude Aitcin. The deck is 30 mm thick and is post-tensioned longitudinally as well as transversally. Post-tensioned diagonals connect the deck to the two bottom arches made of stainless steel tubes of 2 mm thickness and 3.2 m length filled with RPC. The RPC contained a relatively high amount of modified CEM II-type cement that had low hydration heat and silica fumes in addition to crushed quartz, sand, superplasticizer, and water with a low water-to-cement ratio. The elements were steam cured. The RPC reached an

Figure 10.49 Seonyugyo Bridge: 120 m span UHPC pedestrian bridge in Seoul, South Korea. Photo by Balázs.

average strength of 199 MPa with a standard deviation of 9.5 MPa, the modulus of elasticity was 48,000 MPa, and the modulus of rupture was 40 MPa (Aitcin, 2014).

7.5 Seonyugyo Bridge, Seoul, South Korea

A 120 m span UHPFRC pedestrian bridge (Called: Seonyugyo Bridge or Rainbow Bridge) has been erected in Seoul, South Korea to commemorate 100 years of diplomatic relations between Korea and France. It was designed by Rudy Ricciotti (Figure 10.49). The main arch is made of Ductal and contains a high steel fiber content.

7.6 MuCEM footbridge, Marseille, France

The MuCEM footbridge has a particular role to connect the Museum of European and Mediterranean Civilization (MuCEM) to the Fort Saint-Jean in Marseille (Figure 10.50). It is a very elegant solution to bridge the gap between the two constructions with a highly elevated structure. The MuCEM footbridge is constructed of precast segments of Ductal, each measuring 4.60 m, created from a single mold, and including high steel fiber content. The precast elements are post-tensioned together.

The French Association of Civil Engineering (AFGC) developed recommendations for design of UHPFFRC structural elements (AFGC, 2007, 2013).

7.7 Tomai Expressway, Shizuoka, Japan

The new Tomai Expressway, between Tokyo and Kyoto, was constructed parallel to the first Tokai Expressway in order to avoid traffic congestion. The Tomai Expressway is the most heavily used road operated by the Central Nippon Expressway. In some sections, more than 100,000 vehicles travel on it a day.

Figure 10.50 UHPFRC pedestrian bridge between the Museum of European and Mediterranean Civilization (MuCEM) to the Fort Saint-Jean in Marseille.
Photo by Balázs.

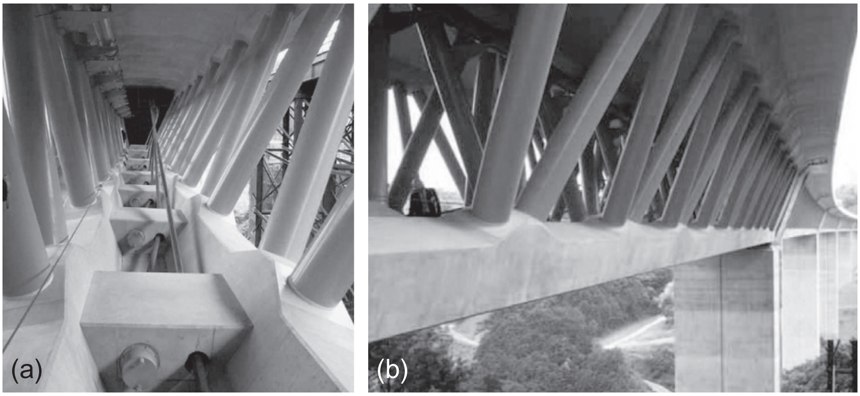

Figure 10.51 Viaduct on the new Tomei freeway between Tokyo and Kyoto at Shizuoka (photo by Balázs).

Earthquake resistance has been one of the main considerations for the design of the freeway viaduct in the vicinity of Shizuoka. A special solution has been developed for the web.

The web consists of steel tubes cast with concrete, providing not only reduced weight but also transparency of the superstructure (Figure 10.51).

7.8 Butterfly Web bridge, Terasako Choucho Bridge, Japan

The Butterfly Web bridge is named after the shape of the prefabricated web of 150 mm thickness (Figure 10.52). The web is prestressed along one of the diagonals, which is subjected to tension with 15.2 mm diameter strands of indented surface. The 80 MPa design strength concrete includes short steel fibers. The web does not contain non-prestressed reinforcement.

Figure 10.52 Side view of Terasako Choucho Bridge with butterfly web, Miyazaki, Japan. Courtesy of Akio Kasuga, Sumitomo Mitsui Construction, Japan.

One of the reasons for this special web is the intention to reduce weight of the structure, hence increasing earthquake resistance. The bridge is constructed using the balanced cantilever method. By using butterfly webs, not only the earthquake resistance but also sustainability improves because less concrete is required compared to an ordinary concrete web box girder.

Terasako Choucho Bridge has been constructed with butterfly webs. It received the Tanaka Award of Japan Society of Civil Engineers in 2013 (Figure 10.53). It is a 10-span continuous butterfly web bridge with a length of 712.5 m, spans of 58.6 m + 87.5 m + 7 × 73.5 m + 49.2 m, and a width of 9.26 m.

7.9 Research and development outlook

Sustainability and durability are major considerations today major in order to construct bridges with minimal materials and increase structures' service life. This is only possible with the optimal selection of materials and systems of bridges. In order to meet the requirements for durability of 100 years or more, durability design should concentrate on all particular details of material selection, conceptual design, detailed design, execution, and use.

High-performance concretes as well as fiber reinforced concretes and lightweight aggregate concretes will provide further innovations.

Various forms of nonmetallic reinforcements are of increasing interest both for prestressed and non-prestressed applications (Research Grant VKE 2018-1-3-1_0003).

Three-dimensional printing started to provide simple solutions even for bridges. The first examples of 3-D concrete printing has been realized for small-span bridges (in Shanghai and in Barcelona). Three-dimensional concrete printing creates new challenges in bridge design and development (Research Grant VKE 2018-1-3-1_0003).

Figure 10.53 Prestressing of main girder by the Terasako Choucho Bridge with butterfly web, Miyazaki, Japan.
Courtesy of Akio Kasuga, Sumitomo Mitsui Construction, Japan.

8. Conclusions

Reinforced and prestressed concrete bridges has been developed over the past 100 years. The present chapter discusses aspects of material specification, different types of cast-in-situ or precast bridge decks and beams, reinforcing and prestressing systems, details, losses, and time-dependent effects in prestressing, design considerations, and construction issues.

Two detailed design examples are presented herein:

- A cast-in-situ non-prestressed girder.
- An externally post-tensioned box girder—the post-tensioning system consisting of polygonal external (unbonded) cables running inside the box (no internal tendons).

In the section about research and development, recent bridge examples were presented based on the speciality of material selection or structural system, such as

- Shell pedestrian bridges Matadero and Invenadero Bridges form Madrid, Spain, owing to their unique form and structural system.
- A large-span arch bridge the Hoover Dam Bridge in Colorado, United States, owing to its special method of construction.
- The Stolma Bridge in Norway, a lightweight aggregate concrete bridge.
- The Passerelle de Sherbrooke, Canada, which is the first large-span pedestrian bridge made of UHPC (ultra high-performance concrete) and RPC (reactive powder concrete).

- The Seonyugyo Pedestrian Bridge, or Rainbow Bridge, in Soul, Korea, which is the largest span (120 m) constructed entirely of UHPFRC.
- The MuCEM (Museum of European and Mediterranean Civilization) footbridge in Marseilles, France, which is constructed of precast segments of Ductal and in which the elements are posttensioned together.
- The new Tomai Expressway Bridge between Tokyo and Kyoto, close to Shizuoka, Japan, where the web consists of steel tubes cast with concrete providing not only reduced weight but also transparency for the superstructure and increased earthquake resistance.
- The Terasako Choucho Bridge in Miyazaki, Japan, which has precast, prestessed butterfly webs for easier construction and increased earthquake resistance.

Acknowledgments

The authors acknowledge the support of the Hungarian Research Grant VKE 2018-1-3-1_0003 "Development of Advanced Concrete Elements Based on New Results of Materials Science."

References

AFGC (Association Francaise de Genie Civil), 2013. Ultra High Performance Fibre-Reinforced Concretes: Recommendations, revised ed. AFGC Publication, Paris.

AFGC (Association Francaise de Genie Civil), 2007. Concrete Design for a Given Structure Service Life: State of the Art and Guide for the Implementation of a Predictive Performance Approach Based upon Durability Indicators. AFGC Publication, Paris.

Aitcin, P.-C., 2014. The first UHSC structure, 15 years later. In: Proceedings of All Russian Conf. on Concrete and Reinforced Concrete. 12–16 May 2014, Moscow, vol. 7, pp. 7–22.

Corres, H.-P., Diestre, S., León, J., Pérez, A., Sánches, J., Cruz, C., 2012. New materials and construction techniques in bridges and building design. In: Fardis, M.N. (Ed.), Innovative Materials and Techniques in Concrete Construction. Springer Science and Business Media, Dordrecht, Netherlands, pp. 17–41, https://doi.org/10.1007/978-94-007-1997-2_22.

Further reading

EN 1992-1-1: 2004 Eurocode 2: Design of concrete structures, Part 1-1: General rules and design rules for buildings.

EN 1992-2: 2005 Eurocode 2: Design of concrete structures, Part 2: Concrete bridges, Design and detailing rules.

fib, 2000a. Lightweight aggregate concrete Part 1—Recommended extensions to Model Code 90, Case studies, *fib* Bulletin 8, Lausanne, ISBN 2-88394-048-7.

fib, 2000b. Guidance for good bridge design Part 1—Introduction; part—Design and construction aspects, *fib* Bulletin 9, Lausanne, ISBN 2-88394-049-5.

fib (2004), "Precast concrete bridges", *fib* Bulletin 29, Lausanne, ISBN 2-88394-069-X.

fib (2013), "Model Code for Concrete Structures 2010", Ernst and Sohn, Wiley, ISBN 978-3-433-03061-5.

Mazzacane, P., Ricciotti, R., Teply, F., Tollini, E., Corvez, D., 2013. MUCEM: The builder's perspective. In: Toutlemonde, F., Resplendino, J. (Eds.), Proceedings of UHPFRC 2013. RILEM Publications Proc 87, pp. 3–16.

Sing, T., Voo, Y.L., Foster, S.J., 2012. Sustainability with ultra-high performance and geopolymer concrete construction. In: Fardis, M.N. (Ed.), Innovative Materials and Techniques in Concrete Construction. Springer Science and Business Media, pp. 81–100, https://doi.org/10.1007/978-94-007-1997-2_5.

This page intentionally left blank

Steel and composite bridges

11

Alessio Pipinato[a,b] *and M. De Miranda*[b]
[a]AP&P, CEO and Technical Director, Rovigo, Italy, [b]Studio de Miranda Associati—DMA, Technical Director, Milan, Italy

1. Introduction

Steel bridges are a design solution that can handle all necessary spans. The advantages of steel bridges include their small foundations; their rapid and efficient construction due to industrialization; the ease of dismantling and reusing their materials; greater control of their members, substructures, and connections; and their lightness when compared to classical r.c. bridges. For small and medium-size spans, girders, and trusses are most commonly used. Commercial or plate girders with superstructures made of composite r.c. decks are the widely used solutions for spans of 30–100 m spans (Figures 11.1 and 11.2). Box girders are more convenient for spans greater than 100 m because of their improved torsional stiffness and aerodynamic behavior (Figures 11.3 and 11.4). For spans longer than 250 m, an orthotropic deck resting on a box girder is a more practical solution. Also, Truss bridges are also employed as a practical and economical solution, especially for railway bridges (Figure 11.5).

2. Design

2.1 Steel bridges

A bridge of which the entire superstructure is made of steel can be referred to as a steel bridge, marking a difference with the steel-concrete composite bridge, where the deck is an r.c. slab: in "pure" steel bridges, the deck is also a steel structure. The weight of a steel deck is around one-third the weight of a concrete deck, but it costs about twice as much as a concrete deck. This has three consequences:

- Steel bridges are usually more expensive than composite bridges up to spans of around 100 m. In fact, for small and medium spans, a steel deck is more costly than a concrete deck, and the increased weight of the main girders is not compensated by the lighter structure. This compensation occurs in movable bridges, which usually have a steel deck.
- A completely steel bridge is more subject to fatigue than a composite one because while the stresses induced by the weight of the bridge are less, those induced by live loads and stress ranges are greater than those subjected to a composite bridge.
- Due to reduced self-weight, steel decks become convenient to construct for the longest spans. The impact of this attribute increases proportionally with the bridge size.

Innovative Bridge Design Handbook. https://doi.org/10.1016/B978-0-12-823550-8.00019-6

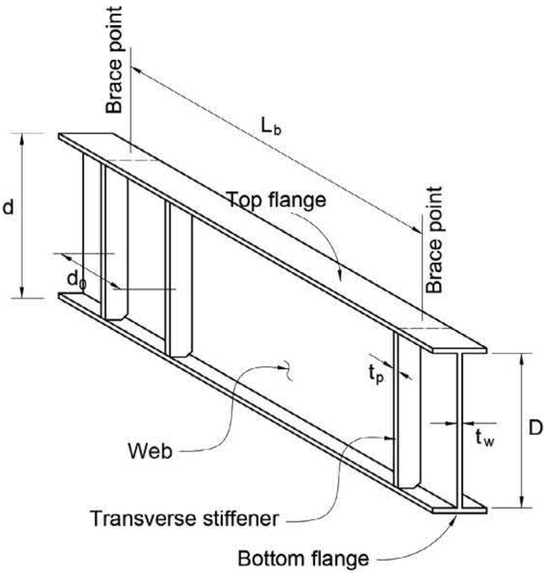

Figure 11.1 Girder components.

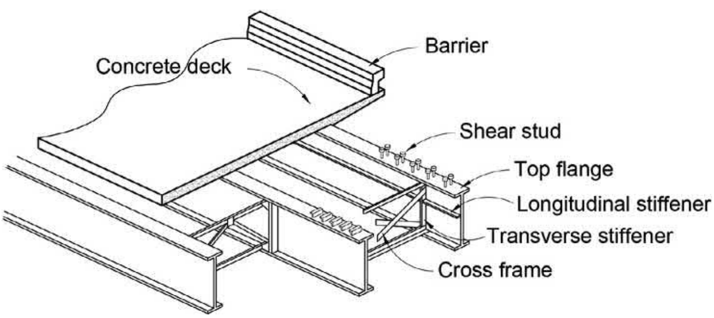

Figure 11.2 Steel-r.c. composite girder components.

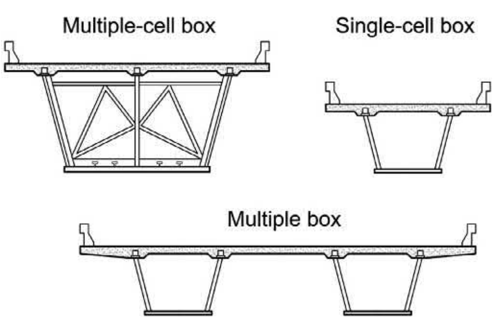

Figure 11.3 Box-girder component types.

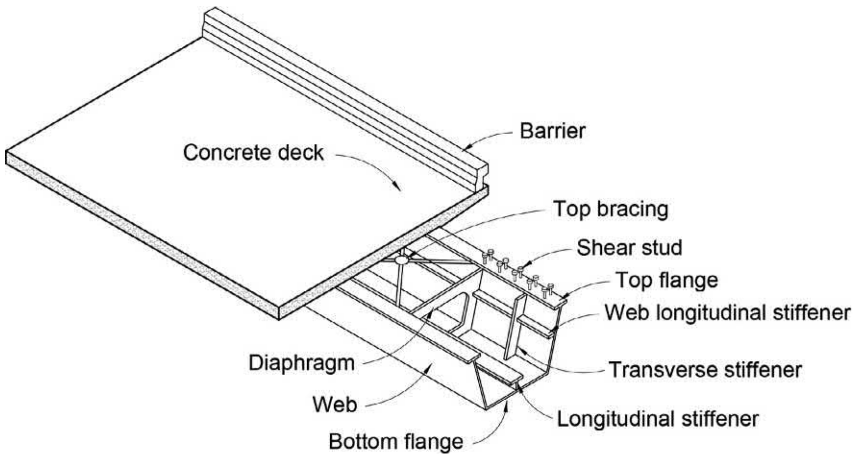

Figure 11.4 Steel-r.c. composite box-girder components.

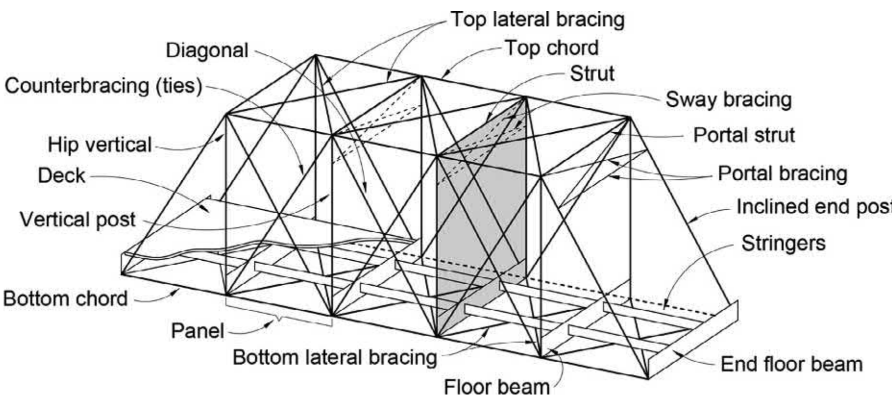

Figure 11.5 Truss main components.

For smaller and medium spans, a steel deck has the advantage of facilitating the full inspection of any part, whereas inspection of rebars and cables is difficult in r.c. or post-tensioned (PT) concrete slab. A steel bridge can be designed using any of the classic bridge types, listed here in increasing order of span:

- *Plate girder type*—Typically with two girders and side cantilevers for spans up to around 120 m.
- *Box girder type*—For curved alignments or longest spans; the shape can be rectangular or trapezoidal.
- *Truss girder*—For medium span bridges, especially used for railway lines.
- *Arch type*—Also called bowstring.
- *Cable-supported bridge*—Cable-stayed or suspension structures.

- *A deck plate*
- *A set of longitudinal stiffeners*
- *A system of transverse girders*—A set of two or more longitudinal girders.

A particular type of steel deck, the orthotropic plate deck, is composed of three elements. The orthogonal mesh and the different stiffness of this double-supporting system is the origin of the name of the orthotropic plate deck. The deck plate, if dimensioned only with regard to strength, could have thickness of 10–12 mm. In any event, a minimum thickness of 14 mm is required today in order to meet the fatigue requirements for road bridges of normal traffic. The longitudinal stiffeners have the scope of supporting the deck plate and can be typically flat plates, angles, tees, or trapezoidal channels. Trapezoidal channels, although involving higher fabrication costs, present greater torsional stiffness and has been popular in Europe in recent decades. Spacing of open stiffeners is of the order of 300 mm; for closed sections, the spacing is twice that value. Their size and depth is proportional to the transverse girder spacing. Transverse girders have the scope of supporting the longitudinal ribs and typically have an inverted T-section, which acts compositely with the deck plate to form an asymmetrical I-section. The spacing of transverse girders can vary from 2.5 to 6 m; a spacing of around 4 m is typical in Europe.

2.2 Composite bridges

2.2.1 General

Composite bridges are becoming more and more popular around the world because they combine some advantages of steel bridges with some key qualities of concrete bridges. A composite bridge has the following advantages:

- A steel main structure that is much easier to erect when compared to the construction of a concrete girder
- A light structure, which imposes smaller loads on piers and foundations, allowing for economy
- A concrete slab, which is cheaper and easier to build than a steel orthotropic deck and has these two additional advantages:
  - A higher mass, which induces fewer vibrations, noise, and dynamic loads on the supporting structure
  - A top surface that allows for easy paving with traditional methods, whereas, in orthotropic decks, it is difficult to create strong bindings, the paving requires delicate execution, and there are some concerns about the durability of paving

While the composite deck has these advantages, a composite deck it also has the following disadvantages:

- Longitudinal tension forces can cause cracks in the slab, and the link with steel causes tensile stresses due to restrained concrete shrinkage.
- A steel deck weighs more than a composite deck, which is a disadvantage for the longest spans.

- A steel structure is usually more expensive than a concrete girder with respect to material costs.

Well-designed composite bridges have proven to be competitive with concrete bridges in all small and medium spans and competitive with steel bridges in spans up to 120 m.

2.2.2 Typical structures

The main structure of a composite bridge is formed by the following elements: (i) main longitudinal girders; (ii) transverse diaphragms or transverse girders; and (iii) concrete slabs. Composite bridges consist of the following elements:

- For spans up to around 70 m, the main girders are typically plate I-girders—two of them for widths up to around 12 m. Two main girders are typically used for widths up to 12 m and even larger widths if a central stringer is used. For longer spans, the structure is typically a box girder of constraint or variable depth. The cross-section shape is usually rectangular, but the trapezoidal shape, even if it is more complicated to fabricate, often has the advantage of a more attractive and slender appearance, as well as a narrower bottom flange, which provides economic benefits.
- Transverse diaphragms in smaller girders are commonly made with simple I-beams. However, a trussed structure is more appropriate for longer spans. For box girders, plated diaphragms are better suited to small boxes, whereas trussed diaphragms work well in larger structures.
- Concrete slabs can be cast in place, cast over prefabricated slabs, reinforced by steel joists, or made of full-thickness, precast elements. Using prefabricated concrete slabs decreases construction time as compared to cast-in-place slabs.

2.2.3 Composite cable-stayed bridges

In self-anchored cable-stayed bridges, composite decks are very competitive for spans ranging between 200 and 500 m. This mainly occurs for the following structural systems:

- Self-anchored three-span cable-stayed bridges
- Two planes of stay cables
- Plated girders of shallow depth both in the longitudinal and transverse directions
- Concrete slab built in partially or fully precast elements

Self-anchored cable-stayed bridges feature a concrete slab fully compressed in two directions:

- Longitudinally, by the horizontal component of stay cables
- Transversally, with the slab being the top flange of the transverse girders simply supported by the stay cables' planes

This biaxial compressive stress is advantageous for strength and durability. The global self-weight of such a structure is much less than the weight of a full concrete deck, requiring fewer stay cables and offsetting the extra costs implied by the steel structure. Construction of this type of structure can be easier and quicker. Further, when compared with the full steel deck, the increased mass of a composite deck has significant benefits: it reduces the vibration both in the deck and the stay cables and has higher aerodynamic stability for larger spans.

2.2.4 Erection

Erection methods of composite bridges typically include the following:

- *Erecting the steel structure from the ground, by using cranes and temporary steel piers*—This is the cheaper and simpler method for small spans that are a short distance from ground.
- *Longitudinal launching*—This is the preferred method for continuous girders, with regular alignment, constant depth, and at least three spans. It is very convenient for girders high above the ground, such as those located over a deep valley, river, or sea strait; by using a long launching nose, this method can be used for even one girder.
- *Building by balanced progressive cantilever*—This is an option primarily for major bridges; when using this method, entire segments are transported by barges or trucks and then lifted and joined to the erected structure.
- *Erecting by rotation*—This is convenient when erection can be done on the sides of the obstacle to be crossed: such as a river or motorway.
- Other special types of erection, such as transversal launching or transporting entire girders by barge, are also possible.

3. Product specifications

Steel is an iron-carbon alloy characterized by specific percentages of the constituent components. Structural steel have a carbon content between 0.1% and 0.3%; the carbon component improves strength but reduces the ductility and weldability of the base material. Structural steels of various strengths are commonly used for bridge structures. Different design standards are used in different countries. In this chapter, North American and European codes are presented. Designs are based on standards such as those shown in Table 11.1, including ASTM A709 (2010a) for North America and Eurocodes for Europe. Additional special requirements are often provided in other codes that are available in Europe and United States, such as National Annexes and American Association of State Highway and Transportation Officials (AASHTO) standards, respectively. These standards mainly differ in notch toughness and weldability requirements.

3.1 Codes

ASTM A709 (2010a) specification covers carbon and high-strength, low-alloy steel structural shapes, plates, and bars and quenched and tempered alloy steel for structural plates intended for use in bridges. Seven grades are available in four yield strength levels, as depicted in Table 11.1. The nominal values of material properties given in EN 1993-1-1 (2014) should be adopted as characteristic values in design calculations. EN 1993-1-1 (2014) covers the design of steel structures fabricated of steel material conforming to the four steel grades listed in Table 11.1.

Table 11.1 Structural Steel Materials According to ASTM and Eurocode

Standard	Designation	Product Categories	Nominal Thickness (mm/in)	f_y (MPa)	f_u (MPa)
ASTM709	36	Plates, shapes, bars	$t<101$, 6/2, 5	250	400
ASTM709	50	Plates, shapes, bars, sheet piles	$t<101$, 6/2, 5	345	450
ASTM709	50S	Shapes	$t<101$, 6/2, 5	345	450
ASTM709	50W	Plates, shapes, bars	$t<101$, 6/2, 5	345	450
ASTM709	HPS 50W	Plates	t < 101, 6/2, 5	345	482
ASTM709	HPS 70W	Plates	$t<101$, 6/2, 5	485	586
ASTM709	HPS 100W	Plates	$t<101$, 6/2, 5	690	690
EN10025-2	S235	Hot-rolled members	$t<40$/1, 57	235	360
EN10025-2	S275	Hot-rolled members	$t<40$/1, 57	275	430
EN10025-2	S355	Hot-rolled members	$t<40$/1, 57	355	510
EN10025-2	S450	Hot-rolled members	$t<40$/1, 57	440	550

3.2 Stress-strain behavior

Both ASTM A370 (2010b) and Eurocode EN 6892-1 (2009) define the testing requirements to determine the tensile strength of steel products. The test method requires the determination of the yield strength, tensile strength, and percent elongation for each test. A stress-strain curve can be measured by graphically or digitally recording the load and elongation of an extensometer during the duration of the test. The elastic modulus or Young's modulus for steel is the slope of the elastic portion of the stress-strain curve. It is conservatively taken as $E = 200.000$ MPa (29,000 ksi) for structural calculations for all structural steels used in bridge construction.

3.3 Hardness

Indentation resistance is the hardness property of steel materials, and it is measurable with a wide variety of testing methods, including the Brinell, Vickers, and Rockwell methods. Rather than being a direct test, it is an indirect measure of tensile and ductility properties. Hardness testing is commonly used to assess the residual properties of structural steel that has been exposed to fire (FHWA, 2012).

3.4 Ductility

A minimum ductility is required for steel. Ductility is expressed in terms of limits for the following:

- The ratio f_u/f_y of the specified minimum ultimate tensile strength f_u to the specified minimum yield strength f_y
- The elongation at failure on a specific gauge length
- The ultimate strain ε_u, corresponding to the ultimate strength f_u

The material ductility is required both by ASTM A709 (2010a) and Eurocode EN 1993-1-1, 2014; however, the material ductility does not automatically translate into structural ductility. The design choice involving connection types, section transitions, bracings, etc., can lead to steel member failing in a brittle mode. To provide structural ductility, the steel must have a sufficient strain-hardening capability to increase the local net section strength sufficiently to allow the gross section to reach yield before rupture occurs at the net section.

3.5 Fracture toughness

The material should have the required material toughness to prevent brittle fracture within the intended design working life of the structure. No further checks against brittle fracture need to be made if the conditions given in codes are met. For example, conditions of EN 1993-1-10 (2010) give the maximum permissible element thickness appropriate to a steel grade, its toughness quality in terms of K_V-value, the reference stress level (σ_{Ed}), and the reference temperature T_{Ed}. According to a well-researched scientific procedure, the linear elastic fracture mechanics (LEFM) approach is the way to predict brittle fracture in bridges and generally in steel structural components. A measure of fracture toughness could be recorded with the Charpy V-notch test (K_V-value).

3.6 Fatigue resistance

A comprehensive overview of fatigue resistance is provided in Chapter 4.

3.7 Strength property variability

Members' property variability is an inherent consequence of the steel manufacturing and is considered in both the resistance factors of Eurocode EN 1993-1-1 (2005) and in load and resistance factor design (LRFD) specifications (AASHTO, 2013).

3.8 Residual stresses

Residual stress is a permanent state of stress in a structure that in itself is in equilibrium and is independent of any applied action. These stresses can result from the rolling processes, cutting processes, welding shrinkage, lack of fit between members, or any loading event that causes part of the structure to yield. Distortion during fabrication is the direct consequence of residual stresses. In order to avoid this problem, mandatory tolerances must be specified during the design stage.

3.9 Durability

According to Eurocode EN 1993-2 (2006), to ensure durability, bridges and their components may be designed to minimize damage or be protected from excessive deformation, deterioration, fatigue, and accidental actions that are expected during the working life of the designed structure. Structural parts of a bridge to which guardrails or parapets are connected should be designed to ensure that plastic deformations of the guardrails or parapets can occur without damaging the structure. The possibility of the safe replacement of any replaceable components of a bridge should be verified as a transient design situation. Permanent connections of structural parts of the bridge should be made with preloaded bolts of specific category connections. Alternatively, closely fitted bolts, rivets, or welding may be used to prevent slipping. Joints where the transmission of forces occurs purely by contact may be used where justified by fatigue assessments.

3.10 Robustness and structural integrity

According to Eurocode EN 1993-2 (2006), the design of the bridge should ensure that when damage occurs to a component due to accidental action, the remaining structure can sustain at least the accidental load combination with reasonable means. The National Annex may define components that are subjected to accidental design situations and also details for the assessments. Examples of such components are hangers, cables, and bearings. The effects of corrosion or fatigue of components and material should be taken into account by appropriate detailing (see also EN 1993-1-9 and EN 1993-1-10).

4. Structural connections

4.1 Bolted connections

EN 1993-1-8 (2005) integrates the general part of EN 1993-1-1 (2014) dealing with verification procedures and requirements for bolted connections. The different classes of bolts—with diameters measured in 12, 14, 16, 18, 20, 22, 24, 27, and 30 mm—can be separated into classes 4.6, 5.6, 6.8, 8.8, and 10.9. For each class, the yield strength f_{yb} and the ultimate strength f_{ub} are given. In the construction of bridges, the last two classes are more diffused. Only bolt assemblies of Classes 8.8 and 10.9 may be used as preloaded bolts with controlled tightening. The reference standard for these bolts in Europe is EN 14399-1 (2005). Bolts with controlled tightening are very sensitive to differences in manufacturing and lubrication.

European regulations on bolts with controlled tightening aim to ensure that, with a given torque, the required preload is obtained with a good reliability and sufficient safety margins to avoid excessive tightening of the screw and consequent plastic deformation. For this reason, a test method to verify the suitability of the components in controlled tightening is included in the Eurocode. The adopted safety factors are given in EN 1993-1-1 (2014) and EN 1993-2 (2006), respectively, for general rules for buildings and bridges. The main safety factors are summarized as follows:

$\gamma_{M0} = 1.05$ strength of gross cross sections
$\gamma_{M1} = 1.25$ strength of net sections at the position of bolts
$\gamma_{M2} = 1.25$ strength of the bolts
$\gamma_{M2'} =$ strength of the contact plates
$\gamma_{M3} = 1.25$ sliding resistance at the ultimate limit state (ULS)
$\gamma_{M7} = 1.10$ preload of high resistance bolts

Diameters and characteristics of bolts in US code (AASHTO, 2013) are different from those in the Eurocode. The standard in the United States for the design of bolted connection (AISC, 2010a) is included in ASTM A325M (2013), ASTM A490M (2013), and related standards. Screws, nuts, and washers are described in AISC (2010a) and ASTM A325M (2013) specifications. The diameters are 15.88, 19.05, 22.23, 28.58, 31.75, 34.93, and 38.10 mm (the smallest diameters approximately correspond to the European 16-, 20-, 22-, 27-, and 30-mm specifications). ASTM A325M and ASTM A490M classes are similar to European classes 8.8 and 10.9, respectively. Under US code, manufacturers' certifications shall be sufficient proof of compliance with the code standard. The use of high-strength bolts is described in RCSC (2009). High-strength bolts are classified in this document according to the strength of the material as follows:

Group A: ASTM A325, A325M, F1852, A354 Grade BC, and A449
Group B: ASTM A490, A490M, F2280, and A354 Grade BD

4.2 Riveted connections

Eurocode 3 EN 1993-1-8 (2005) integrates the general part of EN 1993-1-1 (2014) dealing with verification procedures and requirements for riveted connections. The material properties, dimensions, and tolerances of steel rivets should comply with the requirements given in 1.2.6 Reference Standards, Group 6, of the National Annex. Minimum and maximum spacing and end and edge distances for rivets are the same for bolts and are given in the same Eurocode. Riveted connections should be designed to transfer shear forces, so if tension exists, the design tensile force $F_{t.Ed}$ should not exceed the design tension resistance $F_{t,Rd}$ given in the code. The standard (AISC, 2010a) in the United States does not cover the design of riveted connection. In the evaluation of existing bridges, rivets shall be assumed to be ASTM A502, Grade 1, unless a higher grade is established through documentation or testing (AISC, 2010a), and the same code suggests that because removal and testing of rivets is difficult, assuming the lowest-strength rivet grade simplifies the investigation.

4.3 Welded connections

Submerged arc welding (SAW) is probably the most widely used process for welding bridge web-to-flange fillet welds and inline butt welds in thick plates to make up flange and web lengths. A continuous wire via a contact tip forms a molten pool, and the weld pool is submerged in flux fed from a hopper. The flux immediately surrounding the molten weld pool melts, forming a slag and protecting the weld during solidification; surplus flux is collected and recycled. This process is mainly automatic or robot-assisted. The metal active gas welding (MAG) process is the most widely used manually controlled process for factory fabrication work; it is sometimes known as *semiautomatic* or *carbon dioxide welding*. When the shielding gas used is an inert argon or nonreactive carbon dioxide, the process is named metal inert gas (MIG). The manual metal arc welding (MMA) process remains the most versatile of all welding processes, but its use in the modern workshop is limited.

Eurocode 3 EN 1993-1-8 (2005) integrates the general part of EN 1993-1-1 (2014), which deals with verification procedures and requirements for welded connections; the provisions apply to weldable structural steels conforming to EN 1993-1-1 (2014) and to material thicknesses of 4 mm and greater. The provisions also apply to joints in which the mechanical properties of the weld metal are compatible with those of the parent metal. For welds in thinner material, refer to EN 1993, part 1.3; and for welds in structural hollow sections in material thicknesses of 2.5 mm and greater, guidance is given in Section 7 of EN 1993-1-8 (2005). Welds subjected to fatigue should also satisfy the principles given in EN 1993-1-9. The specified yield strength, ultimate tensile strength, elongation at failure, and minimum Charpy V-notch energy value of the filler metal should be equivalent to or better than that specified for the parent material. A fillet weld with an effective length of less than 30 mm or less than six times its throat thickness (whichever is larger) should not be designed to carry loads. The effective throat thickness a of a fillet weld should be taken as the height of the largest triangle (with equal or unequal legs) that can be inscribed within the fusion faces and the weld surface, measured perpendicular to the outer side of this triangle. The effective throat thickness of a fillet weld should not be less than 3 mm. In determining the design resistance of a deep penetration fillet weld, consider its additional throat thickness, provided that preliminary tests show that the required penetration can consistently be achieved (Figure 11.6). A uniform distribution of stress is assumed on the throat section of the weld, leading to the normal stresses and shear stresses (shown in Figure 11.7) as follows: $\sigma_\perp$ is the normal stress perpendicular to the throat, $\sigma_{||}$ is the normal stress parallel to the axis of the weld, $\tau_\perp$ is the shear stress (in the plane of the throat) perpendicular to the axis of the weld, and $\tau_{||}$ is the shear stress (in the plane of the throat) parallel to the axis of the weld. The design resistance of the fillet weld will be sufficient if the following are both satisfied:

$$\left[\sigma\perp^2 + 3\left(\tau\perp^2 + \tau\|^2\right)\right]^{0,5} \leq f_u/(\beta_w \gamma_{M2}) \text{ and } \sigma\perp \leq 0.9 f_u/\gamma_{M2}, \tag{1}$$

where f_u is the nominal ultimate tensile strength of the weaker part joined, and β_w is the appropriate correlation factor taken from the code (which varies from 0.8 to 1).

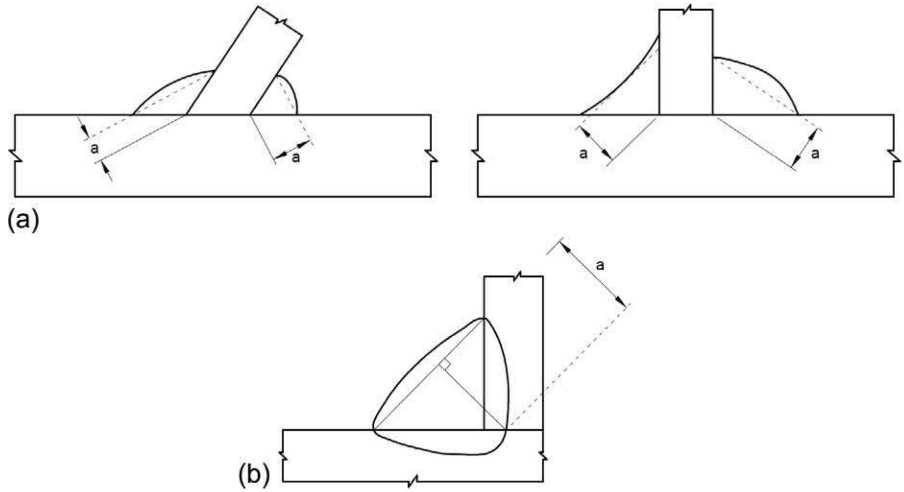

Figure 11.6 (a) Throat thickness of a fillet weld; (b) throat thickness of a deep penetration fillet weld.

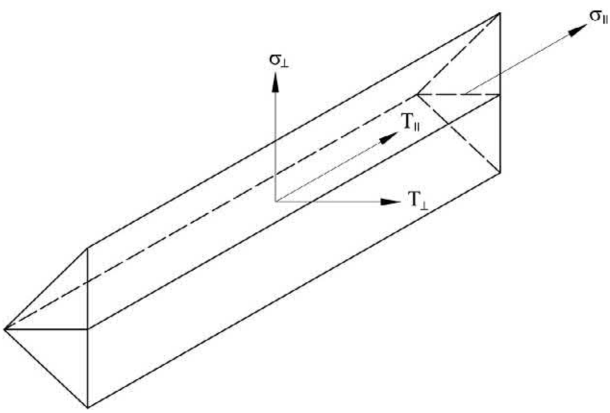

Figure 11.7 Stresses on the throat section of a fillet weld.

Finally, welds between parts with different material strength grades should be designed using the properties of the material with the lower-strength grade. The design resistance of a full penetration butt weld should be taken as being equal to the design resistance of the weaker of the parts connected, provided that the weld is made with a suitable consumable that will produce all-weld tensile specimens with both a minimum yield strength and a minimum tensile strength not less than those specified for the parent metal. The design resistance of a partial penetration butt weld should be determined using the method for a deep penetration fillet weld given in the code. The throat thickness of a partial penetration butt weld should not be greater than the depth of penetration that can be consistently achieved. The design resistance of a T-butt joint, consisting of a pair of partial penetration butt welds reinforced by superimposed fillet welds, may be determined as for a full penetration butt weld if the total nominal throat thickness, exclusive of the unwelded gap, is not less than the thickness t of the part forming the stem of the tee joint, provided that the unwelded gap is not more than (t/5) or 3 mm, whichever is less. In lap joints, the design resistance of a fillet weld should be reduced by multiplying it by a reduction factor β_{Lw} to allow for the effects of nonuniform distribution of stress along its length.

The standard in the United States for the design of welded connection (AISC 2010a) is included in AWS (2010) and related standards. The selection of weld type—complete joint penetration (CJP) groove weld versus fillet versus partial joint penetration (PJP) groove weld—depends on base connection geometry (butt vs T or corner), in addition to required strength and other issues discussed in the code. Consideration of notch effects and the ability to evaluate with NDE may be appropriate for cyclically loaded joints or joints expected to deform plastically (AISC, 2010b).

4.4 Connection choice

Transport needs are commonly a constraint parameter that induces engineers to select the appropriate construction phase and, consequently, the connections design. In general, bolt connections are cheaper than welding, do not require skilled labor, are not difficult to inspect, and can be applied quickly. However, it is not attractive in appearance, and when a good-looking structure is required, bolting is not generally permitted. On the other hand, welded joints require expensive and improved skill labor, and, of course, repair takes more time than it repairing bolted connections.

5. Steel bridge analysis

5.1 Structural modeling

Analysis should be based on calculation models of the structure that are appropriate for the limit state under consideration. The calculation's model and basic assumptions should reflect the structural behavior at the relevant limit state with appropriate accuracy and the anticipated type of behavior of the cross sections, members, joints, and bearings. The method used for the analysis should be consistent with the design assumptions. For the structural modeling of and basic assumptions for bridge components, accurate details are given in the codes and standards adopted. For the structural modeling and basic assumptions pertinent to Eurocode, see EN 1993-2 (2006), and for the design of plated components and cables, see also EN 1993-1-5 (2007) and EN 1993-1-11 (2007). For US codes, FHWA (2012) is a comprehensive reference.

The effects of the behavior of the joints on the distribution of internal forces and moments within a structure and on the overall deformations of the structure may generally be taken into account where significant (such as in the case of semicontinuous joints). If the Eurocode procedure (i.e., EN 1993-1-8) is adopted, the following distinctions among three joint models must be made to identify whether the effects of joint behavior on the analysis need to be considered:

- *Simple*—In which the joint may be assumed not to transmit bending moments
- *Continuous*—In which the behavior of the joint may be assumed to have no effect on the analysis
- S*emicontinuous*—In which the behavior of the joint needs to be taken into account in the analysis

These three models are classified as nominally pinned, rigid and semirigid connections. The requirements of the various types of joints are given in EN 1993-1-8 (2005). Ground-structure interaction should be taken into account, considering the deformation characteristics of the supports where significant. For example, EN 1997-1 (2005) gives guidance for the calculation of soil-structure interaction.

Concerning the global analysis of the structure, the internal forces and moments may generally be determined using either of the following:

- First-order analysis, using the initial geometry of the structure
- Second-order analysis, taking into account the influence of the deformation of the structure

The effects of the deformed geometry (second-order effects) should be considered if they significantly increase the action effects or modify the structural behavior. First-order analysis may be used for the structure if the increase of the relevant internal forces or moments or any other change of structural behavior caused by deformations can be disregarded. This condition may be assumed to be fulfilled if the following criterion is satisfied:

$$\alpha_{cr=}F_{cr}/F_{ed} \geq 10, \text{ for elastic analysis}$$

$$\alpha_{cr=}F_{cr}/F_{ed} \geq 15, \text{ for plastic analysis,}$$

where α_{cr} is the factor by which the design loading would have to be increased to cause elastic instability in a global mode, F_{ed} is the design loading on the structure, and F_{cr} is the elastic critical buckling load for global instability mode based on initial elastic stiffness.

The bridges and components may be checked with first-order theory if the following criteria are satisfied for each section. Elastic analysis should be used to determine the internal forces and moments for all persistent and transient design situations. The National Annex may give guidance for determining when a plastic global analysis may be used for accidental design situations. Concerning the possible presence of imperfections in the structure, appropriate allowances should be incorporated into the structural analysis to cover the effects of imperfections, including residual stresses and geometrical imperfections such as lack of verticality, lack of straightness, lack of flatness, lack of fit, and any minor eccentricities in joints of the unloaded structure. Equivalent geometric imperfections should be used, with values that reflect the possible effects of all type of imperfections unless these effects are included in the resistance formulas for member design. The following imperfections should be taken into account: (i) global imperfections for frames and bracing systems and (ii) local imperfections for individual members. The internal forces and moments may be determined using either elastic global analysis or plastic global analysis. In the first case, elastic global analysis should be based on the assumption that the stress-strain behavior of the material is linear, regardless of the stress level; plastic global analysis allows for the effects of material nonlinearity in calculating the action effects of a structural system.

5.2 Verification for static loading in ULS

According to EN 1993-2 (2006), the partial factors $\gamma_M = R_k/R_d$ shall be applied to the various characteristic values of resistance. Neglecting general information on gross sections, shear lag effects, effective properties of cross sections with class 3 webs, and class 1 or 2 flanges, precise information about the effects of local buckling for class 4 cross sections are given in EN 1993-2 (2006). In this case, the effects of local buckling should be considered by using one of the following two methods specified in EN 1993-1-5 (2007): (i) effective cross-section properties of class 4 sections in accordance with EN 1993-1-5 (2007), Section 4; or (ii) limiting the stress level to achieve cross-section properties in accordance with EN 1993-1-5 (2007), Section 10. Also, for tension members, the general rules of EN 1993-1-1 (2014) apply. For compression members, the design resistance of cross sections for uniform compression $N_{c,Rd}$ should be determined as follows:

Without local buckling:

$$N_{c,Rd} = Af_y/\gamma_{M0} \text{ for class 1, 2, and 3 cross sections.} \tag{2}$$

With local buckling:

$$N_{c,Rd} = A_{eff}f_y/\gamma_{M0} \text{ for class 4 cross sections or} \tag{3}$$

$$N_{c,Rd} = A\sigma_{limit}/\gamma_{M0} \text{ for stress limits,} \tag{4}$$

where $\sigma_{limit} = \rho_x f_y$ is the limiting stress of the weakest part of the cross section in compression; see EN 1993-1-5 (2007).

Concerning the bending moment, the design resistance for bending about the major axis should be determined as follows:

Without local buckling:

$$M_{c,Rd} = \frac{W_{pl}f_y}{\gamma_{M0}} \text{ for class 1 or class 2 cross sections,} \tag{5}$$

$$M_{c,Rd} = W_{el,\min}f_y/\gamma_{M0} \text{ for class 3 cross sections.} \tag{6}$$

With local buckling:

$$M_{c,Rd} = W_{eff,\min}f_y/\gamma_{M0} \text{ for class 4 cross sections or} \tag{7}$$

$$M_{c,Rd} = W_{el,\min}\sigma_{limit}/\gamma_{M0} \text{ for stress limits,} \tag{8}$$

where $W_{el,min}$ and $W_{eff,min}$ are the elastic moduli that correspond to the fiber with the maximum elastic stress, and σ_{limit} is the limiting stress of the weakest part of the cross section in compression. No further details than those provided in EN 1993-1-1 (2014) and EN 1993-1-5 (2007) are needed for shear, whereas torsional and distortional effects should be taken into account for members subjected to torsion. The effects of transverse stiffness in the cross section or effects of diaphragms that are built into reduce distortional deformations may be taken into account by considering an appropriate elastic model that is subject to the combined effect of bending, torsion, and distortion. Distortional effects in the members may be disregarded where the effects from distortion, due to the transverse bending stiffness in the cross section or diaphragm action, do not exceed 10% of the bending effects. Diaphragms should be designed to take into account the action effects resulting from their load-distributing effect. The interaction among bending, axial load, shear, and transverse loads may be determined by using either interaction methods, or the interaction of stresses may be determined by using the yielding criterion (EN 1993-1-5, 2007). Other combinations and specific cases are illustrated in EN 1993-1-1 (2014).

5.3 Verification for earthquake loading

The required provisions are included in EN 1998-2 (2005) and apply to the earthquake-resisting system of bridges designed by an equivalent linear method taking into account a ductile or limited ductile behavior of the structure. Also for bridges provided with isolating devices and for verifications on the basis of results of nonlinear analysis, EN 1998-2 (2005) shall be applied.

5.4 Verification of SLS

According to EN 1993-2 (2006), the following serviceability criteria should be met:

- Restriction to elastic behavior in order to limit excessive yielding, deviations from the intended geometry by residual deflections, and excessive deformations
- Limitation of deflections and curvature in order to prevent unwanted dynamic impacts due to traffic (combination of deflection and natural frequency limitations), infringement of required clearances, cracking of surfacing layers, and damage of drainage
- Limitation of natural frequencies in order to prevent traffic- or wind-induced vibrations that are unacceptable to pedestrians or passengers in cars using the bridge, limit fatigue damages caused by resonance, and limit excessive noise emission
- Restriction of plate slenderness, in order to limit excessive rippling of plates, breathing of plates, and reduction of stiffness due to plate buckling, resulting in an increase of deflection; see EN 1993-1-5 (2007)
- Improved durability by appropriate detailing to reduce corrosion and excessive wear
- Ease of maintenance and repair, to ensure accessibility of structural parts for maintenance and inspection, renewal of corrosion protection and asphaltic pavements; replacement of bearings, anchors, cables, expansion joints with minimum disruption to the use of the structure

5.5 Verification associated with durability

The most relevant indications concerning design for durability in steel bridge design relate to the fatigue endurance, as provided in EN 1993-1-9 (2005). Moreover, EN 1993-2 (2006) provides further insights relating to the specific argument, concerning the following:

- Structural detailing for orthotropic steel decks
- Material
- Fabrication conforming to EN 1090

Finally, according to EN 1993-2 (2006), components that cannot be designed with sufficient reliability to achieve the total design working life of the bridge should be replaceable. These may include the following:

- Stays, cables, hangers
- Bearings
- Expansion joints
- Drainage devices
- Guardrails and parapets
- Asphalt layer and other surface protection
- Wind shields
- Noise barriers

6. Composite bridge analysis

6.1 Introduction

Steel members used in combination with a concrete deck in a bridge structure are often considered under the general nomenclature of composite bridges. In fact, this bridge type has been used throughout the world, mainly in the I-girder and box-girder shapes. Although these are not the only application of composition structures, the structures and codes pertinent two these two types of composite bridges will be explored in this subsection. Other applications include composite steel concrete foundations associating steel beam to concrete piles; towers or special transfer modules at lower-cable anchorages in long-span bridges; special structures for tunnels; and concrete-filled steel tubes (CFST), an interesting application for long-span arches (Pipinato and Modena, 2010).

A typical I-girder composite section is shown in Figure 11.2. A steel I-section or box girder may be a rolled or built-up plated section consisting of top and bottom flange plates welded to a web plate. Hot-rolled steel beams are applicable to shorter-span bridges, and plate girders are used in longer-span bridges (about 40–90 m). If connectors are not provided so that the r.c. deck is simply supported by the deck, the composite action is not provided by this structure, whereas a steel section that acts with the concrete deck to resist flexure is a composite section. Connecting device details are provided in EN 1993-1-8 (2005) for requirements for fasteners and welding consumables. For headed stud shear connectors, refer to EN 13918 (2008).

The various structural members included in a composite steel-r.c. structure should be designed according to the following considerations: The web mainly provides shear strength for the girder and is commonly 1/16–1/18 of the girder span. The web thickness should be as small as the buckling resistance allows, and the height of the web should also be considered where a variable cross-section web would save materials. Longitudinal and transverse stiffeners are usually designed in order to increase flexure resistance of the web, to control lateral web deflection and prevent bending and buckling, respectively, and to control shear resistance in supports and concentrated loads. The bending strength is provided by flanges that have been designed according to the specific code requirements provided in the erection site. The general advantage of r.c. composite bridges is its very slender, aesthetically pleasant shape, made possible by the optimal combination of the high tensile strength of the structural steel, the high compressive strength of concrete, the high durability of normal r.c. decks due to restrictive crack width limitation (Hansville and Sedlacek, 2010). A typical cross section is illustrated in Figure 11.8.

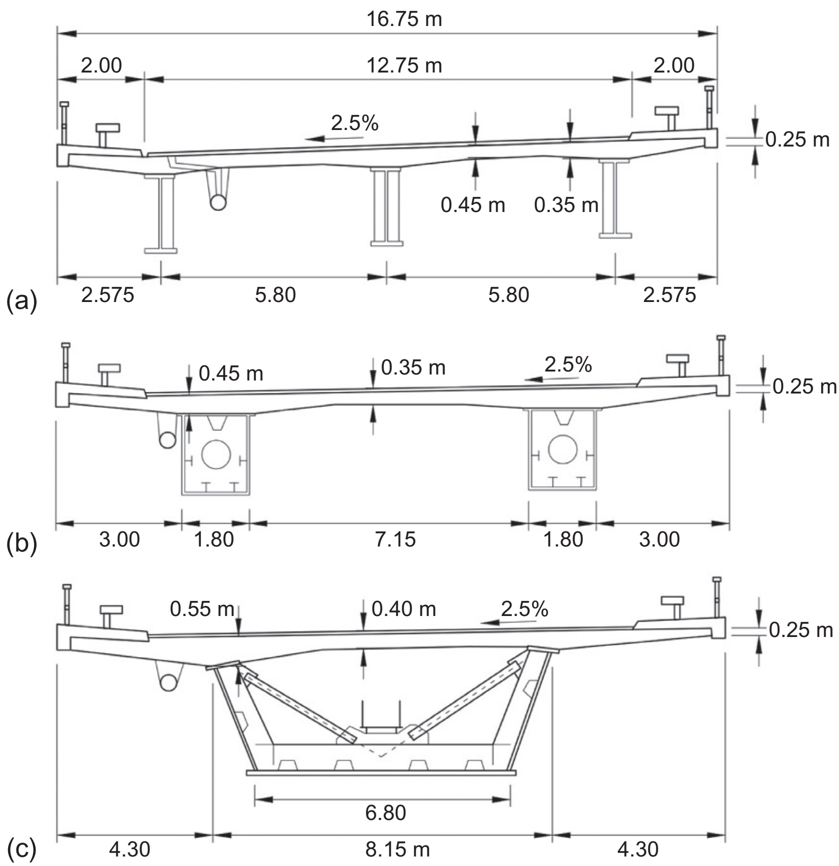

Figure 11.8 Typical cross section of r.c. composite bridges: (a) plate girder bridge with three rolled or welded built-up main girders; (b) cross section with two separated box girders; (c) box girder.

6.2 Structural modeling

The structural model and basic assumptions shall be chosen in accordance with EN 1990 (2005) and reflect the anticipated behavior of the cross sections, members, joints, and bearings. Where the structural behavior is essentially that of a reinforced or prestressed concrete structure, with only a few composite members, global analysis should be generally in accordance with EN 1992-2 (2005). Composite structures should be analyzed in accordance with EN 1994-2 (2006). Concerning joint modeling, the effects of the behavior of the joints on the distribution of internal forces and moments within a structure, as well as on the overall deformations of the structure, may generally be ignored, but where such effects are significant (such as in the case of semi-continuous joints), they should be taken into account; see EN 1993-1-8 (2005). To identify whether the effects of joint behavior on the analysis need to be considered, see the definitions given before for simple, continuous, and semicontinuous joints.

Ground-structure interaction should be taken into account, as discussed in EN 1994-2 (2006). The structural stability is to be taken into account and the action effects may generally be determined using either first-order analysis, using the initial geometry of the structure; or second-order analysis, taking into account the influence of the deformation of the structure. The effects of the deformed geometry (second-order effects) shall be considered if they significantly increase the action effects or modify the structural behavior. Equivalent geometric imperfections should be used with values that reflect the possible effects of system imperfections and also member imperfections unless these effects are included in the resistance formulae; the imperfections and design transverse forces for stabilizing transverse frames should be calculated in accordance with EN 1993-2 (2006).

6.3 Verification for static loading in ULS

According to EN 1994-2 (2006), composite beams should be checked for the following:

- Resistance of cross sections (see Sections 6.2 and 6.3)
- Resistance to lateral-torsional buckling (see Section 6.4)
- Resistance to shear buckling and transverse forces applied to webs (see Sections 6.2.2 and 6.5)
- Shear connections (see Section 6.6)
- Resistance to fatigue (see Section 6.8)

6.4 Verification for earthquake loading

The most relevant requirements are illustrated in EN 1998-2 (2005).

6.5 Verification of SLS

A structure with composite members shall be designed and constructed such that all relevant serviceability limit states (SLS) are satisfied according to the principles of Section 3.4 of EN 1990 (2005). Calculation of stresses for beams at the serviceability limit state (SLS) shall take into account the following effects, as needed:

- Shear lag
- Creep and shrinkage of concrete
- Cracking of concrete and tension stiffening of concrete
- Sequence of construction
- Increased flexibility resulting from significant incomplete interaction due to slip of shear connection
- Inelastic behavior of steel and reinforcement, if any
- Torsional and distortional warping, if any

Moreover, deflections and vibrations are checked according to EN 1990 (2005), EN 1993-2 (2006), and EN 1991-2 (2003).

6.6 Verification associated with durability

The relevant provisions given in EN 1990, EN 1992, and EN 1993 should be followed. Detailing of the shear connection should be in accordance with EN 1994-2 (2006). The corrosion protection of the steel flange should extend into the steel-concrete interface at least 50 mm.

7. Truss bridges analysis

A particular type of bridge is the truss, which is typically all made of steel. Trusses are assumed to be pin-jointed where the straight-force components meet. This assumption means that members of the truss (chords, verticals, and diagonals) will act only in tension or compression. A more complex analysis is required where rigid joints impose significant bending loads upon the elements, as in a Vierendeel truss. Truss bridges' well-known ability to distribute the forces in their structure while assuming different geometric configurations can probably account for the great number truss bridges built around the world. Modern materials and fabrication methods (e.g., automated welding), the specific use of the bridge (roadway, railway, etc.), and other factors such as number of lanes and traffic category influence the choice of truss typology.

7.1 Truss typologies

A wide number of truss types have been developed, and each type has a special use. Many variations on these common schemes could be found in literature. However, following presentation of typologies can be considered an aid in finding the best design solution. In addition, Table 11.2 lists and illustrates the most diffused truss types.

Table 11.2 Truss Typologies

Designation	Geometric Scheme	When First Used	Typical Length	Comments
Pratt	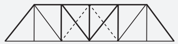	1844	9–75 m	Diagonals in tension, verticals in compression, except for hip verticals adjacent to inclined end post
Baltimore (petit)	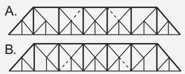	1871	75–180 m	A: With substruts; B: with subties
Warren		1848	15–120 m	Triangular in outline, the diagonals carry both compressive and tensile forces. An original Warren truss has equilateral triangles
Pratt half-hip	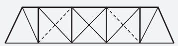	Late 19th century	9–45 m	A Pratt with inclined end posts that do not horizontally extend the length of a full panel
Pennsylvania (Petit)	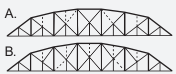	1875	75–180 m	A: Parker with substruts; B: Parker with subties
Warren	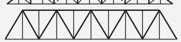	Mid-19th century	15–120 m	Diagonals carry both compressive and tensile forces; verticals serve as bracing for triangular web system
Truss leg bedstead	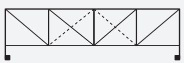	Late 19th century	9–30 m	A Pratt with vertical end posts embedded in their foundations
Lenticular-parabolic	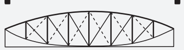	1878	5–110 m	A Pratt with top and bottom chords parabolically curved over the entire length
Double-intersection Warren	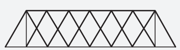	Mid-19th century	23–120 m	Structure is indeterminate; members act in both compression and tension; two triangular web systems are superimposed upon each other with or without verticals

Continued

Table 11.2 Continued

Designation	Geometric Scheme	When First Used	Typical Length	Comments
Parker	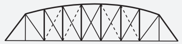	Mid- to late 19th century	12–75 m	A Pratt with a polygonal top chord
Greiner	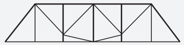	1894	23–75 m	Pratt truss with the diagonals replaced by an inverted bowstring truss
Pegram	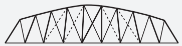	1887	45–195 m	A hybrid between the Warren and Parker trusses; upper chords are all of equal length
Howe	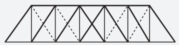	1840	9–45 m	Diagonals in compression; verticals in tension (wood, verticals of metal)
Camelback	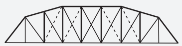	Late 19th century	30–90 m	A Parker with polygonal top chord of exactly five slopes
Double intersection Pratt	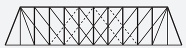	1847	21–90 m	An inclined end-post Pratt with diagonals that extend across two panels
Post	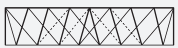	1865	30–90 m	A hybrid between the Warren and the double-intersection Pratt
Bowstring arch-truss	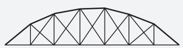	1840	15–40 m	A tied arch with diagonals serving as bracing and verticals supporting the deck
Camelback	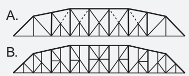	Late 19th century	30–150 m	A: Pennsylvania truss with a polygonal top chord of exactly five slopes; B: same as A, with horizontal struts
Schwelder	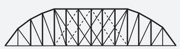	Late 19th century	30–90 m	A double-intersection Pratt positioned in the center of a Parker
Bollman	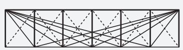	1852	23–30 m	Verticals in compression, diagonals in tension; diagonals run from end posts to every panel point

Table 11.2 Continued

Designation	Geometric Scheme	When First Used	Typical Length	Comments
Waddell A-truss	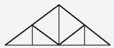	Late 19th century	8–23 m	Expanded version of the king post truss, usually made of metal
Kellogg	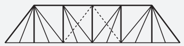	Late 19th century	23–30 m	A variation on the Pratt with additional diagonals running from upper chord panel points to the center of the lower chords
K-truss	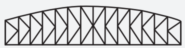	Early 20th century	60–240 m	Takes the name from the particular shape remembering K members
Fink	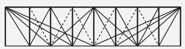	1851	23–45 m	Verticals in compression; diagonals in tension; longest diagonals run from end posts to center panel points
Wichert	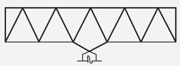	1932	122–305 m	Identified by a characteristic pin connected support system over the piers; truss is continuous over piers
Stearns	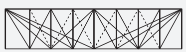	1890	15–60 m	Simplification of fink truss with verticals omitted at alternative panel points

7.2 Analysis methods

The most common analysis method includes force member methods (FMMs), based on the assumption that the truss joints are frictionless pins. This means that as long as loads are applied to the joints and not along the member length, the two forces acting on each member act along its axis. However, this scheme rarely works in real members because, as the physical pins are never really friction-free, secondary bending is present in members. When riveted, bolted, or welded connections start to be used, a common construction method to reduce eccentricities or to compensate for bending involves the alignment of the working line of members into each node. Two variations of this method are used: the method of sections and the method of joints (see, e.g., Krenk and Høgsberg, 2013). However, these methods are scholarly based solutions for simple structures that are statically determinate; and for more complex structures, computer methods are preferred.

8. Research and Development

Steel bridges could be discussed as a paramount in the framework of innovative constructions working toward a more rational and sustainable construction industry, which is growing every year with the increasing number of innovations and futuristic solutions. However, addition R&D is needed, and the most promising areas of exploration could defined be as follows:

- *High-strength steels*—More cost-effective solutions—as well as steel bridges that stronger, lighter, and even more resistant to weather, corrosion, fatigue—are required in the construction market. For this reason, high-strength solutions should be developed and researched. The US Federal Highway Administration (FHWA) reported that high-strength solutions in steel bridges were found to provide lifetime cost savings of up to 18% and weigh 28% less than traditional steel bridge design materials (FHWA, 2002). However, current research in this area is not as concentrated and diffused as necessary.
- *Steel protection technologies*—A design life of 120 years is often required in modern bridges, and the performance of the protective system is a critical factor. Furthermore, reductions in the number of repainting cycles have become significant in the evaluation of whole-life costs. There has been a widely held view that most steel bridges require frequent attention to maintain the original protective coating system. In reality, coating lifetimes have progressively increased from 12 and 15 years to 20 and 25 years. From continued developments in coating technology, modern high-performance coating systems may be expected to not require first major maintenance for more than 30 years.
- *Weathering steel*—Weathering steel is a low-maintenance solution that is used to its advantage less than would be useful. Although it is not an optimal solution for all environmental conditions (e.g., marine locations and highly contaminated sites with deicing salt or SO_2 industrial fumes), there are at least three reasons to prefer the weathering steel alternative: (i) little maintenance with periodic inspection and cleaning; (ii) the cost benefit of not requiring painting (both initially and over the whole life cycle); and (iii) the managing authority's recent preference of the use of nude weathering steel over painted solutions, as mature weathering steel bridges blends well with surrounding protected landscape environments. However, weathering steel has some inherent problems. Superficial debris or the

incorrect maintenance of the superficial patina (high-pressure water washing should be avoided) could accelerate steel decay. Innovative solutions are needed to reduce these problems. Furthermore, the availability of a wide variety of steel components in the market should be increased.

- *Innovative/optimized structural shape*—New advances can be developed by combining the use of new materials with innovative structural and aesthetically pleasing shapes. The principle goals should be to increase cost savings, accelerate construction times, and increase longer lifetimes. Computational and modeling research as well as industry interest and support are needed to achieve these goals.

References

American Association of State Highway and Transportation Officials (AASHTO), 2013. LRFD Bridge Design Specifications. sixth edition with 2013 interim revisions, AASHTO, Washington, DC.

American Institute of Steel Construction (AISC), 2010a. Specification for Structural Steel Buildings. N. 360-10, Chicago.

American Institute of Steel Construction (AISC), 2010b. Commentary on the Specification for Structural Steel Buildings. N. 360-10, Chicago.

American Society for Testing and Materials (ASTM), 2010a. Standard Specification for Structural Steel for Bridges. A 709/A709M, ASTM, West Conshohocken, PA.

American Society for Testing and Materials (ASTM), 2010b. Standard Test Methods and Definitions for Mechanical Testing of Steel Products. A370-10a, ASTM, West Conshohocken, PA.

American Society for Testing and Materials (ASTM) A325M, 2013. Standard Specification for Structural Bolts, Steel, Heat Treated 830 MPa Minimum Tensile Strength (Metric). ASTM International, West Conshohocken, PA.

American Society for Testing and Materials (ASTM) A490M, 2013. Standard Specification for High-Strength Steel Bolts, Classes 10.9 and 10.9.3, for Structural Steel Joints (Metric). ASTM International, West Conshohocken, PA.

American Welding Society (AWS), 2010. AISC Specification Referenced Structural Welding Code—Steel Standard Code AWS D1.1/D1.1M. AWS, Miami, FL.

EN 13918, 2008. Welding. Studs and Ceramic Ferrules for Arc Stud Welding. Comité Européen de Normalisation (CEN), Brussels.

EN 14399-1, 2005. High-Strength Structural Bolting Assemblies for Preloading—Part 1: General Requirements. Comité Européen de Normalisation (CEN), Brussels.

EN 1990, 2005. Eurocode – Basis of Structural Design. Comité Européen de Normalisation (CEN), Brussels.

EN 1991-2: 2003. Eurocode 1: Actions on structures—Part 2: Traffic loads on bridges. CEN, Bruxelles

EN 1992-2, 2005. Eurocode 2: Eurocode 2 – Design of Concrete Structures – Concrete Bridges – Design and Detailing Rules. Comité Européen de Normalisation (CEN), Brussels.

EN 1993-1-1, 2014. Eurocode 3: Design of Steel Structures—Part 1-1: General Rules and Rules for Buildings. Comité Européen de Normalisation (CEN), Brussels.

EN 1993-1-5, 2007. Eurocode 3 – Design of Steel Structures – Part 1–5: Plated Structural Elements. Comité Européen de Normalisation (CEN), Brussels.

EN 1993-1-8, 2005. Eurocode 3: Design of Steel Structures—Part 1–8: Design of Joints. Comité Européen de Normalisation (CEN), Brussels.

EN 1993-1-9, 2005. Eurocode 3: Design of Steel Structures—Part 1–9: Fatigue. Comité Européen de Normalisation (CEN), Brussels.
EN 1993-2, 2006. Eurocode 3: Design of Steel Structures—Part 2: Steel Bridges. Comité Européen de Normalisation (CEN), Brussels.
EN 1993-1-11: 2007. Eurocode 3, part 1-11:Design of structures with tension components. CEN, Bruxelles.
EN 1994-2, 2006. Eurocode 4 – Design of Composite Steen and Concrete Structures – Part 2: General Rules and Rules for Bridges. Comité Européen de Normalisation (CEN), Brussels.
EN 1997-1, 2005. Eurocode 7: Geotechnical Design—Part 1: General Rules. Comité Européen de Normalisation (CEN), Brussels.
EN 1998-2, 2005. Eurocode 8: Design of Structures for Earthquake Resistance—Part 2: Bridges. Comité Européen de Normalisation (CEN), Brussels.
EN 6892-1, 2009. Metallic Materials. Tensile Testing. Method of Test at Ambient Temperature. Comité Européen de Normalisation (CEN), Brussels.
EN 1993-1-10, 2010 Eurocode 3: Design Of Steel Structures—Part 1-10: Material Toughness And Through-Thickness Properties, CEN, Bruxelles.
Federal Highway Administration (FHWA), 2002. High Performance Steel Designers' Guide. US Federal Highway Safety Administration, Washington.
Federal Highway Administration (FHWA), 2012. Steel Bridge Design Handbook: Bridge Steels and Their Mechanical Properties. vol. 1. Publication No. FHWA-IF 12-052, Washington.
Hansville, G., Sedlacek, G., 2010. Steel and composite bridges in Germany. In: State of the Art. Proceedings of the 7th Japanese–German Bridge Colloquium Osaka 2007.
Krenk, S., Høgsberg, J., 2013. Statics and Mechanics of Structures. Springer, https://doi.org/10.1007/978-94-007-6113-1 2.
Pipinato, A., Modena, C., 2010. Il progetto dei ponti ad arco CFST. In: Strade e Autostrade. Edizioni Edi-Cem, Milano. n. 6/2010.
Research Council on Structural Connections (RCSC), 2009. Specification for Structural Joints Using High-Strength Bolts. Chicago.

Further reading

American Society for Testing and Materials (ASTM), 2012. Standard Specification for High-Strength Steel Bolts, Classes 10.9 and 10.9.3, for Structural Steel Joints (Metric). 490M-12, West Conshohocken, PA.
EN 1991-2, 2005. Eurocode 1: Actions on Structures – Part 2: Traffic Loads on Bridges. Comité Européen de Normalisation (CEN), Brussels.
EN 1993-1-10, 2005. Eurocode 3: Design of Steel Structures—Part 1–10: Material Toughness and Through-Thickness Properties. Comité Européen de Normalisation (CEN), Brussels.

Timber bridges

12

K.A. Malo
Department of Structural Engineering, Norwegian University of Science and Technology (NTNU), Trondheim, Norway

1. Wood used in bridges

1.1 Introduction

Throughout the history of societies in the Middle East, the Mediterranean, and China, several massive timber bridges were built. The first bridge built by humans, constructed before 10,000–15,000 B.C., was probably a structure made of timber logs spanning over a waterway. Later, the Romans built timber bridges to ease transport. One of the Roman bridges in particular, known as Caesar's Bridge (55 B.C.), is well documented by the Italian architect Andrea Palladio (1508–1580).

Palladio was also among the first to extend the design of timber bridges into trusses, making longer spans possible. In the 19th century, many timber bridges were built all over the world, using many variants of trusses and arches. An overview of popular structural systems, together with comprehensive information on nearly all relevant topics regarding timber bridges, may be found in Ritter (1990). At the end of the 19th century, steel bridges became popular. From the early 20th century on, reinforced concrete (RC) became available as bridge material, and both RC and steel largely replaced wood for building bridges. Although the use of timber for bridges was low throughout most of the 20th century, interest in this material has grown over the last few decades. Patents for glued and laminated timber (glulam) by the German carpenter K. F. O. Hetzer (1846–1911) made it possible to build large structural members out of very small pieces, which could easily be made straight as well as curved. Modern wood preservation techniques and the growing need for sustainable building materials have resulted in a renewed interest in timber bridges.

Wood is a renewable resource that is readily available in the inhabited parts of the world. Most climatic zones have at least a few tree species that may be used for structural purposes. Older trees are harvested and replaced by young trees, transforming carbon dioxide, water, and small amounts of nutrients from the earth into a structural material via solar energy. The material production by photosynthesis is a natural process, necessary for all life on Earth. When old trees die, the material is broken down and restored by natural and sustainable processes. A piece of wood stores a large amount of carbon dioxide, which makes wood an environmentally friendly material. It is, in fact, the only structural material that has a positive effect on global warming caused by greenhouse gases. Depending on the type, 1 kg of wood can contain about 1.7 kg of carbon dioxide and store it for as long as the wood is used (for instance, in a bridge).

Innovative Bridge Design Handbook. https://doi.org/10.1016/B978-0-12-823550-8.00016-0

Decay and disintegration of wood mainly occur due to activities from fungi, insects, and bacteria. The disintegration of wood is strongly dependent on the moisture content (MC), temperature, and surrounding conditions. By controlling the surrounding conditions, the deterioration of wood can be postponed for a very long time. Well-known examples of this use are the stave churches in the Nordic countries, many of which are still standing after nearly a thousand years. On the other hand, the elements of wood might easily be returned to nature by exposing the material to the natural conditions on the ground. A rough rule of thumb is that wooden structures with moisture content below 20% (by weight) are not prone to decay.

2. Wood as structural material

2.1 Structure of wood

Wood used for structural purposes may broadly be divided into two groups: conifer and deciduous, which are more commonly called *softwood* and *hardwood*. Hardwood trees typically have broad leaves, but solely in the growing season (losing their leaves in winter), whereas conifer species have needle-shaped leaves throughout the year. The terms *softwood* and *hardwood* are somewhat misleading in a general sense, but for the species most commonly used for engineered structures, they have some relevance. Most engineered timber bridges are made of conifer wood (softwood), as explored in the subsequent sections.

Wood is a fibrous, strongly anisotropic material on multiple scales. A useful conceptual model is a composite structure consisting of a bundle of lightly glued, thin-walled drinking straws, conceptually illustrated in Figure 12.1. The tubular structure can be observed for a piece of wood by the human eye, especially by use of a simple magnifying glass. The cell walls in the tubes consist of wood-fiber layers that have inclined orientations relative to each other. The tubes are different sizes but are primarily oriented in the direction of the stem and are held together in a matrix of mainly lignin, an organic polymer. Transport of nutrients and water takes place in the tubes, and in order to serve the branches as well, the trunk also has some tubes (known as *rays*) in the radial directions. The structure of the branches is quite similar to the trunk itself; i.e., the branches also have pith, an annual ring structure, and bark. The connection between the branches and the trunk is known as the *knot*. The knots give rise to some disturbance in the annual ring and tubular structure; some of the tubes are spliced to the branch with tubes, while others have some deviations relative to the longitudinal axes of the stem in order to pass the branching connection. Knots in sawn timber give discontinuities in the fibers, as well as fiber inclinations (grain deviations).

The growth of trees usually depends on the season, and each year creates an additional seasonal ring to the cross section of the stem, commonly denoted as annual rings that typically are a few millimeters thick. Rapid growth gives large tubular cells with small cell thickness and, consequently (on an average volume basis), less load-carrying capacity in the wood material, since it is the fiber material in the cell walls that gives strength to the material.

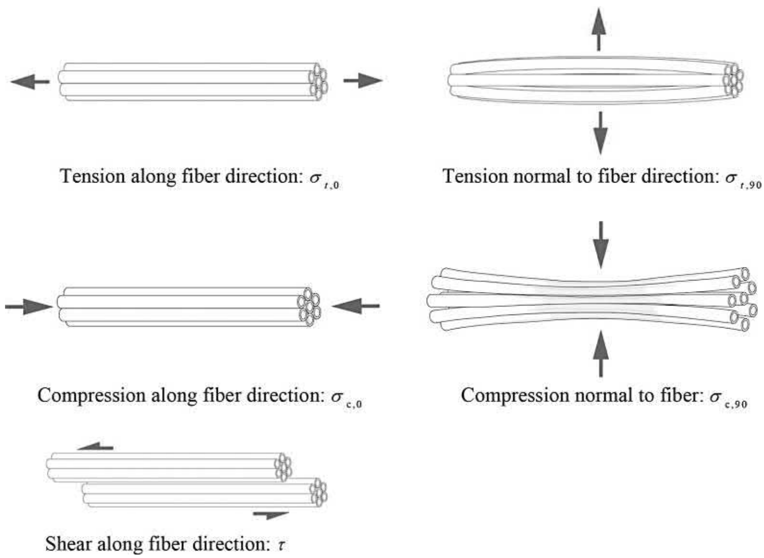

Figure 12.1 Conceptual tube structure of wood subjected to typical stress situations with commonly used symbols for stresses.

The growth along the perimeter produces new wooden fibers by forming wooden cells and strawlike structures held together with a matrix material (gluelike substrate). From the pith in the center of the stem, the annual rings form concentric circles in the stem; hence, the natural coordinate system for a piece of wood is cylindrical with its origin in the pith. The direction along the stem is called *longitudinal (L)*, meaning along grains or fibers, while the outward direction from the pith is called *radial (R),* and the direction along the perimeter is called *tangential (T)* (see Figure 12.2). However, as most pieces of wood are sawn with rectangular shapes and the exact location in the stem is unknown, only longitudinal and transversal directions are used in design calculations. The transversal properties are weighted averages of the R and T properties, which in reality might differ quite significantly. It is common to indicate the L direction (i.e., the stem direction) with a subscript 0 that indicates zero degree angles relative to the grain (fiber) direction, and the transverse direction with subscript 90 (degrees).

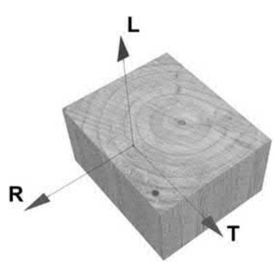

Figure 12.2 Annual rings, pith, and natural material axes at a point for wood.

2.2 Mechanical properties of wood

For anisotropic materials like wood, it is usually necessary to relate all stresses in the material to the material axes in order to evaluate the loading capacity (see Figure 12.1). As already explained, practical design of load-carrying structures is based on strength and stiffness in the grain direction (transversely isotropic). Furthermore, linear material models based on Claude-Louis Navier's hypothesis of plane deformation and Robert Hooke's linear relation between stress and strain are used.

Notations and terms used in the following discussion are those adopted from the European standards for wood materials and design of timber structures (see EN 1995-1-1:2004/A1:2008). For design verification, stresses are denoted by σ (normal stress) and τ (shear stress), and for normal stresses, indices t and c denote tensile and compression, respectively, while indices 0 and 90 indicate the angle between stress direction and fiber direction (e.g., $\sigma_{t,0}$). The stresses are compared to the corresponding strength, denoted by f (e.g., $f_{t,90}$). Note that in general, no stress criterion is available for combined stresses in wood the way that von Mises applies to steel, but certain stress combinations are considered to have significant interactions, which are taken into account. Figure 12.3 shows the usual configurations for strength evaluations, using the same subscript system as for stresses described previously. Although the shear stresses occur with the same value both in the transversal (Figure 12.3f) and longitudinal (Figure 12.3g) directions, the shear strength is much lower along the fibers. Consequently, the shear strength f_v corresponds to the situation shown in Figure 12.3g. Some structural details might be exposed to "peeling" loads (see Figure 12.3h), and in those special cases, it might be necessary to evaluate these stresses and compare them to the corresponding strength (rolling shear strength).

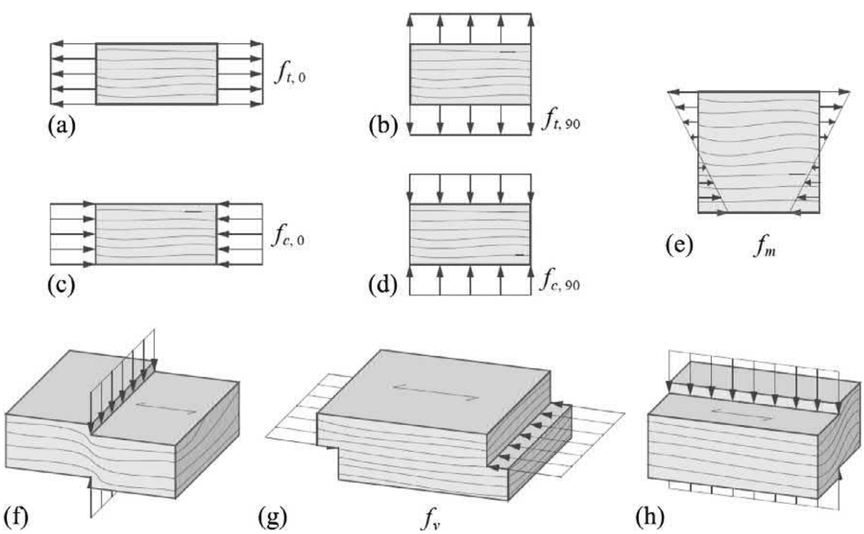

Figure 12.3 Stress exposure and associated strength (drawing: K. Bell).

Numerous experiments have shown that the bending strength is greater than that obtained by simple linear models using tensile or compressive strength at extreme fiber as the strength criterion, and it is well known that with bending, considerable nonlinear stress redistribution occurs. However, this effect is accounted for by the introduction of special design rules for bending. The stresses are computed by linear models (see Figure 12.3e), but are compared to a specific nominal bending strength denoted as f_m—which, in principle, accounts for the nonlinear stress distribution.

Wood is produced by nature, and humans cannot do much to control the production of it. The natural variation in properties is large; to ensure more consistent mechanical and physical properties, sorting procedures are necessary. Many sorting strategies are used, based on either visual grading by the human eye or machine grading by strength, stiffness, density, and visual properties. The mechanical properties for use in structural design calculations are based on statistical distributions and statistical measures like the mean and characteristic (5% fraction) values.

The properties for evaluating the strength and stiffness for wood are specified in standards. In Europe, valid standards are currently EN 338:2009 for solid wood and EN 14080:2013 for glulam. For other locations or species, the *Wood Handbook* (Forest Products Laboratory, 2010) is useful. Some properties of Norway spruce, one of the most frequently used species for structural construction in Europe, are given in Table 12.1 for the European grade C24. The *C* in the grade notation C24 stands for the conifer species (*D* stands for deciduous), and *24* indicates a characteristic bending strength of 24 MPa. For glued laminated members (glulam), the notation *GL* is used in the European codes, and some of these properties are listed in Table 12.1. Further properties and grade classes are given in EN 338 (solid wood) and EN 14080 (glulam).

3. Design of timber components

3.1 Loads on timber bridges

In this discussion, the previously mentioned Eurocodes will be used as the model design code. They are based on the limit state concept used in conjunction with a partial factor method. EN 1990 Basis of Structural Design (EN 1990:2002, commonly denoted Eurocode 0) states how the fundamental limit states shall be verified by design. For each of the two fundamental limit states, the ultimate limit state (ULS) and serviceability limit state (SLS), several scenarios are defined. Eurocode 0 has guidelines as to how the actions in each scenario shall be combined by the use of partial factors giving a design value, indicated by subscript *d,* of the combined effects of the actions. The actions are given by the EN 1991-x series of standards, like EN 1991-2 for traffic loading and EN 1991-1-4 for wind action. Outside Europe, other design codes apply—for instance, for USA, see (AASHTO, 2014). Note that for timber bridges, additional evaluations might be necessary for self-weight due to the effects of moisture and the use of preservatives. Furthermore, moisture might result in considerable dimensional changes that need to be considered, as do the effects of temperature changes.

Table 12.1 Material Properties of Softwood According to EN 338 and EN14080

Symbols	Strength Properties (MPa)						Stiffness Properties (MPa)				
	$f_{m,k}$	$f_{t,0k}$	$f_{t,90k}$	$f_{c,0k}$	$f_{c,90k}$	$f_{v,k}$	$E_{0,mean}$	$E_{0,05}$	$E_{90,mean}$	G_{mean}	$G_{0,05}$
C24	24	14.5	0.4	21	2.5	4.0	11,000	7400	370	690	460
GL30h	30	24	0.5	30	2.5	3.5	13,600	11,300	300	650	540

3.2 Design values

Eurocode 5 Part 1-1, "Design of Timber Structures" (EN 1995-1-1:2004/A1:2008), and Part 2, "Bridges" (EN 1995-2:2004), describe the principles and requirements for safety, serviceability, and durability of timber bridges. The mechanical behavior of wooden materials shows considerable time and moisture dependencies. Long duration of loading (DOL) significantly decreases the measurable strength of the material; this effect is accounted for in modern design codes. Wood is also a hygroscopic material; i.e., water is exchanged with its surroundings. In general, increased moisture content (MC) leads to a decrease in strength and stiffness. In air, the MC and exchange of water are dependent on the relative humidity (RH). Most material properties of wood are related to standardized climatic condition (RH 65% and 20 °C), leading to approximately 12% MC. Furthermore, standardized DOL is used in order to have a common reference for determination of mechanical properties.

The effects from DOL and MC cannot be neglected in the design of timber structures and are taken into account in a simplified manner, through the use of a modification factor k_{mod}, which is dependent on the climatic conditions (i.e., MC) and the DOL, applicable to the timber structure during its design life. The climatic conditions are characterized into three service classes, each of which is related to the expected MC during a given design life EN 1995-1-1:2004/A1:2008. Service class 2 may be applied to timber bridges where the timber parts are properly covered and not exposed directly to rain and water, while in all other cases, service class 3 should be used for timber bridges.

The DOL effect is included in design by characterizing the typical load duration into classes; e.g., self-weight is permanent loading and wind is instantaneous. Traffic loading on bridges is normally assumed to be short-term loading. The design value for a strength property is then calculated by

$$R_d = k_{\text{mod}} \frac{R_k}{\gamma_m}. \tag{1}$$

Recommended values for k_{mod} and the material factor γ_m are stated in EN 1995-1-1:2004/A1:2008 and EN 1991-2. The partial factor for material properties γ_m depends on the type of wood-based product, as well as on the design problem at hand. All the safety and strength properties are based on the use of the characteristic (5%) value R_k (denoted by the use of subscript *k* or *05*), while serviceability issues like deformation and vibration use the mean values of the material properties (subscript *mean*).

3.3 Design strength for structural timber members

Some design formulae essential for timber bridges are presented in the following subsections, but it should be emphasized that these represent only a subset. Readers are encouraged to refer to EN 1995-1-1:2004/A1:2008 and EN 1991-2 for more comprehensive information. In the following discussion, it is assumed that the axis along the structural member is denoted x, while y and z are the principal axes of the cross section. Furthermore, it is assumed that bending about the strong axis is about the y-axis.

3.3.1 Bending and axial actions

The design strength in Eurocode 5 (EN 1995-1-1:2004/A1:2008 and EN 1995-2:2004) is formulated on the basis of linear elastic methods combined with the use of various factors k_{xx}, where the subscript is dependent on the physical effect that it applies to. The factors k_{xx} account for effects neglected by the simplified and linear elastic calculations. For timber members having stresses mainly in the direction of the longitudinal material axes, the following requirements apply:

For bending and axial tension:

$$\frac{\sigma_{t,0,d}}{f_{t,0,d}}+\frac{\sigma_{m,y,d}}{f_{m,y,d}}+k_m\frac{\sigma_{m,z,d}}{f_{m,z,d}}\leq 1 \text{ and } \frac{\sigma_{t,0,d}}{f_{t,0,d}}+k_m\frac{\sigma_{m,y,d}}{f_{m,y,d}}+\frac{\sigma_{m,z,d}}{f_{m,z,d}}\leq 1. \tag{2}$$

For rectangular cross-sectional shapes, the bending stress redistribution shape factor k_m can be set equal to 0.7; it should be set to 1.0 for other cross sections (EN 1995-1-1:2004/A1:2008).

For combined bending and axial compression of members prone to buckling:

$$\frac{\sigma_{c,0,d}}{k_{c,y}f_{c,0,d}}+\frac{\sigma_{m,y,d}}{f_{m,y,d}}+k_m\frac{\sigma_{m,z,d}}{f_{m,z,d}}\leq 1 \text{ and } \frac{\sigma_{c,0,d}}{k_{c,z}f_{c,0,d}}+k_m\frac{\sigma_{m,y,d}}{f_{m,y,d}}+\frac{\sigma_{m,z,d}}{f_{m,z,d}}\leq 1. \tag{3}$$

Here, the buckling effect is brought into the design formulae by use of the factors $k_{c,y}$ and $k_{c,z}$, where subscript c indicates compression, and y or z relates to buckling about the y-axis or z-axis, respectively. The buckling factor $k_{c,i}$ is defined as

$$k_{c,i}=1\Big/\left(k_i+\sqrt{k_i^2-\lambda_{rel,i}^2}\right) \text{ and } k_i=0.5\left[1+\beta_c\left(\lambda_{rel,i}-0.3\right)+\lambda_{rel,i}^2\right], \tag{4}$$

where y or z replace subscript i. The member slenderness λ_i enters the expressions through a material scaled relative slenderness defined as

$$\lambda_{rel,i}=\frac{\lambda_i}{\pi}\sqrt{\frac{f_{c,0,k}}{E_{0,05}}}. \tag{5}$$

The factor β_c reflects the fact that highly industrialized products, like glulam and laminated veneer lumber (LVL), generally have smaller geometrical imperfections, so $\beta_c=0.2$ for solid timber and $\beta_c=0.1$ for glulam and LVL.

Members subjected to bending about the strong axis shall also be checked for lateral-torsional instability by

$$\frac{\sigma_{m,d}}{k_{crit}f_{md}}\leq 1 \text{ and } \left(\frac{\sigma_{m,d}}{k_{crit}f_{md}}\right)^2+\frac{\sigma_{c,0,d}}{k_{c,z}f_{c,0,d}}\leq 1. \tag{6}$$

The latter expression of Eq. (6) takes into account the possible interaction of lateral-torsional instability and weak axis buckling. The reduction factor due to lateral-torsional instability k_{crit} is determined by the simplified expression

$$k_{crit} = \begin{cases} 1 & \text{for}\, \lambda_{rel,m} \leq 0.75 \\ 1.56 - 0.75\lambda_{rel,m} & \text{for}\, 0.75\<\lambda_{rel,m} \leq 1.4 \\ 1/\lambda_{rel,m}^2 & \text{for}\, \lambda_{rel,m}\>1.4 \end{cases} \quad \text{where } \lambda_{rel,m} = \sqrt{\frac{f_{m,k}}{\sigma_{m,crit}}}. \tag{7}$$

The critical bending stress level is determined by classical theory for lateral-torsional instability for elastic members. For timber, warping of cross sections can usually be neglected, leading to

$$\sigma_{m,crit} = \frac{M_{y,crit}}{W_y} = \frac{\pi\sqrt{E_{0,05} I_z G_{0,05} I_{tor}}}{l_{ef} W_y}, \tag{8}$$

where W_y is the section modulus about the strong y-axis, I_z is the second moment of area about the weak axis, and I_{tor} is the torsional moment of area. The effective length of the structural members is denoted l_{ef}; and the ratio of l_{ef}/l is usually in the range 0.5 to 1.0, where l is the actual length of the member.

3.3.2 Shear action

The shear strength along the grain is quite low for most wood species, and for high beams, this might limit the utilization of the timber member. The design requirement is

$$\frac{\tau_d}{k_v f_{vd}} \leq 1. \tag{9}$$

The shear stress along and normal to grain ($\tau_{zxd} = \tau_{xzd}$) is calculated by

$$\tau_d = \frac{V_{zd} S_y}{I_y b_{ef}} = \frac{3V_{zd}}{2h_{ef} b_{ef}}. \tag{10}$$

The latter expression in Eq. (10) is only valid for rectangular cross sections. The introduction of an effective width b_{ef} is meant to account for the risk of cracking due to wetting and drying; it is defined as $b_{ef} = k_{crack} b$, where k_{crack} represents the amount of noncracked material. The effective height h_{ef} will only be smaller than the height of the cross section h in cases where some material is locally removed, as in connections and notches. If a notch leads to a combination of tension normal to grain and shear stresses, a critical stress concentration may occur, and this situation is accounted for by a correction factor k_v for the strength (see Eq. 9), which in such a case will be less than 1.0. In other cases k_v equals unity.

3.3.3 Local effects

Stresses may be transferred between wooden members by compressive contact stresses between mating surfaces or by use of additional elements like metallic fasteners. Contact stresses on inclined surfaces should be related to the material axes of the wood or should be checked against the simplified rules offered by the codes (see, e.g., EN 1995-1-1:2004/A1:2008). For contact stresses normal to grain on some surfaces, an increase in capacity relative to the member size is possible and can be used in design calculations.

The use of fasteners normally requires the removal of material as holes are drilled, grooves are cut, and similar actions are taken. The removal of material reduces the effective load-bearing cross section, which must be taken into account. This is especially important in cases with tensile stresses.

3.3.4 Curved and tapered members

Special rules apply for curved glulam members, taking into account the reduction in strength due to bending of lamellas during production and the occurrence of tensile stresses normal to the grain due to straightening bending moments. In many cases, the interaction of stress components may be the design case. For wooden members with tapered cross sections, the stresses at the surface with inclination relative to the grain direction will have a multi-axial stress state and need special consideration. Most design codes have guidelines for handling these effects (see, e.g., EN 1995-1-1:2004/A1:2008).

3.4 Structural modeling

It is generally sufficient to use linear elastic models in order to distribute the effects of the actions in a wooden structure. Care must be taken regarding the effect of DOL because creep effects may influence the force distribution within a structure, especially in cases where different materials are combined. Put in simplified terms, calculations in ULS, the *characteristic* values of the material properties are used, whereas for SLS, the *mean* values are used. It may be necessary to make further evaluations in cases where second-order deformations affect the internal distribution of forces.

Wood is a strongly anisotropic material and cannot be adequately represented by isotropic material models. While the E/G ratio is about 2.6 for structural metals, it is roughly 16 for wood. Consequently, general isotropic models requiring two parameters as input (E and G, or E and the Poisson ratio) are deemed to fail for wood. The most frequently used material model for three-dimensional (3-D) finite elements is the transverse isotropic linear elastic model, neglecting the difference between the tangential and radial directions but including the difference between transverse and longitudinal directions. In this case, the material axes of the wooden elements have to be represented correctly.

For the overall behavior of beamlike structural members, good results are usually achieved by the use of simple beam elements, provided the shear deformations are included (e.g., use of Timoshenko beam elements).

4. Design of connections

4.1 Connectors

Metallic fasteners made of steel with grades ranging from 4.6 to 8.8 (ISO 898-1:2013) are mostly used. For modern timber bridges, the rod-type connections (dowels, bolts, and screws) are most popular. The fasteners are either axially or shear loaded. Herein, only the shear-loaded dowel-type connection will be discussed. It should be noted that for timber bridges, all metallic parts should have adequate protection against corrosion. Stainless steel dowels are widely used for noncovered bridges, but zinc coating (hot-dipping) is also quite common.

4.2 Dowel-type connections

A dowel is a smooth rod cut in appropriate lengths. Very similar to a bolt, but lacking the threads, nut, and head. The dowel cannot transfer forces in the direction of its own rod axis; otherwise, the nominal capacity of dowels and bolts is similar. The most effective dowel-type connection is achieved by the use of slotted-in steel plates where the capacity of the dowel is balanced with the capacity of the wooden layers between the plates. A conceptual model of a dowel-type connection is visualized on the left side in Figure 12.4. On the right, a similar joint from a bridge is depicted.

Typically, a shear-loaded connection will transmit forces from one structural member to one or more fasteners, which in turn will transfer the forces to the receiving structural member. This leads to three natural steps in the design of timber connection,

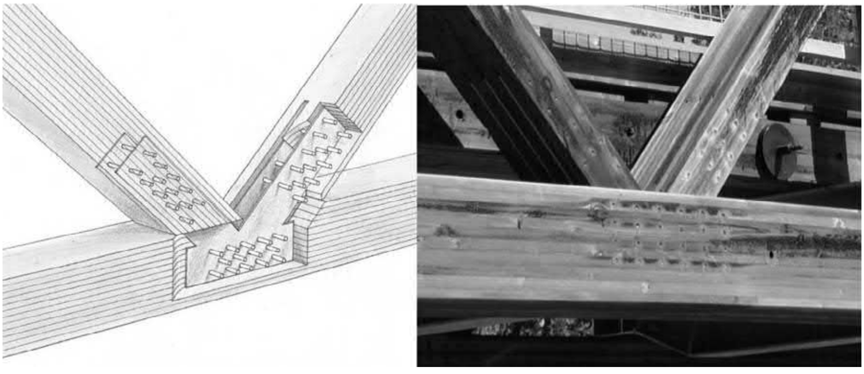

Figure 12.4 Dowel-type joint with slotted-in steel plates.

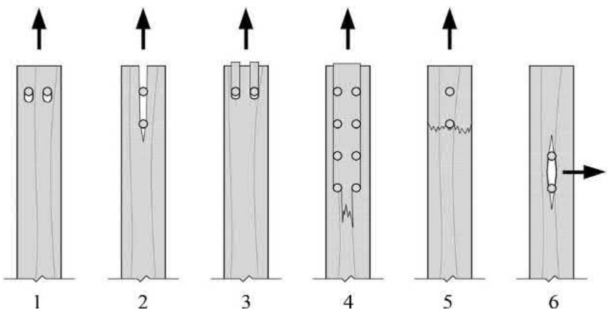

Figure 12.5 Basic failure modes for wood in steel-to-wood dowel type connections.

using connectors: the evaluation of the capacity of the transmitting member, the evaluation of the capacity of the receiving member, and, finally, the evaluation of the capacity of the transferring elements (e.g., the fasteners).

There are several possible failure modes, as illustrated in Figure 12.5. Failure mode 1 is due to the limited embedding strength or capacity of the fasteners; design considerations usually aim at this failure mode because this is the most ductile type of failure. Failure mode 2 includes splitting along a row of fasteners in the grain direction; this failure is minimized by adequate spacing in the fiber direction and end/edge distances. In addition, a reduced computational capacity is used depending on the spacing and the number of fasteners on rows parallel to the grain. Failure mode 3 can be avoided by using proper end distance. Failure mode 4 is a block shear failure that may occur in connections with steel plates and numerous dense groups of fasteners. Failure mode 5 is a tension failure in the net section and may often govern the design capacity. Failure mode 6 is splitting due to tension normal to grain, a load exposure that always should be minimized. However, in many cases, a force component normal grain occurs, and a splitting check should be performed.

4.3 Design expressions for dowel-type connections with multiple slotted-in plates

The theory for the capacity of connections using shear-loaded rod-type connections is usually based on work done by Johansen (1949). The theory is based on the assumptions of rigid plasticity, where the crushing or embedding strength of the wood as well as the yielding of the rods exhibit perfect rigid plastic behavior. A set of possible plastic failure mechanisms is shown in Figure 12.6 for wood-to-steel connections. For multiple slotted-in steel-plates in a structural wooden member, only failure mechanisms (c), (d), and (e) shown in Figure 12.6 are relevant for the external (outermost) shear planes in a connection, whereas (j/l) or (m) will govern the internal shear planes.

The capacity expressions for the external shear planes (per shear plane and connector) are given by Eq. (11), where t_1 is the thickness of the external (outer) wooden

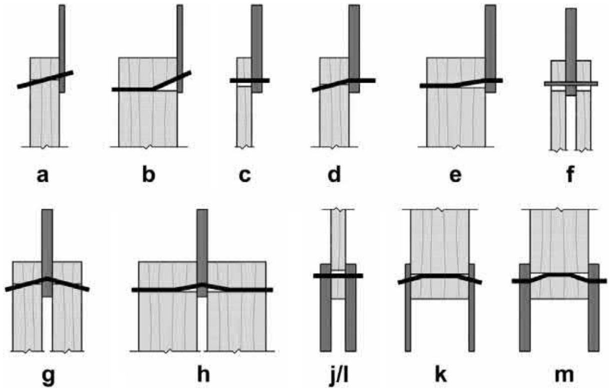

Figure 12.6 Basic failure modes of fasteners for steel-to-wood dowel-type connections.

layer, d is the diameter of the dowel, $f_{h,k}$ is the characteristic embedding strength of the wood, and $M_{y,Rk}$ is the characteristic bending strength of the connector:

$$F_{v,Rk} = min \left\{ \begin{array}{c} f_{h,k} \cdot t_1 \cdot d \quad (\mathrm{c}) \\ f_{h,k} \cdot t_1 \cdot d \left[\sqrt{2 \cdot \dfrac{4M_{y,Rk}}{f_{h,k} \cdot d \cdot t_1^2}} - 1 \right] \quad (\mathrm{d}) \\ 2.3 \cdot \sqrt{\cdot M_{y,Rk} \cdot f_{h,k} \cdot d} \quad (\mathrm{e}) \end{array} \right\}. \tag{11}$$

For the internal shear planes (i.e., all shear planes between the outer steel plates), the capacity per shear plane and connector is expressed in Eq. (12). Note that t_2 is the thickness of the inner wooden layer. Capacity formulations like Eqs. (11) and (12) are often denoted European Yield Models (EYMs), and more on this may be found in EN 1995-1-1:2004/A1:2008:

$$F_{v,Rk} = min \left\{ \begin{array}{c} 0.5 \cdot f_{h,k} \cdot t_2 \cdot d \quad (\mathrm{j/l}) \\ 2.3 \cdot \sqrt{\cdot M_{y,Rk} \cdot f_{h,k} \cdot d} \quad (\mathrm{m}) \end{array} \right\}. \tag{12}$$

5. Design of modern timber bridges

5.1 Building elements

5.1.1 Glulam

Most timber bridges built today use glulam, which is a stack of parallel solid wood lamellas with a thin layer of glue between them, brought together into a single statical element by applied external pressure during the curing of the glue. Several glulam stacks can be glued together side by side, a process usually referred to as *block gluing*. In this way, a wide range of cross-sectional sizes can be made, ranging from the size of solid timber to several square meters. The individual lamella is finger jointed and therefore can be made continuous in any practical length. Usually, the size of a glulam component is limited by transportation obstacles from the factory to the building site—e.g., height under bridges and road curvature.

5.1.2 Stress-laminated decks

The stress-laminated deck system has become popular due to its light weight and high lateral stiffness. In principle, it can be made continuous to any width or length. It consists of parallel wooden lamellas placed with their flatwise faces side by side, but displaced lengthwise relative to each other, spreading the joints to avoid weak sections (see Figure 12.7a). The joints in the lamellas' longitudinal direction are simple butt joints, with just one end facing the other. Depending of the size of the bridge and the loading, lamellas of both solid timber and glulam beams are used.

The lamellas are pressed together by prestressing rods made of high-strength steel, usually placed an equal distance apart. The design of the prestressing system is governed by the need for minimum friction to avoid vertical slip due to concentrated wheel loads (as illustrated in Figure 12.7c), as well as possible occurrence of gaps between the lamellas, which may result in a deck that is too soft (see Figure 12.7b). Most design codes for timber bridges have guidelines for the density of butt joints and necessary prestressing force.

5.1.3 Other materials

A timber bridge usually contains other materials, such as steel and concrete and materials for protection against water access to the wood materials. In addition, RC is used in the abutments and sometimes as decking. Steel is used in the fasteners of the timber

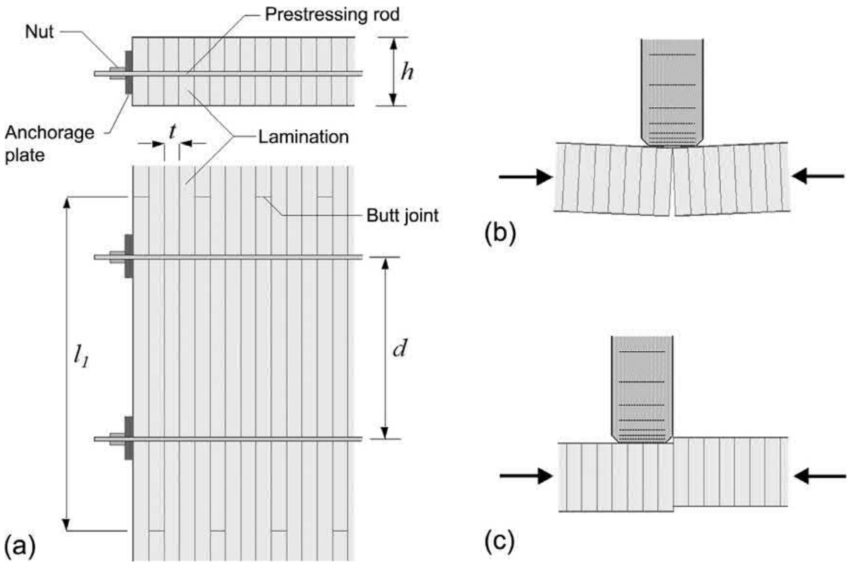

Figure 12.7 Stress-laminated deck plate (drawing: K. Bell).

joints, in hangers located in arches, and sometimes as tension members in truss work. In combination with stress-laminated timber decks, steel crossbeams are often preferred due to their increased stiffness, reduced height, and smaller volume, leading to a more slender appearance of the bridge. Concrete decks can either be designed as a separate plate or in composite action with timber members. In the latter case, concrete will be in compression, and the tension will be handled by the timber members. Two different layouts are used: distributed shear connectors, leading to almost continuous shear force transfer between the parts, or concentrated connections between the concrete plate and the timber structure at the timber joints connecting the concrete slab directly to the slotted-in steel connector plates without contact between wood and concrete.

5.2 Structural systems

5.2.1 Beams and slabs

Short bridges are often built as simple beam-type glulam structures, either as simply supported single-span bridges or multiple-span bridges. The main beams span in the lengthwise direction, and in most cases, crossbeams on top, with close spacing, form the transversal bearing. A top wearing layer of concrete or wooden planks is usually added. An alternative to crossbeams is to use a concrete plate on top of the main beams, with shear connectors in between forming a composite system. However, in some cases, it is preferred to avoid composite action between the wooden structure and the concrete slab due to differences in expected creep and temperature behavior. The bridge depicted in Figure 12.9 has no composite action between the concrete top layer and the timber trusses. A slab-type wooden bridge is often produced by using stress-laminated decks; see Figure 12.7 for the layout and Figure 12.8 for a simple application.

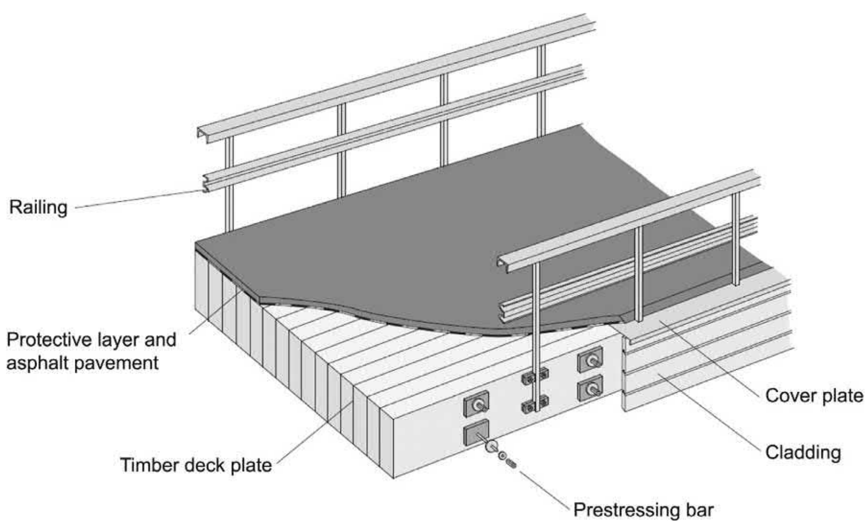

Figure 12.8 Bridge deck using prestressed laminations.
Reproduced with permission from Svenskt Trä, Swedish Wood, 2011.

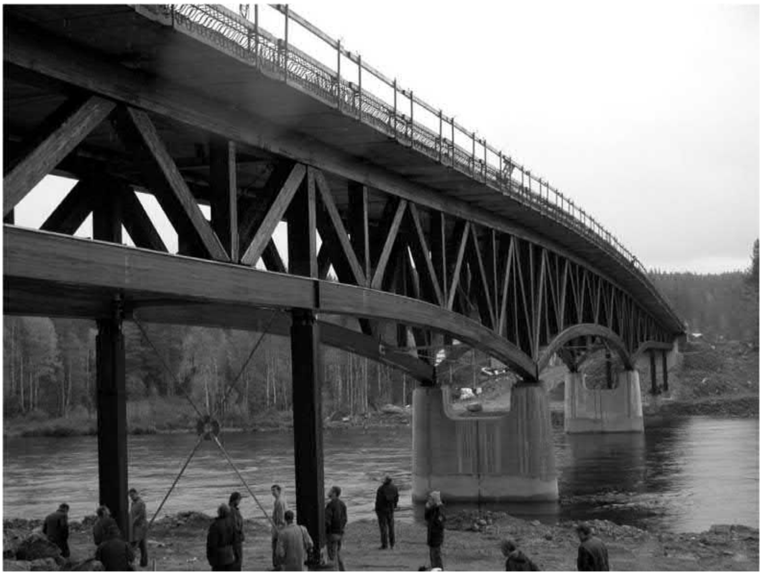

Figure 12.9 Kjøllsaeter Bridge, Norway, whose length is 158 m, features six spans, the longest of which is 45 m.
Photo: Norwegian Public Roads Administration.

Figure 12.10 Flisa Bridge, whose length is 196 m, has three spans, the longest of which is 70 m. Photo K. A. Malo.

5.2.2 Trusses

Trusses in modern bridges are mostly made of glulam members. The truss can be beneath (Figure 12.9) or above the carriageway (Figure 12.10). The choice depends on the available free height under the carriageway and aesthetic, economic, and durability considerations. The trusses are prefabricated in as large pieces as possible, the size of which is commonly limited by transport regulations and road obstacles. Splices in the chords are usually placed at locations suitable for assembling the separate parts on site. All the inclusive splices of the connections are of the slotted-in steel plate and dowel types (see Figure 12.4).

5.2.3 Arches

Arches are often used in the design of timber bridges; they may have massive cross sections (see Figure 12.12) or, for longer spans, may be formed by trusses (see Figure 12.11). The use of a truss arch is beneficial to allow the handling of the considerable moment actions originating from the loads transferred through vertical hangers. A structural feature of the arch is large horizontal thrusts at the footing. These can be accommodated by the use of heavy foundations, which was the chosen solution for the Tynset Bridge in Norway (depicted in Figure 12.11). For shorter bridges, a tension tie can be a better and cheaper solution, and this has been used for the Fretheim Bridge (Figure 12.12), a bowstring bridge in Flåm, Norway. The double tension tie and the chosen detail at the footing of this bridge are shown in Figure 12.13.

Figure 12.11 Tynset Bridge in Norway, whose length is 124 m, has three spans, the longest of which is 70 m.
Photo K.A. Malo.

Figure 12.12 Fretheim Bridge in Flåm, Norway has a span of 38 m.
Photo: Sweco Norway AS.

Figure 12.13 Footing detail at Fretheim Bridge.
Photo: Sweco Norway AS.

The bridges shown in Figures 12.10–12.13 all have stress-laminated timber decks. This type of deck is light and can allow for smaller dimensions in other parts of the bridges, as well as reduced foundation costs. Existing foundations (of an old bridge) can often be reused. This was the case for Flisa Bridge (Figure 12.10), where a one-lane steel bridge was replaced by a timber bridge with a pedestrian lane as well as two road lanes.

6. Design verifications of timber bridges

6.1 Structural information

Some important points concerning an actual timber bridge design are presented in this section. The design specifications are for the Fretheim Bridge in Flåm, Norway, depicted in Figures 12.12 and 12.13. The bridge is a three-hinged bowstring bridge with arches of glulam, tension ties made of steel rods, and a stress-laminated timber deck made of solid timber; the layout is as shown in Figure 12.7a. The hangers are fastened to the arches and to transversal steel crossbeams beneath the timber deck. The arches are slightly slanted inward, with a ratio of 9/100. The span of the bridge is 37.9 m, and the radius of curvature of the circular arches is 35.2 m.

There is no horizontal wind truss between the two arches, and the arches are clamped sideways at the supports. The horizontal stabilization of the arches is increased by replacing the hangers closest to the support with rigid U-shaped steel frames fastened to the deck, which in turn transfer the horizontal forces to the supports. The design load combinations are stated here without further explanation.

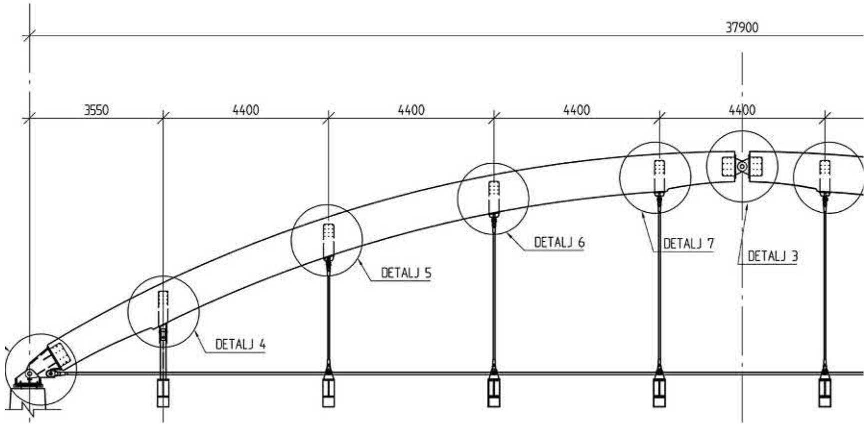

Figure 12.14 Structural system of Fretheim arch bridge.
Design and drawing: Sweco Norway AS.

6.2 Verification of arch in ULS

The structural system is treated as symmetrical about the center hinge, and only the left part is shown on the structural system drawing in Figure 12.14. The cross section of the glulam arch member has a width of 800 mm and height and 1000 mm. The height gradually decreases to 800 mm in the vicinity of the hinges.

The actual loading on the bridge is governed by its location and expected use, together with guidelines from local authorities and requirements from the bridge owner. Furthermore, the loading and load combinations should be in accordance with the current design regulations (e.g., as stated in EN 1990:2002 and EN 1991-2 for Europe). Although the structural system is quite simple, many load combinations need to be investigated, and the results lead to many possible combinations of design actions. The arches are subjected to high compressive forces with moment action about both axes, which vary along the arch. In order to exemplify the use of the timber design verification, this example will use a severely simplified approach by considering just the values stated in Table 12.2, which are based on the original design calculations (Sweco Norway, 2005).

Table 12.2 Design Values of Actions (Load Factors Included)

Symbol	Meaning	Value
N	Axial compressive force	2000 kN
M_y	Moment about y-axes (strong axes)	1500 kNm
M_z	Moment about z-axes (weak axes)	70 kNm
l_{ky}	Buckling length about y-axis (i.e., in the z-x plane)	23 m
l_{kz}	Buckling length about z-axis (i.e., in the y-x plane)	28 m
l_{ef}	Effective length, lateral-torsional instability	15 m

It is assumed that the wooden arches are produced according to EN 14080:2013, fulfilling the requirements for the glulam class GL30h; hence, the properties stated in Table 12.1 are used in the calculations. Furthermore, the traffic loading is treated as short-term loading; and provided that the wooden members are protected against direct water exposure, the modification factor for material strength $k_{\text{mod}} = 0.9$ (EN 1995-1-1:2004/A1:2008). The material factor for glulam members is set to $\gamma_m = 1.25$ (EN 1995-1-1:2004/A1:2008), and, finally, the design strength values are determined by use of the characteristic values given in Table 12.1 modified according to Eq. (1).

The design strength with respect to compression and bending about both cross-sectional axes can be evaluated by using Eq. (3). First, it is assumed that the buckling takes place about the y-axis and that the compression is combined with full moment action about the y-axis and reduced moment action about the z-axis. The slenderness about the y-axis becomes $\lambda_y = {}^{l_{ky}}\!\Big/\!\sqrt{I_y/A} = 79.7$, and the relative slenderness can be evaluated by Eq. (5):

$$\lambda_{rel,y} = \frac{\lambda_y}{\pi}\sqrt{\frac{f_{c,0,k}}{E_{0,05}}} = \frac{79.7}{\pi}\sqrt{\frac{30}{11300}} = 1.31 \tag{13}$$

Next, the buckling parameter $k_{c,y}$ is evaluated by use of Eq. (4), resulting in $k_{c,y} = 0.52$. The stresses are determined by use of common linear elastic relationships. The final step is to evaluate the interaction of compression and bending by use of the left-hand expression of Eq. (3), which reads

$$\frac{\sigma_{c,0,d}}{k_{c,y} f_{c,0,d}} + \frac{\sigma_{m,y,d}}{f_{m,y,d}} + k_m \frac{\sigma_{m,z,d}}{f_{m,z,d}} = 0.26 + 0.57 + 0.02 = 0.85. \tag{14}$$

By comparison of the terms, it is obvious that in this assumed failure mode, the effect of bending about the strong axis dominates the utilization of the member.

Next, it is assumed that buckling takes place about the weak axis, and the following buckling parameters result: $\lambda_z = 121.2$, $\lambda_{rel,\,z} = 1.99$, $k_{c,\,z} = 0.24$. The right-side expression of Eq. (3) becomes

$$\frac{\sigma_{c,0,d}}{k_{c,z} f_{c,0,d}} + k_m \frac{\sigma_{m,y,d}}{f_{m,y,d}} + \frac{\sigma_{m,z,d}}{f_{m,z,d}} = 0.56 + 0.40 + 0.03 = 0.99. \tag{15}$$

In this case, buckling about the weak axis is the dominating effect, and the member is fully utilized.

The buckling lengths in this example have been determined by the use of linearized instability analyses, quantifying the critical axial force P_{cr}. Then, the buckling length is estimated from the simplified relation $l_k = \pi\sqrt{EI/\text{Pcr}}$, where P_{cr} is the axial force at the buckling load level.

Figure 12.15 A dowel-type connection between hanger and arch.
Photo K.A. Malo.

6.3 Verification of a dowel connection in ULS

A dowel-type connection transferring the force from the hanger to an arch is depicted in Figure 12.15. The four slotted-in steel plates are extended outside the arch, and a common pin has been installed through a hole in each plate to create a hinge beneath the arch to avoid any moment action on the dowel connection. It is essential to design the groups of fasteners with no eccentricity, as eccentricities will cause unequal force distribution on the dowels and lead to a more expensive connection.

The detail denoted as "Detalj 5" in the Fretheim Bridge drawing (Figure 12.14) is used here as an example of the calculations. This connection is located 11 m from the center point of the arch and is shown in Figure 12.16. It differs slightly from the design shown in Figure 12.15.

The input parameters for the calculation are four steel plates that are 8 mm thick, with 9 mm slots in the wood. The thickness of the external wood layer is 100 mm, and the internal layers are 188 mm thick. The 12 dowels have diameters of 12 mm and characteristic bending strength $M_{y,\ Rk} = 67152$ Nmm; also, they are installed in a regular pattern with spacing of 100 mm in both directions. The embedding strength of glulam is dependent on the wood density, dowel diameter d, and the angle α between the grain and force directions. This is evaluated by

$$f_{h,\alpha,k} = \frac{f_{h,0,k}}{k_{90}\, sin^2\, \alpha + cos^2\, \alpha}, \tag{16}$$

where $f_{h,\ 0,\ k} = 31.0$ MPa and is the basic embedding strength along the grain, and parameter $k_{90} = 1.53$ for 12 mm dowels in softwood.

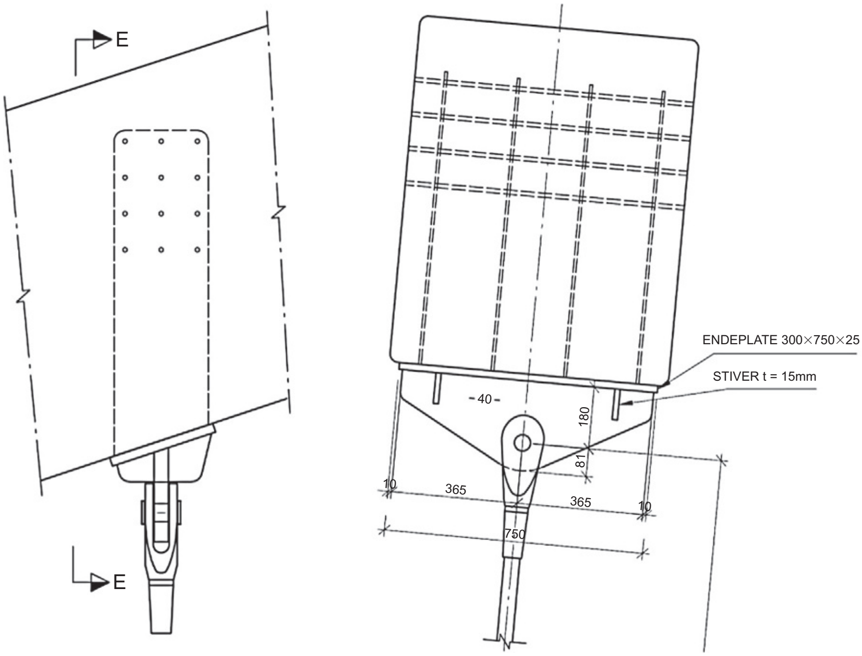

Figure 12.16 Dowel-type connection between hanger and arch (Detalj 5 in Figure 12.14); side view (left); cross section (right).
Design and drawing: Sweco Norway AS.

6.3.1 Transfer of forces from steel plates to wood

The hangers are vertical and the angle between the arch, and the vertical force (at this location) is 71.8 degrees, leading to $f_{h,\ \alpha=71.8,\ k} = f_{h,\ k} = 21.0$ MPa. The characteristic load-bearing capacity of a single dowel is the sum of the individual shear planes acting on the dowel. The shear planes may have different capacities, but they should be compatible with respect to deformation at the ultimate load. Here, the two external shear planes will be identical, due to the symmetry of the layout in the cross section. This is also the case for the six internal shear planes, but the capacities of the internal and external shear planes might very well be different unless they all have the same failure mode.

The capacity of an external shear plane is determined by use of Eq. (11), and an evaluation gives

$$F_{v,Rk,ext} = min\left\{\begin{array}{c} f_{h,k}\cdot t_1\cdot d = 25188\,\text{N} \quad (\text{c}) \\ f_{h,k}\cdot t_1\cdot d\left[\sqrt{2\cdot\dfrac{4M_{y,Rk}}{f_{h,k}\cdot d\cdot t_1^2}}-1\right] = 11371\,\text{N} \quad (\text{d}) \\ 2.3\cdot\sqrt{\cdot M_{y,Rk}\cdot f_{h,k}\cdot d} = 9459\,\text{N} \quad (\text{e}) \end{array}\right\}. \tag{17}$$

The capacity of an external shear plane is determined by using Eq. (12):

$$F_{v,Rk,int} = min \left\{ \begin{array}{c} 0.5 \cdot f_{h,k} \cdot t_2 \cdot d = 23677\,\text{N} \quad (\text{j/l}) \\ 2.3 \cdot \sqrt{\cdot M_{y,Rk} \cdot f_{h,k} \cdot d} = 9459\,\text{N} \quad (\text{m}) \end{array} \right\}. \tag{18}$$

In this connection, the dowels are very slender as compared to the thickness of the wooden layers surrounding the steel plates, and the failure mode is governed by the bending of the dowels. It turns out to give the same failure mode for both external and internal shear planes. The capacity for a single dowel then becomes

$$\begin{aligned} R_{v,Rd} &= R_{v,Rk}\frac{k_{\text{mod}}}{\gamma_m} = \left(\sum_{int} F_{v,Rk,int} + \sum_{ext} F_{v,Rk,ext}\right)\frac{k_{\text{mod}}}{\gamma_m} \\ &= (2 \cdot 9459 + 6 \cdot 9459)\frac{0.9}{1.3} = 52390\,\text{N}. \end{aligned} \tag{19}$$

It is common during the calculation of connections to set material factor $\gamma_m = 1.3$. In this case, the dowels are equally loaded, and the capacity of the dowel connection is, therefore,

$$R_{d1} = 12 \cdot 52.390 = 629\,\text{kN} \tag{20}$$

6.3.2 Splitting along dowel rows caused by force parallel to grain

A complete verification also requires splitting control of the glulam member. This is performed by evaluating the design capacity for splitting along the fibers due to several dowels on a row or due to tension normal to grains caused by the force on the group of fasteners. The capacity of a single dowel, given in Eq. (19), represents the capacity where force and grain directions have a 71.8° angle deviation. For evaluating the risk of splitting due to several dowels on a row, the capacity of a single dowel with the force along the grain is evaluated, and thereafter, the capacity of the rows are determined.

Letting $\alpha = 0$ in Eq. (16), the embedment strength becomes $f_{h,\,k} = f_{h,\,0,\,k} = 31$ MPa. Evaluation of Eqs. (17) and (18) gives $F_{v,\,R,\,k} = 11501$ N; and consequently, by use of Eq. (19), the design capacity of a single dowel along the grain becomes $R_{v,\,Rd} = 63{,}697$ N. The increased risk of splitting along a row of dowels depends on the number of dowels and the spacing between them and is taken into account by use of a reduced average strength or a reduced effective number (n_{ef}) for dowels on a row (EN 1995-1-1:2004/A1:2008). In the dowel connection example shown in Figure 12.16, the dowels are not placed in rows along the fiber direction. However, the deviation from alignment along the grain is too small to satisfy the spacing requirements between rows normal to the grain direction, and consequently, three dowels in a row ($n=3$) are used to verify splitting strength. The effective number in a row is determined by

$$n_{ef} = min\begin{cases} n \\ n^{0.9}\sqrt[4]{\dfrac{a_1}{13d}}. \end{cases} = 2.44, \tag{21}$$

where a_1 is the spacing in the grain direction; in this instance, a_1 equals 105 mm. In this case, all four rows are equally stressed, and the capacity along grain becomes

$$R_{0d} = 4 \cdot 2.44 \cdot 63.697 = 622\,\text{kN}. \tag{22}$$

R_{0d} shall be compared to the force component in the fiber direction, which means that the capacity for vertical hanger force is

$$R_{d2} = R_{0d}/cos\,71.8 = 1990\,\text{kN}. \tag{23}$$

6.3.3 Splitting along grain caused by tensile force Normal to grain

This type of failure may occur on the rear side of a group of fasteners. The current failure criterion in EN 1995-1-1:2004/A1:2008 is based upon simplification of fracture mechanic models; it reads

$$F_{90,Rk} = 14b\sqrt{\frac{h_e}{1-\dfrac{h_e}{h}}} = 14 \cdot 800\sqrt{\frac{900}{1-\dfrac{900}{1000}}} = 1.063 \cdot 10^6\,\text{N}. \tag{24}$$

An increase in the effective height h_e will give increased capacity; and therefore, these types of connections should always be located on the rear side of wooden members (relative to the force direction). In this case, a suitable distance to the rear surface of the member is 50–100 mm. For convenience, 100 mm is used here. The design capacity with respect to tensile failure of the normal grain for a shear force caused by the normal component of the force in the hanger is obtained by

$$F_{90,Rd} = F_{90,Rk}{}^{k_{\text{mod}}}/_{\gamma_m} = 736\,\text{kN}. \tag{25}$$

The design criterion in this case is that the shear force on either side of the connection should be less than $F_{90,Rd}$. The two shear force components shall be determined such that the sum of them equals the normal component of the external force. In principle, the distribution of the shear forces shall be determined from a static analysis, but doing this is not necessary in this case because $F_{90,\,Rd}/sin\,71.8 = 775$ kN, which is greater than the force that can be transferred through the dowels. This failure mode, therefore, will not govern the design, regardless of the distribution of the shear forces.

It can be concluded that the maximum force that can be transferred in the hanger is limited by the capacity of the dowel connectors $R_{d1} = 629$ kN.

7. Verification of fatigue resistance (ULS)

Wooden materials have good resistance against damaging effects from cyclic loading. However, as most connections necessitate the removal of some material and thereby may introduce stress concentrations, wooden structures might also exhibit fatigue failures. In practical timber bridge design, it is mainly the connections that may be prone to fatigue effects. The connections often consist of metallic plates and dowel-type fasteners embedded in wood. The embedded fasteners introduce concentrated stresses in the wooden material, and the most potentially damaging stress concentrations usually involve shear stresses along the grain or tensile stresses normal to the grain or combinations thereof. Note that fatigue verification of the metallic parts must also be performed, as those probably are more vulnerable to fatigue failure than their wooden counterparts.

The fatigue strength of wooden materials are dependent on both stress ranges and the mean stress levels, as is true of most composite materials. Models for the fatigue resistance of wood and connections in timber structures are, so far, not very well developed. In the European standard for timber bridges, EN 1995-2:2004, only an informative annex deals with fatigue resistance of timber structures. Here, the residual strength due to fatigue for some cases is given by S—N curves, relating the fatigue damage to the stress level, the mean stress level and the logarithmic number of stress cycles. However, the expected fatigue loading and, consequently, their load effects on timber bridges are not satisfactorily explored and defined, as the currently available traffic load models (see, e.g., EN 1991-2) are mostly developed and calibrated for steel or reinforced concrete bridges. Consequently, they do not necessarily take into account that other materials show quite different fatigue behavior.

A brief summary on the topic of fatigue of connection in timber structures is that the metallic parts of a connection should be designed and verified against fatigue failure by use of the corresponding regulations for metals. Their wooden counterparts can for some connections, like axially loaded dowel connections, to a certain extent be evaluated by the informative annex in EN 1995-2:2004, but other connections might require experimental testing.

8. Design and durability

Good designers of timber structures follow either of two simple rules:

- Keep water out of the structure.
- If you cannot keep water out, make sure that water can easily escape from the structure.

It is obvious that the durability of wooden bridges is governed by the design. Numerous historical examples (e.g., Sétra, 2007) have shown that timber bridge design resulting in a humidity level in the wood that is too high has led to fungus attacks, which cause the most serious damage. The most important objective of timber bridge design, therefore, is to avoid excessive humidity in the wood. This is not new knowledge, of course. Italian architect André Palladio (1508–1580) published an architectural treatise recommending that if timber bridges were built, they should at least be covered. And in fact, many of the durable timber bridges in Switzerland and the United States are covered by a complete roof (Pierce et al., 2005). But these bridges are mainly pedestrian bridges or made for vehicles that are very different from today's 20-m-long trucks. A modern truck traveling at a high speed on a rainy day will create a considerable blast wave that will throw up a large spray of water and bring it into the bridge structure. In such a situation, the roof, in fact, may reduce the bridge's ability to dry rapid and lead to high moisture in the structure. Hence, the roof is not an ideal approach for modern road bridges. On the other hand, bridges with a deck on top that protects the supporting structure from weathering have demonstrated better preservation than those where the deck was between or below the carrying structure (Kropf, 1996). To obtain good durability, the details of the design are essential (Sétra, 2007). More on recent findings related to durability of timber bridges can be found in Kleppe (2010), Pousette and Sandberg (2010), and Pousette et al. (2017).

The design of a bridge depends on many factors, including topography, required waterway clearance, load, and appearance. Decisions made at an early planning stage can have a decisive influence on the long-term behavior of the structure. The less the structure protects itself, the greater the effort that must be invested in protecting individual endangered parts. Much of this can be resolved at the drawing table, assuming that the design engineer is responsive to the needs and limits of the construction material and keeps in mind that sun exposure and high temperatures might also damage wood (Kropf, 1996). The difference in change of volume due to unequal moisture distribution through a wooden member, together with very low strength normal to the grain, can cause longitudinal checks to develop into large cracks. Large cracks in connection areas may reduce the strength of both connections and members. By combining good detail design with supplemental measures (e.g., cover, water-repellent surface coating, and chemical treatment where needed—but only there), it is possible to equip weather-exposed wooden structures for a service life comparable to other construction materials while maintaining the advantage of wood as an ecological material without disposal problems (Kropf, 1996).

References

AASHTO-LRFD Bridge Design Specifications, 2014. 7th edition with 2015 revisions. American Association of State Highway Transportation Officials, Washington, DC. 1960 p.

Forest Products Laboratory, 2010. Wood handbook - Wood as an engineering material. General Technical Report FPL-GTR-190. U.S. Department of Agriculture, Forest Service, Forest Products Laboratory, Madison, WI. 508 p.

Johansen, K.W., 1949. Theory of Timber Connections. vol. 9 IABSE, Zürich, Switzerland, pp. 341–348.

Kleppe, O., 2010. Durability of Norwegian timber bridges. In: Proc. Intl. Conf. Timber Bridges. ITCB2010 and Tapir Academic Press, pp. 157–168. ISBN 978-82-519-2680-5.

Kropf, F.W., 1996. Durability and detail design—the result of 15 years of systematic improvements. In: Paper presented at the National Conference on Wood Transportation Structures, Madison, Wisconsin. http://www.fs.fed.us/eng/bridges/documents/desinpln/DurabilityAndDetailDesign.pdf.

Pierce, P.C., Brungraber, R.L., Lichtenstein, A., Sabol, S., 2005. Covered Bridge Manual, FHWA-HRT-04-098. Federal Highway Administration, McLean, VA. 327 p.

Pousette, A., Sandberg, K., 2010. Outdoor tests on beams and columns. In: Proc. Intl. Conf. Timber Bridges. ITCB2010 and Tapir Academic Press, pp. 169–178. ISBN 978-82-519-2680-5.

Pousette, A., Malo, K.A., Thelandersson, S., Fortino, S., Salokangas, L., Wacker, J., 2017. Durable Timber Bridges. Final Report and Guidelines. SP Rapport 2017:25, ISSN 0284-5172, RISE Research Institutes of Sweden.

Ritter, M.A., 1990. Timber Bridges. Design, Construction, Inspection, and Maintenance. EM 7700-8 Forest Service, U.S. Department of Agriculture, Washington, DC.

Sétra (Service d'études sur les transports, les routes et leurs aménagements, France), 2007. Timber Bridges. How to Ensure their Durability. Technical Guide. 2007 Sétra - Reference: 0743A - ISRN: EQ-SETRA–07-ED40–FR+ENG. http://www.setra.equipement.gouv.fr.

Sweco Norway, 2005. Drawings and documentation of Fretheim Bridge, Flåm, Norway. Lillehammer, Norway, December 19, 2005.

Swedish Wood, 2011. Design of Timber Structures. Swedish Forest Industries Federation, Stockholm, Sweden. ISBN 978-91-637-0055-2.

Further reading

International Organization for Standardization: International Standard ISO 898-1:2013. Mechanical properties of fasteners made of carbon steel and alloy steel. Part 1: Bolts, screws and studs with specified property classes—Coarse thread and fine pitch thread n.d.

Masonry bridges

13

Alessio Pipinato
AP&P, CEO and Technical Director, Rovigo, Italy

1. Structural theory of masonry structures

In this chapter, the structural theory, history, and technology of masonry structures are introduced.

1.1 History of masonry structures

The history of masonry structures began as a spontaneous process of construction mainly related to simple walls built with stone or caked mud, with mud-smeared mortar to increase stability and to make the edifice watertight. Stone was preferred to brick in many situations, depending on the geographical location and the availability of quarries. An increase in the use of masonry began when quarry capacity, stone workmanship, and using fire to manufacture bricks became more prevalent. Another fundamental development was the introduction of using lime instead of mortar in construction. After buildings in Mesopotamia were erected with stone and natural sun-dried brick and, later, the Egyptian pyramids were constructed, the Greeks built lime and marble constructions of a superior class. Still later, in the first century B.C., Romans introduced a number of refined masonry structures— including arches, massive walls, aqueducts, palaces, and churches—boasting both beauty and durability. Another step forward in masonry construction took place during the medieval period, when masonry was developed at an highly sophisticated level, mainly in Europe but also in the Islamic Empire. The Industrial Revolution, which began in the mid-18th century, fostered further advances in masonry, as quarry and working machines were developed, together with a strong impulse to find advanced mechanical solutions, and the widespread use of Portland cement mortar increased the strength and durability of masonry buildings and bridges. The 19th century saw a drastic change in the use of masonry, as innovations such as reinforced concrete (RC) and steel structures were developed rapidly in order to meet the growing demand for taller buildings. Finally, during the 20th century, innovative solutions —including high-strength mortar, steel-reinforced masonry, and industrialized lighter-masonry blocks—arose and further increased the use of masonry. Masonry bridges developed similar innovations. However, they are mostly no longer used, as masonry bridges have been replaced completely by steel and concrete bridges. For this reason, most of this discussion should be seen as an assessment study on existing structures rather than recommendations for future design. The main masonry bridges built in the last several centuries are listed in Table 13.1.

Innovative Bridge Design Handbook. https://doi.org/10.1016/B978-0-12-823550-8.00012-3

Table 13.1 Main Masonry Bridges in the World

Reference Photo	Name	Place	Nation	Main Span (Total Length)	Year of Construction
	Pont de la Libération	Villeneuve-sur-Lot	France	96 (315)	1919
	Syratalviadukt	Plauen	Germany	90 (295)	1905
	Longmen Bridge	Luoyang	China	90 (295)	1961

Table 13.1 Continued

Reference Photo	Name	Place	Nation	Main Span (Total Length)	Year of Construction
	Solkan Bridge	Nova Gorica	Slovenia	85 (278)	1906
	Adolphe Bridge	Luxembourg City	Luxembourg	84 (275)	1904

Continued

Table 13.1 Continued

Reference Photo	Name	Place	Nation	Main Span (Total Length)	Year of Construction
	Pont de Montanges (Pont-des-Pierres)	River Valserine	France	80 (262)	1910
	Viaduc de la Roizonne	La Mure	France	79 (260)	1928

1.2 Theory of masonry structures

The term *masonry* can be defined as an assemblage of classified stones, bricks, or both, which is often put together with mortar. The geometrical shape of the elementary stone can be either squared and well fitted or unworked units just placed one on top of another to shape the form of the structure. Most interstices have been filled with mortar, which decays over time. The stability of this conventional structure is ensured by compaction under gravity of these elements; the main state of tension relates to compression, and only a low amount of tension can be resisted.

An indirect parameter used to determine the strength of stone is the height at which a prismatic column could be theoretically be built before crushing at its base due to its own weight (Heyman, 1996), and this can be predicted easily. For example, a medium sandstone might have a unit weight of 20 kN/mc and a crushing stress of 40,000 kN/mq, and dividing one number by the other returns the maximum height of the column as 2 km. According to this observation, and belonging to other extensive past studies (e.g., Villarceau, 1854). Heyman (1996) suggested to limit the nominal stress to 1/10 of the crushing stress of the material.

However, observing real cases of existing constructions throughout history is fundamental to understanding how these structures works: for example, from studies of Beauvais Cathedral by Benouville (1891), he observed that the maximum stress of that church was not greater than 1.3 N/mm^2, and if compared to the crushing stress, the safety factor was found to be more than 30. Observing other masonry structures, Heyman (1997) stated that the main portions of the load-bearing structure of a church will be working at 1/100 of the crushing stress, and infill panels or walls that carry little more than their own weight may be subjected to a background stress as low as 1/1000 of the potential of the material. So the safety factor against crushing that is implicit in these statistics makes their rough derivation unimportant. This observation obviously does not consider lateral horizontal forces.

According to Heyman, the three most fundamental assumptions that apply to masonry structures are as follows:

- Masonry has no tensile strength.
- Stresses are so low that masonry has an effectively unlimited compressive strength.
- Sliding does not occur.

Concerning the first assumption, one could consider that individual stones may be strong in tension, but the mortar between stones is weak. The second one will be approximately correct if average stresses are in question, even if stress concentration that could arise in common masonry structures should lead to failure only locally (i.e., splitting or surface spalling). As for the third assumption, even if there were evidence of the slippage of individual stones, the masonry structure generally retains its shape well; only a very small compressive prestress is all that is necessary to avoid the dangers of slippage and general loss of cohesion.

Structure in general also could be analyzed considering the three main structural criteria of strength, stiffness, and stability. The structure must be strong enough to carry whatever loads are imposed, including its own weight. At the same time, it must not deflect unduly, and it must not develop large unstable displacements—either local or overall. If these three criteria are satisfied, then the designer can run through a checklist of secondary limit states to make sure that the structure is otherwise serviceable. Concerning masonry structures, Heyman (1997) observed a paradox: strength and stiffness do not lie in the foreground of masonry design; nevertheless, they are the third criteria of stability relevant for masonry. For example, considering a semi-circular arch structure carrying a given load P and its own weight, stresses are low and deflections negligible, and both will remain so as the value of P is increased. However, a certain value of P destroys the structure's stability, and a point is reached at which the structural forces can no longer be contained within the arch, so stresses remain low, but an instable mechanism of collapse takes place.

1.3 History and technology of masonry arches

The first masonry bridges had only modest span lengths, with partially or completely underground foundations that used the land as an abutment. With the advent of Roman bridges, robust and elegant new constructions were developed. Preferences included an odd number of arches circular arc profiles. Masonry bridges of the Roman period achieved longer spans, and—instead of constructing them in riverbeds—foundations were erected in soil with superior mechanical properties in order to avoid dangers that would undermine the integrity of the bridge. Of course, this solution increased the total length that could be covered with a single span. In the Pont-Saint-Martin in the Aosta Valley, Italy (Figure 13.1a), which has a span of 31.4 m, the low vault is made of large blocks of cube-shaped stone (90 cm wide) configured in five parallel rings, the space between the rings is filled with conglomerate. A typical structure of Roman masonry arches was the aqueduct, generally built with one, two, or three levels of rounded arches. For example, the Pont du Gard (Figure 13.1b), which carried water to Nimes, has three rows of arches, decreasing in width as they move upward, ranging from 4.4 m in the lights of the higher arches are to 15.5 to 24.4 m in the lower arches. In the early Middle Ages, the construction of bridges stops almost completely because of the lack of commercial movement. In constructions during this period in Sicily and Spain, one can see the influence of Eastern culture in such elements as lancet vaults, often with polycentric profiles. In France, however, different forms were used; for example, in the bridge of Avignon (Figure 13.1e), built in the 12th century, the arch is approximately parabolic, with a 20–25 m span length and a thickness of 70 cm.

During the same period in Italy, slim and bold proportions were the trend. The Ponte Vecchio in Florence and Ponte di Castelvecchio in Verona (Figure 13.1c) are examples of this design; the latter has the greater arch of 48.7 m, three smaller lower brick arches are lowered, and mixed masonry brick and stone piles. Another well-known bridge of this period was the Devil Bridge (1321–1341), with a 45 m span (Figure 13.1d).

This evolution led to a decrease in the ratio of the arch thickness to the span length; the materials were often taken from other constructions, even though they were

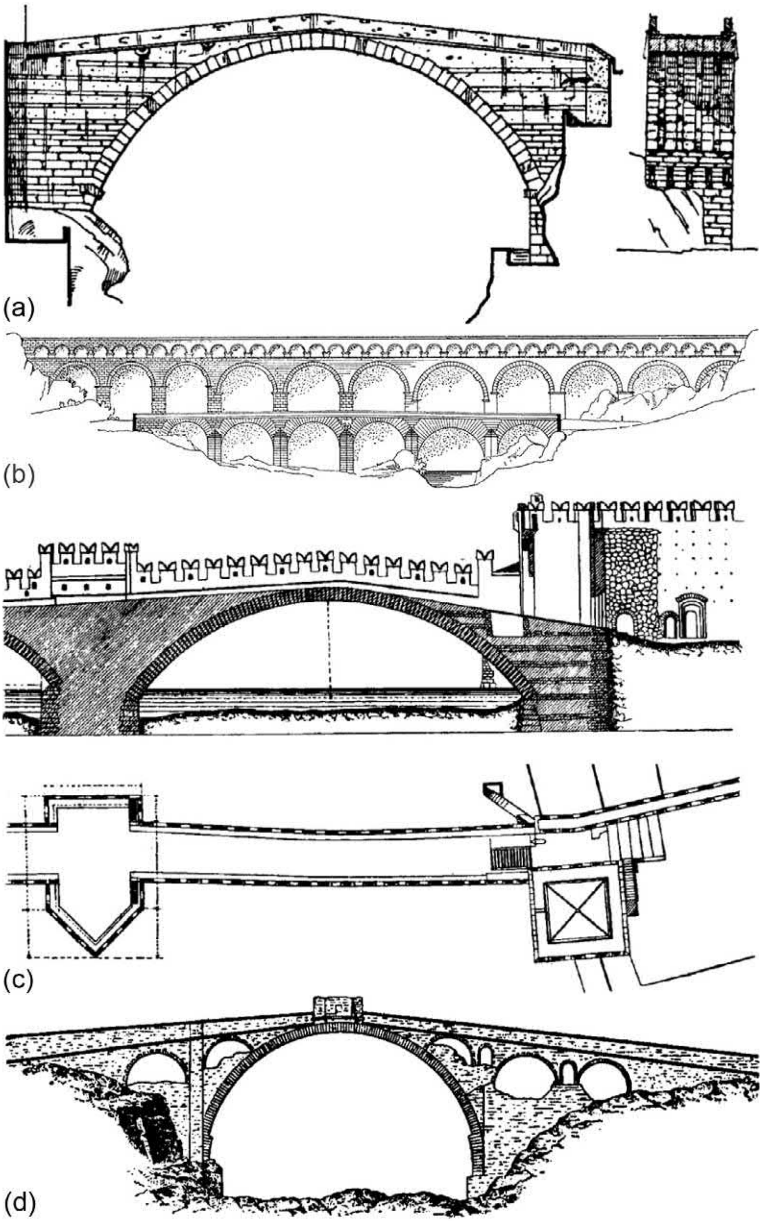

Figure 13.1 (a) Pont-Saint-Martin; (b) Pont Du Gard; (c) Ponte di Castelvecchio (lateral and plan view), (d) Pont du Diable (Ceret), (e) Avignon bridge details.

Continued

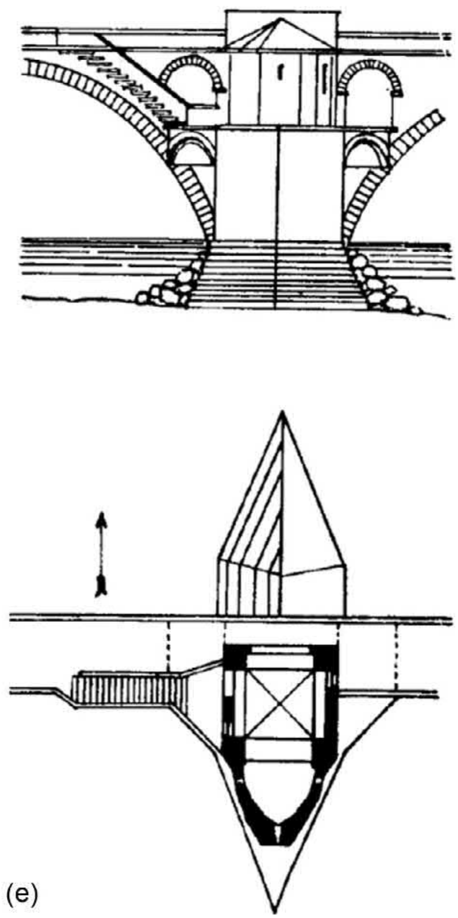

Figure 13.1, cont'd

recycled, the quality of mortar were was improved when compared to that of the previous period.

At the end of the 18th century, the École Nationale des Ponts et Chaussées in Paris introduced many technical innovations: shoulder piles were abandoned, and arches were designed and built directly over the full river level. The Concordia Bridge in Paris is a typical example of this structural shape (Figure 13.2). A new design philosophy was developed, in which the materials were selected with consideration of their characteristics, the walls were built with great care and with suitable binders, and design loadings and consequent stresses in foundations were designed to be uniformly distributed, with adequate design and detail solutions. In addition, greater attention was given to camber and disarmament, from the abutment to the key at midspan, as soon as the mortar cured sufficiently.

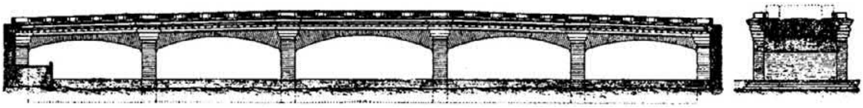

Figure 13.2 Concordia Bridge, Paris.

Figure 13.3 Bridge across the Agout River, Lavaur.

The bridge over the Dora Riparia in Turin is a wonderful example of construction stone cutting. The arch intrados is circular, with a 45 m span and 5.5 m of sag, and the abutment is built with larger blocks for increased stability.

Séjourné built major rail projects using the circular arch. On the Castres–Montauban rail line, the Lavaur Bridge (erected in 1884; Figure 13.3), with a span of 61.5 m; the Castelet Bridge (1883), with a span of 41.2 m; and the Antoinette bridge at Vielmur (1884), with a span of 50 m, are works of interest due to their wide arches and slender shoulders and vaults.

The railway bridges constructed in the second half of the 18th century generally were viaducts, as they were built as a sequence of many spans with small arches (Figure 13.4). This turns out to be the most effective solution to a plan of very irregular

Figure 13.4 Railway viaduct, Lockwood.

Figure 13.5 Railway viaduct, Wiesen.

morphology. The oldest bridges with tall columns usually had several arches, and the lower ones tended to be narrower and shorter. However, you can find some bridges with high columns and a single row of arches of modest span, such as the Lockwood Viaduct (Figure 13.4), as well as multispan solutions with a central large span (e.g., the Wiesen Viaduct, Figure 13.5).

Figures 13.6 and 13.7 illustrates the constitutive elements of a typical masonry arch bridge.

The sizing of these elements was entrusted to empirical work relations that provided a geometric scaling (Corradi, 1998). The sizes of elements were not always supported by theoretical formulations but instead were often based on the builders' past experience.

The shoulders of the bridges were massive pieces of masonry designed to balance the arch and anchor the bridge to the two sides. The shape of the shoulders is usually

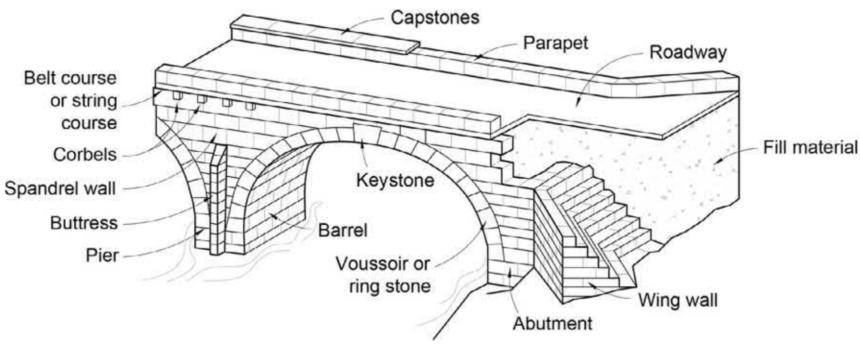

Figure 13.6 Constitutive elements of a masonry bridge.

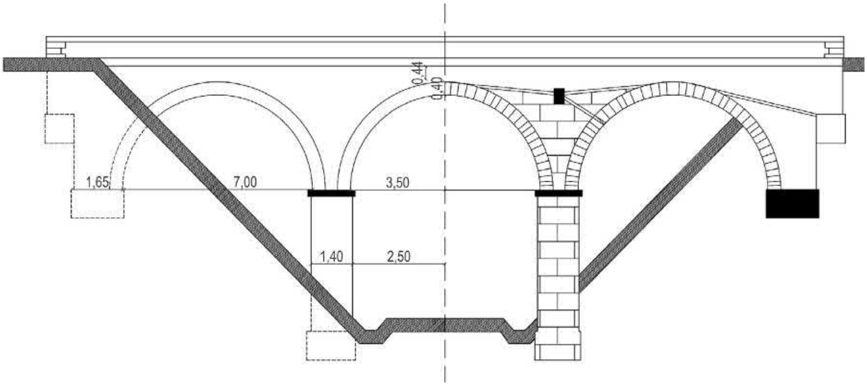

Figure 13.7 Longitudinal arched bridge typical section.

trapezoidal. The masonry, brick, or square blocks generally have horizontal courses; in the abutment area, inclined stone slabs or other special joint pieces were often used to prevent the joints from sliding due to the high thrust of the arc with respect to the weight of the overlying masonry. In the technical manuals of the time there are several formulae for sizing that did not take into account the mechanical characteristics of the masonry and the soil; the most simple and widely used formulae provide the width of the shoulder as follows (in meters):

$$s = 0.005h + 0.2c + c/f\,(0.10 + 0.005c), \tag{1}$$

where h is the height of the shoulder from the floor to the foundation plan, c is the arch span, and f is the sag. Other formulae also take into account the thickness and height of the arch, as well as other specific parameters.

River bridges can be equipped with protections to improve the hydraulic behavior and to avoid problems. Intermediate decks were often placed in the viaducts to limit the buckling of high columns. The columns have rectangular horizontal sections. The vestments of columns have slopes of 1/20–1/25 in the lateral faces and 1/10–1/16 in the frontal ones; the slope can be linear or logarithmic.

For the sizing of columns, various empirical formulae were proposed that provide the width of the columns in the plant s' function of parameters such as the height h' of columns from the foundation plan to the arches, the light or rope arch c, and the thickness of the arch; the Colombo proposes to adopt the greater of these two values (in meters):

$$s' = 0.2h' + 0.6 \tag{2a}$$

$$s' = 0.125c. \tag{2b}$$

The shoulder piles have larger cross sections and are strengthened by pilasters, with a considerable slope; they were included in the multispan bridges because, during the construction of arches, they acted in contrast to the horizontal, unbalanced thrusts. In addition, they protected against the accidental collapse of an arch. As for aesthetics, the shoulder pile breaks up the monotony of similar-looking piles.

The vaults (or arches) were generally used in the barrel and plant straight. The intrados profiles are circular arches, and although they do not represent the optimal shape in relation to the distribution of the loads, they do meet the requirements of construction simplicity (tracing, camber). Three types were generally used: semicircular, lowered arch (circular, semielliptical, or polycentric), and acute or ogive arch. In the viaduct, the semicircular arch is used more frequently; the acute arc is suitable in cases where heavy midspan loads are present; however, it does not hold heavy loads well on the abutments; the lowered arch is necessary only for lower bridges crossing a riverbed.

2. Assessment of the load-carrying capacity of arch masonry bridges

2.1 Historical methods

Past studies, such as La Hire (1695, 1712) and Couplet (1729, 1730), involved theoretical analysis and experimental activities on the line of thrust, and especially on the arch collapse. Then Gregory (1697) deepened the shape of the catenary arch as the most appropriate solution to carry its own shape. Heyman (1982) looked into this last observation in more detail, concluding that it could be interpreted as defining the lower-bound theorem of plasticity. Navier (1833) introduced the middle third rule, which was applied to masonry arches by Rankine (1898), such that the line of thrust was constrained to lie within the middle third of the arch in order to avoid tensile stress. Barlow (1846) and Fuller (1875) worked on graphical solutions on the line of thrust. Castigliano (1879) used the theorem of minimum strain energy to develop elastic methods, and for masonry arches, he performed an iterative analysis quite similar to modern nonlinear finite element model (FEM) analysis (no tension/nonlinear procedure, cutting out tension portion of the arch). Further works developed by Rankine (1898) analyzed the role of backings in masonry arches and recorded the first geometrical/mechanical observations, including the following: (i) strong backings are particularly likely for semicircular or elliptical arches that would probably otherwise have been unstable during constructions; (ii) to give the greatest possible security to a hydrostatic arch, the backings ought to be built of solid rubber masonry up to the level of the crown of the extrados; (iii) and squared side-joints in backings are important to avoid failures.

2.2 Recent methods

The first consistent studies on arch bridges were performed by Pippard and Chitty (1951), Heyman (1876, 1969, 1972, 1980, 1982), Whitey (1982), and Tellet (1983). These studies made significant contributions to our body of knowledge using elastic methods and collapse mechanisms. Pippard also looked into assessment methods: the arch behaved elastically until the first hinge or crack was formed. Then it failed with a four-hinged mechanism. He saw that after the first hinge occurred, there was a significant amount of reserve of strength in the arch before it collapsed. The elastic method enhanced the preliminary estimation of masonry arches: a two-pinned arch with horizontal forces keeping the arch in place is the basic assumption. Pippard's (1948) approach used the partial derivative of the strain energy, U, with respect to a force that is equal to the displacement in the direction of the force (Castigliano's theorems; Castigliano, 1879); the ring was treated as a two-pinned parabolic arch with a secant variation of $I = I_0 \sec\alpha$, where I_0 is the second moment of area at the crown. The axial thrust and shearing force terms in the strain energy equation were ignored in this theory. Hence, the strain energy was assumed to be totally dependent upon the flexural response of the arch.

Therefore, the limiting value of the point load at the crown derived by Pippard would be given by

$$W = \frac{\dfrac{256 f_c h d}{L} - 128\rho L h\left(\dfrac{1}{21} + \dfrac{h+d}{4a} - \dfrac{a}{28d}\right)}{\left(\dfrac{25}{a} + \dfrac{42}{d}\right)}.$$

The following conditions are applied to this simple solution:

- The arch is assumed to be parabolic, with a span-to-rise ratio of 4.
- The arch is assumed to be pinned at the abutments (i.e., it is a two-hinged arch).
- The dispersal of loading applied at the surface of the fill was assumed to occur only in the transverse direction, with a 45-degree load spread angle.
- Pippard considered the case of a single-point load applied at the midspan; the effective width of the arch was taken as twice the fill thickness at the crown ($b = 2h$).
- The fill was assumed to have no structural strength and to only impose vertical loads on the arch.

The fill was assumed to be of the same density as the arch ring (i.e., 22 kN/m3); the limiting compressive stress was taken to be $fc = 1.40\,N/mm^2$, and the limiting tensile stress was taken to be $ft. = 0.7\,N/mm^2$. The expression was then modified by the Military Engineering Experimental Establishment (MEXE) in the form of a nomograph and is currently recommended by the UK Department of Transport in its departmental standard (Department of Transport, 2001). The MEXE method is a long-established system of assessing masonry arch load-carrying capacity. It has been subject to review in recent years, and some shortcomings have been identified. There is now a growing consensus that the current version of MEXE overestimates the load-carrying capacity of short-span bridges, but for spans greater than 12 m, it becomes increasingly conservative. This method was based on the two-hinged elastic analysis by Pippard, which was then calibrated with both field and laboratory tests in the 1930s (Oliveira et al., 2010).

The method was most predominately used in World War II as a way to quickly classify the load-carrying capacity of older masonry arch bridges. However, since that time, the MEXE method has still been used as a way to load-rate masonry arch bridges. The modified axle load (MAL) depends equally on the arch and backfill thickness, although the ring thickness has significantly more influence on the arch behavior than does the backfill. The modification factors are introduced without taking account of the arch geometry; the backfill depth, the ring thickness, and even the mortar thickness could have differing influences on arches with different geometries. The method comprises of the primary calculation of

$$\textit{Modified axle load} = \frac{740(d+h)^2}{L^{1.3}} F_{sr} F_p F_m F_j F_{cm},$$

where d = thickness of arch barrel adjacent to the keystone (m); h = average depth of fill at the quarter points of the transverse road profile between the road surface and the arch barrel at the crown, including road surfacing (m); L = span (m); Fsr is the span/rise factor; Fp is the profile factor; Fm is the material factor; Fj is the joint factor; and Fcm is the condition based, to be determined on-site.

More details about and limitations of this basic formula and its development can be found in Department of Transport (2001).

2.3 Empirical rules

Numerous methods have been employed during the last several decades to assess the load-carrying capacity of masonry arch bridges, using tools ranging from easy-to-use geometrical rules to the most sophisticated finite element software. The first and simplest approach deals with empirical rules, based on geometrical relations, coming from proportions in the construction of arch components (span, rise and thickness, width and height of piers, etc.). There is not always mechanical confirmation of these rules; however, they have been extensively applied in the past in real-life arches. A summary of these methods is reported in Table 13.2.

2.4 Classic solution

A classic solution of arch bridges relies mainly on Heyman's theory (Heyman, 1972, 1996, 1997), which simplifies the calculation of the ultimate load of a masonry arch by making the following assumptions: (i) masonry units have an infinite compressive strength, (ii) masonry units behave as a rigid body, (iii) joints transmit no tension, and (iv) masonry units do not slide at the joints. As a result of these assumptions, the bounding theorems of plasticity can be applied to determine the ultimate load of a masonry arch. Plasticity theories incorporate two theorems: (i) an upper bound, or mechanism solution; and (ii) a lower bound, or equilibrium solution.

The mechanism method is based on upper-bound plastic analysis (Heyman, 1982): masonry arch collapse loads are determined by analyzing the arch as a mechanism instead of an elastic structure. The effects of hinges on the collapse load of masonry arches are analyzed, suggesting that the possible hinge point locations are identified. Then the forces and stresses in the indeterminate structure are calculated.

Table 13.2 Empirical Rules for Crown Arch Thickness (MEXE, 1963)

Date	Author	Deep Arch	Shallow Arch
15th century	Alberti	$t = s/10$	–
1714	Agutier, $s > 10\,cm$	$t = 0.32 + s/15$	–
1777	Perronet	$t = 0.325 + 0.0035\,s$	$t = 0.325 + 0.0694\rho$
1809	Gauthey, $s < 16\,m$	$t = 0.33 + s/48$	–
1809	Gauthey, $16 < s < 32\,m$	$t = s/24$	–
1809	Gauthey, $s > 32\,m$	$t = 0.37 + s/48$	–
1809	Sganzin	$t = 0.325 + 0.3472\,s$	–
1845	Dejardin	$t = 0.30 + 0.045\,s$	$t = 0.30 + 0.025\,s$
1854	L'Eveille	$t = 0.333 + 0.033\,s$	$t = 0.33 + 0.033\,s^{1/2}$
1862	Rankine	$t = 0.19R^{1/2}$	–
1870	Dupuit	$t = 0.20\,s^{1/2}$	$t = 0.15\,s^{1/2}$
1885	Croizette-Desnoyers	$t = 0.15 + 0.20\rho^{1/2}$	–
1885	Lesquiller	$t = 0.10 + 0.20\,s^{1/2}$	$t = 0.10 + 0.20\,s^{1/2}$
1914	Séjourné	$t = 0.15 + 0.15\,s^{1/2}$	–

s = span; R = radius of the circle passing through the crown and intrados springing; ρ = curvature radius.

Next, the locations of the hinges are adjusted based on the calculations, and the process is continued iteratively until the location of the hinges stabilizes (Livesley, 1978).

The thrust analysis is based on lower-bound plastic analysis: Heyman recommended determining the smallest-possible arch thickness in which the thrust line with assumed hinge locations would fit. That thickness is then compared to the actual arch thickness. He considers the ratio of the two values to be the geometric factor of safety for the arch. From his work, he developed what he called the "quick analysis" method. It is based on an arch with inputs of dimensionless parameters and a point load P. The equation is based on a failure occurring with hinges at each of the springings, under the live load, and at the crown.

2.5 FEM analysis

Three-dimensional (3-D) nonlinear FEM analysis offers the opportunity to model entire structures, checking for structural behavior of a well-defined and precise structure. All loads affecting the structure can be modeled.

3. Analysis, repair, and strengthening

Bridge analysis, repair options, and strengthening for existing bridges are reported in detail in this section.

3.1 Material modeling

Masonry is defined as a structural material made by the assemblage of natural (stones) or artificial (bricks) elements, with or without mortar, suitable for the realization of the bearing elements of a construction. The difficulty of modeling masonry depends on the following factors:

- Masonry is a discrete material (blocks and mortar) in which the dimension of the single constituting element is large compared to the dimensions of the structural element.
- The geometry, origin, and placing of the blocks can vary considerably.
- Blocks are stiffer than mortar.
- The mortar thickness is limited (compared to the block dimensions).
- Stiffness of the vertical joints is much less than the stiffness of the horizontal joints.

The physical–chemical and mechanical parameters in the interaction between the stone units and the mortar joints depend on the factors described next.

The parameters depend on the properties of the stone elements, such as the following:

- Compression and tension strength with monoaxial and pluriaxial stresses
- Elasticity module, Poisson coefficient, ductility, and creep
- Waterproof and superficial (roughness) characteristics
- Chemical agent resistance
- Volume variation for humidity, temperature, and chemical reaction
- Weight, shape, and dimension of the holes

The parameters also depend on properties of the mortar, such as the following:

- Compression strength and behavior under pluriaxial stresses
- Elasticity module, Poisson coefficient, ductility, creep, and adhesive force
- Workmanship, plasticity, and capacity of detaining water

Construction formality, such as the following, also determine the parameters

- Geometry and placing of the stone elements
- Filling of the joints at the head
- Ratio of the joint thickness and dimensions of the stone elements
- Handmade construction and consequent lack of uniformity of the layers

Actually, if some monoaxial tests are carried out separately on the constituting masonry elements (mortar and blocks), the typical qualitative behavior shows good compression strength and very poor tensile strength. But while the stone has a nearly linear behavior, larger elastic module, and brittle failure, the mortar shows a nonlinear behavior, larger elastic module, and certain ductility.

Depending on the desired level of accuracy and simplicity, the following methods could be used:

- *Detailed micromodeling*—The block and the mortar in the joints are represented by continuum models, while the unit–mortar interface is represented by discontinuous elements. The Young model, the Poisson coefficient, and the inelastic properties of the units and the mortar are taken into account.

- *Simplified micromodeling*—The blocks are represented by continuum elements, whereas the behavior of the mortar joints and unit–mortar interface is lumped in discontinuous elements. The Poisson coefficient and the inelastic properties of the unit and the mortar are neglected.
- *Macromodeling*—Blocks, mortar, and unit–mortar interface are represented as a continuum. Homogenization theories have been developed in order to derive the global behavior of masonry from the behavior of the constitutive materials (block and mortar).

This physical-mathematic abstraction (i.e., transforming the reality into a scheme governed by mathematically treatable laws) can appear arbitrary when dealing with masonry. In reality, each material is provided with a microstructure, and the assimilation to a continuum implies an operation of stress average on a suitable reference volume. The masonry material, realized through the assemblage of two components, shows a constitutive bond characterized by a nonlinear law and intermediate compression strength to each single component. The limit of the linear behavior coincides with the beginning of the partialization of the cross section. Therefore, micromodeling is necessary to better understand the local behavior of masonry structures; macromodeling is applicable when the structure is composed of walls of sufficient dimensions so that the stresses along the length of the element are uniform. This type of modeling is preferable when accuracy and efficiency are both required. The other two important aspects related to the material in the analysis and behavior of masonry are the size effect (unit size versus structural size) and the influence of the material parameters on the numerical analysis.

3.2 Structural modeling

Another complex topic in masonry is the choice of a suitable model representing the structure. According to the hypothesis of homogeneous material, the following model types can be distinguished:

- *With lumped masses*—This is a rough approximation of the geometry of the structure, but it can be sufficient in order to determinate the structural dynamic response (if the nonlinearity of the material and the resultants effects of the real geometry of the structure are included). Obviously, this type of model cannot be used to predict the local or global collapse mechanisms or the damage levels of the single structural components.
- *With beams and columns*—This defines in greater detail the behavior of the system than the previous item. It is possible to determine the sequential formation of the collapse mechanisms both statically and dynamically.
- *Macro elements*—This considers the structure as a whole of wall panels, each of which is a recognizable and complete part of the building. It can also coincide with an identifiable part of it in architectonical and functional terms (for example: the façade, the apse, or the chapels); usually, it is formed by more panels and horizontal elements connected to each other so that they represent a unitary constructive part, even if it is joined and not independent from the whole of the construction.

Concerning the FEM element types, models that can be distinguished according to the following details:

Two-dimensional or three-dimensional alternatives—2-D or 3-D approaches are available, adopting a 1-D frame, 2-D shell, 3-D brick elements, or a combination thereof. Shell elements produce faster and more controllable models because of the presence of a smaller number of joints compared to the brick elements. On the contrary, the model with brick elements allows the visualization of the stress evolution inside the structure. Notwithstanding, the results gained in the two analysis types are similar, both in terms of structural strains and stress distribution.

Meshing—By increasing the elementary elements, the result's reliability is strongly influenced by convergence problem solution; therefore, using a dense mesh is not the best option. The most appropriate mesh dimension is derived from the engineering judgment, also taking into account the dimension of the investigated structure, and the sophistication of the expected results.

3.3 Damage classification in masonry bridges

This section presents some details on masonry bridge damage classification. One clear and innovative classification was described in Sustainable Bridges (2007). In particular, the general bridge structure damage classification is reported in Figure 13.8; the classification according to the damage localization is depicted in Figure 13.9; the classification for damage discontinuity is illustrated in Figure 13.10; the classification for losses type is highlighted in Figure 13.11; the classification according to the deformation type is reported in Figure 13.12; the classification according to the displacement type is reported in Figure 13.13; finally, Figures 13.14 and 13.15 deal with the description of the overall damage causes and with the contaminations type, respectively.

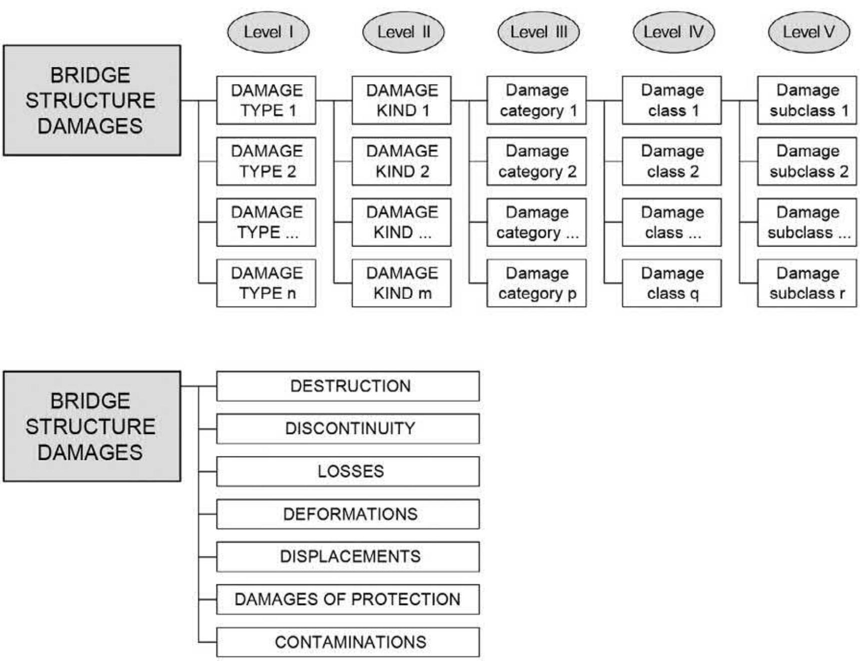

Figure 13.8 Bridge structure damage classification (Sustainable Bridges, 2007).

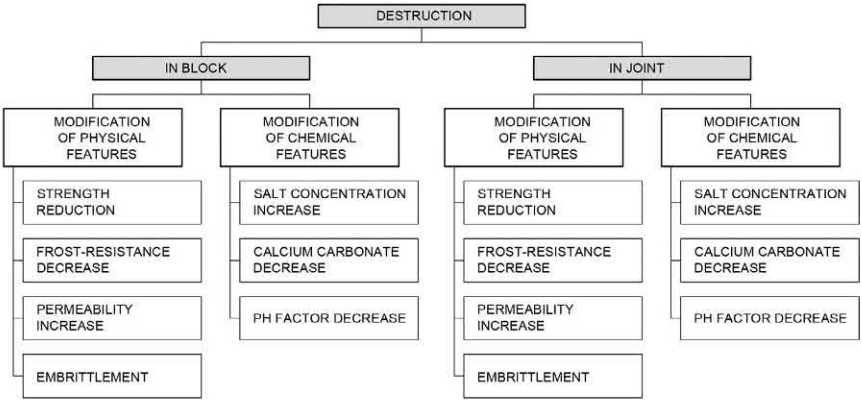

Figure 13.9 Classification according to the damage localization (Sustainable Bridges, 2007).

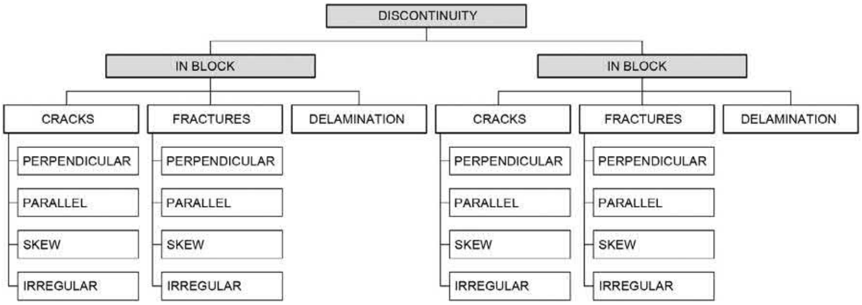

Figure 13.10 Classification for damage discontinuity (Sustainable Bridges, 2007).

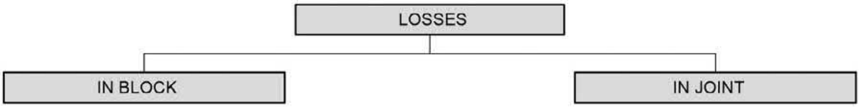

Figure 13.11 Classification for losses type (Sustainable Bridges, 2007).

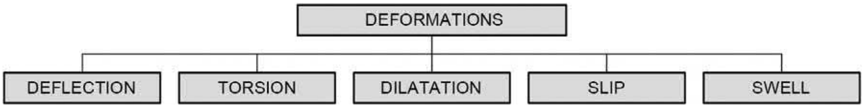

Figure 13.12 Classification for damage deformations type (Sustainable Bridges, 2007).

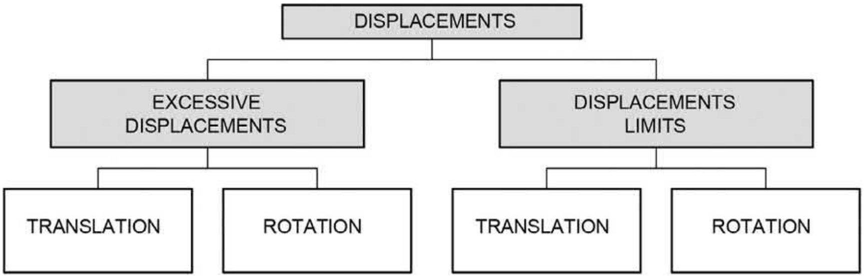

Figure 13.13 Classification according to the displacement type (Sustainable Bridges, 2007).

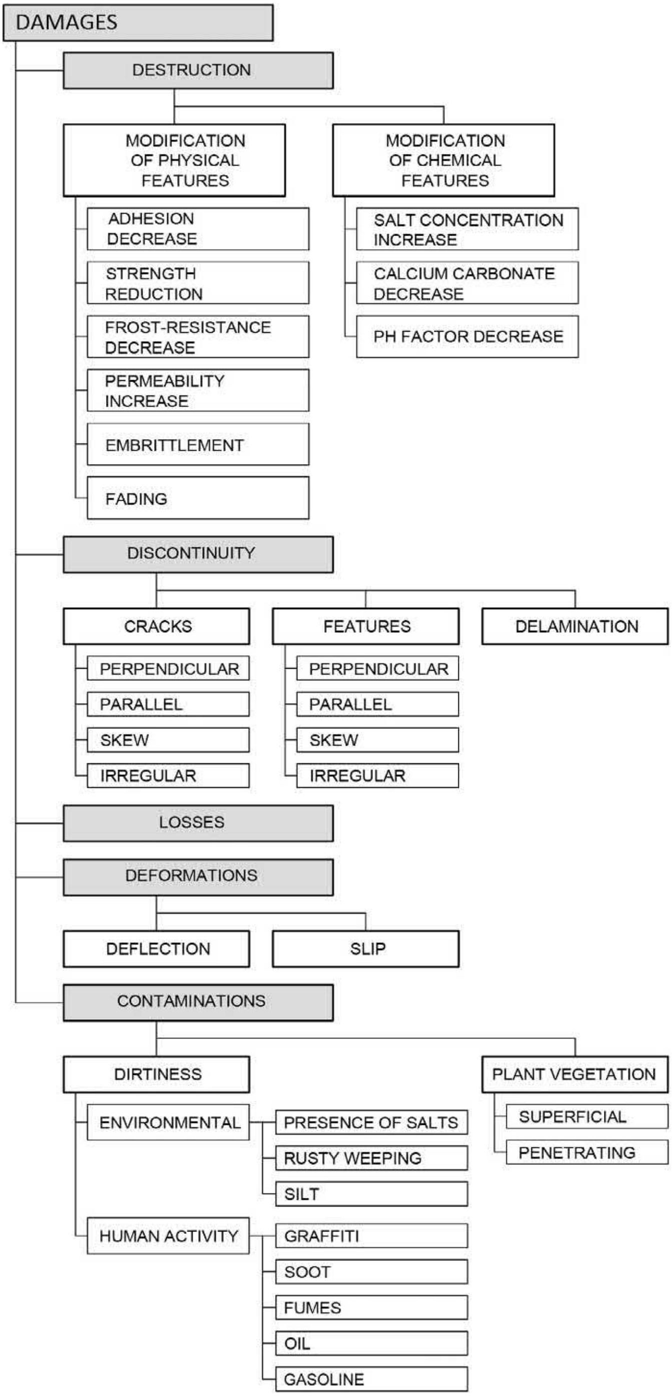

Figure 13.14 Classification for damage type (Sustainable Bridges, 2007).

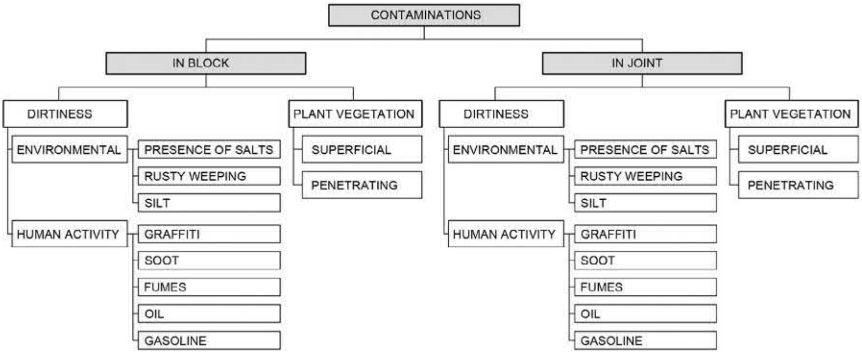

Figure 13.15 Classification of damage according to the contaminations (Sustainable Bridges, 2007).

3.4 Common damages in masonry arch bridges

Structural defects normally fall into the following categories:

- Construction
- Long-term loading
- Transient loading
- Environmental

A combination of all of these types of defects can usually be found in existing masonry bridges. Modern traffic loads, heavier than those in the past, could induce serious problems in an older bridge, but well-maintained masonry arches not subjected to heavy loads are probably among the most durable constructions.

3.4.1 Scour of foundations

One of the most common causes of collapse for masonry arch bridges is scour of foundations, especially for shallow foundations, which are more sensitive than deep foundations. However, this damage type is inherent in the elements of riverbed that make the exacerbate the damage, such as an increase in flow speed in the river (e.g., for environmental reasons) and a local disturbance of the flow due to the design of the piers. Scour problems can be avoided by adding deep foundations linked to the existing structure.

3.4.2 Arch ring issues

The arch ring of a masonry arch can be affected by a wide variety of elements, including the following:

- *Splitting beneath the spandrel walls*—Spandrel walls are employed in order to stiffen the arch ring at its edges; the typical failure here is cracks induced by shear stresses in the ring for traffic loads.
- *Abutment movements*—Foundations' lack of capacity to sustain dead and live loads is the principal cause of this defect, and abutment movements can produce hinge cracks that need

to be repaired; the presence of three well-defined hinges in an arch may allow it to articulate under service loads, resulting in loss of mortar.

- *Spandrel walls*—These walls are the masonry component of arch bridges most exposed to the environmental cyclic action; lapses or small local rotations may be present in the walls as a result.
- *Filling material*—An accurate waterproofing or an efficient drainage system could prevent the long-term water saturation of the infill material; if these systems are not provided, care should be taken to prevent water stagnation, which could also increase lateral pressure on the spandrel walls.
- *Natural stone*—Stone masonry was largely adopted by the Romans, and structures built with natural stone have lasted for thousands of years, reaching medium-span size (i.e., about 150 m); although this material is no longer used, these historic bridges stand as landmarks and probably represent the longest-lasting (if most expensive) construction solution.
- *Salt crystallization*—White efflorescence is often the visible aspect of this defect; it could be concentrated on the top layers or lie deep in the masonry, inducing large-scale decay in the latter case; water or sand brushing solves the problem only for superficial salt crystallization.
- *Air pollutants*—Especially in urban areas and in industrial and marine environments, air pollutants can lead to superficial color changes, and sometimes (in rare cases) damages are enclosed in the masonry.
- *Freezing/thawing*—If it freezes, wet stone can flake, break off, and wash away when the ice melts again. Cycles of freezing/thawing can completely change the structure of bridge components; replacement of the unit, giving consideration to the best material and mortar for such replacements, is the solution, together with treating the surface of the entire masonry.
- *Plant growth*—It is usual for plants to inhabit masonries; although short-term presence does not impact the structural behavior, long-term presence could shorten the life of the structure itself.
- *Load traffic*—Increasing loads on masonry arches may or may not be a structural issue; external signs like visible cracks in key positions such as in the spandrel walls or beneath the arch ring serve as warnings that the bridge should be assessed for its ability to handle actual traffic conditions, and eventually, retrofits should be instituted.

3.5 Structural intervention techniques for masonry arch bridges

3.5.1 Identification of defects

Visual inspection is considered to be sufficient as a first step when analyzing existing arches. The presence of a crack or settlement in parapets could be a sign of the abutment movement, and longitudinal cracks in the arch barrel could indicate spandrel wall detachment. However, some defects can be discovered only with nondestructive testing (NDT).

3.5.2 Structural intervention

Pressure pointing and grouting

Even if it is considered a possible way to reduce voids, fill cracks, and improve the condition of the arch, grouting of the contained ground above and behind the arch should be carefully evaluated, as the distribution of the grouted mass could change the structural behavior of the whole arch in a negative way.

Tie bars

The use of tie bars, a traditional technique widely used in masonry buildings, should be carefully applied with masonry arch bridges; e.g., passing a bar through the full section of the arch to restrain spandrel movements could lead to cracked regions in the nearest of the end plates of the bars.

Rebuilding spandrel/wing walls

If the roadway can be closed, the simplest solution is to excavate behind the wall and refill it, incorporating a reinforced earth system, avoiding excessive pressure against the spandrel walls.

Saddling

Saddling is a common repair technique in which the fill is removed so that the top surface of the arch barrel is exposed. An RC saddle is then put in place over the original barrel. Saddles are typically 150–200 mm thick and made of relatively weak concrete.

Concrete slabs

A concrete slab placed on the existing deck can reduce local loadings, drainage problems, and lateral pressure on walls.

Underpinning

Underpinning includes installing a new foundation for the bridge, excavating material from beneath the foundations, and replacing it with concrete beams or slabs. Using deep foundations as piles could enhance the behavior of the structure, providing a safer ground interface.

Partial reconstruction

When arch ring damage is extensive, the only real solution is to rebuild either the entire structure or a part of it.

Repointing of mortar

Mortar is an element of a masonry bridge that is anticipated to need repointing over time. However, keeping the mortar in good repair is an essential aspect of extending the life of a bridge.

Repair of spalling

The recommended repair of spalling is to use mortar to patch the face. The repair is typically completed for aesthetic purposes only. If the spalling is widespread enough to be a structural concern, in the opinion of an engineer, the delaminated stones will most likely require replacement.

Repair of missing masonry units

This treatment is intended to replace a single stone or a small group of stones. If larger areas of stone are missing or loose, a more extensive rehabilitation or restoration of the masonry is required.

Repair of slipped masonry units

It is recommended that loose slipped stones be removed and replaced (see the preceding missing stone procedure).

Repair of cracked masonry units

Slab bridges that have transverse cracks cannot be repaired. Temporary shoring can be used until a permanent solution can be found, but the cracked slab requires replacement.

Arch deformation repair

If the deformation of the arch is not detrimental to the structural capacity of the structure itself, then it can be repointed to prevent further displacement of the masonry units. However, if the structural capacity of the arch does not meet the safety requirements for the structure, more extensive rehabilitation is required. Three main methods of intervention can be addressed:

(i) *Relieving slabs*—The installation of a reinforced concrete relieving slab is an intervention to adequately distribute the traffic live load to the arch over a wider area than either a directly applied point load.

(ii) *Moment slabs*—If the installation of a lateral barrier system is required, it is often difficult to make it effective without a fixed deck system. One possible solution is the use of a moment slab, which can be placed over a masonry bridge if there is sufficient fill or around an arch if the geometry allows it.

(iii) *Removing arch fill*—An expert engineer should be consulted in this design and construction of this intervention. Before any work and excavation, the use of fixed formwork to be placed under the arch should be taken into consideration. When removing the fill from a stable barrel can lead to local instability. It is extremely important to remove the fill from both sides of the arch in equal lifts, as the unbalanced loading could lead to global instability of the arch.

Maintenance

Routine maintenance consists of the following:

- Keeping the road surface maintained, checking that the waterproofing is in good condition, and minimizing dynamic loading from traffic due to overloading and fast braking/accelerating movements
- Removing vegetation from the structure
- Repairing of lateral guardrails
- Repairing areas of deteriorated mortar

These four areas of maintenance involve modest expense when compared with costs associated with fixing problems resulting from neglect.

4. Structural assessment and retrofit

Masonry bridge assessment and retrofit applied in the field are often the most important lessons to further bridge engineering. Two case studies are presented in the following sections: the first deals with structural assessment, and the second deals with a bridge retrofit.

4.1 Structural assessment: Case study

The case study discussed here has been described in detail in Sustainable Bridges (2007). It concerns a bridge located in Poland, about 30 km from the city of Wrocław. The bridge, built in 1875, is a masonry arch structure with spandrel walls. The basic geometric dimensions are presented in Figure 13.16. The arch is barrel shaped, and the plan shape is rectangular; the span horizontal clearance is 9.93 m, the width is 8.55 m, the vertical clearance is 5.84 m, and the arch radius is 4.97 m. The constituent material is brick, the backfill material is unknown, and the brick dimensions are $6.5 \times 12 \times 25$ cm. The joint thickness is $1 \div 1.5$ cm, and the brick strength and joint strength are unknown. The structure experiences local rail with very low traffic; the available formal documentation about the bridge are an inventory card (1965) and a sketch drawing (1953).

The bridge has defects typical of masonry structures, including an increase in salt concentration, deterioration, loss of material, and longitudinal cracks. Loss of bricks and joints on both spandrel walls of the bridge was filled with concrete and new bricks (Figures 13.17 and 13.18). The displacement measurements were carried out by means of three independent systems:

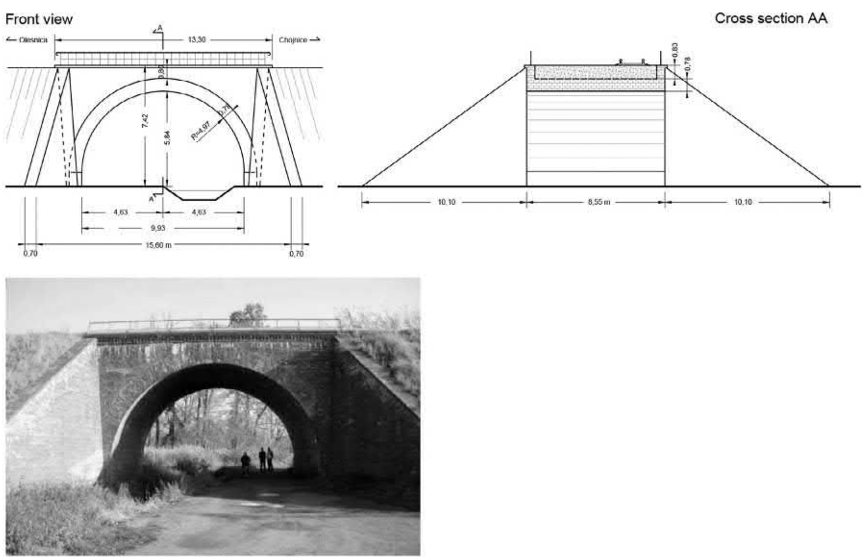

Figure 13.16 Side view, cross section, and photo of the case study (Sustainable Bridges, 2007).

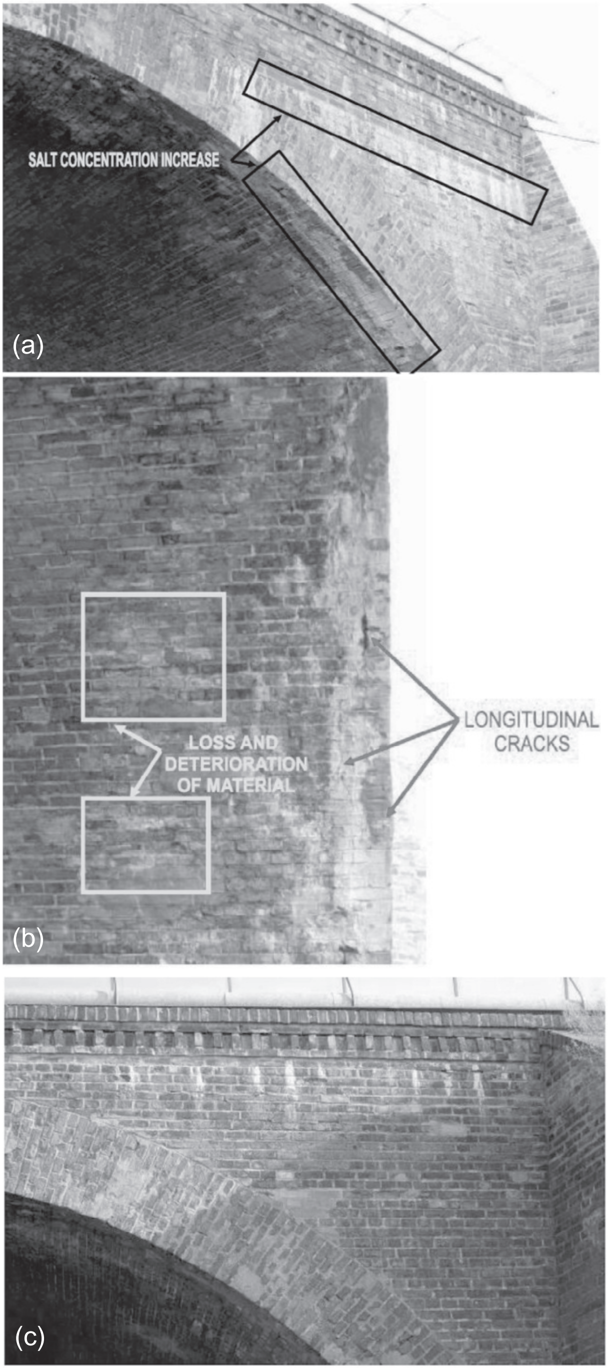

Figure 13.17 (a) Salt concentration increase; (b) material deterioration, loss of material, and cracks; (c) filled losses of masonry (adapted from Sustainable Bridges, 2007).

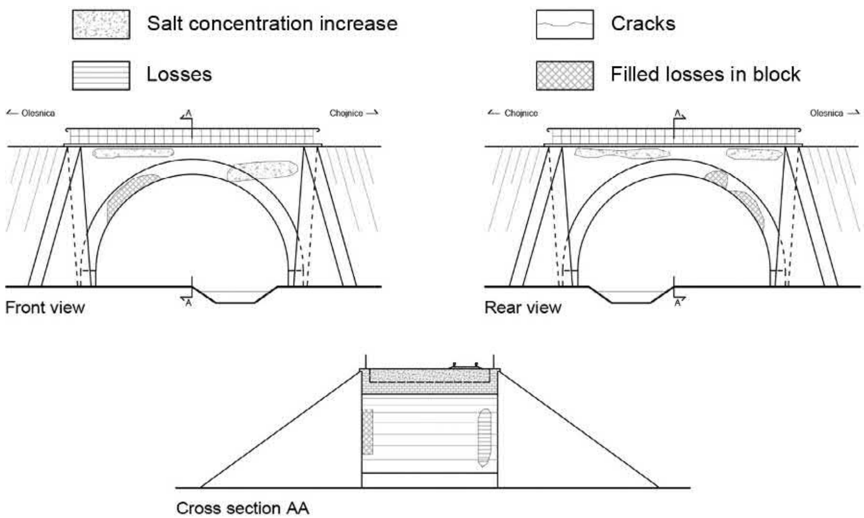

Figure 13.18 Damage localization (adapted from Sustainable Bridges, 2007).

- *Laser measurements* below the axis of the track in the middle of the span (L1)
- *Microradar measurements* from two different radar positions in five points of the middle cross sections (R1–R5) and in two points in quarter-point sections (R6, R7)
- *Linear variable differential transformer (LVDT) measurements* in three points in the middle of the span (D1–D3)

In addition, accelerations of selected points (A1–A4) were monitored.

The configuration of the measurement points for all measuring systems are shown in Figure 13.19.

For the load tests, the Polish railway provided one two-bogie engine with three axles in each bogie, with axle loads equal to 200 kN.

The aim of the test was to measure the deformation under static and dynamic loads.

- *Laser displacement measurements*—The reaction of the middle of the arch was much higher than the reaction of the quarter points, so the backfill and the ballast distribute the load very well. During this testing session, only velocities were measured, so only the relative load distribution was estimated.
- *Microradar displacement measurements*—Two different positions of the radar were applied: A and B. For displacement measurements of points R1–R5 (Figure 13.19) located along the transverse profile, the lateral position (A) of the radar against the bridge was chosen. For displacement measurements of the points R6 and R7 located along the longitudinal profile under the track axis, the radar was located under the bridge (B).
- *LVDT displacement measurements*—LVDT gauges were located in points D1–D3 (Figure 13.19) along the transverse profile, a half-meter from the crown cross section.

The radar measurements were carried out according to recommendations included in Sustainable Bridges (2007). The aim of the test was to measure masonry elements' thicknesses (arch barrel, abutment, and wing walls), detect voids or structural anomalies in masonry elements and backfill, and evaluate moisture or water content.

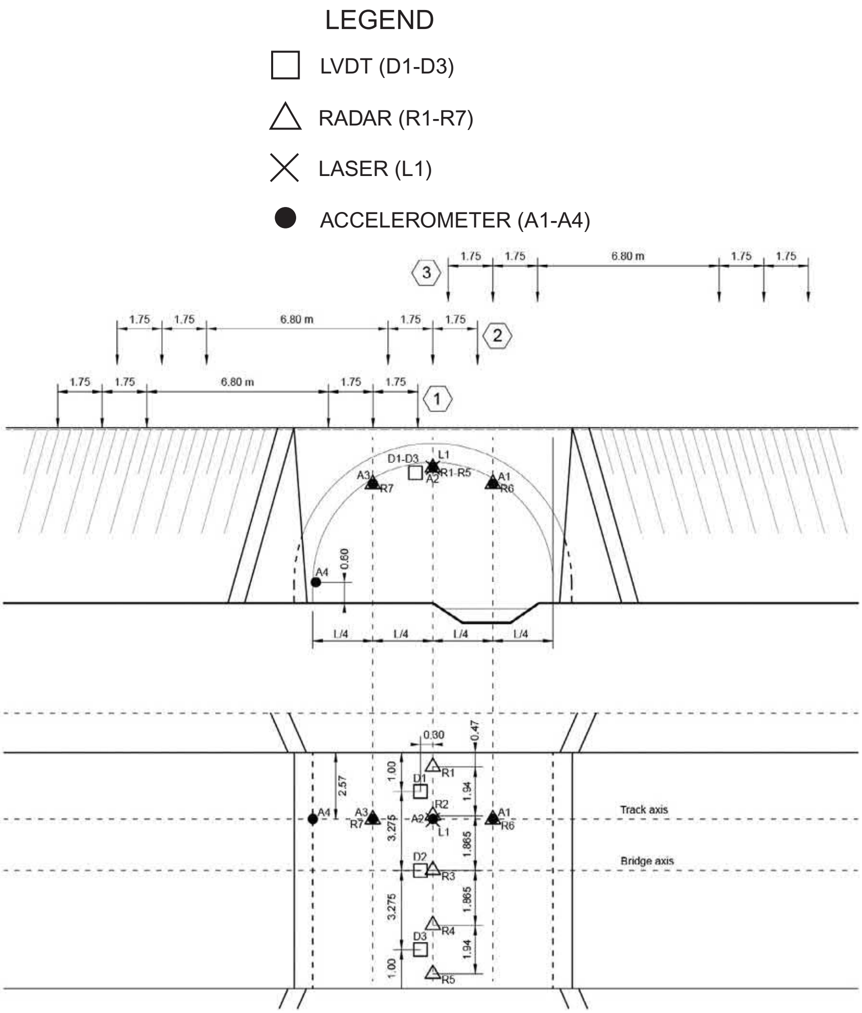

Figure 13.19 Locations of the measurement points and load configurations (adapted from Sustainable Bridges, 2007).

Most results are given in form of radar-grams representing profiles of the structural elements perpendicular to their surfaces (e.g., Figure 13.20).

Darker areas of the radar-grams indicate anomalies in material such as wet areas, boundaries between masonry and backfill or ballast, and brick layer bond, with or without cracks. Radar antennas of different frequencies (with different penetration depths) have been used to estimate the thickness of the walls. Because of high attenuation in the inner masonry structure, the measurements have not produced satisfying results for thickness estimation.

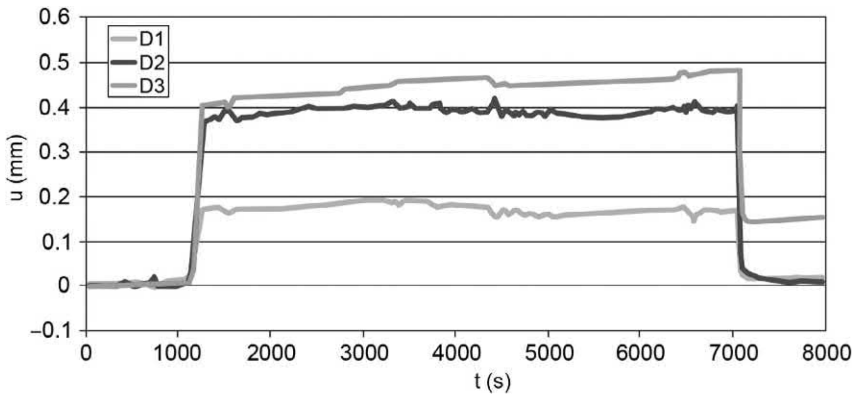

Figure 13.20 Exemplary results for LVDT measurements—displacements of points D1–D3 for loading in 1/4 of the span.

Radar measurements have been successfully applied to investigate the moisture distribution in the masonry. These results have been verified by coring and through geoelectrical measurement.

Crossing the brick layers at the vertical profile, time undulation of the reflection bands of approximately 0.5 ns correspond well with the material changes of brick and mortar between the brick layers. The general structure of the brickwork based on brick layers of different orientation of the bricks (stretcher and header course) is already visible at the small time variation of the reflected signal on the surface. These changes between bricks and mortar are less visible at the horizontal profiles, which is probably caused by a smearing effect of wave propagating to the depth by the antenna movement along the brick layers.

As a result, it could be observed that the concrete cover for the purpose of draining the arch is visible from the top of the bridge with 500 MHz and additionally with the 900 MHz under the ceiling of the arch, and a wall thickness of the abutment of approximately 2 m is expected to be derived from the end of the concrete cover reflection. Other details are reported in Sustainable Bridges (2007).

Electrical conductivity tests were also performed, with the aim of the detection of voids, the analysis of moisture/water content, and the testing and comparison of the NDT technique.

4.2 Structural intervention: Case study

The report on the following case study has been synthetized from Paeglitis and Paeglitis (2000). The bridge over the Venta River was built in 1874 (Figures 13.21–13.25), spanning 164 m with 17 arches. The material used for the reconstruction was chosen in accordance with tests developed at the Riga Technical University labs. The bridge consists of two parts—the 133-year-old initial part and the 81-year-old restored part. Several deteriorations were uncovered in 2006, so a general intervention was chosen as the response. In particular, masonry units of piers had crumbled away;

Figure 13.21 Bridge over Venta River in Kuldiga, built in 1874, after the recent restoration.

Figure 13.22 Bridge over Venta River in Kuldiga, built in 1874: on-site inspection.

corrosion of surfaces and joint material decay existed throughout the structure; the water drainage system of the deck was not working due to damage, which was also leading water filtration in bricks. Lime-based mortar bricks were found to be the best construction components, allowing the water to migrate in masonry. On the contrary, the cement-based mortar for joints with soft bricks revealed a lot of water inside the brick, which was the principle cause of damages due to the freezing/thawing cycles.

The Stone Conservation and Restoration Center of Riga Technical University was asked to research bricks and mortar: all bricks analyzed from the existing construction presented a high level of porosity, and the existing RC components were found to be of considerably lower quality. Chemical tests of salt content in bricks, RC, dolomite stone, and the old dolomite grout indicated very low levels of salt soluble in water. The RC pH level was found to be variable between 8.5 and 9.3, depending on the position of the investigation. After the first assessment phase, supported by on-site investigation of the constituent materials, the retrofit yard started. In the first phase, the road surface was dismantled, and the filling of arches was removed. The bridge was found to be in good condition, and the RC surface did not reveal noticeable damage or cracks. As the traffic load capacity was not good enough, a steel framework for arches 6 and 7 was built. The existing waterproofing and protection layers were restored, and the arches were filled using draining soil. A new RC slab resting on the filling was

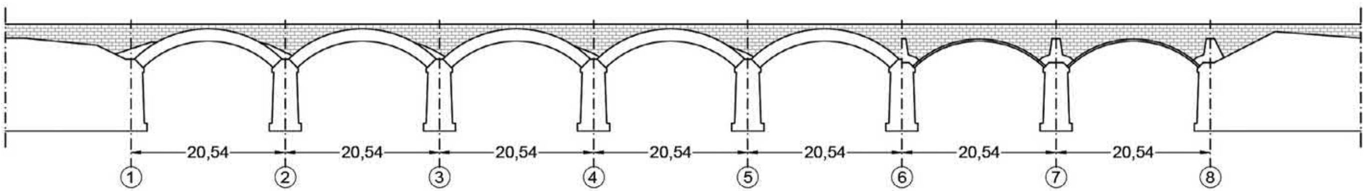

Figure 13.23 Longitudinal view of the bridge over Venta River in Kuldiga, built in 1874 (adapted from Paeglitis and Paeglitis, 2000).

Figure 13.24 Retrofit yard of the bridge over Venta River (adapted from Paeglitis and Paeglitis, 2000): view of the arches reinforcement.

Figure 13.25 Retrofit yard of the bridge over Venta River (adapted from Paeglitis and Paeglitis, 2000): waterproofing of the arches.

built to redistribute loadings and prevent premature damage of the waterproofing. Finally, all structural elements were restored with an external layer washing.

References

Barlow, W.H., 1846. On arches. In: Min. Proc. ICE 5, London, pp. 439–474.

Benouville, L., 1891. Etude sur la Cathédrale de Beauvais. In: De Badout, M.A. (Ed.), Encyclopédie d'Architecture, 40 serie, vol, 3. Librairies imprimeries réunies, Paris, pp. 52–54.

Castigliano, A., 1879. Théorie de l'équilibre des systèmes élastiques et ses applications 1–2. Front Cover. Alberto Castigliano, Auguste Frederic Negro Editeur, Turin.

Corradi, M., 1998. Empirical methods for the construction of masonry arch bridges in the 19th century. In: Sinopoli, A. (Ed.), Arch Bridges: History, Analysis, Assessment, Maintenance, and Repair. Balkema, Rotterdam.

Couplet, P., 1729. De la poussee des voutes. In: Histoire de 1'Academie Royale des Sciences, p. 79.

Couplet, P., 1730. De la poussee des voutes. In: Histoire de 1'Academie Royale des Sciences, p. 117.
Department of Transport, 2001. The assessment of highway bridges and structures, design manual BD 21/01. In: Design Manual for Roads and Bridges, vol. 3, Section 4. Department of Transport Highways Agency, London.
Fuller, G., 1875. Curve of equilibrium for a rigid arch under vertical forces. Proc. I.C.E. 40.
Gregory, D., 1697. Catenaria. Philos. Trans. 231, 637.
Heyman, J., 1876. Copulet's engineering memoirs. In: Hall, A.R., Smith, N. (Eds.), History of Technology. Mansell, London, pp. 1726–1733.
Heyman, J., 1969. The safety of masonry arches. Int. J. Mech. Sci. 11, 363–385.
Heyman, J., 1972. Coulomb's Memoir on Statics: An Essay in the History of Civil Engineering. Cambridge University Press, Cambridge.
Heyman, J., 1980. The estimation of the strength of masonry arches. Proc. Inst. Civ. Eng. 69, 921–937. Part 2.
Heyman, J., 1982. The Masonry Arch. Ellis Horwood, Chichester.
Heyman, J., 1996. Arches, Vaults, and Buttresses: Masonry Structures, and Their Engineering. 418 pp. Collected studies CS546 series. Variorum Edition, Aldershot.
Heyman, J., 1997. The Stone Skeleton, Structural Engineering of Masonry Architecture. Cambridge University Press, Cambridge. 172 p, ISBN 9780521629638.
La Hire, P., 1695. Traité de mécanique, on explique tout ce qui est nécessaire dans la pratique des Arts, et les proprietés des corps pesants lesquelles ont eu plus grand usage dans la Physique. imprimerie Royale, Paris.
La Hire, P., 1712. Sur la eonstruction des voútes dans les édifiees. Mémoires de l'Académie Royale des Sciences, Année. 1712, Paris, pp. 69–77.
Livesley, R.K.A., 1978. Limit analysis of structures formed from rigid blocks. Int. J. Numer. Methods Eng. 12, 1853–1871.
MEXE, 1963. Military Engineering Experimental Establishment - Military Load Classification of Civil Bridges, SOLOG study B. 38. Military Engineering Experimental Establishment, Christchurch, NZ.
Navier, M., 1833. Résumé des leçons de mécanique données à l'Ecole polytechnique. Carilian-Goeury et V. Dalmont, Paris, p. 491.
Oliveira, D.V., Lourenco, P.B., Lemos, C., 2010. Geometric issues and ultimate load capacity of masonry arch bridges from the Northwest Iberian Peninsula. Eng. Struct. 32 (12), 3955–3965.
Paeglitis, A., Paeglitis, A., 2000. Restoration of masonry arch bridge over Venta River in Kuldiga. In: Proceedings of the XXVII Baltic Road Conference, Riga, Latvia.
Pippard, A.J.S., 1948. The approximate estimation of safe loads on masonry bridges. In: Civil Engineer in War, Vol 1. ICE-Institution of Civil Engineers, London, pp. 365–372.
Pippard, A.J.S., Chitty, L., 1951. Study of the Voussoir Arch, National Building Studies. Research Paper 11. HMSO, London.
Rankine, W.J.M., 1898. A Manual for Civil Engineering. 295 Charles Griffin & Co London, pp. 429–432.
Sustainable Bridges, 2007. Possibilities of unification of bridge condition evaluation background document SB3.3. Sustainable Bridges—Assessment for Future Traffic Demands and Longer Lives. Research Programme Developed Under the 6th Framework EU Programme—Priority 6 Sustainable Development Global Change and Ecosystems Integrated Project. Contract number: TIP3-CT-2003-001653.

Tellet, J., 1983. A review of the literature on brickwork arches. In: Proc 8th Int. Symp. on Load Bearing Brickwork, Tech Sec. 2-Structures, Building Materials Section. British Ceramic Society, London.

Villarceau, Y., 1854. On the Arch Bridge Construction. Academie des Sciences of Paris, Imprimerie Imperiale, Paris, p. 325.

Whitey, K., 1982. Assessment of the Masonry Arch Bridge Work Pap. WP/B/28/82 Transport and Road Research Laboratory, Crowthorne, Berks. (unpublished).

Part V

Bridge design based on geometry

This page intentionally left blank

Arch bridges

14

Alessio Pipinato
AP&P, CEO and Technical Director, Rovigo, Italy

1. Introduction

Arched bridges can be defined as vertically curved and axially compressed structural members spanning channels, roads, or railways. Arch bridges can be grouped into three main categories according to the shape of their arch: deck arch bridge, through arch bridge, and half-through arch bridge. The terminology used to describe arch bridges is shown in Figure 14.1, where historical bridges and recent modern structural parts are identified. The main parameters identifying an arch bridge are the clear span (horizontal projection distance between the two intrados abatement), the design rise, and the rise-to-span ratio, which is defined as f_0/l_0, where

$$\left.\begin{aligned} l &= l_0 + d \cdot \sin\varphi_j \\ f &= f_0 + \frac{d}{2}\left(1 - \cos\varphi_j\right) \end{aligned}\right\}, \tag{1}$$

and where l is the design span, d is the depth of main arch, φj is the angle of the center line at the arch springing, and f is the design rise.

2. Historical trends

As illustrated in Chapter 1, one of the most common structural shapes used for bridge construction throughout history is the arch. The frequent use of the arch is strictly related to the availability and capability of use of the compression-resistant materials (stone and sun or furnace-baked bricks) since Romans age, and even before. Around 4000 BCE, Sumerians built arch entrance and small arch bridges with sun-baked bricks (Steinman and Watson, 1941). Well-known arch bridges were built in Europe in the Middle Ages (e.g., the old London Bridge in England, the Pont d'Avignon in France, the Castelvecchio Bridge in Italy) and in the Renaissance Period (e.g.. Ponte di Rialto and Ponte Santa Trinita in Italy, the Pont Notre Dame and Pont Neuf in France).

While Chapter 1 discusses historical arch bridges, this chapter illustrates well-known arch bridges of more recent time periods. For example, Eiffel innovated the modern arched structure as he designed two notable railway wrought-iron two-hinged sickle-shaped arch bridges, the Maria Pia Bridge in Porto, Portugal, with a span of 160 m (Figure 14.2), and the Garabit Viaduct across the Truyeres River at St.-Flour, France, 165 m span (Figure 14.3). Another notable arch bridge of this period, built with an innovative cantilever construction method, is the Eads steel Bridge at

Innovative Bridge Design Handbook. https://doi.org/10.1016/B978-0-12-823550-8.00018-4

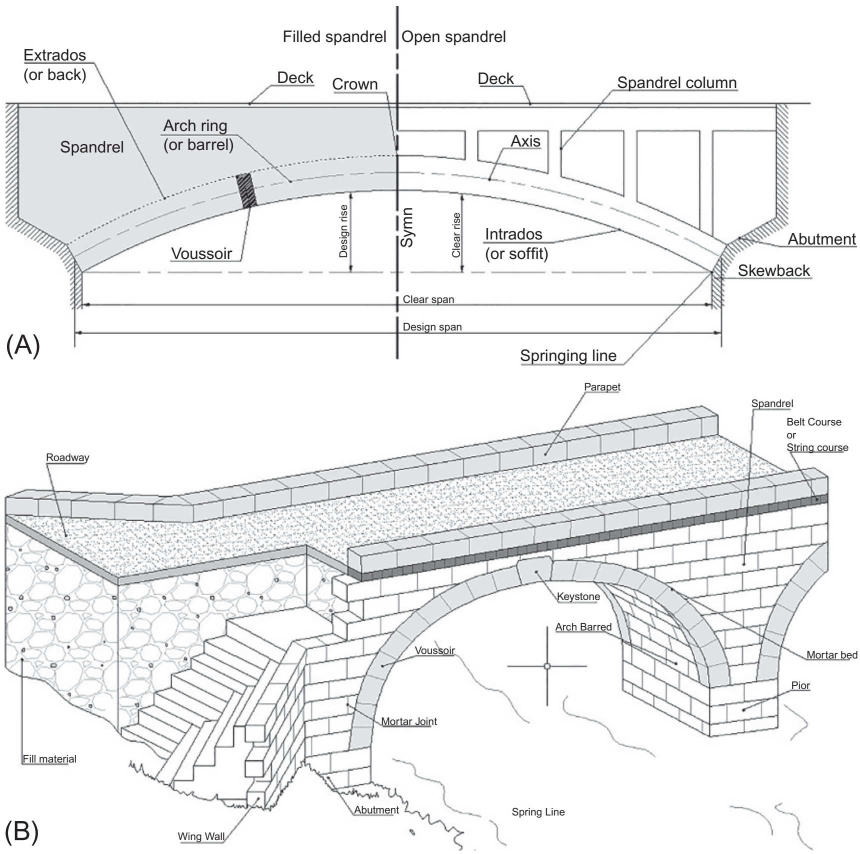

Figure 14.1 Arch bridge components of (a) a modern arch bridge; and (b) an historical arch bridge.

St. Louis, composed of three 158.5 m arches (Figure 14.4). After the iron bridge period, starting in the second half of the 19th century, RC bridges were constructed around the globe. In 1911, using the Hennebique system, the Porcheddu Society built the first concrete bridge with a significant span (more than 100 m) in Italy the Risorgimento Bridge in Rome. Freyssinet designed a series of arch bridges in that period: the Albert Louppe Bridge at Plougastel, France (highway and railway, net span of 172.6 m); the Saint-Pierre-du-Vauvray concrete arch (132 m span); and the Pont De La Libération in Villeneuve-sur-Lot (96 m span). Other relevant arches of this period include the following: (a) Maillart bridges (Tavanasa, Arve, Zuoz, Stauffacher, Salginatobel, Schwandbach, Bohlsbach, Rossgraben, Traubach), slender and pleasant arches that have also been used as references for the construction of more recent structures and buildings (Figures 14.5–14.7); (b) the Martín Gil Viaduct, with a span of 210 m, in Spain, 1942 (Figure 14.8); (c) the Sandö Bridge, with a span of 264 m, in Sweden, 1943 (Figure 14.9); (d) the Hell Gate Bridge by Gustav Lindenthal,

Figure 14.2 Tthe Maria Pia Bridge in Porto, Portugal, with a span of 160 m.

Figure 14.3 The Garabit Viaduct across the Truyeres River at St. Flour, France, with a span of 165 m.

Figure 14.4 The Eads Steel Bridge.

Figure 14.5 The Tavanasa Bridge.

Figure 14.6 The Arve Bridge.

a half-through truss arch bridge supporting four railway tracks with a span of 298 m, New York (Figure 14.10). Soon after the construction of the Hell Gate Bridge, the arch-span record exceeded 500 m with the Bayonne Bridge's main span of 504 m (New York; Figure 14.11) and the Sydney Harbor Bridge's main span 503 m (Australia; Figure 14.12). Span further increased with the New River Gorge Bridge's 518 m (Fayetteville, West Virginia; 1977; Figure 14.13); the Bosideng Bridge's 530 m (China; CFST; 2012; Figure 14.14); the Lupu Bridge's 550 m (China; CFST; 2003; Figure 14.15); and the Chaotianmen Bridge's 552 m (China; CFST; 2009; Figure 14.16).

Figure 14.7 The Salginatobel Bridge.

Figure 14.8 The Martín Gil Viaduct.

Figure 14.9 The Sandö Bridge.

Figure 14.10 The Hell Gate Bridge.

Figure 14.11 The Bayonne Bridge.

Figure 14.12 The Sydney Harbor Bridge.

3. Types

Arch bridges can be classified by the relative positions of the deck (Figure 14.17a) and by hanger type (Figure 14.17b) in the following categories:

- Deck arch
- Half-through arch
- Through deck-stiffened arch
- Through rigid-framed tie
- Fly bird arch

Figure 14.13 The New River Gorge Bridge in Fayetteville, WV.

Figure 14.14 The Bosideng Bridge.

Other details of the bridge classification are reported in Figure 14.17a, considering the number and type of ribs and according to the typology of the deck or the arch. Although it is difficult to classify all arch types, Figure 14.17a provides a comprehensive classification. There are three types of restraint conditions of the arch. The fixed arch is statically indeterminate and, due to its fixed condition, it is subject to internal

Figure 14.15 The Lupu Bridge.

Figure 14.16 The Chaotianmen Bridge.

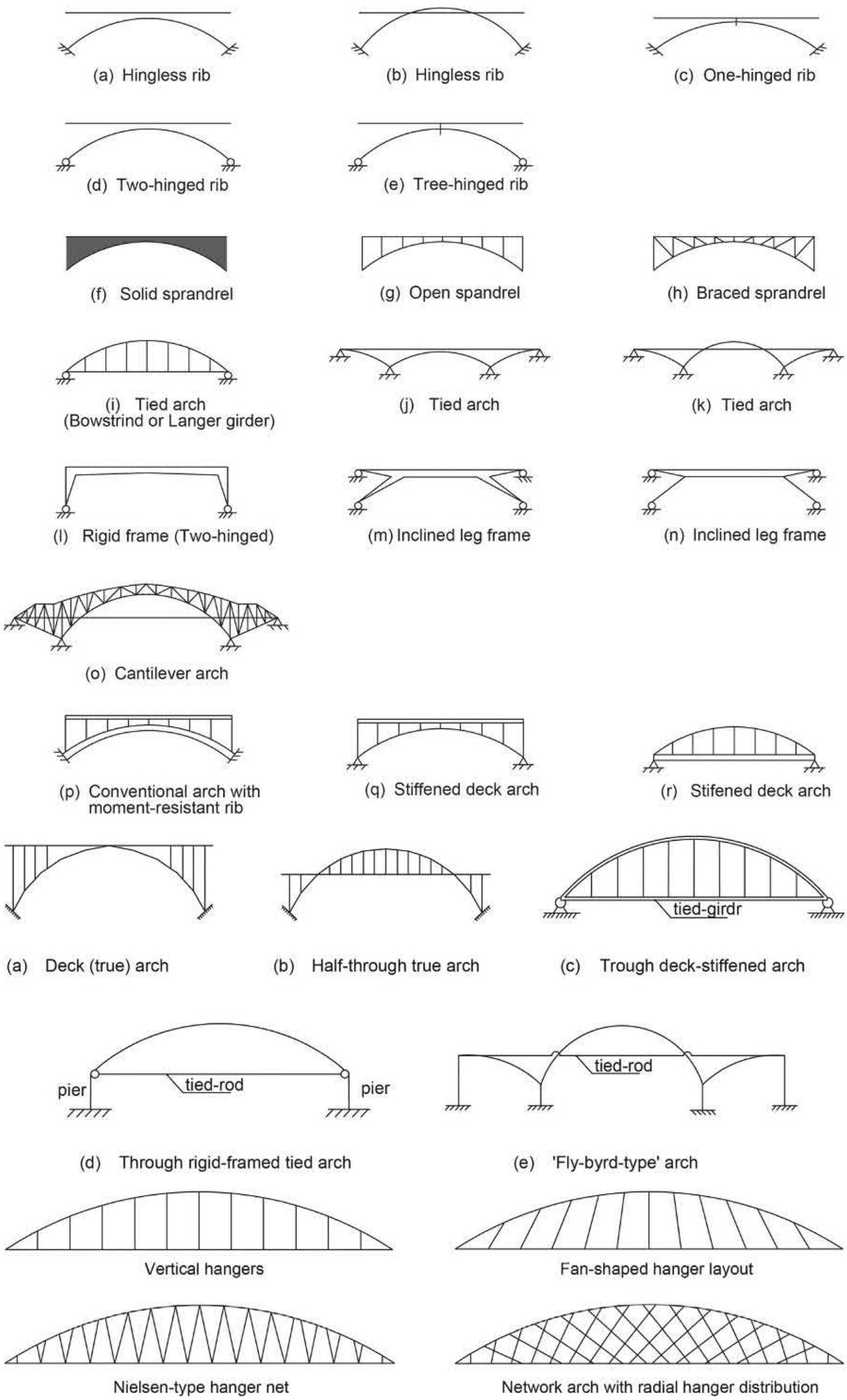

Figure 14.17 Arch bridge types by (a) shape; and (b) hanger type.

stress effected by thermal or time-dependent actions. The two-hinged arch with pinned connections at both springings is statically indeterminate, and its supports are free of stresses incurred by thermal or time-dependent actions. The three-hinged arch with an additional third hinge at the crown is becoming statically determinate; it is, therefore, free of stresses incurred by thermal or time-dependent actions but has the largest deflections of the three types.

4. Selected structures

The longest arched structures are reported in Table 14.1.

5. Construction methods

Differently from other structural types, arch bridges are often constructed in different stages, and only at the closure of the crown do they come together completely as an arch. Consequently, and especially for large structures, various construction methods are used:

(a) *Free cantilever method*—Using this method, the construction of each side of the arch proceeds independently, finally closing at the crown the construction; some of the masterpieces including the Hell Gate Bridge, the Bayonne Bridge in New York, and the Sydney Bridge were built using the free cantilever method.

(b) *Cantilever truss method*—Similarly to the preceding system, a spatial truss is built using cables and trusses in order to join the two sides reciprocally into a unique temporary structure; serving as examples are the twin bridges Krk 1 and Krk 2 in Croatia, designed by Ilija Stojadinović in cooperation with Vukan Njagulj and Bojan Možina, and built by Mostogradnja Belgrade and Hidroelektra Zagreb between 1976 and 1980 (Figure 14.18).

(c) *Cable-stayed cantilever method*—In this method, two temporary pylons are cable-stayed and anchored to the ground at both sides and cables are used to hang up the arch during the cantilever construction; the Tamina Bridge has been built using this method (Figure 14.19);

(d) *Scaffolding method*—As the name suggests, wood or steel scaffolding is employed to incrementally build each side of the arch; worldwide masterpieces have been built with the scaffolding method, such as the Plougastel Bridge, the Salginatobel Bridge (Figure 14.20), the Sandó Bridge, and the Arrabida Bridge.

(e) *Swing method*—To expedite the construction of an arch, the two prefabricated semiarches can be used at each side, they are then affixed by rotating them in a variety of ways (horizontal swing, vertical swing, combined swing method); an example of a bridge constructed using this method is the Alconetar Bridge on Alcantara Reservoir, with a total span of 400 m (Figure 14.21).

(f) *Melan method*—The Melan method utilizes parallel steel beams that are curved to form an arch and embedded within the concrete; steel I-sections are placed in the bottom of the arch. The principle is to construct a relatively light steel arch between abutments, which centers and supports the forms for pouring concrete with stiff reinforcement, to which, when necessary, additional bars could be added. The innovative and economical Melan construction method became a common construction procedure in the late 19th and early 20th centuries

Table 14.1 Arch bridges in the world, main structures realized.

Bridge Reference	Rank	Name	Main Span (m)	Main Material	Opening Year	Location
	1	Chaotianmen Bridge	552	Steel	2009	China
	2	Lupu Bridge	550	Steel	2003	China
	3	Bosideng Bridge	530	CFST	2012	China
	4	New River Gorge Bridge	518	Steel	1977	United States
	5	Bayonne Bridge	510	Steel	1931	United States

	6	Zigui Yangtze River Bridge [zh]	508	CFST	2019	China
	7	Sydney Harbor Bridge	503	Steel	1932	Australia
	8	Wushan Bridge	460	CFST	2005	China
	9	Guantang Bridge	457	Steel	2018	China
	10	Mingzhou Bridge [zh]	450	Steel	2011	China

Continued

Table 14.1 Continued

Bridge Reference	Rank	Name	Main Span (m)	Main Material	Opening Year	Location
	11	Xijiang Railway Bridge	450	Steel	2014	China
	10	Daxiaojing Bridge [zh]	450	CFST	2019	China
	13	Qinglong Railway Bridge	445	Concrete	2016	China
	14	Yachi Railway Bridge	436	CFST	2019	China
	15	Zhijinghe River Bridge	430	CFST	2009	China

	16	Xinguang Bridge	428	Steel	2008	China
	17	Wanxian Bridge	420	Concrete	1997	China
	18	Caiyuanba Bridge	420	Steel	2007	China
	19	Krk Bridge	416	Concrete	1980	Croatia
	19	Nanpan River Qiubei Bridge	416	Concrete	2016	China

Figure 14.18 Krk Bridges I and II.

Figure 14.19 The Tamina Bridge.

(Šavor and Bleiziffer, 2008). One of the first examples of the Melan method is the Schwimmschul Bridge in Steyr (1898), with a span of 42.4 m and a rise of only 2.67 m giving rise-to-span ratio of 1/16. Other examples include the Dragon Bridge in Ljubljiana, with a 33.34 m span (1901); the Echelsbacher Bridge between Augsburg and Oberau, Germany, with a 183 m span (1929); and the Larimer Avenue Bridge in Pittsburgh, Pennsylvania, with a 202 m span (1912). Embedded truss scaffolding has been more recently replaced by embedded CFST (concrete-filled steel tubes) scaffolding, and it has been widely used, especially in China, to build very large arches.

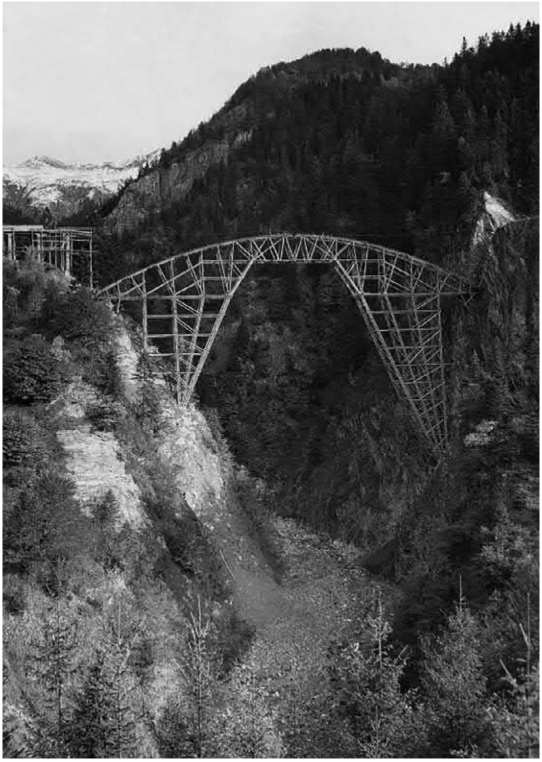

Figure 14.20 The Salginatobel Bridge during the scaffolding operations.

6. Technical innovations and research on arch bridges

Representing one of the most widely used structural solutions, arch bridges advances have been continuously advancing from the Roman era to today. Recent trends and innovations can be summarized as follows:

(a) *Lightweight structures*—Recent arches have increasingly employed light decking systems constructed with composite RC/steel solutions, which can reducing the decking weight up to 35% when compared to concrete current decking. Another lightweight solution is the use of orthotropic decking, which has been employed in movable bridges. Recently, the application of orthotropic decking use has decreased due to maintenance issues such as the fatigue of welding and pavement.

(b) *HPC and UHPC members*—High-performance concrete has been used in long-span concrete arch bridges throughout the world (e.g., Los Tilos Bridge in Spain, 2004, 75 MPa concrete; Colorado River Bridge in USA, 70 MPa concrete). Since the late 20th century, carious research groups have been working to develop the application of UHPC in arch. Trial designs of arch bridges with main spans of 160 m, 420 m and 600 m have been achieved by using UHPC. Compared with conventional concrete bridges, UHPC enables self-weight to be reduced by 35%–42% (Renyuan et al., 2010; Čandrlić et al., 2004).

Figure 14.21 The Alconetar Bridge on Alcantara Reservoir, with a total span of 400 m.

Two examples of UHPC arch bridges are the Sunyu Footbridge in Korea, with a main span of 120 m, which was completed in 2002 (Huh and Byun, 2005), and the Wild Bridge in Graz, Austria, completed in 2009, which is used for load traffic.

(c) *Network arches*—The use of the network arch shape can result in a great reduction in weight: up to a 40% reduction in the weight of the entire arch system (Pipinato, 2016). Network arches can also be constructed with tubular members, to achieve an even greater reduction in weight (Pipinato, 2020).

References

Čandrlić, V., Radic, J., Gukov, I., 2004. Research of Concrete Arch Bridges up to 1000 m in Span, Proceedings of the Fourth International Conference on Arch Bridge, 17–19 Nov. Barcelona, Spain, pp. 538–547.

Huh, S.B., Byun, Y.J., 2005. Sun-Yu Pedestrian Arch Bridge, Seoul, Korea. Structural Engineering International 15 (1), 32–34.

Pipinato, A., 2016. Structural analysis and design of a multispan network arch bridge. Bridg. Eng. 169 (1), 54–66. https://doi.org/10.1680/jbren.14.00013.

Pipinato, A., 2020. Structural optimization of network arch bridges with hollow tubular arches and chords. Mod. Appl. Sci. 12 (2), 36. https://doi.org/10.5539/mas.v12n2p36.

Renyuan, D., Jian, Y., Baochun, C., 2010. Trial design of a reactive powder concrete (RPC) arch bridge with a span of 420m. In: Baochun, C., Jiangang, W. (Eds.), Proceedings of 6th International Conference on Arch Bridges. New Art Color-plate & Printing Co., LTD., Fuzhou, China, pp. 126–132.

Steinman, D.B., Watson, S.R., 1941. Bridges and Their Builders. G. P. Putnam's Sons, New York, NY.

Šavor, Z., Bleiziffer, J., 2008. Proceedings of Chinese-Croatian Joint Colloquium on Long Span Arch Bridges, Structural Engineering Conference, Zagreb, Brijuni Islands, pp. 171–180.

This page intentionally left blank

Girders

15

R.K. Bharil
Biggs Cardosa Associates, San Jose, CA, USA

1. Introduction

Girder bridges are the most natural and simplest form of bridging between two points. Chances are very high that today, a bridge engineer will learn how to design a bridge girder before any other bridge type. The use of girders as a natural bridging element is abundantly evident in nature—such as a fallen tree trunk over a stream or rock formations over eroded soil—providing both people and animals dry and safe access across an obstacle. The use of girders as a human-made bridging element probably evolved as an outdoor extension of an indoor dwelling's floor or roofing system.

The span length and the site conditions often dictate the type of bridge that can be feasible at a given site. There are physical and economic limitations, and the bridge selection process often starts by considering a simple culvert, progressing to a slab or girder system, and ultimately evolving to truss and other more complex systems if and when needed. Figure 15.1 shows the commonly used and economical span ranges of various bridge types. Keep in mind that there are often exceptions to the recommended bridge type selection driven by aesthetic preferences, special site conditions, environmental regulations, political influence, and many other factors.

Originally, the girder selection relied on time-proven depth-to-span ratios that controlled deflections and served the function of carrying the load. The most commonly used span-to-depth ratios for various popular bridging elements are described in Figure 15.2. The primary function of these ratios is to control live load deflections and vibrations; however, modern innovation is constantly pushing these ratios toward leaner and more efficient systems.

As structural analysis methods evolved, moments and shear were added to the beam equation, and factors of safety were used to guard against uncertainties in building materials and prevalent loads. As the girder shape evolved from untreated logs, sawn timber, and cut stones to steel, the material's properties began to play a greater role in its selection. As analysis and design methodologies progressed, girder bridges became more complex—from simple rectangular beams to fabricated or rolled shapes, concrete with steel reinforcement, concrete with prestressing strands, and various other complex structural systems such as stringer-floor beams and box girders.

Today's girder bridges consist of the elements described next.

The primary structural elements are as follows:

- *Girders*—Transfer load to substructure elements (the primary focus of this chapter)
- *Deck*—Provides a riding surface and transfers external loads to stringers or girders
- *Stringers*—Transfer load from slab to floor beams (not always present)
- *Floor beams*—Transfer load from stringers to girders (not always present)

Innovative Bridge Design Handbook. https://doi.org/10.1016/B978-0-12-823550-8.00007-X

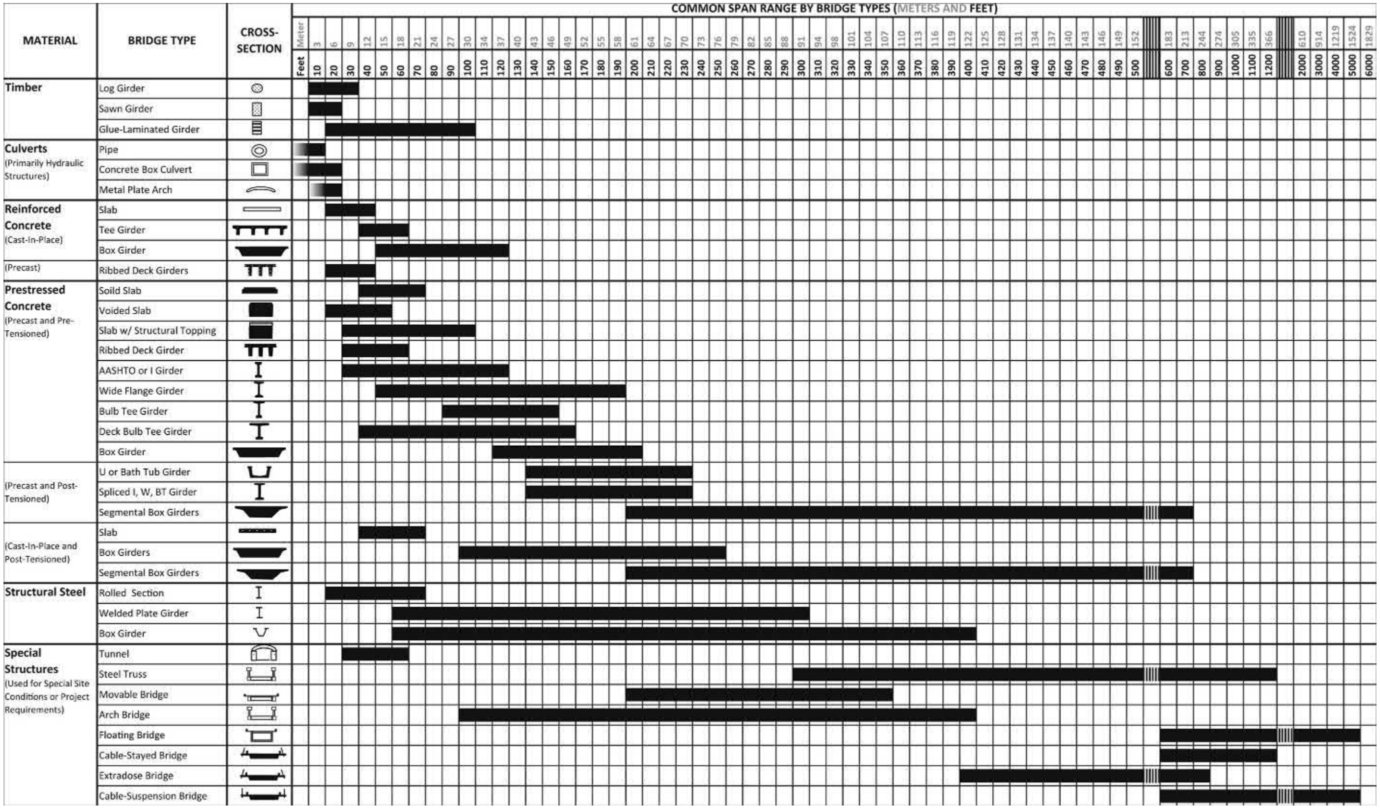

Figure 15.1 Common span range, by bridge type. Compiled in part from California Department of Transportation (2019) and Washington State Department of Transportation (2020).

MATERIAL	BRIDGE TYPE	DEPTH TO SPAN RATIO (%)																				
		0.00	0.50	1.00	1.50	2.00	2.50	3.00	3.50	4.00	4.50	5.00	5.50	6.00	6.50	7.00	7.50	8.00	8.50	9.00	9.50	10.00
Timber	Log Girder																	■				
	Sawn Girder															■						
	Glue-Laminated Girder															■						
Reinforced Concrete (Cast-In-Place)	Slab										■	■	■	■								
	Tee Girder														■	■						
	Box Girder												■	■								
(Precast)	Ribbed Deck Girders													■	■	■						
Prestressed Concrete (Precast and Pre-Tensioned)	Soild Slab							■														
	Voided Slab							■														
	Slab w/ Structural Topping								■													
	Ribbed Deck Girder												■	■								
	AASHTO or I Girder											■	■									
	Wide Flange Girder									■	■											
	Bulb Tee Girder										■	■										
	Deck Bulb Tee Girder												■	■								
	Box Girder										■	■	■	■								
(Precast and Post-Tensioned)	U or Bath Tub Girder												■	■								
	Spliced I, W, BT Girder									■	■											
	Segmental Box Girders									■	■											
(Cast-In-Place and Post-Tensioned)	Slab							■														
	Box Girders									■	■											
	Segmental Box Girders									■	■											
Structural Steel	Rolled Section									■	■											
	Welded Plate Girder									■	■											
	Box Girder									■	■											
	Steel Truss									■	■	■	■									

Figure 15.2 Common bridge girder depth-to-span ratios. Compiled in part from California Department of Transportation (2020) and Washington State Department of Transportation (2020).

The secondary structural elements are as follows:

- *Diaphragms*—Provide stability to girders during construction (often eliminated due to their initial cost)
- *Barriers and railings*—Serve as a traffic safety element and confine external loads to the designated riding surface
- *Bearings*—Transfer loads to substructure elements while providing for superstructure rotation and translation
- *Joints*—Allow movements of superstructure segments to thermal, shrinkage, and seismic demands (used sparingly to reduce maintenance costs)

The substructure elements are as follows:

- *Abutments, wing walls, and approach slabs*—Connect the bridge structure to the roadway embankment
- *Pier caps and crossbeams*—Transfer loads to columns or piles
- *Piers, bents, and columns*—Transfer loads to foundation interface elements
- *Footing and pile caps*—Transfer loads to soil/rock strata or other foundation elements
- *Piles, shafts, and caissons*—Transfer loads to final soil/rock strata via bearing, friction, or both

Before discussing a design based on geometry, let's define a bridge girder correctly. Many bridge inspection manuals define a *girder* as a longitudinal bridge element that supports the deck slab carrying external loads and transmits the load to substructure elements such as bearings or abutment/pier caps or crossbeams. A *stringer* is defined as a similar longitudinal element that transmits loads to other superstructure elements (such as a floor beams) and is typically a part of a more elaborate bridge type such as a truss or a cable-supported system. Other names such as *beam* and *joist* are also interchangeably used but do not necessarily refer to the term *girder* that defines the bridge. This chapter defines a girder bridge as a bridge whose primary load-carrying members are girders oriented along the direction of the traffic.

Due to its inherent simplicity, the girder bridge is the most common form of bridge. The bridging of two distant points by joining them by a straight line is not only intuitive but also a very efficient form of overall space planning. For example, with girders, there is little loss of vertical clearance below to accommodate an arch springing line or deck truss, there are no overhead constraints to accommodate the lateral bracings of a through truss, and there is no complicated geometry of overhead cables or tied arches. It requires relatively simple formwork or erection procedures and is often a first choice. However, a girder bridge eventually loses out to other complex forms as new geometry constraints begin to play key roles, spans become longer, or construction access becomes difficult. Such limitations are further given in Figure 15.1 and are described in detail in the following sections.

2. Planning

Every successful design begins with a solid plan. Before a bridge project is conceived, the project need, data collection, funding procurement, project delivery methods, and other key steps must be identified, as shown in Figure 15.3.

2.1 Project need identification

The planning for a bridge begins with identification of the project—for example, a route alignment that needs to cross an obstacle, followed by data collection and preliminary studies to identify the type of bridge needed and the estimated cost to plan, design, and build the bridge. Traffic demands and freight mobility needs typically dictate a new crossing, and the condition and capacity of an existing bridge lead to

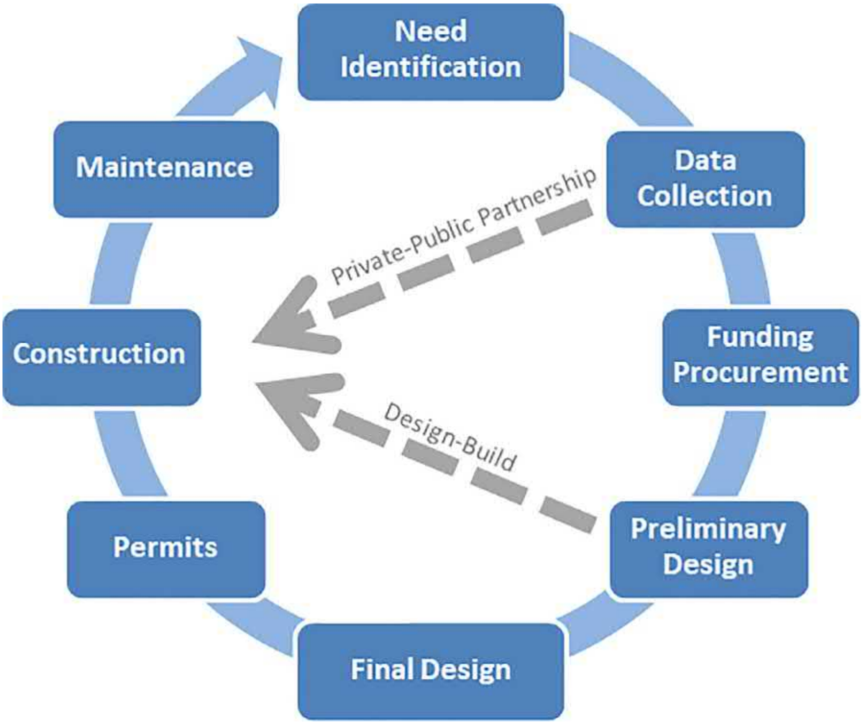

Figure 15.3 Typical bridge project planning cycle—From inception to preservation.

rehabilitation or replacement alternatives. The bridge type selection process depends heavily upon site, funding constraints, and, to some extent, on the preferences of the bridge owners. Generally, the first preference is a girder bridge unless other, more complex bridge systems seem to make sense.

2.2 Data collection and preliminary design

Once a project need is identified, the next step is to collect preliminary site data to develop several viable options. Topographic surveys are needed after a field reconnaissance so that a route can be laid out and an approximate bridge size can be determined. The advent of newer and faster surveying techniques such as three-dimensional (3-D) laser scanning (also known as LiDAR) can enable the collection of a vast amount of survey data in days, instead of weeks, to an accuracy of 0.1 ft (about 2–4 cm). The use of scanning has been found to be very beneficial in verifying existing as-built plans needed for a bridge widening or rehabilitation project. Some level of preliminary design is essential to identify the estimated cost; to begin the permitting process; and to plan the funding, design, and construction tasks. Preliminary design, described in detail in Section 2.4, is one of the most important tasks.

2.3 Funding procurement

Obtaining funding (whether public or private) is one of the most critical steps in making any project a reality, and it requires a significant amount of planning and effort. Public (i.e., government) funding is the most common funding used for bridges. However, private funding is becoming increasingly popular, as the cost of a bridge project can be directly charged to the public in the form of a toll or user fee. Public–private partnership (PPP, also sometimes P3) is changing how some very large public projects throughout the world can be funded and maintained, usually in a very short time frame. Typically, bridge cost estimates at the funding level are very approximate and use a conventional cost per square foot (or meter) of the bridge footprint for estimating purposes. Since the cost per square foot (or meter) of various bridge types can vary a great deal, and delays, planning, and procurement costs can consume a lot of money very early on, early consideration needs to be given to better bridge costing to secure an adequate level of financing. It is customary to use 150% to 300% of the bridge's square foot (or meter) cost during the planning stage to arrive at the overall funding needs. This takes into account the additional costs of approach roadway and channel improvements; traffic control during construction; aesthetic requirements; public input process; administrative, planning, and design; construction management fees; uncertainties of bidding climates; inflation delays due to utility relocations and permitting; and construction contingencies.

2.4 Project development, delivery, and execution

The project delivery method—whether it is a conventional design-bid-build, design-build (DB), engineer-procure-construct (EPC), PPP, or general contractor–construction manager (GCCM, or construction at risk)—can have an impact on the bridge planning process, but this decision is often deferred. In the past, the amount of project funding precluded certain types of project delivery methods. For example, it used to be considered that DB procurement should be used only for projects costing more than US $20 million, and PPP would be worth the additional effort for projects exceeding US $100 million. However, such boundaries now no longer apply, and the procurement methods are based more often on comfort level (e.g., agency size, prior experience, etc.) and needs (e.g., urgency, resources, etc.) of the bridge owners rather than cost and complexity of the project. The procurement method plays a much greater role in the final design of bridges and delivery of the bridge project. By using DB delivery, the bridge owner is no longer limited by the size of the available workforce. Often, outside consultants are hired as the project manager and construction manager to facilitate such deliveries. Another method, known as *construction at risk* or *general contractor–construction manager (GCCM)*–is where a contractor is retained earlier in the design process, which helps to sync both the design and construction together so that the cost of the project is more certain. An early determination of probable project delivery methods can be very helpful in the planning process and very cost effective for the bridge owners as well.

The other steps of the bridge project cycle, such as construction and preservation, are described in later sections of this chapter.

3. Preliminary bridge design

The process of determining a bridge type, size, and location is commonly known as *preliminary bridge design,* but it is also referred to by other names, such as *project study report*, *advance planning study*, *type selection process*, or *type size and location (TS&L)* study, depending on the naming preferences of the bridge owners. Preliminary design is often more detailed than the feasibility or planning studies, and it has a great bearing on the final design and project costs.

All successful bridge projects owe a great deal to the bridge type selection process since this selection basically seals the bridge's fate, whether it is iconic or just an ordinary bridge. Will it be perceived as aesthetically pleasing or an eyesore for decades to come? Will it meet the construction budget or blow a hole in it? Will it create traffic nightmares during its construction, or will most not even notice it is being built? The list goes on.

It is difficult to understate how important this early design process is and how much impact it has on almost every aspect of a bridge project. Most engineers, with some training, can design a bridge once its cross section, location, and size have been determined, but the process of successful type selection requires years of experience in bridge engineering; understanding of the multidisciplinary nature of bridge projects; and consideration of funding, construction, inspection, maintenance, hydraulics, traffic, highway geometrics, and many other constraints—as described in this section. Even though a girder bridge may clearly be the best option in most locations, there are many more specific choices that must be made to arrive at the final bridge type that require additional considerations. A thorough type selection process should include the following elements:

- *Site constraints*—Topography, utilities, traffic, right-of-way, geometry
- *Function*—The facility serves a function to carry or cross stream, railroad, highways, canals, navigational waterways
- *Span length*—Total length and lengths of individual spans, limitations, and types
- Substructure—Caps, columns, walls, footings, piles, shafts
- *Seismic considerations*—Seismic zone, stiffness ratio, balanced spans
- *Material selection*—Constraints, cost effectiveness, availability
- *Aesthetics*—Form and function, requirements, public input, local influence
- *Environmental considerations*—Sustainability, permitting, construction constraints
- *Schedule*—Fabrication, delivery, construction sequencing, and in-service deadlines
- *Cost*—Funding, cost effectiveness, life cycle cost analysis (LCCA)

3.1 Site constraints

A topographic map showing existing utilities, right-of-way boundaries, topographic contours, hydraulic boundaries, photographic layers, and other site features is essential to correctly lay out a bridge. Site constraints can play a major role in determining the feasible bridge types and will typically dictate how the bridge can be built successfully. For example, a deep ravine may make the placement of falsework very expensive and require the girders to be launched from the banks, therefore limiting the

Figure 15.4 Tied arch bridge was selected due to its shallow superstructure depth was compared to a high level multiple-span girder bridge option for McKinley Grade Separation, Corona, California. Courtesy of its Design Consultant, Biggs Cardosa Associates.

bridge selection to prefabricated concrete or steel plate girders. The existence of underground utilities may require that the bridge footings are placed only at certain locations, which may affect the span layout. Limited or difficult construction access to the site may limit the use of large cranes and the length of a prefabricated girder that can be delivered to the site. A very active railroad overpass may dictate an entirely different type of span that will limit the falsework placement and construction closure of tracks (Union Pacific Railroad – BNSF Railway, 2016). For example, a girder bridge may not be the most appropriate (Figure 15.4) when multiple site constraints—such as railroad clearance, together with adjacent channel and local streets—exist in a highly urbanized area. Site constraints make each bridge unique, even among bridges that most casual viewers think look the same.

3.2 Function

Besides the main traffic on the bridge deck, what needs to be carried across a bridge may dictate the most efficient type of construction. For example, deflection and pedestrian comfort may require a transit bridge to have a certain level of stiffness and may preclude certain types of flexible spans. If a bridge will receive a combination of railway and highway traffic, it may require a double-deck system that is better suited to a deck truss, and the combination of pedestrian and truck loading on a long-span bridge may need some modification of standard bridge codes to ensure that the bridge is not overdesigned due to rather unrealistic load combinations. Unusual combinations, such as waterway canal and highway traffic, also have been used in some cases, and these situations require that careful attention is given to the design loads and the bridge's performance criteria.

3.3 Span length

Nothing has a more direct influence on the bridge type than its span length. The placement of piers is typically based on the site constraints, and it often decides the span arrangement. There are some basic guidelines that are difficult to bypass when it comes to selecting the bridge type based on span. For example, it will be difficult to justify erecting a cable-stayed bridge with a span of 150 ft (50 m) where a girder bridge is better suited. The addition of superficial elements without providing a function does not fare well in bridge design. Figure 15.1 illustrates which bridge types are generally suited for specific span ranges. For a long crossing, the span arrangements can play a critical role in minimizing the overall project cost. The selection of the number of spans and span lengths requires some consideration of the basic principles of engineering economics. The optimal bridge project cost can be achieved, at least in theory, when the cost of superstructure is almost equal to the cost of substructure, which means balancing individual spans. For the example shown in Figure 15.5, the most cost-effective individual span for this bridge crossing will be about 180 ft (55 m). There are other factors as well—such as construction risks of a deep foundation, availability of erection equipment, and ease of access and delivery of materials to the site—which can play a big role in the final selection.

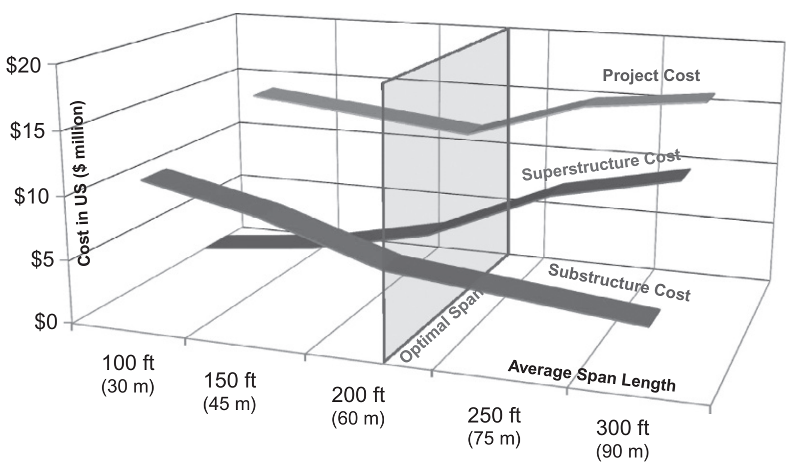

Figure 15.5 Optimizing bridge project cost by balancing superstructure and substructure.

3.4 Substructure

The type of substructure can play a significant role in overall bridge type selection. For example, if the foundation soil is relatively poor, requiring a deep foundation, then it may be worth using longer spans and fewer piers; however, increased loading and dead weight due to longer spans may adversely affect the foundation design, particularly in a high-seismicity region. From an economic point of view alone, the most preferred footing type is a spread footing, followed by driven piles, and then drilled shafts (also called *caissons* or *cast-in-drilled-hole piles*). The connection of the pier column to the superstructure also plays a major role in the transfer of superstructure forces to the foundation, which can affect the cost of the foundation. Substructure design in a high-seismic area requires an entirely different set of considerations, as compared to substructures located in a relatively low-seismic region. The proportion of substructure with respect to superstructure, bent arrangement, and column heights not only affects the overall aesthetics; it can also have a large impact on the seismic design. Typically, substructure thickness, when viewed from the bridge elevation profile, should be smaller than substructure depth (subject to additional requirements in high-seismic zones to force plastic hinging in columns). Fortunately, most common substructure configurations work well for girder bridges.

3.5 Seismic considerations

In high-seismic zones, the type selection process can have a substantial impact, and in some cases, it is better to size the substructure, span arrangements, joint locations, column width, and length for seismic forces in the preliminary design phase than to shift such responsibilities to the final design phase. Experience shows that planning for balanced structural stiffness—for example, uniformity in girder spans and column heights within various frames of the bridge—pays off in the final design. A detailed discussion of this topic can be found in the *Caltrans Seismic Design Criteria* (California Department of Transportation, 2020). In general, uneven stiffness, although often necessary to lay out a functional bridge, attracts additional seismic forces to substructure elements and can be costly to mitigate in the final design phase. Seismic design should be used early on to plan for joint spacing (e.g., continuous girder lengths), in-span hinges, span lengths, and the number and length of bents and columns.

3.6 Material selection

The material selection goes hand in hand with span lengths. Steel offers a lot of flexibility in span length and curvature, but its use is often restricted by the location of the nearest certified fabrication shops and long-term maintenance considerations such as painting. Cast-in-place reinforced concrete has its limitations due to span length and can exhibit extensive cracking if overload vehicle control cannot be enforced. Prestressed (pretensioned or post-tensioned) concrete permits longer spans and is a very popular choice of material in western United States or where concrete precast plants are located within an economical shipping distance from the bridge site. The use of structural timber (sawn or glue-laminated) is often limited by the availability of harvestable forests and fabricated timber treatment facilities. Structural composite [i.e., fiber-reinforced polymer (FRP)] bridge decks have been used in special applications due to their light weight and low maintenance; however, their use as a common bridge material is still limited due to the lack of rational design codes, difficulties in assessing service life, relatively high cost, and limited commercial availability (Bharil, Time-Dependent Reliability Framework for Durability Design of FRP Composites, 2020). Concrete, steel, and timber, in that order, make up the vast majority of materials for modern girder bridges.

3.7 Aesthetics of girder bridges

There is an enormous amount of research and publications on the aesthetics of bridges, and an ordinary girder bridge design can also benefit from the very same aesthetic principles applied to the design of signature bridges. Some simple rules specifically applicable to girder bridges are as follows:

- Form follows function, so do not add extraneous items to a bridge since they typically create long-term inspection/maintenance issues and do not work well.
- Keep all horizontal lines (e.g., girders, railing, and deck) continuous and smooth flowing, if they must break (such as at piers or abutments), incorporate vertical features of functional elements (e.g., posts and pedestals).
- Pay special attention to span ratios of adjacent spans; keep them as constant as possible, and if they must change, keep the rate of change uniform.
- Pair spans in odd numbers if possible. Three spans look better than two or four. Place end spans with a slightly smaller span to help create balance. Span proportion will also aid in the total design savings later (Figure 15.6).
- Abutment components (e.g., end joints, approach slab, bridge/wall railing, wing walls, or retaining walls) are often designed separately and sometimes do not match the main structure elements. For example, uneven heights of two abutment walls may help with the design but may form a distraction when viewed together.
- When abutments are flanked by retaining walls, match the bottom of the bridge barrier rails with the coping of the retaining wall barrier. This detail is often left to nonbridge engineers (e.g., standard plans, wall supplies, etc.) and can be very noticeable. Any incongruity at bridge–roadway transition will detract from the smooth horizontal lines of the bridge spans.

Figure 15.6 Aesthetic elements of Sandifer Memorial Bridge over the Spokane River in Washington State. This design included varying spans of timber, steel, and concrete. Courtesy of its Design and Construction Management Consultant, CES, Inc.

- Use mild vertical slopes and flares to accentuate the column shape that supports the heavy girder superstructure. For example, thickening at the tops of columns appears to be logically correct, but it may not be needed. In high-seismic zones, care should be taken to isolate architectural add-ons from the core structural functions.
- If girder depth must change between the spans, use gradual variations or use vertical elements (i.e., extended pier façade) to break the disrupted horizontal lines, but it is best not to use variable depths at all.
- Traffic barriers and safety railings provide ample opportunities to bring life to an otherwise plain girder superstructure. Care should be taken by offsetting barriers from girders to not give a visual perception large superstructure depth. Architectural features on bridge exterior (elevation view) and interior (roadway side) fascia—such as lights, castings, and fractured ribs concrete finish—help in delineating their form and functions better.
- Nothing makes a statement like a slender superstructure over proportionally sized piers, so do not use anything thicker than necessary. Instead, invest in better materials and post-tensioning, and employ other schemes to preserve the serviceability of the structure without sacrificing aesthetic value.
- Visualize your bridge design in actual settings to see how it will look. Also, get bridge architects involved, use computer animation and 3-D visualization to iron out the kinks, see how it will look when illuminated at night, to the public, and to local businesses and residents from afar. Use the most contemporary tools you can get to refine the structural features early in the design process (Figures 15.9 and 15.10).
- Visual imperfections can be magnified along very long straight lines, such as with concrete barriers, metal or cable railings, wall copings, girder soffits, and sidewalk curbs. Accept the fact that it is almost impossible to build a perfectly visually aligned large structure, so it is better to break up these lines (e.g., by incorporating light posts or pedestals) so that imperfections are less noticeable.

3.8 Environmental considerations

A bridge project can come to a dead halt due to an unmitigated environmental permitting issue. The key to avoiding this is to start early and identify permitting issues as soon as possible and work with regulatory agencies to see what can be realistically permitted. For example, a short construction window for a bridge over a fish-bearing stream may limit you to only prefabricated girder types. Floodways also affect how large the bridge opening must be to limit the rise in backwater. Scour and the potential for meandering channels may often preclude spread footings and dictate where abutments can be located. In addition, wetlands and sensitive cultural resources may require a special type of bridge construction (e.g., temporary construction platforms) that may exclude certain types of bridges that require extensive falsework (Figure 15.8).

3.9 Schedule

Most projects are very schedule driven, which can often influence the bridge selection. If the lead time for girder prefabrication is long, cast-in-place options may be preferred. If the incentives for opening to traffic early are great enough, prefabricated options may take precedence. If the in-water work window is very short, the bridge span may be increased to keep the piers out of the natural water boundaries (often referred to as the *ordinary highwater mark*) of a river. A preliminary schedule for

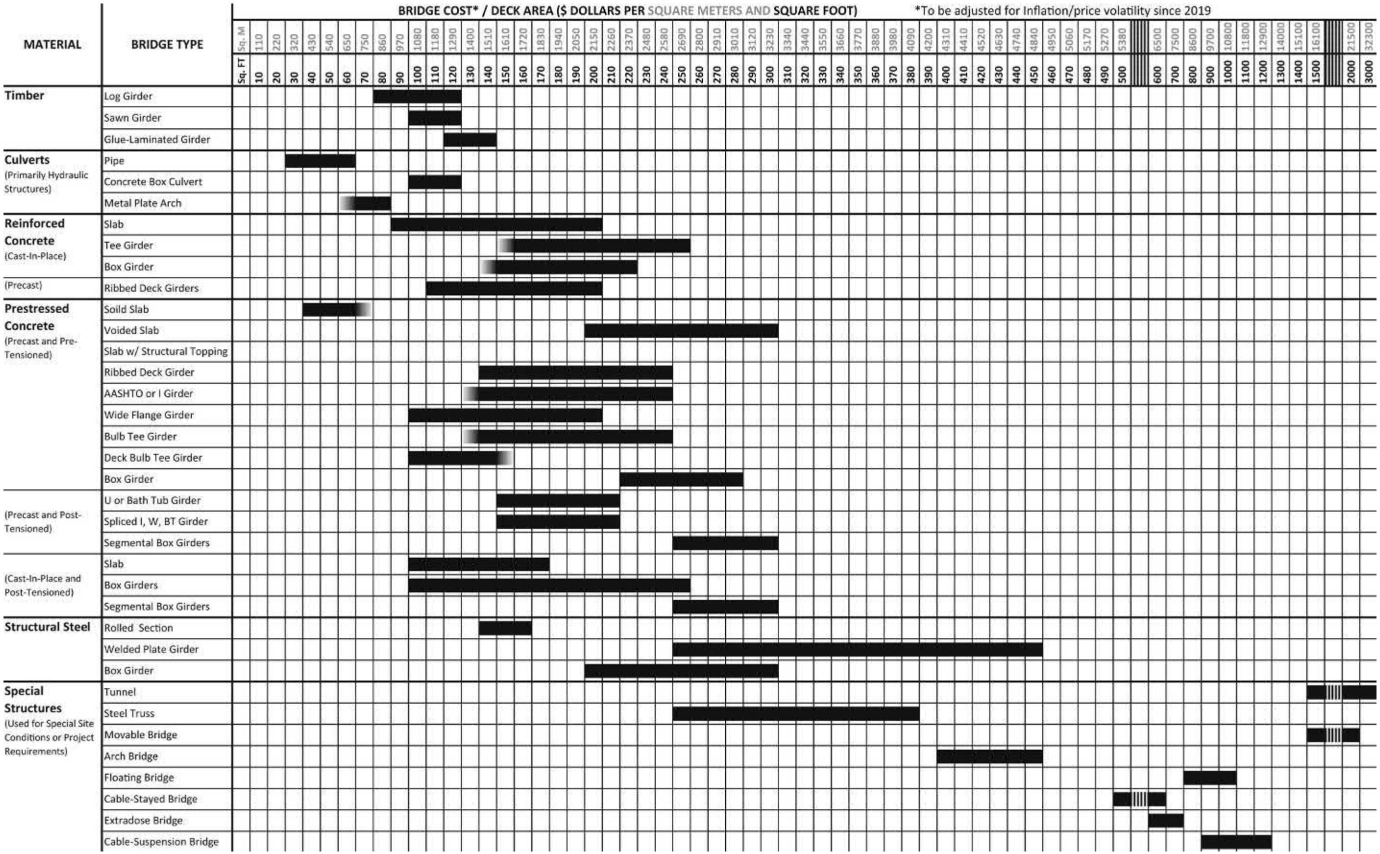

Figure 15.7 Common bridge girder cost (in US dollars) per square foot or meter of deck area. Compiled in part from California Department of Transportation (2019) and Washington State Department of Transportation (2020).

a bridge project should be prepared to analyze if the funding, permitting, design, and construction, timelines are realistic to avoid surprises later.

3.10 Cost

It is important to consider the overall and life cycle costs, rather than just the initial construction costs, to assess the real benefits of certain bridge types. For example, on a heavily traveled freeway, prefabricated options such as steel or precast concrete spans may result in a lower overall cost when traffic delays and traffic safety during construction are taken into account. A weathering steel option may offset the cost of repainting a structural steel bridge every 20 to 40 years. The following factors should be kept in mind with regard to bridge costs (California Department of Transportation, 2019; Washington State Department of Transportation, 2020):

- Factors that can result in a lower-unit-cost project include short and simple spans, low structure heights, low seismicity, no special environmental constraints, being a very large project (i.e., mass and repeat structural quantities), no aesthetic treatment, dry conditions, square bridge (no skew), easy access (not a very remote location), short abutments, spread footings, bridge site being closed to general traffic, and no staged construction.
- Factors that can result in a higher-unit-cost project include long spans, tall piers/bents, complex falsework (e.g., over a deep ravine), environmental constraints, high-seismicity/seismic faults/liquefaction potential, being a small project (i.e., no repeat element or small quantities), complex aesthetic treatment, wet conditions (i.e., cofferdams required), skewed bridges, highly urbanized areas (e.g., complex traffic staging, expensive easement/right-of-way, overhead and underground utilities), very remote location, tall cantilever abutments, and deep foundations (i.e., piles, drilled shafts, micropiles).
- Some factors that can have a very high impact on the unit cost (from 25% to as much as 150%) are unique urban conditions requiring more than two construction stages and very narrow widenings (less than 15 ft or 5 m). Although architectural and aesthetic requirements for bridges may seem costly, they actually do not significantly impact the overall bridge cost.

The bridge cost ranges (based on deck square footage or meter as shown in Figure 15.7) are calculated using "Bridge Replacement Unit Costs," as defined by the U.S. Federal Highway Administration for the western United States in 2019. These

Figure 15.8 Wishkah River Bridge over sensitive wetlands in Washington State. Existing bridge (left) as traffic detour and work platform (right). Courtesy of its Design Consultant, CES, Inc.

costs do not include items such as time-related overhead, mobilization, existing bridge removal, bridge approach slabs, abutment slope paving, soundwalls, retaining walls, or unusually large wing walls. Due to the worldwide COVID-19 pandemic (2020–21), most unit costs have been reported to be volatile (showing higher inflation trend) at the time of this publication (Mid-2021).

4. Final design

Once a girder type is selected and the preliminary design is carried out, the final design process is relatively straightforward. There are plenty of resources available—including software, literature, guidelines, examples, and codes—to help in the design development process. A constructability evaluation (that is, designing backward with construction in mind during various phases of design) is highly recommended to reduce project risk. The following elements govern the design development process:

- *Design criteria*—Codes, specifications, and guidelines
- *Material properties*—Steel, cast-in-place concrete, precast concrete, timber, and FRP
- *Loading type*—Highway, railroad, transit, pedestrian, and utility
- *Design considerations*—Structural analysis, seismicity, and software applications
- *Detailing practice*—Standards, computer-aided design and drafting (CADD), and automation
- *Construction specifications*—General specifications and special provisions
- *Construction cost*—Engineer’s estimate of cost of hard bid
- *Construction schedule*—Engineer’s estimate of construction working days

4.1 Design criteria

Unlike buildings, bridges are almost always designed for public use, are subject to public scrutiny due to funding sources, and require that the safety of the traveling public remains paramount. There are numerous specifications and codes governing bridge design that are often regulated by the bridge owners or the jurisdiction where the bridge is located. For example, in the United States, almost every year or two, new American Association of State Highway and Transportation Officials (AASHTO) specifications are adopted and supplemented by additional special publications by various state agencies, which become the governing design criteria for all bridges under the state jurisdiction (AASHTO, 2020). The American Railway Engineering and Maintenance-of-Way Association (AREMA) publishes a guide every year and becomes the code for designing all heavy railroad bridges since it is developed by all Class 1 railroad companies (AREMA, 2019). Modern bridge design is based on probabilistic analysis, which is geared to provide an acceptable probability of failure for all elements instead of the previous factor of safety-based design. Most codes oversimplify the bridge girder design, and therefore, it is important to understand how bridge codes evolved when encountering an unusual condition that may not be covered in the codes. Codes are often years behind the latest technology and can cover only common conditions. As bridge design gets more complicated, understanding the intent of code becomes more important, and only experienced and well-informed engineers can make full use of innovations in materials, loading, and construction.

4.2 Material properties

Use of high-strength and unique materials is advancing faster than the development of bridge codes or specifications. For example, yield strength of steel and compressive strength of concrete is much higher today than it has ever been. It is also worth keeping in mind that many of the material properties, such as concrete strength, can depend heavily on the local region and cannot be adopted easily outside the region. For example, the superb quality of coarse aggregates in the Pacific Northwest of the United States can help easily produce a concrete strength of more than 10,000 psi (70 MPa), which is not possible elsewhere.

4.3 Loading type

The type of traffic that a bridge carries can and should heavily influence bridge design. Highway loading is relatively lighter than railway loading and may allow the girders to be placed much farther apart. The use of two or even three girders is often discouraged due to lack of redundancy. Special loads—such as airplanes, barge impacts, heavy ice, frequent mining trucks, special permit trucks, and transit systems—require special consideration, but they are not covered in most codes. Incidence of load impact damage on highway bridge overpasses has been well documented and should be considered in the design of critical bridges.

4.4 Utilities

In urban areas, utility relocation can have a huge impact on the bridge design and construction schedule and can be extremely costly if not planned correctly. Utilities should be surveyed and potholed (i.e., water jetting to determine the exact location of buried pipes) early in the design phase so that they can be avoided if possible. Overhead utilities (such as high-voltage power) can interfere with girder erections and crane movements and wet utilities (i.e., water and sewer) are heavy and need to be accounted for in the design. Inflammable utilities (oil and gas) and electrical utilities should be handled with extreme care, and fiber optic lines are difficult to splice. Utilities mounted on bridges should be given special design considerations in the final design phase to ensure that essential services are not disrupted and do not cause unintended consequences to the bridge or the utility (Bharil et al., 2001).

4.5 Design considerations

Depending on the materials and loadings, design considerations vary. Unique bridge design guidelines exist for a wide variety of bridges; however, they should be verified to include concerns of the stakeholders and to comply with the jurisdictions. For large projects, the number of stakeholders and jurisdictions can be large and may have conflicting interests that must be handled carefully. Questions in the following categories should be asked to arrive at the final design considerations:

- *Bridge location and ownership*—Where is the bridge located? Who owns the bridge now, and who will maintain it? Typically, this is a major factor in deciding which design codes and manuals will be used. For example, if the bridge is located in the City of Los Angeles, the Caltrans design codes will apply, but various city codes will also have to be followed.
- *Bridge funding*—Who is funding the bridge? Most bridges are funded by public agencies, but the source and type of funding may impose some additional conditions and design considerations. For example, if the project funding includes federal funds, the bridge project may require more rigid review and oversight, while purely state, local, or private funding may allow more leeway on the project design. Funding may also preclude certain types of bridges or materials.
- *Bridge traffic*—What will be carried on the bridge? The type of traffic, such as bikes and pedestrians, heavy rail, light rail, vehicular traffic, water, airplanes, oil/gas, and mining trucks will determine the technical and functional design criteria for the bridge. For example, a bridge carrying heavy rail traffic over a highway will require the bridge to be designed by AREMA codes (AREMA, 2019) and *Railroad Grade Separation Guidelines* (Union Pacific Railroad – BNSF Railway, 2016) but also satisfy the state design manuals for highway safety features for pier and abutments located underneath.

4.6 Detailing practices

The use of CADD is widespread in design, and its use in construction [e.g., geographic information system (GIS), and building information modeling (BIM)] will become a reality for bridge design in the upcoming years. Tools and programs are available to make better use of the available technology, and bridges form an integral part of the overall project CADD package. CADD for bridges is less standardized than it is for roadways, and most states and agencies allow some flexibility. The use of CADD is also widespread at the engineering design level, and most recent engineering graduates already have some level of CADD training and knowledge of popular platforms such as AutoCAD and MicroStation. There are some good design practices for bridges, and due to the close interfaces with other disciplines, these practices should be followed closely to accommodate changes and to make key bridge information, such as the bridge foundation footprint, readily available for utility coordination. The use of BIM in bridges is also increasing to enable a more streamline construction interface to the design drawings.

4.7 Construction specifications

Many designers do not realize that in the order of precedence, certain specifications can supersede the design plans and cause a great deal of confusion, schedule delays, claims, and budget overruns. For example, most agencies have standard construction specifications (published almost yearly) that are typically modified by special provisions written for unique bridge elements, which may conflict with the design drawings and create unanticipated change orders. The process of construction specification writing for bridges should be done by seasoned professionals and should be reviewed to balance the risks to both the owner and contractors.

4.8 Construction cost estimates and schedule

The engineer's estimate of the probable construction cost and likely construction schedule complete the construction bid package on a bridge project. Again, a good estimate of the cost and schedule will determine if there will be surprises at the day of the bid (tender) opening and whether there is adequate funding and time allocated for the project. At this stage, a more detailed estimate of probable construction cost based on actual quantities and the prevailing bid cost of the various items will be required. It is customary to allocate some percentage (10% to 25%, depending on the complexities of the project) of the estimated construction cost to contingency and administration cost. The total project cost can be almost double or even triple the hard-bid construction cost when all costs (from project planning phase to construction closeout and routine maintenance) are taken into account.

5. Construction

A wide variety of methods are used in girder fabrication, erection, and casting. In addition, bidding, award, and delivery methods affect the construction methods. The construction procurement can also have a huge impact on the schedule and cost. In addition to conventional design-bid-build (DBB) procurement, alternate project delivery (APD) methods such as design-build (DB), engineer-procure-construct (EPC), general contractor–construction manager (GCCM or CMGC), and private-public partnership (PPP) are typically used for large bridges and for major highway segments involving scores of bridges. Schedule saving is a primary goal achieved in APD methods, where—after a certain level of preliminary design—the project can be designed, built, operated, and financed by an APD contractor (typically a consortium of contractors, designers, financiers, and concessionaires). APD methods have been used for many years in other industries; however, their application in public infrastructure has increased manifold in the last decade and will continue to do so.

Construction of girder bridges requires attention to the following:

- *Bid/tender advertisement, selection, award, and execution*—Bid advertisement and contractor selection
- *Preconstruction and mobilization*—Construction schedule, progress payments, equipment, shop drawings, material certifications, preconstruction conference, and mobilization
- *Removal and demolition*—Often used in staged construction and can be tricky
- *Delivery and erection*—Site safety, cranes, launching, etc.
- *Resident engineering and construction methods*—Cast-in-place construction using falsework, maintenance of traffic; precast and prefabricated construction using fabrication, on-site casting, shop drawings, shipping, and storage
- *Project closeout*—Record of materials, as-built drawings, final acceptance

In general, the construction of bridges requires special expertise and should be performed by experienced construction personnel. The risk mitigation of an unexpected bridge failure (due to higher probability of fatalities) is many times more costly than similar risks of adjacent roadway construction. One of the biggest causes of unbalanced bids is the allocation of construction risks between the owners and contractors. The cost and schedule penalties to amend construction problems are much higher, and some risks (e.g., foundation impacts due to uncertainly in subsurface conditions or unexpected discovery of hazardous waste or archeological finds) cannot be easily mitigated. It is best if they are shared among the owner and the contractor. It is beneficial to perform thorough constructability reviews by construction personnel at various phases of the design (e.g., preliminary design, intermediate design, and final design).

6. Preservation

Modern bridges must be designed to allow easy access to preservation activities such as inspection, maintenance, and common repair. Some design considerations for bridges for preservation activities are described in the next sections.

6.1 Provide arm's-reach inspection access

Provide ladders, maintenance walkways, cables, and access doors for full manual access throughout the bridge elements. Use current specifications of under-bridge inspection trucks (UBITs) to reach various parts of the bridge without rope-assisted climbing. For example, providing a gap of at least 7 ft (2 m) between two adjacent bridges will facilitate the UBIT arm to reach under the bridge (Washington State Department of Transportation, 2020). Not providing these essential amenities during the design phase will only increase the cost of future preservation activities multifold.

6.2 Design for rope-assisted inspection

If full manual climbing or bucket truck access cannot be provided due to cost or other site constraints, access for rope-assisted climbing must be provided. Such access can be easily facilitated by providing rope anchorage points (predrilled holes or brackets) at selected locations. Providing lifeline cables along the girders during original construction is not expensive and facilitates easier and less expensive rope access operations in the future. If access is too difficult, the bridge element is likely not to be inspected often or properly. More detailed rope-assisted work requirements have been issued by two organizations: the Society of Professional Rope Access Technicians (SPRAT) and the International Rope Access Trade Association (IRATA).

6.3 Design to account for maintenance

All bridges require routine and special repairs over time. For example, bearings and joints need replacement, drains get plugged, and the deck may eventually need an overlay. The designer should provide jacking locations for bearing replacement or repositioning, the joint style should allow for gland replacement, drains should have a cleanout pipe, and the deck should have enough clear cover over the top-reinforcing steel to allow for future scarification (up to 1 in. or 25 mm) and enough structural capacity to absorb the added weight of 2–3 in. (50–75 mm) of overlay (future wearing surface). Other future maintenance items include accounting for stream bed scour and aggradation, ability to clear river debris and ice accumulation underneath, accounting for reduction of vertical clearance due to surface overlay underneath, and added cover and protection for corrosion due to soil and climate. Most of these items are common sense, but they can be easily neglected when designing a new bridge with the idea of minimizing construction cost only.

6.4 Consider the life cycle cost of bridge

There is too much focus on the upfront cost of a construction project; the life cycle cost of bridges is often ignored. New bridges are expected to last 75–100 years, and repair, retrofit, and rehabilitation typically can extend the life by 20–40 years. During the expected life of the bridge, maintenance expenses such as painting, deck overlays, joint replacements, and scour mitigation can really add up. For example, choosing between a replacement versus repair, retrofit, and rehabilitation should be based on the life cycle cost, not just upfront costs. The general rule indicates that if the cost of rehabilitation approaches 50% of replacement, extreme caution should be taken before embarking on rehabilitation. The life of an aging bridge can be increased by reducing the number of lanes or changing the type of traffic (restricting to automobiles only, for example), and a rigid deck overlay can reduce impact loading while extending the life of the deck by 20 or more years. A simple economic analysis of the bridge (using a present worth or sensitivity analysis) can provide enough information to provide a valuable comparison of feasible alternatives.

Once a girder bridge is built, it needs to be preserved, which includes the following required elements:

- *Inspection and testing*—Types of inspection include crack inspection and fracture-critical and fatigue-prone details, testing, and instrumentation. An inspection interval of every two years is common.
- *Load rating, posting, and overloads*—Once a load rating has been performed, it needs to be updated to reflect the condition of the bridge. Special permits for bridge use by overload trucks need to be reviewed, evaluated, and permitted.
- *Bridge maintenance and management*—Preventative maintenance activities such as instrumentation, testing, repairs, overlays, widening, strengthening, scour mitigation, and seismic retrofit can play a key role in keeping girder bridges functioning. The use of bridge management practices can prioritize maintenance and repair funding.
- *Rehabilitation*—This typically involves a major upgrade to the structural capacity and may also involve retrofits (with no change in capacity), widening, and strengthening. It typically uses inspection findings and a bridge management system to prioritize work.
- *Seismic*—Vulnerability evaluation, prioritization, and seismic retrofitting to prevent collapse during a designated seismic event (for older structures not designed per current seismic codes).

7. Innovation

Innovation has been generally slow in the field of bridge engineering due to the heavy emphasis placed on public safety and the relatively long process of adapting changes to the existing code and practices by bridge owners. Girders were very quick to evolve at an early stage, but many significant innovations, such as wide-flange prestressed supergirders or high-strength welded plate girders, took a long time to develop compared to other industries. Many trends still in their infancy today may one day become the norm. Innovation will continue to change how girder bridges are planned, selected, designed, constructed, monitored, and maintained. Some of these innovations are described as follows:

7.1 Predominance of APD procurement

APD procurement of megaprojects costing billions and encompassing hundreds of bridges to be built in short duration will boost an unprecedented level of innovation in all sectors of girder bridges. APD may lead to mass girder production, new and rapid fabrication techniques, longer girder spans, the use of high-performance materials, the advent of special shipping trucks, heavier erection cranes, efficient girder shapes (Figures 15.9 and 15.12), the integration of GIS/BIM technology into CADD

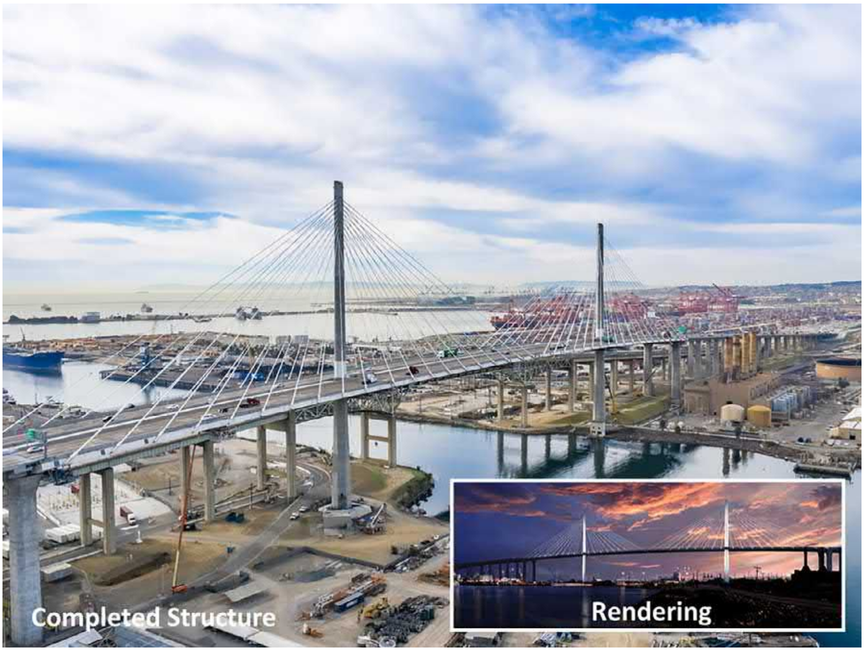

Figure 15.9 Design-build delivery of Gerald Desmond Cable-Stayed Bridge for the Port of Long Beach, Long Beach, California. Courtesy of its Design Consultants, Arup and Biggs Cardosa Associates.

design drawings, and the use of drones for remote data collection and construction monitoring. In addition, shifting of maintenance responsibilities to the private sector will lead to innovation in bridge health monitoring, jointless and low-maintenance bridges, and designing for preservation.

7.2 High-performance materials

The general trend is increasing strength and versatility of cast-in-place and precast concrete. The purpose of using higher-strength materials is not always increasing capacity but, rather, increasing structural service performance in terms of durability, imperviousness, and chemical resistivity. Similarly, high-performance structural steel continues to break new ground in terms of tension strength, ductility, and corrosion resistance. The use of new coating techniques in bridges is also evolving to make the cost of a steel bridge as a girder bridge very competitive with precast and cast-in-place concrete bridges.

7.3 Use of structural composites

Although the use of structural composites for bridges has diminished, primarily due to cost and lack of technical expertise, the promise of developing lighter-weight materials with greater strength remains. The use of structural composites in bridges, particularly in everyday girder bridges, from new construction to retrofit, has come a long way from the early testing and instrumentation phases, but more adaptation work is needed to make FRP composites comparable to other construction materials (Iyer and Bharil, 2004). The recent research shows that FRP composites can be economically designed to suit a particular environment, exact life span, and loading conditions (Bharil, 2020).

7.4 Automatic bridge health monitoring

This area is evolving fast from its experimental stages to real-life applications. The advancement in durable and less expensive instrumentation techniques, as well as remote monitoring via the Internet and wireless technology, will enable bridge engineers to understand and track bridge deterioration better. These innovations will also help bridge owners to remotely monitor damages during catastrophic events such as earthquakes and take actions to save lives and program special inspections and repairs.

7.5 Improved girder fabrication and shipping lengths

Girder fabrication and shipping lengths are improving as the trucking and shipping industry applies more modern technology to maneuver tight radii and other roadway constraints. Pre-cambering of precast girders allows for vertical clearance below, the casting cycle of concrete girders is much shorter, and steel girder fabrication is mostly automated. It is not uncommon to see a single 150-ft (45 m) precast concrete girder being shipped today, whereas only 120 ft (35 m) was the norm in the past. Megaprojects are also contributing to this trend to meet a constant demand for increasing efficiency and maneuvering longer spans to avoid traffic closures and to minimize environmental permitting constraints.

7.6 Longer Jointless bridges

Deck joints—whether due to seismic, thermal, or shrinkage demands—are a maintenance headache and generally expensive. Elimination of these joints can entail a tedious design and approval process that most bridge engineers prefer to avoid. Secondary effects can be substantial and should be avoided to circumvent new maintenance problems. In the future, more of these expensive joints will be eliminated, as jointless bridges of 1000 ft (300 m) or longer become more commonplace.

7.7 Better girder erection procedures

Modern erection methods and the use of supercranes have increased the lifting and launching weight and girder length capabilities and have reduced the construction turnaround time. The use of special machinery in lifting/moving of fully constructed superstructure (e.g., ABCD techniques) can enable the use of girder bridges at locations that were previously not possible due to low overhead clearance, constricted staging areas, environmental regulations, or heavy traffic volumes. Such innovations can dramatically increase the use of girder bridges (Figure 15.10).

Figure 15.10 Steel truss, steel girder, and concrete box girder bridges of Fullerton Road grade separation project for San Gabriel Valley Council of Governments, City of Industry, California. Courtesy of Design Consultant, Biggs Cardosa Associates.

7.8 Highly efficient girder shapes

Partnerships between precasters/fabricators and bridge engineers, researchers, suppliers, and the trucking/shipping industry have prompted the refinement of the precast concrete girder shape from a box-shaped beam to highly refined wide-flanges, bulb-tees, and supergirders capable of spanning up to 240 ft (75 m). As the demand for longer clear spans increases, the impetus to push the girder shapes beyond what is deemed possible today will continue.

7.9 Hybrid girders

Combining various materials and shapes will push the limits of spans and load-carrying capacity well beyond the classic marriage of concrete deck over steel beams. The use of new materials such as structural composites, time-proven materials such as steel, and glue-laminated timber can yield very high strength-to-weight ratios and can be cost effective as well (Figure 15.6).

7.10 Improved design codes

Nothing can have a greater impact than making refinements in current design codes, and effecting changes in the bridge owners' mindsets to push the limits of girder bridges. The codes were designed to keep things simple so that complex analyses were not required for everyday bridge designs. Codes facilitate the use of more detailed analysis, but the engineer will need to substantially expand the design effort to justify a nonstandard approach. Sophisticated software can be used to create a very efficient design, but it may not be easy for the results to pass the reviews of bridge engineering peers. Change does not come easy in this old-fashioned industry, which has served the public well for hundreds of years. The risk of litigation also keeps much innovation at bay, but the question remains: are consultants, contractors, funding agencies, and bridge owners willing to take advantage of newfound knowledge, particularly when the established codes may be ambiguous (or just silent) on those topics?

8. Conclusions

There is no doubt that the girder bridge remains the most popular form of bridge worldwide. Given this popularity, innovations will continue despite the mundane appearance of a girder form (Figures 15.11 and 15.12). Girder bridges will continue to break records in terms of span length, material strength, and longevity, resulting in slender, clutter-free systems. Innovation comes from the bridge engineering community— designers, fabricators, constructors, and bridge owners who constantly demand more, care about the impact of their work products, and challenge themselves to improve both the engineering processes and design codes to move bridge engineering practices forward.

Figure 15.11 Prestressed concrete box girders span the SR-85/SR-87 interchange in San Jose, California. Courtesy of its Design Consultant, Biggs Cardosa Associates.

Figure 15.12 California prestressed concrete wide-flange girders are widely used for California High Speed Rail Project, Design-Build Construction Packages 2 & 3, Central Valley, California, Courtesy of its Independent Design Check Consultant, Biggs Cardosa Associates.

We see and drive over run-of-the-mill girder bridges almost daily, and the bridge engineering community thus has the opportunity to make a real impact on people every day. An ugly bridge will remain an eyesore throughout its life (which can be more than a hundred years), but a beautiful, elegant, and well-constructed girder bridge will not only provide safe travel (as all bridges must) but also complement or even improve its setting. It is very easy to get lost in the everyday practice of bridge design and not look back and consider if we could have done a little better. If we can all promise only one thing to ourselves today, it is our hope that it will be that, as bridge engineers, we will never design another ugly girder bridge.

References

American Association of State Highway and Transportation Officials (AASHTO), 2020. AASHTO LRFD Bridge Design Specifications, ninth ed. Washington, DC.

American Railway Engineering and Maintenance-of-Way Association (AREMA), 2019. AREMA Manual of Railway Engineering, Structures. Vol. 2. Lanham, MD.

Bharil, R., 2020. Time-Dependent Reliability Framework for Durability Design of FRP Composites. Doctoral Dissertation, West Virginia University, Morgantown, WV.

Bharil, R.K., et al., 2001. Guidelines for bridge water pipe installations. In: Proceedings from ASCE Pipeline 2001 Conference, San Diego, CA.

California Department of Transportation, 2019. Caltrans Comparative Bridge Costs.

California Department of Transportation, Caltrans Publications, 2020. Seismic Design Criteria, SDC Version 2.0, and Memos to Designers.

Union Pacific Railroad – BNSF Railway, 2016. Guidelines for Railroad Grade Separation Projects.

Iyer, S.L., Bharil, R.K., 2004. Testing and evaluation of the FRP deck system for the Douglas County in Washington State. In: SAMPE Spring Conference Proceedings. Long Beach, CA.

Washington State Department of Transportation, WSDOT Publications, 2020. Bridge Design Manual (LRFD), Version M 23–50.13, and Washington State Bridge Inspection Manual. Version M 36–64.03.

Long-span bridges

16

M. De Miranda
Studio de Miranda Associati—DMA, Technical Director, Milan, Italy

1. Introduction

1.1 Concepts and problems of long-span bridges

The definition of the term *long-span bridge* derives from the context and the historical epoch, in terms of the limits reached at that time by the builders of bridges as large span. In Roman times, the maximum spans were in the order of a few tens of meters. At the start of the Industrial Revolution, with the first railways and roads for vehicles, long spans were in the order of 150 m.

In the 20th century, with the construction of bridges with spans exceeding 1000 m, and up to nearly 2000 m in this century, *large span* generally means a span over 300–500 m. However, spans of these lengths present problems that are mainly linked to the method of construction, aerodynamic stability, and the effect of self-weight on the bridge's static load. In fact, large span structures can be seen today as structures in which the so-called scaling law is dominant.

Scaling law was described as early as 1638 by Galileo Galilei in the *Discorsi* (Galileo, 1638); it expresses the circumstance where, upon increase of the geometrical dimensions of an object (even if the shape does not vary), the stress to which the object is subjected due to its weight increases.

A cube with side l and specific weight γ is stressed at the base with a tension of

$$\gamma \cdot 1^3/1^2 = \gamma 1,$$

which expresses a stress that is directly proportional to l, by a factor of γ.

It is for this reason that the elephant has a more massive bone structure and much wider feet than the gazelle: that is, when considering a geometric scale ratio of 1:10, if the shape remains unvaried, the pressure on the feet and the ground would be 10 times higher in the case of the larger animal. Nature has adapted by changing the animal's shape and limiting its size.

In the same way, if the same shape and material is maintained in the structures, as the dimensions increase, the stress increases proportionally. Then a larger amount of structural material is required, which in turn would lead to an increase in weight. This implies that there is a limit in the dimension of structure that is proportional to the ratio between the resistance and specific weight of the structural materials.

For a vertical tension rod of uniform cross section A, length l, and unit weight γ, the maximum stress will be

Innovative Bridge Design Handbook. https://doi.org/10.1016/B978-0-12-823550-8.00021-4

$$\sigma_{MAX} = \frac{\gamma \cdot l \cdot A}{A} = \gamma \cdot l \rightarrow l = \frac{\sigma_{MAX}}{\gamma} \rightarrow l_{MAX} = \max\left(\frac{\sigma}{\gamma}\right).$$

For a strong steel, this means

$$L_{MAX} = \frac{\sigma_{ULT}}{\gamma} = \left(1.9E6\frac{\mathrm{kN}}{\mathrm{m}^2}/78.5\frac{\mathrm{kN}}{\mathrm{m}^3}\right) \cong 24,200\,\mathrm{m}.$$

This gives the stress-weight ratio σ/γ a suggestive physical meaning.

For a parabolic rope that has span L, sag f, and section A and is made of the same material, with a uniform weight that is a good approximation if $f/L < 1/8$ (as is usually the case with bridges), the maximum tension force results:

$$T_{MAX} \cong (\gamma \cdot A) \cdot \frac{L^2}{8 \cdot f} \cdot \left(1 + \left(\frac{4f}{L}\right)^2\right)^{0.5}.$$

The second term, for a typical value if $f/L = 1/10$, is 1.08. Therefore:

$$\sigma_{MAX} = \frac{T_{MAX}}{A} = \left(\gamma \cdot \frac{L^2}{8 \cdot f}\right) \cdot 1.08 = \gamma \cdot \frac{L}{0.1 \cdot 8} \cdot 1.08 = 1.35\,\gamma L,$$

and

$$L_{MAX} = \frac{\sigma}{\gamma} \cdot 0.74 = 17,900\,\mathrm{m},$$

which is only 26% less than the vertical rod.

For a realistic allowable stress for suspension bridge cables of 650 MPa, we get:

$$\sigma/\gamma = 650\,\mathrm{MPa}/78.5\,\mathrm{kN/m}^3 = 8280\,\mathrm{m}$$

and results in the following:

$$L_{MAX} = 6127\,\mathrm{m}.$$

Considering, then, that the load supported by the rope must include the weight of the bridge deck, hangers, and the live load, and assuming that the ratio k between the total load and the self-weight of the cable must be of the order of 1.80, we get:

$$L'_{MAX} = L_{MAX}/k = 3400\,\mathrm{m}.$$

It can be seen from the previous examples that large-span structures must have, from the point of view of theoretical feasibility, the following features:

- To be built, as much as possible, using materials with a high σ/γ ratio; therefore, today, high-tensile steel is used.

- As the elements subjected to traction are not subjected to phenomena of instability, they can be used with the maximum tension and have the minimum weight for the force transmitted, so they are highly efficient.
- As a result, the large-span structures are formed mainly from high-tensile steel tension elements (that is, cables).

However, from the point of view of feasibility, a large-span structure must have a structural shape that allows it to be built safely, even when it has large dimensions.

The types of structures that have these features and thus are the most suitable for large spans are suspension bridges and cable-stayed bridges (CSBs).

1.2 Historical evolution of long-span bridges

It is interesting to give a brief history of these bridge types in order to highlight their origin, as well as present and future developments.

1.2.1 Suspension bridge

The suspension bridge has the ancient origins. Crossing a body of flowing water or a ravine using textile ropes anchored to the ends was the first archetype of a suspension bridge. The first data regarding these can be traced back to the fifth century, from Asia and Latin America.

These structures were lightweight and flexible, and they put the following two concepts into practice at the base:

- To suspend the loads on one or more ropes anchored to the ground and configured as a catenary.
- To realize the structure by laying a carrying cable from one side of the obstacle to the other and successively equipping it with secondary structures and elements.

The culture of textile rope bridges never developed in the Western world.

The first rope bridge, with a layout that is known today as cable stayed, dates back to 1615, when the Italian polymath and inventor Fausto Veranzio demonstrated an idea for military bridging supported by inclined cables in a book of inventions called *Machinae Novae* (Figure 16.1) (Veranzio, 1968). The cables were formed of iron bar chains.

It is not known if the bridge was actually constructed, but it remains the first example of a bridge supported by metal ropes.

The first iron chain suspension bridges were built in Europe in 1730–40 in Prussia and in the Brittany region of France. The modern suspension bridge was developed as a response of 19th-century engineers to the requirements that the Industrial Revolution imposed in terms of new roads, railways, and crossings. It therefore had to provide suitable tensile strength and stiffness, especially regarding the heavy and concentrated moving loads of trains. The stiffness of the structure was brought about by a stiffening beam lattice in the first bridges, which distributed the localized loads onto the ropes in such a way as to guarantee reduced deformations and angular distortions of the road surface.

The first experiences with such bridges were in the United States in the early 19th century, by James Finley in Pennsylvania. These were pioneering ventures, hindered

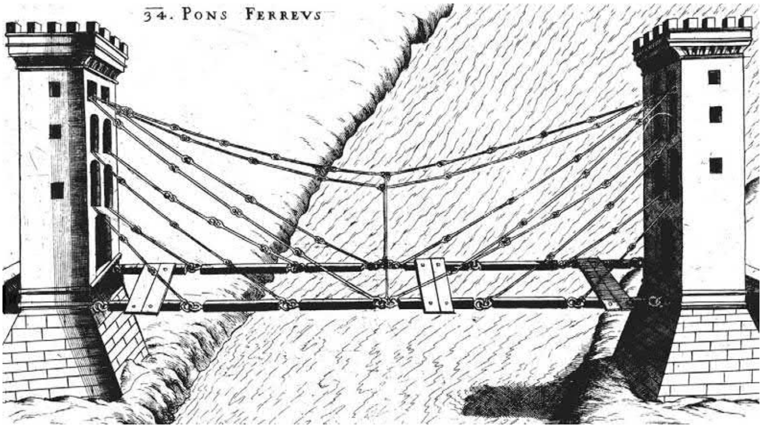

Figure 16.1 The Faustus Verantius bridge, first idea of cable-stayed bridge. It is not sure that it was actually built, although it's possible.

by several accidents, collapses, and immediate reconstructions; but these problems quickly increased the existing store of technical expertise.

In Europe, Finley's concept was released by Thomas Pope in *A Treatise on Bridge Architecture* and was developed in England starting with the Dryburgh Abbey Bridge, with a span of 79.30 m, built in 1818. This bridge collapsed six months after its construction; it was then rebuilt and stiffened with stays (Figure 16.2). This was the first integration of the two structural systems.

Other bridges followed, with increasing spans and varying technical details, in England, France, and Italy, reaching a span of 280 m with the Fribourg Bridge in 1835. This was followed by the Lewiston-Queenston Bridge in the United States in 1850 and the Roebling Bridges at Niagara Falls, New York, in 1870 with 380 m (Roebling, 1854) and the Brooklyn Bridge in 1883, with a 486-m span (Figure 16.3).

Spans increased fourfold in the 20th century. They exceeded 1000 m in 1931 with the George Washington Bridge ($L = 1067$ m) designed by Othmar Amman and Leon

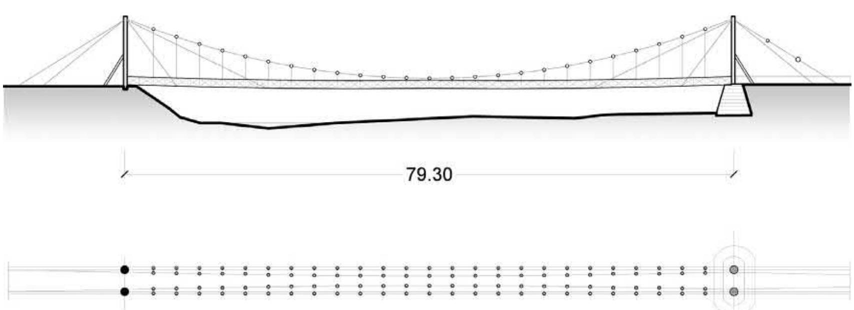

Figure 16.2 The Dryburgh bridge, first suspension bridge in Europe, successively stiffened by stay-cables.

Figure 16.3 The Brooklyn bridge, in New York, first long-span suspension bridge in America.

Moisseiff, and they continued to increase even after the Tacoma Bridge collapsed due to wind and other not fully known aeroelastic forces. Later bridges that even exceeded this length include the Verrazano Narrows Bridge ($L = 1298$ m), built in 1964, the Humber Bridge ($L = 1410$ m) in England, erected in 1981; and the Storebaelt Bridge ($L = 1624$ m) in Denmark, (Figure 16.4) and the Akashi Kaikyo Bridge in Japan ($L = 1991$ m), both built in 1998. These latter two bridges represented two completely different concepts. The Japanese bridge, with its deep and weighting lattice-stiffening girder, represented the continuation and evolution of the American way after the Tacoma event. The Danish bridge, designed by Danish engineers and built by an international pool of companies, has its slender, light, and streamlined deck that represented the evolution of the European concept of the suspension bridge, with a box-girder deck with an aerodynamically efficient shape.

1.2.2 Cable stayed bridges

After several pioneering ventures at the end of the 19th century, and the canal bridge of Tamul by Eduardo Torroja in the 1920s, the development of modern CSBs began in Europe, immediately after World War II. The first CSBs had very high, rigid girders and very widely spaced stays.

The static pattern recalled the concept of a girder resting on quite distant elastic supports, made from the stays. Examples of this type are the Donzère Mondragon Bridge in France (with a main span of 81 m), designed by Albert Caquot in 1952; the Stromsund Bridge in Sweden (182 m), designed by Franz Dischinger, opened in 1956; the Theodore-Heuss Bridge (260 m), in Mainz, Germany (Figure 16.5); and the Knie Brücke Bridge in Düsseldorf, Germany, designed by Fritz Leonhardt

Figure 16.4 (a) The longest span in the word today, the Akashi Kaykio Bridge, Japan. (b) The longest span in western countries: the Storebaelt East Bridge.

Figure 16.5 Theodor-Heuss bridge, Germany, stiff deck in steel plated girders, harp shaped stay cables, 260 m main span.

Figure 16.6 Rhine Bridge in Bonn, Germany, box girder steel deck, central stay cables, harp-fan layout.

(Leonhardt et al., 1969) and built in 1958; and the Wye Bridge in Scotland, with just two couples of stay cables for each tower.

These bridges were fashioned completely of steel, except for the Tempul reinforced concrete canal bridge by Torroja and the prestressed concrete bridges with PC cables of Riccardo Morandi.

The first bridges with a central suspension and box girder with high torsional rigidity were developed by Hellmut Homberg, including the Rhine Bridge in Bonn, erected in 1967 (Figure 16.6).

The requirement of a torsionally stiff deck girder took the consequence of deck with high flexural stiffness, and in turn the structural behavior corresponded to a girder on elastic supports, well distributed in this case due to the short spacing among the stay cables.

The setting for the development of a new conception of CSBs was an international design competition (Figure 16.7), and studies by Fabrizio de Miranda (de Miranda, 1971, 1980), which can be resumed by the following concepts discussed next.

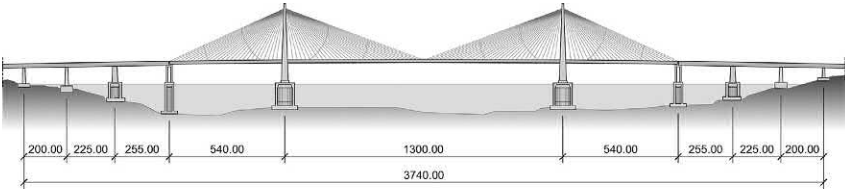

Figure 16.7 Design of a stay cable bridge for the Messina Strait Crossing, 1969, Ref. 5, Design Competition, 1300 m central span, A-shaped towers, box girder deck, cross-tie cables designed for stiffening the cable system. This design was improved in 1982 and 2016 with a central span of 2000m.

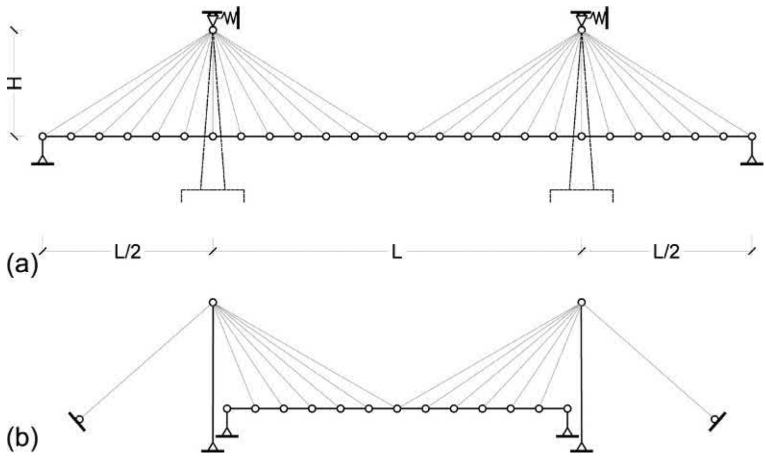

Figure 16.8 Structural systems of truss-like concept of cable-stayed bridge: statically determinate systems obtained by neglecting the deck stiffness. The equilibrium is fully insured only by axial forces in cables and deck. Two typical systems can be defined: (a) The lattice girder of Gerber type. (b) An overturned trussed arch.

By interrupting the bridge deck with articulations in the stay-coupling points, the structural layout can be seen as the large lattice girder type Gerber, a Gerber girder is a statically determinate continuous beam (Figure 16.8a) or that of an overturned trussed arch (Figure 16.8b). In both these diagrams, the diagonals (stays) reach the bridge deck starting from the top of the towers.

The static behavior of these structures is characterized by the prevalent "normal-force" status in various areas, determined by the axial stress in the stays and in the bridge deck, while the "flexure" status in the girder becomes almost secondary if the spacing of the stays to the bridge deck are closer to each other. Densifying of the stays also simplifies the construction details relative to said couplings.

These innovative concepts, together with others expressed in the first design for the Messina Bridge (1968), as well as in the design and construction of the Paranà (1970) and Rande (1973) bridges (de Miranda, 1971; Baglietto et al., 1976; de Miranda et al., 1979), started the development of a new generation of CSBs. These structures were characterized by the following features:

- Slender and streamlined bridge decks.
- Closer stays.
- A "lattice" structure, whereas the main resisting system can be idealized by a statically determinate system obtained by neglecting the low flexural stiffness of deck (that is, by ideally placing hinges at the intersection of deck cables)..
- Continuous suspension of the deck by stay cables for all bridge lengths.
- Towers laid out with inclined legs in an A shape, as proposed in the Messina Bridge.

By further developing and improving these concepts, modern CSBs have today surpassed 1100 m of free span.

Comprehensive discussions of suspension and CSBs can be found in a number of books (Podonly and Scalzi, 1976; de Miranda, 1980; Leonhardt, 1982; Gimsing, 1983; Walter et al., 1999).

2. Cable-stayed bridges

2.1 Structural principles and concepts

Basically, a CSB is a deck structure suspended by inclined cables. This suspension system can be realized in many different forms, and this leads to various structural concepts, described in the next sections.

2.1.1 Suspension system

As already mentioned, a CSB can be interpreted in two different ways:

- As a girder on elastic supports, given by the stay cables system.
- As a trusslike structure; that is, a bridge in which the equilibrium is guaranteed by a system made of elements such as stay cables, decks, and pylons, arranged in a triangulated layout and subjected to axial forces.

The first concept corresponded with the idea of replacing some support points of a continuous girder with a series of supports made of the stays. These supports were at a distance of several meters from each other and required very high and heavy girders, making assembly difficult.

2.1.2 Deck slenderness

The modern concept of the CSB has replaced the discrete distribution of the suspension points with widespread distribution, reducing the distance between the stays. In this way, the decks could be made more slender, as bending stiffness was no longer necessary to guarantee resistance and stability to the structural system, but just axial stiffness. The thickness of the deck was no longer related to the length of the central span; rather, it depended mainly on the width of the deck itself.

For example, the Rande Bridge (Figure 16.9), designed in 1970 and completed in 1977, had a slenderness (i.e., a ratio between central span and thickness of the deck) equal to 400 m/2 m = 200, when the largest CSB realized up to that moment, with spans of the order of 300 m had girder depth of 3–4 m, with a slenderness ratio of less than 100.

2.2 Structural systems

On the basis of internal restraints and restraints attached to the ground, CSBs can be realized according to two different structural systems:

- Earth-anchored system
- Self-anchored system

These will be described in the next sections.

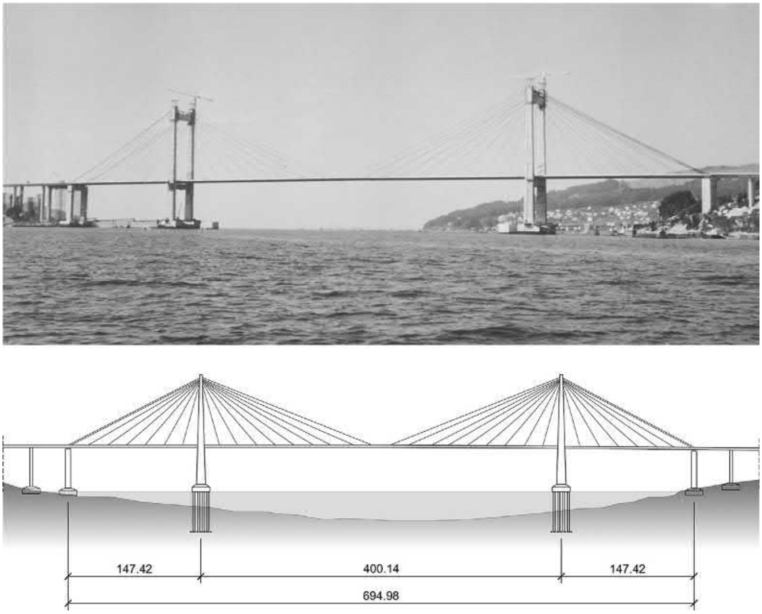

Figure 16.9 The Rande Bridge, Spain, 400 m of main span, longest span at time of design and construction, 1970–77, first composite deck cable-stayed bridge, first application of multi-strand system for stay-cables.

2.2.1 *Earth-anchored*

In the Earth-anchored bridge, the horizontal forces induced by the horizontal components of the stays are transferred to the Earth. The resulting structure is therefore a true and proper "tensile structure," as the deck girder is subject to traction and the only elements compressed are the pylons (Figures 16.10 and 16.11).

The structural system is, therefore, similar as that of classical suspension bridges, with the following relative advantages and disadvantages:

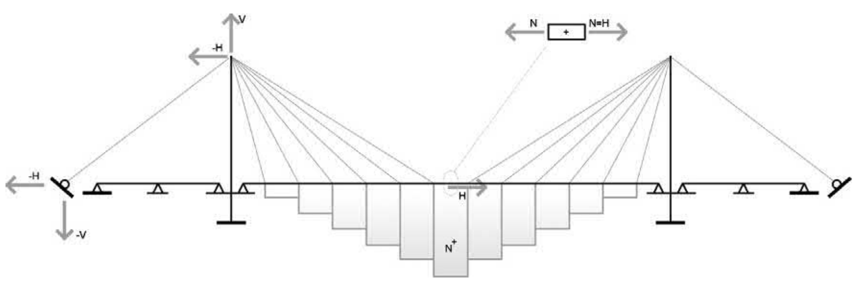

Figure 16.10 Earth anchored system: the horizontal thrust is equilibrated by the deck, in tension, and by the foundation blocks.

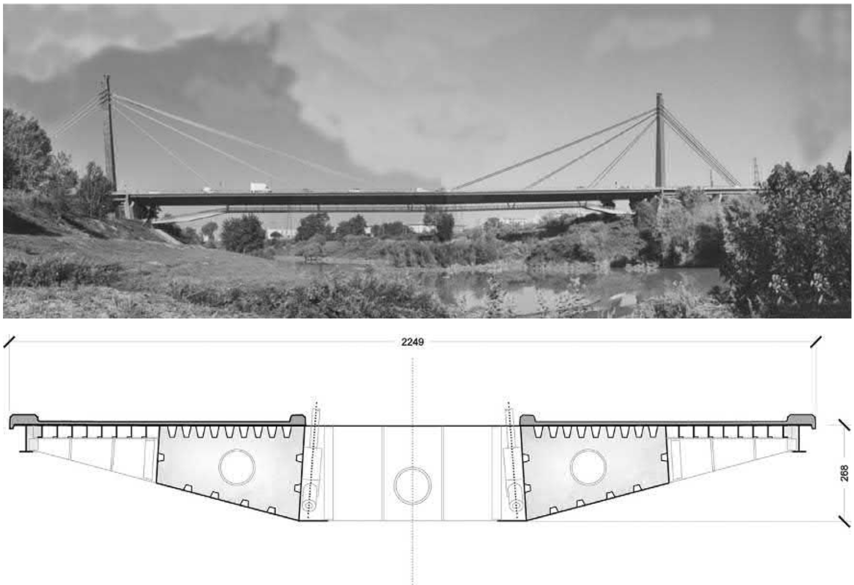

Figure 16.11 The Indiano Bridge, Ref. 6, 200 m of main span, 1968–76, first earth-anchored cable stayed bridge, first twin-deck bridge.

- The deck, in traction, is subject to positive effects of the second order, which reduces their bending moments.
- High horizontal forces must be transmitted to the Earth, and this constitutes a technical problem that is sometimes difficult, and always expensive, to solve.

2.2.2 Self-anchored

In the self-anchored bridge, the horizontal components of the stay tensions are balanced by the deck girder, which is therefore subjected to compression (Figures 16.12 and 16.13).

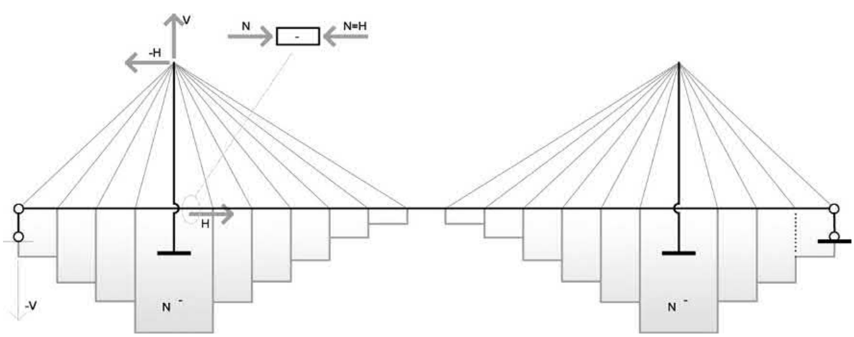

Figure 16.12 Self-anchored system: the deck only, in compression, equilibrates the horizontal thrust.

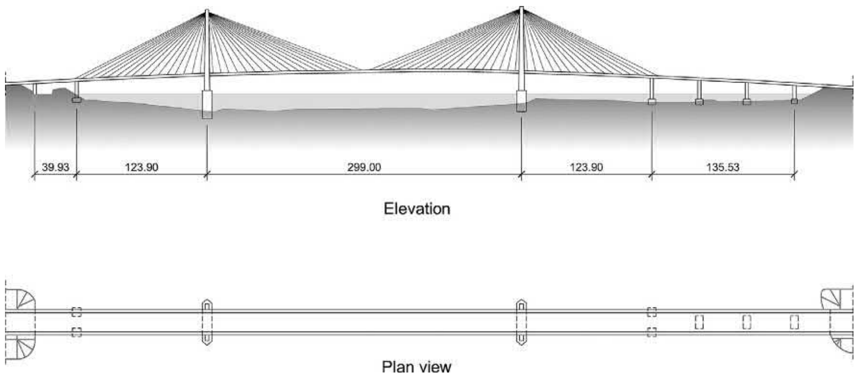

Figure 16.13 Pasco-Kennewick Bridge, Ref. 29: first long-span, slender concrete deck, cable-stayed bridge in America, self-anchored. The horizontal thrust is equilibrated in a really economical way by the concrete deck.

This compression induces negative effects of the second order, as the bending moments tend to increase. But the great advantage of the self-anchored bridge consists in the absence of horizontal reactions to the Earth due to the effect of vertical loads acting on the structure.

Moreover, as we will see later in this chapter, this system allows for the realization of the construction using the progressive symmetrical cantilevers method (i.e., one of the most simple and effective construction methods), which has been the main reason of the success of the CSB in the medium- to large-span field.

2.3 Cable configuration

The positioning of the cables in CSBs can follow two different basic configurations:

- Fan (Figure 16.14)
- Harp (Figure 16.15)

In the fan layout, the stays are anchored to the upper end of the pylons and branch in various ways toward the deck. In this way, the main structure is effectively a lattice, formed from a series of triangular links, in which axial action prevails.

If articulations should occur or be formed in the nodes, equilibrium would be guaranteed by the main lattice system. The result is a highly efficient structure, whose structural dimensions can be set at minimum values.

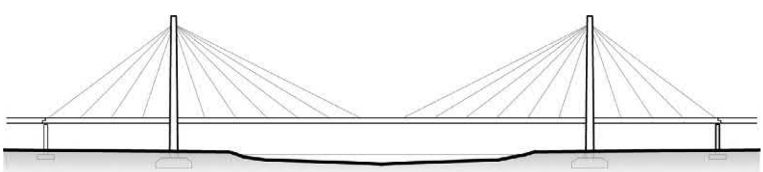

Figure 16.14 Fan configuration: forces are transferred by a clear truss behaviour, minimum weight, maximum stiffness.

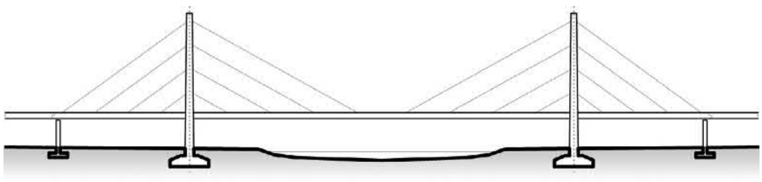

Figure 16.15 Harp configuration: high stiffness of deck or towers are required for transferring of forces by bending; equal inclination of the stay cables leads to very ordered visual image.

In the harp layout, the stays are anchored along the pylons and are parallel. The bending moments in the pylon toward the calibration of the tensions in the stays can be eliminated for permanent loads. This is not possible for mobile loads, however, and the pylons and the deck are greatly stressed by bending.

In reality, these moments can be eliminated with the introduction of intermediate supports in the back spans (Figure 16.16). Otherwise, the deck or girder or both are subjected to the combined action of compression and bending moment and require greater stiffness and thickness than the case showing the fan configuration.

However, the fan layout leads to a high concentration of stress at the top of the pylons. This consequently creates difficult technical problems that must be solved. Therefore, in many cases, it is preferred to distribute the upper anchorages of the stays, placing them at short distance on the upper pylon.

The result is an intermediate configuration between the two described previously. This is called *harp-fan,* and it maintains the advantages of the fan structure to the extent that the distribution of the upper anchorages is compact (Figure 16.17).

Two planes of stays are typically envisioned in the transversal plane, which suspend the deck at the two transversal ends. In this case, the deck can be very slender and simple from a construction point of view and does not require great torsional stiffness.

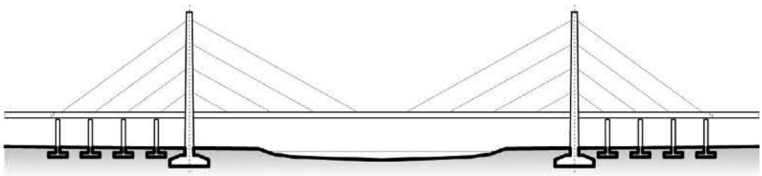

Figure 16.16 Harp configuration with side piers; main forces are transferred by truss behaviour: deck and towers can be slender.

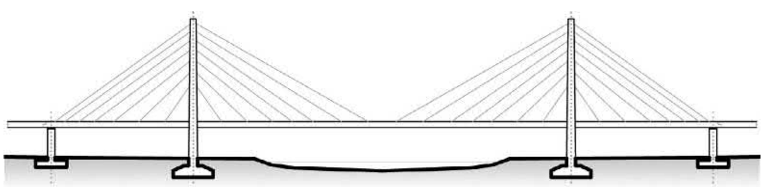

Figure 16.17 Fan-Harp or Semi-Fan configuration: anchorages on top of pylon, shared on a certain length, can be simply detailed.

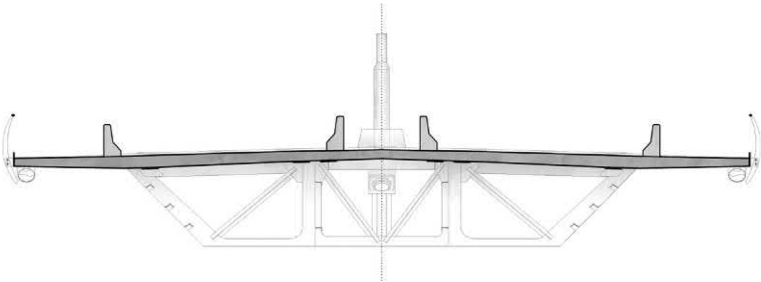

Figure 16.18 Box girders cross sections for central suspension of cable-stayed decks.

Several planes of stays can be realized for very wide decks. By envisioning box-shaped girders under torsion, the deck can be suspended via just one central plane of stays (Figure 16.18).

In this case, high torsional stiffness is typically accompanied by significant bending stiffness, and as a consequence, bending moments are high due to the effect of the mobile loads. The result is more complex and often heavier decks than in the first case. The requirement of high torsional stiffness calls for a great girder depth and higher aerodynamic drag, which makes this configuration less adapt for large-span bridges.

For long spans, the best layout comprises two planes of stay cables anchored at the top of A-shaped pylons in order to get the maximum torsional stiffness of the deck and thus increase its aerodynamic stability.

2.4 Structural elements

The main structural elements of CSBs are as follows:

- Decks
- Pylons
- Stay cables

These will be discussed next.

2.4.1 Decks

Decks can be realized entirely in steel, entirely in concrete, or as a steel-concrete composite structure. Generally, the concrete solution is the most convenient for spans up to approximately 250 m. The composite structure can be used successfully in all spans up to about 600 m, but it adapts well to spans from 200 to 500 m (i.e., crossings of large rivers). The steel solution is the most expensive, but it is also the most suitable for bridges with spans exceeding approximately 500 m (that is, for long-span bridges).

Bridge deck (Figure 16.9a) with two planes of stays are realized effectively with two lateral girders, a series of cross-members with pitches varying from 3.50 to 7.00 m, and one slab in a concrete or orthotropic deck. Aerodynamic fairings, improving aerodynamical stability, and reducing drag, can be required for larger spans or higher winds (Figure 16.19b and c, and see de Miranda and Bartoli, 2001). The decks

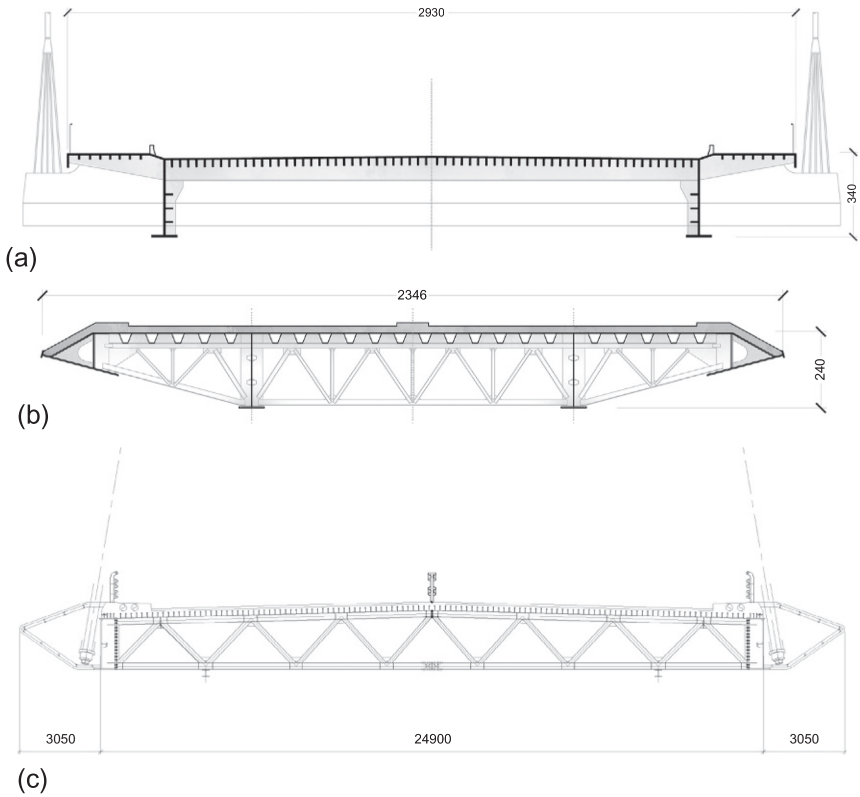

Figure 16.19 Typical cross sections for side suspension of deck: (a) Kniebrucke; (b) Rande Bridge; and (c) Higuamo Bridge.

of bridges with a unique central plane of stays are always realized with a central box girder; two lateral overhangs are usually envisioned with variable length from 2 to 8 m. Bridge decks, mainly for longer spans, must be streamlined, with minimum depth and good aerodynamic properties (Figure 16.19b). This not only reduces the wind drag and increases the deck flutter stability, but also reduces vibration amplitudes in the deck so it can withstand vibrations of the stay cables.

2.4.2 Towers

Like decks, towers can be realized in steel, concrete, or in a steel-concrete composite. Typical configurations are illustrated in Figure 16.20.

The main technical problems are related to the upper part of the pylons, where very high vertical loads must be transferred in a limited space to the tower shaft and the horizontal components of the stay cables have to be equilibrated. Towers are not only a fundamental structural element, but they become the main aesthetical element in a CSB. For this reason, their design is a difficult, challenging task of integrations of structural/engineering statements and aesthetical/architectural aspects.

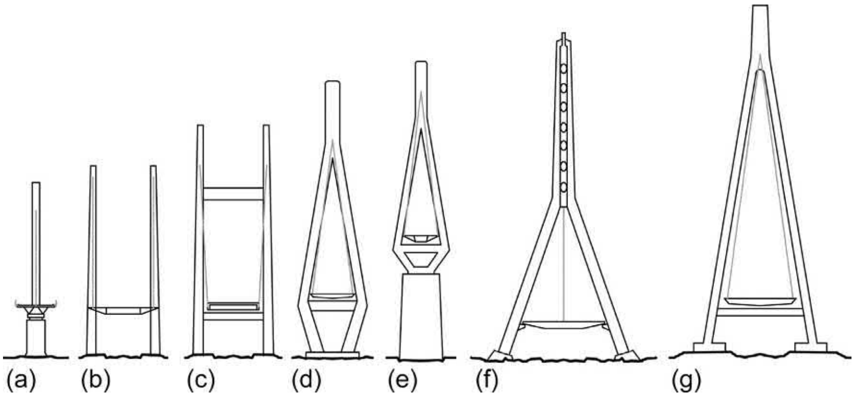

Figure 16.20 Types of towers for cable stayed bridges.

2.4.3 Stay cables

Stay cables are the main and more special elements in this type of bridges. Their behavior, and mainly their axial stiffness due to the sag effect, are nonlinear. The nonlinear axial stiffness can be taken into account in an effective engineering form by the equivalent Ernst modulus (Figure 16.21).

The following types of cable are mainly used (Figure 16.22):

- Locked coil rope
- Parallel wire cables
- Parallel strand cables

Solid bars and twisted ropes are used less frequently today.

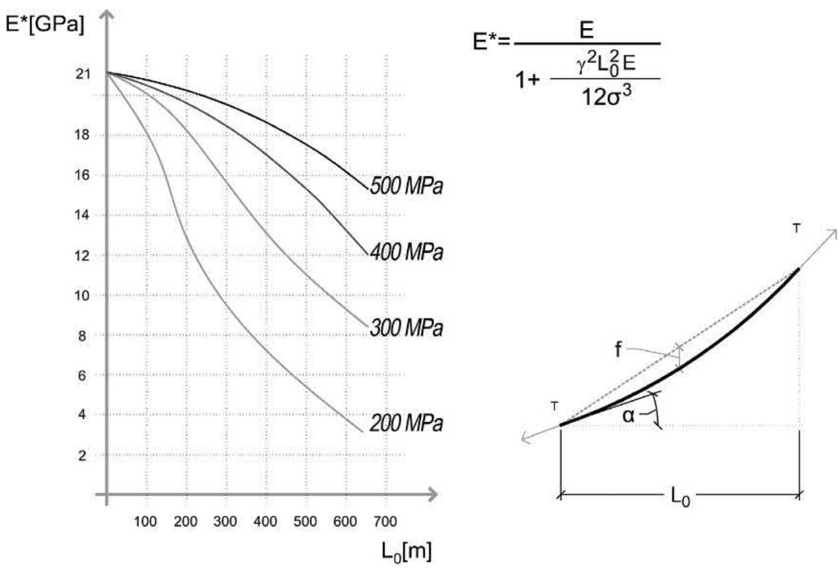

Figure 16.21 Equivalent Elastic Modulus for stay cables.

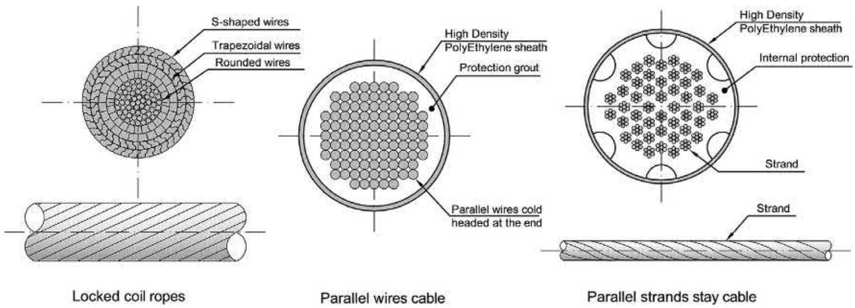

Figure 16.22 Typical cross sections of stay cables.

The locked coil rope system was used in the first German CSBs, and it is still used today, especially for bridges with small and medium spans. The advantages of prefabrication and the consequent high executive quality are balanced by the difficulties regarding transport and installation of these very long elements (which, for larger bridges, may weigh a great deal).

Cables with parallel wires are very stiff and have high resistance to fatigue and low aerodynamic resistance and therefore, except for the difficulty of installation of the large prefabricated elements, they are suitable for bridges with large spans. Cables with parallel strands, in which the strands are installed on site one after the other, are currently the most popular system just by virtue of their easy installation, which requires light and easy tensioning in the cantilevered construction.

The design of stay cables is influenced by four main aspects: strength, fatigue, durability, and aerodynamic stability, listed in order of increasing severity. In fact, strength aspects are well addressed, knowledge is sufficient, and the codes seem to cover all aspects. Fatigue, although there is more uncertainty, is a clear issue from a design point of view, even if the uncertainties of aerodynamic aspects must be taken into account. The durability of stay cables, related to frequent lack of proper inspection and maintenance, is an important issue that requires more research.

Although much knowledge has been acquired over the last decades, the aerodynamic stability of stay cables still presents some degree of uncertainty. This instability is basically due to direct aerodynamic sources, such as:

- Von Karman vortices
- Wake galloping of closely spaced cables
- Buffeting, induced by wind turbulence
- Galloping of inclined cable, or ice accumulation
- Rain/wind induced vibration

In addition, there can be dynamic sources, like cable excitation due to deck/towers vibration from wind or traffic.

The aerodynamic causes depend on the wind actions on the cables. The parameters involved are:

- Wind speed V
- Cable diameter D

- Cable damping c, ρ
- Cable unit mass m

Their relative influence can be studied by looking at the dynamic equilibrium equation:

$$\ddot{y} \cdot m + \dot{y} \cdot c + y \cdot k = F(V(t), D),$$

where

y = transverse displacement of cable
k = stiffness of cable, inversely proportional to its length: $k \, \alpha \, L^{-1}$
c = damping.

Also, it can be seen that the response y to wind action F are directly proportional to V, D, and L, and inversely proportional to c and m.

The nondimensional Scruton number takes most of these factors into account:

$$Sc = \frac{m \cdot \left(\frac{c}{c_{CR}}\right)}{\rho \cdot D^2}.$$

In order to avoid cable instability, the following empirical/experimental criteria were proposed:

- Von Karman vortices usually induce small oscillations and the inherent damping of stay cables results sufficient.
- Wind/rain oscillations can be kept small enough if
  $Sc \geq 10$ for smooth cable surfaces
  $Sc \geq 5$ for cable surfaces with helical ribs or protuberances that can prevent the stabilization of rain rivulets on the cable

According to this criteria, for Sc lower than 5, an additional damping system should be provided in most stay cables, independently of their length. Since the vibration of cables that are shorter than approximately 100 m is rare, the Sc criteria should be used only above this length threshold.

- Wake galloping of closed-spaced cables and dry galloping of inclined cables occurs (PTI, 2007) only above a critical speed of

$$V'_{CR} = (25 \div 80) \cdot f \cdot D \cdot \sqrt{Sc}.$$

Further investigations (FHA, 2007) showed that this statement is too conservative for real stay cables, and that, if Sc is greater than 3 and if the criteria for wind/rain vibration are fulfilled, no risk of dry galloping occurs.

The last cause of vibration is the forced oscillation of the cable ends. This effect does not depend on aerodynamic effects on cables and is often more difficult to control.

In this case, there are two control criteria:

- To increase damping of the cable
- To tune the cable frequencies in order to avoid the range of forcing frequencies

The increase of damping, for this and other instabilities, can be achieved in various ways:

- By installing internal dampers between the cable and the protection pipe, which can be made by high-damping elastomers and viscous or friction dampers
- By installing tuned mass dampers on the stay cable
- By installing external hydraulic/oil/viscous fluid dampers

The change (typically an increase) in the cable frequencies can be achieved by means of cross-cables, or cross-ties, or "aiguilles," interconnecting the stay cables in various ways.

The idea of introducing cross-cables connecting the main stay cables was first proposed by Fabrizio de Miranda, who patented the system (de Miranda, 1969) in the previously mentioned design of a CSB for the Messina Strait Crossing. The purpose of the cross-cables was mainly to reduce the sag effect of the longest cables in order to increase their stiffness. These cables can accomplish this very well, but also intuitively, to reduce their tendency to move and vibrate.

Later, the first experiences of cross-ties with the purpose of stabilizing vibrating cables occurred with the Stormsund Bridge in Denmark in 1971 and later in Japan. And more recently, cross-ties have been used in many large bridges which, after their opening, presented excessive cable vibrations, like the Dames Point Bridge and the Pont de Normandy.

Cross-ties segment the free length of the stay cables, in the cable planes, increasing their first vibration frequencies and adding damping to the system due to interference due to the connected cables vibrating at different frequencies. Research on optimal cross-tie configurations is in progress, but cross-ties have already proved to be effective, and they are the most efficient way of counteracting the vibration of cables in very long-span bridges.

2.5 Analysis and design

The analysis of a CSB is divided into three different phases:

- Equilibrium conditions for permanent loads
- Construction phases
- Analysis of the structure in service

The first phase defines the forces to be applied to the stay cables at the end of construction such that:

- The deck will have design geometry and present a design distribution of bending moments, usually as uniform as possible.
- The tower will stay vertical; i.e., in equilibrium under the action of the horizontal components of the stay cables from side and central spans. (Figure 16.23).

This phase defines the initial state of the bridge.

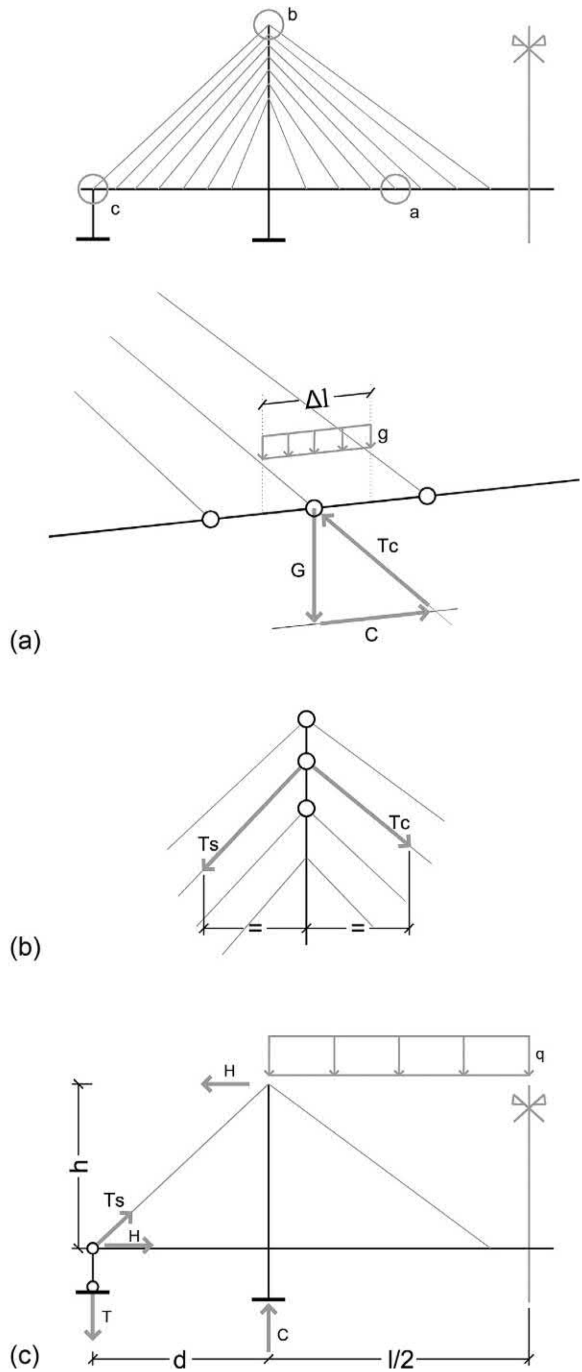

Figure 16.23 Equilibrium conditions and pre-design fundamental equations of stay-cables of a three-span self-anchored cable stayed bridge. (a) Stay cable-deck equilibrium: define design forces in main span stay-cable. (b) Horizontal equilibrium of side-spans and central span stay cables: define the side spans cables. (c) Global half-central span rotational equilibrium: define design forces in tie-down and anchor cables.

The second phase defines the forces to apply to the stay cables and the precambers to apply to the deck so that:

- The deck under construction will be in a safe condition: i.e., checking of the bending moments in deck and towers and forces in stay cables.
- The final force distribution in the stay cables and the final bending moment distribution in deck and towers will be that defined in the initial-state analysis.
- The deck profile will be the design geometry at the end of all construction phases.

The third phase is the elastic, linear, and nonlinear analysis for all in-service load conditions: live load, wind, earthquake, temperature, etc. Although FEM methods are used for the final checks, the design phase can utilize equilibrium handmade analysis and the result of useful closed-form formulations.

Bending moments in the deck girder (Figure 16.24) are inversely proportional to the deck stiffness since they are related to the imposed deformation of the cable system; for a three-span fan-shaped CSB, they were calculated in closed form by a differential equation (de Miranda, 1980); the maximum value at midspan can be estimated by the following equation:

$$M(L/2) = 0.165 * q * \sqrt{4 \cdot E \cdot J \cdot d \cdot \Delta},$$

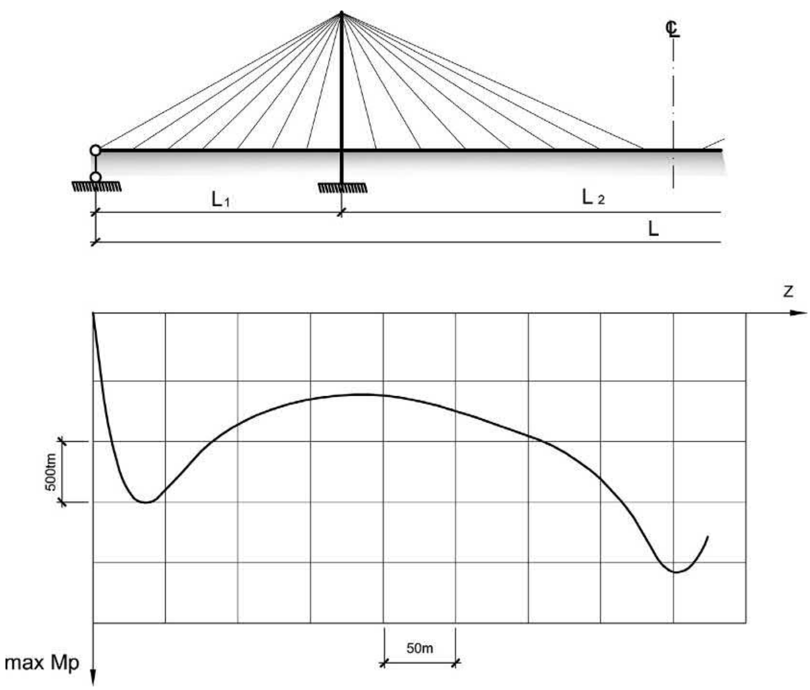

Figure 16.24 Typical bending moment diagram in deck of three spans cable-stayed bridge with slender deck and continuous suspension.

where

q = live load per unit length
E = elastic modulus of deck
J = deck moment of inertia
Δ = spacing of the stay cables
d = maximum flexibility of the cable system for a unit-concentrated load, given by

$$\frac{N_b^2 \cdot s_b}{E_b^* \cdot A_b} + \frac{N_m^2 \cdot s_m}{E_m^* \cdot A_m} + \frac{N_g^2 \cdot s_g}{E_g \cdot A_g},$$

where

N = element force
s = element length
E^* = Ernst modulus
A = element area
Cable index m = midspan cable
b = back cable
g = deck girder

The circular frequency of the first vertical mode of the deck can be estimated in a very synthetic manner still, for a three-span bridge and neglecting the deck stiffness as reasonable for long-span bridges (Wyatt, 1991). If C is a function of geometric ratio, and for $L_{SIDE}/L_{MAIN} = 0.36$ and $H/L_{MAIN} = 0.22$, $C = 1.3$. If h is the pylon height above the deck, σ is the average stress in cables for permanent loads, and g is gravity acceleration, the following results:

$$\omega^2 = C \cdot E \cdot g \cdot h / \left(\sigma \cdot L^2{}_{MAIN}\right).$$

CSBs have a very wide variety of structural systems, shapes, and technologies that make this bridge type conducive to strong innovations and development all over the world. In the last 25 years, the main span lengths have increased by a factor of 2. Remarkable long-span CSBs in the last 15 years have been the Pont du Normandy, France (built in 1995, 856 m), Tatara, Japan (built in 1998, 890 m), Sutong, China (built in 2008, 1088 m) and Stonecutter, Hong Kong (2009, 1018 m).

The longest span of a CSB today belongs to the Vladivostok Bridge, at 1104 m, which was built in 43 months and completed in July 2012 (Figure 16.25; also see SK Most, 2012).

2.6 Construction methods

The following procedures are typically adopted:

- Installation with provisional supports, which includes:
- Installation of the deck on temporary supports, with possible longitudinal launching
- Erection or construction of the towers
- Installation and tensioning of the stays

Figure 16.25 Vladivostok bridge, the presently longest span cable stayed bridge.

This procedure is necessarily adopted for Earth-anchored type decks, but it also can be used for all bridge types, provided there is easy access for the deck propping. Therefore, it is not suitable for long-span bridges.

- Installation by progressive cantilever (Figure 16.26), which includes:
- Realization of the towers
- Lifting off the ground and installation (or assembly on site) of the segments of deck, proceeding symmetrically from the piers
- Progressive installation of the stays, in parallel with the assembly of the segments
- Key joints between the two half-bridges

This procedure is adopted when it is not possible (or inconvenient) to install provisional supports. It is the typical procedure for self-anchored CSBs, and is also suitable for long-span bridges.

A detailed description of the construction of two bridges by cantilever method are given by de Miranda (2001, 2003).

- Longitudinal launching of the entire bridge, which includes:
- Preassembly on deck scaffolding, tower and stays of each half-bridge on the access abutments
- Longitudinal translation of the two half-bridges to the final position and subsequent closure in the key
- Launching by rotation, which includes:
- Preassembly on deck scaffolding, antenna, and stays on each half-bridge perpendicular to the alignment of the definitive deck
- Rotation of about 90° of each half-bridge around a vertical axis, coinciding with the axis of the mast, to reach the final position and the subsequent closing in key

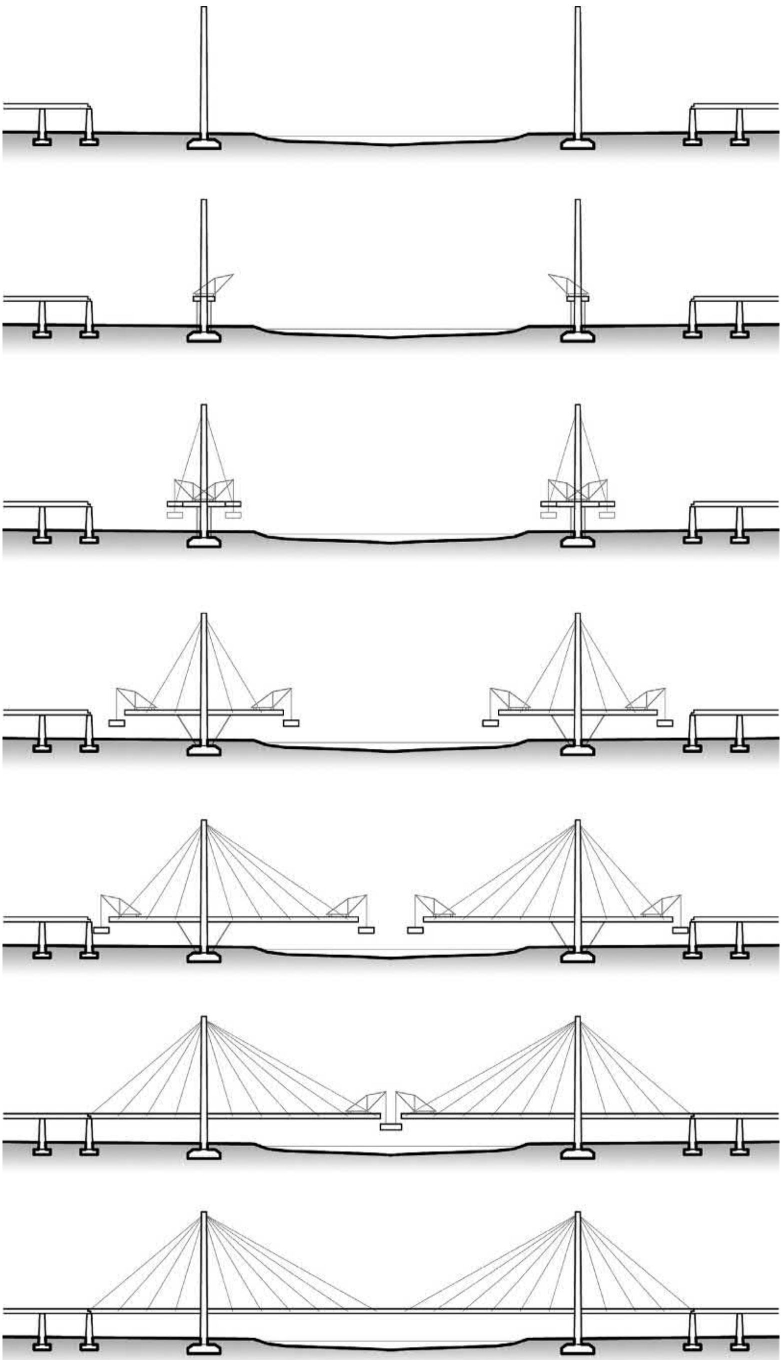

Figure 16.26 Typical erection procedure by balanced symmetrical cantilevering of a CSB. A temporary bracing system by means of bottom counter-stays is shown.

The procedures outlined here, described with reference to typical three-span bridges with two towers, are generally also applied to bridges with a single antenna or multiple spans.

For bridges with span over 200 m, the progressive cantilever is typically the most affordable system, so it is generally used. For long-span bridges of the earth-anchored type, a progressive assembly of the segments of deck is possible, starting from the center line of the central span and proceeding to the towers.

3. Suspension bridges

3.1 Static principles and structural form

As stated previously, in a suspension bridge, the deck is sustained by means of vertical or subvertical cables and by one or more parabolic main cables supported by vertical pylons. The following points are key:

- The main cables take the profile of the funicular curve of the loads applied to them. The funicular curve of the cables self-weight is a catenary.
- The funicular curve of the weight of deck is a second-order parabola. The actual cable profile is a curve that will stay between these two, and also, for small sag/span ratios, stays very close to the parabola.
- The suspenders, or hangers, simply transmit the load from the deck to the main cables.
- The deck has the simple function of transferring self-weight and live load to the hangers. Therefore, if its function were limited to this purpose, it can be very light and slender.

The main cables, being shaped like a funicular curve, generally have low stiffness for localized loads, related mainly to second-order effects. Therefore, excessive slenderness, and in turn excessive flexibility of the deck, lead to large displacements under localized loads, as well as aerodynamic instability. For this reason, the deck structure also has the function of stiffening the entire structure, and it is assigned the correct stiffness in the design phase.

3.1.1 Self-anchored versus earth-anchored

Similar to the CSBs, the main cables of a suspension bridge can be anchored to the ground or to the deck girder. The first case is the classical configuration, which has the following advantages:

- The construction can be realized without intermediate supports, since the main cables can be installed before the deck and this can be erected by suspending its segments to the cables.
- The second-order effect given by the tensile force in the main cables increases system stiffness and reduces the bending moments in the deck.

The disadvantages of Earth anchoring occurs in the difficulty of anchoring very large horizontal forces, which amount to hundreds of thousands of tons and are usually applied meters above the strong layers of soil. The self-anchored suspension bridge removes this last difficulty, transmitting only vertical loads to the soil.

Inversely, construction is more difficult—at least for long-span bridges—since the deck must be present when the cables are installed. Therefore, the deck must be erected on temporary supports. Furthermore, the positive second-order effects due to the tension in main cables are fully compensated by the negative second-order effect of the compression force on the deck. The latter forces are typically very high, meaning the deck structure must be strengthened.

For long-span bridges, the Earth-anchored system is usually more convenient.

3.1.2 Cable layout

The main cables can be arranged in many configurations, according to the dimensions and number of the spans to be crossed (Figure 16.27). The typical sag/span ratio is in the order of 1/8 ÷ 1/10; a deeper profile gives economy of cable steel, while a tight profile gives greater stiffness and fewer deck bending moments.

In order to reduce system flexibility for asymmetrical load conditions (i.e., those giving maximum displacement), a link between the main cables and the deck at midspan is very useful: the horizontal movement of cables is prevented and, in turn, the vertical displacements are reduced.

The hangers are usually vertical. However, it is possible to incline them in order to form a trussed layout. In this way, they tend to behave like shear-resistant structures in which the inclined cables, pretensioned by the deck self-weight, act as the diagonal of an ideal truss structure.

The positive result of this is a stiffer structure. The disadvantage, however, is an increase in the stress range in the hangers, which increases fatigue.

3.1.3 Deck

The deck structure is usually of an orthotropic plate type; for smaller spans, it can be a concrete slab. Deck girders basically come in three types:

- Truss structure
- Plate girder
- Box girder

The trusslike girder was chosen by American engineers when building bridges until 1970 in order to give great stiffness to the whole structure while maintaining relatively low aerodynamic drag.

For the longest spans, the weight of steel is higher than for other systems.

The longest suspension bridge in the world today, the Akashi Kaikyo (Figure 16.28; also see Kashima, 1998), has a truss-stiffened girder.

Plate girders allow the lighter and simplest structural system. But its disadvantages are that its aerodynamic behavior is worse than that of a streamlined box girder, relatively low flexural stiffness and, mainly, very low torsional stiffness. Nevertheless, the use of aerodynamic fairings can improve their aerodynamic performance, and a bottom bracing can improve torsional stiffness.

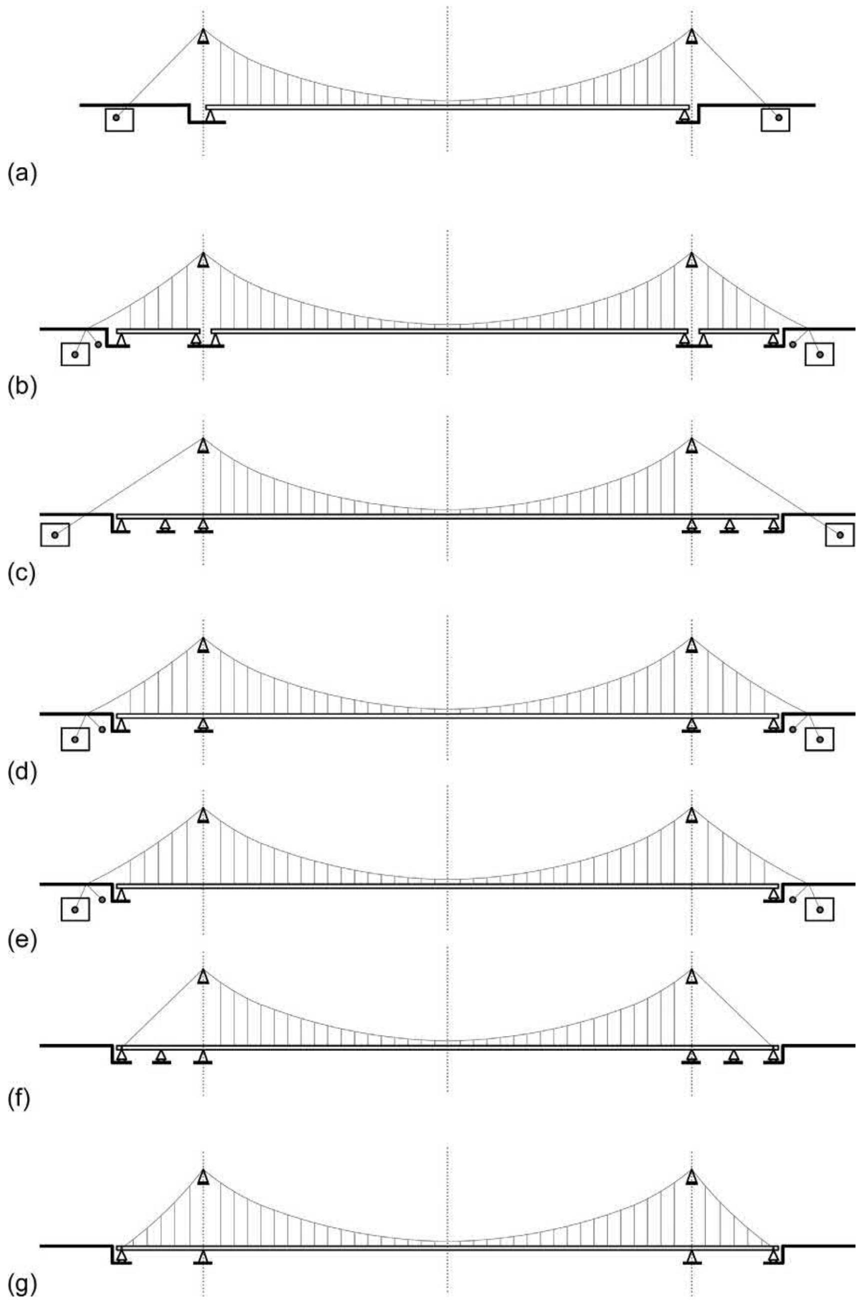

Figure 16.27 Different types of suspension bridge configurations: (a) simple span; (b) three spans simply supported; (c) continuous deck, side spans earth supported; (d) continuous three spans, fully cable supported; (e) continuous suspension between anchor blocks; (f) self-anchored central span cables supported; and (g) self-anchored three spans cable supported.

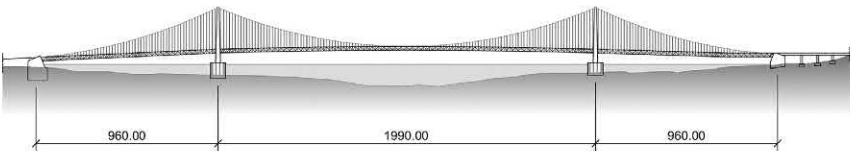

Figure 16.28 Akashi Kaikyo bridge, with deep but transparent truss stiffening girder, simply supported spans. Layout and erection phases.

Box girders, which have a streamlined-aerodynamic profile, apart from a relatively high fabrication cost, present many advantages, just like the deck of suspension bridges, as follows:

- Flexural and torsional stiffness are high.
- Aerodynamic drag is low.
- Aerodynamic properties of the cross section, related to the flutter stability, are good.

However, the aerodynamic stability for a classical box girder suspension bridge depends on its first-mode torsional frequencies, and therefore on its main span length. For very long spans (i.e., >1600 m), or for very high design wind speed, the stability of a single box girder would not be good enough.

Splitting the deck into two streamlined box girders increases flutter stability greatly. This circumstance was observed in the wind tunnel tests of the Indiano Bridge in Florence, with a double box-girder deck, at the National Physical Laboratory (NPL), London, in 1970, and later formalized by Richardson (1984).

The higher stability of decks with central openings, however, was already out looked by Farquharson (1950–1958) in the wind tunnel tests in 1950, and put in practice in the Mackinac Bridge in Michigan by David Steinman in 1965.

3.1.4 Pylons and anchor blocks

The pylons of suspension bridges (Figure 16.29) can be steel structures, as is usually the case for U.S. and Japanese bridges, or concrete structures, like the Storebaelt Bridge. Concrete structures are typically more economical, at least in areas of low seismicity and with good soil conditions.

The tops of pylons have to accommodate the cable saddles, where practically all the load of the half bridge is concentrated. The anchor blocks, always set in concrete, have the purpose of transmitting both vertical and horizontal forces to the soil, transferred by the cable anchorages. They are massive structures, which contribute to much of the total cost of the bridge, as well as lengthening construction time.

3.2 Analysis: Special aspects

The global analysis includes static and dynamic analysis, linear and nonlinear aeroelastic checks, and examining the stability of the tower cables and deck. This analysis includes the local stress and fatigue checks of the elements of the deck, as well as checking the local forces on cables, transverse forces at saddles and hanger clamps, and bending moments localized in the vicinity of saddles.

3.2.1 Analysis for vertical loads

The classic theme in the analysis of suspension bridges consists of determining the state of deformation and stress of the cables and the stiffening girder of the bridge deck, taking into account the interaction between them. Starting in the early 19th century, basically, three theories have been developed: first was the theory of Rankine (1869), which was simple but only approximate, then the first-order theory (elastic theory), by Ritter, Levy, and Melan, which leads to correct results at the first order

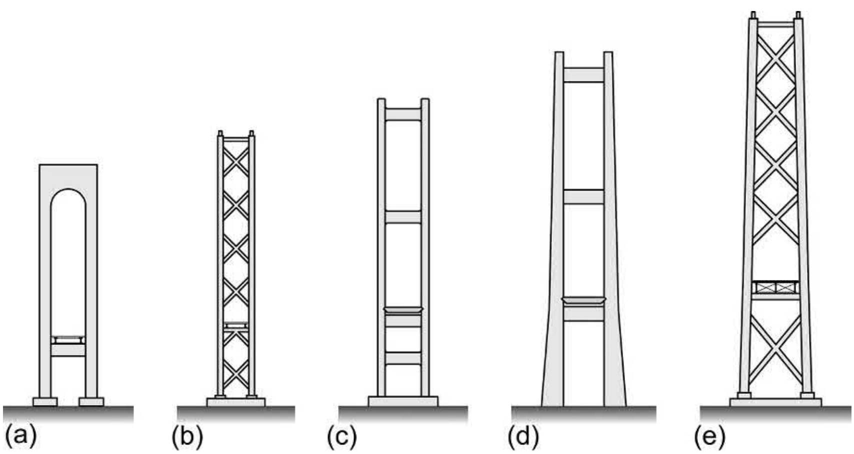

Figure 16.29 Typical layouts of suspension bridge towers, in size ascending order. (a) simple frame; (b) multiple frame; (c) trussed; (d) stain lined frame; and (e) stain lined truss.

for self-anchored bridges, and precautionary but acceptable for bridges with very stiff girders. Finally, the second-order theory (i.e., deflection theory), expressed by Mélan (1888) and firstly applied by Moisseiff and Lienhard (1933), which made it possible to obtain accurate results for bridges with deformable decks and, in essence, made it possible to realize the modern long-span suspension bridges.

Geometry and forces for permanent loads

We typically assume that the stiffening girder appears devoid of bending moments at the end of construction, and therefore, the shape of the cable corresponds to the funicular of applied permanent loads. This is actually achieved by proper erection procedures.

The geometry of the cable in the central span, with distance L between the ends of the cable and sag f, is defined by the following function:

$$y(x) = M_o(x)/H = \text{ordinate axis of the cable,}$$

where

$$H = M_o(L/2)/f$$
$$= \text{horizontal component of the cable force for permanent loads, and}$$

$$M_o(x) = \text{moment of permanent external loads on a beam in simple support of span } l.$$

In the case of the permanent p load uniformly distributed, on a beam of span L, we get:

$$\mathrm{y} = 4f/L^2 \cdot (L - x) \cdot x$$

and

$$H = pL^2/8f.$$

Geometry and loads for moving loads

The differential equation of vertical equilibrium of deck, in the theory of second-order, can be written in the following form:

$$p = EJ\frac{d^4y}{dx^2} - h \cdot \frac{d^2y}{dx^2} - (H+h)\frac{d^2y}{dx^2},$$

where h represents the variation of the horizontal component of the force of the cable due to the movable load.

The last term of the equation, which depends on the variation of load applied to the beam because of the tension in the cable produced by the change of geometry, is neglected in the first-order theory, which then provides acceptable results when:

$$(H+h)\cdot\frac{d^2y}{dx^2}\text{ is negligible compared to the term}: h\cdot\frac{d^2y}{dx^2},$$

which happens to girders with very stiff decks.

This equation can be solved through different methods for succesive iterations, and the bending moment in deck girder can then be expressed by

$$M = M' - hy\ (\text{first}-\text{order}),$$

$$M = M' - hy - (H+h)v\ \ (\text{second}-\text{order}),$$

where M' represents the moment of moving loads on a simply supported beam of span l.

It may be noted that in a generic section of the deck, the bending moment is equal to the product between the horizontal component of the cable force and the displacement between the actual deformed configuration of the cable and the configuration that it would assume in the absence of a deck; that is, the funicular of the external forces (Figure 16.30).

In the first approximation, if we consider, instead of the actual deflected profile, the configuration that the cables assume for the action of permanent loads, we obtain the results of the theory of first order.

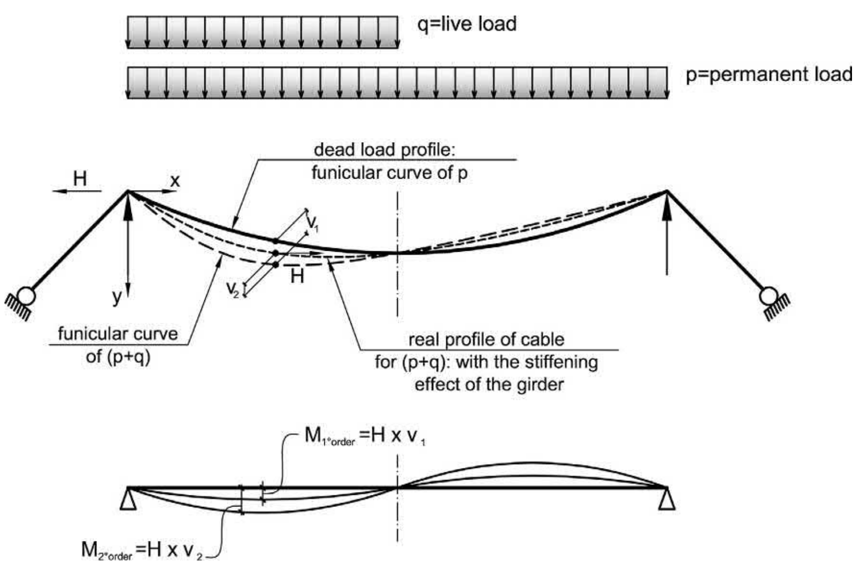

Figure 16.30 Cable profile: (a) Permanent loads (p) shape: funicular curve of p. (b) Real cable profile after loading live load (q), with stiffening effect by girder: total load = $p + q$. (c) Funicular curve of cable for $p + q$.

Predimensioning

For the analysis of the final suspension bridges, numerical procedures are adopted in nonlinear regimes of large displacement, for both the analysis of the construction phases and computing initial geometries, and then for the analysis of the bridge in service. However, for the first dimensioning calculation, it is possible to use the following approximate expressions, derived in part from the theory of linearized second-order.

- Geometry and balance of the cable for permanent loads (Pugsley, 1968):

  Development length of the cable: $l = L\left(1 + \frac{8}{3}\left(\frac{f}{L}\right)^2 - \frac{32}{5}\left(\frac{f}{L}\right)^4\right)$

  Horizontal component of the cable force: $H = \frac{\rho L^2}{8f}$

  Max. cable force: $T = H(1 + 16\, f^2/L^2)^{1/2}$

  Variation of the cable length $\Delta l = \frac{Hl}{AE}\left(1 + \frac{16}{3}\frac{f^2}{L^2}\right)$

  Vertical displacement of the center line due to Δl: $v = \dfrac{\Delta l}{\frac{16}{15}\frac{f}{-L}\left(5 - \frac{24f^2}{L^2}\right)}$

Vertical displacement at the center line for the horizontal displacements ΔL of the heads of the towers, neglecting the stiffness of the deck:

$$v' = \frac{\Delta L\left(15 - 40\dfrac{f^2}{L^2} + 288\dfrac{f^4}{L^4}\right)}{16\dfrac{f}{L}\left(5 - 24\dfrac{f^2}{L^2}\right)}$$

Variation of cable force and vertical displacement at the load section, due to the action of a concentrated load P applied at abscissa x, neglecting the stiffness of the deck:

$$\begin{gathered}\Delta H = \frac{3}{4}\frac{Pl}{f} \cdot k(1-k) \\ v = 4/3 \cdot f \cdot \Delta H/(H - \Delta H) \cdot (3k^2 - 3k + 1), \\ \text{with:} \\ k = x/l\end{gathered}$$

The bending moment for maximum traffic load distributed over a stretch ($o < x < a$) for a simply supported girder of deck:

$$M_{MAX} \cong 0.161 \cdot p \cdot L^2 \cdot \left(4/\alpha \cdot EJf/wL^4\right)^{1/2}$$

in which is the equivalent stiffness of the cables system, and can be approximated as

$$\alpha \cong 1100\,\text{kN/m}^2.$$

3.2.2 Analysis for horizontal loads

The great amount of slenderness of the deck in the horizontal plane for large-span suspension bridges ($L/B = 40$–60) have significant second-order geometric effects on the calculation of displacements and bending moments in the horizontal plane of the deck.

In short, the supporting cables, which are connected to the deck by means of the hangers, follow the movement of the deck to the action of the wind arranging the hangers on inclined planes, thus absorbing part of the horizontal actions and transferring them to the top of the towers (Figure 16.31).

The deck is then subject to directly applied horizontal actions and to the opposite reactions provided by the hangers and transmitted to the cables; by this mechanism, the resulting bending moments and displacements are significantly less than with those calculated with the theory of the first order, and a huge transfer of horizontal transverse force from deck to the top of the towers occurs.

3.3 Methods of construction

In classic suspension bridges, the operational sequence must pass through the following stages:

- Construction of towers and mooring blocks
- Formation of the supporting cables and installation of hangers
- Installation of the girder deck

The installation of the deck is performed by lifting the structural elements of the deck (or panels of the truss segments or whole segments) from the sea (or river, or from the

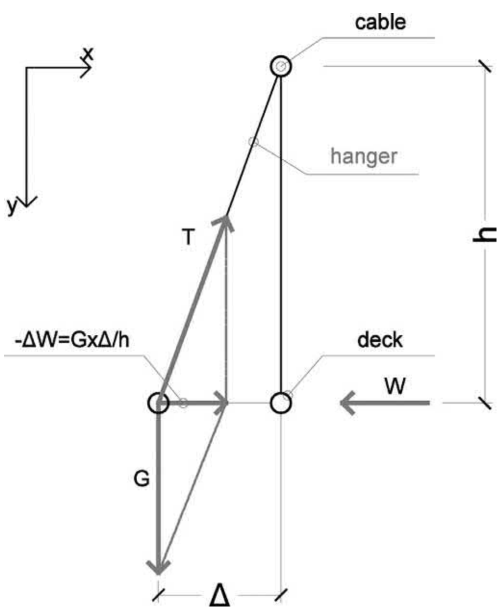

Figure 16.31 Pendulum effect of hanger and restraining force, windward directed, responsible of a substantial reduction of horizontal bending moment in deck.

ground, depending on the environment) by a crane positioned on the cables or on the already-erected deck.

In bridges with trussed decks, it is normal to start from the towers and proceed symmetrically toward the middle of the central span and toward the end of moorings (Figure 16.32b). In bridges with box-girder decks, the segments are assembled initially starting from the center line and proceed symmetrically to the towers to reduce the risk of flutter during construction (Figure 16.32a).

After lifting, the segments are connected temporarily with devices designed to allow mutual rotation during the erection of the adjacent segments, but also to guarantee the necessary stability due to the dynamic effects of the wind. A detailed description of the erection phases, as well as of problem solved in building a suspension bridge, is given by de Miranda and Petrequin (1998).

3.4 Technology of main cables and hangers

Supporting cables are always made of strong steel in parallel wires and are galvanized, with diameters of 5.2–5.7 mm. The following two methods are distinguished by the mode of formation of the cable systems:

- Aerial spinning method, which was the traditional system used for over a century in the construction of suspension bridges, which consists of cable assembly on site, working with individual wires (Figure 16.33)
- With bundles of prefabricated strands of parallel wires, the system that allows (theoretically) greater independence from environmental conditions and a higher execution speed.

The realization of the cables typically comprises the following steps:

1. Installation of walkways (i.e., catwalks) made of stranded steel wire, wooden sleepers, and network security, arranged approximately 1.00–1.50 m below the axis of the cable
2. Mounting of a catwalk bracing and stabilizing system consisting of cross-cables and hangers and of transverse walkways; installation of saddles
3. Installation of a cable car, placed over the cable and stabilized by catwalk
4. Spinning of the wires (or strands) from an anchoring end block to the other block and formation of the cable through tiling of the wires, according to the geometry of the project
5. Progressive compaction of the cables
6. Installation of hanger clamps
7. Installation of the surface protection system, consisting typically of a painting and a bandage with galvanized wire with small diameter (3–4 mm)

The cables of the longest suspension bridges that exist today have diameters of 0.82 m (Storebaelt, Denmark) and 1.12 m (Akashi Kaikyo, Japan).

Hangers are made with wire ropes or spiral cables or locked coil ropes or parallel wire ropes, always in galvanized steel and protected by sheaths, often in high-density polyethylene. The clamps that support and anchor the hangers to the main cables are typically made of cast steel, with bolt anchors.

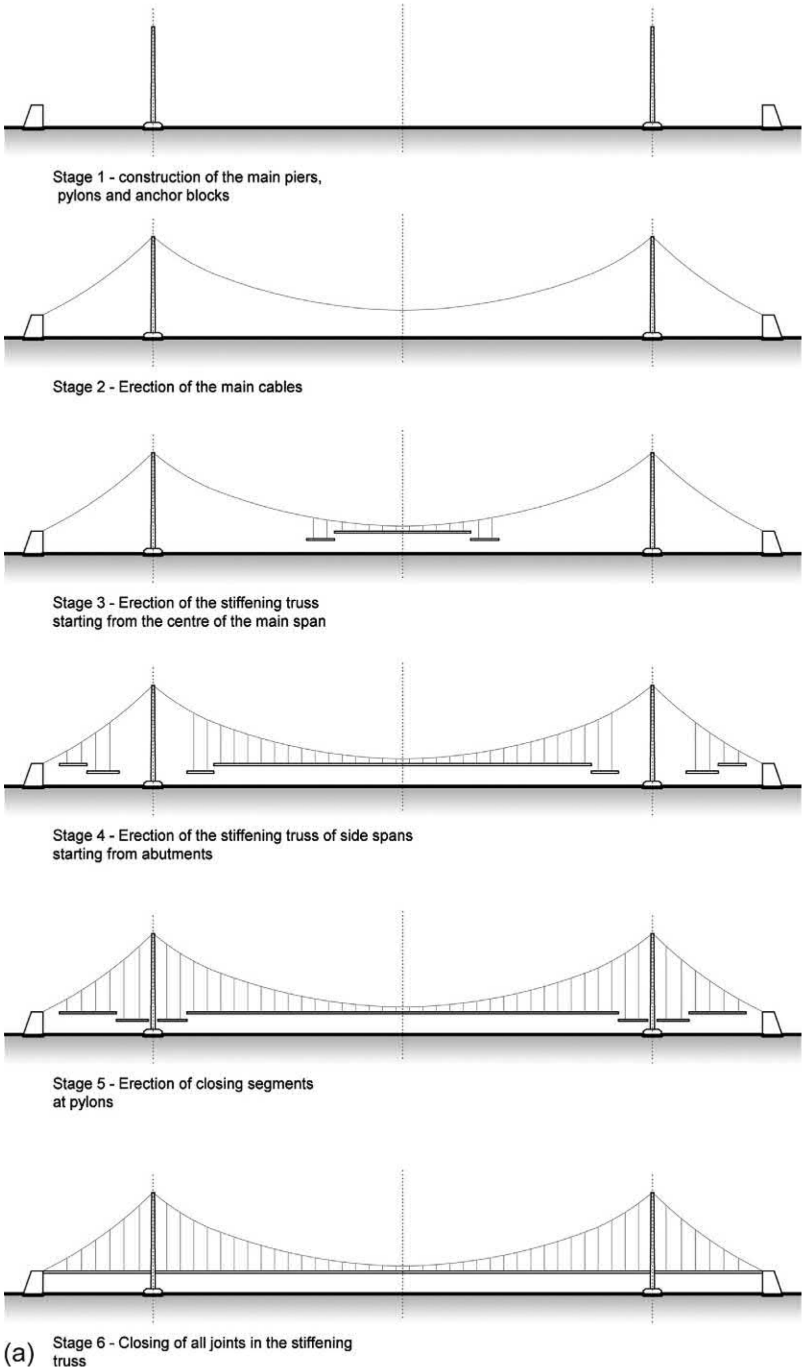

Figure 16.32 (a) Erection sequence of typical box-girder suspension bridge, by starting from mid-span in order to minimize the risk of flutter during construction.

(Continued)

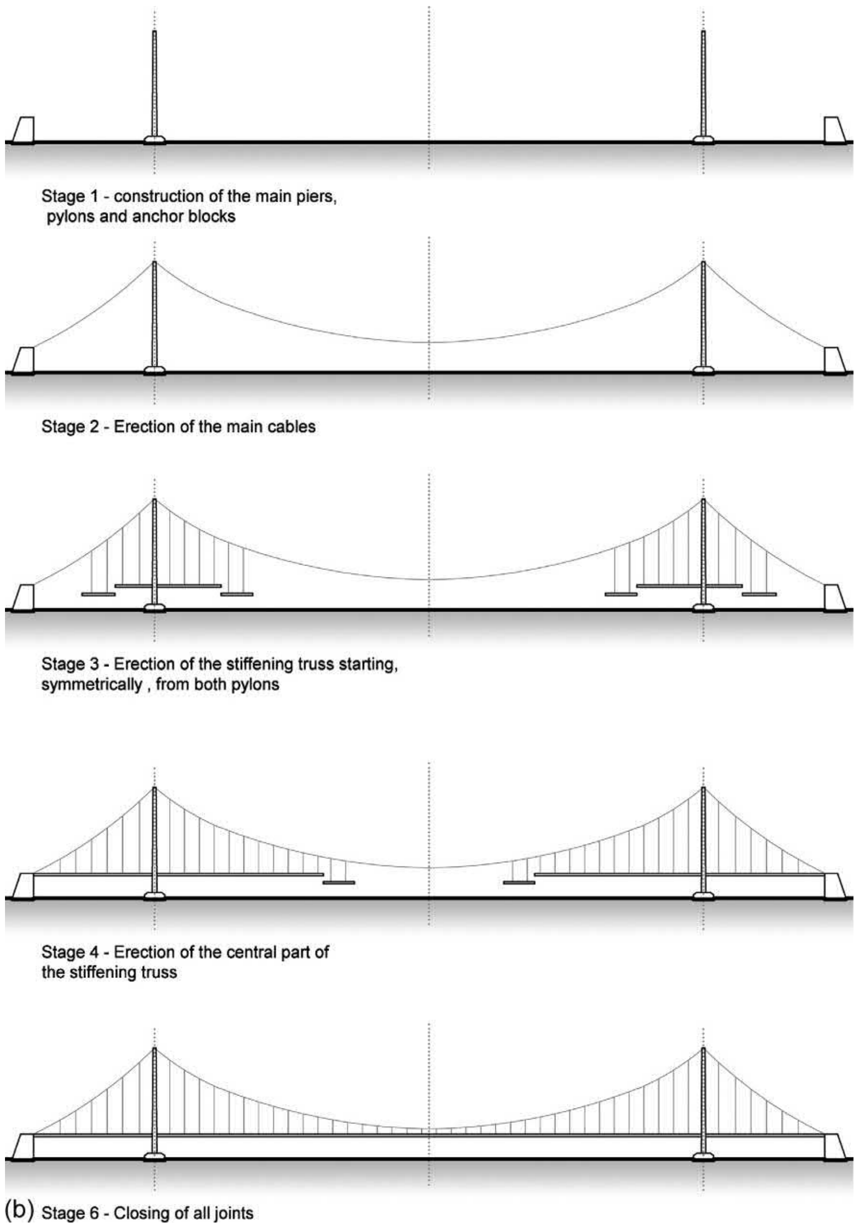

Figure 16.32, cont'd (b) Erection sequence of deck starting from pylons.

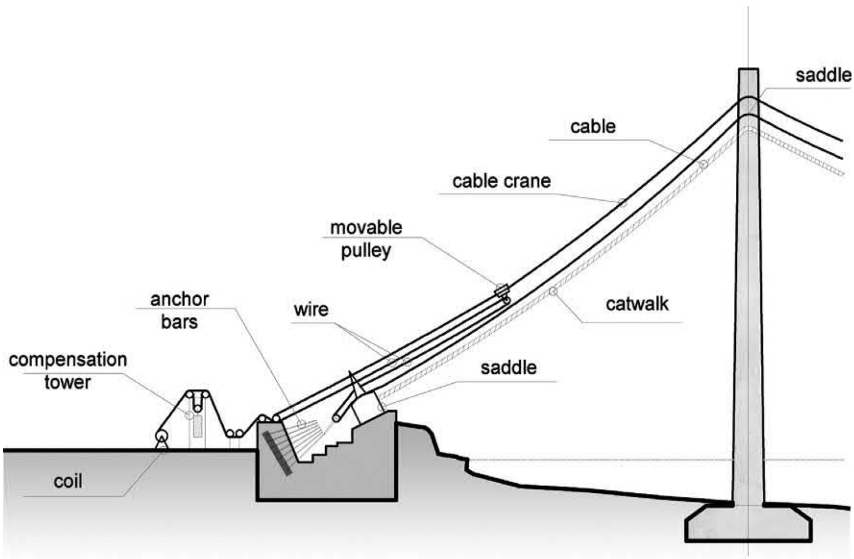

Figure 16.33 Traditional erection method of cables, by wires spinning.

The anchorages to the deck are necessarily of the hinge type for the hangers next to the mooring blocks, where the longitudinal rotation of the hangers is at its maximum, while they may be of the rigid type, with possible adjustment rings, for the intermediate hangers.

3.5 Aerodynamic stability

3.5.1 Deformable structures

For deformable bridge structures, the dynamic effects of the wind must be considered. In particular, these effects are mainly the following:

- Dynamic amplification of the structural response of the turbulent component of the wind and the impulsive action of periodic gusts (buffeting)
- Dynamic action induced by the detachment of vortex wakes (Von Karman vortices)
- Actions induced by aeroelastic instability, that can formally be divided into the following areas:
- Divergence for pure torsion
- Flutter for pure bending (galloping)
- Flutter for pure torsion (stall-flutter)
- Flutter for coupling of bending and torsion (classical flutter).

For spans typically longer than 200 m, the low vibration frequencies determine the need to verify the conditions of aerodynamic stability, briefly summarized here along with some verification criteria.

Von karman vortex

The alternating vortex street wake downwind of the deck induces aerodynamic pulsing actions which, when resonating with the frequency of vibration of the deck, can induce bending and torsional oscillations. The critical speed, for which the vortex shedding occurs at the same frequency of the deck, is equal to

$$V_{cr} = n_r \cdot d/S_t \,(\mathrm{m/s}),$$

where n_r = natural frequency of mode r in the plane normal to the wind direction (Hz) with:

b = effective width of the deck (m)
d = height of the deck (m)
S_t = Strouhal number, $\cong 0.08$ for $b/d \geq 10$

$$0.08 < S_t < 0.15 \text{ for } 10 < \frac{b}{d} < 5$$

$$S_t \cong 0.15 \text{ for } b/d \leq 5$$

Vertical oscillations can occur if

$$V_{cr} \leq 1.2x\,V_m,$$

where V_m = average characteristic wind speed (average of $10'$) (m/s).

In such a case, the aerodynamic loads applied to the structure, the amplitude of the oscillations, and the stress induced must be evaluated.

The maximum flexural displacement is given, in first approximation, by the following expression:

$$y_{MAX} = \frac{b^{1/2} \cdot d^{5/2} \cdot \rho}{4 \cdot m \cdot \delta_s},$$

with values generally overestimated with respect to the actual displacements, especially in the case of continuous, very long bridge decks.

The extent of the structural response to the wind action depends on the aerodynamic shape of the cross section of the deck, atmospheric turbulence (and therefore orography and the height above the ground), and the actual aerodynamic damping.

Torsional-flexural flutter

The torsional-flexural flutter phenomenon consists, in synthesis and with some simplification, of coupled oscillations in bending and torsion of the deck, fed and amplified by the action of the wind. Instability occurs when the wind speed has the effect of reducing the torsional frequency (which is decreased by the aerodynamic torque) to the same value as the bending frequency.

The critical speed for flutter, provided the ratio between flexural and torsional frequencies are far from unity, results in a first approximation by a modified Selberg formula:

$$V_f = k_f \cdot 3.7\,(1 - \eta_B/\eta_T)\left(m \cdot r/\rho b^3\right)^{1/2} \cdot b \cdot \eta_T \text{ (m/s)}$$

where

η_B = first bending frequency (Hz)
η_T = first torsional frequency (Hz)
m = mass unit (kg/m)
ρ = density of air (kg/m^3)
b = width of deck (m)
r = polar radius of inertia of the section center line (m)

k_f = shape coefficient equal to unity for flat plate or aerodynamically well profiled sections, and lower up to 0.2 for not streamlined sections.

For safety, it should be:

$$V_f \geq 1.5 \cdot V_m,$$

in which the multiplier 1.5 takes into account the possible increase of the wind speed for short periods and a safety margin, and V_m is the average characteristic speed for a period of 10 min at the height of the deck.

For sections that are not aerodynamically profiled (that is, for "bluff" sections), V_f is lower than the relative value at profiled sections, and is evaluated based on tests run on similar sections in the wind tunnel.

It's interesting to note that the aerodynamic torque, responsible for the reduction of the torsional frequency and in turn of the critical speed, is due to the forward shift of the lift force in a simple wing airfoil that is proportional to the profile width or chord. But in the case of a twin airfoil, the halved airfoil chord more or less also halves the aerodynamic torque and then increases flutter speed. The following points are important:

- In several suspension bridges, severe oscillations have occurred due to wind as a result of Von Karman vortices and buffeting. In some cases, remedial actions (usually aerodynamic devices like winglets or fairings) are taken to reduce or eliminate them. However, the oscillations for flutter, which rarely occur, can have catastrophic results.
- The aerodynamic stability is, therefore, a primary issue in the design of suspension bridges.
- The conditions for aerodynamic stability are more important in the construction phase than during service, since the structure is incomplete and more flexible during construction. However, the design speed can be considered during the construction phase, related to a shorter window time and then to a shorter return period that is less than the desired life of service.
- On bridges of significant length (300 m), the oscillations due to Von Karman vortices can be triggered even on relatively high eigenmodes, unlike what occurs in girder bridges.
- The action of cross-winds on deck over long spans has a mostly dynamic character: the effects of buffeting, which are often prevalent, must be added to the effects of the uniform component of the wind pressure.

4. Limits of long-span bridges

As was stated at the beginning of this chapter, long spans are generally intended for bridges for which the structural weight is overwhelming, and it becomes necessary to adopt a structural system based on lightweight, strong cables. Effective discussions of the limits and optimal structural systems of long-span bridges were proposed several decades ago by Steinman (1922), Stussi (1954), and Gimsing (1983).

The choice of the structural system depends on the following three aspects, as stated previously:

- Optimization of weight and cost of the structural material
- Guarantee of aerodynamic stability during service and during construction
- Feasibility of the construction system

From the point of view of the quantity of material used, for spans of between 500 and 1500 m, CSBs are more convenient than suspension bridges of the same span (Figure 16.34; also see de Miranda, 1971).

It involves, however, towers higher by 60%–70% and, in the self-anchored layout, requires the realization of large cantilevers in the construction phase, which are sensitive to the effects of the wind. They are, in fact, the construction aspects and aerodynamic stability during construction which until now have favored the suspension bridge for longer spans.

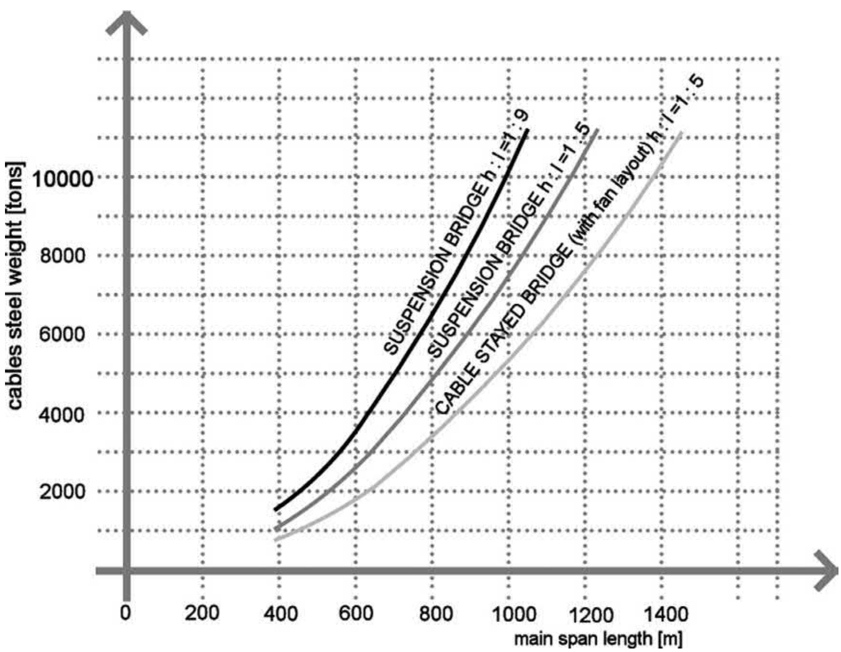

Figure 16.34 Comparison of weight of cables for suspension and cable-stayed bridges. A cost comparison will also include the increase of tower weight and deck weight in cable-stayed bridge, and the large cost of anchor blocks in suspension bridge.

Currently, the longest spans of the various types of bridges are:

- CSB, wing deck: $L = 1104\,\text{m}$ (in Vladivostok, Russia erected in 2012)
- CSB, twin deck: $L = 1018\,\text{m}$ (Stonecutter, Hong Kong, erected in 2009)
- Suspension bridge with wing deck: $L = 1650\,\text{m}$ (Xihoumen Bridge, China, 2009)
- Suspension bridge with trussed stiffening girder: $L = 1991\,\text{m}$ (Akashi Kaikyo, Japan, erected in 1998).

These bridges represent the culmination of a long and gradual evolution (Figure 16.35) of the structural systems and cross sections of traditional decks, where it seems that the limits of free spans have been achieved, at least for suspension bridges. To overcome these limitations, and mainly to increase the aerodynamic stability of even longer spans, various solutions have been proposed along the last decades, such as the following, which appear promising:

- Decks with central openings or with multiple box girders to improve aerodynamic stability
- Cross bracings between cables and decks in suspension bridges
- Mono-cable suspension systems
- Cross-tie in CSBs
- Use of aerodynamic fixed or active control
- Systems of CSBs that are partially earth-anchored
- Mixed suspension systems: cable stayed and suspension, net systems

The effective design implementation and integration of these solutions, together with the use of high performance materials should help to overcome the current limit of 2000 m and achieve progressively even larger spans.

Anyway, most of the abovementioned solutions introduce erection complications, and the effects of wind, temperature, and heavy weights of structural elements

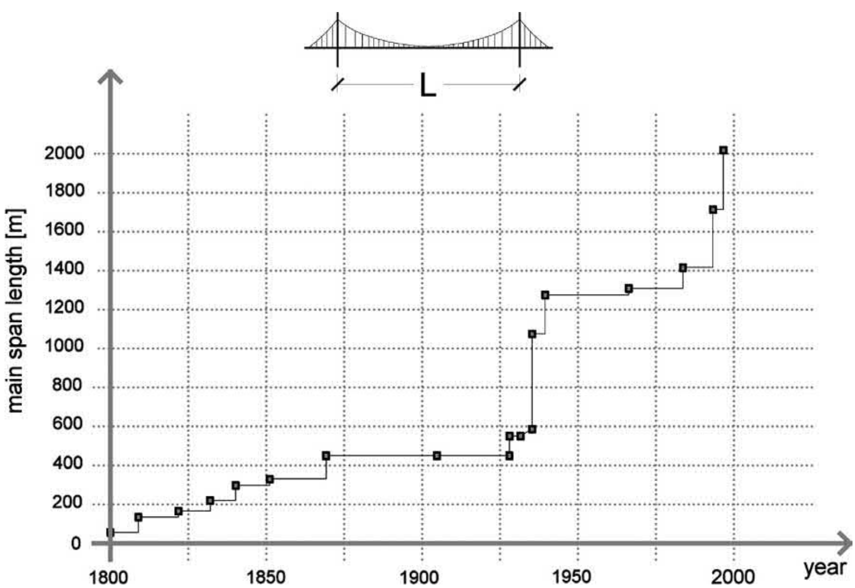

Figure 16.35 Increase in maximum span length of suspension bridges along the time.

increase with the bridge dimension. Then, to overcome spans still longer than those achieved so far, these problems must be solved by the construction methods, as well as by all those activities for which it is difficult to extrapolate a real assessment of the operational difficulties to the new size.

Looking at the graph that shows the progress in the free spans of the bridges over the past two centuries, we note that progress has not been continuous and regular, and that when growth was sudden and too rapid, it also abruptly stopped. In 1940, the cause of this discontinuation was the collapse of the bridge in Tacoma, Washington, which led to a season of projects characterized by great caution and conservatism, and certainly excessive in the light of current knowledge. This incident is not derived from errors or chance, but rather from the lack of perception (or even of the lack of the relevant scientific knowledge at that time) of a technical problem: the aeroelastic stability of the unstreamlined sections.

It is interesting to note that, despite the great advances in wind engineering over the last 70 years, stimulated by that incident, only recently has a realistic explanation (Larsen, 2000) on the aerodynamic and aeroelastic mechanism that led to the collapse of the Tacoma bridge been found.

Ultimately, it seems reasonable to say that the future progress of long-span bridges must follow solutions that do not deviate too far conceptually from those already tested and implemented and that they should not stray too far from the previous ones regarding size and spans, creating and developing both continuous and gradual progress.

5. Future perspective

5.1 Development of long-span bridges

5.1.1 Materials

The main material for building long-span bridges is steel and will remain so for years, even if knowledge and experience on polymeric materials is growing and will lead to their greater use in future.

High-strength laminated steel will be used increasingly for decks.

For high-strength cold-drawn steel for cables, no large improvements are foreseen.

Unfortunately, the use of innovative materials in long-span bridges suffers of a major controversy:

- Their adoption would be effective due to the low unit weight and, mainly, to the high strength-to-weight ratio, which is higher than that of steel. And the importance of strength-to-weight ratio greatly increases with span length.
- But their adoption in "strategic" bridges, such as long-span bridges, calls for high material reliability; that means high knowledge and experience on the adopted materials.

Maybe a crossing point between these two needs will be found in some decades, mainly when the cost of polymeric material drops to a really positive cost-benefit level.

Polymeric materials, and in particular carbon fibers, have two large advantages:

- High strength, of the same order of high-strength steel, and low unit weight. These two features give a very high strength-to-weight ratio, arounds five times higher than high-strength steel.
- High corrosion resistance, leading to lower maintenance and, hopefully, higher durability.

The disadvantages are as follows:

- Lower ductility
- Lower critical wind speeds against flutter since the lower weight reduces the vibrating mass
- Less experience in bridge construction
- Higher cost today.

The cost of carbon fiber has reduced by 300% in last 10 years. Today it is still higher, at equal strength, than steel, but it is expected to still decrease in next few decades.

5.1.2 Construction and structural systems

Construction methods are closely linked to structural systems.

The availability of large-capacity equipment, large barges, and real-time systems for control of geometry and vibrations facilitates the offshore erection work.

The main issue of construction works is the control of the large movements of structures in an incomplete structural configuration, due to wind and to erection loads.

Suspension bridge stiffness, in many stages of construction, is only given by the cable stiffness, relying on second-order effects of displacements, so low in transverse direction (only "pendulum" behavior) and low for localized loads (deck segments) in vertical direction.

Even if large displacements are accompanied by long vibration periods and, in turn, low movement speed, these displacements can be of the order of tenths of meters and need to be confidently taken under control. That is not a simple task as spans increase.

CSB stiffness during construction can be higher than for suspensions bridges due to the continuity of deck during the progress of construction and due to three-dimensional stiffening behavior of stay cables, when starting from an A-shaped pylon.

5.2 Ultra-long-span bridges

Bridges considered ultra-long-span bridges today have spans larger than 2 km, so none are built yet at this point in time.

5.2.1 Limit spans

Limit spans depend on a synergic combination of constructability, structural system efficiency, and material efficiency.

- Constructability was discussed briefly in the preceding points. To achieve ultra-long spans, this is the main precondition.
- An analysis of structural systems shows that efficiency of CSB, seen as the minimum required material for a certain span, is higher than in SB. It was also shown that V-shaped pylons

present lower quantities than vertical pylons, but the extra cost for construction neutralizes that advantage.

- The present efficiency of materials can allow limit spans of the order of more the 4 km to be reached, but these spans seem today too far from present experience.

5.2.2 Challenges

- Cable corrosion

Corrosion of main cables of suspension bridges is an important issue.

Traditional protection of cables has been found to be insufficient to prevent corrosion of internal parallel wires in many cases.

So dehumidification systems for cables were envisaged as retrofit of existing cables and as a built-in system in recent bridges.

This way, the durability of suspension bridges is made dependent on mechanical installation.

In cable-stayed bridges the corrosion of stay cables is controlled today by the three protection levels of modern cables:

- Galvanization or, better, Galfanization
- Individual HDPE sheaths
- Global HDPE pipes

In any case, the key feature of cables of CSB is the replaceability of stay cables; that is a substantial benefit.

5.2.3 Sustainability

Sustainability can be an issue for long-span bridges in two aspects: size and cost.

The size of towers, which can reach more than 300 m, can conflict or appear disproportionate or gigantic in the context of existing construction, houses, roads, and so on, if the towers are placed on-shore or close to the coast. In this case, the issue is the aesthetic sustainability.

The cost of very long-span bridges can be very high and difficult to be recovered in a realistic timeframe by standard and acceptable tolls.

Elements that can positively influence the cost-benefit ratio are the possible economic or social development and growth of the connected areas and populations.

Elements that can negatively influence the cost-benefit comparison are the possibility of delays and extra costs due to the exceptionality of the span and dimensions and the corresponding lack of direct experience.

In this case, the issue, to be controlled by an economic realistic feasibility study, is investment sustainability.

5.3 Concluding remarks

Even if suspension bridges are typically adopted for spans greater than 1000 m, the CSB can be a valid alternative even for these spans because of its higher stiffness, cable replaceability, and lower cost.

Recent research carried out by DMA studying a three-span CSB with a 2000 m central span for the Messina Strait showed lower deformation, lower impact of towers, and lower cost—around the half—than a single 3300 m span suspension bridge.

Moreover, the future development of long- and ultra-long-span bridges will depend only in part on technical aspects like structural forms, materials, and construction methods. It also will depend on social aspect and, in general, on sustainability.

References

Baglietto, E., Casirati, M., Castoldi, A., de Miranda, F., Roberto Sammartino, R., 1976. Modelli matematici e strutturali del comportamento statico e dinamico dei ponti. Zarate—Brazo Largo Costruzioni Metall. 4, 151–161.

de Miranda, F., 1969. Stay cables anchored to the deck by means of stiffening additional cables. Patent 7368 A/69–Genova, October, 7 (in Italian).

de Miranda, F., 1971. Il ponte strallato—soluzione attuale del problema delle grandi luci (The cable stayed bridge—an actual solution for long spans bridges). Costruzioni Metalliche 1. and Ponti a struttura d'acciaio, Collana Tecnico Scientifica, ITALSIDER (then CISIA), Milano.

de Miranda, F., 1980. Ponti strallati di grande luce. Zanichelli, Bologna.

de Miranda, M., 2001. Il ponte sul rio Higuamo. Il Giornale dell'Ingegnere n. 5–Milano, 15 Marzo 2008.

de Miranda, M., 2003. Cable-stayed bridge over the Guamà River. Brazil. Struct. Eng. Int. 3, 171–173.

de Miranda, M., Bartoli, G., 2001. Aerodynamic optimization of decks of cable stayed bridges. In: IABSE, International Association of Bridges and Structural Engineers, Symposium in Kobe, 1998. "Long-Span and High-Rise Structures," vol. 79, pp. 143–148.

de Miranda, M., Petrequin, M., 1998. Storebaelt Bridge, Aspects du Montage et de la Realisation, Construction Metallique, 2-2000, Costruzioni Metalliche n. 6, 1998. In: Beyond the Limits of Erection Activities, IABSE Conference, Kobe, 1998.

de Miranda, F., Leone, A., Passaro, A., 1979. Il ponte strallato sullo Stretto di Rande presso Vigo (Spagna) della Autopistas del Atlantico. Costruzioni Metall. 2, 55–62.

Farquharson, F.B., 1952. Aerodynamic Stability of Suspension Bridges With Special Reference to the Tacoma Narrows Bridge. Bulletin n 116, part III, June, University of Washington, Engineering Experimental Station.

Federal Highway Administration (FHA), 2007. Wind Induced Vibrations in Stay Cables. Report FHWA-RD-05-083, FHA, Washington, DC.

Galileo, G., 1638. Discorsi e Dimostrazioni Matematiche. Intorno a due Nuove Scienze Attenenti Alla Meccanica e i Movimenti Locali.

Gimsing, N., 1983. Cable-Supported Bridges. John Wiley & Sons, New York.

Kashima, S., 1998. Technical advance in the Honshu-Shikoku bridges. In: IABSE, Kobe Conference Proceedings, pp. 23–34.

Larsen, A., Lessons learned. Bridge Design and Engineering 20, Third Quarter: 44–46.

Leonhardt, F., 1982. Brucken, Bridges. Deusche Verlags-Anstalt, Stuttgart, Germany.

Leonhardt, L., Andra, W., Wintergest, L., 1969. Kniebrücke—Dusseldorf—Ed. Tamms-Beyer—Beton–Verlag.

Mélan, J., 1888. Theorie der eisernen Bogenbrücken und der Hängebücken. In: Handbuch der Ingenieuwissenschaten, second ed. vol. 2. Wilhelm Engelmann, Leipzig, Germany. Part 4.

Moisseiff, L., Lienhard, F., 1933. Suspension bridges under the action of lateral forces. Trans. Am. Soc. Civil Eng. 98, 1080–1095. 1096–1141.

Podonly, W., Scalzi, J., 1976. Construction and Design of Cable Stayed Bridges. John Wiley & Sons, New York.

Post-Tensioning Institute (PTI), 2007. Recommendations on Stay Cables. Phoenix, AZ.

Pugsley, A.G., 1968. The Theory of Suspension Bridges. Edward Arnold, London.

Rankine, W.J.M., 1869. A Manual of Applied Mechanics. Charles Griffin, London.

Richardson, J.R., 1984. The influence of aerodynamic stability on the design of bridges. In: 12th IABSE Congress, Vancouver, BC, Canada.

Roebling, J.A., 1854. Final Report on the Niagara Railway Suspension Bridge. Lee, Mann and Co., Rochester, N.Y.

SK Most, 2012. Construction of the Bridge Crossing to Russky Island over the Eastern Bosphorus Strait in Vladivostok. http://www.skmost.com.

Steinman, D.B., 1922. A Practical Treatise of Suspension Bridges. John Wiley & Sons, London.

Stussi, F., 1954. Das Problem der Grossen Spannweite. VSB Verlag, Zurich.

Veranzio, F., 1968. Machinae Novae—Ferro Edizioni. Milano via Brera, 6.

Walter, R., Houriet, B., Isler, W., Maia, P., Klein, J.F., 1999. Cable Stayed Bridges. Thomas Telford, London.

Wyatt, T.A., 1991. The dynamic behaviour of cable stayed bridges: fundamental and parametric studies. In: Ito, M., Fujino, Y., Miyata, T., Narita, N. (Eds.), Cable Stayed Bridges—Recent Developments and their Future. Proceedings of a Seminar, Yokohama, Japan, 10–11 December 1991. Elsevier, pp. 151–170.

Part VI

Special topics

This page intentionally left blank

Integral bridges

17

Murat Dicleli
Middle East Technical University

1. Introduction

Bridges are traditionally built with expansion joints at the ends to allow for longitudinal displacements of the superstructure due to temperature variations. Thus, most conventional bridges possess expansion joints and bearings, which are expensive in terms of material and installation costs. Furthermore, expansion joints may allow water, salt, and deicing chemicals to penetrate through them and cause extensive deterioration to the bearings, substructure, and superstructure components. Consequently, for many years, expansion joints have caused considerable maintenance problems for transportation agencies (Wolde-Tinsae et al., 1988a,b; Burke Jr., 1988, 1990; Steiger, 1993). The elimination of expansion joints in bridges may reduce the construction cost, overcome many of the maintenance problems, and increase the stability and durability of the bridges. These economic and functional advantages are generally recognized by bridge engineers (Dicleli, 2000a,b), which leads to the concept of integral construction or integral bridges. The lack of expansion joints in integral bridges results in reduced repair and maintenance costs throughout the service life of the bridge. In addition, when used as part of highways or railways, the lack of expansion joints in integral bridges enhances the riding comfort and provides better lateral rigidity to breaking loads, and the reduced lateral displacement of the continuous railway construction minimizes the likelihood of rail buckling. Moreover, modern integral bridges are known to have performed well in recent earthquakes due to their monolithic construction (Erhan and Dicleli, 2014).

2. Historical background

The use of Integral bridges began thousands of years ago in the form of masonry arches, and today there exist many similar arches that have survived for more than a hundred years (Hambly, 1997). The construction of reinforced concrete arch bridges in North America began in the early decades of the 20th century. Bridge engineers started the practice of eliminating the deck joints at piers and abutments after the moment distribution method was first developed in early 1930s (Cross, 1932), allowing engineers to analyze statically indeterminate structures such as rigid-frame bridges. By mid-century, concrete rigid frame bridges became a standard type of construction for many departments of transportation (Burke, 1990). Ohio and Oregon were the first states to use integral bridges in the 1930s. Illinois and Iowa followed them in the 1940s. Washington State had its first integral bridge in 1960s, and

Innovative Bridge Design Handbook. https://doi.org/10.1016/B978-0-12-823550-8.00029-9

New York State began building integral bridges in the late 1970s. By 1980, 30 states were using integral abutment bridges as a standard form of construction. In the past few decades, engineers started to notice the benefits of integral bridges over jointed bridges in terms of their superior stability and serviceability and lower maintenance demand. Consequently, most bridge engineers focused their attention on the design and construction practice of integral bridges. Nowadays, most departments of transportation in the United States, Canada, and Europe consider the integral bridge construction as a standard form of construction.

3. Modern integral bridges

Modern integral bridges are single-span or multiple-span bridges with a continuous deck and a flexible movement system composed primarily of abutments supported on a single row of piles (Hambly, 1997; Chen, 1997; Dicleli, 2000a,b). A typical slab-on-girder integral bridge is shown in Figure 17.1. The details of a typical integral bridge are shown in Figure 17.2. In these types of bridges, the road surfaces are continuous from one approach embankment to the other, and the abutments and occasionally the piers are cast integrally with the girders and the deck slab. A flexible abutment with a single

Figure 17.1 Single-span integral bridge with slab-on-steel-girder deck (Blackmud Creek Bridge Edmonton, Canada).

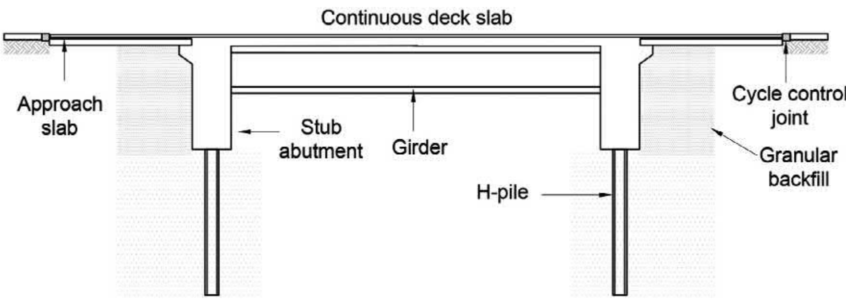

Figure 17.2 Details of a typical single-span integral bridge.

row of piles is essential to allow for the longitudinal bridge movements due to temperature variations, shrinkage, and creep. The most common type of piles used at the abutments of integral bridges is steel H-piles. Cycle control joints are provided at the ends of the approach slabs to accommodate the longitudinal movements of the bridge.

4. Thermal effects in integral bridges

The daily and seasonal temperature changes result in imposition of cyclic horizontal displacements on the continuous bridge deck of integral bridges and thus on the abutments, backfill soil, steel H-piles at the abutments, and cycle control joints at the ends of the approach slabs. The magnitude of these temperature-induced cyclic displacements is a function of the temperature difference and the length of the bridge. Thermal-induced cyclic displacements are especially important for the performance of the steel H-piles at the abutments and the abutments themselves. In the following subsections, the effect of cyclic thermal displacements on the steel H-piles and abutments will be discussed.

4.1 Thermal effects in integral bridge piles

The daily and seasonal temperature changes result in imposition of cyclic horizontal displacements on the continuous deck of integral bridges and thus on the steel H-piles at the abutments. As the length of integral bridges increases, the temperature-induced displacements in the steel H-piles may increase as well. Consequently, the piles may experience deformations beyond their elastic limit. The ability of steel H-piles to accommodate such large displacements is an important factor that affects the maximum length of an integral bridge.

The displacement capacity of steel members, including steel H-piles at the abutments of integral bridges, is affected by their buckling instability. Instability in steel structural members includes local buckling of the plates forming the cross section of the member as well as lateral-torsional and global buckling of the steel member. Local buckling instability in steel H-piles may occur in either the flange or web or both, depending on the width-to-thickness ratios of the flange and web plates. Lateral-torsional buckling, which occurs when steel members are subjected to bending about their strong axis, is critical for steel sections with relatively narrow flanges and is not much of a concern in steel H-piles that have wider flanges. Furthermore, as the steel H-piles in integral bridges are laterally supported by the surrounding soil, the lateral-torsional or global buckling instability need not be considered. Thus, local buckling is the only instability type that will be considered when determining the displacement capacity of steel H-piles. The width-to-thickness ratios of the flanges and the web for steel H-piles must be limited to prevent local buckling. Many researchers worked out limits for the width-to-thickness ratios of web and flange to prevent local buckling effects and hence to ensure a ductile behavior of the steel member. Most of these studies have been implemented in design codes such as the AISC (American Institute of Steel Construction) Load and Resistance Factor Design (LRFD) Manual for steel structures (2010). AISC LRFD Design Manual (2010) divides the steel sections into three categories based on their ability to reach a certain compressive stress level and deform without experiencing local buckling problems: compact sections, non-compact sections, and sections with slender plate elements (web and/or flange). Compact sections are capable of developing full plastic flexural capacity. Non-compact sections cannot develop full plastic capacity but are capable of developing yield stress in compression elements. The third category covers steel sections with slender plate elements that experience local buckling before the yield stress is achieved. The divisions between these three categories are defined by slenderness parameters λ_p and λ_r that define the limiting width-to-thickness ratios for compact and non-compact sections, respectively. For compact sections, the width-to-thickness ratios for the web and flange are smaller than λ_p. For non-compact sections, they are larger than λ_p but smaller than $\lambda_{r,}$ and for slender sections, they are larger than λ_r. Table 17.1 displays the expressions for λ_p and λ_r for web and flange under monotonic loading.

In Table 17.1, b_f is the flange width; d_w is the clear height of the web plate between flanges t_f and t_w are the flange and web thickness, respectively; P_u and P_y are the required and yield axial forces; and F_y is the yield stress in ksi.. Under cyclic thermal movements, the steel H-piles are expected to reach their plastic capacity. Thus, it is recommended that compact steel HP sections are used to avoid local buckling instability.

Fatigue of steel H-piles is another important problem that should be considered in design. Steel H-piles supporting the abutments of integral bridges are subjected to cyclic loading due to temperature changes. In the summer, the superstructure expands and pushes the abutment and the piles toward the backfill, and in the winter, the superstructure pulls the abutment and the piles in the opposite direction. Consequently, the piles may be subjected to one dominant cyclic displacement each year due to seasonal (summer and winter) temperature changes (Girton et al., 1991). Additionally, the piles may be subjected to numerous small cyclic displacements due to daily and/or weekly temperature fluctuations (Girton et al., 1991). The magnitude of these temperature-induced cyclic displacements is a function of the temperature difference and the length of the structure. As the length of the integral bridges becomes longer, the

Table 17.1 Limiting Width-to-Thickness Ratios for Compression Elements in Steel Sections (LRFD, 2010)

Width-to-Thickness Ratio	Limiting Width-to-Thickness Ratios: λ_p	λ_r
b_f/t_f	$\frac{163}{\sqrt{F_Y}}$	$\frac{250}{\sqrt{F_Y}}$
d_w/t_w	For $P_U/\varphi_b P_Y \leq 0.125$ $\frac{640}{\sqrt{F_Y}}\left(1-\frac{2.75P_U}{\varphi_b P_Y}\right)$ For $P_U/\varphi_b P_Y \geq 0.125$ $\frac{500}{\sqrt{F_Y}}\left(2.33-\frac{P_U}{\varphi_b P_Y}\right) \leq \frac{665}{\sqrt{F_Y}}$	$\frac{665}{\sqrt{F_Y}}$

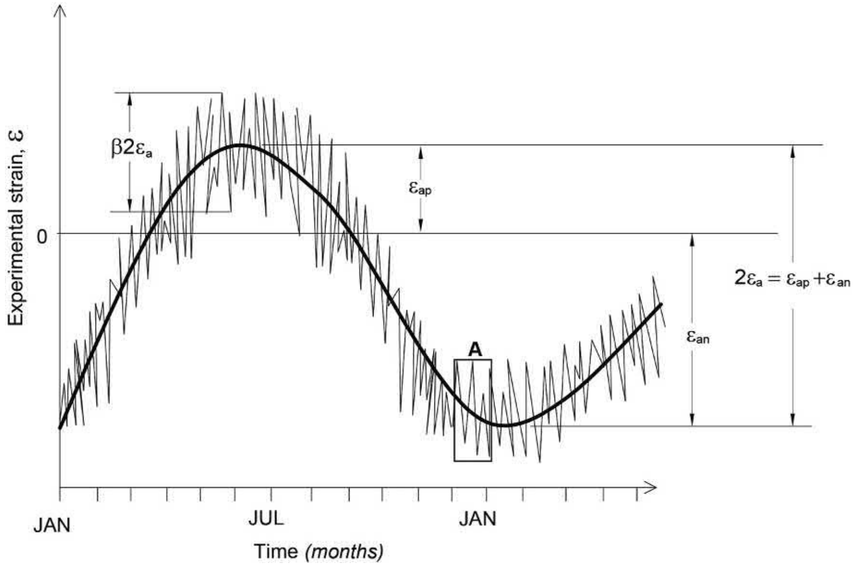

Figure 17.3 General experimental strain versus time for integral bridges piles.

temperature-induced cyclic displacements in steel H-piles may become larger as well. As a result, the piles may experience cyclic deformations beyond their elastic limit. This may result in the reduction of their service life due to low-cycle fatigue effects.

Examination of records of strain versus time for the instrumented steel H-piles for two integral abutment bridges in the state of Iowa (Girton et al., 1991) revealed that both bridges exhibited one large strain cycle per year due to seasonal temperature changes and about 52 small strain cycles per year due to weekly temperature fluctuations, as illustrated schematically in Figure 17.3. Moreover, the field test records demonstrated that the strain amplitude of the small cycles in the piles supporting the abutments fall within 20% to 40% range of the strain amplitude from the large cycles, as shown in Figure 17.3.

It is noteworthy that the net difference between the seasonal and reference (construction) temperatures may be disparate in the summer and winter based on the climatic conditions of the area where the bridge is located. Therefore, the amplitudes of the positive (ε_{ap}) and negative (ε_{an}) strain cycles corresponding to the summer and winter may not be equal, as can be observed in Figure 17.3. However, as the range of strain amplitudes rather than the strain amplitude itself defines the extent of fatigue damage, the positive and negative strain amplitudes may be assumed to be equal.

4.2 Thermal effects in integral bridge abutments

The earth pressure that is exerted on the abutment by the backfill soil depends on the extent of movement of the abutment An integral bridge will experience elongation and contraction due to temperature variations during its service life. Thus, the earth pressure at the abutments should be considered in correlation with temperature variation. A very small displacement of the bridge away from the backfill soil can cause the development of active earth pressure conditions (Barker et al., 1991). Therefore, when the bridge contracts due to a decrease in temperature, active earth pressure will be developed behind the abutment. At rest, earth pressure behind the abutment is assumed when there is no thermal movement. When the bridge elongates due to an increase in temperature, the intensity of the earth pressure behind the abutment depends on the magnitude of the bridge displacement toward the backfill soil. Thus, the actual earth pressure coefficient, K, may change between at rest, $K_{o,}$ and passive, K_{P}, earth pressure coefficients depending on the amount of displacement.

5. Conditions and recommendations for integral bridge construction

5.1 Length of the bridge

For the present, where overall length of the bridge is less than 150 m, it shall be considered for design as an integral bridge. For structure lengths larger than 150 m, the consent of the governing bridge authority (the owner) should be given in order to proceed. In considering the movement requirements, due consideration should be given to the place and type of joints, joint seal, backfill and approach slab details, and construction temperatures. The limitation placed on the total length of the structure is mainly a function of local soil properties, seasonal temperature variations, resistance of abutments to longitudinal movements, and the type of superstructure being considered.

The integral bridge length limits as governed by the low-cycle fatigue performance of steel H-piles and flexural strength of the abutments are given in what follows (Dicleli and Albhaisi, 2004, 2005):

5.1.1 Integral bridge length limits as governed by low-cycle fatigue performance of the piles

$$L := \frac{2}{\gamma_T \alpha_T \Delta T}\left[\frac{M_y(\lambda l_c)^2}{6E_pI_p}\left(1+\frac{M_y}{M_p}\right)+\frac{0.0085(\lambda l_c)^2}{6d_p}\left(2-\frac{M_y}{M_p}-\left(\frac{M_y}{M_p}\right)^2\right)\right], \tag{1}$$

where l_c is the critical length of the pile defined as the length beyond which the pile's top displacement and rotations have practically no effect and is defined as

$$l = 4\sqrt[4]{\frac{E_pI_p}{k_h}}, \tag{2}$$

where for clay:

$$k_h = \frac{9C_u}{2.5\varepsilon_{50}} \text{ (Soft to medium} - \text{stiff clay)} \tag{3}$$

$$k_h = \frac{9C_u}{4.0\varepsilon_{50}} \text{ (Stiff clay).} \tag{4}$$

In the absence of geotechnical data, for soft, medium, medium-stiff, and stiff clay, corresponding values of $C_u = 20$, 40, 80, and 120 kPa (Bowles, 1996) and $\varepsilon_{50} = 0.02$, 0.01, 0.0065, and 0.0050 (Evans, 1982) shall be used.

For sand:

$$k_h = kx \tag{5}$$

$$x = H + 8d_p \tag{6}$$

In the absence of geotechnical data, for loose, medium, medium-dense, and dense sand, corresponding values of $k = 2000$, 6000, 12,000, and 18,000 kN/m^3 shall be used.

In most cases, the subsoil is composed of layers of soils with different stiffness properties. In such cases, the soil stiffness shall be averaged over the top $10 \times b_p$ length of the pile and used in Eqs. (3), (4), and (5), where b_p is the width of the pile perpendicular to the direction of the movement.

The λ values are given in Table 17.2.

In lieu of adequate structural and geotechnical data at the bridge site, integral bridge length limits for different pile sizes are given in Table 17.3.

5.1.2 Integral bridge length limits as governed by flexural strength of abutments

Abutments have adequate shear strength to accommodate thermal induced shear forces, and hence, the shear strength of the abutments does not govern the integral bridge length limits. Although the flexural strength of the abutments generally does

Table 17.2 λ Values for Different Soil and Abutment–Pile Connections Types

Soil	Abutment–Pile Connection	Strong Axis	Weak Axis
Clay	Fixed	0.5	0.55
	Pinned	1.15	1.40
Sand	Fixed	0.65	0.75
	Pinned	1.1	1.40

Table 17.3 Maximum Length Limits for Steel and Concrete Integral Bridges Based on Pile's Low-Cycle Fatigue Performance

Pile Size	Steel Bridges		Concrete Bridges	
	Moderate Climate	**Cold Climate**	**Moderate Climate**	**Cold Climate**
	L (m)	L (m)	L (m)	L (m)
HP310 × 125	220	145	320	265
HP310 × 110	205	135	300	250
HP250 × 85	160	110	240	195
HP200 × 63	125	80	180	150

not govern the bridge length limits either, for abutments taller than 4 m, the following equations may be used to calculate the length limits of integral bridges based on the flexural strength of the abutments (Dicleli, 2005):

For clay:

$$L = \frac{2H}{\alpha_T \alpha \Delta T m^{\frac{1}{n}}}\left[\left(\frac{1}{\alpha_E \gamma S}\right)\left(M_r - n_p\left(M_p + \frac{M_p}{\lambda_v l_c}(H - h_D)\right)\right)\left(\frac{6}{(h_D + 2H)(H - h_D)^2}\right) - K_0\right]^{\frac{1}{n}}. \tag{7}$$

For sand:

$$L = \frac{2H}{\alpha_T \alpha \Delta T m^{\frac{1}{n}}}\left[\left(\frac{1}{\alpha_E \gamma S}\right)\left(M_r - n_p M_p\left(1 + (H - h_D)\sqrt[4]{\frac{k(H + 8d_p)}{2E_p I_p}}\right)\right)\left(\frac{6}{(h_D + 2H)(H - h_D)^2}\right) - K_0\right]^{\frac{1}{n}}, \tag{8}$$

where $\lambda_v = 0.30$, m = 10, and $n = 0.33$ for compacted backfill and m = 28 and $n = 0.56$ for uncompacted backfill (Dicleli, 2005).

5.2 Superstructure type

Types of structures to be used with integral bridges include the following:

1. Steel girders with concrete deck.
2. Prestressed concrete girders with concrete deck.
3. Prestressed concrete box girders with concrete deck.

Post-tensioned construction is not suitable for integral design, as the abutments supported on single row of piles may not be able to accommodate the lateral forces exerted during the post-tensioning process.

5.3 Geometry of the bridge

The geometry of the structure should be considered in deciding the feasibility of integral bridge design. Owing to the nonuniform distribution of loads and difficulties in establishing the movement and its direction, structures with skew greater than 35° or where an angle subtended by a 30 m arc along the length of the structure is greater than 5° are not considered suitable for integral designs. Skews greater than 20° but not exceeding 35° may be considered if a rigorous analysis is carried out to account for the skew effects. In carrying the analysis for skew, the effects such as torsion, unequal load distribution, lateral translation, pile deflection in both longitudinal and transverse direction, and increase in the length of the abutment exposed to soil pressure shall be considered.

5.4 Abutments and wing walls

It is recommended that abutment height and wing-wall length shall be limited to 4.0 m and 7.0 m, respectively. The abutment should be kept as short as possible to reduce the soil pressure; however, the minimum penetration required for frost protection should be provided. The frost penetration requirement can be reduced to minimize abutment height by providing insulation at the bottom of the abutment. It is recommended to have abutments of equal height at the bridge ends. A difference in abutment heights causes unbalanced lateral load resulting in sidesway, which should be considered in the design by balancing the earth pressure which is consistent with the direction of sidesway, at the abutments. This procedure requires an iterative process, which may result in a pressure ranging from active to at rest on the taller abutment and at rest to passive on the shorter abutment. Wing walls parallel to the roadway, carried by the structure, shall be used, and their size should be minimized to allow the substructure to move with minimum resistance.

5.5 Multiple-span integral bridges

The spans and the articulation at the supports of multispan structures should be selected so that equal movement occurs at each end of the structure. The deck diaphragms may be integral with the piers, made fixed in the lateral direction, or move laterally, as appropriate. The piers should be flexible and supported on flexible foundations if made integral with the deck diaphragms.

5.6 Foundation soil conditions

Subsoil condition is an important consideration in the feasibility of integral arrangement of a structure. The primary criteria is the need to support the abutments on relatively flexible piles. Therefore, where load-bearing strata is near the surface or where the use of short piles (less than 5.0 m in length) or caissons is planned, the site is not considered suitable for integral bridges. Where piles are driven in dense and stiff soils, pre-augured holes filled with loose sand shall be provided to reduce resistance to lateral movement. Where soil is susceptible to liquefaction, slip failure, sloughing, or boiling, the use of integral arrangement should be avoided.

6. Construction methods of integral bridges

Construction considerations and sequence shall be given on the drawings to specify the following requirements:

1. The abutments, including wing walls, shall be constructed first to bearing seat elevation.
2. The girders shall be placed on a support that allows rotation and deflection of the girders due to self-weight and dead weight of the deck. A 20 mm thick natural rubber sheet is generally adequate to accommodate the rotations of the girders.
3. The deck and the portion of the abutment above bearing seat elevation shall be cast integrally with the girders.
4. The deck and the abutment to the bearing seat level shall be poured in sequence so that the structure becomes integral with no residual stresses. This may require a careful consideration of the concrete pouring sequence and the use of retarder. The ends of deck and the abutments shall be placed last unless concrete can be retarded sufficiently to allow the placement from one end to the other in a single pour.
5. The stability and the integrity of the structure shall be maintained at all stages of the construction.
6. Backfill shall not be placed behind the abutments until the deck has reached 75% of its specified strength.
7. Backfill shall be placed simultaneously behind both abutments, keeping the height of the backfill approximately the same. At no time shall the difference in heights of backfill be greater than 500 mm.

7. Design of integral bridges

The design procedure defined here is applicable to integral bridges with slab-on-steel or prestressed-concrete girder deck.

7.1 Construction stages, loads, and load combinations

The construction of an integral bridge is done in stages. Therefore, it must be analyzed for each construction stage to ensure that the structure has adequate capacity to sustain the applied loads particular to the stage under consideration.

Two construction stages are considered for the design of slab-on-prestressed-concrete-girder integral bridges. The loads applied at each construction stage are listed in Table 17.4. In the first stage, the slab concrete is assumed to be wet. Accordingly, the prestressed-concrete girders alone resist the applied loads. The structure is analyzed for the effects of prestressing force, dead weight of the girders, weight of wet concrete slab, and weight of the diaphragms. In the second stage, the bridge is assumed to be in service. Full composite action is considered between the slab, girders, and abutments.

Table 17.4 Summary of Stage Loading for Slab-on-Prestressed-Concrete-Girder Deck Integral Bridges

Stage #	Stage Name	Load ID	Load Description
1	Simply supported beams	1	Own weight of girder
		2	Pretensioning
		3	Weight of wet concrete slab, diaphragms, and abutment
2	Composite structure	4	Superimposed dead load
		5	Asphalt/ballast weight
		6	Long-term prestress losses
		7	Highway/railway live loading at fatigue limit state
		8	As load 7 but at serviceability limit state
		9	As load 7 but at ultimate limit state
		10	Thermal load due to longitudinal expansion
		11	Thermal load due to longitudinal contraction
		12	Passive earth pressure
		13	At rest earth pressure
		14	Active earth pressure

The effects of superimposed dead loads, ballast weight, temperature variation, soil pressure, and live loads are considered in this stage.

Three stages are considered for the design of slab-on-steel-girder integral bridges. The loads applied at each stage are listed in Table 17.5 In the first stage, the naked steel girders are assumed to be fully assembled and supported on the abutments and piers, but the slab concrete is assumed to be wet. Therefore, the steel girders alone resist the applied loads. The loads due to the wet concrete slab, diaphragms, and self-weight of the steel girders are considered in this stage. In stage two, the steel girders are assumed to be composite with the concrete slab. However, the modulus of elasticity of the concrete slab is assumed as one-third of its actual final value to consider the effect of creep due to superimposed dead loads. In addition to the loads applied in the first stage, ballast load and superimposed dead loads are considered in this stage. In the final stage, the bridge is assumed to be in service. Full composite action is assumed between the slab, girders, and abutments. The effects of temperature variation, soil pressure, and live load are considered in this final stage.

7.2 Modeling integral bridges for analysis under gravitational loads

For the analysis of integral bridges subjected to gravitational loads, a separate structure model is proposed for each construction stage. The proposed structure models are subject to the following assumptions:

Table 17.5 Summary of Stage Loading for Slab-on-Steel-Girder-Deck Integral Bridges

Stage #	Stage Name	Load ID	Load Description
1	Naked steel beam	1	Own weight of steel beam and diaphragms
		2	Weight of wet concrete slab, diaphragms, and abutment
2	Composite structure (3n)—superstructure only	3	Superimposed dead load
		4	Asphalt/ballast weight
3	Composite structure (n)	5	As load #3
		6	As load #4
		7	Highway/railway live loading at fatigue limit state
		8	As load 7 but at serviceability limit state
		9	As load 7 but at ultimate limit state
		10	Thermal load due to longitudinal expansion
		11	Thermal load due to longitudinal contraction
		12	Passive earth pressure
		13	At rest earth pressure
		14	Active earth pressure

(i) The analysis of bridges having a slab-on-girder-type deck is reduced to the consideration of one beam and an effective width of the slab for the purpose of gravity load analysis. Accordingly, the abutments are idealized to have a tributary width equal to that of the slab. Similarly, the number of piers and piles per tributary width is calculated, and their stiffness is lumped to obtain a single pier or pile element for analysis purposes.

(ii) The effect of frictional forces between the approach slab and soil as well as between the wing walls and soil, resulting from movements due to temperature variations, is ignored.

(iii) An equivalent pile length or Winkler spring model is assumed in the structural model.

(iv) The live load applied on the structure is proportioned to one girder considering the transverse distribution of the live load effects.

Figure 17.4 illustrates a typical two-span, prestressed-concrete-girder integral bridge and its 2-D structure model for construction stage 1. The naked girder alone is considered in the structure model assuming that the concrete is not hardened. Accordingly, the composite action between the girder and slab and the continuity between the girders of adjacent spans and at the deck-abutment joints are ignored. The bridge is modeled considering each span as a simply supported beam. The structure is analyzed for stage 1 loads tabulated in Table 17.4. The resulting internal forces (stresses) are then kept in order to superimpose them onto the ones resulting from the loads to be applied in stage 2.

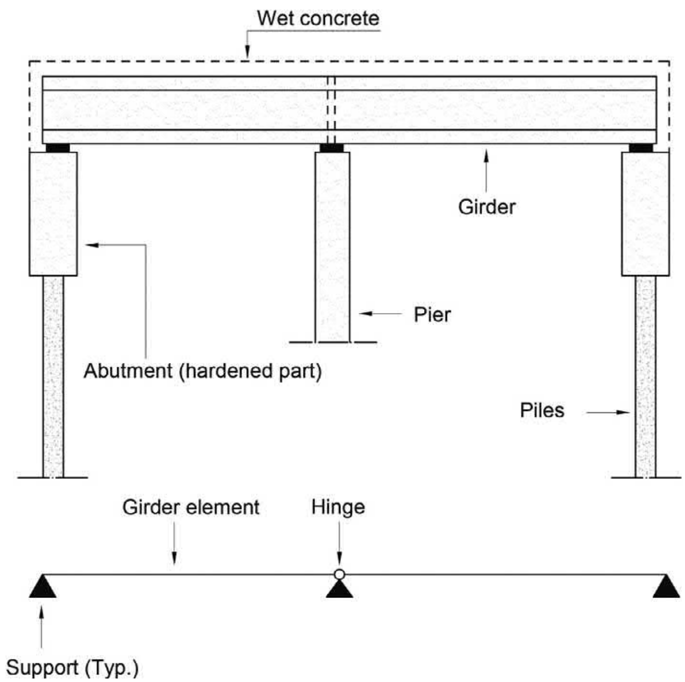

Figure 17.4 Typical two-span integral bridge and analytical model for construction stage I.

For slab-on-steel-girder integral bridges, the steel beams are fully assembled to form a continuous beam before the slab is cast in construction stage 1. Therefore, the hinge shown at the middle support of the structure model depicted in Figure 17.4 is removed for this type of integral bridge. Furthermore, if steel columns are rigidly connected to the steel girders, the middle simple support shown in Figure 17.4 is replaced by a column element rigidly connected to the beam. Each span is idealized using 2-D beam elements. The structure is then analyzed for stage 1 loads tabulated in Table 17.5. The resulting internal forces (stresses) are stored in order to superimpose them onto the ones resulting from the loads, to be applied in subsequent stages.

Figure 17.5 illustrates the structure model for the rest of the construction stages for the same bridge shown in Figure 17.4. The structure model shall be used for the analysis of both steel and prestressed concrete, slab-on-girder, integral bridges. The bridge is idealized as a plane frame considering only one girder and an effective width of slab. Full continuity at the intermediate supports and at the abutment–deck connection joints is considered assuming that the concrete is fully hardened. The idealized abutment and pier members are connected to the deck nodes by abutment–deck or pier–deck connection elements. The pile member is connected to the abutment member by a pile–abutment connection element. If the connections between the abutment and deck as well as pile and abutment are normally assumed to be rigid, then the connection elements may be removed from the model.

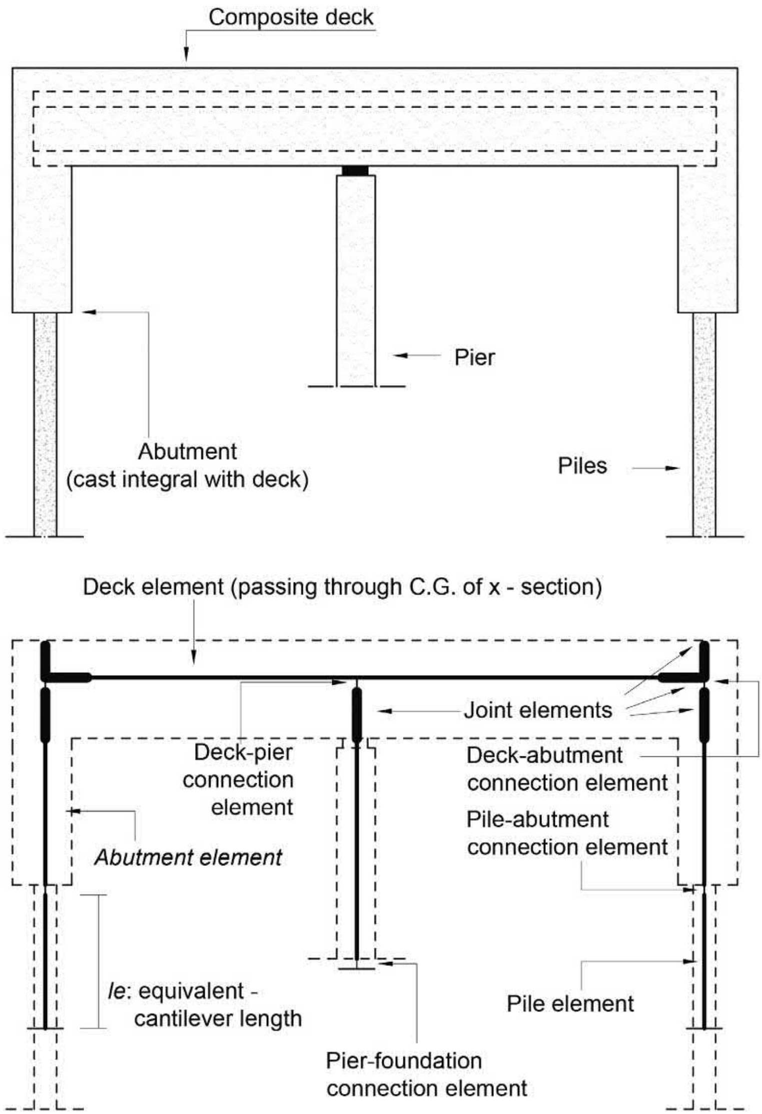

Figure 17.5 Typical two-span integral bridge and analytical model for the final construction stage.

7.3 Thermal variations and associated soil–bridge interaction

The earth pressure coefficient is a function of the displacement or rotation of the earth retaining structure. An integral bridge will experience elongation and contraction due to temperature variations during its service life. Thus, the earth pressure at the abutments should be considered in correlation with temperature variation. A very small displacement of the bridge away from the backfill soil can cause the development of active earth pressure conditions. Therefore, when the bridge contracts due to a decrease in temperature, active earth pressure will be developed behind the abutment. At-rest earth pressure behind the abutment is assumed when there is no thermal movement. When the bridge elongates due to an increase in temperature, the intensity of the earth pressure behind the abutment depends on the magnitude of the bridge displacement toward the backfill. The actual earth pressure coefficient, K, may change between at rest, $K_{O,}$ and passive, K_P, earth pressure coefficients depending on the amount of displacement. The dependency of the earth presure coefficient on the thermal displacement of the bridge shall be taken into consideration in the design of the bridge using the following equation:

$$K = \frac{2K_o + \alpha\,\delta T\,L\phi}{2 + \dfrac{LH^2 S\gamma_s \phi}{2E_g\left(A_g + nA_s\right)}} \le K_P \tag{9}$$

Where φ is the rate of the variation of the earth pressure coefficient between at rest and passive states. In lieu of geotechnical data for the properties of granular soil (backfill), $\varphi = 24\,\text{m}^{-1}$. For bridges with unequal abutment heights, the preceding equation shall be used cautiously by considering unequal movements at both ends of the bridge due to the difference in abutment heights.

7.4 Live load distribution in integral bridges

The maximum live load effect in a bridge is based on the position of the truck both in the longitudinal and transverse direction, the number of loaded design lanes and the probability of the presence of multiple loaded design lanes. To calculate the maximum live load effects in an integral bridge, the position of the truck in the longitudinal direction as well as both the position and the number of trucks in the transverse direction need to be considered in a three-dimensional finite element model of the bridge. Furthermore, in the estimation of live load effects, the probability of the presence of multiple loaded design lanes need to be taken into consideration by using the multiple-presence factors defined in design specifications such as AASHTO (2010). Although using 3-D finite element models to determine live load effects in bridge components is possible due to the readily available computational tools in design offices, using such complicated methods throughout the design process is tedious and time consuming. Therefore, most bridge engineers use simplified two-dimensional structural models and live load distribution factors (LLDFs) readily available in bridge design specifications to determine live load effects in bridge girders. LLDFs have been used in bridge design since the 1930s.

LLDFs are needed for the composite interior and exterior girders of integral bridges for the loading cases where only a single design lane is loaded (fatigue limit state) and two or more design lanes are loaded (service and ultimate limit state). For this purpose, first the maximum live load effects (moment and shear) from 3-D analyses for the composite girders are calculated as the summation of the maximum effects in the girder element and within the tributary width of the slab at the same location along the bridge. For the case where two or more design lanes are loaded, the transverse loading case producing the maximum girder live load effect after multiplying by the multiple presence factors is used to obtain the LLDFs. The LLDFs are then calculated as the ratio of the maximum live load effects obtained from 3-D analyses to those obtained from 2-D analyses under a single truck load. In the calculation of LLDFs the AASHTO HL-93 truck is used AASHTO (2010). n this section LLDFs are provided for the interior and exterior girders of commonly used slab-on-girder integral bridges. Using these LLDFs, it is possible to obtain the actual three-dimensional live load effects in bridge girders by multiplying the response from a two-dimensional model of a bridge represented by a single girder over a tributary width of girder spacing by appropriate LLDFs. In what follows, live load distribution equations (LLDEs) are provided for the interior and exterior girders of commonly used slab-on-girder integral bridges.

Interior Girder Moment—Two or More Design Lanes Loaded:

$$LLDE_{IAB} = \frac{S^{0.82}}{500L^{0.06}} \tag{10}$$

Interior Girder Moment—One Design Lane Loaded:

$$LLDE_{IAB} = \frac{3S^{0.72}}{500L^{0.13}} \tag{11}$$

Interior Girder Shear—Two or More Design Lanes Loaded:

$$LLDE_{IAB} = 0.2 + \frac{S}{3600} - \left(\frac{S}{10700}\right)^{2.0} \tag{12}$$

Interior Girder Shear—One Design Lane Loaded:

$$LLDE_{IAB} = 0.36 + \frac{S}{7600} \tag{13}$$

Exterior Girder Moment—Two or More Design Lanes Loaded:

$$LLDE_{IAB} = \frac{L^{0.09}S^{0.53}t_s^{0.06}}{80K_g^{0.04}}\left(0.5 + \frac{d_e}{5000}\right) \tag{14}$$

Exterior Girder Moment—One Design Lane Loaded:

$$LLDE_{IAB} = \frac{L^{0.06}S^{0.45}}{18t_s^{0.02}K_g^{0.04}}\left(0.4 + \frac{d_e}{6000}\right) \tag{15}$$

Exterior Girder Shear—Two or More Design Lanes Loaded:

$$LLDE_{IAB} = \frac{L^{0.10}S^{0.43}t_s^{0.03}}{14K_g^{0.07}}\left(0.4 + \frac{d_e}{3000}\right) \tag{16}$$

Exterior Girder Shear—One Design Lane Loaded:

$$LLDE_{IAB} = \frac{2L^{0.05}S^{0.34}}{15t_s^{0.01}K_g^{0.04}}\left(0.5 + \frac{d_e}{3000}\right) \tag{17}$$

In the preceding equations, where S = girder spacing, L = span length, t_s = slab thickness, d_e = cantilever length measured from the centroid of the exterior girder up to the face of the barrier wall length, and K_g = a parameter representing the longitudinal stiffness of the composite slab-on-girder section of the bridge expressed as

$$K_g = n\left(I + Ae_g^2\right), \tag{18}$$

where n = the ratio of the modulus of elasticity of the girder material to that of the slab material, I = the moment of inertia of the girder, A = cross-sectional area of the girder, and e_g = distance between the centers of gravity of the girder and the slab.

7.5 Design for seismic loads

Compared to conventional jointed bridges, Integral bridges perform better during an earthquake due to the fixity and restraint at the abutments. However, caution should be exercised in the design of substructures to minimize damage in the event of an earthquake. Nonlinear time history analysis method considering the passive backfill resistance behind the abutments is more appropriate for the seismic design of integral bridges. In lieu of nonlinear time history analyses, the maximum earth pressure acting on the abutment in the longitudinal direction shall be assumed to be equal to the maximum longitudinal earthquake force transferred from the superstructure to the abutment. To minimize abutment damage, the abutment should be designed to resist the passive pressure being mobilized by the backfill, which should be greater than the maximum estimated longitudinal earthquake force transferred to the abutment. When longitudinal seismic forces are also resisted by piers or columns, it is necessary to estimate the stiffness of the components in order to compute the proportion of earthquake load transferred to the abutment. The wing walls should be treated similarly for transverse seismic forces. The capacity of piles in both directions should be checked to resist the earthquake forces. It may be necessary in some cases to batter the piles sufficiently in the transverse direction, to adequately transfer the earthquake forces or provide stability in the transverse direction.

8. Nonlinear modeling of integral bridges for seismic performance assessment

The monolithic construction of integral bridges provides a better transfer of seismic loads to the backfill and pile foundations and results in larger damping due to cyclic soil–pile–structure interaction. Therefore, soil–pile and backfill–abutment interaction become an important part of the seismic performance assessment of integral bridges. Consequently, soil–structure interaction must be considered in the nonlinear structural model of integral bridges used to perform time history analyses for seismic performance assessment or design. In this section, the modeling of integral bridges for seismic performance assessment with particular emphasis on soil–structure interaction is introduced using an existing integral bridge built in Ontario, Canada.

To assess the seismic performance of integral bridges via nonlinear time history analyses, a 3-D nonlinear structural model is necessary. A 3-D model is especially necessary to study the response of integral bridges in the transverse direction including the transverse direction responses of the wing walls, backfill, piers, and piles (to simulate the frame action of the piers and piles in the transverse direction), which are not possible to simulate accurately in a 2-D model.

8.1 Description of the integral bridge to introduce modeling procedure for seismic performance assessment

A two-span integral bridge is considered to introduce the modeling procedure for seismic performance assessment. The bridge was built in 2000 on Highway 400 underpass at Major Mackenzie drive in Ontario, Canada. The total length of the bridge is 82 m, and its width is 16 m. The bridge has two spans with lengths of 41 m each and a slab-on-prestressed concrete girder deck supported by low-damping elastomeric bearings under each girder at the pier. The bridge deck is composed of seven AASHTO type VI girders spaced at 2.4 m and supporting a 225 mm thick reinforced concrete slab. A 75 mm thick asphalt pavement is provided on the deck surface. The bridge pier is composed of three 1400 mm diameter circular reinforced concrete columns supporting a cap beam. The abutments of the integral bridge are 4 m tall and 1.5 m thick and are supported by 12×15 m long end-bearing steel HP 310×174 piles oriented to bend about their strong axes. The strength of the concrete used for the prestressed concrete girders is 50 MPa, whereas the strength of the slab, abutment, and pier concrete is 30 MPa. The granular compacted backfill behind the abutments is assumed to have a unit weight of 20 kN/m^3. The foundation soil surrounding the piles is assumed to be medium sand.

8.2 Modeling of superstructure

The bridge superstructure may be modeled using 3-D beam elements, as shown in Figure 17.6a. The composite action between the slab and the girders should be considered in the structural model. The superstructure may be divided into a number of segments, and its translational and rotational mass may be lumped at each nodal point connecting the segments. At the abutment and pier locations, the bridge deck may be modeled as a transverse rigid bar of length equal to the center-to-center distance between the two exterior girders supporting the deck slab, as shown in Figure 17.6a. The transverse rigid bar is used to simulate the interaction between the axial deformation of the columns and torsional rotation of the bridge deck as well as the interaction between the in-plane rotations of the deck and relative displacements of the bearings.

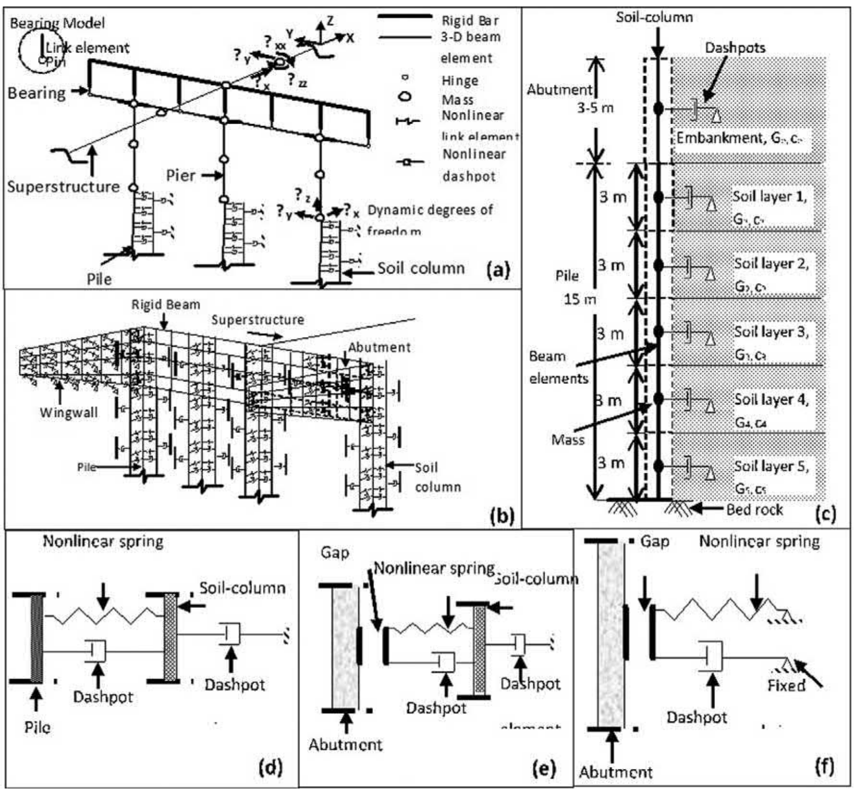

Figure 17.6 (a) Structural modeling details at the pier and bearings; (b) structural modeling details at the abutments; (c) soil–column modeling details; (d) soil–pile interaction modeling; (e) abutment–backfill interaction modeling with embankment; (f) abutment–backfill interaction modeling without embankment.

8.3 Modeling of the bearings

For the example bridge, the bearings supporting the superstructure at the pier are regular low-damping rubber bearings. It is a known fact that, in this type of bearings, loading and unloading paths nearly overlap; that is, their behavior is linear elastic (Warn and Ryan, 2012). Accordingly, the lateral stiffness of the bearing may be estimated by the following equation:

$$K_b = \frac{G_R A_b}{h_b}. \tag{19}$$

In the preceding equation, G_R is the shear modulus of rubber material, A_b is the bonded plan area of the rubber bearings, and h_b is the thickness of the rubber bearing (or height of the rubber). The calculated lateral stiffness of the bearing may be increased by a factor of 1.35 to obtain an effective shear stiffness ($K_b = 1.35 \times K_{bmin}$), which considers the effect of aging and low-temperature conditions throughout the service life of the bridge. The calculated lateral stiffness of the bearing may be implemented in the structural model by means of linear spring elements.

8.4 Modeling of the pier, reinforced concrete piles, abutments, and steel H-piles

The reinforced concrete cap beam, columns, and piles underneath the piers may be modeled as 3-D beam elements (Figure 17.6a). Specific software may be used to obtain the moment curvature relationships of the pier columns. The moment curvature relationships are then used in a nonlinear hinge element in the structural model to define the envelope of the hysteresis loops simulated by Takeda model (Takeda et al., 1970). Typical hysteretic behavior of the pier column of the example bridge is illustrated in Figure 17.7a. It is worth mentioning that capacity design approach is usually used to prevent plastic hinging and, hence, damage to the piles. Thus, plastic hinging should be assumed only in the pier columns. The abutments may be modeled using a grid of frame elements, as shown in Figure 17.6b. In most cases, the steel H-piles at the abutments yield before the abutment. Therefore, there is no need for the nonlinear modeling of the integral bridge abutments for seismic performance assessment. In the transverse direction, wing walls are similarly modeled using a grid of frame elements, as shown in Figure 17.6b. The steel H-piles are also modeled using frame elements. The current state of design practice does not use capacity design approach to prevent plastic hinging in the steel H-piles at the abutments under seismic excitations. This is mainly due to the much larger size and associated larger flexural capacity of the abutments compared to that of the piles. Therefore, the cyclic behavior of steel H-piles may be modeled using an elasto-plastic hysteretic behavior using Plastic–Wen hysteresis rules (Dicleli, 2007). Typical hysteretic behavior of the steel H-piles is illustrated in Figure 17.7b.

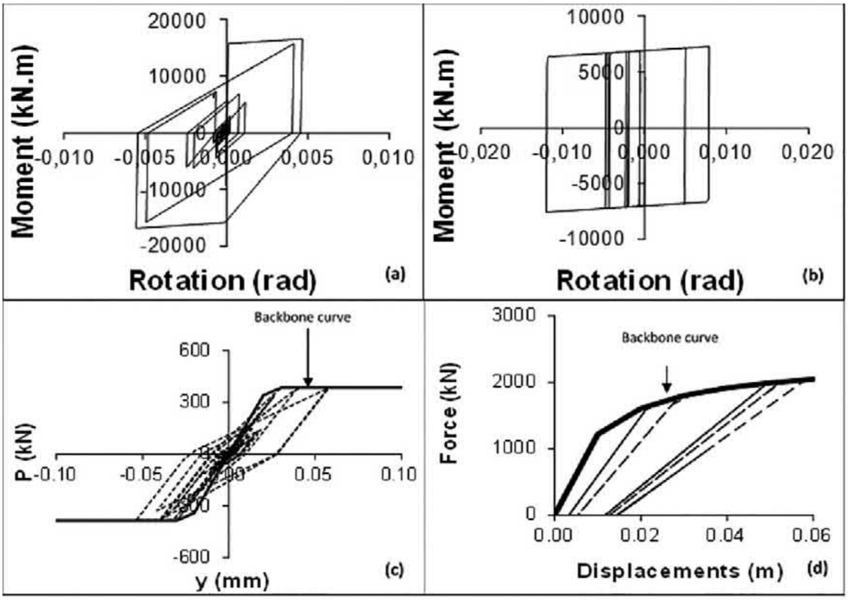

Figure 17.7 (a) Typical pier column moment-rotation hysteresis loop; (b) typical steel H-pile moment rotation hysteresis loop; (c) sample hysteresis loop simulating soil–pile interaction from structural analyses; (d) sample hysteresis loop simulating abutment–backfill interaction from structural analyses (San Fernando Earthquake Ap = 0.8 g).

8.5 General Information on the modeling of soil–structure interaction

It is a known fact that soil–pile and abutment-embankment interaction simulation is an important structural modeling aspect of seismic response prediction of integral bridges. There are several ways of simulating the soil–pile and abutment–embankment interaction in the structural model of integral bridges. For instance, one way is to build a complex 3-D finite element model of the foundation and embankment soil using a specialized software capable of modeling both nonlinear structural and continuum soil elements as well as surface contact interactions and conducting nonlinear time history analysis for soil materials (Zhang and Makris, 2002; Kotsoglou and Pantazopoulou, 2007, 2009, 2010). For such finite element models, if a coarse mesh is selected, the level of accuracy will be lost (Shamsabadi, 2007). However, when a refined mesh is used, the model becomes very tedious to build and computationally requires extensive run times. Therefore, such complex models are generally not used in engineering practice (Shamsabadi, 2007). Accordingly, for practical applications, the soil–bridge interaction may be simulated in the structural model by using a soil–column model.

The soil–column modeling approach consists of replacing the continuum soil elements with a soil–column having spring-dashpot components that are attached to the frame model of the bridge structure and its pile foundation. The local nonlinear force-displacement behavior of springs and viscous damping coefficients of the dashpots at the soil–pile and abutment–backfill contact interfaces may be obtained from research studies involving models generated via calibration with experimental results. The properties of the soil column to simulate the free-field behavior of the foundation soil (degraded shear modulus and equivalent damping ratios) for a given ground motion scaled to a specific peak ground acceleration may be obtained by modeling separately the foundation soil and approach embankments with specialized software for soil response analysis.

The research studies of Franchin and Pinto (2014) revealed that the soil column model is capable of providing reasonably good predictions of both maximum and residual bending moments of structural members and their cumulative displacements. Furthermore, Zhang and Makris (2002) have compared the dynamic properties of a 3-D model of a long embankment with that of a 1-D tapered soil column and found that soil column approximation captures most of the longitudinal and transverse response of the approach embankment in comparison to the 3-D models. On the other hand, the main disadvantage of the soil column modeling approach for the embankment is that it fails to estimate the deformations along the length of the embankment and associated soil damping. However, as the main focus of an integral bridge design is the structural response of the bridge components, the deformations along the length of the embankment are not of interest to the designer.

The soil–structure interaction model proposed here could be classified into three forms. The first one is the local abutment–backfill interaction where the interaction between the backfill and the laterally moving abutment under seismic effects is considered locally. The second one is the local soil–pile interaction where the interaction between the pile and soil under seismic effects is simulated locally by so called p–y curves. The third one is the free-field motion of the foundation soil and the embankment (backfill) with respect to the bridge, which is considered by using a soil column in the structural model. Details of the modeling procedures for these three soil–bridge interaction forms are given in what follows.

8.6 Modeling of local abutment–backfill interaction

The local abutment backfill (and, in the transverse direction, wing wall–backfill) interaction behavior under cyclic loads may be simulated by using the hysteresis model proposed by Cole and Rollins (2006) (Figure 17.8a and b) that takes into consideration the possible formation of a gap behind the abutment at each loading cycle (as the abutment pushes toward the backfill and pulls back under seismic effects). In this hysteresis model, the hyperbolic load (P)-deflection (Y) envelope curve for the abutment–backfill system must first be defined. The following hyperbolic p–y relationship purposed by Duncan and Mokwa (2001) (Figure 17.7d) may be used for this purpose:

$$P = \frac{y}{\dfrac{1}{K_{\max}} + R_f \dfrac{y}{P_{ult}}}, \tag{20}$$

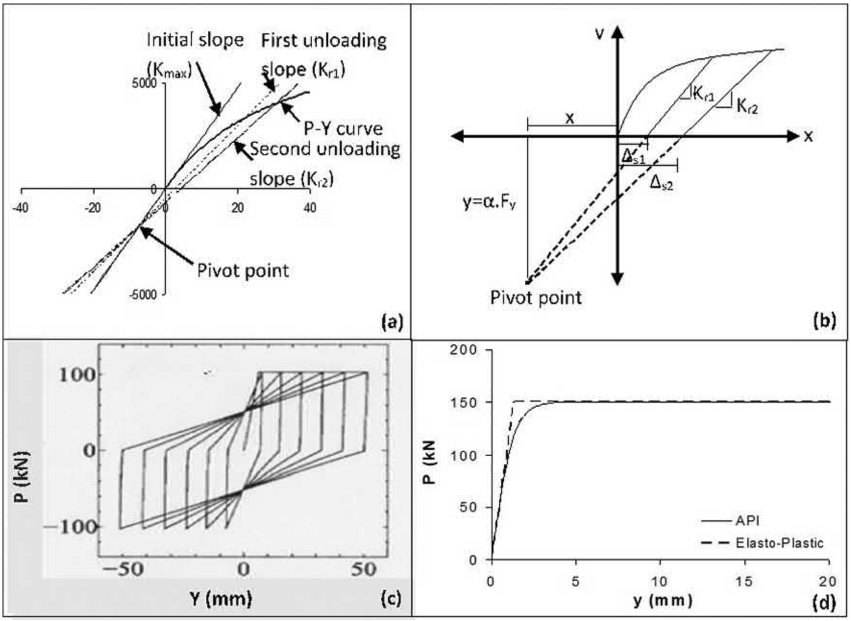

Figure 17.8 (a) Hysteretic abutment–backfill interaction diagram; (b) pivot parameter of α; (c) hysteretic soil–pile interaction diagram proposed by Shirato et al. (2006); (d) elasto-plastic envelope p–y curves for soil–pile interaction.

where P is the passive resistance of the backfill, P_{ult} is the ultimate passive resistance, y is the backfill deformation, K_{max} is the initial slope of the load–deformation curve, and R_f is the failure ratio assumed as 0.85 (Duncan and Chang, 1970).

The pivot hysteresis model (Dowell et al., 1998) may be used to simulate the hysteretic behavior of the backfill behind the abutment by assigning appropriate values to the hysteresis model parameters. The pivot hysteresis model (Dowell et al., 1998) requires the force-deformation envelope (for the backfill defined by Eq. 20) as well as two additional parameters for capturing the pinching and stiffness degradation effects. In the pivot hysteresis model, α refers to the stiffness degradation parameter, and β corresponds to pinching parameter. However, in the full-scale tests performed by Cole and Rollins (2006) on several abutment–backfill systems, no pinching behavior is observed. Accordingly, pinching effect should be excluded from the pivot model by setting $\beta = 1$. The parameter α in the pivot model may be calculated from the intersections of the two consecutive unloading lines K_{r1} and K_{r2} and corresponding permanent displacements Δ_{s1} and Δ_{s2} in the backfill hysteresis model proposed by Cole and Rollins (2006), as shown in Figure 17.8a and b to simulate the force-displacement behavior of the backfill. Accordingly, in the structural model, the hysteretic behavior of the abutment–backfill system may be simulated by using nonlinear elements available in the structural analysis software with pivot hysteresis model connected between the nodes along the length of the abutment and the soil column (Figure 17.6c) for the case where the embankment is included in the structural model (Figure 17.6e).

However, for the case where the embankment is not included in the structural model, while one end of the nonlinear link element is connected to the abutment, the other end is attached to a node fixed in space (Figure 17.6f). A typical abutment–backfill hysteresis loop obtained from the analyses is presented in Figure 17.7d.

The radiation damping effects (as the abutment impacts the backfill) for the abutment–backfill system may be simulated in the structural model using dashpots (Figure 17.6e and f). The radiation damping coefficient for these dashpots may be obtained from the following equation proposed by Jain and Scott (1989):

$$c = \sqrt{\frac{2}{1-\nu} G\rho}, \tag{21}$$

where $G, \rho,$ and ν are the dynamic shear modulus, mass density, and Poisson's ratio of the backfill, respectively. For a typical compacted backfill, $G, \rho,$ and ν may be taken as 6000 kN/m^2, 2.05 ton/m^3, and 0.3, respectively. For uncompacted backfill, however, G, $\rho,$ and ν may be taken as 5000 kN/m^2, 1.84 ton/m^3, and 0.3, respectively. During seismic excitation, there is a compression-only interaction between the abutment and backfill. Accordingly, gap elements with a zero gap length connected in series with the nonlinear springs/elements and dashpots may be incorporated in the structural model to simulate this behavior (Figure 17.6e and f).

8.7 Modeling of local soil–pile interaction

The local soil–pile interaction behavior under cyclic loads for sand may be simulated using the hysteresis model proposed by Shirato et al. (2006). In this hysteresis model, a monotonic load–deflection envelope curve must first be defined. The lateral soil resistance–deflection (p–y) relationship for sand available in API (2001) may be used to define this envelope curve at any specific depth, H, as follows:

$$P = A_f P_u \tanh\left[\frac{kH}{A_f P_u} y\right], \tag{22}$$

where A_f is a factor to account for cyclic or static loading condition and may be assumed as 0.9 for cyclic loading (API, 2001), P_u is the ultimate lateral bearing capacity of the foundation soil at depth H (kN/m), and k is the initial subgrade reaction modulus (kN/m^3) given in the API design code (2001) as a function of the angle of internal friction (φ). The properties of granular soils (sand) that may be used in the analyses are given in Table 17.6.

In the hysteresis model proposed by Shirato et al. (2006), the envelopes of the *p–y* curves of the foundation soil are assumed as elasto-plastic (Figure 17.8c and d). The p–y curves obtained from the API (2001) recommendation are also nearly elasto-plastic and, hence, suited well for the model proposed by Shirato et al. (2006), as shown in Fig.ure 17.8d. The hysteretic rules of the Takeda's hysteresis model (Takeda et al., 1970). available in many structural engineering software are similar

Table 17.6 The Properties of Sand With Different Stiffness

Sand Type	k (kN/m^3)	φ (deg)	γ (kN/m^3)	N	G_{max} (kPa)	V_s (m/s)
Dense	61,000	38	20	40	224,000	330
Medium-dense	40,650	35	19	27	163,400	290
Medium	21,680	32	18	18	118,000	250
Loose	2170	29	16	7	55,000	150

to those proposed by Shirato et al. (2006)—unloading curves are parallel to the initial slope of the elasto-plastic p–y curves (Figure 17.8c). Accordingly, in the structural model, the hysteretic behavior of the soil–pile system may be simulated by using nonlinear spring elements with Takeda's hysteresis model connected between the nodes along the length of the pile and the soil column representing free-field effects (Figure 17.6d).

A typical soil–pile hysteresis loop obtained from nonlinear time history analyses is presented in Figure 17.7c. To simulate radiation damping as the piles impact the soil under seismic effects, dashpots may be placed between the nodal points along the pile and the soil column representing free-field effects (Figure 17.6d). The radiation damping coefficient for these dashpots may be obtained from the following equation (Anandarajah et al., 2005):

$$c = A\rho V_s, \tag{23}$$

where A is the tributary area between the nodal points along the pile, ρ is the mass density of the soil, and V_s is the shear wave velocity.

8.8 Modeling of free-field effects by soil column model

In bridge design, the relative movement of the surrounding soil (free-field motion) during the earthquake is generally not considered. However, this may result in an incorrect simulation of the overall behavior of the bridge during a potential earthquake, especially for soft soil conditions where free-field movements may be considerable (Boulanger et al., 1999). Therefore, a soil column model may be used to simulate the relative movement of the surrounding soil around the piles at the pier and abutments as well as the embankments at the abutments (free-field soil) in the structural model.

The soil column used in the structural model may be modeled using equivalent linear properties of the soil field such as equivalent shear modulus and equivalent damping using any commercially available soil response analysis software. In such software, first, the soil profile above the bedrock needs to be divided into layers, where the soil in each layer is defined by two properties: the maximum shear modulus, G_{max}, and the shear wave velocity, ν_s, given in Table 17.6. The embankment may also be included as a layer on top of the foundation soil with a height equal to the integral abutment height. Then, time history analyses of the model (free-field soil) are performed using spectrum compatible earthquake records. The equivalent degraded shear modulus and equivalent damping ratios at each soil layer and embankment are then obtained from the analyses' results for each earthquake record and associated peak ground acceleration considered in the analyses. These parameters are then used to build linear soil column models integrated with the bridge structural model in the structural engineering software.

In the structural model of the bridge, the free-field effect of the foundation soil should be simulated by introducing soil columns at the pier and abutments. For the soil column model, beam elements (as many discrete beam elements as the number of soil layers and embankment connected in series at nodal points along the height of the soil column), having a high flexural rigidity but a shear stiffness computed using the equivalent degraded shear modulus obtained from soil response analyses, are used (Figure 17.6c) to simulate the free-field behavior of the foundation soil and the embankment. To determine the stiffness properties of the shear beam elements used in the soil column model, the shear area of the free field soil first needs to be determined, since the beam stiffness is equal to $G_S \times A_S$, and A_S is the shear area of the free-field soil. Using the unit weight, shear area, and height of the soil layer, the mass of each soil layer should be calculated and lumped at each node along the soil column. Dashpots should be used to simulate the equivalent damping effects in the soil.

In the structural model with the bridge and the soil column, the free-field motion of the foundation soil together with the embankment (e.g., displacements or accelerations of the soil layers simulated by the soil column) should not be affected by the response of the bridge due to the very large size of the soil field compared to the size of the bridge in actual conditions (the bridge is very small compared to the free-field soil). This could be achieved by selecting a very large shear area for the soil column in the structural model. However, if the shear area selected for the soil column is too large, it may produce numerical instability during the nonlinear solution procedure, as the stiffness of the soil column would be much larger than those of the structural members of the bridge. Accordingly, in the structural model, the size of the shear area of the soil column must be selected carefully to prevent such numerical instability during the nonlinear solution procedure. To define the optimum shear area of the soil columns used in the structural models, sensitivity analyses may be conducted.

9. Important considerations in integral bridge design

9.1 Superstructure

The bridge deck components are designed assuming a continuous frame action at the joints linking the bridge deck to the abutments. A connection detail consistent with the degree of continuity assumed at the joints shall be provided. A typical reinforcement detail that provides full continuity at the deck–abutment joints is illustrated in Figure 17.9. The effect of temperature variation and axial compression in the steel and prestressed girders due to backfill soil pressure is considered in the design.

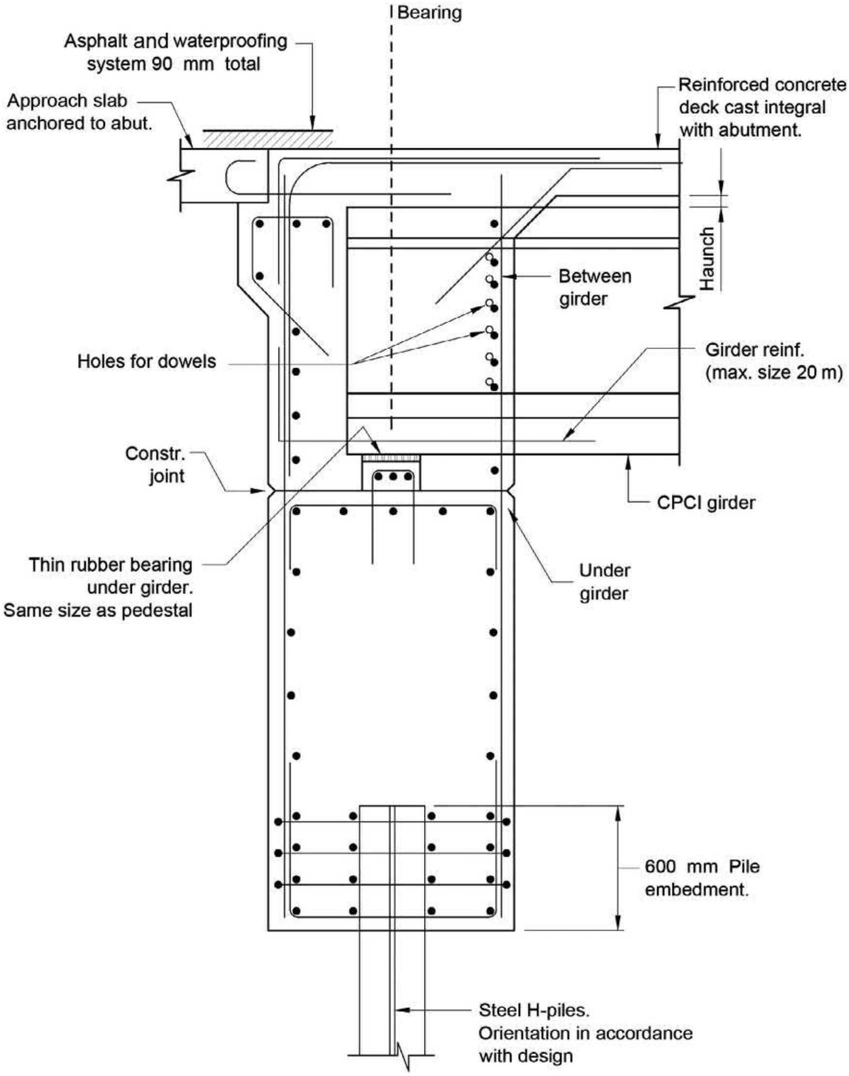

Figure 17.9 Typical reinforcement details of deck–abutment–pile joints.

9.2 Abutments, wing walls, and approach slab

The abutment shall be connected monolithically to the deck as shown in Figure 18.8.1.1., to avoid any expansion joint. The abutment height shall be restricted to the minimum practical value to reduce the soil pressure and to limit the weight, which moves with the deck. However, the minimum penetration required for frost protection shall be provided. The frost penetration requirement can be reduced to minimize abutment height by providing insulation at the bottom of the abutment. It is

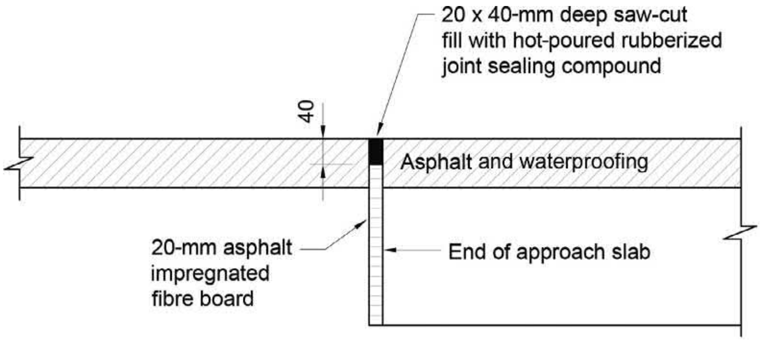

Figure 17.10 Typical joint detail at the end of approach slab.

recommended that abutments at both sides of the bridge be of equal height since a difference in abutment heights causes unbalanced lateral load, which results in sidesway. Additionally, the soil under the approach slab should be sloped to reduce the height of the soil behind the abutment. This practice is also useful in preventing the compaction of the soil behind the abutment wall due to rail traffic. It also reduces the resistance of frictional forces between the soil and the approach slab to bridge movement.

It is preferred that turn-back wing walls, parallel to the railway and carried by the structure, are used. Their size should be minimized to allow the substructure to move with minimum resistance.

The approach slab should be built integral with the abutment to prevent water penetration. An expansion joint shall be provided at the end of the approach slab, as shown in Figure 17.10. The approach slab shall be designed as a simply supported structure spanning over the backfill behind the abutment to prevent compaction of backfill material.

9.3 Piles at abutments

A single row of piles shall be used to support the abutments. The design of piles may be carried out using the equivalent cantilever method as a beam-column with a fixed base at some distance below the ground surface or using a Winkler soil model. A pin connection is recommended between the pile top and abutment to allow free rotation of the pile top about an axis perpendicular to bridge longitudinal direction. If the connection is designed as fixed, plastic bending moments may be produced at the pile top due to thermal movements and the effect of live loads. Low-cycle fatigue effects due to thermal movements should be considered in estimating the maximum integral bridge length.

If the pile-supporting system utilizes the frictional forces between the piles and the soil, consideration shall be given to the effect of lateral displacement of the piles on the frictional resistance. As the piles will be moving laterally with temperature variations, a gap may be produced between the disturbed soil and the pile. This may result in a

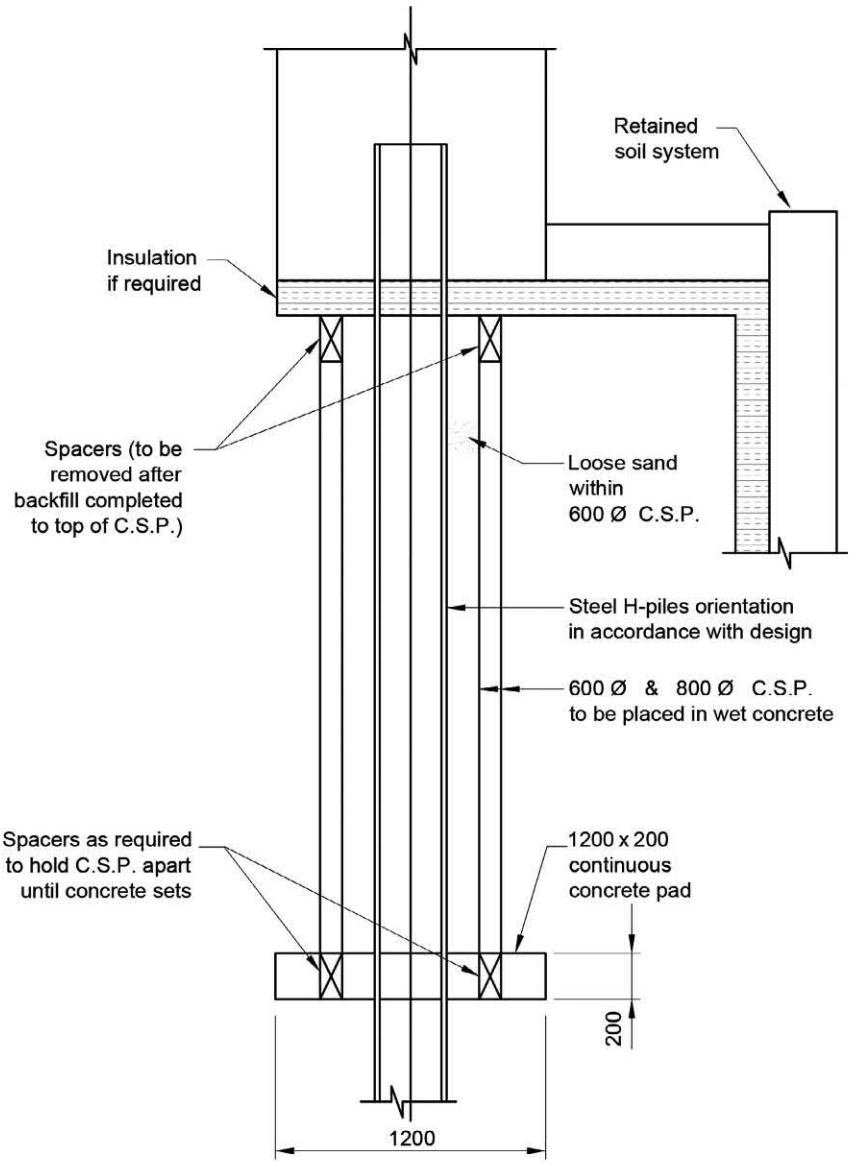

Figure 17.11 Example of pile in stiff soil.

considerable decrease in the frictional resistance of the piles. Therefore, the piles should be designed using the effective frictional pile length reduced by pile displacements.

If the piles are driven into stiff soils, their longitudinal displacement may somehow be restrained. Predrilled oversize holes filled with loose sand may be provided to reduce the resistance to lateral movements. A typical example of this arrangement is illustrated in Figure 17.11.

9.4 Bearings, piers, and foundations

The pier is expected to deflect and rock on its foundation when the structure contracts or expands due to temperature variation. Elastomeric bearings of adequate thickness may be used to reduce the flexibility demand of the pier. The bearings are designed to accommodate the movements of the bridge and to support vertical loads coexisting with rotation of the deck. The pier footing is designed as narrow as possible in the longitudinal direction of the bridge to allow partial rotation of the pier at its base. If the footing is supported on piles, the pile group is designed to allow some rotation of the footing.

10. Conclusions and closing remarks

This chapter provides important information on thermal effects in integral bridges, required conditions for their design and construction method as well as modeling for seismic performance assessment. The information provided in this chapter also presents useful tools that may aid bridge design engineers to properly model and design integral bridges under gravitational, thermal, and seismic loads.

References

AASHTO, 2010. LRFD Bridge Design Specifications, fourth ed. Washington, DC.
AISC (American Institute of Steel Construction), 2010. Load and Resistance Factor Design (LRFD) Manual for steel structures. AISC LRFD Design Manual.
Anandarajah, A., Zhang, J., Ealy, C., 2005. Calibration of dynamic analysis methods from field test data. Soil Dyn. Earthq. Eng. 25 (7–10), 763–772.
API (American Petroleum Institute), 2001. Recommended Practice and Planning, Designing, and Constructing Fixed Offshore Platforms. Washington, DC.
Barker, R.M., Duncan, J.M.K., Rojiani, K.B., Ooi, P.S.K., Kim, S.G., 1991. Manuals for the Design of Bridge Foundations, NCHRP Report 343. Transportation Research Board, National Research Council, Washington, DC.
Boulanger, R.W., Curras, C.J., Kutter, B.L., Wilson, D.W., Abghari, A., 1999. Seismic soil-pile-structure interaction experiments and analyses. J. Geotechn. Geoenviron. Eng. ASCE 125 (9), 750–759.
Bowles, J.E., 1996. Foundation Analysis and Design, fifth ed. McGraw-Hill, New York, NY.
Burke Jr., M.P., 1988. Bridge Deck Joints. Transportation Research Board, National Research Council, Washington, DC. NCHRP Synthesis of Highway Practice, No 141.
Burke Jr., M.P., 1990. Integral bridge design is on the rise. AISC Mod. Steel Construct. 30 (4), 9–11.
Chen, Y., 1997. Assessment on pile effective lengths and their effects on design – I. Assessment. Comput. Struct. 62 (2), 265–286.
Cole RT, Rollins KM (2006) Passive earth pressure mobilization during cyclic loading. J Geotech Geoenviron Eng 132(9):1154–1164.
Cross, H., 1932. Analysis of continuous frames by distributing fixed-end moment. Trans. Am. Soc. Civ. Eng. 96, 1–156.
Dicleli, M., 2000a. A rational design approach for prestressed-concrete-girder integral bridges. Eng. Struct. 22 (3), 230–245.
Dicleli, M., 2000b. Simplified model for computer-aided analysis of integral bridges. ASCE J. Bridge Eng. 5 (3), 240–248.

Dicleli, M., 2005. Integral abutment-backfill behavior on sand soil - pushover analysis approach. J. Bridg. Eng. 10 (3), 354–364.

Dicleli, M., 2007. Supplemental elastic stiffness to reduce isolator displacements for seismic-isolated bridges in near fault zones. Eng. Struct. 29 (5), 763–775. Elsevier Science.

Dicleli, M., Albhaisi, S.M., 2004. Effect of cyclic thermal loading on the performance of steel H-piles in integral bridges with stub-abutments. J. Constr. Steel Res. 60 (2), 161–182.

Dicleli, M., Albhaisi, S.M., 2005. Analytical formulation of maximum length limits for integral bridges built on cohesive soils. Can. J. Civ. Eng. 32 (5), 726–738.

Dowell, R.K., Seible, F., Wilson, E.L., 1998. Pivot hysteresis model for reinforced concrete members. ACI Struct. J. 95 (5), 607–617.

Duncan, M.J., Chang, C.Y., 1970. Nonlinear analysis of stress and strain in soils. J. Soil Mech. Found. Div. ASCE 96 (5), 1629–1653.

Duncan MJ, Mokwa RL (2001) Passive earth pressure: theories and tests. J Geotechn Geoenviron Eng 127(3):248–257.

Erhan, S., Dicleli, M., 2014. Comparative Assessment of the Seismic Performance of Integral and Conventional Bridges with Respect to the Differences at the Abutments, Bulletin of Earthquake Engineering. Springer, https://doi.org/10.1007/s10518-014-9635-8.

Evans, L.T., 1982. Simplified Analysis of Laterally Loaded Piles. Ph.D. Thesis, University of California, Berkeley, CA, p. 211.

Franchin, P., Pinto, E.P., 2014. Performance-based seismic design of integral abutment. Bridges Bull. Earthq. Eng. 12, 939–960.

Girton, D.D., Hawkinson, T.R., Greimann, L.F., 1991. Validation of design recommendations for integral-abutment piles. ASCE J. Struct. Eng. 117 (7), 2117–2134.

Hambly, E.C., 1997. Integral bridges. Proc. Inst. Civ. Eng. Transp. 123 (1), 30–38.

Jain, S.K., Scott, R.F., 1989. Seismic analysis of cantilever retaining walls. In: Proceedings of Structural Mechanics in Reactor Technology (SMIRT), Anaheim, CA, pp. 241–246.

Kotsoglou, A., Pantazopoulou, S., 2007. Bridge–embankment interaction under transverse ground excitation. Earthq. Eng. Struct. Dyn. 36, 1719–1740.

Kotsoglou, A., Pantazopoulou, S., 2009. Assessment and modeling of embankment participation in the seismic response of integral abutment bridges. Bull. Earthq. Eng. 7, 343–361.

Kotsoglou, A., Pantazopoulou, S., 2010. Response simulation and seismic assessment of highway overcrossings. Earthq. Eng. Struct. Dyn. 39, 991–1013.

Shamsabadi, A., 2007. Three-dimensional nonlinear seismic soil abutment-foundation-structure interaction analysis of skewed bridges. PhD thesis, University of Southern California, Los Angeles, CA.

Shirato, M., Koseki, J., Fukui, J., 2006. A new nonlinear hysteretic rule for Winkler type soil-pile interaction spring that consider loading pattern dependency. Soil Found. Jap. Geotechn. Soc. 46 (2), 173–188.

Steiger, D.J., 1993. Jointless bridges provide fuel for controversy. Roads and Bridges 31 (11), 48–54.

Takeda, T., Sozen, M.A., Nielsen, N.N., 1970. Reinforced concrete response to simulate earthquake. J. Struct. Div. ASCE 96 (12), 2557–2573.

Warn, P.G., Ryan, K.L., 2012. A review of seismic isolation for buildings: historical development and research needs. Buildings 2 (3), 300–325.

Wolde-Tinsae, A.M., Klinger, J.E., Mullangi, R., 1988a. Bridge Deck Joint Rehabilitation or Retrofitting. Final Report, Department of Civil Engineering, Maryland University, College Park, MD.

Wolde-Tinsae, A.M., Klinger, J.E., White, E.J., 1988b. Performance of jointless bridges. ASCE J. Perform. Constr. Facil. 2 (2), 111–128.

Zhang, J., Makris, N., 2002. Kinematic response functions and dynamic stiffnesses of bridge embankments. Earthq. Eng. Struct. Dyn. 31, 1933–1966.

This page intentionally left blank

Movable bridges

18

R. Saul and K. Humpf
Leonhardt, Andrä und Partner Beratende Ingenieure VBI AG, Stuttgart, Germany

1. Introduction

1.1 General

One of the great beneficiaries of globalization is the transport sector, especially maritime transport. With the cost of DVD player being about $2 and a television set being about $20 between the Far East and Europe of about $2 for a DVD player and $30 for a television set, even the longest transport pays off! This has led to an explosive increase of container traffic (e.g., between 2004 and 2005, an increase of 24% in Shanghai, 17% in Dubai, and 17% in Hamburg) (BMVBS, n.d.). Consequently, the number and size of container ships has increased permanently (Figure 18.1). In places with sufficient space for long-ramp bridges, high-level bridges are normally built (Figure 18.2). In places with restricted space, road bridges may still be built as high-level bridges, but railway bridges may be built as low-level movable bridges (Figure 18.3). Because in many ports high-level bridges are unfeasible due to the very restricted space, movable bridges have experienced a veritable renaissance during the last decades.

1.2 Short description of movable bridge types

1.2.1 Lift bridges

Lift bridges are suitable for great spans, but their clearance is limited by the lift towers, which have a great impact on the environment, even when the bridge is closed (Figure 18.4). The cables linking the bridge and the counterweights may suffer from significant wear.

1.2.2 Swing bridges

Swing bridges are also suitable for great spans and do not limit the clearance. The biggest bridge of this type crosses the Suez Canal at El Ferdan, Egypt, with a free span of about 300 m (Figure 18.5). The disadvantages of swing bridges include the following:

- When opened, they occupy the embankment over a length of about their main span.
- Due to geometrical reasons, it is impossible to have separate bridges for railways and highways in close vicinity.

Innovative Bridge Design Handbook. https://doi.org/10.1016/B978-0-12-823550-8.00001-9

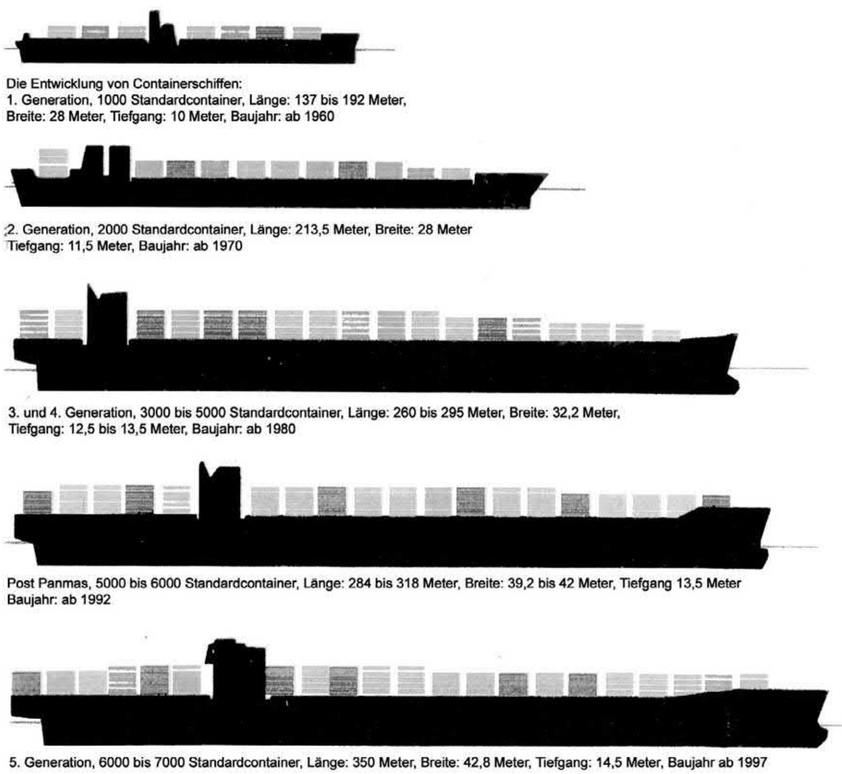

Figure 18.1 Development of container ships.

1.2.3 Bascule bridges

Bascule bridges may have a single flap or two flaps and are also adequate for long spans without limiting the clearance. The connection between the two flaps may transmit shear forces only, or shear forces and bending moments. For great heights above the water, the counterweight may be attached to the rear arm as a pendulum (Figure 18.6); for reduced heights, it has to be integrated with it (described further in Section 4).

1.2.4 Balance beam bridges (draw bridges)

Drawbridges, the precursors of bascule bridges, are most probably the oldest type of movable bridge (Figure 18.7). Compared to bascule bridges, they have the advantage of rather simple piers and a high architectural potential (Figure 18.8), but their disadvantage is that they permit only rather reduced spans.

Figure 18.2 High-level bridge for road and railway traffic: the Zárate–Brazo Largo bridges across the Paraná, Argentina (Leonhardt et al., 1979).

2. Lift and lower bridges

2.1 Example of a lift bridge: The Guaiba River bridge with concrete towers at Porto Alegre, Brazil (1954–1960)

2.1.1 General information

The Guaiba River Bridge (Leonhardt and Andrä, 1963) has a total length of 5665 m. It consists of the following:

- A 2013 m long access bridge and a flyover, linking roads parallel to the river with the road crossing it.

Figure 18.3 High-level bridge for long distance road traffic and low-level bridge for local road and railway traffic: the Strelasund Crossing at Stralsund, Germany (Kleinhanß and Saul, 2007).

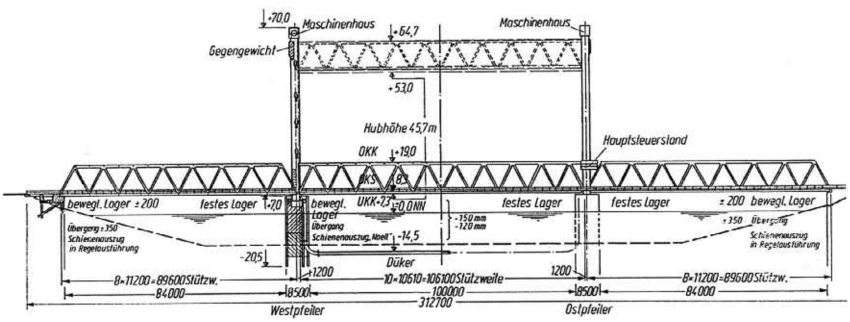

Figure 18.4 Kattwyk Liftbridge at Hamburg, Germany (Rüster, 1974).

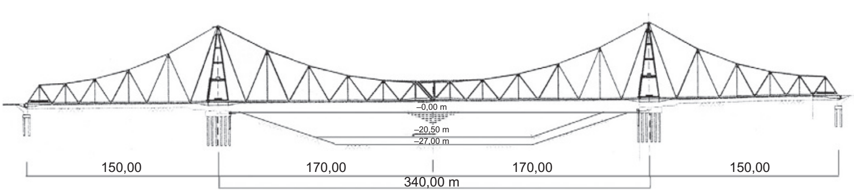

Figure 18.5 Swing bridge across the Suez Canal at El Ferdan, Egypt (Binder et al., 2001).

- The bridge across the Guaiba River, with a total length of 777 m. Its main span, with a clear span of 50 m and a clearance of 40 m, is designed as a lift bridge.
- The 344 m long bridge across the Furado Grande River.
- The 774 m long bridge across the Saco Alamôa Bay.
- The bridge across the Jacui River, with a total length of 1757 m and main openings of 50×20 m.

With the exception of the lift bridge, the entire bridge is made of prestressed concrete, with regular spans of 43 m above water and 21.5 m over land.

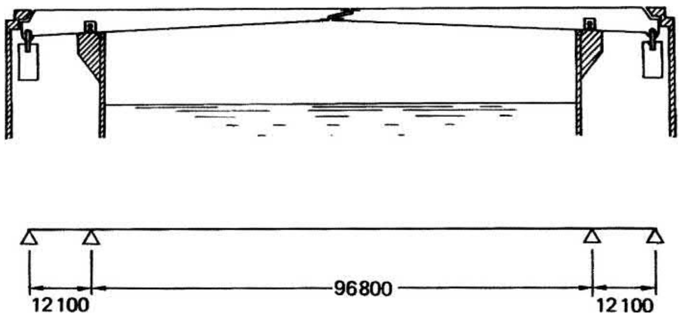

Figure 18.6 Bascule bridge with hang-on counterweight: Bridge across the bay of Cádiz, Spain (Freudenberg, 1971).

Figure 18.7 Vincent van Gogh: Langlois Bridge at Arles, France. Courtesy of Rheinisches Bildarchiv Köln rba_c012712.

Figure 18.8 Diffené Bridge at Mannheim, Germany (Freudenberg, 1989).

2.1.2 The lift bridge

General information

The lift bridge has a free span of 50 m and a clearance above the low-water level of 13.5 m when in service and 40 m when opened. The lifting height, therefore, is 26.5 m. It consists of the bridge deck, a steel bridge with orthotropic plate, and four rounded towers made of reinforced concrete, which hoist (and hide) the concrete counterweights and machinery. Thanks to the graceful design of these towers, the often-ugly appearance of lift bridges is avoided (Figure 18.9).

Bridge deck

The bridge deck has a span of 55.8 m and hoists a four-lane roadway 16.00 m, the walkways 2 × 1.15 m totaling 2.30 m, for a combined span of 18.30 m.

The distance of the main girders is 13 m and the two cantilevers are 2.65 m long (Figure 18.10). The orthotropic deck consists of the deck plate, with a thickness of 12 mm; the bulb-shaped longitudinal ribs, with a distance of 310 mm and a depth of 160 mm; the narrowly spaced (d = 1.65 m) cross-girders, with a depth of 640 mm corresponding to 1/20 of their span; the 60-mm-thick asphalt layer.

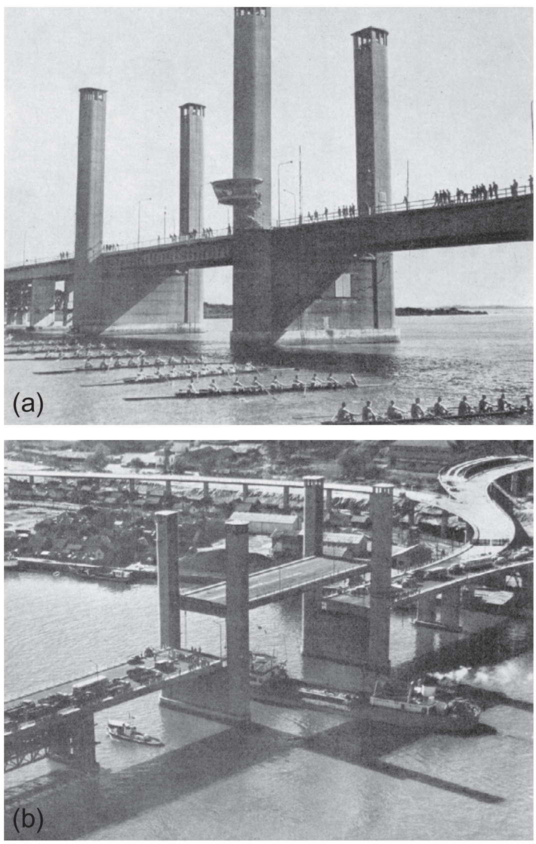

Figure 18.9 View of the lift bridge: (a) under service, (b) opened to a major ship.

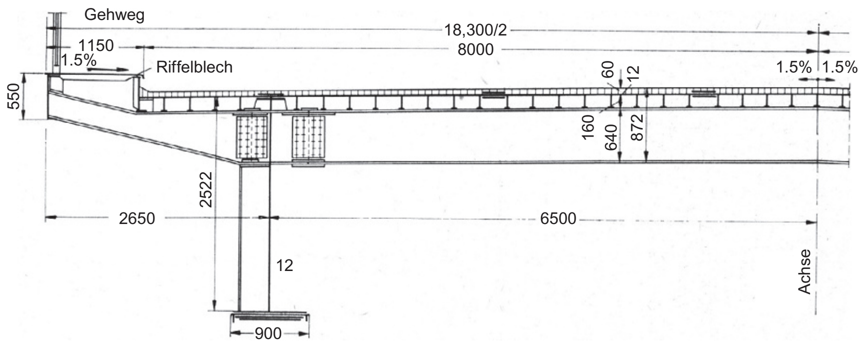

Figure 18.10 Section of the bridge deck.

The main girders have a depth—as the approach viaducts—of 2.64 m corresponding to 1/21 of their span. They are stiffened by vertical stiffeners on the outside only, and, therefore, they are an early application of the tension field theory. The weight of the steel structure is 381 tons, corresponding to 360 kg/m^2, and the total weight of the bridge deck is 540 tons.

Towers and piers

The towers and piers have a total height of 48.2 m above the lowest water level. They consist of the following (Figure 18.11):

- Four freestanding towers, with a distance of 51.8 m in the longitudinal direction, 18.6 m in the transverse direction, and a height of 35 m. They have overall dimensions of 4 × 4 m and are rounded on their outer faces. Their walls parallel to the bridge axis are 300 mm thick, and the other walls are 250 mm thick. The towers surround the counterweight Ø 3 m × 6 m of heavyweight concrete.
- The 11.6 m high piers connecting the towers underneath the bridge deck. They have two walls with a distance of 3.0 m and a thickness of 250 mm.
- Pile caps with dimensions of 28.4 m × 4.9 m × 2.0.
- A total of 66 driven piles Ø 0.52 m per pier, in a Franki piling system.

Mechanical installations

The wheels for turning around the cables, which connect the bridge deck and the counterweights, and the entire machinery at the top are also included in the towers. These features improve the aesthetical appearance of the bridge substantially. The hoisting and lowering of the bridge deck are controlled from a cabin on the outside of one of the towers (Figure 18.9a).

2.2 Lower (submergible) bridges

At a first glance and in view of their corrosion protection, it may seem crazy to submerge a bridge into water, especially into salty seawater. But, if corrosion protective systems, like for hydraulic steel structures, are applied, this is not really a problem. On

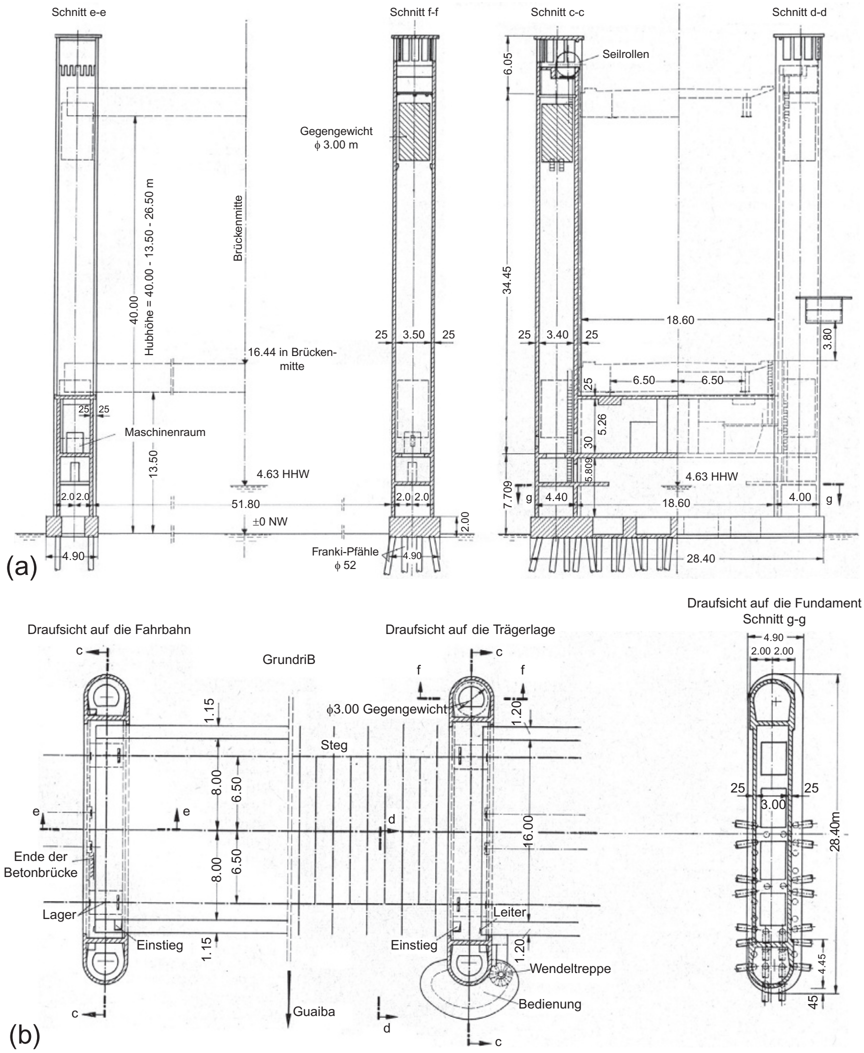

Figure 18.11 Towers and piers.

the other hand, compared to lift bridges, lower or submergible bridges have the following advantages:

- The vertical movement is substantially reduced, as the draught of ships is only about one-fifth of their height above the water line.
- Consequently, the energy consumption is reduced, especially if the bridge is designed in such a way that it is hovering in the water.
- The surrounding landscape is not disturbed by the high and voluminous lifting towers.

Nevertheless, this bridge type is very rare. An example is the bridge across the Corinth Canal (opened to shipping in 1893) near the city of Isthmia, Greece (Figure 18.12).

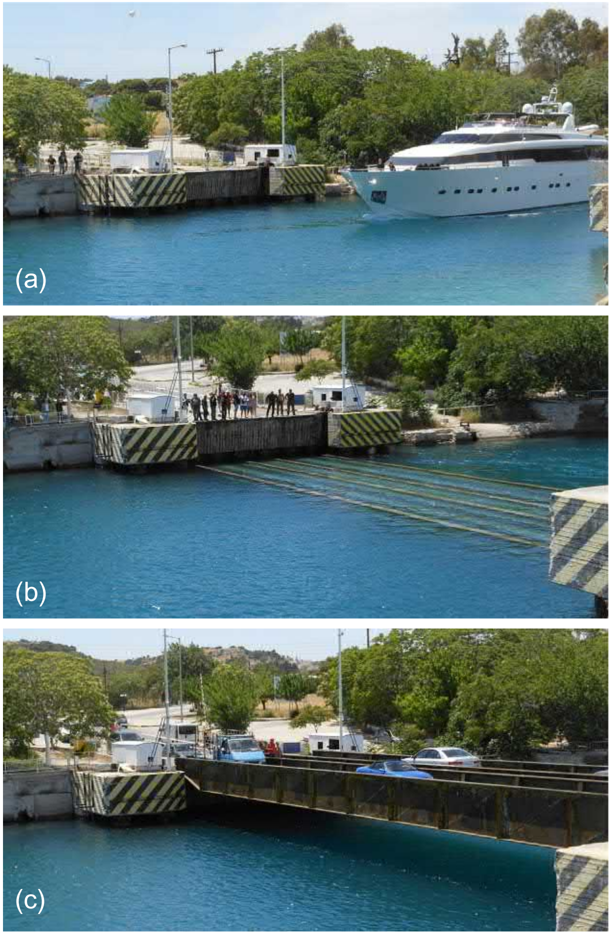

Figure 18.12 Lower (submergible) bridge at Isthmia, Greece (Saul and Humpf, 2007): (a) submerged; (b) emerging; (c) service condition.

3. Swing bridges

3.1 The Prestressed concrete bridge across the Shatt-Al-Arab, Iraq (1972–1978)

3.1.1 General

The prestressed concrete bridge across the Shatt-Al-Arab (Seifried and Wittfoth, 1979) consists of the following (Figure 18.13):

- The western section, with a total length of 331.75 m
- The eastern section, with a total length of 430.15 m
- A viaduct linking the main bridge to Sinibad Island

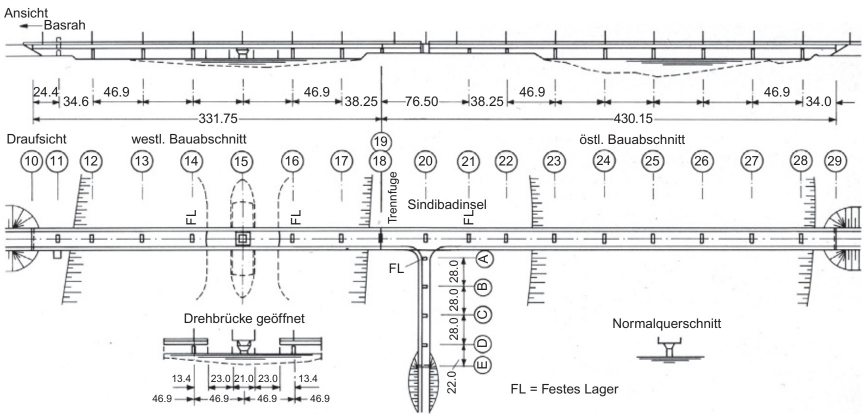

Figure 18.13 General layout.

The center part of the western section is a swing bridge with a total length of 67 m, providing space for two shipping canals of 23 m each. The main bridge has regular spans of 46.9 m and a width of 21 m; the viaduct has regular spans of 28 m and a width of 10.75 m. The entire bridge deck, including the swing bridge, is made of prestressed concrete. The main bridge was built by incremental launching, with a unit length of 15.63 m corresponding to 1/3 of the regular span. With respect to this construction procedure, its depth is 3.65 m, corresponding to 1/12.8 of the regular span.

3.1.2 The swing bridge

Bridge deck

The swing bridge has two cantilevers of 33.5 m each (Figure 18.14a). The cross section consists of the following:

- A trapezoidal box girder with a width of 7 m at the bottom and 10.5 m at the top
- Two 5.25 m wide cantilevers

The bridge deck is prestressed in the longitudinal and the transverse directions (Figure 18.14b). For the launching, continuity tendons were introduced at both bridge ends, which were cut after the bridge had reached its final position.

Main pier

The main pier (Figure 18.15a) consists of the following:

- A solid pier Table 12.8 m square
- A hollow shaft 6.5 m square, with a wall thickness of 1.0 m
- A 2.0 m thick pile cap
- 16 drilled piles Ø 2 m, with a length of about 40 m

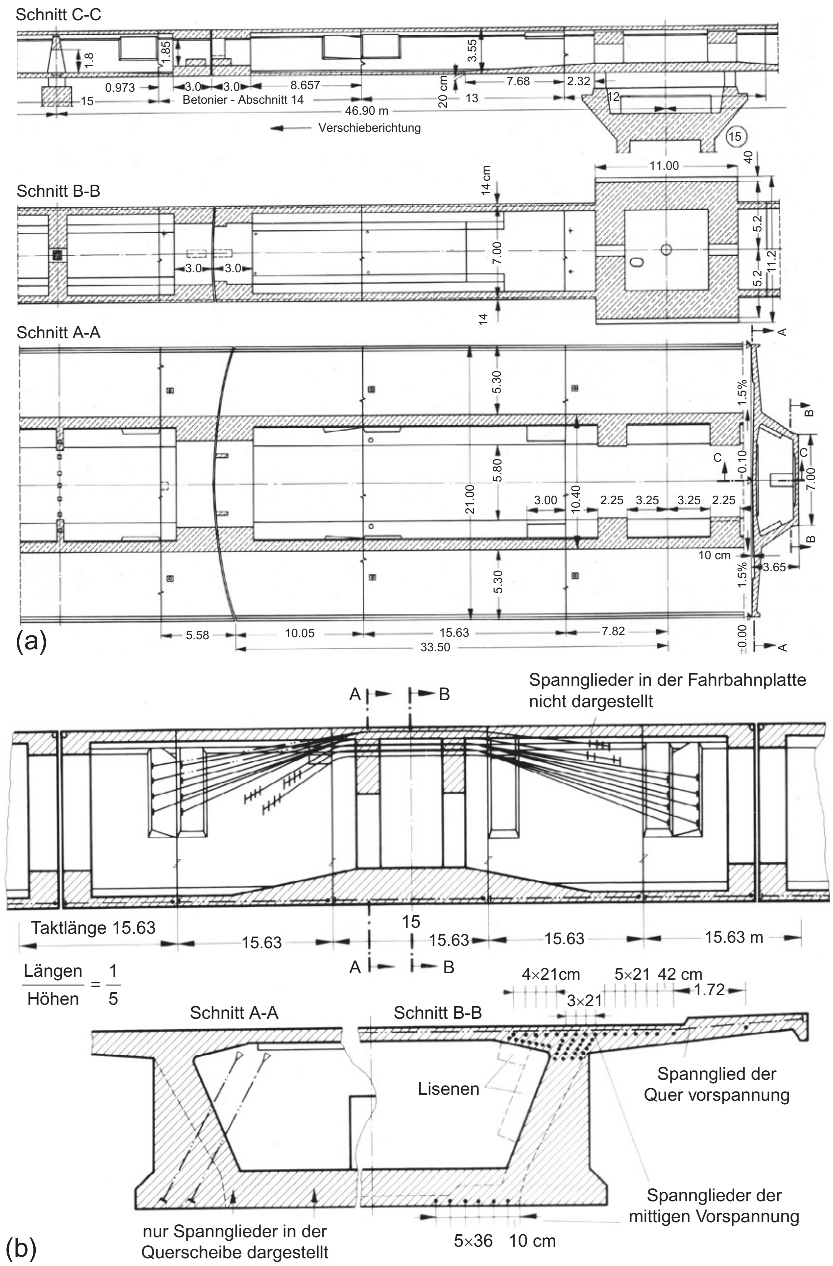

Figure 18.14 Swing bridge: (a) layout; (b) prestressing.

The pier table is heavily prestressed (Figure 18.15b). The bridge deck rests at the pier on a turning circle with a radius of 10 m (Figure 18.15c).

3.1.3 Joint to the fixed part

The swing bridge is locked to the fixed part by locking devices that can be retracted to facilitate the opening of the bridge (Figure 18.16, top). The circular expansion joint is open, with a gap of 30 mm (Figure 18.16, bottom).

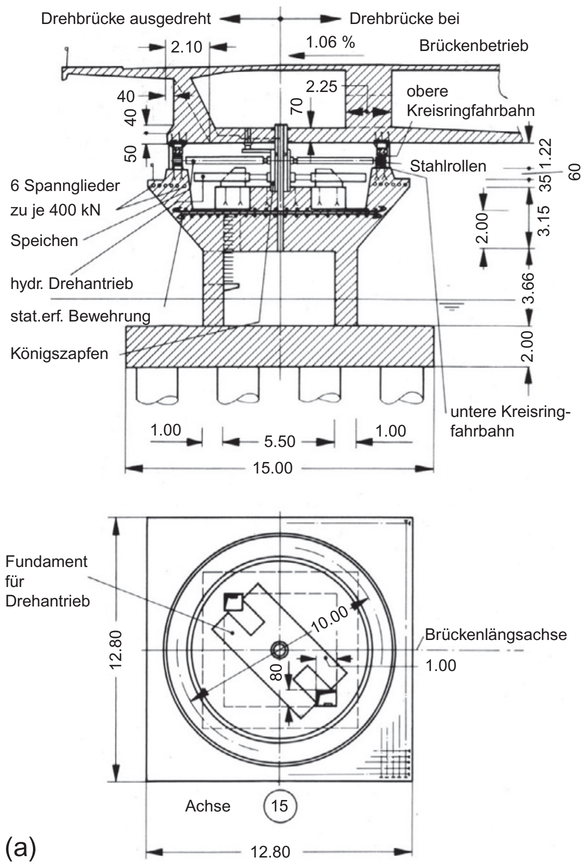

Figure 18.15 Main pier: (a) layout;

(Continued)

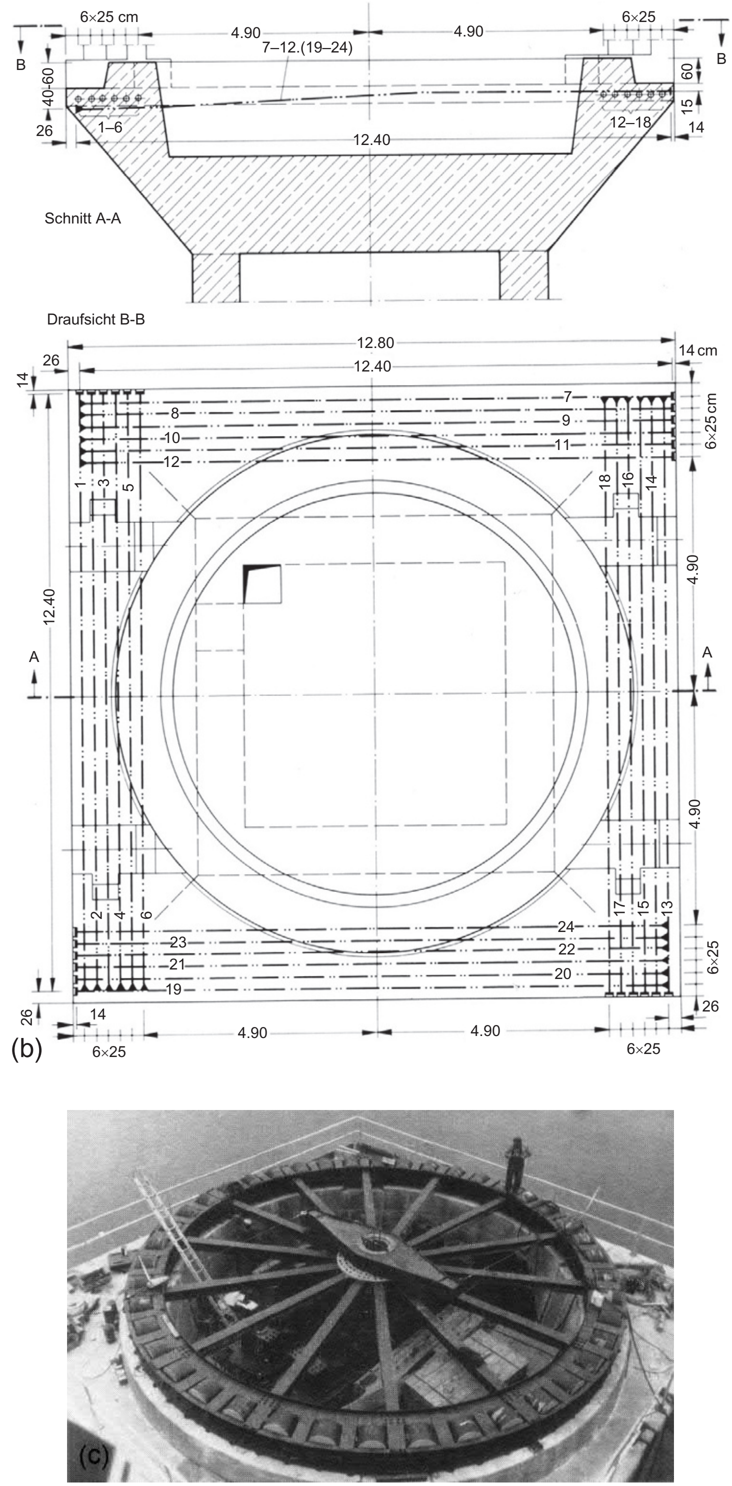

Figure 18.15, cont'd (b) prestressing of the pier table; (c) turning circle.

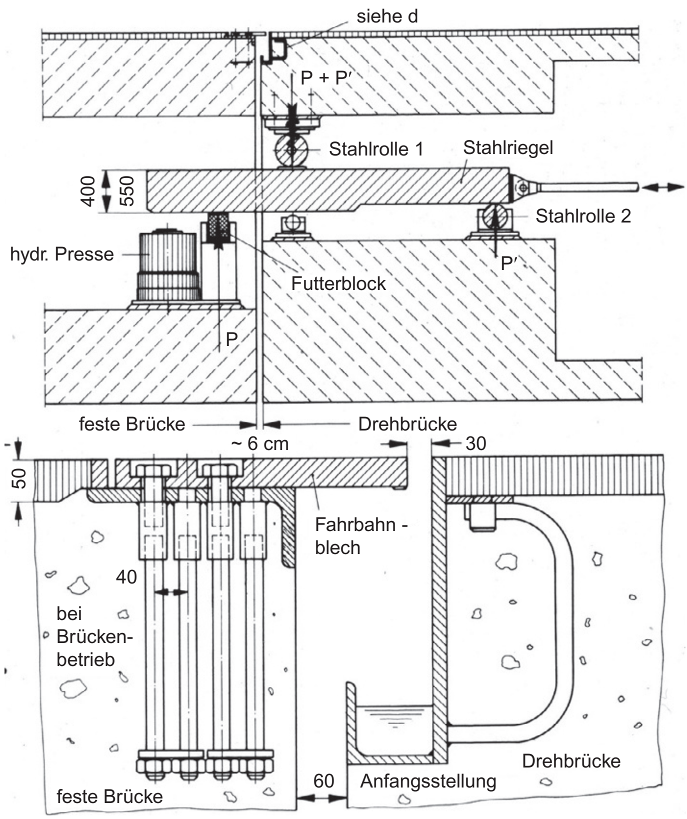

Figure 18.16 Joint to the fixed part: top-locking device; bottom: expansion jointing.

3.2 Cable-stayed bridge in the port of Barcelona, Spain

3.2.1 Introduction

The bridge in the port of Barcelona was the first of a growing number of movable bridges built during the last decade the ports of in Spain with the aim of adapting these ports to the needs of modern ship traffic. The tender design called for a double flap bascule bridge with a free span of 85 m (Figure 18.17). This span is small for the design ship— 20,000 dwt, L = 250 m, W = 35 m, sailing at 2.2 m/s— and left the main piers, founded on piles, in the water. Hence, they would be exposed to impact from ships.

LAP (Leonhardt, Andrä, Partner GmbH, 1997), with a group of Spanish contractors, prepared an alternative design as a swing bridge. The main aim of this design was to avoid the expensive piers in the water, thereby increasing the safety of navigation. Unfortunately, this alternative was not selected for construction. Nevertheless, for readability, we use the language corresponding to a built bridge.

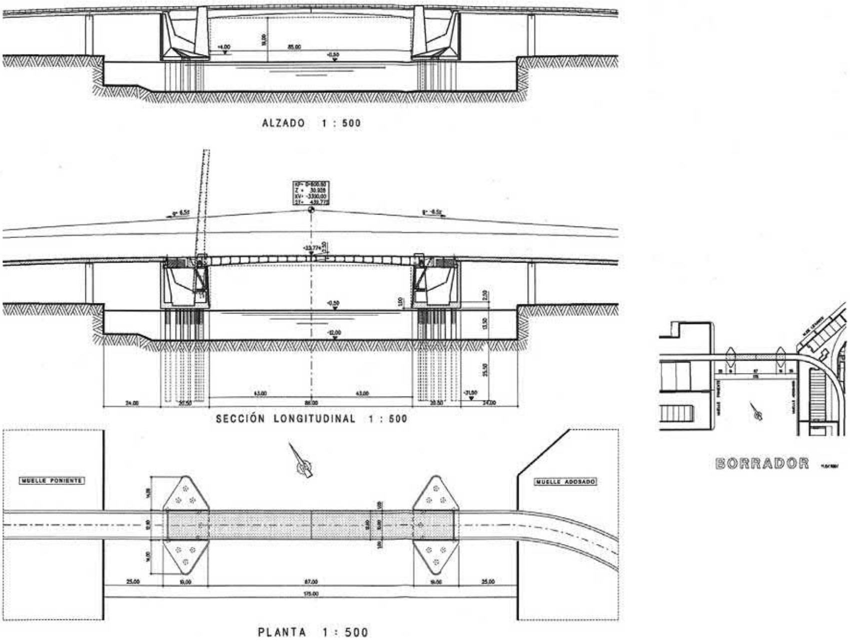

Figure 18.17 Bascule Bridge of Tender Design.

3.2.2 Description of the design

Main structural system

The main structure of the swing bridge is a cable-stayed bridge with spans of 180 m and 75 m and a single tower with four legs (Figure 18.18). The effective span lengths are reduced by cantilevers of the approach viaducts to 159 m and 68 m, respectively. In order to have the permanent loads centered with respect to the axis of the towers, the steel composite deck of the main span is counteracted by a concrete side span. In the longitudinal direction, the cables are anchored at regular intervals of 17 m at both borders of the deck.

Bridge deck

The bridge deck consists of a two-lane, 10 m wide roadway and two 2.25 m wide walkways and cable anchorage zones, yielding a total width of 14.50 m.

The steel composite bridge deck (Figure 18.19a) is built up from

- The two 2.3 m deep main girders with a distance of 12.3 m
- 2.10 m deep cross girders spaced 4.25 m apart.
- The 225 mm thick roadway slab with an 80 mm thick asphalt layer; in the walkway and cable anchorage zone, the slab thickness is 500 mm.
- Concrete cable anchorages at the outside of the main girders.

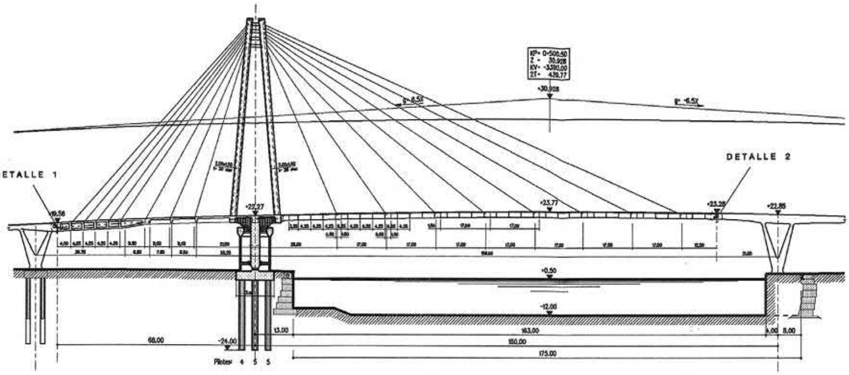

Figure 18.18 Layout of the Alternative.

The bridge deck in the side span, close to the pier, made of prestressed concrete, is a plate-beam structure with a depth of 2.3 m (Figure 18.19b). It consists of the following:

- The main girders, with an outer distance of 12.3 m and a width of 1.75 m to 2.0 m
- Cross girders with a spacing of 8.5 m
- A 600 mm thick slab.

In the sidespan counterweight area, the bridge deck is a box girder with outer dimensions of 12.3 × 3.2 m (Figure 18.19c). The box is filled with heavyweight concrete to counteract the long main span.

Tower and pier

The steel tower has a height of 67.7 m above the bridge deck (Figure 18.20). It consists of four legs with outer dimensions of 1.5 m × 2 m and is stiffened by four cross girders at their top. The tower is supported by a solid part of the bridge deck that is prestressed in both the longitudinal and transverse directions. The circular pier has an outer diameter of 11.2 m and a wall thickness of 400 mm, which is thickened to 2 m at the top, where it hoists the turning table with a diameter of 10.8 m. The pier is founded on fourteen 24 m long drilled piles Ø 2 m and a 3 m thick pile cap.

Mechanical equipment

The bridge deck is turned around a pivot of 3 m, which takes horizontal forces only, by two hydraulic cylinders (Figure 18.21).

3.2.3 Construction

The bridge was assembled parallel to the embankment. Later, it was turned into its service position.

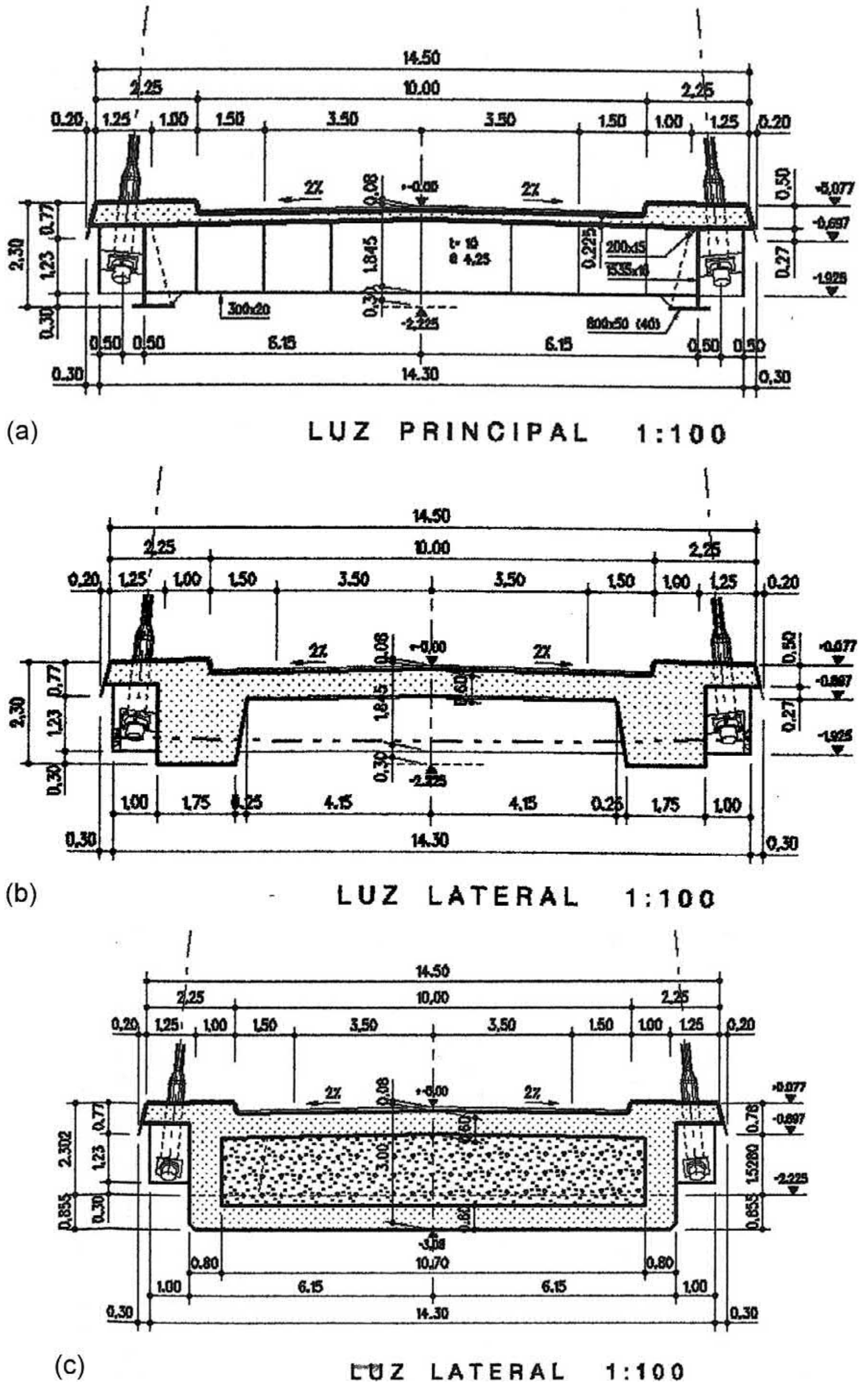

Figure 18.19 Cross sections of bridge deck: (a) at mainspan; (b) at sidespan; (c) at counterweight.

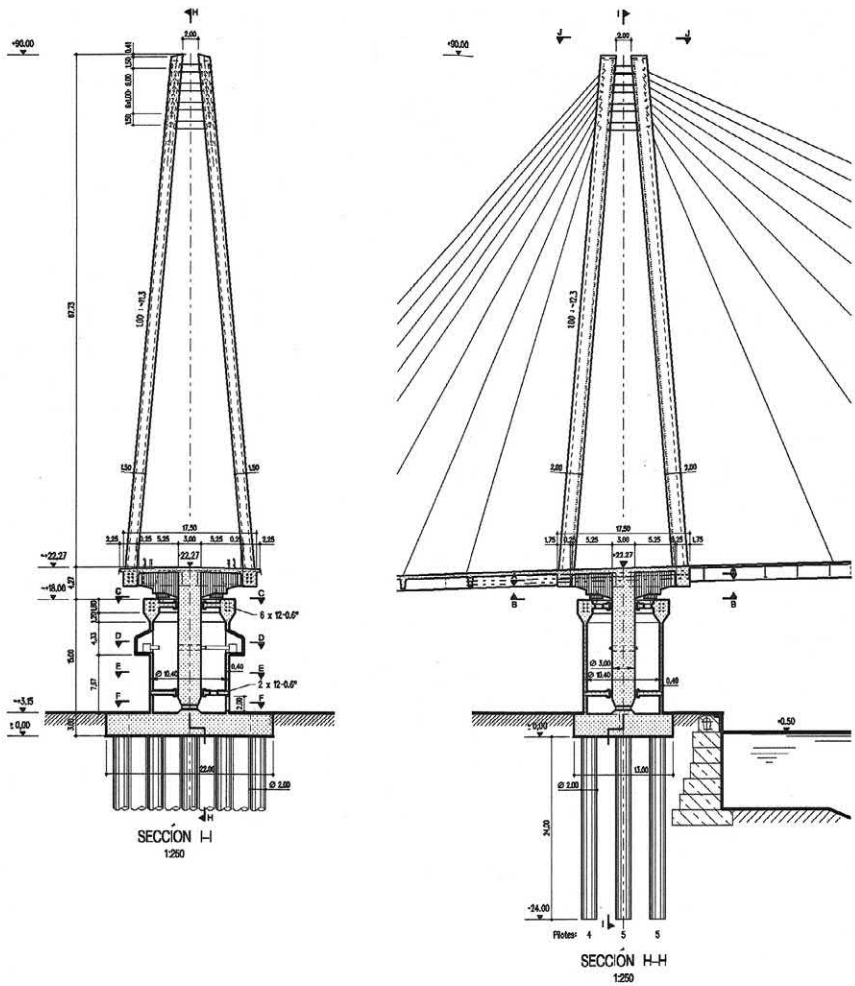

Figure 18.20 Towers and piers.

3.3 Railroad bridge across the Sungai Perai River, Malaysia (2008–2013)

3.3.1 Introduction

A double-track electrified railway line between Padang Besar and Ipoh crosses the Sungai Perai River in Malaysia from west to east on a railway bridge designed by LAP (Leonhardt, Andrä, Partner GmbH, 2008) with two spans of 45 m. LAP prepared link the concept and tender design, including the mechanical and electrical elements, for the contractor responsible for the construction of the complete rail.

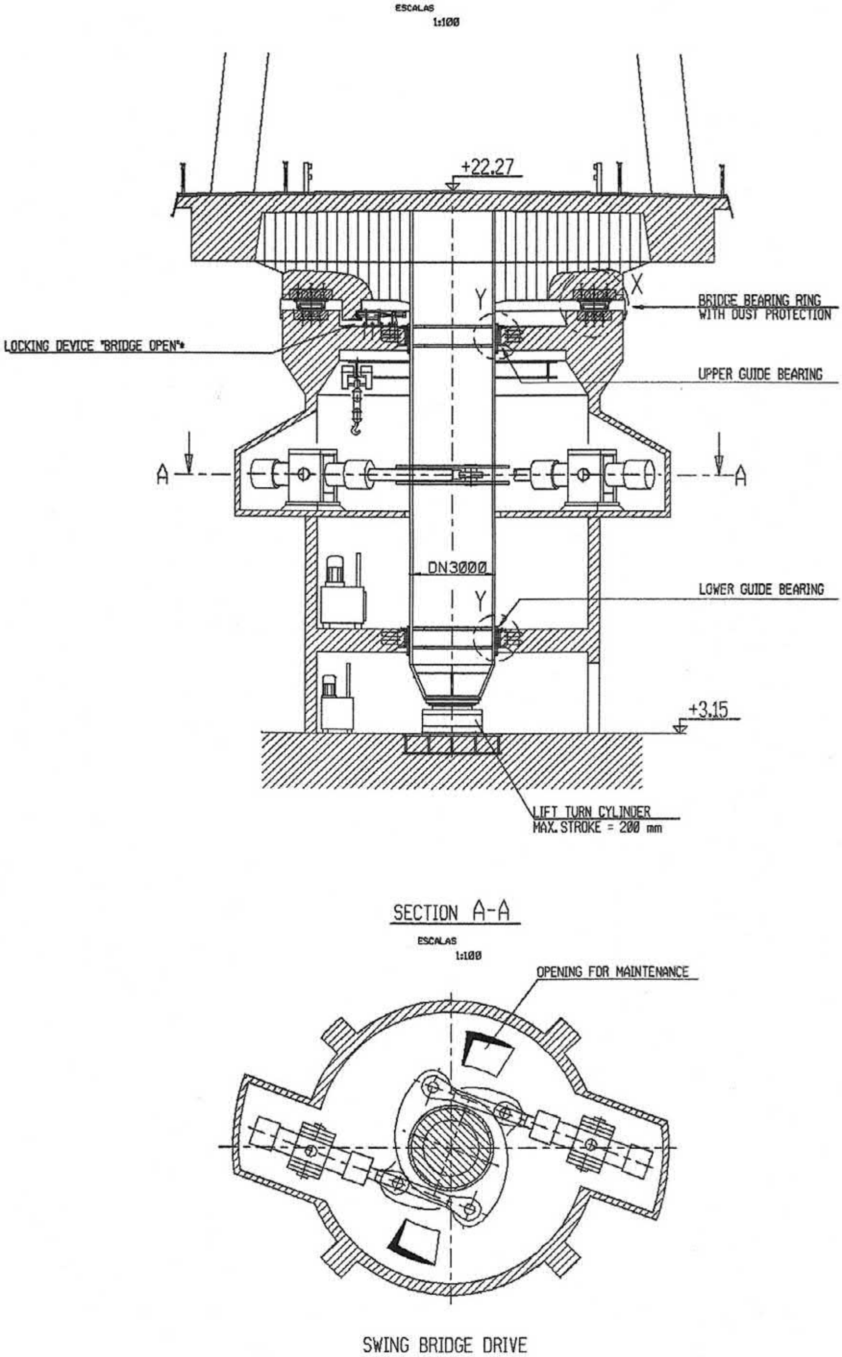

Figure 18.21 Mechanical equipment.

3.3.2 Description of the design

The main structure consists of two balanced spans composed of a steel grid supporting the concrete slab and of two steel sails at the edges as main load-carrying members. The deck width is 11 m, and together with the steel sails of 1 m each, the overall width is 13 m (Figure 18.22). Crossbeams of 1.40 m depth at 4 m distance carry the traffic loads to the main girders, which consist of a plate girder of variable depth (between 2 and 12 m), a V-shaped strut in the axis of the central pier, and two openings in the web of the plate girder. All stiffeners of the plate girders are located at the inner side, providing a smooth outside face of the structure. The supply of electricity for the railway can be held independent of the structure, with typical posts and contact wire supports throughout the railway link. Below the center pier, all turning equipment and rotational bearings are located in a hollow pier partially underwater. The center pivot shaft provides vertical and horizontal support during the swinging operation. A hydraulic lift/turn cylinder allows the torque to transmit to turn and lower the structure on bearings for the railway service situation. The pivot shaft is free from loads under service conditions. In the service position, the bridge is locked with wedge-shaped end locks, and a rail-locking device is engaged to provide continuity of the rail. In the open position parallel to the river, the bridge is protected by a guidance steel structure that keeps the footprint of the bridge in open position free from navigation.

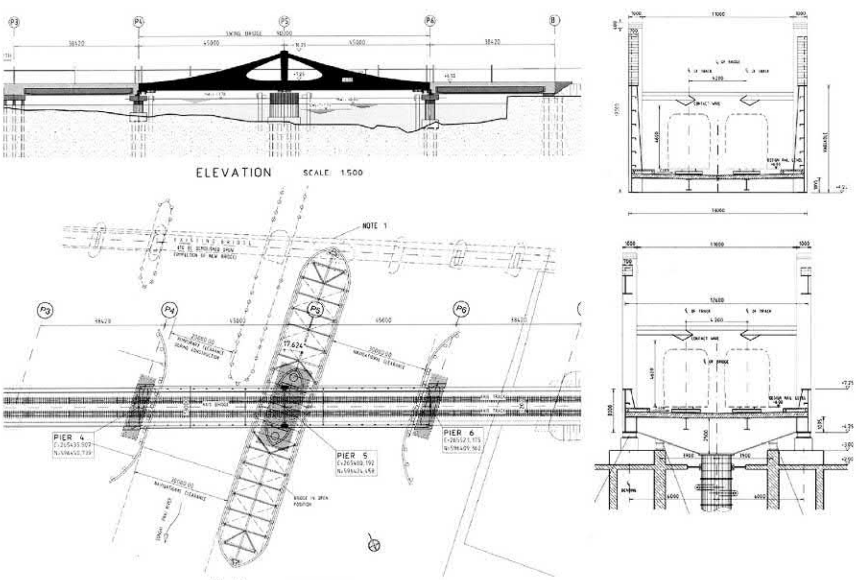

Figure 18.22 Railroad bridge across the Sungai Perai River, Malaysia: layout and sections (Leonhardt, Andrä, Partner GmbH, 2008).

4. Bascule bridge: The new Galata bridge with twin double flaps at Istanbul, Turkey (1985–1993)

4.1 Introduction

The New Galata Bridge across the Golden Horn (Saul et al., 1992) in Istanbul, Turkey, links the quarters of Eminönü and Karaköy, close to a steel floating bridge built in 1912.

The 477.45 m long and 42 m wide bridge (Figures 18.23 and 18.24) primarily consists of the following elements:

- A center bascule bridge with a clearance of 80 m and the corresponding bascule bridge piers
- Double deck approach bridges with eight spans of 22.3 m each, with road and light railway traffic on the upper deck and shops, restaurants, and similar establishments on the lower deck
- The abutments

Between these 2×3 elements and between the bascule bridge piers and their piles, buffer bearings are provided.

Due to a water depth of up to 40 m and poor soil of another 40 m, the bridge is founded on driven or drilled hollow steel piles with a diameter of 2 m, a wall thickness of 20 mm, and cathodic corrosion protection.

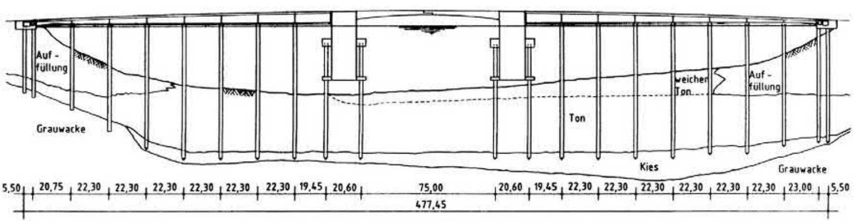

Figure 18.23 General layout.

Figure 18.24 The near to finished bridge.

4.2 Design

4.2.1 Bascule bridge

The free span of 80 m and a total width of 42 m render this as the world's largest bascule bridge (Figures 18.25 and 18.26). The total length of the flaps (54.5 m each) is divided by the axis of rotation into two cantilevers of 42.8 m and 11.7 m.

In the design of the bascule bridge piers, two contradictory requirements had to be fulfilled: they had to be still to absorb ship impact, but they needed to be flexible for earthquakes. This could be achieved by a pier going down to the seabed and founded on 12 piles, which are fixed to the pier between −13 m and − 7.5 m and elastically supported at −32 m (Figure 18.27). To avoid an overloading of the pile or the addition of piles, the piers are made hollow. In spite of being exposed to a water pressure of up to 35 tons/m^2, the pier walls are not waterproofed; rather, they are reinforced for a crack width of w95 = 0.2 mm.

4.2.2 Approach bridges

Structural design

Both decks of the approach bridges have four T-beams with a constant depth of about 1.2 m and a width of 3 m, enlarged to 4 m at the piers (Figure 18.28). The prestressing consists transversely of 4 Ø 0.6 in. St 1570/1770 per linear meter, and longitudinally of 9 tendons, with 15 Ø 0.6 in. St 1570/1770 each, per beam.

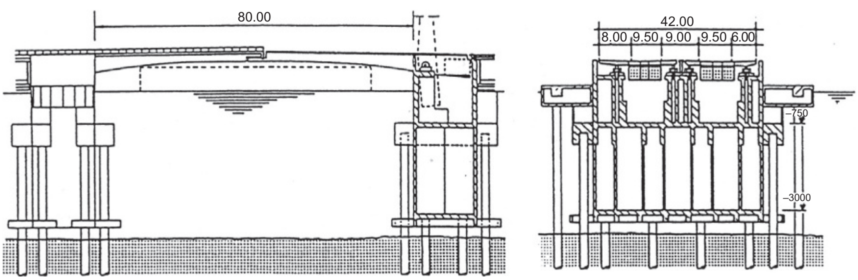

Figure 18.25 General arrangement of the bascule bridge.

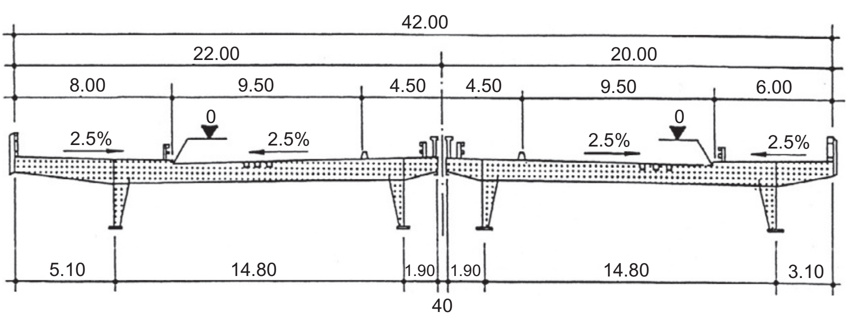

Figure 18.26 Cross section of the bascule bridge.

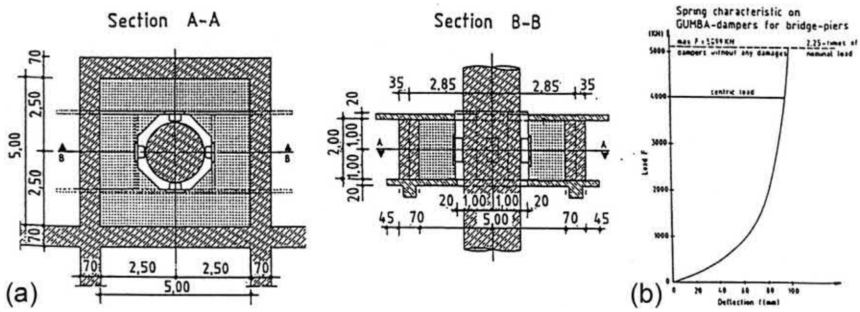

Figure 18.27 Bearings at −32 m: (a) layout, b) load–displacement diagram.

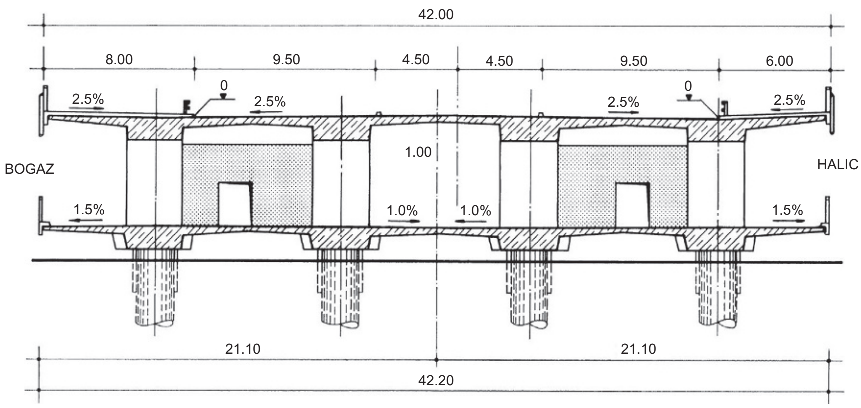

Figure 18.28 Approach bridge.

Bearings

Bearings for vertical loads are needed at the bridge ends and the main piers only due to the longitudinal elasticity of the piles. In order to keep them out of the splash water zone, they support the upper deck only, so the end walls are tension walls. The displacement of these bearings has been sized generously in order to avoid a dripping-down of the end spans in case of an unforeseen strong longitudinal earthquake.

Bearings for transverse forces are also at the abutment and the main piers only; they are designed as Teflon sliding bearings. Longitudinal forces are absorbed at both ends of the approach bridges by buffer bearings, which are working under compression only. In order to avoid bending of the walls, these bearings are at both deck levels. They consist of rubber disks and have a pronounced hysteresis (Figure 18.29).

4.2.3 Piles

In order to reduce the masses involved in an earthquake and to save costs, the pile shafts are designed as hollow steel pipes, with an outer diameter of 2 m and a wall thickness of only 20 mm, with steel quality of St 52–3. The piles of the bascule bridge

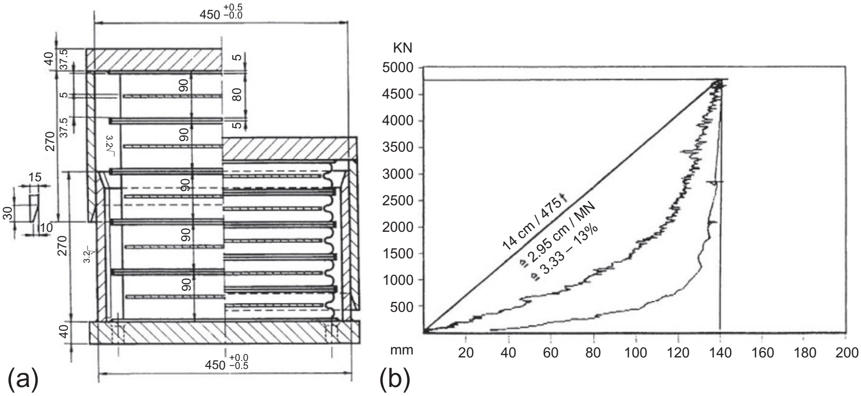

Figure 18.29 Longitudinal buffer bearings: (a) design, b) load–displacement diagram.

piers are filled with tremie concrete B35 and are reinforced in the upper parts. The design of these piles as composite columns proved that shear connectors were only needed at both ends.

4.3 Special aspects of dimensioning

4.3.1 Ship impact

The bridge had to be designed to withstand the head-on impact of an 8000-dwt ship sailing at 2.5 m/s. The corresponding impact force is, according to the Nordic Road Council Regulations for Ship Impact,

$$P_{[\mathrm{kN}]} = 500 \cdot \sqrt{dwt} = 500 \cdot \sqrt{8000} = 45.000\,\mathrm{kN}.$$

As a consequence of an eventual ship impact, the loss of buoyancy of the upper or lower part of the pier due to breaching of its walls also had to be considered. As the bascule bridge could not be designed against ship impact, of course, two worst-case scenarios were investigated (Figure 18.30):

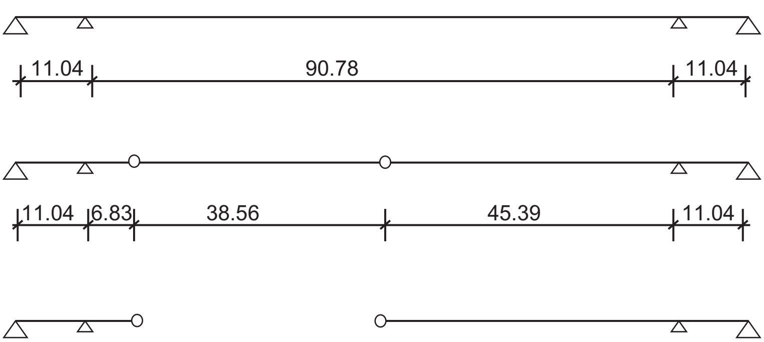

Figure 18.30 Worst-case scenarios.

- Formation of a hinge in front of the pier
- Loss of a flap between this hinge and the center

These scenarios led to a loss neither of the other flap nor of the rear arm with the counterweight.

4.3.2 Earthquake analysis

For the check of the structure's safety during earthquakes, two methods were used. In a first step, a response-spectrum analysis was performed, assuming that the six elements of the bridge are completely independent in the longitudinal direction. In order to determine the displacements of bearings and joints and the forces acting on the buffers, a time-history analysis was performed next.

Response-Spectrum analysis

A response-spectrum analysis was performed for closed flaps, opened flaps, and construction stages. It was done with a spectrum given in the tender documents and with the spectrum according to an American Association of State Highway and Transportation Officials (AASHTO, Guide Specifications for Seismic Design of Highway Bridges, Washington 1983) earthquake code that yields substantially higher accelerations for the governing, rather low frequencies (Figure 18.31). The response modification factor was assumed to be 1.0 for the spectrum according to the tender documents and 3.0 for the spectrum according to AASHTO. Under the first spectrum, the bridge behaved in a completely elastic manner. That means that the safety against yield is 1.0 at the maximum stressed point of the maximum stressed pile.

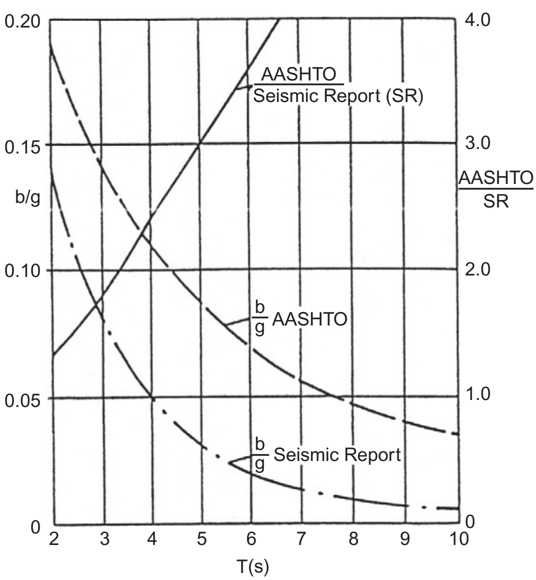

Figure 18.31 Peak acceleration versus natural frequency.

Time-history analysis

The velocity of the surface (Love) waves may be assumed to be 3 km/s, whereas the governing eigenfrequency of the bridge is in the range of 0.25 per second. An earthquake, hence, moves along the bridge in 470/3000 = 0.15 s, which is substantially less than the period of eigenvibration $t = 1/0.25 = 4$ s. Therefore, it was assumed that the bridge would accelerate uniformly over its entire length, which means no phase difference was considered.

Acceleration diagrams

For the time-history analysis, six acceleration diagrams compatible with the energy content of the response spectrum have been generated (Figure 18.32a).

Investigated systems

Corresponding to the progress of design, and especially of the buffers, different connections between the main elements of the bridge were assumed—e.g., elastic springs and springs with a gap for the displacements under service conditions, friction, and assumed and real hysteresis of the buffers (Figure 18.32b).

Results

The results were given graphically—for example, the displacements between the abutment and the approach bridge and the reactions of the corresponding buffers (Figure 18.32c and d).

The design was jointly prepared by LAP and Temel Muhendislik, of Istanbul, Turkey. The main contractor was a joint venture of STFA, of Istanbul, and Thyssen Engineering GmbH, of Essen, Germany.

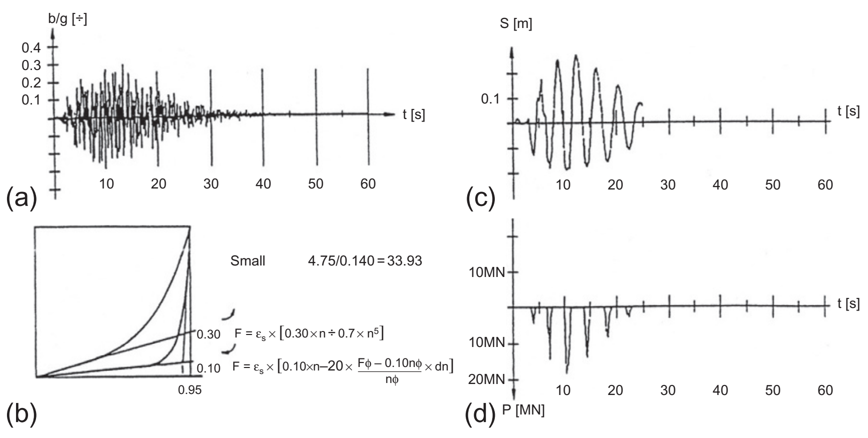

Figure 18.32 Time-history analysis: (a) acceleration diagram; (b) analytical description of buffers; (c) deformation of buffer 1, approximately symmetric; (d) forces in buffer 1, pronouncedly nonsymmetric: upwards friction only, downwards friction + buffer force.

5. Double balanced beam bridge (DBBB)—Design proposal

5.1 Design concept

This section discusses the design for a DBBB proposed by Saul and Humpf (2007). So far, balance beam bridges have been built as single-span bridges. Due to the articulation of the balance beam, this system takes permanent loads only. In DBBBs, the joint at the center would have to transmit under live loads the bending moment of a single-span beam. If, instead, the rotation of the balance beam is blocked by a second bearing, the staying system also participates in handling the live loads. This allows balance beam bridges to be built with two flaps, thereby doubling their span range. This solution is advantageous in areas where the piers of a bascule bridge have to be built in water or groundwater. In more detail, we make use of the fact that, for cinematic reasons, the balance beam has to have an eccentricity toward land. With an additional bearing with eccentricity toward the water—which can take compression only and is automatically activated when lowering the flaps (Figure 18.33)—the live loads can also be taken by the balance beam and the pylon, and thereby, the moments of the bridge deck—especially at the center—are substantially reduced.

5.2 Comparison of section forces

5.2.1 System and loads

The free span is 80 m, and the bridge width 12 m. The permanent load, including surfacing, is 5 kN/m2, and the equivalent live load was also 5 kN/m2. Only the live load over the full main span is considered.

5.2.2 DBBB

The static system for a DBBB is as follows:

- For permanent loads, a span and a cantilever of 22 m each
- For live loads, a continuous beam with spans of 22–44–22 m and elastic, intermediate supports.

The tensile rod is inclined by 1:3, and the distance of the counterweight from the axis of rotation is 80% of that of the rod. The stiffness of the balance beam and the tower are five times that of the bridge deck. The governing bending moments and reaction forces are given in Figure 18.34.

5.2.3 Double bascule bridge

The static system for a double bascule bridge is as follows:

- For permanent loads, a span and a cantilever of 11 m and 45 m, respectively
- For live loads, a continuous beam with span of 11–90–11 m.

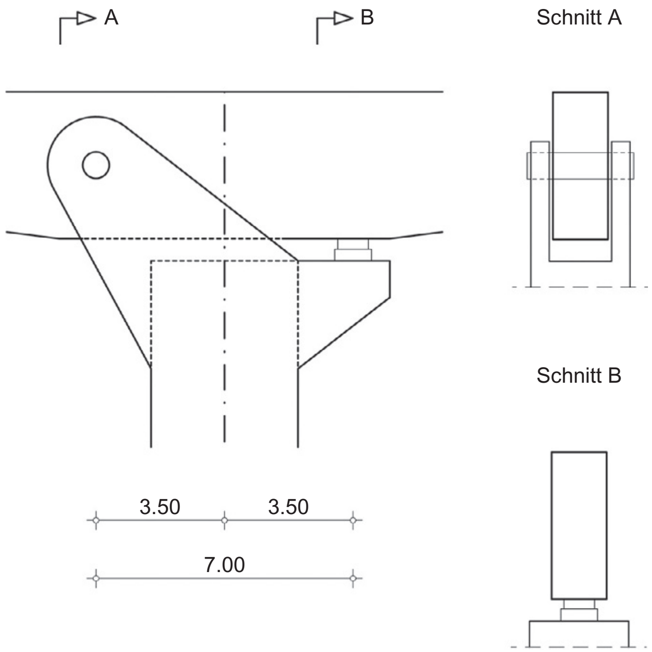

Figure 18.33 Bearing at the top of the tower.

The stiffness at the axis of rotation is five times that at the center. The governing bending moments and reaction forces are given in Figure 18.35.

5.2.4 Comparison of DBBB and the double bascule bridge

See Figures 18.34c and 18.35c:

- The maximum bending moment of the bridge deck of the DBBB is only about 15% of that of the double bascule bridge. This reduces the construction depth and lowers the gradient.
- At the center joint, the live load moments of both bridge types are virtually the same.
- The counterweight of the DBBB (3165 kN) corresponds to only 45% of that of the double bascule bridge (7140 kN), due to the longer lever arm.
- The reaction force of the rotation bearing of the DBBB (6900 kN) corresponds to 40% of that of the double bascule bridge (17,450 kN) only.
- The governing moments of the balance beam (72,100 kNm) and the pylon (43,000 kNm) of the DBBB corresponds to 70% and 40% of the maximum moment of the double bascule bridge (107,600 kNm).
- The bending moments acting on the foundation of the DBBB (42,940 kNm) and the double bascule bridge (46,850 kNm) are basically the same.

5.2.5 Comparison of DBBB with the single bascule beam bridge

The live load moments of the single bascule beam bridge are that of a beam with a span of 44 m (that is, 13,200 kNm). The comparison shows the following:

- The governing moments of the bridge deck are basically the same.
- The governing force of the rotation bearing is that under permanent loads (6900 kN). The live load (−4200 kN) reduces it but does not invert it.
- The force of the tensile rod is about 70% bigger.
- The governing moment of the balance beam is increased by about 12% from 64,300 kNm to 72,100 kNm.
- The governing moment at the base of the tower is increased from 7800 kNm to 42,900 kNm, but this is not a problem, however, due to the large dimensions of the tower.

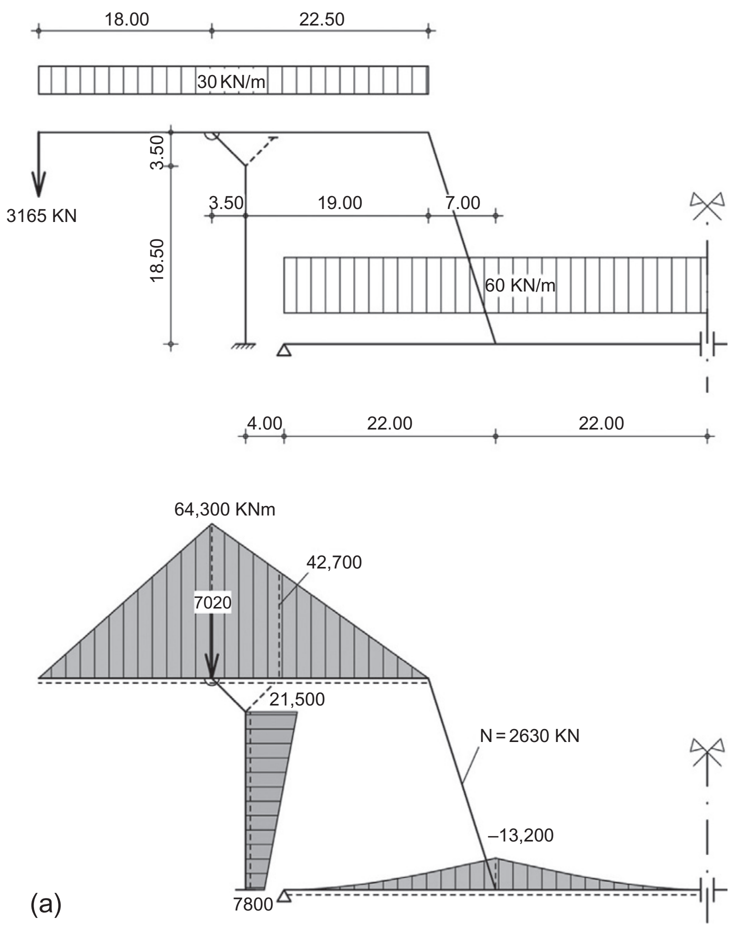

Figure 18.34 Section forces of a double balance beam bridge: (a) permanent loads;
(Continued)

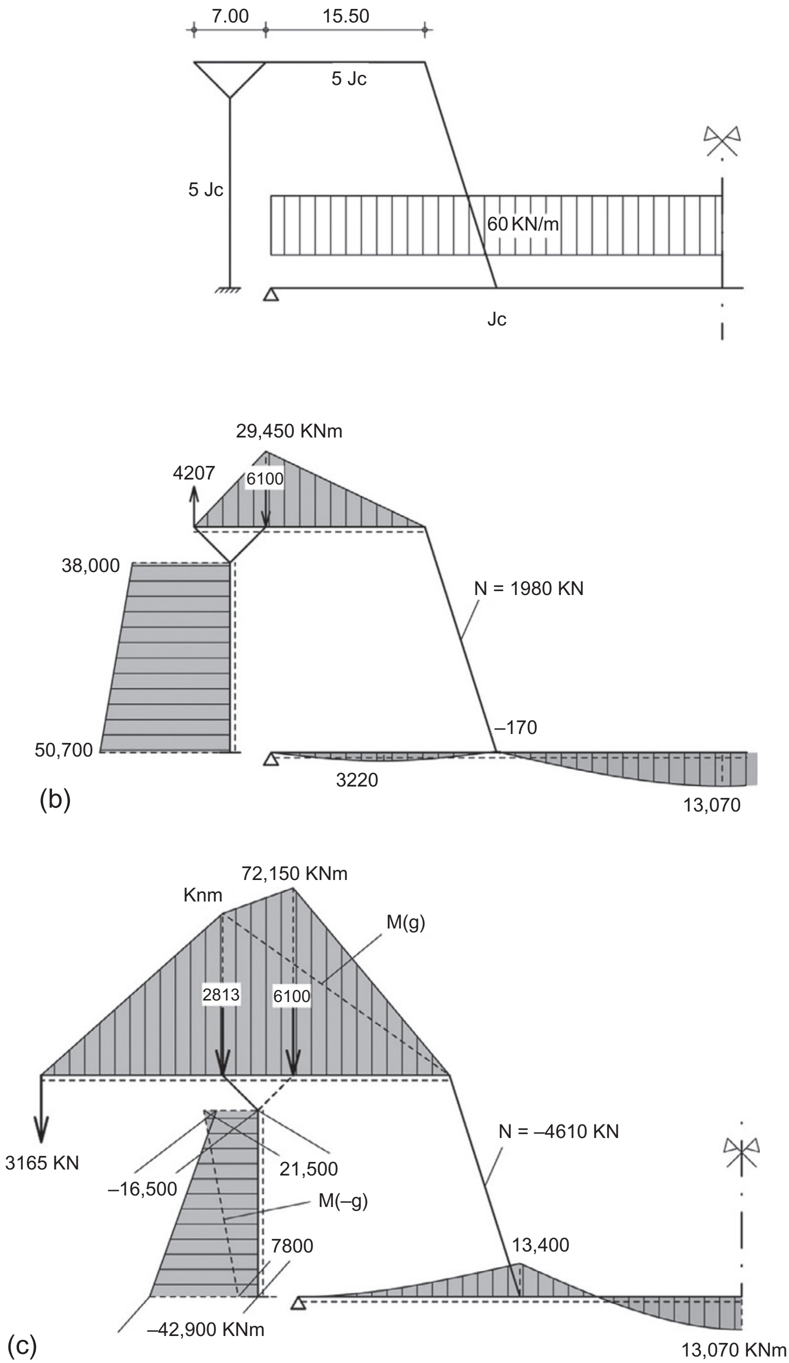

Figure 18.34, cont'd (b) traffic; (c) permanent loads + traffic.

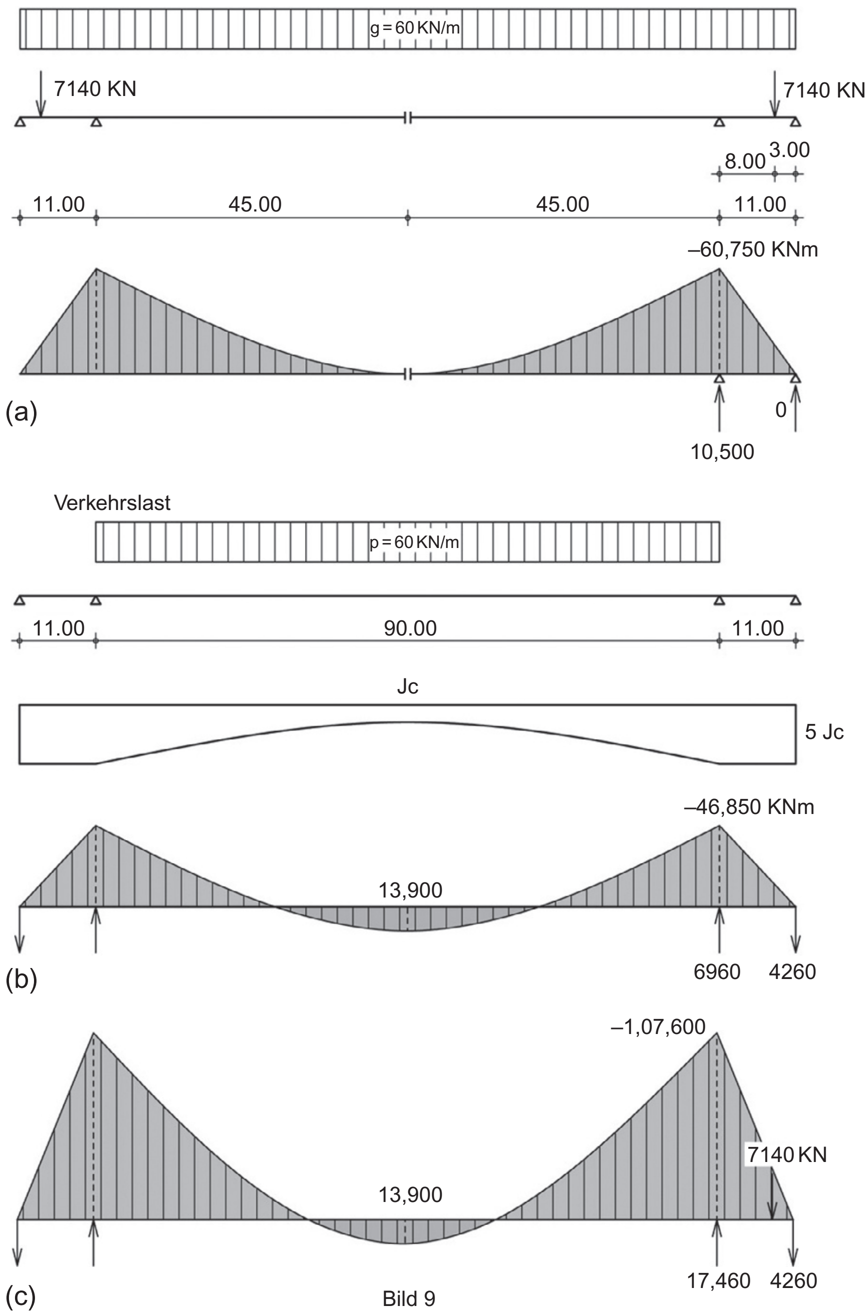

Figure 18.35 Bending moments of a double bascule bridge: (a) permanent loads; (b) traffic; (c) permanent loads + traffic.

5.3 Summary

The presented innovative system of a DBBB allows for taking all loads by a simple blockage of the rotational axis. Compared to a double-flap bascule bridge, it enables a substantial reduction of the cost of the bascule bridge pier—especially when situated in water, poor soil, or both—and a reduction of the construction depth of the bridge deck. Compared to a single balance beam bridge, it allows the span to be doubled. The increased normal force of the tensile rod and bending moment at the bottom of the tower may be absorbed without serious problems.

References

Binder, B., Pfeiffer, M., Weyer, U., 2001. Die El-Ferdan Brücke-Konstruktion, Fertigung und Montage der größten Drehbrücke der Welt über den Suez-Kanal (The El-Ferdan Bridge - design, shop fabrication, and erection of the biggest swing bridge worldwide). Stahlbau 70, 231–244.

BMVBS: Zukunft Elbe, eine Initiative für Norddeutschland (Future of Elbe River, an initiative for northern Germany). Undated folder n.d.

Freudenberg, G., 1971. Die größte Doppelklappbrücke der Welt über die Bucht von Cadiz (The worldwide biggest double flap bascule brideg across the Cadiz Bay). Steel, 463–472.

Freudenberg, G., 1989. Zwei neue Waagebalken-Klappbrücken in Mannheim (Two new scale beam bascule bridges at Mannheim). Stahlbau 58, 35–43.

Kleinhanß, K., Saul, R., 2007. The second Strelasund crossing—a modern cable-stayed bridge in close vicinity to the world cultural heritage, Stralsund, Germany. Struct. Eng. Intl., 30–34.

Leonhardt, F., Andrä, W., 1963. Die Guaiba-Brücken bei Porto Alegre, Brasilien (The Guaiba Bridges at Porto Alegre, Brazil). Beton Stahlbetonbau 58, 273–279.

Leonhardt, Andrä, Partner GmbH, 1997. Puerto de Barcelona, Puente entre Muelle de Poniente y Muelle Adosado. Puente principal, Alternativa: Sistema giratorio atirantado (port of Barcelona, bridge between Muelle de Poniente and Muelle Adosado. Main bridge, cable-stayed swing bridge alternative). Stuttgart.

Leonhardt, Andrä, Partner GmbH, 2008. Design Documents for the Sungai Perai River Bridge, Malaysia. Stuttgart.

Leonhardt, F., Zellner, W., Saul, R., 1979. Zwei Schrägkabelbrücken für Eisenbahn und Straßenverkehr über den Rio Paraná/Argentinien (two cable-stayed bridges for railway and highway traffic across the Paraná River, Argentina). Der Stahlbau 48 (225–236), 272–277.

Rüster, R., 1974. Die Kattwyk Hubbrücke in Hamburg, eine vollständig geschweißte Fachwerkbrücke (The Kattwyk lift bridge at Hamburg, a completely welded truss girder bridge). Stahlbau 43, 257–267.

Saul, R., Humpf, K., 2007. Doppelwaagebalkenbrücke – Vorschlag für einen innovativen Klappbrückentyp (double balance beam bridge – proposal of a new type of bascule bridge). Stahlbau 76, 559–564.

Saul, R., et al., 1992. Die neue Galata Brücke in Istanbul (the new Galata bridge at Istanbul). Bauingenieur 67, 433–444. and 1993;68:43–51.

Seifried, G., Wittfoth, H., 1979. Die Brücke über den Shatt-al-Arab in Basrah (Irak) [the bridge across the Shatt-al-Arab in Basrah (Iraq)]. Beton Stahlbetonbau 74, 77–85.

Highway bridges

19

B.T. Martin
Modjeski and Masters, Inc., Poughkeepsie, NY, USA

1. Introduction

In a report called “The Three Mentalities of Successful Bridge Design,” De Miranda (1991) stated that a successful bridge design must address three areas: (1) creative and aesthetic, (2) analytical, and (3) technical and practical considerations. The lack of any of these conceptualizations leads to a less-than-successful design. In today’s “team” approach, it is fairly easy to achieve the first two of these considerations, but the last is the one that is often the most troubling. Without an in-depth familiarity with economical construction alternatives, the selected bridge type, though innovative in its technical aspects, will not be practical.

2. Practical considerations for selection of a highway bridge type

The selection of a bridge type for a given site is driven by many variables, and there is no single correct solution to the problem. For any given span length, there are always many bridge types that can satisfy the design objectives of the project. The type of bridge that is selected can be driven by such variables as the availability and cost of certain materials, the skill set of the local labor force, and the experience of local contractors. It is entirely possible that, for a given set of constraints, the bridge type that is preferred in one jurisdiction or country will be entirely different from the one selected in another.

2.1 Selecting a bridge type

2.1.1 Geometric demands of the roadway

Quite often, the type of bridge selected will be driven by the geometric alignment of the approach roadways. The vertical and horizontal geometry of the bridge approaches are driven by such factors as desired vertical clearances, roadside elements, and roadway facilities either up-station or down-station of the bridge. For example, if vertical clearance beneath the proposed structure is critical and the elevation of the approach roadways cannot be raised, a shallow, beam-type bridge might be in order. Or if the approach roadways demand the use of a curved structure and the site is such that aesthetic considerations are important, then a continuous curved box-girder bridge might

Innovative Bridge Design Handbook. https://doi.org/10.1016/B978-0-12-823550-8.00011-1

be used, due to its pleasing lines and great torsional resistance. If the purpose of the bridge is to cross a navigable channel where a large amount of vertical and horizontal clearance is needed, an entirely different bridge type would be used than a bridge selected to serve as an elevated roadway in an urban area.

2.1.2 Utilization requirements

The utilization demands on a bridge will play a major role in its final configuration. The bridge must have a sufficient number of lanes to carry not only today's traffic volume, but also the demands projected for the future. Will the bridge carry pedestrians? Will it also have bicycle pathways? Is there a need to separate opposing traffic lanes with a median barrier? Is there a need to separate sidewalks/bicycle pathways from the roadway with a barrier? The answers to all of these questions will drive the ultimate width of the bridge. Another consideration is future expansion. Are there conditions in the geographic area that might lead to an increase in traffic volume, but is there a high degree of uncertainty? If that is the case, then bridge types with the capability of future widening, such as multiple-girder bridges, should be considered.

2.1.3 Surface site conditions

The terrain of the site will play a major role in selection of a bridge type. Bridges over wide canyons with inaccessible side slopes will require long-span bridge types such as arch spans. Depending on the type of vessel traffic, bridges over navigable waterways may require large spans and high vertical clearances such as truss spans, cable-stayed bridges, or suspension bridges. If the approach constraints will not allow long, high approaches, then a moveable bridge might be required. Does the bridge cross a flood plain? If so, the elevation of the bottom of structure, span lengths, and impacts to flow during flood season will have to be taken into consideration. All of these factors will play a major role in the selection of bridge type.

2.1.4 Subsurface site conditions

The subsurface condition at a proposed bridge site will play a major role in the selection of a bridge type. Basic questions have to be asked, such as the following:

- Will the soil conditions allow spread footings, or will piles be required?
- Can drilled shafts be used, and are there economic advantages to using them?
- Are the soil types such that future settlement might occur? If so, the bridge type selected must be able to accommodate such movement.
- Does the site have a potential for seismic activity? If it does, the resulting configuration of the substructure may drive the superstructure loads and vice versa.
- Are foundation conditions such that high lateral loads can be resisted? For example, if geometric requirements and utilization requirements result in the need for a long-span bridge, can the subsurface conditions allow the large loads that would result later at the anchorages of a suspension bridge, or would it be best to use a cable-stayed bridge that results primarily in vertical loads?

2.1.5 Construction considerations

Erection and construction processes often dictate the type of bridge that is selected to be built. As stated previously, the type of bridge that is selected is often driven by such elements as the availability and cost of certain material, the skill set of the local labor force, and the experience of local contractors. For example, if there is a preponderance of steel fabricators in the area of the bridge site but no precast concrete fabricators nearby, then one might lean toward using steel. If the local workforce does not have the skill set required for steel erection, then bridge types that maximize the use of cast-in-place concrete might be the best solution. Cast-in-place concrete is well suited for grade separation structures with limited restrictions under them in regions of the world where the workforce can build falsework quickly and cheaply.

The time allotted by the owner for construction can also influence the bridge type. If time is short, then maximizing the use of precast elements might be in order. This would lead to the potential use of segmental concrete bridges or some of the newer accelerated bridge construction techniques.

It is always recommended to use bid histories for previous jobs in the selection of bridge types. In some parts of the world, such information does not exist; therefore, the construction advantages of one bridge type comprised of one material or the other is difficult to discern. In this case, there is a definite advantage to bid alternative designs. This typically is cost effective only for large projects.

2.1.6 Project delivery system

In the recent past, most projects in the United States have used a design–bid–build project delivery system. Even more recently, the United States, like most other countries of the world, has started using a design–build delivery system. This is actually a return to the system used in the early years of bridge building in the United States (Barker and Puckett, 2007). During the great bridge-building era of the 19th century, an owner would express an interest in having a bridge built at a particular location and then solicit proposals from engineers not only for the design but also for the construction. In many cases, the engineer would recognize a need and then present the concept to the affected parties. All services, in the areas of both design and construction, were the responsibility of one entity.

The design–bid–build approach was meant to provide a quality product while also providing a system of checks and balances between the designer/owner and the contractor. As is often the case, the problem with design–bid–build is not the concept but its execution. Often, problems that develop during construction result in an attempt to assign blame rather than seek a practical solution that decreases the financial risks of all parties.

Because design–build more clearly defines lines of responsibility, this delivery system is being used more and more in the United States. That being said, the successful application of this delivery system is dependent on a knowledgeable owner that has staff capable of judging the quality of work provided. This delivery system seems to work best on large bridge projects, though it is being applied in some jurisdictions to smaller bridge projects that are consolidated into a single contract.

2.1.7 Regulatory requirements

Almost every bridge design project in the world has to comply with the regulatory requirements of the jurisdiction in which the bridge is built. These requirements can have a profound impact on the bridge type that is selected and the location of the bridge. There are many environmental regulations and agencies with which coordination must take place, all of which require permits with stipulations that will impact the design process. It is essential that the engineer be knowledgeable about these agencies, regulations, and permits prior to the beginning of the design process.

Local and regional politics also have to enter into the bridge selection process. Often, national, state, or local officials have made commitments to their constituents that must be understood and included by the designer. In some cases, such political drivers override many of the engineering-driven criteria.

2.1.8 Aesthetics

It should be the desire of every engineer to design a bridge that is aesthetically pleasing. That being said, in the opinion of this writer, one should not begin with the desire to achieve “uniqueness” at all costs, nor should structural efficiency be abandoned for the sake of appearance. A detailed discussion of the aesthetics of bridge design is discussed by others in this volume.

3. Bridge types

On the basis of this site criteria, a general idea of the required span length can be established, and studies can be performed to determine the most desirable bridge type to be used at the site. There are various publications that can assist in the selection of bridge type as a function of span, but span length alone is not the determining factor. The other factors mentioned here must also be taken into consideration. The following sections include a discussion of the bridge types that are most often used for different span lengths, and this is based primarily on the information contained in the Pennsylvania Department of Transportation Design Manual, Part 4, Page A.2 (PennDOT, 2012), and data collected by Barker and Puckett (2007).

3.1 Short-span bridges

Short-span bridge types (i.e., span lengths up to 15 m) include single-unit or multiunit culverts, concrete slab bridges, precast I-beam bridges, and rolled I-beam bridges.

3.1.1 Culverts

Most often used to provide passage through roadway embankment for small streams, drainage channels, pedestrians, livestock, and, in some cases, vehicles, culverts far outnumber bridges in the United States. The National Bridge Inventory in the United States lists culverts as bridges only if the span exceeds 6.5 m. Almost 20% of all bridges in the United States are classified as culverts. Culverts take many structural forms and are composed of many materials ranging from concrete to steel, aluminum, and thermoplastics.

3.1.2 Slab-span bridges

Slab-span bridges are simple and cost effective for spans up to 12 m. They can be built on falsework or precast and shipped to the site. They can be used as simple spans or, if a topping slab and reinforcement is added, they can be made continuous over intermediate bents, thereby limiting the number of joints. The spans can be extended to approximately 15 m if prestressing is used. These structure types are shallow and project a simple, slender appearance. Maintenance is rather low, except where transverse joints are used.

3.1.3 T-beam

Traditionally, these bridges have been built on scaffolding and poured in place. They are generally economical for spans of 10–20 m. Formwork can be rather complex for the bridge if built in the field. It was a workhorse bridge throughout the middle of the 20th century but has been pretty much replaced by prestressed slab bridges and precast box-beam bridges. Should a designer choose to use this bridge type, careful attention should be given to reinforcement for crack control, as well as clearance above waterways, as the underside collects debris, resulting in potential damage to the stems of the T-beam. The bridge has a neat, clean appearance, with the exception of the underside. Maintenance costs are low, except in the case where transverse deck joints are used.

3.1.4 Wooden beams

Most often used for secondary roads where truck traffic volume is low, wooden beam bridges remain a primary bridge type for rural locations. The bridges are used for spans up to 15 m and usually have a wood pile substructure. With the exception of elements coming in direct contact with pedestrians, the components of the bridge are chemically treated for preservation. Main members are usually precut and drilled prior to chemical treatment and installation. The bridge can accommodate a spiked wooden deck, concrete deck, or a combination of wood planking and asphalt. Because of the propensity of the bents and abutments to catch debris when over water, the substructure units are built parallel to the stream. These bridges can be visually appealing in the right environment though they don't lend themselves to urban environments.

3.1.5 Precast concrete box beams

Fast becoming a mainstay in the short-span bridge market, the precast box-beam bridge can have spread boxes or adjacent boxes. This bridge type is typically used for spans of 10–45 m. It is not advised to use the top of the boxes as the riding surface due to the uneven riding surface that results from variable camber between boxes. The boxes are often transversely post-tensioned with grouted shear keys between the boxes. The riding surface is often comprised of an asphalt topping or a concrete slab. It is common for differential movement between the boxes to result in the cracking of the asphalt or concrete topping along the joint between the boxes. This is often alleviated by using a highly reinforced concrete deck. The boxes can be used as simple spans or made continuous by pouring concrete between the ends of the boxes. The bridge has an appearance similar to that of the T-beam bridge—except that, in the case of adjoining boxes, a smooth underside results. This bridge, like all concrete bridges, requires little maintenance, except where transverse deck joints are used.

3.1.6 Precast concrete I-beams

Competitive with steel girders for spans of 10–45 m, precast, prestressed concrete I-beams have many of the same advantages and disadvantages as precast concrete box beams. In most cases, the beams are designed as noncomposite simple spans for dead loads and as composite continuous spans for live loads and superimposed dead loads. Maintenance is low, except in the case where transverse deck joints are used. The appearance of the bridge is clean from above, but, like the T-beams, very "busy" underneath.

3.1.7 Noncomposite rolled steel I-beams

Often used because of their lower fabrication costs, rolled steel wide-flange beam bridges are cost effective for spans up to 15 m. To be cost effective, spans longer than this need to be made composite and utilize cover plates. Though weathering steel can be used to eliminate the need for painting, it cannot be used in situations where the site conditions will result in constant wetting. If weathering steel cannot be used, the cost of painting must be used in all cost comparisons with concrete spans. The overall aesthetic appearance is much like that of the concrete I-beams—clean lines in elevation but cluttered underneath.

3.2 Medium-span bridges

Bridge types that can be used in the medium-span range (span lengths up to 75 m) include precast concrete box-beam bridges, precast I-beam bridges, composite rolled wide-flanged beam bridges, composite steel plate girder bridges, reinforced cast-in-place concrete box-girder bridges, post-tensioned, cast-in-place concrete box-girder bridges, and composite steel box-girder bridges.

3.2.1 Precast Prestressed concrete beams (box beams and I-beams)

The general characteristics of both the concrete box-beam and I-beam bridges were discussed in the previous section. Transportation of these types of bridge elements become a major issue as the span lengths increase. Virtually every jurisdiction has length and load limitations for trucks hauling such elements. In addition, as the length of the elements increase, on-site storage requires special support conditions and lateral stability becomes an issue in the case of the I-girders during lifting and placement.

Temporary bracing becomes essential. Extremely long girders may require precasting in segments and joined together once erected.

3.2.2 Composite rolled I-beams

The general characteristics of composite rolled steel beam bridges were discussed in the previous section. Composite rolled I-beam bridges are economical up to spans of 30 m. To economically achieve these span lengths, it is necessary to make the bridge composite for live load and add steel cover plates in maximum moment regions. Special care must be taken at the ends of such cover plates due to a susceptibility to fatigue cracking if improper detailing is used. Though different types of shear connectors have been used through the years to accommodate composite action, the most common today are welded studs.

3.2.3 Composite steel plate girders

Bridges comprised of composite steel plate girders (such as the Harpers Ferry Bridge, shown in Figure 19.1) are economically feasible for spans of 20–40 m, although they have been used for spans exceeding 90 m. The girders typically comprise an asymmetric section consisting of a top and bottom flange welded to a web. Many such girders consist of hybrid sections using steels of different strengths for the webs and the flanges. As the prices of different grades of steel have become more uniform over the years, this has become less common. The use of such girders results in low dead loads, making them quite desirable for use in areas of poor foundation conditions. The tall, slender girders that result for longer spans must be handled and erected with care. Lateral stability is an issue during fabrication, transportation, and erection. It is imperative that careful thought be given to proper lateral bracing during all phases of the project. Because each one is fabricated using plate steel, the girders can have variable

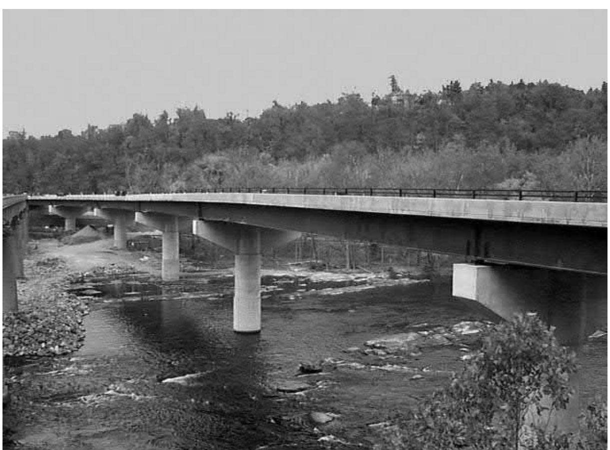

Figure 19.1 Harpers Ferry Bridge, Harpers Ferry, West Virginia, USA. Courtesy of Modjeski and Masters, Poughkeepsie, NY.

depths for maximum section efficiency. Such variation in section depth can be visually appealing.

3.2.4 Reinforced cast-in-place concrete box girder

As in the case of the concrete T-beam option, reinforced cast-in-place concrete box girders typically require a ground-based scaffolding system; therefore, their use is often restricted by site limitations. They are suitable for spans of approximately 15–35 m and result in very torsionally rigid structures. In some cases, they can be more economical than steel and concrete I-girder bridges, but only when local industry is geared up for such construction. They are visually attractive structures with a clean, simple, and smooth appearance from all directions, making them very appealing for use in urban environments. They have the additional advantage of allowing all utilities to be run inside the boxes, hiding them from view.

3.2.5 Post-tensioned, cast-in-place concrete box girder

Post-tensioned, cast-in-place box girders have the capability of providing much longer spans than cast-in-place reinforced box girders. They have been used in bridges with spans up to 180 m and result in cost-effective, low-maintenance bridges that are pleasing in appearance. The boxes have a very high torsional resistance, making them well suited for curved or skewed bridges. The use of post-tensioning can minimize dead load deflections and cracking in the boxes and decks. The use of post-tensioning does result in creep shortening of the elements, and provisions must be made to accommodate such movements. As is the case for most concrete bridges, maintenance is low (with the exception of the bearings and any transverse joints). It is recommended that consideration be given to an overlay system on the bridge deck in areas with high use of deicing chemicals. Care also must be given in the deck drainage system in such cases.

3.2.6 Composite steel box girder

Composite box girders may be rectangular or trapezoidal in shape and possess high torsional resistance once the deck is poured. They are used for spans of 20–150 m. Though they are most cost effective in the longer-span ranges, they are often used for shorter spans in highly curved situations or when a shallow section is required. Due to their size, steel boxes face the same shipping challenges as all of the other large component systems. With all their benefits, steel boxes do come with their own set of challenges. The shapes and intersecting elements present fabrication issues. Even though they are shop-fabricated, there are many opportunities for welding and detailing errors that lead to fatigue issues. If a decision is made to use steel box girders, close and careful attention must be given to the structural detailing. Steel box-girder spans have very clean lines and can be aesthetically pleasing. The same issues regarding painting and the use of weathering steel raised for the other steel sections apply to steel boxes as well.

3.3 Long-span bridges

Bridge types that can be used in the long-span range (span length up to 150 m) include composite steel plate girder bridges, post-tensioned, cast-in-place concrete box-girder bridges, post-tensioned segmental bridges, steel and concrete arch bridges, and steel truss bridges.

3.3.1 Composite steel plate girder bridge

The same issues presented in the previous discussion of steel plate girders in the medium-span range also apply to the long-span range. As the spans get longer, the sections get deeper, and the issues regarding lateral stability and transportation become even more critical.

3.3.2 Post-tensioned, cast-in-place concrete box-girder bridge

The same issues presented in the previous discussion of post-tensioned, cast-in-place concrete girders in the medium-span range also apply to the long-span range. As spans get longer, time-dependent effects such as creep and shrinkage become even more critical and require even more attention.

3.3.3 Post-tensioned, concrete segmental bridges

Though primarily used for box sections, post-tensioned segmental construction methods can be used for numerous bridge types (see Figure 19.2), including spliced concrete I-girders. Cost savings are realized through the reuse of standard form systems. Segmental construction can be used for cast-in-place elements using traveling forms or precast cast elements. Erection methods include span-by-span construction, balanced cantilever erection, and launching the bridge from one end. Typical span lengths for segmental bridges are as follows: (i) cast-in-place post-tensioned box

Figure 19.2 I-96-295 ramp, Jacksonville, FL, USA.
Courtesy of John Corven.

girder of constant depth, 30–90 m; (ii) precast post-tensioned box girder of constant depth erected using balanced cantilever, 30–90 m; (iii) variable-depth precast balanced cantilever segmental, 60–180 m; and (iv) cast-in-place cantilever, 60–300 m. More detailed information is available in various sources, such as Hewson (2003), the American Segmental Bridge Institute (ASBI, 2003), and Podolny Jr. and Muller (1982).

3.3.4 Steel and concrete arches

Span lengths for arches range from 90 to 420 m for concrete arches and from 90 to 420 m for steel arches. They can be either above or below the roadway deck. The distinctive features of arch-type bridges have been very effectively summarized by O'Connor (1971) as follows:

- The most suitable site for this form of structure is a valley, with the arch foundations located on dry rock slopes.
- The erection problems vary with the type of structure; erection is the easiest for the cantilever arch and possibly the most difficult for the tied arch.
- The arch is predominately a compression structure. The classic arch form tends to favor concrete as a construction material.
- Aesthetically, the arch can be the most successful of all bridge types. It appears that through experience or familiarity, the average person regards the arch form as understandable and expressive. The curved form is almost always pleasing.

3.3.5 Steel trusses

Steel truss bridges (Figure 19.3) were the major structure of choice during the 19th and 20th centuries. Their spans range from 240 to 550 m. These trusses are typically classed as through trusses and deck trusses. Through trusses have the truss above the roadway, and deck trusses have the roadway above the truss. Some bridges feature

Figure 19.3 Huey Long Bridge, New Orleans, LA, USA.
Courtesy of Modjeski and Masters, Poughkeepsie, NY.

both kinds of trusses. O'Connor (1971) offers an excellent summary of the features of a truss bridge:

- A bridge truss has two major structural advantages: (1) the primary member forces are axial loads, and (2) the open web system permits greater overall depth than an equivalent solid web girder. Both of these factors lead to economy in material and a reduced dead weight. The increased depth also leads to a more rigid structure and reduced deflections as a result.
- The conventional truss bridge is most likely to be economical for medium spans. Traditionally, it has been used for intermediate spans between the plate girder and the stiffened suspension bridge. Modern construction techniques and materials have tended to increase the economical span of both steel and concrete girders. The cable-stayed bridge has become a competitor to the steel truss for intermediate spans. These factors, all of which are related to the high fabrication cost of a truss, have tended to reduce the number of truss spans built in recent years.

In addition to the fabrication costs mentioned by O'Connor, recent issues with the gussets of truss bridges have led some to be hesitant to use this structure type. Recommendations resulting from ongoing research regarding the design of gusset plates should alleviate this concern.

3.4 Very long-span bridges

3.4.1 Suspension bridges

Suspension bridges (Figure 19.4) typically consist of two (and sometimes four) parallel cables separated by a distance approximately equal to the roadway deck width that they support. These cables act as tension elements and extend from anchors at each of their ends over the tops of the intermediate towers. The deck is suspended by strong ropes running from the deck level to the main cables. The main cables

Figure 19.4 Forth Road Bridge, Queensferry, Scotland.
Courtesy of Barry Colford.

can consist of parallel strong wires that are aerially spun in place or prefabricated wire ropes. The deck can be stiffened by a truss or by girder elements. The purpose of the stiffening element is to ensure aerodynamic stability and to limit the local angle changes in the deck. Suspension bridges are used for spans of 300–2300 m. The bridge can be erected without any ground-based towers. The resulting bridge is very elegant in appearance, and its form clearly expresses its function. As the existing inventory of suspension bridges have aged, inspections have revealed active corrosion and stress corrosion cracking in many of the wires comprising the main cables. This has led to the installation of dehumidification systems in many of the new and existing bridges.

3.4.2 Cable-stayed bridges

Cable-stayed bridges (Figure 19.5) were introduced immediately following World War II to replace many of the bridges lost during the war. Unlike the suspension bridge, the cables extend from the towers directly connecting to the deck. In most bridges, the cables come to a "dead end" at the deck and the tower. There have been some recent bridges where the cables pass through a "saddle" at the tower, and then to the deck at each end. The cables are typically in two planes separated by the width of the roadway, though numerous bridges have been built with a central plane of stays between the two opposing lanes of traffic. This requires a torsionally resistant superstructure. The cables are straight, resulting in greater stiffness than a suspension bridge. By anchoring the cables to the deck, compressive forces are applied to the

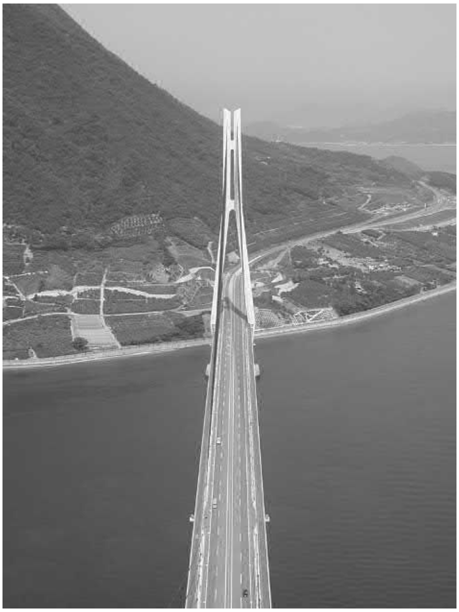

Figure 19.5 Tatara Bridge, Japan.
From author's collection.

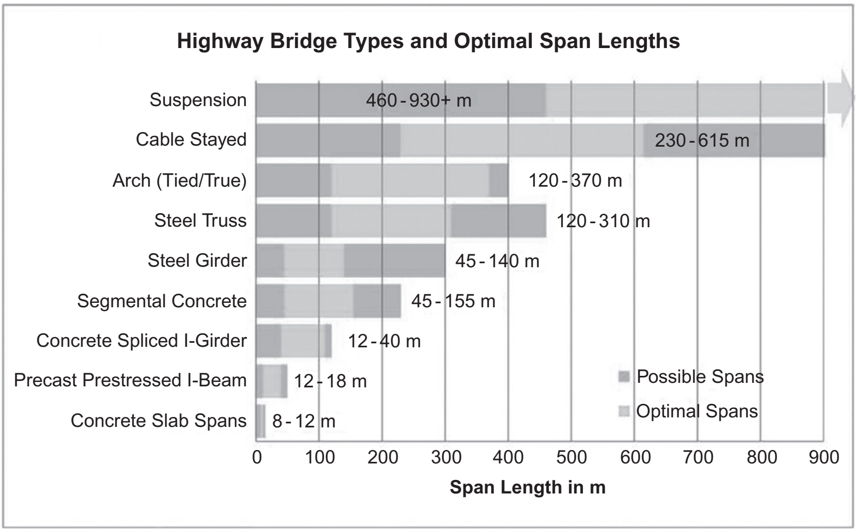

Figure 19.6 Possible and optimal highway bridge span lengths.

deck, resulting in it participating in handling those loads. This can be problematic should deck replacement be necessary. In general, a cable-stayed bridge is less efficient in carrying dead load than a suspension bridge but is more efficient in carrying live load. The most economical span length for a cable stayed bridge is 100–350 m, though some designers have extended this range to as much as 800 m. There have been some problems with cable excitation during rain/wind events, particularly on the longer stays. A cable-stayed bridge is very modern and pleasing in appearance and fits extremely well in almost any environment.

A visual representation of the data presented here can be seen in Figure 19.6, where the possible and optimal span lengths for various bridges are presented.

4. Methods of analysis (emphasizing highway structures)

All of the design specifications used in the world today for highway bridges allow the use of any method of analysis that satisfies the requirements of equilibrium and compatibility and utilizes stress–strain relationships for the proposed materials. These methods include, but are not necessarily limited to, the following:

- Classical force and displacement methods
- Finite element method
- Finite difference method
- Finite strip method
- Folded plate method
- Grid analogy method
- Series or other harmonic methods
- Methods based on the formation of plastic hinges
- Yield line method

It is imperative for the designer to realize that he or she is responsible for the implementation of computer programs used to facilitate structural analysis and for the interpretation and use of the results. The designer must understand all limitations of programs used, as well as the nuances of commercial software regarding automatically set material properties. For the sake of clarity and for future reference, the designer should indicate the name, version, and release date of any software used during the project.

5. Design method

The present method used to design highway bridges in the United States is called the load and resistance factor design (LRFD) method. This is basically a limit-state design approach similar to that used in Canada and also contained in the Eurocodes used throughout Europe.

In the early days of structural design, most structures were composed of metallic elements that had a well-defined yield point. Therefore, all designs were based on some "allowable" stress that was based on some fraction of the yield stress. That fraction was referred to as a *factor of safety*. The factor of safety varied depending on the utilization of the member: tension, compression, or bending. Using the allowable stress and the force effects on a member, the net area required for a tension member, the gross area required for a compression member, and the section modulus required for a bending member could easily be determined.

There are numerous shortcomings to this method:

- The method does not lend itself to other materials, particularly nonmetallic materials.
- It is based on the assumption that there are no existing stresses in a member (i.e., no residual stresses resulting from the manufacturing process).
- Factors of safety are arrived at rather subjectively and are only applied to the resistance of the element. Furthermore, the resistance is based solely on the elastic behavior of materials.
- The method does not take into consideration the fact that different loads have different levels of uncertainty.

It became evident in the middle of the 20th century that an effective design method needed to take into account the variability of the loads, as well as the resistance to those loads. Thus, the limit state design methods were developed.

The primary advantages of the limit state design methods are as follows:

- The method accounts for the variability in the loads and resistances.
- The method results in more consistent levels of factor of safety.
- The method is more rational and consistent.

Detailed discussions of the limit-state methods of design are presented elsewhere in this volume and will not be discussed in detail in this chapter. The following design example is based on the Eurocode, which is based on the concept of a limit-state design.

6. Design example

An in-depth presentation of a bridge example illustrating all the requirements of the Eurocode would require a number of pages well beyond what is appropriate for a single book chapter. For this reason, this text will explore portions of a detailed example prepared by Crespo et al. (2012) that was contained in a scientific and technical report by the European Commission's Joint Research Centre (JRC), titled "Bridge Design to Eurocodes, Worked Examples, 2012." Much of the following discussion is taken from that report, and full attribution is given to those authors. This is an excellent example that can be very helpful for those seeking a greater understanding of the application of the Eurocode requirements.

6.1 Selecting the bridge type

This example is a road bridge that is to be designed to have a 100-year working life with a total length of 200 m consisting of three spans (60 m, 80 m, and 60 m). The bridge is on a tangent alignment and has no grade or vertical curvature. Traffic studies have resulted in the determination that the bridge will need to carry two lanes of traffic. It is to cross a deep canyon with access (though limited) to the proposed location of the pier footings. The subsurface conditions at the proposed location of the bridge are very good, allowing the construction of shallow foundations bearing on dense sand. (See Figure 19.7 for an elevation of the proposed bridge.) Due to the difficult access, a decision has been made to launch the bridge from one end. As a result, for ease of construction, the bridge will be a constant depth.

There is an established steel industry in the area, as well as access to numerous concrete suppliers in close proximity to the site. Therefore, there is no preference of materials based on availability. The bridge is located in a developed country outside the United States with ready access to highly experienced construction workers; therefore, any bridge type would be acceptable. Following a cost study, it was determined that a steel, two-girder composite bridge is the best solution for this site. It should be noted that two-girder systems are not allowed in the United States due to redundancy concerns; therefore, it would not be considered if this bridge was in the United States.

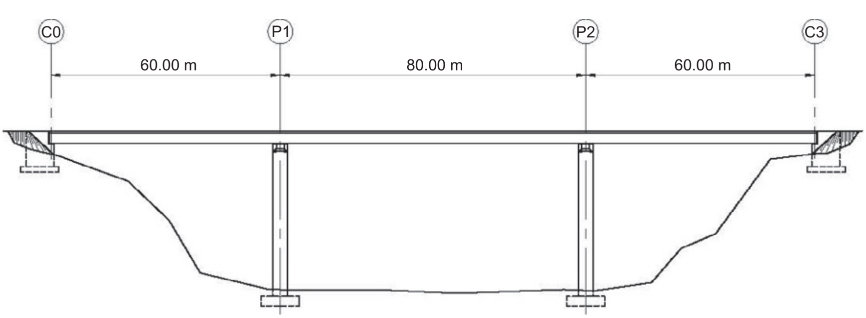

Figure 19.7 Elevation of proposed bridge.
Courtesy of JRC.

6.2 The structural concept

The superstructure is composed of a symmetrical, two-girder composite cross section. Preliminary studies established that the most effective depth for the girders would be a constant 2800 mm. Since the bridge is to be launched, all the "steps" in the thickness of the steel flanges will be made on the flange web side of the flanges. The deck slab has a 2.5% symmetrical cross slope with a variable thickness ranging from 400 mm (over the girders) to 250 mm (at its free edges) and 307.5 mm (at the center line of the deck). The roadway will have two traffic lanes that are 3.5 m wide apiece, with 2 m shoulders on each side. This results in an 11 m carriageway with 0.5 m parapets on each side. The total width of the resulting deck slab is 12 m, and the center-to-center spacing between the main girders is 7 m, resulting in a slab cantilever on both sides, each of which is 2.5 m. (See Figure 19.8 for a typical cross section of the deck.)

The piers and abutments are analyzed in accordance with the relevant chapters of EN 1992 (2004) and EN 1998 (2004). The height of the piers is approximately 40 m, and they consist of concrete circular hollow sections with an external diameter of 4.0 m and walls 0.4 m in thickness. The footings for each column are 10.0 m × 10.0 m × 2.5 m. The abutment is to be a standard stub abutment of the geometry resulting from a straight alignment. It will rest on a footing that is 10.0 m × 15 m × 1.5 m.

6.3 Design parameters

6.3.1 Dead loads

For the determination of dead loads, in addition to the self-weight of the concrete deck and steel girders, the following nonstructural elements are to be included: two parapets, two cornices, a 3 cm waterproof layer, and an 8 cm thick asphalt wearing surface. Each of these elements is shown in Figure 19.9.

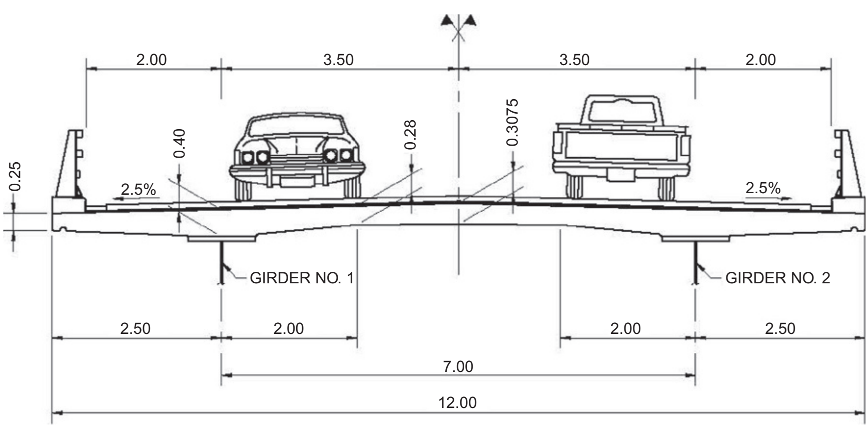

Figure 19.8 Typical cross section of the deck.
Courtesy of JRC.

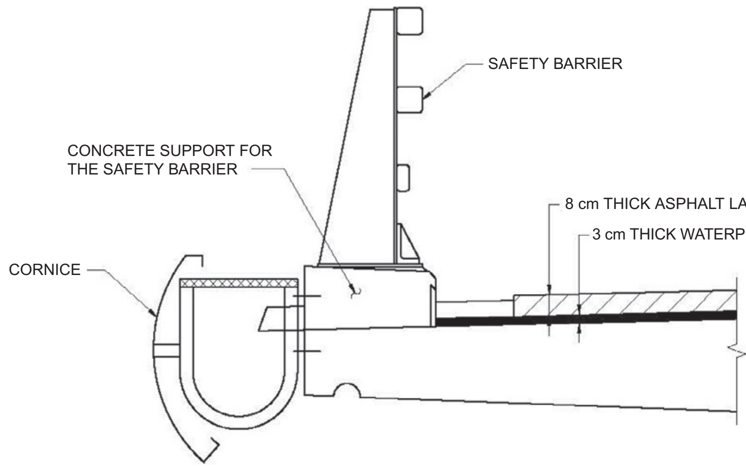

Figure 19.9 Nonstructural elements.
Courtesy of JRC.

6.3.2 Live loads

Traffic loads will be represented by Load Model 1 (LM1). According to EN 1991-2 (2003), LM1, which is formed by a uniformly distributed load (UDL) and the concentrated loads of the tandem system (TS), can be adjusted by α-coefficients. The values of these α-coefficients are given by the National Annexes based on different traffic classes. In accordance with EN 1991-2 (2003), 4.3.2, in the absence of specifications about the composition of the traffic, the values $\alpha_{Qi} = \alpha_{qi} = \alpha_{qr} = 1.0$ are recommended. No abnormal vehicles are to be considered for this bridge.

6.3.3 Temperature range/humidity

The minimum shade air temperature at the bridge location to be considered for steel quality selection is −20 °C. This corresponds to a return period of 50 years. The maximum shade air temperature at this bridge location to be used in the calculations, as required, is 40 °C. The variation in the temperature along the depth of the superstructure between the concrete and steel parts will be ±10 °C. The ambient relative humidity (RH) is assumed to be equal to 80%.

6.3.4 Wind conditions

The bridge is spanning a valley with few and isolated obstacles like a tree or house. It is located at an area where the fundamental value of the basic wind velocity is $v_{b,0} = 26$ m/s. No launching operations of the steel beams will be allowed if the wind velocity is greater than 50 km/h.

6.3.5 Exposure class

The bridge is located in a moderate freezing zone where deicing agents are frequently used. To determine the concrete cover, the following exposure classes, according to Table 4.1 of EN 1992-1-1 (2004), will be used:

- XC3 for the top face of the concrete slab (under the waterproofing layer)
- XC4 for the bottom face of the concrete slab

6.3.6 Subsurface conditions

Soil conditions are such that no deep foundations are needed. Both piers and abutments have swallow foundations. A settlement of 30 mm at Pier 1 will take place for the quasi-permanent combination of actions. It can be assumed that this displacement occurs at the end of the construction stage.

6.3.7 Seismic data

For the seismic analysis, the ground under the bridge is considered to be formed by deposits of very dense sand (it can be identified as ground type B, according to EN 1998-1 (2004), Table 3.1). The bridge has a medium importance for the communications system after an earthquake, so the importance factor I will be taken as equal to 1.0. No special regional seismic situation is considered. The reference peak ground acceleration will be $a_{gR} = 0.30\,g$. In this case, a limited elastic behavior is selected and, according to Table 4.1 of EN 1998-2 (2005), the behavior factor is taken as $q = 1.5$ (reinforced concrete piers).

6.3.8 Other considerations

The action of snow is considered to be negligible. Hydraulic actions are not relevant. Accidental design situations are analyzed in the referenced example.

6.3.9 Materials

Structural steel

For the girders, the steel used is grade S355 with the subgrades used as a function of thickness, as shown in the following table.

Thickness	Subgrade
$T \leq 30\,\text{mm}$	S355K2
$30 \leq t \leq 80\,\text{mm}$	S355N
$80 \leq t \leq 135\,\text{mm}$	S355NL

Concrete

Concrete class C35/45 is used for all the concrete elements in the referenced example (deck slab, piers, abutments, and foundations).

Reinforcing steel

The reinforcing bars used in the referenced example are class B high bond bars with a yield strength $f_{sk} = 500\,MPa$.

Shear connectors

Steel grade S235J2G3 stud shear connectors are used in the referenced example. Their ultimate strength is $fu = 450\,MPa$.

6.4 Details on structural steel and slab reinforcement

6.4.1 Resulting Main steel girder configuration

The structural steel distribution for a main girder is presented in Figure 19.10. The two main girders have a constant depth of 2800 mm, and the variations in thickness of the upper and lower flanges are found on the web side of the flanges. The lower flange is a constant 1200 mm wide, whereas the upper flange is a constant 1000 mm wide.

The two main girders have transverse bracing at abutments and at internal supports, as well as every 7.5 m in the side spans (C0-P1 and P2-C3) and every 8 m in the central span (P1-P2). Figures 19.11 and 19.12 illustrate the geometry and dimensions adopted for this transverse cross-bracing. The transverse girders in the span are made of IPE600 rolled sections, whereas the transverse girders at the internal supports and abutments are built-up, welded sections. The vertical T-shaped stiffeners are duplicated and welded on the lower flange at the supports, whereas the flange of the vertical T-shaped stiffeners in span has a V-shaped cutout to help prevent fatigue.

6.4.2 Resulting slab reinforcement

For both steel reinforcing layers, the transverse bars are placed outside the longitudinal ones, on the side of the slab free surface (Figure 19.13). High bond bars are used. Other specifications are as follows:

- Longitudinal reinforcing steel located in the in-span region consists of $\Phi = 16\,mm$ every 130 mm in the upper and lower layers (i.e., $\rho_s = 0.92\%$ of the concrete section in total).
- Longitudinal reinforcing located in the intermediate support regions consists of $\Phi = 20\,mm$ every 130 mm in the upper layer $\Phi = 16\,mm$ every 130 mm in the lower layer.
- Transverse reinforcing steel located at the midspan of the slab (between the main steel girders): $\Phi = 20\,mm$ every 170 mm in the upper layer and $\Phi = 25\,mm$ every 170 mm in the lower layer
- Transverse reinforcing steel located over the main steel girders consists of $\Phi = 20\,mm$ every 170 mm in the upper layer and $\Phi = 16\,mm$ every 170 mm in the lower layer.

6.4.3 Construction process

Launching of the steel girder

As stated earlier, it is assumed that the steel structure is launched, and it is pushed from the left abutment (C0) to the right one (C3) without the addition of any nose-girder.

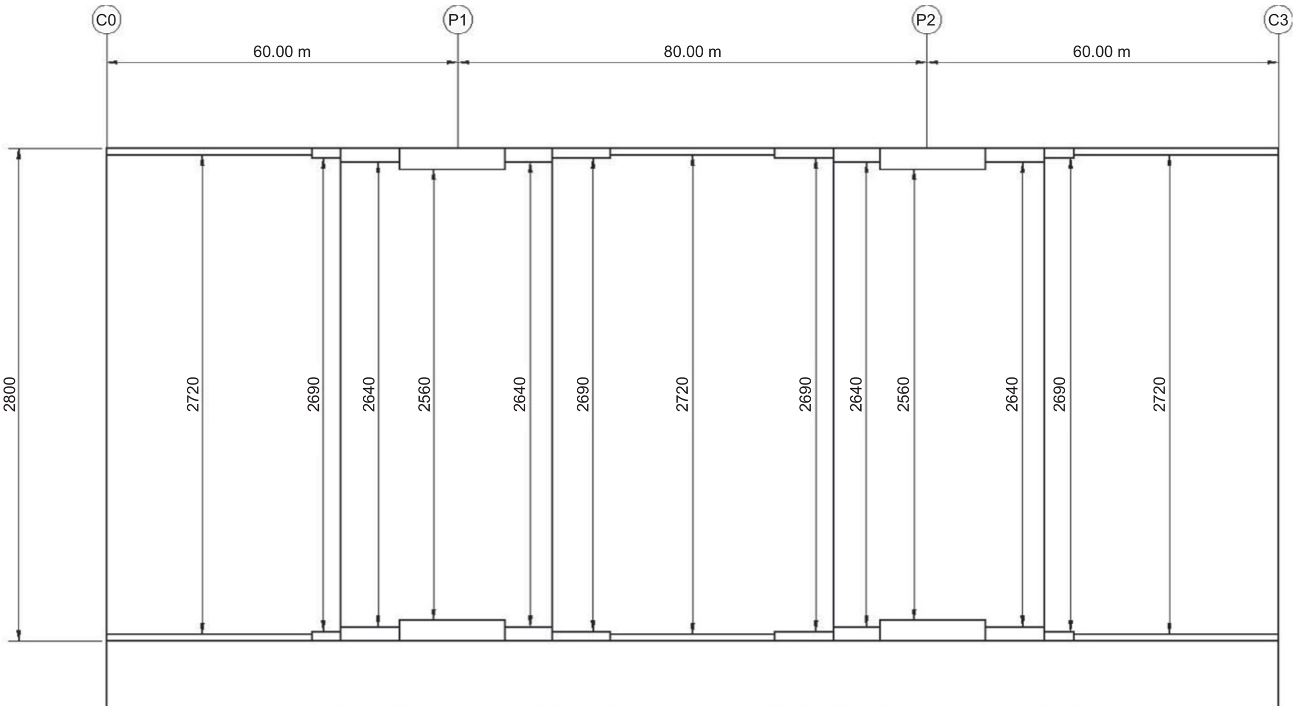

UPPER FLANGE Constant width 1000 mm	35,000×40	5000×55	10,000×80	18,000×120	8000×80	10,000×55	28,000×40	10,000×55	8000×80	18,000×120	10,000×80	5000×55	35,000×40
WEB	18×40,000		26×36,000			18×48,000			26×36,000			18×40,000	
LOWER FLANGE Constant width 1200 mm	35,000×40	5000×55	10,000×80	18,000×120	8000×80	10,000×55	28,000×40	10,000×55	8000×80	18,000×120	10,000×80	5000×55	35,000×40

Figure 19.10 Structural steel distribution.
Courtesy of JRC.

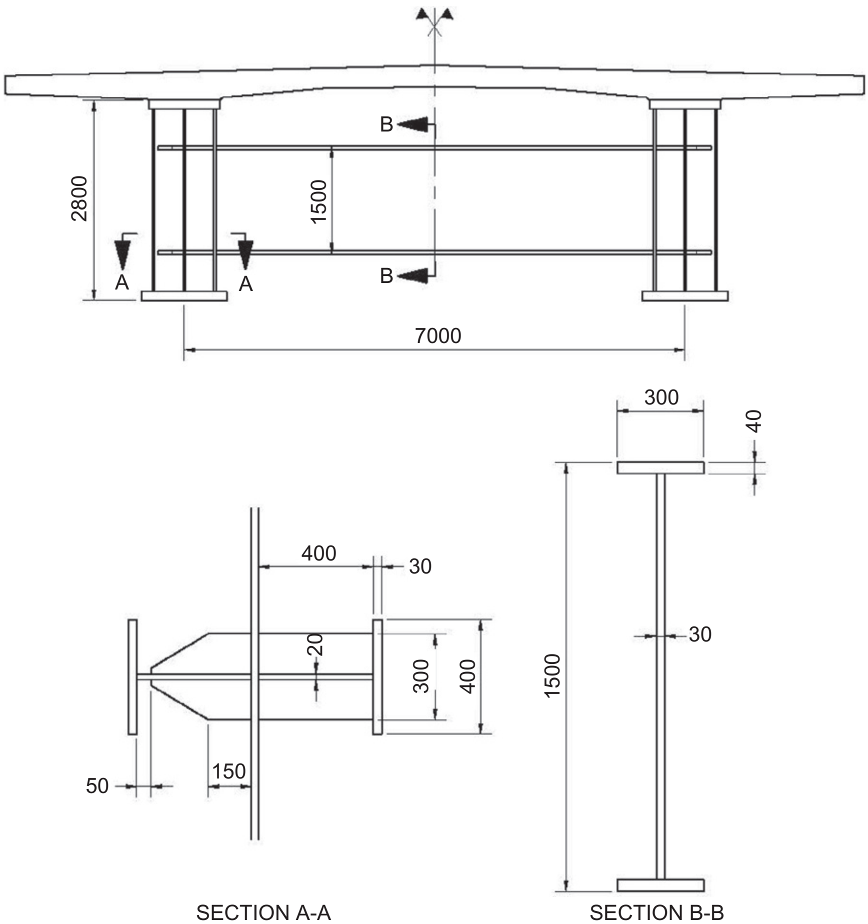

Figure 19.11 Transverse cross-bracing at bearings.
Courtesy of JRC.

Slab concreting

After the installation of the steel structure, concrete is poured on-site, casting the slab elements in a selected order: the total length of 200 m is split into 16 identical 12.5 m long concreting segments. They are poured in the order indicated in Figure 19.14. The start of pouring the first slab segment is the time origin ($t=0$). Its definition is necessary to determine the respective ages of the concrete slab segments during the construction phases. The time taken to pour each slab segment is assessed as three working days. The first day is devoted to the concreting, the second day to its hardening, and the third to moving the formwork. This sequence respects a minimum concrete strength of 20 MPa before the formwork is removed. The slab is thus completed within 66 days (including weekend days when no work is done). It is assumed that the

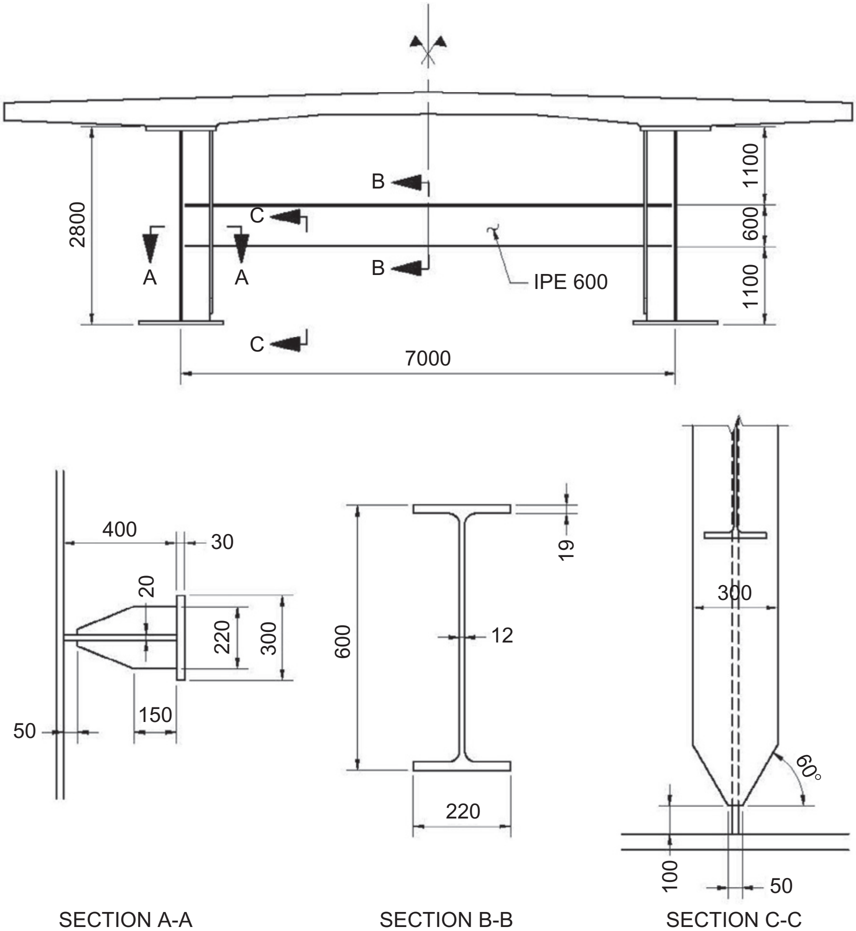

Figure 19.12 Transverse cross-bracing in spans.
Courtesy of European Commission's JRC.

installation of nonstructural bridge equipment is completed within 44 days, so that the deck is fully constructed at the date $t = 66 + 44 = 110$ days.

7. Research needs for highway bridges

Highway bridges have been designed and built since the advent of the wagon, and the general structure types used and described in this chapter are not likely to change. That being said, there are areas where these structure types can be improved—hence the need for future research. It is this author's opinion that the research needs for highway bridges (and for that matter, bridges of all uses) fall into five general areas:

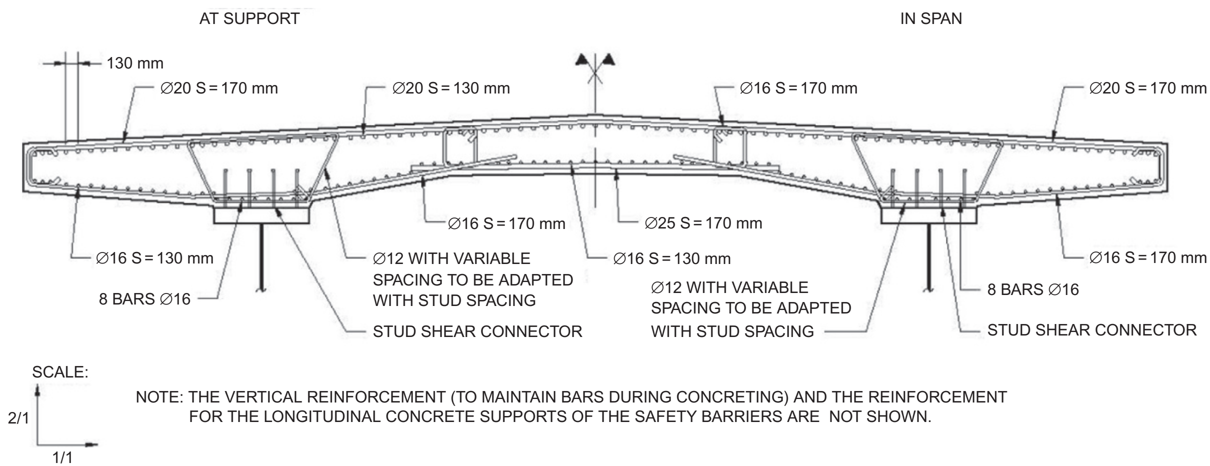

Figure 19.13 Slab reinforcing.
Courtesy of JRC.

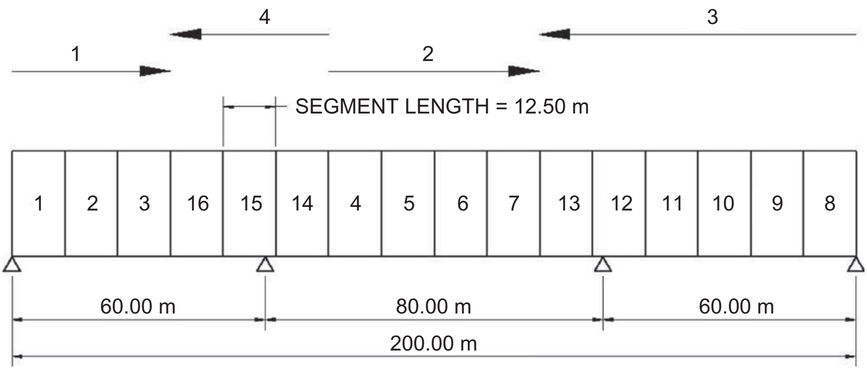

Figure 19.14 Slab pouring sequence.
Courtesy of JRC.

- Optimize structural systems
- Develop ways to extend service life
- Develop systems to monitor bridge conditions
- Develop details and methods to accelerate bridge construction
- Develop a full life cycle approach to bridge data management

7.1 The need to optimize structural systems

Though the general types of bridge structures have remained unchanged over time, the materials that comprised those types of structures have been constantly changing. The introduction of high-strength steel, high-performance concrete, and fiber-reinforced polymer composite materials has resulted in structures that are, in many cases, easier to build, more durable, and more economical. To take full advantage of these materials and their properties, optimization of structural shapes, details, components, and construction procedures must take place. Though research work in these areas is underway, there is much remaining to do.

7.2 Develop ways to extend service life

The bridges in the developed world are getting older, and the maintenance of that aging inventory is placing a strain on the budgets of bridge owners. Therefore, it is imperative to develop ways to extend the service life of existing bridge structures. Research into the processes that decrease the service life of bridges and the most promising preservation methods that will address these processes is needed.

7.3 Develop systems to monitor bridge performance

Often called *health monitoring,* bridge monitoring in real time holds great promise for prolonging bridge life. New data acquisition systems and monitoring devices allows the efficient collection of data dealing with virtually every component of a bridge.

The question is, "What information should be collected?" Terabytes of data may be collected, and this is being done on some bridges, without really having a means of sifting that data or use it in a meaningful manner. So the question remains of what data should be collected from which bridge components to establish the condition of the bridge.

7.4 Develop details and methods to accelerate bridge construction

In the United States, as well as most developed countries, traffic demands vastly limit the amount of time available for bridge repair and construction. There is a real need to reduce on-site construction time, while ensuring long lasting structures. More research needs to be done on erection technology and prefabricated elements while developing a means to balance the cost of such technologies against user costs.

7.5 Develop a full life cycle approach to bridge data management

This last element is not so much a need for research as it is a need to take existing available technology and use it more effectively in bridge management. By using building information technology, it is possible to collect data regarding a bridge over its complete life cycle. Using building information modeling (BIM) and other developing technology, every stage in the development, design, construction, maintenance, and eventual demolition of a bridge can be maintained in an easily searchable form. This information can be used to effectively maintain a bridge over the life of a bridge and to modify the structure as needs arise.

References

American Segmental Bridge Institute (ASBI), 2003. Recommended Practice for Design and Construction of Segmental Bridges. American Segmental Bridge Institute, Phoenix, AZ.

Barker, R.M., Puckett, J.A., 2007. Design of Highway Bridges: An LRFD Approach. John Wiley & Sons, Hoboken, NJ, pp. 87–108. Chapter 2.

Crespo, P., Davaine, L., Cornejo, M.O., Raoul, J., 2012. Bridge Design to Eurocodes, Worked Examples. Publications Office of the European Union, Luxembourg. Chapters 1 and 6. Entire publication can be found at http://eurocodes.jrc.ec.europa.eu/doc/1110_WS_EC2/report/Bridge_Design.

De Miranda, F., 1991. The three mentalities of successful bridge design. In: Bridge Aesthetics Around the World. Committee on General Structures, Transportation Research Board, National Research Council, Washington, DC, pp. 89–94.

EN 1991-2, 2003. Eurocode 1: Actions on Structures - Part 2: Traffic Loads on Bridges. European Committee of Standardization, Brussels, Belgium.

EN 1992, 2004. Eurocode 2: Design of Concrete Structures - Part 1–1: General Rules and Rules for Buildings. European Committee of Standardization, Brussels, Belgium.

EN 1998, 2004. Eurocode 8: Design of Structures for Earthquake Resistance - Part 1: General Rules, Seismic Actions and Rules for Buildings. European Committee of Standardization, Brussels, Belgium.

EN 1998-2, 2005. Eurocode 8 - Design of Structures for Earthquake Resistance - Part 2: Bridges. European Committee of Standardization, Brussels, Belgium.
Hewson, N.R., 2003. Prestressed Concrete Bridges: Design and Construction. Thomas Telford Publishing, London, pp. 179–281.
O'Connor, C., 1971. Design of Bridge Superstructures. Wiley Interscience, New York.
Pennsylvania Department of Transportation (PennDOT), 2012. Design Manual, Part 4. Harrisburg, PA.
Podolny Jr., W., Muller, J.M., 1982. Construction and Design of Prestressed Concrete Segmental Bridges. Wiley, New York.

Railway bridges

20

Alessio Pipinato
AP&P, CEO and Technical Director, Rovigo, Italy

1. Introduction

Railway bridge engineering has evolved extensively since the construction of the first modern rail bridge in the 1820s. Locomotives have changed from steam to diesel electric along with the weight of railway freight car loads and equipment. While future freight equipment weights will be limited by economics associated with railway infrastructure, maintenance, and renewal, it is most likely that train shipments and axle loads will increase. The first working model of a steam rail locomotive was designed and constructed by John Fitch in the United States in 1794. The first full-scale working railway steam locomotive was built in the United Kingdom in 1804. Stockton and Darlington Railway was a railway company that operated in northeast England from 1825 to 1863. The world's first public railway to use steam locomotives, which connected Shildon with Stockton-on-Tees and Darlington, was officially opened on September 27, 1825. The movement of coal to ships rapidly became a lucrative business, and the line was soon extended to a new port at Middlesbrough. Passengers were carried in coaches drawn by horses until carriages hauled by steam locomotives were introduced in 1833. In 1839, the first Italian railway line was laid between Naples and Portici. In the United States, the Baltimore and Ohio Railroad was incorporated in 1827 and officially opened in 1830. In the same period, engineers faced the problem of adapting bridge structures to railway traffic for the first time, and in most cases, principal structures were constructed of metal.

One of the first large bridge "experiments" was in 1845, when plans for carrying the Chester and Holyhead Railway over the Menai Straits in Wales were considered, and the conditions imposed by the admiralty in the interests of navigation involved the adoption of a new type of bridge (Britannica, 1910). Suspension chains combined with a girder was seen as a possible construction scheme, and in fact, the tower piers were built to accommodate chains. But the theory of such a combined structure could not be formulated at that time, and it was proved, partly by experiment, that a simple tubular girder of wrought iron was strong enough to carry a railway (Britannica, 1910). The bridge, then called Britannia, has two spans of 140 m and two of 70 m at 30 m above the water (Figure 20.1). It consists of a pair of tubular girders with solid or plate sides stiffened by angle irons and one line of rails passing through each tube. Each girder weighs nearly 4680 tons. In cross section, it is 4.5 m wide and varies in depth from 7 m at the ends to 9 m at the center. Partly to counteract any tendency to buckling under compression, and partly for convenience in assembling a great mass of plates, the top

Innovative Bridge Design Handbook. https://doi.org/10.1016/B978-0-12-823550-8.00003-2

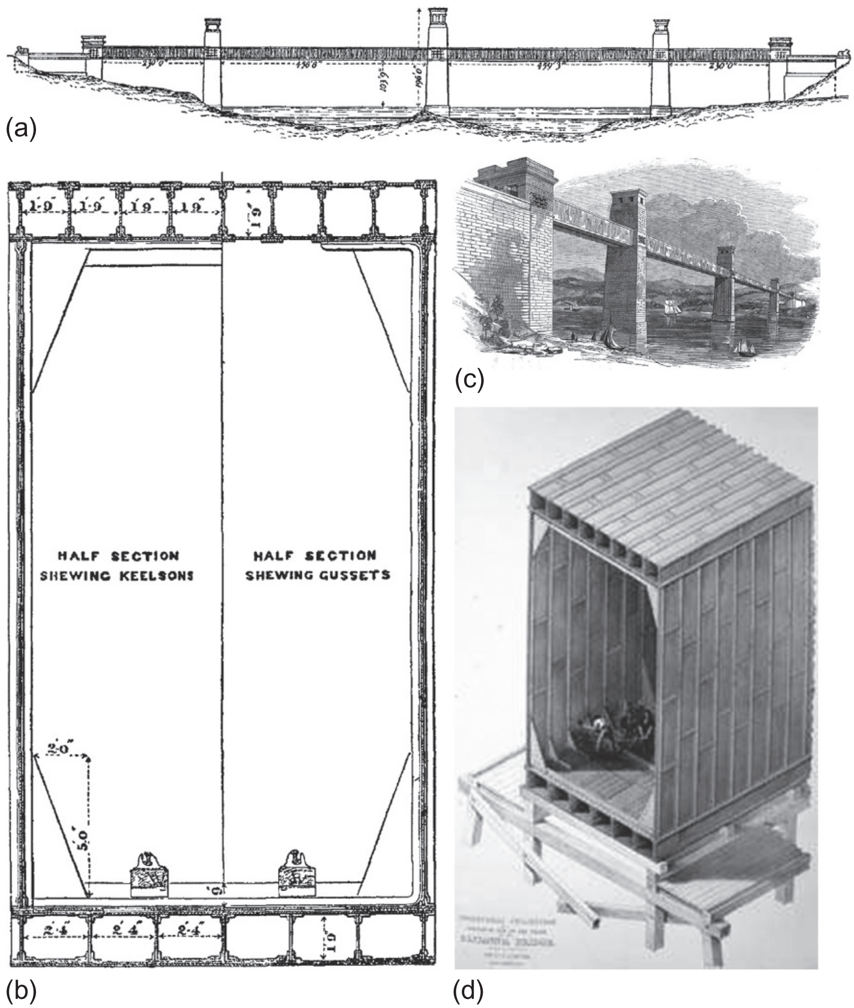

Figure 20.1 The original design of the Britannia Bridge (1850): (a) lateral view; (b) cross section; (c) bridge preliminary sketch; (d) three-dimensional view.

and bottom were made cellular, with the cells just large enough to permit passage for painting. As no scaffolding could be used for the center spans, the girders were built on shore, floated out, and raised by hydraulic presses (Britannica, 1910). Robert Stephenson (son of George Stephenson, well known as the "Father of Railways"), William Fairbairn, and Eaton Hodgkinson (who assisted in the experimental tests and in formulating the imperfect theory then available) together shared in creating this impressive, successful structure.

The first train passed over the Britannia Bridge in 1850. Though each girder is continuous over the four spans, it does not quite have the proportions over the piers that a continuous girder should have, so it must be regarded as an imperfectly continuous girder. The spans were, in fact, designed as independent girders, as the advantage of continuity was imperfectly known at that time. The vertical sides of the girders are stiffened so that they amount to 40% of the whole weight. This was partly necessary to meet the uncertain floating conditions in that the distribution of supporting forces was unknown and there were chances of distortion (Britannica, 1910). From that period up to now, large advances in the construction of railway bridges have been made, both in materials and in construction methods. However, fundamental principles in railway bridge engineering remain the same.

2. Type classifications

2.1 Bridge layout

The two main factors affecting the choice of a bridge structure are the main span and the obstacle type (e.g., a river, a railway, a highway). Different alternatives could be chosen for the same span length; functional, construction, and economic issues could lead to the final decisions. The main structural types of bridges could be subdivided as follows:

- Plate girders or box section beams (0–250 m)
- Truss beam (up to 400 m)
- Arches and cantilever bridges with suspended center span (up to 600 m)
- Cable-stayed bridge (up to 1200 m)
- Suspension bridge (up to 1900 m).

These requirements are general and apply to all bridges; with railway bridges, stringent deformation requirements often govern their design. As a result, structures inherently stiff in bending are required to be trusses or composite sections rather than cable-stayed or suspension bridges (Hirt and Leben, 2013).

2.2 Materials and code references

Materials of railway bridge constructions are provided by specific national codes such as Eurocodes, while additional documents and specifications are provided by railway associations such as the International Union of Railways (UIC). There is no predominant material; however, steel and composite structures are preferred for their simplicity of construction; lighter weight; and ease of inspections, intervention, and replacement. High-strength materials are employed (but not mandatory), as they provide a lighter and more economical solution considering the minimum rail standard requirement. In Europe, steel rail bridges today are commonly realized with S355 grade carbon steel, bolted or welded, even if higher grades have been employed in special cases; general provisions for metal structures are provided by EN 1993-1-1 (2014). Concrete solutions actually include the concrete category provided in EN 1992-1-1 (2004). In the United States, the use of materials conforms to American Society for Testing and Materials (ASTM) specifications (AREMA, 2014). Finally, national standards usually provide minimum material requirement specifications.

2.3 Substructures and foundations

Foundations are commonly made up of deep structures, as piles; shallow foundations are not normally adopted for railway bridges. The substructure consists of abutments and piers and includes foundations: this substructure transmits to the underlying soil the forces comprising the dead load of the superstructure and substructure, the live load effect of passing traffic, and forces from wind, water, etc. The substructure is generally represented by pile foundations, spread footings, piers and abutments, or any combination of these (AREMA, 2013). Careful soil investigation is needed before construction: extensive recommendations are given in specific codes and standards (AREMA, 2014; Eurocode 7-2, 2007).

As the stability of the structure is obviously related to that of the substructures, these should be under observation during the whole life of the bridge, and special inspections should be performed during and after freshets, ice gorges, cloudbursts, and other unusual happenings, which could have the potential of seriously affecting the safety of the structure. The most railway bridge foundations are piles or caissons, which are mainly made of reinforced concrete (RC): these piles are heavy structures with a high bearing capacity. In some cases (e.g., when a specific requirement of temporarily constructions are needed), steel H-piles are used. In order to resist lateral forces, concrete-filled pipe piles with an adequate diameter and moment of inertia are required. Finally, for very large loads with minimum settlement, caissons are needed. Two main configurations could be used: isolated piles or sheet piles. The latter are piles built close together to form a wall, which can act as a retaining structure for water, earth, or other material. While concrete sheet piles are tongued and grooved, steel sheet piles are usually interlocked. The capacity of a pile as a structural member is based on allowable stresses established by the American Railway Engineering and Maintenance-of-Way Association (AREMA, 2014 in Chapter 8 or 15). For European standards, indications are given in Eurocode 7-1-7 (2007).

2.4 Superstructures

The objective of a railway bridge designer is to maximize the structural stiffness while reducing the self-weight of the construction material; this concept is maximized in truss structures. Another design tip for railway bridges is the presence of a hierarchical structure that can carry forces among a series of components. The vertical loads are transferred from their point of application (the rails) to the supports via sleepers and longitudinal beams (tertiary structural members), and then the cross bracing (secondary structural members), before being transferred to the primary structural members—namely, the main beams (Hirt and Leben, 2013). Some older bridges could not be ballasted; however, most bridges today are ballasted in order to reduce impact and improve train ride quality due to a relatively constant track modulus on the approaches and across the bridge. Concerning the deck solution, an upper slab is preferred because it provides protection from the weather (so long as the structure itself is protected by waterproofing), bridge widening is simple, maintenance is allowed during operations, and derailment does not result in damage to the principal structures.

3. Analysis and design

3.1 Loads and load combinations

In the following section, load specifications are presented according to European and other relevant codes. Concerning load combinations, specific guidance is given by standards such as EN 1990 (2006); however, appropriate indications are included in international codes, standards, and National Annexes.

3.1.1 Dead loads

The weight of the structure itself, the track it supports, eventual ballasting, and any other superimposed loads attached to the bridge are dead loads. These act due to gravity and are applied to the structure, either permanently or until the structure changes its configuration throughout its life. Unit weights for calculation of dead loads are given in codes and standards. The self-weight of nonstructural elements includes the weight of elements such as noise and safety barriers, signals, ducts, cables, and overhead line equipment (except the forces due to the tension of the contact wire, etc.).

3.1.2 Live loads

The load models defined in codes and standards do not describe actual loads. The bridge designer should always be mindful of this in order to evaluate the possible use of heavier convoys, which is not an impossible situation. In fact, load models have been selected so that their effects, with dynamic enhancements taken into account separately, represent the effects of service traffic. This is the specific case of EN 1991-2 (2005): rail traffic actions are defined by means of load models. Five models of railway loads are given:

- Load Model 71 (and Load Model SW/0 for continuous bridges), to represent normal rail traffic on mainline railways (Figures 20.2 and 20.3)
- Load Model SW/2, to represent heavy loads (Figure 20.3)
- Load Model HSLM, to represent the loading from passenger trains at speeds exceeding 200 km/h (Figure 20.4 and 20.5)
- Load Model “unloaded train,” to represent the effect of an unloaded train; this consists of a vertical uniformly distributed load with a characteristic value of 10.0 kN/m.

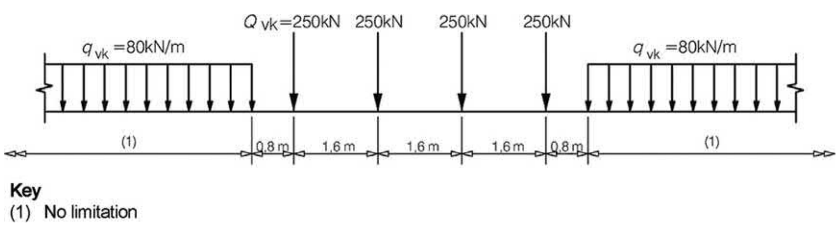

Figure 20.2 Load Model 71 and characteristic values for vertical loads (EN 1991-2, 2005).

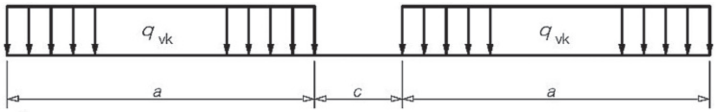

(a)

Load Model	q_{vk} (kN/m)	a (m)	c (m)
SW/0	133	15,0	5,3
SW/2	150	25,0	7,0

(b)

Figure 20.3 Characteristic values for vertical loads for Load Models SW/0 and SW/2 (EN 1991-2, 2005): (a) geometrical disposition; and (b) characteristic values.

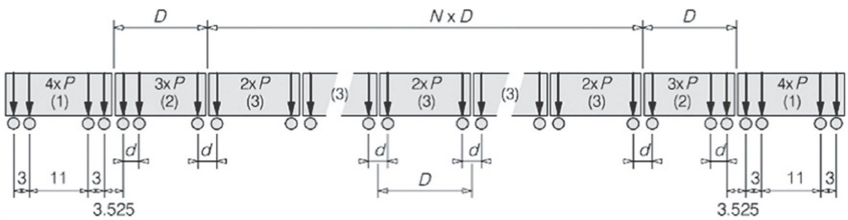

Key
(1) Power car (leading and trailing power cars identical)
(2) End coach (leading and trailing end coaches identical)
(3) Intermediate coach

(a)

Universal Train	Number of Intermediate Coaches N	Coach Length D (m)	Bogie Axle Spacing d (m)	Point Force P (kN)
A1	18	18	2.0	170
A2	17	19	3.5	200
A3	16	20	2.0	180
A4	15	21	3.0	190
A5	14	22	2.0	170
A6	13	23	2.0	180
A7	13	24	2.0	190
A8	12	25	2.5	190
A9	11	26	2.0	210
A10	11	27	2.0	210

(b)

Figure 20.4 Characteristic values for vertical loads for HSLM-A (EN 1991-2, 2005): (a) geometrical disposition; and (b) universal train details.

Concerning load schemes, it should be considered that a point force or wheel load may be distributed over three rail supports. For the design of local floor elements, the longitudinal distribution beneath sleepers should be taken into account, where the reference plane is defined as the upper surface of the deck. The standard loading scheme incorporated by North American Railways and AREMA (2013) is the Cooper

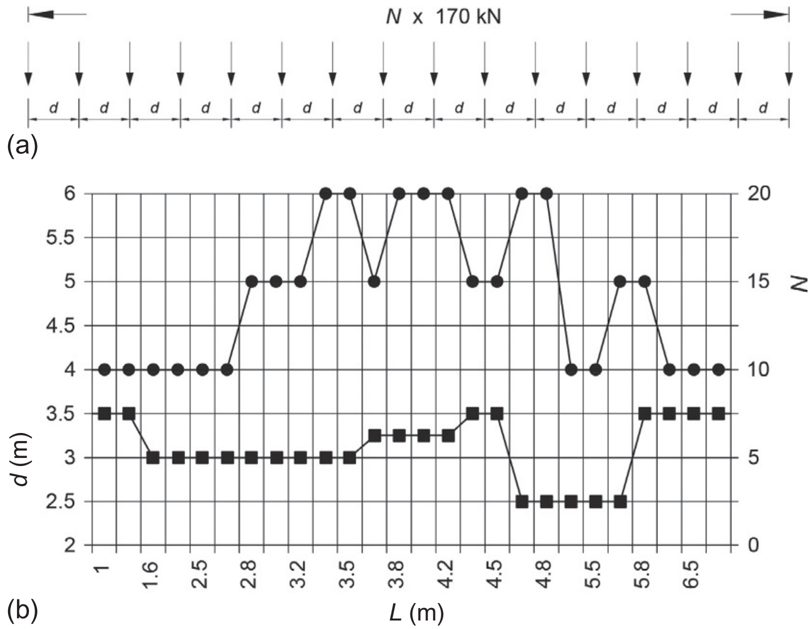

Figure 20.5 Characteristic values for vertical loads for HSLM-B (EN 1991-2, 2005): (a) geometrical disposition; and (b) graph for d (m) – L (m) – N (kN) correlation (b).

E-Series loading: AREMA (2013) recommends that E-80 loadings (two locomotives coupled together in doubleheader fashion, with a maximum axle load of 335.84 kN) be used for the design of steel, concrete, and most other structures. Yet the designer must verify the specific loading to be applied from the railway, as this may require a design loading other than the E – 80 Cooper E-Series.

3.1.3 Dynamic effects

The static stresses and deformations (and associated bridge deck acceleration) induced in a bridge are increased and decreased by moving traffic by the following factors (EN 1991-2, 2005):

- The rapid rate of loading due to the speed of traffic crossing the structure and the inertial response (impact) of the structure
- The passage of successive loads with approximately uniform spacing, which can excite the structure and under certain circumstances create resonance (where the frequency of excitation or a multiple thereof matches a natural frequency of the structure or a multiple thereof)
- The possibility that the vibrations caused by successive axles running onto the structure will be excessive
- Variations in wheel loads resulting from track or vehicle imperfections (including wheel irregularities)

For determining the effects (stresses, deflections, bridge deck acceleration, etc.) of rail traffic, these effects shall be taken into account. The principal factors that influence dynamic behavior are as follows:

- The speed of traffic across the bridge
- The span L of the element and the influence line length for deflection of the element being considered
- The mass of the structure
- The natural frequencies of the whole structure and the associated mode shapes (eigenforms) along the line of the track
- The number of axles, axle loads, and the spacing of axles
- The damping of the structure
- Vertical irregularities in the track
- The unsprung mass and suspension characteristics of the vehicle
- The presence of regularly spaced supports of the deck slab, track, or both (cross girders, sleepers, etc.)
- Vehicle imperfections (wheel flats, out-of-round wheels, suspension defects, etc.)
- The dynamic characteristics of the track (ballast, sleepers, track components, etc.)

A static analysis generally shall be carried out with the load models defined in the specific code that is adopted. The results shall be multiplied by the dynamic factor specifically defined in the reference code. Simplified criteria for determining whether a dynamic analysis is required are given in codes and standards. For specific cases, codes should require a dynamic analysis: i.e., high speed lines and the particular geometry of the investigated bridge (Figure 20.6). Moreover, codes usually provide useful graphs that include the limits of the bridge's natural frequency n_0 (in hertz) as a function of the length L (in meters); in order to establish this for bridges with a first natural frequency n_0 within the limits given and a maximum line speed at the site not exceeding 200 km/h, a dynamic analysis is not required (i.e., Figure 20.7). Finally, for a simply supported bridge subjected only to bending, the natural frequency may be estimated using simplified approaches: EN 1991-2 (2005) suggests the formula $n_0 = 17.75/d_0^{-0.5}$ (expressed in hertz), where d_0 is the deflection at midspan due to permanent actions (in millimeters) and is calculated using a short-term modulus for concrete bridges, in accordance with a loading period appropriate to the natural frequency of the bridge.

AREMA (2013) has developed empirical relationships based on experimental observations to evaluate design impact values (percentage of live load) for various bridge types. The impact produced is represented as a vertical load applied to the top of the rail at the same location as the Cooper axle loadings, expressed as a percentage of the live load. The impact on a ballasted deck structure can sometimes be reduced compared to that for an open-deck structure because of the absorbing effect of the ballasted track. For steel bridge design, the percentage of live load attributed to impact is a function of the spacing of the structure-supporting elements (girder or stringer spacing) relative to the spacing of the rails (rocking effect) and the distance between supports for the member being designed (span length); reduction in impact design

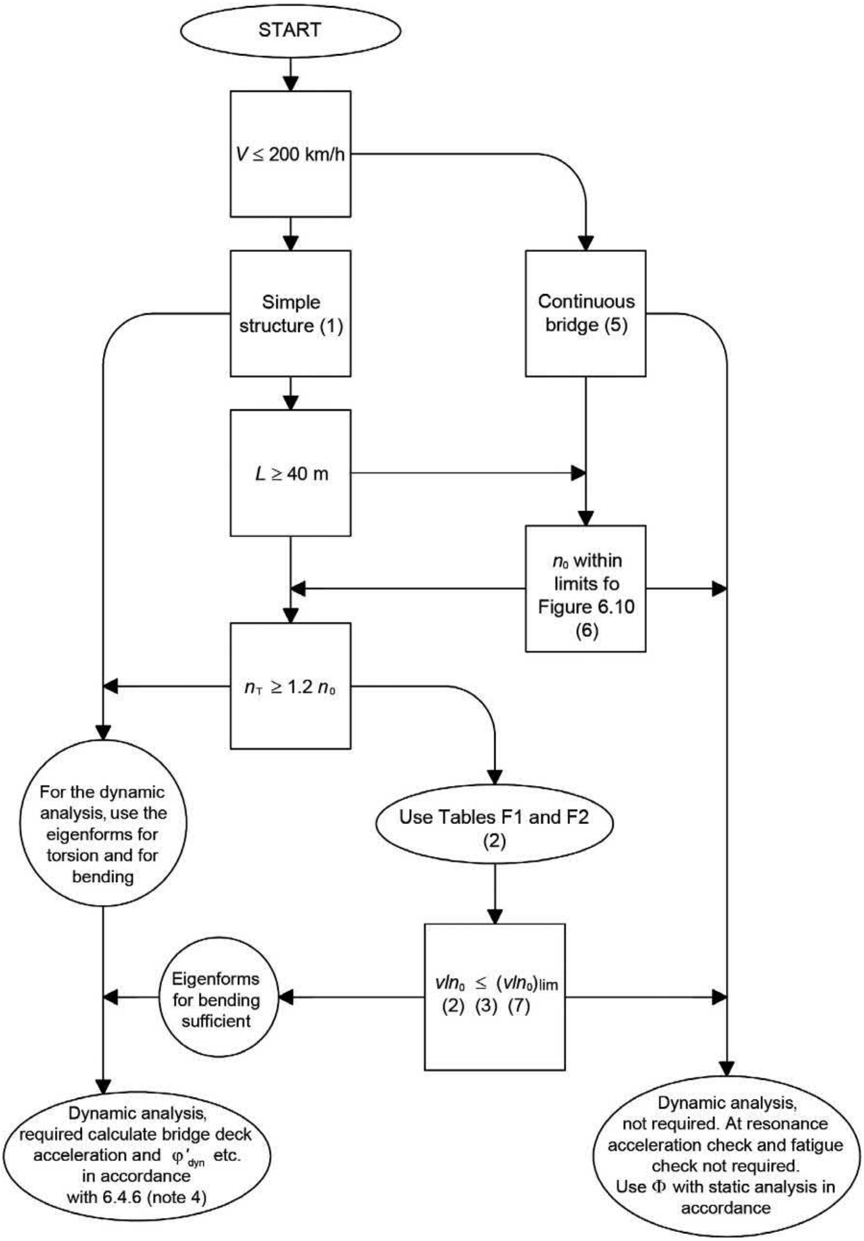

Figure 20.6 Flowchart for determining whether a dynamic analysis is required according to EN 1991-2 (2005).

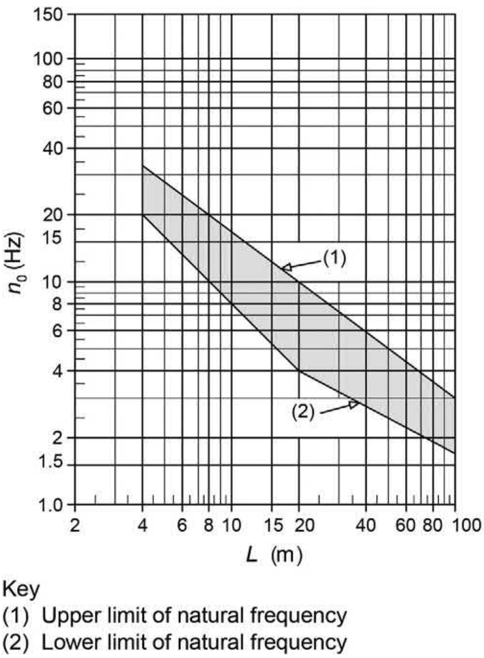

Figure 20.7 Limits of a bridge's natural frequency n_0 (Hz) as a function of L (m) according to EN 1991-2 (2005).

values are given for speeds below 96 km/h. Impact is also considered when performing fatigue analysis and design: when checking fatigue stresses, impact forces may be reduced for members greater than 9 m in length. For concrete bridges, AREMA (2013) utilizes live load and dead load values to develop a modified ratio, and the span length of prestressed members for evaluating the impact percentage (Figure 20.8).

3.1.4 Horizontal forces

Horizontal forces are the result of a variety of physical factors and include the following:

- *Centrifugal forces*, where the track is curved over the whole or part of the length of the bridge; both the centrifugal forces and the track shall be taken into account. The centrifugal forces should be taken to act outward in a horizontal direction at a specific height above the running surface.
- The *nosing force* shall be taken as a concentrated force acting horizontally at the top of the rails, perpendicular to the center line of the track. It shall be applied to both straight track and curved track;
- *Traction and braking forces* act at the top of the rails in the longitudinal direction of the track. They shall be considered as uniformly distributed over the corresponding influence length $L_{a,b}$ for traction and braking effects for the structural element considered. The direction of the traction and braking forces shall take account of the permitted directions of travel on each track.

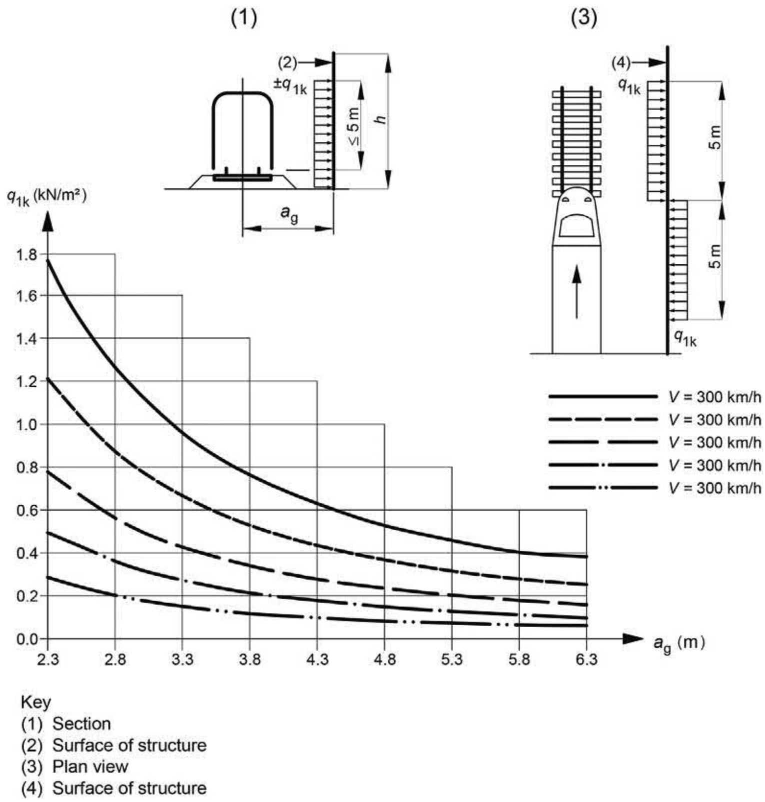

Figure 20.8 Characteristic values of actions q_{1k} for simple vertical surfaces parallel to the track (e.g., noise barriers) according to EN 1991-2 (2005).

According to AREMA (2013), lateral loads are applied to the structure as a result of routine train passage, excluding centrifugal forces. The magnitude and application point of these loads vary depending on the constitutive material of the bridge; e.g., for steel, a load of one-quarter of the heaviest axle of the specified live load is applied at the base of the rail as a moving concentrated load that can be applied at any point along the span in either horizontal direction. Experience has shown that very great lateral forces may be applied to structures due to the lurching of certain types of cars, wheel hunting, or damaged rolling stock (slewed trucks, binding center plates, etc.).

3.1.5 Aerodynamic actions from passing trains

When designing structures adjacent to railway tracks, aerodynamic actions from passing trains shall be taken into account. The passing of rail traffic subjects any structure situated near the track to a traveling wave of alternating pressure and suction. The magnitude of the action depends mainly on the speed of the train, the aerodynamic shape of the train, the shape of the structure, and the position of the structure, particularly the clearance between the vehicle and the structure. When checking ultimate and serviceability limit states and fatigue, the actions may be approximated by equivalent loads at the head and rear ends of a train (CHSRA, 2011). Characteristic values of the equivalent loads are given specifically in codes and standards.

3.1.6 Derailment and other actions for railway bridges

The limitation of damages due to derailment is often included in codes and standard design requirement in order to minimize the effects. Codes could differentiate derailment cases as extreme and minor by differentiated vertical loads/accidental load cases, to be applied commonly at the edge of the railway.

3.2 Verifications regarding deformations and vibrations for railway bridges

Due to the particular and inherent construction types that are included in the specific case of railway bridges, detailed verifications are necessary to ensure safety, security, and comfort to train passengers. Specific limits of deformation and vibration to be taken into account for the design of new railway bridges are included in standards such as EN 1990 (2006). Bridge deformation checking includes the following:

- Vertical accelerations of the deck (to avoid ballast instability and unacceptable reduction in wheel rail contact forces)
- Vertical deflection of the deck throughout each span (to ensure acceptable vertical track radii and generally robust structures)
- Unrestrained uplift at the bearings (to avoid premature bearing failure)
- Vertical deflection of the end of the deck beyond bearings (to avoid destabilizing the track, limit uplift forces on rail fastening systems, and limit additional rail stresses)
- Twisting of the deck measured along the center line of each track on the approaches to a bridge and across a bridge (to minimize the risk of train derailment)
- Rotation of the ends of each deck about a transverse axis or the relative total rotation between adjacent deck ends (to limit additional rail stresses, uplift forces on rail-fastening systems, and angular discontinuity at expansion devices and switch blades)
- Longitudinal displacement of the end of the upper surface of the deck due to longitudinal displacement and rotation of the deck end (to limit additional rail stresses and minimize disturbance to track ballast and adjacent track formation)
- Horizontal transverse deflection (to ensure acceptable horizontal track radii)
- Horizontal rotation of a deck about a vertical axis at the ends of a deck (to ensure acceptable horizontal track geometry and passenger comfort)
- Limits on the first natural frequency of lateral vibration of the span (to avoid the occurrence of resonance between the lateral motion of vehicles on their suspension and the bridge)

Concerning the vertical acceleration of the deck, to ensure traffic safety, where a dynamic analysis is necessary, the verification of maximum peak deck acceleration due to rail traffic actions shall be regarded as a traffic safety requirement checked at the serviceability limit state for the prevention of track instability. The maximum peak values of bridge deck acceleration calculated along each track shall not exceed the appropriate design values, and according to EN 1990 (2006), recommended values are $\gamma_{bt}=3{,}5\ m/s^2$, $\gamma_{df}=5\ m/s^2$ (where γ_{bt} deals with ballasted track), and γ_{df} (for direct-fastened tracks with track and structural elements designed for high-speed traffic).

The twist of the bridge deck shall be calculated taking into account, where Eurocode applies, the characteristic values of Load Model 71 (as well as SW/0 or SW/2, as appropriate) multiplied by Φ and α and Load Model HSLM (including centrifugal effects), all in accordance with EN 1991-2 (2005). Twisting shall be checked on the approach to the bridge, across the bridge, and on the departure from the bridge.

Also, the vertical deformation of the deck should be checked. If Eurocode applies, for all structure configurations loaded with the classified characteristic vertical loading in accordance with EN 1991-2 (2005) (and, where required, classified SW/0 and SW/2), the maximum total vertical deflection measured along any track due to rail traffic actions should not exceed L/600. In addition, angular rotations of the deck's end is specified in codes and standards.

The transverse deflection δ at the top of the deck should be limited to ensure that a horizontal angle of rotation of the end of a deck about a vertical axis is not greater than the values provided in codes; the change of radius of the track across a deck is not greater than fixed values; and at the end of a deck, the differential transverse deflection between the deck and adjacent track formation or between adjacent decks does not exceed the specified value.

Finally, limitations of the values for the maximum vertical deflection for passenger comfort are provided in codes and standards. Comfort criteria depends on the vertical acceleration inside the coach during travel on the approach to, passage over, and departure from the bridge. Also, the levels of comfort and associated limiting values for the vertical acceleration should be specified in each project; however, recommended levels of comfort are given in codes and standards [e.g., for EN 1990, 2006]; the level of comfort/vertical acceleration (m/s^2) could be defined as very good (<1.0), good (<1.3), or acceptable (<2.0).

3.3 Fatigue strength

Cracking or fracture due to repetitive loading is the result of fatigue. The repetitive loading that causes fatigue fracture produces stresses in the material below its yield stress. Stress reversals in railway bridges are commonly higher than those found in current road bridges because of the different load rates. However, a correct detailing design could avoid fatigue stress concentrations and the fracture in the bridge members that could also lead to collapse. Codes and standards provide construction details, including the description and requirements of common structural members. In Europe, EN 1993-1-9 (2005) deals with fatigue in metal structures; in the United States, AREMA (2014) provides general design specifications, as well as other requirements of the governing railway that must be adopted.

4. Static scheme and construction details

4.1 Static scheme

The durability and deformation limits under service loads are severe inputs for the design stage. Also for this reason, the most preferred static scheme is the continuous beam, as this scheme helps to reduce vertical deformations under loadings and the joints and bearing points. These characteristics are also relevant for recent high-speed railways, with trains exceeding 200 km/h. However, the designer should be careful: continuous beam static scheme solutions imply an increased deformation to settlement of the supports and a terrible distribution of braking forces through the bridge substructure. Finally, it is difficult to replace deck parts.

4.2 Expansion joints

The railway bridge structure is not normally able to move without introducing forces onto the rails and deck in the absence of expansion joints. This interaction is to be considered upon code provisions, which give the designer the possibility of avoiding calculations in a particular case. If these requirements are not met, the structure–rail interaction has to be included in the design calculation procedure.

4.3 Ballasting

Ballasted tracks on bridges are currently a common rule, even if codes and standards have specific exceptions. The inherent advantages of the ballasted tracks are commonly related not only to noise and vibration reduction but also to decreased maintenance expenses, even if structural improved performance could be discovered, as well as the reduction of the dynamic amplification, improved redistribution of loads on the deck, and consequent reduction of stress reversals/peak stresses on deck structural details more prone to fatigue.

4.4 Rainwater evacuation

Waterproofing systems must be enclosed in every railway bridge project, and the surfaces of carriageways and footpaths should be sealed to prevent the water access (EN 1993-2, 2005). The drainage layout should be based on the slope of the bridge deck as well as the location, diameter, and slope of the pipes. Free fall drains should carry water to a point clear of the underside of the structure to prevent water entering the structure.

Drainage pipes should be designed so that they can be cleaned easily. The distance between centers of the cleaning openings should be shown on drawings. Where drainage pipes are used inside box girder bridges, provisions should be made to prevent the accumulation of water when leaks occur or pipes break. For road bridges, drains should be provided at expansion joints on both sides where it is appropriate. Often, for small bridges, rainwater evacuation can be concentrated into abutment: for instance, EN 1993-2 (2005) suggests, for railway bridges up to 40 m long carrying ballasted tracks, that the deck may be assumed to be self-draining to abutment drainage systems, and no further drainage provisions need to be provided along the length of the deck. Provision should be made for the drainage of all closed cross sections unless they are fully sealed by welding.

4.5 Fatigue details

The best solution to avoid fatigue in structural details is to adopt practical detailing solutions commonly described in codes and standards. EN 1993-1-9 (2005) provides a wide variety of solutions, including plain members and mechanically fastened joints, welded built-up sections, transverse butt welds, weld attachments and stiffeners, load-carrying welded joints, hollow sections, lattice girder node joints, orthotropic decks (open and closed stringers), and top-flange-to-web junction of runway beams. For each of these details, the code includes information on the detail category and the detail requirements.

4.6 Accessibility

All bridge parts should normally be designed to be accessible for inspection, cleaning, and painting. Where such access is not possible, either all inaccessible parts should be effectively sealed against corrosion (e.g., the interior of boxes or hollow portions) and long-term damage or they should be constructed with improved atmospheric resistance.

4.7 Construction process

Railway bridges are specific structures requiring a deep knowledge not only of structural engineering but also of the operations and safety requirements of lines used daily by great numbers of passengers. For this reason, the following considerations arise:

- *Timing*—When dealing with the construction or replacement process in railway engineering, the driving factor of the design is track time; so operations, maintenance, and new construction are all relevant factors that should be carefully evaluated by the designer in order to produce the best bridge in the shortest time. For this reason, the design efficiency could be sacrificed for a shorter construction period.
- *Simplifying construction*—Simple constructions are generally preferred to complex solutions, and elements such as simple spans and bolted construction (i.e., stiffeners bolted to web plates) are still widely used for railway bridges, whereas continuous spans with welded stiffeners are standard practice in highway bridge design. The use of bolted construction reduces fatigue requirements, and simple spans enable the replacement of each individual span, thus minimizing traffic interruptions.
- *Precasting*—A direct consequence of the previous points is that it is becoming a common practice to design and erect spans in nearly complete form in order to expedite span realization. Steel spans and precast concrete box beams, as well as other superstructure types,

may be shipped to a construction site fully assembled and lifted in place quickly in order to restore traffic as soon as possible (AREMA, 2013).

- *Material savings*—Often the outcome of a design is counterintuitive to the standard practice of producing highly efficient structural systems that use a minimum amount of material. In the long term, this break from common practice proves more beneficial to railway companies due to the savings yielded from a design that lasts many years, requires minimal maintenance, and provides a construction period that keeps trains moving (AREMA, 2013).

5. R&D on railway bridges

Special emphasis on recent relevant research on railway bridges can be seen in the following fields:

- *High-speed lines (HSLs)*—The inherent advantages of increased speeds on railway vehicles has led to an increased interest in research on improved structures that can carry such vehicle loads and speeds. For example, in Italy, HSLs have been recently realized and accordingly, new bridges to carry HS vehicles have been designed and realized (Figure 20.9). Depending on the vehicle type and the maximum design speed allowed on the line, bridge structures becomes more sophisticated to be designed and built; the framework of studies is very large and deals with different key problems. For instance, Doménech et al. (2014) recently investigated the influence of the vehicle model on the prediction of the maximum bending response of simply supported bridges under high-speed railway traffic; Johansson et al. (2014) deepened a methodology for the preliminary assessment of existing railway bridges for high-speed traffic; Xu et al. (2014) performed a complete evaluation of track geometry on a long-span steel-trussed cable-stayed bridge; and Vega et al. (2012) studied the dynamic response of underpasses for high-speed train lines.
- *Improved/innovative materials*—As railway bridges have relevant requirements in terms of stiffness and vertical and lateral displacement limitations, an improvement on the materials employed could help to minimize material weight and accelerate the construction speed, if possible, at the same time. Current improvements are represented by higher-strength steel grades, working with ultra-high-performance fiber-reinforced cement (UHPFRC). Recent research on this issue includes the local bending tests and punching failure of a ribbed UHPFRC bridge deck (Toutlemonde et al., 2007), an experimental study on the bond between carbon fiber-reinforced polymer (CFRP) bars and ultra-high-performance fiber-reinforced concrete (Ahmad et al., 2011), innovative calculation formula of shear connectors in UHPFRC composite structure (Guo and Wang, 2012), and the rehabilitation and strengthening of concrete structures using UHPFRC (Brühwiler and Denarié, 2013).
- *Strengthening existing bridges*—A strong international interest has concentrated on the upgrading and structural strengthening of these bridge types, especially for metal bridges, but also for more recent steel bridges,. This is because a lot of them were built between the late 18th and the mid-19th centuries, and all of them need to be repaired or replaced. As the complete renovation of entire national rail lines (amounting to thousands of kilometers) sounds difficult to develop, appropriate strengthening solutions are needed. Some general hints concerning this specific issue are presented in several studies by this author: for instance, in Pipinato (2010), the step-level procedure for remaining fatigue life evaluation of one railway bridge is deepened, whereas in Pipinato (2011), safety and security issues in the assessment of existing bridges considering codes and standard are presented. In Pipinato and

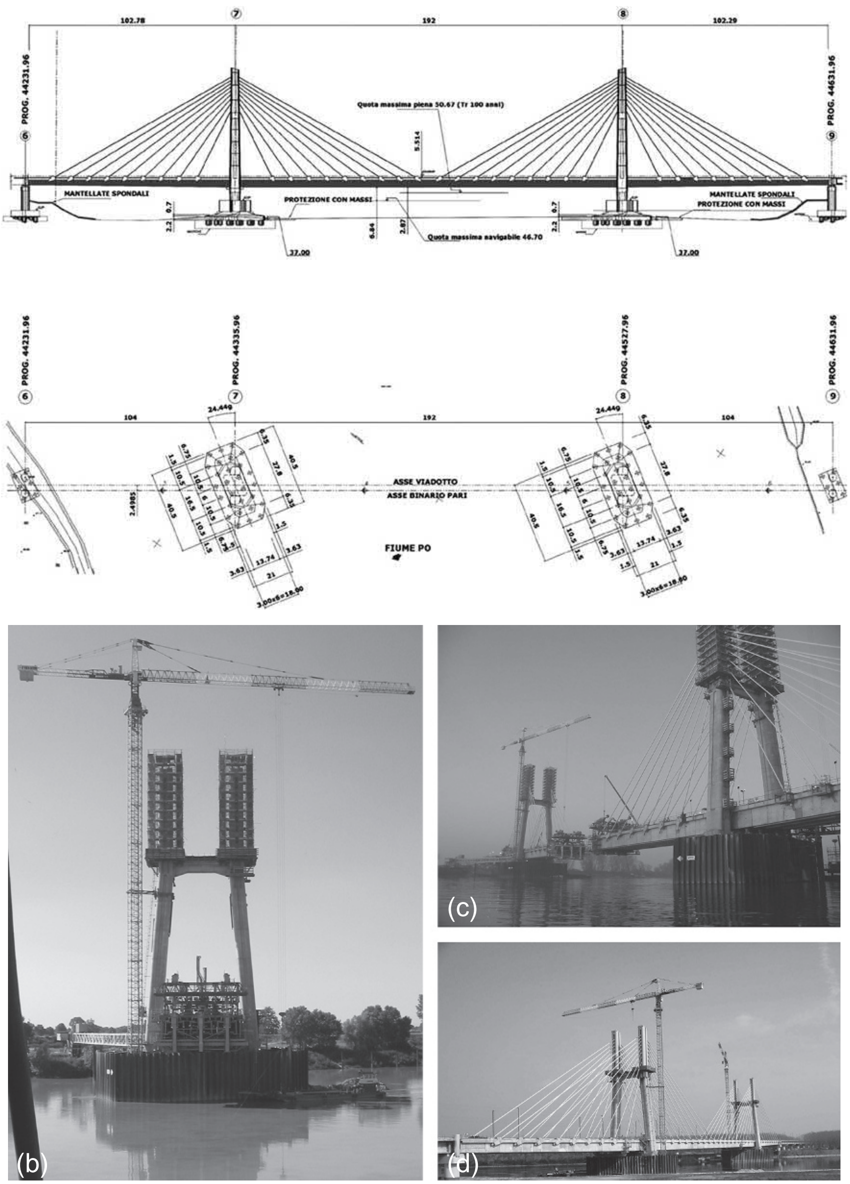

Figure 20.9 The recent bridge over the Po River, for the HSL Milano-Bologna: (a) plant and elevation scheme; (b) north side antenna; (c) entire bridge view during the yard; (d) final phase of the bridge yard.

Modena (2010), the structural analysis and fatigue reliability assessment of the Paderno Bridge, a mixed road and railway bridge with a significant cultural heritage value, is presented, and in Pipinato et al. (2009), the high-cycle fatigue behavior of riveted connections for railway metal bridges is analyzed. In addition, in Pipinato et al. (2011a), real-scale tests are presented dealing with the fatigue behavior on riveted steel elements taken from a railway bridge. It is useful to cite Pipinato et al. (2011b) as well, as in this study, the fatigue assessment of highway steel bridges in the presence of seismic loading is presented as an assessment approach that could be useful for railway bridges; a similar approach, including on-site dynamic testing, was applied in Pipinato et al. (2012a) for the assessment procedure and rehabilitation criteria for the riveted railway Adige Bridge. Dealing with retrofit procedures, in Pipinato et al. (2012b), the fatigue behavior of steel bridge joints strengthened with FRP laminates is presented, and finally, an analytical approach, including dynamic analysis applied in historic riveted steel bridges, is presented in Pipinato (2014). Other research includes Lin et al. (2014a), who investigated the rehabilitation and restoration of old steel railway bridges; Lin et al. (2014b), who deepened the preventive maintenance on welded connection joints in aged steel railway bridges; and Stamatopoulos (2013), who studied the fatigue assessment and strengthening measures to upgrade a steel railway bridge. Finally, a research project carried out in Europe, called Sustainable Bridges (Bień et al., 2008), has investigated a wide variety of problems dealing with existing bridges—analyzing nondestructive testing technologies, testing new intervention methodologies on-site, and performing much analysis on retrofit issues dealing with existing bridges in Europe.

References

Ahmad, F.S., Gilles, F., Le Roy, R., 2011. Bond between carbon fibre-reinforced polymer (CFRP) bars and ultra-high performance fibre-reinforced concrete (UHPFRC): experimental study. Constr. Build. Mater. 25 (2), 479–485.

American Railway Engineering and Maintenance-of-Way Association (AREMA), 2013. Practical Guide to Railway Engineering. AREMA, Lanham, MD.

American Railway Engineering and Maintenance-of-Way Association (AREMA), 2014. Manual for Railway Engineering. AREMA, Lanham, MD.

Bień, J., Elfgren, L., Olofsson, J., 2008. Sustainable bridges: Assessment for future traffic demands and longer lives. In: Research Project TIP3-CT-2003-001653 within the Sixth Framework Programme. European Commission, Bruxelles.

Britannica, 1910. The Encyclopædia Britannica: A Dictionary of Arts, Sciences, Literature and General Information, eleventh ed. vol. IV Edited by The Encyclopædia Britannica Company, New York, pp. 539–540.

Brühwiler, E., Denarié, E., 2013. Rehabilitation and strengthening of concrete structures using ultra-high performance fiber reinforced concrete. Struct. Eng. Int. 23 (4), 450–457. Iabse Edition, Zurich, ISSN: 1016-8664. ISSN: 1016-8664.

California High-Speed Railway Authority (CHSRA), 2011. Technical memorandum: structure design loads TM 2.3.2. California high-speed train project. California High-Speed Railway Authority, Sacramento, CA.

Doménech, A., Museros, P., Martínez-Rodrigo, M.D., 2014. Influence of the vehicle model on the prediction of the maximum bending response of simply-supported bridges under high-speed railway traffic. Eng. Struct. 72, 123–139.

EN 1990, 2006. Basis of Structural Design. CEN, Bruxelles.

EN 1991-2, 2005. Actions on structures. Part 2: Traffic loads on bridges. CEN, Bruxelles.

EN 1992-1-1, 2004. Eurocode 3: Design of Concrete Structures—Part 1-1: General Rules. CEN, Bruxelles.

EN 1993-1-1, 2014. Eurocode 3: Design of Steel Structures—Part 1-1: General Rules. CEN, Bruxelles.

EN 1993-1-9, 2005. Eurocode 3: Design of steel structures. Part 1–9: Fatigue. CEN, Bruxelles.
EN 1993-2, 2005. Eurocode 3: Design of steel structures. Part 2: Steel Bridges. CEN, Bruxelles.
EN 1997, 2007. Geotechnical design. CEN, Bruxelles.
EN 1997-2, 2007. Eurocode 7—Geotechnical Design—Part 2: Ground Investigation and Testing. CEN, Bruxelles.
Guo, Y.H., Wang, Z.Q., 2012. Proposed calculation formula of shear connectors in UHPFRC-NSC composite structure. Appl. Mech. Mater. 166-169, 2851–2854. TTP, 05/2012.
Hirt, M.A., Leben, J.P., 2013. Steel Bridges. Conceptual and Structural Design of Steel and Steel—Concrete Composite Bridges. EPFL Press, Lausanne, Switzerland.
Johansson, C., Nualláin, N.Á., Pacoste, C., Andersson, A., 2014. A methodology for the preliminary assessment of existing railway bridges for high-speed traffic. Eng. Struct. 58, 5–35.
Lin, W., Yoda, T., Taniguchi, N., 2014a. Rehabilitation and restoration of old steel railway bridges: laboratory experiment and field test. J. Bridg. Eng. 19 (5). Technical paper n. 04014004.
Lin, W., Yoda, T., Taniguchi, N., Shinya, K., 2014b. Preventive maintenance on welded connection joints in aged steel railway bridges. J. Constr. Steel Res. 92, 46–54.
Pipinato, A., 2010. Step level procedure for remaining fatigue life evaluation of one railway bridge. Baltic J. Road Bridge Eng. 5 (1), 28–37.
Pipinato, A., 2011. Assessment of existing bridges: safety and security issues [Problemi di sicurezza nelle valutazioni strutturali di ponti esistenti]. Ingegneria Ferroviaria 66 (4), 355–371. in (Italian).
Pipinato, A., 2014. Residual life of historic riveted steel bridges: an analytical approach. Journal of ICE - Bridge Eng. 167 (1), 17–32. https://doi.org/10.1680/bren.11.00014. Institution of Civil Engineers, Thomas Telford Ltd, London, ISSN: 1478–4637.
Pipinato, A., Modena, C., 2010. Structural analysis and fatigue reliability assessment of the Paderno bridge. Prac. Period. Struct. Des. Construct. 15 (2), 109–124.
Pipinato, A., Pellegrino, C., Bursi, O.S., Modena, C., 2009. High-cycle fatigue behavior of riveted connections for railway metal bridges. J. Constr. Steel Res. 65 (12), 2167–2175.
Pipinato, A., Molinari, M., Pellegrino, C., Bursi, O.S., Modena, C., 2011a. Fatigue tests on riveted steel elements taken from a railway bridge. Struct. Infrastruct. Eng. 7 (12), 907–920.
Pipinato, A., Pellegrino, C., Modena, C., 2011b. Fatigue assessment of highway steel bridges in presence of seismic loading. Eng. Struct. 33 (1), 202–209.
Pipinato, A., Pellegrino, C., Modena, C., 2012a. Assessment procedure and rehabilitation criteria for the riveted railway Adige bridge. Struct. Infrastruct. Eng. 8 (8), 747–764.
Pipinato, A., Pellegrino, C., Modena, C., 2012b. Fatigue behavior of steel bridge joints strengthened with FRP laminates. Mod. Appl. Sci. 6 (9), 1–14.
Stamatopoulos, G.N., 2013. Fatigue assessment and strengthening measures to upgrade a steel railway bridge. J. Constr. Steel Res. 80, 346–354.
Toutlemonde, F., Renaud, J.-C., Lauvin, L., Brisard, S., Resplendino, J., 2007. Local bending tests and punching failure of a ribbed UHPFRC bridge deck. In: Proc. 6th Intl. Conf. Fracture Mech. of concrete and concrete Struct. FRAMCOS 6, Catania, pp. 1481–1489.
Vega, J., Fraile, A., Alarcon, E., Hermanns, L., 2012. Dynamic response of underpasses for high- speed train lines. J. Sound Vib. 331 (23), 5125–5140.
Xu, J.H., Wang, B., Wang, L., Wang, P., 2014. Evaluation of track geometry on a long span steel trussed cable-stayed bridge. Appl. Mech. Mater. 501–504, 1403–1407. TTP edition, Dürnten.

Further reading

EN 1993-1-10, 2005. Eurocode 3: Design of Steel Structures—Part 1-10: Material Toughness and Through-Thickness Properties. CEN, Bruxelles.

EN 1993-1-2, 2003. Design of steel structures. Part 1–2: General Rules—Structural Fire Design. CEN, Bruxelles.

Lamine, D., Pierre, M., Gomesb, F., Tessiera, C., Toutlemondec, F., 2013. Use of UHPFRC overlay to reduce stresses in orthotropic steel decks. J. Constr. Steel Res. 89, 30–41.

Pipinato, A., 2012. Coupled safety assessment of cable stay bridges. Mod. Appl. Sci. 6 (7), 64.

Footbridges

21

Alessio Pipinato
AP&P, CEO and Technical Director, Rovigo, Italy

1. Introduction

In this chapter, footbridge design is presented. Wherever footpaths or cycling paths are interrupted by a physical obstacle, footbridges are needed to cross the obstacles. Lighter loads are carried by these structures when compared to highways and railroads. Consequently, lighter and more slender structures are required. However, short-, medium-,and in some cases long-span structures are needs. This requires a careful analysis of the vibration imposed by human loads and wind loads, so stiffness becomes a relevant consideration. At the same time, as footbridges are inserted into the urban context, pleasant and attractive architectural forms are required. Requirements of footbridges include a clear span, simply supported unique structures, and height sufficient to cross over urban obstacles. Footbridges also must be accessible to wheelchairs and cyclists, so a ramps are designed with restricted gradient. These ramps need to be long enough to carry the foot traffic from the road level onto the footpath level. However, the length of such ramps may need to be reduced for river footbridges, depending on the specific orographic context. Particular attention should be given to the architectural of the ramp structure, which can influence the final shape of the entire bridge. The width depends on the traffic that the bridge carries. If only a footpath is required, 2 m clear width is often sufficient to permit the free passage of two pedestrians; however, if a cycle path is required, a wider passage should be considered, depending on the specific code and standard adopted for the cycle path design.

2. Conceptual design

A safe access onto the footbridge should be the first concern: The width and form of and access should be designed according to the client indications, including at minimum the type and consistency of traffic to be carried (whether the bridge is open pedestrians only, or also accessible to cyclists, wheelchairs, etc.). As previously mentioned, a minimum clear of 2 m should be considered, and this should be increased to 4 m if cyclists and pedestrians use the footbridge simultaneously. These different use needs to be adequately and signaled and clearly marked with a separation line, colors, a smooth curb, or railings. At the edge of the path, two parapets must be installed at a minimum height of 1.15 m, and up to 2.2 m if a railway line or a dangerous obstacle stands under the footbridge. In recent years, high parapets have also been installed on

Innovative Bridge Design Handbook. https://doi.org/10.1016/B978-0-12-823550-8.00013-5

highway passages to prevent vandalism. Required dimensions for footbridges are reported in the section of this chapter devoted to codes and standards. When designing drainage systems the presence or absence of a curb should be considered in order to ensure adequate deck draining to prevent hazards to the public. The span may or may not be aligned with the crossed obstacle, depending on the footpath's content within its environment. The clear span dimensions are derived from the sum of the obstacle width and the planimetric clearance (4 m or more from the edge of the pathway) to avoid danger in case of derailed trains and errant vehicles, considering that, due to the reduced load carried, piers are designed with smaller dimensions compared to road or railway bridge elevations and consequently provide reduced protection from such dangers. Height clearance has must consider the codes and standards governing the surpassed obstacle, which normally specify around 5 m or more of clearance. Concerning footbridge elevation, a minimum vertical camber is suggested in order to maintain drainage of the footbridge to the ends, where the runoff can be carried directly to the ground and not upon the obstacle surpassed. Where needed, stairs and ramps should be designed according to national rules and standards not included in structural design codes. Finally, service lines should be adequately designed so that maintenance can easily be performed without service disruption.

3. Construction

Most footbridges up to spans of about 45 m can be prefabricated as a complete length of the span and then transported. Although fabrications greater than a specific length (e.g., greater than 16.5 m in Italy) require special permission to travel on public highways, most fabricators prefer to prefabricate the structure whenever possible and are familiar with necessary arrangements to transport long lengths (SC, 2021). Some examples of footbridge launched as complete or partial structures are the following: In Figure 21.1, the complete Derby Footbridge was lifted on-site in 2020 (192 t); in Figure 21.2, one segment of the Greystone Road Footbridge over the M62 was lifted on-site in 2015; in Figure 21.3, one segment of the footbridge in Bremerhaven was lifted onsite in 2009.

4. Footbridge types

4.1 Type selection

Depending on the span to be covered and the obstacle to be surpassed, girder or truss bridges are the most suitable and economic solutions for small to medium spans of up to 60 m; however, when the span is greater than 60 m and the height of the deck is a design input for nearest constraints, arches are mainly adopted. Alternatively, suspended or cable-stayed construction can be employed in spans greater than 50 m and 80 m, respectively. A summary of various bridge types suitable for approximate span ranges is given in Table 21.1.

Figure 21.1 Derby footbridge lifted on-site in 2020.

Figure 21.2 Greystone Road Footbridge over the M62 lifted on-site in 2015.

4.2 Truss and girders

While the Warren truss and modified Warren truss are generally used for footbridges (see Chapter X for a complete analysis of truss types), a Pratt truss occasionally may be used. The Vierendeel solution used as a spatial girder has no diagonal members that

Figure 21.3 Footbridge in Bremerhaven lifted on-site in 2009.

Table 21.1 Span Ranges for Different Types of Footbridge

Construction Type	Span Range (m)
Truss	15–60
Vierendeel girder	15–45
Twin steel girders	10–25
Steel girders + steel floor plate	10–30
Steel box girder	20–60
Composite beams	10–50
Arches	25 and greater
Cable-stayed bridge	50 and greater
Suspension bridge	80 and greater

would carry loads combining axial loading and bending, so this solution is appropriate only for small-span footbridges. Coupled girders—connected in the lower flange as a small, open box section—are increasingly used for steel girders with a steel or a composite deck. This is the most economical solution for bridging obstacles spanning up to 25 m; for obstacles spanning longer lengths, girder solutions of variable heights can be adopted.

Examples of truss and girder footbridges include the following. Figure 21.4 depicts the Saint-Omer footbridge, standing with a girder solution enriched with a plated external skin. Variations of the girder solution can lead to elegant bridge aesthetics,

Figure 21.4 Saint-Omer Footbridge.

Figure 21.5 Technion University Entrance Bridge.

such as he Technion University entrance depicted in Figure 21.5. A rare lightweight and attractive solution is the Millénaire structure in Paris, presented in Figures 21.6 and 21.7, where the bridge shaped a new urban park. Figure 21.8 depicts the Saint-Omer Footbridge which was completed in a single launch. Truss footbridges are well represented in many locations, as they provide a very economical solution up to

Figure 21.6 The Millénaire Footbridge in Paris, erection phase.

Figure 21.7 The Millénaire Footbridge in Paris, lateral view.

medium-span obstacles. Figure 21.9 shows the Vakwerkbrug Simon Vestdijkpark Footbridge, covering a narrow river spanning 17 m. Figure 21.10 shows the Disneyland access pedestrian bridge, covering a span of 40 m. Trusses can also help to overpass large obstacles, as in the case of Milan Expo Footbridge, crossing the four-plus-four-lane A8 Highway (Figure 21.11).

Figure 21.8 The Saint-Omer Footbridge.

Figure 21.9 The Vakwerkbrug Simon Vestdijkpark Footbridge.

4.3 Arches

Arched structures for footbridge increase the options for small- to medium-span structures, conferring an elegant and pleasing shape to footbridges. There are many relevant worldwide, with a large amount using steel arches, which stand as urban landmarks. Arches are also designed with various inclined configurations, in particular for curved plan situations (e.g., see Figure 21.12, the Zubizuri Footbridge in Bilbao). However, arches structures are normally employed as straight bridges, such as in the Rhine Bridge (Figure 21.13), the Chiswick Park structure (Figure 21.14), and the Humber Bay Bridge in Toronto (Figure 21.15).

Figure 21.10 The Disneyland pedestrian bridge access.

Figure 21.11 The Milan Expo Footbridge access.

Figure 21.12 The Zubizuri Footbridge in Bilbao.

Figure 21.13 The Rhine Bridge.

Figure 21.14 The Chiswick Park Footbridge.

Figure 21.15 The Humber Bay Bridge in Toronto.

4.4 Cable-stayed and suspension footbridges

Large-span structures can also be adopted for footbridges, where the term "large" in terms of obstacle covered is quite different when compared to the rail or road bridges. In footbridges, in fact, the structures adopted to carry light loads such as pedestrians and cyclists introduce difficulties of the dynamic behavior of the bridge in wind and seismic loads. However, light and also complicated geometric solutions can be realized in footbridges today, such as in the Bob Kerry Pedestrian Bridge (Figure 21.16), the Trinity structure (Figure 21.17), or the Delta Footbridge (Figure 21.18), all located in Omaha, Nebraska.

Figure 21.16 The Bob Kerry Pedestrian Bridge in Omaha.

Figure 21.17 The Trinity Bridge in Omaha.

Figure 21.18 The Delta Footbridge in Omaha.

4.5 Spatial structures

Spatial structures with uncommon engineering solutions to achieve the minimal stiffness and strength necessary to ensure footbridge safety use of steel or steel composite material in ways not defined as precise classical solutions. Examples of such structures include the Oberhausen Bridge (stress ribbon bridge 20–66-20 m span, for an overall length of 406 m, Figure 21.19), the High-Tech Park Bridge (Figure 21.20), and the Calgary Peace Bridge (Figure 21.21).

5. Codes, standards, and literature

For the design of steel and composite footbridges in Europe and related countries, the following sections of Eurocodes are applicable: EN 1990 Eurocode, EN 1991 Eurocode 1: Actions on Structures; EN 1992 Eurocode 2: Design of Concrete Structures; EN 1993 Eurocode 3: Design of Steel Structures; and EN 1994 Eurocode 4: Design of Composite Steel and Concrete Structures. BS (2006) deals with the permissible vibrations for footbridges and cycle track bridges. In the USA, LRFD Guide Specifications for Design of Pedestrian Bridges (2009) is available. Guidelines are also available for specific situations:

- For concrete footbridges, FIB (2005) has prepared a guide for best practices.
- For vibration control in footbridges, EU (2010) has sponsored research on the human-induced vibration of steel structures.

Also pertaining to vibration control in footbridges, SETRA (2006) has improved the assessment of vibrational behavior of footbridges under pedestrian loading.

Figure 21.19 The Oberhausen Bridge.

Figure 21.20 The High-Tech Park Bridge.

Figure 21.21 The Calgary Peace Bridge.

References

BS, 2006. Permissible Vibrations for Footbridges and Cycle Track Bridges. BS 5400 - Appendix C.

EU, 2010. Human-Induced Vibration of Steel Structures (Hivoss). ISSN 1018-5593, ISBN 978-92-79-14146-1, https://doi.org/10.2777/79056.

FIB, 2005. Guidelines for the Design of Footbridges. Guide to Good Practice. (160 pages, ISBN 978-2-88394-072-7, November 2005).

SC, 2021. Design of Steel Footbridges. Steel Construction Institute, Silwood Park, Ascot, UK.

SETRA, 2006. Footbridges Assessment of Vibrational Behavior of Footbridges under Pedestrian Loading.

Part VII

Bridge components

This page intentionally left blank

Seismic component devices

22

A.K. Agrawal[a], *M. Amjadian*[b]
[a]Department of Civil Engineering, The City College of the City University of New York, New York, NY, USA, [b]Department of Civil Engineering, The University of Texas Rio Grande Valley, Edinburg, TX, USA

1. Introduction

Seismic component devices are innovative structural elements designed to protect bridges during extreme hazards, such as earthquakes, by absorbing or dissipating input external energy. Two of the most commonly used seismic component devices are seismic isolators and dampers. Performance of these devices have been demonstrated through numerous studies, including several large-scale tests (Kelly et al., 1986; Constantinou and Symans, 1992; Yang et al., 2002, 2004; Phillips et al., 2010; Zhou et al., 2020) and theoretical research studies (Spencer et al., 1997; Dyke et al., 2003; Agrawal and Nagarajaiah, 2009; Agrawal et al., 2009; Tan and Agrawal, 2009; Nagarajaiah et al., 2009; Clemente, 2017; Makris, 2019). These devices protect the structural safety and stability of bridges by modifying their dynamic characteristics, such as their natural period, damping, or energy dissipation behavior. Bridges with these devices are designed such that damage during earthquakes and other hazards is localized in these devices, thereby protecting key structural members, such as piers. This chapter presents a brief overview of different types of seismic isolators and dampers used widely around the world to enhance seismic behavior of bridges. The standard methods employed for the analysis and design of seismic component devices in bridges are discussed, and applications of these devices are presented.

2. Seismic protective devices

2.1 Seismic isolators

Seismic isolators, such as elastomeric or sliding bearings, reduce seismic demand on key structural members of bridges, such as piers, during an earthquake. In bridges, piers are subjected to considerable shear force and flexural and torsional moments during an earthquake because of a large mass concentrated in the deck. Seismic isolators are typically installed between the deck and piers or deck and abutments (as illustrated in Figure 22.1) to decouple the movement of the superstructure (deck) from the substructure (piers). The fundamental objective of seismic isolation is to elongate the natural period of a bridge beyond the predominant period of ground motions. Figure 22.2

Innovative Bridge Design Handbook. https://doi.org/10.1016/B978-0-12-823550-8.00027-5

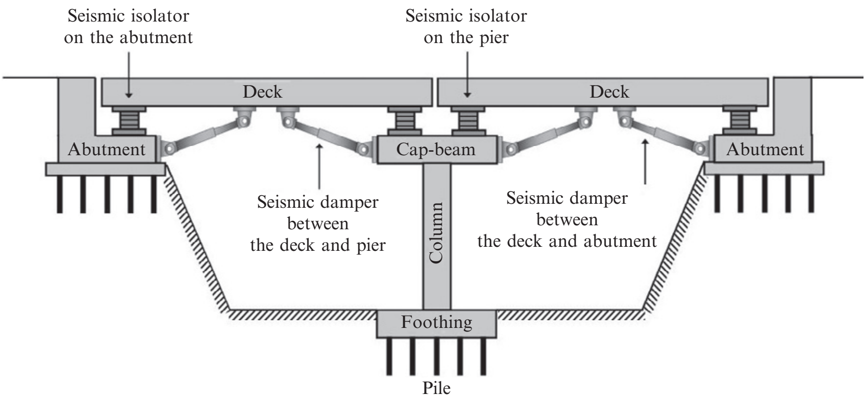

Figure 22.1 Placement of seismic protective systems in a typical two-span highway bridge (not drawn to scale).

Figure 22.2 Influence of period shift and damping increase on acceleration and displacement of an isolated bridge: (a) acceleration response spectrum; (b) displacement response spectrum.

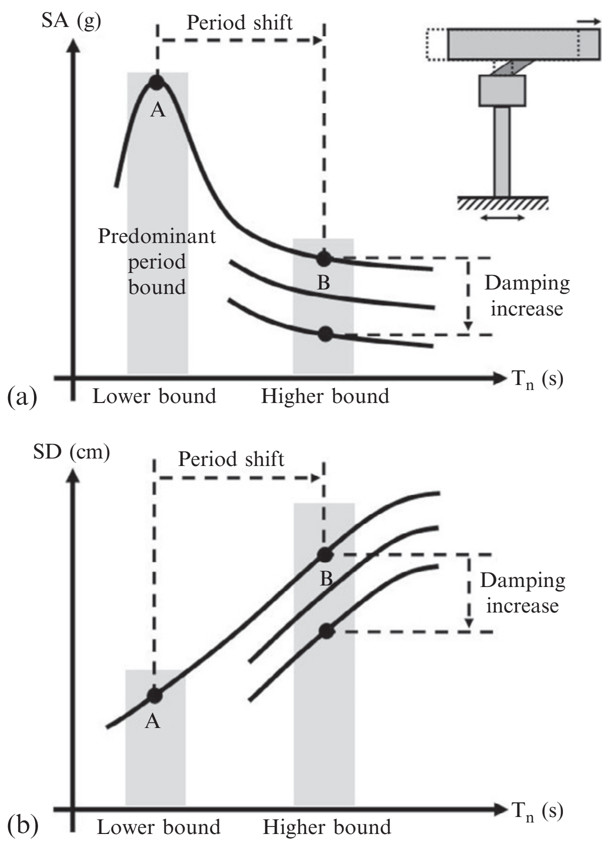

shows typical acceleration and displacement response spectra for structures. For a bridge with its period at point A in Figure 22.2, the period of the bridge with seismic isolation will be lengthened to B, resulting in significant reduction in spectral acceleration, as seen from Figure 22.2a. However, the spectral displacement of the isolated bridge may increase significantly, as illustrated in Figure 22.2b. The displacement of the isolated deck can be reduced further by increasing damping through supplemental devices, such as energy-dissipating lead core in bearings, friction in bearings, or dampers parallel with bearings. Figure 22.1 illustrates the installation of dampers parallel with bearings.

Seismic isolation has not been found to be efficient for flexible bridges whose natural periods are longer than predominant periods of earthquakes (Kunde and Jangid, 2006; He et al., 2020). The flexibility of bridges can be attributed to a flexible substructure (e.g., high-elevation piers), superstructure (e.g., elastic slender deck), or soft soil surrounding the piers (Tongaonkar and Jangid, 2003; Soneji and Jangid, 2008; Stehmeyer and Rizos, 2008; Dezi et al., 2012).

Seismic isolation of bridges near regions prone to fault ruptures is also not efficient because of the presence of long pulses in seismic waves that are destructive for flexible structures (Shen et al., 2004; He and Agrawal, 2008; Losanno et al., 2017). For serviceability, seismic isolators should have self-centering properties so that the deck can return to its original position after an earthquake.

2.1.1 Theoretical concept of seismic isolation in bridges

The theoretical concept of seismic isolation is illustrated for the lateral response of an isolated highway bridge using an idealized 2-DOF (degrees of freedom) model, as shown in Figure 22.3. It is assumed that the isolation system behaves linearly, and columns also remain elastic during the ground motion excitation.

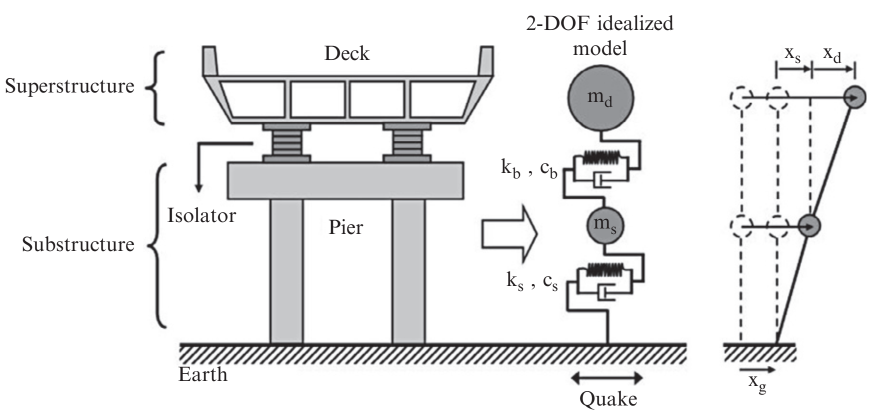

Figure 22.3 Simulation of lateral motion of an isolated highway bridge.

The equation of motion based on relative displacement of superstructure and substructure can be written as

$$\begin{bmatrix} m_d & m_d \\ m_d & m_d+m_s \end{bmatrix}\begin{Bmatrix} \ddot{x}_d \\ \ddot{x}_s \end{Bmatrix}+\begin{bmatrix} c_b & 0 \\ 0 & c_s \end{bmatrix}\begin{Bmatrix} \dot{x}_d \\ \dot{x}_s \end{Bmatrix}+\begin{bmatrix} k_b & 0 \\ 0 & k_s \end{bmatrix}\begin{Bmatrix} x_d \\ x_s \end{Bmatrix}$$
$$=-\begin{bmatrix} m_d & m_d \\ m_d & m_d+m_s \end{bmatrix}\begin{Bmatrix} 0 \\ 1 \end{Bmatrix}\ddot{x}_g, \tag{1}$$

where x_d is the relative displacement of the deck with respect to the top of the pier, x_s is the relative displacement of the top of the pier with respect to the ground, $\ddot{x}_g$ is the ground acceleration, m_d is the mass of the superstructure, m_s is the mass of the substructure, k_b and c_b are the effective stiffness and damping coefficients of the isolation system, and k_s and c_s are the stiffness and damping coefficients of the substructure. We define following parameters to further simplify Eq. (1):

$$\gamma=\frac{m_d}{m_d+m_s},\quad \omega_b=\sqrt{\frac{k_b}{m_d}}=\frac{c_b}{2\xi_b m_d},\quad \omega_s=\sqrt{\frac{k_s}{m_d+m_s}}=\frac{c_s}{2\xi_s(m_d+m_s)}, \tag{2}$$

where γ is the ratio of mass of superstructure to the total mass of the bridge ($\gamma \approx 0.85$–0.95), ω_b is the natural frequency of the isolation system, ω_s is the natural frequency of the bridge before isolation, ξ_b is the critical damping ratio of the isolation system, and ξ_s is the critical damping ratio of the bridge before isolation. Using Eqs. (1) and (2), ratios of natural periods of the bridge with and without isolation can be calculated as

$$\frac{T_1}{T_s}=\sqrt{\frac{2(1-\gamma)}{1+\varepsilon-\sqrt{(1-\varepsilon)^2+4\gamma\varepsilon}}},\quad \frac{T_2}{T_s}=\sqrt{\frac{2(1-\gamma)}{1+\varepsilon+\sqrt{(1-\varepsilon)^2+4\gamma\varepsilon}}}, \tag{3}$$

in which ε is defined as the square of the ratio of the natural frequency of the isolation system to the natural frequency of the bridge before isolation [i.e., $\varepsilon=(\omega_b/\omega_s)^2=k_b/\gamma k_s$], which takes a small value between 0.01 and 0.1. Assuming a first-order approximation for small values of ε, the modal vectors and modal participation factors for the isolated bridge are obtained as

$$\phi_1 \approx \begin{Bmatrix} 1 \\ \gamma\varepsilon \end{Bmatrix}\ \Gamma_1 \approx \frac{1+\gamma\varepsilon}{1+(1+\gamma^2)\varepsilon+\gamma^2\varepsilon^2},\quad \phi_2 \approx \begin{Bmatrix} 1 \\ (1-\gamma)\varepsilon-1 \end{Bmatrix}$$
$$\Gamma_2 \approx \frac{\varepsilon}{1-(1-\gamma)\varepsilon+(1-\gamma)\varepsilon^2}. \tag{4}$$

The contribution of a mode to seismic response of a bridge in a given direction can be demonstrated by modal participation factor (Carr, 1994). Figure 22.4 displays the natural periods, mode shapes, and modal participation factors of the isolated bridge versus ε. It is observed from Figure 22.4a that the isolated bridge vibrates predominantly in the first mode for the values of ε in the range of 0.01–0.1. For this range of ε, the ratio of T_1/T_s varies from 10 to approximately 3.5. On the other hand, the ratio of T_2/T_s is generally less than 1.0. Since the first mode is significantly more

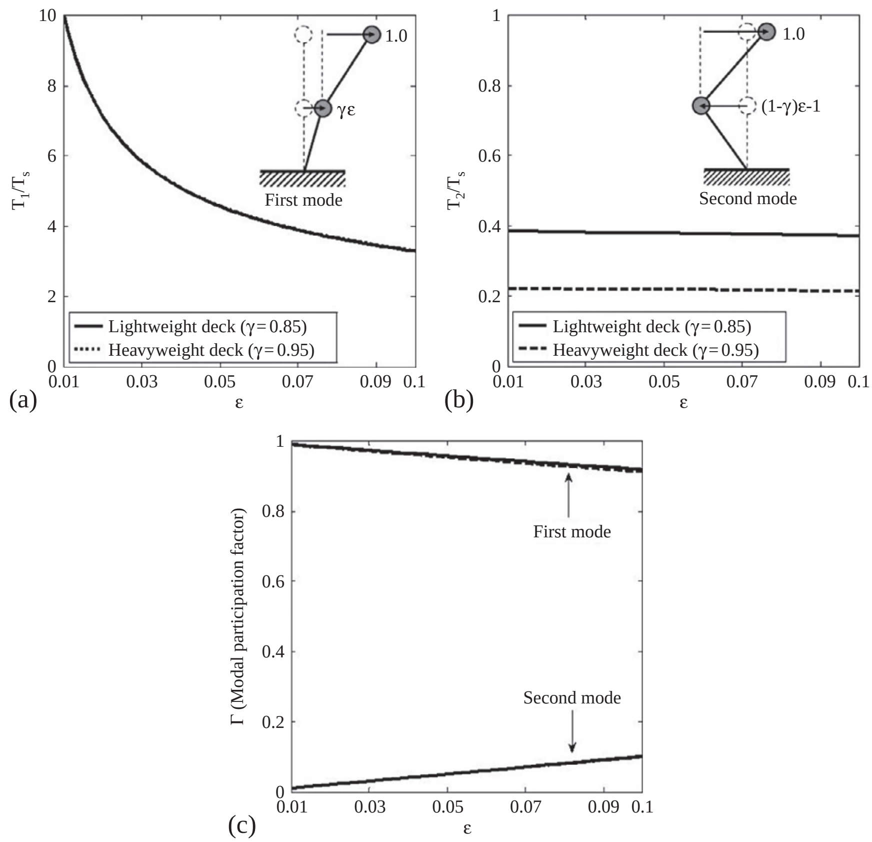

Figure 22.4 Influence of seismic isolation on dynamic characteristics of a conventional bridge: (a, b) first and second natural periods and mode shapes; (c) modal participation factor.

flexible (having a longer period) than the second mode, the bridge deck vibrates predominantly in this mode. The spectral acceleration of the bridge deck decreases drastically because of lengthening of the natural period of the first mode of the isolated bridge, compared to the relatively shorter natural period of the bridge without isolation, as illustrated in Figure 22.2. In fact, an isolated bridge can be modeled as a single-DOF system with the natural period and damping of the first mode. Such an assumption is valid and is used by seismic guidelines to design isolated bridges in the initial phase of the design process (American Association of State Highway and Transportation Officials (AASHTO), 2010; Eurocode 8, 2005).

2.1.2 Types of seismic isolators

Seismic isolators for bridges can be generally grouped into two main classes: elastomeric and sliding (Kelly et al., 1986; Naeim and Kelly, 1999; Buckle et al., 2006; Yoshida et al., 2004; Robinson, 1982; Mokha et al., 1991). This classification is based on the way that these protective systems provide the restoring force or flexibility to the bridge.

2.1.2.1 Elastomeric-based isolators

Elastomeric-based isolators consist of alternate layers of natural or synthetic rubber (elastomer) vulcanized and bonded with steel plates to carry desired vertical loads while allowing horizontal deformations (Naeim and Kelly, 1999; Kelly and Konstantinidis, 2011; Kelly, 1997). Figure 22.5a–c shows three types of elastomeric-based isolators commonly used for bridges. The isolators are installed between the superstructure and substructure using top and bottom steel plates, as shown in Figure 22.5. Information on other types of elastomeric-based isolators

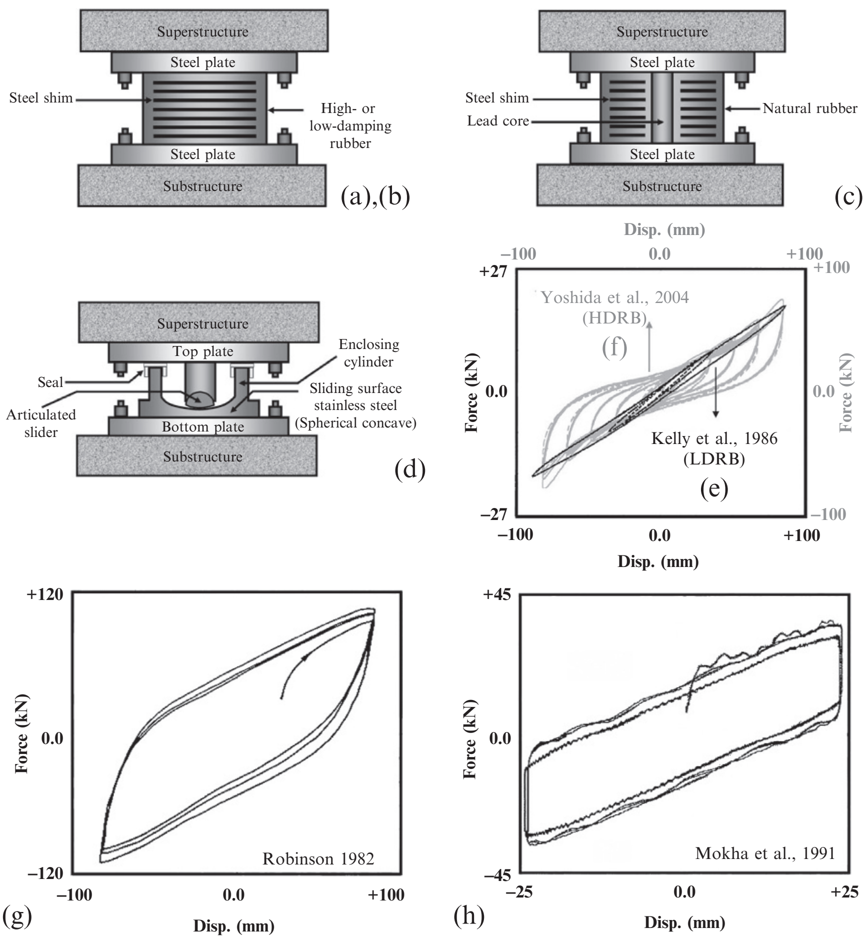

Figure 22.5 Typical seismic isolators implemented on bridges: (a) low-damping rubber bearing; (b) high-damping rubber bearing; (c) lead rubber bearing; (d) friction pendulum system and hysteretic loops; (e) Kelly et al. (1986); (f) Yoshida et al. (2004); (g) Robinson (1982); and (h) Mokha et al. (1991), respectively.

can be found in the literature (e.g., Naeim and Kelly, 1999). These isolators can be considered as efficient successors to neoprene bearings in bridges in a low-seismicity region because they can carry vertical loads and braking forces and can resist temperature variations and creep. Moreover, these bearings, unlike neoprene bearings, are less vulnerable to separation from supports during strong earthquakes (Naeim and Kelly, 1999; Buckle et al., 2006).

Low-damping rubber bearings (LDRBs), shown in Figure 22.5a, are simple to manufacture, are designed to resist creep and temperature effects, and have a small amount of damping in the range of 2% of critical damping. Their lateral force displacement behavior is predominantly linear (mostly because of elastic stiffness of rubber), as shown in Figure 22.5e (Kelly et al., 1986). Hence, a supplemental damper is often installed parallel with these isolators to provide a desired level of damping. *High-damping rubber bearings (HDRBs)* with an inherent damping ratio in the range of 10%–20% of critical damping are used to eliminate the need for supplemental dampers. Lateral force versus displacement of these isolators is nonlinear, with stiffness increasing (hardening) at large deformation, as shown in Figure 22.5f (Yoshida et al., 2004). The area under the force-displacement curve (hysteresis loop) represents the damping capacity of isolators.

The three important parameters controlling the design of rubber bearings are horizontal stiffness (K_h), vertical stiffness (K_v), and critical axial load (P_{cr}). The horizontal stiffness of the isolator system due to rubber layers is calculated as follows (Naeim and Kelly, 1999; Buckle et al., 2006; Kelly and Konstantinidis, 2011; Kelly, 1997):

$$K_h = \frac{G_r A_r}{t_r}, \tag{5}$$

where G_r is the shear modulus of rubber ($G_r \simeq 0.7\,\text{MPa}$ for rubber with average hardness), A_r is the gross area of rubber, and t_r is the total thickness of rubber. The vertical stiffness of the bearing is calculated as follows (Naeim and Kelly, 1999; Buckle et al., 2006; Kelly and Konstantinidis, 2011):

$$K_v = \frac{E_r A_s}{t_r}, \tag{6}$$

where E_r is the modulus of elasticity of rubber and A_s is the cross-sectional area of steel shims. The value of E_r for a common bearing with a circular cross section is given by (Kelly and Konstantinidis, 2011):

$$E_r = \frac{1}{\left(\frac{1}{6G_r S^2} + \frac{4}{3K}\right)}, \tag{7}$$

where S is the shape factor of a layer of rubber and K is the bulk modulus of rubber ($K \simeq 2000\,\text{MPa}$). The critical buckling load of rubber bearings with bolt-type connections in undeformed and deformed states are calculated as follows (Naeim and Kelly, 1999; Buckle et al., 2006):

$$\begin{aligned} P_{cr1} &= \sqrt{G_r A_s \frac{\pi^2 E_c I_s}{3t_r^2}} \quad \text{(Undeformed)} \\ P_{cr2} &= P_{cr1} \frac{A_{eff}}{A_s} \quad \text{(Deformed)} \end{aligned}, \tag{8}$$

where I_s is the second moment of area of A_s, and A_{eff} is the area of overlap between the top and bottom of the bearing due to maximum lateral deformation. The stability of rubber bearings, especially those with dowel-type connections, should also be checked for the rollout condition in which the rubber is subjected to tension, and its force-displacement curve suffers a decreasing slope (Naeim and Kelly, 1999; Kelly and Konstantinidis, 2011).

Lead rubber bearings (LRBs) have one or several lead cores installed at the center of the rubber layers, as shown in Figure 22.5c. The lead plug acts as a damper by dissipating input seismic energy through yielding (Robinson, 1975, 1982). The steel reinforcing plates provide confinement to the lead core and vertical stiffness to carry the vertical loads. They push the lead plug laterally to yield during a seismic event. The lead plug has a high-preyield horizontal stiffness, making it resistant against lateral movements due to nonseismic loads, such as wind, and vehicle braking force (service loads; Naeim and Kelly, 1999; Buckle et al., 2006). However, because of low-postyield stiffness, the horizontal stiffness of the isolator is predominantly contributed by rubber layers after yielding of lead core. A typical hysteresis behavior of lead rubber bearings, shown in Figure 22.5g, can be modeled by a bilinear behavior (Robinson, 1982). In order to design the areas and thickness of rubber layers, the area of the lead core should be subtracted from the rubber cross section. The yield force of lead core is given by (Buckle et al., 2006)

$$f_y = \frac{1}{R_c}\left(\frac{\pi}{4}\sigma_{yl} d_l^2\right), \tag{9}$$

where σ_{yl} is the yield stress of lead (10 MPa), d_l is diameter of lead core, and R_c is the creep load factor, which is equal to 1 for seismic loads and 2 for service loads. Figure 22.6a displays the installation of an LRB in a bridge (Dynamic Isolation Systems Company, 2006).

2.1.2.2 Sliding-based isolators

In sliding-based isolators, flexibility in the horizontal direction is provided through slippage between the support and the sliding surface, whereas restoring force is provided through geometry of the support, such as concave surface, or supplemental springs. The friction between the support and the sliding surface provides damping through the dissipation of input seismic energy by converting it to heat. Although there are different kinds of friction-based bearings [e.g., polytetrafluoroethylene (PTFE)

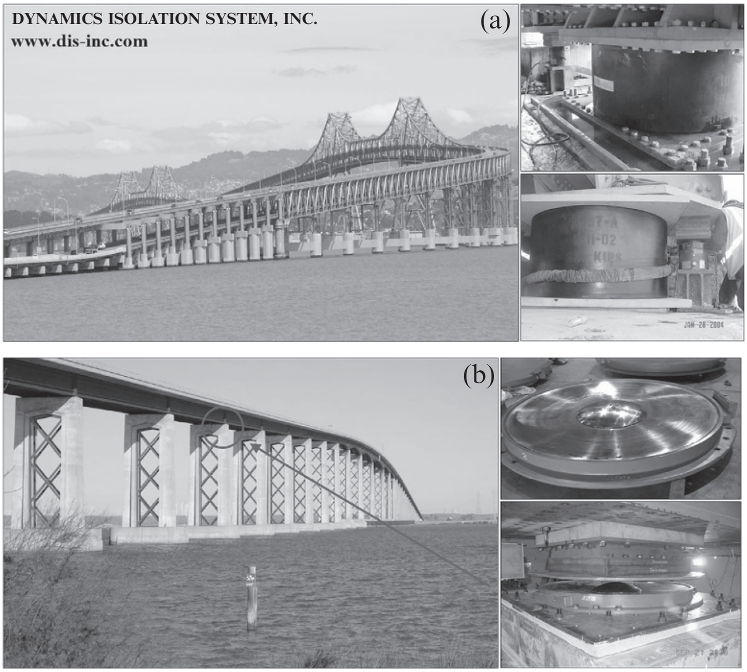

Figure 22.6 Seismic isolator full-scale implementation: (a) LRB (Richmond-San Rafael Bridge); and (b) FPS (Antioch Bridge).

spherical bearings (Constantinou et al., 2011), double (Constantinou et al., 2011; Fenz and Constantinou, 2006) and triple (Constantinou et al., 2011; Fenz and Constantinou, 2008) friction pendulum systems, and the EradiQuake isolator (Buckle et al., 2006)], friction pendulum systems (FPSs) with a single slippage surface are the most common type and have been used extensively in bridges (Mokha et al., 1991).

Figure 22.5d shows the cross section of a typical FPS used for bridges. Figure 22.6b shows the photograph of a FPS installed in a bridge. An FPS includes an articulated slider sliding on a spherical concave surface, both made of stainless steel. The surface of the articulated slider, which makes contact with the concave surface, is coated with low-friction composite materials. The curvature of the concave surface provides lateral stiffness and restoring force to the superstructure during earthquake ground excitation. These isolators are capable of carrying large axial loads in the range of large lateral displacement (Naeim and Kelly, 1999; Buckle et al., 2006).

2.1.3 Standard design method for isolation bearings

The isolated bridges are designed according to standard seismic codes such as AASHTO (American Association of State Highway and Transportation Officials (AASHTO), 2010) and Eurocode 8 (2005). These two codes support very similar methods for seismic analysis of isolated bridges. The analysis procedures used by

American Association of State Highway and Transportation Officials (AASHTO) (2010) are (i) simplified method, (ii) single mode spectral method, (iii) multimode spectral method, and (iv) time-history method. The first three methods are based on representing the nonlinear behavior of the isolated system by an equivalent elastic model with an effective natural period (T_{eff}) and damping (ξ_{eff}). The time-history method is the most accurate procedure, and it is used to analyze the isolation systems in bridges with a highly curved or skewed geometry (Kalantari and Amjadian, 2010; Amjadian and Agrawal, 2016) or bridges with a large demand of ductility ($T_{eff} > 3$; see American Association of State Highway and Transportation Officials (AASHTO), 2010) or damping [$\xi_{eff} > 50\%$, American Association of State Highway and Transportation Officials (AASHTO), 2010; or 30%, Eurocode 8, 2005; Buckle et al., 2011]. In this procedure, the bridge is analyzed using a three-dimensional (3-D) model with nonlinear isolators. A bilinear model is permitted by seismic codes (American Association of State Highway and Transportation Officials (AASHTO), 2010; Eurocode 8, 2005) to be used to simplify the hysteretic behavior of the isolator unit, as shown in Figure 22.7.

The basic principles of seismic design of isolated bridges provided by American Association of State Highway and Transportation Officials (AASHTO) (2010) and Eurocode 8 (2005) are generally similar; although it is believed that Eurocode 8 (2005) adopts a more rational design criteria in some cases such as recentering capability requirements (Constantinou et al., 2011). The design of the isolation systems of ordinary bridges according to AASHTO can be briefly described as follows. First, the effective period T_{eff} (1.5–2.5 s) and damping ξ_{eff} (20%–30%) of the isolated bridge are assumed based on the required performance. Then the simplified method is used, and the initial value of maximum displacement of the deck is calculated from the design response spectrum developed for the region in which the bridge is located. Therefore,

F^{iso}_{max} = Maximum force
F^{iso}_{y} = Yield force
Q^{iso} = Characteristic strength
D^{iso}_{max} = Maximum displacement
D^{iso}_{y} = Yield displacement
k^{iso}_{1} = Elastic (unloading) stiffness
k^{iso}_{2} = Postelastic stiffness
k^{iso}_{eff} = Effective stiffness

$$k^{iso}_1 = nk^{iso}_2$$

$$k^{iso}_{eff} = k^{iso}_2 + \frac{Q^{iso}}{D^{iso}_{max}}$$

$$Q^{iso} = (k^{iso}_1 - k^{iso}_2)D^{iso}_y$$

$$4Q^{iso}(D^{iso}_{max} - D^{iso}_y) = 2\pi k^{iso}_{eff} {D^{iso}_{max}}^2 \xi^{iso}_{eff}$$

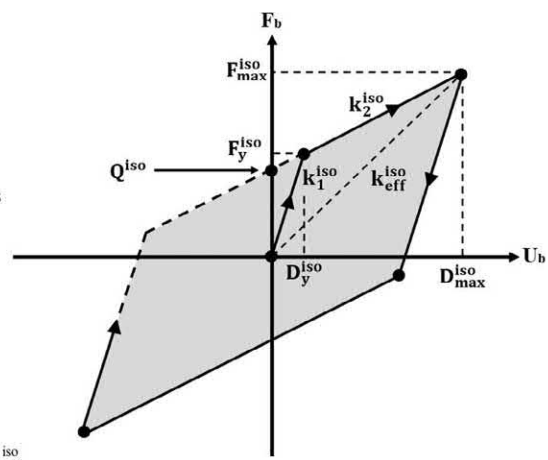

Figure 22.7 The idealized bilinear hysteretic behavior of isolation systems in American Association of State Highway and Transportation Officials (AASHTO) (2010).

initial properties of the isolators can be estimated. In the next step, the multimode spectral method is used to iteratively analyze a 3-D model of the bridge, by assuming isolators to be equivalent linear elements.

This analysis is carried out along both longitudinal and transverse directions of the model, and results are obtained. The design values of isolators are calculated by combining these results using the 30%–100% rule (Constantinou et al., 2011; Buckle et al., 2011). Then a type of isolator is selected, and its physical features are designed. For example, the dimensions of the isolator (e.g., the gross area of rubber, the thickness of steel shims, and the diameter of lead core for a lead rubber bearing) are determined in this stage (see Figure 22.5c). Finally, the design is evaluated to determine whether the seismic performance objective is satisfied; if it is not, then the design needs to be revised.

2.1.4 Dampers

Although different types of dampers have been developed for response control of structures during the last few decades, fluid viscous and friction dampers have been applied most frequently to bridges. In recent years, smart dampers, such as magnetorheological (MR) fluid dampers, have also been developed and have been applied for vibration mitigation of stay cables of cable-stayed bridges. The following is a brief description of three types of these devices.

2.1.4.1 Fluid viscous damper

Fluid viscous dampers work based on the principle of dissipation of energy due to fluid flowing through orifices. The damper consists of a stainless steel piston, a steel cylinder divided into two champers by the piston head, a compressible hydraulic fluid (silicone oil), and an accumulator for smooth fluid circulation. A typical fluid damper, manufactured by Taylor Devices, Inc., is shown in Figure 22.8 (Taylor Devices Company, 1956). In fluid viscous dampers, as the piston moves (e.g., from left to right or right to left), fluid flows from one chamber to another chamber through the orifice.

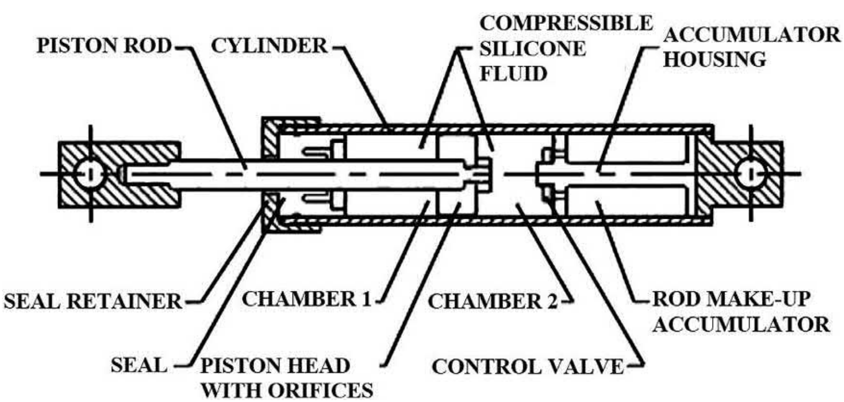

Figure 22.8 A typical fluid viscous damper manufactured by Taylor Devices, Inc.

This movement of fluid from a larger area (cylinder chamber) to a smaller area (orifice) and from a smaller area (orifice) to a larger area (cylinder chamber) results in the dissipation of energy because of head loss. Fluid viscous dampers can operate in an ambient temperature ranging from −40°C to 70°C (Constantinou and Symans, 1992).

The damping force of the damper is proportional to the pressure difference across the piston head and is expressed as a function of velocity of the piston, as follows (Constantinou and Symans, 1992; Konstantinidis et al., 2012):

$$F_d = C_\alpha \left|\dot{U}_d\right|^\alpha \operatorname{sgn}\left(\dot{U}_d\right), \tag{10}$$

where C_α is the damping ratio depending on pressure difference, $\dot{U}_d$ is the velocity of piston, sgn (.) is the sign function, and α is a constant parameter controlled by orifice shape to alter flow characteristics with fluid speed. For seismic protection, α is designed to be typically in the range of 0.3 and 1.0. For $\alpha = 1$, the viscous damper behaves as a linear device with $F_d = C_\alpha \dot{U}_\alpha$. For $\alpha < 1$, the force applied by the damper is nonlinear with velocity (Makris and Zhang, 2002). Figure 22.9a shows a photograph of four fluid viscous dampers installed between the deck and one of the abutments of a highway bridge in California (Makris and Zhang, 2002). The typical hysteresis loop of these dampers for $\alpha = 0.35$ and $\alpha = 1.00$ is shown in Figure 22.9b. Since the force applied by a viscous damper is proportional to the velocity, it is 90 degrees out of phase with displacement response of the bridge. Therefore, viscous dampers do not contribute to peak column forces at the instant when columns experience their maximum deflection during the ground motion excitation.

Viscous dampers have been found to be effective in reducing base shear on bridge piers. However, it is possible that the dampers may add some stiffness to the structure during high-frequency excitations and show viscoelastic behavior beyond the cutoff frequency (Constantinou and Symans, 1992; Reinhorn et al., 1995). In contrast to other kinds of dampers, such as viscoelastic dampers, the variation in temperature has a minor influence on the behavior of viscous dampers (Constantinou and

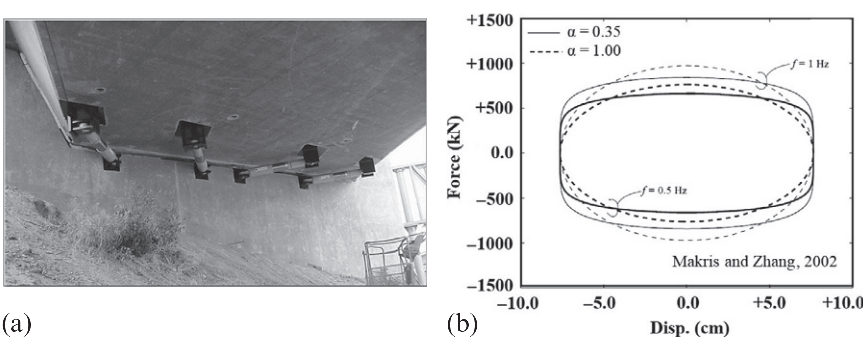

(a) (b)

Figure 22.9 Fluid viscous damper: (a) full-scale implementation (of viscous damper) on 91/5 (bridge name) overcrossing in California; and (b) typical hysteresis loop (Makris and Zhang, 2002).

Symans, 1992). On the other hand, the device needs to be maintained over a long period of operation against wear in seals to prevent oil leakage (Sadek et al., 1996).

Approaches to improving the effectiveness of viscous dampers using real-time control of orifice have been investigated by researchers worldwide. Kawashima and Unjoh (1994) have proposed a variable viscous damper to control seismic response of bridges. Neff Patten et al. (1999) tested three hydraulic actuators in semiactive mode to investigate the performance of viscous dampers in reducing traffic induced response of the Walnut Creek Bridge in Oklahoma. Feng et al. (2000) showed that viscous dampers are more effective than viscoelastic dampers in reducing the relative displacement at expansion joints of bridges with narrow seat widths to minimize the risk of deck unseating during strong earthquakes.

2.1.4.2 Friction damper

Friction dampers dissipate input seismic energy through friction between two rough sliding surfaces. Over the past few decades, many different kinds of friction dampers have been proposed to maximize the dissipation of input seismic energy in buildings and bridges (Pall and Marsh, 1982; Aiken et al., 1992, 1993; Amjadian and Agrawal, 2017, 2018). One of the most widely used friction dampers is the Pall friction device, which was originally developed for braced steel frames in buildings (Pall and Marsh, 1982). Another commonly used friction damper device is the Sumitomo damper, which was originally designed and manufactured by Sumitomo Metal Industries in Osaka, Japan, as a shock absorber in railway rolling stock (Aiken et al., 1992, 1993). It includes a piston equipped by several friction pads sliding on the inner surface of a damper cylinder. Figure 22.10a and b shows the schematics of the Sumitomo friction damper and its hysteresis loop subjected to a given base acceleration in the lab.

Many mathematical models have been proposed to simulate friction in dynamics (Olsson et al., 1998). One of the main common friction models, which is acceptable in range of engineering measurements, is the classical model of friction called the Coulomb friction model. In most friction devices, the friction force can be developed based on the Coulomb friction law with a typical rectangular hysteretic behavior, as shown in Figure 22.10b. The friction damper force based on this simple model can be characterized as

$$F_d = \mu N \,\mathrm{sgn}\left(\dot{U}_d\right), \tag{11}$$

where μ is friction ratio, N is normal reaction between two sliding surfaces, $\dot{U}_d$ is velocity of the damper, and sgn (.) is the sign function, which ensures that the damper force is applied in the direction opposing the motion. Although the behavior of friction can be modeled by a simple formula in Eq. (11), the actual dynamic behavior of a structure with frictional dampers is quite complex because of the presence of stick (no sliding) and slip (sliding) phases in the damper, depending on the slip force and earthquake ground motion characteristics (Olsson et al., 1998; Amjadian and Agrawal, 2017).

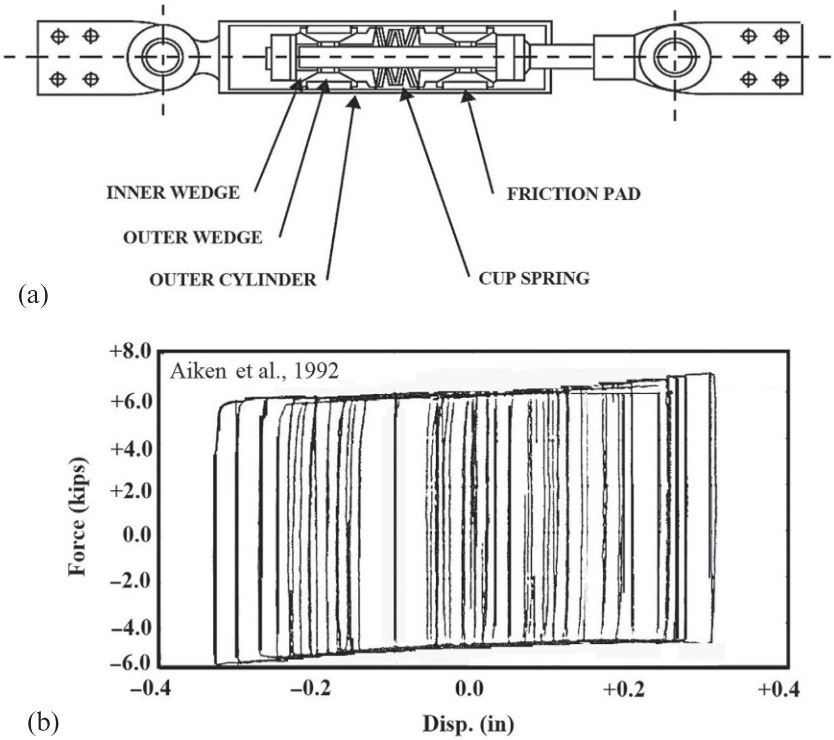

Figure 22.10 Sumitomo friction damper: (a) sectional view; and (b) typical hysteresis loop (Aiken et al., 1992, 1993).

The energy dissipated by the friction damper for a given maximum force is greater than that by the viscous damper (which has an elliptical hysteresis loop). Friction dampers are designed to have slippage beyond a certain slippage force that depends on the ground motion time history. Hence, these dampers provide added stiffness (without any dissipation) of energy during low-level wind and braking forces. Long-term reliability of sliding surfaces because of their susceptibility to corrosion and wear is one of the primary concerns in actual applications of this damper. Moreover, the normal load on the sliding interfaces cannot be reliably maintained, and some relaxation (loss of stress) may be expected over time. A passive friction may also experience permanent displacement after a strong earthquake (Sadek et al., 1996) because of a significantly higher level of slip force than the magnitude of the restoring force at the end of the earthquake.

Many researchers have investigated controllable friction dampers to address deficiencies of passive friction dampers because of slip forces (i.e., stick-slip phases or permanent displacement in the damper). Two of the most commonly investigated friction devices are piezoelectric (Madhekar and Jangid, 2011; Wieczorek et al., 2014) and electromagnetic friction dampers (Agrawal and Yang, 2000; Amjadian and Agrawal, 2019). In these devices, damper slip force can be varied based on real-time measurement of velocity and displacement across the damper to guarantee continuous slippage in the dampers (Agrawal and Yang, 2000). At the end of the earthquake, the slip force can be set to a very low value to return the damper piston to its original position.

2.1.4.3 MR dampers

MR dampers are similar in construction to fluid viscous dampers and utilize MR fluids instead of hydraulic oil. The MR fluids typically consist of micron-sized, magnetically polarizable particles dispersed in a carrier medium such as mineral or silicone oil. The particle form of fluid can be changed by the applied magnetic field, transforming the behavior of the fluid to a plastic or semisolid state in a few milliseconds because of the alignment of iron particles to the magnetic field. MR devices can change the stiffness of their fluid up to 100 Hz and can operate over a wide range of the ambient temperature, usually from −40°C to +150°C. They have a large yield shear stress routinely between 50 and 100 kPa for applied magnetic fields of 150–250 kA/m (Carlson et al., 1996). MR fluids react to external stimulus in a few milliseconds and can be readily controlled by standby batteries with a voltage in range of 12–24 V (Spencer et al., 1997). Figure 22.11 shows the operation and construction of an MR damper developed by the LORD Corporation Company (1924).

MR dampers have been investigated extensively both theoretically and experimentally, and they have several advantages over other semiactive devices. One of these is that the force of MR dampers is not fully dependent on the velocity, as is the case with variable orifice dampers (Xu et al., 2006). This fact enables significant mitigation of a broader range of seismic activity. Another merit of MR dampers is the broad range of the maximum to the minimum force; i.e., the range is much bigger than that of any other controllable damper, especially at low velocities. An MR damper has no moving parts in valves, thereby reducing maintenance and malfunction concerns. Their response time is also significantly faster than that of variable orifice dampers. An MR damper can be made in a smaller device than can a hydraulic damper, and it is also fail-safe; i.e., it operates as a passive device when the power source is disconnected for any reason (Yoshioka et al., 2002; Gavin and Dobossy, 2001).

Mathematically, the behavior of MR dampers can be modeled by a phenomenological model based on the Bouc-Wen model or a hyperbolic tangent model to capture the nonlinear force response of large-scale MR dampers over the dynamic range of interest (Spencer et al., 1997; Gavin and Dobossy, 2001; Dyke et al., 1996).

Both these models have been found to have good agreement with experimental results. The typical hysteretic behavior of an MR damper is shown in Figure 22.12.

Investigation of performance of MR dampers to bridges have been carried out primarily through theoretical studies, although MR dampers have been applied to bridges for mitigating vibration of stay cables (Chen et al., 2003). Figure 22.13 shows the first full-scale implementation of MR dampers used for this purpose in Dongting Lake Bridge, China (Chen et al., 2003). Erkus et al. (2002) have investigated the

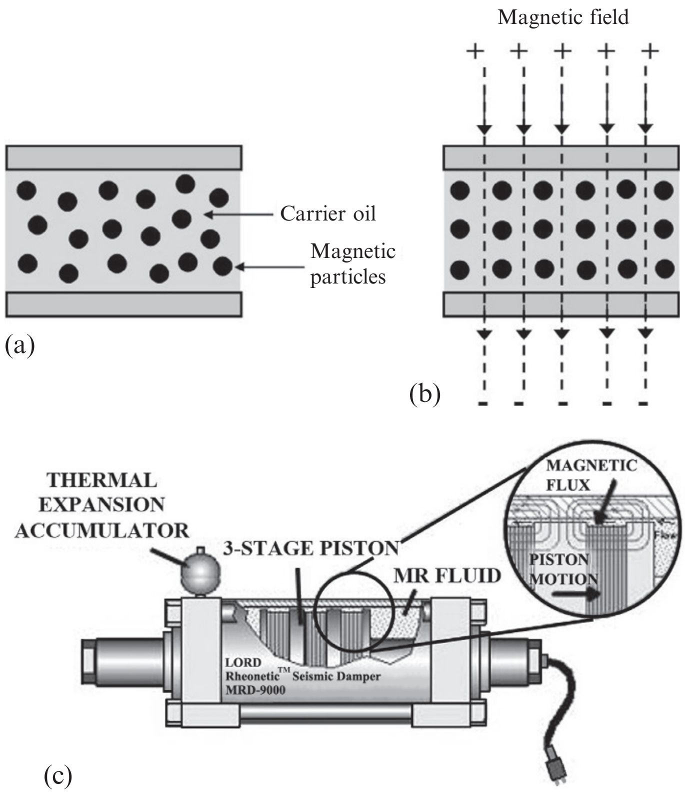

Figure 22.11 MR fluid damper: (a) randomly dispersed particles when the fluid is in its own neutral condition; (b) particle chains formation when the fluid is exposed to a magnetic field; (c) a typical seismic MR damper manufactured by the LORD Corporation.

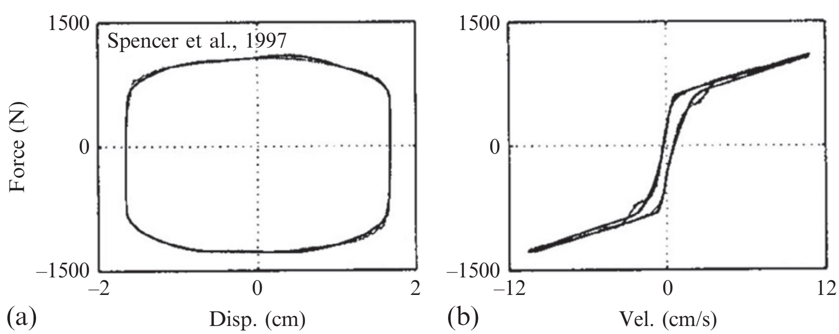

Figure 22.12 MR fluid damper hysteresis loops: (a) force displacement; and (b) force velocity (Spencer et al., 1997).

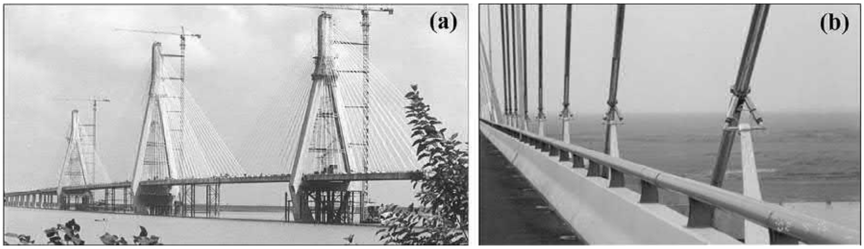

Figure 22.13 First full-scale implementation of MR dampers for mitigation vibration of stay cables: (a) Dongting Lake Bridge, China, and (b) MR damper configuration.

performance of semiactive MR dampers for reducing bearing deflection and column force using a simple bridge model. It is shown that MR dampers can perform the dissipating role of an active actuator and a passive damper to control the bridge's response, depending on the design goal. Sahasrabudhe and Nagarajaiah (2005) studied analytically and experimentally the performance of a sliding isolated bridge model equipped with a semiactive controllable MR damper subjected to near-fault earthquakes. They have shown that semiactive MR dampers can exhibit better performance in reducing bearing displacement in semiactive mode as compared to that in passive mode. Loh and Chang (2006) have applied a semiactive MR damper with different semiactive control algorithms to the American Society of Civil Engineers (ASCE) benchmark model of a cable-stayed bridge. This numerical study has shown that the MR damper is able to reduce the bridge response if it is commended by a mixed H_2 and H_1 algorithm. They have also studied the efficiency of MR dampers to control vibration of cables in the Gi-Lu cable-stayed bridge using a numerical model (Chang and Loh, 2006). Ok et al. (2007) proposed a fuzzy control technique to control the input voltage of several MR dampers implemented on the benchmark cable-stayed bridge model. Guo et al. (2009) investigated the effectiveness of MR dampers to control displacement and pounding of the deck in an experimental bridge model. Pradono et al. (2009), using the concept of negative stiffness, have proposed a control method to command an MR damper to produce larger hysteretic loops for absorbing the earthquake energy as much as possible. This algorithm was implemented on the base-isolated benchmark bridge.

Jung et al. (2009) have proposed a smart passive control system to generate the current required to launch the inner magnetic field of an MR damper without any external power supply. The system includes an electromagnetic induction (EMI) part consisting of a coil connected to the piston rod of damper exposed to a permanent magnetic field. By implementing the new passive system on the highway bridge benchmark model, they have shown that it has superior performance to the passive-optimal control system. Yang et al. (2011) proposed a new nonlinear mechanical model to simulate hysteretic behavior of MR dampers. By comparison with an experimental model simulating the vibration of a suspension bridge in its own first mode, they have shown that the numerical model is reliable and can be efficiently applied to control longitudinal seismic response of suspension bridges. Heo et al. (2014) studied the performance of a 30 kN MR damper controlled by Lyapunov and clipped-optimal control algorithms to decrease the seismic response of a scaled asymmetrical cable-stayed bridge in laboratory. The bridge was a large-scale model with 28 m length and a tower with 10.2 m height. It has been shown that the MR damper when commanded by the semiactive algorithm control can reduce the displacement of the bridge by 75% compared to the case when the MR damper is set to its passive-off mode. MR dampers have also an important role in reducing the vibration of cables in cable-stayed bridges, as demonstrated by different researchers around the world (Wang et al., 2019; Zhou et al., 2021).

3. Applications of seismic protective systems in bridges

Over the past few decades, many full-scale seismic protective systems have been implemented on bridges worldwide. These systems primarily include seismic isolators and passive fluid viscous dampers. Bridges designed or retrofitted by these devices before 2000 are well documented in the literature (Spencer and Nagarajaiah, 2003; Earthquake Engineering Research Center (EERC), 1995, 1996). Table 22.1 lists some important bridges protected by such seismic devices after the year 2000. The bridges in this table include major ones located in regions with high levels of seismic hazards.

4. Conclusions

Bridges are key elements of transportation networks in urban areas. The reduction in functionality of bridges after strong earthquakes is a matter of great concern. These infrastructures must be fully operational immediately after the disaster to lessen economic and safety impacts of earthquakes. The response of bridges to earthquakes can be controlled by installing seismic protective devices in these structures as a cost-effective method of design or retrofit.

In this chapter, a brief review of seismic protective devices, such as isolators and dampers, and their application in bridges has been given. It has been shown that seismic isolation is effective in increasing ductility of a bridge by shifting its natural period away from the predominant period of earthquake. Two main classes of isolators used in bridges are elastomeric and sliding-based bearings. The mechanisms of most common isolation systems of each class—including HDRBs, LDRBs, LRBs, and FPS—are described in detail. The capability of different types of dampers—such as fluid viscous, MR, and friction dampers—in dissipating the input seismic energy to bridges has been discussed. A list of full-scale implementation of these devices in important bridges around the world has also been presented.

Table 22.1 Full-Scale Implementation of Seismic Component Devices on Bridges Worldwide

Bridge	Location (Country, City/State)	Type	Length (m)	Seismic Component Device	Year	Notes
Marga Marga	Chile, Vinã del Mar	Composite	383	HDRB	1996	Undamaged in 2010 Maule earthquake (Sarrazin et al., 2013)
San Diego-Coronado Bay	United States, California	Steel girder	3407	Rubber bearing and viscous damper	2000	
Amolanas	Chile, Los Vilos	Steel girder	268	Sliding bearing and viscous damper	2000	
Shin-Tenno	Japan	Steel girder		Elastomer bearing	2002	Undamaged in 2011 Tohoku earthquake (Kawashima, 2012)
Benicia-Martinez	United States, California	Steel truss	1875	FPS (Earthquake Protection System, Inc.)	2003	
Hernando de Soto	United States, Tennessee	Steel girder	5950	FPS (Earthquake Protection System, Inc.)	2003	
Loureiro Viaduct	Portugal, Lisbon	Prefabricated posttensioned box girder	1050	Rubber bearing and viscous damper, $F_{max} = 4000\,kN$ (FIP Industriale, Inc.)	2003	
Bill Emerson Memorial	United States, Illinois	Cable-stayed	1206	Shock transmission device, $F_{max} = 6670$ kN (Taylor Devices, Inc.)	2003	The structural model of the bridge is a benchmark for seismic protection of cable-stayed bridges (Dyke et al., 2003)
George Washington	United States, Washington	Steel truss	1450	FPS (Earthquake Protection System, Inc.)	2004	

Continued

Table 22.1 Continued

Bridge	Location (Country, City/State)	Type	Length (m)	Seismic Component Device	Year	Notes
Rion Antirion	Greece, Patras	Cable-stayed	2252	Viscous Dampers, $F_{max} = 3500$ kN (FIP Industriale, Inc.)	2004	
Bolu Viaducts	Turkey	Reinforced concrete	2300	FPS (Earthquake Protection System, Inc.)	2006	
Richmond-San Rafael	United States, California	Steel truss	8850	LRB (Dynamic Isolation System, Inc.)	2006	
Sutong Bridge	China, Jiangsu	Cable-stayed	8206	Elastomeric spring and viscous damper, $F_{max} = 10{,}000$ kN (Taylor Device, Inc.)	2008	The performance of the system reported as "very good" during the 2008 Wenchuan earthquake (Yongqi et al., 2008)
Yabegawa	Japan	Prestressed concrete cable-stayed	517	LRB and stopper damper	2009	
Antioch	United States, California	Steel girder	2900	FPS (Earthquake Protection System, Inc.)	2010	
Stonecutters	China, Hong Kong	Cable-stayed	1600	Shock transmission device, $F_{max} = 8000$ kN	2011	
Erqi	China, Wuhan	Cable-stayed	2922	Viscous Dampers, $F_{max} = 1000$ kN (FIP Industriale, Inc.)	2011	
Dumbarton	United States, California	Reinforced concrete	2620	FPS (Earthquake Protection System, Inc.)	2013	

Han Jia Tuo	China, Chong Qing	Cable-stayed	866	Shock transmission device, $F_{max} = 2300$ kN, and viscous damper, $F_{max} = 2500$ kN (FIP Industriale, Inc.)	2013	
Jiashao	China, Zhejiang	Cable-stayed	2680 m (length of main span)	Viscous damper, $F_{max} = 2500$ kN (FIP Industriale, Inc.)	2013	World's longest cable-stayed bridge with a total length of 10,138 m

References

Agrawal, A.K., Nagarajaiah, S., 2009. Benchmark structural control problem for a seismically excited highway bridge: phase I and II. Struct. Control. Health Monit. 16, 503–508.

Agrawal, A., Yang, J., 2000. A semi-active electromagnetic friction damper for response control of structures. In: Proceedings of Structures Congress 2000, Philadelphia, PA, USA, May 8–10, pp. 1–8.

Agrawal, A., Tan, P., Nagarajaiah, S., Zhang, J., 2009. Benchmark structural control problem for a seismically excited highway bridge—part I: phase I problem definition. Struct. Control. Health Monit. 16, 509–529.

Aiken, I.D., Nims, D.K., Kelly, J.M., 1992. Comparative study of four passive energy dissipation systems. Bull. N. Z. Natl. Soc. Earthq. Eng. 25, 175–192.

Aiken, I.D., Nims, D.K., Whittaker, A.S., Kelly, J.M., 1993. Testing of passive energy dissipation systems. Earthq. Spectra 9, 335–370.

American Association of State Highway and Transportation Officials (AASHTO), 2010. Guide Specifications for Seismic Isolation Design, third ed. Washington, DC.

Amjadian, M., Agrawal, A.K., 2016. Rigid-body motion of horizontally curved bridges subjected to earthquake-induced pounding. J. Bridg. Eng. 21 (12), 04016090.

Amjadian, M., Agrawal, A.K., 2017. A passive electromagnetic eddy current friction damper (PEMECFD): theoretical and analytical modeling. Struct. Control Health Monit. 24 (10), e1978.

Amjadian, M., Agrawal, A.K., 2018. Modeling, design, and testing of a proof-of-concept prototype damper with friction and eddy current damping effects. J. Sound Vib. 413, 225–249.

Amjadian, M., Agrawal, A.K., 2019. Seismic response control of multi-story base-isolated buildings using a smart electromagnetic friction damper with smooth hysteretic behavior. Mech. Syst. Signal Process. 130, 409–432.

Buckle, I.G., Constantinou, M., Dicleli, M., Ghasemi, H., 2006. Seismic isolation of highway bridges. In: Technical Report, MCEER-06-SP07, Multidisciplinary Center for Earthquake Engineering Research, Univ. at Buffalo, State Univ. of New York, Buffalo, NY, USA.

Buckle, I.G., Al-Ani, M., Monzon, E., 2011. Seismic isolation design examples of highway bridges. In: Technical Report, NCHRP 20-7/Task 262(M2), National Cooperative for Highway Research Program, Transportation Research Board, Washington, DC, USA.

Carlson, J.D., Catanzarite, D.M., St. Clair, K.A., 1996. Commercial magneto-rheological fluid devices. Int. J. Mod. Phys. B 10, 2857–2865.

Carr, A.J., 1994. Dynamic analysis of structures. Bull. N. Z. Natl. Soc. Earthq. Eng. 27, 129–146.

Chang, C.-M., Loh, C.-H., 2006. Seismic response control of cable-stayed bridge using different control strategies. J. Earthq. Eng. 10, 481–508.

Chen, Z.Q., et al., 2003. MR damping system on Dongting Lake cable-stayed bridge. In: Proceeding of Smart Structures and Materials, Smart Systems and Nondestructive Evaluation for Civil Infrastructures, 5057, pp. 229–235.

Clemente, P., 2017. Seismic isolation: past, present and the importance of SHM for the future. J. Civ. Struct. Health Monit. 7 (2), 217–231.

Constantinou, M.C., Symans, M.D., 1992. Experimental and analytical investigation of seismic response of structures with supplemental fluid viscous dampers. In: Technical Report, NCEER-92-0032, Multidisciplinary Center for Earthquake Engineering Research, Univ. at Buffalo, State Univ. of New York, Buffalo, NY, USA.

Constantinou, M.C., Kalpakidis, I., Filiatrault, A., Lay, R.A.E., 2011. LRFD-based analysis and design procedures for bridge bearings and seismic isolators. In: Technical Report, MCEER-11-0004, Multidisciplinary Center for Earthquake Engineering Research, Univ. at Buffalo, State Univ. of New York, Buffalo, NY, USA.

Dezi, F., Carbonari, S., Tombari, A., Leoni, G., 2012. Soil-structure interaction in the seismic response of an isolated three span motorway overcrossing founded on piles. Soil Dyn. Earthq. Eng. 41, 151–163.

Dyke, S.J., Spencer, B.F., Sain, M.K., Carlson, J.D., 1996. Modeling and control of magnetorheological dampers for seismic response reduction. Smart Mater. Struct. 5, 565–575.

Dyke, S.J., Caicedo, J.M., Turan, G., Bergman, L.A., Hague, S., 2003. Phase I benchmark control problem for seismic response of cable-stayed bridges. J. Struct. Eng. 129, 857–872.

Dynamic Isolation Systems Company, 2006, McCarran, NV, USA. http://www.dis-inc.com/ (accessed 05.07.15).

Earthquake Engineering Research Center (EERC), 1995. Isolated Bridges in Japan. From http://nisee.berkeley.edu/prosys/japanbridges.html. accessed 23.11.14.

Earthquake Engineering Research Center (EERC), 1996. Isolated Bridges in the US. From http://nisee.berkeley.edu/prosys/usbridges.html. accessed 23.10.14.

Erkus, B., Abé, M., Fujino, Y., 2002. Investigation of semi-active control for seismic protection of elevated highway bridges. Eng. Struct. 24, 281–293.

Eurocode 8 (Ed.), 2005. Design of Structures for Earthquake Resistance. Part 2: Bridges. Eurocode 8, Brussels.

Feng, M.Q., Kim, J.-M., Shinozuka, M., Purasinghe, R., 2000. Viscoelastic dampers at expansion joints for seismic protection of bridges. J. Bridg. Eng. 5, 67–74.

Fenz, D.M., Constantinou, M.C., 2006. Behaviour of the double concave Friction Pendulum bearing. Earthq. Eng. Struct. Dyn. 35, 1403–1424.

Fenz, D.M., Constantinou, M.C., 2008. Spherical sliding isolation bearings with adaptive behavior: theory. Earthq. Eng. Struct. Dyn. 37, 163–183.

Gavin, H.P., Dobossy, M.E., 2001. Optimal design of an MR device. In: Proceeding of SPIE's 8th Annual International Symposium on Smart Structures and Materials, Newport Beach, CA, USA, March 3–8, pp. 273–280.

Guo, A., Li, Z., Li, H., Ou, J., 2009. Experimental and analytical study on pounding reduction of base-isolated highway bridges using MR dampers. Earthq. Eng. Struct. Dyn. 38, 1307–1333.

He, W.-L., Agrawal, A.K., 2008. Analytical model of ground motion pulses for the design and assessment of seismic protective systems. J. Struct. Eng. 134, 1177–1188.

He, W., Jiang, L., Wei, B., Wang, Z., 2020. The influence of pier height on the seismic isolation effectiveness of friction pendulum bearing for Double-Track railway bridges. Structures 28, 1870–1884.

Heo, G., Kim, C., Lee, C., 2014. Experimental test of asymmetrical cable-stayed bridges using MR-damper for vibration control. Soil Dyn. Earthq. Eng. 57, 78–85.

Jung, H., Jang, D., Choi, K., Cho, S., 2009. Vibration mitigation of highway isolated bridge using MR damper-based smart passive control system employing an electromagnetic induction part. Struct. Control Health Monit. 16, 613–625.

Kalantari, A., Amjadian, M., 2010. An approximate method for dynamic analysis of skewed highway bridges with continuous rigid deck. Eng. Struct. 32, 2850–2860.

Kawashima, K., 2012. Damage of bridges due to the 2011 Great East Japan earthquake. In: Proceedings of the International Symposium on Engineering Lessons Learned From the 2011 Great East Japan Earthquake, Tokyo, Japan, March 1–4, pp. 82–101.

Kawashima, K., Unjoh, S., 1994. Seismic response control of bridges by variable dampers. J. Struct. Eng. 120, 2583–2601.

Kelly, J.M., 1997. Earthquake-Resistant Design With Rubber. Springer London, London.

Kelly, J.M., Konstantinidis, D., 2011. Mechanics of Rubber Bearings for Seismic and Vibration Isolation. John Wiley & Sons, Chichester, UK.

Kelly, J.M., Buckle, I.G., Tsai, H.C., 1986. Earthquake simulator testing of a base isolated bridge deck. In: UCB/EERC-85/09.

Konstantinidis, D., Makris, N., Kelly, J.M., 2012. Health monitoring of fluid dampers for vibration control of structures: experimental investigation. Earthq. Eng. Struct. Dyn. 41, 1813–1829.

Kunde, M.C., Jangid, R.S., 2006. Effects of pier and deck flexibility on the seismic response of isolated bridges. J. Bridg. Eng. 11, 109–121.

Loh, C.-H., Chang, C.-M., 2006. Vibration control assessment of ASCE benchmark model of cable-stayed bridge. Struct. Control Health Monit. 13, 825–848.

LORD Corporation Company, 1924. Cary, NC, US. http://www.lord.com/ (accessed 22.10.14).

Losanno, D., Hadad, H.A., Serino, G., 2017. Seismic behavior of isolated bridges with additional damping under far-field and near fault ground motion. J. Earthq. Struct. 13 (2), 119–130.

Madhekar, S.N., Jangid, R.S., 2011. Seismic performance of benchmark highway bridge installed with piezoelectric friction dampers. IES J. Part A Civ. Struct. Eng. 4, 191–212.

Makris, N., 2019. Seismic isolation: early history. Earthq. Eng. Struct. Dyn. 48 (2), 269–283.

Makris, N., Zhang, J., 2002. Structural characterization and seismic response analysis of a highway overcrossing equipped with elastomeric bearings and fluid dampers: a case study. In: PEER 2002/17.

Mokha, A., Constantinou, M.C., Reinhorn, A.M., Zayas, V.A., 1991. Experimental study of friction-pendulum isolation system. J. Struct. Eng. 117, 1201–1217.

Naeim, F., Kelly, J.M., 1999. Design of Seismic Isolated Structures: From Theory to Practice. John Wiley & Sons, New York, USA.

Nagarajaiah, S., Narasimhan, S., Agrawal, A., Tan, P., 2009. Benchmark structural control problem for a seismically excited highway bridge—part III: phase II sample controller for the fully base-isolated case. Struct. Control Health Monit. 16, 549–563.

Neff Patten, W., Sun, J., Li, G., Kuehn, J., Song, G., 1999. Field test of an intelligent stiffener for bridges at the I-35 Walnut Creek Bridge. Earthq. Eng. Struct. Dyn. 28, 109–126.

Ok, S.-Y., Kim, D.-S., Park, K.-S., Koh, H.-M., 2007. Semi-active fuzzy control of cable- stayed bridges using magneto-rheological dampers. Eng. Struct. 29, 776–788.

Olsson, H., Åström, K.J., Canudas de Wit, C., Gäfvert, M., Lischinsky, P., 1998. Friction models and friction compensation. Eur. J. Control 4, 176–195.

Pall, A.S., Marsh, C., 1982. Seismic response of friction damped braced frames. J. Struct. Div. 108, 1313–1323.

Phillips, B.M., Chae, Y., Jiang, Z., Spencer, B.F., Ricles, J.M., Christenson, R., Dyke, S.J., Agrawal, A.K., 2010. Real-time hybrid simulation benchmark study with a large-scale MR damper. In: Proceeding of 5th World Conference on Structural Control and Monitoring, Tokyo, Japan, July 12–14, Paper No. 10335.

Pradono, M.H., Iemura, H., Igarashi, A., 2009. Passively controlled MR damper in the benchmark structural control problem for seismically excited highway bridge. Struct. Control Health Monit. 16, 626–638.

Reinhorn, A.M., Li, C., Constantinou, M.C., 1995. Experimental and analytical investigation of seismic retrofit of structures with supplemental damping. Part 1: fluid viscous damping devices. In: NCEER-95-0001.

Robinson, W.H., 1975. Cyclic shear energy absorber. In: US Patent No. 4117637.
Robinson, W.H., 1982. Lead-rubber hysteretic bearings suitable for protecting structures during earthquakes. Earthq. Eng. Struct. Dyn. 10, 593–604.
Sadek, F., Mohraz, B., Taylor, A., Chung, R., 1996. Passive energy dissipation devices for seismic applications. In: NISTIR 5923.
Sahasrabudhe, S.S., Nagarajaiah, S., 2005. Semi-active control of sliding isolated bridges using MR dampers: an experimental and numerical study. Earthq. Eng. Struct. Dyn. 34, 965–983.
Sarrazin, M., Moroni, O., Neira, C., Venegas, B., 2013. Performance of bridges with seismic isolation bearings during the Maule earthquake, Chile. Soil Dyn. Earthq. Eng. 47, 117–131.
Shen, J., Tsai, M.-H., Chang, K.-C., Lee, G.C., 2004. Performance of a seismically isolated bridge under near-fault earthquake ground motions. J. Struct. Eng. 130, 861–868.
Soneji, B.B., Jangid, R.S., 2008. Influence of soil–structure interaction on the response of seismically isolated cable-stayed bridge. Soil Dyn. Earthq. Eng. 28, 245–257.
Spencer, J.B.F., Nagarajaiah, S., 2003. State of the art of structural control. J. Struct. Eng. 129, 845–856.
Spencer, B.F., Dyke, S.J., Sain, M.K., Carlson, J.D., 1997. Phenomenological model for magnetorheological dampers. J. Eng. Mech. 123, 230–238.
Stehmeyer, E.H., Rizos, D.C., 2008. Considering dynamic soil structure interaction (SSI) effects on seismic isolation retrofit efficiency and the importance of natural frequency ratio. Soil Dyn. Earthq. Eng. 28, 468–479.
Tan, P., Agrawal, A.K., 2009. Benchmark structural control problem for a seismically excited highway bridge-part II: phase I sample control designs. Struct. Control Health Monit. 16, 530–548.
Taylor Devices Company, 1956, North Tonawanda, NY, USA. http://taylordevices.com/ (accessed 16.06.14.).
Tongaonkar, N.P., Jangid, R.S., 2003. Seismic response of isolated bridges with soil-structure interaction. Soil Dyn. Earthq. Eng. 23, 287–302.
Wang, W., Hua, X., Wang, X., Wu, J., Sun, H., Song, G., 2019. Mechanical behavior of magnetorheological dampers after long-term operation in a cable vibration control system. Struct. Control Health Monit. 26 (1), e2280.
Wieczorek, N., Gerasch, W.-J., Rolfes, R., Kammerer, H., 2014. Semiactive friction damper for lightweight pedestrian bridges. J. Struct. Eng. 140, Paper No. 04013102.
Xu, Z., Agrawal, A.K., Yang, J.N., 2006. Semi-active and passive control of the phase I linear base-isolated benchmark building model. Struct. Control Health Monit. 13, 626–648.
Yang, G., Spencer, B.F., Carlson, J.D., Sain, M.K., 2002. Large-scale MR fluid dampers: modeling and dynamic performance considerations. J. Eng. Struct. 24, 309–323.
Yang, G., Spencer, B.F., Jung, H., Carlson, J., 2004. Dynamic modeling of large-scale magnetorheological damper systems for civil engineering applications. J. Eng. Mech. 130, 1107–1114.
Yang, M.-G., Chen, Z.-Q., Hua, X.-G., 2011. An experimental study on using MR damper to mitigate longitudinal seismic response of a suspension bridge. Soil Dyn. Earthq. Eng. 31, 1171–1181.
Yongqi, C., Liangzhe, M., Tiezhu, C., Schneider, R., Winters, C., 2008. Shock control of bridges in China using Taylor devices' fluid viscous dampers. In: Proceeding of 14th World Conference on Earthquake Engineering, Beijing, China, October 12–17.
Yoshida, J., Abe, M., Fujino, Y., Watanabe, H., 2004. Three-dimensional finite-element analysis of high damping rubber bearings. J. Eng. Mech. 130, 607–620.
Yoshioka, H., Ramallo, J.C., Spencer, B.F., 2002. "Smart" base isolation strategies employing magnetorheological dampers. J. Eng. Mech. 128, 540–551.

Zhou, P., Liu, M., Li, S., Li, H., Song, G., 2020. Experimental study on seismic control of towers in cable-supported bridges by incorporating fluid viscous dampers between sub-towers. Adv. Struct. Eng. 23 (10), 2086–2096.

Zhou, P., Liu, M., Kong, W., Xu, Y., Li, H., 2021. Modeling and evaluation of magnetorheological dampers with fluid leakage for cable vibration control. J. Bridg. Eng. 26 (2), 04020119.

Cables

23

E. Caetano
Laboratory of Vibrations and Monitoring ViBest, Faculty of Engineering of the University of Porto, Porto, Portugal

1. Introduction

In the context of the design of cable-stayed and suspension bridges, the composition and mechanical characteristics of cables are described, including reference to related components (namely, guides, pipes, anchorages, and vibration mitigation devices). Recent developments based on the use of polymeric materials are addressed, and some of the most relevant suspension and cable-stayed bridges are listed. Focusing on these structures, some design bases and requirements are presented, as well as methodologies to assess the static and dynamic behavior, characterize vibrations, and design devices for vibration mitigation.

2. Cable components

2.1 Tension members

Although chains and bars have been used to form the cables of early cable-supported bridges, modern cables are made from steel wires, which are typically cylindrical in shape, and have a diameter of 3–7 mm. These wires are arranged in strands and ropes. Strands can be formed from the parallel or else from the helical assembling of wires. The parallel arrangement is typical of the main cables of long span suspension bridges (Figure 23.1a), while the helical arrangement is normally employed in smaller suspension spans and in hangers and stay cables. The simplest and most common arrangement is the seven-wire strand made from the helical winding of six 5 mm wires around a core wire (Figure 23.1b), with a nominal diameter of 15 mm. Modern stay cables are frequently formed from bundles of such strands, reaching diameters close to 470 mm. Alternatively, cables can be formed from multiwire helical strands. These so-called spiral strands result from the spinning of various layers of wires around a core center (Figure 23.1c) and reach diameters of 150–170 mm. Previously, cable-stayed bridges employed fully locked coil strands made from the assembling of wires with different shapes: a core helical strand, one or more layers of wedge-shaped wires, and a number of outer layers formed by z-shaped wires arranged helically (Figure 23.1d). The maximum diameter of fully locked coil cables available in the market is of the order of 180 mm.

Due to a higher carbon content in the composition when compared with structural steels (see Table 23.1), the strength of steel wire is significantly high, reaching values

Innovative Bridge Design Handbook. https://doi.org/10.1016/B978-0-12-823550-8.00046-9

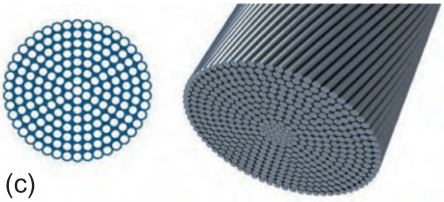

Figure 23.1 Types of strands: (a) parallel-wire (copyright) Nippon Steel Corporation; (b) seven-wire strand; (c) multiwire helical strand (Bridon-Bekaert catalog);

(Continued)

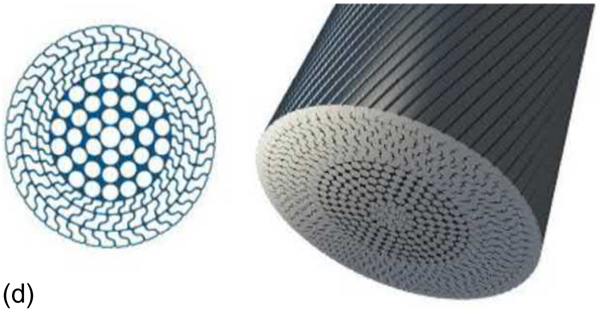

(d)

Figure 23.1, cont'd (d) full locked coil strand (Bridon-Bekaert catalog).

Table 23.1 Comparison Between Cable Steel and Structural Steel (Based on Typical Values) (Gimsing and Georgakis, 2012)

			Structural Steel	
	Unit	**Conventional Cable Steel (5 or 7 mm Wires)**	**Mild**	**High Strength**
Yield stress (=2% proof stress)	MPa	1180	240	690
Tensile strength	MPa	1570	370	790
Strain at breaking	%	4	24	
Modulus of elasticity	GPa	205	210	210
Typical chemical composition				
C		0.80%	0.20%	0.15%
Si		0.20%	0.30%	0.25%
Mn		0.60%		0.80%
Cu		0.05%	0.20%	0.30%
Ni		0.05%		0.80%
Cr		0.05%	0.30%	0.50%
P		0.03%	0.04%	0.03%
S		0.02%	0.04%	0.03%

of 1570–1860 MPa. For very long spans, strengths of 1860–1960 MPa have been used (Hauge and Andersen, 2011). Recently, 2160 MPa grade strands have become available on the market for use in stay-cable applications (Guesdon et al., 2020).

It is important to note that the ductility of the steel wire is lower than that of the structural steel. According to Table 23.1, the strain at breaking of the steel wire is one-sixth of that corresponding to a mild steel. Regarding the modulus of elasticity, a common value for the 5–7 mm wires is 205 GPa. The simple helical and the spiral strand have a lower-elasticity modulus, with current values of 190 and 170 GPa, respectively. For locked coil cables, the modulus is normally 180 GPa (Gimsing and Georgakis, 2012).

Despite the lower-elasticity modulus, helical strands have the advantage of the self-compacting with the tensioning and not requiring wrapping, in contrast to parallel wire strands. Furthermore, helical strands have null elongation when reeling, due to the alternate position of the wires in the compression and tension areas. Therefore, these strands can be prefabricated in very long lengths. Parallel wire strands are normally fabricated on-site by aerial spinning.

The z-shaped wires of locked coil cables present a strength of the order of 1370–1570 MPa (EN 1993-1-11, 2006), slightly lower than that of circular wires. However, the tensioning of these wires leads to a higher degree of compaction than that of spiral strands (of the order of 15%–20%), resulting in void ratios of the order of 10%. Clearly, this is an advantage from the point of view of wind excitation, as the surface exposed to wind is minimum. The locking of the inner spiral strand by the *z*-wires when stretched provides an additional barrier to corrosion (see Section 2.2), although, in fact, cables employed in several early cable-stayed bridges have been replaced earlier than expected (Gimsing, 1983; Saul and Svensson, 1990; Sandberg and Hendy, 2010). Finally, locked coil cables need to be delivered entirely fabricated, including the sockets. The longest fabricated locked coil cable had a length of the order of 1250 m (Gimsing and Georgakis, 2012).

2.2 Corrosion protective systems

Most modern cable systems for suspension and cable-stayed bridges are designed for an intended working life of 100 years or more. This requires that adequate protective systems against corrosion and fatigue are used. Despite the fact that different practices can be found worldwide, the most recent specifications impose two levels of barriers. Zinc coating of the wires, achieved by galvanization, is a first barrier level and is applied individually to all wires of parallel wire cables in a suspension bridge cable, or to all wires of stay cables in Europe and Japan, although this has not been a current practice in USA (TRB 20015, 2005). In suspension bridge cables, a second barrier is given by a zinc dust paste filling of voids of the compacted cable and is further complemented by the wrapping with a galvanized wire. A third barrier can be created by painting. In stay cables formed by bundles of spiral strands, the second barrier consists of the individual greasing and sheathing, and a third barrier is also used, consisting of the encasing of the strands in a high-density polyethylene (HDPE) pipe. This pipe has a role of protecting the bundle of stays from moisture and weather agents. In locked coil cables, the core helical wires are not galvanized and are locked by the wedge or *z*-wires, which are themselves galvanized. A filling of zinc dust paint may help protecting the inner wires, while the outer wires may be additionally painted or else made of stainless steel. The zinc coating achieved with galvanization is not stable, and a more recent coating combining zinc (95%) and aluminum (5%), the GALFAN, has been used (ISO 19203, 2018).

Grouting inside a steel or a polyethylene pipe was one of the previously used protective systems, by analogy with the post-tensioning technique. However, it has been verified that voids in the concrete or cracks due to vibrations and long-term deformation may lead to the penetration of water and promote degradation of the wires from

Figure 23.2 Compact stay cable with permanent dehumidification system Copyright VSL (VSL, 2002).

inside the cable. Moreover, cracks in the pipes due to the stresses generated during grouting have also been observed (TRB 20015, 2005). The irreplaceability of the strands and the difficulty in accessing the wires' condition have made this technique fall out of use in recent years, in favor of the bundle of individually sheathed strands encased in an HDPE pipe.

A recent evolution of the parallel strand bundle is the compact cable developed for very long stay cables, as those of the Russky Bridge (FREYSSINET, 2010, 2012). This compact cable is made with individual sheaths of smaller diameter than usual to allow a denser allocation of the strands in the pipe, providing a wind load reduction of the order of 25%–30%, but installing this compact cable requires special tools. Coextrusion of a common sheath to the bundle of strands is another option offered by manufacturers (FREYSSINET, 2014a). An even more compact system can be achieved by the removal of the individual sheath and the use of a permanent dehumidification system to provide an equivalent protection against corrosion (see Figure 23.2). These systems have also been introduced in cables from suspension bridges, as the Akashi Kaikyo Bridge, and require humidity and pressure monitoring to detect leakage and prevent the development of conditions that would corrode the cables (Bloomstine, 2006; Beabes et al., 2015).

2.3 Anchorages

Anchorages provide the means for the transfer of cable loads to the soil or to the attaching parts of the structure and should be designed in order to exhibit optimal performance in terms of the mechanical behavior and fatigue resistance. These are composed of two main components: the anchorage heads, which constitute an intermediate mechanical part and are formed by wedges and anchor blocks, designed to secure the strands and transmit their force to the structure or the soil; and a transition zone, where the strands fan out, eventually with the help of deviators and are guided to the anchor head by means of guide pipes (see Figure 23.3). These pipes may also contain sealing

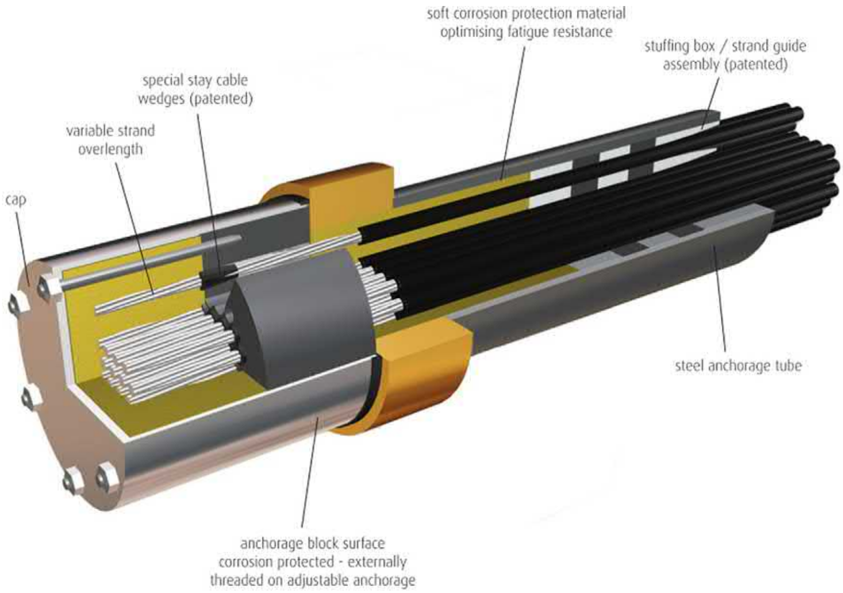

Figure 23.3 Typical components of stay cable anchorage (FREYSSINET, 2010).

systems, in order to ensure protection against corrosion, as well as internal dampers, to preclude cable vibrations. In suspension bridges, cable splay chambers may have dehumidification systems. In stay cables, the guide deviators normally incorporate neoprene rings in the end, allowing for the accommodation of limited angular variation (± 25 mrad, according to Fédération Internationale du Béton, FIB, 2005, or ± 20 mrad static and ± 10 mrad, according to PTI Guide Specification, 2007). These neoprene rings contribute to limiting bending stresses.

2.4 Fire protective systems

The increase of heavy traffic in long-span bridges has contributed to an increased risk of fire. The occurrence of a truck fire in 2013 on the New Little Belt Bridge in Denmark exposed the risk of loss of integrity of the main cable in the lower part, motivating the development and installation of a fire protection system (FPS) based on an insulation mat and an encasing steel cap up to the height of 10 m above the deck level (Kragh et al., 2020). The same type of protection is already being offered to hangers and cables from cable-stayed bridges (VSL, 2018).

2.5 Vibration mitigation devices

The very low intrinsic damping of cables makes them vulnerable to vibrations. In order to prevent or mitigate such vibrations, several measures can be taken, involving an aerodynamic or structural approach.

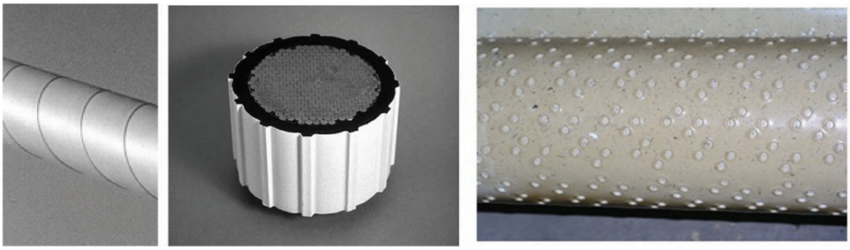

(a) (b) (c)

Figure 23.4 Examples of nonsmooth surfaces of cable coating to prevent rain-wind-induced vibration: (a) helical wire whirling, Vasco da Gama Bridge; (b) protuberated, Higashi Kobe Bridge; (c) dimpled, as in Tatara Bridge (Sham and Wyatt, 2016).

Referring to the aerodynamic approach, one of the most common measures consists in the fabrication of the HDPE pipes with an helical wire whirling (see Figure 23.4a) or with indented protuberances (Figure 23.4b and c), which have been shown to disrupt the formation of rivulets associated with rain and wind vibrations (see Section 3.3.6). Helical wire whirling has been first employed in the Normandy Bridge (Virlogeux, 1998) and is presently a measure adopted for most stay cables (Vo-Duy and Nguyen, 2020). In the Tatara Bridge, in Japan, a dimpled surface (Figure 23.4c) was adopted, which was shown to lead to lower drag forces by comparison with other alternative tested protuberances. This aspect is extremely important in very long stay cables, considering that the wind loads on the cables can exceed 50% of the overall wind loads (Virlogeux, 1998).

The structural control of cable vibrations can be achieved both by the installation of interconnection ropes and by dampers installed close by the cables anchorages. Interconnecting ropes constitute the most evident form of attenuating cable vibrations in a cable-stayed bridge and have been widely used both as temporary and permanent measures.

In terms of structural behavior, the addition of cross-ropes to the stay-cable system creates intermediate supports at those elements and, consequently, increases their natural frequencies for in-plane vibrations. Another effect of the installation of cross cables is an increase of the damping. A study by Yamaguchi (1995) showed that this increase is higher for soft secondary cables than for taut ties. However, the initial tension on these cables should have a sufficiently high value so that, under extreme effects, the cross cables are not detensioned, producing shocks and causing damage of the tie devices, as reported by Virlogeux (1998) in the Farø and some of the Honshū-Shikoku Bridges.

The installation of hydraulic or viscous dampers close to the stay cables' anchorages is the most efficient solution for suppressing cable vibrations. The damping capacity of external dampers is defined according to a specified requirement. In general, it is considered that viscous dampers have low maintenance costs but show a dependence of damping characteristics with temperature and frequency, while hydraulic dampers have high maintenance costs and a complex adjustment

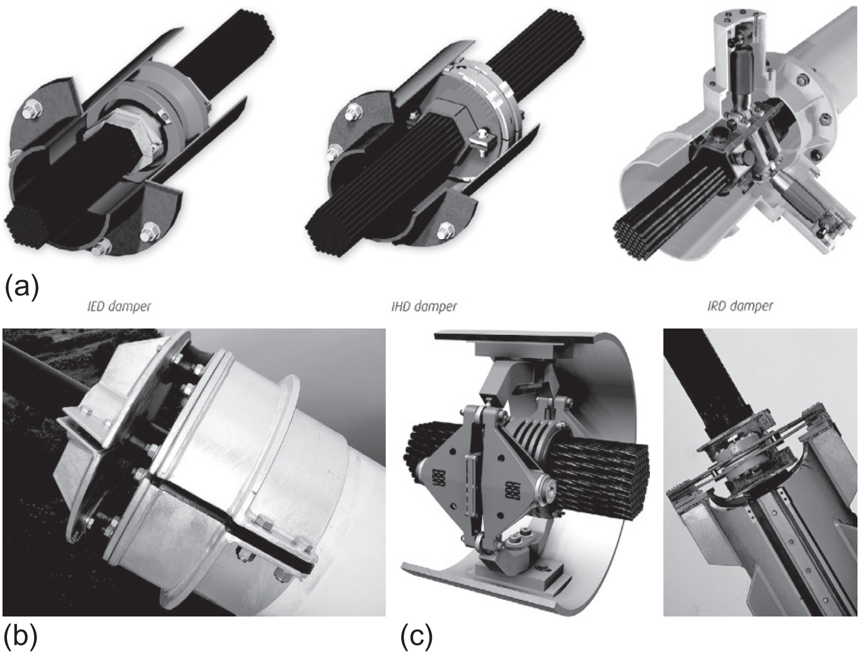

Figure 23.5 Different types of internal dampers: (a) elastomeric (IED), hydraulic (IHD), and radial (IRD) dampers (FREYSSINET, 2014b,c,d); (b) elastomeric damper (Copyright VSL); (c) friction dampers (Courtesy of BBR VT International Ltd (BBR, 2011) Copyright VSL (VSL, 2002)).

(Bournand, 1999). Another reported inconvenience associated with these mechanical devices is the lowering of the aesthetic quality of the bridge. In order to overcome this aspect, internal ring dampers have been developed that are inserted in the deviator guide pipe of the cable. Different principles can be applied to activate damping, as exemplified in Figure 23.5 by the proposals of different manufacturers, which respect elastomeric, hydraulic, and friction dampers. Elastomeric devices are based on the shearing deformation of high-damping rubber devices disposed as cylinders (Figure 23.5a) or as pads (Figure 23.5b) and are activated at low levels of vibration. These devices are adequate for small and medium-length cables. Hydraulic dampers are based on the shear motion of a viscous fluid inside a cylinder deposit activated by the moving cable or else on the compression of viscous fluid by a piston, in the case of the two configurations shown in Figure 23.5a. These devices are adequate for long-span cables and should be installed at a distance from the anchorage of the order of 0.015–0.02 L, L being the chord length of the stay. Figure 23.6 shows the implementation of the internal hydraulic dampers at several cables of the Russky Bridge. Friction dampers, as shown in Figure 23.5b, are based on the mechanical friction activated by the cable vibration. Due to this principle, the activation of these devices only occurs for a certain amplitude of vibration. This can be both a benefit and an inconvenience from the points of view of damper durability and cable vibration limits, respectively.

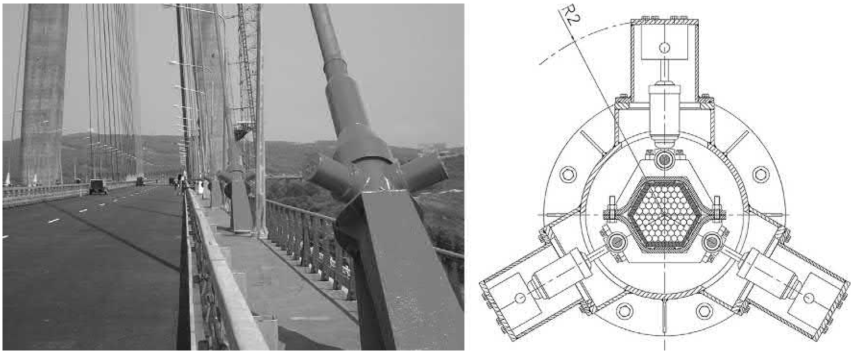

Figure 23.6 Internal radial dampers installed at the Russky Bridge (*left*) (FREYSSINET, 2014d).

Figure 23.7 Combined hydraulic and elastomeric internal dampers installed on a stay cable of Vasco da Gama Bridge.

The possibility of combining in the same cable two types of dampers can then be considered. Figure 23.7 shows an internal damper installed at one stay of Vasco da Gama Bridge, which combines a high-damping rubber ring with a viscous damper.

2.6 Recent developments

Besides the technological developments related to cables made of steel, there has been continuous research using glass, aramid, or carbon-fiber-reinforced polymers (TRB 20015, 2005; Liu et al., 2015). These materials use epoxy-based resins as a matrix for the composite and have the advantages of lighter weight, higher tensile strength, almost no thermal expansion, and high corrosion resistance. However, their implementation has not been made on a regular basis due to some particular difficulties, such as high cost and low shear strength, which limits the gripping capacity of anchorages and demands dedicated solutions. Despite this, some applications have been made for research purposes. In this context, reference is made to the first cable-stayed bridge employing composite stays, the footbridge over the Gave de Pau River in Laroin, France. The structure has an only steel/concrete span of 110 m suspended by 16 carbon-fiber stays, while backstays are traditional bundles of steel strands (Geffroy, 2002). The composite stays, with lengths of 20–45 m, are made of pultruded carbon-fiber-epoxy rods bundled in groups of seven, encased in an HDPE pipe. Another case study is the Stork Bridge in Winterthur, Switzerland, a roadway bridge with two spans of 63 and 61 m, where two of the stays are carbon composite (CFRP) and have been installed with a monitoring system for continuous assessment of the corresponding condition. In this case, each stay cable is made of a bundle of 241 carbon epoxy wires with 5 mm diameters. These wires have tensile strength of 3300 MPa, an elastic modulus of 165 GPa, and a density of 1.56 g/cm^3 (Meier, 2012).

2.7 Major realizations

Lists containing information concerning major world realizations in suspension (Table 23.2) and cable-stayed bridges (Table 23.3) are presented in this section. These include bridge spans, lengths, diameters and types of employed cables, and the country and year of construction.

Table 23.2 Major World Suspension Bridges: Main Cable Characteristics

Name	Location	Year	Span (m)	Total Length (m)	Cable Characteristics
Akashi Kaikyo	Kobe-Naruto, Japan	1998	1991	3911	Diameter: 1.122 m High-strength galvanized PPW, UTS 1800 MPa 5.23 mm dia. × 127 wires × 290 strands Strand length: 4071–4074 m
Yangsigang Bridge	Hubei, China	2019	1700	4317.8	Diameter: 1.090 m High-strength galvanized PPW, UTS 1960 MPa 6.2 mm dia. × 91 wires × 271 strands Strand length: 2850 m

Table 23.2 Continued

Name	Location	Year	Span (m)	Total Length (m)	Cable Characteristics
Nansha Bridge (East)	Guangdong, China	2019	1688	12,891	Diameter: 1.012 m Guangzhou side span (west); 1.000 m central span and Dongguan side span (east) High-strength galvanized PPW, UTS 1960 MPa 5 mm dia. × 127 wires × 252 strands Strand length: approximately 3000 m
Xihoumen Bridge	Zhejiang, China	2009	1650	2588	Diameter: 0.870 m High-strength galvanized PPW, UTS 1770 MPa 5.25 mm dia. × 127 wires × 169 strands Strand length: 2880 m
Great Belt East Bridge	Halsskov-Sprogø, Denmark	1998	1624	2694	Diameter: 0.827 m High-strength galvanized AS, UTS 1770 MPa 5.38 mm dia. × 504 wires × 37 strands
Osman Gazi	Kocaeli, Turkey	2016	1550	2682	Diameter: 0.781 m High-strength galvanized PPW, UTS 1760 MPa 5.9 mm dia. × 127 wires × 110 strands
Yi Sun-sin Bridge	Yeosu, South Korea	2012	1545	2260	High-strength galvanized AS, UTS 1860 MPa 5.35 mm dia. × 400 wires × 32 strands
Runyang	Zhenjiang, China	2005	1490	35,660	Diameter: 0.900 m High-strength galvanized PPW, UTS 1670 MPa 5.3 mm dia. × 127 wires × 184 strands Strand length: 2580 m
Humber	Hull, Great Britain	1981	1410	2220	Diameter: 0.68 m High-strength galvanized AS, UTS 1540 MPa 5 mm dia. × 149,948 wires

Continued

Table 23.2 Continued

Name	Location	Year	Span (m)	Total Length (m)	Cable Characteristics
Yavuz Sultan Selim	Istanbul, Turkey	2016	1408	1875	Suspension bridge with cable stays Diameter: 0.720 m central span, 0.75 m side spans High-strength galvanized WS, UTS 1960 MPa 5.4 mm dia. × 127 wires × 113 strands Stays: 65–151 strands, dia. 0.25–0.315 m, longest cable 588 m

AS, fabrication of cable by air spinning; *PPW*, prefabricated parallel wire strand.

Table 23.3 Major World Cable-Stayed Bridges: Main Characteristics

Name	Location	Year	Span	Cable Type	Materials
Russky Bridge	Vladivostok, Russia	2012	1104	13–85 No. PWS 56 Internal dampers	Steel/ concrete
Sutong Yangtze	Suzhou, China	2008	1088	PW 7 mm wires UTS: 1770 MPa, added dampers	Steel/ concrete
Stonecutters	Hong Kong, China	2009	1018	PWS 7 mm wires Longest cable: 540 m	Steel/ concrete
Edong Bridge	Hubei, China	2010	926	PW 7 mm wires UTS: 1670 MPa Longest cable: 493.6 m, added dampers	Steel/ concrete
Jiayu Yangtze	Hubei, China	2019	920	PW 7 mm wires UTS: 1770 MPa, added dampers	Steel/ concrete
Tatara	Onomichi-Imabari, Japan	1999	890	$D = 170$ mm 7 mm dia. PW349 wires UTS: 1770 MPa Longest cable: 460 m	Steel
Pont de Normandie	Le Havre, France	1995	856	31–53 PWS Longest cable: 460 m	Steel/ concrete

PW, parallel wire; PWS, parallel wire strand

3. Analysis and design

3.1 Loads and basis of design

The design of cables for cable-stayed and suspension bridges is commonly based on the limit-state verifications. This philosophy has been promoted in particular by the Eurocodes, which define actions, combinations of actions, and partial safety factors (EN 1990, 2002; EN 1993-1-11, 2006). This section addresses the basic design concepts. Accordingly, the design of cables should be based on the verification of the following limit states:

- Ultimate limit state (ULS) for design tension
- Serviceability limit state (SLS) for stress and strain levels, for sag, and for amplitudes of vibration
- Fatigue limit state (FLS) for stress and stress variation due to traffic and wind loads

Considering the diverse actions and combinations of actions on cables and supporting members defined in the various parts of Eurocodes (EN 1991-1-4, 2005; EN 1991-1-5, 2003; EN 1991-2, 2003; EN 1993-3-1, 2006) and national standards and annexes, the following criteria should be satisfied:

- For the verification of cable stays in the ULS, two partial safety factors should be applied to the so-called guaranteed ultimate tensile strength (GUTS) of the cable, addressing (i) the condition of the structure (in service or under construction) and the provisions taken in terms of the mechanical qualification tests; and (ii) construction imperfections. When precautions have been taken in order to limit bending stresses at the end of cable stays, the design tension F_{ULS} should satisfy the relation $F_{ULS} < 0.70\ F_{GUTS}$ for in-service conditions, or $F_{ULS} < 0.75\ F_{GUTS}$ for construction and accidental situations (Service d'Etudes Techniques des Routes et Autoroutes (SETRA), 2002).
- For the verifications in the SLS, the design tension F_{SLS} should satisfy the relation $F_{SLS} < 0.50\ F_{GUTS}$, when stay cables are tested for fatigue considering axial and bending effects (Fédération Internationale du Béton (FIB), 2005). If bending effects are not addressed, the relation $F_{SLS} < 0.45\ F_{GUTS}$ should be satisfied. In addition to tension verification, vibration limit criteria should be checked in order to ensure users' comfort. Eurocode 3 (EN 1993-1-11, 2006) proposes to limit the amplitude of stay-cable vibration to $L/500$ (L being the chord length) for a moderate wind velocity of 15 m/s.
- For verification of stays in the FLS, if the cable systems adopted are qualified by mechanical tests defined in recommendations and standards (Service d'Etudes Techniques des Routes et Autoroutes (SETRA), 2002) and provisions are adopted to prevent bending effects close to the anchorages (namely, by adopting cable guide systems and limiting angular deformations and vibrations), it is sufficient to verify that the so-called stress demand (determined as the interval of variation of stress associated with fatigue loads) is below the fatigue-limit truncation point of the cable-stay system.

3.2 Structural analysis

Cables are characterized by significant geometrical nonlinear behavior. A precise idealization of a cable suspended between two fixed points (Figure 23.8) should include

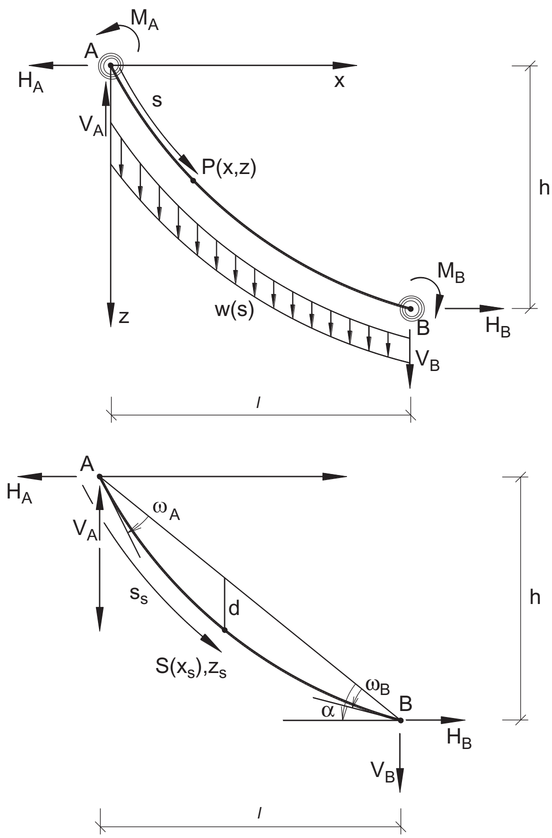

Figure 23.8 Suspended cable subject to self-weight and axial tension. Cable deformation parameters.

the bending and axial deformation. It should also take into consideration the applied axial tension T_0, the self-weight, and the end conditions. The complexity of this problem is further exacerbated by the difficulty of doing a rigorous assessment of the degree of restraint of rotations at anchorages.

However, in the modeling of the structural behavior of a cable, some simplifications are possible, which still result in an accurate calculation of the cable profile and tension.

3.2.1 Static behavior

As a basic assumption, a suspended cable is considered a perfectly flexible elastic structural element. In this condition, the Cartesian coordinates x and z of a generic point P (see Figure 23.8) are defined as a function of the unstrained length s associated with the cable segment AP as (Irvine, 1981)

$$x(s) = \frac{H_A s}{EA_0} + \frac{H_A L_0}{W} \cdot \left[\sinh^{-1}\left(\frac{V_A}{H_A}\right) - \sinh^{-1}\left(\frac{V_A - Ws/L_0}{H_A}\right) \right] \tag{1}$$

$$z(s) = \frac{Ws}{EA_0} \cdot \left(\frac{V_A}{W} - \frac{s}{2L_0}\right) + \frac{H_A L_0}{W} \cdot \left\{ \left[1 + \left(\frac{V_A}{H_A}\right)^2\right]^{1/2} - \left[1 + \left(\frac{V_A - Ws/L_0}{H_A}\right)^2\right]^{1/2} \right\}. \tag{2}$$

These coordinates depend on the reactions at the end A, V_A, and H_A, on the cable weight $W = mgL_0$, on the unstrained length L_0, and on the axial stiffness EA_0 (A_0 being the area of the undeformed cable cross section and E being the elasticity modulus of the cable).

The transcendental equations (Eqs. 1 and 2) of the cable profile define the so-called elastic catenary and constitute the most precise description of the cable geometry under self-weight. The resolution of these equations requires the knowledge of the reactions H_A and V_A, which are obtained by introduction of the boundary conditions $[x(L_0) = \ell;\ z(L_0) = h]$.

The approximation of the catenary profile by an elastic parabola applies to shallow cables (i.e., cables with a small sag-to-span d/L ratio, typically no greater than 1:8). This range covers stays from cable-stayed bridges and most of the cables from suspension bridges. The assumption of a unit ratio between the deformed and undeformed cable length yields the simple equations for the cable profile defined in Cartesian coordinates:

$$z(x) = \frac{1}{2}\frac{mg}{H} \cdot \sec\alpha \cdot x \cdot (\ell - x) + \frac{h}{\ell} \cdot x, \tag{3}$$

where the quantity $T = H \cdot sec\ \alpha$ represents the cable tension at the section whose tangent is parallel to the chord.

The parabolic approach provides significant error in the description of the static behavior of the cable in local quantities, like sag and the angles of deviation to the chord at the anchorages. This error increases with both the angle of inclination of the cable to the horizontal and the chord length. Although very practical and useful for an approximate analysis during design phase, the parabolic approach is not convenient for design and installation purposes.

3.2.2 Dynamic behavior

The dynamic behavior of a cable integrated both in a suspension or in a cable-stayed bridge can generally be described by the linear theory of vibrations derived by Irvine and Caughey (1974) for shallow cables. According to this theory, the circular frequencies ω_n and the corresponding transversal modal components $v_n(x)$ of out-of-plane vibration modes of a horizontal cable with chord length ℓ and horizontal component of the tension H can be obtained from

$$\begin{aligned} \omega_n &= \frac{n\pi}{\ell} \cdot \sqrt{\frac{H}{m}} \quad n = 1,2,3,\ldots \\ v_n(x) &= A_n \cdot \sin\left(\frac{n\pi x}{\ell}\right) \ n = 1,2,3,\ldots \end{aligned} \tag{4}$$

where A_n *is* an arbitrary constant.

In-plane vibration modes are characterized as *symmetric* and *antisymmetric*, according to the profile of the transversal component of motion. The circular frequencies ω_n and the in-plane transversal components w_n of the antisymmetric modes are given by

$$\begin{aligned} \omega_n &= \frac{2n\pi}{\ell} \cdot \sqrt{\frac{H}{m}} \quad n = 1,2,3,\ldots \\ w_n(x) &= A_n \cdot \sin\left(\frac{2n\pi x}{\ell}\right) \ n = 1,2,3,\ldots. \end{aligned} \tag{5}$$

For the symmetric in-plane modes, the circular frequencies are extracted from the solution of

$$\tan\frac{\overline{\omega}}{2} = \frac{\overline{\omega}}{2} - \frac{4}{\lambda^2}\left(\frac{\overline{\omega}}{2}\right)^3, \tag{6}$$

where $\overline{\omega}$ is the adimensional natural frequency given by $\overline{\omega} = \omega\ell/(H/m)^{1/2}$, and λ^2 is the Irvine parameter (Irvine, 1981). This parameter incorporates both the geometric and deformational characteristics of the cable and is defined as

$$\lambda^2 = \left(\frac{mg\ell}{H}\right)^2 \cdot \frac{\ell}{\frac{HL_e}{EA_0}}, \tag{7}$$

where L_e is a virtual length of cable defined by

$$L_e = \int_0^\ell \left(\frac{ds}{dx}\right)^3 dx \approx \ell \cdot \left\{1 + 8\left(\frac{d}{\ell}\right)^2\right\}. \tag{8}$$

The in-plane modal shape transversal components w_n associated with these frequencies are defined by

$$w_n(x) = A_n \cdot \left(1 - \tan\frac{\overline{\omega}}{2}\sin\frac{\overline{\omega}x}{\ell} - \cos\frac{\overline{\omega}x}{\ell}\right). \tag{9}$$

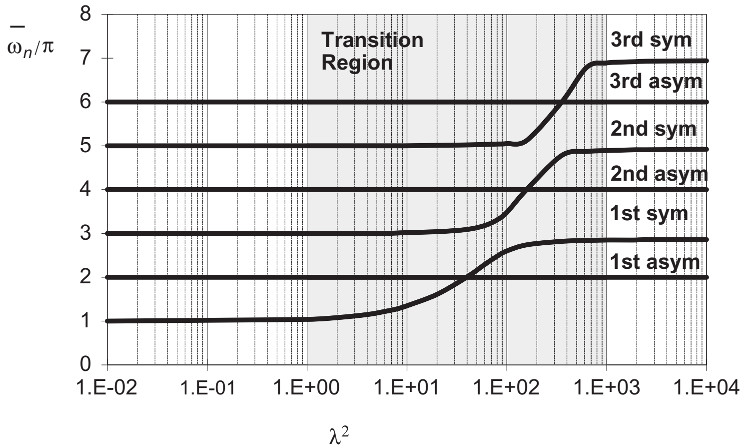

Figure 23.9 Variation of the natural frequencies of the first three symmetric and antisymmetric modes of vibration with λ^2.

The sole dependence of the natural frequencies of *in-plane symmetric modes* on the Irvine parameter λ^2 illustrates the importance of λ^2 as an intrinsic characteristic of the cable.

Typical values of λ^2 attained by stay cables vary in the range of 0–1, while for suspension bridges, λ^2 is normally greater than 100. Very large stay cables can have a λ^2 value greater than 1. Small values of λ^2 reflect relatively highly stressed and low-sagged cables, whose deformation is achieved essentially by extensibility, while large values are typical of very low-tensioned and higher-sagged cables, whose deformation is mainly of a geometric nature, therefore exhibiting a relative inextensibility.

According to the representation in Figure 23.9 of the variation of the quantity $\overline{\omega}_n/\pi$ with λ^2 for the first six vibration modes, the transition from the dynamics of a taut string ($\lambda^2 = 0$) to that of an inextensible cable ($\lambda^2 = \infty$) is marked by a shift of almost 2π in the value of the adimensional frequency $\overline{\omega}_n$ of symmetric modes. This transition is evidenced by the occurrence of the so-called crossovers, corresponding to values of λ^2 beyond which the natural frequency of the symmetric modes becomes higher than the natural frequency of the same order antisymmetric modes.

Considering the typical values of λ^2 for stay cables, it can be concluded from Figure 23.9 that the corresponding natural frequencies lie outside the transition region and can be obtained using the equations for taut strings. On the contrary, the cables from suspension bridges are generally in the transition range; consequently, their vibration characteristics should consider both the cable geometry and elasticity.

The linearized theory of cable vibration that is on the basis of Eqs. (4)–(6) for the circular frequencies of a vibrating cable does not account for the sag and bending stiffness of these members. In practice, the bending stiffness EI of a cable modifies its dynamic behavior. This effect is more pronounced for short cables, whose sag can be neglected. A simplified formula for the circular frequencies ω_n of a cable clamped at both ends with nonnegligible bending stiffness is given by (Morse and Ingard, 1968)

$$\omega_n = \frac{n\pi}{\ell} \cdot \sqrt{\frac{H}{m}} \cdot \left[1 + 2\sqrt{\frac{EI}{H\ell^2}} + \left(4 + \frac{n\pi^2}{2}\right) \cdot \frac{EI}{H\ell^2}\right]. \tag{10}$$

This expression is valid so long as the value of $EI/H\ell^2$ is small. The relative deviation ε_{EI}^n to the vibrating chord theory of the natural frequencies of a taut cable characterized by a stiffness EI is then given by

$$\varepsilon_{EI}^n = \frac{2}{\zeta} + \frac{\left(4 + \frac{n\pi^2}{2}\right)}{\zeta^2}, \tag{11}$$

where $\zeta = \sqrt{H\ell^2/EI}$. This deviation increases with the order of the mode shape. Considering as negligible differences associated with a value of ε_{EI}^n lower than 5% for the first five modes, it can be concluded that bending stiffness effects are negligible for stay cables with $\zeta \geq 50$.

The difficulty in assessing bending stiffness effects lies in the evaluation of the inertia of the cable, which depends on the degree of constraint of the strands. This degree of constraint varies according to the cable type and protection (locked coil, stranded, parallel wire, with or without grout), and also with the cable length and the curvature. Therefore, although an estimation of EI can be obtained from laboratory tests, it is only from site measurements that an average EI can be assessed. According to Yamagiwa et al. (1997), typical values of EI are around 50%–70% of the stiffness of a solid bar with the same diameter of the cable. Reported values on a cable-stayed bridge employing locked coil cables are of the order of 65%–85% that stiffness (Geier and Wenzel, 2003).

The inclusion of sag effects in the dynamic behavior of the cable is important for long-span cables. In this context, mention is made of the simplified formulae derived by Mehrabi and Tabatabai (1998), which are valid for cables where ζ is no less than 50 and for Irvine parameters λ^2 of less than 3.1 (these authors state that this is the case in 95% of the stay cables on cable-stayed bridges around the world). Accordingly, the nth-order circular frequency of a cable ω_n is given by

$$\omega_n = \frac{\pi n}{\ell} \cdot \sqrt{\frac{H}{m}} \cdot \left(\alpha\beta_n - 0.24\frac{\mu}{\zeta}\right), \tag{12}$$

with

$$\alpha = 1 + 0.039\mu;\ \beta_n = 1 + \frac{2}{\zeta} + \frac{\left(4 + \frac{n\pi^2}{2}\right)}{\zeta^2},$$

where $\mu = \lambda^2$, $n = 1$; $\mu = 0$, $n > 1$ for in-plane modes; and $\mu = 0$ for out-of-plane modes.

The importance of considering sag and bending effects when analyzing the dynamic behavior of a cable lies in the fact that the vibration method can be used for the identification of the installed tension in constructed structures (Caetano et al., 2013). Therefore, this requires an accurate identification of the frequencies and a valid description of their relation to the installed force.

3.2.3 Numerical modeling

The numerical modeling of cables integrated in suspension and cable-stayed bridges can incorporate different levels of simplification. For stay cables, the simplest and also the most common approach consists on the idealization of each cable using the so-called truss element. This is a two-node elastic finite element characterized by no bending stiffness and an axial stiffness EA_0/L, whose weight is concentrated at the nodes (see Figure 23.10). These characteristics correspond to the treatment of the cable as a spring element, not accounting for geometric effects and providing a poor description of the local deformational characteristics: both the sag and angles of deviation at anchorages have null values, the cable's undeformed length is equal to the chord length, and the tension is assumed to be constant along the cable.

Despite the high level of simplification, the linear model is of great interest for a global analysis of the bridge, allowing a good estimation of the force distribution in the cable-stayed bridge, and therefore providing important information for the design of the stay cables. The major source of error associated with the linear model results from geometric effects. So, for taut stay cables with a low λ^2 value, small errors are expected, whereas for less tensioned or very long cables with high values of λ^2, the errors may be significant.

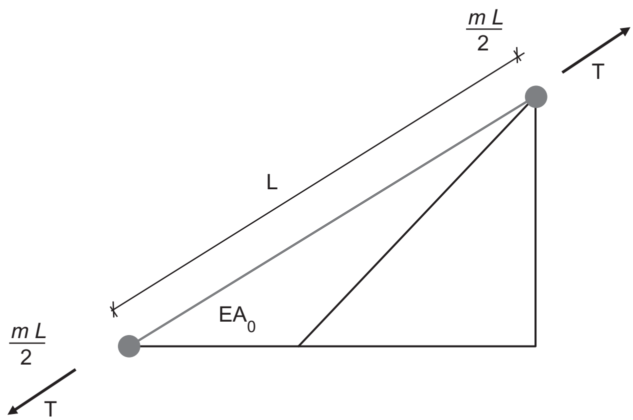

Figure 23.10 Truss element.

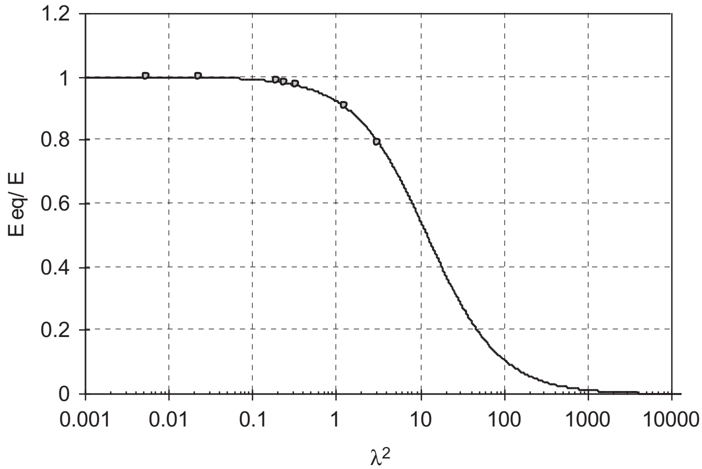

Figure 23.11 Variation of the ratio E_{eq}/E with λ^2.

It is possible to introduce in a simplified form the nonlinear geometric behavior through the use of an equivalent modulus of elasticity E_{eq} incorporating the cable stress condition according to (Ernst, 1965)

$$E_{eq} = \frac{E}{1 + \frac{\gamma^2 \ell^2}{12\sigma^3} E} = \frac{E}{1 + \frac{\lambda^2}{12}}, \tag{13}$$

where γ is the specific weight and σ is the tensile stress of the cable. The variation of E_{eq} with λ^2 is represented in Figure 23.11, showing that for standard taut stay cables ($\lambda^2 < 1$), the introduced correction is very small ($\lambda^2 = 1, E_{eq} = 0.92E$), while for very long stay cables, it becomes significant (for the largest of the Normandy cables, $\lambda^2 = 3.1$, $E_{eq} = 0.79E$).

A natural extension of the idealization of the stay cable as a simple truss element to a series of truss elements (Figure 23.12) has been proposed by Liu (1982) as a computational improvement that allows for the accounting of geometric effects, so long as the discretization is complemented by a geometric nonlinear analysis. Due to the resulting large dimension of numerical models and to computational limitations, the implementation of this modeling technique has not been a current trend in the global modeling of a cable-stayed bridge. It should be noticed, however, that currently available commercial software and computer memory allow for reasonable computing times in face of the advantages obtained: using an adequate number of elements to discretize a stay cable, the corresponding weight, applied at the nodes, approximates the distributed weight of the cable, and the resulting profile approximates the elastic catenary profile. As for the number of necessary elements to adequately represent the deformational and vibrational behavior of a stay cable, it has been shown (Caetano, 2007) that a discretization of a short and a long cable in 20 truss elements provides

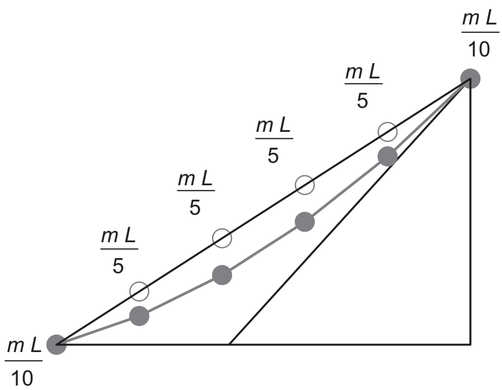

Figure 23.12 Multilink approach: undeformed and deformed mesh under self-weight.

relative errors of less than 5% in the parameters that characterize the cable deformation and vibration. A lower number of truss elements (10 per cable) can be used when local parameters, like rotations, and only the first three vibration modes are of interest.

The multilink approach is the most adequate to model suspension bridge cables. However, given that suspension cables have low stress, convergence problems may occur in the determination of the deformation under self-weight. The addition of bending stiffness to the cable by replacing truss elements by beam elements can mitigate this difficulty, with the advantage of representing the actual behavior of cables.

3.3 Cable vibrations and damping

3.3.1 Cable damping

Suspension and cable-stayed bridges typically exhibit a very low amount of structural damping. This damping decreases with the span length. Lower-limit values of the structural damping ratio for suspension and cable-stayed bridge vibration modes driven by the cables are systematized in Table 23.4 based on the experience achieved with the construction of the bridges of the Honshū-Shikoku Project (Fujino et al., 2012).

Table 23.4 Limit Lower Structural Damping ξ of Cable Vibration Modes in Suspension and Cable-Stayed Bridges (Fujino et al., 2012)

Bridge Type	Deck Type	Vertical Modes	Torsion Modes
Suspension	Truss	0.6%	0.3% ÷ 0.6%
	Box	0.3%	0.3%
Cable-stayed	Truss	1.1%	1.1%
	Box	0.3%	0.3%

Individual cables, typically from cable-stayed bridges, and hangers from suspension bridges, exhibit an intrinsic damping ξ of 0.05%–0.5% (Tabatabai and Mehrabi, 2000). This interval covers most of the values indicated by other authors based on their experience (Macdonald, 2001; Yamaguchi and Fujino, 1998; Caetano and Cunha, 2011), although it should be stressed that damping varies with the amplitude of vibration, and also that different methodologies in the corresponding assessment explain the wide dispersion of values found in the literature.

When actuated by wind, an additional aerodynamic damping appears due to the friction of the cable with the surrounding air. For relative displacement of the cable in the downwind direction, this damping, expressed in terms of the logarithmic decrement of the nth mode, can be determined from (Service d'Etudes Techniques des Routes et Autoroutes (SETRA), 2002)

$$\delta_a = \frac{\rho \pi U D C_D}{m \omega_n}, \tag{14}$$

where ρ is the density of the air (1.23 kg/m^3 for standard temperature and pressure), U is the mean wind velocity, D is the outer diameter of the cable, C_D is the drag coefficient, m is the distributed mass of the cable, and ω_n is the nth-order circular frequency of the cable.

In the crosswind direction, the aerodynamic damping of the cable is half that of the downwind direction.

The total damping of a cable, δ_t, is then given by the sum of the intrinsic damping with the aerodynamic damping:

$$\delta_t = 2\pi\xi + \delta_a. \tag{15}$$

Even though aerodynamic damping has the same order of magnitude of intrinsic damping for design wind velocities, the total damping of cables is generally low. The simultaneous flexibility of these members makes them vulnerable to vibrations induced by the wind and by traffic on a bridge. Even though the mechanisms behind cable vibration are not yet fully understood, some of the phenomena have been identified and characterized (namely, buffeting, vortex shedding/lock-in, galloping, aerodynamic interference, rain-wind-induced vibration, dry galloping, and parametric excitation). The following sections will briefly describe the main characteristics of these phenomena. An additional section will focus on the design of vibration mitigation devices.

3.3.2 Buffeting

When immersed in a flow (the wind) a cable is subjected to surface pressures that, integrated along the section, represent the applied wind loads. These loads can be split into two parcels: one constant, associated with the mean wind velocity; and one varying with time, representing the turbulent component. The corresponding effects are also treated separately, the former parcel leading to average stresses and deformations and the latter being responsible for the vibrational component of the response. The turbulent component of the wind loads, which is the subject of the present section, varies directly with the mean wind velocity and with the intensity of turbulence (Caetano, 2007).

As an elastic system, the amplitude of the cable response increases with the growth of buffeting forces, and hence with the mean wind velocity. However, the growth of wind velocity also leads to an increase of the aerodynamic damping, as evidenced by Eq. (14). The significant increase of the aerodynamic damping at high wind velocities prevents the occurrence of important cable oscillations under buffeting loads in most situations. Therefore, even though the amplitudes of vibration caused by buffeting forces in cables under extreme winds should be assessed and limited in order to prevent local damage at the anchorages and shock effects in stabilizing cables (Service d'Etudes Techniques des Routes et Autoroutes (SETRA), 2002), no fatigue problems are posed.

3.3.3 Vortex shedding/lock-in

In the presence of a circular cylinder with diameter D, a uniform wind flow detaches from the surface and generates a turbulent wake, characterized by alternate shedding of vortices at the top and bottom detachment points at a frequency f_v defined as a function of the Strouhal number St as follows:

$$f_v = \frac{USt}{D}. \tag{16}$$

The Strouhal number St depends upon the cross-section shape and is approximately constant with the Reynolds number Re for a wide range of values. For practical applications with circular cylinders, a constant value of St of 0.2 can be considered.

The shedding of vortices in the wake of the cylinder induces approximately sinusoidal excitation components that result in oscillations, normally characterized by very small amplitudes. If the frequency of vortex shedding approximates the frequency of the cable, a resonance effect takes place, which is designated as *vortex resonance*. An increased oscillation leads the cylinder to interact strongly with the flow and control the vortex-shedding mechanism for a certain range of variation of the wind velocity; i.e., an increase of the flow velocity by a few percentage points won't change the shedding frequency, which coincides with the cable natural frequency. This aeroelastic phenomenon is commonly known as *lock-in* or *synchronization* and originates additional across-wind loads.

According to Dyrbye and Hansen (1996), the risk of vortex-induced vibrations is higher when the flow is smooth, a situation that is typical of isolated structures located by the sea. It can also be high for structures located in the wake of slender nearby structures of similar size. On the contrary, large-scale turbulence reduces the aerodynamic damping.

The occurrence of violent vortex-induced vibrations depends on the intensity of large-scale turbulence, as well as on the intrinsic structural damping, which is characterized by the *Scruton number* S_c, a nondimensional parameter defined by

$$S_c = \frac{2\delta m_e}{\rho D^2}, \tag{17}$$

where δ is the logarithmic decrement of the structural damping and m_e is an equivalent mass per unit length (for a uniform cylinder, $m_e = m$).

High Scruton numbers reduce the risk of violent vortex-induced vibrations. According to Dyrbye and Hansen (1996), no risk of lock-in exists for S_c values greater than about 20. On the contrary, the risk of *lock-in* is very significant if S_c is less than 10.

Eq. (16) for the definition of the vortex-shedding frequency f_v can also be used to predict the so-called critical velocity at lock-in, U_{cr}, assuming a constant St of 0.2:

$$U_{cr} = 5 f_v D. \tag{18}$$

For the shortest stay at the Vasco da Gama Bridge—with a length of 35 m, a diameter of 160 mm, and a fundamental frequency of 3 Hz—the critical velocity associated with the occurrence of lock-in in the first mode would be 2.4 m/s. This velocity is clearly too low to provide a significant energy input for the occurrence of cable oscillations. On the contrary, fixing a critical wind velocity of 12 m/s, relevant for deck vibrations, a shedding frequency of 15 Hz would be obtained, meaning the possible occurrence of vortex resonance of this cable in the fifth mode of vibration.

It is possible to estimate the amount of damping ξ required to avoid vortex-shedding vibrations, based on the practical rule of ensuring a S_c value greater than 20:

$$\xi \approx \frac{\delta}{2\pi} \geq \frac{6D^2}{\pi m}. \tag{19}$$

The study by Tabatabai and Mehrabi (2000) centered on a database formed by all the stays of 16 cable-stayed bridges has shown that a damping coefficient ξ of 0.7% would lead to Scruton numbers greater than 20 for 90% of the stay cables and, therefore, to stable cables. The application of Eq. (19) to the cable of the Vasco da Gama Bridge (as mentioned previously) leads to a required damping coefficient of around 0.12%.

With regard to the characterization of the vortex-shedding phenomenon in terms of the definition of wind forces and evaluation of the response, no completely successful analytical method has been developed yet. Instead, several empirical analytical models have been developed to represent the vortex-induced response of bluff cylinders, whose parameters are obtained from experimental data (Simiu and Scanlan, 1996). This is, for example, the case of the formula obtained by Griffin et al. (1975), which gives the maximum relative amplitude of vibration y_0/D as

$$\frac{y_0}{D} = \frac{1.29}{\left[1 + 0.43\,(2\,\pi\, St^2 S_c)\right]^{3.35}}. \tag{20}$$

Considering the usual values found for the S_c numbers for cables of cable-stayed bridges, it becomes evident that the amplitudes of vibration are generally very small.

Davenport (1994) states that the amplitude of vortex-shedding vibration rarely attains half the cable diameter.

In the case of the Vasco da Gama Bridge, where the measured logarithmic decrement damping of the shortest stays is about 0.0085 (without damping devices) and the S_c number is 23.7, the maximum amplitude of vortex-induced vibration would be $0.0183D$ (3 mm). Although irrelevant for vortex-induced vibration, damping devices were installed in all stays, leading to a S_c number of 233 for the shortest stays.

3.3.4 Galloping

Galloping is an instability phenomenon typical of slender structures with rectangular or "*D*" cross sections, which is characterized, in a similar manner to vortex shedding, by oscillations transverse to the wind direction that occur at frequencies close to some natural frequency of the structure. The phenomenon is, however, quite different from vortex-induced vibration. In effect, while the latter originates small amplitudes of oscillation in restricted ranges of wind velocity, galloping occurs for all wind speeds above a critical value and produces high-amplitude vibrations, which may be 10 times the typical body dimension or even more.

The onset condition for the occurrence of galloping is given by the occurrence of a negative aerodynamic damping generated by the vibration of a cable in a wind flow. This is achieved when

$$\left(\frac{dC_L}{d\beta}+C_D\right)_{\beta=0}<0, \tag{21}$$

where C_D and C_L are the drag and lift coefficients and β is the angle of attack of the wind flow. Eq. (21) is the so-called *Glauert-Den Hartog* criterion for incipient galloping instability (Simiu and Scanlan, 1996).

The analysis of Eq. (21) shows that circular cross sections are never subjected to instability by *galloping*, as the derivative $dC_L/d\beta$ is always null. So, except for the cases where the external shape has been altered, by the presence of either ice or water rivulet (see Sections 3.3.7 and 3.3.8), instability of the cables by galloping should not be expected in cable-stayed bridges employing circular cross sections for these elements. However, the studies of Matsumoto et al. (1992) and Saito et al. (1994) have shown that galloping can occur for inclined circular cables. The reason presented is the appearance of an axial flow behind the cable for certain yawing angles, which favors instability. More recently, other aspects have been investigated, which will be discussed in Section 3.3.7.

Based on experimental testing, some authors have developed formulae for the evaluation of the onset wind velocity of divergent oscillation, as a function of the Scruton number. Honda et al. (1995) proposed the following formula for the critical reduced velocity $\overline{U}_{cr}$:

$$\overline{U}_{cr}=\frac{U_{cr}}{fD}=10\cdot S_c{}^{2}/_{3}, \tag{22}$$

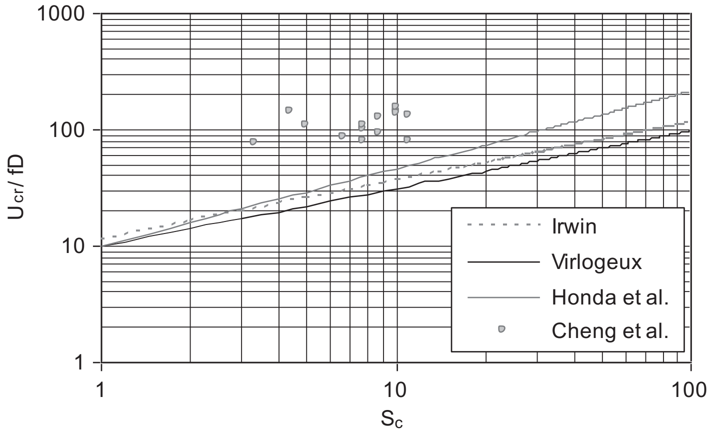

Figure 23.13 Critical reduced wind velocity versus *Sc*.

where f is the cable natural frequency and U_{cr} is the critical wind velocity for the onset of divergent oscillation. Irwin (1997) proposed for the PTI Guide Specification (2007) that

$$\overline{U}_{cr} = \frac{U_{cr}}{fD} = c \cdot \sqrt{S_{c0}}, \tag{23}$$

where $S_{c0} = S_c/(4\pi)$ and the constant c is 40 for circular cross sections. Virlogeux (1998) referred to an identical formula but considered a constant c of 35. These authors have stressed, however, that one should be cautious in the use of Eq. (23), as very conservative estimates are obtained. Figure 23.13 represents the variation of the critical wind-reduced velocity with S_c according to the three referred formulae. This figure also includes experimental values obtained by Cheng et al. (2003) in laboratory tests and can be further used to define a minimum damping necessary to avoid galloping.

Other strategies for avoiding galloping are based on the modification of the cross section. Kubo et al. (2003) proposed a stranded configuration composed by a bundle of individual strands wrapped with a spiral strand. A similar solution was implemented at the hangers of the Akashi Kaikyō Bridge (Fujino et al., 2012). Matsumoto et al. (1995) proposed the introduction of helical plates along the smooth surface of the cable. In both cases, the axial flow in the wake of the cable is disturbed by the presence of the strand and plates.

3.3.5 Aerodynamic interference

Aerodynamic interference occurs whenever a cable or a group of cables lies in the wake of other cables or structural elements. The perturbation introduced by the first obstacle "seen" by the wind affects the wind flow around the close obstacles, creating local turbulent conditions. The high flexibility of cables makes these elements

Figure 23.14 Multiple parallel stay cables at Oresund Bridge (Gimsing and Nissen, 1998). Reprinted by permission of Taylor & Francis Ltd. (http://www.tandfonline.com).

extremely vulnerable to oscillations. These oscillations occur more easily in locations of low turbulence.

A typical situation of aerodynamic interference occurs with groups of parallel cables. These have been used in several cable-stayed bridges, particularly in Japan, with the purpose of reducing the size of the cables. Multiple cables are distant from each other by only a few diameters and are anchored at the same level in the tower and deck. Figure 23.14 shows the twin stay cables employed on the Oresund Bridge, linking Denmark and Sweden. Figure 23.15 shows the possible arrangements of cables.

It has been observed that, under particular conditions, the cable assembly may undergo vibrations. These oscillations are due to *vortex resonance*, to *galloping* of the cable assembly, or to so-called *interference* or *wake galloping*. The last phenomenon is no more than a *galloping* that occurs on the downstream cable(s) induced by the turbulent wake of the upstream cable(s). The oscillation of the downstream cable (s) may induce also a perturbation of the flow around the upstream cable(s), generating oscillation of these cables, designated as *interference galloping*.

The EC1 (EN 1991-1-4, 2005) proposes some conservative formulae for the evaluation of instability by wake effects. Matsumoto et al. (1989), Miyata (1991), and Tanaka (2003) define the main aspects of the phenomenon, concluding that instability

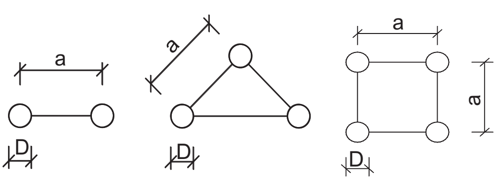

Figure 23.15 Possible arrangements of grouped stay cables.

can be found both for close-spaced ($D \leq x \leq 4D$ and $-2D \leq y \leq 2D$; see Figure 23.15), and largely spaced cables ($8D \leq y \leq 20D$), where the interference effects occur only for the downstream cable. Interference galloping was observed in several cable-stayed bridges in Japan, such as the Hitsuishijima, Iwakurojima, Yobuko, and Shima Maruyama bridges (Narita and Yokoyama, 1991). For the particular case of the Yobuko Bridge, amplitudes of oscillation of $2.5D$ were reported. Kubo et al. (1994) and Kubo (1997) proposed the following measures to prevent interference effects: adopt a close spacing between cables in the range of 1.2–1.3D, which proved to show no galloping at a reduced wind velocity $\overline{U} = U/fD$ of 200; connect parallel cables by spacers or stringers at lengths defined by a deflection of the connecting points no greater than $0.2D$.

It is still relevant to mention the interference effects observed in stranded cables. The use of bundles of individually protected strands clamped with collars at distances of 30–50 m is a technology introduced in 1988. Although recently constructed bridges normally employ an encasing of the strands in HDPE pipes, many bridges constructed in the late 1980s and early 1990s employ the former described technology and have suffered from diverse vibration problems. The most frequent vibrations are associated with interference phenomena of a similar type to the previously described ones and occur due to the aerodynamic interaction between strands, which shock against each other, generating global vibration of the cable and producing a significant and disagreeable rattling noise. Virlogeux (1998) defines these movements as "breathing of strands." Vibrations are started by wind and attain significant amplitudes of around $1D$-$2D$. This breathing of the cables produces damage of the collars, and so it may be necessary to encase the bundles in pipes. However, there is the risk of "slapping" the pipes against the bundles, as the latter are not normally blocked inside the former. This problem has been reported at the Glebe Island Bridge in Australia (Service d'Etudes Techniques des Routes et Autoroutes (SETRA), 2002).

3.3.6 Rain-wind-induced vibration

Although rain-wind-induced vibration of power lines, designated as *rain vibration*, had been reported in the literature 10 years earlier (Hardy et al., 1975; Hardy and Bourdon, 1979), it was only in 1986 that Hikami identified the phenomenon of cable vibration in cable-stayed bridges induced by the combined action of wind and rain during the construction of the Meiko-Nishi Bridge (Hikami, 1986; Hikami and Shirashi, 1988). The general characteristics identified by these authors were soon associated with several past and many subsequent occurrences of vibrations in cable-stayed bridges. It is presently considered that rain-wind-induced oscillations are in the origin of about 95% of the reported vibration problems in cable-stayed bridges (Wagner and Fuzier, 2003).

Despite the intense research developed both through wind tunnel testing and through observation of prototypes, the mechanisms of rain-wind-induced vibrations are yet to be fully understood. Some main aspects of this complex phenomenon can be outlined, however (Tanaka, 2003): first, it is under the combined action of rain and wind, at specific angles of attack and intensity of rainfall, that rivulets can be

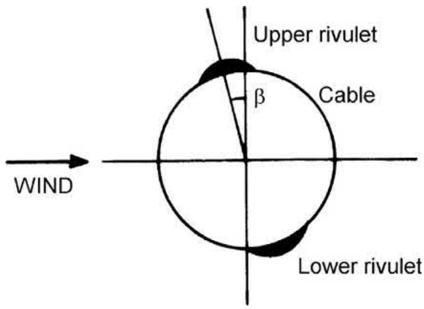

Figure 23.16 Formation of water rivulet on the upper and lower surfaces of cable in rainy and windy conditions.

formed at the upper and lower surfaces of the cable (see Figure 23.16). The formation of these rivulets as the result of a balance between gravitational, aerodynamic, and surface capillarity forces leads to a loss of symmetry of the cable cross section and, therefore, to a variation of aerodynamic forces on the cable. Eventually, a decrease in the drag coefficient and a negative slope of the lift coefficient associated with a small variation of the angle of attack may result in a negative aerodynamic damping and, therefore, in a galloping instability of Den Hartog type (see Section 3.3.4). Once the cable starts oscillating, the rivulets tend to oscillate circumferentially with the same frequency. A coupling of this oscillation with the flexural oscillation of the cable may lead to aerodynamic instability, which may intensify the vibrations.

Research conducted all over the world (e.g., Matsumoto, 1998; Yamaguchi, 1990; Peil and Nahrath, 2003; Verwiebe, 1998) has further led to the identification of different excitation mechanisms behind the phenomenon of rain-wind-induced excitation. The complexity of the phenomenon is evident and can still be enhanced when considering other variables to the problem, like the adhesion property of the cable's coating material (Flamand, 1994) or the intensity of the rainfall (Ohshima and Nanjo, 1987; Main and Jones, 1999). Based upon the experience gathered from the observation of rain vibration in prototypes of cable-stayed bridges and on wind tunnel tests, the main conditions and characteristics associated with the occurrence of the phenomenon can be summarized as follows (Hikami and Shirashi, 1988; Matsumoto, 1998; Main and Jones, 1999; Sarkar et al., 1994; Tanaka, 2003):

- The wind speed varies in the range 5–20 m/s, the majority of reported cases lying in the interval 8–12 m/s, corresponding to reduced wind velocities U_{cr} ($U_{cr} = U/fD$) of 20–90.
- The wind direction varies in the range of 20°–60° to the longitudinal axis of the bridge.
- The cables are inclined to the horizontal of angles of 20°–45°.
- There is rain (whether heavy, light, or drizzle), although in most cases, moderate rain is more likely to produce the effect.
- The cable surface is smooth, such as polyethylene or painted metal cased cables.
- The cable diameter is in the range of 80–200 mm.
- Typical vibration frequencies are in the range 0.3–3 Hz.
- Typical amplitudes of vibration are about twice the cable diameter. However, amplitudes of 7D have been observed.

- The structural damping of the cables is very low (with logarithmic damping decrement less than 0.01).
- The cable is located behind the bridge pylon and declines in the direction of the wind.
- The cable-stayed bridge is located in an area where the intensity of turbulence is low.
- The vibration orbit varies according to the intensity of the rainfall: for light rain and drizzle, vibration occurs essentially in the vertical plane, whereas for heavy rainfall, the orbit may exhibit significant two-dimensionality.

With respect to possible measures against rain-wind vibrations, two strategies can be followed—one based in the application of aerodynamic measures to the cable cross section and the other based in the increment of damping through the addition of special devices.

As for the implementation of aerodynamic measures, and given that it seems conclusive that the motion of rivulets worsens oscillations, the adoption of nonsmooth surfaces has proven an adequate strategy. Protuberances, helical wire whirling, and a dimpled surface (Figure 23.4) have shown to disrupt the formation of rivulets.

With respect to the addition of damping devices and, in the absence of other study, the indication proposed by the *PTI Guide* (PTI Guide Specification, 2007) to ensure that the Scruton number S_{c0} (calculated as $S_{c0} = m\,\xi/\rho\,D^2$) is greater than 10 in order to avoid rain-wind-induced vibrations can be employed as a practical rule. Given the very low intrinsic damping ratios of cables, the necessity to design dampers for the majority of cables seems evident.

3.3.7 Dry galloping

The observation of important cable vibrations with characteristics similar to those reported for rain-wind-induced vibration, but occurring under dry weather, has motivated further research of the phenomenon identified presently as dry galloping. Matsumoto (1998) discussed the high-speed vortex shedding associated with the formation of an axial flow in the wake of the cable. Other authors (e.g., Larose and Zan, 2001; Larose et al., 2003; Tanaka, 2003) noticed these vibrations occurred in the critical Reynolds number range. For smooth cylinders, this range is (2×10^5)–(8×10^5) (Service d'Etudes Techniques des Routes et Autoroutes (SETRA), 2002), meaning that for a circular stay cable with a diameter of 0.20 m, the critical Reynolds range would occur for mean wind velocities of 20–60 m/s. Assuming the vibration of the cable in that particular range, a small increase of the mean wind velocity might create a sudden decay of the drag force, hence of the lift force over the cable, resulting in reduced motion. The approximation to the equilibrium position would cause an increase of the relative velocity of the flow and so a slight increase of the drag force and of cable vibration, with the consequence of reducing the relative wind velocity of the flow. An oscillation of the cable could then be created merely by slight fluctuation of wind flow. This phenomenon was designated as "drag crisis." More recently, a bistable behavior of a cable has been identified (Nikitas et al., 2012; Matsumoto, 2014), characterized by random jumps of the drag and lift forces. These may be associated with the asymmetry created by the alternate detachment of air bubbles from the cylinder section, and they are increased by asymmetries of geometric nature as those resulting from the deformation of the cable pipes associated with fabrication tolerances or storage (Flamand et al., 2014).

3.3.8 Ice galloping

The accumulation of ice on a circular cable during an ice or freezing rain storm originates a modification of the cross section, which may become aerodynamically unstable. Galloping vibrations of cables due to ice accretion have been reported frequently in cables of transmission lines. Regarding bridges, ice galloping in cables has been investigated more recently (Demartino and Ricciardelli, 2017). Despite the fatigue problems that can result from the very high amplitudes observed, cable vibrations can also trigger the shedding of ice, what presents an important safety risk for vehicles and passengers, as well as for circulating pedestrians. According to Demartino et al. (2015) referring to Gimsing and Georgakis (2012), between 2004 and 2007, the Storebælt Bridge was closed an average of 14.3 h a year, 12 of which were due to falling ice and snow. Several other bridges of the Northern Hemisphere had similar problems.

The simplest approach to define the onset wind velocity of ice galloping is the formula presented in Eurocode 1 (EN 1991-1-5, 2003),

$$U_{cr} = V_{cG} = \frac{2\,S_c}{a_G}.f.D, \tag{24}$$

where a_G is the factor of galloping instability, defined as 1 for ice accreted circular cylinders. This corresponds to the Den Hartog (1932) formula derived for vertical galloping of conductors of power lines under perpendicular wind where

$$a_G = -\left(\frac{\partial C_L}{\partial \beta} + C_D\right). \tag{25}$$

The unit value of a_G results from the assumption of $C_D = 1$ and $C_L' = \frac{\partial C_L}{\partial \beta} - 2$.

When applied to stay cables, this formula is considered conservative. Furthermore, it addresses a specific mode of galloping in which the wind is perpendicular to the direction of vibration, which does not correspond to the reality in most stay cables. Jones (1992) formulated a 2-degree-of-freedom (2-DOF) model of galloping in which a coupling between in-plane and out-of-plane vibrations appears, with the consequence that, although predominantly vertical, galloping vibrations may have horizontal component or even lead to elliptical orbits, depending on the values of the aerodynamic coefficients and their derivatives.

Macdonald and Larose (2008) also developed a 2-DOF formulation of the galloping problem evidencing similar behavior and including the dependence of the aerodynamic coefficients and their derivatives on the Reynolds number. These authors derived the quasi-steady aerodynamic damping ζ_a of a cylinder of arbitrary cross section yawed/inclined to the flow as (Macdonald and Larose, 2006)

$$\zeta_a = \frac{\mu Re}{4m\omega_n}\cos\beta\left\{\cos\beta\left[C_D\left(2\sin\phi+\frac{\tan^2\beta}{\sin\phi}\right)+\frac{\partial C_D}{\partial \mathrm{Re}}\mathrm{Re}\sin\phi+\frac{\partial C_D}{\partial \phi}\cos\phi-\frac{\partial C_D}{\partial \beta}\frac{tan\beta}{\sin\phi}\right]\right.$$
$$\left.-\sin\beta\left[C_L\left(2\sin\phi-\frac{1}{\sin\phi}\right)+\frac{\partial C_L}{\partial \mathrm{Re}}\mathrm{Re}\sin\phi+\frac{\partial C_L}{\partial \phi}\cos\phi-\frac{\partial C_L}{\partial \beta}\frac{tan\beta}{\sin\phi}\right]\right\}. \tag{26}$$

In this formula, μ is the dynamic viscosity of the fluid, and ϕ is the angle between U and the cable axis. This formula can be understood as addressing a general galloping problem, containing as particular case the aerodynamic damping leading to the Den Hartog formula ($\beta = 90°$; $\phi = 90°$),

$$\zeta_a = \frac{\rho DU}{4m\omega_n}\left(C_D+\frac{\partial C_L}{\partial \beta}\right); \tag{27}$$

and also the one associated with drag crisis, in the region of critical Reynolds number ($\beta = 0°$; $\phi = 90°$),

$$\zeta_a = \frac{\mu Re}{4m\omega_n}\left(2C_D+\frac{\partial C_D}{\partial \mathrm{Re}}\mathrm{Re}\right); \tag{28}$$

and, finally, it can be applied to ice accreted cables. The difficulty in application of these formulae lies in the need of available experimental data.

Referring to experimental data, it is relevant to mention the studies of Demartino and Ricciardelli (2017), who analyzed instability regions using aerodynamic coefficients determined from wind tunnel tests on ice accreted hanger in order to determine the requirement of damping. These authors concluded that for the subcritical *Re* number, the instability observed was of Den Hartog type, with no dependence of aerodynamic coefficients on the Reynolds number. In the critical *Re* number region, an instability was observed with characteristics of a combined Den Hartog and drag crisis type. Another very important test, although not focusing on ice accreted galloping, respects the study at NRC of an inclined cable with diameter of 0.219 m over the critical and supercritical Reynolds region (McTavish et al., 2018). In the critical *Re* region, it was observed that the drag coefficient dropped and the lift coefficient increased, exhibiting fluctuations that contributed to destabilize pressures and define instabilities. Imperfections of the surface may trigger instability for which the PTI criterion defined in terms of a minimum Scruton number may be insufficient. On the contrary, in the supercritical *Re* region tested, it appears that, although instability appeared again, the damping determined from the Scruton number limit condition in PTI was sufficient to attenuate vibrations.

Finally, it should be noted that the application of the Den Hartog formula refers to an assumption of a uniform and constant cross section, which may not be the case in ice-accreted cables. This aspect was studied by Svensson (2004). It is possibly not easy to define an extension of the cable prone to galloping, but a reduction factor might help to alleviate the damping measures for the higher wind velocities extracted from a probabilistic analysis of ice deposition along the cable.

3.3.9 Parametric excitation

The vibration of the deck and towers caused by wind, traffic, and earthquake, produces an *indirect excitation* of the cables through motion of their anchorages. In certain circumstances, the induced cable vibrations attain very high amplitudes. Two phenomena can be identified under these circumstances, here designated as *external* and *parametric* excitation. The *external excitation* corresponds to an amplification of motion applied at some anchorage perpendicularly to the cable chord, while the *parametric excitation* corresponds to oscillations in the direction of the chord. The phenomena of *external* and *parametric excitation* have been observed in several bridges in the past (some examples are the Brotonne Bridge in France, Ben-Ahin and Wandre Bridges in Belgium, and the Annacis Bridge in Canada).

For simplicity, external and parametric excitation of stay cables are normally analyzed by separating these members from the bridge structure (see Figure 23.17). The amplification of the deck/tower motion due to a sinusoidal excitation applied at one end is then calculated in order to define the amount of damping necessary to prevent the cable system to undergo large vibrations.

Using this approach and a series of simplifications (namely, neglecting the sag effect and the contribution of modes other than the resonant), the following equations have been obtained for the amplitude of oscillation of a stay cable with distributed mass m and chord length ℓ tensioned with a force T subjected to a harmonic excitation perpendicular to the chord with frequency ω and amplitude z_B at one end (Caetano, 2007):

$$w(x,t) = z_B \cdot \frac{x}{\ell} \cdot \sin(\omega t) + \alpha_1(t) \sin\frac{\pi x}{\ell} \tag{29}$$

with

$$\alpha_1(t) = a\sin(\omega_1 t - \gamma) + \frac{3\lambda}{2\pi\sqrt{X_0 \ell}} a^2 \cdot \left[1 - \frac{1}{3}\sin(2\omega_1 t - 2\gamma)\right], \tag{30}$$

where ω_1 is the first circular frequency of the cable, given by the taut string formula

$$\omega_1 = \frac{\pi}{\ell}\sqrt{\frac{T}{m}}. \tag{31}$$

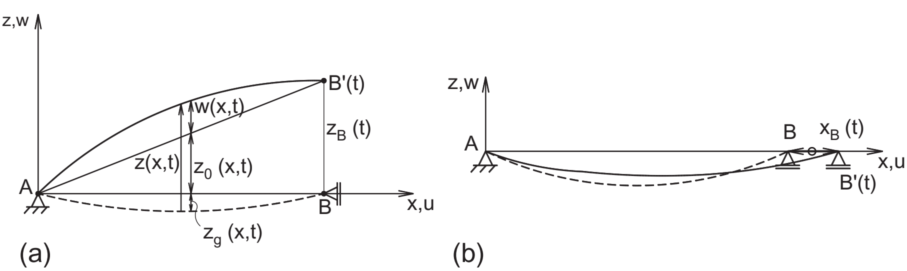

Figure 23.17 Stay cable subjected to harmonic (a) transverse and (b) longitudinal motion at one anchorage.

The amplitude of vibration a (that governs the total response) and the phase of the response γ in Eq. (30) are given as a function of the Irvine parameter λ^2 and the damping ratio of the first mode ξ_1 by

$$a = \frac{z_B}{\pi \xi_1} \cdot \frac{1 - \left(\frac{\lambda}{\pi}\right)^2}{\left[1 + \frac{1}{2}\left(\frac{2}{\pi}\right)^4 \lambda^2\right]^{1/2}} \cdot \sin\gamma \tag{32}$$

and by the solution of

$$\sin^2\gamma \cdot \tan\gamma = \frac{32}{3} \cdot X_0 \ell \cdot \frac{\left[1 + \frac{1}{2}\left(\frac{2}{\pi}\right)^4 \cdot \lambda^2\right]^4}{\left[1 - \left(\frac{\lambda}{\pi}\right)^2\right]^2 \cdot \left[1 - 32\frac{\lambda^2}{\pi^4}\right]} \cdot \frac{\xi_1^3}{z_B^2}. \tag{33}$$

External excitation is not an instability phenomenon; rather, it represents the amplification of a support oscillation in which amplitude varies nonlinearly with the amplitude of the former. This oscillation is slightly dependent on the damping coefficient for very large amplitudes of vibration. This can be observed in Figure 23.18 for two cables with different characteristics: one from the Ben-Ahin Bridge in Belgium, with a length of 110 m and Irvine parameter $\lambda^2 = 0.0727$, and another from the Vasco da

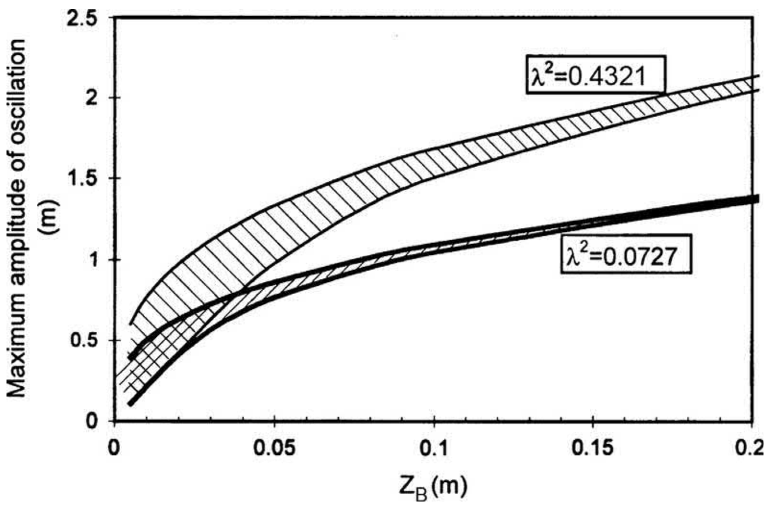

Figure 23.18 Variation of maximum steady-state amplitude of oscillation at primary resonance with amplitude of transversal support oscillation for damping coefficients within the range 0.1%–1.5%.

Gama Bridge, with a length of 226 m and $\lambda^2 = 0.4321$, for damping coefficients in the range 0.1%–1.5%.

Now, considering a longitudinal harmonic oscillation of the support (Figure 23.17b) with amplitude x_B and frequency 2ω, the vertical vibration $w(x,t)$ of the stay cable is again determined by separation of variables considering the contribution of the first mode according to

$$w(x,t) = \alpha_1(t) \cdot \sin \frac{\pi x}{\ell}. \tag{34}$$

The coefficient $\alpha_1(t)$ is given by the solution of

$$\begin{aligned}
&\ddot{\alpha}_1(t) + 2\xi_1\omega_1\dot{\alpha}_1(t) + \omega_1^2 \cdot \left(1 + \frac{\lambda^2}{\pi^2} + \frac{x_B}{X_0}\sin 2\omega t\right) \cdot \alpha_1(t) \\
&\quad + 2\frac{\omega_1^2}{\pi\sqrt{X_0\,\ell}} \cdot \lambda \cdot \left(1 + \frac{\pi^2}{16}\right) \cdot \alpha_1^2(t) + \frac{\pi^2}{4} \cdot \frac{\omega_1^2}{X_0\,\ell} \cdot \alpha_1^3(t) \\
&\quad = \frac{\omega_1^2 \cdot \ell}{2\pi\sqrt{X_0\,\ell}} \cdot \lambda \cdot x_B \sin 2\omega t,
\end{aligned} \tag{35}$$

where X_0 is the elastic elongation of the cable, $X_0 = T\ell/(EA_0)$. This equation has the form of a so-called modified Mathieu equation, which is characterized by a set of secondary resonances; i.e., the response to a harmonic of frequency 2ω is not increased exclusively at resonance, but also at specific ratios between the exciting frequency and the system's natural frequency: 1/2, 1/3, 2, and 3. It is possible then to define instability regions (i.e., intervals of frequency oscillation of the supports where high amplitudes of vibration occur) and also to characterize both the threshold amplitude for the occurrence of instability and the maximum amplitude of oscillation inside the instability regions. These regions are represented in the diagram of Figure 23.19, called a

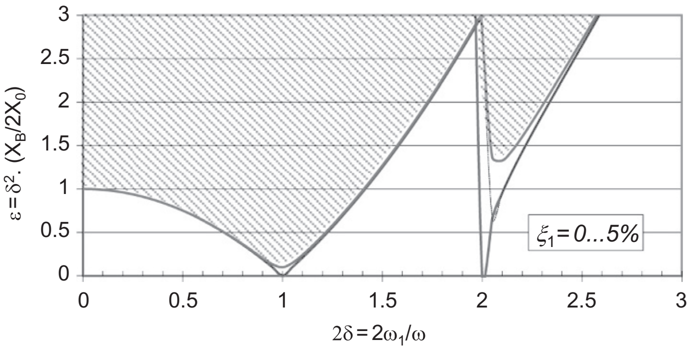

Figure 23.19 Transition curves for different values of the damping coefficient ξ_1: 0 (*in bold*), 0.5%, and 5%.

Strutt diagram (*hatched regions* are unstable) and emanate from $\delta^2 = (\omega_1/\omega)^2 = n^2$ ($n = 1, 2, \ldots$) for each instability region of order n. The lift of the instability regions with the increase of damping means that higher amplitude of support oscillations are required to attain instability for a given excitation frequency ratio δ. This effect is more pronounced for the second-order resonance ($\delta^2 \approx 4$).

Considering the first parametric resonance $\delta^2 \approx 1$, the threshold amplitude for the occurrence of instability is given by

$$\frac{x_B}{2X_0} = 2\xi_1. \tag{36}$$

Once parametric excitation occurs, the oscillation builds up. Tagata (1977), Pinto da Costa et al. (1996), and Clement and Cremona (1996), employing the method of harmonic balance; and Nayfeh and Mook (1979), using the method of multiple scales, obtained an approximation of the steady-state response in the vicinity of this first resonance:

$$\alpha_1(t) = a \sin\left(\omega t - \frac{1}{2}\psi\right), \tag{37}$$

where

$$a = \frac{4}{\pi}\cdot\sqrt{\frac{X_0\ell}{3}}\cdot\frac{1}{\delta}\cdot\left\{1-\delta^2 \pm \left[\delta^4\cdot\left(\frac{x_B}{2X_0}\right)^2 - 4\delta^2\xi_1^2\right]^{1/2}\right\}^{1/2} \tag{38}$$

and

$$\tan\psi = -\frac{2\,\xi_1\delta^2}{2(1-\delta) - \delta^4 a^2}. \tag{39}$$

Eq. (38) is plotted in Figure 23.20 for the Ben-Ahin cable, with 110 m, considering two values of the relative support motion $x_B/(2 \times {}_0)$, of 0.05 and 0.3, and a damping coefficient of 1%. The nonlinearity of the differential equation induces a bending of the frequency-response curves into the right, as can be observed in this figure, which leads to multivalued responses and, consequently, to a so-called *jump* phenomenon. The evolution of the amplitude of the response is represented by the *arrows* in Figure 23.20, where it can be observed that in a vicinity of the first parametric resonance ($\delta \approx 1$), the trivial solution is not stable.

In order to understand the characteristics and importance of parametric excitation by comparison with external excitation, a study is conducted for the aforementioned Ben-Ahin cable (length 110 m, $\lambda^2 = 0.0727$) using both the analytical expressions given here and a numerical modeling with a FE discretization. The amplitude of steady-state response under longitudinal harmonic motion at the anchorage at twice the linear natural frequency of the cable was calculated considering different

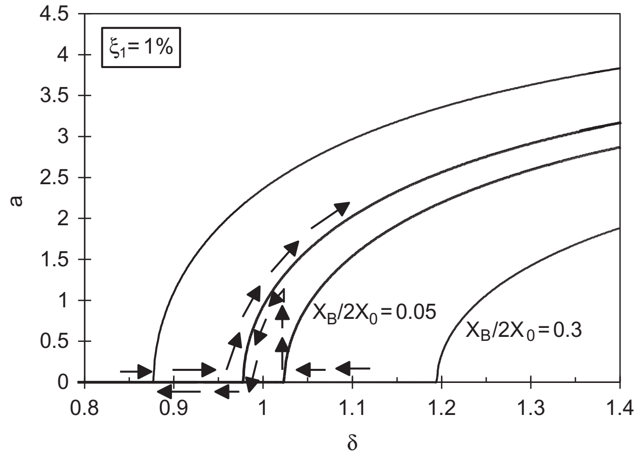

Figure 23.20 Frequency-response functions for a stay cable subjected to two different amplitudes of support motion: $x_B/(2\ X_0) = 0.05$, and $x_B/(2\ X_0) = 0.3$.

amplitudes of support motion and a damping coefficient of 1%. The representation in Figure 23.21 shows that, in comparison with the external excitation response represented in Figure 23.18, parametric excitation induces amplitudes of vibration that almost double the amplitude of oscillations induced by external excitation for identical amplitudes of oscillation. However, as opposed to external excitations, parametric excitation does only occur for longitudinal oscillations greater than 0.006 or 0.012 m for damping coefficients of 0.5% and 1%, respectively.

It is further noted that damping is only important to prevent parametric excitation. Once the oscillations occur, the amplitude is almost independent of the corresponding value.

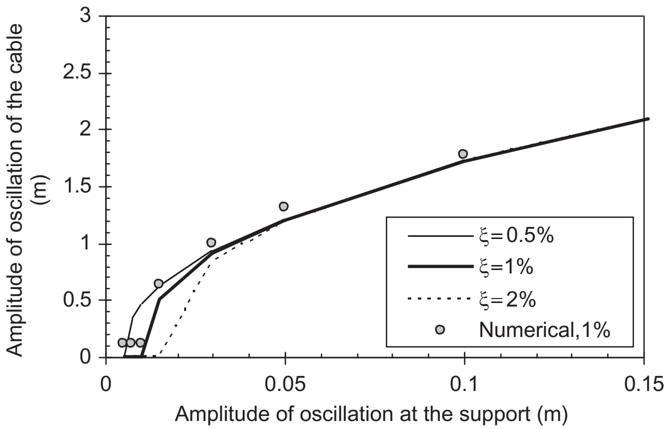

Figure 23.21 Amplitude of a steady-state response of Ben-Ahin cable at the principal parametric resonance.

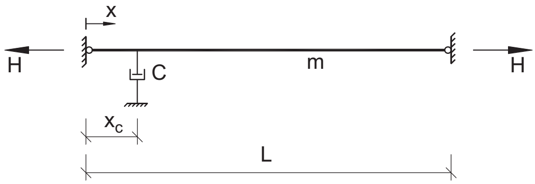

Figure 23.22 Cable with viscous damper.

3.3.10 Design of vibration mitigation devices

The problem of defining the optimal characteristics of a damper installed at a point close to the anchorage of a cable was formerly studied by Kovàcs (1982), who proposed a practical optimal damping estimation method and empirically defined the maximum attainable modal damping.

According to Kovàcs and the illustration of Figure 23.22, the effect of adding a viscous damper with constant c at a distance x_c to the anchorage of a cable of mass per unit length m and length L submitted to a static tension H can be framed by two limiting conditions, under the assumption of null intrinsic damping:

- If $c = 0$, the first vibration mode is undamped (Figure 23.23a), and the dynamic amplification curve associated with the cable tends to infinity at the fundamental frequency ω_{01}.
- When $c =$ infinity (i.e., when a very large damper is installed), the force generated is so large that it blocks the cable at the damper, therefore acting as if there was a support at that location (Figure 23.23b). The consequence is a slight modification of the fundamental cable frequency to $\omega_{01}/(1 - x_c/L)$, but once more, the mode of vibration is undamped, and the corresponding dynamic amplification curve tends to infinity at the frequency $\omega_{01}/(1 - x_c/L)$.

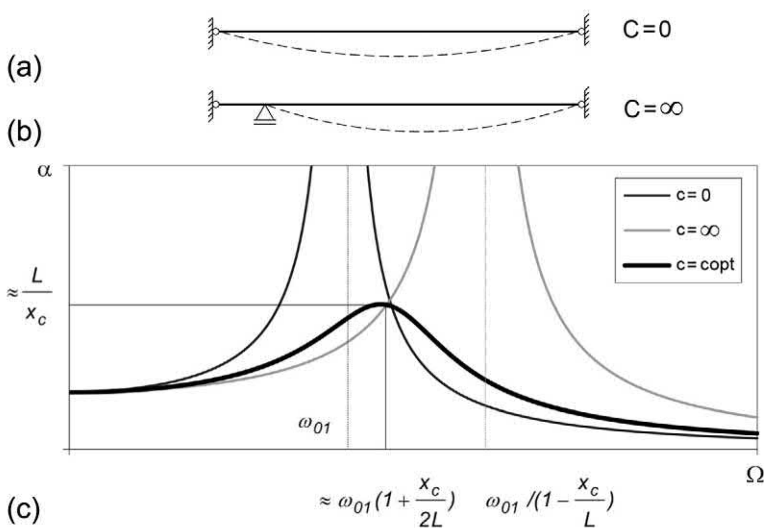

Figure 23.23 Limiting amplification behavior characteristics of cable with attached viscous damper: (a) $c = 0$; (b) $c = \infty$; (c) dynamic amplification curves for $c = 0$, $c = \infty$, and $c = c_{opt}$.

The optimal damper is characterized by a constant c_{opt} that provides the amplification curve represented by the *solid bold line* in Figure 23.23c, whose maximum value is approximated by L/x_c and occurs at the frequency for which the two previously referred amplification curves intersect, $\Omega \approx \omega_{01}(1 + x_c/2L)$. The modal damping associated with this system is the maximum and is given by

$$\xi_{\max} \approx \frac{1}{2} \cdot \frac{x_c}{L}. \tag{40}$$

Kovàcs estimated the optimum damper size c_{opt} as

$$\frac{c_{opt}}{mL\omega_{01}} \approx \frac{1}{2\pi\left(\frac{x_c}{L}\right)}. \tag{41}$$

It is important to note that the ratio x_c/L is normally no greater than 0.015, meaning that the maximum damping added by a viscous damper attached close to the anchorage does not normally exceed 0.75%. Pacheco et al. (1993) have shown that these equations can be extended for higher-order modes. In order to provide a damping coefficient as a function of the constant c, and assuming small values of x_c/L, Pacheco et al. (1993) obtained a curve (Figure 23.24) representing the modal damping of any taut cable for the first few modes of vibration. This universal curve is characterized by a maximum that corresponds to the maximum attainable damping ratio $\xi_{n,\max}$ of the vibration mode of order n, achieved by the attachment of a damper with optimum constant $c_{opt,n}$. These quantities are given by

$$\xi_{n,}\max = 0.52 \cdot \frac{x_c}{L} \tag{42}$$

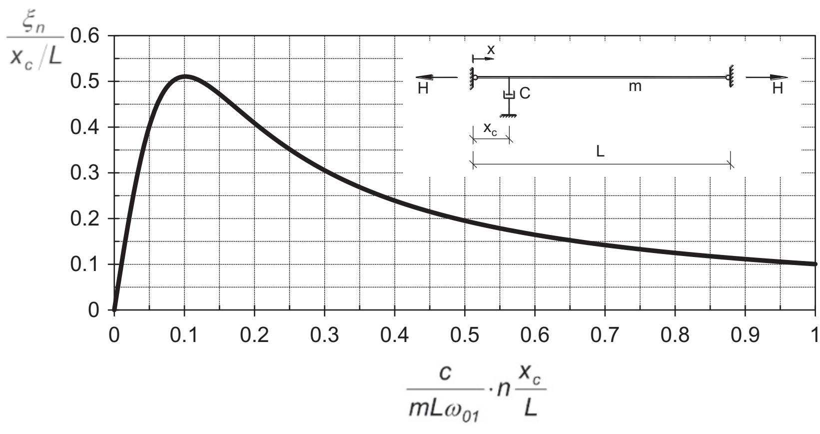

Figure 23.24 Universal curve relating modal damping ratio ξ_n with damper size c, location of damper x_c, and cable parameters, m, L, and ω_{01}.

$$c_{opt,n} = 0.10 \cdot \frac{mL\omega_{01}}{n\dfrac{x_c}{L}}. \tag{43}$$

The interest in the use of the universal curve is that not only can an optimum viscous damper be designed for a particular vibration mode of a cable whose damping coefficient has been specified, but the achieved damping coefficient for other vibration modes can also be estimated.

The universal curve deduced by Pacheco et al. (1993) can be applied to taut cables ($\lambda^2 < 1$), where the distance between damper and anchorage is within a few percentage points of cable length (e.g., 1%–10%). The difficulty in defining this universal curve on the basis of the design applications motivated the development by Krenk (2000) of an analytical representation that can be expressed in the following form:

$$\frac{\xi_n}{x_c/L} = \frac{\eta\, n\, \pi\, x_c/L}{1 + (\eta\, n\, \pi\, x_c/L)^2}, \tag{44}$$

where η is a nondimensional damping parameter, defined as

$$\eta = \frac{\pi\, c}{m\, L\, \omega_{01}}. \tag{45}$$

Eq. (44) provides a good approximation of the universal curve for the first few modes of vibration, so long as the ratio x_c/L is small.

Considering that current applications of cable-stayed bridge construction have resulted in longer cables, with Irvine parameters $\lambda^2 \geq 1$, and where sag effects can be significant, leading to a decrease of damper effectiveness, Crémona (1997) extended the universal curve introduced by Pacheco et al. (1993) to inclined cables with a maximum sag/span ratio of 1:8, and with an Irvine parameter no greater than $4\pi^2$ (first transition region), therefore covering all stays from cable-stayed bridges. Krenk and Nielsen (2002) derived an extended asymptotic solution for shallow cables, evidencing the reduction of efficiency of the damper as a function of the Irvine parameter.

Hoang and Fujino (2007) provided a deeper investigation of the effects of bending stiffness on the performance of viscous dampers installed in taut cables. These authors (Fujino and Hoang, 2008; Hoang and Fujino, 2008) and Krenk and Hogsberg (2005) explored the effect on the performance of dampers induced by other factors, such as the damper flexibility or the flexibility of the support and the nonlinearity of behavior. This research has been systematized by Caetano (2007).

In the context of the design of a damper to control cable vibrations, it is of interest to combine the effects of sag, bending stiffness, and flexibility of the support in order to obtain a global estimate of the reduction of efficiency and the increase of the optimal damping coefficient with respect to the taut cable approach. This can be achieved using the simplified formulae derived by Fujino and Hoang (2008). For the sagged cable with nonnegligible bending stiffness with an installed viscous damper on a flexible support (Figure 23.25), these authors propose the following expression for the attained modal damping ratio:

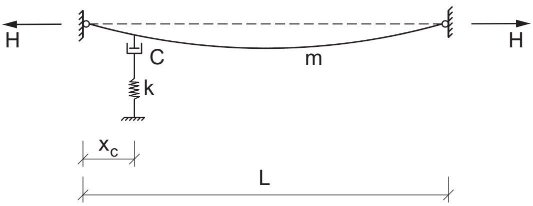

Figure 23.25 Sagged cable with tandem association of viscous damper and spring.

$$\frac{\xi_n}{x_c/L} = R_n \cdot R_{EI} \cdot R_{kEI} \cdot \frac{\eta_n \cdot \eta_{EI} \cdot \eta_{kEI}}{1 + (\eta_n \cdot \eta_{EI} \cdot \eta_{kEI})^2}, \tag{46}$$

where η_n and R_n are the nondimensional damping parameter and the reduction factor due to sag effect, η_{EI} and R_{EI} are the nondimensional damping parameter and the reduction factor due to the bending stiffness EI of the cable, and η_{kEI} and R_{kEI} are, respectively, the nondimensional damping parameter and associated reduction factor related to the stiffness k of the support. These parameters are defined in Table 23.5.

The maximum modal damping ratio is then obtained by

$$\frac{\xi_n^{\max}}{x_c/L} = 0.5 \cdot R_n \cdot R_{EI} \cdot R_{kEI} \tag{47}$$

and occurs for a nondimensional optimal damping parameter η_n^{opt} defined as

$$\eta_n^{opt} = \frac{1}{\eta_{kEI} \cdot \eta_n}. \tag{48}$$

It should be noted that Eqs. (47) and (48) have been derived based on the assumption that the viscous damper is linear. The nonlinearity of the damper is probably one of the

Table 23.5 Definition of Nondimensional Parameters and Reduction Factors for the Efficiency of a Damper Due to Sag, Bending Stiffness, and Flexibility of the Damper Support

Effect	Nondimensional Parameter η_i	Reduction Factor R_i
Sag	$\eta_n = \eta k_n \pi \frac{x_c}{L}$	$R_n = \frac{\left[\tan\left(\frac{k_n\pi}{2}\right) - \left(\frac{k_n\pi}{2} \cdot \frac{x_c}{L}\right)\right]^2}{\tan^2\left(\frac{k_n\pi}{2}\right) + \frac{12}{\lambda^2} \cdot \left(\frac{k_n\pi}{2}\right)^2}$, with $k_n = \frac{\omega_n}{\omega_{01}}$, n is the mode order
Bending stiffness of cable	$\eta_{EI} = 1 - q - \frac{r.q^2}{2}$	$R_{EI} = \frac{(1-q)^2}{1-q-rq^2/2}$, with $q = \frac{1-e^{-r}}{r}$ and $r = \zeta \cdot \frac{x_c}{L}$
Support stiffness k	$\eta_{kEI} = \eta_{EI} + \frac{1}{\overline{\eta}_k}$, with $\overline{\eta}_k = \frac{k\,x_c}{H}$	$R_{kEI} = \frac{\overline{\eta}_k \cdot \eta_{EI}}{1 + \overline{\eta}_k \cdot \eta_{EI}}$

most important causes of reduction of the efficiency; therefore even though small curvature, bending, and support stiffness effects are associated with a typical medium-sized cable, the damper effectiveness can be, in practice, of the order of 50%–70% of the theoretical (Sun et al., 2005).

It is further remarked that the installation of a single damper may not provide sufficient damping to a stay cable. From a study with different combinations of dampers located close to the cable anchorages, Hoang and Fujino (2008) concluded that the combination of two dampers close to the same anchorage does not provide increased damping with respect to the effect of the damper located at the highest distance from the anchorage. On the contrary, the installation of a damper close to each anchorage of a cable leads to an increased damping effect that is asymptotically the sum of the individual contributions from the single dampers.

4. Present challenges and future improvements

The technology of cable construction has greatly evolved during the last decades and the experience from past failures has enabled manufacturers, designers, and researchers to develop more compact, durable, and resistant solutions. Provided with adequate construction, inspection, and maintenance, cables can comply with life cycles of 100 years and even more.

In Europe, where a great number of cable-supported structures were constructed since the beginning of the 20th century, many of such structures are reaching the end of their life, often sooner than expected, as a consequence of increased traffic demands, improper maintenance, and insufficient understanding of the structural behavior and construction errors. An important challenge for the next decade is, therefore, the investment in the accurate characterization of cable condition, namely by early identification of damage, and the improvement of the understanding of vibration phenomena and mitigation devices.

Cable vibrations have been investigated worldwide, with important discoveries and a general understanding of the different sources and mechanisms, as explained throughout this chapter. Nevertheless, the simultaneous presence of several of those sources and the costs and difficulties in the implementation of mitigation devices still result presently in excessive vibrations in many structures, contributing to an accelerated degradation by fatigue. The combination of traffic and wind vibrations is an exacerbating aspect that needs further research. Modern instrumentation and computational power can assist in the observation of cable prototypes to enhance such knowledge, contributing to extend their lifetime.

References

BBR, 2011. BBR HiAM: strand stay cable system. In: Brochure. www.bbrnetwork.com.

Beabes, S., Faust, S., Cocksedge, C., 2015. Suspension bridge main cable dehumidification—an active system for cable preservation. In: Mahmoud, K. (Ed.), Sustainable Bridge Structures. CRC Press, ISBN: 9780429225796 (Chapter 1).

Bloomstine, M., 2006. Main cable corrosion protection by dehumidification—experience, optimization and new development. In: IABSE Symposium Report, January 2006., https://doi.org/10.2749/222137806796236.

Bournand, Y., 1999. Development of new stay cable dampers. Cable-stayed bridges—past, present, and future. In: IABSE Conference, 2–4 June 1999, Malmo, Sweden.

Caetano, E., 2007. Cable vibrations in cable-stayed bridges. In: Structural Engineering Documents. No. 9. Published in English by IABSE. Published in Chinese by CABP, 2012.

Caetano, E., Cunha, A., 2011. On the observation and identification of cable-supported structures. In: Eurodyn'2011 4–6 July, Leuven, Belgium.

Caetano, E., Bartek, R., Magalhães, F., Keenan, C., Tryppick, G., 2013. Assessment of cable forces at the London 2012 Olympic stadium roof. Struct. Eng. Int. 4, 489–500.

Cheng, S., Tanaka, H., Irwin, P., Jakobsen, J., 2003. Aerodynamic instability of inclined cables. In: Fifth International Symposium on Cable Dynamics, 15–18 September, Santa Margherita Ligure, Italy, pp. 69–76.

Clement, H., Cremona, C., 1996. Étude Mathématique du Phénomène d'Excitation Paramétrique Appliqué aux Haubans de Pont. Études et Recherches des Laboratoires des Ponts et Chaussées. LCPC, Paris.

Crémona, C., 1997. Courbe Universelle pour le Dimensionnement d'Amortisseurs en Pied de Haubans. Rev. Fr. Gén. Civ. 1 (1), 137–159.

Davenport, A., 1994. A simple representation of the dynamics of a massive stay cable in wind. In: Proc. IABSE/FIP Intl. Conf. Cable-Stayed and Suspension Bridges, pp. 427–438.

Demartino, C., Ricciardelli, F., 2017. Aerodynamics of nominally circular cylinders: a review of experimental results for Civil Engineering applications. Eng. Struct. 137, 76–114.

Demartino, C., Hoss, H., Georgakis, C., Ricciardelli, F., 2015. Effects of ice accretion on the aerodynamics of bridge cables. J. Wind Eng. Ind. Aerodyn. 138, 98–119.

Den Hartog, J.P., 1932. Transmission line vibration due to sleet. AIEE Trans. 51 (12), 1074–1076.

Dyrbye, C., Hansen, S., 1996. Wind Loads on Structures. John Wiley & Sons, New York.

EN 1990, 2002. EN 1990:2002. Eurocode—Basis of Structural Design.

EN 1991-1-4, 2005. Eurocode 1: Actions on Structures—Part 1–4: General Actions—Wind Actions.

EN 1991-1-5, 2003. Eurocode 1: Actions on Structures—Part 1–5: General Actions—Thermal Actions.

EN 1991-2, 2003. Eurocode 1: Actions on Structures—Part 2: Traffic Loads on Bridges.

EN 1993-1-11, 2006. Eurocode 3: Design of Steel Structures—Part 1–11: Design of Structures With Tension Components.

EN 1993-3-1, 2006. Eurocode 3: Design of Steel Structures—Part 3-1: Towers, Masts, and Chimneys—Towers and Masts.

Ernst, H.J., 1965. Der E-Modul von Seilen unter Berücksichtigung des Durchhangers. Bauingenieur 40 (2), 52–55.

Fédération Internationale du Béton, FIB, 2005. Acceptance of stay cable systems using prestressing steels. In: Bulletin No. 30.

Flamand, O., 1994. Rain-wind-induced vibration of cables. In: Proc. IABSE/FIP Intl. Conf. Cable-Stayed and Suspension Bridges, pp. 523–531.

Flamand, O., Benidir, A., Gaillet, L., Dimitriadis, G., 2014. Wind tunnel experiments on bridge stays cable protection tubes in dry galloping conditions processing method for bi-stable phenomenon. In: Symposium on the Dynamics and Aerodynamics of Cables, 25–26 September, Copenhagen, Denmark.

FREYSSINET, 2010. HD stay cable. In: Freyssinet Brochure. www.freyssinet.com.

FREYSSINET, 2012. Pont de l'ile Russky. In: Freyssinet Brochure. www.freyssinet.com.
FREYSSINET, 2014a. Cohestrand. In: Freyssinet Brochure FT EN CI33. www.freyssinet.com.
FREYSSINET, 2014b. Internal elastomeric damper. In: Freyssinet Brochure FT EN CI116. www.freyssinet.com.
FREYSSINET, 2014c. Internal hydraulic damper. In: Freyssinet Brochure FT EN CI117. www.freyssinet.com.
FREYSSINET, 2014d. Internal radial damper. In: Freyssinet Brochure FT EN CI118. www.freyssinet.com.
Fujino, Y., Hoang, N., 2008. Design formulas for damping of a stay cable with a damper. J. Struct. Eng. 134 (2), 269–278.
Fujino, Y., Kimura, K., Tanaka, H., 2012. Wind-Resistant Design of Bridges in Japan: Developments and Practices. Springer, Tokyo.
Geffroy, R., 2002. The Laroin footbridge with carbon composite stay cables. In: Footbridge 2002, 20–22 November, Paris.
Geier, R., Wenzel, H., 2003. Field Testing of Ludwigshafen Cable-Stayed Bridge, Deliverable D10, IMAC (Project GRD1-2000-25654).
Gimsing, N.J., 1983. Cable-Supported Bridges: Concept and Design. Wiley Interscience, Chichester, UK.
Gimsing, N.J., Georgakis, C., 2012. Cable-Supported Bridges: Concept and Design, third ed. Wiley, Chichester, UK.
Gimsing, N., Nissen, J., 1998. The pylons on the Øresund Bridge. Struct. Eng. Int. 8 (4), 263–264. IABSE.
Griffin, O., Skop, R., Ramberg, S., 1975. The resonant vortex-excited vibrations of structures and cable systems. In: Offshore Technology Conference, Paper OTC-2319, Houston, TX.
Guesdon, M., Herdogan, J., Zivanovic, I., 2020. The Third Bosphorus Bridge: a milestone in long-span technology development and hybrid bridges. Struct. Eng. Int. 30 (3), 312–319. IABSE.
Hardy, C., Bourdon, P., 1979. The Influence of Spacer Dynamic Properties in the Control of Bundle Conductor Motion. In: IEEE PES Summer Meeting, Vancouver, British Columbia, Canada, July.
Hardy, C., Watts, J.A., Brunelle, J., Clutier, L.J., 1975. Research on the dynamics of bundled conductors at the Hydro-Quebec Institute of Research. In: Trans. E. & O. Div., CEA, 14, Part 4.
Hauge, L., Andersen, E.Y., 2011. Longer. In: 35th Annual Symposium of IABSE/52nd Annual Symposium of IASS/6th International Conference on Space Structures, London, 20–23 September 2011.
Hikami, Y., 1986. Rain vibrations of cables of a cable-stayed bridge. J. Wind Eng. (Japan) 27, 17–28 (in Japanese).
Hikami, Y., Shirashi, N., 1988. Rain-wind-induced vibrations of cables in cable-stayed bridges. J. Wind Eng. Ind. Aerodyn. 29, 409–418.
Hoang, N., Fujino, Y., 2007. Analytical study on bending effects in a stay cable with a damper. J. Eng. Mech. 133 (11), 1241–1246.
Hoang, N., Fujino, Y., 2008. Combined damping effect of two dampers on a stay cable. J. Bridg. Eng. 13 (3), 299–303.
Honda, A., Yamanaka, T., Fujiwara, T., Saito, T., 1995. Wind tunnel test on rain-induced vibration of the stay-cable. In: Proceedings of the International Symposium on Cable Dynamics, 19–21 October, Liège, Belgium.
Irvine, H.M., 1981. Cable Structures. MIT Press, Cambridge, MA.

Irvine, H.M., Caughey, T.K., 1974. The linear theory of free vibrations of a suspended cable. Proc. R. Soc. Lond. A 341, 299–315.

Irwin, P., 1997. Wind vibrations of cables on cable-stayed bridges. Proc. ASCE Struct. Congr. 1, 383–387.

ISO 19203, 2018. Hot-Dip Galvanized and Zinc-Aluminium Coated High Tensile Steel Wire for Bridge Cables—Specifications.

Jones, K., 1992. Coupled vertical and horizontal galloping. J. Eng. Mech. 118 (1), 92–107.

Kovàcs, I., 1982. Zur Frage der Seilschwingungen und der Seildampfung. Bautechnik October, 325–332.

Kragh, E., et al., 2020. Fire protection of bridge cables. Struct. Eng. Int. 30 (4), 530–533.

Krenk, S., 2000. Vibrations of a taut cable with an external damper. Trans. ASME 67, 772–776 (Dec.).

Krenk, S., Hogsberg, J., 2005. Damping of cables by a transverse force. J. Eng. Mech. 131 (4), 340–348.

Krenk, S., Nielsen, S., 2002. Vibrations of a shallow cable with a viscous damper. Proc. R. Soc. Lond. A 458, 339–357.

Kubo, Y., 1997. Aeroelastic instability and its improvement of bundle cable for cable-stayed bridge. In: Proc. Intl. Sem. Cable Dyn, pp. 49–56.

Kubo, Y., Kato, K., Maeda, H., Oikawa, K., Takeda, T., 1994. New concept on mechanism and suppression of wake galloping of cable-stayed bridges. In: Proc. IABSE/FIP Intl. Conf. Cable-Stayed and Suspension Bridges, pp. 491–498.

Kubo, Y., Kimura, K., Tanaka, H., Isobe, T., Fujita, M., Higashi, H., Kato, K., 2003. Aerodynamic responses of inclined cables in section model test and full model test. In: Fifth International Symposium on Cable Dynamics, 15–18 September, Santa Margherita Ligure, Italy, pp. 383–390.

Larose, G., Zan, S., 2001. The aerodynamic forces on the stay cables of cable-stayed bridges in the critical Reynolds number range. In: Proceedings of the 4th International Symposium on Cable Dynamics, 27–30 May, Montréal, Canada, pp. 77–84.

Larose, G., Jakobsen, J., Savage, M., 2003. Wind-tunnel experiments on an inclined and yawed stay cable model in the critical Reynolds number range. In: Fifth International Symposium on Cable Dynamics, 15–18 September, Santa Margherita Ligure, Italy, pp. 279–286.

Liu, P., 1982. Static and dynamic behaviour of cable assisted bridges. In: Ph.D Thesis. University of Manchester Institute of Science and Technology (UMIST), Manchester, UK.

Liu, Y., et al., 2015. Carbon fiber reinforced polymer for cable structures—a review. Polymers 7 (10). https://doi.org/10.3390/polym7101501.

Macdonald, J.H.G., 2001. Susceptibility of inclined bridge cable to large amplitude vibrations considering aerodynamic and structural cable damping. In: Proc. 4th ISCD, pp. 243–250.

Macdonald, J., Larose, G., 2006. A unified approach to aerodynamic damping and drag/lift instabilities and its application to dry inclined cable galloping. J. Fluids Struct. 22, 229–252.

Macdonald, J., Larose, G., 2008. Two-degree-of-freedom inclined cable galloping—part 1: general formulation and solution for perfectly tuned system. J. Wind Eng. Ind. Aerodyn. 96, 308–326.

Main, J., Jones, N., 1999. Full-scale measurements of stay cable vibration. In: Proc. 10th Intl. Conf. Wind Eng, 21–24 June, Copenhagen.

Matsumoto, M., 1998. Observed behaviour of prototype cable vibration and its generating mechanism. In: Larsen, A., Esdahl, S. (Eds.), Bridge Aerodynamics. Balkema, pp. 189–211.

Matsumoto, M., 2014. Stall-type galloping and VIV-initiated galloping of inclines stay cable aerodynamics and its aerodynamic stabilization. In: Proc. Symp. Dyn. Aerodyn. Lyngby, Denmark. Cables, September 2014.

Matsumoto, M., Yokoyama, K., Miyata, T., Fujino, Y., Yamaguchi, H., 1989. Wind- induced cable vibration of cable-stayed bridges in Japan. In: Proc. Canada-Japan Workshop on Bridge Aerodyn., Ottawa, Canada, September, pp. 101–110.

Matsumoto, M., Shiraishi, H., Shirato, H., 1992. Rain-wind-induced vibration of cables of cable-stayed bridges. J. Wind Eng. Ind. Aerodyn. 44, 2011–2022.

Matsumoto, M., Ishizki, H., Kitazawa, M., Aoki, J., Fujii, D., 1995. Cable aerodynamics and its stabilization. In: Proc. Intl. Symp. Cable Dyn., 19–21 October, Liège, Belgium.

McTavish, S., Raeesi, A., D'Auteuil, A., Yamauchi, K., Sato, H., 2018. An investigation of the mechanisms causing large-amplitude wind-induced vibrations in stay cables using unsteady surface pressure measurements. J. Wind Eng. Ind. Aerodyn. 183, 19–34.

Mehrabi, A., Tabatabai, A., 1998. A unified finite difference formulation for free vibration of cables. J. Struct. Eng. 124 (11), 1313–1322.

Meier, U., 2012. Carbon fiber reinforced polymer cables: why? Why not? What if? Arab. J. Sci. Eng. 37, 399–411.

Miyata, T., 1991. Design considerations for wind effects on long-span cable-stayed bridges. In: Ito, M., et al. (Eds.), Cable-Stayed Bridges: Recent Developments and Their Future. Elsevier, 10–11 December, Yokohama, pp. 235–256.

Morse, P., Ingard, K., 1968. Theoretical Acoustics. Princeton University Press, Princeton, NJ.

Narita, N., Yokoyama, K., 1991. A summarized account of damping capacity and measures against wind action in cable-stayed bridges in Japan. In: Ito, M., et al. (Eds.), Cable-Stayed Bridges: Recent Developments and Their Future. Elsevier, pp. 257–278.

Nayfeh, A., Mook, D., 1979. Nonlinear Oscillations. John Wiley & Sons, USA.

Nikitas, N., MacDonald, J.H.G., Jakobsen, J.B., Andersen, T.L., 2012. Critical Reynolds number and galloping instabilities: experiments on circular cylinders. Exp. Fluids 52, 1295–1306.

Ohshima, K., Nanjo, M., 1987. Aerodynamic stability of the cables of a cable-stayed bridge subject to rain (a case study of the Ajigawa Bridge). In: Proc. US-Japan Seminar on Natural Resources, pp. 324–336.

Pacheco, B., Fujino, Y., Sulekh, A., 1993. Estimation curve for modal damping in stay cables with viscous damper. J. Struct. Eng. 119 (6), 1961–1979.

Peil, U., Nahrath, N., 2003. Modeling of rain-wind-induced vibrations. Wind Struct. 6 (1), 41–52.

Pinto da Costa, A., Martins, J., Branco, F., Lilien, J., 1996. Oscillations of bridge stay cables induced by periodic motions of deck and/or towers. J. Eng. Mech. 122 (7), 613–622.

PTI Guide Specification, 2007. Recommendations for Stay Cable Design, Testing, and Installation, fifth ed. PTI.

Saito, T., Matsumoto, M., Kitazawa, M., 1994. Rain-wind excitation of cables on cable-stayed Higashi-Kobe Bridge and cable vibration control. In: Proc. IABSE/FIP Intl. Conf. Cable-Stayed and Suspension Bridges, pp. 507–514.

Sandberg, J., Hendy, C., 2010. Replacement of the stays on a major cable-stayed bridge. In: Proceedings of the Institution of Civil Engineers—Bridge Engineering 2010, 163:1, pp. 31–42.

Sarkar, P., Jones, N., Scanlan, R., 1994. Identification of aeroelastic parameters of flexible bridges. J. Eng. Mech. 120 (8), 1718–1743.

Saul, S., Svensson, H., 1990. On the corrosion protection of stay cables. Stahlbau 59 (6), 165–176.

Service d'Etudes Techniques des Routes et Autoroutes (SETRA), 2002. Cable Stays. Recommendations of French Interministerial Commission on Prestressing. SETRA, Bagneux, ISBN: 2110934026.

Sham, S.H.R., Wyatt, T.A., 2016. Construction aerodynamics of cable-stayed bridges for record spans: Stonecutters Bridge. Structures 8, 94–110.

Simiu, E., Scanlan, R., 1996. Wind Effects on Structures: Fundamentals and Applications to Design, third ed. John Wiley & Sons, New York.

Sun, L., Shi, C., Zhou, H., Zhou, Y., 2005. Vibration mitigation of long stay cable using dampers and cross-ties. In: Proceedings of the Sixth International Symposium on Cable Dynamics, Charleston, South Caroline, 19–22 September.

Svensson, E., 2004. Galloping, beams and taut strings. Only fraction of member length galloping prone. In: 5th International Conference on Bridges Across the Danube, IABSE, Novi Sad, 24–26 June.

Tabatabai, H., Mehrabi, A., 2000. Design of mechanical viscous dampers for stay cables. J. Bridg. Eng. 5 (2), 114–123.

Tagata, G., 1977. Harmonically forced, finite amplitude vibration of a string. J. Sound Vib. 51 (4), 483–492.

Tanaka, H., 2003. Aerodynamics of cables. In: Fifth International Symposium on Cable Dynamics, 15–18 September, Santa Margherita Ligure, Italy, pp. 11–25.

TRB 20015, 2005. NCHRP synthesis 353: inspection and maintenance of bridge stay systems. In: National Cooperative Highway Research Program. American Transportation Research Board, Washington.

Verwiebe, C., 1998. Rain-wind-induced vibrations of cables and bars. In: Larsen, A., Esdahl, S. (Eds.), Bridge Aerodynamics, 10–13 May, Balkema, Copenhagen, pp. 255–263.

Virlogeux, M., 1998. Cable vibrations in cable-stayed bridges. In: Larsen, A., Esdahl, S. (Eds.), Bridge Aerodynamics, 10–13 May, Balkema, Copenhagen, pp. 213–233.

Vo-Duy, H., Nguyen, C.H., 2020. Mitigating large vibrations of stayed cables in wind and rain hazards. Shock. Vib. 2020, 5845712.

VSL, 2002. VSL SSI 2000 stay cable system. In: Brochure. www.vsl.com.

VSL, 2018. VSL stay cable systems. In: Technical Catalogue. www.vsl.com.

Wagner, P., Fuzier, J.-P., 2003. Health monitoring of structures with cables—which solutions? Dissemination of the results of the IMAC European project. In: Fifth International Symposium on Cable Dynamics, 15–18 September, Santa Margherita Ligure, Italy.

Yamagiwa, I., Utsuno, H., Endo, K., Sugii, K., Morimoto, T., 1997. Simultaneous identification of tension and flexural rigidity of bridge cables. Annu. Proc. Steel Struct. 5, 15–22.

Yamaguchi, H., 1990. Analytical study on growth mechanism of rain vibration of cables. J. Wind Eng. Ind. Aerodyn. 33, 73–80.

Yamaguchi, H., 1995. Control of cable vibrations with secondary cables. In: Proc. International Symposium on Cable Dynamics, 19–21 October, Liège, Belgium, pp. 445–452.

Yamaguchi, H., Fujino, Y., 1998. Stayed cable dynamics and its vibration control. In: Larsen, A., Esdahl, S. (Eds.), Bridge Aerodynamics, 10–13 May, Balkema, Copenhagen, pp. 235–253.

Further reading

Holmes, J.D., 2001. Wind Loading of Structures. Spon Press.

This page intentionally left blank

Orthotropic steel decks

24

H. De Backer
Department of Civil Engineering, Ghent University, Ghent, Belgium

1. Introduction

An orthotropic steel deck (OSD) consists of a deck plate, which is supported by stiffeners working in two orthogonal directions: the transversal stiffeners (or crossbeams) and the longitudinal stiffeners. The system can thus be compared to a uniform deck plate having different stiffness characteristics in two directions or, in other words, an orthogonal anisotropic steel deck. Because of this, the OSD can take part in the overbridge actions, such as the upper flange of a box-girder bridge, the tie of a tied-arch bridge, the stiffening girder of a suspension or cable-stayed bridge, or another part of the overall structural bridge system.

The basic composition of an OSD is shown in Figures 24.1 and 24.2. The component showing the most variation is the longitudinal stiffener. This stiffener can be open—using strips or L-profiles—or closed—using trapezoidal, V-shaped, or rounded sections. The most important structural characteristics of an OSD can be summarized as follows:

- Low dead load: The dead load of an OSD is considerably lower when compared to other similar steel and concrete deck types.
- Strength and stiffness: An OSD has a considerable plastic deformation capacity under its ultimate load.
- Structural efficiency: The system is perfectly capable of spreading the high patch loads in both longitudinal and transversal directions.
- The ability to take part in the overall structural actions of the bridge in both the longitudinal and transversal directions.
- A reduced structural height, when compared to a classic combination of deck, stringer, crossbeam, and main beams. All of these components are combined in one plane.
- Since this is a continuous deck system, the number of connections within the deck plate is quite low.
- Ease of construction using large prefabricated sections.
- Durability and long-term economy of a well-designed OSD, since the deck system can have the same life span as the overall bridge system.

These characteristics are extremely important for the design of new bridges, as well as for renovation projects. Low weight and height and high carrying capacity seem to be the most determining factors for choosing this bridge type. These factors have allowed the OSD to become the standard choice for record-breaking bridge spans.

Innovative Bridge Design Handbook. https://doi.org/10.1016/B978-0-12-823550-8.00028-7

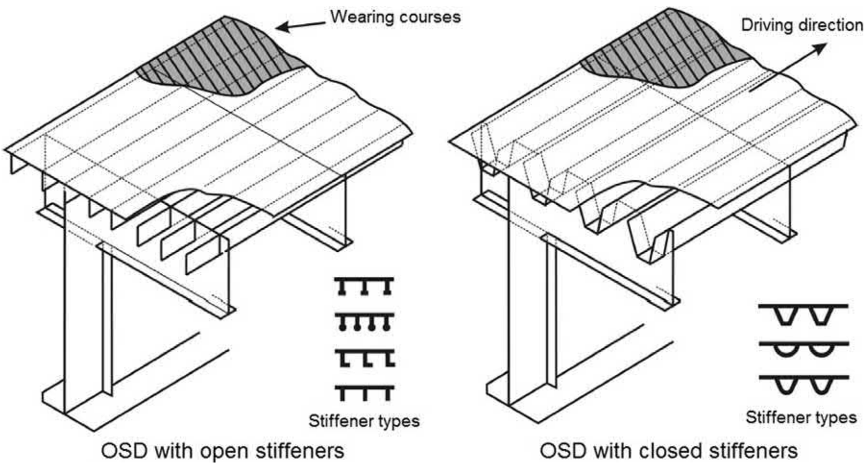

Figure 24.1 Two basic types of OSDs.

Figure 24.2 Orthotropic deck plate of the Temse Bridge in Flanders, Belgium.

2. History

The origin of OSD can be found with the development of "battledeck floors" in the 1930s. These decks consisted of a steel deck plate welded to longitudinal I-shaped stringers, which were attached to the underlying crossbeams. One of the first applications was in 1932, on the North Saginaw Road/Salt River Bridge in Michigan. An important thing to note is that, in this concept, the deck plate does not function as a stiffener of the crossbeams or an upper flange of the main beams. Its only function is spreading the local patch loads to the other components. The same principle was applied frequently to the German Autobahn network from 1934 onward.

Reconstruction after World War II was an important factor in stimulating development and construction of multiple OSD bridges, mainly in Germany during the 1950s. Examples of these bridges that use open stiffeners are the Kurpfalz Bridge, which crosses the Neckar in Mannheim, and the Keulen-Mülheim Bridge, which crosses the Rhine River. The first application of closed stiffeners dates from 1954 in Duisburg, Germany. The first North American application of the OSD concept was the Port Mann Bridge in Vancouver, Canada, in 1964. During the following years, several other OSD bridges were built, including the Severn Crossing Bridge in Britain, the Poplar Street Bridge in St. Louis, Missouri, and the San Mateo Bridge in California. The first design guides were published in 1972 by the Japan Road Authority and were closely followed by the inclusion of OSDs in the AASHTO design rules in 1973.

OSDs have also been used for the redecking of a number of famous bridges, such as the Golden Gate Bridge in San Francisco and the Benjamin Franklin Bridge in Philadelphia. Most of the record-span suspension bridges also use an OSD. Table 24.1 illustrates that an OSD is used in 8 of the 10 largest bridge spans. Other applications include the Millau Viaduct and the recently opened San Francisco–Oakland Bay Bridge.

3. OSD concept

This section describes the most useful manual design methods for OSDs. These analytical methods are based on the groundbreaking efforts of Pelikan and Esslinger (1957) and Wolchuk (1963), who were the pioneers of the OSD concept. The analytic calculation of an OSD can be quite complex because of its lack of symmetry, which is caused by all stiffeners working on the same side of the steel deck plate. A detailed design method would become labor-intensive and complicated, so a number of simplified OSD models have been developed. The results of these models are quite conservative but allow for a quick determination of the internal forces and initial design dimensions. These methods are as follows:

- Simplification as a rectangular beam grid (Cornelius, 1952): The deck plate and all stiffeners are considered to be individual, discrete beams working together. The method assumes that the deck is cut halfway between longitudinal stiffeners. These stiffeners are then considered virtual beams with the deck plate as an upper flange. Provided the effective width is larger than the distance between stiffeners, this method considers the entire OSD. Stiffness of the

Table 24.1 Record Span Suspension Bridges

	Bridge	Length of Main Span (m)	City, Country	Year	Deck Type
1	Akashi Kaikyō	1991	Kobe-Naruto, Japan	1998	OSD
2	Great Belt	1624	Korsor, Denmark	1998	OSD
3	Runyang	1490	Zhejiang, China	2005	OSD
4	Humber	1410	Kingston-Upon-Hull, UK	1981	OSD
5	Jiangyin	1385	Jiangsu, China	1999	OSD
6	Tsing Ma	1377	Hong Kong, China	1997	OSD
7	Verrazano Narrows	1298	New York, United States	1964	Concrete
8	Golden Gate	1280	San Francisco, United States	1937	OSD
9	Höga Kusten	1210	Kamfors, Sweden	1997	OSD
10	Mackinac	1158	Mackinaw City, United States	1957	Concrete

OSD in the transversal direction is neglected and must be considered separately. These types of methods have difficulty in describing the effects of torsion within the OSD concept.

- Simplification as an idealized orthotropic plate (Pelikan and Esslinger, 1957; Wolchuk, 1963): The actual OSD is replaced by a singular deck plate with equivalent characteristics. The sections of deck plate and stiffeners are spread out over the width of the deck. Afterward, the effect of the actual loads on this idealized plate is calculated and used as an input for separate calculations of each stiffener. This method will be discussed in more detail later in this chapter.

It has to be stressed that purely linear elastic theories are only allowed when displacements are small. Otherwise, membrane action might develop in the deck plate. Due to the high ductility of steel, membrane action will be responsible for the large post-critical strength reserve of the OSD concept.

An idealized orthotropic plate is defined as a plate with different stiffnesses in two orthogonal directions x and y within the surface of the plate, as shown in Figure 24.3. Other assumptions include a constant thickness and a continuous and homogenous material. The different stiffnesses in each direction will thus be defined by different stiffness moduli E_x and E_y, as well as by different Poisson's ratios ν_x and ν_y. Structural anisotropy is thus replaced by material anisotropy quite similarly, as in the behavior of a wooden beam. A natural example of this type of plate structure is a wooden board, which has different stiffness ratios parallel and perpendicular to the veins. The initial assumptions for such a calculation are a homogenous material, constant thickness, limited purely elastic deformations according to Hooke's law, negligible vertical normal stresses, and strictly vertical supports.

All of the properties can then be described based on the affective bending stiffnesses in both directions, as well as the torsional stiffness of the plate.

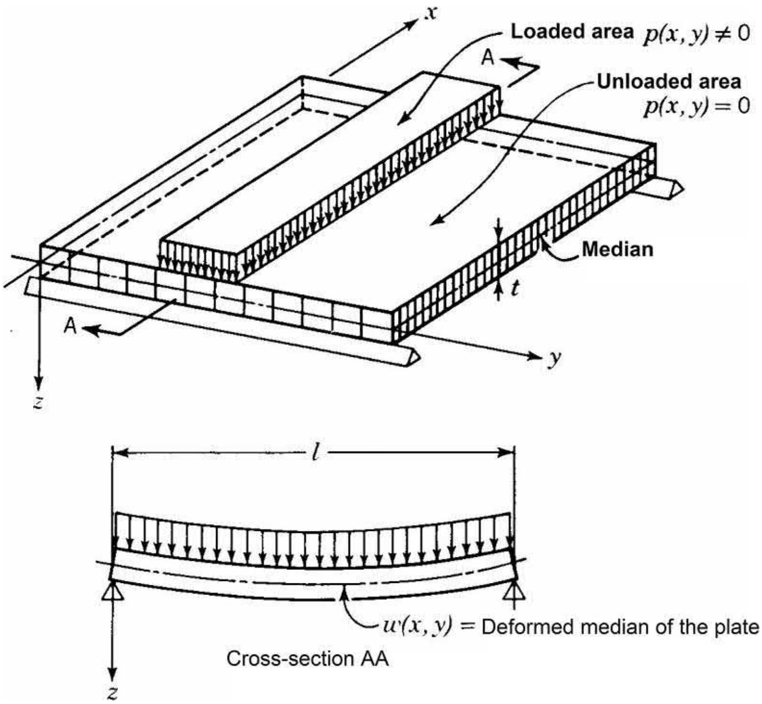

Figure 24.3 Design assumptions for an idealized orthotropic plate.

The calculation is thus a combination of three separate structural systems (Wolchuk, 1963; Vandepitte, 1979):

- The deck plate working as a transfer medium of the local patch loads to the longitudinal and transversal stiffeners
- The orthotropic behavior of the combination of stiffeners and deck plate, which can be calculated as an idealized orthotropic plate
- The overall bridge actions

More information about these calculation methods can be found in Pelikan and Esslinger (1957), Wolchuk (1963), Vandepitte (1979), American Institute for Steel Construction (AISC, 1938), and Klöppel and Roos (1960).

4. Practical design

4.1 Fatigue design

Fatigue is the process by which an accumulation of damages is caused by a repeating load of variable magnitude. Fatigue damage normally occurs under purely elastic stresses. However, due to stress concentrations, plastic stresses are possible in very small areas of the construction. Once enough damage is accumulated, fatigue fracture will initiate and propagate through the plasticized regions. Fatigue calculations are quite complex. Codes and standards will use simplified models to describe the fatigue behavior. Most methods, such as Eurocode 3 (2009), use a combination of S-N curves and the Palmgren-Miner rule for OSDs.

Specific S-N curves or Wöhler curves have been determined for each fatigue sensitive weld detail in an OSD. They offer a relation between the nominal stress, $\Delta\sigma$, at the location and the number of cycles, N, until failure, as described by the Paris–Erdogan law:

$$N = \frac{A}{\Delta\sigma^m}. \tag{1}$$

Parameters A and m are determined based on the considered weld detail. The stress concentrations are calculated using elastic material laws and based on the occurring stress concentrations and possible secondary effects (Kiss et al., 1998). Although nominal stresses combined with elastic theories are basically inaccurate because only the S-N curves are to be used for constant amplitude loading, and they are generally accepted as a simplified calculation method. As an example, the Eurocodes use the following failure criterion, combined with the Palmgren-Miner rule, wherein all realistic stress cycles are replaced by constant amplitude stress cycles resulting in equivalent damage:

$$\gamma_{Ff} \Delta\sigma \le \frac{\Delta\sigma_c}{\gamma_{Mf}}. \tag{2}$$

Herein, γ_{Ff} and γ_{Mf} are partial safety factors for the fatigue loads and fatigue strength, respectively, while $\Delta\sigma$ is the nominal stress cycle and $\Delta\sigma_c$ is the fatigue strength for the considered weld category for the expected number of stress cycles N during the assumed fatigue life.

Although most methods and standards follow these simplifications, some cautionary remarks must be made here. The method totally neglects the probabilistic background of the phenomenon. In addition, actual load histories—i.e., the actual order of the stress cycle—is neglected, although fracture mechanical principles take into consideration that this can be influential. Furthermore, all standards are based on a certain safety level that is guaranteed. For fatigue of OSDs, this level is based on the determination of the weld categories using prototype measurements and laboratory testing. Due to the development of production methods, steel qualities, and weld methods, the overall quality has greatly improved over the years. Since weld categories are still based on all available tests, this implies that they become more and more conservative each year.

4.2 OSD design based on AASHTO

The American standards use two approaches for fatigue problems, shown in Figure 24.4. Load-induced fatigue considers details subjected to axial tension over their entire cross section. The actual calculation is based on the determination of the number of stress cycles and the use S-N curves and weld categories.

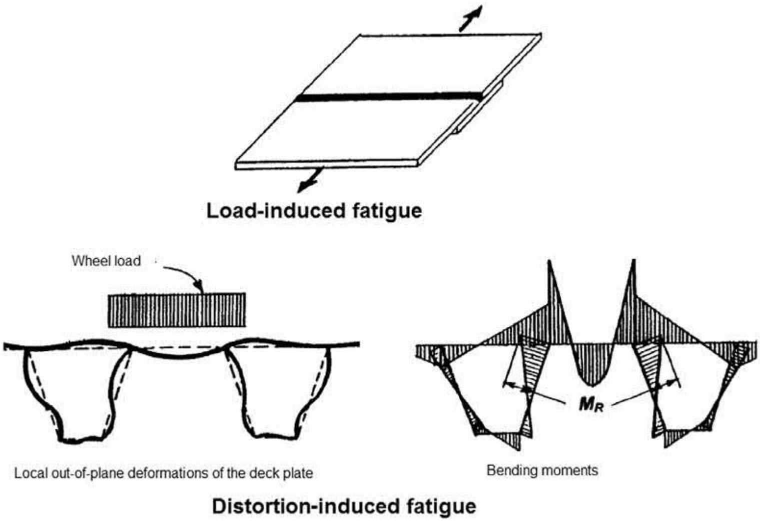

Figure 24.4 Examples of fatigue types according to AASHTO (2014).

Distortion-induced fatigue, on the other hand, concerns details wherein out-of-plane deformations of the steel plate elements occur. No detailed calculation is necessary, but safety is guaranteed based on the geometrical rules for each detail.

Load-induced fatigue details need to meet the following criterion:

$$(\Delta \mathrm{F})_n = \left(\frac{A}{N}\right)^{\frac{1}{3}} \geq \frac{1}{2}(\Delta F)_{TH}, \tag{3}$$

with

$$N = (365)(75)n(ADTT)_{SL}. \tag{4}$$

In Eqs. (3) and (4), n equals the number of stress cycles caused by the passage of a standardized truck, $(\Delta F)_{TH}$ equals the constant amplitude fatigue strength, and $(ADTT)_{SL}$ equals the average daily traffic volume for trucks on a single lane. The corresponding S-N curves are shown in Figure 24.5. These curves are linked to 12 weld categories in OSDs. These categories are summarized in Table 24.2.

The stiffener-to-deck-plate detail is not included in this list, strangely enough. This fatigue detail is considered to be deformation induced. This should not be calculated in detail, but it is assumed that no fatigue will occur if a number of geometric design rules are met. From a design point of view, this can be seen as an oversimplification of the problem. These empirical design rules are aimed at minimizing the moment M_R, which is found in the stiffener flank. The moment M_R occurs because the wheel load causes localized, out-of-plane movements of the stiffener flank, which causes potential fatigue cracks. In order to be certain that the moment M_R is as small as possible,

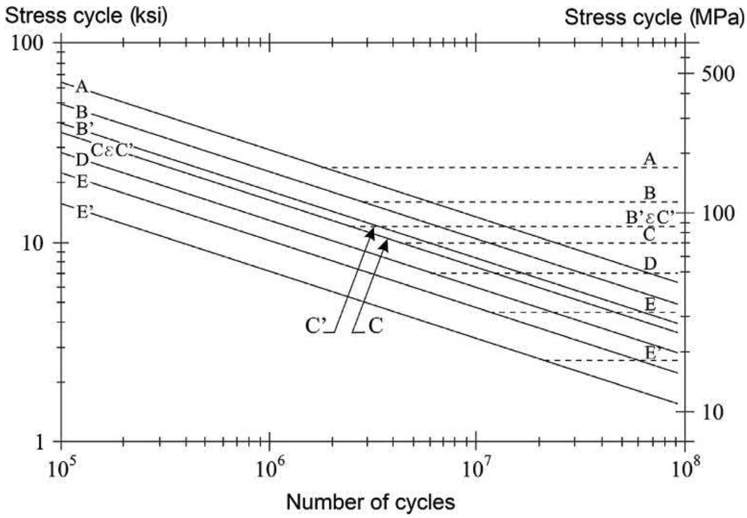

Figure 24.5 S-N curves for OSD according to AASHTO (2014).

Table 24.2 AASHTO Fatigue Details

	Description	Category
1	Welded connections within the deck plate, using	B
2	different types of backing strips	C
3		D
4	Bolted connections in the deck plate	B
5	Welded connections in deck plate and stiffeners under	B
6	workshop conditions	C
7	Welds of the stiffener window	D
8	Weld between longitudinal stiffener and crossbeam,	C
9	with or without internal diaphragm	C
10	Weld of crossbeam web to stiffener, with or without	<C
11	internal diaphragm	<C
12	Weld between crossbeam web and deck	E

measures should be taken to ensure that the deck plate has a sufficient thickness and has a sufficiently high rigidity, while the stiffener, on the other hand, should be slender and flexible.

4.3 Eurocode design principles

Eurocode mandates that detailed fatigue checks should be performed for all components, except when the geometry of the considered detail meets certain design rules drawn up based on experimental work and practical experience. As for the connection

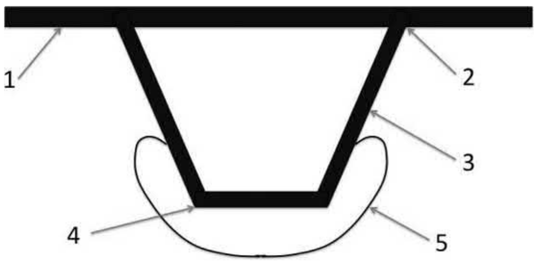

Figure 24.6 Eurocode fatigue details.

Table 24.3 Eurocode Fatigue Details

	Detail	Category
1	Longitudinal stresses in transversal welds of the deck	71
2	Longitudinal stresses in the deck plate at the connection of longitudinal stiffener with the deck	100 80
3	Welded connection of a closed longitudinal stiffener with the crossbeam	80
4	Welded connection between closed longitudinal stiffeners, with backing strip	71
5	Free edge of the cutout in the crossbeam web to allow for continuous longitudinal stiffeners	112
6	Welded connections between closed longitudinal stiffeners and the deck plate	71

of the longitudinal stiffeners to the deck plate and the connection of the longitudinal stiffeners to the crossbeam, these are discussed in the annexes. All of the fatigue details around the stiffeners to be considered are shown in Figure 24.6 and listed in Table 24.3. The calculation methods for stiffeners are defined as well. Longitudinal stiffeners should be studied using a realistic model of the entire structure. Only the longitudinal stiffeners of railway bridges may be analyzed as continuous beams on elastic supports. The influence of the cutouts in the web plate at the location of the longitudinal stiffeners should be taken into account in the design of the crossbeams. The fatigue in the deck plate is assumed to be mainly caused by the deflection of the deck plate under the wheel load.

4.4 Open or closed stiffeners

The selection of open versus closed longitudinal stiffeners involves three major issues: design (steel weight or economy), ease of fabrication, and ease of construction. In addition, maintenance issues, such as ease of inspection and the percentage of superstructure exposed to exterior elements, are important. Weight savings in superstructures are the weightiest concern in the use of an orthotropic system. For most bridges, the stiffeners are connected to the crossbeams by welding. The crossbeams or transversal stiffeners can be steel hot-rolled beams, small plate girders, box girders, or full-depth diaphragm plates. When full-depth diaphragms are used, access openings are needed for bridge maintenance purposes. The holes also reduce dead load and provide a passageway for mechanical or electrical utilities. A small number of bridges have the stiffeners perpendicular to the main girders, which is more common in pedestrian bridges (Mangus, 2014).

An open stiffener has virtually no torsional capacity. The open stiffeners were initially very popular in because of simpler analysis and welding. The switch to closed stiffeners occurred to reduce dead weight of the superstructure. In the tension zones, the shape of the stiffener can be any shape, open or closed, depending on the preference of designers. Also, closed stiffeners have 50% less surface area to protect from corrosion. A closed longitudinal stiffener is torsionally stiff and is essentially a miniature box girder. The closed stiffener is more effective for lateral distribution of the individual wheel loads than the open stiffener system.

The trapezoidal (closed) stiffener shows greater bending efficiency in load-carrying capacity and stiffness. The original shapes were patented by the Germans (Sedlacek, 1992), later adopted in United States by Bethlehem Steel, and then also adopted in Japan and other countries (Institution of Civil Engineers, 1972). U-shaped as well as V-shaped and Y-shaped stiffeners have been developed. It is readily apparent that a series of miniature box girders placed side by side is much more efficient than a series of miniature T-girders placed side by side. Weight savings in total steel weight has lead designers to switch to the trapezoidal stiffeners with a large range of choices. The trapezoidal longitudinal stiffener is quite often field-welded completely around the superstructure's cross section, rather than field bolting, to achieve full structural continuity (Hubman et al., 2013).

5. Innovative applications and research topics

5.1 Fracture mechanics and residual stresses

Fatigue in steel structures is the most important type of fracture, and because of its complexity, it is less understood than other types of failure. In the past, fatigue problems were sometimes overlooked during design. With the current design codes, a fatigue problem is assessed based on S-N curves. However, these curves should be updated for every project where a different design approach or installation procedure is used. Since this has mostly not been done, a misunderstanding of the fatigue behavior of the detail has occurred. In addition, the Palmgren-Miner method is used to calculate the lifetime of each detail. However, this method is not very accurate because the load history and the load sequences do not have any effect on the fatigue resistance. These design imperfections lead to the overestimation of the dimensions when considering OSDs (Nagy et al., 2014).

Residual stresses are present in many steel structures due to manufacturing actions causing plastic deformations. Nevertheless, these stresses are not often taken into account when considering the design of these structures. This is acceptable when only focusing on the stress variations, which eliminates the initial stress state of the structure. However, the effect of residual stresses may either be beneficial or detrimental—depending on the magnitude, sign, and distribution of these stresses—with respect to load-induced stresses (Barsoum and Lundbäck, 2009). Therefore, the initial stress state due to a welding operation has to be introduced into a finite element method (FEM) model. Basically, there are two different methods to introduce an initial stress state into a model. The easiest and preferred way is to apply the residual stresses according to literature or test data. This can be done by imposing the stresses directly into the model or by imposing complementary normal forces and bending moments. Results from similar fillet welds as those in the orthotropic bridge decks that have already been studied. Therefore, N_{deck} is chosen in order to have tensile yield stresses into the deck plate at the weld, as shown in Figure 24.7. For the stresses into the stiffener, an additional bending moment $M_{stiffener}$ and normal force $N_{stiffener}$ are also introduced. The bending moment is necessary because the weld is completed from one side only, and the filler metal and the corresponding heat zone is larger at the weld toe compared to the weld root. For the magnitude of this bending moment and normal force, an assumption is made based on the distribution of the filler metal.

Linear elastic fracture mechanics (LEFM) calculations can be carried out with a detailed three-dimensional (3-D) model of a stiffener-to-deck-plate connection. The method described refers to the automatic crack propagation method based on extended finite element method (XFEM) techniques (Polak, 2007). With this method, it is possible to evaluate the whole crack propagation without remeshing the model for every crack propagation step. In addition, not only can the crack growth rate be evaluated, but the crack growth direction can be evaluated as well. At first, an initial crack length should be chosen according to the welding detail and construction technology. Often, an initial crack length between 0.1 and 1 mm is chosen (De Backer, 2006). If the weld is perfectly accessible to smoothen the surface afterward, the initial crack length can be very small. However, the welds used for longitudinal stiffeners in OSDs are welded from only one side, and even the lack of penetration can be questioned. Therefore, due to the large uncertainties, initial elliptical crack lengths of 1 mm in the longitudinal direction and 0.5 mm in the transversal direction are assumed. This was also confirmed in a microscopic study of the present weld details of a stiffener-to-deck-plate connection (De Backer, 2006). Although the fatigue crack often propagates

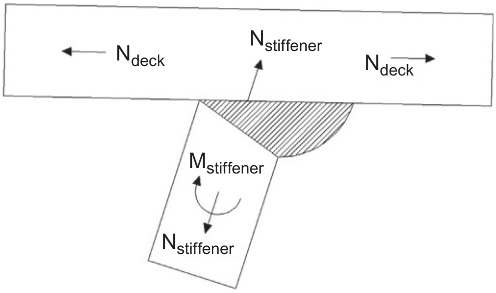

Figure 24.7 Complementary normal forces and bending moments to simulate residual stresses.

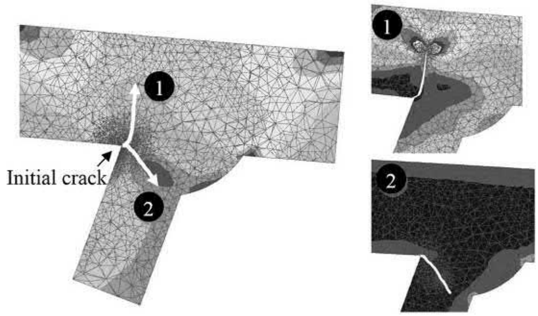

Figure 24.8 Detailed small-scale 3-D model: possible crack growth directions.

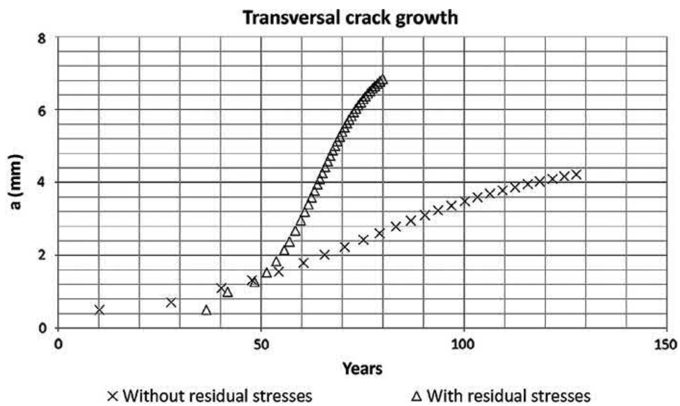

Figure 24.9 Transversal crack growth: a comparison with residual stresses or without them.

through the deck plate, the initial crack length is chosen parallel to the deck plate and at the weld root. After implementing an initial crack length into the model, the XFEM calculation can be performed, as shown in Figure 24.8.

Figures 24.9 and 24.10 visualize the evolution of the crack length as a function of the years of service life for both the transversal and longitudinal crack growth directions. At this point, the fatigue life is evaluated due to constant stress amplitude with wheel type *B* from Eurocode 3 (2009) and an axle load of 130 kN. Without residual stresses, the crack does not develop quickly, but its development remains faster than that of the crack with residual stresses for approximately 52 years. After that, the crack with residual stresses grows progressively. The continuity of the stress distribution due to membrane forces is interrupted because the crack is growing through the deck plate. The stresses are forced into the less rigid body of the closed stiffeners. This explains why the crack propagation through the deck plate is much faster than the crack propagation through the stiffener. The same conclusions hold for the longitudinal crack growth direction—however, it should be noted that the speed of the longitudinal crack growth is much faster than in the transversal

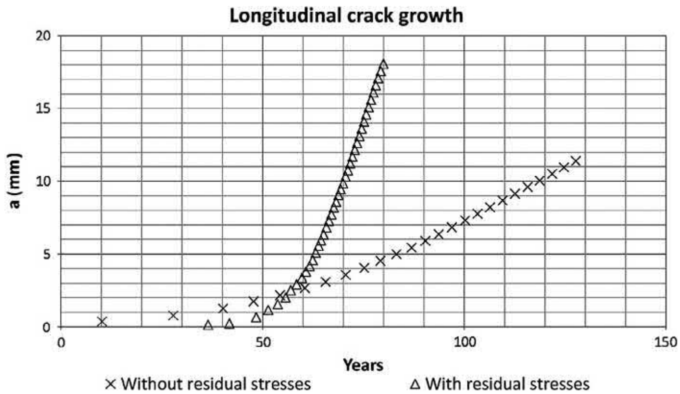

Figure 24.10 Longitudinal crack growth: a comparison with residual stresses or without them.

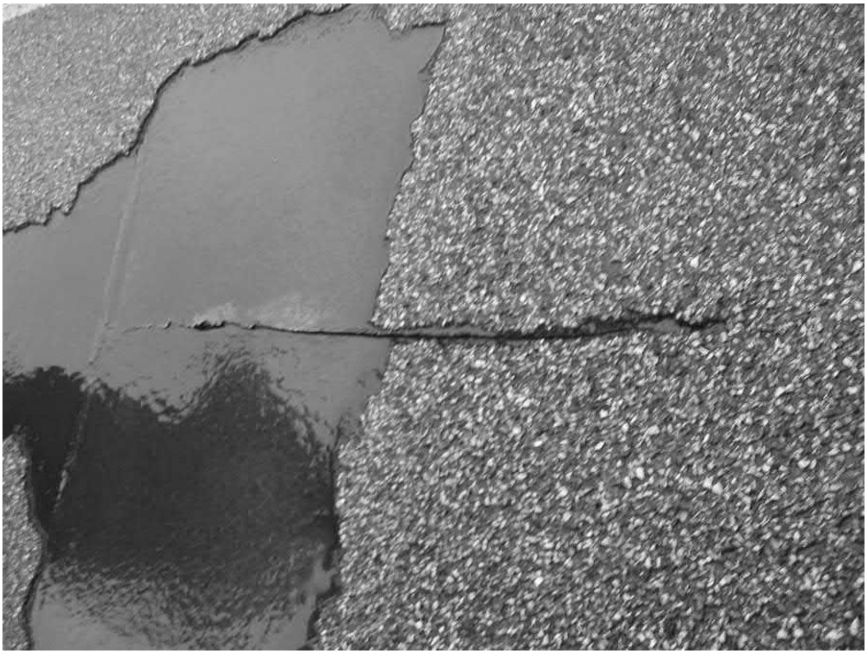

Figure 24.11 Longitudinal crack through the deck plate at a stiffener-to-deck-plate connection on the Temse Bridge, Flanders, Belgium.

direction. These conclusions are illustrated by the fatigue problem detected in the Temse Bridge in Flanders, Belgium, shown in Figure 24.11. The crack first grows longitudinally before fully penetrating the deck plate (or the stiffener). Therefore, the crack stays invisible through visible detection unless there is already sufficient damage (Kühn et al., 2008).

5.2 Refurbishment techniques

Since a number of bridges suffered fatigue damage early in their lives, possible repair and refurbishment techniques have been researched in detail and used on actual bridges. This section will focus on two of the most promising options: adding a high-performance concrete plate to the deck or gluing an additional steel plate to the existing deck surface.

Two separate lightweight systems for reinforcing OSDs have been researched (Teixeira de Freitas et al., 2010, 2011): the bonded steel plate system and the sandwich steel plate system. The main idea of these types of reinforcement is to stiffen the existing deck plate, thereby reducing the stresses at the fatigue-sensitive details and, thus, extending the fatigue life of the OSD. Both reinforcement systems consist of adding a second steel plate to the existing steel deck. The behavior and the effect of the reinforcement systems have been investigated using full-scale static tests and finite element analyses, using realistic wheel loads. The results showed at least 40% of stress reduction close to the fatigue sensitive details after applying both reinforcements. The two suggested reinforcement systems showed good performance and proved to be efficient, lightweight solutions to refurbish OSDs and extend their life-spans (Teixeira de Freitas et al., 2013).

A sandwich plate system (SPS) is composed of two steel plates and a solid polymer (polyurethane) core, sandwiched together. The sandwich action is generated through the bond between the polymer core and the steel plates. This ensures a high-bending resistance and bending stiffness of the sandwich if it is loaded as a plate, so that the stiffeners usually utilized to reinforce thin plates can be abandoned. Because of the low density of the core material, SPS plates have the advantage of being lightweight. They provide minimum steel surfaces exposed to corrosion, have excellent fatigue properties (due to the absence of welded stiffeners or attachments), and also exhibit good damping (noise emission) and insulation properties (temperature and fire resistance). SPS plates are most suitable for both building new steel decks and refurbishing existing steel decks by overlay and underlay techniques to make them durable and fit for the increasing traffic loads (Feldmann et al., 2007).

A developed renovation technique for fixed bridges is a surfacing of high-performance concrete (De Jong and Kolstein, 2004; Buitelaar et al., 2004). Fixed bridges often have a wearing course of approximately 50 mm mastic asphalt, with low stiffness. It is possible to replace this with a wearing course with a higher stiffness. A wearing course of reinforced, high-performance concrete with the same thickness as the mastic asphalt layer is a good solution to lower the stress cycles. If a good intermediate layer between steel and concrete is possible, composite action between steel and concrete is also possible. In that case, the total stiffness of the composite deck plate structure might be enlarged with factors. Then the stress cycles in the steel deck plate are strongly reduced, and subsequently, the fatigue life is far better. This is a very promising solution since it turns the deck plate in a much more rigid construction behaving as an actual uniform plate, due the monolithic composite interaction between the reinforced high-performance concrete (RHPC; shown in

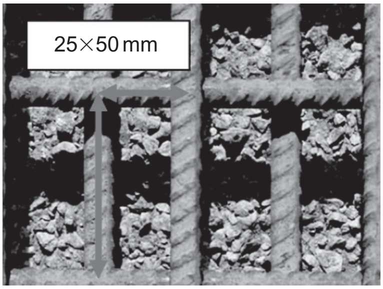

Figure 24.12 Very dense RHPC reinforcement (Buitelaar et al., 2004).

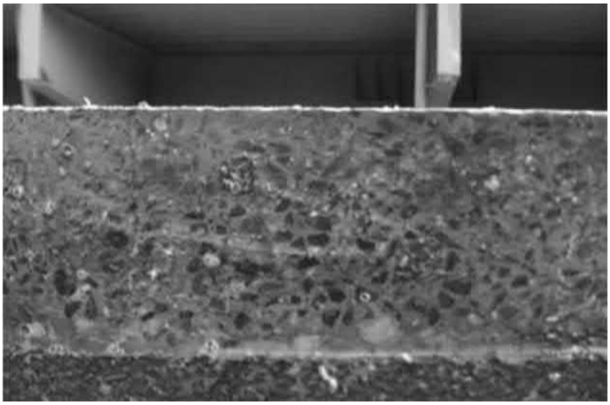

Figure 24.13 RHPC overlay on OSD deck plate (Buitelaar et al., 2004).

Figures 24.12 and 24.13) overlay and the steel deck plate. The RHPC overlay with a thickness of a minimum of 5 cm will result in a stress reduction with a factor of 4–5 in the deck plate and a factor of 3–4 in the trough wall, thus extending the service life of the OSD for extra decades without additional maintenance.

5.3 Innovative concepts

In recent years, alternative deck systems have been proposed that also aim to focus on orthotropic behavior but try to avoid the numerous welds and resulting fatigue problems. Possibilities include the use of other materials (high-strength steel/aluminum), alternative arrangements of the stiffeners, or combinations of both (combining two steel plates with an orthogonal concrete grid between them). While research is available, no actual realizations exist at present. Further research and development is ongoing.

6. Conclusions

OSDs have been employed worldwide, particularly in Europe, Asia, and South America. However, the use of orthotropic steel has been fairly limited, such that the use of OSDs represents a very small percentage of total bridges. The construction and fabrication techniques employed are very important to the successful use of OSDs. OSDs typically require detailed construction specifications and special quality-control procedures during fabrication. While fatigue effects remain the most important design issue, it should be stressed that recent research and development and a detailed design will avoid these problems, resulting in one of the most lightweight and slender deck structures available. Overall, it can be stated that the OSD remains a valuable bridge concept, especially for larger-span bridges.

References

American Association of State Highway and Transportation Officials (AASHTO), 2014. LRFD Bridge Design Specification. Sections 2, 4, 6, and 9. American Association of State Highway and Transportation Officials.

American Institute of Steel Construction (AISC), 1938. The Battle-Deck Floor for Highway Bridges. American Institute of Steel Construction, p. 34.

Barsoum, Z., Lundbäck, A., 2009. Simplified FE welding simulation of fillet welds—3D effects on the formation of residual stresses. Eng. Fail. Anal. 18, 2281–2289.

Buitelaar, P., Braam, R., Kaptijn, N., 2004. Reinforced high-performance concrete overlay system for rehabilitation and strengthening of orthotropic steel bridge decks. In: Proceedings of Orthotropic Bridge Conference, Sacramento, CA, pp. 384–401.

Cornelius, W., 1952. Die Berechnung der Ebenen Flächentragwerke mit Hilfe der Theorie der Orthogonal-Anisotropen Platten. Der Stahlbau 21, 21–43 (in German).

De Backer, H., 2006. Optimization of the Fatigue Behavior of the Orthotropic Bridge Concept by Improved Dispersion of Traffic Loads. Ghent, Belgium., p. 516 (Ph.D. thesis, in Dutch).

De Jong, F.B.P., Kolstein, M.H., 2004. Strengthening a bridge deck with high-performance concrete. In: Proceedings of Orthotropic Bridge Conference, Sacramento, CA, pp. 328–345.

Eurocode 3, 2009. NBN EN 1993-1-9:2005. Eurocode 3: Design of Steel Structures—Part 1–9: Fatigue. European Committee for Standardization, Brussels, Belgium.

Feldmann, M., Sedlacek, G., Gessler, A., 2007. A system of steel-elsatomer sandwich plates for strengthening orthotropic bridge decks. Mech. Compos. Mater. 43 (2), 183–190.

Hubman, M., Gunther, H.P., Kuhlman, U., 2013. Maintenance of orthotropic steel bridge decks with longitudinal Y-stiffeners. In: Proceedings of IABSE Conference. Assessment, Upgrading and Refurbishment of Infrastructures, Rotterdam, Netherlands, pp. 498–499.

Institution of Civil Engineers (ICE), 1972. Steel box girder bridges. In: Proceedings of the International Conference. Thomas Telford Publishing, London.

Kiss, K., Szekely, E., Dunai, L., 1998. Fatigue analysis of orthotropic highway bridges. In: Proceedings of the 2nd International Ph.D. Symposium in Civil Engineering, Budapest, pp. 1–8.

Klöppel, K., Roos, E., 1960. Statische versuche und dauerversuche zur frage der bemessung von flachblechen in orthotropen platen. Der Stahlbau 29, 361 (in German).

Kühn, B., et al., 2008. Assessment of Existing Steel Structures: Recommendations for Estimation of Remaining Fatigue Life. Joint Research Centre - European Convention for Constructional Steelwork, Aachen, Germany, p. 92.

Mangus, A.R., 2014. Orthotropic steel decks. In: Chen, W.F., Duan, L. (Eds.), Bridge Engineering Handbook, second ed. Taylor & Francis Group, Boca Raton, FL, pp. 589–645.

Nagy, W., Van Bogaert, P., De Backer, H., 2014. Improved fatigue assessment techniques of connecting welds in orthotropic bridge decks. In: Proceedings and Abstracts of the Eurosteel Conference, Naples, Italy. ECCS (European Convention for Constructional Steelwork), Brussels, Belgium, pp. 737–738.

Pelikan, W., Esslinger, M., 1957. Die Stahlfahrbahn Berechnung und Konstruktion. MAN-Forshungsheft 7, Augsburg-Nurnberg, Germany (in German).

Polak, J., 2007. Cyclic deformation, crack initiation, and low-cycle fatigue. In: Milne, I., Ritchie, R.O., Karihaloo, B. (Eds.), Comprehensive Structural Integrity, Vol. 4: Cyclic Loading and Fatigue. Elsevier Applied Science, London, pp. 1–39.

Sedlacek, G., 1992. Orthotropic plate bridge decks. In: Dowling, P.J., Harding, J.E., Bjorhovde, R. (Eds.), Constructional Steel Design: An International Guide. Elsevier Applied Science, London, pp. 227–245.

Teixeira de Freitas, S., Kolstein, M.H., Bijlaard, F., 2010. Composite bonded systems for renovations of orthotropic steel bridge decks. Compos. Struct. 92, 853–862.

Teixeira de Freitas, S., Kolstein, M.H., Bijlaard, F., 2011. Sandwich system for renovation of orthotropic steel bridge decks. J. Sandwich Struct. Mat. 13 (3), 279–301.

Teixeira de Freitas, S., Kolstein, M.H., Bijlaard, F., 2013. Lightweight reinforcement systems for orthotropic bridge decks. In: Proceedings of IABSE Conference. Assessment, Upgrading, and Refurbishment of Infrastructures, Rotterdam, the Netherlands, pp. 500–501.

Vandepitte, D., 1979. Brugvloeren. In: Berekening van Cconstructies. Story Scientia, Ghent, Belgium, pp. 593–638.

Wolchuk, R., 1963. Design Manual for Orthotropic Steel Plate Deck Bridges. American Institute of Steel Construction (AISC), New York.

This page intentionally left blank

Bridge foundations

25

V. Modeer[a] *and R.K. Bharil*[b]
[a]Luminant, Naperville, IL, USA, [b]Biggs Cardosa Associates, San Jose, CA, USA

1. Introduction

To design the interface between a bridge structure and the earth-supported footings, abutments, embankments, retaining walls, and settlement slabs, a structural engineer relies heavily on geotechnical investigation reports and interaction with various geo-professionals, including geotechnical engineers, seismologists, and engineering geologists. The bridge foundation design process involves the planning for field exploration, field and laboratory investigations, development of foundation design parameters, field testing, and geotechnical analysis regarding various site-specific soil and geologic conditions. Special situations of foundation installations such as the end-bearing design on fractured to solid rock, development of seismic response spectrum or time-history analysis, and analyses/testing methods to obtain foundation capacity (without damaging the piles) play integral roles in today's bridge foundation engineering practice. The bridge foundation design is a highly iterative process between the structural engineer and the geotechnical engineer due to stiffness/displacement compatibility, load configuration, and geo-constructability. The bridge foundation risks can be significantly reduced by applying innovative techniques to predict the subsurface conditions accurately, number and depths of exploratory boreholes, ground improvements to manage future settlements and liquefaction potential, proper selection of the bridge foundation type (e.g., spread footings, driven piles, and drilled shafts), field monitoring and testing during construction, and factoring of subsurface conditions during the bridge type selection process.

This chapter introduces bridge engineers to various geotechnical design considerations involved in the planning, design, and construction of conventional as well as innovative bridges. It also reinforces the importance of roles geotechnical professionals play in developing the most suitable bridge foundation design. This chapter is not intended to provide specific or detailed geotechnical engineering design guidance; instead, it outlines the design requirements and overview of the services that geotechnical professionals are required to provide for major bridge projects. A bridge design team will require the service of the geotechnical profession's most highly regarded foundation specialists to successfully complete a major bridge project. Careful considerations should be given in selecting a professional engineering firm with experienced geo-professional teams that can provide such services.

Geotechnical professionals include geotechnical engineers, geotechnical engineers experienced in rock mechanics, geologists, seismologists, geophysicists, and engineering geologists. Structural engineers require the service of geotechnical

Innovative Bridge Design Handbook. https://doi.org/10.1016/B978-0-12-823550-8.00002-0

professionals in order to properly vet foundations for the geologic conditions at a specific site. Geotechnical professionals and structural engineers interface at the ground surface in the design of a bridge structure.

Most, if not all, major bridges cross bodies of water, and the geologic and geotechnical-related concerns are magnified at the location of rivers, streams, lakes, and ocean crossings. The primary reason that a body of water exists in a given location is due to geologic processes such as tectonics, volcanism, glaciation, rifting, and faults. For example, the lower Mississippi River is maintained to the west by the adjacent Pleistocene Terrace, the Nile River crosses five major regions that differ in geologic history (Butzer, 1980), the Rhine River flows through 11 geologic regions (Preusser, 2008; Woodward, 2007), and the Yangtze River (Zheng, 2013) flow was directed from the Tibetan uplift across the Jiangnan Basin, developing deep fluvial deposits. Such cited information is the beginning of the data that geotechnical professionals consider when recommending foundations for bridges.

The need for geotechnical professionals should be recognized from the planning to the construction phase on bridge projects. The design team must have a geotechnical professional thoroughly involved in the design and construction of major bridges. The following sections describe various steps involved.

2. Determination of the geologic setting

A professional or engineering geologist should be engaged in the design phase, which involves determining the geologic setting for the construction. The professional geologist will use many sources to determine the geologic setting. Many, if not most, countries have extensive geologic mapping by a natural resource agency or similar group. A geologist will review any published work on the geology of the bridge area. It is not uncommon for a bridge location to be moved or the location of foundation elements to be changed in the type, size, and location (TS&L, TSL, or Type Selection) phase of design due to the findings of a geologist at this stage of the work. The scope of a geologic setting report will depend on the complexity of the geology. An example of complex geology is the discovery of Karst topography, as discussed in Section 8.7.

All major bridge locations require geotechnical specialists to work closely with the structural engineer and project leads. Bridge design and construction require that both geotechnical and geology professionals are vital contributors to the project team. There is a vast amount of accessible, published technical reports and papers that reference the contributions of geotechnical and geology professionals in projects' success.

3. Geotechnical investigation report

A geotechnical investigation report is based on (i) the results of the geologic setting and assimilated geologic research provided by a professional geologist and principal geotechnical engineer and (ii) the range of geotechnical issues and potential solutions for selecting the foundation type. The geologist and geotechnical engineer work with the structural engineer to develop the engineering design of the proposed bridge concept. This phase is most likely completed concurrently with the TSL structural project phase. Often, prior geotechnical investigations completed on nearby projects serve as the starting point for early project planning and programming of a more thorough on-site geotechnical investigation. The geotechnical reports are often revised to correctly reflect the preliminary design, final design, and construction phases of major bridge projects.

The borings are drilled, and samples are taken at the proposed location of foundation or bridge pier locations. Typical field investigations are performed by a drill rig that obtains soil samples to be laboratory tested (Figure 25.1). Granular or sandy soils are sampled through the Standard Penetration Test (SPT), as described in ASTM D1586, ISO 22476, and Australian Standards AS 1289.6.3.1. The SPT provides disturbed samples only suitable for laboratory index property tests. The sample tube is driven 150 mm into the ground, and then the number of blows needed for the tube to penetrate each additional 150 mm up to a depth of 450 mm is recorded. The sum of the number of blows required for the second and third 150 mm of penetration is termed the *standard penetration resistance* or the *N-value*. The blow count is used to estimate the density of granular soils and shear strength of clay soils for empirical geotechnical correlations of the sampled stratum (Lunne et al., 1989; Robertson et al., 1983; Meyerhof, 1956; Rogers, 2006).

Figure 25.1 Warren George drill rig, drilling on the Hudson River for the new Tappen Zee Bridge.
Courtesy Tom Cooling and the New York State Thruway Authority.

Relatively undisturbed samples of fine-grained or clay soils are taken. The Standard Practice for Thin-Walled Tube Sampling of Soils for Geotechnical Purposes (ASTM D 1587) describes the process of taking samples of fine-grained soils. Kontopoulos (2012) describes various causes and avoidance techniques of fine-grained sample disturbance in his Ph.D. thesis. Soil testing is a professional geotechnical field that employs test methods appropriate for geotechnical analyses required to design and construct bridge foundations. The tests are too numerous to describe in this chapter. The design methodology is outlined next for the specific foundation type.

Depending on the soil type, the Cone Penetrometer Test (CPT) (ASTM Standard D 3441and ASTM D-5778) (Figure 25.2) or the Dilatometer Test (DMT) (ASTM D6635) can provide correlations of soil shear strength, consolidation characteristics, and soil classification information on the soils encountered. The seismic CPT (or SCPT), and the seismic DMT (or SDMT) can be used to determine shear wave velocity by means of an accelerometer on the SCPT or the SDMT that records shear wave velocity by recognizing the vibrations of a ground-level vibration source. Most CPT testing is completed with a porous tip that records the pore pressure of the soil as the CPT is advanced. Stopping the CPT at various depths in cohesive soils and recording the time to dissipation of the increase in pore pressure by CPT advance can be correlated with soil types to obtain an estimate of the coefficient of consolidation and permeability (CPT: Lunne et al., 1989; Mayne, 2007; Tumay et al., 1981; Tumay, 1997; Iliesi et al., 2012; DMT: Marchetti et al., 2001). This CPT resistance or N-value also serves as a quick indicator of the probable foundation condition for structural engineers as well.

Geophysical exploration methods are used to supplement borings and other intrusive sampling and testing of soil and rock stratigraphy. Geophysical methods are extremely valuable in investigating karst conditions (see Section 8.7). There are

Figure 25.2 CPT rig on the Hudson River for the new Tappen Zee Bridge. Courtesy Tom Cooling and the New York State Thruway Authority.

various methods, as described in *Principles of Applied Geophysics* (Parasnis, 1996). Geophysical methods include seismic reflection, seismic refraction, magnetic, electromagnetic and electrical resistivity, and conductivity surveys. Advanced methods of geophysical testing are multichannel and spectral analyses of surface waves (MASW and SASW). Geophysics is a highly specialized field of the geotechnical profession, and an expert should be used for this type of exploration (Dobrin and Savit, 1988; Kearey et al., 2002).

Rock coring is the sampling method for hard rock. Standard Practice for Rock Core Drilling and Sampling of Rock for Site Exploration (ASTM D2113) provides the standard method used in the United States. Rock core testing is also a professional geotechnical field that employs test methods for rock testing. The testing on core samples is only part of the analysis for determining the strength of a rock mass. The tests are too numerous to describe in this chapter. The other methods to determine rock mass design characteristics are the rock quality designation (Deere and Deere, 1988) and the rock mass rating (Bieniawski, 1989). The design methodology for rock foundations is outlined next.

4. Foundation selection during the type selection (TSL) project phase

The bridge structural engineer will develop the TSL report based on the results and constraints developed by influencers such as bridge architects, public opinion and input, waterway width constraints such as maintaining a clear zone for navigation, and other government-related regulatory constraints. These influences will allow the structural engineer to develop estimated foundation loads for further interaction with the geotechnical engineer. The location of the foundation elements and the foundation loads will determine the next phase of the geotechnical investigation.

The bridge engineer should consult with the geotechnical engineer during this phase to develop the potential foundation types. The type selection process will determine foundations that can resist vertical loads, dead loads, and traffic-induced live loads and lateral forces from potential vessel collision, wave and tidal forces, and seismic loads. TSL is a critical phase of the project, where the geotechnical and geology professionals combine the structural elements with the geologic conditions to develop innovative foundation solutions and realistic cost estimates for planning/funding purposes. The main tower foundations and anchorage of the Akashi Kaikyō Bridge are examples of this interaction. Kashima and his team developed an innovative robotic system to clean the seabed rock surface and place concrete in the submerged large-diameter caissons (Kashima, 1991).

Foundation selection for innovative and major bridges requires a lead geotechnical engineer and supporting team that is very experienced in foundation design and has a proven ability to be innovative in finding unique foundation solutions. The geologist should review the stratigraphic interpretations by the geotechnical engineer for geologic implications to the selected foundation type.

5. Geotechnical design report

The geotechnical design report will be detailed specifically for the bridge type selected in the TSL phase. The soil and underlying rock will be characterized in detail. The vertical, uplift, and lateral loads will be estimated so that foundation types can be reviewed and analyzed for applicability.

The offshore oil and offshore wind turbine foundation industry has been responsible for significantly improving innovative bridge foundations. The extreme depth and constant lateral loading from wave action have created a vacuum in foundation requirements that traditional onshore foundation design and foundations could not fill (Byrne, 2011). For example, large 3 m and larger-diameter driven piles or reusable spud piles on jack-up platforms or oil investigation drill rigs are common. There is a significant difference in foundation design for onshore versus offshore structures. Offshore foundations or substructures design approaches are based on much more flexible piles and are more concerned with lateral capacity than stiffness (Houlsby et al., 2005). Though this is a departure from the stiffness requirements of bridge foundations and structures, many of the offshore concepts can be and have been applied to bridges over deep channels and in heavy wave conditions.

The geotechnical design report will also identify potential construction-related problems. Such conditions could be glacial sands and gravels that will require hard driving for driven piles. The same sands and gravels would likely require full casing advanced during drilling for a drilled shaft foundation. Soft soil deposits are also commonly present in major river crossings in deltaic deposits such as in the lower Mississippi River and the Yangtze River delta (Liu et al., 1992).

6. Foundation design

6.1 Driven pile foundations

6.1.1 Steel H-piles

Steel H-section piles (designated as HP shapes in AISC tables) are normally designed as end-bearing piles (Figures 25.3 and 25.4) (ASTM A690/A690M, Eurocode 3, Part 5: Piling). H-shaped piles are used because of their structurally compact section. A structurally compact H-section allows high driving stresses and a more predictable location of the tip relative to the pile top. Driving a steel beam that has a high section modulus about one axis will allow bending, permanent deformation, and damage about the weak axis during driving. H-piles are typically used for end bearing in dense sand, hard clay, clay shale, or a hard rock formations. Many of the formations that are suitable for end bearing are overlain by weathered zones, vary in elevation across the top of the stratum, or have overlying inclusions such as cobbles or boulders and require a “driving shoe” to be added to the tip to aid in preventing damage and penetrating through obstacles. End bearing H-piles should have wave equation analyses performed for the subsurface conditions to better match the pile driving hammer to the

Figure 25.3 Route 490 Ramp Bridge at Exit 27, Delmag, D 19–32.
Courtesy New York State DOT.

Figure 25.4 West Dodge Project H pile driving.
Courtesy Nebraska DOT.

pile and not cause damages to the pile during driving. The wave equation analysis can provide pile capacity estimates but is much better suited to determining driving stresses for a given pile and hammer system in a given soil profile when driven to refusal.

6.1.2 Steel pipe piles

Pipe piles can be fabricated as extruded or rolled thin-walled pipe piles, spiral welded steel, extruded steel, and rolled steel (ASTM A252, Standard Specification for Welded and Seamless Steel Pipe Piles). The available size range of pipe piles and the stiffness that can be enhanced by increasing the pipe wall thickness has made pile piles desirable for major bridge foundations. Pipe piles can also be driven with a closed end and filled with reinforced concrete as a structural element. Depending on location, the steel wall's corrosion can be a concern and should be accounted for in sizing the pipe. Typically, pipe piles greater than 1 m in diameter are open-ended. Driving very large 3 m and larger-diameter piles became possible as a result of the offshore foundation construction (Figures 25.5–25.7). Pile-driving equipment also became available for these piles as a result of the need to drive large piles for the

Figure 25.5 Driving 1.82 m diameter, 85 m long open-end pipe piles for the New Tappan Zee Bridge over the Hudson River, New York.
Courtesy New York State Thruway Authority.

Figure 25.6 Driving 2.5 m piles for the San Francisco–Oakland Bay Bridge with hydraulic impact hammer.
Courtesy California DOT.

Figure 25.7 Menck, MHU1700T Hammer.
Courtesy California DOT.

offshore industry. There is a likelihood that thin-walled pipe piles used for friction and end bearing could be damaged during the driving if the pile and hammer system are not appropriately matched. Wave equation analyses should be performed for thin-walled pipe pile driving to determine driving stresses for a given pile-and-hammer system in a given soil profile.

6.1.3 Concrete piles

Driven concrete pile, which is typically precast and prestressed—often manufactured in circular, square, hexagonal, or octagonal shapes—sometimes makes for an economic foundation in certain areas such as Florida and California in the United States, where casting yards are available (Figure 25.8). Square concrete piles from 60 to 90 cm are commonly used with larger sizes up to 3 m that are less common but used for major bridges. These are typically used as friction piles but can be outfitted with steel driving tips for driving to rock or very dense soil to develop high end bearing. Precast, prestressed concrete cylinder piles, up to 140 cm in diameter, are also common in coastal areas and are driven as primarily as friction piles. Concrete piles provide high durability in marine environments and can provide high capacity. However, concrete piles are more difficult to splice, are more easily damaged during driving, and typically require larger lifting equipment than steel piles. Wave equation analysis is required to estimate driving stresses and drivability during the pile design phase. Dynamic testing during pile installation of *indicator piles* in each cap is needed to monitor driving stresses to verify the integrity and pile capacity. Concrete piles are designed based on the Guide to Design, Manufacture, and Installation of Concrete Piles (ACI 543R).

Figure 25.8 Concrete pile driving, Napa, CA (Argyriou, licensed under Wikipedia Commons, 2006).

6.1.4 Integrity testing of driven piles

- ASTM D-4945— 00 Standard Test Method for High Strain Dynamic Testing of Piles (Pile Driving Analyzer, PDA).

6.1.5 Load testing of driven piles

- ASTM D1143, Standard Test Methods for Deep Foundations Under Static Axial Compressive Load
- ASTM D3689, Standard Test Methods for Deep Foundations Under Static Axial Tensile Load
- ASTM D 3966—90 Standard Test Method for Piles Under Lateral Loads
- ASTM D-4945— 00 Standard Test Method for High Strain Dynamic Testing of Piles (Pile Driving Analyzer, PDA) (Using CAPWAP option for pile load estimate).

6.1.6 Design methodology for driven piles

There are many published design manuals that can be used for driven pile design. Very comprehensive manuals have been published by the US Federal Highway Administration (FHWA) and are available in the public domain. Also, several authored and edited references (Hannigan et al., 2006; Washington State Department of Transportation, Geotechnical Design Manual, 2020; Fellenius, 2014; Sands, 1992; Smoltczyk, 2003; Fang, 1991; Tomlinson, 1994; Das, 2011; Rowe, 2001; Naser et al., 2011; and others) prove quite valuable.

6.2 Drilled foundations

There are many types of drilled foundations that are appropriate for various types of bridges. One major advantage of any drilled foundation is the minimal vibration and noise that occur during installation and the drilled foundation's ability to provide a very large range of vertical load bearing and lateral load capacities. The drilled shaft is also called caissons, drilled piers, cast-in-drilled-hole piles (CIDH piles), or cast-in-situ piles (Figures 25.9–25.12).

Drilled foundations include augered piles with diameters less than 75 cm. These augered piles include continuous flight auger (CFA) hollow stem augered piles. These are normally suitable for use as friction piles. The auger is drilled to the designated depth, and pressurized grout is installed through the hollow stem as the auger is withdrawn from the excavated hole. Another type of augered pile is the drilled displacement pile. While not as common as the CFA pile, the stated principal advantage of the drilled displacement pile is that the displaced soil is compacted or densified. The developers state that this process creates a larger effective diameter pile and, therefore, a higher-capacity augered pile. The advocates of this type of pile state that they can provide an accurate capacity of the pile from the installation measurements. This pile type cannot be confidently designed without field load tests coupled with consistent soil stratigraphy. Micropiles (e.g., pin piles, needle piles, and root piles) are a drilled foundation type that has advantages in supporting foundation underpinning, foundations in confined areas, adding foundation capacity, and as a drilled foundation

Figure 25.9 Large crane mounted drilled shaft rig. Bond Bridge, MoDOT, Kansas City. Courtesy Dan Brown, Dan Brown and Associates.

Figure 25.10 Top-driven remote-controlled drill rig.
Courtesy Dan Brown, Dan Brown and Associates.

Figure 25.11 Auger retrieving rock from shaft. Courtesy of MnDOT and WisDOT St. Croix River Bridge, Extradosed Cable-Stayed Structure.

alternative (Cadden, 2004). Micropiles founded in rock have been tested to vertical capacities up to 4500 kN (Cadden, 2004). All of these pile types can provide sufficient vertical capacity by using a pile group with a structural cap. The need for lateral capacity or structural rigidity for seismic loads needs to be evaluated in detail for micropiles (Cadden and Gomez, 2002).

Figure 25.12 Cleaning a rock auger into a spoils barge.
Courtesy of MnDOT and WisDOT St Croix River Bridge, Extradosed Cable-Stayed Structure.

Most, if not all, major bridges have drilled shaft foundations that have diameters greater than or equal to 24 in. (60 cm). Drilled shaft foundations can typically be open auger drilled and/or cased after drilling. If the drilled shaft diameter is generally 6 ft. (180 cm) or greater, or if the soil is determined to collapse in an uncased drilled open hole, the shaft may be encased in a phased manner during the advancing of the shaft or with a telescoping casing (Brown et al., 2010). The soil in the shaft is removed by the auger drilling process and replaced with concrete. The concrete shaft is normally reinforced to some depth below the ground surface with a steel rebar cage to increase stiffness to align with the structural design. Use of temporary and permanent steel casing should be evaluated if subsurface springs, unsuitable soil, or voids may be present. However, some bridge owners (e.g., railroads) require temporary and/or permanent steel casings regardless of the soil type. Large-diameter shafts typically speed up the construction by providing large foundation capacities in a few piles but also impose risks to the project schedule if major unanticipated subterranean soil conditions are discovered during drilling. The contractor ultimately selects the drilling method, but the recommendations of an experienced geotechnical engineer should be considered a professional assessment and should be included in the design documents. Excellent summaries of drilled shaft design considerations are included in Brown's works (Brown et al., 2010; Brown, 2012).

6.2.1 Integrity testing of drilled shafts

Drilled shafts and auger-cast piles require integrity testing to verify that the infilled concrete is a minimum diameter and free of anomalies (blowouts or voids). This testing is necessary since, unlike the exposed surface of a concrete bridge column, a drilled shaft's surface is not accessible for visual or manual examination after the concrete pour. There are three accepted methods for the integrity testing of drilled foundations:

- The first is low-strain impact integrity or low-strain dynamic tests (ASTM D5882 Standard Test Method for Low-Strain Impact Integrity Testing of Deep Foundations). This is a simple test in principle. Accelerometers are attached to the top of the concrete shaft or pile, and the concrete is struck with a blow that sends a compressive wave into the pile. The return times that are less than what is calculated for a full length indicate changes in the cross section of the pile. Near-surface construction deformities and reinforcement can return reflected waves that interfere with the deeper reflections. The testing company should provide the ratio of length to maximum diameter at which its equipment can be effective, which is normally 30 or less. These tests are commonly used with CFA piles with lengths of 10 to 15 m or less.
- The second test type is cross-hole sonic logging (ASTM D6760–08 Standard Test Method for Integrity Testing of Concrete Deep Foundations by Ultrasonic Crosshole Testing). This method was derived from cross-hole shear wave testing in geotechnical boreholes. Cross-hole sonic logging requires the attachment of a minimum of three steel tubes to the reinforcing steel cage. The tubes must accommodate the ultrasonic transmitter and receivers. The sonic wave arrival times are converted to wave speed that must be compared to standard concrete at various set times. Differences in the wave speed along the shaft indicate changes in the shaft circumference. A drawback of this test is that it only evaluates concrete within the reinforcing cage.
- The third type, thermal integrity testing of drilled shafts, is not yet an ASTM standard, and yet it is a very accurate method to determine shaft integrity. Mullins, 2009 states:

  > *Thermal Integrity testing utilizes the thermal signature generated during the hydration phase of the concrete curing process. Deviations in the thermal signature from a gradient predicted by modeling the concrete mix design and soil profile can indicate anomalies in the shaft cross-section. A decrease in the measured temperature may indicate a decrease in shaft cross-section, whereas an increase in measured temperature may be indicative of a bulge or increase in the shaft cross-section is capable of detecting anomalies outside the reinforcing cage such as bulging outward and necking inward (Mullins et al., 2007).*

6.2.2 Load testing of drilled shafts

- ASTM D1143 Standard Test Methods for Deep Foundations under Static Axial Compressive Load
- ASTM D3689 Standard Test Methods for Deep Foundations under Static Axial Tensile Load
- ASTM D3966 Standard Test Method for Piles under Lateral Loads

6.2.3 Design methodology for drilled shafts

There are many published design manuals that can be used for the design of drilled shafts and drilled piles. These very comprehensive manuals (Fang, 1991; Smoltczyk, 2003; Brown, 2012; Brown et al., 2010; Sands, 1992; Cadden, 2004; Sabatini et al., 2005) are published by the US Federal Highway Administration (FHWA) and are available in the public domain. Various state departments of transportation publish their requirements for drilled shafts design and construction. Bridge engineers using the soil–structure interaction parameters developed by geotechnical engineers design the drilled shaft's final section and depth. Various assumptions made in the vertical and lateral load demands and shaft capacities must be reconciled for various computed load combinations prescribed by bridge design codes. Seismic requirements (e.g., plastic hinge location, displacements, collapse) typically play a significant role in drilled shafts designs in earthquake-prone areas and liquefiable soils.

6.3 Foundations on rock

Bridge footing or mat-type foundations on bedrock are designed as described in Wyllie (1999), Smoltczyk (2003), and Rock Foundations (1994). An example will best illustrate the type of footing or mat foundation for major bridges. The methodology for the example described here could be used for foundations as innovative as the Salginatobel Bridge near Schiers, CH (completed in 1930), and the Schwandbach Bridge near Bern, CH (completed in 1933), both designed by Robert Maillart. These bridges are considered works of art and have parapet thrust or bearing type foundations on rock (Billington, 2003). The Hoover Dam Bypass Arch Bridge, Mike O'Callaghan–Pat Tillman Memorial Bridge, has nine precast segmental column sets founded on rock that utilized structural, geotechnical/rock mechanics, and geology professionals to investigate and design. The bridge received the International Federation of Consulting Engineers (FIDIC) Centenary Award in 2013.

Suspension bridges require the uplift and horizontal forces at the bridge abutments to be held in place by tiedown shafts, rock anchored mats, or very large gravity anchorages or anchor blocks. The largest suspension bridges require extremely large anchorage. The Golden Gate Bridge and the world's longest suspension bridge, the Akashi Kaikyō Bridge, have very large concrete anchorage blocks. The anchorage block system is subjected to both uplift and lateral forces from the suspension cable end. The main towers for many major bridges are often supported on rock by means of a large caisson. Similarly, conventional arch bridges also require sound foundation conditions to resist an enormous amount of horizontal thrust exerted by arch action. Some cable-stayed bridges may need end soil anchorages but often use the structural means to self-balance their horizontal forces.

The Akashi Kaikyō Bridge anchorage is an example of rock foundation design for the anchorage and main towers:

> *Anchorages measure 63 m by 84 m in plan and extend into the Kobe and granite layers at the site. This required special foundation construction technology. The Honshu anchorage had to be embedded 61 m below sea level, and the anchorage excavation had to be performed in the open air. Therefore, an 85-m-diameter circular slurry wall, 2.2 m thick, was constructed and subsequently used as a retaining wall. Excavation within the slurry wall was followed by the placement of roller-compacted concrete to complete anchorage foundation construction. The Awaji anchorage foundation was constructed using steel pipes and earth anchors to support the surrounding soil. The excavated foundation was filled with specially designed flowing-mass concrete. Both anchorages were completed with the construction of a huge steel supporting frame used to anchor the main suspension cable strands (Cooper, 1998).*

Each anchor weighed an average of 390,000 metric tons. “The foundation (main towers) was constructed using a newly developed laying down caisson method. Steel caissons, 80 meters in diameter and 70 meters in height, were towed to the tower sites, submerged, and set on the pre-excavated seabed (pre-excavated to rock)” (Cooper, 1998). The seabed rock was evaluated to support the 181,000 metric tons of vertical force along with the forces from wind, earthquake, wave action, and vessel collision. Before setting the caisson and concreting, the seabed was prepared by using “a cleaning robot to clean the undersea bedrock surface” (Kashima, 1991).

Rock mass properties and accurate definition of the rock surface area are necessary to design and construct a foundation on rock. The previous example of the Akashi Kaikyō Bridge foundation construction is an example of the geotechnical engineer, the geologist, and the geotechnical rock mechanic professional working together with the structural team.

7. Foundation construction

The easiest to access and most complete manuals for construction monitoring and inspection is the FHWA manuals. The Pile Driving Contractors Association for driven piles and the Deep Foundations Institute for drilled piles provide excellent construction guidelines and sample specifications. Performing an independent constructability evaluation or soliciting input from the foundation contractors or organizations can often limit surprises during the bidding and construction phases of the bridge projects. There are other excellent sources for foundation construction in various publications (Sabatini et al., 2005; Brown et al., 2010; Hannigan et al., 2006b; Smoltczyk, 2003).

8. Special considerations

8.1 Liquefaction

Bridge foundations are inevitably located in seismically active regions. A geoscience-based seismic hazard analysis, which will determine structural design considerations to resist the earthquake loadings, will be performed. In addition, the most serious impact to foundations that may be revealed in the hazard analysis is liquefaction. Liquefaction occurs when earthquake ground-motion vibrations cause pore water pressure within a mass of mainly granular soil particles to lose contact with one another. The saturated granular soil mass behaves like a liquid and loses shear strength. Foundations lose support, and mat or shallow foundations sink or tilt, pile foundations lose lateral support during the earthquake ground motions, and saturated slopes will slide (Idriss and Boulanger, 2008; Ashford et al., 2011; Fellenius and Siegel, 2008). Ground improvements and accounting for liquefaction into the structural design are commonly used methods to mitigate liquefaction effects.

8.2 Lateral pile loads

The analyses of lateral pile loads with computed P-Y curves is that lateral load analysis is necessary for the design of pile foundations that can withstand seismic, wind, ice, wave action, river, and tidal current loading of the bridge piers and superstructure. The lateral analysis of piles is defined in detail in Bearing Capacity of Soils (1992), the United States Army Corps of Engineers (USACE) Manual, and Duncan et al. (1994). Currently available software for P–Y-based analysis is described in Pando (2013). Structural designers will typically account for such lateral pile loads in the structural design of the foundation.

8.3 Downdrag and drag force on driven and drilled foundations

Fellenius (2014) defines *downdrag* as the pile settlement caused by soil adhering to the pile shaft. He defines drag force as the sum or integration of the unit negative skin friction. These are important distinctions to understand the neutral plane or unified design approach for pile design. The neutral plane method provides an understanding of the load distribution along the pile shaft (Allen, 2005). Siegel et al. (2014) provide an excellent summary of the neutral plane method, as well as a comparison to the former state of practice explicit method. These forces can be mitigated, to some degree, by proper construction staging schemes; however, the residual effects must be accounted for in the foundation design of the new and adjacent old foundation.

8.4 Vessel collision

The most complete and concise source of information on the design of foundations subject to various types of vessel collision is in *AASHTO Guide Specifications and Commentary for Vessel Collision Design of Highway Bridges*, 2nd Edition, with 2010 Interim Revisions, 2009. There is also guidance for assessing the risk of a bridge foundation to a vessel collision in the aforementioned document. The design of the foundation for accidents/collisions is risk-based.

8.5 Coastal storms

Bridge foundation loads from coastal storms are design elements for every bridge along or near a coast. The storm does not have to be a hurricane or typhoon, yet these represent the most extreme coastal storms. High winds causing tidal surges and earthquake-induced tsunamis are an example of conditions identical to coastal storms. The publications *AASHTO Guide Specifications for Bridges Vulnerable to Coastal Storms* (2008) and Douglass and Krolak (2008) provide detailed information for designing foundations to resist coastal storms.

8.6 Scour

Erosion of the soil around the bridge foundation is defined as scour. Scour is the primary cause of bridge failure in the United States. There are more than 20,000 highway bridges that are rated *scour critical* (Hunt, 2009). Scour can occur from coastal storms; streambed elevation changes due to upstream or downstream conditions; lateral shifting of a stream, harbor, or river dredging; and tidal action. The publication by Arneson et al. (2012) describes evaluation and monitoring methodologies and mitigation methods. Additional references for scour are Lagasse et al. (2007), Thompson and Beasley (2012), *Countermeasures to Protect Bridge Piers from Scour*, and Hunt's (2009) *Monitoring Scour Critical Bridges*. The primary cause of many bridge failures is scour, so the scour design must be accounted for in new bridge foundations. It is good practice to place spread footings well below the anticipated scour depth (for extreme flooding), limit the use of spread footings to only on bedrock, use deep foundation (i.e., piles and shafts) on erodible soil, ignore any soil resistance above the anticipated scour depths, assume most waterways are dynamic, and provide redundancy in the structural system from collapse whenever possible.

8.7 Karst conditions

Karst landforms are evident in every hemisphere and specifically where there are carbonate rock formations at or near the ground surface. The geologist will recommend a very detailed geotechnical investigation report to determine where the epikarst begins and downward to the top of unweathered rock or the karst surface. The epikarst is essentially the upper boundary of a karst system where groundwater leaches a weak carbonic acid into the soil and organic elements to cause an acid reduction by the calcium chloride rock. The calcium chloride is removed by this reaction, and the process continues (Kutschke, 2011; Kannan, 2005). Karst geologic conditions should be avoided as the investigation, design, and construction in this condition is generally very expensive. If karst cannot be avoided, the areal and vertical extent must be determined. Geophysical and field boring explorations are combined to evaluate the karst extent. There is not a singular process to explore, characterize, design, and construct foundations in karst. The karst in Florida is very different from the karst in Georgia, though they are less than 700 km apart in the United States. Excellent compilations of various case histories from around the world can be found in Beck (1995, 2005).

9. Foundation design standards and codes

The following publications are updated frequently, and only the latest edition should be used for designing bridge foundations.

- AASHTO, LFRD Bridge Design Specifications, Foundations Section. American Association of State Highway Officials. Adopted by states in the United States as bridge design code.
- Canadian Standard Council, Canadian Highways Bridge Design Code, Foundation Section. Canadian Standard Association, CSA-S6–06, Code and Commentary.

- Chinese National Standard (CNS), Chinese Code (TB10002.5–2005).
- Eurocode, EN. Geotechnical Design, Part 1: General Rules.
- Indian Code, Indian Code of Practice for Design and Construction of Pile Foundations IS: 2911.
- United Kingdom— BS 8004: Code of Practice for Foundations. Replaced by Eurocode 7.
- United States, ASTM, ASCE 70–5, IBC/BOCA.

References

Allen, T., 2005. Development of Geotechnical Resistance Factors and Downdrag Load Factors for LRFD Foundation Strength Limit State Design. Federal Highway Administration, Washington, DC. Publication No. FHWA-NHI-05-052.

American Association of State Highway and Transportation Officials (AASHTO), 2008. Guide Specifications for Bridges Vulnerable to Coastal Storm. Washington, DC.

Arneson, L.A., et al., 2012. Evaluating Scour at Bridges, fifth ed. FHWA Office of Bridge Technology, Washington, DC. FHWA-HIF-12-003 HEC-18.

Ashford, S.A., Boulanger, R.W., Brandenberg, S.J., 2011. Recommended Design Practice for Pile Foundations in Laterally Spreading Ground. PEER Report 2011/04. Pacific Earthquake Engineering Research Center, University of California, Berkeley, Berkeley, CA.

Bearing Capacity of Soils, 1992. USACE EM 1110–1-1905. Department of the Army, Washington, DC.

Beck, B. (Ed.), 1995. Karst Geohazards: Engineering and Environmental Problems in Karst Terrains. A.A. Balkema, Rotterdam, Netherlands.

Beck, B. (Ed.), 2005. 10th Multidisciplinary Conference on Sinkholes and the Engineering and Environmental Impacts of Karst. American Society of Civil Engineers. GSP 144.

Bieniawski, Z.T., 1989. Engineering Rock Mass Classifications. Wiley, New York.

Billington, D.P., 2003. The Art of Structural Design: A Swiss Legacy. Princeton University Art Museum, Princeton, NJ.

Brown, D.A., 2012. Factors affecting the selection and use of drilled shafts for transportation infrastructure projects. In: ADSC EXPO 2012 Geo-Construction Conference Proceedings, March 14–17, 2012, San Antonio, TX, pp. 25–35.

Brown, D., Turner, J., Castelli, R., 2010. Drilled shafts: construction procedures and LRFD design methods. NHI Course No. 132014. Geotechnical Engineering Circular No. 10. FHWA NHI-10-016. May 2010.

Butzer, K.W., 1980. Pleistocene history of the Nile valley in Egypt and lower Nubia. In: Williams, M.A.J., Faure, H. (Eds.), The Sahara and the Nile: Quaternary Environments and Prehistoric Occupation in Northern Africa. A.A. Balkema, Rotterdam, Netherlands, pp. 253–280.

Byrne, B., 2011. Foundation design for offshore wind turbines. In: PowerPoint Presentation. Géotechnique Lecture 2011 British Geotechnical Association. Institution of Civil Engineers.

Cadden, A., 2004. Micropiles: recent advances and future trends. Geotechnical Special Publication No. 125. American Society of Civil Engineers, Reston, VA.

Cadden, A.W., Gomez, J.E., 2002. Buckling of Micropiles – A Review of Historic Research and Recent Experiences. ADSC-IAF Micropile Committee.

Cooper, J.D., 1998. World's Longest Suspension Bridge Opens in Japan. Public Roads. 62 (1). FHWA, Washington, DC.

Das, B., 2011. Principles of Foundation Design, seventh ed. Cengage Learning, Stamford, CT.

Deere, D.U., Deere, D.W., 1988. The rock quality designation (RQD) index in practice. In: Kirkaldie, L. (Ed.), Rock Classification Systems for Engineering Purposes. ASTM Special Publication 984, Philadelphia, PA, pp. 91–101.

Dobrin, M.B., Savit, C.H., 1988. Introduction to Geophysical Prospecting, fourth ed. McGraw-Hill Book Co, New York, NY.

Douglass, S., Krolak, J., 2008. Highways in the Coastal Environment, second ed. Federal Highway Administration, Washington, DC. Hydraulic Engineering Circular 25. FHWA Office of Bridge Technology. Publication No. FHWA-NHI-07-096.

Duncan, J.M., Evans Jr., L.T., Ooi, P.S.K., 1994. Lateral load analysis of single piles and drilled shafts. J. Geot Div. ASCE 120 (5), 1018–1033.

Fang, H. (Ed.), 1991. Foundation Engineering Handbook, second ed. Springer Science+Business Media, New York, NY.

Fellenius, B., 2014. Basics of Foundation Design (The Red Book). Electronic Edition.

Fellenius, B.H., Siegel, T.C., 2008. Pile drag load and downdrag in a liquefaction event. J. Geot. Environ. Eng. ASCE 134 (9). New York.

Hannigan, P.J., et al., 2006. Design and Construction of Driven Pile Foundations. National Highway Institute, Federal Highway Administration, Washington, DC. Publication No. FHWA-NHI-05-042.

Hannigan, P.J., et al., 2006b. Design and Construction of Driven Pile Foundations Volume I and II. Publication No. FHWA NHI-05-042 and FHWA NHI-05-043, Washington, DC.

Houlsby, G.T., Ibsen, L.B., Byrne, B.W., 2005. Suction caissons for wind turbines. Invited Theme Lecture. In: Proc. International Symposium on Frontiers in Offshore Geotechnics, September 19–21. Taylor and Francis, Perth, Australia, pp. 75–94.

Hunt, B., 2009. Monitoring Scour Critical Bridges, a Synthesis of Highway Practice. NCHRP SYNTHESIS 396. Transportation Research Board, Washington, DC.

Idriss, I.M., Boulanger, R.W., 2008. Soil Liquefaction During Earthquakes. Monograph MNO-12. Earthquake Engineering Research Institute, Oakland, CA.

Iliesi, A., Tofan, A., Prestiuse, D., 2012. Use of Cone Penetration Tests and Cone Penetration Tests With Porewater Pressure Measurement for Difficult Soils Profiling. Bulletin of the Technical University of Ias¸i, Ias¸i, Romania.

Kannan, R., 2005. Essential elements of estimating engineering properties of karst for foundation design. In: Proceedings: Sinkholes and the Engineering and Environmental Impacts of Karst, ASCE, New York. ASCE, New York, pp. 322–330.

Kashima, S., 1991. Automation and robotics of underwater concreting in huge scale steel caisson, the main tower foundation of the Akashi Kaikyo bridge. In: 1991 Proceedings of the 8th ISARC. Stuttgart, Germany. International Association for Automation and Robotics in Construction (IAARC), the Netherlands.

Kearey, P., Brooks, M., Hill, I., 2002. An Introduction to Geophysical Exploration, third ed. Blackwell Science Ltd, London, UK.

Kontopoulos, N., 2012. The effects of sample disturbance on preconsolidation pressure for normally consolidated and overconsolidated clays. PhD Thesis, Massachusetts Institute of Technology, Boston, MA.

Kutschke, W., 2011. Geotechnical roadway design for karst environments. PowerPoint Presentation. In: 11th Annual Technical Forum Geohazards in Transportation in the Appalachian Region, August 3, Chattanooga, TN.

Lagasse, P.F., et al., 2007. Countermeasures to protect bridge piers from scour. In: NCHRP Synthesis 593. Transportation Research Board, Washington, DC.

Liu, K., Sun, S., Jiang, X., 1992. Environmental change in the Yangtze River delta since 12,000 years B.P. Quat. Res. 38, 32–45.

Lunne, T., Lacasse, S., Rad, N.S., 1989. General report/discussion session 2: SPT, CPT, pressuremeter testing and recent developments in in-situ testing part 1: All tests except SPT. In: Proceedings of the Twelfth International Conference on Soil Mechanics and Foundation Engineering. 4 (August), Rio De Janeiro, BR, pp. 2339–2403.

Marchetti, S., et al., 2001. The flat dilatometer test (DMT) in soil investigations. In: Report of the ISSMGE Technica1 Committee 16 on Ground Property Characterization from in- Situ Testing. International Society for Soil Mechanics and Geotechnical Engineering (ISSMGE).

Mayne, P., 2007. Cone penetration testing - a synthesis of highway practice. In: NCHRP Synthesis 368. Transportation Research Board, Washington, DC.

Meyerhof, G., 1956. Penetration tests and bearing capacity of cohesionless soils. J. Soils Mech. Found. Div. ASCE SM1, 82.

Mullins, G., 2009. Thermal integrity testing of drilled shafts. In: Presentation to AASHTO SOC Conference, August 4, Chicago, IL.

Mullins, G., Stokes, M., Winters, D., 2007. Thermal integrity testing of drilled shafts. Final Report - Contract BD544-20. Florida Department of Transportation, Tallahassee, FL.

Naser, A., DiMaggio, J., Kramer, W., 2011. Implementation of LRFD geotechnical design for bridge foundations. NHI Courses No. 132083. Publication No. FHWA NHI-10-039.

Pando, M.A., 2013. Analyses of lateral loaded piles with P-Y curves - observations on the effect of pile flexural stiffness and cyclic loading. In: NCDOT 7th Geo3 T2, Raleigh, NC.

Parasnis, D.S., 1996. Principles of Applied Geophysics. Chapman and Hall, London, UK.

Preusser, F., 2008. Characterisation and evolution of the river Rhine system. J. Geosci. Geol. Mijnbouw 87 (1), 7–19. Kluwer Academic Publishers, Dordrecht, Netherlands.

Robertson, P.K., Campanella, R.G., Wightman, A., 1983. SPT-CPT correlations. J. Geot. Eng. ASCE 109 (11). New York.

Rock Foundations, 1994. USACE EM 1110–1-2908. Department of the Army, Washington, DC.

Rogers, J.D., 2006. Subsurface exploration using the standard penetration Test and the cone penetrometer Test. The Geological Society of America. Env. Eng. Geoscience 8 (2), 161–179. Boulder, Colorado.

Rowe, K., 2001. Geotechnical and Geoenvironmental Engineering Handbook. Kluwer Academic Publishers, Dordrecht, Netherlands.

Sabatini, P., et al., 2005. Micropile Design and Construction (Reference Manual for NHI Course 132078). FHWA-NHI-05-039.

Sands, M. (Ed.), 1992. Piling: European Practice and Worldwide Trends. Institution of Civil Engineers, Thomas Telford House, London, UK.

Siegel, T.C., et al., 2014. Neutral plane method for drag force of deep foundations and the AASHTO LRFD bridge design specifications. In: Proceedings of the 62nd University of Minnesota Annual Geotechnical Engineering Conference, St. Paul, MN.

Smoltczyk, U. (Ed.), 2003. Geotechnical Engineering Handbook. Vols. 1–3. Ernst & Sohn, Berlin, DE.

Thompson, D., Beasley, D., 2012. NAVFAC Handbook for Marine Geotechnical Engineering (SP-2209-OCN). Naval Facilities Engineering Command, Washington Navy Yard, Washington, DC.

Tomlinson, M.J., 1994. Pile Design and Construction Practice, fourth ed. E & FN Spon, an Imprint of Chapman and Hall, London, UK.

Tumay, M.T., 1997. In-situ testing at the national geotechnical experimentation sites (Phase II). Final Report. FHWA Contract No. DTFH61-97-P-00161. Louisiana Transportation Research Center, Baton Rouge, LA.

Tumay, M.T., Boggess, R.L., Acar, Y., 1981. Subsurface investigations with piezocone penetrometers. Cone penetration testing and experience. In: Proceedings ASCE National Convention, St. Louis, MO, pp. 325–342.

Washington State Department of Transportation, 2020. Geotechnical Design Manual. M 46-03.23. Olympia, WA.

Woodward, J.C., 2007. The Nile: evolution, quaternary environments and material fluxes. In: Gupta, A. (Ed.), Large Rivers: Geomorphology and Management. John Wiley & Sons, Chichester, UK, pp. 261–292.

Wyllie, D.C., 1999. Foundations on Rock: Engineering Practice, second ed. E & FN Spon, an Imprint of Chapman and Hall, London, UK.

Zheng, H., 2013. Pre-Miocene birth of the Yangtze River. Proc. Natl. Acad. Sci. U. S. A. 110 (19), 7556–7561.

Further reading

American Association of State Highway and Transportation Officials (AASHTO), 2009. Guide Specifications and Commentary for Vessel Collision Design of Highway Bridges, second ed. with 2010 Interim Revisions. Washington, DC.

American Association of State Highway and Transportation Officials (AASHTO), 2020. AASHTO LRFD Bridge Design Specifications, Ninth ed. Washington, DC.

Engineering and Design: Standard Penetration Test, 1988. Technical Letter No. ETL 1110-1-138. U.S. Army Corps of Engineers, Washington, DC.

Standard Penetration Test, 2015. ISO 22476-3, ASTM D1586 (Wiki article). Available from http://en.wikipedia.org/wiki/Standard_penetration_test.

Expansion joints and structural bearings

26

Alessio Pipinato
AP&P, CEO and Technical Director, Rovigo, Italy

1. Introduction

Expansion joints and structural bearings are commonly produced according to codes and standards, and for railways, they are also created according to specific railway authority sanctions. Expansion joints for bridges are used to ensure the continuity of the running surface as well as the bearing capacity and the movement of the bridges, whatever the nature of the structure constitutive material. Bridge bearings ensure adequate mutual connection of different parts of a bridge, allowing the transfer of vehicular and external loads from the superstructure down to the substructure. Seismic bearings can mitigate the seismic damage to bridge structures with the mutual support of energy dissipation and dynamic isolation.

2. Expansion joints

2.1 Overview

Expansion joints are connecting elements between decks or between the deck and the abutment with the capacity to bear both vertical and horizontal actions, allowing free movements without perceptible resistance and ensuring safety to passing traffic. Joints, besides giving continuity to the road surface and allowing deformation of the connected structural parts, should provide additional features, such as

- Waterproofing
- Safety by ensuring maximum tire grip
- Providing ultimate comfort for passengers in transit by minimizing noise and vibrations
- Corrosion resistance
- Joint production in modulus, for simple and cost-effective installation, inspection, and maintenance
- Optimum functioning and durability of all components, with a reduction of the frequency of maintenance
- Minimal interference with the structure
- Availability of different mechanical anchorage solutions to suit customers' requirements.

Innovative Bridge Design Handbook. https://doi.org/10.1016/B978-0-12-823550-8.00020-2

The expansion joints can be divided into the following groups:

- Reinforced rubber joints: Reinforced rubber joints with bridge plates are made of elastomeric elements reinforced with hot vulcanized metal inserts. The displacement is obtained by rubber deformation. Two main alternatives are available:

a) Medium-displacement expansion joints: Modular reinforced rubber pads consist of a central connection plate and side-bearing elements vulcanized on steel plates. The mechanical anchoring system is composed of threaded rods fixed with epoxy resin or, alternatively, multidirectional clamps and anchor bolts, depending on the site requirements and a water-gutter in reinforced fabric with polyester, PVC-coated, or reinforced Hypalon mesh. An L-shaped aluminum profile is used for water drainage under pavement. The expansion joints offer in-service displacements from 50 mm (±25 mm) up to 400 mm (±200 mm), and up to double that in the seismic phase.

b) Large-displacement expansion joints (Figure 26.1): The deformation capacity is given by the axial deformation of rubber bellows placed horizontally at the sides of a central steel bridge plate covering the gap. They are similarly built as medium-displacement joints, except for the larger steel central plate. They are used for longitudinal movements in service from 300 to 1000 mm, and by increasing the size of the gap cover plate, they can ensure seismic movements greater than 1 m.

- Finger joints (Figure 26.2): Steel joints composed of modules attached to each other at the opposing header, where the finger-joint configuration of the complementary modules allows the movement. Modular finger elements are often made of weathering steel (CORTEN), suitably dimensioned and shaped stainless steel gutters reinforced with mesh, fixed to the two heads of the slab by means of epoxy resin. They have an L-shaped aluminum profile for water drainage under pavement. There are different solutions available on the market, covering longitudinal displacements from 50 mm (±25 mm) to 1000 mm (±500 mm).
- Nosing joints (Figure 26.3): Installed at pavement level, they are characterized by a flexible elastomer element at the gap, which allows the movement. They allow longitudinal displacements up to 100 mm (±50 mm) and small transverse displacements.
- Under-pavement joints: The joints are positioned at reinforced concrete slab level below the road surface and are covered by the pavement. They are made of either an extruded elastomeric profile, composed of two T-shaped metal profiles anchored to the slab or reinforced

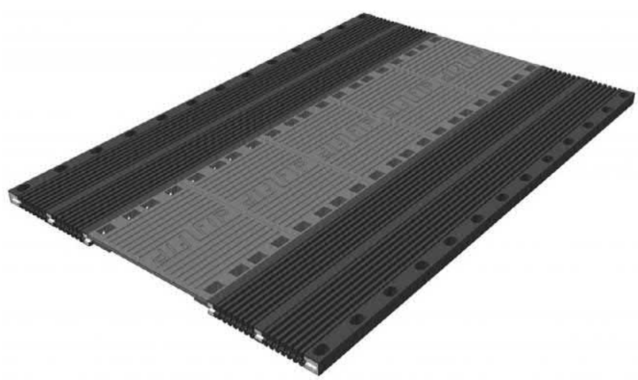

Figure 26.1 Reinforced rubber large-displacement expansion joint (FIP, 2020).

Figure 26.2 Finger joint (FIP, 2020).

rubber joints laid on the extrados of the slab and mechanically fixed to it; they allow a maximum displacement of up to 20 mm (±10 mm).

- Longitudinal joints: Reinforced rubber joints that through different mechanisms ensure the connection between two structures or two parts of the structure are arranged in a parallel configuration or slightly inclined with respect to the direction of traffic flow, while accepting differential movements between the parts. They are composed of reinforced rubber and allow for a maximum displacement of 30 mm (±15 mm) in the deck plane and up to 50 mm vertically.
- Railway joints: Railway joints are rubber joints with bridge plate made of elastomeric elements reinforced with hot vulcanized metal inserts. Their displacement is obtained through the sliding of internal elements and occurs at low friction, thanks to the coupling of PTFE and stainless steel. They offer dielectricity as an additional feature and prevent the ballast from penetrating the gap. Railway joints allow a maximum displacement of 600 mm (±300 mm) free transverse movement without limits and vertical deformations up to 50 mm. They are often subjected to detailed homologation according to the governing railway authority standard.

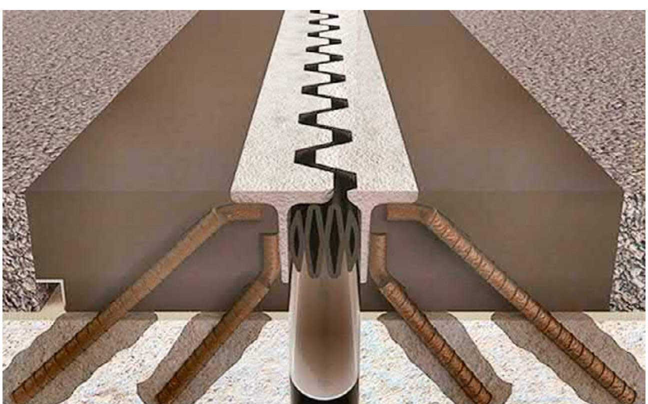

Figure 26.3 Nosing joint (FIP, 2020).

The main type of joints is modular, and therefore, they are particularly suitable for applications where it is necessary to operate only on part of the deck, as they allow operations without a complete closure of the bridge. Expansion joints should be produced, tested, installed, and monitored during their life according to codes and standard, which are different in each nation worldwide.

2.2 Design criteria

Expansion joints are designed to allow the movements of the following phenomena imposed upon the bridge. Concrete shrinkage, thermal variation, and long-term creep are the three most common primary sources of movement. Calculation of the movements associated with each of these phenomena must include the effects of superstructure type, tributary length, fixity condition between superstructure and substructure, and pier flexibilities. According to WSDOT (2019), a general formulation for the expansion joint calculation is

$$\Delta L,\mathrm{tot} = \Delta L_{\mathrm{shrink}} + \Delta L_{\mathrm{temp}} = \beta \cdot \mu \cdot L_{\mathrm{trib}} + \alpha \cdot L_{\mathrm{trib}} \cdot \delta T \tag{1}$$

where L_{trib} is the tributary length of the structure subject to shrinkage and thermal variation, β is the ultimate shrinkage strain after expansion joint installation (estimated as 0.0002 in lieu of more refined calculations), μ is the restraint factor accounting for the restraining effect imposed by superstructure elements installed before the concrete slab is cast (0.0 for steel girders, 0.5 for precast prestressed concrete girders, 0.8 for concrete box girders and T-beams, and 1.0 for concrete flat slabs), $\alpha =$ is the coefficient of thermal expansion of the structure, δT is the bridge superstructure average temperature range as a function of bridge type and location.

2.3 Codes and standard

The main codes and standard dealing with expansion joints are D.M. 17/1/2018 (Italy), ETAG032 (2013) in Europe as guidelines, and WSDOT Bridge Design Manual (WSDOT, 2019) and AASHTO LRFD Bridge Design Specifications (AASHTO, 2017) in the United States.

2.4 Working life

The expansion joint is a "kit" (ETAG032, 2013) composed of a set of at least two separate components that need to be put together to be installed permanently in the works (i.e., to become an "assembled system"). Its working life depends on the external loads or the imposed movements, the cycle frequency, the number of cycles and the durability (including fatigue, wear resistance, etc.) of the expansion joint and its components. It is also linked to the ability to replace components and the installation quality. The manufacturer shall declare the assumed working life of the joint (including its components). The assumed working life of the kit is based on the working life categories provided by ETAG032 (2013)—differentiating four increasing categories spanning from 10, 15, 25, and 30 years, respectively. The assumed working life of replaceable components shall be declared in the ETA.

2.5 Jointless structures

To avoid expansion joint maintenance, continuous spans built integrally with their abutments (also called integral or continuous bridges) can be designed. Detailed specifications can be found in Steiger (1991) and Burke (2009). In this situation, superstructure movements are restrained, and secondary stresses induced in superstructure and substructure should be addressed during design; otherwise, these stresses can damage structural elements and the road pavement. While continuous bridges are now prevalent, in existing bridges, simple-span structures are the most common solution. In order to avoid bridge deterioration due to lack of joint maintenance, a vast amount of techniques have been implemented to make continuous and existing simple-span bridges. The most common solution is the realization of a continuous bridge deck over multiple simple spans in order to reduce joint maintenance costs, and this also improves riding quality, lowers impact loads, and improves seismic resistance (Safty and Okeil, 2008).

3. Bearings

3.1 Overview

Structural bearings are devices installed in bridges to transfer loads and to restrain or release certain degrees of freedom of both displacement and rotation. Depending on design requirements, bearings can be divided into the main categories of structural bearings and seismic devices.

3.1.1 Structural bearings

Structural bearings are built to transfer design loads from the superstructure to the substructure. The main structural bearings produced worldwide are reported in Table 26.1.

3.1.2 Seismic devices

The seismic analysis and the design of the isolation system of a bridge is governed by different codes and standards (e.g., EN 1998-2, 2005 in Europe). In the seismic analysis of the isolation system of an entire structure, design action effects on individual components, including antiseismic devices, are assessed based on the design seismic action deduced from the structural seismic analysis. The main seismic devices produced worldwide are reported in Table 26.2. Figure 26.4 reports the corresponding types 3d scheme of the devices illustrated in Table 26.2.

Table 26.1 Structural Bearings

Description of the device			*Relevant clause*	*Graphic Representation*	*Notes*
				Plan view	
Rigid Connection Devices (RGDs)	*Permanent connection devices (PCDs)*	*Fixed*	5.2		This type of devices corresponds to type 8,1 (Restraint bearing) in of EN 1337 1:2000 Table 1
		Moveable	5.3		This type of device corresponds to type 8,2 (Guide bearing) in EN 1337 1:2000 Table 1
	Fuse Restraints	*Mechanic al fuse restraints (MFRs)*	5.3	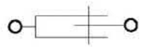	
		Hydraulic Fuse Restraints (HFRs)	5.3	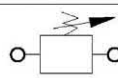	
	Temporary connection Devices (TCDs)		5.4		This type of devices is usually referred to as Shock Transmission Unit (STU)
Displacement Dependent Devices (DDDs)	*Linear devices (LDs)*		6.1		
	Non Linear devices (NLDs)		6.2		
Velocity Dependent Devices	*Fluid Viscous Dampers (FVDs)*		7.1	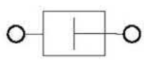	This graphic representation applies also to two-shaft dampers
	Fluid Spring Dampers (FSDs)		7.1		
Seismic Isolators	*Elastomeric*		8.2		The isolators are ahown in the deformed position to underscore their horizontal flexibility
	Lead Rubber Bearings		8.2		
	Curved Surface Sliders		8.3	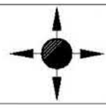	The symbols apply to both single and multiple curved surface sliders
	Flat Surface Sliders		8.3		The symbols apply to both types of sliders as given in EN 1337 1:2000, Table 1, 2.3 (free sliding pot bearing) and 3.5 (free sliding sphericl bearing)

Table 26.2 Seismic Devices for Bridges

N°	Symbol in the plan view	Type	Displacements			Rotation		
			υ_x	υ_y	υ_z	α_x	α_y	α_z
1.1	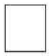	Elastomeric bearing (EB)	deforming	deforming	reduced	deforming	deforming	deforming
1.2		Elastomeric bearing with restraints for one axis (RS)	deforming	none	reduced	deforming	deforming	deforming
1.3	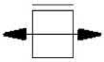	EB with unidirectional movable sliding part and RS for the other axis	sliding and deforming	none	reduced	deforming	deforming	deforming
1.4	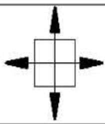	Elastomeric bearing with multi-directional movable sliding part	sliding and deforming	sliding and deforming	reduced	deforming	deforming	deforming
1.5	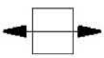	Elastomeric bearing with unidirectional movable sliding part	sliding and deforming	deforming	reduced	deforming	deforming	deforming
1.6		Elastomeric bearing with securing device for two axes	none	none	deforming	deforming	deforming	deforming
1.7	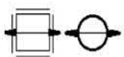	Elastomeric bearing with unidirectional movable sliding part and RS for two axes	sliding	none	deforming	deforming	deforming	deforming
1.8	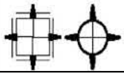	Elastomeric bearing with multi-directional movable sliding part and RS for two axes	sliding	sliding	deforming	deforming	deforming	deforming

N°	Symbol in the plan view	Type	Relative movements					
			Displacements			Rotation		
			υ_x	υ_y	υ_z	α_x	α_y	α_z
2.1		Pot bearing	none	none	very small	deforming	deforming	sliding and deforming
2.2		Pot bearing with unidirectional movable sliding part	sliding	none	very small	deforming	deforming	sliding and deforming
2.3		Pot bearing with multidirectional movable sliding part	sliding	scorrimento	very small	deforming	deforming	sliding and deforming
3.1		Spherical bearing with RS beyond the rotating part	none	none	almost none	sliding	sliding	sliding
3.2		Spherical rotating part likewise a RS	none	none	almost none	sliding	sliding	sliding
3.3		Spherical bearing with unidirectional movable sliding part (ext. guidance)	sliding	none	almost none	sliding	sliding	sliding
3.4		Spherical bearing with unidiractional movbale sliding part (int. guidance)	sliding	none	almost none	sliding	sliding	sliding
3.5		Shperical bearing with multidirectional movable sliding part	sliding	sliding	almost none	sliding	sliding	sliding

Continued

Table 26.2 Continued

N°	*Symbol in the plan view*	*Type*	*Relative movements*					
			Displacements			*Rotation*		
			υ_x	υ_y	υ_z	α_x	α_y	α_z
4.1		Steel point rocher bearing	none	none	almost none	rocking	rocking	sliding
4.2		Steel point rocker bearing with unidirectional movable sliding part	sliding	none	almost none	rocking	rocking	sliding
4.3	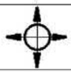	Steel point rocker bearing with multi-directional movable sliding part	sliding	sliding	almost none	rocking	rocking	sliding
5.1		Steel linear rocker bearing	none	none	almost none	none	rocking	none
5.2	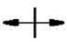	Steel linear rocker bearing with uni-directional movable sliding part	sliding	none	almost none	none	rocking	none
5.3	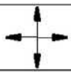	Steel linear rocker bearing with multi-directional movable sliding part	sliding	sliding	almost none	none	rocking	sliding
6.1		Steel roller bearing	rolling	none	almost none	none	rocking	none
6.2	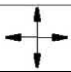	Single roller bearing with sliding part movable in the other direction	rolling	sliding	almost none	none	rocking	none
N°	*Symbol in the plan view*	*Type*	*Relative movements*					
			Displacements			*Rotation*		
			υ_x	υ_y	υ_z	α_x	α_y	α_z
7.1		Cylindrical fixed bearing	none	none	almost none	none	sliding	none
7.2		Cylindrical guided bearing along y direction	none	sliding	almost none	none	sliding	none
7.3	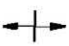	Cylindrical guided bearing along x direction	sliding	almost none	almost none	none	sliding	none
7.4	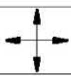	Cylindrical guided bearing along x and y direction	sliding	sliding	almost none	none	sliding	sliding
8.1		Fixed retain	none	none	sliding	sliding and deforming	sliding and deforming	sliding and deforming
8.2	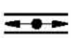	Mobile retain	sliding	none	sliding	sliding and deforming	sliding and deforming	sliding

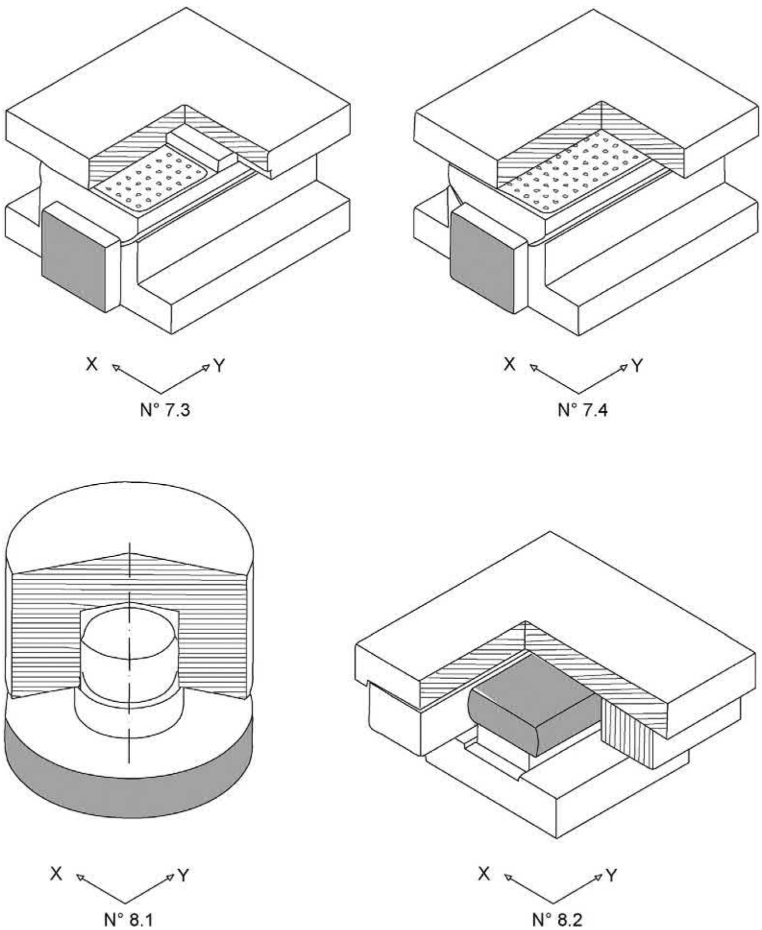

Figure 26.4 Seismic devices, types illustrated in Table 26.2.

(Continued)

3.2 Design criteria

Bridge bearings are built to transfer design loads from the superstructure to the substructure. Design loads that must be considered include dead loads; live loads; wind loads; seismic loads (in all direction, including the possibility of vertical uplift).

3.3 Codes and standards

The main codes and standards dealing with bearings are D.M. 17/1/2018 (Italy), WSDOT Bridge Design Manual (WSDOT, 2019) and AASHTO LRFD Bridge Design Specifications (AASHTO, 2017) in the United States, and EN1337 (2001) and EN15129 (2009) in Europe.

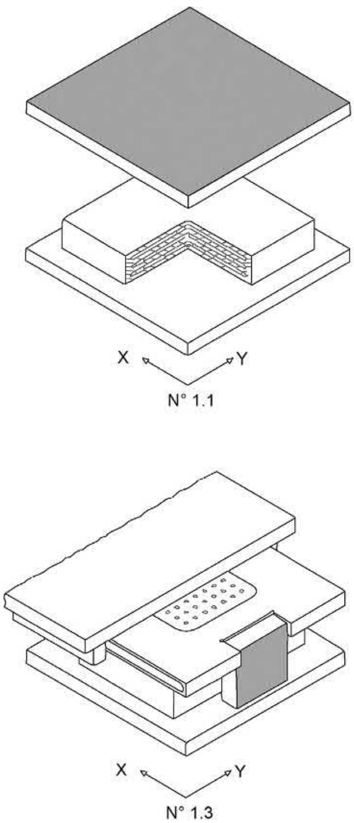

Figure 26.4, cont'd

(Continued)

3.4 Working life

The service life is based on declarations made by the device manufacturer as part of the validation procedure provided by the reference code. In accordance with EN1990, the service life of the device may be less than the design life of the bridge structure.

4. Case study: Rion-Antirion bridge

4.1 Introduction

The Rion-Antirion Bridge (Teyssandier et al., 2003), located in the Gulf of Corinth—an area prone to strong seismic events and windstorms—comprises a cable-stayed bridge and two approach viaducts (986 m long on the Rion side and 228 m long on

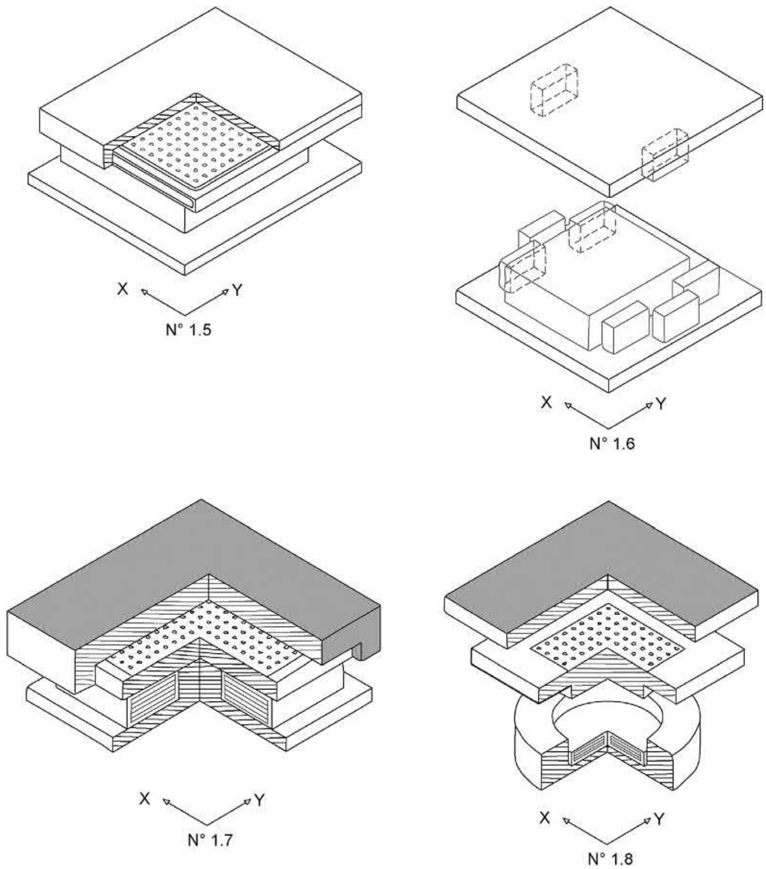

Figure 26.4, cont'd

(Continued)

the Antirion side). The main bridge, which has four pylons, was the cable-stayed bridge with the longest suspended deck in the world (2252 m) until to 2004, its span distribution comprising 286 m + 560 m + 560 m + 560 m + 560 m + 286 m. The critical factor in the design of the main bridge was its resistance to earthquakes, with a 2000-year return period and a PGA of 0.48 g. The fully suspended, continuous deck is free to accommodate all thermal and seismic movements in the longitudinal direction, whereas movements in the transverse direction are controlled by the protection system described in what follows, comprising fluid viscous dampers and fuse restraints. The cable-stayed deck is a composite steel structure made of two longitudinal plate girders 2.2 m high on each side of the deck, with transverse plate girders spaced at 4 m intervals and a concrete slab, with a total width of 27 m. Each pylon is composed of four 4 $\times$ 4 m legs made of high-strength concrete and joined at the top to provide the

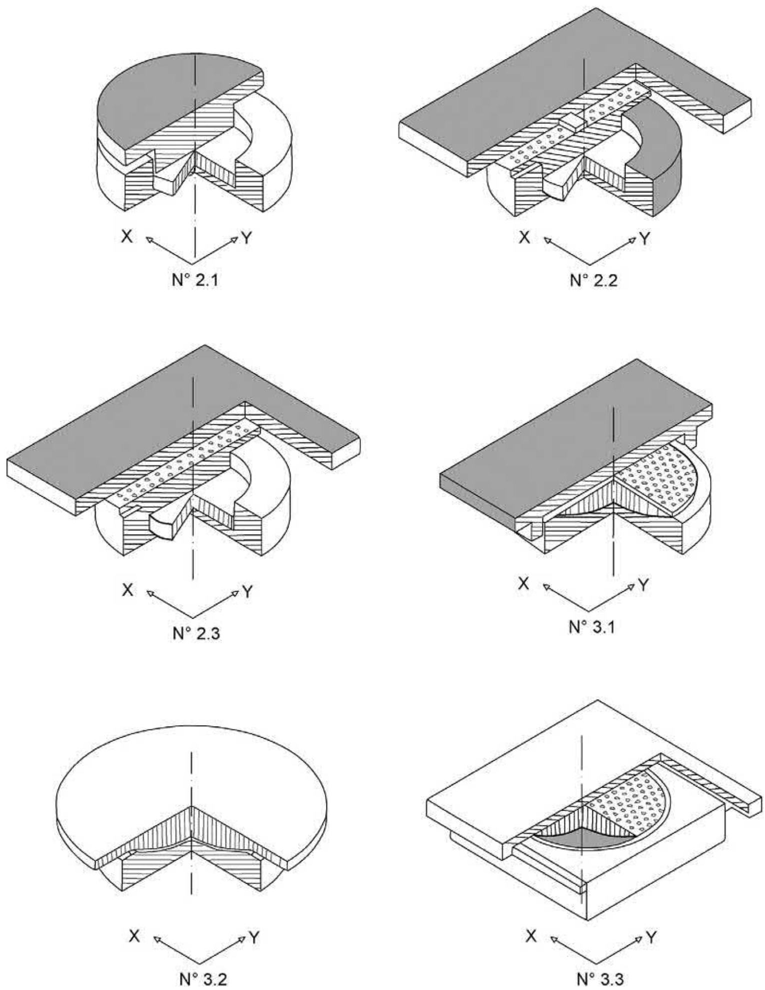

Figure 26.4, cont'd

(Continued)

necessary rigidity to support asymmetrical service loads and seismic forces. The pylons are rigidly embedded in the pier head to form a monolithic structure, up to 230 m high from the sea bottom to the pylon top (Figure 26.4). The approach viaducts are also seismically protected by a seismic isolation system comprising elastomeric isolators designed to provide the bearing function as well as the required period-shift effect, and the approach viaducts are also protected by viscous dampers that provide energy dissipation.

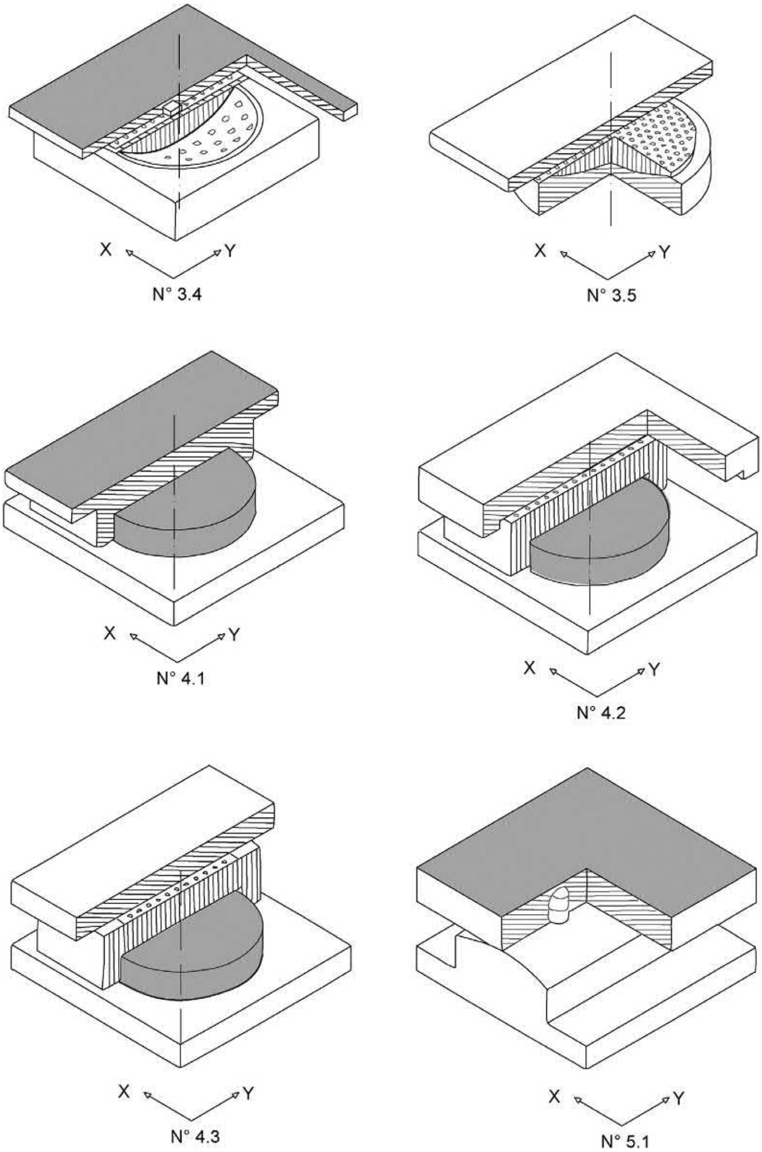

Figure 26.4, cont'd

(Continued)

4.2 Main bridge seismic protection system

The main bridge is equipped with a seismic viscous dampers of dimensions and design capacity never built before that connect the fully suspended deck to the pylon base in the transverse direction to reduce the transverse swing of the deck during an

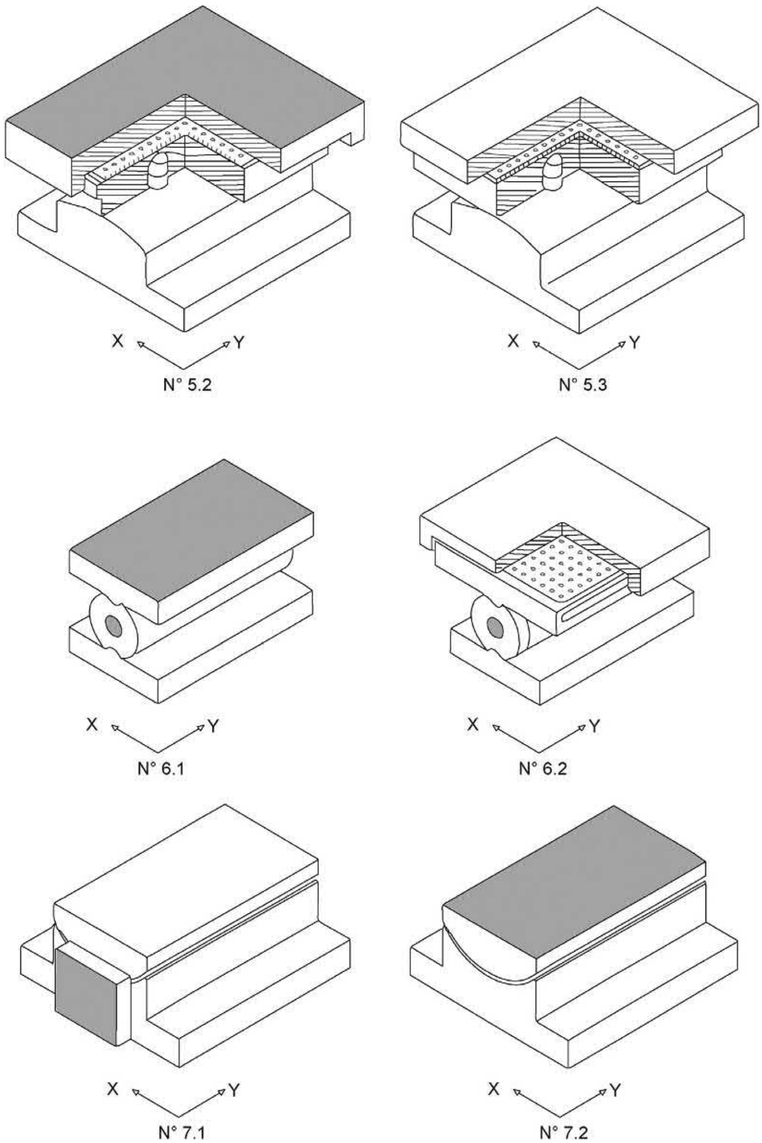

Figure 26.4, cont'd

earthquake. Large structural displacements induced by moderate earthquakes or windstorms are prevented by an additional restraint system, which fails at the occurrence of a major design event and allows the structure to freely oscillate with its damping system. This restraining system comprises fuse restraints installed in parallel with the dampers, so the deck is linked rigidly to the substructure when subjected to lateral loads not exceeding their design capacity. After their failure, it leaves the deck free to swing coupled to the dampers. The design failure force of the four viscous dampers (F_{max} 3500 kN, stroke ±1750 mm) and one fuse restrainer are installed at each pylon, and at the transition piers, there are two viscous dampers (F_{max} 3500 kN, stroke ±2600 mm) and one fuse restrainer. Figures 26.5 and 26.6 show the general arrangement of the viscous dampers and the restraint devices at each of the four pylons, as well as at the transition pier. The fluid viscous dampers used are nonlinear—i.e., with a force versus velocity law $F = c\ va$ with $a = 0.15$, (see Castellano et al. 2004; Infanti

Figure 26.5 The Rion-Antirion main bridge structure.

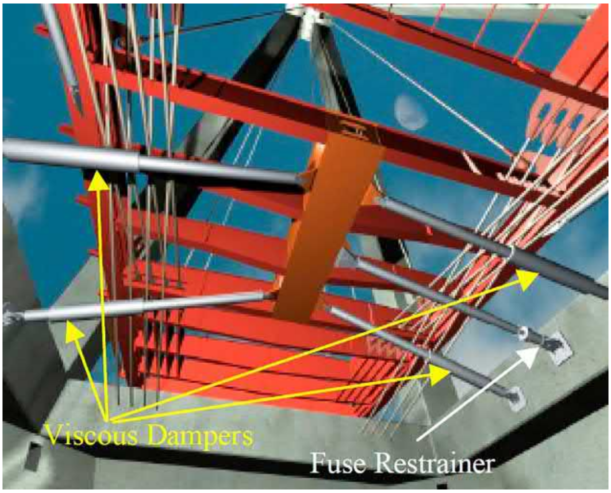

Figure 26.6 Rion-Antirion Main Bridge: arrangement of fluid viscous dampers on the main piers.

Figure 26.7 Rion-Antirion Main Bridge: arrangement of fluid viscous dampers on the transition piers.

and Castellano, 2001). The nonlinear viscous dampers were tested at an independent facilities in the United States according to HITEC protocol (see Infanti, 2001; Technical Report, 1998, 2000). The fuse restraints located on the main pylons are characterized by a failure load of 10,500 kN and are designed as single units equipped with spherical hinges at their ends. This configuration allows for design rotations as well as the correct alignment of the load along the device axis for any deck position. The element that fails when it reaches a desired design load—the so-called fuse element—is installed in the middle of the unit (Figure 26.7). Similarly, the units installed at the transition piers, as components of the dampers, are characterized by a failure load of 3400 kN. Particular specifications were imposed during the design stage: the dampers' reactions shall be within ±15% of the theoretical constitutive law, and fuse restrainer failure shall be within ±10% of the design value. Full-scale tests aimed at verifying the design characteristics are briefly described in this chapter, and further details are given by Benzoni and Seible (2002) and Infanti et al. (2003a, b).

4.3 Viscous damper full-scale testing

The main results of the qualification tests performed at both FIP Industrial Testing Laboratory and at the Seismic Response Modification Device (SRMD) Testing Laboratory of Caltrans at the University of California at San Diego (UCSD) were performed on a full-scale prototype of the viscous dampers.

4.3.1 Qualification tests on prototype

The prototype is characterized by a 3220 kN reaction at the maximum design velocity of 1.6 m/s [damping constant C = 3000 kN·(s/m) 0.15] and a ±900 mm stroke. Table 26.3 compares its characteristics with the characteristics of dampers installed on the pylons and transition piers, which are deemed to be the largest ever built to date (Table 26.4).

Table 26.3 Fluid Viscous Dampers Characteristics

Characteristics	Pylons	Transition Piers	Prototype
Damper series	OTP350/3500	OTP350/5200	OTP350/1800
Design capacity (kN) at 1.6 m/s	3220	3220	3220
Stroke (mm)	–1650/+1850	±2600	±900
Pin-to-pin length (mm)	10,520	11,320	6140
Total length (mm)	11,310	12,025	6930
Maximum diameter (mm)	500	550	500
Damper weight (kg)	6500	8500	3300
Total weight (kg)	9000	11,000	5500

Table 26.4 Test Protocol on Viscous Damper Prototype FIP OTP 350/1800

Test #	Test Name	Input	Number of Cycles	Stroke	Testing Conditions (V = Peak Velocity)
1	Thermal	Linear	1	895 mm	$V < 0.05$ mm/s for 5 min Increase velocity to 1 mm/s up to completion of the displacement
2	Velocity Variation	Sinusoidal	5 5 5 3 2	300 mm	$V = 0.13$ m/s $V = 0.40$ m/s $V = 0.80$ m/s $V = 1.20$ m/s $V = 1.60$ m/s
3	Full-stroke velocity	Sinusoidal or step loading	1	850 mm	$V_{max} = 1.6$ m/s
4	Wear	Linear	20,000	±5 mm	$V = 15$ mm/s Every hour, change position of the piston of about 100 mm
5	Velocity variation	Sinusoidal	2	300 mm	$V_{max} = 1.6$ m/s

The prototype is equal in every detail to the dampers designed for final installation with the exception of their length (and consequently their stroke), which is shorter (6.14 m pin to pin) in order to fit into the existing test rig of the SRMD Laboratory. The prototype was officially tested up to its maximum design conditions under the client supervision (Kinopraxia Gefyra—Greece) and the bridge design checker (Buckland & Taylor—Canada). Before shipping the prototype to the SRMD Laboratory, preliminary tests were carried out at FIP Testing Laboratory, which is equipped with a power system providing 630 kW at 1200 L/min. Results are reported in Figure 26.9, together with the results of tests carried out at the SRMD Laboratory. The matrix of tests carried out at the SRMD Laboratory is reported in what follows. Figure 26.8 shows the damper installed on the testing frame: average forces measured at different velocity levels (test # 2) are reported in Figure 26.9, together with those measured at a lower velocity at FIP laboratory. Maximum forces appear to be very symmetric in the entire range of velocities: a difference of 7% was recorded at maximum speed (1.6 m/s) only during the first cycle. The second cycle of the same test instead shows a deviation of 1.6%. The comparison among peak forces of different cycles shows that the damper provides stable reaction within a very wide velocity range (0.002–1.6 m/s): a reduction of the peak force of 3.8% between the fifth cycle and the first cycle was measured in test velocity A (0.13 m/s); for the high-speed tests, the maximum force reduction is equal to 10.4%. The typical force versus displacement response of the damper is reported in Figure 26.10 for the sinusoidal tests (#2) with 0.8 and 1.2 m/s peak velocity. The calculated energy dissipated per cycle (EDC) for the full-stroke and velocity test (test #3) was 11,035 MNm (+6% of the theoretical EDC). To perform this test, a 3.3 MW average power input was required. Thermocouples were installed both inside and outside the damper body to monitor any temperature rise during and after the motions. Air and nitrogen gas was used in a cooling box to restore the ambient temperature on the damper before a new test. Temperature increases were recorded for each test. The maximum increase took place at the end of the test velocity variation B, with 40°C recorded from the sensor installed inside the damper. Wear tests were completed with 10 sets of 2250 cycles, at constant velocity of 0.015 m/s and 10 mm total stroke. All the test results were deemed to be in agreement with the design specifications.

4.4 Production quality control tests on main bridge dampers

The aim of the production tests was to verify the compliance of the production units with the contract specification or, in other words, to verify whether their reaction and damping characteristics fall within the design tolerance range. The tests were performed at FIP in Italy (see Figure 26.11 for the testing configuration of a production unit). The contractual test program requires the following tests:

- Proof pressure test: The test aimed to verify whether the damper vessel can withstand 125% of the design internal pressure with no damage or leakage.

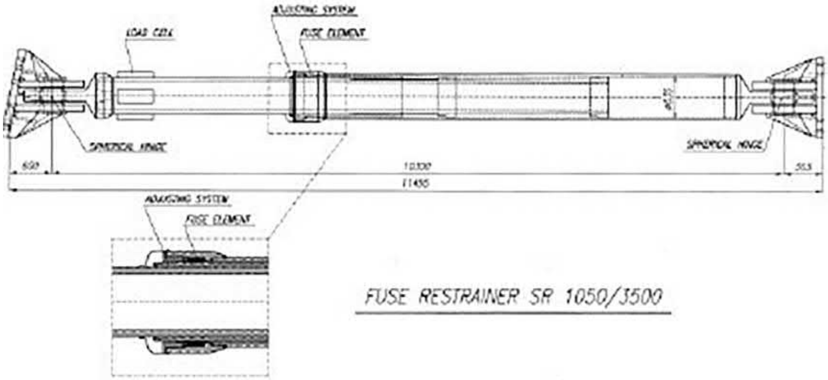

Figure 26.8 General configuration of fuse restraint installed on main pylons.

Figure 26.9 Prototype testing at SRMD facility (UCSD).

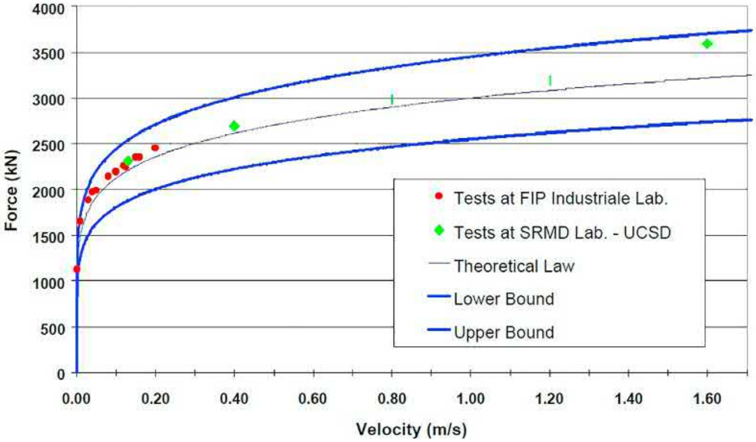

Figure 26.10 Experimental versus theoretical—damper constitutive law

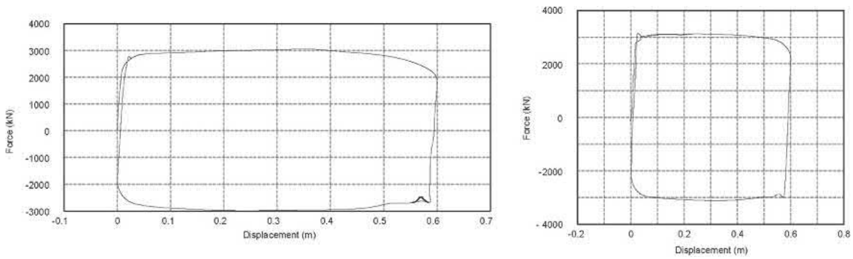

Figure 26.11 Experimental damper hysteresis loop ($V = 0.8$ m/s—left; $V = 1.2$ m/s—right).

- Low velocity test: The test aimed to verify whether the damper reaction at low velocity (less than 0.1 mm/s) is less than 200 kN to allow for ease of length adjustment as well as to prevent fatigue loads on the bridge.
- Dynamic test: The test aimed to verify whether the units can provide a reaction that follows the theoretical constitutive law with a maximum deviation of ±15%.

All the aforementioned tests yielded a positive outcome. Figure 26.13 shows the measured reaction for all the units of the first two production lots (serial numbers from 414946 to 414953), normalized with reference to the theoretical reaction, obtained imposing by three sinusoidal cycles of 250 mm stroke amplitude and reaching a peak velocity of 100 mm/s. Figure 26.14 shows a typical force versus displacement loop, obtained on one of the longest dampers—i.e., those to be installed in the transition piers, in a sinusoidal test with amplitude ±250 mm and a peak velocity of 175 mm/s.

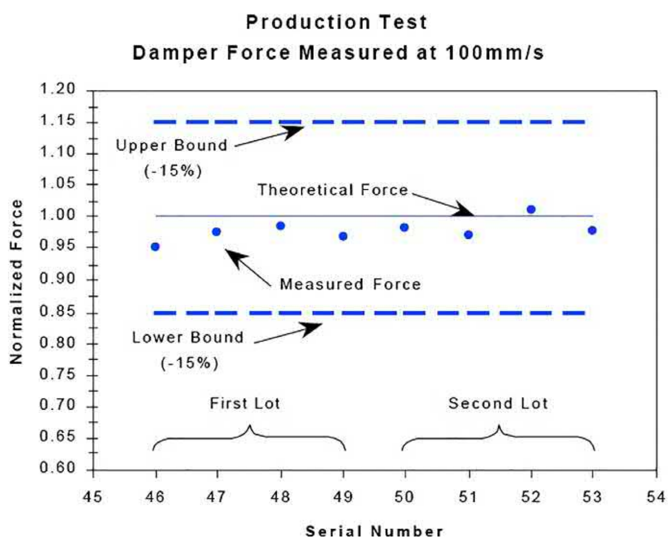

Figure 26.12 Normalized reaction of the production units

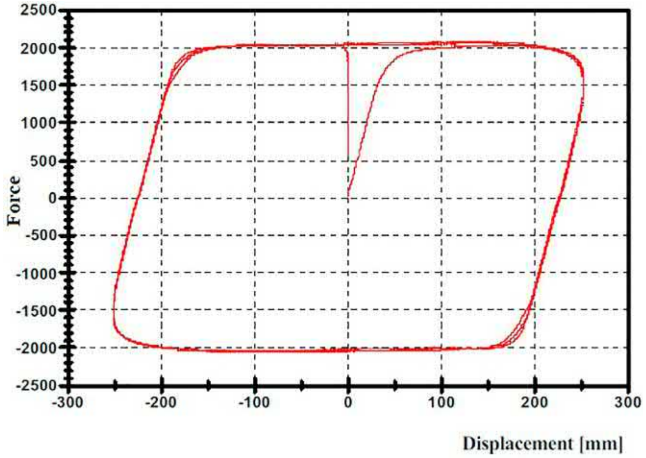

Figure 26.13 Hysteresis loop measured in sinusoidal dynamic tests at Vmax = 175 mm/s on a transition pier damper.

Figure 26.14 SR1050 Fuse element during fatigue test.

4.5 Fuse restraints testing program

The testing program was carried out on two full-scale prototypes of fuse elements of each type. It comprised a first test performed on one unit monotonically increasing the load up to failure, followed by a second test performed on the other prototype imposing two millions of cycles at a load level equal to 10% of the design failure load and then monotonically increasing the load up to failure. Since the restraints' first function is that of withstanding everyday actions (service loads), a second test was required to evaluate fatigue life as well as any influence of fatigue on failure strength. Failure test and fatigue test were carried out on different test rigs, the first one is a 8000 kN capacity rig commonly used for bearing tests while the second is a 3000 kN dynamic test rig: the same used for damper testing. Test results showed that both prototypes failed within design tolerances. All test results are presented in Table 26.5. Figure 26.14 shows the fuse element during fatigue test (Figures 26.15 and 26.16).

Table 26.5 Test Results

Device Type	Failure Load Capacity (kN)	Tolerance Range (kN)	Measured Load (kN)	Deviation (%)
SR340	3400	3060–3740	3545	+4.3
SR340	3400 (Fatigue)		3591	+5.6
SR1050	10,500	9450–11,550	10,382	−1.1
SR1050	10,500 (Fatigue)		11,765	+12.0

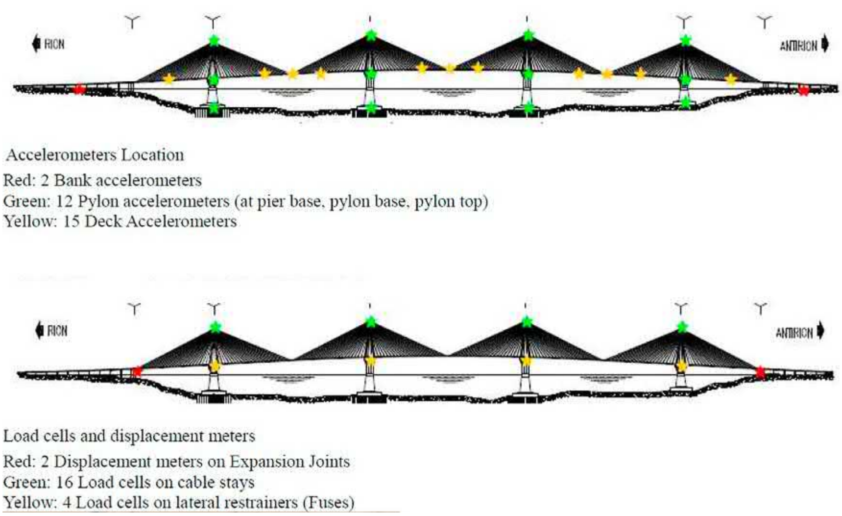

Figure 26.15 Monitoring system deployed onto the bridge.

Figure 26.16 Production tests at FIP laboratory on a fluid viscous damper for the main bridge.

4.6 The behavior of the bridge during the Earthquake of Achaia-Ilia

After a strong earthquake in June 8, 2008, named "Achaia-Ilia" Earthquake, a complete visual and geometrical monitoring was performed in order to evaluate the condition of the Rion-Antirion Bridge. Moreover, the data recorded by the instrumented monitoring (Figure 26.12) system provided valuable information for the behavior of the bridge, the characterization of the earthquake, and its intensity. The best estimated seismic free-field motions at the foundations of the bridge were computed. The maximum PGA recorded onshore was 0.127 g (at Rion Bank) while the maximum estimated at pier bases was 0.184 g (at M3). The results show that the corresponding acceleration response spectra remain below the 475-year return period design spectrum of EAK 2000 and in the range of the 120-year return period design spectrum of the bridge. The response of the main bridge, as from inspections and monitoring, was for all elements within the SLS while the lateral restrainers (sacrificial elements) were released to prevent damages on the structure. The structural status was completely recovered after the replacement of the fuses. The behavior of the seismic protection system confirmed all the design assumptions and the testing verification performed prior to the installation on both viscous dampers and fuse restraints. Furthermore, the easy fuse replacement operation demonstrated the soundness of the design. The main parameters recorded during the seismic event are reported in Table 26.6.

Table 26.6 Maximum Displacement and Velocity of Dampers

Location	Eastward Displacement (mm)	Eastward Velocity (mm/s)	Westward Displacement (mm)	Westward Velocity (mm/s)
M1 Fuse	−47.89	–	+48.55	–
M1 NE Damper	−50.11	−179.8	2.42	152.3
M1 SW Damper	−51.84	−199.5	+47.99	159.0
M2 Fuse	−28.55	–	+123.35	–
M2 NE Damper	–	–	–	–
M2 SW Damper	−30.09	**−150.6**	+114.28	**276.5**
M3 Fuse	−48.19	–	+74.79	–
M3 NE Damper	−43.35	−158.9	+70.69	148.4
M3 SW Damper	−37.01	−203.6	+77.62	155.2
M4 Fuse	−51.50	–	+60.57	–
M4 NE Damper	−45.73	−157.5	+56.64	143.6

References

AASHTO (2017), AASHTO LRFD Bridge Design Specifications. Eighth Edition, November 2017, AASHTO, US.

Teyssandier, J.P., de Maublanc, G., Morand, P., Papanikolas, P., 2003. The Rion-Antirion bridge. In: Proceedings of fib Symposium Concrete Structures in Seismic Regions, Athens, Greece.

Burke, M.P., 2009. Integral and Semi-Integral Bridges. Wiley-Blackwell, ISBN: 978-1-444-31637-7.

Castellano, M.G., Colato, G.P., Infanti, S., 2004. Use of viscous dampers or shock transmission units for seismic protection of buildings. In: Proceedings of the 13th World Conference on Earthquake Engineering, Vancouver BC, Canada. Paper No. 2172.

EN 1998-2, 2005. Eurocode 8: Design of Structures for Earthquake Resistance. Part 2. Bridges. CEN, Brussels.

ETAG032, 2013. Guideline for European Technical Approval of Expansion Joints For Road Bridges. EOTA-European Organisation for Technical Approvals, Brussels.

FIP, 2020. Structural Bearings Typologies. Official Web-site of FIP MEC, Italy.

Infanti, S., 2001. Seismic protection of Sehoharie bridge approaches through viscous dampers. In: Proceedings of IABSE Conference Cable-Supported Bridges—Challenging Technical Limits, Seoul, Korea.

Infanti, S., Castellano, M.G., 2001. Viscous dampers: a testing investigation according to the HITEC protocol. In: Proceedings of Fifth World Congress on Joints, Bearings and Seismic Systems for Concrete Structures, Rome, Italy.

Technical Report, 1998. Guidelines for Testing of Seismic Isolation and Energy Dissipating Devices. Highway Innovative Technology Evaluation Center.

Technical Report, 2000. Evaluation Findings of FIP Industriale Viscous Dampers According to the HITEC Testing Protocol. Rocketdyne Division of Boeing, Canoga Park, CA, USA.

Benzoni, G., Seible, F., 2002. Rion-Antirion Bridge—Prototype Tests of Damper FIP OTP 350/1800. Caltrans SRMD Test Facility Report N. 2002/01, San Diego, CA, USA.

Infanti, S., Papanikolas, P., Theodossopoulos, G., 2003a. Rion-Antirion bridge: full-scale testing of seismic devices. In: Proceedings of Fib Symposium Concrete Structures in Seismic Regions, Athens, Greece.

Infanti, S., Papanikolas, P., Castellano, M.G., 2003b. Seismic Protection of the Rion-Antirion Bridge. In: Proceedings of 8th World Seminar on Seismic Isolation, Energy Dissipation and Active Vibration Control of Structures, Yerevan, Armenia.

Safty, A., Okeil, A.M., 2008. Extending the service life of bridges using continuous decks. PCI J., 96–111. Precast/Prestressed Concrete Institute, Chicago.

Steiger, D.J., 1991. Field evaluation and study of jointless bridges. In: Stoyle, J.E. (Ed.), Third World Congress on Joint Sealing and Bearing Systems for Concrete Structures. American Concrete Institute, Farmington Hills, MI, p. 227.

WSDOT, 2019. Bridge Design Manual. WSDOT—Washington State Department of Transportation, Washington.

This page intentionally left blank

Part VIII

Bridge construction

This page intentionally left blank

Case study: The San Giorgio Bridge

27

Alessio Pipinato
AP&P, CEO and Technical Director, Rovigo, Italy

1. Introduction

After the collapse of the historical Morandi Bridge in Genoa, Italy, the new Polcevera Bridge (also called the San Giorgio Bridge) was built and opened to traffic in less than two years. In this chapter, the new Polcevera Bridge is described, and detail information about its engineering approach and design solution is provided.

2. The historical bridge collapse

On August 14, 2018, a heavy storm engulfed Genoa, Italy. The Morandi Bridge, crossing the Polcevera River in the center of the city, was busy as always, as it is a vital section of the highway system connecting France and Italy. Named after its engineer, Riccardo Morandi, the iconic bridge was a feat of Italian architecture when it opened in 1967. An innovative technique was used to encase steel supports in concrete, and the bridge became a landmark for the port city. At 11:36 a.m. on that fateful day, a steel-enforced concrete cable stay broke and collapsed, taking a supporting tower and a 210 m (690 ft) section of the bridge with it. Vehicles cascaded to the ground. Apartment blocks below were crushed.

3. Dismantling operation

The dismantling phase involves the use of several combined methods: cutting and disassembling, crumbling, and, in some cases, demolition by explosives. The execution of this phase was impacted by safety and health requirements for workers and for the population as well as by the need to carry out the demolition operations as expeditiously as possible, in order to free building site for future construction. Project planning and deconstruction of the remaining parts of the bridge superstructure started on December 15, 2018. In Figure 27.1, the controlled demolition of the tower of the historical bridge with the use of explosives, taking place at 9:37 a.m. on June 28, 2019, is depicted.

Innovative Bridge Design Handbook. https://doi.org/10.1016/B978-0-12-823550-8.00025-1

Figure 27.1 Controlled demolition with explosives (ECRP, Extraordinary Commissioner for the Reconstruction of the Polcevera Viaduct of the A10 Motorway, official website).

4. The new bridge

4.1 Generalities

The new bridge, which is valued in excess of 200 €M, carries approximately 60,000 vehicles per day. The architectural design of the bridge was signed by Renzo Piano Building Workshop, while the executive structural design was guided by Italferr Spa (2019). The proposed solution for the reconstruction of the Polcevera crossing is a continuous orthotropic caisson bridge. The main deck is a continuous girder with a total length of 1067.17 m consisting of 19 spans, described as follows:

- 14 steel-concrete spans, 50 m long
- Three steel-concrete spans, 100 m long
- One steel-concrete span, 40.9 m long
- One steel-concrete span, 26.27 m long

Furthermore, a long steel-concrete ramp is structurally connected to the main deck approximately; it measures 109.91 m and is divided into three spans (34 m + 43.45 m + 32.46 m). The piers, with an elliptical section, are realized in reinforced concrete with a constant section for the entire height. The deck structure was planned to be seismically isolated from the piles, through the use of "friction pendulum" seismic devices. This solution enabled the structures, substructures, and foundations to be optimized, limiting their size in a highly urbanized and anthropized context. The road axis is essentially straight—except for a sharp curve with a radius of 300 m, located in the last 250 m west of the connection with the Coronata tunnels. The architectural conception of the bridge, by Renzo Piano–RPBW office, highlights a particular attention to details and to the environment in which the bridge is realized: the new bridge is depicted in Figure 27.2 (site plan), Figure 27.3 (general elevation), Figure 27.4

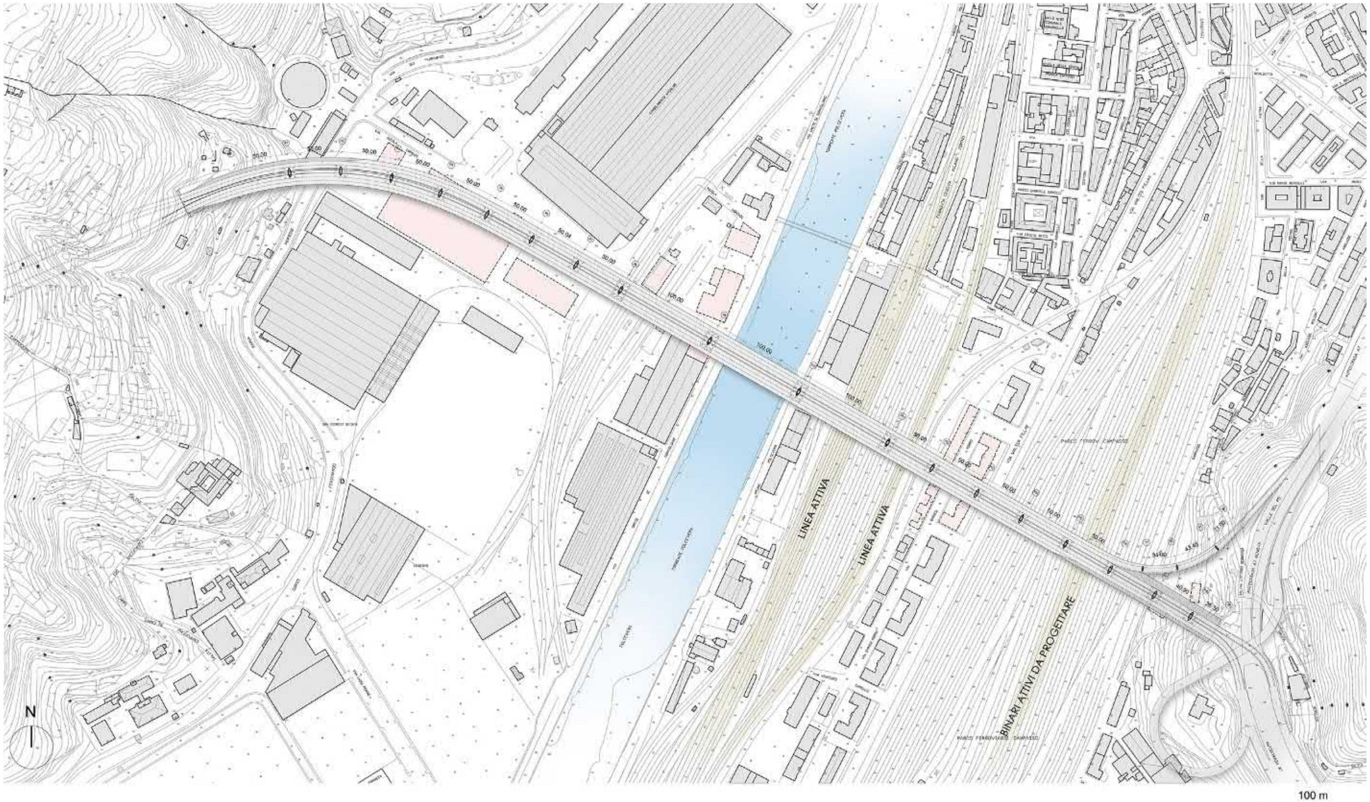

Figure 27.2 Site plan.
Credit: © Renzo Piano.

Figure 27.3 General elevation.
Credit: © Renzo Piano.

Figure 27.4 Model of a bridge pier.
Photo by Stefano Goldberg.

(model of a bridge pier), and Figure 27.5 (cross section of a column). The engineering cross section is illustrated in Figure 27.6 (cross section of a column) and Figure 27.7 (current cross section). The construction yards, due to the reduced timing at disposal (as the highway was to be reopened as soon as possible), was organized in order to industrialize every construction step. In the following figures, some of the impressive procedures are shown: Figure 27.8 (drilling foundations), Figures 27.9–27.11 (building basement footings of RC steel, Figure 27.10 (a typical pile disposal), Figures 27.11 and 27.12 (an elevation pile under construction), Figures 27.13–27.16 (orthotropic deck construction, welding operation at the base of the column, and deck vertical launching), Figure 27.17 (load testing of the bridge), and Figure 27.18 (the new bridge at night, with a particular lighting from below that illuminates the bridge with the colors of the Italian flag).

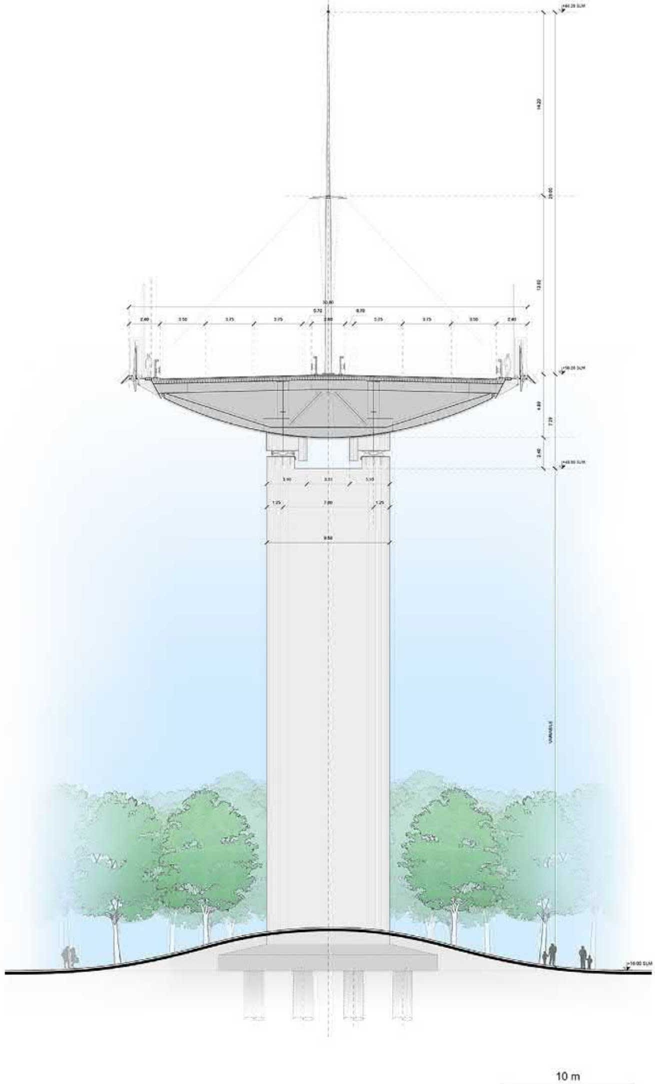

Figure 27.5 Cross section of a column.
Credit: © Renzo Piano.

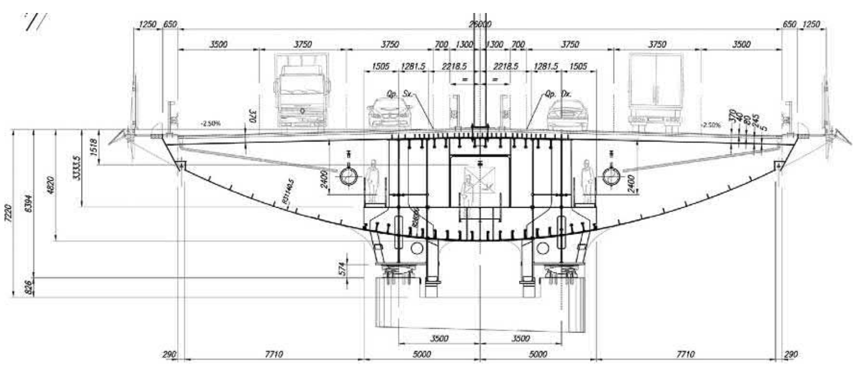

Figure 27.6 Cross section of column (final design by Italferr Spa).

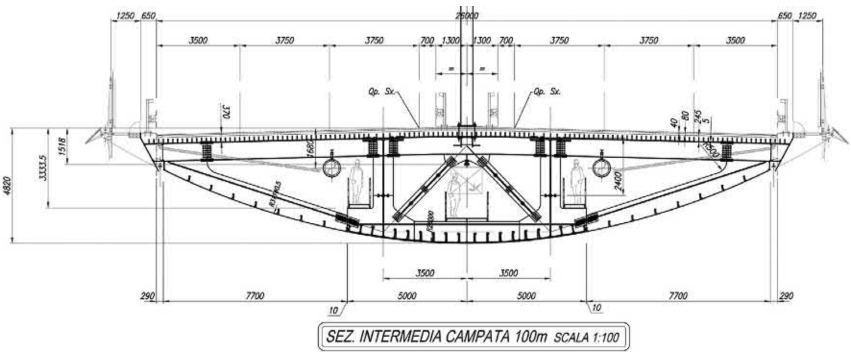

Figure 27.7 Current cross section (final design by Italferr Spa).

Figure 27.8 Drilling foundations (ECRP, Extraordinary Commissioner for the Reconstruction of the Polcevera Viaduct of the A10 motorway, official website).

Figure 27.9 Basement construction (ECRP, Extraordinary commissioner for the reconstruction of the Polcevera viaduct of the A10 motorway, official website).

4.2 Deck system

The spans are all built with a mixed steel-concrete orthotropic structure with a central metal caisson to which the side "oars" are welded, to complete the support structure of the roadways and side walkways. The connection between the reinforced concrete slab and the steel structure is provided with a Nelson shear connector welded to the extrados of the central caisson and side oars. Prefabricated reinforced concrete predalles have been employed for the support of the concrete casting that forms the slab of the spans with smaller spans (50 m, 40.9 m, and 26.27 m), and steel predalles have been used to support the casting for the 100 m spans. The following are some geometric data pertaining to the structure:

- The maximum height between the intrados of the caisson and the extrados of the reinforced concrete slab for the main deck is equal to 4.72 m.
- The width of the slab, in the straight section of the main deck, is equal to 27.20 m (it is variable in the curved section).
- The overall thickness for the road pavement is 12 cm.

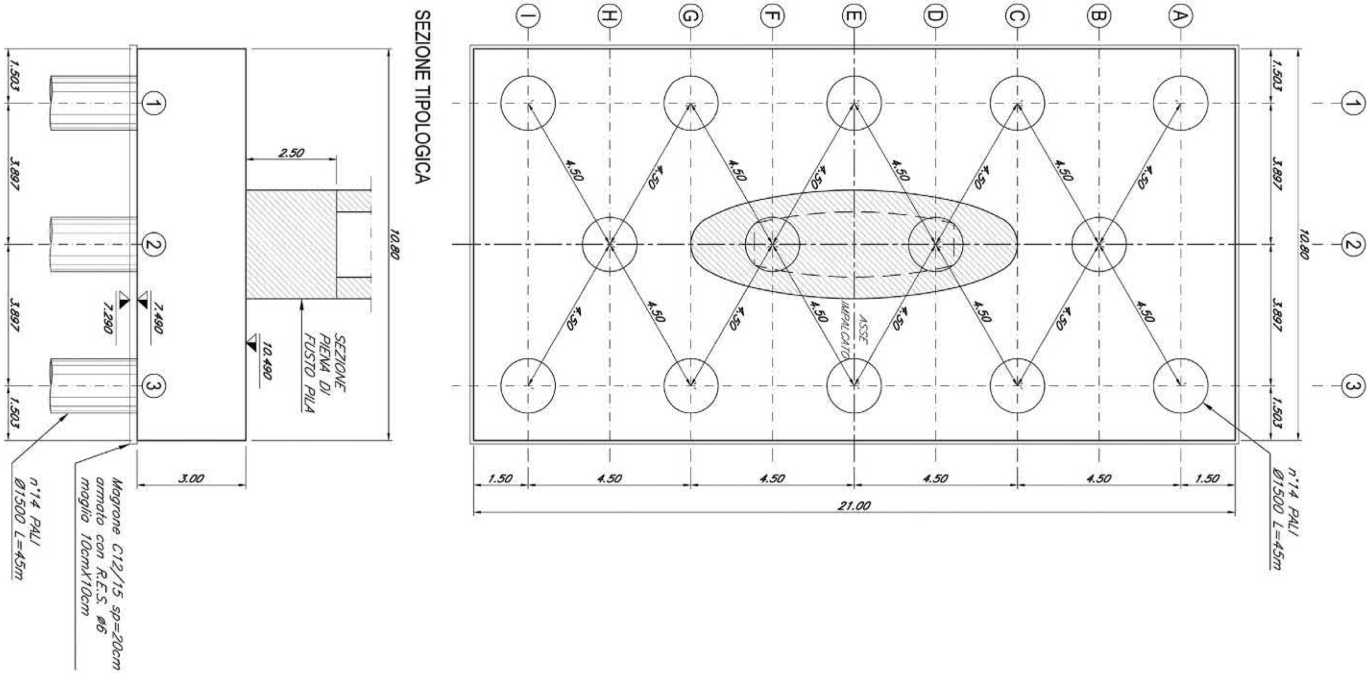

Figure 27.10 Typical foundation geometry (final design by Italferr Spa).

Figure 27.11 Elevation-reinforcing steel ready for column construction (ECRP, Extraordinary Commissioner for the Reconstruction of the Polcevera Viaduct of the A10 Motorway, official website).

- The center distance of the transverse is approximatively constant and equal to 4545 mm.
- The center distance of the supports for the main deck is approximatively 7 m.
- The center distance of the supports for the ramp deck is approximatively 3.2 m.

This solution makes the construction of several spans in sequence simple and fast on-site. The segments of the central caisson are mutually connected on-site by means of full penetration welding. The geometries of all the diaphragms inside the caisson and the manholes allow the bridge to be fully inspected at every point. The side "oars" are preassembled, welded, and connected to the central box by means of friction-bolted joints at the ends to facilitate quick assembly directly on-site. To minimize construction site activities and ensure the best-possible quality of individual processes—and, therefore, of the finished product—the segments of the lower part of the central box (such as the internal diaphragms) are made in the workshop.

4.3 Elevation design

The piles are entirely built in reinforced concrete. The identified section has an elliptical shape, as does the external shell of the deck. The external dimensions of 9.00×3.00 m are the same for both 50 m and 100 m spans. Such a choice brings significant benefits, including

- Perspective uniformity of the work
- Speed of realization of external formwork (one single type).

Figure 27.12 Elevation column construction (ECRP, Extraordinary Commissioner for the Reconstruction of the Polcevera Viaduct of the A10 Motorway, official website).

Internally, the pile is made up of a single-celled caisson. The piles are made with the aid of self-lifting formworks. The casting shots are planned at a 4.5 m pitch starting from above, to have them all aligned. The reinforcement is made with prefabricated cages with a total height of 7.50 m, with two overlapping orders. Particular attention is given to the durability of the batteries. An appropriate mix of concrete with cements suitable for use in a coastal environment is used. The same attention is given to the appropriate choice concrete covers to avoid corrosion of the reinforcement. As an additional protection of the pile, all the external surfaces have been painted with a waterproof product on polyurethane elastomers with aliphatic isocyanates. The solution adopted for the constraint system provides for all piles, except for piers 1 and 18, the use of single-curved curved-surface sliding isolators (simple friction pendulum). For piers 1 and 18 and for the abutment, multidirectional supports with spherical caps

Figure 27.13 Orthotropic deck construction, welding operation at the base of the column.
Photo by Shunji Ishida.

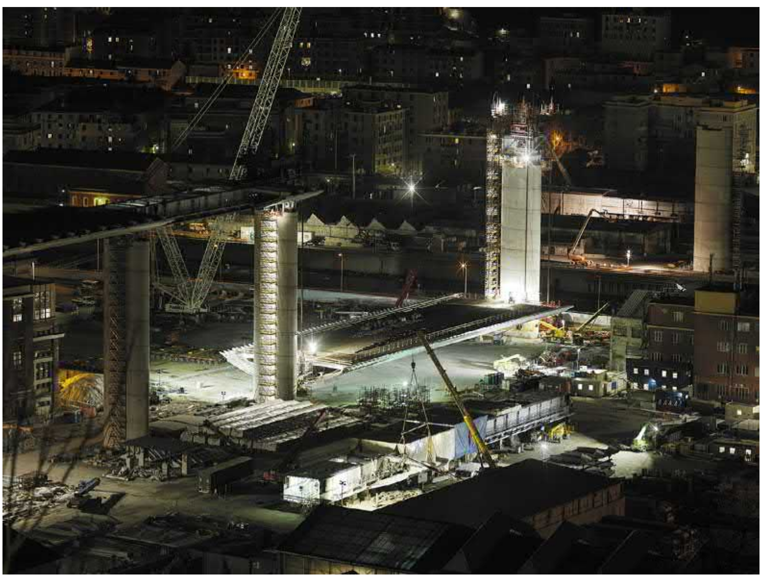

Figure 27.14 Orthotropic deck vertical launching, 100 m long span between pier P8 and P9, 11.02.2020.
Photo by Enrico Cano.

Figure 27.15 Orthotropic deck vertical launching, 50 m long span P3–P4 08.01.2020 (© PERGENOVA).

are adopted. A prismatic guide is also provided only on the abutment in the centerline. Transverse seismic retainers are arranged on the header, whereas the longitudinal seismic retainers are arranged on the abutment. The abutments are built adjacent to the existing abutments of the Morandi Bridge. From the static point of view, they are movable in the longitudinal direction. They are only cross-linked to the bridge. This constraint scheme allows the forces to be restricted to the minimum, limiting their dimension.

4.4 Foundations

The new bridge is supported by deep foundations, to transfer the loads coming from the structures in elevation to the most rigid base soil. For this purpose, 250 reinforced concrete large diameter drilled piles (1500 mm) have been realized up to 45 m long.

Figure 27.16 Orthotropic deck vertical launching, 50 m long span 14–15, 15.12.2019. Photo by Stefano Goldberg.

Figure 27.17 Load-testing of the bridge (ECRP, Extraordinary Commissioner for the Reconstruction of the Polcevera Viaduct of the A10 Motorway, official website).

The deep foundations transfer the loads coming from the structures in elevation to the most rigid base formations. The length has been calculated as to effectively transfer loads below the altered portion of the base formation. Where new foundations interfere with existing bridge foundations, it is planned to adopt ad hoc design configurations for piling, considering possible interaction effects with the structures' existing

Figure 27.18 New bridge completed.
Photo by Enrico Cano.

seabed. For foundation excavations, the use of protective structures (sheet piling and/or pile/micropile bulkheads) is envisaged, where necessary to ensure the safety of the works and to resolve any interference with adjacent works and services. The foundations project has been conducted on the basis of the geotechnical model of the subsoil, starting from the results of the geological survey campaign.

4.5 Structural devices

The structural scheme of a continuous deck creates a kinematic chain that is isolated from the elevation columns by simple friction pendulum devices, which also perform the function of supporting the deck. Multidirectional devices and a prismatic guide are employed onto abutments.

4.6 Structural monitoring system

The monitoring system must ensure the identification of significant parameters—in terms of absolute physical and relative qualities, to represent the structure's compliance with design principles and their natural modifications both during assembly and during the useful life of the work. The following parameters will be monitored and evaluated over time, thanks to maintenance activities:

(a) *Weight in motion*: The under-floor sensors allow the measurement of the weight of the vehicles in motion and allow a statistical analysis and monitoring of loads, an evaluation of the number of steps, and any preselection for the next legal measure. The measuring system must be able to detect the passage of heavy and light vehicles with an expected sensitivity of detection of weights of 3kN per axle, therefore only excluding motorcycles, and must be integrated with media optics detection.

(b) *Temperature*: Fifteen sensors along the deck are installed with a precision of 1°C.

(c) *Strain devices*: Six strain gauges for deformation measurements on steel and three temperature sensor are installed for each span. The strain gauges positioned on the metallic structure will have a longitudinal measurement axis and will be positioned as follows:
- Two on the upper wings of the deck beams at the core
- Two on the lower wings of the two deck beams at the core
- One in the middle of the closed bottom
- One on a side cover

The goal is to measure the longitudinal deformations of the beams.

(d) *Displacement devices:*
- At the interface between the pile and the deck, a monitoring system consisting of one measurement system for measuring the reciprocal transverse and longitudinal displacements between the top of the pile and the metal deck is installed. The system must be provided on each beam of the right side, but on the P3, P7, P9, P11, P16, and P2 ramps, the system must be provided for both beams. The sensitivity required is 1 mm.
- The columns' verticality must be detected in operation during the whole life of the bridge. A monitoring system is provided for each pile, it consists of one biaxial inclinometer in the pile head and one biaxial inclinometer at the pile base. These records have been integrated by an initial geometric topographic survey of the verticality of each pile.
- On the two abutments of the main deck and on the abutment of the ramp, the movement of the expansion joints is monitored. This information, combined with the temperature information, allows for the definition the position of the deck and the actual recentering of the structural devices.

(e) *Dynamic devices:* Multiaxial accelerometers sensors operating in OMA mode are installed on the deck to measure the dynamic behavior of the bridge. They monitor the vertical bending modes, the torsional modes of some significant spans and horizontal modes.

4.7 Special equipment

The bridge is equipped with an innovative dehumidification system; this will have the function of reducing the moisture content to such levels as to avoid formation of condensation inside the deck-box system in order to preserve the characteristics of the sheet over time and avoid phenomena corrosion, which can compromise the mechanical characteristics of the structure itself. The dehumidification system will use an adsorption dehumidifier, which is used in cases where it is necessary to keep the box low in humidity and to reduce maintenance interventions. The system is subdivided into two parts: the local system and the global system. In the local system, each dehumidifier will have its own regulation system, which—in relation to the local parameters recorded—will decide the set point of machine work. The dehumidifier will be sized to work with a mixture of recirculated air and external air. The two channels, fresh air and recirculation air, will be equipped with a manual adjustment damper. Each local plant described previously will be networked and will be part of a centralized global level. The seven planned plants will be networked through a multimode fiber that will connect the seven controllers.

4.8 Construction material details

Gathering, testing, and factory inspection of the material, as well as checking during temporary approval and structural assembly, have been developed in accordance with D. M. 17/01/2018 and Specifications RFI DTC SI PS SP IFS 001C. The execution class, in accordance with EN 1090–2, is EXC4 except, for the following elements, for which execution class EXC3 is required:

- Deck lateral shell composed of 10 mm thick metal plate, longitudinal ribs, and assembling welding included
- Structure of internal pathways and relative grids

Structural steel has been designed with hot-rolled (laminated) angles, plates, and wide plates, in accordance with UNI EN 10025 1/2/3 (2005). The yielding strength in mechanical tests and CEV in chemical tests must be in the limits imposed by D.M. 17/01/2018. The minimum temperature of service was set at −10 °C. Structural steel details are provided in Table 27.1.

Shear bolts were of Nelson Type ST 37-3 K (S235J2G3 + C450, yielding strength: 350 N/mm^2; tensile strength: 450 N/mm^2, stretching >15%, necking >50%. In accordance with UNI EN 10025/UNI EN ISO 13918):

High resistance bolts:

- Bolts: Class 10.9 UNI EN ISO 898-1, UNI EN 14399–10 HCR, rounded/hexagonal head functional class K2 (HCR system, bolt, and nut assembly with calibrated tightening).
- Nuts: Class 10 UNI EN ISO 898-2, UNI EN 14399–10 (HCR system, bolt, and nut assembly with calibrated tightening).
- Washers: Steel C 50 UNI EN 10083–2, hardened and tempered HCR 32–40, UNI EN 14399–6
- Friction joints: m = 0.3, sanded surfaces at almost white-metal level, coated with suitable varnish.

In accordance with D.M. 17/01/2018 and RFI DTC SI PS SP IFS 001C, coating procedure were designed according the following details:

- Atmospheric—corrosion category: C5 "Very High (VH)" (EN 12944–2018), which corresponds to a painting cycle of total coating thickness ≥ 320 μm, with 3 being the minimum number of layers. Support preparation: sandblasting to SA2 1/2 grade. Painting color: RAL, as specified in architectural design.

Table 27.1 Structural Steel

Element	Standard and Steel Grade	Thickness	Toughness Subgrade
Main beams, welded elements and joint covers	S355	≤40 mm	J2
	S355	>40 mm	K2
	S460	≤40 mm	N
	S460	>40 mm	NL
Angles, profiles, and fastened plates	S355	≤40 mm	J2
Metallic predalles	S355	–	J0

Table 27.2 Reinforcement Steel Details

Grade		fk B450C	fk Stainless Steel
Characteristic yielding strength	fyk > fy,nom	450 MPa	450 MPa
Characteristic tensile strength	ftk > ft.,nom 1.15 < (ft/fy)k < 1.35 (fy/fy,nom)k < 1.25	540 MPa	540 MPa
Percentage elongation	Agt,k > 7.5%	–	–
Young's modulus	Ec	210,000 MPa	210,000 MPa

Table 27.3 Concrete Details.

Element		Slab	Curb
Strength class	–	C45/55	C45/55
Characteristic compressive strength	fck	$\geq$45 N/mm^2	$\geq$45 N/mm^2
Minimum cement content	–	450 kg/m^3	450 kg/m^3
Maximum water/cement ratio	a/c	0.45	0.45
Slump	–	S4	S4
Maximum aggregate diameter	ϕ	22 mm	25 mm
Exposure class		XC4+XS1+XF4	XC4+XS1+XD3+XF4
Concrete cover		55 mm	55 mm

Concerning the reinforced concrete structure, material details are reported in Tables 27.2 and 27.3. For concrete admixtures, shrinkage-reducing additive, containing expansive agents, has been employed.

References

Italferr Spa, 2019. Final Design of the New Polcevera Bridge. Environmental Ministry (public project published onto the Italian Environmental Ministry website for the environmental impact evaluation).

This page intentionally left blank

Case study: The Russky Bridge

28

Alessio Pipinato
AP&P, CEO and Technical Director, Rovigo, Italy

1. Introduction

The bridge to Russky Island has a 1104 m central span length, which established a new world record in the bridge-building practice in 2012 (Figure 25.1), as the bridge has the highest bridge towers and the longest cable stays. Approaching spans are 60 m, 72 m, and 384 m at each side, and the central span is 1104 m. The total bridge length is 1885.53 m, the total length of the inclined viaducts is 3100 m, the total bridge roadway breadth is 21 m, the number of driving lanes is four, the under clearance measure is 70 m, the bridge pylons' height is 324 m, and the longest and shortest cable stays are approximately 580 m and 136 m, respectively. The design of the bridge location was determined based on the shortest coast-to-coast distance, 1460 m at the bridge crossing location (Figure 25.2). Navigable channel depth is up to 50 m. The locality of the bridge crossing construction site is characterized by severe climate conditions (e.g., temperatures varying from −31 °C to 37 °C, storm wind velocity of up to 36 m/s, storm wave height of up to 6 m, and ice formation in winter of up to 70 cm thick). Most of the information provided in this chapter comes from SK Most (2012).

2. Design

2.1 Bridge tower

Regarding the bridge tower construction, piles with a diameter of 2000 mm have been driven as deep as 77 m below ground, and on the island side, the 120 auger piles have been piled under each of the two 320 m bridge towers. The bridge towers have been constructed with custom self-climbing forms of 4.5 m. A crane was used on the first three sections, and afterwards, the formwork moved through a hydraulic motion of modular elements. The pylons are A-shaped, with nonstandard scaffolding and self-climbing forms, which made it possible to achieve a faster production. The bridge piers, M1 on the Nazimov Peninsula and M12 on Russky Island, are the heaviest and most complex structures. They are each 35 m high and take up the horizontal load from the cable-stayed, span-stiffening girder. The builders used self-compacting B35 grade sulfate-resistant Portland cement concrete to erect the bridge pier and pylon grillage. This material protects the footing against corrosive fluids and prevents rebar corrosion.

Innovative Bridge Design Handbook. https://doi.org/10.1016/B978-0-12-823550-8.00032-9

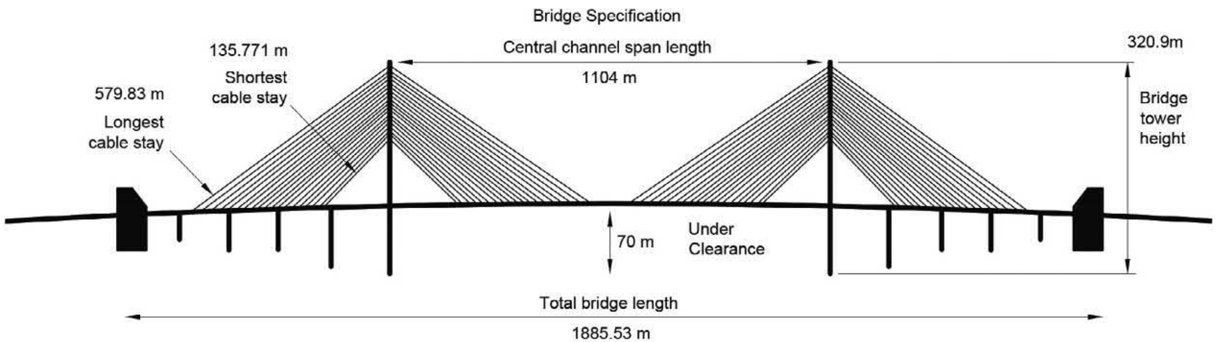

Figure 25.1 Main measures of the bridge.

Figure 25.2 The Russky Bridge: a general view of the completed structure. Courtesy of SK MOST Group.

2.2 Bridge deck

The deck cross-section shape was determined based on aerodynamic analysis and was optimized following the results of experimental wind tunnel testing in a scaled model in order to predict the deck's resistance to squall wind loads. Welded on-site connections are used for longitudinal and transversal joints of the cap sheet for the orthotropic plate and lower ribbed plate. High-strength bolts have been adopted for vertical walls of the block's joints, longitudinal ribs, transversal beams, and diaphragms. The premounted sections were transported to the site by barges and then were hoisted by crane to 76 m elevation at the erection site. Then, every section was linked, and the cable stays were attached (Figure 25.3). The approaching viaducts with total lengths of more than 900 m serve the bridge. The piers of this structure are columns, 9 to 30 m high. The span decks are made of steel and reinforced concrete, which consist of steel inclined-wall box sections and a cast-in-place reinforced concrete slab.

2.3 Cable-stay system

A penetration sealing system (PSS) was implemented in the cable stays in order to reduce wind loads by 25%–30%. Moreover, the cost of materials for pylons, the stiffening girder, and foundations was reduced by 35%–40%. PSS cable stays consist of 13 to 85 parallel strands of 15.7 mm in diameter, with each strand consists of seven galvanized steel wires enclosed in high-density polyethylene sheathing. The length of the shortest cable stay is 135.77 m, and the longest is 579.83 m. The protective sheath of the cable stay is made of high-density polyethylene (HDPE) and is resistant to UV and the specific local climate conditions of Vladivostok (design temperature range from −40°C to 40°C). The detail of a cable stay hanger is depicted in Figure 25.4. The stay-cable system weighs 3720 tons and has a total length of more than 54 km.

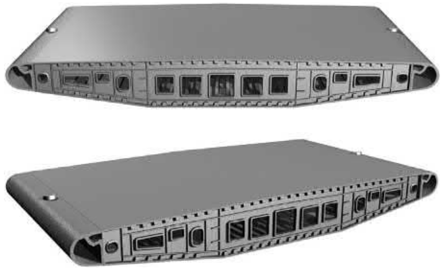

Figure 25.3 Deck 3-D model and section view.
Courtesy of SK MOST Group.

Figure 25.4 Detail of a cable-stay hanger.
Courtesy of SK MOST Group.

2.4 Seismic devices

The Russky Bridge could experience an earthquake with a magnitude of up to 8.1 on the Richter scale. This represents a safety margin comparable to the very high requirements of other bridges (e.g., the Akashi Kaikyo Bridge's resistance is 8.5). The designed system of two-hinged stiffening girders was conceived in order to allow seismic loads up to 8.1 points, along with strong sea currents. Pendulum-type bearing structures were introduced to reduce the active loads, ensuring the seismic isolation of the span deck. Movement joints have endured large axial displacements of the span deck, and lead-cored rubberized metal bearings have been adopted to dissipate energy under large stresses.

2.5 Production facilities

Two production facilities were put in place for running efficient construction operations. One facility was located on the Nazimov side of the bridge, and the other on the Russky side. The facilities included a rebar welding workshop, building laboratories, and a concrete mixing plant. Each production facility had an office building; living quarters; and mechanical, woodworking, and equipment repair workshops. More than

1 km of new railway tracks were built to ensure timely delivery of building materials. About 320 pieces of state-of-the art equipment were used in the construction of the bridge to the Russky Island. Unique 40-ton and 20-ton tower cranes, which can telescope up to 340 m, were used to erect the pylons. Derrick cranes with up to 400 tons of lifting capacity were used to install the channel span deck. Crawler cranes with 1350-ton lifting capacities were installed in the record time to lift the first 10 sections of the steel span deck (SK Most, 2012).

3. Construction phase

3.1 Bridge foundations

Drilling and pile concreting operations were done in seawater that varies from 14 to 20 m in depth. A total of 120 drilled piles with a 2000 mm diameter were put in place to build the footing of each pylon, with permanent steel-cased piles 46 m deep (under the M7 pylon), while those on the Nazimov side reach 77 m deep. The total length of the wells' drilling operations was more than 5000 m. The drilled soil was a very heterogeneous rock siltstone with a strength of 90 MPa and compressed sandstone lens with a strength up to 180 MPa. The most labor-intensive operation of the bridge construction project was the building of the pier-side foundations. Strain gauges were embedded in the grillage body for in order to monitor the conditions of these footings (Figures 25.5 and 25.6).

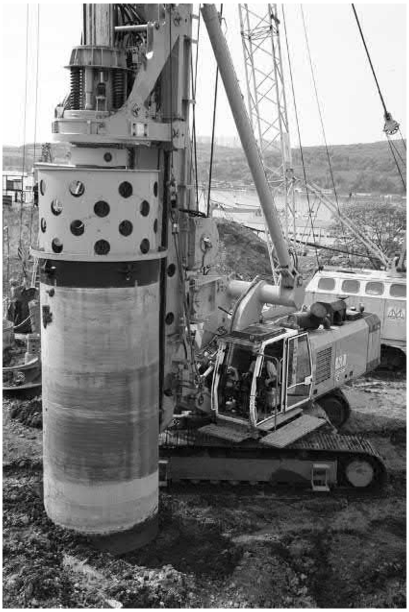

Figure 25.5 Operating welling machine.
Courtesy of SK MOST Group.

Figure 25.6 Construction yard of one pylon.
Courtesy of SK MOST Group.

Figure 25.7 Detail of one antenna during construction and the scaffolding system erecting bridge concrete segments.
Courtesy of SK MOST Group.

3.2 Bridge tower and girder

Self-lift shutters were used to concrete the pylons: seven working tiers, each with a total height of 19 m, facilitated the preparation of the construction joint, reinforcement, concreting, concrete curing, and finishing to be run simultaneously in three, 4.5 m high sections. The hydraulically powered self-lift shutters reduced the erection time for the cast-in-place reinforced concrete structure by a factor of 1.5. This is significant, considering the amount of concreting necessary for each pylon (20,000 m^3). The symmetrically built anchor span structures are each 316 m long (Figure 25.7).

The continuous span is made of prestressed, cast-in-place reinforced concrete, which required approximately 21,000 m^3 of concrete mix to complete. High-tensile prestressing steel bundles were installed and tensioned by the application of a tensioning force of 300–370 tons by prestressing jacks. After tensioning, voids are filled with a special cement-based mortar. The all-metal stiffening girder of the central navigation span is comprised of the bottom and top orthotropic plates and a system of transverse diaphragms. The steel-stiffening girder is composed of 103 panels, each 12 m long and 26 m wide, and two transition panels of 6 m each. The panels weigh a total of 23,000 tons. The stiffening girder is 1248 m long.

3.3 Preassembly of the deck panels

The main steel-stiffening girder panels of the bridge were built in a nearby, specially equipped yard, which delivered thousands of tons of steel structures for the bridge's main steel-stiffening girder from the preassembly site. This procedure has reduced the number of joints and significantly accelerated the procedure of installation at 70 m high. Also, the 30 km of first-class welded joints with 100% ultrasound flaw detection were completed quickly in this yard, rather than on-site (Figure 25.8).

3.4 Panel lifting

The panels delivered to the installation site by barges were then lifted by crane to the 70 m elevation. The barge was positioned under the installation unit using a global navigation satellite system. After Section 20 was installed, 24 m long paired panels were delivered for installation to expedite the installation of the steel-stiffening girder (Figure 25.9).

3.5 Installation of the longest stay cables

The closing pair of white-colored stay cables are 579.83 m long, which sets a world record in bridge construction. The world's longest stay cables are installed at an elevation of 317 m at M6 Pylon and are attached to the 50th panel of the

Figure 25.8 Preassembled segment of the main steel-stiffening girder.
Courtesy of SK MOST Group.

Figure 25.9 A deck panel segment lifted up on-site.
Courtesy of SK MOST Group.

Figure 25.10 A close view of the starting anchorage of the longest stay cable in the world.
Courtesy of SK MOST Group.

main steel-stiffening girder, which extends over the distance of 534 m toward Russky Island. The white jackets of each stay cable contain 80 strands of high-tensile wire with a design strength of 1860 MPa. Freyssinet developed the ultra-compact stay cable design specifically for this bridge, as depicted in Figure 25.10 (Freyssinet, 2014).

Figure 25.11 Final tasks of the deck construction: lifting the key deck segment from a river barge.
Courtesy of SK MOST Group.

3.6 Key deck segment erection

The key segmental deck was erected during the night of April 11–12, 2012. Section 52 was lifted from the pontoon, which was custom-equipped for the purpose in order to close the two 546 m long cantilever sections (Figure 25.11).

4. Monitoring system

The bridge is equipped with an automated precision monitoring system, which enabled the continuous monitoring of the installation's status to be conducted using two satellite-based global positioning systems simultaneously. This system integrates more than 500 state-of-the-art sensors, allowing for real-time monitoring of bridge health parameters, along with the weather conditions and wind loads. A huge display board in the control center that monitors the bridge over the Eastern Bosphorus Strait presents all incoming data such as visibility, wind velocity, roadway temperature, traction coefficient, water film thickness, lane traffic intensity, traffic flow density, and many other data points in real time. Acquiring data determines the actions taken by the 24-h control team: e.g., a safe speed limit is set up for traffic via the bridge. The innovative monitoring system integrates a variety of sensor types—including global positioning satellite (GPS) receivers, tachymeters, inclinometers, seismometers—which provide the precise position monitoring and data on the structural components.

Color coding is used to show the bridge's health: the green light on the screen means that everything is fine, yellow warns of the approaching alarm level in the preset range, and red is the alarm level.

References

Freyssinet, 2014. Stay Cable System Installation. Russky Island Bridge. Freyssinet official website.

SK Most, 2012. Russky Bridge: Construction of the Bridge Crossing to Russky Island over the Eastern Bosphorus Strait in Vladivostok. SK Most, Vladivostok, Russia.

Case study: The Akashi Kaikyo bridge

29

Alessio Pipinato
AP&P, CEO and Technical Director, Rovigo, Italy

1. Introduction

The Akashi Kaikyo Bridge passes across the Akashi Strait between the Tarumi ward of Kobe prefecture and the Awaji Island in Hyogo prefecture. The bridge was built as part of the Kobe–Naruto segment of the Honshu–Shikoku construction projects (Figures 29.1 and 29.2). The distance between the bridge's two cables is 35.5 m. While the original plan was for the bridge to carry both rail and road traffic, in 1985, it was decided that the bridge should carry only highway traffic (Nagai et al., 2000). The construction started in May 1987, and the bridge opened to traffic in 1998. The side view of the bridge is shown in Figure 29.1. The main cables have diameters of approximately 1 m and weigh 50,500 tons, which allows them to carry the 87,000 tons of the stiffening girder. The Akashi Strait is a busy shipping port, so engineers had to design a bridge that would not block shipping traffic. They also had to consider the weather, as Japan experiences very severe weather conditions—e.g., hurricanes, tsunamis, and earthquakes that rattle and thrash the island almost annually. The bridge deck has been constructed with a truss featuring a complex network of triangular braces beneath the roadway. The open network of triangles makes the bridge very rigid, but it also allows the wind to blow right through the structure. In addition, 20 tuned mass dampers (TMDs) were placed in each tower. The TMDs swing in the opposite direction of the wind sway, so when the wind blows the bridge in one direction, the TMDs sway in the opposite direction, effectively balancing the bridge and canceling out the wind's sway. With this design, the Akashi Kaikyo Bridge can handle high-speed winds and withstand an earthquake with a magnitude of up to 8.5 on the Richter scale. Aerodynamic stability was investigated through a boundary layer wind tunnel test with a 1:100 full model. In the design standard adopted, it is specified that flutter must not occur under a wind speed of 78 m/s in the wind tunnel test within the attack angle from $-3°$ to $3°$ (Fuchida et al., 1998). To determine the type of the stiffening girder to be used, several types of girders were investigated; from these comparisons, the truss girder and compound stiffness box girder were selected as prospective types (the compound stiffness box girder is a bridge system that arranges high-torsional-stiffened girders around the tower and aerodynamically well flat girders at the central portion of the bridge). As a result of the experiment on a scaled model (1:100), it was confirmed that the required wind resistance could be obtained by installing some gratings on the road deck and a vertical stabilizing device along the truss girder (Fuchida et al., 1998). The bridge cost was estimated at US$3.6 billion, according to Cooper (1998).

Innovative Bridge Design Handbook. https://doi.org/10.1016/B978-0-12-823550-8.00006-8

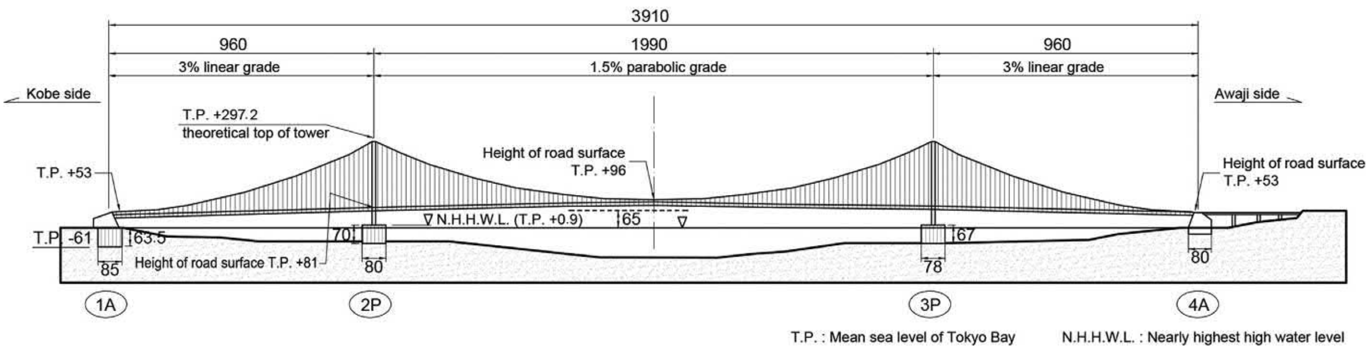

Figure 29.1 Side view of the Akashi Kaikyo Bridge.

Figure 29.2 The Akashi Kaikyo Bridge.

2. Design

2.1 Bridge tower

The tower pier foundations were designed to transmit 181,400 tons of vertical force to bedrock, approximately 60 m below the water surface. The foundation was constructed using a newly developed laying-down caisson method: the steel caissons, each 80 m in diameter and 70 m in height, were first towed to the sites and then submerged and set on the preexcavated seabed (Figure 29.3). Pier foundation construction was completed with the placement of concrete. Then the main steel towers were erected on the concrete piers with an independent, self-supporting 145-metric-ton tower crane. Each main tower height was 282.8 m (297.3 m with a cable saddle in place) and was erected by stacking 30 prefabricated steel segments, which were approximately 10 m in height, on top of each other. The segments were formed with three separate main cells in plan view. Special procedures were used during the fabrication of each segment to ensure accurate tolerances for proper tower alignment. The tolerances were maintained using laser-measuring technologies to control all dimensions. The use of this technology resulted in no major erection problems during the field bolting and splicing together of the steel tower segments (Cooper, 1998). The allowable inclination of the tower was specified to be 1/5000 (about 6 cm at the top of the tower). TMDs were installed inside the tower to control wind-induced vibration. TMDs were attached to each tower at varying stages of completion to reduce wind-driven tower motion and tower vibration in the event of an earthquake (Figure 29.4).

2.2 Bridge deck

The bridge roadway surface is constructed on top of a truss girder system (14 m in depth, 35.5 m in width) that is suspended from main cables passing over two steel towers that rise 298 m above sea level. A 65 m clearance is maintained over the

Figure 29.3 Steel caissons.

Figure 29.4 Steel towers: (a) climbing crane used for tower erection;

(Continued)

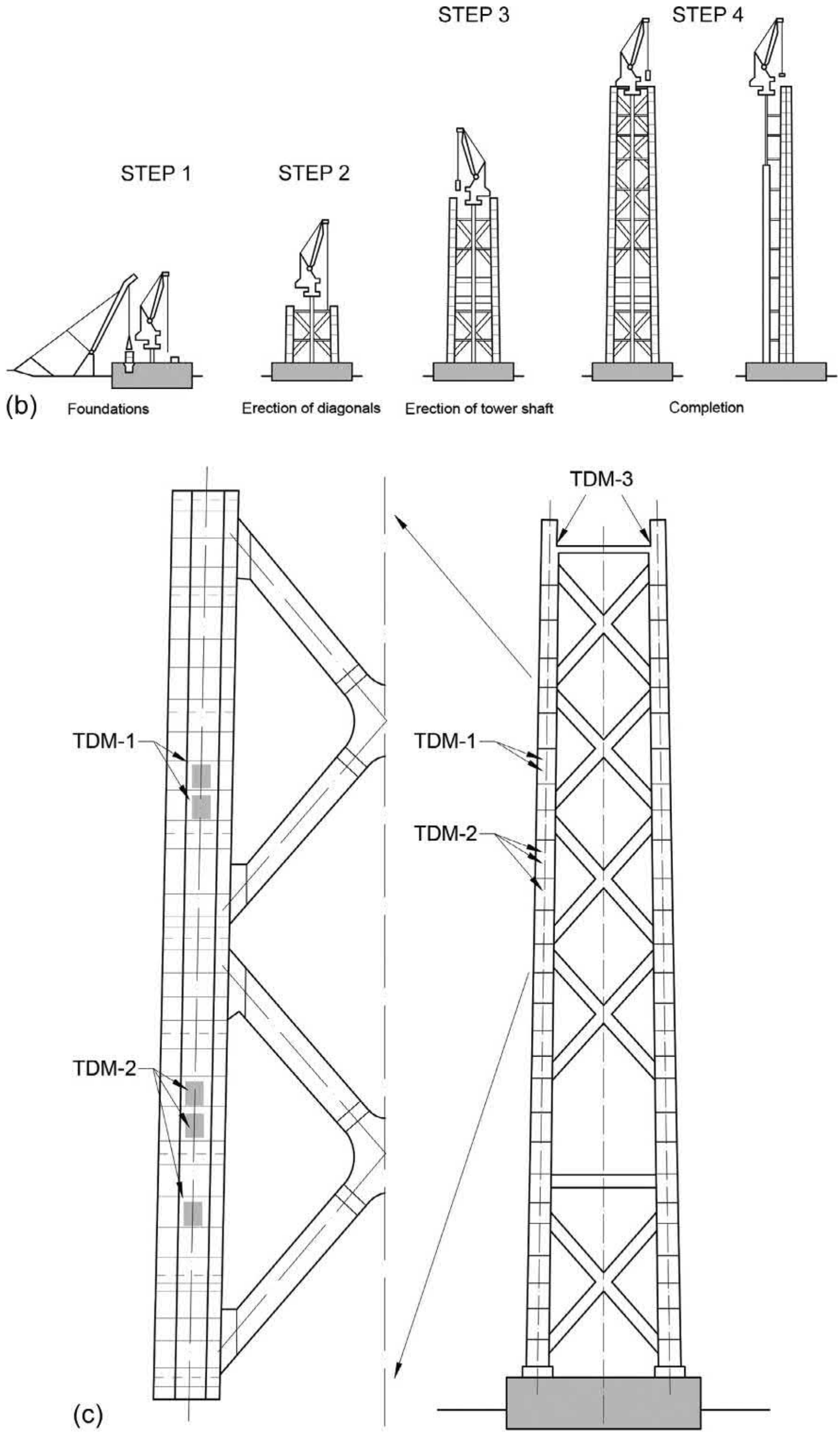

Figure 29.4, cont'd (b) erection procedure; (c) location of TMDs;

(Continued)

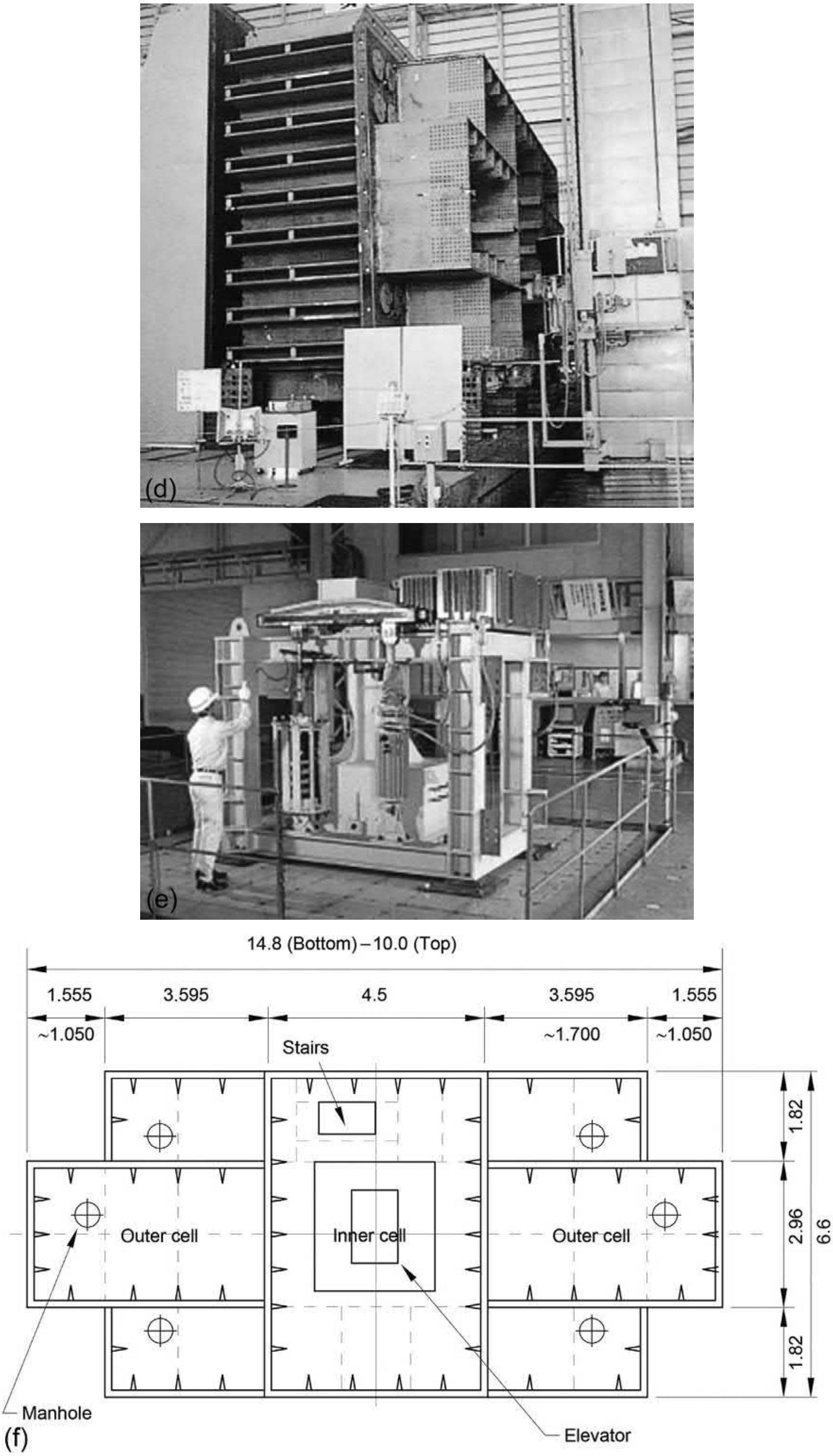

Figure 29.4, cont'd (d) polishing the cross section of a tower shaft using a large-scale facing machine; to control the inclination of the towers and to assure the metal touch at connections, each end of the tower shaft blocks was polished up to 0.0125 mm ruggedness; (e) tuned mass damper (TMD); (f) cross section of tower shaft (measurements in m).

shipping lane. The block was constructed using a special barge because of the severe environmental conditions: e.g., strong currents (5 m/s), deep water (maximum depth = − 100 m), and heavy traffic (1000 vessels/day). The barge was equipped with computer-controlled, omnidirectional propellers mounted at each corner of the barge, and it could maintain its position at a fixed point without mooring ropes. As a result, working time per cycle was drastically reduced from the conventional 3 h to only 30 min. After comparing the streamlined box girder with the truss girder, the latter was chosen because of its aerodynamic stability and economy. In order to reduce the weight of the girders, high-strength steel was used. Stiffening girder sections, each about 36 m in length, are fabricated and placed on the barge for transport to a site below each erection point. Then they are hoisted into position using lifting beams and are secured to hanger ropes. Since the barge cannot access the construction point when in shallow waters or on the ground, stiffening girder blocks are moved to the area using two lifting beams (Figure 29.5).

2.3 Cable-stay system

Before stringing the cable, a pilot hauler rope was attached to each anchorage and placed over the tower tops by helicopter. The pilot rope was used to suspend the catwalk, from which work on the main cable attachment proceeded. The main cables, which have a 1:10 sag ratio, were assembled using the prefabricated strand method: each strand was transported to the construction site, where it was pulled from one anchorage over the saddle of each tower and fastened to the opposite anchorage frame. This procedure was repeated 289 times to fabricate each main cable. Before attaching it to the steel frame inside the anchorage, each main cable was separated at the anchorage by a splay saddle to equally distribute cable tension

Figure 29.5 Steel truss deck.

to the foundation. A specially designed cable-squeezing machine was used to compress the 290 parallel wire strands into the final 1.12 m diameter cable. Cable bands were placed to circumferentially compress the cable and to maintain its circular shape. Finally, suspender cable hangers were attached to the main cable to support the main stiffening truss (Cooper, 1998). Further, the pilot rope, which is lightweight and made of high-strength polyaramid fiber (measuring 10 mm in diameter), was spanned using a helicopter. Newly developed high-tensile-strength wire of 1760 N/mm^2 made it possible to use only one cable per side, rather than two. The suspender ropes are prefabricated parallel-wire strands (PPWS) covered by a polyethylene tube, and there are two suspender ropes at one panel point. The span of each rope at one panel point is about 9 times that of its diameter, and generating an oscillation can be difficult in this condition. However, a large-amplitude oscillation was observed at the downstream side suspender rope. Therefore, in order to improve the aerodynamic characteristic of the ropes, the generating conditions were investigated in detail, including the oscillation characteristics and their ability to withstand a vibration obtained through the wind tunnel test. It was found that the vibration was controlled by spirally winding trip wires (10 mm in diameter) around a suspender rope. Moreover, the most suitable wire diameter and twisting pitch were obtained through the wind tunnel test, and set at longer suspender ropes of the bridge using a newly developed machine. By this countermeasure, the oscillation was controlled and has not been observed in large amplitude. Many analyses have been performed on the bridge—including experiments on the dynamic behavior of the bridge under wind forces, especially flutter and buffeting, as both are issues of utmost concern in the wind-resistant design of long-span bridges. Multimode flutter and buffeting analysis of the Akashi Kaikyo Bridge was performed by Katsuchi et al. (1999), and the analytical results were compared with the wind-tunnel test data obtained from an aeroelastic, full model of the bridge. The multimode flutter analysis corresponded well with the measurements and exhibited a significant coupling among modes. The multimode buffeting analysis also showed excellent agreement between the analysis and measurements in vertical and torsional response. Significant coupling among modes was also observed in the buffeting analysis, and the multimode analysis predicted the measurement better than an alternate single-mode analysis method did (Katsuchi et al., 1999). Anchorages measure 63 m by 84 m and extend into the Kobe and granite layers at the site. These anchorages required special foundation construction technology. The Honshu anchorage had to be embedded 61 m below sea level, and the anchorage excavation had to be performed in open air. Therefore, a slurry wall 85 m diameter and 2.2 m thick was constructed and subsequently used as a retaining wall. Excavation within the slurry wall was followed by the placement of roller-compacted concrete to complete the anchorage foundation construction. The Awaji anchorage foundation was constructed using steel pipes and earth anchors to support the surrounding soil. The excavated foundation was filled with specially designed, flowing-mass concrete. Both anchorages were completed with the construction of a huge steel-supporting frame that was used to anchor the main suspension cable strands (Cooper, 1998). See Figures 29.6 and 29.7.

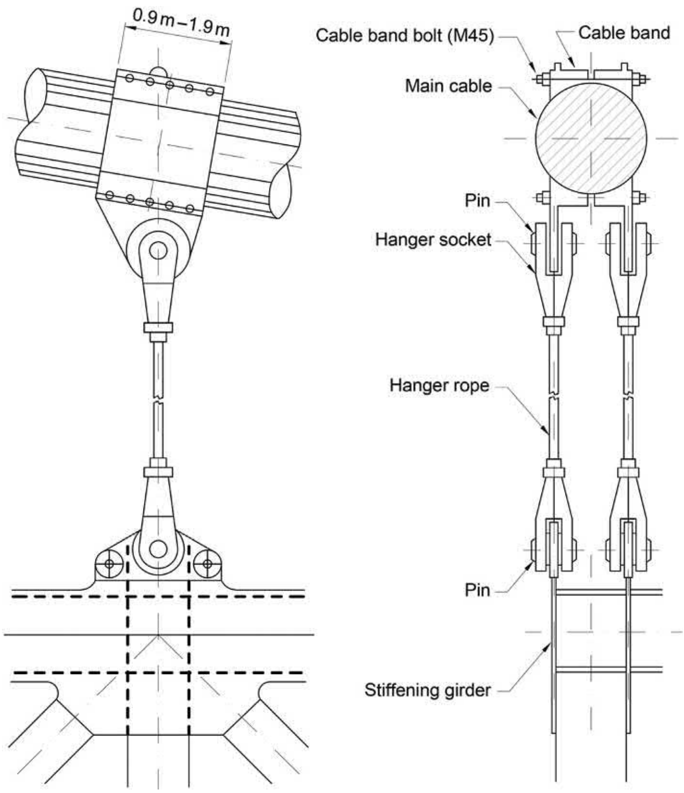

Figure 29.6 Cable band and hanger structure.

2.4 Seismic devices

The complete bridge structure was designed to resist a 150 km distant, 8.5 Richter magnitude earthquake. Of particular interest was the performance of the bridge during the January 17, 1995, Hyogo-ken Nanbu earthquake, which provided a full-scale test of tower response during the bridge construction. Fortunately, the bridge-stiffening truss had not begun at that time, being the yard at the stage of cable squeezing. The Nojima fault zone passes between the towers of the bridge, and the earthquake caused a permanent lateral and vertical offset of the Awaji tower and anchorage. Ground fault rupture was visible on the northern tip of Awaji Island, approximately 2 km from the Awaji anchorage. According to the bridge authority, the following observations were reported (Nasu and Tatsumi, 1995):

- According to the results of an analysis in which the earthquake-induced foundation displacement is added to the completed structure, there appear to be no problems from a stress viewpoint as regards to the bridge's towers, cables, stiffening girder, etc.

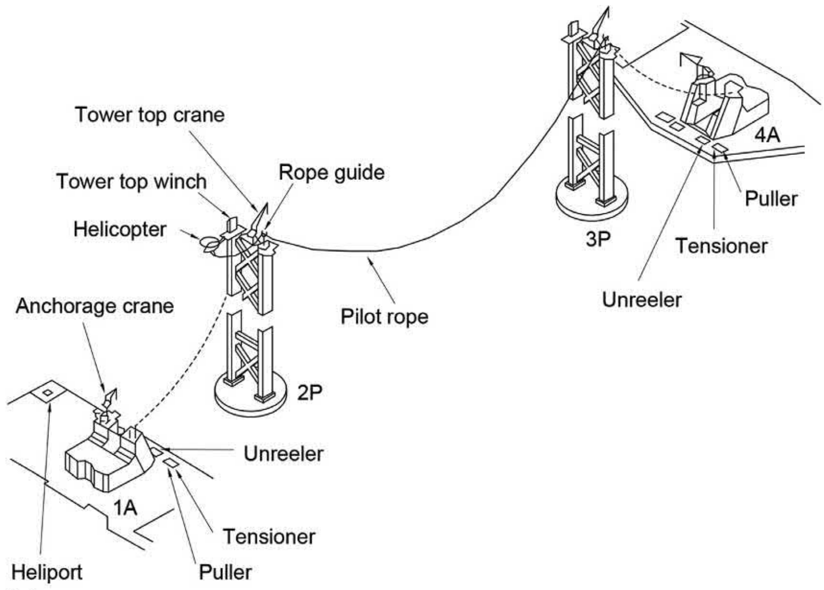

(a)

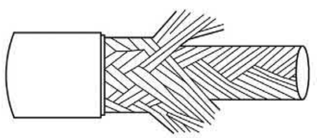

Type	Construction	Material	Characteristic
008B-BC	◎	Inner layer: Aramid fiber Middle layer: Polyester fiber Outer layer: Urethane resin (#129)	Rotation-resistant, waterproof construction

Diameter (standard) (mm)	Inner layer aramid fiber diameter (braid) (mm)	Outer layer thickness (urethane + fiber) (mm)	Aramid fiber cross-sectional area (mm²)	Weight (g/m)	Tensile strength [kN(tf)]
10	8,0	1,0	25,9	91,7	46,1 [4,70]

(b)

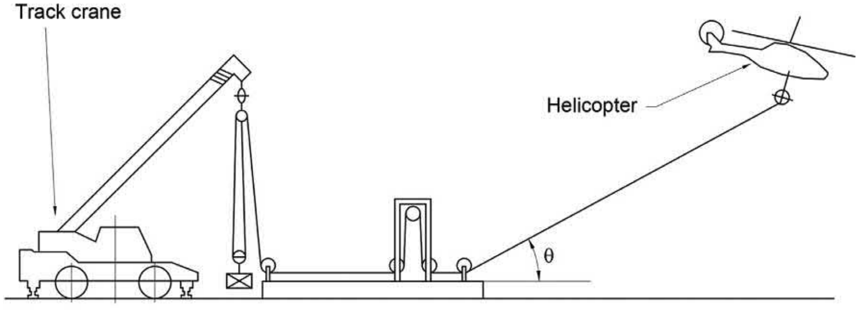

(c)

Figure 29.7 Procedure of crossing a pilot rope: (a) general layout; (b) specifications of pilot rope; (c) helicopter pulling force experiment;

(Continued)

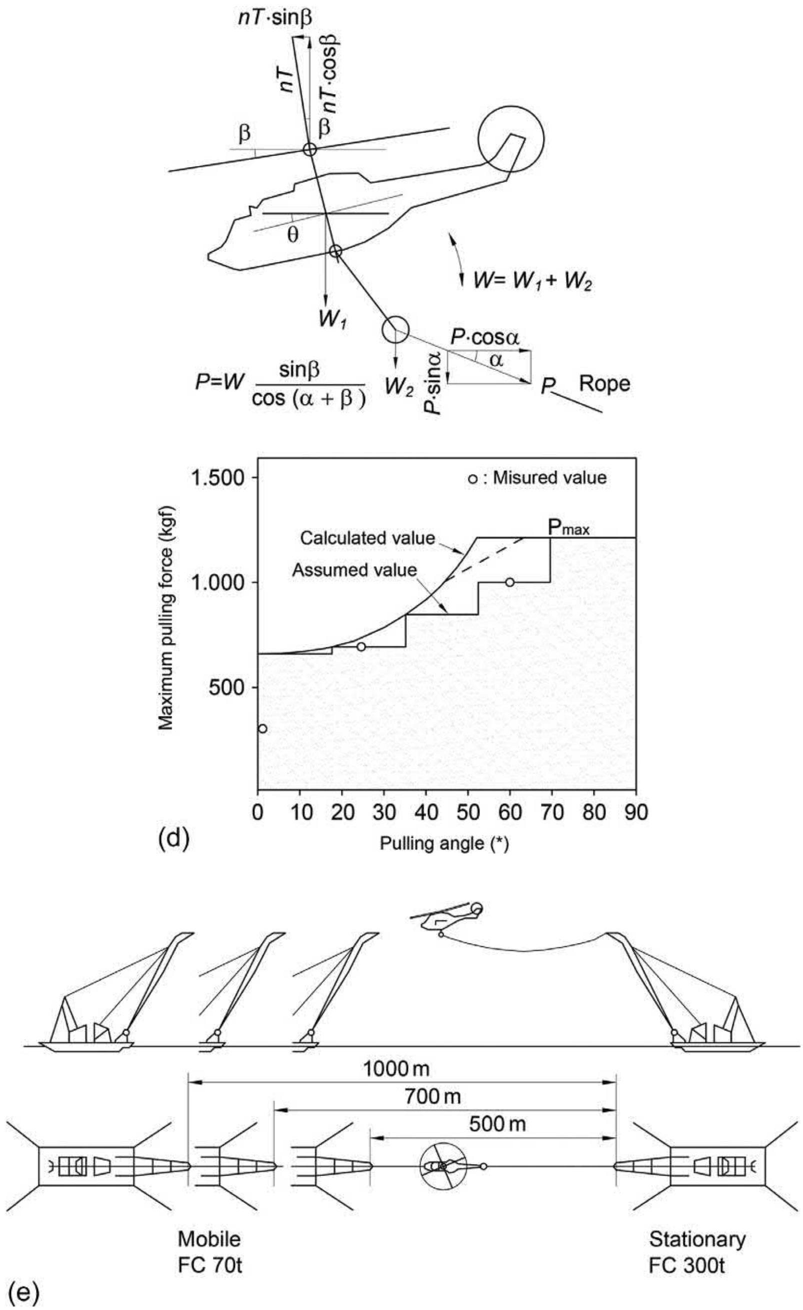

Figure 29.7, cont'd (d) relationship between helicopter pulling force and angle; (e) experiment to confirm the entire system;

(Continued)

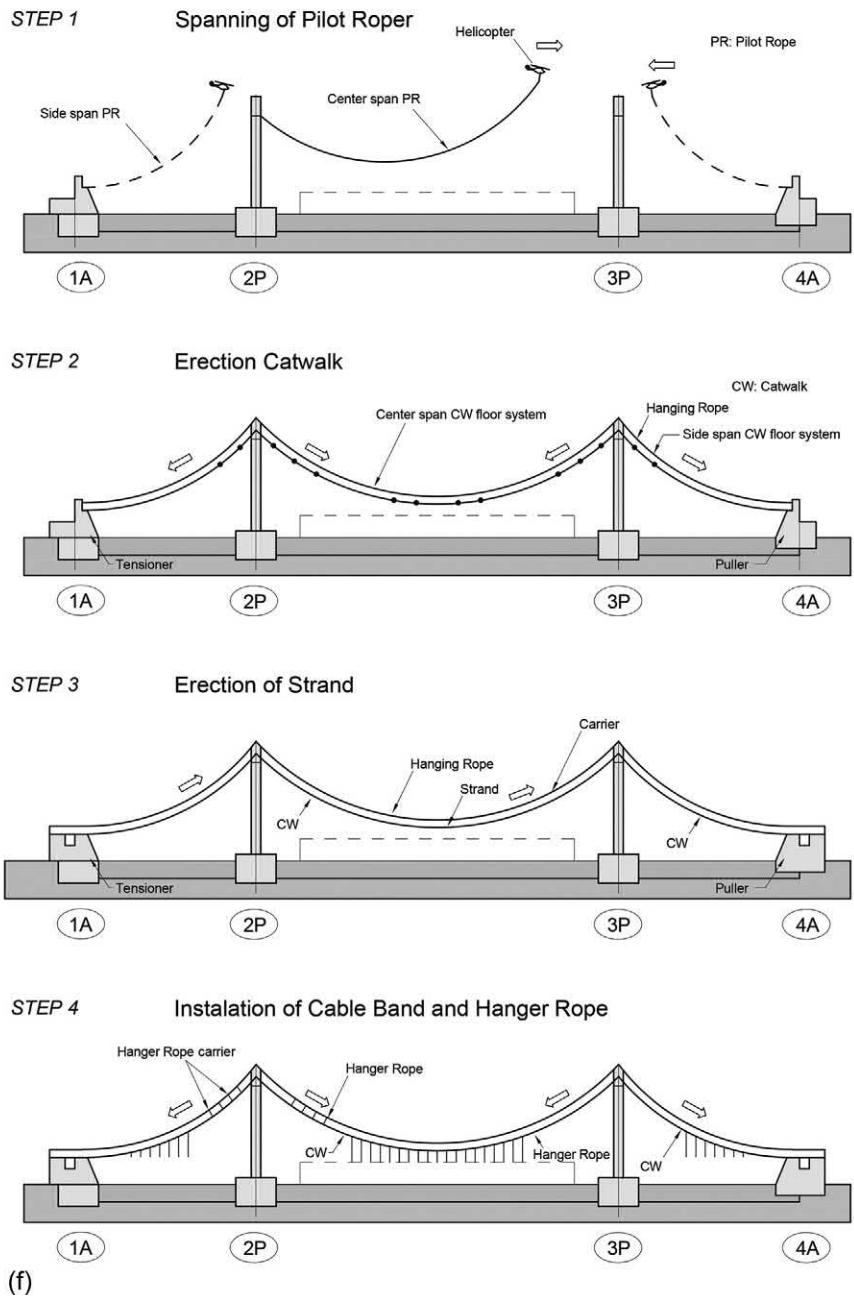

Figure 29.7, cont'd (f) construction phases.

- Although the part of vertical alignment exceeds 3% due to the lessened cable sag in the center and side spans, no problem will occur under the conditions of the highway structure. Also, the horizontal alignment is now off by about 0.03° at the tower, which is not expected to present problems as far as the passage of cars is concerned.
- The increased 2P-3P and 3P-4A spans will be handled by adjusting the length of the stiffening girder, which is now being fabricated.

The modified position of the structural elements is reported in Figure 29.8 (Nasu and Tatsumi, 1995). The Awaji tower was displaced 1.3 m to the west, while the Awaji anchorage was displaced 1.4 m to the west, relative to the Kobe tower and anchorage. This resulted in a 0.8 m increase in span length between the main towers and a 0.3 m increase in the southern side span length. The Awaji tower pier was displaced 0.2 m downward, while the Awaji anchorage rose by 0.2 m. The sag in the main cable was reduced by 1.3 m. The earthquake caused a one-month delay in the construction schedule, during which the bridge was carefully inspected for damage. This lost time was made up during the remaining three-year construction period, and the bridge was opened to traffic on schedule. The redesign of the two center stiffening panels, each 0.4 m longer than originally designed, accommodated for the increased distance between towers. The cable-squeezing machine suffered minor damage but was quickly repaired. Anchorages, piers, and towers were otherwise undamaged. (Cooper, 1998; Nasu and Tatsumi, 1995).

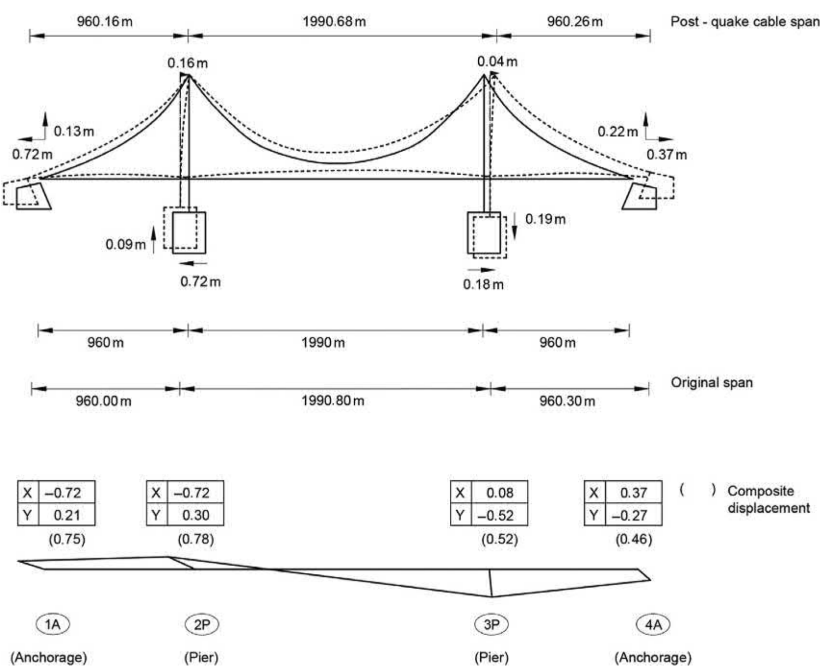

Figure 29.8 Effect of the Hyogo-ken Nanbu earthquake on the structural skeleton of the bridge (Nasu and Tatsumi, 1995).

3. Innovations and special construction details

3.1 Innovative technologies

Several technologies were developed to support the design and construction of the Akashi Kaikyo Suspension Bridge. One of the most relevant developments was the aerodynamic stability of a long suspension bridge, which has often posed major challenges to bridge designers. To verify the wind design, the bridge authority contracted the Public Works Research Institute to construct the world's largest wind tunnel facility and tested full-section models in laminar and turbulent wind flows. Other innovations that resulted from wind tunnel testing included the installation of vertical plates at the bottom center of the highway deck to increase flutter speed. A second innovative technology for that time was the development of individual parallel wire strands that were fabricated off-site, transported to the bridge site, and strung parallel to each other to form the main cable. The advantage of using this method was that the strands are then continuous from anchorage to anchorage, eliminating the in-place spinning of cables, and thus reducing the probability of accidents while ensuring a higher level of safety. In order to create the parallel wire strand, a unique cable-squeezing machine was designed to form the parallel strands into the final circular shape. The use of higher-strength wires reduced the number of strands required (saving construction time and cost), and the number of suspender ropes (which dropped from four to two) needed to connect each stiffening truss panel point to each cable hanger attachment on the main cable (Cooper, 1998).

3.2 Bridge foundations

At the center of the strait, the topography consists of a wide valley with steeply sloping sides and a water depth of 100 m. The geology comprises granite from the Mesozoic Era as the site's bedrock. This bedrock is covered roughly with the Kobe stratum of the Mesozoic epoch of Neocene, the Akashi layer of the diluvial epoch of the Quaternary Period, an upper diluvial formation, and an alluvial formation (Nasu and Tatsumi, 1995).

The severe conditions were the strong tidal currents (4.5 m/s) and deep water (−100 m at the central span site, − 50 m circa under the pylon). As a result, the foundations were constructed safely by the *laying-down caisson* method. State-of-the-art technologies, such as scour protection and underwater concrete desegregation, were developed for substructure construction. Concerning anchorages, anchorage 1A, located on the Kobe side, was located on the soft ground, and the foundation was constructed using the *underground slurry wall method*. Various kinds of concrete, from slurry wall (rich mixed concrete) to inner concrete foundation (lean mixed concrete), were used. Precast concrete panels were installed, considering the aesthetics of the outside walls. Highly workable concrete was used for the anchorage body (Figures 29.9–29.11) (Cooper, 1998).

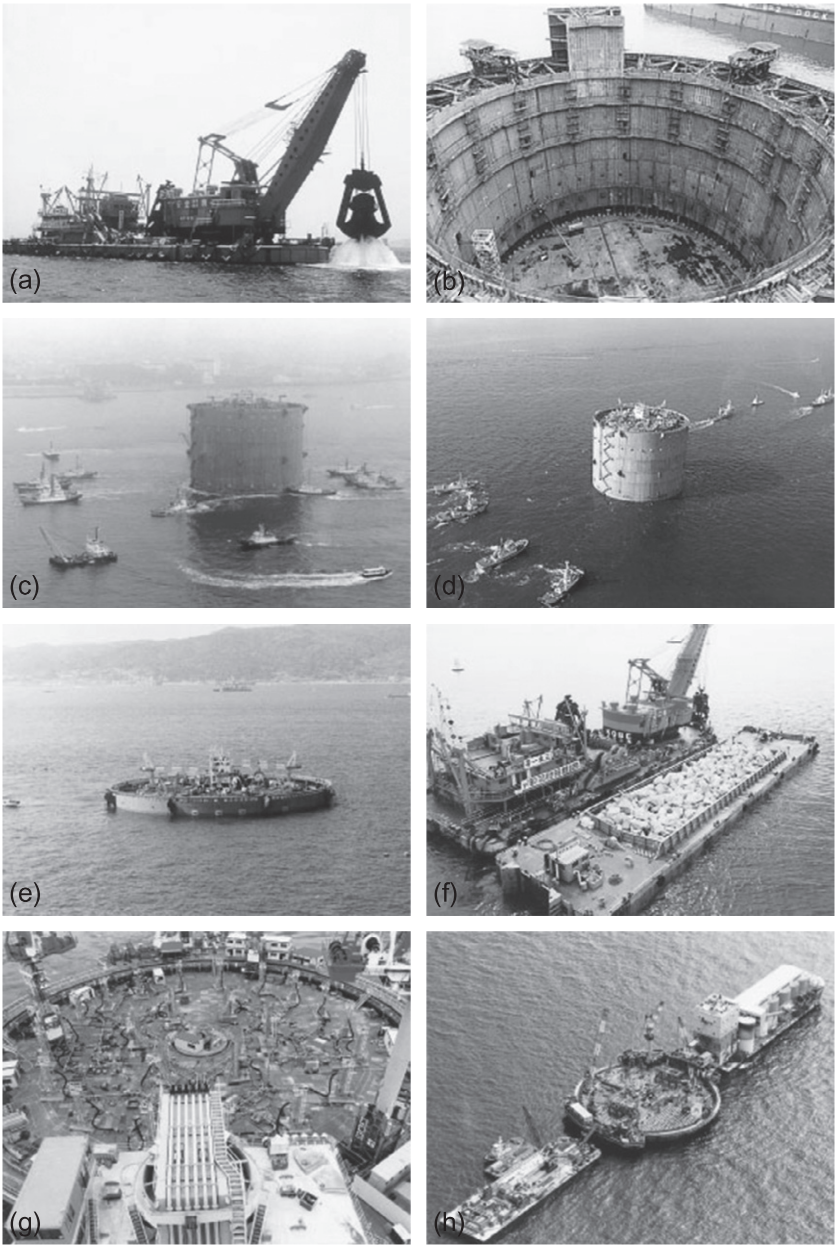

Figure 29.9 Foundation construction phases: (a) excavation of the seabed using a large-grade bucket dredger; (b) manufacturing a steel caisson; (c) mooring; (d) towing; (e) sinking; (f) dropping riprap (scour protection); (g) casting underwater desegregate concrete; (h) casting the top slab of concrete in the open air.

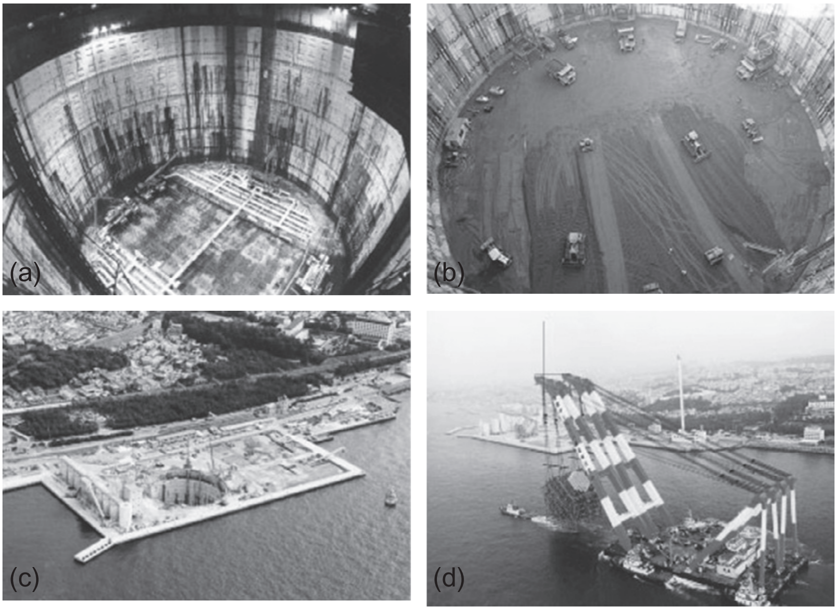

Figure 29.10 Anchorage construction phases: (a) construction of the bottom slab of concrete; (b) inner concrete [roller-compacted concrete (RCC)]; (c) distant view of 1A anchorage foundation work; (d) transportation of a cable anchor frame using a floating crane.

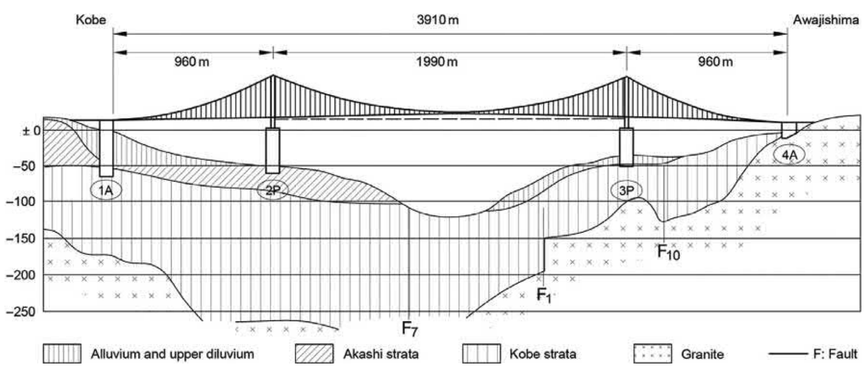

Figure 29.11 Geological profile at the bridge construction site.

3.3 Installation of cables

The cable installation work of a bridge begins when the main towers and the cable anchorages are completed. The first phase of the work starts with the installation of a pilot rope that acts as a foothold over the entire span of the bridge, connecting the main towers and anchorages. The pilot rope is then used to install a drive rope system, mount service catwalks, and, finally, suspension cables. Due to the channel's high traffic and the rapid current, the pilot rope (a polyaramid fiber rope 10 mm in diameter) was put into place by a large helicopter on November 10, 1993. The helicopter carried an extending machine with a reel of pilot rope and strung the pilot rope from one anchorage to the first main tower, then to the second main tower, and finally to the other anchorage, while unreeling the pilot rope. All these phases were previously confirmed by testing, and then they were performed with the same helicopter and ship cranes, in order to test all the on-site stresses of the cable during the final construction phase—including a pulling force experiment—and the experimental relationship between the rope tension and the critical pulling angle (Takeno and Kishi, 1997).

4. Monitoring system

Various monitoring devices such as seismography, anemometers, and accelerometers have been installed to record data on the Akashi Kaikyo Bridge. Figure 29.12 shows the layout of the monitoring devices. The records are accumulated and analyzed to ensure structural safety through monitoring the behavior of the bridge and provide information on the characteristics of the bridge during use. In addition to this system, a global positioning system (GPS) was introduced to monitor the seasonal, daily, and hourly behavior of the bridge, which may be governed mainly by temperature and live loads (HSBE, 2005).

5. Maintenance system

It is very difficult to inspect this bridge due to its extended and high structures above sea level, and also because of the large number of vehicles passing over and ships passing under the bridge. Under these circumstances, maintenance vehicles have been installed on the bridge to inspect the structures safely and effectively. There are different maintenance vehicles for outside girders, inside girders, and cables, according to each structural type used (Figure 29.13). Furthermore, the concept of *preventive maintenance* has been introduced to keep this long-span bridge in good condition for the future and allow it to withstand severe natural actions, including:

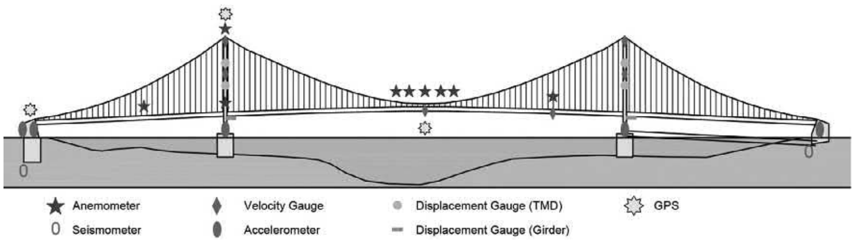

Figure 29.12 Monitoring system for the Akashi Kaikyo Bridge.

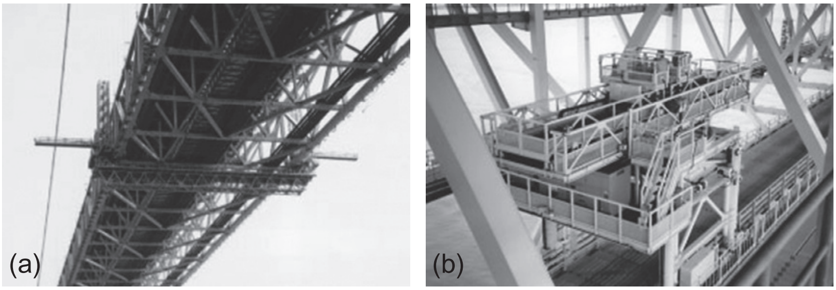

Figure 29.13 Maintenance vehicles: (a) outside girder vehicle; (b) inside girder vehicle.

- For *substructures*, continuous testing is applied for out-of-water parts of the construction—including sampling of concrete core, examination of salt damage, neutralization, cracks diffusion, steel rebar state, etc.—and adopting interventions when required as a result of non-destructive testing (NDT). For underwater structures with pitting corrosion on the surface of the steel laying-down caissons, the electrodeposit (EDP) method has been used as a countermeasure to prevent further corrosion.
- For *superstructures*, a wide array of maintenance actions are utilized: (a) long-lasting paint has been used for metal structures; in particular, the base consists of a thick-coating type of paint and inorganic zinc-enriched paint, which includes a rich amount of zinc powder and has excellent anticorrosion performance due to electrical and chemical sacrificial anode action; the undercoat, which protects the base coat, is epoxy resin paint, which has excellent durability and performance against alkalinity. In addition, fluorine resin paint, whose performance is excellent against chemical action and weather action, is applied as the surface coat (HSBE, 2005). (b) A dry air injection system for main cables has been installed, ensuring a 40% level of relative humidity, far below the 60%, which is critical. (c) An electromagnetic method (called the *main flux method*) to identify internal corrosion of suspender ropes is adopted in order to provide appropriate and concentrated interventions on ropes. (d) As unexpectedly large amplitude oscillation had been observed in suspender ropes at the downstream side, vibration control of wind-induced oscillation was introduced after construction through the winding of trip wires around a suspender rope. (e) A preventive action for the vibration control for cables is the use of an indent cable, which has dispersive concave marks on its surface, and a high-damping rubber, which was installed at the cable anchorage in the girder, as an anti-vibration measure for cables against vortex-induced oscillation. (f) A dry air injection system was installed in the box girders to avoid corrosion on the inner surface of unpainted steel pieces. Thus, the repainting costs have been avoided, and humidity controlled. (g) To maintain the undamaged bridge pavement while avoiding cut and cast expensive procedures, the surface (made of an adhesive layer of 35–40 mm of guss asphalt and 30–35 mm of improved asphalt) is treated regularly with a microsurfacing composed of a thin slurry admixture of aggregates, early strength-improved asphalt emulsion, water, and cement. This treatment allows for a timely reopening of the traffic lanes.

References

Cooper, J.D., 1998. World's longest suspension bridge opens in Japan. ASCE Public Roads 62 (1).

Fuchida, M., Kurino, S., Kitagawa, M., 1998. Design and construction of the Akashi Kaikyo bridge's superstructure. IABSE Report, 79/1998. pp. 63–68. Zurich.

Honshu-Shikoku Bridge Expressway (HSBE), 2005. Maintenance Technology. Honshu-Shikoku Bridge Expressway Company Limited. Official Website.

Katsuchi, H., Nicholas, P.J., Scanlan, R.H., 1999. Multimode coupled flutter and buffeting analysis of the Akashi-Kaikyo bridge. J. Struct. Eng. 125, 60–70.

Nagai, M., Yabuki, T., Suzuki, S., 2000. Design practice in Japan. In: Chen, W., Duan, L. (Eds.), Bridge Engineering Handbook. CRC Press, Boca Raton, CA.

Nasu, S., Tatsumi, M., 1995. Effect of the Southern Hyogo Earthquake on the Akashi-Kaikyo Bridge. In: Proceedings of the 4th International Workshop on Accelerator Alignment (IWAA 1995), 14–17 November 1995, Tsukuba, Japan-Ground Motion and Active Damping Session, Tsukuba, pp. V-305–V-316.

Takeno, M., Kishi, Y., 1997. Cable erection technology for world's longest suspension bridge—Akashi Kaikyo bridge. Nippon steel tech. Rep. 73. Nippon Steel & Sumitomo Metal Corporation, Tokyo, pp. 59–70.

This page intentionally left blank

Bridge construction equipment

30

Alessio Pipinato
AP&P, CEO and Technical Director, Rovigo, Italy

1. Introduction

The construction method to be chosen for a bridge depends on the geometrical characteristics of the superstructure, the layout of the bridge, the elevation, and the deck type, the height of the piers, the geographic context, the length of the bridge and of each span, and the spans' uniformity—as well as logistic issues such as the availability of materials and equipment, the ground properties, the context of the bridge (deep valleys, crossing a waterway or a road, open field or urban area, ease of access, size of space available, etc.), labor costs, designer and contractor expertise, site accessibility, and so on. In this chapter, bridge construction equipment (BCE) alternative methods are presented together with mechanized procedures to be used in the complex construction of medium- to long-span bridges that are often concrete made. The choice of the BCE is correlated with the types of concrete bridge deck, each of which should be used in different circumstances. Table 30.1 shows a layout of bridge types versus bridge span, which gives a broad outline of the options.

The bridge types may be split into in situ and precast options (CBDG, 2015). In situ options are the following:

- In situ *solid or voided slab*— Cast on a scaffold system or a series of beams/girders
- In situ *twin rib*— Cast on scaffold/beams or using traveling gantries
- In situ *span-by-span box girder*—Cast on scaffold/beams or using traveling gantries
- In situ *balanced cantilever*—Short box sections cast using a traveling formwork system

Precast options are the following:

- *Standard precast beam* —Inverted T, Y, or U beams erected by a crane
- *Bespoke precast beam*—T, I, or U beams erected by a crane or by using a gantry system
- *Precast segmental box girder*—Short segments erected with cranes or gantries
- *Whole-span precast box girder*—Erected span-by-span with gantries
- *Incrementally launched box girder*—Erected using sliding equipment
- *Modular precast*—Short shell segments erected on scaffold/beams or launched into place

Table 30.2 displays the concrete bridge production rates together with the suggested erection BCE.

The installation or assemblage, operation, and dismantling of bridge construction equipment systems are usually performed by a specialized subcontractor, selected

Innovative Bridge Design Handbook. https://doi.org/10.1016/B978-0-12-823550-8.00022-6

Table 30.1 Concrete Bridge Types vs. Span (Adapted From CBDG, 2015)

Bridge Type	Span (m)									
	10 to 20	20 to 30	30 to 40	40 to 50	50 to 60	60 to 70	70 to 80	80 to 90	90 to 100	100 to 150150 to 200 200 to 250 250 to 300
In-Situ Flat Slabs										
In-Situ Voided Slabs										
In-Situ Twin Ribs										
Standard Precast Arches/Portals										
Standard Precast Beams										
Bespoke Precast Beams										
In-Situ Span by Span Boxes										
Modular Precast System										
Precast Segmental Span by Span										
Incremental Launching										
Whole Span Precast										
In-Situ Balanced Cantilevering										
Precast Segmental Balanced Cantilevering										
Bespoke Arches/Frames										
Stressed Ribbons										
Extradosed										
Cable-Stayed										

The typical range is shown in blue (light gray in print version), and most competitive range for the UK market is depicted in gray.

Table 30.2 Concrete Bridge Production Rates and Erection Methods (Adapted From CBDG, 2015)

Bridge Type	Erection Method	Typical Production Rate (m/week)	10	20	30	40	50	60	70	80	90	100
Whole span precast	Gantry	100										
Precast segmental	Gantry	50										
Precast segmental	Crane	30										
Incremental launching	Launched	25										
In-situ span by span boxes	Gantry	25										
In-situ twin ribs	Gantry	25										
Bespoke precast I beams	Gantry	25										
Bespoke precast U beams	Crane	25										
Standard precast Y beams	Crane	20										
Modular precast	Launched	20										
Modular precast	Scaffolding	15										
In-situ span by span boxes	Scaffolding	10										
In-situ twin ribs	Scaffolding	10										
In-situ slabs	Scaffolding	10										
In-situ balanced cantilever	Travellers	5 to 10										

during the construction phase, who normally follows the construction method specified in the tender documents. The temporary structures project must fulfill the design philosophy and requirements indicated in the detailed design project of the permanent structure. Therefore, each BCE plan, design, and operation is unique and project specific. Expert-level experience of the specific matter is required to design a BCE machine to prevent a possible collapse during erection, which would result in human losses and injuries; considerable economic, financial, environmental, and political costs; damage to reputations; and increased insurance premiums.

2. Balanced cantilever erection with launching gantry

The balanced cantilever erection with launching gantry (Figure 30.1) enhances the delivery of segments along the completed deck to the rear of gantry, minimizing disruption to existing traffic networks. Moreover, temporary works require little ground improvement and are generally elevated, therefore causing only minimal disruption to existing roads, structures, and services. The necessary level support craneage is reduced because temporary works are relocated by a gantry crane. Unobstructed access to all work fronts is provided within the gantry system, and work can proceed on multiple fronts—i.e., pier segment erection, cantilever construction, and closure pour construction—simultaneously within the gantry. Temporary loads are introduced directly into the piers, and quick construction is possible; most BCE expert firms can erect up to six pairs of segments per shift (VSL, 2020). Examples of this method are reported in Figures 30.2 and 30.3.

3. Span-by-span erection with launching gantry

The span-by-span erection with launching gantry (Figure 30.4) increases the project's flexibility and enables the use of overhead or underslung gantries. Using this method facilitates fast rates of erection due to the use of external post-tensioning. Because segment delivery along the completed deck to rear of gantry or at ground level is possible, a smaller crew size is required compared to balanced cantilever construction, and good access to all work fronts is provided within the gantry. Typical erection rates are 1 span per 2.5 days with underslung gantries, and 1 span per 4 days with overhead gantries. If allowed to work 24 h a day, many contractors are able to achieve an erection cycle of 1 span every 24 h (VSL, 2020). Examples of this method are reported in Figures 30.5 and 30.6.

4. Balanced cantilever erection with lifting frames

The method of balanced cantilever erection with lifting frames (Figure 30.7) starts after the completion of piles and the pier, and the erection of the first segment onto those components by crane. After that, the lifting frame is installed on the first pier, and production begins. This is a relatively simple temporary machine, capable of

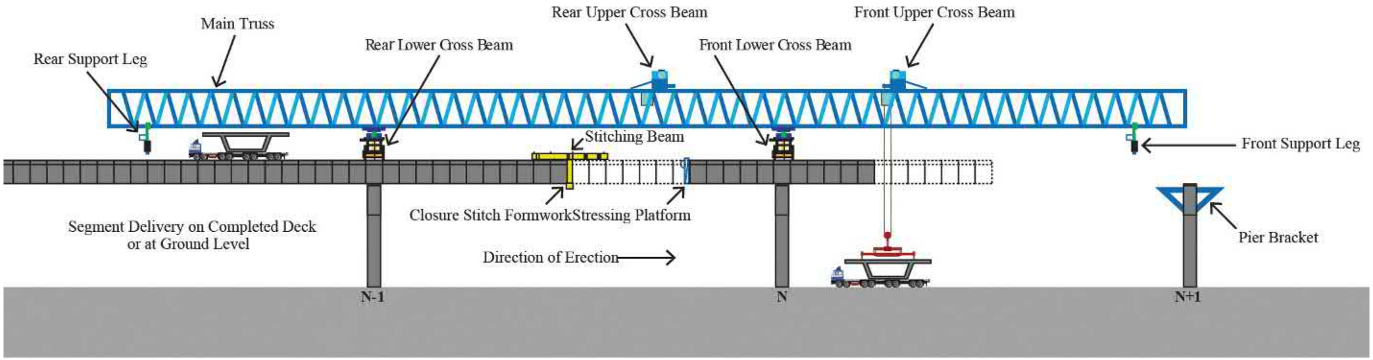

Figure 30.1 Balanced cantilever erection, launching gantry yard type.

Figure 30.2 Shenzhen Western Corridor, Hong Kong (2004–2005), 90,800 m^2 of deck, 1879 segments (VSL International).

Figure 30.3 Telok Blangah, Singapore (1998–2001), 61,440 m^2 of deck, 1460 segments (VSL International).

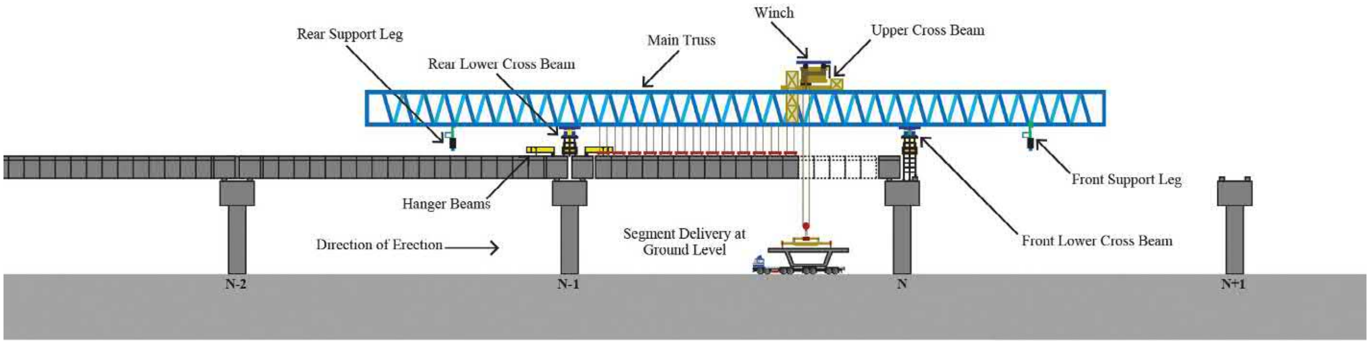

Figure 30.4 Span-by-span erection, launching gantry yard type.

Figure 30.5 West Rail, Hong Kong (1999–2002), 116,667 m^2 of deck, 8642 segments (VSL International).

Figure 30.6 Deep Bay Link, Hong Kong (2004–2005), 108,000 m^2 of deck, 3014 segments (VSL International).

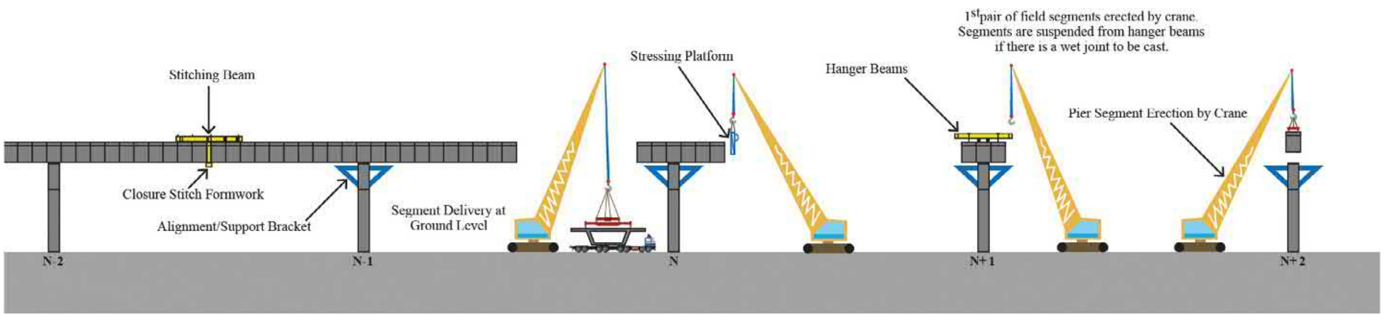

Figure 30.7 Balanced cantilever erection, lifting frames yard type.

constructing large segments quickly. It should be noted that optimized crew cycles enhance multiple levels of segment alignment and adjustment, where strand lifting units can be adopted to provide advanced levels of safety (VSL, 2020). Examples of this method are reported in Figures 30.8 and 30.9.

5. Balanced cantilever erection with cranes

The balanced cantilever erection with cranes method (Figure 30.10) is very similar to the balanced cantilever erection with lifting frames, substituting cranes in sites that are accessible from the ground. With minimal calculation requirements, this is a speedy method that minimizes the time and work area required to complete the project (VSL, 2020). Examples of this method are reported in Figures 30.11 and 30.12.

6. Precast beam method

The precast beam method (Figure 30.13) uses a variety of launching girders, beam launchers, and lifting frames that are capable of receiving precast beams directly behind, below, or parallel to the erection system. Precast I beams, U beams, and T beams are readily available around the world. Beams can be delivered from the ground

Figure 30.8 West Tsing Yi, Hong Kong (2004–2005), 14,000 m^2 of deck, 250 segments (VSL International).

Figure 30.9 Quarashia Bridge, Saudi Arabia (1989–1990), 12,820 m^2 of deck, 143 segments (VSL International).

or along the completed deck to the rear gantry, thus minimizing the working area and accessibility issues (VSL, 2020). Examples of this method are reported in Figures 30.14 and 30.15.

7. Full-span precast method

The full-span precast method (Figure 30.16) is particularly suited to projects comprising multiple spans of similar lengths that have minimal horizontal radii (e.g., railway viaducts). The construction of rail networks is typically suitable for this method of erection, as mechanization is required for beam precasting. Rapid rates of erection are achievable, and full-span production in a factory environment enhances the quality

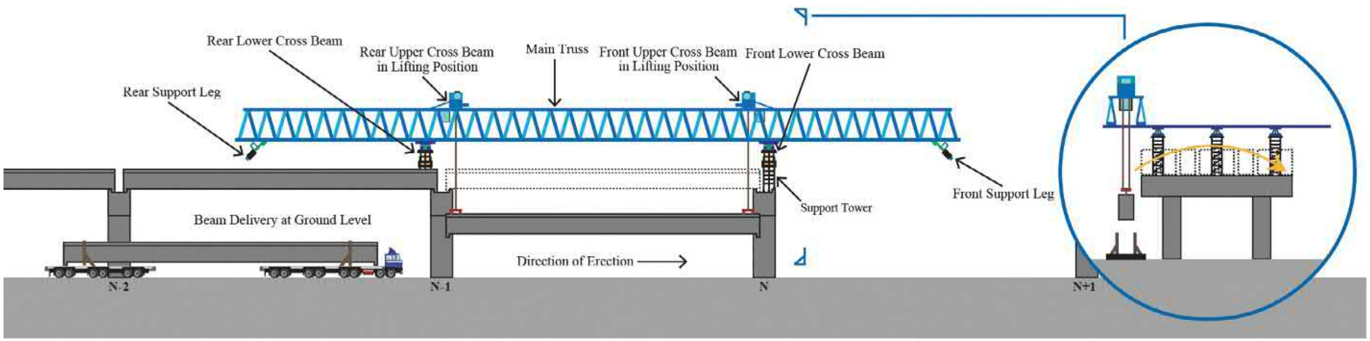

Figure 30.10 Balanced cantilever erection, cranes yard type.

Figure 30.11 West Rail, Hong Kong (1999–2002), 8330 m^2 of deck, 617 segments (VSL International).

Figure 30.12 Shatin T3, Hong Kong (2004–2007), 65,800 m^2 of deck, 1806 segments (VSL International).

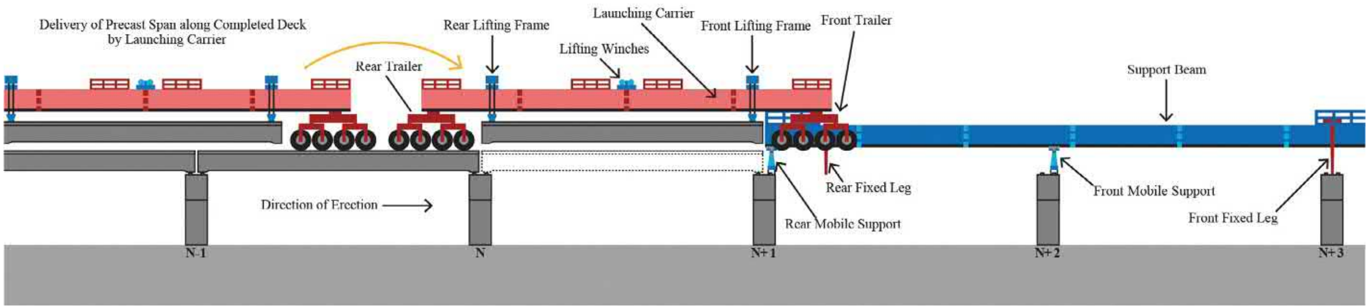

Figure 30.13 Precast beam method yard type.


Figure 30.14 N-S Link, Jakarta (1989–1991), 2000 beams (VSL International).


Figure 30.15 Cebu Coastal Road, Philippines (2001 – 2002), 24,000 m^2 of deck, 320 beams (VSL International).

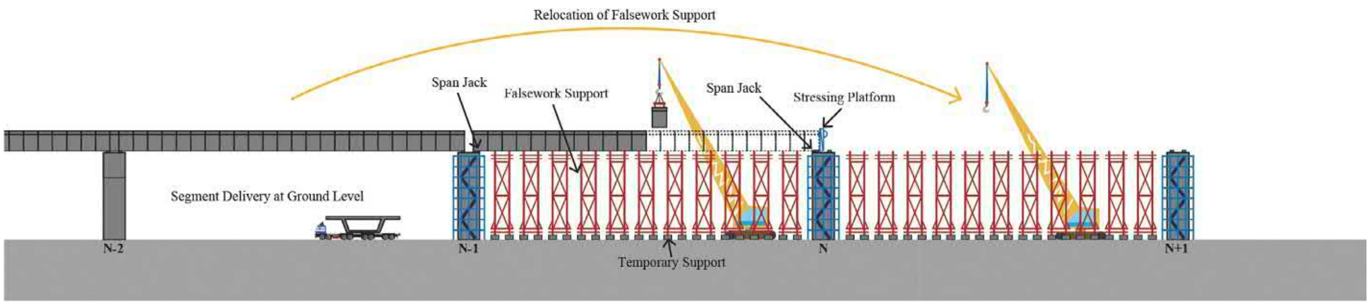

Figure 30.16 Full-span precast method yard type.

of the precast elements, which are completely prefabricated and checked outside the yard. Similarly to the precast beam method, full-scale elements are delivered to rear of the gantry along the completed deck, minimizing the yard dimensions (VSL, 2020). Examples of this method are reported in Figures 30.17 and 30.18.

8. Span-by-span erection on falsework

The span-by-span erection on falsework (Figure 30.19) is adopted where other method are not suitable (e.g., temporary loads on piers are restricted, so full-span precast, precast cantilever, or full cantilever methods are not suitable). Using this method, multiple fronts can be working simultaneously. Conventional scaffold supports or heavy shoring systems are used and commonly reused in similar yards (VSL, 2020). Examples of this method are reported in Figures 30.20 and 30.21.

9. Incremental launching method

In the incremental launching method (Figure 30.22), the deck segments is casted in a yard located behind the bridge abutment. Each segment is casted against and prestressed to the section of the superstructure that has already been built. The entire

Figure 30.17 Taiwan High-Speed Rail C215, Taiwan (2000–2004), 260,000 m^2 of deck, 602 spans (VSL International).

Figure 30.18 MRT, Singapore (1985–1989), 114,000 m^2 of deck, 1000 spans (VSL International).

prebuilt deck is then moved forward a distance equal to the length of this segment. This process is repeated until the bridge is in its final position. Additional continuity prestress is then installed. Bridges suitable for this method (a) have a constant cross-sectional shape along the entire length, (b) are straight, or (c) are either constant horizontal or vertical curvature bridges (VSL, 2020). Examples of this method are reported in Figures 30.23 and 30.24.

10. Form traveler method

The form traveler method (Figure 30.25) enhances the mechanized production of variable cross sections of deck segments. In this method, long-span segments cast in situ segments can be erected with a remarkably fast production times and very precise control, using a lightweight modular system (VSL, 2020). Examples of this method are reported in Figures 30.26 and 30.27.

11. Automatic climbing formwork systems

Automatic climbing formwork systems are used to build the columns. These systems climb hydraulically and are always anchored to the structure by guiding rails. Climbing operations are available also can be used in high wind speeds (often up to 70 km/h) and are designed specifically for each bridge and column shape. Formwork panels are beam timber made with steel walings. The maximum pouring height

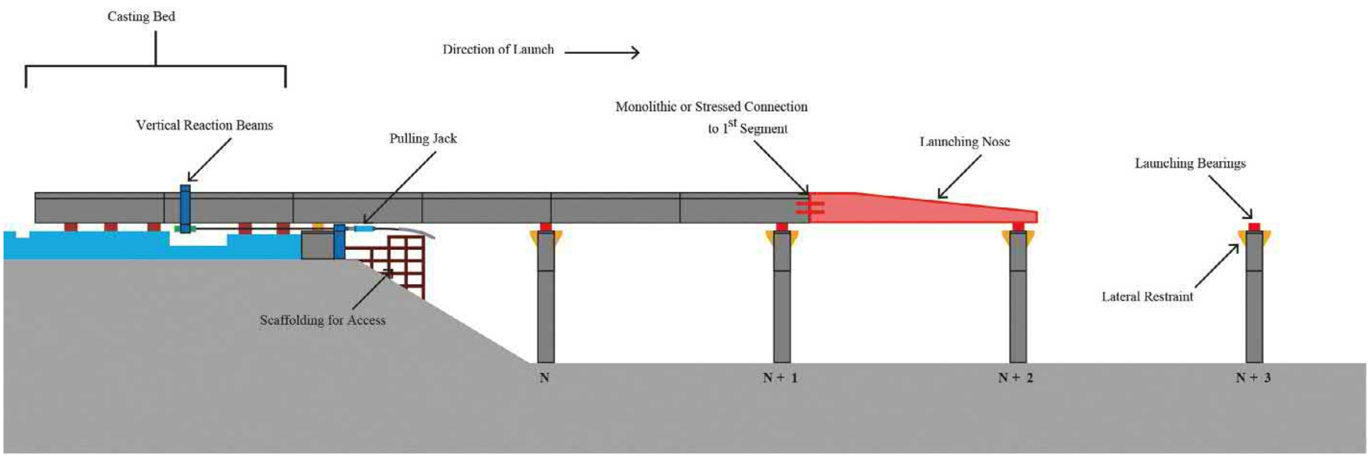

Figure 30.19 Span-by-span erection on falsework yard type.

Figure 30.20 Deep Bay Link, Hong Kong (2004–2005), 108,000 m^2 of deck, 3014 segments (VSL International).

Figure 30.21 East Rail, Hong Kong (2000 – 2003), 58,320 m^2 of deck, 4449 segments (VSL International).

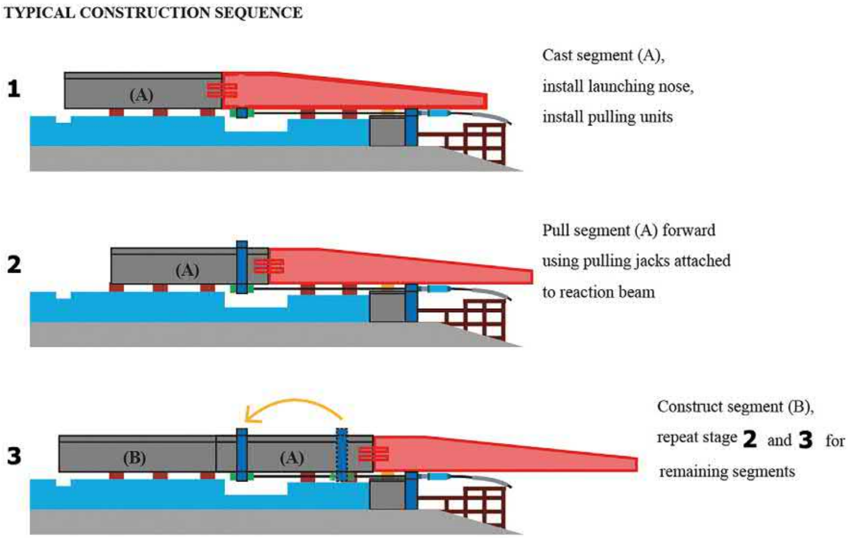

Figure 30.22 Incremental launching method yard type.

Figure 30.23 Kemena Bridge, Malaysia (2003–2005), 32–53 m of span length, 4947.6 m^2 of surface (VSL International).

Figure 30.24 Ryby Potok, Czech Republic (2005), 58 m of span length, 10,858 m^2 of surface (VSL International).

is also designed for the specific project. A ladder system is always provided within the system to ensure safe vertical movement and access between the different platform levels. An example of this method is reported in Figure 30.28.

12. Heavy lifting

Due to the growing amount of prefabrication solutions, preferable in large construction projects, very large primary structural elements of a bridge often need to be installed directly on the bridge structure. In those cases where no other solutions

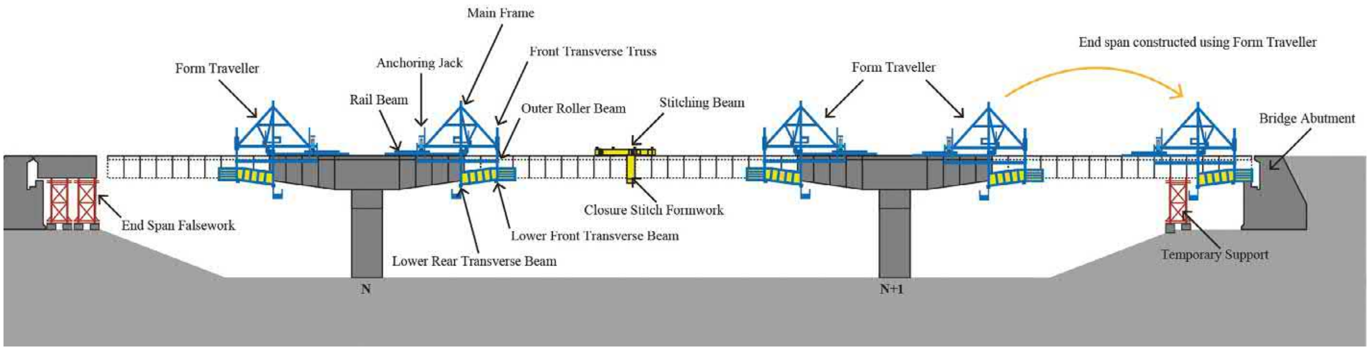

Figure 30.25 Form traveler method yard type.

Figure 30.26 Taiwan High Speed Rail, Taiwan (2002 – 2003), 80–100 m of span length, 22 cantilevers (VSL International).

Figure 30.27 Sinu Bridge, Columbia (2005), 150 m of main span length, 2 cantilevers (VSL International).

Figure 30.28 Automatic climbing formwork for the Lanthal Viaduct (DOKA).

are available, heavy lifting is the only way to accomplish this task. A vast array of hydraulic jacks, pumps, controls units, monitoring devices, and modular lifting/jacking frames are available to lift loads weighing more than 10.000 t, allowing very large-scale elements to be installed on-site. An example of this method is reported in Figure 30.29.

Figure 30.29 Bridge at Miraflores, Spain (2005). Two lowering operations of main arch, 1360 t each (VSL International).

References

CBDG, 2015. Best Construction Methods for Concrete Bridge Decks—Cost Data: A state-of-the-art report. CBDG-TG 14. Published April 2015, ISBN 978-1-904482-85-6, Concrete Bridge Development Group, Camberley.

VSL, 2020. Bridge Mechanized Methods. Available on VSL International website www.vsl.com.

Part IX

Assessment, monitoring, and retrofit of bridges

This page intentionally left blank

Bridge diagnostics, assessment, retrofit, and management

31

Alessio Pipinato
AP&P, CEO and Technical Director, Rovigo, Italy

1. Introduction

This chapter provides an analysis of the causes of structural and material decay in bridges. It also includes the investigation procedures used to analyze and understand the condition state of a particular bridge. Assessment procedures, which are not all standardized, are also described using a multilevel approach, which considers research and common standards. In the final part of the chapter, retrofit and strengthening solutions for bridge structures are reported, taking various constituent materials into consideration. Finally, the most common BMSs are presented.

2. Materials decay and on-site testing

2.1 Degradation causes

The classification presented in Table 31.1 deals with degradation causes in bridge structures; these are partly based on factors that are proposed in Silano (1993) and Radomski (2002). The factors leading to bridge deterioration can be classified into five fundamental groups: (a) basic factors, (b) load factors, (c) weather and environmental factors, (d) maintenance factors, and (e) construction defects.

2.2 Concrete structures

A concrete structure may not perform satisfactorily during its intended life-span with only an efficient design; experience has shown that durability design is required to ensure adequate structural performance (FIB, 2010). Parameters such as loading, traffic growth analysis, material types, material strength, element geometry, environmental analysis, etc., made during the design phase should also be checked during the construction stage by quality and performance control. Recent works such as the FIB bulletins (FIB, 1999) and the DuraCrete project (DuraCrete, 1998, 2000a,b) provide valuable information about the durability characteristics of concrete structures. The principle of the DuraCrete model has been adopted in the FIB model code for service life design (FIB, 2010). Environmental conditions that have an effect on the development of the deterioration processes (either their initiation or their progress over time) also need to be accounted for. The next section describes factors affecting

Innovative Bridge Design Handbook. https://doi.org/10.1016/B978-0-12-823550-8.00026-3

Table 31.1 Classification of Degradation Causes

A. Basic factors
A.1. Age of the bridge structure
A.2. Quality of the project
A.3. Sensitivity to damage
A.4. Adequacy of the design to the increasing service conditions
A.5. Time-dependent effect on constituent materials
B. Load factors
B.1. Frequency, speed, and traffic loads spectra
B.2. Dynamic effects
B.3. Accidents on the bridge
B.4. Accidents under the bridge
B.5. Vessel collision under the bridge
B.6. Overloading
B.7. Fatigue-induced damage
B.8. Time-dependent effects
B.9. Resonance and lateral effects at high speeds
B.10. Horizontal forces due to speed changes
C. Weather and environmental factors
C.1. Rain events
C.2. Snow events
C.3. Variation of the water level and its frequency
C.4. Ice-float run-off and its pressure on bridge substructures
C.5. Wind pressure and its effects on bridge elements
C.6. Earthquake and soil displacement
C.7. Temperature-induced deformations
C.8. Solar-induced deformations
C.9. Chloride attack originating from the action of sea water
C.10. Chloride attack originating from the use of deicing products
C.11. Freeze–thaw cycles
C.12. Aggressive chemicals
C.13. Penetration of CO_2 from atmosphere (carbonation effect in concrete)
C.14. Aggressive chemicals in rivers and underground water
C.15. Seawater attacks by its sulfates and chlorides
C.16. Vagabond currents
C.17. Fire
C.18. Hurricane
D. Maintenance factors
D.1. Whether design solutions are easy for maintenance or not
D.2. Inspection timing and quality
D.3. Timely maintenance works
D.4. Timely renewal of consumed secondary structures (e.g., drainage system, plants, pavement, parapets etc.)
D.5. Painting renewal
D.6. Use of deicing salts
E. Construction defects
E.1. Quality of the construction
E.2. Quality of the structural materials
E.3. Bridge yard-quality control protocol
E.4. Construction interruption
E.5. Partial collapse and repair during erection

the durability of a concrete structure, focusing on the main deterioration mechanisms and the role of the environment.

2.2.1 Affecting factors

After the design stage, the execution phase of a structure is one of the most crucial stages. Several examples exist of durability deficiencies due to poor workmanship that have resulted in insufficient compaction, curing, and concrete cover depth (BRE, 2001; FIB, 2010). Certain environmental conditions can benefit from an emphasis on the degradation of concrete structures, environmental effects, various transport mechanisms, and deterioration processes. These effects eventually will affect the appearance of the structure—e.g., the formation of cracks—and one thing will lead to another until, by acceleration of the progress of some deterioration mechanisms, there will be a resulting loss of safety for the users, loss of the resistance of the structure, and loss of the bridge's serviceability. However, design and construction controls may enable a reduction in unwanted results, such as the weakening of the structure's durability and structural performance. Furthermore, during its service life, regular inspections should catch any deficiencies in their early stages.

Deterioration of concrete structures occurs mainly from physical processes, or as a result of chemical reactions. Mechanisms such as temperature variations (i.e., freezing and thawing), sulfate attack, carbonation, chloride penetration, alkali–silica reactions, etc., may all result in severe damage of the concrete and/or the reinforcement through different steps and lead to events such as scaling, cracking, spalling, and corrosion. These mechanisms, with their individual steps and effects, are well described in a number of references—such as FIB (2010), Bentur et al. (1997), and Broomfield (1997)—and, thus, are only briefly described in the following sections. For reinforced concrete structures, the most common cause of damage is corrosion of the reinforcement. Theoretically, corrosion of the reinforcement should not occur, as the reinforcement is supposed well protected by the concrete cover. In fact, noncarbonated concrete has a high alkalinity ($pH = 13$) that is a result of the presence of sodium, potassium, and calcium hydroxides produced during the hydration of the cement. In this alkaline environment, an oxide layer is formed on the steel surface, the so-called passive film that prevents the corrosion of the reinforcement. However, there are two processes that may break down this passive film: the aggression of chlorides and carbon dioxide.

2.2.2 Temperature

Freezing and thawing is a common cause of concrete deterioration. Concrete subjected to alternating freezing and thawing is damaged due to the expansion of frozen water. Moisture is collected in the voids that result from entrapped air during placement. Consequently, damage occurring from frost action depends mainly upon the degree of saturation of the concrete's pore system with water (Mullheron, 2000). During a freeze cycle, water expands about 9% (White et al., 1992). This change in volume results in expansive pressures, causing gradual scaling, cracking, and eventually spalling of the concrete. Dry concrete is generally unaffected by freezing.

Nonetheless, most concrete structures are exposed at some stage to wet and/or cold environments. To prevent the effects of freezing and thawing, specific requirements are included in codes and standards (e.g., in EN 206-1/2000, 2005).

2.2.3 Sulfate

Sulfates carried into the inner sections of concrete may cause disruptive forces leading to cracking and scaling of the concrete. Sulfates are found in some clay soils, in seawater, and in many industrial environments where the combustion leads to the release of sulfur dioxide (FIB, 2010). The best way to protect concrete from the adverse effects of sulfates is by producing impermeable cement. Where there are known high levels of sulfates, protective epoxy coatings, or the traditional bitumen, should be applied to the concrete surface (Mullheron, 2000). Also in this case, the specific requirements of EN 206-1/2000 (2005) should be applied.

2.2.4 Alkali–silica reaction

Some decades ago, it was observed that certain concrete structures exposed to moisture penetration, developed cracks, with discoloration of the concrete adjacent to the cracks, (Liebenberg, 1992). Alkali–silica reactions (ASRs) can develop on concrete mixes containing reactive aggregates. Reactive aggregates are aggregates found in natural rocks containing reactive forms of silica such as chert, flint, chalcedony, and opaline sandstone (Mullheron, 2000). The ASR results in the formation of an alkali–silicate gel able to absorb large quantities of water that can cause expansive forces that lead to the cracking of concrete (Sukumaran, 1998). This type of deterioration may cause significant problems because the rate of deterioration is relatively slow and the first signs of cracking may take several years to appear. This makes it difficult to identify the deterioration mechanism and take measures to arrest it at an early stage, where no serious damage has been caused. To prevent this issue, lithium compounds have been found to be effective in mitigating ASR in concrete since the early 1950s. Supplementary cementitious materials such as silica fume, fly ash, and slag cement may also be used to control ASR in concrete.

2.2.5 Corrosion process

The corrosion of steel in concrete is an electrochemical process that involves two reactions, namely the anodic and the cathodic reactions, which take place simultaneously but not necessarily at the same rate. At the anode, ferrous atoms are ionized to ferrous ions that dissolve in the water solution around the steel:

$$Fe \rightarrow Fe^{2+} + 2e^{-}. \tag{1}$$

The electrons produced at the anode flow through the steel to be consumed at the cathode, where—combined with dissolved oxygen and water—form hydroxyl ions ($OH-$) that flow through the concrete to the anode:

$$½O_2 + H_2O + 2e^{-} \rightarrow 2OH^{-}. \tag{2}$$

The ferrous ions released at the anode react with the hydroxyl ions and yield ferrous hydroxide (Fe $(OH)_2$), which is unstable and reacts with water to form hydrated ferric oxide (Fe_2O_3), also known as rust:

$$2Fe(OH)_3 \rightarrow Fe_2O_3H_2O + 2H_2O. \tag{3}$$

Rust develops on the surface of the reinforcement and normally has a brown-green color. In cases of lack of oxygen, such as in submerged structures, the resulting product of $Fe(OH)_3$ is Fe_2O_4, which is known as black rust. The two ways to prevent corrosion are to improve the corrosion resistance of the metal and to add silica fume to reduce concrete permeability by providing an additional hydration product that reduces the number and size of capillary pores.

2.2.6 Chloride penetration

Chloride-induced corrosion is the most serious and widespread deterioration mechanism of concrete structures (FIB, 2010). Chlorides can either be cast into the concrete or may penetrate from the environment through pores to the interior of the concrete. The addition of calcium chloride accelerators (which was widely used until the mid 1970s; Broomfield, 1997) and the use of seawater in the concrete mix, as well as contaminated aggregates, increase the risk of premature corrosion. The dominant source of chlorides that diffuse into concrete is the seawater exposure and the application of deicing salts. A comprehensive literature review on the chloride penetration resistance of concrete can be found in Stanish et al. (2000) and is the result of a FWHA-sponsored study.

2.2.7 Carbonation

Carbon dioxide gas (CO_2) penetrates into the concrete from the environment and reacts with the calcium hydroxide ($Ca(OH)_2$) that is contained in the pores and maintains the high alkalinity of the concrete, providing the passive protective layer to the reinforcement:

$$Ca(OH)_2 + CO_2 \rightarrow CaCO_3 + H_2O. \tag{4}$$

This reaction leads to a reduction of the pH of the concrete, which—when it falls below approximately 9—signifies its full carbonation (Concrete Society, 2000). When the carbonation front reaches the reinforcement, the protective layer depassivates and corrosion initiates. Therefore, the depth of the concrete cover plays a significant role in the corrosion initiation time, as reported in the specific requirements of EN 206-1/2000 (2005).

2.3 Metal structures

2.3.1 Corrosion process

The process is the same as what was described in the previous section concerning concrete structures.

2.3.2 Fatigue phenomena

Repeated application of static load in structural components may produce fracture and fail if the same load, or even a smaller load, is applied a large number of times. The fatigue failure is due to progressive propagation of flaws in steel under cyclic loading. This is partially enhanced by the stress concentration at the tip of such flaws or cracks. Fatigue and fracture is entirely dedicated to the fatigue phenomenon.

2.4 Earthquakes

Real experience and observations of postseismic events have indicated that bridges have been often damaged by earthquake events, most commonly by the following causes (Priestley et al., 1996): span failures due to unseating at movement joints; amplification of displacements due to soil effects; and pounding of bridge structures. Structural dynamics are given in the thematic chapters of this book.

3. Investigation procedures

3.1 Bridge inspection

Bridge inspection is based on a methodology that takes into consideration instructions, guidelines, standards, and other official regulations. Bridge inspection can be classified into the following groups, depending on its scope and frequency (Radomski, 2002; Branco and Brito, 1996): cursory inspections, carried out by maintenance staff during routine inspections, normally taking place every day; basic inspections, carried out usually at least once a year by local bridge inspectors; detailed inspections, carried out at least every five years on selected bridges by regional bridge inspectors; and special inspections, carried out by highly qualified experts and researchers according to technical needs, normally as a consequence of questionable results from basic or detailed inspections. It is necessary to determine the capacity and assess the safety of a bridge after unexpected or accidental loads in order to establish its ability to resist to loads, or to indicate the need for rehabilitation and strengthening.

Bridge inspection is crucial in the evaluation and assessment of an existing bridge, and is directly related with the following phase of bridge rehabilitation decisions, because inspections help in investigating the existing condition of the structure from which recommendations for repairs, if necessary, can be formulated (Brinckerhoff, 1993).

3.2 On-site tests for concrete structures

Concrete bridges should be tested if the bridge inspection reported doubts regarding the structural performance of the existing structure. The tests available range from the completely nondestructive to those where the concrete surface is slightly damaged, to partially destructive tests such as core tests and pullout and pull off tests, where the surface has to be repaired after the test. The following methods, with some typical applications, have been used for the nondestructive testing (NDT) of concrete, considering that a preliminary visual inspection is an essential precursor to any intended NDT phase:

(a) Half-cell electrical potential method, used to detect the corrosion potential of reinforcing bars in concrete
(b) Radiographic testing, used to detect voids in the concrete and the position of stressing ducts
(c) Ultrasonic pulse speed testing, mainly used to measure the sound speed of the concrete and, hence, the compressive strength of the concrete
(d) Sonic methods, using an instrumented hammer that provides both sonic echo and transmission methods
(e) Schmidt/rebound hammer test, used to evaluate the surface hardness of concrete
(f) Carbonation depth measurement test, used to determine whether moisture has reached the depth of the reinforcing bars and hence whether corrosion may be occurring
(g) Permeability test, used to measure the flow of water through the concrete
(h) Cover meter testing, used to measure the distance of steel reinforcing bars beneath the surface of the concrete, and also possibly to measure the diameter of the reinforcing bars
(i) Penetration resistance or Windsor probe test, used to measure the surface hardness and hence the strength of the surface and near-surface layers of the concrete

3.3 On-site tests for metal structures

In the same situation of concrete structures, steel bridges also need to be assessed during their lifetime. NDT techniques for steel bridges are mostly coded (e.g., in ISO standards), and include the following.

3.3.1 Magnetic particle inspection

In magnetic particle inspection, one is able to detect discontinuities in metal structures through the use of magnetization. To visualize the magnetic field, a suspension, usually with fluorescent steel splinters, is used. A damage or fatigue crack discontinuity results in the formation of the magnetic field. Ultraviolet (UV) light visualizes the alignment of the field. This inspection method can be used for the detection of surface cracks in ferromagnetic materials only. Cracks in nonmagnetic material or in sandwiched elements cannot be detected. The method can be applied as quality control of precise setting of drilled holes to stop active fatigue cracks (Kühn et al., 2008).

3.3.2 Liquid penetration inspection

Fatigue cracks in structural members can be detected with a liquid penetration method. After surface cleaning, a developer is applied to reveal locations were the dye has penetrated.

3.3.3 Radiographic evaluation

The radiography procedure (e.g., X-ray, γ-ray) can be adopted to detect cracks and flaws in steel sections. The radiographic source can be placed on one side, while the receivers are placed on the other side of the inspected cross section.

3.3.4 Ultrasonic inspection

The back face of an element, or the damage inside the investigated material, reflects the ultrasonic signal and propagates as an ultrasonic wave. Typical applications are on corroded members, where the remaining thickness can be easily obtained.

3.3.5 Eddy current inspection

This technique is not widely applied to old steel structures; however, feasibility studies can be found in the literature. An application of the method to old structures to detect fatigue cracks in built-up sections of a truss girder after laboratory fatigue tests was described by Helmerich (2005); and after rivets have been removed, the sensors can indicate whether there is a crack in the rivet hole in one of the layers (Kühn et al., 2008).

3.3.6 Acoustic emission techniques

This technique is widely used, as it is able to produce interesting and profitable results, including the characteristic frequencies emitted by cracks if the structure is excited by the traffic load. The monitoring, collecting, filtering, and analyzing activities should be done by specialized personnel in order to obtain useful results. Examples on the applications of acoustic emission techniques for monitoring crack growth are given in Kühn et al. (2008), Nair and Cai (2010), and Lédeczi et al. (2011).

4. Assessment procedures

4.1 Introduction

The aim of an assessment of an existing bridge is obtain evidence to demonstrate whether it will function safely over a specified residual service life, taking into account a specific code reference. It is mainly encompasses an assessment of the hazards and load effects to be anticipated in the future, the material properties, the geometry, and the structural state of the bridge. Guidelines for the assessment of existing structures have been developed in many countries; however, the existence of bridge assessment guidelines based on codes or standards is rare. More frequently, such guidelines are prepared at a detailed level by scientific groups or research organizations. Whatever the source, the first issue deals with fixing risk acceptance criteria, which is quite difficult since it must be compatible with the code for new structures (e.g., limit-state analysis, safety factor format, etc.). The second issue deals with the process of the assessment procedure, which is commonly separated into phases, from preliminary evaluation to detailed investigation, expert investigation, and, finally, advanced assessment, depending on the structural condition of the investigated structure (Pipinato, 2011, 2014). See Figure 31.1.

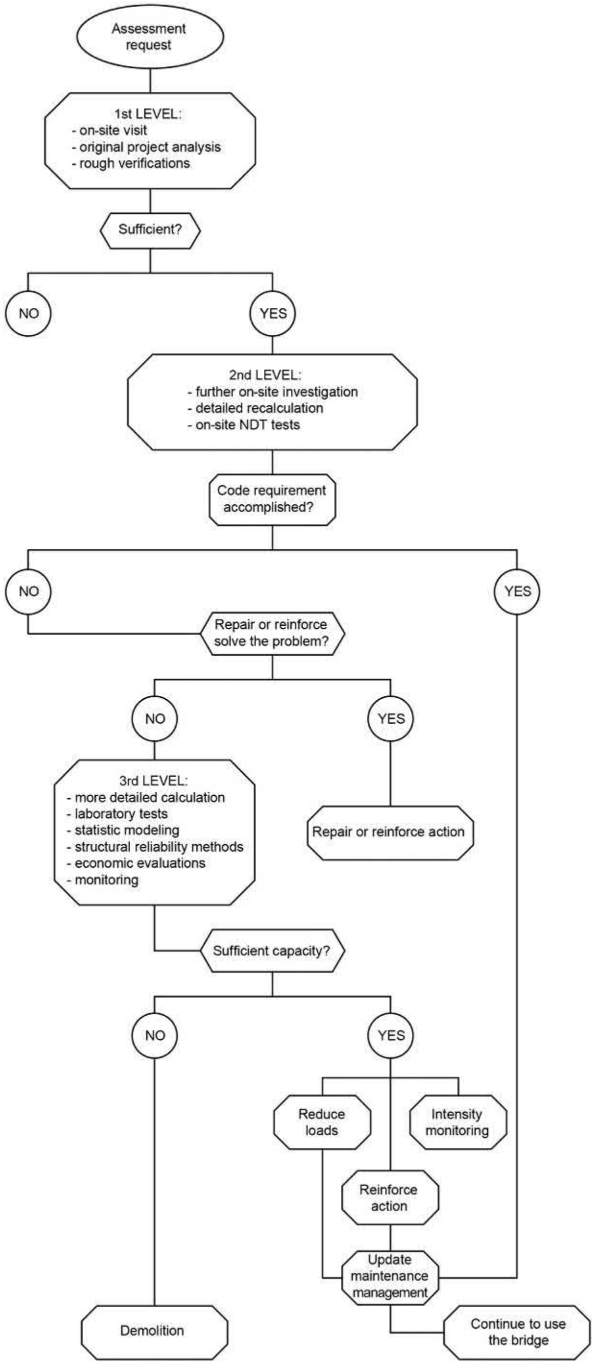

Figure 31.1 Step-level assessment procedure.

4.2 First level: Preliminary evaluation

The preliminary evaluation is the first level of investigation, the aim of which is to remove existing doubts about the safety of existing structures by adopting fairly simple method and identifying critical parts or members in the structure. In order to identify critical members, it is necessary to carry out an intensive study of the available original design documents, a visual inspection of the structure, and a photographic survey. The inspection procedure is often coded by infrastructural agencies manuals and procedures; however, at minimum, the following points must be checked:

- The bridge construction's conformity to the original drawings and/or differences between the structure as built and those drawings
- Bridge modification during service (e.g., rehabilitation, strengthening, changes in the static system, etc.)
- Presence of any visual evidence of degradation (e.g., damaged expansion joints, supports, corrosion, cracks, vibration or loose rivets, collision, lack of structural members, etc.)

Moreover, if available, inspection and maintenance reports can be used, and reference should be made to the evaluation report. The preliminary evaluation should include codes and recommendations analysis procedures where available, and conservative assumptions where information is lacking or doubtful. In this way, critical construction details can be identified.

4.3 Second level: Detailed investigation

The aim of the detailed investigation is to update the information obtained in other analyses by carrying out a refined assessment, especially for those members for which adequate safety was not confirmed by preliminary evaluation. At this stage, a specialized consultant should assist. In this phase, a finite element method (FEM) numeric model of the entire structure is developed. Based on the current code provisions, the structure should be recalculated, and verification tables should report whether the structural members are safe or not. Concerning specific issues, such as the fatigue and seismic behavior of the bridge, detailed code provisions should be referred to. From this step-level investigation, NDT can be used in order to characterize the basic material properties of the structure. The final report of the investigation should establish whether the structure is secure against specific issues and has sufficient static strength against actual loadings.

4.4 Third level: Expert investigation

In case of key structures that have major consequences in terms of risks or costs related to a decision, a team of experts is needed to carefully check the conclusions and proposals reached in the last phase. Discussions and further assessments using specific tools can also be carried out to help reach decisions. At this level, on-site testing can be adopted in order to provide the dynamic identification of the structure, as reported in the following example.

4.5 Fourth level: Advanced testing

This advanced level of investigation should be reserved for recurrent bridges along infrastructural nets, in which a rational procedure of analysis and intervention could help in determining if retrofitting interventions could be adopted or if rational dismantling large-scale operations are required. The procedure is based on a detailed survey of the existing bridge, a FEM analysis, a code verification procedure, NDT diffused sampling, and, based on these data for real-scale testing of one case study structure, determines the global static and cyclic behavior of the bridge. In specific cases, on-site dynamic identification can be performed. Concerning the fatigue assessment, in this case, a linear elastic fracture mechanics (LEFM) investigation is required. Concerning seismic analysis, nonlinear analysis is required. Specific material testing analysis should be performed regarding the case analyzed. The advanced testing result should report on the various analyses performed, and should clearly state verification results that indicate the specific retrofit needed for recurrent interventions.

The problem of existing bridges and their assessments has recently increased. Indeed, the current low funding in the infrastructure sector of many European countries forces the bridge owners, as well as the operators, to postpone investments in new road and railway bridges and consequently stretch the service life of their existing structures. Therefore, the owner of the infrastructure currently faces two main challenges: the need for further continuing the safe operation of aging bridges and the need for cost-effective maintenance. Methods must be provided that enable engineers to offer safe and cost-effective assessment and maintenance methods to their clients (Kühn et al., 2008). In the following sections, some key procedures are reported in order to reproduce different step-level assessments dedicated to bridge management analysis. This advanced level is not shown in Figure 31.1, as it is mostly avoided in the structural common practice, except for special and large-scale constructions.

4.6 Critical member identification procedure

An alternative and faster solution could be adopted in some cases. Existing bridges are often exposed to an effective risk of collapse for a single and specific structural member state; this could be discovered by an identification procedure that is called a *top-down bridge collapse identification (TDBCI) procedure,* which is effectively able to find out critical situations. This process should not only be theoretical and analytical but also should be combined with a survey of the structure to identify failure or incipient mechanisms (Figure 31.2).

5. Repair and strengthening

5.1 General information

As there is great confusion regarding different but similar terms, a definition of the common terms used in this field should be outlined here. We can define *maintenance* as every operation applied to an existing bridge and finalized to maintain

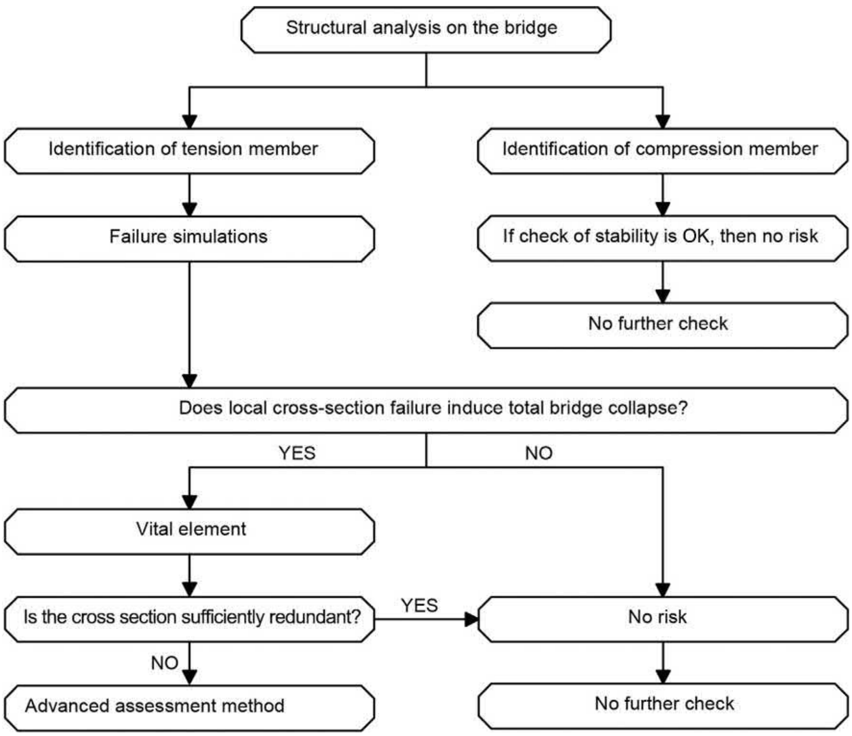

Figure 31.2 Identification procedure of critical elements.

its actual strength and geometry without extraordinary interventions; *rehabilitation* as the process to restore under service level/handicap of an existing structure with concentrated actions; *repair* as concentrated actions to restore damaged points; *stiffening* as singular action used to enhance the bridge capacity where in-service limits have been passed (e.g., cracks, rotations, deflections etc.); and *retrofit/strengthening* as a comprehensive work of renovation including a large amount of structural and technological actions that lead to a complete modernization of the bridge structure, in order to upgrade its load carrying capacity, even against horizontal actions.

5.2 Lightweight components

Dead load in existing bridges is relevant: for this, load reduction is a possible intervention, considering deck substitution and safe barrier changes. This choice should be finalized to a precise improvement in the bridge service level, at least on the load carrying capacity; if not, extensive work on the deck is not necessary.

5.3 Composite actions

To increase the flexural strength of existing deck systems, the modification to a composite system is a common method used. Where analytically verified, the flexural stiffness is upgraded as the deck combines with the steel profiles in a composite manner to adopted the welded stud: this solution could also be adopted for existing composite bridges, in which the composite action is very low, by the use of shear connectors between the deck and the stringers. Deck materials are generally made of concrete, such as normal-weight reinforced concrete (precast, cast in place, partly precast, and partly cast in place) or lightweight reinforced concrete. If a decision is made on an existing structure, the first issue to focus on is the weldability of steel stringers.

5.4 Improving bridge member strength

Cover plating is a widely adopted technique used in steel bridges: steel plates are connected to existing steel members by riveting, bolting, or welding in order to enhance the structural capacity of nodes or members by increasing the section modulus and, consequently, the flexural capacity. If jacketing is feasible during the cover plate's application, this ensures that the both dead and live load stresses will be carried; otherwise, an increased amount of steel would be necessary. This technique can also be explored for reinforced concrete (RC) bridges at the tension face of the beam, by bolting or doweling to strengthen the flexural capacity, and by cover plates for shear lacks. In RC bridges, jacketing should be adopted before interventions to reduce the dead load influence.

5.5 Post-tensioning applications

Post-tensioning technique is useful where undesirable deflections or high-tension levels have to be reduced: local (e.g., cracks) or global (e.g., deflections) problems should be solved in this way while considering the limit imposed by post-tensioning. Moreover, this technique has been widely used to change the static scheme of bridges and viaducts, from a series of simple spans to a continuous span. However, post-tensioning can also change the stress state in structural members: e.g., one or more concentric tendons straight in the median height of the deck section will induce an axial compression force that, depending on magnitude, can eliminate part or all of an existing tension force in a member, or even place a residual compression force sufficient to counteract a tension force under other loading conditions (Klaiber et al., 1987).

5.6 Modification of the structural configuration

The modification of the structural configuration of a generic structure could induce variations in internal force distribution. Two main methods are available:

- Introducing new support points and reducing the maximum positive moment in the midspan; in this case, a problem could arise if deep water is present or if bridge obstacles are present below.

- Changing a series of simple spans to a continuous span scheme in order to lower the stress level in the structure while simultaneously enhancing the structural capacity versus live load. This is a feasible technique if girders are located at a reasonable height and if the existing bridge is overall in well maintained. Cost analysis of alternatives should be carefully considered for this type of application.

5.7 Concrete Bridges

5.7.1 Crack repair

There are various types of cracks; however, in the context of repair, they can be classified into two categories: inactive cracks, which are unable to propagate, and moving cracks, which are active and able to increase under applied loads. The most appropriate solutions to these cracks are epoxy resin injection and/or cement grouting; however, the former is preferable for small cracks (<4 mm). Admixtures ready for use are widely available and can be easily adopted for this specific purpose. In the case of grouting, the water-to-cement ratio could be established according to testing or, if available, to code and standards prescriptions.

5.7.2 Stitching

Stitching occurs when U-shaped metal bars are encased or epoxy-fixed in the near side of the crack, along the whole crack line. This technique is possible only if the crack is exposed on one surface of the element to be reinforced (e.g., in bending members); otherwise, the technique has to be adopted at both sides (e.g., in tension members).

5.7.3 Reinforcement

Local or extended steel bar reinforcement is needed if an extended large crack (>4 mm) is found on an existing bridge component. In this case, superficial decortication is used before adding a new RC layer, which is dimensioned according to the analytical results of the assessment. If deep cracks are found (e.g., going over the removed layer), further strengths should be adopted (e.g., injections, steel member addiction, etc.).

5.7.4 Overlays and surface treatment

Where the aforementioned case evidenced a net of microcracks (<4 mm), surface treatments/coatings should be enough to remedy this. As these situations come from surface over tensions (e.g., due to drying shrinkage), epoxy resin or silane/siloxane coats are the most appropriate solution.

5.7.5 Flexible sealant

To repair or bond cracked concrete surfaces, sealants developed especially for forming permanent, waterproof, and weatherproof seals in all exterior gaps and joints are required. The sealant must be elastic, remaining flexible to expand and contract with construction material movement and to protect and retain the original seal. Excellent adhesion to the sealed concrete and high movement quality are required for these sealants, which include epoxy polysulfides, silicones, and acrylic polyurethanes. If the surface is not used or hidden, the application could be without a recess, which is required if the surface is exposed to traffic.

5.7.6 Patch repairs

To repair specific and closed zones of the concrete members, a patch application could be employed. In this case, a polymer-reinforced, high-strength, cement-based patching and resurfacing mortar is adopted. This solution type should be avoided if it is enclosed in a traffic lane.

5.8 Steel Bridges

5.8.1 Stop-hole drilling

Hole drilling is the most commonly applied means of arresting fatigue cracks. A hole drilled at the tip of a crack essentially blunts the crack tip and greatly reduces local stress concentration. This technique has been successfully applied to various types of structures, including navigation lock gates and several bridges (Fisher, 1984). Hole drilling is effective for through-thickness cracks in plates or plate components of structural members.

5.8.2 Weld-toe grinding

Weld-toe grinding reduces the geometrical stress concentration and extends the fatigue life of undamaged details. Grinding can be used to remove shallow fatigue cracks that may exist in the weld toe. Grinding should always be done in the direction of applied stress. A pencil or rotary burr grinder can be used. Magnetic particle inspection of the ground area should be conducted after grinding to ensure that embedded flaws are not exposed. Penetrant inspection may reveal false indications due to grinding marks.

5.8.3 Peening

Peening is effective as a retrofit for shallow surface cracks that commonly occur at fillet weld toes. Peening imposes compressive residual stresses resulting from the plastic deformation induced by the peening hammer and reduces the geometrical stress concentration similar to that with grinding. Air hammer peening is effective in arresting fillet weld toe surface cracks with a depth of up to 3 mm if the tensile stress range does not exceed 40 MPa (6 ksi). Peening can also be applied to uncracked fillet welds to improve the fatigue resistance of the detail. The expected benefit of peening under favorable conditions (low stress range, low minimum stress) is an increase in fatigue life approximately equivalent to one fatigue design category (Fisher et al., 1979). Peening should be done using a small pneumatic air hammer with all sharp edges of the peening tool ground smooth. Although peening intensity can be easily varied by changing air pressure, multiple-pass peening at lower air pressures is most effective. Initial passes of the peening hammer may reveal some cracks that were not initially visible, and peening should be continued until the weld toe is smooth and no cracks are apparent. Penetrant inspection of the peened area should be conducted after peening to ensure that embedded flaws are not exposed. Peening is most effective when it is performed under dead load so that the imposed compressive residual stress has to be effective only against the live load.

5.8.4 Gas tungsten arc Remelting

The gas tungsten arc (GTA) remelting process is also an effective procedure for the repair of shallow surface cracks that occur at fillet weld toes. This procedure is generally effective for surface cracks with a depth of up to 5 mm (slightly greater depths than peening) and is not limited to small stress ranges and minimum stress levels. Like peening, GTA remelting can also be used to improve the performance of uncracked fillet welds, approximately doubling the fatigue life. However, it is less easily performed in the field, and it requires highly skilled welders and good accessibility.

With the GTA remelting procedure, a small volume of the weld toe and base metal is remelted with a gas-shielded tungsten electrode. After the area cools, the geometric stress concentration is improved, and nonmetallic inclusions that might exist along the weld toe are eliminated. When the procedure is applied to crack repair, sufficient volume of the metal surrounding the crack must be melted so that upon solidification, the crack is eliminated. The effectiveness of the procedure is dependent on the depth of the remelted zone, since insufficient penetration would leave a crack buried below the surface. Such a crack would simply continue to propagate, resulting in premature failure. Proper selection of shielding gas and electrode cone angle is crucial in obtaining maximum penetration of the remelted zone. Argon-helium shielding and an electrode cone angle of 60 degrees were found to be most effective (Fisher et al., 1979). For any retrofit procedure, the depth of penetration should be verified by metallographic examination of test plates before the procedure is applied in the field.

5.8.5 Rivet replacement

Missing, loose, or headless rivets and rivets with rosette heads should be replaced (Fisher, 1984). Deteriorated rivets missing more than half of the head should be replaced if the rivet is subject to an applied tensile force or tension resulting from prying action. The most useful riveting repair is represented by high-strength bolting: the rivet should be knocked off before bolting with a pneumatic buster. Welding or other interventions that can cause metallurgical damage (adversely affecting, e.g., the fatigue strength) to the adjacent material are to be avoided.

5.8.6 Welding

Welding solutions should be carefully used in existing steel structures only where continuous welding connections are present, and if no other bolting solutions are practicable, weld repair should be introduced. Avoid welding in fracture critical members, in nonweldable steels, in low Charpy members, and, if possible, in tensile areas.

5.8.7 FRP strengthening

An alternative technique for strengthening steel structures consists of the application of externally bonded fiber reinforced polymer (FRP) sheets, used mainly to increase the tensile and flexural capacity of the structural element. FRP materials have a high strength-to-weight ratio, do not present problems due to corrosion, and are manageable. Some examples of guidelines for the design and construction of externally bonded FRP systems for strengthening existing metal structures include the ICE design and practice guide (Moy, 2001), CIRIA Design Guide (Cadei et al., 2004), US Design Guide (Schnerch et al., 2007), and CNR-DT 202/2005 document (Italian Research Council, 2005).

The benefits of composite strengthening have been applied, for example, in a steel bridge on the London Underground (Moy and Bloodworth, 2007). The benefits of strengthening large cast-iron struts with carbon FRP (CFRP) composites in the London Underground are illustrated in Moy and Lillistone (2006). A state-of-the-art review of FRP-strengthened steel structures was recently developed by Zhao and Zheng (2007). Among materials, apart from the well-known e-glass, HS CFRP, and aramid, high-modulus CFRP (HM CFRP),materials are becoming widely used and have been developed with a tensile modulus approximately twice that of steel. Diverse applications are reported in literature concerning this type of material and are discussed next.

Among the most common techniques of FRP-strengthening systems in bridge engineering, three should be cited. The first is the wet lay-up system, which consists of multidirectional or unidirectional dry or fiber sheets on-site, saturated with resin, which provides the binding matrix of the fiber and bonds the FRP to the material. Common types are represented by dry unidirectional fiber sheets with the fiber running predominantly in one planar direction, dry multidirectional fiber sheets or fabrics with fibers oriented in at least two planar directions, and dry fiber tows that are wound around or otherwise mechanically applied to the material surface. Another system is represented by precured FRP fibers, bonded with an adhesive on the surface. Externally applied epoxy bonded FRP sheets to the tension face of structural elements have been widely accepted for practical use as the bonding solution between FRP and steel, even if the durability of this application has to be extended with direct applications and monitoring (e.g., attention where there is danger of fire).

5.8.8 Cover plating

To strengthen existing bridges, steel plates are connected to existing steel members by riveting, bolting, or welding in order to enhance the structural capacity of nodes or members, by increasing the section modulus and consequently the flexural capacity.

If jacketing is feasible during the cover plate application, this ensures that the both dead and live load stresses will be carried. Otherwise, an increased amount of steel should be used.

5.8.9 Painting

To protect steel against corrosion, a protective coating is the most commonly adopted technique. The first stage of a corrosion protection system application is the surface preparation: the preferable situation for rapid intervention is if the rust grades comply with grade A or B (BS EN ISO 8501-1 (2007)), as grades C and D involve a longer and costlier cleaning operation. The standard grades of cleanliness for abrasive blast cleaning are as follows:

- Sa 1–Light blast cleaning
- Sa 2–Thorough blast cleaning
- Sa 2½–Very thorough blast cleaning
- Sa 3–Blast cleaning to visually clean steel

Specifications for bridge steelwork usually require either Sa 2½ or Sa 3 grades. The protective system is then applied. This is defined by a sequence of applications, including the primer, the intermediate(s), and the finishing. Special codes and standards for railway or highway applications can be found in literature. Regarding unpainted solutions in weathering steel structures (EN 10025-5, 2004), paints should be adopted if surface damage becomes a concern. Weathering steels can be protected with the same maintenance paint systems recommended for new structures.

6. Bridge management

6.1 Overview on BMSs

Due to the rapid growth of automobile and truck usage and the development of massive transportation infrastructures in past decades, there are increasing demands to improve the management methods of bridges, which constitute the most vulnerable elements of the road network. Many agencies responsible for infrastructural networks have recognized the difficulties of the available bridge management approaches, in which decisions are made only on a single project level. As a result, a significant effort has been undertaken in many countries to develop bridge management systems (BMSs) to evaluate the condition of a single bridge in the global network level during its life cycle and, at the same time, to provide efficiency information when allocating resources and establishing management policies in a bridge network.

A BMS is a rational and systematic approach to organizing all finalized activities related to managing network-level bridges (Hudson et al., 1993). Decision makers should select optimal solutions from an array of possibilities and must evaluate and compare alternatives for all bridges in the road network from the viewpoint of life cycle management in order to avoid similar problems in the near future. Several BMSs have been developed for specific purposes: e.g., Gralund and Puckett (1996) developed a BMS for the rural environment, Markow (1995) developed a BMS for highways, Thoft-Christensen (1995) developed BMS analysis—including a reliability approach, in particular—and Kitada et al. (2000) developed a detailed BMS for steel bridges. Some studies on evaluation criteria for bridge maintenance that also take into account seismic risk and fatigue evaluation are described in Pipinato (2008a,b).

Innovative techniques that include the implementation of new technologies and BMSs have given bridge inspectors and engineers the necessary information to determine an appropriate action. Such a decision is often dependent on a combination of the quantitative information obtained from various measurements, qualitative information obtained from bridge recognition, and general engineering knowledge about the entire bridge system. In order to allocate funds, a bridge owner needs a BMS that uses historical deterioration trends and predictive relationships. Combining existing management system specifications with bridge-specific deterioration models, which consider the system's structural behavior and the aging of the infrastructural network investigated, will improve an infrastructural owner's ability to make bridge-specific decisions and allocate funds for specific and accurate programmed interventions. Probably one of the most significant applications of contemporary BMSs relates to the United States. In 1991, the Intermodal Surface Transportation Efficiency Act (ISTEA) required all states to develop, establish, and implement a BMS by October 1998. The ISTEA requirements, first distributed in 1991, stated that a BMS must be implemented on all state and local bridges. New federal legislation, however, required implementation of BMSs only for bridges on the National Highway System (NHS); therefore, the use of BMS inspection for non-NHS bridges was optional (Sunley, 1995). The principle that BMS used in the United States is PONTIS, which was developed in the early 1990s for the Federal Highway Administration (FHWA) and became an American Association of State Highway and Transportation Officials (AASHTO) practice in 1994. It performs functions such as recording bridge inventory and inspection data, simulating condition and suggesting actions, developing preservation policy, and developing an overall bridge program. The system allows the representation of a bridge as a set of structural elements, with each element reported based on its condition.

In 2002, 46 agencies throughout the nation had PONTIS licensing, and each state highway administration (SHA) could customize the system according to its needs (Robert et al., 2003). BRIDGIT was developed in 1985 by the National Cooperative Highway Research Program (NCHRP) and the National Engineering Technology Cooperation in an attempt to improve bridge management networks. This system has capabilities similar to the PONTIS system. There have been many research projects throughout the nation on which local agencies have worked with universities to develop their own BMSs. Other BMSs developed by individual state agencies have good specific functions and qualities but lack features that can satisfy all the demands of effective bridge management and maintenance procedures on a national scale. Other notable research and development efforts on BMSs took place in Iowa, Washington, Connecticut, Texas, and South Carolina (Czepiel, 1995). Among recent European experiences that are noteworthy is the TISBO Infrastructure Maintenance Management System, currently being developed by the Netherlands Ministry of Transportation, Public Works, and Water Management. It is a system that integrates inspection registration and maintenance management. Owner agencies in Italy usually manage their network with self-developed codes/procedures regarding BMSs. The policy of the main Italian agencies is briefly presented in the following:

- Rete Ferroviaria Italiana (RFI) is the national agency for the whole Italian railway network, consisting of about 16,000 km. The BMS is based on periodical visual inspections supported by special testing trains. All data are elaborated with specific software developed by the agency with the aim of defining economical and technical convenience of possible maintenance, rehabilitation, and/or strengthening interventions.
- Autostrade per l'Italia is the most relevant highway agency in Italy; it manages a network of about 3400 km. The BMS is based on the SAMOA program for surveillance, auscultation, and maintenance of structures.
- ANAS (1997) is the Italian agency for roads with a national interest, and manages a network of about 26,700 km. The BMS is based on the national road inventory and in situ surveys, and is a web-based management application that is developed by the agency and updated regularly.

Not only are large networks monitored and regularly inspected in Italy; municipal, provincial, and regional authorities also have recently increased their surveillance of bridge networks, as requested from the innovative Guideline for the Surveillance of Bridges (2020), developed by the Italian Infrastructure Ministry. In this framework, a wide range of possibilities of BMS are present in the market—such as ProPonti (2020), an innovative BMS developed in Italy by a group of Italian researchers and engineers, which includes a framework of active bridge monitoring system with wireless and MEMs devices.

During the last decade, numerous research projects have been financed by the European Commission, and some guidelines from these projects that deal with the assessment of existing bridges in Europe have been published; i.e., BRIME (2001), COST345 (2004), SAMARIS (2005), and Sustainable Bridges (2006). All of these guidelines are meant for highway bridges specifically, except for Sustainable Bridges (2006), which is particularly pertains to railway bridges. The purpose of BRIME (2001) was to develop the modules required for a BMS that enable bridges to be maintained at minimum overall cost while taking a number of factors into account, including effect on traffic, life of the repair, and the residual life of the structure. COST345 (2004) investigated the procedures and documentation required to inspect and assess the condition of in-service highway structures, not only bridges. SAMARIS (2005) focused on inventorying the condition of highway structures in European countries, choosing the optimal assessment and strategy selection for rehabilitation through the use of ultra-high-performance fiber-reinforced concrete (UHPFRC) and similar technologies. *Sustainable* Bridges (2006) deals, in particular, with railway bridges and structural reliability assessment based on in situ NDT.

6.2 Network and bridge level

While the bridge-level management relies more on the previously described structural monitoring and interventions, the network management of a set of bridges involves the significance of "prioritization": a vast amount of existing bridges are impossible to maintain and retrofit at the same time, so a prioritization system should be employed in an advanced BMS. Network- and project-level information should be interrelated (Thompson et al., 2003). The final output of a prioritization system is represented by a priority-rated list, with the bridges with a higher needs for intervention at the top (Li and Love, 1998). At the project level, the network-level information is used in order to accurately define the individual bridge intervention, with a precise cost analysis boundary (Soderqvist and Veijola, 2000).

6.3 Network level and prioritization methods

Prioritization methods include priority ranking [e.g., sufficiency rating (SR), level-of-service (LOS), deficiency rating (DR), and incremental-benefit–cost (B/C) analysis] and mathematical optimization. Subjective method ranking has been demonstrated to be ineffective for large networks (Mohamed, 1995), and this conclusion should also be made for priority ranking in general, not considering the importance of the bridge in a certain network. The SR method is applied, for example, by FHWA in the United States, where the sufficiency rating formula is a method of evaluating a bridge's sufficiency to remain in service, based on a combination of several factors; the result of the formula is a percentage in which 100% represents an entirely sufficient bridge, and 0% represents an entirely insufficient or deficient bridge (FHWA, 2015). Bridge deficiencies are represented by two main categories: structurally deficient (structurally deficient means that a bridge requires repair or replacement of a certain component) and functionally obsolete (functional obsolescence is assessed by comparing the existing configuration of each bridge to current standards and demands). The SR does not enter into the domain of the appropriate intervention to be performed on the single bridge. The LOS system includes information on the load capacity, clear deck width, and vertical roadway clearance (Johnston and Zia, 1984). The B/C alternative is a system created to allocate benefits for the user and the agency by employing a certain amount of money for a precise bridge repair, considering the consequence of different types of interventions. Then, an analytical approach is used for translating these alternatives to all the network bridges.

6.4 Project level

At this level, some alternatives are available, including B/C techniques and life cycle cost (LCC) optimization. B/C techniques include the analysis of different intervention strategies for a singular bridge, allocating funds to the alternative represented by the highest value of B/C; this method is limited to a one-bridge analysis and neglects all network information and needs. The LCC approach considers all costs required during the life of the structure, allocating funds over the life-span of the bridge. Integrated solutions, considering funding availability over the time and intervention alternatives, are available.

6.5 Network- and project-level decision making

Recent attempts have been made to try to use a multipurpose decision scheme that includes the project and the network level. Artificial neural networks (ANNs) and genetic algorithms (GAs) have been employed in the optimization of BMS integrated solutions, even if not directly employed by agencies. Liu and Hammad (1997) presented the application of the multiobjective optimization of bridge deck rehabilitation only. The objective function was to minimize both the total LCC and the average degree of deterioration weighted by the bridge deck area. The total rehabilitation cost (C) was determined by the following equation:

$$\text{Minimize}\, C = \sum_{i=1}^{N} \sum_{t=1}^{T} \left[(1+r)^{-t}.c.s(i).n(i,t) \right],$$

where N is the number of bridges, T is the length of the planning period, r is the discount ratio, c is the unit area cost of rehabilitation, $s(i)$ is the deck area of bridge i, and $n(i,t) = 1$ if a rehabilitation cost is calculated or 0 otherwise. The binary values are defined as $0 =$ do nothing, and $1 =$ rehabilitation action. After this first attempt, good solutions have been found. Dogaki et al. (2000) developed a most complex analysis and presented a GA model for planning the maintenance of reinforced concrete decks, considering a probability-based transition matrix for the deteriorating model, linked with the crack density. The objective function relies on the minimization of the maintenance cost and on the maximization of the benefit derived from the maintenance. The constraints included traffic capacity, detours, the possibility of extending the bridge width, traffic constraints, and the importance of the bridge. The model includes the user cost, the LCC, and the environmental cost. Frangopol and Liu (2007) present the application of multiobjective optimization for safety and LCC for civil infrastructure. Neves et al. (2006a,b) also proposed the multiobjective optimization system for different bridge maintenance types.

6.6 Economic approaches for bridge network management: Repair or replace

The decision to repair or replace is an increasingly painful decision for bridge authorities who manage thousands of bridges. For this reason, this decision should be supported by appropriate theoretical instruments. To perform this analysis, a global cost function C was developed by BRIME (2001):

$$\mathrm{C} = \mathrm{CC} + \mathrm{C1} + \mathrm{CM} + \mathrm{CR} + \mathrm{CF} + \mathrm{CU} + \mathrm{C0} - \mathrm{VS},$$

where CC is the construction costs, CI is the inspection costs, CM is the maintenance costs, CR is the repair costs, CF is the failure costs, CU is the road user costs, CO is other costs, and VS is the salvage value of the bridge. The objective stands on the minimization of C, while keeping the lifetime reliability of the structure above a minimum allowable value. To implement an optimum lifetime strategy, the following problem must be solved:

$$\text{Minimize C subject to } \mathrm{P_{f,\,life}} \leq \mathrm{P*_{f,\,life,}}$$

where $\mathrm{P_{f,\ life}}$ represents the maximum acceptable lifetime failure probability (also called the *lifetime target failure probability*). The actions considered in this method are intended to restore the initial service level (design) of the bridge, without considering an improvement of its initial performances, dimensions, load carrying capacity, etc. Nevertheless, this method also can be also when all the considered alternatives lead to the same level of improvement in the bridge.

A method that consists of the proposal of alternatives for the repair or replacement of a deteriorated bridge or a bridge with issues regarding its correct functionality considers the following phases (BRIME, 2001):

- Identification of factors
- Evaluation of factors
- Comparison of alternatives and selection

If, in the year T_i (taking as a reference T_0 = the moment when the study is done), cost C_i is produced, this actualized cost in the instance T_0 will be

$$C_{i,T_0} = C_i \frac{1}{(1+r)^{T_i}}.$$

In this instance, r is the net discount rate of money, and C_i represents the costs of the T_i year.

In this way, all other costs during the analysis period will be discounted to T_0, with a total cost being

$$C = \sum_{i=1}^{n} C_i \frac{1}{(1+r)^{T_i - T0}}.$$

This cost will be used for the comparison of alternatives.

The following list contains the most relevant factors affecting the intervention alternatives considered:

- CM: maintenance costs
- CI: inspection costs
- CR: repair costs, which include the following:
- $\mathrm{CR_A}$: structural assessment costs
- $\mathrm{CR_R}$: structural repair costs
- CU: road user costs, which include the following:
- CUD: traffic delay costs
- CUR: traffic reroute costs
- CURT: time costs
- CURO: vehicle operating costs
- CURA: accident costs

- CF: failure costs
- VS: salvage value
- CO: other costs

The following warnings should be considered:

- Some of these factors are affected by subjective considerations.
- A rough estimate can be calculated for some costs.
- Social, financial, and economic factors can both positively and negatively influence the final cost attribution.

Each cost is considered and detailed as follows:

- *Inspection cost:* These costs can be estimated considering direct costs (e.g., personnel hours and equipment) and a calendar of inspections.
- *Maintenance costs:* These can be estimated as a percentage of the construction cost, or as a percentage of previous work performed on the bridge during the exercise; annual rates of 1%–2% are expected.
- *Repair costs:* This is a summation of the works to be delivered during repair operations (CR_R) and the assessment/design procedure performed (CR_A). It is easy to demonstrate that, if an accurate assessment is performed, CR_R is reduced by an appropriate incremental increase of CR_A.
- *Failure costs:* Bridge replacement costs; loss of lives, cars; and equipment; and architectural, cultural, and historical costs should be accounted for. The failure costs should be calculated for every bridge, as a probability of failure linearly increases during the timeline of the structure; this consideration should be done for every bridge and maintained by the owner as an insurance cost.
- *Road user costs:* A summation of C_{UD}, the costs due to delayed traffic, and C_{UR}, the costs due to traffic detours; both terms can analytically calculated by adopting various mathematical schemes.
- *Salvage value:* This is the value of the structure at the end of the analysis period; this is not always null at the end of a bridge's service life.
- *Other costs:* Additional costs could arise during the lifetime of a bridge; they should be included in this category.

A repair index (RI) is defined as a value indicating how the proposed repair alternative costs compare with the no-action option, or with respect to any other alternative used as a reference. The smaller the coefficient for a particular option, the better investment that option represents (considering a determinate serviceability level). For each option, the RI may be quantified by

$$RI = \frac{(C_I + C_M + C_R + C_F + C_U + C_O - V_S)_{\mathrm{Re}pair\_or\_replacement}}{(C_I + C_M + C_F + C_U + C_O - V_S)_{No\_action\_or\_rerference\_alternative}}.$$

7. Case study

7.1 The Macdonald Bridge, Halifax, NS

A pertinent project to mention is the ongoing large-scale repair yard for the redecking and retrofitting of the Macdonald Bridge in Halifax, NS (Figure 31.3). On April 2,

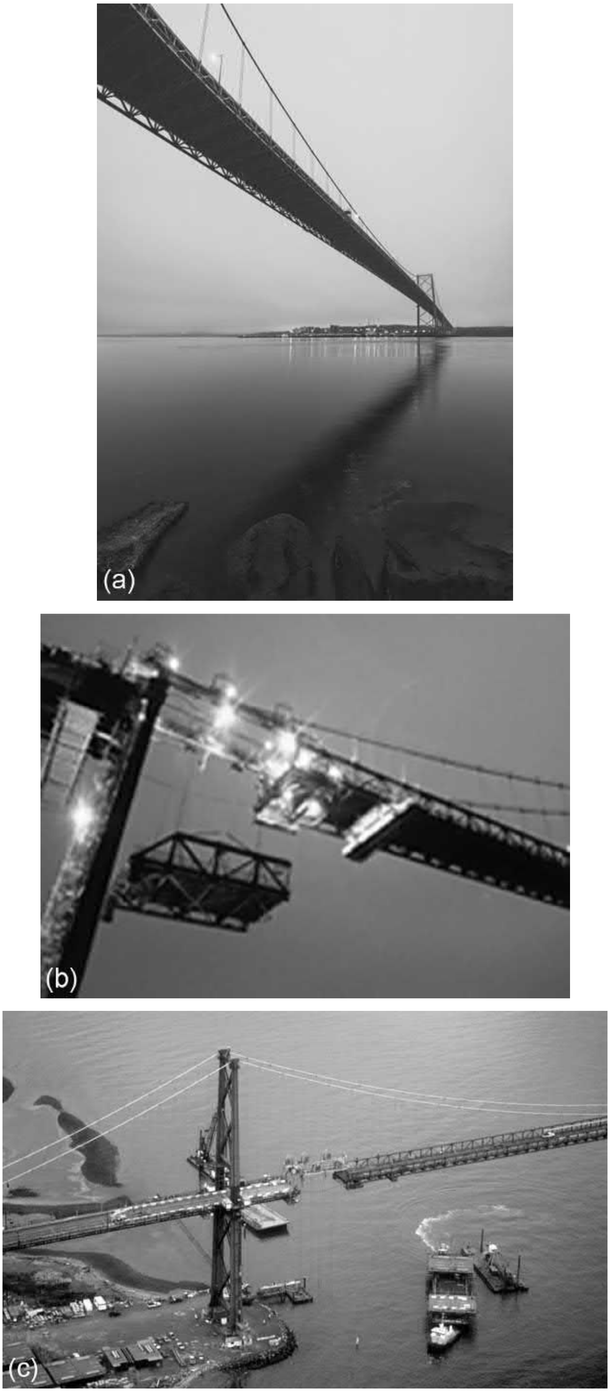

Figure 31.3 The Macdonald Bridge in Halifax: (a) overview; (b, c) redecking works, lifting the deck from the river barges;

(Continued)

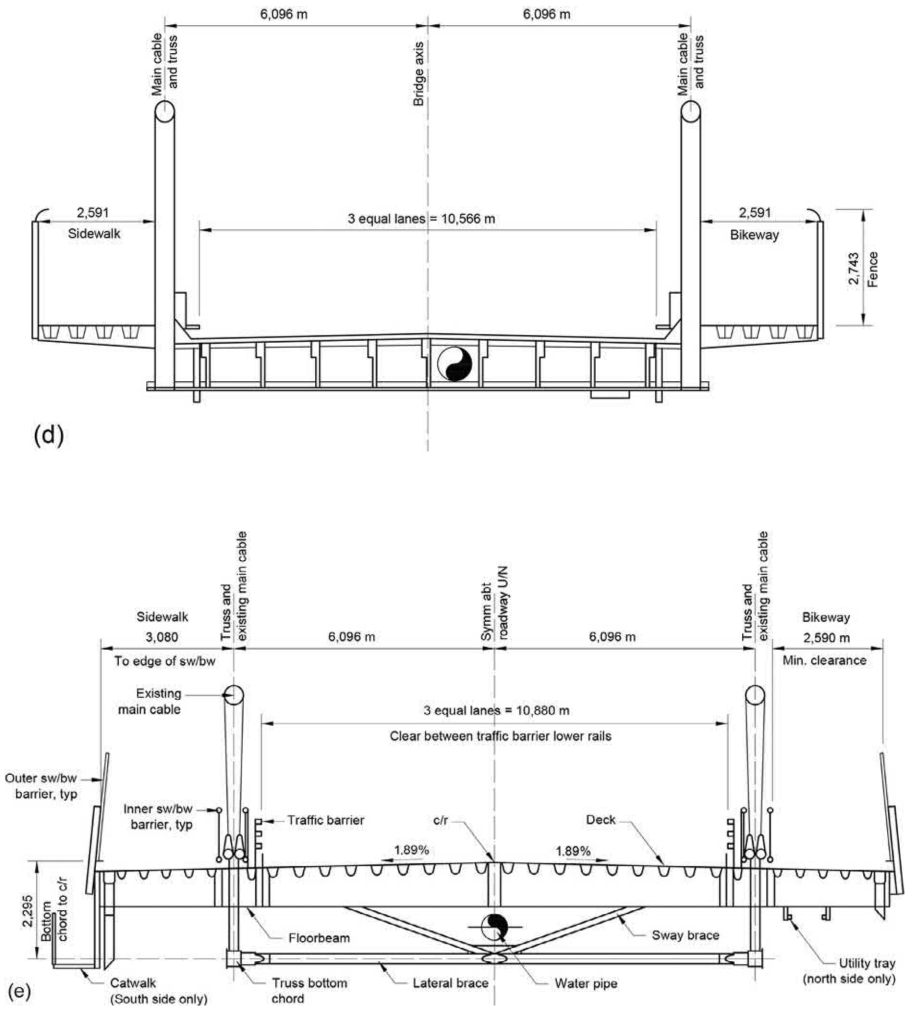

Figure 31.3, cont'd (d) existing deck scheme (in m); (e) new deck scheme (in m).

1955, the Angus L. Macdonald Bridge opened, uniting the communities of Halifax and Dartmouth for the first time. The Macdonald Bridge was converted from a two-lane to a three-lane structure with a pedestrian walkway and bicycle lane in 1999. There are approximately 48,000 crossings on the Macdonald Bridge on an average workday. The Macdonald Bridge has a reversible center lane. In the morning, there are two lanes to Halifax. At noon, it switches and there are two lanes to Dartmouth and one to Halifax (HHB, 2015). The existing deck system is deteriorating in three ways: (i) water penetrating the concrete-filled, welded steel grid has caused corrosion between the bottom of the grid and the tops of the supporting stringers, resulting in the deck becoming separated from the stringers; (ii) the continual wearing of the thin asphalt running surface in the traffic wheel paths exposes the upper steel surface of the T-grid and reduces the skid resistance; and (iii) the deck stiffening truss, a through truss, is composed of riveted, built-up steel members with large exposed areas that require labor-intensive maintenance painting (Kirkwood et al., 2014). For these reasons, in addition to the new requirements for naval traffic (the deck will be raised by 2.9 m at midspan to increase shipping clearance), a global restoration of the bridge has been designed. The principal requirement of the bridge authority was to keep the bridge open during the day and carry out the replacement of the deck at night in order to avoid traffic delays. To achieve this, deck segments will be supported from above by a movable erection gantry so they can be detached from the existing deck system by cutting the top and bottom chords and diagonals, and then they will be lowered onto barges below by strand jacks. The new deck will be orthotropic with a 14 mm thick deck plate in the carriageway with 300 mm wide longitudinal trough stiffeners at 600 mm centers and a 10 mm thick deck for the footway and cycle track. The new top and bottom chords are designed as closed sections and are tucked under the deck plate to protect them from rain and deicing salt. The deck plate then forms the top plate of the top chord, which is an efficient structural arrangement (Kirkwood et al., 2014). Other minor works include the installation of a dehumidification system for cables.

7.2 The Luiz I Bridge, Porto, PT

The Luiz I Bridge is a metallic arch bridge over the Douro River (Figure 31.4). The bridge was strengthened for the passage of metro trains on the upper deck. It is monitored continuously for the need for repair work. The main objectives of upgrading the Luiz I Bridge for metro traffic were (i) to replace the roadway upper deck by a new steel deck for the new metro line and strengthen the main truss girders of the deck; and (ii) strengthen the arch, hangers (suspending the lower deck), and main truss piers (Lopes et al., 2008). The main purpose for the railroad addition was to replace the existing deck with a lighter one. The new deck's structural system, widened from 8.2 m to 9.8 m, was made of a new steel grid in S355K2J3 and composed of four IPE400 stringers (each 4 m long), which were supported by IPE500 cross beams. The stringers directly support wooden sleepers; welded steel sections cantilevered from the deck made up the sidewalks. In order to reduce fatigue in the existing structural elements and avoid direct traffic loading, the wooden sleepers lie only over new steel stringers (Lopes et al., 2008). The constituent material was wrought iron (E = 193 kN/mmq; v = 0.25; fy = 160 MPa; unit weight = 84 kN/mc). Loosened rivets in the existing structure were found, and for this reason, new rivets were adopted to replace the existing ones; bolts were never adopted to replace rivets. In the new structure, bolted connections were adopted, and some of them were prestressed. A comprehensive fatigue verification was performed: a C = 71 for riveted connection was used according to category D of AASHTO, in accordance with UIC International Union of Railways recommendations for the 19th-century metal-riveted structures. For new structural elements, such as crossbeams or stringers, a category C = 160 was used in bending and a C = 100 for shear stress; for bolted connections, C = 100 (shear) and C = 36 (tension) were used. The procedure adopted in order to verify the fatigue strength of the modified structure was the EC3 equivalent damage verification.

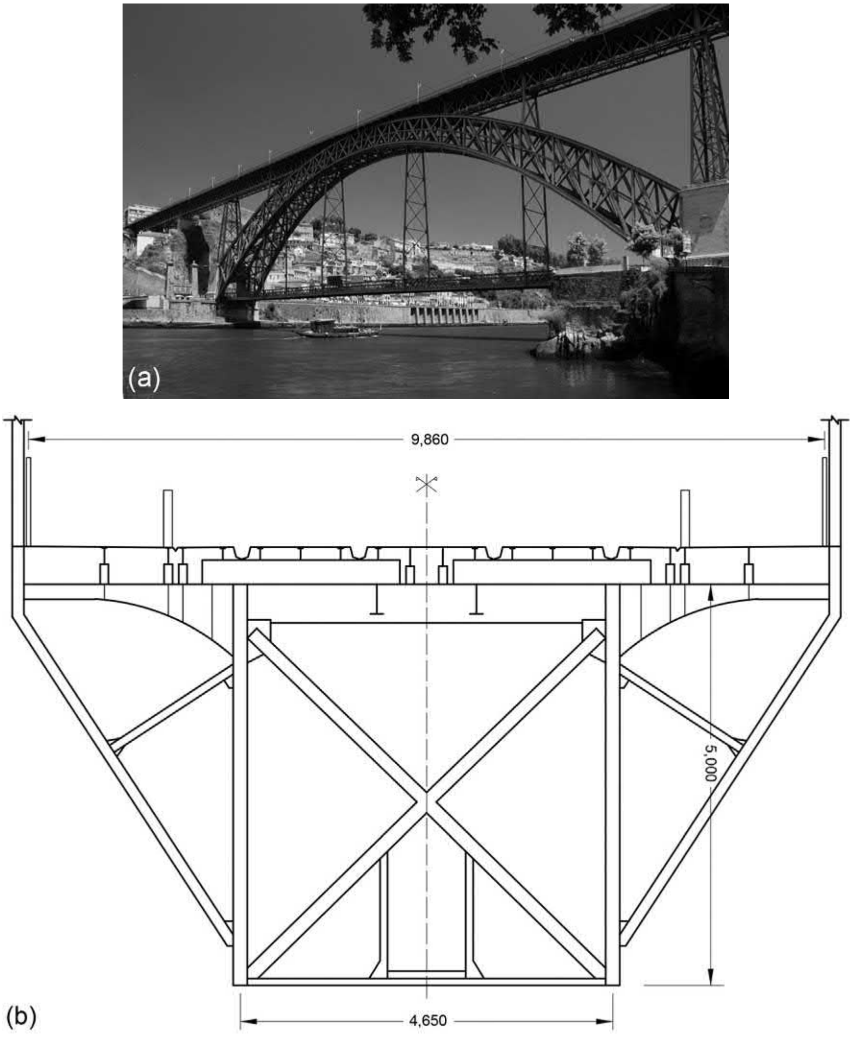

Figure 31.4 The Luiz I Bridge: (a) overview; (b) new deck cross section (in m);

(Continued)

Concerning the past damage accumulated, a consumption of 11% of the structure's service life was calculated via the Palmgren-Miner procedure (Lopes et al., 2008).

7.3 The Broadway Bridge, Portland, OR

The Broadway Bridge (Figure 31.5) carries an average daily volume of 30,000 vehicles in four lanes of traffic. An FRP deck application can be observed in this bascule bridge; as reported by Sams (2005), the project dealt with the requirement of a new

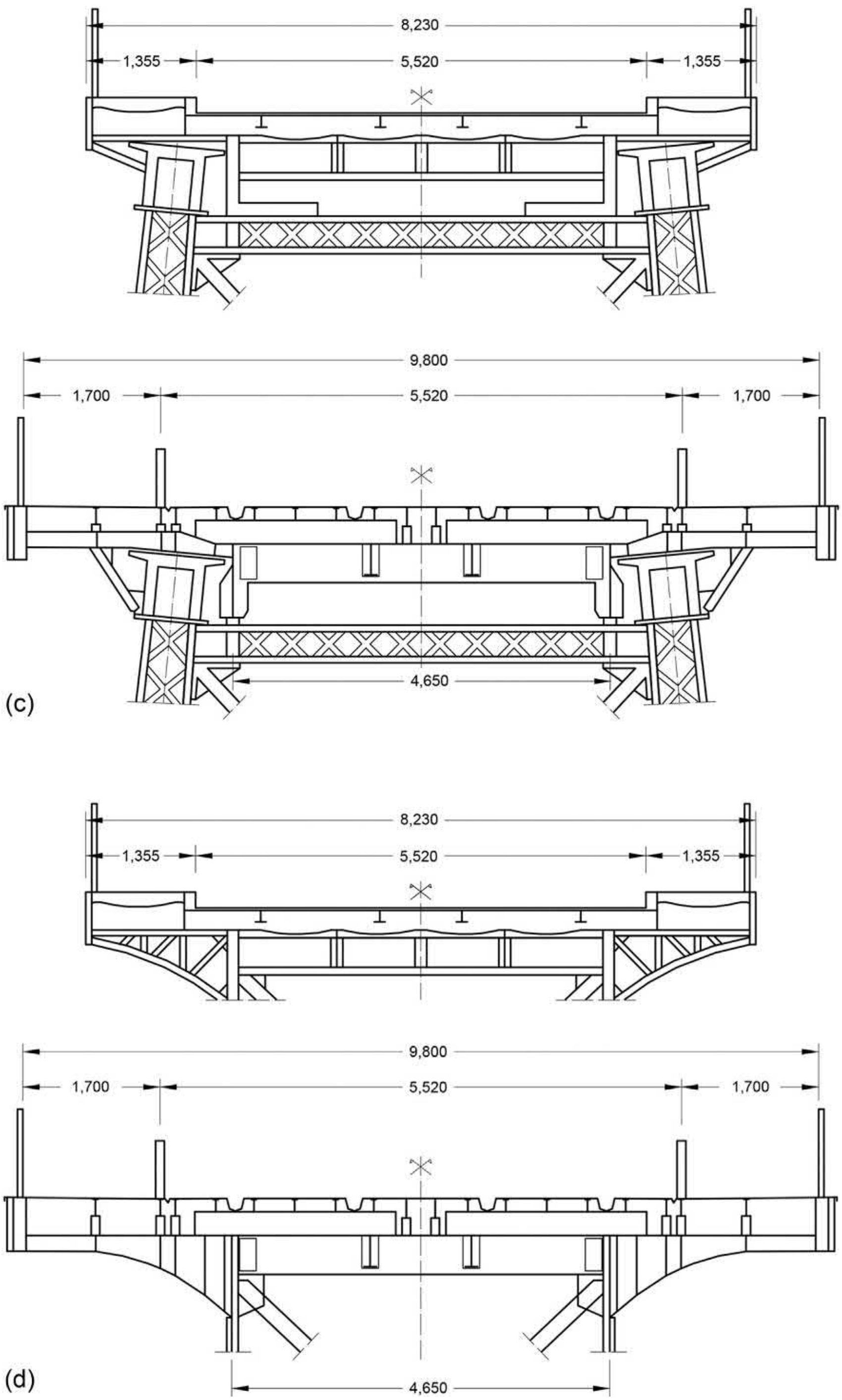

Figure 31.4, cont'd (c) upper deck on the arch before and after rehabilitation; (d) upper deck cross section before and after rehabilitation.

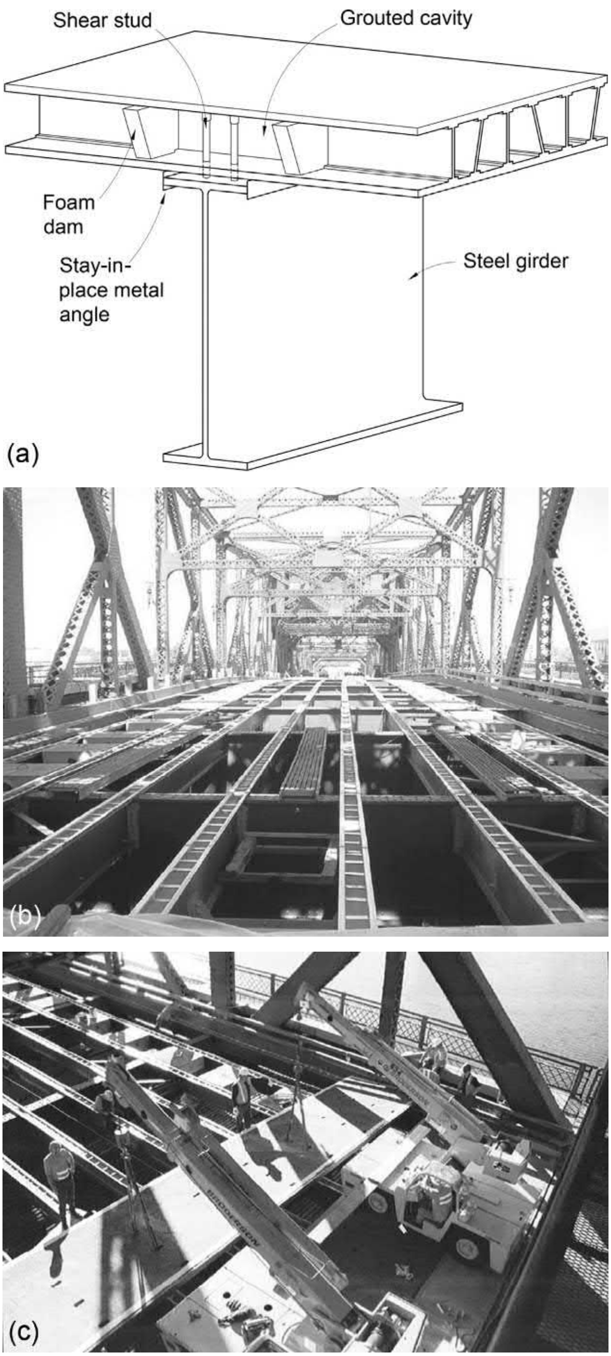

Figure 31.5 The Broadway Bridge interventions: (a) new deck scheme; (b) girders and crossbeams without the deck structure; (c) redecking operations.

deck that matched the weight of the bridge's existing steel grating, offering improved skid resistance that could be installed quickly. The deck-to-beam connections are similar to conventional shear studs and grout-filled cavities to connect the new deck to the bridge's longitudinal beams. Grout was poured through the deck into a cavity formed by stay-in-place metal angles, providing a variable haunch along each longitudinal beam. Because of this connection's inherent ability to transfer shear, the Broadway Bridge's beam–deck system likely exhibits some level of composite behavior. However, the beams were sized to carry loads without consideration of the composite action. The prefabricated FRP panels arrived at the yard in $2.4\,\text{m} \times 14\,\text{m}$ modules, ready for installation on the beam's variable haunches. The length of each panel matched the width of the bridge deck because the FRP panels span perpendicular to the bridge's longitudinal beams. Shop workers had predrilled all holes to accommodate the connections to the bridge's longitudinal beams. At the heel of each bascule leaf, the FRP deck connected to a concrete transition deck, which was designed to accommodate dynamic vehicular forces. At the bridge's center open joint, the deck interfaced with heavy steel angles to accommodate dynamic forces. At the side edges, workers bonded an FRP curb to the deck along its full length. By their own weight, the pultruded panels matched the parabolic crown (6 cm) on the bridge's approach spans, so cambering was analyzed in the shop, and panels arrived at the job site in their curved state. Another key geometric feature of the existing bridge was its vertical alignment. In the portions of the bridge where the longitudinal stringers were vertically curved, each panel was placed on the stringers and conformed to the existing profile with a chord effect. Each panel was straight, whereas the field joints accommodated incremental, extremely slight rotations before adhesive curing. Both accommodations facilitated the use of FRP on the unique structure and are expected to have minimal negative effects on the integrity of the deck system. At the time of construction, no AASHTO design criteria were established for FRP decks, so the supplier took full responsibility for the design and performance of this system.

8. Research on bridge assessment, retrofit, and management

The research and development relating to decay of materials and on-site tests, in particular, deal with advances in the concrete field relating to the following: the decay of fracture parameters of concrete under sulfate environments (Xu et al., 2013); a factorial design study to determine the significant parameters of fresh concrete lateral pressure and initial rate of pressure decay (Santilli et al., 2011); studies on concrete degradation during molten core–concrete interactions (Yu et al., 2006); studies on the stability of a concrete bay bridge pier under freeze–thaw action (Jia et al., 2010); mechanisms of long-term decay of tension stiffening (Beeby and Scott, 2006); numerical modeling for predicting service life of reinforced concrete structures exposed to chloride environments (Gang et al., 2010); advanced studies on the improved application technique of the adaptive probabilistic neural network for predicting concrete strength (Jong et al., 2009); the characterization of flaws embedded in externally bonded CFRP on concrete beams by infrared thermography (Lai et al., 2009); a study on concrete degradation during molten core–concrete interactions (Maruyama et al., 2006); and the load of reinforced concrete columns by seawater corrosion (Lin, 2012). Research and development for assessment procedures include simplified site-specific traffic load models for bridge assessment (Getachew and Obrien, 2007); site-specific traffic load modeling for bridge assessment (O'Connor and Eichinger, 2007); rapid and global bridge assessment for the military and also for urgent situations (Ray and Butler, 2004); assessment procedures concerning the probability-based bridge (O'Connor and Enevoldsen, 2007); and assessment procedures concerning the reliability-based bridge assessment using risk-ranking decision analysis (Stewart et al., 2001). However, it is well established that bridge structural reliability assessment should be based on health monitoring data in order to get precise information on existing structures (Jiao and Sun, 2011). Similar studies that could be useful for the same scope relate to bridge system performance assessment from structural health monitoring (Ming et al., 2009). There are valuable resources that cover other assessment procedures regarding specific issues, such as the probability analysis and risk assessment of vessel–bridge collision reported in Yin et al. (2011). The argument to pursue research and development for repairing and strengthening operations has been widely cited in recent studies. In the following, we have reported some of the most relevant recent studies, divided by the specific constituent material. Aidoo et al. (2006) discuss a full-scale experimental investigation for the repair of a reinforced concrete interstate bridge using CFRP materials; Tedesco et al. (1999) describes a finite element method analysis of a concrete bridge repaired with fiber-reinforced plastic laminates; Hyman (2005) explores inspection, repair, and rehabilitation of concrete structures due to corrosion; and Alampalli (2005) investigates the effectiveness of FRP materials with alternative concrete removal strategies for reinforced concrete bridge column wrapping. Regarding steel structures; Hollaway et al. (2006) report advances in the adhesive joining of carbon fiber–polymer composites to steel members for repair and rehabilitation of bridge structures; Chang et al. (2008) discuss the weldability studies of the replacement repair welded joints of a damaged steel bridge; Clubley et al. (2006) deal with heat-strengthening repairs to a steel road bridges; and Pipinato (2011) explores the specific topic of railway bridge assessment. Advances in BMSs are commonly investigated directly by management authorities.

References

Aidoo, J., Harries, K.A., Petrou, M.F., 2006. Full-scale experimental investigation of repair of reinforced concrete interstate bridge using CFRP materials. J. Bridg. Eng. 11 (3), 350–358.

Alampalli, S., 2005. Effectiveness of FRP materials with alternative concrete removal strategies for reinforced concrete bridge column wrapping. Int. J. Mater. Prod. Technol. 23 (3–4), 338–347.

ANAS, 1997. Material and Techniques of Intervention for the Restoration of the Concretes of the Bridges and Viaducts (in Italian). Gangemi Ed, Rome.

Beeby, A.W., Scott, R.H., 2006. Mechanisms of long-term decay of tension stiffening. Mag. Concr. Res. 58 (5), 255–266.

Bentur, A., Diamond, S., Berke, N.S., 1997. Steel Corrosion in Concrete. E & FN Spon, London.

Branco, F.A., Brito, J., 1996. Bridge management from design to maintenance, Recent advances in bridge engineering. In: Proceedings of the US-Europe Workshop on Bridge Engineering, July 15–17, 1996, Barcelona, Spain.

Bridge Management in Europe (BRIME), 2001. Final Report D14, IV Framework Program. Brussels.

Brinckerhoff, P., 1993. In: Silano, L.G. (Ed.), Bridge Inspection and Rehabilitation. John Wiley & Sons, New York.

Broomfield, J.P., 1997. Corrosion of Steel in Concrete. E & FN Spon.

BS EN ISO 8501-1, 2007. Preparation of steel substrates before application of paints and related products. Visual assessment of surface cleanliness. Rust grades and preparation grades of uncoated steel substrates and of steel substrates after overall removal of previous coatings.

Building Research Establishment (BRE), 2001. Modeling Degradation Processes Affecting Concrete. BRE 434. ISBN 1 86081 5316. Construction Research Communications Ltd, Watford, UK.

Cadei, J.M.C., et al., 2004. Strengthening Metallic Structures Using Externally Bonded Fiber-Reinforced Polymers (C595). CIRIA Design Guide. CIRIA, London.

Chang, K.H., Park, H.C., Lee, C.H., Jang, G.C., Lee, S.H., Choi, E.H., Shin, Y.E., Kim, J.M., Lee, J.H., 2008. Weldability studies on the replacement repair welded joints of a damaged steel bridge. Mater. Sci. Forum 580–582, 655–658.

Clubley, S.K., Winter, S.N., Turner, K.W., 2006. Heat-straightening repairs to a steel road bridge. Proc. Inst. Civil Eng. Bridge Eng. 159 (1), 35–42.

Concrete Society, 2000. Diagnosis of Deterioration in Concrete Structures: Identification of Defects, Evaluation and Development of Remedial Action. Technical Report No. 54. ISBN 0 94669 1818, The Concrete Society, Berkshire, UK.

COST345, 2004. Procedures Required for the Assessment of Highway Infrastructures – Final Report. European Research Project under the Framework of European Cooperation in the Field of Scientific and Technical Research, EU Commission-Directorate General Transport and Energy, Bruxelles. 182 pp.

Czepiel, E., 1995. Bridge Management Systems Literature Review and Search. Technical Report No. 11. Northwestern University BIRL Industrial Research Laboratory, Evanston, IL.

Dogaki, M., et al., 2000. Optimal maintenance planning of reinforced concrete decks on highway network. In: Conference Proceedings. US169 Japan Workshop on Life-Cycle Cost Analysis and Design of Civil Infrastructure Systems. ASCE, Honolulu.

DuraCrete, 1998. Modeling of Degradation. BRITE –EURAM-Project BE95-1347/R4-5.

DuraCrete, 2000a. Statistical Quantification of the Variables in the Limit State Functions. BRITE – EURAM-Project BE95-1347/R9.

DuraCrete, 2000b. Probabilistic Calculations. BRITE–EURAM-Project BE95-1347/R14B.

EN 10025-5, 2004. Structural steels with improved atmospheric corrosion resistance.

EN206-1/2000, 2005. EN 206-1, Concrete: Specification, Performance, Production, and Conformity. CEN—European Committee for Standardization.

Federal Highway Administration (FHWA), 2015. Bridge Ratings. Federal Highway Administration, Washington.

FIB (Fédération internationale du béton), 1999. Structural Concrete, Textbook on Behavior, Design and Performance, Updated Knowledge of the CEB/FIP Model Code 1990. Vol. 3 Sprint-Druck, Stuttgart, DE.

FIB (Fédération internationale du béton), 2010. FIB Model Code for Concrete Structures 2010. Edited by Ernst & Sohn–Wiley, Berlin. ISBN: 978-3-433-03061-5, 434 pp.

Fisher, J.W., 1984. Fatigue and Fracture in Steel Bridges: Case Studies. John Wiley & Sons, New York, NY. 336 pp.

Fisher, J.W., Yen, B.T., Frank, K.H., 1979. Minimizing Fatigue and Fracture in Steel Bridges. American Society of Mechanical Engineers (ASME), pp. 155–161.

Frangopol, D.M., Liu, M., 2007. Multiobjective optimization for risk-based maintenance and life-cycle cost of civil infrastructure systems. In: System Modeling and Optimization, Volume 199 of the Series IFIP International Federation for Information Processing, Proceedings of the 22nd IFIP TC7 Conference Held from July 18–22, 2005, in Turin, Italy. Springer, New York, pp. 123–137.

Gang, L., Yinghua, L., Zhihai, X., 2010. Numerical modeling for predicting service life of reinforced concrete structures exposed to chloride environments. Cement Concr. Comp. 32 (8), 571–579.

Getachew, A., Obrien, E.J., 2007. Simplified site-specific traffic load models for bridge assessment. Struct. Infrastruct. Eng. 3 (4), 303–311.

Gralund, M.S., Puckett, J.A., 1996. System for bridge management in a rural environment. J. Comput. Civ. Eng. 10 (2), 97–105.

Helmerich, R., 2005. Alte Stähle und Stahlkonstruktionen–Materialuntersuchungen, Ermüdungsversuche an originalen Brückenträgern und Messungen von 1990 bis 2003. BAM. Forschungsbericht 271, Berlin, DE.

HHB, 2015. History of the Macdonald Bridge. HHB—Halifax Harbour Bridges Authority, Dartmouth.

Hollaway, L.C., Zhang, L., Photiou, N.K., Teng, G., Zhang, S.S., 2006. Advances in adhesive joining of carbon fibre/polymer composites to steel members for repair and rehabilitation of bridge structures. Adv. Struct. Eng. 9 (6), 791–804.

Hudson, R., Carmichael III, R., Hudson, S., Diaz, M., Moser, L., 1993. Microcomputer bridge management system. J. Transp. Eng. 119 (1), 59–76.

Hyman, A.E., 2005. Inspection, repair and rehabilitation of concrete structures due to corrosion. Int. J. Mat. Product Tech. 23 (3–4), 309–337. Inderscience Publishers.

Italian Infrastructure Ministry, 2020. Guideline for the Surveillance of Bridges - Linee guida per la classificazione e gestione del rischio, la valutazione della sicurezza ed il monitoraggio dei ponti esistenti, Ministero delle Infrastrutture e dei. Trasporti, Roma.

Italian Research Council, Italian Advisory Committee on Technical Recommendations for Construction, 2005. Guidelines for the Design and Construction of Externally Bonded FRP Systems for Strengthening Existing Structures. Preliminary Study. Metallic Structures (CNR–DT 202/2005). Italian Research Council, Rome.

Jia, C., Sheng-Zhen, J., Zhang, F., 2010. Study on the stability of concrete bay bridge pier under freeze-thaw action. Sichuan Daxue Xuebao (Gongcheng Kexue Ban). J. Sichuan Uni. (Eng. Sci. Ed.) 42 (3), 7–13.

Jiao, M., Sun, L., 2011. Bridge reliability assessment based on the PDF of long-term monitored extreme strains. In: Proc. SPIE. 7983. Nondestructive Characterization for Composite Materials, Aerospace Engineering, Civil Infrastructure, and Homeland Security 2011, April 18, 2011, p. 79830J.

Johnston, D.W., Zia, P., 1984. A Level of Service System for Bridge Evaluation, Transportation Research Record. No. 962. TRB, Washington, DC, pp. 1–8.

Jong, J.L., et al., 2009. An improved application technique of the adaptive probabilistic neural network for predicting concrete strength. Comput. Mater. Sci. 44 (3), 988–998.

Kirkwood, K., Radojevic, D., Buckland, P., 2014. A deck dilemma. Bridge Design Eng. November.

Kitada, T., et al., 2000. Bridge management system for elevated steel highways. Comput. Aided Civ. Infrastruct. Eng. 15 (2), 147–157.

Klaiber, F.W., et al., 1987. Methods of Strengthening Existing Highway Bridges. NCHRP 293. Transportation Research Board.

Kühn, B., Lukic, M., Nussbaumer, A., Günther, H.-P., Helmerich, R., Herion, S., Kolstein, M. H., Walbridge, S., Androic, B., Dijkstra, O., Bucak, O., 2008. In: Sedlacek, G., Bijlaard, F., Géradin, M., Pinto, A., Dimova, S. (Eds.), Assessment of existing steel structures: recommendations for estimation of remaining fatigue life– joint report prepared under the JRC-ECCS cooperation agreement for the evolution of Eurocode 3 Background Documents in Support to the Implementation, Harmonization and Further Development of the Eurocodes. Office for Official Publications of the European Communities 2007, Luxembourg. 89 pp., Scientific and Technical Research Series, ISSN 1018-5593, published by JRC-Joint Research Centre, Ispra.

Lai, W.L., et al., 2009. Characterization of flaws embedded in externally bonded CFRP on concrete beams by infrared thermography and shearograph. J. Nondes. Ev. 28 (1), 27–35.

Lédeczi, A., et al., 2011. Self-sustaining wireless acoustic emission sensor system for bridge monitoring. New developments in sensing technology for structural health monitoring. Lect. Notes Elec. Eng. 96, 15–39.

Li, H., Love, P.E., 1998. Site-level facilities layout using genetic algorithms. J. Comput. Civ. Eng. 12 (4), 227–231.

Liebenberg, A.C., 1992. Concrete Bridges: Design and Construction. Longman Group, UK Ltd., London.

Lin, Y., 2012. On the load of reinforced concrete column by seawater corrosion. Adv. Mater. Res. 368–373, 975–978, TTP Edition, Pfaffikon.

Liu C. Hammad A. (1997). Multiobjective optimization of bridge deck rehabilitation using a genetic algorithm. Microcomputers in civil engineering, n.12-1997, pp. 431–443. Blackwell publischers, Oxford, UK

Lopes, N., Ribeiro, D., Reis, A., 2008. Upgrading the Luiz I Bridge in Porto. In: Proceedings of the 7th International Conference on Steel Bridges, Guimaraes, Portugal.

Markow, M.J., 1995. Highway management systems: state of the art. J. Infrastruct. Syst. 1 (3), 186–191.

Maruyama, Y., et al., 2006. A study on concrete degradation during molten core/concrete interactions. Nuc. Eng. Des. 236 (19–21), 2237–2244.

Ming, L., Frangopol, D.M., Kim, S., 2009. Bridge system performance assessment from structural health monitoring: a case study. J. Struct. Eng. 135 (6), 733–742.

Mohamed, H., 1995. Development of Optimal Strategies for Bridge Management Systems. Ph. D. Thesis, Dept. of Civil and Environmental Engineering, Carleton University, Ottawa, Canada.

Moy, S.S.J. (Ed.), 2001. FRP composites: life extension and strengthening of metallic structures. In: ICE Design and Practice Guide. Thomas Telford, London.

Moy, S.S.J., Bloodworth, A.G., 2007. Strengthening a steel bridge with CFRP composites. Proceedings of the Institution of Civil Engineers (ICE). Struct. Build. 160 (SB2), 81–93.

Moy, S.S.J., Lillistone, D., 2006. Strengthening cast iron using FRP composites. Proceedings of the Institution of Civil Engineers (ICE). Struct. Build. 159 (6), 309–318.

Mullheron, M., 2000. Durability of Bridges and Structures. Module in the MSc in Bridge Engineering. Internal Publication, University of Surrey, Surrey, UK.

Nair, A., Cai, C.S., 2010. Acoustic emission monitoring of bridges: review and case studies. Eng. Struct. 32, 1704–1714.
Neves, L.A.C., Frangopol, D.M., Cruz, P.J.S., 2006a. Probabilistic lifetime-oriented multi-objective optimization of bridge maintenance: single maintenance type. J. Struct. Eng. 132 (6), 991–1005.
Neves, L.A.C., Frangopol, D.M., Petcherdchoo, A., 2006b. Probabilistic lifetime-oriented multi-objective optimization of bridge maintenance: combination of maintenance types. J. Struct. Eng. 132 (11), 1821–1834.
O'Connor, A., Eichinger, E.M., 2007. Site-specific traffic load modelling for bridge assessment. Proc. Inst. Civ. Eng. Bridge Eng. 160 (4), 185–194.
O'Connor, A., Enevoldsen, I., 2007. Probability-based bridge assessment. Proc. Inst. Civ. Eng. Bridge Eng. 160 (3), 129–137.
Pipinato, A., 2008a. New Approaches for the Management, Maintenance and Control of Bridge Networks (in Italian). Strade e Autostrade. EDI-CEM ed, Milan, Italy.
Pipinato, A., 2008b. High-Cycle Fatigue Behavior of Historical Metal Riveted Railway Bridges. PhD thesis, University of Padova, Italy.
Pipinato, A., 2011. Assessment of existing bridges: safety and security issues [Problemi di sicurezza nelle valutazioni strutturali di ponti esistenti]. Ingegneria Ferroviaria 66 (4), 355–371.
Pipinato, A., 2014. Assessment and rehabilitation of steel railway bridges using fiber-reinforced polymer (FRP) composites. In: Karbhari, V.M. (Ed.), Rehabilitation of Metallic Civil Infrastructure Using Fiber-Reinforced Polymer (FRP) Composites. Elsevier, New York, pp. 373–405. ISBN: 978-0-85709-653-1.
Priestley, M.J.N., Seible, F., Calvi, G.M., 1996. Seismic Design and Retrofit of Bridges. John Wiley & Sons, New York. ISBN: 978-0-471-57998-4, 704 pp.
ProPonti, 2020. ProPonti Software: BMS and Monitoring System. https://www.proponti.it/.
Radomski, W., 2002. Bridge Rehabilitation. Imperial College Press, London.
Ray, J., Butler, C.D., 2004. Rapid and global bridge assessment for the military. J. Bridg. Eng. 9 (6), 550–557.
Robert, W., et al., 2003. The Pontis bridge management system: state-of-the-practice in implementation and development. In: Proc., 9th Int. Bridge Management Conf. Transportation Research Board, Washington, DC, pp. 49–60.
SAMARIS, 2005. Sustainable and Advanced Materials for Road Infrastructure. Final report. VI Framework Program. European Commission's Directorate General for Mobility and Transport, Brussels.
Sams, M., 2005. Bridge deck application of fiber-reinforced polymer. Transp. Res. Rec. J. Transport. Res. Board, 175–178. CD 11-S. Transportation Research Board of the National Academies, Washington, DC.
Santilli, A., et al., 2011. A factorial design study to determine the significant parameters of fresh concrete lateral pressure and initial rate of pressure decay. Construct. Build. Mat. 25 (4), 1946–1955.
Schnerch, D., Dawood, M., Rizkalla, S., 2007. Proposed design guidelines for strengthening of steel bridges with FRP materials. Construct. Build. Mat. 21, 1001–1010.
Silano, L.G., 1993. Bridge Inspection and Rehabilitation—A Practical Guide. John Wiley & Sons, Inc, New York.
Soderqvist, M.K., Veijola, M., 2000. Finnish project level bridge management system. Transp. Res. Circular 498 (TRB), F-5/1–F-5/7.
Stanish, K.D., Hooton, R.D., Thomas, M.D.A., 2000. Prediction of Chloride Penetration in Concrete. Testing the Chloride Penetration Resistance of Concrete: A Literature Review.

FHWA Contract DTFH61-97-R-00022 by Department of Civil Engineering University of Toronto, Toronto, Ontario, Canada.

Stewart, M.G., Rosowsky, D.V., Valc, D.V., 2001. Reliability-based bridge assessment using risk-ranking decision analysis. Struct. Saf. 23 (4), 397–405.

Sukumaran, B., 1998. A Review of Inspection Maintenance and Assessment of Reinforced Concrete and Prestressed Concrete Bridges and a Case Study. MSc dissertation, University of Surrey, Surrey, UK.

Sunley, W., 1995. Pontis: A Bridge Inspection. Illinois Department of Transportation, Illinois Municipal Rev, pp. 13–15.

Sustainable Bridges, 2006. Guideline for load and resistance assessment of existing European railway bridges – advices on the use of advanced methods. In: European Research Project Under the EU 6th Framework Program.

Tedesco, J.W., Stallings, J.M., El-Mihilmy, M., 1999. Finite element method analysis of a concrete bridge repaired with fiber reinforced plastic laminates. Comput. Struct. 72 (1–3), 379–407.

Thoft-Christensen, P., 1995. Advanced bridge management systems. Struct. Eng. Rev. 7 (3), 151–163.

Thompson, P., et al., 2003. Implementation of Ontario bridge management system. In: Ninth International Bridge Management Conference, Orlando, FL, pp. 112–127.

White, K.R., Minor, J., Derucher, K.N., 1992. Bridge Maintenance, Inspection and Evaluation. Marcel Dekker, Inc., New York.

Xu, H., Zhao, Y., Cui, L., Xu, B., 2013. Sulphate attack resistance of high-performance concrete under compressive loading. J. Zhejiang Univ.-Sci. A (Appl. Phys. Eng.) 14 (7), 459–468.

Yin, Z.H., Li, Y.F., Li, Y., 2011. Probability analysis and risk assessment about vessel- bridge collision of Xihoumen Bridge. Adv. Mater. Res. 179–180, 464–469.

Yu, M., et al., 2006. A study on concrete degradation during molten core/concrete interactions. In: National Nuclear Center of the Republic of Kazakhstan, Konechnaya, Pavlodar, Kazakhstan. Nuclear Engineering and Design. 236. Elsevier, New York, pp. 2237–2244.

Zhao, X.L., Zheng, L., 2007. State-of-the-art review on FRP strengthened steel structures. Eng. Struct. 29, 1808–1923.

This page intentionally left blank

Bridge monitoring

32

P.J. Vardanega[a], *G.T. Webb*[b], *P.R.A. Fidler*[c], *F. Huseynov*[c], *K.K.G.K.D. Kariyawasam*[c], and *C.R. Middleton*[c]
[a]University of Bristol, Bristol, UK, [b]WSP, London, UK, [c]University of Cambridge, Cambridge, UK

1. Introduction

In his classic book on geotechnical instrumentation, Dunnicliff (1988) wrote:

> *"Every instrument on a project should be selected and placed to assist with answering a specific question: if there is no question, there should be no instrumentation."*

Structural Health Monitoring (SHM) is an important topic for the bridge engineering community. Rapid technological developments have made it easier to install extensive bridge monitoring systems. It is hoped that by obtaining quantitative data, it will be possible to develop smart structures, with monitoring systems that are able to supplement the subjective and variable visual inspection practices that are currently employed as the primary means of evaluating bridge conditions (Moore et al., 2001; Graybeal et al., 2002; Middleton, 2004; Lea, 2005; Bennetts, 2019; Sony et al., 2019; Bennetts et al., 2020).

There are many studies describing efforts to monitor individual bridges (e.g., Brownjohn et al., 1999; Chang and Im, 2000; Wong, 2004; Lynch et al., 2006; Staquet et al., 2007; Hoult et al., 2010; Hussain et al., 2010; Koo et al., 2013; Middleton et al., 2016; Moreu et al., 2017; Selvakumaran et al., 2018; Cusson and Ozkan, 2019; Kariyawasam et al., 2019a). Webb (2014) observed that often monitoring systems do not deliver the necessary insights desired by bridge owners and managers; a clear statement upfront of what value the system may deliver is often lacking. Middleton et al. (2014) discuss the current and future potential of SHM for bridges concluding (in part) that many SHM systems have not realized the promise of supplying useful information to the asset owner. Many of the reported SHM projects are simply records of the capabilities of new sensors and sensor deployments. Some specific cases were found to demonstrate value e.g., Hammersmith Flyover (Webb et al., 2014), where a specific issue of concern was investigated using remote SHM techniques.

The primary aim of SHM systems is commonly perceived as a desire to detect damage or deterioration. Relevant information may then be used to optimize maintenance interventions in a cost-effective manner. This is an objective that would provide value to bridge operators. Yet this alone is not sufficient to capture the entire spectrum of potential uses of SHM. SHM should provide data that can be transformed into useful information to enhance decision making by bridge engineers and asset managers.

Innovative Bridge Design Handbook. https://doi.org/10.1016/B978-0-12-823550-8.00023-8

Therefore, it is necessary to consider what is meant by value and to identify who can benefit from the information derived from SHM data.

Before implementing an SHM system the following guiding questions should be asked:

(a) What are the overall objectives of the monitoring activities?
(b) What information is needed from a monitoring system to fulfill these objectives?
(c) What raw data are required to provide this information?
(d) What are the expected values of the readings that will be obtained from measurements, and how are these affected by various uncertainties?
(e) What accuracy (and frequency of readings) is needed from the measurements to allow for decisions to be taken based on the measurements?
(f) What technology will be able to take the necessary measurements?
(g) How and at what cost will the information be recorded, interpreted, disseminated, and stored, and what communications strategy will be used to transfer data to the end user?
(h) What input is required from all the relevant stakeholders so that all expectations can be understood and managed?
(i) Who will bear the capital and ongoing operational costs associated with the system, and are these costs affordable?
(j) How can the value/benefit of the information obtained be quantified?

It is important to note that the choice of monitoring technology itself is a consideration that happens much later in the specification process than the definition of the overall objectives of the monitoring activities.

2. Objectives of SHM deployments

SHM can be used to fulfill many objectives, and it is extremely important for these objectives to be clearly defined at the outset, *before* any monitoring technologies are specified. Without a clear reason for *why* monitoring is needed, it is highly unlikely that the expected value will be obtained. In general, there is usually a desire to ensure that bridges are safe and perform as required, and for this to be achieved at a reasonable cost. However, to define specific objectives for a system within this overarching goal, there are many considerations, some of which will be introduced in this section.

Firstly, there are several potential beneficiaries of SHM who each can derive different benefits from bridge monitoring. A monitoring system that is targeted to provide information to one individual stakeholder may provide limited or no value to other stakeholders. It is therefore vital that the target stakeholders and their objectives are identified. It is also noted that the end users of the information obtained by a monitoring program may not be the ones who are responsible for paying for the system. Andersen and Vesterinen (2006) identified seven key stakeholders of SHM projects—"Authorities," "Owners," "Users," "Researchers," "Designers," "Contractors," and "Operators"—showing that each stakeholder has varying objectives to be met by SHM systems.

The objectives of a monitoring system can also vary depending on the project phase. Before a construction project commences, SHM can be used to provide information to support design work. For example, field tests can be used to determine ground conditions so that these can be incorporated into the design. It may also be necessary to undertake measurements to support the assessment of the condition of existing structures to determine whether they can continue to remain in service. During the construction phase, there are several different areas where monitoring systems have the potential to add value. This may include the monitoring of nearby structures to provide assurance to their owners that they are not being adversely affected by construction processes. In some cases, it may also be possible to use a monitoring system to improve the efficiency of the construction process by allowing adjustments to be made as the project progresses. Additionally, it may be beneficial in some cases to collect data to allow key design assumptions to be verified, reducing the risk of unforeseen phenomena impacting a structure's functionality. There are many different aims that can be realized during the operational life of a structure. These include systems designed to ensure safe and efficient operation of the structure, and to assist those investigating the behavior of structures and materials over long periods of time to support future design developments.

It is also necessary to consider whether there is a desire for information to support decisions relating to individual structures or to inform wider strategic decisions associated with a portfolio of structures. At the individual structure level, there is likely to be a need for specific, reliable, and precise information. Measurement errors or uncertainties could potentially have a large influence on the decisions taken. Conversely, if the objective of a monitoring project is to inform strategic decisions across a portfolio, then the level of detail required for each structure may be much lower. Information from the monitoring system is also likely to be combined with that from multiple information sources, thus reducing the impact that erroneous or anomalous readings may have.

3. Interpreting monitoring data

Many studies explaining the academic outcomes from bridge monitoring projects have been published; however, it is often more difficult to demonstrate findings that offer conclusive insights into structural condition. Webb et al. (2015) developed a classification system that can be used to describe the different ways in which data can be interpreted to obtain different types of information. This can be used by designers of monitoring systems as a "toolkit" of potential interpretation techniques, to support the development of monitoring objectives that are truly useful. The interpretation of data from bridge monitoring systems can be classified as one or a combination of the following (Webb et al., 2015): (1) "Anomaly detection"—systems used to detect that something has changed or that something is changing over time, which can then potentially be used to support the prioritization of further inspection or maintenance work; (2) "Sensor deployment studies"—systems used to demonstrate new sensor or communication technologies; (3) "Model validation"—systems used to compare the performance of a structure with the performance that is predicted by structural analysis models; (4) "Threshold check"—systems that compare key parameters against thresholds that are usually derived from a structural model to warn of potential problems or trigger physical interventions; and (5) “Damage detection” systems that aim to detect and locate specific areas of damage.

Webb (2014) and Webb et al. (2015), after a detailed review of the literature, reported that the majority of published SHM papers often only reported the deployment of an SHM system for validation of structural models (Figure 32.1; category 3), with little discussion or explanation of the purpose of the system in terms of the needs of one or more key stakeholders (e.g., the asset owner). The second-most-common type of deployment identified by Webb et al. (2015) is sensor deployment studies (category 2). These deployments are typically carried out by researchers to demonstrate new sensor or communication technologies (e.g., MEMS sensors or wireless sensor networks). Gunner et al. (2017) report a sensor deployment on the Clifton Suspension Bridge in Bristol, UK, demonstrating a rapid SHM deployment. There may be no intent to provide immediate value to the asset owner or operator from such deployments, but such field demonstrations may ultimately lead to greater industry confidence in new SHM technologies. Attempts have been made to implement damage detection (category 5); e.g., Çatbaş et al. (2013) and Wenzel (2009) detail methodologies for using structural identification and ambient vibration measurements, respectively. While it is acknowledged that the original reasons for many of these deployment studies may not always be reported in academic papers (and arguably that there is a greater volume of papers produced by academics than by practicing engineers) it is nevertheless interesting that the value derived by asset owners is rarely mentioned in the reviewed literature.

In addition to reviewing monitoring systems described in the literature, the authors can also make the following observations from their experiences of implementing monitoring systems within the bridge engineering industry. Practitioners rarely implement sensor deployment studies because such systems rarely provide relevant

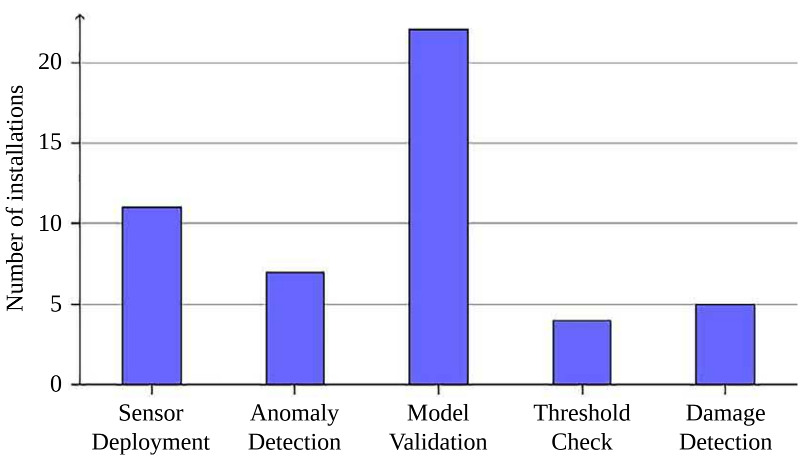

Figure 32.1 Categorization of some existing monitoring systems reported in the literature. Adapted from Webb et al. (2015).

information for the immediate needs of the bridge engineer. Threshold checks are frequently implemented, either to provide controls during construction works to prevent damage to existing structures or, with existing structures, to trigger the implementation of reactive restrictions or maintenance interventions. Model validation exercises are also reasonably common during the assessment of existing structures where value can be obtained by confirming that a structural model does accurately represent aspects of the real structure in its current condition. "Validated models" can then be used with greater confidence to assess the impact of any deterioration. In some cases, if the objectives of a monitoring system have not been clearly defined, anomaly detection can be used to highlight the fact that something has changed, but it can be extremely difficult to confidently identify a physical reason for any changes detected.

4. SHM technologies

4.1 Prevalence of different SHM technologies

Many different sensors can be used in bridge SHM systems both to measure the loading applied to a structure as well as its response. After reviewing 31 publications detailing SHM deployments, Webb et al. (2014) showed approximate levels of prevalence of various monitoring technologies (Figure 32.2). The monitoring technologies discussed in detail within this chapter are listed in Table 32.1. Monitoring technologies can be broadly categorized into three types: "discrete" (Section 4.2), "distributed" (Section 4.3), and "earth observation" (i.e., remote monitoring; Section 4.4), all of which are discussed in the following sections with case studies. Discrete monitoring

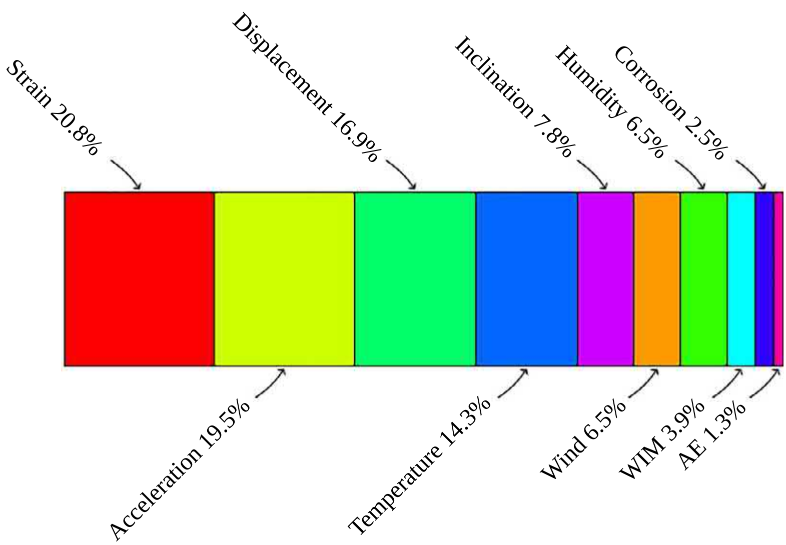

Figure 32.2 Sensor types used in 31 bridge monitoring installations.
Adapted from Webb (2014) (WIM = weigh-in-motion; AE = acoustic emission).

Table 32.1 Types of SHM Technology Described within This Chapter

	SHM Technology	**Description and Example Case Studies**	
1	Strain gauges	Measure the change in strain at a location Examples: strain gauges (Huseynov et al., 2017), piezoelectric transducers (Wang, 2004), vibrating wire strain gauge (Sreeshylam et al., 2008) and fiber optic cables (Rodrigues et al., 2010)	Discrete sensors
2	Scour monitoring	Indicates the presence (and, in some cases, the extent and the location) of scour around a bridge foundation Examples: Sonar (Falco and Mele, 2002), ground-penetrating radar (Anderson et al., 2007), and magnetic sliding collar (Briaud et al., 2011)	
3	Vibration/ acceleration monitoring	Used to derive the modal parameters from the vibration captured from a bridge, and these parameters show some sensitivity to damage Examples: vibration-based crack detection (Farrar et al., 1994), vibration-based scour detection (Kariyawasam, 2020)	
4	Displacement monitoring	Captures the displacement between the sensor and an object Examples: laser displacement sensors (Zhao et al., 2015), linear proximity sensors, ultrasonic displacement sensors, linear voltage differential transformer (Sarwar and Park, 2020)	
5	Inclinometers/ tiltmeters	Measure the change in inclination of an object using the constancy of the direction of gravity; see Hou et al. (2005)	
7	MEMS	Small, typically low-cost electromechanical sensors that capture various parameters, e.g., MEMS accelerometers (Kariyawasam, 2020)	
8	Optical	Captures high-level understanding of a physical space by interpreting digital videos or images. e.g., laser scanning (Riveiro et al., 2011)	Distributed sensors
9	Acoustic Emission	Captures the elastic strain sound waves generated by cracks or steel wire breaks; see Yuyama et al. (2007)	
10	Fiber Optic	Measures distributed/point measures of strain and/or temperature of an object by observing the optical wave propagation and scattering along a cable attached to the object; e.g., Brillouin fiber optic sensors (Minardo et al., 2012), fiber-Bragg grating sensors (Rodrigues et al., 2010)	
11	Weigh-in-motion (WIM)	Allows for automatic collection of traffic data, such as axle loads, gross vehicle loads (weights), traffic volume, and speed (Yu et al., 2016)	

Table 32.1 Continued

	SHM Technology	Description and Example Case Studies	
12	Corrosion	Captures the level of corrosion present in metallic objects such as prestressing tendons and reinforcing bars; see Budelmann et al. (2014)	
13	Earth Observation	Techniques such as satellite-based synthetic aperture radar (SAR) allow remote measurement of displacement variations; see Selvakumaran et al. (2018)	

technologies have sensors placed at specific, discrete locations on a structure and hence provide localized information, which needs to be integrated with certain assumptions to understand the global behavior of the structure. Distributed monitoring technologies provide measurements at any location covered by the sensor (e.g., any point within the field of view of an image sensor, or any position along the length of a fiber optic cable). Finally, earth observation systems such as InSAR are now also emerging for use in bridge monitoring (Selvakumaran et al., 2018). Table 32.2 lists some monitoring technologies adapted from Gastineau et al. (2009). An in-depth study of all these technologies would be beyond the scope of this chapter.

An automated monitoring system is not the only way in which data about a structure can be collected. Manual inspections and on-site testing can also provide information and therefore should also be considered a form of monitoring. Such visual inspection methods are the most common form of "damage detection" monitoring, but the results are subjective (e.g., Moore et al., 2001; Graybeal et al., 2002; Middleton, 2004; Lea, 2005; Bennetts et al., 2018; Bennetts, 2019; Bennetts et al., 2020). Visual inspection-derived condition indices are arguably of limited use for understanding the condition of a single asset but can be more useful at the portfolio level (Bennetts et al., 2018). Current visual inspection frameworks are also not well suited to detecting changes in condition with time (see Bennetts, 2019; Bennetts et al., 2021).

4.2 Discrete sensors

4.2.1 Strain gauges

Strain is a nondimensional value that represents the deformation of an object relative to its initial length. It is one of the most common types of measurements used in SHM and is traditionally sensed using electrical resistance strain gauges, piezoelectric transducers, or vibrating wire strain gauges. An electrical resistance strain gauge typically consists of an insulating flexible backing pad that supports a conductive and resistive foil. Strain is measured through the change in resistance of the foil caused by the deformation of an object due to the applied load. Similarly, a piezoelectric transducer generates an electrical signal, which is proportional to the magnitude of deformation.

Table 32.2 25 Types of SHM System Technologies Described in Gastineau et al. (2009), Incorporating Adaptions Provided by the Present Authors

	System Technology	System Capabilities (Further Information Provided in Gastineau et al., 2009)
1	3-D laser scanning	Used to build 3-D "point cloud" models of structures. See Park et al. (2007).
2	Accelerometers	Used to determine modal properties of structures. See Matsumoto et al. (2010).
3	Acoustic emission	Detects sound waves generated by cracks propagating or steel wires breaking. See Nair and Cai (2010).
4	Automated laser total Station	3-D displacement monitoring of a number of targets. See Psimoulis and Stiros (2013).
5	Chain dragging	Acoustic technique used to detect shallow delamination in concrete decks. See Perenchio (1989).
6	Concrete resistivity	Provides an indication of the likelihood of corrosion occurring.
7	Digital image correlation (DIC)	Also known as particle image velocimetry (PIV). An image processing technique to track relative movements between sets of images taken at different times, allowing a continuous strain field to be derived. See Lee et al. (2012) and White et al. (2003).
8	Electrochemical fatigue sensing system	A nondestructive technique developed to detect fatigue cracks in metal structures by continually monitoring current flow at the surface.
9	Electrical impedance (post-tensioned tendon)	Technique for detecting defects in the corrosion protection of post-tensioned tendons using a change in electrical resistance. Relies on the tendons being enclosed by a polymer duct that electrically isolates the tendon and grout from the surrounding concrete. See Elsener (2005).
10	Electrical resistance strain gauges	Common form of strain gauge, but susceptible to thermal variations. Issues include variation in the quality of attachment.
11	Fatigue life indicator	Sacrificial sensor intended to indicate the likely remaining fatigue life of a component. See Zhang et al. (2007b).
12	Fiber optics	Can provide discrete or continuous measurement of a variety of parameters, such as strain, temperature, and chloride ion concentration. See Rodrigues et al. (2010).
13	Global positioning system (GPS)	Satellite based system to provide 3-D position information.
14	Ground-penetrating radar (GPR)	A technique involving radar pulses to view subsurface features such as reinforcement or prestressing tendons.
15	Impact echo	Analysis of reflected sound waves from a hammer tap is able to detect some subsurface flaws.

Table 32.2 Continued

	System Technology	System Capabilities (Further Information Provided in Gastineau et al., 2009)
16	Infrared thermography	Disrupted heat flows through structures can be indicative of damage such as delamination of concrete slabs. See Washer et al. (2010).
17	Linear polarization resistance (LPR)	Provides an indication of the likelihood of corrosion in concrete.
18	Linear potentiometer	Displacement transducer based on the principle of a potential divider.
19	Linear variable differential transformer	Robust displacement transducer consisting of three solenoidal coils around a sliding ferromagnetic core.
20	Macrocell corrosion rate monitoring	Technique to provide an indication of the likelihood of corrosion.
21	Half-cell potential measurements/chloride content	Measuring the electrochemical potential or the chloride ion concentration in concrete can provide an indication of the likelihood that corrosion is occurring.
22	Scour measurement	Ultrasonic and radar technologies have been used in attempt to detect scour, but inspection by a diver may be the only reliable way to assess the extent of any scour.
23	Tiltmeters/inclinometers	Used to measure the angle of an object with respect to the earth's gravitational field, typically using a force balance sensor.
24	Ultrasonic C-scan	Ultrasonic testing can be used to detect some imperfections within materials.
25	Vibrating wire strain gauges	Strain gauge comprising a taut steel wire attached to the structure, the natural frequency of which varies with applied strain. See DiBiagio (2003).

The vibrating wire strain gauge, on the other hand, measures the resonant frequency of a wire to record strains. It consists of a tensioned wire attached to a plate at each end. When the plates (which are attached to a structure or test specimen) move the tension in the wire changes. This changes the resonant frequency of the wire that is measured and then converted into a strain value. It is now also possible to measure strains using fiber optic sensors (see Section 4.3.3).

Case study: Exe north bridge load testing (Huseynov et al., 2017)

A load test on the Exe North Bridge (a three-span simply supported bridge spanning the River Exe in Exeter, UK) was conducted (for more details see Huseynov et al., 2017). The bridge is 18.9 m wide and carries four lanes of traffic with a superstructure of 1 m depth comprising 12 composite precast girders, with embedded steel beams in the reinforced concrete I-girders. The purpose of the field testing was to obtain the

Figure 32.3 Elevation view of Exe North Bridge.
Photo: Authors.

transverse load distribution factors of the deck structure, which is an essential parameter for obtaining the accurate load rating factor of the main load-carrying elements. Figure 32.3 shows the elevation view of the test structure.

ST350 model strain transducers, supplied by Bridge Diagnostics Inc. (BDI), were installed to measure the strain response of the bridge. The sensors were attached to the soffit of each main girder, as shown in Figure 32.4. These resistive sensors were encased in a ruggedized transducer package mounted to the bridge using bolted tabs and epoxy glue. The sensor was 76 mm in length. The measurement length was increased using 0.6 m long aluminum extension rods to account for local microcracks typically occurring in reinforced concrete surfaces. Thus average strain values were recorded. The bridge was loaded with a four-axle 32-ton truck during testing; the test truck remained stationary in each lane for approximately 45 s. A typical strain-time history from the test records is depicted in Figure 32.5a. Transverse load distribution factors were calculated by dividing the average strain measured on the soffit of each

Figure 32.4 ST350 strain transducers being installed on the beam soffit.
Photo: Authors.

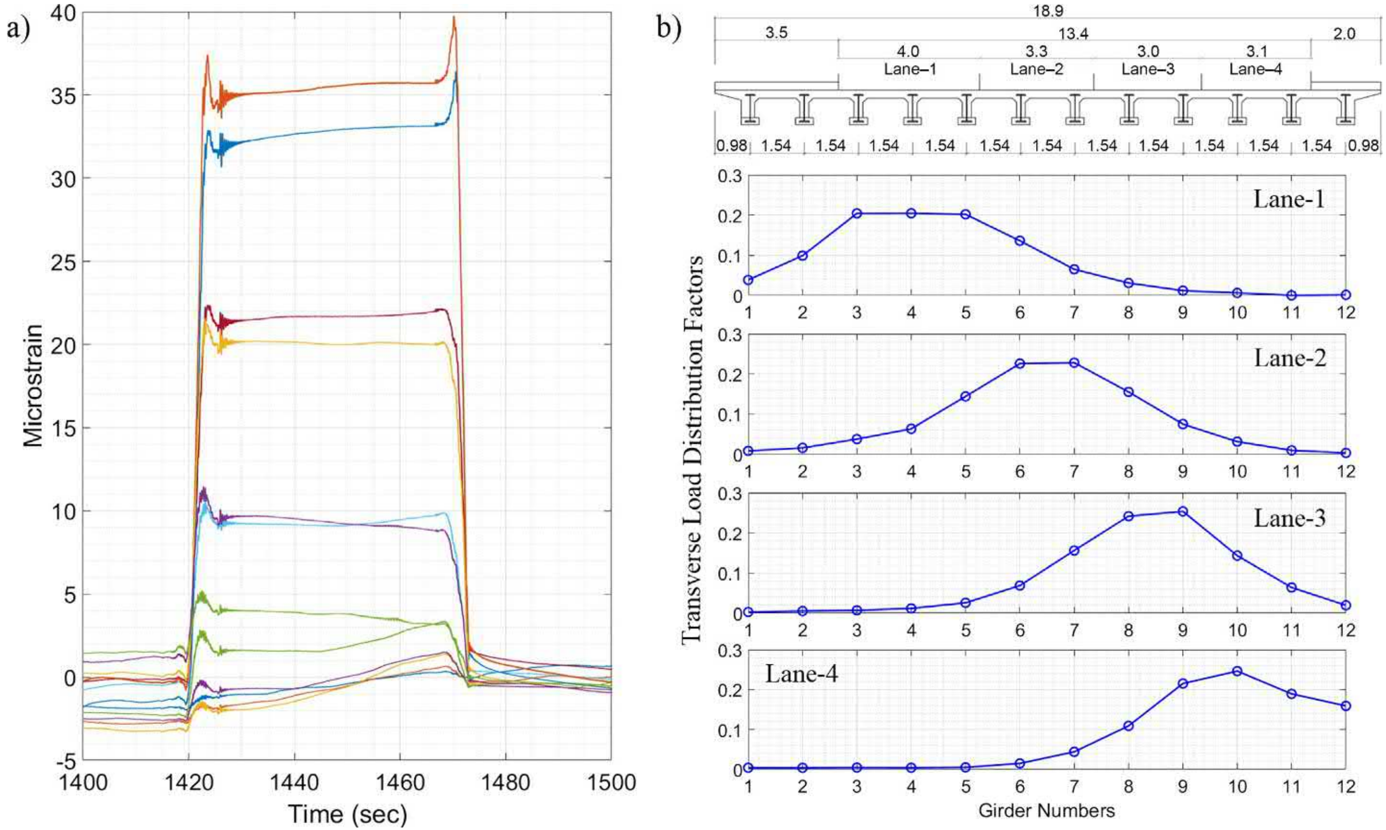

Figure 32.5 Field testing results (a) Typical strain time history response (b) calculated transverse load distribution factor of the deck for each lane loading.

girder while the truck remained stationary by the total sum of the average strains of all girders. Figure 32.5b shows the calculated transverse load distribution factors for each lane, providing insights into the true behavior of the structure that would not have been possible to verify without the monitoring system.

4.2.2 Scour monitoring

Scour is the removal of soil around pier and abutment foundations of bridge structures due to the action of water. Scour has been reported as the most prominent cause of historical bridge failures (Wardhana and Hadipriono, 2003). Various scour monitoring techniques have been proposed; however, traditional inspection by human divers is still common (e.g., Elsaid and Seracino, 2012). Most scour monitoring techniques use discrete sensors, except for the wave-based techniques such as sonar and ground-penetrating radar (GPR), which use the return time of a sound or radio wave to measure the distance from the water surface to the riverbed (e.g., Prendergast and Gavin, 2014). There are numerous discrete scour monitoring techniques such as vibration-based techniques, float-out devices, and magnetic sliding collars. Some of the common challenges of these scour monitoring techniques are lack of durability, high-cost, labor-intensive installation, and loss of function during flooding (Kariyawasam, 2020).

4.2.3 Vibration/acceleration monitoring (Kariyawasam, 2020)

Vibration-based monitoring aims to identify changes in bridge vibration properties to better understand the performance of a structure and to potentially detect damage. Vibrations are typically present in bridges as a result of ambient random excitations caused by vehicles, flooding, wind, and other environmental sources. Individual bridges have their own intrinsic vibration properties, such as natural frequency and mode shape. Under normal (undamaged) conditions, such vibration-based properties remain constant as bridge stiffness, mass, and damping are unchanged. However, when damage occurs, either locally or globally, there will be a reduction in stiffness and other modal characteristics. Hence, monitoring bridge vibrations may allow any damage to be detected as a change in modal characteristics.

There have been numerous attempts in past studies to use natural frequency as an indicator of superstructure damage (e.g., Döhler et al., 2014; Kim et al., 2003; Farrar et al., 1994). However, these damage detection studies have shown little practical potential except for some recent studies on scour damage detection. Only small changes in natural frequency have been observed even when there is considerable damage. For example, for cracks as considerable as 50% of the depth of a bridge beam or pier, the frequency changes observed were only 7% (Döhler et al., 2014), 5.6% (Kim et al., 2003), and 0.4% (Farrar et al., 1994). These sensitivities to damage are not sufficiently higher than the natural frequency changes expected due to environmental and/or operational changes (e.g., Peeters and De Roeck, 2001; Kim et al., 2003; Magalhães et al., 2009). Such low sensitivity may be due to the local stiffness change due to concrete/steel cracking. Scour is a special damage case that changes the boundary condition and the global stiffness of the bridge. Therefore, vibration-based scour detection may have greater potential than vibration-based crack detection. Significant changes in natural frequency, as high as 20%–40%, have been reported for the scour depths analysed in studies focused on numerical simulations (Prendergast et al., 2016), laboratory experiments (Kariyawasam et al., 2020), and field studies (Ko et al., 2010). Vibration-based techniques typically require a set of accelerometers placed at various locations of the bridge piers and decks to capture the modal characteristics. Some recent research has proposed that the modal characteristics of bridges can also be obtained by "drive-by" monitoring i.e., accelerometers placed on a vehicle traversing a bridge (Fitzgerald et al., 2019).

Case study: Vibration-based monitoring at Baildon Bridge (Kariyawasam, 2020)
It has been difficult to evaluate the potential of vibration-based damage detection in real bridges, particularly with regards to scour, due to its unpredictable nature. At Baildon Bridge (Figure 32.6a), due to existing scour and a planned repair program, there was an opportunity to monitor the vibrational characteristics of the bridge during a repair program and to capture "scour in reverse." As shown in Figure 32.6b, a sonar scan before and after the repair program showed the scour backfilling to have occurred primarily near the south bridge pier. The modal characteristics obtained before and after the repair indicated that natural frequency was too uncertain to be able to detect the change predicted by the numerical models. However, as shown in Figure 32.6c and d, other parameters such as mode shape and modal spectral densities showed a clear and significant change before and after repair, indicating that there is potential for scour to be detected in real bridges (Kariyawasam et al., 2019a,b). The mode shapes changed primarily at the pier undergoing scour backfilling (the south pier), and thus, mode shapes could be used to detect the location of scour. Modal spectral density gradually reduced during the scour backfilling process, indicating that modal spectral density would increase if the bridge were to experience scour. Further research with various types of small-scale models tested in the geotechnical centrifuge at the Schofield Centre at the University of Cambridge has confirmed these findings that mode shapes and modal spectral densities show significant sensitives to scour at bridge foundations (Kariyawasam et al., 2020).

4.2.4 Inclination and displacement monitoring

The inclination of an object is traditionally measured using tiltmeters or inclinometers. The main operating principle of an inclinometer is that it measures various responses generated by pendulum behavior due to gravitational effects. Inclination is perhaps the least adopted parameter in the bridge SHM field due to the insufficient accuracy of the commercially available sensors failing to capture tiny rotations occurring on bridges. However, in a recent study, Huseynov et al. (2020) developed a novel approach of

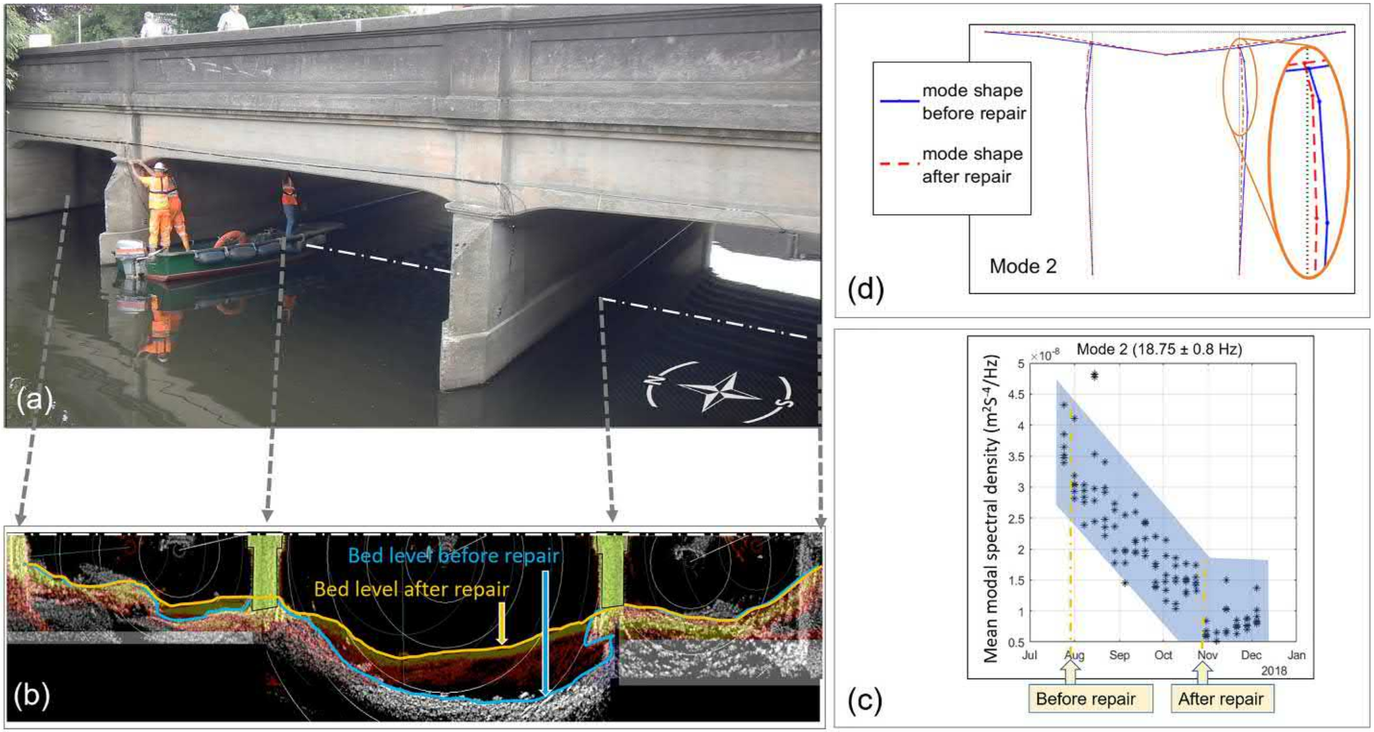

Figure 32.6 (a) Baildon Bridge; (b) riverbed level before and after repair, captured by sonar images; (c) modal spectral density for Mode 2 over the repair period captured by an accelerometer on the pier near the scour hole; (d) mode shapes before and after the repair.
(a) Photo: Authors. (b) Image courtesy of Jenny Roberts.

measuring rotations of an object to microradian accuracy using high-grade force balance type accelerometers. Similarly, Faulkner et al. (2020) demonstrated the application of accurate rotation measurements using the combination of accelerometers and gyroscopes. In this study, authors demonstrated through field trials that the accuracy of the rotation measurements can be significantly improved by applying sensor fusion techniques using a Kalman filter.

Case study: Mineral line bridge field testing (Faulkner et al., 2018)

The test structure is a 14.8 m long simply supported historical railway bridge owned by West Somerset Railway (Faulkner et al., 2018). The bridge deck consists of two cast iron main girders and cast-in-situ reinforced deck, which carries a single railway track. In the summer of 2017 the famous locomotive, the Flying Scotsman, was visiting the West Somerset Railway. This provided a unique opportunity to capture some bridge deformation data due to the passage of the Flying Scotsman at the deck level. The field testing was established (i) to measure deck rotations due to the Flying Scotsman using accelerometers and (ii) to determine resulting deflections from the measured deck rotations. Figure 32.7 shows the Flying Scotsman locomotive crossing the bridge site.

The rotation was determined by projecting the gravity vector on the axes of acceleration, similar to the methodology described by Huseynov et al. (2020) and Hester et al. (2020). The bridge deck was instrumented with five high-grade force balance type accelerometers, oriented in the horizontal direction, placed at two supports, quarter-, mid-, and three-quarter span locations, as shown in Figure 32.8. Figure 32.9a shows the typical acceleration time history response recorded during the passage of the Flying Scotsman. The rotations obtained from the measured acceleration response are plotted on Figure 32.9b. The first peak in the plot represents the passage of the locomotive, which is the heaviest part of the train, and the following peaks correspond to the passage

Figure 32.7 Flying Scotsman locomotive crossing bridge site.
Photo: Karen Faulkner.

Figure 32.8 Test layout showing sensor locations.
Photo: Authors.

of eight carriages. During field testing it was not possible to deploy another type of rotation sensor to validate the accuracy of the rotation measurements obtained using accelerometers. Instead, the accuracy of recorded rotations was validated by comparing the displacement values predicted using measured rotations and through direct measurements (i.e., using an optical camera system).

The displacement values were obtained from measured rotations applying the procedure reported in Helmi et al. (2015). An optical camera system (see also Section 4.3.1) was deployed to compare the displacements obtained using the rotation response of the bridge deck. Figure 32.10 shows an Imetrum camera pointing to an optical target attached on the main girder at the midspan location. Figure 32.11 presents the deflection time history recorded during the train loading. The black plot with square data markers represents the displacement values obtained using the rotation response measured by accelerometers. The red plot was recorded using the Imetrum camera system. Figure 32.11 shows that the two displacement values match very well, confirming that the methodology applied for measuring rotations was reliable.

4.2.5 MEMS sensors

Advances in silicon chip manufacturing processes have made it possible to fabricate small electro-mechanical sensor devices within the same packaging as integrated circuits. Examples of these microelectromechanical systems (MEMS) devices include accelerometers, inclinometers, and solid-state gyroscopes, which can be found in everyday consumer devices such as smartphones and tablets. MEMS sensors can be produced rapidly in large numbers and are cheap to manufacture. They tend to have low power requirements, which facilitates their use in wireless sensor networks (WSNs). Wireless devices incorporating MEMS sensors may offer a cost-effective solution for extensive, scalable remote monitoring of bridges.

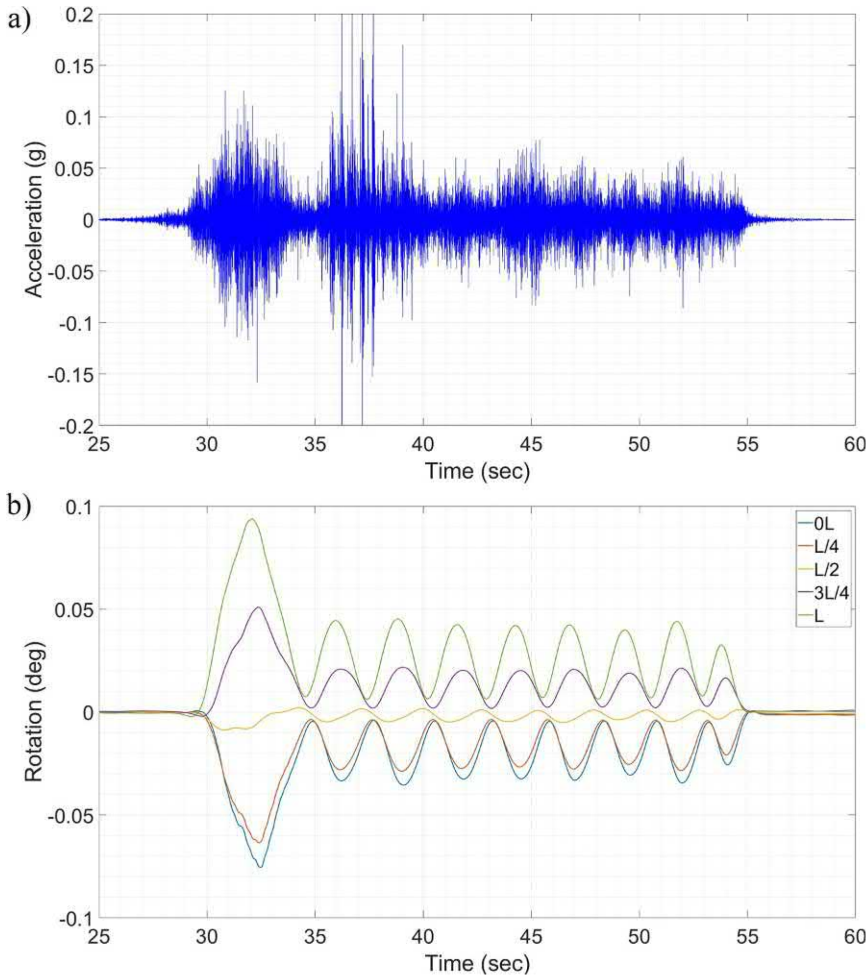

Figure 32.9 Bridge response to Flying Scotsman: (a) horizontal acceleration time history signal from the accelerometer at the support location; (b) inferred rotations at five locations using horizontal accelerations.

4.3 Distributed sensors

4.3.1 Computer vision

Computer vision systems allow for the extraction of information from the scanning and/or interpretation of digital images. Computer vision can be employed for a wide variety of tasks, including 3-D reconstruction, construction progress monitoring, geometric checks, component compliance, and deflection detection. It offers new opportunities to enhance SHM efforts, especially with the emerging prominence of building information modeling (BIM). Computer vision has the potential to remove some of the inherent subjectivity in visual inspection. If defect detection can be more automated, computer vision could potentially add significant value to construction or operation processes.

Figure 32.10 Imetrum camera pointing to the optical target at the midspan location. Photo: Authors.

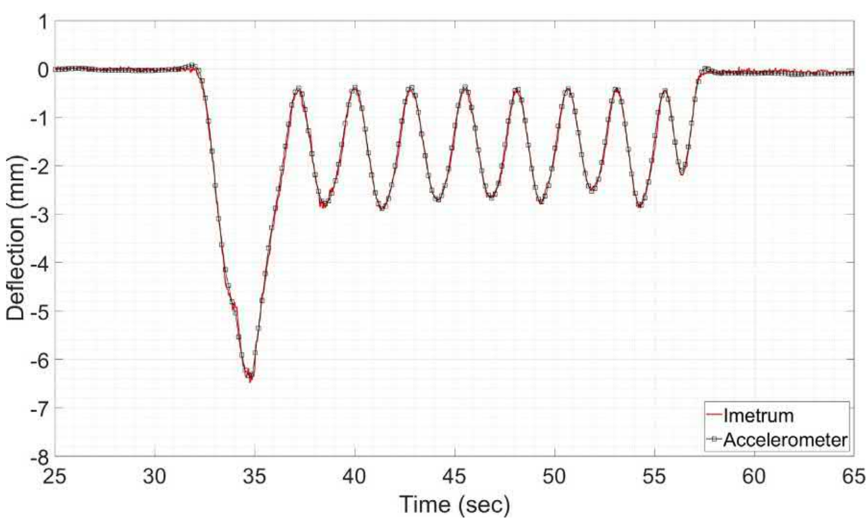

Figure 32.11 Displacement response of the bridge to the Flying Scotsman.

Case study: Abutment Wall crack movement monitoring using computer vision (Huseynov et al., 2019)

The test structure is a masonry-type cantilever abutment of a historical railway bridge dating back to the Victorian era. The bridge was constructed in the 1870s in England (Huseynov et al., 2019). The abutment structure consists of a main wall (with a height approximately 5 m above the ground surface) and two integrated wing walls (with heights approximately 3.8 m above the ground surface). The bridge was extensively renovated in 2011. During the latest visual inspection, the condition of the bridge was deemed to be sufficient to carry the regular daily traffic; however, some defects were found on the abutment structure. One of the abutment wing walls experienced a vertical crack running along its full length approximately 2 m from the face of the main wall. Figure 32.12a shows the vertical crack on the abutment wing wall.

The crack movement was initially monitored by the operator using a Moiré Tell Tale device to obtain the cumulative displacement of the wall over time and to identify its direction of movement. The inset in Figure 32.12a shows a Moiré Tell Tale device installed on the surface of the wall at the crack location. The results from the Moiré Tell Tale device revealed that the wing wall was moving relative to the main wall. However, it was not possible to establish if the abutment was moving, the wing wall was moving, or if both were moving, due to the limitations of the device.

The main objective of the field testing was established after a detailed discussion with the bridge operator to address the following questions:

- What is the magnitude of crack movement in 3-D?
- What is the displacement of the wing wall relative to the abutment main wall?

Figure 32.12 Test layout: (a) vertical crack on the abutment wing wall; (b) test setup. Photo: Authors.

- What is the relationship between the applied load and the magnitude of the crack movement?
- Is the structure continuing to move (for some time) once the train passed?
- Does the crack movement remain in the elastic range (i.e., does the wall movement return to its initial state after the train passage)?

To answer the preceding questions, the wall movements on both sides of the crack were monitored using an optical camera system. Figure 32.12b shows the real view of the test layout. Two Imetrum cameras were used to measure the crack movement in three dimensions. One of the cameras was pointed perpendicular to the wall, whereas the other one was placed almost parallel to the surface of the wall (see Figure 32.12b). Two L-shaped optical targets were mounted on the wing wall at each side of the crack line, as shown in Figure 32.12a.

Figure 32.13 shows the crack movement on both sides of the wall due to a train's passage. The plots on the left-hand side (plotted in red) show the results on the left-hand side of the crack line (TP-1 location, closer to the main wall), whereas plots on the right-hand side represent the corresponding results on the opposite side of the movement (TP-2 location, closer to the wing wall end). Overall, the following conclusions were made from the study:

- The abutment wall is exposed to cycling loading due to passing trains. The dominant direction of movement is in the longitudinal bridge direction. The maximum magnitude of movement recorded during the test day was approximately 0.4 mm.
- The monitoring results revealed that the left-hand side of the crack (closer to the main wall) moves significantly more than the opposite side of the crack.
- The magnitude of the movements appears to be approximately in proportion to the magnitude of the applied load, and the wall movements remain in the elastic range.

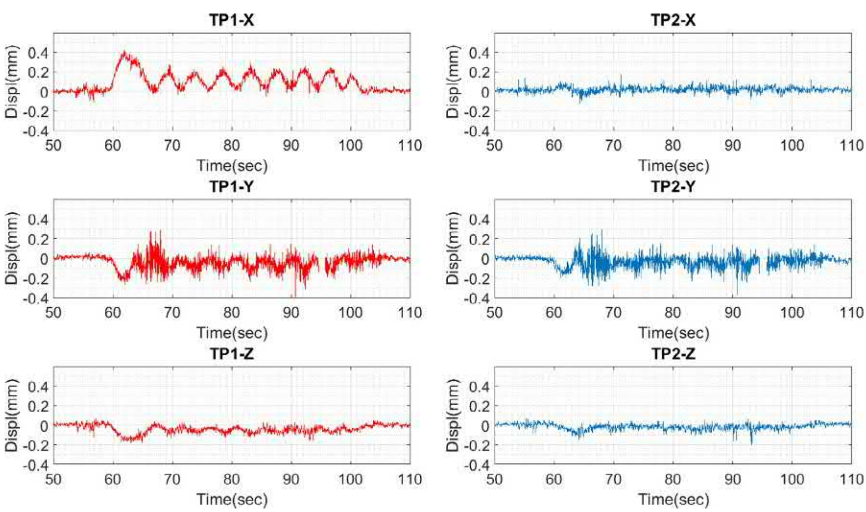

Figure 32.13 Wall movements in 3-D on both sides of the crack line due to the passage of a train.

4.3.2 Acoustic emission (AE)

Acoustic emission involves the use of sensitive acoustic transducers to detect small elastic strain waves that are generated as cracks in steel plates propagate or as pre-stressing wire cable strands break. For the latter, interpreting the historical number of wire breaks that have occurred and, hence, quantifying the effect on the whole bridge cable remains a challenge (unless the AE system has been in place since the construction of the bridge).

Case study: Hammersmith flyover (Webb et al., 2014)

Acoustic emission sensors were used by a contractor (Watson, 2010) on the Hammersmith Flyover in London to detect loss of prestress (wire breaks), and the data were made available to the research team at the University of Cambridge for analysis (Webb et al., 2014). The rate of wire breaks began to increase around March 2011 (see Figure 32.14), and the increasing concern over the ensuing months led to closure of the bridge to traffic in December 2011. This led to a program of intrusive investigation and subsequent retrofitting activities. This monitoring technique is an example of damage detection (category 5; Webb et al., 2015) being used to investigate a specific problem (i.e., corrosion/wire breaks) and subsequently yielding value to the asset owner, who would then make an informed decision on the refurbishment strategy.

4.3.3 Fiber optic strain sensing

It is possible to measure strain using fiber optic cables. While most light shone through a fiber optic cable will travel to the end via total internal reflection, imperfections in the glass result in the backscattering of some of the input signal. By analyzing the frequency of the backscattered light relative to the input frequency, it is possible to

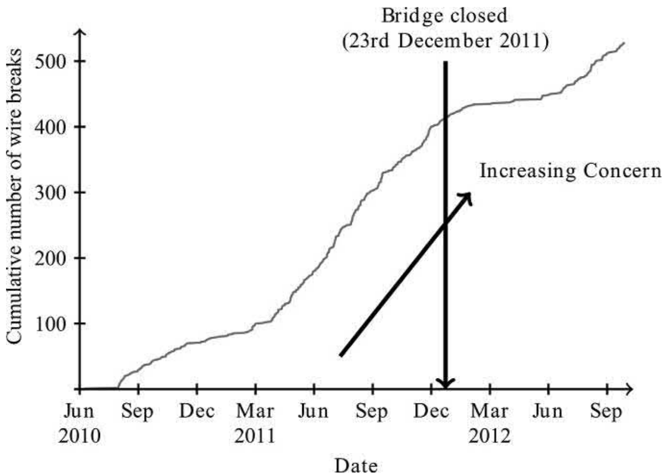

Figure 32.14 Cumulative wire breaks detected during the acoustic emission monitoring on Hammersmith Flyover.
Plot from Webb et al. (2014).

determine the strain (either mechanical strain or temperature induced strain) in the fiber optic cable, at any point along its length. This is the basis for distributed fiber optic sensing (DFOS). Fiber optic analyzers that make use of Brillouin scattering can measure strain with data rates of one measurement every few seconds or even minutes, so they are best suited for measurement of dead loads (or known static loads) rather than for situations with varying live loads such as traffic.

Another type of fiber optic sensor is the fiber-Bragg grating (FBG). Rather than relying on light backscattered from imperfections in the glass, in FBG sensors, a portion of the fiber optic cable is inscribed with a grating that strongly reflects a particular frequency of light. As the FBG sensor is strained, the spacing between the grating lines also changes resulting in a change to the frequency of light that is strongly reflected, and this change in frequency can be measured. Several FBG sensors can be placed on the same fiber, provided they have different grating spacings. These sensors are only able to measure strain at discrete points along the fiber optic cable but can measure strains with data rates of multiple kHz, making them suitable for dynamic measurement applications.

Case study: Nine Wells Bridge (Webb et al., 2017)

The Nine Wells Bridge, located in Cambridgeshire, UK, is an example of an experimental deployment of fiber optic strain measurement (further details on this sensor deployment study are given in Hoult et al., 2009; Webb 2014 and Webb et al., 2017). Six beams in the western span of this three-span prestressed concrete bridge were constructed with optical fibers cast into the concrete in the precasting factory (see Figures 32.15–32.17), allowing distributed strain measurements to be taken along the lengths of the prestressed beams. Fiber optic cables enter at one end of the beam and run along the lower prestressing strands, up one of the shear links at the end of each beam, and then return along the upper prestressing strands, thus completing

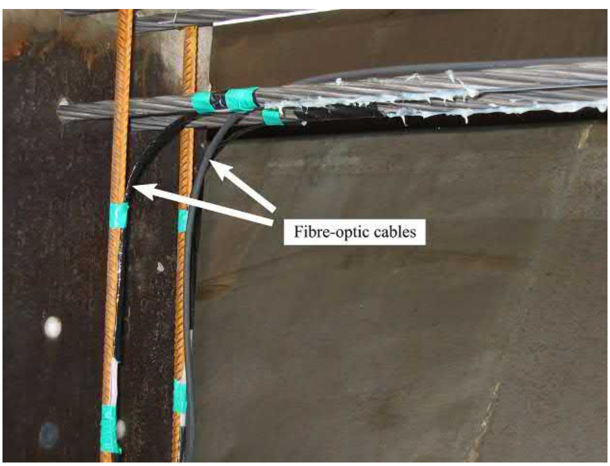

Figure 32.15 Close-up of fiber optic cables attached to rebar and pretensioned tendons. Photo: Neil Hoult.

Figure 32.16 Finished beam ready for transport to site.
Photo: Neil Hoult.

Figure 32.17 Taking baseline readings with fiber optic analyzer.
Photo: Neil Hoult.

the loop of fiber in the beam. Readings were taken after release of the pretensioned cables, immediately after installation, and also after casting of the composite in situ deck slab. The results enabled an investigation of various phenomena including the debonding of prestressing tendons, initial elastic shortening, concrete creep and shrinkage, and the effects of temperature (more details are provided in Webb, 2014 and Webb et al., 2017). In this case, researchers gained value from the installed system as it leads to greater confidence in the use of this fiber optic technology for measuring distributed strain in bridge beams.

4.3.4 Weigh-in-motion (WIM) systems

A WIM system allows for automatic collection of traffic data, such as axle loads, gross vehicle loads (weights), traffic volume, and speed—all taken as real-time or near-real-time measurements (e.g., Zhang et al., 2007a). Live loading is usually an important load-case for bridges and is needed to make predictions of the expected response to compare with measured data. Some difficulties encountered in calibrating WIM data have been discussed in Zhi et al. (1999). For example, it is difficult to measure vehicle live loads accurately due to complex interactions of the vehicles, their suspension, and the bridge deck. Cantero and González (2015) suggest that WIM technology may be used to monitor change in structural condition for short- to medium-span bridges more effectively than using conventional vibration techniques. Webb (2014) estimated live loads on a bridge deck by inverse analysis of deflection measurements, and this work highlighted the difficulty faced in uniquely characterizing live loads indirectly.

4.3.5 Corrosion detection systems

Techniques such as the use of corrosion ladders and linear polarization resistance gauges may provide an indication of the likelihood of corrosion being present rather than the actual loss of steel section. Agrawal et al. (2009) present a detailed review of corrosion monitoring systems. Most corrosion detection systems only provide an indirect indication of the likelihood of corrosion.

4.4 Earth observation

Satellite-based synthetic aperture radar (SAR) provides a means for acquiring remote measurements covering most of the Earth's surface. This technique is a form of radar, in which the sensing system transmits pulses of radio waves and records the echoes received from reflections of those waves from the area of interest. The true potential of SAR techniques results from combining multiple images covering the same area but acquired at different times. This allows changes in the line-of-sight distance between the satellite and objects in the observed area to be deduced. These systems have been used since the 1990s to study ground deformations over large areas, such as those resulting from earthquakes or volcanoes. Early systems had a coarse spatial resolution, so they were not suitable for collecting information about individual structures; however, more recently deployed sensors are able to collect imagery with spatial resolutions of the order of a meter, or even smaller. This allows specific parts of individual structures to be identified within an image, meaning effective monitoring of bridges is becoming a realistic proposition.

Recent work by Selvakumaran et al. (2018) has demonstrated the potential for InSAR measurements to detect settlement of bridge piers resulting from scour. Tadcaster Bridge is a nine-span masonry bridge over the River Wharfe in Tadcaster, UK, which suffered a partial collapse due to scour following a period of flooding in December 2015. In this study, Selvakumaran et al. (2018) undertook retrospective analysis of 48 images acquired over a two-year period. The plot in Figure 32.18

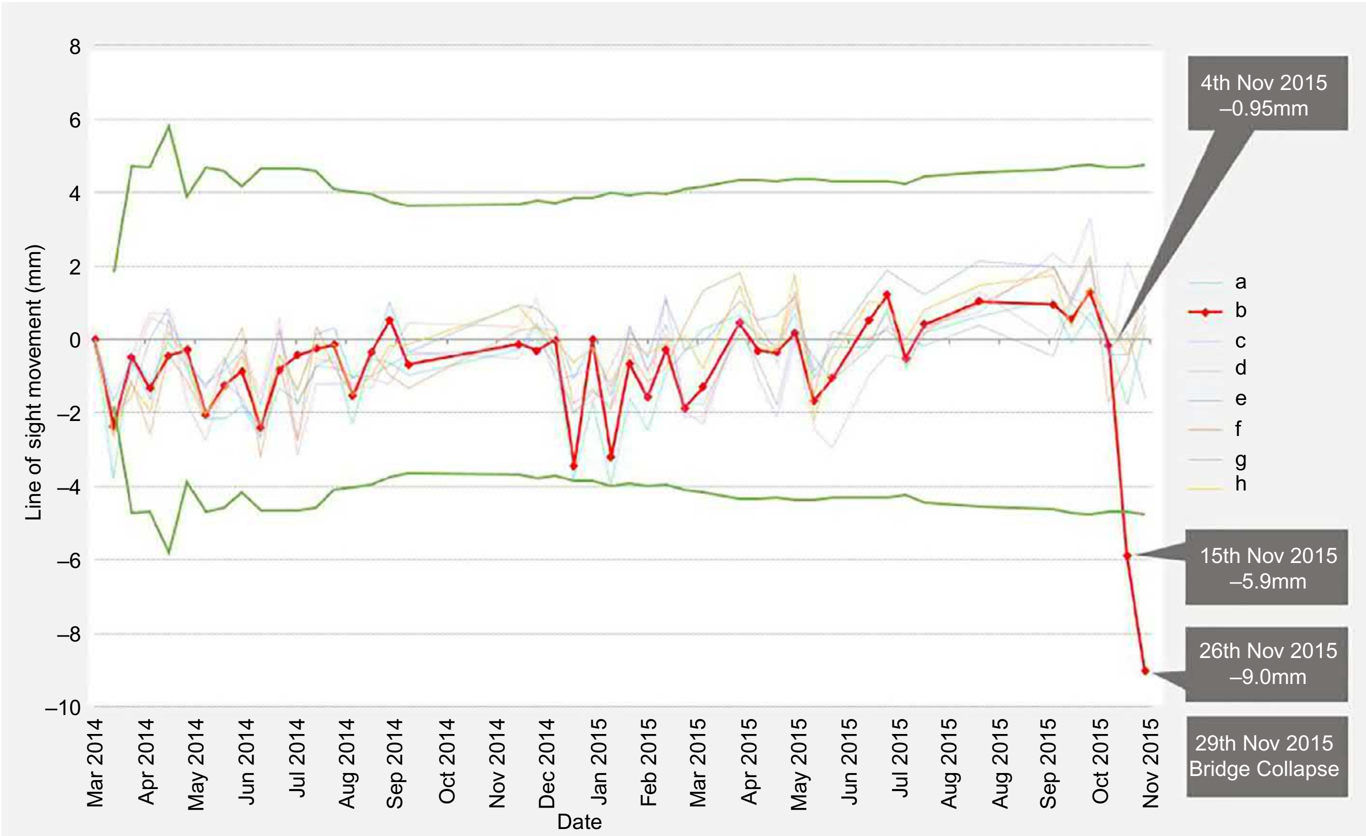

Figure 32.18 Plot showing movements of points on Tadcaster Bridge over time.
Plot from Selvakumaran et al. (2018).

shows the measured movements of points on the structure derived from the InSAR imagery. The green lines mark a boundary for outliers, meaning that any data points outside of this region should be considered to represent unusual bridge behavior. It can clearly be seen that there was a distinct movement of point b, which was located near to one of the bridge's piers, shortly before the bridge partially collapsed. This demonstrates the potential for the technique to be used as an early warning system.

If a structure reflects radio waves sufficiently well that it is visible in SAR imagery, then remote monitoring can be undertaken with no requirement for any equipment to be installed on the structure itself. Additionally, individual SAR images typically cover areas of hundreds of square kilometers, so there is the potential for large numbers of structures to be monitored at a low cost per structure. This monitoring technique is dependent on there being a clear line of sight between the structure and the sensing satellite. InSAR satellites typically use a side-looking image geometry, meaning that the satellite's sensor is not orientated vertically. One implication of this is that the line of sight to some structures can be obstructed by tall objects (such as vegetation or buildings) nearby. In addition, any displacement measurements are one-dimensional, representing the observed change in line-of-sight distance between the satellite and the structure being monitored. This complicates the interpretation of results unless it can be assumed that most movements of a structure will occur in a single direction.

4.5 Further information on measurement techniques used for bridge monitoring

A complete in-depth review of all available measurement techniques and sensing technologies useful for bridge monitoring would be beyond the scope of this chapter—or, indeed, this book. A more comprehensive list is presented in Gastineau et al. (2009); Table 32.2 lists different monitoring technologies described therein.

5. Deployment and operation

5.1 Sensor deployment strategies

5.1.1 Wired sensor networks

Wired sensor networks utilize dedicated cabling to provide both power and data transfer to the system's sensors. Wong (2004) describes the Wind and Structural Health Monitoring System (WASHMS) that is deployed on a number of significant bridges in Hong Kong. This complex and expensive system is arguably more robust than many wireless systems but does not have the level of flexibility and expandability that wireless solutions offer and requires installation of cable runs to connect the sensors to a suitable data logger.

5.1.2 Wireless sensor networks

Wireless sensor networks are being developed as an alternative lower-cost and more flexible solution to wired deployments. Each sensor is completely self-contained and transmits readings wirelessly to a receiver and data logger located somewhere on or near the structure. The lack of cables means that wireless systems can be much more easily reconfigured than wired systems, a key benefit. The research project *Smart Infrastructure: Wireless sensor network system for condition assessment and monitoring of infrastructure* (2006–2009), funded by the Engineering and Physical Sciences Research Council (EPSRC) in the United Kingdom, trialed several wireless SHM deployments on bridges, including systems installed on the Humber Bridge (Hoult et al., 2008), Ferriby Road Bridge (Hoult et al., 2010), and Hammersmith Flyover (Webb et al., 2014). Figure 32.19 shows an example of the type of wireless sensor device typically used for these deployments.

5.2 Deployment challenges

Many of the research papers reviewed by the authors discuss the technology itself but do not discuss the difficulties and challenges that must be overcome when an SHM system needs to be designed, installed, and then operated. Practical considerations for the design and specification of new SHM systems include the following:

(a) Sensor placement (and access): for example, the need for specialized equipment to access certain parts of the structure (Figure 32.20)

(b) Wiring placement, or wireless relay placement if using a wireless sensor network

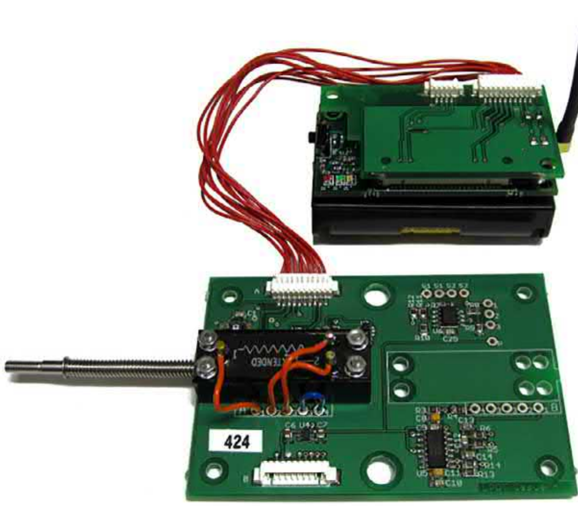

Figure 32.19 A wireless sensor "mote" connected to an LPDT displacement gauge.
Photo: Authors.

Figure 32.20 Installing wireless sensors on Hammersmith Flyover.
Photo: Authors.

Figure 32.21 Example of nonideal location for wireless sensors—pier pit at the Hammersmith Flyover, which flooded during remediation work, destroying some installed sensors.
Photo: Authors.

(c) Environmental considerations (indoor/outdoor, International Protection Marking (IP) rated enclosures): remember to expect the unexpected (Figure 32.21)

(d) Data-logger placement, communications (if remote access to data is required), power supply (backup batteries) (Figure 32.22)

Stajano et al. (2010) elucidated 19 key considerations that must be kept in mind when deploying a wireless sensor system (listed in Table 32.3) in relation to communications and security.

Figure 32.22 Data logger for wireless humidity sensors at Humber Bridge.
Photo: Authors.

5.3 Data quality

5.3.1 Reliability and robustness

Adequate redundancy must be provided if the data is to be relied upon to influence decisions concerning the safe operation of the bridge. An independent method of measurement should be installed to provide an alternative "check" of the measurement system e.g., installation of electrical resistance strain gauges or vibrating wire strain gauges to verify fiber optic strain measurements. There is also a need for the SHM system to be able to quickly notify the system operator of instances of failure of individual sensors or, indeed, of the entire system.

5.3.2 Accuracy and resolution

The accuracy and resolution of analog sensors will often be determined by the analog-to-digital converter used to measure the output of the sensor, along with the characteristics of any filtering or signal conditioning circuits used. The way in which a sensor is packaged and attached to the structure will also have an effect. This means the system needs to be considered, not just the specification for the individual sensor devices.

5.4 Sensor calibration

It should be a condition of any SHM project that a sufficient, up-front investment be devoted to proving that all the equipment is appropriately calibrated and functioning. Some suppliers may provide calibration certificates for their sensors. If provided, these certificates should be kept as part of the documentation for the system. It should be established whether the calibration is for individual sensors or for a batch of similar

Table 32.3 Stajano et al.'s Principles for Successful WSNs

Principle	Description
1	Multidimensional optimization: you must choose a goal function
2	Planning for shortest deployment time: ensure the multi-hop network will achieve end-to-end connectivity within a reasonable time
3	Assume access time to the site will be limited: you must plan in advance where to put the nodes
4	Radio is like voodoo: it affects you even if you do not understand or believe it
5	Radio propagation modeling: to minimize the number of nodes to be deployed you need an accurate, efficient, and robust propagation model
6	Radio propagation measurements: you must calibrate your radio propagation model with physical measurements that can only be obtained on-site
7	Once a node's position is fixed and you experience fading, you must be able to overcome it
8	Risk assessment: you must talk to the stakeholders and find out what they want to protect
9	As far as sensor data is concerned, you should probably pay more attention to integrity and availability than to confidentiality
10	Your risk rating must be a function of the use to which the network will be put and of its side effects on the environment
11	You must assess whether a vulnerability of the wireless sensor network can be used to attack other networks connected to it
12	Evaluation: you must perform independent penetration testing of the COTS equipment you use, even if it claims to offer a "secure" mode of operation
13	Deployment in harsh environments: you must ensure your sensors keep working and do not fall off
14	If sensors that measure what you want do not exist, you must make your own
15	Sensor failures: you must be prepared for the unexpected to happen
16	You must be able to find out exactly what happened
17	You must think about what you're measuring and why
18	You must understand the end users and their workflow and find a way to present the data that makes sense to them
19	You must strive to preserve and present the spatial origin of the data

COTS, commercial-off-the-shelf.
Adapted with permission from Stajano et al. (2010). (Extracts reprinted from Ad Hoc Networks, Vol 8. No. 8, Stajano et al., Smart bridges, smart tunnels: Transforming wireless sensor networks from research prototypes into robust engineering infrastructure, 872–888, 2010, with permission from Elsevier.)

sensors. A guiding principle of SHM deployments should be that calibration studies form an integral part of the setting-up of a field deployment.

5.5 Future proofing

Future proofing is a popular topic amongst knowledge management professionals. An asset owner who undertakes SHM should remember that the specified system should (1) be maintainable, (2) be replaceable, (3) incorporate redundancy of sensors, and

(4) be aligned with well-maintained data storage protocols. This implies the need for digital archive maintenance to ensure against loss of data. Installation of SHM itself may be a form of future proofing; for example, it may be relatively inexpensive to embed fiber optic cables into a newly built concrete structure so that these can be used to measure the response to the structure to increased loading requirements in the future.

5.6 Data processing

Data from bridge monitoring systems is unlikely to be useful without a degree of processing to turn it into information that may be used by a bridge owner/operator to make operational decisions. At the simplest level, this data processing can be performed by a human. For example, a wind speed sensor on a long-span suspension bridge could be referred to directly by an operator in a control room to determine whether to close the bridge in high winds—usually by reference to a pre-agreed threshold. In this case, the only "processing" done is a simple *threshold check* on whether the wind speed exceeds a particular value. In general, however, automated processing by a computer will be required to convert data into usable information. It is imperative that there is some plan as to what is done with data collected—what decisions the data will be used to support. This will often guide the data processing requirements.

5.6.1 Data size and duality

Some processing may be required to reduce the size of the data prior to transmission to the owner/operator (see Vann et al., 1996 for discussion of 'intelligent logging' case studies including on-site filtering of data). For example, in the case of a monitoring system in a remote location with only a mobile broadband connection, the monthly bandwidth and total data allowance may be limited. In this case, processing to filter out irrelevant data points or outliers may be necessary at the monitoring system. Data compression can also be used to minimize the amount of data transmitted if the data is highly redundant such as comma separate value (CSV) files. Examples of filtering could include an accelerometer-based parapet collision or bridge strike detection system; it is important to read from the accelerometers at a rate that will ensure that any impact is not missed, but there is little point in transmitting accelerations below a threshold likely to be from an impact, other than when commissioning and calibrating the system.

5.6.2 Use of cloud services

Some infrastructure owning organizations may have the resources and expertise to run a high-availability computer system and network. Others may choose to outsource this to a cloud service provider. There are several subscription services available—such as Amazon Web Services, Microsoft Azure, or Google Cloud, which provide Internet-based computing and storage facilities. It is usually possible to scale up services with demand by buying additional credits. In the case of a bridge monitoring system, the computing resources required are unlikely to increase much over time; the number of sensors will generally remain constant. However, the storage requirements for the data collected will only ever increase over time unless a decision is taken to remove data no longer considered useful.

Some monitoring solution vendors may provide a cloud-based system and dashboard intended for use only with their sensor systems, while others provide services that may be used with any sensor system via an open application programming interface (API). Examples of specialist sensor-optimized cloud services include SensorCloud and ThingsBoard. Some issues to consider when choosing between a generic cloud service, a sensor-application cloud service, and locally based computing solutions are the following:

- Local resources (people, hardware, and communications infrastructure) necessary to run a locally based solution.
- Service Level Agreements (SLAs) of the various cloud services. How secure is the data? Is it backed up? How long is it kept in the event of an administrative error (such as failing to pay the subscription)? How likely is the service provider to still be in business in a year? In two years?
- Subscription costs. Is the subscription charged per sensor, per data point, or per megabyte? Is it charged by computation hour? Is data transmission (both in and out) of the service charged separately to data storage?
- What services are provided? (A time-series database? Or a dashboard visualization?)
- Finally, consider how costly it would be to switch to another provider. Is there an element of vendor "lock-in"?

5.6.3 Model-based versus model-free analysis

In many monitoring situations, a simple threshold check alarm is sufficient, and for some anomaly detection systems, a simple time-based chart visualization is likely to be sufficient to be able to show a trend in an undesirable direction. More sophisticated systems that attempt to perform model validation and damage detection will require additional computing resources and structural engineering and computing expertise.

Model-based systems

Model-based structural health monitoring systems will use some underlying physics-based model of the bridge, such as a finite element or grillage analysis model—sometimes to predict the response of the bridge to certain expected in-service conditions, such as wind loading, traffic loading, and temperature. Data from the monitoring system may be used to refine assumed values for loadings, and the results of the analysis model are compared against the measured response. The parameters of the model are then updated, and the simulation is rerun until the response of the model is close to that of the real structure. The extent to which the parameters need to be adjusted will determine whether the original analysis model gives a reasonably realistic prediction of behavior and could be considered a "valid" model. Some systems go a stage further. If the measured values from the monitoring system start to differ significantly from those predicted by the (updated) model, then individual parameters—each corresponding to a particular structural element on the bridge—may be adjusted in an attempt to predict the location or any damage. Significant computational resources may be required to continually run analysis models of the bridge for each new set of data points—potentially multiple times—to discover which model parameters are most likely to no longer be representative of the real structure.

Model-free systems

The difficulty and complexity of first creating and then continually updating a physics-based model of the bridge have resulted in an alternative approach. In model-free systems, data collected from the monitoring system is processed using one or more statistical or artificial intelligence techniques to identify sets of data that deviate from the expected response of the structure.

6. Summary

This chapter has summarized some of the practical considerations that bridge engineers need to consider when specifying, installing, and operating SHM systems. A key requirement for a successful SHM program is that a clear idea of what data is required for decision making is known up front. Ensuring that the specified system can produce data of sufficient quality that will allow for decisions to be taken will assist in making the case for monitoring.

6.1 Future industry directions

SHM is becoming standard on many large-span, newly constructed bridges (Hussain et al., 2010). Additionally, SHM is often commissioned when a specific problem identified on an existing bridge requires investigation e.g., the AE monitoring on Hammersmith Flyover (Webb et al., 2014). In the future, industry best-practice guides detailing how to specify, install, manage the data, and, most importantly, use it to make engineering decisions will need to emerge (see the sample monitoring specifications included in Middleton et al., 2016).

6.2 Future research directions

There remains considerable scope for improving the ability for bridge engineers to model, predict, detect, and quantify the location, extent, and rate of deterioration of bridges resulting from mechanisms of deterioration or damage such as corrosion, fatigue, and scour. Increased focus should also be given to developing and using better techniques for reliably determining the actual loading on the bridge (real-time load evaluation), the available additional load-carrying capacity (or margin of capacity), and, finally, the residual life of the bridge, so that transport corridors can be more effectively utilized and managed. Many studies on damage detection in the literature focus on numerical modeling and laboratory experiments, whereas more practical field demonstrations on bridges are necessary for the advancement of bridge monitoring techniques (An et al., 2019; Casas and Moughty, 2017).

There has been substantial progress made in bridge monitoring, especially in the categories of (1) anomaly detection, (2) sensor deployment studies, (3) model validation, and (4) threshold check-based studies but less in the category of (5) damage detection. As damage detection is one of the crucial capabilities required by bridge managers to safeguard their bridge assets, there is a need and scope for improvement in bridge damage detection SHM systems and scope for incorporation of machine learning and digital twin technologies to complement bridge monitoring systems (Ali and Cha, 2019; Moughty and Casas, 2017; Nguyen et al., 2019; Sofia et al., 2020).

Acknowledgments

The authors would like to acknowledge Kevin Dentith from the Devon County Council and Andrew Young from the West Somerset Railway for facilitating the field tests on Exe North Bridge and Mineral Line Bridge. Additionally, the authors also wish to thank the Vibration Engineering Section (VES) research group at the University of Exeter and Full-Scale Dynamics Limited Company for their support of the work. The authors also thank Prof. James Brownjohn (University of Exeter), Prof. Eugene O'Brien (University College Dublin), Dr. David Hester (Queens University Belfast), Karen Faulkner (University of Exeter), and Nick Trump (University of Exeter) for their support. Authors would like to gratefully acknowledge the partners and funders of Baildon Bridge scour monitoring project, Bradford Metropolitan Council, Gaist Solutions, TMS Maritime Ltd., Centre for Smart Infrastructure and Construction, Laing O'Rourke Centre, and Gates Cambridge Foundation with special thanks to Naveed Anwar, Jenny Roberts, and TMS scour repair team for their help at various stages of this project.

References

Agrawal, A.K., Yi, Z., Alampalli, S., Ettourney, M., King, L., Hui, K., Patel, M., 2009. Remote corrosion monitoring systems for highway bridges. Pract. Period. Struct. Des. Constr. 14 (4), 152–158. https://doi.org/10.1061/(ASCE)1084-0680(2009)14:4(152).

Ali, R., Cha, Y.J., 2019. Subsurface damage detection of a steel bridge using deep learning and uncooled micro-bolometer. Constr. Build. Mater. 226, 376–387. https://doi.org/10.1016/j.conbuildmat.2019.07.293.

An, Y., Chatzi, E., Sim, S., Laflamme, S., Blachowski, B., Ou, J., 2019. Recent progress and future trends on damage identification methods for bridge structures. Struct. Control Health Monit. 26 (10). https://doi.org/10.1002/stc.2416, e2416.

Andersen, J.E., Vesterinen, A., 2006. Structural Health Monitoring Systems. COWI Futuretec. Available from: http://www.shms.dk/COWI_ISBN-87-91044-04-9.pdf. (Accessed 14 January 2021).

Anderson, N.L., Ahmed, M.I., Thitimakorn, T., 2007. Ground-penetrating radar: a tool for monitoring bridge scour. Environ. Eng. Geosci. 13 (1), 1–10. https://doi.org/10.2113/gseegeosci.13.1.1.

Bennetts, J., 2019. The Management of Bridges (Eng.D. thesis). University of Bristol, Bristol, UK.

Bennetts, J., Webb, G., Denton, S., Vardanega, P.J., Loudon, N., 2018. Quantifying uncertainty in visual inspection data. In: Powers, N., Frangopol, D.M., Al-Mahaidi, R., Capriani, C. (Eds.), Maintenance, Safety, Risk, Management and Life-Cycle Performance of Bridges: Proceedings of the Ninth International Conference on Bridge Maintenance, Safety and

Management (IABMAS 2018), 9–13 July 2018, Melbourne, Australia. CRC Press/ Balkema, Leiden, The Netherlands, pp. 2252–2259.

Bennetts, J., Vardanega, P.J., Taylor, C.A., Denton, S.R., 2020. Survey of the use of data in UK bridge asset management. Proc. Inst. Civ. Eng. Bridge Eng. 173 (4), 211–222. https://doi.org/10.1680/jbren.18.00050.

Bennetts, J., Denton, S.R., Webb, G.T., Nepomuceno, D.T. & Vardanega, P.J. (2021). Looking to the future of bridge inspection and management in the UK. In: Bridge Maintenance, Safety, Management, Life-Cycle Sustainability and Innovations: Proceedings of the Tenth International Conference on Bridge Maintenance, Safety and Management (IABMAS 2020), Sapporo, Japan, 11-15 April 2021 (Yokota, H. & Frangopol, D.M. (eds.)). CRC Press/Balkema Taylor & Francis Group, The Netherlands, pp. 3858–3866. https://doi.org/10.1201/9780429279119-526.

Briaud, J., Hurlebaus, S., Chang, K., Yao, C., Sharma, H., Yu, O., Darby, C., Hunt, B.E., Price, G.R., 2011. Realtime monitoring of bridge scour using remote monitoring technology. Report 0-6060-1, Austin, TX, USA. Available from: https://static.tti.tamu.edu/tti.tamu.edu/documents/0-6060-1.pdf. (Accessed 14 January 2021).

Brownjohn, J.M.W., Lee, J., Cheong, B., 1999. Dynamic performance of a curved cable-stayed bridge. Eng. Struct. 21 (11), 1015–1027. https://doi.org/10.1016/S0141-0296(98)00046-7.

Budelmann, H., Holst, A., Wichmann, H.J., 2014. Non-destructive measurement toolkit for corrosion monitoring and fracture detection of bridge tendons. Struct. Infrastruct. Eng. 10 (4), 492–507. https://doi.org/10.1080/15732479.2013.769009.

Cantero, D., González, A., 2015. Bridge damage detection using weigh-in-motion technology. J. Bridge Eng. 20 (5). https://doi.org/10.1061/(ASCE)BE.1943-5592.0000674, 04014078.

Casas, J.R., Moughty, J.J., 2017. Bridge damage detection based on vibration data: past and new developments. Front. Built Environ. 3. https://doi.org/10.3389/fbuil.2017.00004, 4.

Çatbaş, F.N., Kijewski-Correa, T., Aktan, A.E. (Eds.), 2013. Structural Identification of Constructed Systems: Approaches, Methods, and Technologies for Effective Practice of St-Id. American Society of Civil Engineers, Reston, VA, USA.

Chang, S.P., Im, C.K., 2000. Thermal behavior of composite box-girder bridges. Proc. Inst. Civ. Eng. Struct. Build. 140 (2), 117–126. https://doi.org/10.1680/stbu.2000.140.2.117.

Cusson, D., Ozkan, I.F., 2019. Satellite-based InSAR monitoring –validation on Victoria Bridge in Montreal, Canada. In: SMAR 2019 – Proceedings of the Fifth Conference on Smart Monitoring, Potsdam, Germany. Available from: https://www.ndt.net/article/smar2019/papers/We.4.D.6.pdf. (Accessed 14 January 2021).

DiBiagio, E., 2003. A case study of vibrating-wire sensors that have vibrated continuously for 27 years. In: Myrvoll, F. (Ed.), Field Measurements in Geomechanics, Proceedings of the 6th International Symposium, Oslo, Norway, 23–26 September 2003. Taylor & Francis, London, UK, pp. 445–458.

Döhler, M., Hille, F., Mevel, L., Rücker, W., 2014. Structural health monitoring with statistical methods during progressive damage test of S101 Bridge. Eng. Struct. 69, 183–193. https://doi.org/10.1016/j.engstruct.2014.03.010.

Dunnicliff, J., (with the assistance of Green, G. E.) 1988. Geotechnical Instrumentation for Monitoring Field Performance. John Wiley & Sons, USA.

Elsaid, A.H., Seracino, R., 2012. Vibration based damage detections of scour in coastal bridges. Homeland Secur. Aff. Suppl 4 (2). Available from: https://www.hsaj.org/articles/212. (Accessed 14 January 2021).

Elsener, B., 2005. Long-term monitoring of electrically isolated post-tensioning tendons. Struct. Concr. 6 (3), 101–106.

Falco, F.D., Mele, R., 2002. The monitoring of bridges for scour by sonar and sedimetri. NDT&E Int. 35, 117–123. https://doi.org/10.1016/S0963-8695(01)00031-7.

Farrar, C.R., Baker, W.E., Bell, T.M., Cone, K.M., Darling, T.W., Duffey, T.A., Eklund, A., Migliori, A., 1994. Dynamic characterization and damage detection in the I-40 bridge over the Rio Grande (Technical report). Los Alamos National Lab, California, USA, https://doi.org/10.2172/10158042.

Faulkner, K., Huseynov, F., Brownjohn, J., Xu, Y., 2018. Deformation monitoring of a simply supported railway bridge under varying dynamic loads. In: Powers, N., Frangopol, D.M., Al-Mahaidi, R., Capriani, C. (Eds.), Maintenance, Safety, Risk, Management and Life-Cycle Performance of Bridges: Proceedings of the Ninth International Conference on Bridge Maintenance, Safety and Management (IABMAS 2018), 9–13 July 2018, Melbourne, Australia. CRC Press/Balkema, Leiden, The Netherlands, pp. 1484–1491.

Faulkner, K., Brownjohn, J.M.W., Wang, Y., Huseynov, F., 2020. Tracking bridge tilt behavior using sensor fusion techniques. J. Civ. Struct. Heal. Monit. 10 (4), 543–555. https://doi.org/10.1007/s13349-020-00400-9.

Fitzgerald, P.C., Malekjafarian, A., Cantero, D., Obrien, E.J., Prendergast, L.J., 2019. Drive-by scour monitoring of railway bridges using a wavelet-based approach. Eng. Struct. 191, 1–11. https://doi.org/10.1016/j.engstruct.2019.04.046.

Gastineau, A., Johnson, T., Schultz, A., 2009. Bridge health monitoring and inspections – a survey of methods. Minnesota Department of Transportation. Report No. MN/RC 2009-29., p. 194. Available from: http://www.lrrb.org/pdf/200929.pdf. (Accessed 14 January 2021).

Graybeal, B., Phares, B., Rolander, D., Moore, M., Washer, G., 2002. Visual inspection of highway bridges. J. Nondestruct. Eval. 21 (3), 67–83. https://doi.org/10.1023/A:1022508121821.

Gunner, S., Vardanega, P.J., Tryfonas, T., Macdonald, J.H.G., Wilson, R.E., 2017. Rapid deployment of a WSN on the Clifton Suspension Bridge, UK. Proc. Inst. Civ. Eng. Smart Infrastruct. Constr. 170 (3), 59–71. https://doi.org/10.1680/jsmic.17.00014.

Helmi, K., Taylor, T., Zarafshan, A., Ansari, F., 2015. Reference free method for real time monitoring of bridge deflections. Eng. Struct. 103, 116–124. https://doi.org/10.1016/j.engstruct.2015.09.002.

Hester, D., Brownjohn, J., Huseynov, F., Obrien, E., Gonzalez, A., Casero, M., 2020. Identifying damage in a bridge by analysing rotation response to a moving load. Struct. Infrastruct. Eng. 16 (7), 1050–1065. https://doi.org/10.1080/15732479.2019.1680710.

Hou, X., Yang, X., Huang, Q., 2005. Using inclinometers to measure bridge deflection. J. Bridge Eng. 10 (5), 564–569. https://doi.org/10.1061/(ASCE)1084-0702(2005)10:5(564).

Hoult, N.A., Fidler, P.R.A., Wassell, I.J., Hill, P.G., Middleton, C.R., 2008. Wireless structural health monitoring at the Humber Bridge UK. Proc. Inst. Civil Eng. Bridge Eng. 161 (4), 189–195. https://doi.org/10.1680/bren.2008.161.4.189.

Hoult, N.A., Bennett, P.J., Middleton, C.R., Soga, K., 2009. Distributed fiber optic strain measurements for pervasive monitoring of civil infrastructure. In: Proceedings 4th International Conference on Structural Health Monitoring of Intelligent Infrastructure (SHMII-4), 22nd to 24th July 2009, Zurich, Switzerland.

Hoult, N.A., Fidler, P.R.A., Hill, P.G., Middleton, C.R., 2010. Long-term wireless structural health monitoring of the Ferriby Road Bridge. J. Bridge Eng. 15 (2), 153–159. https://doi.org/10.1061/(ASCE)BE.1943-5592.0000049.

Huseynov, F., Brownjohn, J.M.W., O'Brien, E.J., Hester, D., 2017. Analysis of load test on composite I-girder bridge. J. Civ. Struct. Health Monit. 7 (2), 163–173. https://doi.org/10.1007/s13349-017-0223-x.

Huseynov, F., O'Brien, E., Brownjohn, J., Faulkner, K., Xu, Y., Hester, D., 2019. Monitoring crack movement on a masonry type abutment using optical camera system—a case study.

In: Proceedings of the 6th International Symposium on Life-Cycle Civil Engineering (IALCEE 2018), pp. 28–31.

Huseynov, F., Kim, C., OBrien, E.J., Brownjohn, J.M.W., Hester, D., Chang, K.C., 2020. Bridge damage detection using rotation measurements – experimental validation. Mech. Syst. Signal Process. 135. https://doi.org/10.1016/j.ymssp.2019.106380, 106380.

Hussain, N., Falbe-Hansen, K., Kite, S. (Eds.), 2010. Stonecutters Bridge Hong Kong: Design and Construction. Arup & COWI, Hong Kong.

Kariyawasam, K.K.G.K.D., 2020. A Vibration-Based Bridge Scour Monitoring Technique (Ph.D. thesis). University of Cambridge, Cambridge, UK, https://doi.org/10.17863/CAM.58843.

Kariyawasam, K., Fidler, P., Talbot, J., Middleton, C., 2019a. Field assessment of ambient vibration-based bridge scour detection. In: Structural Health Monitoring 2019. Stanford, CA, USA, pp. 374–381, https://doi.org/10.12783/shm2019/32137.

Kariyawasam, K., Fidler, P., Talbot, J., Middleton, C., 2019b. Field deployment of an ambient vibration-based scour monitoring system at Baildon Bridge, UK. In: Proceedings of the International Conference on Smart Infrastructure and Construction. ICE UK, Cambridge, UK, pp. 711–719, https://doi.org/10.1680/icsic.64669.711.

Kariyawasam, K., Middleton, C., Madabhushi, G., Haigh, S., Talbot, J.P., 2020. Assessment of bridge natural frequency as an indicator of scour using centrifuge modelling. J. Civ. Struct. Heal. Monit. 10 (5), 861–881. https://doi.org/10.1007/s13349-020-00420-5.

Kim, J.T., Yun, C.-B., Yi, J., 2003. Temperature effects on modal properties and damage detection in plate-girder bridges. KSCE J. Civ. Eng. 7 (6), 725–733. https://doi.org/10.1007/BF02829141.

Ko, Y.Y., Lee, W.F., Chang, W.K., Mei, H.T., Chen, C.H., 2010. Scour evaluation of bridge foundations using vibration measurement. In: 5th International Conference on Scour and Erosion (ICSE-5). ASCE, CA, USA, pp. 884–893, https://doi.org/10.1061/41147(392)88.

Koo, K.Y., Brownjohn, J.M.W., List, D.I., Cole, R., 2013. Structural health monitoring of the Tamar suspension bridge. Struct. Control. Health Monit. 20 (4), 609–625. https://doi.org/10.1002/stc.1481.

Lea, F.C., 2005. Uncertainty in Condition and Strength Assessment of Reinforced Concrete Bridges (Ph.D. thesis). University of Cambridge, Cambridge, UK.

Lee, C., Take, W.A., Hoult, N.A., 2012. Optimum accuracy of two-dimensional strain measurements using digital image correlation. J. Comput. Civ. Eng. 26 (6), 795–803. https://doi.org/10.1061/(ASCE)CP.1943-5487.0000182.

Lynch, J.P., Wang, Y., Loh, K.J., Yi, J.-H., Yun, C.-B., 2006. Performance monitoring of the Geumdang Bridge using a dense network of the high-resolution wireless sensors. Smart Mater. Struct. 15 (6), 1561–1575. https://doi.org/10.1088/0964-1726/15/6/008.

Magalhães, F., Cunha, Á., Caetano, E., 2009. Online automatic identification of the modal parameters of a long span arch bridge. Mech. Syst. Signal Process. 23 (2), 316–329. https://doi.org/10.1016/j.ymssp.2008.05.003.

Matsumoto, Y., Yamaguchi, H., Yoshioka, T., 2010. A field investigation of vibration-based structural health monitoring in a steel truss bridge. In: Proceedings of the IABSE-JSCE Joint Conference on Advances in Bridge Engineering-II, pp. 8–10.

Middleton, C., 2004. Bridge management and assessment in the UK. In: Proceedings of the Austroads 2004 Bridge Conference: Bridges Another Dimension. Austroads, Sydney, NSW, Australia. Available from: http://www.bridgeforum.org/files/pub/2004/austroads5/Middleton%20keynote.pdf. (Accessed 14 January 2021).

Middleton, C., Vardanega, P., Webb, G., Fidler, P., 2014. Smart infrastructure – are we delivering on the promise? In: Proceedings 6th Australian Small Bridges Conference, Sydney, Australia, 27th to 28th May 2014., https://doi.org/10.13140/RG.2.1.1463.5288.

Middleton, C.R., Fidler, P.R.A., Vardanega, P.J., 2016. Bridge Monitoring: A practical guide. ICE Publishing, London, UK.

Minardo, A., Bernini, R., Amato, L., Zeni, L., 2012. Bridge monitoring using Brillouin fiber-optic sensors. IEEE Sensors J. 12 (1), 145–150. https://doi.org/10.1109/JSEN.2011.2141985.

Moore, M., Phares, B., Graybeal, B., Rolander, D., Washer, G., 2001. Reliability of visual inspection for highway bridges, vol. 1. US Department of Transportation, Federal Highway Administration, Washington, United States. Report no. FHWA-RD-01-020. Available from: http://www.fhwa.dot.gov/publications/research/nde/01020.cfm. (Accessed 14 January 2021).

Moreu, F., Kim, R.E., Spencer, B.F., 2017. Railroad bridge monitoring using wireless smart sensors. Struct. Control Health Monit. 24 (2). https://doi.org/10.1002/stc.1863, e1863.

Moughty, J.J., Casas, J.R., 2017. A state of the art review of modal-based damage detection in bridges: development, challenges, and solutions. Appl. Sci. 7 (5), 510. https://doi.org/10.3390/app7050510.

Nair, A., Cai, C.S., 2010. Acoustic emission monitoring of bridges: review and case studies. Eng. Struct. 32 (6), 1704–1714. https://doi.org/10.1016/j.engstruct.2010.02.020.

Nguyen, D.H., Bui, T.T., Roeck, G.D., Wahab, M.A., 2019. Damage detection in Ca-non bridge using transmissibility and artificial neural networks. Struct. Eng. Mech. 71 (2), 175–183. https://doi.org/10.12989/sem.2019.71.2.175.

Park, H.S., Lee, H.M., Adeli, H., Lee, I., 2007. A new approach for health monitoring of structures: terrestrial laser scanning. Comput. Aided Civ. Infrastrut. Eng. 22 (1), 19–30. https://doi.org/10.1111/j.1467-8667.2006.00466.x.

Peeters, B., De Roeck, G., 2001. One-year monitoring of the Z24-bridge: environmental effects versus damage events. Earthq. Eng. Struct. Dyn. 30 (2), 149–171. https://doi.org/10.1002/1096-9845(200102)30:2<149::AID-EQE1>3.0.CO;2-Z.

Perenchio, W.F., 1989. The condition survey. Concr. Int. 11 (1), 59–62.

Prendergast, L.J., Gavin, K., 2014. A review of bridge scour monitoring techniques. J. Rock Mech. Geotech. Eng. 6 (2), 138–149. https://doi.org/10.1016/j.jrmge.2014.01.007.

Prendergast, Hester, D., Gavin, K., 2016. Determining the presence of scour around bridge foundations using vehicle-induced vibrations. J. Bridge Eng. 21 (10). https://doi.org/10.1061/(ASCE)BE.1943-5592.0000931, 04016065.

Psimoulis, P.A., Stiros, S.C., 2013. Measuring deflections of a short-span railway bridge using a robotic total station. J. Bridge Eng. 18 (2), 182–185. https://doi.org/10.1061/(ASCE)BE.1943-5592.0000334.

Riveiro, B., Morer, P., Arias, P., Arteaga, I.D., 2011. Terrestrial laser scanning and limit analysis of masonry arch bridges. Constr. Build. Mater. 25 (4), 1726–1735. https://doi.org/10.1016/j.conbuildmat.2010.11.094.

Rodrigues, C., Félix, C., Lage, A., Figueiras, J., 2010. Development of a long-term monitoring system based on FBG sensors applied to concrete bridges. Eng. Struct. 32 (8), 1993–2002. https://doi.org/10.1016/j.engstruct.2010.02.033.

Sarwar, M.Z., Park, J.W., 2020. Bridge displacement estimation using a co-located acceleration and strain. Sensors 20 (4). https://doi.org/10.3390/s20041109, 1109.

Selvakumaran, S., Plank, S., Geiß, C., Rossi, C., Middleton, C., 2018. Remote monitoring to predict bridge scour failure using interferometric synthetic aperture radar (InSAR) stacking techniques. Int. J. Appl. Earth Obs. Geoinf. 73, 463–470. https://doi.org/10.1016/j.jag.2018.07.004.

Sofia, H., Anas, E., Faiz, O., 2020. Mobile mapping, machine learning and digital twin for road infrastructure monitoring and maintenance: case study of Mohammed VI Bridge in Morocco. In: IEEE International Conference of Moroccan Geomatics, Casablanca, Morocco., https://doi.org/10.1109/Morgeo49228.2020.9121882.

Sony, S., Laventure, S., Sadhu, A., 2019. A literature review of next-generation smart sensing technology in structural health monitoring. Struct. Control Health Monit. 26 (3). https://doi.org/10.1002/stc.2321, e2321.

Sreeshylam, P., Ravisankar, K., Parivallal, S., Kesavan, K., Sridhar, S., 2008. Condition monitoring of prestressed concrete structures using vibrating wire sensors. Int. J. COMADEM 11 (3), 46–54.

Stajano, F., Hoult, N., Wassell, I., Bennett, P., Middleton, C.R., Soga, K., 2010. Smart bridges, smart tunnels: transforming wireless sensor networks from research prototypes into robust engineering infrastructure. Ad Hoc Netw. 8 (8), 872–888. https://doi.org/10.1016/j.adhoc.2010.04.002.

Staquet, S., Kalogiannakis, G., Detandt, H., Van Hemelrijck, D., Epsion, B., 2007. Field testing of a 30-year-old composite Preflex railway bridge. Proc. Inst. Civ. Eng. Bridge Eng. 160 (2), 89–98. https://doi.org/10.1680/bren.2007.160.2.89.

Vann, A.M., Cairns, J., Davis, J.P., Linfoot, B.T., 1996. Intelligent logging strategies for civil engineering applications. Proc. Inst. Civil Eng. Struct. Build. 116 (2), 194–203. https://doi.org/10.1680/istbu.1996.28287.

Wang, M., 2004. Embedded Strain Sensor with Power Scavenging from Bridge Vibration (Masters thesis). University of Maryland, MD, USA.

Wardhana, K., Hadipriono, F.C., 2003. Analysis of recent bridge failures in the United States. J. Perform. Constr. Facil. 17 (3), 144–150. https://doi.org/10.1061/(ASCE)0887-3828(2003)17:3(144).

Washer, G., Fenwick, R., Bolleni, N., 2010. Effects of solar loading on infrared imaging of subsurface features in concrete. J. Bridge Eng. 15 (4), 384–390. https://doi.org/10.1061/(ASCE)BE.1943-5592.0000117.

Watson, J., 2010. Watching brief. Bridge Des. Eng. 60. August.

Webb, G., 2014. Structural Health Monitoring of Bridges (Ph.D. thesis). University of Cambridge, Cambridge, UK.

Webb, G.T., Vardanega, P.J., Fidler, P.R.A., Middleton, C.R., 2014. Analysis of structural health monitoring data from Hammersmith flyover. J. Bridge Eng. 19 (6). https://doi.org/10.1061/(ASCE)BE.1943-5592.0000587, 05014003.

Webb, G.T., Vardanega, P.J., Middleton, C.R., 2015. Categories of SHM deployments: technologies and capabilities. J. Bridge Eng. 20 (11). https://doi.org/10.1061/(ASCE)BE.1943-5592.0000735, 04014118.

Webb, G.T., Vardanega, P.J., Hoult, N.A., Fidler, P.R.A., Bennett, P.J., Middleton, C.R., 2017. Analysis of fiber-optic strain-monitoring data from a prestressed concrete bridge. J. Bridge Eng. 22 (5). https://doi.org/10.1061/(ASCE)BE.1943-5592.0000996, 05017002.

Wenzel, H., 2009. Health Monitoring of Bridges. John Wiley, USA, ISBN: 9780470031735, https://doi.org/10.1002/9780470740170.

White, D.J., Take, W.A., Bolton, M.D., 2003. Soil deformation measurement using particle image velocimetry (PIV) and photogrammetry. Geotechnique 53 (7), 619–631. https://doi.org/10.1680/geot.2003.53.7.619.

Wong, K.Y., 2004. Instrumentation and health monitoring of cable-supported bridges. Struct. Control. Health Monit. 11 (2), 91–124. https://doi.org/10.1002/stc.33.

Yu, Y., Cai, C.S., Deng, L., 2016. State-of-the-art review on bridge weigh-in-motion technology. Adv. Struct. Eng. 19 (9), 1514–1530. https://doi.org/10.1177/1369433216655922.

Yuyama, S., Yokoyama, K., Niitani, K., Ohtsu, M., Uomoto, T., 2007. Detection and evaluation of failures in high-strength tendon of prestressed concrete bridges by acoustic emission. Constr. Build. Mater. 21 (3), 491–500. https://doi.org/10.1016/j.conbuildmat.2006.04.010.

Zhang, L., Haas, C., Tighe, S.L., 2007a. Evaluating weigh-in-motion sensing technology for traffic data collection. In: 2007 Annual Conference and Exhibition of the Transportation

Association of Canada: Transportation – An Economic Enabler (Les Transports: Un Levier Economique), (14–17 October 2007) Saskatoon Saskatchewan, Canada. Transportation Association of Canada. Available from: http://conf.tac-atc.ca/english/resourcecentre/readingroom/conference/conf2007/docs/s15/zhang.pdf. (Accessed 14 January 2021).

Zhang, Y.H., Tubby, P.J., Allen, C., Mawella, J., 2007b. Evaluation of crack- first TM fatigue sensor. In: CF/DRDC International Defence Applications of Materials Meeting. Available from: http://www.twi-global.com/technical-knowledge/published-papers/evaluation-of-crackfirst-fatigue-sensors-june-2007/. (Accessed 14 January 2021).

Zhao, X., Liu, H., Yu, Y., Xu, X., Hu, W., Li, M., Ou, J., 2015. Bridge displacement monitoring method based on laser projection-sensing technology. Sensors 15 (4), 8444–8643. https://doi.org/10.3390/s150408444.

Zhi, X., Shalaby, A., Middleton, D., Clayton, A., 1999. Evaluation of weigh-in-motion in Manitoba. Can. J. Civ. Eng. 26 (5), 655–666. https://doi.org/10.1139/l99-025.

Application of fiber-reinforced polymers to reinforced concrete bridges

33

G. Hegemier[a] *and L. Stewart*[b]
[a]School of Civil and Environmental Engineering, Georgia Institute of Technology, Atlanta, GA, USA, [b]Department of Structural Engineering, Jacobs School of Engineering University of California, San Diego, La Jolla, CA, USA

1. Introduction

It is well known that the ductility and strength of concrete in certain regions of stress space (e.g., where the principal stresses are negative, such as compression), can be increased (the former, substantially) by the application of confining pressure (e.g., as measured by the average of the principal stresses; Mander et al., 1988a; Saatcioglu and Razvi, 1992; Xiao and Wu, 2000). This concept is reinforced by Figure 33.1, which displays the ratio of confined concrete compressive strength, f_{cc}, to the unconfined compressive strength, f'_c, for both steel and concrete jackets used as confining systems. It is also understood that concrete exhibits increased volume expansion, or dilatancy, as a stress point approaches the failure surface in such regions. Figure 33.2 shows where the volumetric strain, ε_V, is calculated with respect to the axial strain, ε_c and the lateral strain, ε_l, as given in Eq. (1) (Bezant and Kim, 1979; Vermeer and DeBorst, 1984). This phenomenon allows the passive generation of the confining pressure necessary to attain the desired strength and ductility by the application of an appropriate confining "jacket" to a reinforced concrete (r.c.) column.

$$\varepsilon_V = \varepsilon_c + 2\varepsilon_l \tag{1}$$

2. Jacket materials and processes

The jacket concept has been successfully utilized for the past three decades for both seismic and other load environments (e.g., blast) via a variety of jacket materials. The most common and widely used of which include steel and FRPs, in the form of carbon, glass, or aramid fiber-reinforced polymers (respectively, CFRP, GFRP, and AFRP). In the case of existing bridge or building structures, the jacket takes the form of a retrofit. For new constructions, it may consist of a stay-in-place form.

The FRP jackets, for retrofit purposes, are typically fabricated in the field using dry uniaxial fabrics and plant-manufactured uniaxial strips. The fabrics are saturated with a two-part epoxy system at the job site using such tools as a small saturation machine

Innovative Bridge Design Handbook. https://doi.org/10.1016/B978-0-12-823550-8.00034-2

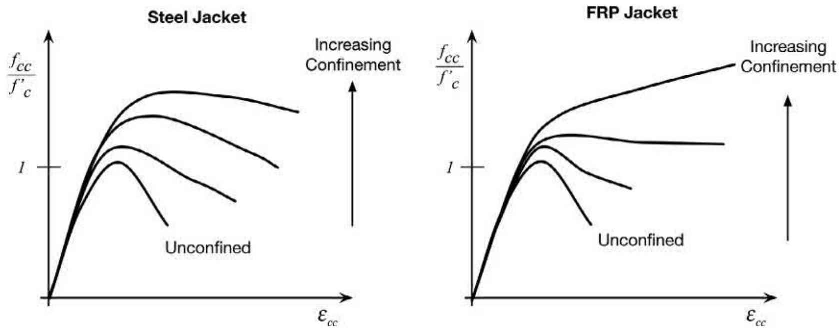

Figure 33.1 Influence of confinement on concrete response.

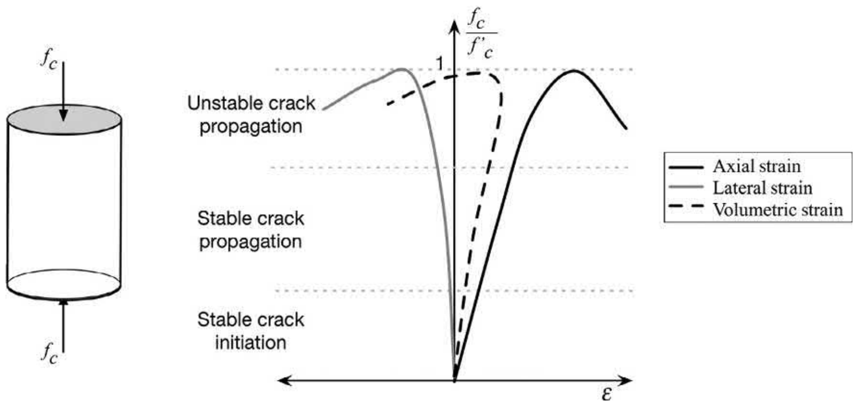

Figure 33.2 Concrete dilation under uniaxial compression.

(Bank, 2006; Mallick, 2007). Primer epoxy and other primer materials are placed to achieve appropriate surface preparation before the strips are applied with a technique similar to the application of wallpaper. The FRP/resin system is then subsequently cured under ambient conditions.

The resulting layer thickness is typically approximately 1–1.5 mm, and a jacket may consist of two to eight layers (or sometimes even more) and can be layered in both the axial (for flexural stiffness) and the hoop direction (for confinement) depending on the level of lateral force required. The strips are usually CFRP with high strength and stiffness, fabricated by pultrusion (or a related manufacturing method), and bonded to the column using an adhesive (Barbero, 1991). Typical strip geometries are in the 1-mm thickness and 5–10 cm width ranges, with lengths adjusted as necessary. The epoxy/adhesive chemistries for such field operations are adjusted for expected local temperature and humidity in an effort to obtain a proper cure (e.g., a desired glass transition temperature, T_g) and a sufficient resin workability time. Depicted in Figure 33.3a is an example jacket design for blast and seismic retrofit, based on the use of fabrics and strips (Hegemier et al., 2007).

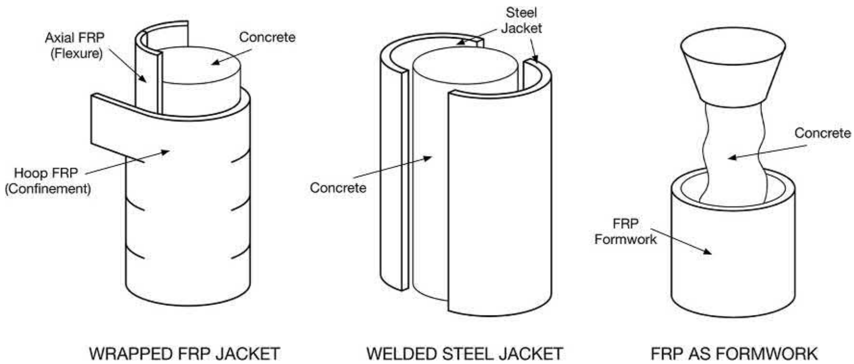

Figure 33.3 Illustration of FRP jacket techniques: FRP wrap, steel jacket, and FRP jacket as stay-in-place formwork.

In contrast to the fabrication of FRP jackets, steel jackets (Figure 33.3) are typically fabricated from two half shells or additional segments that are welded together at the site along two seams. Since the segments do not conform to the column surface, they are positioned with a small standoff from the column and a small gap is typically present. The gap is subsequently filled with a grout or similar material (Priestley et al., 1994; Ramirez et al., 1997).

For new construction, the FRP jacket can be applied as a stay-in-place form, which is plant-manufactured. This may be accomplished by *wet winding* or by methods such as vacuum assisted resin transfer molding (VARTM) (Rigas et al., 2001). In the former case, an epoxy resin system is typically used; in the latter, the resin system may be expanded to include vinylesters and polyesters depending upon the fiber system employed. In both methods, fabrication may include a low temperature post-cure.

3. Advantages of fiber-reinforced polymer systems (FRPS)

FRP systems have been used in practice over the course of the past three decades because under many circumstances, they can offer significant performance, economic, and aesthetic advantages over other materials (such as steel) for many applications.

With respect to performance, the anisotropic nature of FRPs allows the tailoring of jacket mechanical properties (Reddy, 1987; Pipes and Pagano, 1970) to a given design objective. For example, with the use of FRPs rather than steel, which is isotropic, one can create confinement (and hence column ductility) without considerably increasing the overall bending stiffness of a column (which can attract additional load for certain events, such as seismic events). This can be accomplished by fabricating a jacket with reinforcing fibers only in the circumferential (hoop) direction. On the other hand, additional flexural strength can be obtained by adding longitudinal fibers to the jacket design using unidirectional fabric or premanufactured unidirectional FRP strips, if needed.

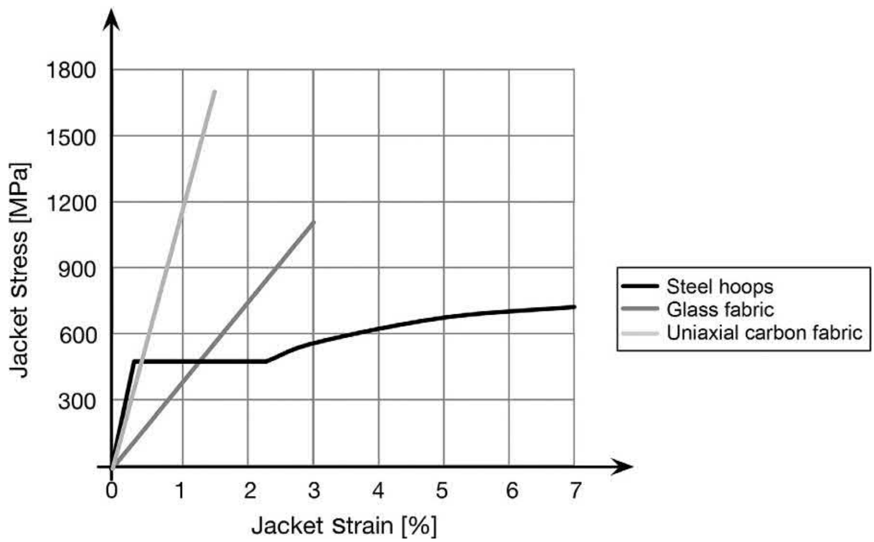

Figure 33.4 Idealized confining pressure for steel and composite jacket materials.

Other performance differences between steel and FRPs exist due to the inelastic, ductile behavior of steel. For example, since FRPs are essentially elastic to failure in direct tension along the fiber direction, the confining pressure associated with FRP jackets continues to increase with concrete deformation, whereas the confinement pressure essentially reaches a peak as a steel jacket enters the plastic state (as shown in Figure 33.4). This leads to eventual strain softening for steel, whereas FRP wraps of sufficient thickness and stiffness will exhibit strain hardening up to a failure.

In addition to short-term mechanical properties, FRPs such as CFRP offer considerable resistance to corrosion and advantageous long-term durability under a wide variety of environmental conditions. Durability data are available from experiments on various materials, which were conducted by Karbhari and Engineer (1996), Karbhari et al. (1997), Karbhari et al. (2003), Karbhari (2007).

With respect to economics, the use of FRPs can lead to much shorter application times than those for steel. Thus, even with the use of carbon fiber, the reduced labor costs can, depending on location, result in a lower overall system cost. In addition, whereas a constant jacket thickness with a lower bound is typically used for steel jackets for to constructability reasons, the thickness distribution of an FRP jacket is easily optimized for minimum cost for a given performance objective.

Finally, with respect to aesthetics, typically the use of FRPs will not alter the basic architecture of a column since the jacket generally conforms to the original geometry and the jacket thickness required is usually quite small (Hegemier et al., 2007).

4. Performance—Columns

In what follows, a number of data samples are presented in an effort to demonstrate the efficacy of the FRP jacketing concept for retrofit (Section 4.1), repair (Section 4.2), and new construction (Section 4.3). In an effort to avoid scaling issues, the discussion is restricted to large or full-scale tests. The summary includes results from USCD Powell Laboratory tests conducted since the mid-1990s. Since then, there have been a multitude of experiments considered by researchers all over the world studying the effects of FRP jacketing and all its intricacies in great detail (e.g., Mirmiran et al., 1998; Parvin and Wang, 2001; Rochette and Labossiere, 2000; Xiao and Rui, 1997; Nanni and Norris, 1995; Monti et al., 2001; Pantazopoulou et al., 2001).

4.1 Laboratory tests—Seismic retrofit

Experiments were developed and conducted by Seible et al. (1997a) for the retrofit of pre-1971-design rectangular and circular 40% scale bridge columns subject to combined axial and hysteretic lateral (simulated seismic) loads. The experiments studied three main seismic retrofits as they pertained to shear, plastic hinge development and lap-splice clamping. The shear retrofits consisted of wraps of three thicknesses, localizing the thickest regions towards the connection (i.e., the location with maximum shear). The flexural retrofits for the case with single bending also used three varying thicknesses, localized in the location of plastic hinge development. Finally, the lap-splice retrofit included the jacket only at the local connection over the lap. The results for the three series of tests are given in Figure 33.5, with drawings of the specimens tested and respective force-displacement curves. It can be seen that the application of confining pressures, both with CFRP and steel jackets, can lead to large increases in the ductility of the bridge column.

FRP jacket design criteria for various column failure modes were originally proposed by researchers at the University of California, San Diego (UCSD), and are described in Seible et al. (1995a, 1997b) and Inmamorato et al. (1995, 1996), along with detailed examples of their applications to retrofits of columns with circular and rectangular geometries, different reinforcing ratios, and detailing. A concrete model (Mander et al., 1988b) was employed in the development of the key aspects of the initial UCSD design equations for the seismic retrofit of r.c. columns. Unfortunately, such models do not provide information concerning concrete dilation that, in turn, loads the FRP jacket. As a result, the portion of the jacket strain due to concrete dilation cannot be directly computed. In an effort to remedy this situation, UCSD researchers developed a concrete model that allows one to directly predict the concrete dilation strain; a detailed description of their work can be found in Lee (2006). The implications here are twofold: First, use of the new model, which has been subjected to extensive validation, allows one to directly predict jacket failure, which is a function of both dilation and shear. Second, dilation tends to reduce the shear capacity of the column section, especially in the plastic hinge region. As a result, if one does not account for the dilation contribution to the jacket tensile strains, the shear capacity can be overestimated.

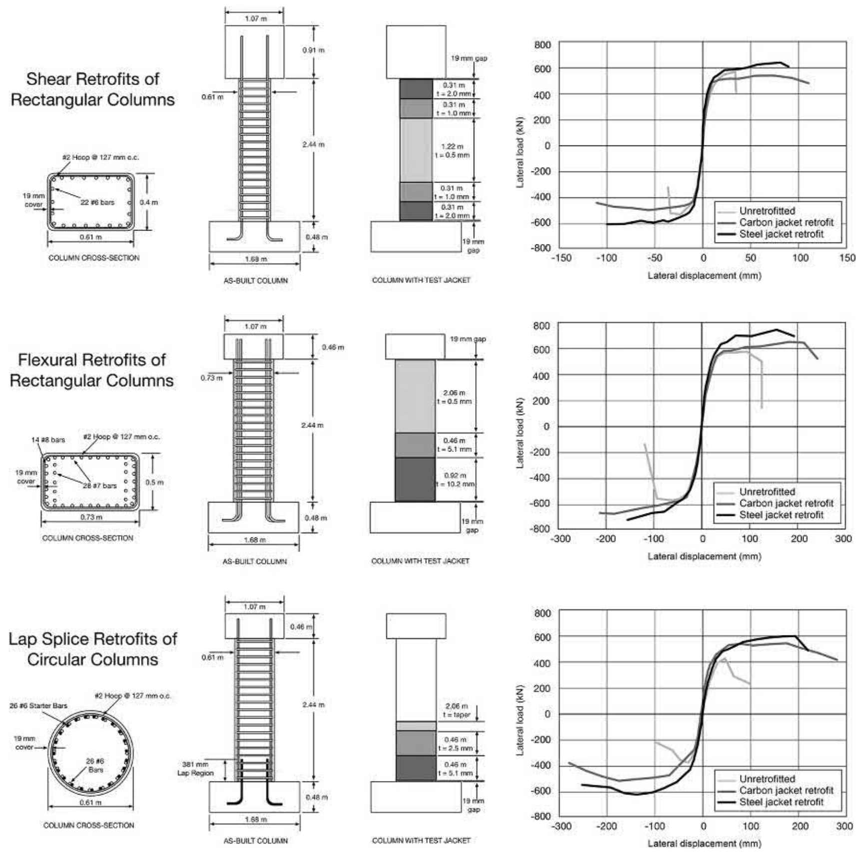

Figure 33.5 Experimental results from shear: (a) flexure, (b) splicing, and (c) bridge column retrofits (data from Seible et al., 1997a).

The model, which gives a better estimate for concrete dilation strain, was utilized to study the effects of corner radius on the stress strain response under direct compression. The results from the study are discussed in detail in Lee (2006) and are summarized in Figure 33.6. Additional studies using various models conducted by other researchers can be found in Al-Salloum (2007) and Wang and Wu (2008).

It should be noted that codes and design guidelines for various agencies (i.e., ACI, AASHTO) have a framework for these systems, as well as for the mechanisms under discussion (i.e., shear, flexure, and splicing). These are discussed briefly in Section 6 of this chapter. The designer should use engineering judgment with regard to the selection of analysis techniques and code requirements for implementation.

4.2 Laboratory tests—Seismic repair

The previous example concerned the FRP retrofits of undamaged specimens. The example discussed in this section illustrates the efficacy of the FRP jacket concept as a repair measure for bridge columns. The tests described in this section were

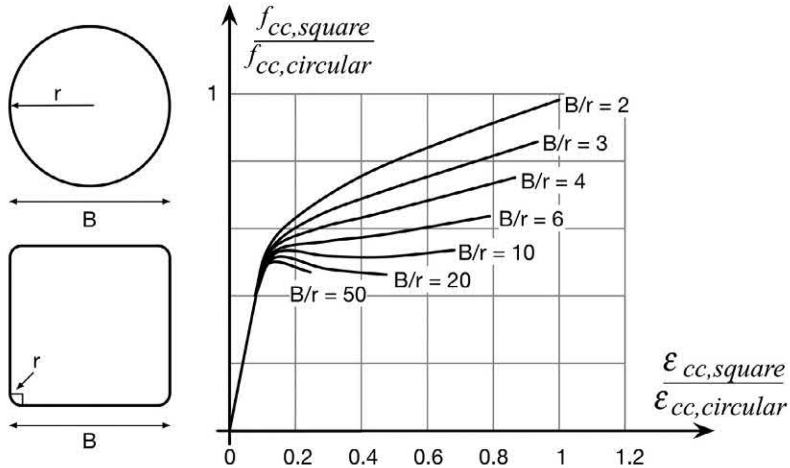

Figure 33.6 Effect of corner radius on stress–strain response (reproduced from data from Lee, 2006).

conducted by Ohtaki, Benzoni, and Priestley at UCSD. Additional details regarding these experiments are given in Ohtaki et al. (1996). This research highlights the use of FRP for repair, while also demonstrating the effectiveness of the procedure for large diameter columns.

The test setup for these experiments is shown in Figure 33.7. For this purpose, a shear-dominated bridge column with a 1.83-m diameter and an aspect ratio of 2.0 is considered with a pre-1971 design. In this case, the jacket was 9.8 mm of uniaxial GFRP, which was applied as hoop reinforcement via a wet layup of a glass fabric saturated with an epoxy resin system. The GFRP was applied after cement grout injection of the damaged specimen. Comparisons of the lateral force (no axial load was applied) versus displacement envelopes of the "as-built" and repaired specimens are provided in Figure 33.7. As can be seen, the repaired specimen exhibits a large ductility improvement over the "as-built" version with a displacement ductility up to $\mu = 6$ with no strength degradation.

4.3 Laboratory tests—New construction

For the application of FRP to new construction, the jacket is typically used as a stay-in-place formwork and consists of an FRP shell manufactured in a plant. These jackets can be circular or noncircular and are filled with concrete on the construction site. The concrete provides the compression force transfer and the shell serves as the formwork for the concrete, the reinforcement for the tension force transfer in bending and shear, and the confinement of the concrete core. The shell can be fabricated with internal circumferential ribs, which provides a mechanism for the transference of tensile forces and acts as a mechanical interlock between the concrete and the shell. With the use of this system, a steel reinforcement cage is often not necessary except for starter bars

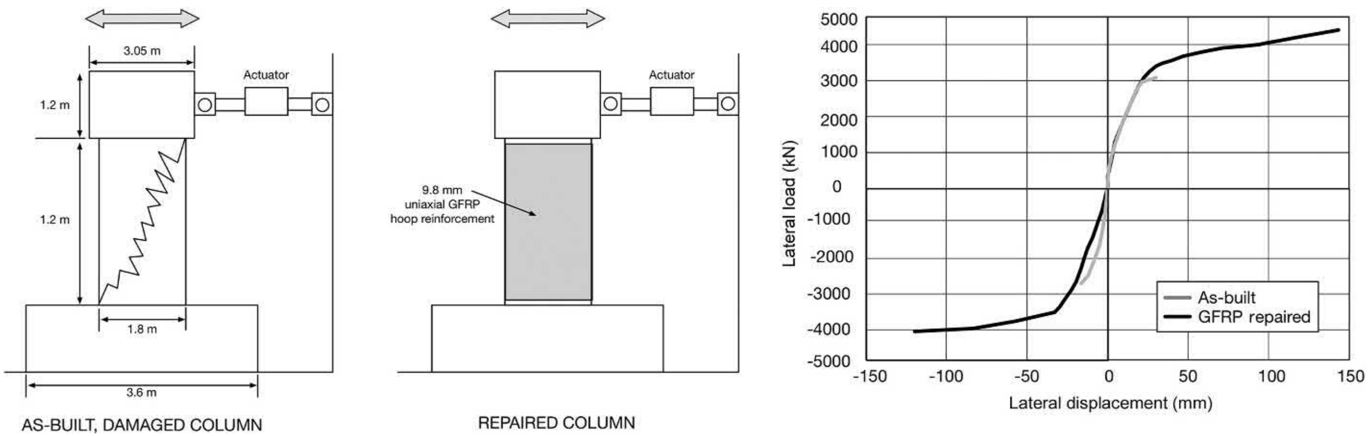

Figure 33.7 Experimental results from as-built and repaired reinforced concrete column (reproduced from data from Ohtaki et al., 1996).

that provide load transfer from the concrete-filled shell to termini elements, such as a footing. A variation of this theme employs the shell for confinement purposes only, in which case the ribs are not required (Hegemier et al., 2007).

A series of laboratory tests were conducted at UCSD on the *composite shell system (CSS),* with internal ribs as discussed previously and shown in Figure 33.8. In these experiments, the CSS was used for a column with a 610-mm diameter, a 3.43-m length, and a 9.52-mm jacket. The CFRP jacket was fabricated by the wet-filament winding method [see Burgueño et al., 1995 and Seible et al., 1995b for system material properties; and Fitzer and Terwiesch, 1972 for information on the wet-filament winding method]. As can be observed in Figure 33.8, although no primary steel reinforcement cage exists, the use of mild reinforcement splice bars in the concrete core across the column-footing joint and the confinement of the concrete by the shell result in a ductile response under hysteretic lateral loading with no strength degradation up to $\mu = 8$ (Burgueño et al., 1995). For comparison, the response of a conventional reinforced concrete column (seismic design) is also shown.

5. Performance—Superstructure

In what follows, two concept designs are presented in an effort to demonstrate the feasibility and response of FRP use in hybrid bridge systems as part of the bridge decking. The summary includes results from USCD Powell Laboratory tests conducted by UCSD researchers. Since that time, the use of composites for bridge deck applications has extended into alternative uses and applications, such as retrofits of steel structures, bonded/bolted sandwich panels, and innovative prestressing systems, as discussed in Shaat et al. (2004), Mosallam et al. (2015), and Ghafoori and Motavalli (2015).

5.1 Laboratory experiments—CSS for short- and medium-span bridges

The CSS technology discussed in Section 4.3 has also been applied to the use in bridge systems as part of the bridge superstructure. The cable stayed-bridge, which was conceptually designed and experimentally tested for proof of concept by Davol (1998) and Seible et al., included a 137-m-long deck supported by a 59-m-high A-frame pylon, utilizing concrete-filled CSS tubes (Seible et al., 1997b). The structural design concept, which is shown in schematic form in Figure 33.9, of the bridge consisted of an FRP panel stiffened, steel-free deck system and was supported on, and composite with, transverse CSS crossbeams. These crossbeams were spaced 2.4 m from the center and supported on the longitudinal CSS edge girders. The CSS edge girders are concrete filled and held up at 4.9-m intervals by the cable stays. These CSS sections were experimentally tested in the lab for flexure using a four-point bend setup, as shown in Figure 33.10. Results from these tests, including extensive strain gauge data from the FRP CSS section, are available in Davol (1998).

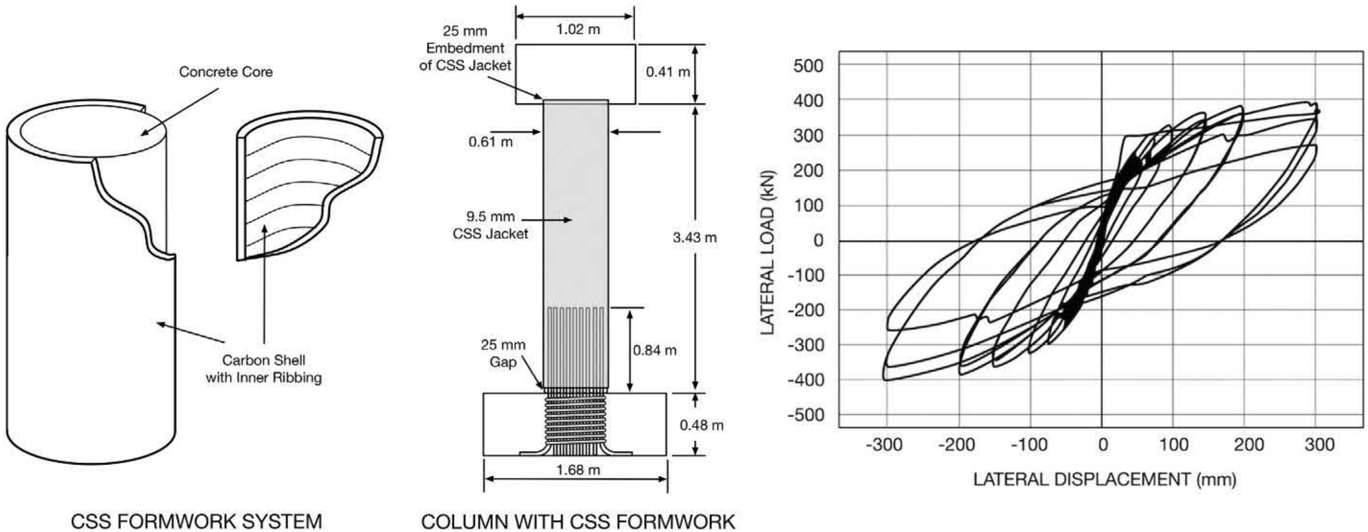

Figure 33.8 Experimental results from a column with CSS jacket (reproduced from data from Burgueño et al., 1995).

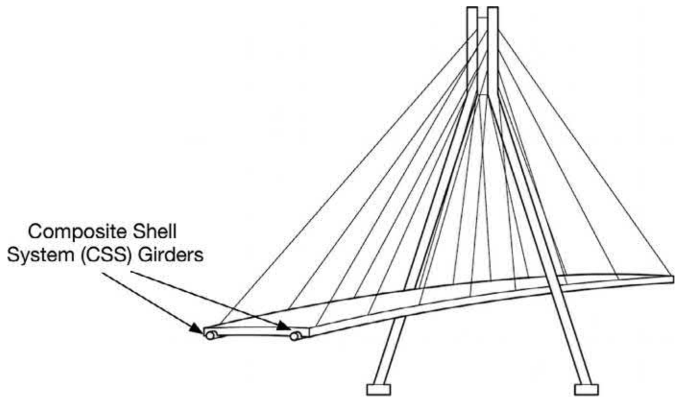

Figure 33.9 CSS section as girder of cable-stayed bridge system (reproduced from the concept described in Zhao, 2001).

5.2 Laboratory experiments—FRP for rapid rehabilitation

Composite systems have also been tested for use in rapid rehabilitation and construction of bridge decks. Experiments were conducted at UCSD by Pridmore (2008) to validate the use of FRP composite panels both for stay-in-place formwork and as the bottom longitudinal and transverse reinforcement in the deck of concrete box girder bridges. Performance assessments for full-scale, two-cell box girder bridge specimens, through monotonic and extensive cyclic loading, provided evidence that the FRP panel system bridge deck was a viable rehabilitation solution for box girder bridge decks. The experiments showed that the FRP panel system performed comparably to a conventionally reinforced concrete bridge deck in terms of serviceability, deflection profiles, and system-level structural interaction, and performed superior to the r.c. bridge deck in terms of residual deflections and structural response under cyclic loading (Pridmore, 2008).

Furthermore, this research utilized results from the development and characterization of a modular bridge system incorporating FRP composite girders connected by stiffened FRP deck panels which serve as both formwork and flexural reinforcement for a steel-free concrete deck cast on top. These systems were tested by Cheng and Karbhari (2004). The experimental results showed that capacity of the modular FRP hybrid system is substantially greater than the design demand levels. The researchers also developed analytical predictions, based on laminated beam theory using progressive ply failure criteria, moment-curvature analysis, and finite element models; also discussed in Cheng et al. (2005).

6. Design guides and codes

In the preceding sections, design applications using FRP technology was discussed in the context of experimental programs conducted for feasibility studies and tool development. Such analysis and design tools have contributed, along with many other

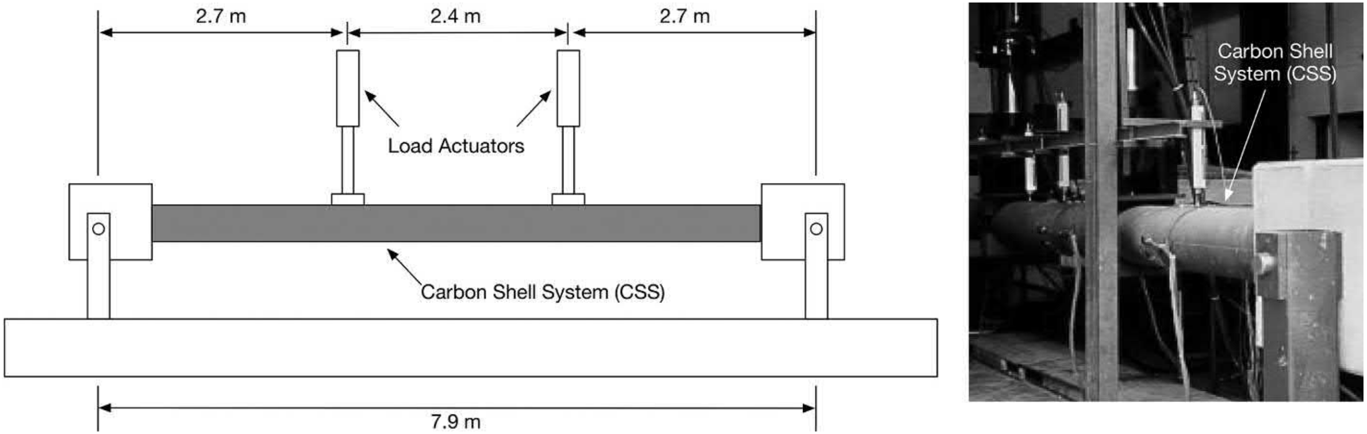

Figure 33.10 Experimental setup of flexural testing of CSS section (reproduced from Davol, 1998).

experiments conducted by researchers outside of UCSD, to the development of application-specific design codes and recommended guidelines. Such codes are often specific to location and purpose; thus, the designer should choose the appropriate tool given their context. What follows is a brief summary of available US codes and guidelines to date in the areas discussed in this chapter, as well as codes and recommendation guidelines from various locations and governances.

6.1 Bridge strengthening and repair with FRP

In the United States in 2010, the Transportation Research Board (TRB) published the National Cooperative Highway Research Program (NCHRP) Report 655 (TRB, 2010), which presents a recommended guide specification for the design of externally bonded FRP systems for the repair and strengthening of concrete bridge elements. This guide specification provides a review of current practices from various countries such as the Canadian ISIS Design Manual (Canada Design Manuals, 2001), the Italian CNR-DT 200 (2006), and those from the Japanese Society of Civil Engineers (2001), among others (e.g., French Association of Civil Engineers, 2003; German Provisional, 2003; Gorski and Kryzywon, 2007; Caltrans, 2007; Zureick, 2002; TRB NCHRP, 2004; TRB, 2008). The report addresses the design requirements for members subjected to different loading conditions (e.g., flexure, shear and torsion, and combined axial force and flexure). The report is presented in the load and resistance factor design (LRFD) method for complementary use with the American Association of State Highway Transportation Officials (AASHTO) LRFD bridge design specifications (2015).

In the case of pedestrian bridges, which primarily serve human and bicycle traffic, the use of FRP is covered by the AASHTO Guide Specifications for Design of FRP Pedestrian Bridges (AASHTO, 2008), which should be used in conjunction with the Guide Specifications for Design of Pedestrian Bridges (AASHTO, 2009a).

6.2 FRP tubes as stay-in-place formwork

Many researchers have studied the use of FRP tubes as a formwork for concrete construction (e.g., Deskovic et al., 1995; Hall and Mottram, 1998; Hollaway and Head, 2001). This technique is covered in the AASHTO LRFD Guide Specifications for Design of Concrete-Filled FRP Tubes (AASHTO, 2012). The specifications present provisions for the analysis and design of concrete-filled fiber-reinforced polymer tubes (CFFTs) for use as structural components (i.e., beams, arches, columns, and piles) in bridges subjected to flexure, axial compression, or combined loading.

6.3 Design of FRP bridge decks

In 2009, AASHTO developed a specification, the LRFD Bridge Design Guide Specifications for GFRP-Reinforced Concrete Bridge Decks and Traffic Railings (AASHTO, 2009b), for glass fiber-reinforced polymer (GRFP) use in the application of design and construction of concrete bridge decks and railings, in which the GFRP are used as reinforcing bars.

7. Other loading applications

In addition to seismic loading, reinforced concrete columns retrofitted with FRP jackets have also proved to be an effective system for lateral loading induced by explosive events. The confining pressure created by the jackets, as with seismic loading, aids in mitigating the effects of the blast loading. Experiments using CFRP retrofits for blast response have been conducted by Morrill et al. (2000, 2004), Crawford et al. (1996, 1997), Muszynski and Purcell (2003), and Winget et al. (2005). UCSD also demonstrated the mitigating nature of the column jackets using their blast simulator (Gram et al., 2006; Stewart et al., 2014) with experiments conducted by Rodriguez-Nikl et al. (2011) which showed that reduced column displacements can be achieved with as few as two layers of CFRP. Test results of the retrofitted concrete columns subjected to blast loading can be found in (Rodríguez-Nikl, 2006). Recommendations of concrete columns subjected to blast loadings is covered in the recently published ACI 370R-14 Report for the Design of Concrete Structures for Blast Effects (ACI, 2014). This report is based on the use of single degree-of-freedom (SDOF) systems as the main analysis technique to develop response. The designer should take care to use these methods where applicable, based on standoff, charge size, and other relevant parameters.

Similarly, FRP applications have also been shown to be an effective strategy for the retrofitting of reinforced concrete bridge decks or for new construction techniques. Field tests showing the response of decks or concrete slabs retrofitted with FRP to blast loading can be found in testing conducted by Seible et al. (2008), Buchan and Chen (2007), Millard et al. (2010), Wu et al. (2009), Coughlin et al. (2010), Schenker et al. (2008), and Silva and Binggeng (2007).

8. Conclusions

This chapter provided a summary of applications of FRP to bridge systems, as demonstrated through experimental testing conducted at the UCSD Powell Laboratories over the past three decades. The laboratory tests confirmed the effective use of FRP with reinforced concrete columns for retrofit, repair, and new constructions. Additionally, FRP systems were shown to be effective when used in various bridge deck system designs. These experiments, combined with investigations and implementation of these systems from many other researchers, have motivated the development of design codes and guidelines, many of which are actively used by bridge engineers all over the world.

References

Al-Salloum, Y.A., 2007. Influence of edge sharpness on the strength of square concrete columns confined with FRP composite laminates. Comps. Part B: Eng. 38 (5), 640–650.

American Association of State Highway and Transportation Officials (AASHTO), 2008. Guide Specifications for Design of FRP Pedestrian Bridges. Washington, DC.

American Association of State Highway and Transportation Officials (AASHTO), 2009a. LRFD Guide Specifications Pedestrian Bridges, second ed. Washington, DC.
American Association of State Highway and Transportation Officials (AASHTO), 2009b. Guide Specifications for GFRP-Reinforced Concrete Bridge Decks and Traffic Railings. Washington, DC.
American Association of State Highway and Transportation Officials (AASHTO), 2012. LRFD Guide Specifications for Design of Concrete-Filled FRP Tubes, first ed. Washington, DC.
American Association of State Highway and Transportation Officials (AASHTO), 2015. LRFD Bridge Design Specifications, seventh ed. Washington, DC.
American Concrete Institute (ACI), 2014. 370R-14 Report for the Design of Concrete Structures for Blast Effects. Farmington Hills, MI.
Bank, L.C., 2006. FRP Flexural Reinforcement, in Composites for Construction: Structural Design with FRP Materials. John Wiley & Sons, Inc., Hoboken, NJ.
Barbero, E., 1991. Pultruded structural shapes - from the constituents to the structural behavior. SAMPLE J. 27 (1), 25–30.
Bezant, Z., Kim, S., 1979. Plastic-fracturing theory for concrete. J .Eng. Mech. Div. 105 (3), 407–428.
Buchan, P.A., Chen, J.F., 2007. Blast resistance of FRP composites and polymer strengthened concrete and masonry structures–a state-of-the-art review. Comps. Part B: Eng. 38 (5), 509–522.
Burgueño, R., Seible, F., Hegemier, G.A., 1995. Report No. ACTT-95/12, Concrete Filled Carbon Shell Bridge Piers Under Simulated Seismic Loads–Experimented Studies. University of California, San Diego, La Jolla, CA.
Caltrans, 2007. Bridge Memo to Designers-MTD 20–4: Seismic Retrofit Guidelines for Bridges in California. Technical Publication, Sacramento, CA.
Canada Design Manuals, I.S.I.S., 2001. Strengthening Rein- Forced Concrete Structures with Externally-Bonded Fiber-Reinforced Polymers. Winnipeg, Manitoba, Canada.
Cheng, L., Karbhari, V.M., 2004. Development of FRP composite modular system for slab-on-girder bridges. In: Proceedings of the Fourth International Conference on Advanced Composite Materials in Bridges and Structures, Calgary, Alberta, July, pp. 20–23.
Cheng, L.J., et al., 2005. Assessment of a steel-free fiber reinforced polymer-composite modular bridge system. J. Struct. Eng. 131 (3), 498–506.
CNR-DT 200, 2006. Guide for the Design and Construction of Externally Bonded FRP Systems for Strengthening Existing Structures. Italian Advisory Committee on Technical Recommendations for Construction, Rome.
Coughlin, A.M., et al., 2010. Behavior of portable fiber reinforced concrete vehicle barriers subject to blasts from contact charges. Int. J. Imp. Eng. 37 (5), 521–529.
Crawford, J.E., et al., 1996. Retrofit of Reinforced Concrete Columns Using Composite Wraps to Resist Blast Effects. Karagozian and Case, Glendale, CA.
Crawford, J.E., et al., 1997. Retrofit of reinforced concrete structures to resist blast effects. ACI Struct. J. 94 (4), 371–377.
Davol, A., 1998. Ph.D dissertation. Structural Characterization of Concrete Filled Fiber Reinforced Shells. University of California, San Diego, La Jolla, CA.
Deskovic, N., Triantafillou, T., Meier, U., 1995. Innovative design of FRP combined with concrete: short-term behavior. J. Struct. Eng. 121 (7), 1069–1078.
Fitzer, E., Terwiesch, B., 1972. Carbon—carbon composites unidirectionally reinforced with carbon and graphite fibers. Carbon 10 (4), 383–390.
French Association of Civil Engineers, 2003. Réparation et renforcement des structures en béton au moyen des matériaux composites. AFGC, Paris.

German Provisional Regulations, 2003. Nr. Z-36.12–65 vom 29, Allgemeine Bauaufsichtliche Zulassung. Deutsches Institut für Bautechnik, Berlin.

Ghafoori, E., Motavalli, M., 2015. Innovative CFRP-Prestressing system for strengthening metallic structures. J. Compos. Constr. https://doi.org/10.1061/(ASCE)CC.1943-5614.0000559.

Gorski, M., Kryzywon, R., 2007. Polish standardization proposal for Design procedures of FRP strengthening. In: Triantafillou, T. (Ed.), Proceedings, CD, FRPRCS-8. University of Patras, Patras, Greece.

Gram, M.M., et al., 2006. Laboratory simulation of blast loading on building and bridge structures. Struc. Under Shock and Imp. IX. 87, 33–44.

Hall, J., Mottram, J., 1998. Combined FRP reinforcement and permanent formwork for concrete members. J. Compos. Constr. 2 (78), 78–86.

Hegemier, et al., 2007. The use of fiber-reinforced polymers to mitigate natural and manmade hazards. In: FRPCS-8, Patras, Greece, pp. 1–24.

Hollaway, L., Head, P., 2001. Advanced Polymer Composites and Polymers in the Civil Infrastructure. Elsevier, Oxford, UK.

Inmamorato, D., et al., 1995. Report No. ACTT-95/19. Carbon Shell Jacket Retrofit Test of a Circular Shear Column with 2.5% Reinforcement. University of California, San Diego, La Jolla, CA.

Inmamorato, D., et al., 1996. Report No. ACTT-96/10. Full Scale Test of Two Column Bridge Bent with Carbon Jacket Retrofit. University of California, San Diego, La Jolla, CA.

Japan Society of Civil Engineers (JSCE), 2001. Recommendations for Upgrading of Concrete Structures with Use of Continuous Fiber Sheets. Tokyo, Japan.

Karbhari, V.M. (Ed.), 2007. Durability of Composites for Civil Structural Applications. Elsevier, Woodhead Publishing, Sawston, Cambridge.

Karbhari, V.M., Engineer, M., 1996. Effect of environmental exposure on the external strengthening of concrete with composites-short term bond durability. J. Reinf. Plastics Comps. 15 (2), 1194–1216.

Karbhari, V.M., Engineer, M., Eckell II, D.A., 1997. On the durability of composite rehabilitation schemes for concrete: use of a peel test. J. Mats. Sci. 32 (1), 147–156.

Karbhari, V.M., et al., 2003. Durability gap analysis for fiber-reinforced polymer composites in civil infrastructure. J. Comps. Constr. 7 (3), 238–247.

Lee, C.S., 2006. Ph.D dissertation, Modeling of FRP-Jacketed RC Columns Subject to Combined Axial and Lateral Loads. University of California, San Diego, La Jolla, CA.

Mallick, P.K., 2007. Fiber-Reinforced Composites Materials, Manufacturing, and Design, third ed. CRC Press, Boca Raton.

Mander, J., Priestley, M., Park, R., 1988a. Observed stress-strain behavior of confined concrete. J. Struct. Eng. 114 (8), 1827–1849.

Mander, J.B., Priestly, M.J.N., Park, R., 1988b. Theoretical stress-strain model for confined concrete. J. Struct. Eng. 114 (8), 1804–1826.

Millard, S.G., et al., 2010. Dynamic enhancement of blast-resistant ultra high performance fibre-reinforced concrete under flexural and shear loading. Int. J. Impact Eng. 37 (4), 405–413.

Mirmiran, A., et al., 1998. Effect of column parameters on FRP-confined concrete. J. Compos. Constr. 2 (4), 175–185.

Monti, G., Nisticò, N., Santini, S., 2001. Design of FRP jackets for upgrade of circular bridge piers. J. Compos. Constr. 5 (2), 94–101.

Morrill, K.B., et al., 2000. RC column and slab retrofits to survive blast loads. In: Advanced Technology in Structural Engineering, Structures Congress 2000, Philadelphia, Pennsylvania, United States, pp. 1–8.

Morrill, K.B., et al., 2004. Blast Resistant Design and Retrofit of Reinforced Concrete Columns and Walls. Proceedings of Structures Congress-Building on the Past-Securing the Future. Nashville, Tennessee, United States.

Mosallam, A., et al., 2015. Structural evaluation of reinforced concrete beams strengthened with innovative bolted/bonded advanced FRP composite sandwich panels. Compos. Struct. 124, 421–440.

Muszynski, L.C., Purcell, M.R., 2003. Composite reinforcement to strengthen existing concrete structures against air blast. J. Compos. Constr. 7 (2), 93–97.

Nanni, A., Norris, M.S., 1995. FRP jacketed concrete under flexure and combined flexure- compression. Constr. Build. Mater. 9 (5), 273–281.

Ohtaki, T., Benzoni, G., Priestly, M.J.N., 1996. Report No. SSRP-96/07, Seismic Performance of a Full-Scale Bridge Column–As Built and Repaired. University of California, San Diego, La Jolla, CA.

Pantazopoulou, S.J., et al., 2001. Repair of corrosion-damaged columns with FRP wraps. J. Compos. Constr. 5 (1), 3–11.

Parvin, A., Wang, W., 2001. Behavior of FRP jacketed concrete columns under eccentric loading. J. Compos. Constr. 5 (3), 146–152.

Pipes, R.B., Pagano, N.J., 1970. Interlaminar stresses in composite laminates under uniform axial extension. J. Comp. Mats. 4 (4), 538–548.

Pridmore, A., 2008. Ph.D Dissertation, Structural Characterization of Concrete Filled Fiber Reinforced Shells. University of California, San Diego, La Jolla, CA.

Priestley, M.J.N., et al., 1994. Steel jacket retrofitting of reinforced concrete bridge columns for enhanced shear strength—part 1: theoretical considerations and test design. ACI Struct. J. 9 (4), 394–405.

Ramirez, J.L., et al., 1997. Efficiency of short steel jackets for strengthening square section concrete columns. Construc. Build. Mat. 11 (5), 345–352.

Reddy, J.N., 1987. A generalization of two-dimensional theories of laminated composite plates. Comms. App. Num. Methods. 3 (3), 173–180.

Rigas, E.J., Walsh, S.M., Spurgeon, W., 2001. Development of a novel processing technique for vacuum assisted resin transfer molding (VARTM). In: 46th International SAMPE Symposium and Exhibition. CRC Press, Long Beach, CA.

Rochette, P., Labossiere, P., 2000. Axial testing of rectangular column models confined with composites. J. Compos. Constr. 4 (3), 129–136.

Rodríguez-Nikl, T., 2006. Experimental simulations of explosive loading on structural components: Reinforced concrete columns with advanced composite jackets. PhD Dissertation, University of California, San Diego, La Jolla, CA.

Rodriguez-Nikl, T., et al., 2011. Experimental performance of concrete columns with composite jackets under blast loading. J. Struct. Eng. 138 (1), 81–89.

Saatcioglu, M., Razvi, S., 1992. Strength and ductility of confined concrete. J. Struct. Eng. 118 (6), 1590–1607.

Schenker, A., et al., 2008. Full-scale field tests of concrete slabs subjected to blast loads. Int. J. Imp. Eng. 35 (3), 184–198.

Seible, F., et al., 1995a. Advanced Composite Carbon Shell Systems for Bridge Columns Under Seismic Load. Report No. ACTT/BIR-95/27. Dept. of Structural Engineering, University of California, San Diego, La Jolla, CA.

Seible, F., et al., 1995b. Report No. ACTT-95/03, Rectangular Carbon Jacket Retrofit of Flexural Column with 5% Continuous Reinforcement. University of California, San Diego, La Jolla, CA.

Seible, F., et al., 1997a. Seismic retrofit of RC columns with continuous carbon Fiber jackets. J. Compos. Constr. 1 (2), 52–62.
Seible, F., et al., 1997b. The carbon shell system for modular short and medium span bridges. In: Proceedings of International Composite Expo, Nashville, TN, January, pp. 1–6.
Seible, F., et al., 2008. Protection of our bridge infrastructure against manmade and natural hazards. Struct. Infrastruct. Eng. 4 (6), 415–429.
Shaat, A., et al., 2004. Retrofit of steel structures using fiber-reinforced polymers (FRP): State-of-the-art. In: Transportation Research Board (TRB) Annual Meeting, Washington, DC, USA.
Silva, P.F., Binggeng, L., 2007. Improving the blast resistance capacity of RC slabs with innovative composite materials. Composites Part B: Eng 38 (5), 523–534.
Stewart, L.K., et al., 2014. Methodology and validation for blast and shock testing of structures using high-speed hydraulic actuators. Eng. Struct. 70 (1), 168–180.
Transportation Research Board of the National Academies, 2004. NCHRP Report 655: Bonded Repair and Retrofit of Concrete Structures Using FRP Composites—Recommended Construction Specifications and Process Control Manual. Washington, DC.
Transportation Research Board of the National Academies, 2008. NCHRP Report 609: Recommended Construction Specifications and Process Control Manual for Repair and Retrofit of Concrete Structures Using Bonded FRP Composites. Washington, DC.
Transportation Research Board of the National Academies, 2010. NCHRP Report 655: Recommended Guide Specification for the Design of Externally Bonded FRP Systems for Repair and Strengthening of Concrete Bridge Elements. Washington, DC.
Vermeer, P., DeBorst, R., 1984. Non-associated plasticity for soils, concrete, and rock. Heron 29 (3), 1–64.
Wang, L.M., Wu, Y.F., 2008. Effect of corner radius on the performance of CFRP-confined square concrete columns: test. Eng. Struct. 30 (2), 493–505.
Winget, D.G., Marchand, K.A., Williamson, E.B., 2005. Analysis and design of critical bridges subjected to blast loads. J. Struct. Eng. 131 (8), 1243–1255.
Wu, C., et al., 2009. Blast testing of ultra-high performance fibre and FRP-retrofitted concrete slabs. Eng. Struct. 31 (9), 2060–2069.
Xiao, Y., Rui, M., 1997. Seismic retrofit of RC circular columns using prefabricated composite jacketing. J. Struct. Eng. 123 (10), 1357–1364.
Xiao, Y., Wu, H., 2000. Compressive behavior of concrete confined by carbon fiber composite jackets. J. Mater. Civ. Eng. 12 (2), 139–146.
Zhao, L., 2001. Design and evaluation of modular bridge systems using FRP composite materials. In: Proceedings of the Fifth International Conference on Fiber-Reinforced Plastics for Reinforced Concrete Structures. Cambridge, UK, July, pp. 16–18.
Zureick, 2002. GDOT Specification: Proposed Specifications-Polymeric Composite Materials for Rehabilitating Concrete Structures.

Bridge collapse

34

Arturo E. Schultz[a], *Alesso Pipinato*[b], *and Andrew J. Gastineau*[c]
[a]School of Civil and Environmental Engineering, and Construction Management, The University of Texas at San Antonio, San Antonio, TX, USA, [b]AP&P, CEO and Technical Director, Rovigo, Italy, [c]KPFF Consulting Engineers, Seattle, WA, USA

1. Introduction

Historically, bridge collapses have been caused by a variety of factors and from a combination of those factors. These include poor engineering judgment, use of substandard materials, extreme loading, and inadequate maintenance. In all cases, much can be learned from these failures. Most bridge collapses have been closely scrutinized, and reasons for the collapse are generally agreed upon. Entire books have been dedicated to significant collapses, and yet they barely cover the vast number of historic bridge failures. This chapter attempts to present some major bridge failures and their consequences to highlight broad categories of the causes of bridge collapses. Åkesson (2008) described a variety of collapses but identified five key bridge collapses that have changed the way in which engineers understand bridges. The key collapses identified are the Dee Bridge, the Tay Bridge, the Quebec Bridge, the Tacoma Narrows Bridge (Figure 34.1), and a series of box-girder bridge failures that took place from 1969 to 1971. In addition to the collapses highlighted by Åkesson, others have documented bridge failures that led to major design changes. This chapter covers bridge collapses in North America, as well as significant bridge failures worldwide. Not all of the bridges described in the chapter underwent a complete collapse because a bridge failure is defined as an event in which a bridge does not perform to meet design goals and cannot be safely operated. The bridge failures highlighted in this chapter are classified into three main categories: construction failures, in-service failures, and extreme events. Each of these broad categories provides insight and caution that should be incorporated into bridge design, construction, and maintenance.

2. Construction failures

From their invention, bridges have been essential for transportation, trade, communication, and defense, and their construction has posed many challenges. While unintended and completely undesirable, bridge collapses and failures have often served as an indicator of what is impossible in bridge design and construction. In modern times, a variety of failures have demonstrated that the engineering criteria and processes that go into the construction sequence are just as important as the design for service conditions of a bridge. Without thoughtful construction analysis, a well-designed bridge may never be successfully placed into service.

Innovative Bridge Design Handbook. https://doi.org/10.1016/B978-0-12-823550-8.00030-5

Figure 34.1 Tacoma Narrows Bridge, Library of Congress, Prints and Photographs Division, LC-USZ62-46682.

Manitoba Free Press

EIGHTY-FOUR KILLED IN COLLAPSE OF BRIDGE

SOUTH SPAN FALLS INTO ST. LAWRENCE

CAUSE OF ACCIDENT A MYSTERY

Figure 34.2 Quebec Bridge collapse, Manitoba Free Press.

During construction of the Quebec Bridge, a cantilever steel truss structure, in 1907, a compression chord was found to have distorted out of plane, and the designer ordered construction to be halted. However, in spite of this, the contractor was falling behind schedule and continued construction anyway. Buckling failures resulted in a complete collapse of the bridge (Figure 34.2), killing 75 workers. Multiple reasons led to the bridge collapse; first, the bridge had been designed using higher working stresses, and second, the designers underestimated the self-weight of the steel. The large allowable stresses caused the buckling of a compression member, which led to further overstressing of additional members, causing complete collapse (Quebec Bridge Disaster, 1908; Biezma and Schanack, 2007; Åkesson, 2008). A new bridge was planned and erected using compression chords with almost twice the cross-sectional area to avoid buckling; however, the bridge partially collapsed again in 1916, killing an additional 13 workers. The second collapse was blamed on a weak connection detail, which was redesigned, and the bridge was finally completed in

1917. These collapses highlighted the need for designs that are not only economical but also safe. Increasing working stresses without proper testing and safety assessment can lead to devastating consequences. These experiences also highlighted the importance of connections, as well as the need to carefully evaluate design changes made during construction.

A series of steel box-girder bridge failures occurred in the late 1960s and early 1970s, with the majority of failures occurring during the erection stage of construction (Biezma and Schanack, 2007; Subramanian, 2008; Åkesson, 2008). By using the cantilever construction method during erection, high moment regions at the supports produced a buckling failure in Austria's Fourth Danube Bridge. As the final box-girder piece was placed to close the gap between the two cantilevers, the piece had to be shortened on the top due to sag of the cantilevered segments, which the design did not take into account. The additional sag had been caused by expansion of the bridge deck due to a full day of sun exposure. The bridge was designed as a continuous span so that the inner pier supports needed to be lowered to produce the correct stress distribution; however, this activity had been moved to the next day. As the bridge cooled that evening, tension was introduced in the shortened region, and compression was introduced in the bottom flange. Areas designed to be in tension for in-service loads were instead loaded in compression, causing buckling failures of the bottom flanges of the box section (see Figure 34.3). Four other box-girder failures occurred in the next four years, all of which had buckling issues during erection (one was kept secret for more than 20 years due to the controversy). Because of the large number of collapses in a small period of time, it was clear that erection loads and practices needed to be included in the design process and that local buckling problems were not well understood.

While the River Verde Viaduct was being erected in Spain, the movable scaffolding system collapsed (Figure 34.4), killing six workers (Tanner and Hingorani, 2013). While this event was not technically a bridge collapse, these systems are critical for building long-span bridges. The scaffolding was a movable system, and while being moved, there was a power failure because of damage to an electrical cable. This allowed excessive movement of the scaffolding, which caused a connection failure, after which collapse ensued. The failure highlights the fact that, in addition to the scaffolding having the required strength and stiffness, it is necessary for any peripheral electrical and mechanical systems to be designed adequately and that fail-safe systems

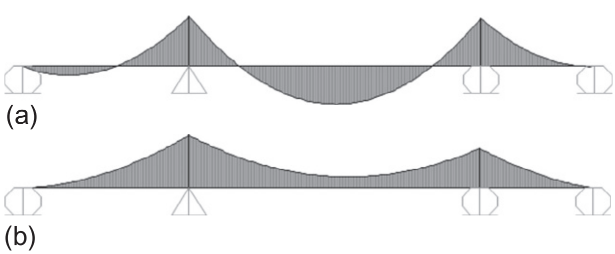

Figure 34.3 Fourth Danube Bridge moment diagrams: (a) in-service design moments; (b) temporary condition due to construction method and temperature loading.

Figure 34.4 River Verde Viaduct scaffolding collapse (Image Courtesy Fred Nederlof).

are necessary in case any one of these components fail during construction. Without safe and robust designs, bridges cannot be safely constructed, and public opinion of the engineering profession can be undermined.

A dramatic case of bridge collapse during construction unraveled in Miami, Florida, USA in March 15, 2018. The Florida International University (FIU) Bridge (Figure 34.5) was intended to provide pedestrian access from Florida International University to University City Prosperity Project, an urban renewal project in the adjacent town, Sweetwater. The bridge was located approximately 18 km from downtown Miami and crossed SW 8th Street (also designated as US Highway 41 and Florida State Route 90) and the Tamiami Canal. The structure was a two-span concrete truss with a 53 m main span over the roadway and a 30 m back span over the Tamiami Canal. The U.S. National Transportation Safety Board (NTSB) investigated the

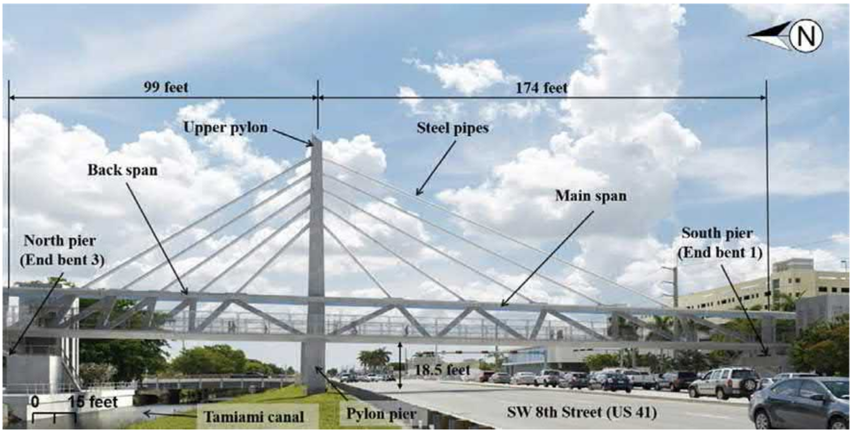

Figure 34.5 FIU Bridge (NTSB, 2019 Fig. 2, p. 2).

collapse and concluded that it was due to a combination of errors in design, peer review, construction, and communication between the various project entities (2019).

Concrete truss bridges are rare, and the unique FIU bridge truss was post-tensioned longitudinally and transversely, and the truss members were also post-tensioned. The bridge was supported on two end piers and an intermediate pier between the roadway and the canal. The intermediate pier that supported a pylon and steel pipe stays that were architectural fixtures to enhance the esthetics of the bridge. Another unusual feature of the FIU bridge was its accelerated bridge construction (ABC) method, in which innovative procedures were used to reduce on-site construction time. The main span was built at a nearby casting site and transported, using a self-propelled modular transporter, for placement on the piers. The back span of the bridge was constructed in place since it was not located immediately over the roadway.

The FIU bridge experienced a catastrophic failure and collapsed onto SW 8th Street before it was fully built. A team of construction workers was in the process of retensioning the post-tensioning rods in one of the truss members (member 11) connecting the canopy and the deck at the pier along the Tamiami Canal (Figure 34.5). A construction vehicle equipped with a video recorder captured the collapse at approximately 1:46 p.m. (Figure 34.6). The video indicates an explosive concrete failure of the north end of the bridge. The collapsed main span crushed several vehicles that were located below the bridge, killing five occupants and one construction worker. Ten other people were injured during the mishap.

The FIU bridge suffered a history of crack distress for nearly three weeks prior to the collapse, beginning on February 24, 2018, during the construction of the main space in the casting site. When the falsework was removed at the casting site, concrete cracking in truss node 11/12 (Figure 34.7) was observed visually and audibly. The width and depth of the cracks continued to grow during this time until the bridge collapsed on March 15.

As an intervention to mitigate the cracking, the design engineer prescribed that the rods in truss member 11 be detensioned and then retensioned. However, the cracks

Figure 34.6 FIU Bridge during collapse (NTSB, 2018 Fig. 10, p. 12).

Figure 34.7 Cracking in truss member 11 at node 11–12 (NTSB, 2018 Fig. 25, p. 37).

opened wider upon detensioning because the clamping force afforded by the post-tensioning was no longer present to enhance the shear strength of the concrete. Additionally, the structural plans did not specify surface roughening at cold joints between the truss members and the deck or canopy. Thus, the combination of premature cracking and smooth cold joints reduced the horizontal shear resistance at the node sufficiently to enable collapse of the bridge. Other extenuating circumstances included disturbed anchorage regions for some of the post-tensioning rods, due to concrete cracking, and placement of nonstructural hollow pipes in the affected region, further reducing the capacity of the concrete to resist combined compression and shear forces.

The NTSB investigation (2019) identified a number of errors made during design and construction that likely led to collapse of the FIU bridge. First, during the design of the bridge, the design engineering firm underestimated the load demands acting on node 11/12 and overestimated its capacity to resist horizontal shear forces, such that the demand-to-capacity ratio calculated by the NTSB investigators approached a value of 2. Second, peer review of the bridge design by an independent firm did not identify the errors in the design of the truss, because the reviewing firm did not calculate loads and capacities for the truss nodes, and they lacked the expertise to perform such work. Third, in spite of the numerous reports by the construction and inspection firms regarding concrete cracking in the main span, the design firm repeatedly deemed the cracks to be of no safety concern. Fourth, being a pedestrian bridge, the FIU bridge lacked structural redundancy in the load path, and as soon as node 11/12 failed, the bridge collapsed.

Ultimately, NTSB faults the construction management firm, the design engineering firm, the inspecting firm, the bridge owner, and the bridge authority for not stopping bridge construction when the crack in the main span exceeded acceptable norms. Moreover, the NTSB takes strong exception for these entities not taking measures to temporarily halt traffic under the bridge to protect the public.

The Chirajara Bridge (Figure 34.8) was a cable-stayed bridge projected to span the 150 m deep Chirajara Gorge of the Rio Negro near the municipality of Guayabetal in central Colombia. The project was part of a major infrastructure expansion in Colombia to modernize the highway from the capital city Bogotá to the city of Villavicencio. It was one of 47 bridges in the project and was intended to carry two of the four lanes of the expanded highway. While it was nearing completion, one-half of the Chirajara Bridge collapsed on January 15, 2018. The West Tower (Axis B in Figure 34.8) collapsed (Figure 34.9), killing nine construction workers and compromising a critical artery in the Colombian national highway network.

The bridge was constructed using the cantilever method with the towers and abutments built first. The abutments balanced the loads imposed by the unsymmetrical spans on either side of the towers. Subsequently, the deck was extended from each abutment toward the adjacent tower, and afterwards from each tower toward the center of the middle span. Each segment was shored during construction and supported by additional stay cables, with the weight of each segment balanced by a corresponding segment on the opposite side of the tower.

The roadway was supported on a composite structure with steel longitudinal girders and steel transverse beams supporting a reinforced concrete slab with an asphalt wearing course. Two 107 m tall reinforced concrete towers supported the roadway by means of 52 cable stays (Figure 34.8). The stay cables consisted of bundles of high-strength steel strands meeting US requirements for Grade 270 (270 MPa) prestressing strand. The tower masts were supported by a framed structure with a diamond-shape elevation, and the roadway was placed through the widest part of the diamond. The lower part of the tower included a thick wall acting as a web between the columns (Figure 34.9). At the top of this web and below the deck was a thick "tower" slab (Figure 34.10) that acted as a tie between the columns at the elevation, with the widest separation between the columns.

Tower slab reinforcement (Figure 34.10) included twelve 15 mm diameter unbonded post-tensioning Grade 270 strands that were anchored in the columns. Other reinforcement in the tower slab consisted of deformed reinforcing bars that were

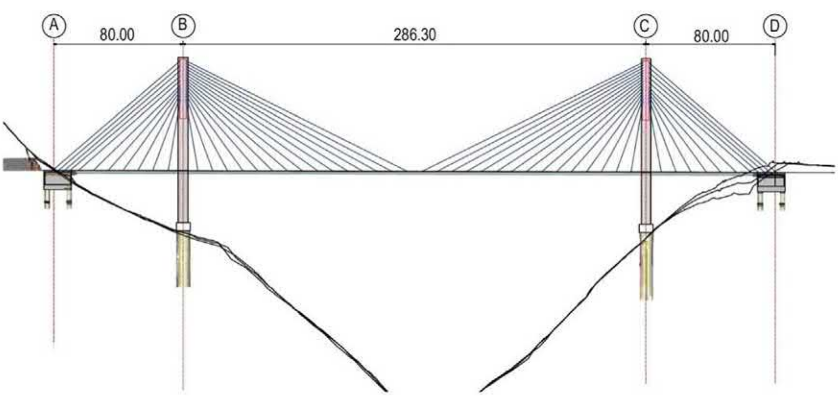

Figure 34.8 Schematic of the Chirajara Bridge (Pujol et al., 2019).

Figure 34.9 East Tower after bridge collapse (image courtesy Arturo Schultz).

terminated near each column face. Because the construction process resulted in cold joints between the concrete in the tower slab and the columns, the deformed bars would have been incapable of transferring tension forces between the tower slab and the columns. Mill certificates provided to the company supervising the highway expansion project indicate that the reinforcing bars met the specifications for US Grade 420 mild steel reinforcement. Additionally, standard cylinder test reports provided to the supervision company show results exceeding the specified strength.

At the time of collapse, bridge construction was near completion, with the cantilever ends approximately 30 m from each another. At the time, neither portion of bridge was carrying significant live load, and the planned asphalt wearing course had not yet been placed on the concrete deck. No construction activities involving heavy weights or large forces are reported to have been taking place on the collapsed portion of the bridge at the time of failure. Additionally, there were no reports of seismic activity or strong winds, nor were there indications of foundation distress at the base of the towers.

A security video camera recorded the West Tower during the collapse (Figure 34.11). The sequence shows clearly that the dominant feature of the collapse involved separation between the columns on opposing sides of the tower, suggesting a tensile failure at or near the tower slab. Examination of the debris revealed that failure involved: fracture of the horizontal deformed reinforcing bars in the web-to-column joint (below the tower slab), limited cracking elsewhere in the web, no failures in stay-cable anchorages in the bridge deck, and deck girder fractures at splice locations.

The video of the collapse (Figure 34.11) as well as debris examination strongly suggest that the failure was related to gravity demands overcoming the vertical load capacity of the West Tower of the Chirajara Bridge. Collapse was inevitable because post-tensioned reinforcement placed in the tower slab (a slab meant to act as a tie

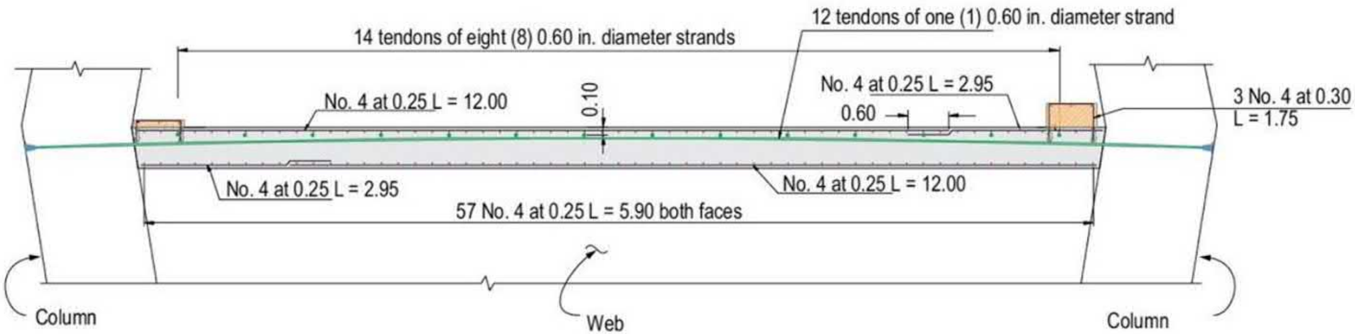

Figure 34.10 Section through the tower slab (Pujol et al., 2019).

between columns) was insufficient to resist tie force demands from bridge weight by a large margin. Surprisingly, in the perpendicular direction (i.e., in the deck longitudinal direction), where no large stresses would have been expected, the tower slab was provided with nine times more reinforcement. It is surmised that had the provided reinforcement been rotated 90 degrees, the collapse would not have occurred. Inspection by the supervision company did not notice the discrepancy in these reinforcement amounts.

The insufficient lateral restraint provided to the West Tower by the post-tensioned reinforcement in the tower slab, which was meant to act as a tie between columns, forced the reinforced concrete web between the columns to work in tension. Conditions were worsened by the small amount of reinforcement in the webs (meeting code minimum) and the cold joint formed at the connection between the tower slab and the columns. The discontinuity at the cold joint forced large strain concentrations to the small amount of reinforcement (i.e., with tensile capacity comparable that of the concrete). These conditions ultimately led to brittle fracture of the web reinforcement,

Figure 34.11 Frames extracted from security camera video (Pujol et al., 2019).

leaving the post-tensioned reinforcement in the tower slab to resist a force much larger than its capacity. The failure of the project can be traced to (1) a design error, (2) an error in the peer review process that was implemented, and (3) and an error in the construction inspection process.

3. In-service failures

Bridges are designed to carry trains, pedestrians, or vehicles over obstacles. Due to the complex nature of both loads and structural behavior, simplifying assumptions must be made during design. However, these assumptions may not fully represent either the loading or the physical behavior of the bridge, and sometimes the flaws from oversimplification can lead to catastrophic consequences. This section discusses in-service failures in four categories: design flaws, material inadequacy, overloading, and maintenance issues.

3.1 Design flaws

As societies progress, new technology is continuously developed, and engineers are constantly trying to innovate and improve design effectiveness. Untested materials and unique designs can lead to unexpected loads and poorly understood static or dynamic behavior. The Tay Bridge was built in 1878 to cross the Firth of Tay in Scotland. The bridge was the longest train bridge in the world at the time and consisted of wrought-iron trusses and girders supported by trussed towers. In 1879, while a mail train was crossing it at night during a storm with high winds, the bridge collapsed, killing 75 people (Figure 34.12), and 13 of the tallest spans, having higher clearances to allow for ship passage beneath, collapsed. It was determined that wind loading had not been included in the design of the bridge. The open-truss latticework was assumed to allow the wind to pass through; however, it was not considered that, when loaded

Figure 34.12 Tay Bridge after collapse (National Library of Scotland).

with a train, the surface area of the train would transfer wind loading to the structure. During the gale, the extremely top-heavy portion of the bridge, upon which the train rode, acted like a mass at the end of a cantilever. The narrow piers could not withstand the lateral thrust and collapsed into the water (Biezma and Schanack, 2007; Åkesson, 2008). In addition, defective joints also led to fatigue cracking, which contributed to the collapse of the bridge (Lewis and Reynolds, 2002). This collapse highlighted problems for tall structures in windy environments, which required the consideration of the stability of the structure and repeated loading, the effects of load combinations, and continued problems with fatigue in iron structures.

The collapse of the Tacoma Narrows Bridge in 1940 (Figure 34.1) is one of the most well-known and well-studied bridge disasters (Reissner, 1943; Billah and Scanlon, 1991; Larsen, 2000; Green and Unruh, 2006; Biezma and Schanack, 2007; Åkesson, 2008; Subramanian, 2008; Petroski, 2009). Multiple videos made from films of the collapse have been widely disseminated on the internet and are very popular (Figure 34.13). The narrow and elegant suspension bridge spanned the Puget Sound, and a gale caused the bridge to oscillate excessively. Vortices formed on the leeward side of the deck, causing oscillations at one of the natural frequencies in a torsional mode of the very flexible bridge deck. The bridge was driven to resonance, responded with extremely large deflections, and after more than an hour, it eventually collapsed. The bridge had been designed to withstand a static wind pressure three times as large as the one that resulted in collapse, but the dynamic effects of the wind loading on the bridge had not been taken into account. After the collapse, the bridge was rebuilt with a wider bridge deck and deeper girders to yield a much stiffer design, especially in torsion. The new bridge was also tested in a wind tunnel prior to erection. These design changes helped form the standard for future suspension bridge design and drew attention to the need for wind tunnel testing of special structures. A large number of existing bridges were subsequently retrofitted to mitigate the torsional hazards.

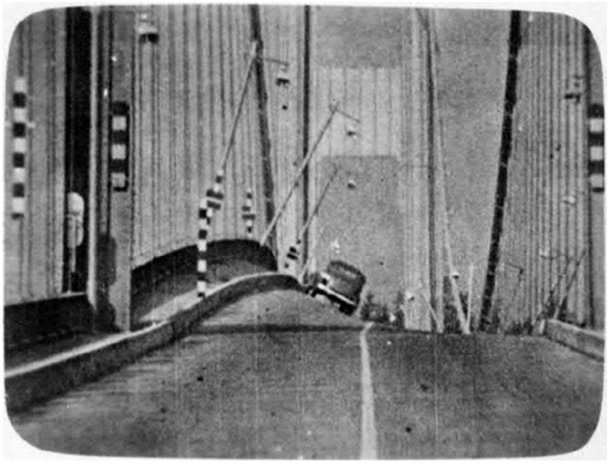

Figure 34.13 Tacoma Narrows Bridge oscillations, Library of Congress, Prints and Photographs Division, HAER WASH, 27-TACO,11-35.

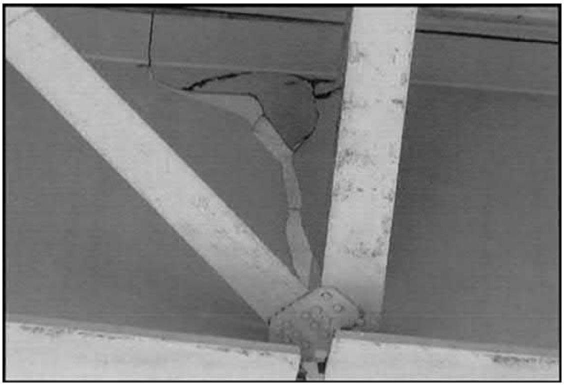

Figure 34.14 Hoan Bridge girder full-depth cracking (Image Courtesy FHWA (FHWA, 2001)).

In 2000, the Hoan Bridge failed in Milwaukee, Wisconsin (Figure 34.14). This steel plate-girder bridge built in 1970 had full-depth cracking in two of its three girders in one of the approach spans (Fisher et al., 2001). The bridge was immediately taken out of service, and the damaged span was demolished. The cracks initiated where the diaphragm and diagonal bracing connected to the girder near the tension flange, at which stress concentrations led to stress levels 60% larger than the nominal yield stress for the steel in the girder web. Steel toughness levels met the American Association of State Highway and Traffic Officials (AASHTO) requirements, but due to the excessive stress levels, cracking still occurred. This area of stress concentration led to brittle fracture initiating from microscopic defects, and the failure has shown that details that amplify stress levels are problematic.

While the Millennium Bridge in London has never collapsed (Figure 34.15), the need for an emergency retrofit shortly after its opening represented a failure in design

Figure 34.15 Millennium Bridge (Image Courtesy Arturo Schultz).

objective. Immediately after the June 10, 2000, opening of the long, shallow suspension bridge for pedestrians, patrons felt large movements in the bridge. The unique design of the lightly loaded structure was very flexible laterally. Due to lateral forces generated by pedestrians, small oscillations initiated and were immediately amplified by other pedestrians reacting to the motion (Dallard et al., 2001; Strogatz et al., 2005; MacDonald, 2009). The loading excited the resonant response of the bridge, and the oscillations were characterized by very large displacements. Both tuned mass dampers (TMDs) and viscous dampers were added to the bridge to dampen the lateral bridge motions. The design flaws of the Millennium Bridge highlighted gaps in knowledge and gaps in bridge codes for certain load conditions, specifically synchronous lateral pedestrian loads.

3.2 Material inadequacy

The modern history of bridges parallels the development of new construction materials, and as material characterization has evolved, previously unknown material limitations have led to bridge collapses. This linkage was best seen when forged iron was introduced in bridge construction and was eventually superseded by wrought iron, and in turn, wrought iron was replaced by low-carbon structural steel. Even after the introduction of low-carbon structural steel, problems associated with material production, member jointing (i.e., riveting, bolting, and welding), and material response (i.e., fatigue, fracture, and corrosion) have been involved in numerous bridge failures worldwide. These failures have underscored the need for quality assurance and control during material fabrication, enforcement of stringent material and construction specifications, and periodic inspections and maintenance of bridges.

Following the success of the first iron bridge in Shropshire, UK, in 1779, more iron bridges were erected, including the Dee Bridge in Chester, UK. The Dee Bridge is a three-span, iron girder train bridge that was built in 1846. The bridge's design incorporated tension flanges reinforced with a Queen Post truss system (tension bars attached with a pin to the girder; Figure 34.16). Prior to the bridge's collapse, cracking had been found in the lower flanges during inspection, and it was assumed that improper installation of the tension bars was responsible for the damage. The tension bars were subsequently reset, but, in 1847, the bridge collapsed as a train was crossing, killing five people. While lateral instability and fatigue cracking have been proposed (Petroski, 2007) as potential causes of the failure, Åkesson (2008) believed that repeated loadings caused the pin holes in the web plate to elongate. Åkesson posited that this elongation undermined the composite action of the girders and tension rods, leaving the girder to carry the entire load, which fractured and caused the collapse. Regardless of the actual cause of the collapse, the failure of the Dee Bridge forced engineers to realize that the brittle and weak nature of cast iron in tension is dangerous; consequently, more ductile materials like wrought iron and, eventually, steel were used. Additionally, this collapse highlighted the fact that bridge design assumptions are not always correct, and if problems such as cracking occur, all possible causes should be investigated.

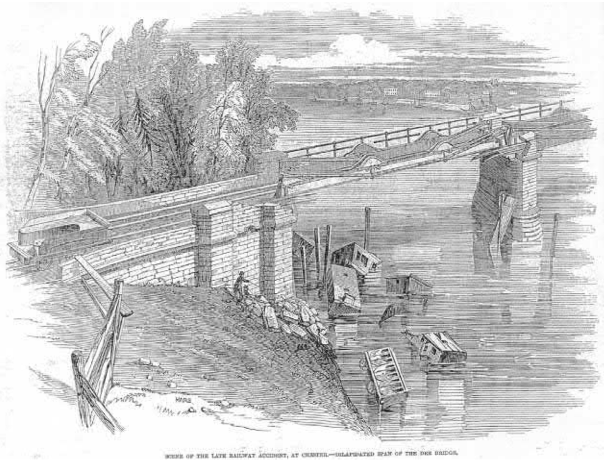

Figure 34.16 Newspaper etching of the Dee Bridge Collapse (The Illustrated London News, 1847).

Not only can certain materials have poor ductility, but materials can also be poorly crafted. A 48 m span of Seongsu Bridge in Seoul, South Korea, collapsed suddenly in 1994 (Figure 34.17). The 672 m long bridge, which spanned the Han River and connected the Kanan district and the Seoul city center, was built in 1977. The collapsed span was a suspended steel truss bridge. Due to public complaints about the excessive motion of the bridge, the bridge authority had begun repair work the previous night. As a result of the collapse, a school bus and six passenger cars fell 20 m to the river below, resulting in the death of 32 persons and injury of 17 others. The failure was attributed to the cracking of the steel truss members due to a variety of factors, including poor quality of welding, other poor construction practices, and poor maintenance (NEMA, 2004; Kunishima, 1994; Moon, 2011). There were no technical standards in

Figure 34.17 The collapsed Seongsu Bridge (Photo Credit: Kwangmo, 1994).

place for the maintenance and repair of the Seongsu Bridge at the time of its collapse, and periodic inspections were not conducted due to limited fiscal resources. It is also noteworthy that no flaws were found in the design of the bridge.

3.3 Overloading

Arguably the most important consideration in the structural design of a bridge is load resistance, but bridges are often required to resist loads that exceed those considered in their design. Thus, the ability to resist overloading is often the threshold between safe performance and collapse. Overloading is best resisted through the redistribution of loads that is possible when alternate load paths are present in a bridge structure. This feature of bridge design and performance is often referred to as *redundancy*, also known as *robustness*, and many catastrophic bridge collapses were due, in part, to a bridge's inability to resist overloading through redundancy.

Issues with gusset plate design have caused recent truss bridge collapses (Richland Engineering Limited, 1997; Subramanian, 2008; Hao, 2010; Liao et al., 2011). In 1996, the Grand Bridge (Figure 34.18), a suspended deck truss bridge built in 1960 near Cleveland, Ohio, suffered a gusset plate failure (Huckelbridge et al., 1997). The failed gusset plate buckled under the compressive load and displaced, but the bridge only shifted 75 mm both laterally and vertically and did not collapse completely. The Federal Highway Administration (FHWA) found that the design thickness of the plate was only marginal and had noticeably decreased due to corrosion. An independent forensic team concluded that the plates had lost up to 35% of their original thickness in some areas. On the day of the failure, the estimated load compared to the design load was approximately 90%, and it was concluded that sidesway buckling occurred in the gusset plates. The damaged gusset plates were replaced and other plates throughout the bridge deemed inadequate were retrofitted with supporting angles.

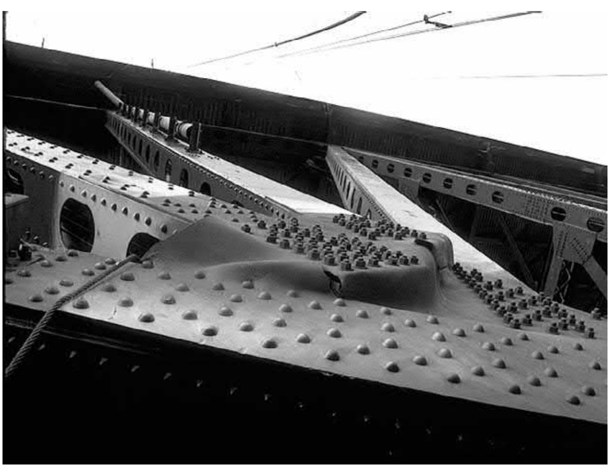

Figure 34.18 Grand Bridge gusset plate failure (Image Courtesy Art Huckelbridge).

Figure 34.19 I-35 W Bridge collapse (Photo Credit: Mike Wills).

The I-35 W (St. Anthony Falls) Bridge in Minneapolis, Minnesota, collapsed on August 1, 2007, killing 13 people (Figure 34.19). The National Transportation Safety Board (NTSB) determined that undersized gusset plates were the cause of the collapse (NTSB, 2008), and subsequent investigations have independently verified these findings (Subramanian, 2008; Hao, 2010; Liao et al., 2011). The design forces in the diagonal members were not correctly incorporated into the initial gusset plate design, and significantly higher forces dominated the actual stresses in the gusset plates. These higher stresses in the undersized plates led to significant yielding under service loads and ultimately to collapse (Liao et al., 2011). These two collapses indicated that gusset plates on bridges designed during the 1960s need to be reanalyzed for sufficient design and load capacity strength, and that proper maintenance of steel bridges is essential for adequate performance.

An indoor, two-story pedestrian walkway in the Hyatt Regency Hotel in Kansas City, Missouri, collapsed onto a dance floor in 1981, claiming the lives of 114 people. The steel walkway suddenly collapsed when the washer and nut at the end of a hanger pulled through the supporting beam (Figure 34.20; Hauck, 1983; Rubin and Banick,

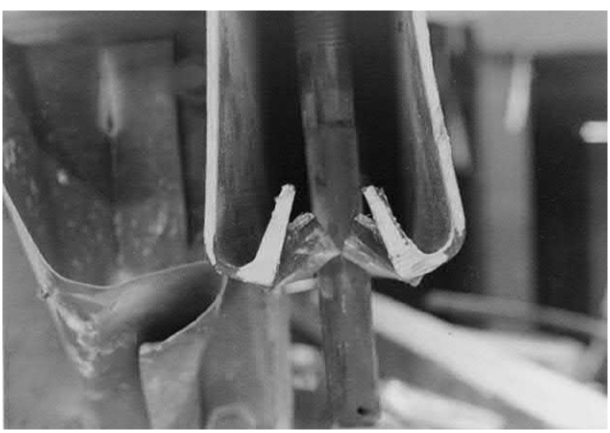

Figure 34.20 Hanger–rod connection failure of the Hyatt Regency walkway (Photo Credit: Dr. Lee Lowery, Jr., P.E.).

1987; Pfatteicher, 2000; Morin and Fischer, 2006). At the time of the collapse, the walkways were heavily loaded with patrons watching a performance below. The as-built connection supported the weight of two floors of the walkway, instead of the initial design, which was meant to support only one. The connection was changed during construction for constructability reasons, and poor communication between the designer and fabricator meant that it was never verified for design strength. The engineer of record and project engineer both lost their licenses due to their negligence and ultimate failure.

3.4 Maintenance

Of all causes of bridge failure, lack of maintenance is the most preventable. Initial design assumptions usually rely on boundary conditions for bridge connections. As bridges degrade from environmental exposure, aging, and exposure to deicing chemicals, connections that were meant to rotate or move longitudinally can become fixed and alter the expected transfer of internal forces and reactions, which causes damage and, in some cases, failure. In addition, corrosion can cause section loss in steel members and concrete reinforcement, which leads to strength degradation and increases the likelihood of bridge failure.

For example, the Sgt. Aubrey Cosens VC Memorial Bridge in Ontario, Canada, a steel tied-arch bridge built in 1960, partially collapsed in 2003 (Figure 34.21), when a large truck was crossing (Biezma and Schanack, 2007; Åkesson, 2008). Previously, some components of the bridge had failed, but the problem had gone unnoticed, and, when the truck crossed, the first three vertical hangers connecting the girder to the arch failed in rapid succession. When the first two hangers failed, the next few were able to redistribute and carry the load; however, when the third hanger fractured, a large portion of the deck was displaced. The hangers were designed with the ends free to rotate, but these ends had seized up with rust over time and had become fixed. When fixed, the hangers were subjected to bending, which caused fracturing to

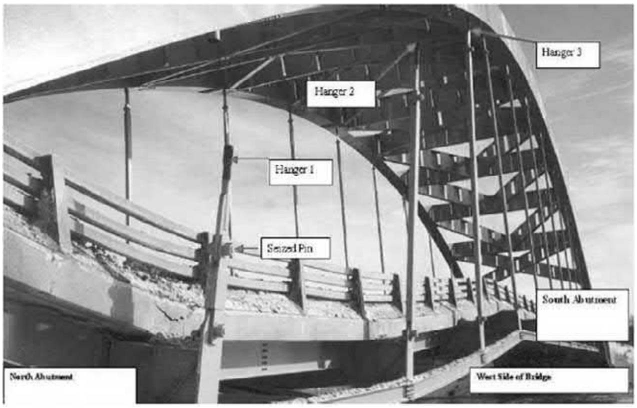

Figure 34.21 Partial collapse of the Sgt. Cosens Memorial Bridge (Bagnariol, 2003).

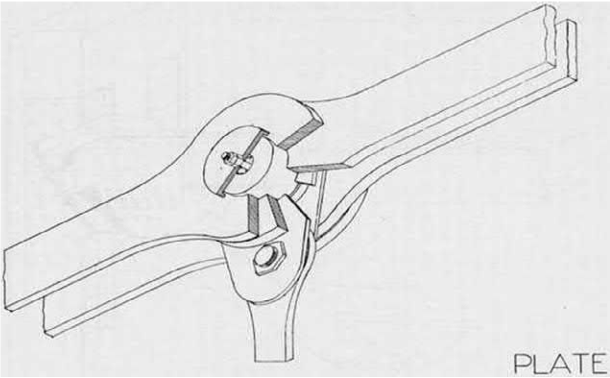

Figure 34.22 Silver Bridge typical eyebar connection detail (NTSB, 1970).

occur on the portions of the hangers tucked inside the arch. Fortunately, no lives were lost in this partial collapse, but this failure highlighted the necessity of understanding initial bridge design assumptions and of ensuring that these original design assumptions continue to hold true through a program of maintenance and regular inspections.

Constructed in the late 1920s, the Silver Bridge connecting Ohio and West Virginia was the first suspension bridge in the United States to use high-strength, heat-treated steel eyebars as tension members connecting the stringers to the suspension cable. During rush hour in 1967, an eyebar (Figure 34.22) fractured at its head and caused a complete collapse of the bridge, killing 46 people. Corrosion, fatigue, and non-redundant design of the eyebars were the major reasons for failure (Lichtenstein, 1993; Subramanian, 2008). This tragedy led the US Congress to adopt systematic inspections of all bridges in the country and made engineers aware of the consequences of questionable choices in design specifications made to save money.

The Hintze Ribeiro bridge in Portugal, built in 1887, collapsed in 2001 (Figure 34.23), claiming the lives of 59 people traveling in a bus and three cars. The steel truss bridge with superimposed concrete deck built was supported by granite piers on timber piles, spanning 336 m over the Douro River in northwestern Portugal. The stability of one of the piers was undermined by the lowering of the river depth due to a combination of sand mining and dam operations (Sousa and Bastos, 2013; Antunes do Carmo, 2014). The lower water depth led to scour of the foundation of the pier and the eventual collapse of the bridge. The collapse led to immediate inspections and repair of bridges around Portugal.

Scour, the removal of backfill around the pier by river flow, caused the collapse of the Schoharie Creek Bridge (Figure 34.24) in 1987 in the United States (Storey and Delatte, 2003). The two-girder steel bridge was supported by closely spaced floor beams and longitudinal stringers on concrete piers. The scour, estimated to have been 8.5–13.5 m, undermined the support of one of the piers introducing unexpected stress, which led to unstable cracking and the ultimate failure (Swenson and Ingraffea, 1991). Scour from ice flows is also suspected to have contributed to the failure (Hains and Zabilansky, 2006). Two spans fell into the river, killing 10 people. The collapse

Figure 34.23 Hintze Ribeiro Bridge post-collapse (Photo Credit: Enciclofurgo, 2001).

highlighted the importance of post-flood pier inspections and the vulnerability of shallow footings in riverbeds.

A combination of corrosion, lateral motion, bridge skew, and fatigue cracking caused the Mianus River Bridge to fail (Figure 34.25) in 1983, killing several people (Fisher et al., 1998; Gorlov, 1984). Corrosion in this steel plate girder bridge led to geometric changes in the joint and generated unanticipated forces. The joint failure led to increased inspection standards on fracture-critical bridges, as well as new nondestructive testing (NDT) methods to observe internal changes.

The Polcevera Bridge in Italy, built in 1960–1967, collapsed in 2018 (Figure 34.26–34.28), killing 59 people who were traveling in a bus and three cars. The bridge was an exceptional and unique design production, similar to but not identical to other bridges' designs. The cable-stayed bridge was realized with single post-tensioned concrete stays and spans exceeding 200 m. The deck was temporarily

Figure 34.24 Schoharie Creek Bridge collapse due to pier scour (USGS, 1987).

Figure 34.25 Mianus Bridge collapse (NTSB, 1984).

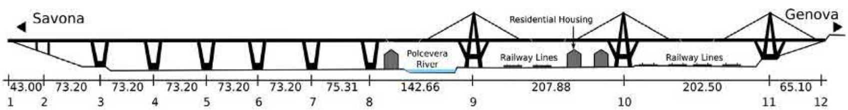

Figure 34.26 Schematic of the piers and distances between each support of the Morandi Bridge, with the three balanced systems shown to pass over residential areas, numerous transportation lines and the Polcevera river (although not shown, the area between piers 1 and 8 is also heavily industrialised) (m).

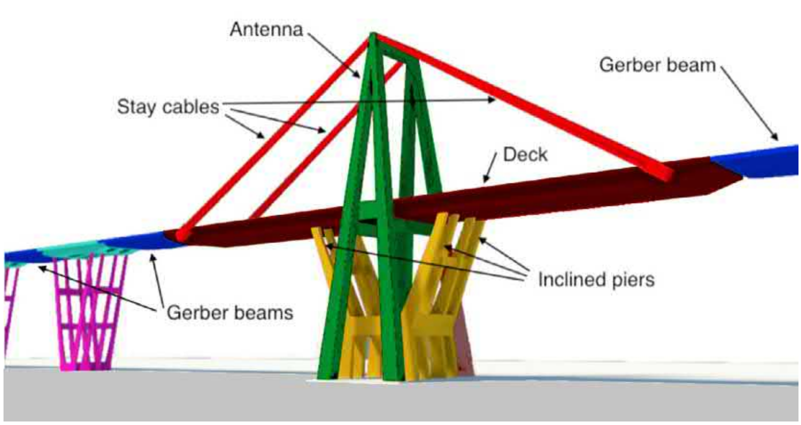

Figure 34.27 Structural scheme of pier 9 and 10, Morandi Bridge.

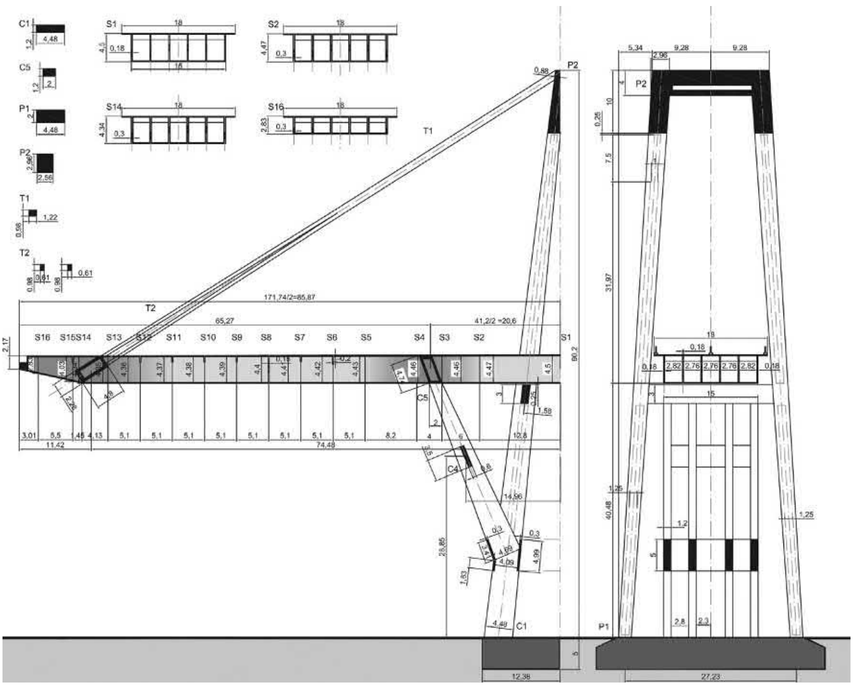

Figure 34.28 Longitudinal and transversal section of one of the "balanced systems" that constituted the large span portions of the viaduct (m).

prestressed during construction and locally post-tensioned in its final configuration. The connecting simply supported spans were made of 36 m precast prestressed Gerber beams. The 12 supports of the bridge were numbered from the Savona side. Each balanced system at supports 9, 10, and 11 comprises the following main elements (Calvi et al., 2019):

- One pier with eight inclined struts carrying the deck for 42 m
- An antenna with two A-shaped structures;
- A main deck with a five-sector box section of variable depth between 4.5 and 1.8 m, an upper and lower slab 160 mm thick, and six deep webs with thicknesses ranging from 180 to 300 mm
- Four transverse link girders, connecting stays and pier trusses to the deck
- Four cable stays, hanging from the antenna's top and intersecting the deck at an angle of about 30°
- Two Gerber beam spans connecting the balanced system to the adjacent parts of the bridge

One of the notable and innovative systems used in this bridge was the so-called Morandi Pre-compression M5 system (Morandi, 1970); it was realized by means of seven wire strands (d = 12.7 mm, minimum strength 163 kN, minimum elongation capacity 3.5%, recommended working stress 1000 MPa) with no mortar injection applied. Each cable stay contained a total of 464 strands with a nominal diameter of ½ inch; 352 strands were located first and connected to the deck to bear its dead weight

(Calvi et al., 2019). According to the maintenance and inspection surveillance document (Martinez y Cabrera et al., 1993; Martinez y Cabrera et al., 1994) in the early 1990s, "during maintenance and repair activities, it was discovered that the stays of the three balanced systems were suffering from widespread general deterioration, as well as several instances of concentrated degradation." Due to this dangerous state, the stays of pier 11 were strengthened with a massive steel external tendon system, transferring all carried load to this new system. However, this retrofit solution was adopted only for this pier and not for the similar pier 9 and 10, as they were discovered in a good state in the 1990s. In the following years, an intense monitoring champaign was launched on the whole bridge, to preserve the integrity and the structural safety of the bridge; however, specific issues were discovered over time (Calvi et al., 2019):

- The absence of injection mortar on pre-compression duct led to increasing oxidation and consequently increasing section loss of the steel pre-compression system.
- Strands that were free to move under live loads were discovered.
- In two cables, some wires were fractured.
- Dynamic identification procedures led to unexpected results in 2017, as four natural vibration periods in the range of 0.7–0.82 s were found to be inconsistent with the numerical models.

All these highlighted issues posed an unsafe situation with a clear deterioration of the structure; however, no particular repairs were made. Although, up to now, no evidence has been published concerning the evident collapse mechanism, the following hypothesis has been made: as the bridge has been found within a consistent margin of safety under live loads in its redundant structures, the possible initial cause of the collapse therefore may be related to fatigue problems in the tendons near the tip of the antenna or the deterioration of the connection between the stay and the transverse link. These local phenomena have not been explored because of the lack of detailed data, as reported in Calvi et al. (2019). From another point of view, the recent collapse of the Morandi Bridge has been analyzed in order to verify the possible influence of fatigue to trigger the failure; it is concluded that the combined effect of very-high-cycle, low-amplitude fatigue and corrosion degradation can be at the origin of the collapse. In particular, the aggressive environment, as well as the structural size effect, both may change Wohler's curve, translating it downwards and eliminating the horizontal asymptote at the basis of the concept of fatigue limit. Therefore, if a structure is subjected to a number of cycles higher than 10 million, even the lowest stress range can provide relevant damage accumulation. This could have been the case of Morandi Bridge. Against this terrible collapse, a new bridge was built and opened to traffic less than 2 years later, in June 2020 (see Chapter 28).

4. Extreme events

Environmental loads from natural events such as earthquakes, cyclonic storms (e.g., hurricanes, typhoons, and tornados), and floods are difficult to predict or quantify for design, but they can cause major damage to bridge structures. Other events, like

Figure 34.29 I-40 barge strike post collapse (Photo Credit: Robert Webster).

vehicle strikes and vehicle fires under bridges, can be foreseen, but the loadings can be extreme, are due to user error, and can be difficult to quantify. However, these can also lead to catastrophic failure.

In 2002, a towboat traveling on the Arkansas River in Oklahoma struck a pier of the Interstate 40 Bridge, causing a section to collapse (Figure 34.29) and killing 14 people. The bridge, constructed in 1967, was a twin-girder, continuous-span structure with a concrete deck supported by steel plate girders and a steel superstructure that was, in turn, supported by RC piers and abutments. The boat captain had a cardiac event and was incapacitated, resulting in the loss of control of the vessel (NTSB, 2004). Many of the deaths were the result of trucks and automobiles driving into the void left after the bridge collapsed. This event caused some to call for bridge collapse warning systems to alert motorists of a bridge outage. In 1993, a similar accident occurred in New Orleans, Louisiana, when the Judge William Seeber Bridge was struck by a barge, causing two spans to collapse and killing one person (NTSB, 1994).

In 1989, the magnitude 7.1 Loma Prieta earthquake struck the west coast of the United States. Many structures were damaged, including a span collapse of the Oakland Bay Bridge in California as well as the Cypress Street Viaduct. Figure 34.30 shows a striking image of the upper deck of the viaduct collapsed onto the lower deck. At the time, both bridge structures were considered to have a low risk of damage from earthquakes (GAO, 1990). It was later realized that the soft soil supporting the Cypress Street Viaduct amplified the global bridge response. While previous earthquakes, such as the San Fernando earthquake, had resulted in changes to earthquake design standards and some retrofits, the Loma Prieta earthquake led to the implementation of widespread seismic retrofitting of bridges. Subsequent large earthquakes have continued to expose certain vulnerabilities, and design codes have been updated accordingly.

In 2008, the Great Wenchuan earthquake, with a magnitude of 8.0, struck central China and caused widespread structural damage. More than 400 bridges were damaged, which exposed a variety of problems including ground fault displacement,

Figure 34.30 Collapsed Cypress Street Viaduct (Photo Credit H. G. Wilshire).

landslides, unseating of spans (Figure 34.31), and damaged piers (Wang and Lee, 2009). The damage revealed the need to consider near-fault ground motion in bridge design, especially for bridges that cross active known faults. Additionally, landslides were also determined to be an important concern, but landslides are generally not considered by bridge designers.

More recently, a span of the I-5 Skagit River Bridge collapsed north of Seattle, Washington (Figure 34.32; Lindblom, 2013; Johnson, 2013). The four-span, 339 m steel truss bridge opened in 1955 and was fracture critical, meaning the bridge lacked redundancy. If a single member failed, the truss would become unstable. An oversized load struck an overhead support girder, causing the truss to become unstable, resulting in a complete collapse of the span (Lindblom, 2013). While no one perished in this collapse, individuals had to be rescued, and travel times along the Washington coast were impacted significantly. Clearances and weight issues are a concern for many bridges, especially those with nonredundant, above-deck truss systems.

Bridge collapse following vehicle fires is uncommon, but there have been historic cases in which large vehicle fires under bridges have led to the partial or full collapse of these bridges. In the United States, historic fires occurred in 2002, on Interstate Highway I-65 in Birmingham, Alabama (Figure 34.33); in 2007, in Oakland,

Figure 34.31 Collapsed bridge unseated during the Great Wenchuan earthquake (EERI, 2008).

Figure 34.32 Skagit River Bridge collapse (Photo Credit: Martha Thornburgh).

Figure 34.33 Effects of fire on Interstate Highway I-65 bridge (Image Courtesy FHWA (Bergeron, 2006)).

California, on an interchange connecting interstate highways I-80, I-580, and I-880; and in 2009, on Interstate Highway I-75 in Detroit, Michigan, under the Nine Mile Road overpass. In all cases, tanker trucks carrying large amounts of fuel crashed and created intense fires (Wright et al., 2013). Fires in crashed vehicles usually do not last for long enough to affect bridge overpasses, but the fires resulting from tanker truck fires can last a longer amount of time and produce enough heat to undermine the strength of many bridges.

5. Concluding remarks

A variety of factors can lead to bridge collapse, including construction issues, in-service problems, and extreme events. Throughout history, these collapses have given engineers important data and have led to changes in the design process, and many of these lessons have been learned as a result of the bridge collapses described in this chapter. As bridge construction material technology progresses, new design concepts and construction methods will continue to be developed. Each new design concept poses new challenges and can lead to unexpected structural demands that may not be accounted for in design. The lessons learned include the need for careful consideration of new materials, wind stability, structural safety, local buckling, construction practices, inspection and maintenance practices, design flaws, and overload resistance through redundancy. While the majority of designs are safe and reliable, the bridge engineer must always keep previous bridge disasters in mind when considering daring new design concepts and construction methods that would push the envelope of previous practices. Moreover, with the evolution of design and construction technologies, existing bridges may no longer meet contemporary expectations on bridge safety, and maintaining updated databases on deficient bridges becomes a necessity (FHWA, 2012). For a bridge engineer, a small mistake can lead to fatalities, injuries, and monetary losses.

Databases of bridge failures, such as the one reported by Lee et al. (2012), have been compiled to better understand the characteristics of bridge failure and their impact on design. Alternatively, formal attempts to model bridge collapse, given the consequences of such events, have been advanced in order to offer engineers and planners the potential to carefully evaluate collapse conditions when designing a bridge. For example, fault-tree analysis has been used to model the conditions that have led to the collapse of specific bridges (LeBeau and Wadia-Fascetti, 2007) and has been generalized to create a framework for investigating the resilience of bridges (Chavel and Yadlosky, 2011). However, Lwin (2013) recognizes that such efforts cannot cover the entire set of conditions that can lead to collapse, and that collapse associated with design and construction errors, for example, has to be addressed separately by quality assurance and quality control programs. Nonetheless, these formal approaches to analyze bridge collapse potential hold promise for enhancing bridge resilience in the future.

References

Åkesson, B., 2008. Understanding Bridge Collapses. Taylor and Francis, London, UK.

Antunes do Carmo, J.S., 2014. Environmental impacts of human action in watercourses. Nat. Hazards Earth Syst. Sci. Discuss. 2, 6499–6530.

Bagnariol, D., 2003. Sgt. Aubrey Cosens V.C. Memorial Bridge over the Montreal River at Latchford, Investigation of Failure: Final Report. Ministry of Transportation of Ontario, St. Catharines, Ontario, Canada. 25 pp.

Bergeron, K.A., 2006. Helping roadway contractors fulfill public expectations. Public Roads 69 (5). https://www.fhwa.dot.gov/publications/publicroads/06mar/04.cfm. (May 8, 2015).

Biezma, M.V., Schanack, F., 2007. Collapse of steel bridges. J. Perform. Constr. Facil. 21 (5), 398–405.

Billah, K.Y., Scanlon, R.H., 1991. Resonance, Tacoma narrows bridge failure, and undergraduate physics textbooks. Am. J. Phys. 59 (2), 118–124.

Calvi, G.M., Moratti, M., O'Reilly, G.J., Scattarreggia, N., Monteiro, R., Malomo, D., Calvi, P. M., Pinho, R., 2019. Once upon a time in Italy: the tale of the Morandi bridge. Struct. Eng. Int. 29 (2), 198–217. https://doi.org/10.1080/10168664.2018.1558033.

Chavel, B., Yadlosky, J., 2011. Framework for Improving Resilience of Bridge Design. Report No. FHWA-IF-11-016, Federal Highway Administration, Washington, DC.

Choi Kwangmoa, 1994. Collapse of Seongsu Bridge. Available from. http://commons.wikimedia.org/wiki/File:1994%EC%84%B1%EC%88%98%EB%8C%80%EA%B5%90_%EB%B6%95%EA%B4%B4_%EC%82%AC%EA%B3%A001.jpg. [6 May 2015b]. Licensed under http://creativecommons.org/licenses/by-sa/4.0/.

Dallard, P., Fitzpatrick, T., Flint, A., Low, A., Smith, R.R., Willford, M., Roche, M., 2001. London millennium bridge: pedestrian-induced lateral vibration. J. Bridg. Eng. 6, 412–417.

Earthquake Engineering Research Institute (EERI), 2008. The Wenchuan, Sichuan Province, China, Earthquake of May 12, 2008. EERI Special Earthquake Report - October 2008. 12 pp.

Enciclofurgo, 2001. Hintze Ribeiro Collapse. Available from. http://commons.wikimedia.org/wiki/File:Puente_hintze_ribeiro.jpg. (25 April 2015).

Federal Highway Administration (FHWA), 2012. Deficient Bridges by Highway System. http://fhwa.dot.gov/bridge/deficient.cfm. (June 30, 2021).

FHWA, 2001. Hoan Bridge Investigation. Memorandum. Available from. http://www.fhwa.dot.gov/bridge/steel/010710.cfm. (18 May 2015).

Fisher, J.W., Kaufmann, E.J., Pense, A.W., 1998. Effect of corrosion on crack development and fatigue life. Transp. Res. Rec. 1624, 110–117.

Fisher, J.W., Kaufmann, E.J., Wright, W., Xi, Z., Tjiang, H., Sivakumar, B., Edberg, W., 2001. Hoan Bridge Forensic Investigation Failure Analysis. Final Report. Wisconsin Department of Transportation and FHWA.

General Accounting Office (GAO), 1990. Loma Prieta Earthquake: Collapse of the Bay Bridge and Cypress Viaduct. GAO, Washington, DC.

Gorlov, A.M., 1984. Disaster of the I-95 Mianus River bridge. Where could lateral vibration come from? J. Appl. Mech. 51 (3), 694–696.

Green, D., Unruh, W.G., 2006. The failure of the Tacoma bridge: A physical model. Am. J. Phys. 74 (8), 706–716.

Hains, D.B., Zabilansky, L.J., 2006. Scour under ice: potential contributing factor in the Schoharie Creek Bridge collapse. In: Cold Regions Engineering 2006. ASCE, pp. 1–9.

Hao, S., 2010. I-35W bridge collapse. J. Bridg. Eng. 15 (5), 608–614.

Hauck, G.F.W., 1983. Hyatt-regency walkway collapse: design alternates. J. Struct. Eng. 109, 1226–1234.

Huckelbridge, A.A., Palmer, D.A., Snyder, R.E., 1997. Grand gusset failure. Civ. Eng. ASCE 67 (9), 50–52.

Johnson, K., 2013. Washington state bridge collapse could Echo far beyond interstate. The New York Times. www.nytimes.com. October 4, 2013.

Kunishima, M., 1994. Collapse of the Korea Seoul Seongsu Bridge. www.sozogaku.com/fkd/en/cfen/CD1000144.html.

Larsen, A., 2000. Aerodynamics of the Tacoma narrows bridge: 60 years later. Struc. Eng. Intern. 10 (4), 243–248.

LeBeau, K.H., Wadia-Fascetti, S.J., 2007. Fault tree analysis of Schoharie Creek bridge collapse. J. Perform. Constr. Facil. 21 (4), 320–326.

Lee, G.C., Mohan, S.B., Huang, C., Fard, B.N., 2012. A Study of U.S. Bridge Failures (1980-2012), MCEER Report 13-0008. State University of New York, Buffalo. 148 pp.

Lewis, P.R., Reynolds, K., 2002. Forensic engineering: A reappraisal of the Tay bridge disaster. Interdiscip. Sci. Rev. 29 (2), 177–191.

Liao, M., Okazaki, T., Ballarini, R., Schultz, A.E., Galambos, T.V., 2011. Nonlinear finite-element analysis of critical gusset plates in the I-35W bridge in Minnesota. J. Struct. Eng. 137 (1), 59–68.

Library of Congress, Prints and Photographs Division, LC-USZ62–46682. 1940. Washington, Tacoma. Suspension bridge collapses into the Tacoma Narrows. Available from. http://www.loc.gov/pictures/item/2006687436/. (23 April 2015).

Library of Congress, Prints and Photographs Division, HAER WASH, 27-TACO,11- -35. 1940. Tacoma Narrows Bridge, Spanning Narrows at State Route 16, Tacoma, Pierce County, WA. Available from. http://www.loc.gov/pictures/item/wa0453.photos.370520p/. (23 April 2015).

Lichtenstein, A., 1993. The silver bridge collapse recounted. J. Perform. Constr. Facil. 7 (4), 249–261.

Lindblom, M., 2013. NTSB update: trucker in bridge collapse felt crowded, moved right. The Seattle Times. www.seattletimes.com. (October 4, 2013).

Lowery Jr., L., 1981. View of the 4th Floor Support Beam, during the First Day of the Investigation of the Hyatt Regency Walkway Collapse. Available from. http://commons.wikimedia.org/wiki/File:Hyatt_Regency_collapse_support.PNG. (6 May 2015).

Lwin, M.M., 2013. Resilient bridge design. In: 7th New York City Bridge Conference, August 26–27. Bridge Engineering Association.

MacDonald, J.H.G., 2009. Lateral excitation of bridges by balancing pedestrians. Proc. R. Soc. A 465, 1055–1073.

Manitoba Free Press, 1907. Quebec Bridge, west of Quebec City, Canada. Available from. http://io9.com/these-are-some-of-the-worst-architectural-disasters-in-512561209. (15 December 2015).

Martinez y Cabrera, F., Camomilla, G., Pisani, F., Marioni, A., 1993. Il risanamento degli stralli del viadotto Polcevera. Atti delle Giornate AICAP 581–590, 1993.

Martinez y Cabrera, F., Camomilla, G., Donferri Mitelli, M., Pisani, F., 1994. Rehabilitation of the stays of the Polcevera viaduct. In: International Symposium on Cable Stayed Bridges, Shanghai, pp. 640–665.

Moon, J.H., 2011. Cracks Everywhere: How the Seongsu Bridge Collapse Changed Seoul's Urban Personality. Master's Thesis. 55 pp.

Morandi, B., 1970. La precompressione sistema Morandi M5. CESAP S.p.A.

Morin, C.R., Fischer, C.R., 2006. Kansas City Hyatt hotel skyway collapse. J. Fail. Anal. Prev. 6 (2), 5–11.

National Emergency Management Agency, 2004. Collapse of Seongsu Bridge. Available from. www.nema.go.kr/eng/m4_seongsu.jsp. (7 December 2014).

National Library of Scotland, 1879. Scottish Bridges, (53) 139B. J,V. - Fallen girders, Tay Bridge. Available from. http://digital.nls.uk/74585164. (3 May 2015).

National Transportation Safety Board, 2019. Pedestrian Bridge Collapse Over SW 8th Street Miami, Florida March 15, 2018. Highway Accident Report. NTSB/HAR-19/02. National Transportation Board, Washington, DC. 152 pp.

National Transportation Safety Board (NTSB), 1970. Highway Accident Report: Collapse of U. S. 35 Highway Bridge, Point Pleasant, West Virginia, December 15, 1967: Report Number NTSB-HAR-71-1. National Transportation Safety Board, Washington, DC. Image Available from: http://failures.wikispaces.com/Silver+Bridge+(Point+Pleasant)+Collapse. (1 December 2014).

National Transportation Safety Board (NTSB), 1984. Highway Accident Report: Collapse of a Suspended Span of Interstate Route 95 Highway Bridge over the Mianus River, Greenwich, Connecticut, June 28, 1983: Report Number NTSB-HAR-84-03. National Transportation Board, Washington, DC.

National Transportation Safety Board (NTSB), 1994. Highway Accident Report: U.S. Towboat Chris Collision with the Judge William Seeber Bridge. NTSB/HAR-94/03 PPB940916203. www.ntsb.gov/investigations/summary/HAR9403.htm.

National Transportation Safety Board (NTSB), 2004. U.S. Towboat Robert Y. Love Allison with Interstate 40 Highway Bridge Near Webbers Falls, Oklahoma. NTSB/HAR-04/05 PB2004–916205 Notation 7654, Washington, DC.

National Transportation Safety Board (NTSB), 2008. Collapse of I-35W Highway Bridge, Minneapolis, Minnesota, August 1, 2007. Highway Accident Report NTSB/HAR-08/03, Washington, DC.

Petroski, H., 2007. Engineering: why things break. Am. Sci. 95 (3), 206–209.

Petroski, H., 2009. Tacoma narrows bridges. Am. Sci. 97 (3), 103–107.

Pfatteicher, S.K.A., 2000. The Hyatt horror: failure and responsibility in American engineering. J. Perform. Constr. Facil. 14, 62–66.

Pujol, S., Kreger, M.E., Monical, J.D., Schultz, A.E., 2019. Investigation of the Collapse of the Chirajara Bridge. Concrete International, American Concrete Institute, pp. 29–37. June.

Quebec Bridge Disaster, 1908. Eng. Rec. 57, 504–510.

Reissner, H., 1943. Oscillations of suspension bridges. T. ASME 65, A23–A32.

Richland Engineering Limited, 1997. Truss Gusset Plate Failure, Analysis, Repair and Retrofit: Interstate 90 Bridge over Grand River. Final Report, 15 April 1997.

Rubin, R.A., Banick, L.A., 1987. The Hyatt regency decision: one view. J. Perform. Constr. Facil. 1, 161–167.

Sousa, J.J., Bastos, L., 2013. Multi-temporal SAR interferometry reveals acceleration of bridge sinking before collapse. Nat. Hazards Earth Syst. Sci. 13, 659–667.

Storey, C., Delatte, N., 2003. Lessons from the collapse of the Schoharie Creek bridge. Forensic Eng., 158–167.

Strogatz, S.H., Abrams, D.M., McRobie, A., Eckhardt, B., Ott, E., 2005. Crowd synchrony on the millennium bridge. Nature 438, 43–44.

Subramanian, N., 2008. I-35W Mississippi River bridge failure - is it a wake up call? Indian Concrete J. 82 (2), 29–38.

Swenson, D.V., Ingraffea, A.R., 1991. The collapse of the Schoharie Creek bridge: A case study in concrete fracture mechanics. Int. J. Fract. 51, 73–92.

Tanner, P., Hingorani, R., 2013. Collapse of the River Verde Viaduct Scaffolding System. IABSE Symposium Report: Safety, Failures and Robustness of Large Structures, pp. 162–169.

The Illustrated London News, 1847. The Illustrated London News etching of Dee bridge disaster. Available from. http://commons.wikimedia.org/wiki/File:Dee_bridge_disaster.jpg. (10 December 2014).

Thornburgh, M., 2013. Skagit Bridge Collapse. Available from. https://commons.wikimedia.org/wiki/File:05-23-13_Skagit_Bridge_Collapse.jpg. [20 April 2015]. Licensed under http://creativecommons.org/licenses/by/2.0/.

United States Geological Survey (USGS), 1987. Schoharie Creek Bridge collapsed. Available from. http://commons.wikimedia.org/wiki/File:Schoharie_Creek_Bridge_02.gif. (25 April 2015).

Wang, Z., Lee, G.C., 2009. A comparative study of bridge damage due to the Wenchuan, Northridge, Loma Prieta, and San Fernando earthquakes. Earthq. Eng. Eng. Vib. 8, 251–261.

Webster, R., 2002. Collapsed I-40 Bridge, near Webers Falls, Sequoyah County, Oklahoma - in 2002. Available from. http://commons.wikimedia.org/wiki/File:I40_Bridge_disaster.jpg. (6 May 2015).

Wills, M., 2007. The Scene at the I-35W Mississippi River Bridge, the First Morning after its Collapse. Available from. http://commons.wikimedia.org/wiki/File:I35_Bridge_Collapse_4crop.jpg. [6 May 2015a]. Licensed under http://creativecommons.org/licenses/by-sa/2.0/.

Wilshire, H.G., 1989. Collapsed Cypress Street Viaduct in Oakland, from the 1989 Loma Prieta Earthquake. United States Geological Survey. Available from. https://commons.wikimedia.org/wiki/File:022srUSGSCyprusVia.jpg. (25 April 2015).

Wright, W., Lattimer, B., Woodworth, M., Nahid, M., Sotelino, E., 2013. Highway Bridge Fire Hazard Assessment Draft Guide Specification for Fire Damage Evaluation in Steel Bridges. NCHRP Report 12-85. Nat. Acad. of Sciences, Washington, DC.

This page intentionally left blank

Index

Note: Page numbers followed by *f* indicate figures and *t* indicate tables.

E

U

Second Edition

INNOVATIVE BRIDGE DESIGN HANDBOOK

Construction, Rehabilitation and Maintenance

Edited by Alessio Pipinato

Innovative Bridge Design Handbook: Construction, Rehabilitation and Maintenance, Second Edition, brings together the essentials of bridge engineering across design, assessment, research, and construction. Written by an international group of experts, each chapter is divided into two parts: the first covers design issues, while the second presents current research into the innovative design approaches used across the world.

This new edition includes new topics such as foot bridges, new materials in bridge engineering, and soil foundation structure interaction. All chapters have been updated to include the latest concepts in design, construction, and maintenance to reduce project cost, increase structural safety, and maximize durability. Code and standard references have been updated.

Key Features

- Completely revised and updated with the latest in bridge engineering and design
- Provides detailed design procedures for specific bridges with solved examples
- Presents structural analysis including numerical methods (FEM), dynamics, risk and reliability, and innovative structural typologies

This book will be of special interest to academics, engineers, and students working on structural, civil and bridge engineering, and design.

About the Editor

Alessio Pipinato is the CEO as well as the Technical and Scientific Director of the engineering consulting firm Alessio Pipinato and Partners. He is an engineer for the executive design and construction supervision of bridges, viaducts, and public buildings. He is a member of international associations, including the American Society of Civil Engineers (ASCE), the Structural Engineering Institute, the International Association for Bridge and Structural Engineering, the International Association for Bridge Maintenance and Safety, the Collegio Ingegneri Ferroviari Italiani, and the American Institute of Architects. He has also served as the national expert member of the UNI-CT21 Technical Commission on Structural Engineering, and as Associate Editor of the Journal of Bridge Engineering, ASCE. Across his career, which included over a decade as Professor of Structural Engineering and Bridge Engineering at the University of Padova, Italy, he has authored more than 250 publications in international journals, books, and conference proceedings.

ISBN 978-0-12-823550-8

9 780128 235508

ELSEVIER

Butterworth-Heinemann
An imprint of Elsevier
elsevier.com/books-and-journals